AFRL-RQ-WP-TR-2016-0144

FUELS AND COMBUSTION TECHNOLOGIES FOR AEROSPACE PROPULSION

Steven Zabarnick, Matthew J. DeWitt, Richard C. Striebich, Thusitha S. Gunasekera, Jamie S. Ervin, Alejandro M. Briones, Linda M. Shafer, Shiral K.A. Fernando, John L. Graham, Zachary J. West, Scott D. Stouffer, Marlin D. Vangsness, and Barbara A. Harruff-Miller

University of Dayton Research Institute

SEPTEMBER 2016
Final Report

AIR FORCE RESEARCH LABORATORY
AEROSPACE SYSTEMS DIRECTORATE
WRIGHT-PATTERSON AIR FORCE BASE, OH 45433-7541
AIR FORCE MATERIEL COMMAND
UNITED STATES AIR FORCE

NOTICE AND SIGNATURE PAGE

*//Signature//
_____
DONALD K. MINUS
Program Manager
Fuels and Energy Branch
Turbine Engine Division

//Signature//
_____
MIGUEL A. MALDONADO, Branch Chief
Fuels and Energy Branch
Turbine Engine Division
Aerospace Systems Directorate

//Signature//
_____
CHARLES W. STEVENS
Lead Engineer
Turbine Engine Division
Aerospace Systems Directorate

REPORT DOCUMENTATION PAGE

1. REPORT DATE *(DD-MM-YY)*	2. REPORT TYPE	3. DATES COVERED *(From - To)*
September 2016	Final	11 December 2009 – 30 September 2016

4. TITLE AND SUBTITLE	5a. CONTRACT NUMBER
FUELS AND COMBUSTION TECHNOLOGIES FOR AEROSPACE PROPULSION	FA8650-10-2-2934
	5b. GRANT NUMBER
	5c. PROGRAM ELEMENT NUMBER
	62203F

6. AUTHOR(S)	5d. PROJECT NUMBER
Steven Zabarnick, Matthew J. DeWitt, Richard C. Striebich, Thusitha S. Gunasekera, Jamie S. Ervin, Alejandro M. Briones, Linda M. Shafer, Shiral K.A. Fernando, John L. Graham, Zachary J. West, Scott D. Stouffer, Marlin D. Vangsness, and Barbara A. Harruff-Miller	3048
	5e. TASK NUMBER
	5f. WORK UNIT NUMBER
	Q0HS

7. PERFORMING ORGANIZATION NAME(S) AND ADDRESS(ES)	8. PERFORMING ORGANIZATION REPORT NUMBER
University of Dayton Research Institute 300 College Park Avenue Dayton, OH 45469	

9. SPONSORING/MONITORING AGENCY NAME(S) AND ADDRESS(ES)	10. SPONSORING/MONITORING AGENCY ACRONYM(S)
Air Force Research Laboratory Aerospace Systems Directorate Wright-Patterson Air Force Base, OH 45433-7541 Air Force Materiel Command United States Air Force	AFRL/RQTF
	11. SPONSORING/MONITORING AGENCY REPORT NUMBER(S)
	AFRL-RQ-WP-TR-2016-0144

12. DISTRIBUTION/AVAILABILITY STATEMENT
DISTRIBUTION STATEMENT A: Approved for public release. Distribution is unlimited.

13. SUPPLEMENTARY NOTES
PA Case Number: 88ABW-2016-5958; Clearance Date: 23 Nov 2016.

The appendices in this report are a series of published papers and articles.

14. ABSTRACT

This report is a compilation of highlights of research accomplishments completed under Cooperative Agreement No. FA8650-10-2-2934, "Fuels and Combustion Technologies for Aerospace Propulsion," with the Air Force Research Laboratory, Aerospace Systems Directorate, Turbine Engine Division. This report covers work performed during the period December 11, 2009 to September 30, 2016. Research efforts covered a wide range of topics toward development of advanced fuels and combustion systems. These efforts included Analysis, Analytical Measurement, and Diagnostics Technologies for Fuels, Additives, and Combustion Processes; Advanced/Alternate Fuels Development, Evaluation, Demonstration, and Management; Advanced, Affordable Fuel/Combustion Additive Technologies; Support of Alternative Fuel Development; Materials Compatibility; Modeling and Simulation; Technology Integration and Demonstration for Thermal Management and Fuel System Operability, Supportability, and Maintainability.

15. SUBJECT TERMS
jet fuel, alternative fuels, fuel additives, fuel system icing inhibitor, thermal stability, particulate emissions, combustion emissions, combustion, gas turbine engines

16. SECURITY CLASSIFICATION OF:			17. LIMITATION OF ABSTRACT:	18. NUMBER OF PAGES	19a. NAME OF RESPONSIBLE PERSON (Monitor)
a. REPORT	b. ABSTRACT	c. THIS PAGE	SAR	403	Donald Minus
Unclassified	Unclassified	Unclassified			19b. TELEPHONE NUMBER *(Include Area Code)* N/A

TABLE OF CONTENTS

LIST OF FIGURES

PREFACE

This final report was submitted by the University of Dayton Research Institute (UDRI) under Cooperative Agreement FA8650-10-2-2934, sponsored by the U.S. Air Force Research Laboratory, Aerospace Systems Division, Wright-Patterson AFB, OH. Mr. Robert W. Morris, Jr. and Mr. Donald K. Minus of AFRL/RQTF were the Contract Monitors during the performance period. Dr. Dilip R. Ballal and Dr. Steven Zabarnick of the Energy & Environmental Engineering Division of UDRI were the Principal Investigators. This report covers work performed during the period December 11, 2009 to September 30, 2016.

The authors would like to acknowledge the support and encouragement of the AFRL Fuels and Energy Branch and Turbine Engine Division Leadership, including: Mr. Miguel Maldonado, Dr. Tim Edwards, Mr. Bob Morris, Mr. Donald Minus, Mr. Edwin Corporan, Dr. Chris Bunker, Ms. Milissa Griesenbrock, Dr. Donald Phelps, Dr. Oscar Ruiz, Dr. Robert Hancock, and Dr. Chuck Cross.

This material is based on research sponsored by the Air Force Research Laboratory under agreement number FA8650-10-2-2934. The U.S. Government is authorized to reproduce and distribute reprints for Governmental purposes notwithstanding any copyright notation thereon. The views and conclusions contained herein are those of the authors and should not be interpreted as necessarily representing the official policies or endorsements, either expressed or implied, of Air Force Research Laboratory or the U.S. Government.

1   EXECUTIVE SUMMARY

This report is a compilation of highlights of research accomplishments completed under Cooperative Agreement No. FA8650-10-2-2934, "Fuels and Combustion Technologies for Aerospace Propulsion," with the Air Force Research Laboratory, Aerospace Systems Directorate, Turbine Engine Division. This report covers work performed during the period December 11, 2009 to September 30, 2016. Research efforts covered a wide range of topics toward development of advanced fuels and combustion systems. These efforts included Analysis, Analytical Measurement, and Diagnostics Technologies for Fuels, Additives, and Combustion Processes; Advanced/Alternate Fuels Development, Evaluation, Demonstration, and Management; Advanced, Affordable Fuel/Combustion Additive Technologies; Support of Alternative Fuel Development; Materials Compatibility; Modeling and Simulation; Technology Integration and Demonstration for Thermal Management and Fuel System Operability, Supportability, and Maintainability.

2 INTRODUCTION

2.1 Background

The University of Dayton is pleased to submit this final report to the Air Force Research Laboratory, Aerospace Systems Directorate, (AFRL/RQTF), under Cooperative Agreement No. FA8650-10-2-2934, "Fuels and Combustion Technologies for Aerospace Propulsion." The goal of this program was to investigate and evaluate advanced (conventional and alternative) fuels and combustion technologies for aerospace propulsion systems. This research has extended the technology base for development, validation, and fielding of alternative (synthetic) jet fuels, high heat sink fuels, low-temperature fuels, fuel-additive material compatibility, mitigating biological contaminants, modeling and simulation of fuels and combustion processes, reduced emissions of gaseous and particulate matter, and technology integration for optimizing thermal management systems for use in 21st century aircraft and weapons systems.

This program was comprised of seven component areas: (1) Analysis, Analytical Measurement, and Diagnostic Technologies for Fuels, Additives and Combustion Processes; (2) Advanced/Alternate Fuels Development, Evaluation, Demonstration, and Management; (3) Advance Affordable Fuel/Combustion Additive Technologies; (4) Support of Alternative Fuel Development; (5) Materials Compatibility; (6) Modeling and Simulation; and (7) Technology Integration and Demonstration for Thermal Management and Fuel System Operability, Supportability, and Maintainability.

Here we highlight the research accomplishments during the program (Sections 3.1 to 3.7); summarize subcontract programs used to augment the research effort (Section 3.8); provide copies of journal publications that show the most important research successes achieved during the research period (Appendices A to AA); and provide a list of publications, presentations, honors, and awards during the performance period (Appendix BB).

3   HIGHLIGHTS OF RESEARCH STUDIES

3.1   Analysis, Analytical Measurement, and Diagnostic Technologies for Fuels, Additives, and Combustion Processes

3.1.1   GCxGC Hydrocarbon Type Determination for Comprehensive Fuels Analysis

A hydrocarbon type analysis method using the GCxGC system was developed and used to examine alternative fuels, blends, high temperature thermally stressed fuel samples, thermal oxidative stressed fuel samples, combustion samples, samples from chemical processing streams and biological samples. The system was first used to compare to existing hydrocarbon type speciation techniques such as ASTM D2425 and ASTM D6379 for conventional jet fuels (Striebich et al., 2011). Because the technique is excellent at measuring aromatics accurately while speciating alkylbenzenes and naphthalenes, it was used for several research studies into the effect of aromatics in jet fuel (DeWitt et al., 2012a; DeWitt et al., 2013a; DeWitt et al., 2014). The technique is used to conduct comprehensive analyses (analyses of all parts of the fuel) and so it has been widely used as a hydrocarbon type determination (Striebich et al., 2014a) and for general analytical work for alternative fuels analysis because of its use of flame ionization detection (FID) with consistent response factors (Corporan et al., 2012; Corporan et al., 2013a; DeWitt et al., 2014). Hydrocarbon type analysis is also useful for determination of whole fuel changes and cracked product analysis for endothermic work (DeWitt et al., 2013), off-line supercritical decomposition (McMasters et al., 2012), and fuel processing studies (Robota et al., 2012). Next, because of its quantitative and qualitative abilities, GCxGC has been used in tracking the activity of microbes as they consume jet fuel hydrocarbons in water/fuel mixtures which simulate fuel tank contamination (Gunasekera et al., 2013; Gunasekera et al., 2014; Striebich et al., 2014b). Most recently, GCxGC is being used in conjunction with solid-phase extraction to separate, identify, and quantify the important components of the polar fraction of jet fuels (Shafer et al., 2015).

3.1.2   GCxGC (SPE) Polar Species Identification and Quantitation

The link between heteroatomic (polar) species in fuels and thermal stability continues to drive research into developing improved methods for quantifying polar species in fuels. The GCxGC (with FID/MS) method developed (Shafer et al., 2015) employs an initial solid-phase extraction (SPE) step to effectively separate and concentrate the polar fraction of the fuel. The SPE procedure had been used previously; however, it was refined to yield a more complete separation. This coupled with the capability of the GCxGC to separate the polar species enables quantitation of the major polar species (phenols, anilines, indoles carbazoles, etc.) using the FID. Other polar species that were previously found mainly in alternative fuels (ketones, alcohols, aldehydes, etc.) can also be quantified by this method. Polar sulfur-containing species, as well as those containing both sulfur and nitrogen, have been shown to be among the more detrimental to thermal stability. These types of compounds are typically very difficult to detect with the GCxGC-FID/MS system. Within the last year a GCxGC-MS system has been developed at University of Dayton's Shroyer Park Center with increased mass spectral sensitivity that has the capability to identify more of these "atypical" compounds.

3.1.3 Biofuels Evaluation

An extensive analytical effort has been performed on approximately 200 biofuel samples from nearly 30 different companies as part of the "Alternative and Experimental Jet Fuel and Jet Fuel Blend Stock Evaluation" program, which included the "DARPA Biojet" program. The initial (Tier I) evaluations of the experimental biofuels included hydrocarbon type composition by ASTM D2425 (and GCxGC beginning in late 2011), normal alkanes composition and chromatographic comparison by GC-MS, thermal stability by QCM, as well as specification tests for a few key properties conducted by the Air Force Petroleum Agency (AFPA). Upon "passing" the initial evaluations, larger samples of the experimental fuels were subjected to the second tier of evaluations (Tier II) as neat samples and/or blends with a representative JP-8. Additional testing as part of the Tier II evaluations included phenolic polars quantitation by HPLC (and other polars identification by SPE/GC-MS), metals by ICP-MS, low-temperature Scanning Brookfield viscosity, initial material compatibility testing (three materials), and full specification testing. The results of this testing along with comparisons to representative fuels were reported in over 120 Technical Memoranda during the 7-year period. Four of the hydroprocessed esters and fatty acid (HEFA) synthetic paraffinic kerosenes (SPKs), formerly referred to as hydroprocessed renewable jets (HRJs), were produced in sufficient quantity for the full certification process (AFRL-RQ-WP-TR-2013-0108). The certification process followed was initially developed for Fischer-Tropsch –SPKs (AFRL-RQ-WP-TR-2013-0124).

3.1.4 Analysis of Engine Emissions and Research Combustors for Hazardous Air Pollutants (HAPs)

Aircraft turbine engines are a significant source of particulate matter (PM) and gaseous emissions in the vicinity of airports and military installations. Hazardous air pollutants (HAPs) (e.g., formaldehyde, benzene, naphthalene and other compounds) associated with aircraft emissions are an environmental concern both in flight and at ground level. Therefore, effective sampling, identification, and accurate measurement of these trace species are important to assess their environmental impact. This effort evaluated two established ambient air sampling and analysis methods, U.S. Environmental Protection Agency (EPA) Method TO-11A and National Institute for Occupational Safety and Health (NIOSH) Method 1501, for potential use to quantify HAPs from aircraft turbine engines. The techniques were used to perform analyses of certified gas standards and the exhaust from a T63 turboshaft engine (Anneken et al., 2015; Cain et al., 2012; Cain et al., 2013, Corporan et al., 2010). Test results show that the EPA Method TO-11A (for aldehydes) and NIOSH Method 1501 (for semivolatile hydrocarbons) were effective techniques for the sampling and analysis of most HAPs of interest. This technique was also used to support combustion studies in HAPs emissions for the Well Stirred Reactor (WSR) system for traditional and alternative fuels (Blunck et al., 2012).

3.1.5 Use of High Performance Liquid Chromatography- Mass Spectrometry (HPLC-MS) to Investigate Fuel Polars

Our experiences in the analytical laboratory have been most often related to gas chromatography because the overwhelming majority of compounds in jet fuel are amenable to this technique. However, some compounds in jet fuel, due to their low concentration or polarity, may be better analyzed by HPLC-MS with Electrospray Ionization (ESI). In this cooperative agreement, we have purchased, installed and operated a HPLC-MS with ESI to examine, identify and quantify

4

the trace polar components in jet fuel. This method was described and a variety of jet fuels were examined (Adams et al., 2013). In addition, this technique has been combined with derivatization methods to examine the difficult components of the important polar fraction of fuel with regards to additives, sensitivities, etc. (Johnson et al., 2012). It was important to develop this technique because while the polar fraction can be adequately analyzed using conventional GC-MS, GCxGC, and specific detectors, HPLC may be more likely to identify acid or basic components which may not be able to be transported through a gas chromatographic column.

3.1.6 Analytical Support of the Assured Aerospace Fuels Research Facility (AAFRF) Operations

We conducted regular monitoring of AAFRF operations, which included examination of waxes, liquid fuel products and gases that were released. Generally, waxes were analyzed by dilution in carbon disulfide or some other suitable solvent and by using a high temperature GC system with a cold, on-column inlet and flame ionization detector (FID). A high temperature metal column with metal connector and retention gap "pre-column" was used so that the GC oven temperature could be programmed to 410 C, which allowed the elution of compounds up to C90 carbon number. Fuel range samples were examined on a more conventional GC with a HP-5MS column and traditional split-splitless injector and FID, using hydrogen carrier gas, which provided more resolving power to separate complex mixtures. Gas analysis to support AAFRF operations included both the micro GC system and the more traditional GC systems which included a molecular sieve column for hydrogen, methane, air and other fixed gases (thermal conductivity dectection - TCD), and a Poraplot column for C2-C6 gases, using an FID. The micro GC system could be operated on-line while the traditional gas analysis system was used off-line using sampling bags and injection of samples using gas phase syringes.

In addition to supporting AAFRF operations, research was conducted on small scale reactor systems to investigate catalysts and processes which could then be scaled up to larger systems like the AAFRF. Several studies of alternative fuel sources were performed involving algae to diesel fuel schemes as well as isomerization studies (Robota et al., 2012; Robota et al., 2013).

3.1.7 Hydrocarbon Decomposition by Microbes

Air Force fuel systems can be contaminated by bacteria, fungi, and other microbes, creating operational problems with filters, materials degradation, fuel pump degradation and a decline in overall fuel system cleanliness. In order to understand the degradation of hydrocarbons and the organisms that consume them, we used GC, GC-MS and GCxGC to measure individual hydrocarbon concentrations with and without bacteria as a function of time. We have studied this degradation in small systems (less than 8 mL), and up to a five L bioreactor with varying concentrations of bacteria, mineral media, and jet fuel. These studies aided the investigation of transcriptomics for *Pseudomonas aeruginosa*, for which we identified genes that were activated when certain hydrocarbons (n-alkanes) were consumed (Gunasekera et al., 2013; Gunasekera et al., 2014). We also investigated many different types of bacteria, each with tendencies to consume different components in jet fuel. For example, *Marinobacter hydrocarbonoclasticus* was very adept at consuming light aromatics (toluene, ethylbenzene, etc.) (Striebich et al., 2014b) while *Pseudomonas putida* could consume naphthalene and 2-methylnaphthalene quickly and nearly completely (Striebich et al., 2015). Bioreactor experiments involving the hydrocarbon

5

monitoring of biological activity also show that a competition exists between bacteria using the same resources; inhibition of the growth of one bacteria was caused by the immediate growth of another (Striebich et al., 2015). These studies have allowed biological researchers to understand how the microbes function in a fuel tank system, so that any contamination may be better controlled.

3.1.8 Development of a Leco GCxGC-TOFMS with Thermal Modulation

UDRI has been involved in two-dimensional gas chromatography for the past 15 years, including Multidimensional GC with a linear actuating modulator (Striebich et al., 2014a). Since these initial studies, we have purchased a flow modulated GCxGC as described above. Recently, however, we have been able to acquire a LECO GCxGC-Time of Flight Mass Spectrometer (GCxGC TOFMS) system. This two year old system was not being used and so was provided to us for use as a second GCxGC on which to conduct research using a reverse-phase column combination (polar primary column, non-polar secondary column) with thermal modulation. This instrumentation is fairly large so it was deployed on the UD campus with additional space for a larger computer system, liquid nitrogen access, gas generators and bottles, etc. In December 2015, this room was completed and the GCxGC was installed and operated. Since that time, contributions have been made for identification of polar components in SPE samples, field storage stability problems, and general analysis of existing fuels. While no publications have resulted from this effort as yet, several are planned including comparisons of thermal modulation with flow modulation, as well as publications in the area of the analysis of polar fuel components.

3.1.9 Alternative Fuels Analysis using GCxGC (DLA sponsored project)

The alternative aviation fuel specifications that are approved, or in development, have more compositional constraints than current specifications. In addition, the on-going fit-for-purpose testing results in data for properties where the petroleum jet fuel baseline is lacking or poorly known (e.g., isentropic bulk modulus). The ultimate goal of this effort was to link fluid composition (hydrocarbon class distribution) with properties and performance. The effort was divided in three tasks as follows: Task 1 – Characterization of hydrocarbon class composition of JP-5/8, Jet A and alternative fuel blendstocks and blends; Task 2 - Fit-for-purpose baseline determination; and Task 3 – Trace impurity technique evaluation and baseline determination

The role of UDRI in this program was to conduct various methods for aromatic content (ASTM D1319, D5186, and D6379), hydrocarbon composition (D2425 and GCxGC), and hydrogen content (D3701, D7171, and GCxGC), as well as total and reactive sulfur analysis (GC-FPD).

In general, good interlaboratory reproducibility was seen for the aromatic and hydrogen content methods. The D2425 method showed reasonable interlaboratory agreement, as well as general agreement with some of the GCxGC data for the petroleum-derived fuels. D2425 is not as useful as GCxGC for quantifying the saturated hydrocarbon sub-classes, because it does not distinguish between normal and iso-paraffins, and it does not identify conventional cycloparaffin sub-classes (i.e., monocycloparaffins, dicycloparaffins, and tricycloparaffins). These results were carefully documented for more than 25 different bio-derived fuels. GCxGC was found to be practiced differently in each laboratory, and while the UDRI GCxGC was confidently and accurately used

to perform hydrocarbon type analysis, GCxGC quantitation from other laboratories were less successful at precise and accurate quantitation of the composition of these fuel samples.

3.1.10 Detection and Mitigation of Microbiological Contamination in Fuel

Microbial growth in fuel is a significant concern to fuel users. Alkanes and aromatic compounds in fuel can serve as rich carbon sources for microbial proliferation. Microbial growth in fuel can deteriorate fuel quality and has been linked to tank corrosion, fuel pump failures, filter plugging, injector fouling, topcoat peeling, and engine damage. The Environmental Microbiology Group in the Energy & Environmental Engineering Division (EEE) at UDRI recognizes this need and has performed extensive research in biological contamination in biodiesel and other alternative fuels during this effort. UDRI has developed rapid detection assays to track microorganisms in fuel. Multiple bacterial species have been isolated from contaminated fuels and the environments exposed to fuel. The Environmental Microbiology group at UDRI is a leading laboratory in this area, supporting military and commercial aviation by evaluating microbial contamination of fuel systems and developing mitigation techniques.

3.1.10.1 Rapid Detection Methods

During this contract period, our laboratory has developed methods to enumerate fuel-degrading bacteria in contaminated fuel samples/tanks using culture and culture-independent methods. We have developed highly sensitive molecular biology tools (e.g., quantitative polymerase chain reaction - qPCR) to enumerate bacterial and fungal cells. We have designed broad range probes to detect bacterial and fungal load in contaminated fuel samples. Primers with broad interspecies specificity have been designed and have been used to determine bacterial loads in fuel samples. The qPCR methods developed by our group can be used to estimate 16S rDNA copy numbers of all the bacteria including complex, fastidious microbial communities growing in fuel that cannot be estimated by plate count methods. In addition organisms' specific probes have been designed to detect specific bacteria or bacterial sub-groups such as sulfate-reducing bacteria (SRB) or bacteria responsible for alkane degradation using *alk* genes specific primers. We have evaluated a number of contaminated fuel samples from the Air Force /Army and have estimated microbial loads on these samples. Multiple bacterial and fungal species have been isolated and their identities were confirmed by sequencing 16S/18S rRNA genes. Additionally, their fuel degradation profiles were characterized by gas chromatographic analyses (Striebich et al., 2014b).

3.1.10.2 Genomics and Transcriptomic Approach to Detect Novel Targets for Biocide Development

We have employed advanced genomic and transcriptomic technologies to characterize the transcriptional response of bacteria in the presence of fuel (Gunasekera et al., 2013; Brown et al., 2014). We initiated a whole genome approach using Affymetrix microarray chips of the *P. aeruoginosa* PAO1 strain to study the transcriptional profile of the fuel degrading strain *P. aeruginosa* ATCC 33988. Transcriptional profiling has revealed that *P. aeruginosa* ATCC 33988 required multiple adaptive mechanisms to proliferate in fuel-containing environments (Gunasekera et al., 2013). Additionally, we investigated fuel specific transcriptomic differences between fuel adapted ATCC 33988 and fuel less-adapted PAO1 in order to ascertain the underling mechanisms utilized by the ATCC 33988 strain to proliferate in fuel. Using microarray techniques and bioinformatics tools we have identified candidates of genes responsible for fuel adaptation. One example of a uniquely induced gene in ATCC 33988 is a homolog of PA5359 in

the PAO1 strain. Differentially expressed genes and novel genes discovered using this methodology have been used as targets to control bacterial growth. In addition to microarray techniques, in collaboration with Lawrence Livermore National Laboratories (LLNL), we used ribosome profiling and proteomic technology to identify differences in gene expression that allow the *P. aeruginosa* 33988 isolate to grow more rapidly in normal alkanes than the closely related strain PAO1.

Knowledge of the genome sequences of microorganisms degrading bacteria enable us to understand how the genetic information determines the degradation of fuel and what type of microbial adaptive mechanisms support surviving the harsh environment. During this work, we have sequenced complete genomes of *Pseudomonas aeruginosa* ATCC 33988 (Brown et al., 2013), *Gordonia sihwensis* Strain 9 (Brown et al., 2014), *Rhodovulum* sp. Strain NI22 (Brown et al., 2015), *Pseudomonas frederiksbergensis* SI8 (Ruiz et al., 2015a), and *Nocardioides luteus* (Brown et al., 2016). Sequencing several microbial genomes of bacteria helped to understand the underlying mechanisms that are involved in hydrocarbon degradation. Metagenomic sequencing of 16S rDNA sequences allowed differentiation of microorganisms into different subgroups and functional classes (Ruiz et al., 2016). High-throughput sequencing methods, such as 454 pyrosequencing have been applied to investigate the microbial diversity and expressions of specific genes in these microbial communities. Our metagenomic studies helped to differentiate taxonomic groups to their ecological functions and monitor structural and functional community shifts in different aviation and diesel fuels under varied conditions (Ruiz et al., 2016). Experiments using both conventional and alternative fuels with larger scale bioreactors were also conducted to confirm the results observed in small scale experiments. Sulfate-reducing bacteria (SRB) in fuel tanks have been receiving increasing attention because they not only degrade fuel, but also play a role in metal corrosion. Our group has carried out preliminary experiments to understand the growth of SRB in fuel in the presence of other aerobic bacteria.

3.1.10.3 Biocidal/Biostatic Additive Development and Testing

The need for novel biocides against fuel contaminants has been emphasized by the Air Force. Our lab, in collaboration with the Brown University (Providence, RI) has discovered novel di-peptides against fuel contaminating bacteria. Dipeptides can block efflux pumps in bacterial cell membranes, thereby inhibiting the cell's ability to remove toxic substances, causing cell death. We have screened a wide range of antimicrobial peptides and found several di-peptides that are highly effective against bacteria contaminating jet fuel. The other biocide types that we tested in our laboratory were Protegrins (PG-1). Protegrins are small proteins with potential antimicrobial activity against microbes found in a fuel environment. Our lab has evaluated the minimal inhibitory dosage of antimicrobial peptides for various fuel contaminants. We are studying the efficacy of these peptides with various organisms, as a function of fuel composition, test conditions, and additive concentration. These new biocides appear to be effective at much lower concentrations than currently used additives, offering the potential of reduced additive costs and minimal negative impact on fuel properties. In addition, we tested biocide delivery mechanisms (such as carrier solvents) to fuel water layer without affecting fuel composition. We also extended our research to develop cost-effective methods to produce large quantities of antimicrobial peptides using microorganisms and plants. With this objective in mind, our laboratory has cloned the PG-1 gene into bacterial plasmids. In collaboration with University of Pennsylvania, we have tested commercially produced plant derived protegrins. These plant derived protegrins were effective against a number of fuel contaminants.

3.1.10.4 Graphene oxide-based nano-filters to remove bacteria from fuel

We have demonstrated that graphene oxide (GO) does not have antibacterial properties, instead GO supports bacteria to attach and proliferate (Ruiz et al., 2011). However, silver-decorated GO (Ag-GO) in the form of free-standing films and coatings were shown to be antimicrobial against Gram positive and Gram negative bacteria. The solubility of GO in water is highly dependent on the degree of surface functionalization imparted during oxidation. Based on these findings, our group has developed a GO based filter to remove water and bacteria from jet fuel (Ruiz et al., 2015b), providing a new tool to prevent fuel biodeterioration. One unique feature of the designed nano-filter is that it allows fuel filtration at a high flow rate. We have procured a patent on this technology (US patent No. 20140199777).

3.1.11 Bench Level Raman Investigation Spectroscopy of Fuels

Bench level fuel diagnostics are of great interest and the ability to test small quantities of fuel is quite attractive. Our group has successfully built a custom Raman system that will be used to investigate bulk properties, on the order of ones of percent, of classes of compounds. The current configuration includes a 785 nm excitation, which fixes the problem of the 532 nm background fluorescence issue. We have also mocked up a surrogate to mimic what a thermal background would look like to the instrument. Using a commercial spectrometer, we found that the thermal background became a serious issue around 325 °C and then switched to using a monochromator and a sensitive detector, along with a lock-in amplifier to successfully overcome the thermal issue. We demonstrated that the bench level set up works quite well for both stressed and non-stressed fuels. Future work will include locating a more sensitive detector, conducting Raman gas cell studies, and miniaturization/simplification of the system.

3.1.12 Home-built Supersonic Quadruple (Suzie Q) Mass Spectrometer Applications

A significant effort has been made in developing applications for the Suzie Q mass spectrometer (Extrel CMS, Pittsburgh, PA). Because this instrument is modular, allowing one to easily change the reaction and sample introduction chamber, it results in an instrument that is powerful (both in sensitivity and the information generated) and extremely versatile. This versatility has allowed us to perform experiments beyond that which was initially conceived for Suzie Q as opportunities have arisen; from monitoring hydrogen production produced by E. coli bacteria, to performing nanoparticle-catalyzed methanol oxidation experiments at high temperatures. Each of these studies has required the development of a home-built reaction chamber to be interfaced to the instrument.

The primary purpose of this instrument and the focus of much of its operating time, has been the study of endothermic fuels and fuel precursors under supercritical conditions for the purpose of more accurately understanding the kinetics of endothermic fuel breakdown at flight conditions. Our long-term goals are to use the knowledge obtained about detailed reaction mechanisms and intermediate identification to improve simulations and better predict the performance of proposed endothermic fuels for high speed flight. This instrument is unique in that by separating intermediates and quenching further reactions as they are transferred via molecular beam for detection, these fragile and short-lived species can be detected before molecule(radical)-molecule collisions induce further reactions, therefore giving an accurate description of the various species produced across the high-temperature and high-pressure supercritical regime.

Our initial efforts were focused on developing the reaction and sample introduction chamber to be interfaced with the Suzie Q mass spectrometer. The operating parameters for supercritical reactions will require heating of the sample to ~900 °C and compressing it to pressures up to 75 atm. To withstand the extreme conditions, a custom built, high-pressure nozzle from Lenox Laser featuring a 3 μm diameter flow orifice to generate the molecular beam for transfer of the intermediates to the instrument was purchased. In addition to the previously mentioned high pressure nozzle, we have constructed and operated a heated, effusive source to induce pyrolysis of the endothermic fuel precursors at reduced pressures by recording data sets and monitoring kinetics of pyrolysis as samples are heated to 900 °C at reduced pressures (1.3×10^{-7} atm). Our initial focus was on the pyrolysis of simple, straight-chained hydrocarbon surrogates such as hexane, ethane, and dodecane, all of which have been well studied and provide comparison for our results. These sets of data will be used for comparison of the rate of hydrocarbon cracking once the supercritical inlet is operating.

We have concluded our survey of the gas-phase pyrolysis dynamics of *n*-hexane and its branched analogs as a function of pyrolysis temperature in isolation and upon exposure to a variety of boron nitride and graphene oxide-based catalysts. We have used our high-pressure supercritical pyrolysis source to investigate hexane pyrolysis under supercritical conditions. The results are compared with those previously obtained under gas-phase conditions. Our preliminary supercritical results seemed to indicate an interesting fluid density-dependence of the pyrolysis kinetics. Also, we have now observed a number of reaction intermediates/products not seen in the gas phase experiments. Using our accelerated measurement capability, we have completed a series of experiments examining the pyrolysis of supercritical dodecane and hexane fluids. We have captured the *in-situ* speciation data for the two fluids from room temperature up to ~800 °C. The preliminary overlap (or sometimes non-overlap) between theoretical predictions and our experimental observations suggests that these data will be able to further our understanding of the supercritical pyrolysis chemistry under investigation.

3.2 Advanced /Alternative Fuels Development, Evaluation, Demonstration, and Management

3.2.1 Planning, Construction, and Operation of the Assured Aerospace Fuels Research Facility (AAFRF)

The Air Force has previously committed to using alternative (non-petroleum-derived) fuels in existing and future aircraft. This commitment consisted of two goals: (1) qualifying all its assets to use a 50/50 blend of conventional/alternative fuels by the year 2011 and (2) being prepared to cost competitively acquire 50 percent of the Air Force's domestic aviation fuel requirements via an alternative fuel blend (derived from domestic sources produced in a manner that is "greener" than fuels produced from conventional petroleum) by the year 2016.

In order to meet these goals, work was performed to understand the characteristics of fuels produced from alternative sources and the variables that impact their characteristics. To produce research quantities of fuel, UDRI worked with Battelle Memorial Institute to design, build, and operate an Assured Aerospace Fuels Research Facility to produce quantities of alternative jet fuels and jet fuel components for testing. The upgrader Sample Preparation Unit (SPU) was the first unit brought online.

DISTRIBUTION STATEMENT A: Approved for public release. Distribution is unlimited.

The SPU at the AFRL Assured Aerospace Fuels Research Facility (AAFRF) was designed to meet a critical government and industry need to produce alternative fuels in research quantities (10-50 gallons per day). This meets a market need between small testing amounts produced in a laboratory and larger quantity production using pilot-scale production plants.

The facility was purpose-built for the production of fuels. It features a modular design to accommodate a variety of processing methods, is highly instrumented for maximum data generation and analysis, and boasts a suite of excellent safety features. Potential fuel feedstocks for use in the facility include, but are not limited to, coal-derived waxes and liquids, camelina, salicornia, palm, jatropha, soy, algae, waste animal fats, and other renewable resources.

The SPU is rated for high temperature/high pressure hydrogen use. The sample preparation bay is highly configurable to accommodate a variety of processing systems, including the ability to operate up to four fixed-bed reactors in series, parallel, or independently. The facility has three distillation columns for intermediate and fuel product separation. The modular nature of the facility allows test rigs to be added and integrated into the facilities' processing, instrumentation, and control systems.

The facility is extensively instrumented, including mass flow measurements on all streams. The data is essential for the optimization of production techniques as well as the design of large-scale production facilities. The AAFRF boasts an array of safety features, including six H_2 detectors at key locations, integrated ventilation and facility alarms, remote H_2 storage, an O_2 sensor on the vacuum column, and full audio/video monitoring.

The system is capable of fully recycling materials and catalysts in a manner similar to large-scale manufacturing. Catalytic transformation processes include gaseous-gaseous feeds and liquid-gaseous feeds, and oligomerization projects are possible.

The system was used for a variety of programs during the Cooperative Agreement period. These programs included upgrading of Fischer-Tropsch waxes to specification jet fuels, conversion of renewable crude to jet fuel, and production of variable fuel compositions for evaluation of composition to performance relationships.

3.2.2 Assembly and Study of Atomic & Molecular Clusters via Helium Droplet Beam Methods

We have brought online a new and exciting capability to investigate atomic and molecular clusters. These are materials in which ones-tens of atoms/molecules are assembled into a cluster, often with sub-nm size, and typically exhibiting extremely strong quantum effects. We have constructed a helium droplet beam instrument which allows us to assemble and study virtually any cluster imaginable. This capability follows on earlier work by Will Lewis in this area. Briefly, a beam of helium droplets is formed and then directed through various "pickup cells" that dope the droplets with atoms/molecules of interest. Owing to the low temperature (0.4 K) and liquid nature of the droplets, any dopant species picked up tend to be frozen into a cluster inside the droplet. Due to the fact that helium is a very weak "solvent" the properties of the cluster are virtually unchanged from those of an isolated gas-phase cluster. The real beauty of the technique is that by controlling the pressure in the pickup cells (or temperature in the case of ovens) the number of atoms/molecules picked up can be controlled with single-atom precision.

Additionally, because the low temperature of the droplet typically prevents rearrangement of the cluster as it is assembled, the order of the pickup cells can be used to control which species will be used to form the interior of the cluster and which will be attached to the exterior. Via these methods, we can assemble virtually any cluster imaginable. We will use this new capability to investigate novel clusters.

We have successfully assembled Cn carbon clusters from n=2 to n=13 and we have developed two different experimental procedures for producing these clusters: one which was based upon a pulsed laser, and allows time-dependent measurements to be made, but the signal-to-noise ratio resulting from the low duty cycle of these experiments was marginal. Another which was based upon CW-laser heating that yields much improved signal-to-noise. We have used the two sources to study the cluster assembly process in detail. The latter precludes time-dependent measurements but offers much higher signal-to-noise ratios for steady-state measurements. Modeling was also performed to better understand the structure and energetics of the clusters produced.

Additionally, we have examined the reactivity with H_2 and H_2O reaction partners (no reactivity was observed) and ethylene. These fundamental studies will support development of mechanisms for fuel pyrolysis and combustion. We also examined clusters composed of Al atoms and organic molecules in support of advanced aluminized fuel programs. While not conceptually different from carbon-fuel studies, stable operation of the aluminum evaporation ovens is easier to achieve.

We also added mid-IR spectroscopy capability to our existing instrument in order to allow spectroscopic interrogation of the structure and vibrational dynamics of the species formed. We have added a tunable quantum cascade laser head and the associated optics and diagnostics to the instrument. We have a total of five laser heads yielding a spectral range of roughly 1700-2400 cm^{-1}.

These efforts are detailed in journal publications (Thomas et al., 2015; Lewis et al., 2012; Lewis et al., 2014). Future work includes improving the stability of the carbon evaporation source (stable operation for several hours is necessary) and studying various chromophores, metal clusters, and other novel fuel based novel structures via the mid-IR spectroscopy method.

3.2.3 Algae Carbon Sequestration and Biofuel Generation

Microalgae are known for their high photosynthetic efficiency and high lipid content. Therefore, microalgae have the potential to be used to feed CO_2 and other gases (NO_x, SO_x etc.) from flue gas emitted from various combustion sources to reduce greenhouse gas (GHG) emissions and generate biomass that can be used for biofuel. However, the prevailing weather conditions (solar insolation and its duration and temperature) at the geographical location of the system affects microalgae growth and hence the carbon capture efficiency. Thus, it is necessary to evaluate systems at conditions relevant to their operating environment.

Given the potential benefits, the Air Force was interested in evaluating and developing algae biomass production systems to minimize GHG emissions from its boilers at WPAFB, OH and to generate biofuel in an effort to reduce its carbon footprint. Therefore, this effort involved

designing and building an outdoor facility suitable for operating and evaluating photobioreactors throughout the year, including cold weather conditions.

Under this effort, a 10,000 sq ft outdoor facility was constructed that includes a 2,000 sq ft greenhouse that can be used as a staging area, as well as to house support systems. The facility is fenced and gated. Compacted gravel covers most of the open area with a 10 ft wide driveway to the greenhouse and the greenhouse flooring asphalted. The total power supplied is 350 kVA at 480 V of which 75 kVA is available as 120/208V service with GFCI receptacles placed at selected locations throughout the facility. A power monitoring system monitors all circuits fed from the panels for process energy consumption. A boiler (450 kBtu/hr) and chiller (350 kBtu/hr) with multiple connection locations also provide the necessary heating and cooling for operation during cold and warm weather conditions. A compressor feeds air distribution manifolds distributed throughout the facility up to 110 CFM of air at 120 psi. Non-potable water is provided to the facility and multiple drainage points connect to the sewer line. The green house and the open area are well illuminated. Propane gas heating is available to the green house for winter operation.

Since the completion of the facility buildup under this effort, it has been used to build and evaluate a modular pilot scale photobioreactor system designed by UDRI for algae biomass production complete with all required support systems. The facility also serves as a place to evaluate other algae biomass production related technologies.

3.3 Advanced, Affordable Fuel/Combustion Additive Technologies

3.3.1 Improvements in Fuel System Icing Inhibitor Use

UDRI performed extensive work related to the use of Fuel System Icing Inhibitor (FSII) additives in military aviation fuels. FSII, a mandatory additive in JP-5 and JP-8, is used to prevent solidification of free water in the fuel and to provide protection against microbial growth in fuel systems. We performed detailed analytical and experimental studies and directly supported full-scale flight testing to identify if required anti-icing and biostatic capabilities could be maintained at lower additive dose concentrations (DeWitt et al., 2011l; DeWitt et al., 2013b). Studies completed under a prior cooperative agreement with AFRL/RQTF provided the basis for the specific efforts performed. We completed experimental studies to investigate the effect of temperature and concentration on FSII partitioning between aqueous and fuel phases (West et al., 2014). We completed large scale component studies to verify FSII efficacy at reduces dose concentrations. We evaluated the impact of reduced FSII concentration on the ASTM D5006 quantitation method (DeWitt et al., 2013c). We provided critical support to B-52 Flight Testing of reduced FSII levels with elevated total water content performed at Edwards AFB Flight Test Center, including developing the analytical and fuel preparation methods used, developing the flight test plan, and on-site direct support during the flight tests. These efforts resulted in the successful reduction of the JP-8 minimum FSII use limit to 0.04% by volume (in USAF T.O. 42B-1-1), and the JP-8 procurement range to 0.07-0.10% by volume (in MIL-DTL-83133H). The reduced FSII limits have resulted in an immediate cost savings for DoD (estimated > $5M annually) and a potential reduction in the frequency of Fuel Tank Topcoat Peeling (FTTP). UDRI has provided extensive support to AFRL and AFPA efforts to obtain concurrent reductions in FSII use and procurement limits in NATO and ASIC fuel specifications.

UDRI performed extensive efforts to improve the understanding of the effect of FSII on FTTP occurrences in integral aircraft fuel tanks. We performed basic and applied experimental studies to improve the understanding of the effect of operational conditions (e.g., temperature, concentration) on FTTP (Zabarnick et al., 2010). We identified an alternate FSII, TriEGME, which could provide equivalent anti-icing performance with reduced propensity for FTTP (Zabarnick et al., 2011). Flight testing was performed with TriEGME for further demonstration of capability. UDRI provided extensive support to the USAF Coatings Technology Integration Office (CTIO) and various SPOs regarding the compatibility of varying topcoat formulations with FSII. This included a recent study to directly support the KC-46 SPO (West et al., 2016).

3.3.2 Spectroscopic Interrogation of Energetic Materials Incorporating Metal Nanomaterials

We have begun a collaboration with researchers at AFRL/RWME to characterize the full-scale performance of metal nanoparticle-based energetic materials. Such work has traditionally been quite challenging due to the short timescales associated with energy release (reaction is generally complete on μs-ms timescales), the lack of methods to reliably measure temperatures on those timescales, and the sheer complexity of the chemistry occurring. Recently we have developed and published spectroscopic methods to remotely measure temperature and follow reaction dynamics of selected species on sub-microsecond or longer timescales. These methods allow us to monitor the time-evolution of chosen species within the overall chemical dynamics of the system and to correlate these measurements with the energy release process. We first applied our spectroscopic methods to explosives incorporating oxide-passivated materials.

High explosives experiments were conducted on RDX charges incorporating energetic nanomaterials, including those developed at RQTF. The experiments were jointly sponsored by RQTF and RWME. Temperatures and chemical dynamics were characterized as a function of time and space following detonation, and indicated the RQTF-developed nano-aluminum released energy faster than any other known metal nanoparticle (Lewis et al., 2010; Lewis et al., 2011). In fact, the energy release was so rapid we could only estimate a lower bound for the rate. From these exciting results, we prepared two manuscripts which have now been published (Lewis et al., 2013a; Lewis et al., 2013b). Our current efforts are focused towards examining the chemical dynamics of these materials on the detonation timescale. Future work will involve explosive compositions that include organically-passivated materials instead. Additionally, we are working to further develop our time-resolved methods to include spatial resolution.

3.3.3 Synthesis of Novel Alanes for Energetic Nanoparticles

Current commercially available alanes, such as N-dimethylethyl alane are highly unstable and pyrophoric at ambient conditions. In principle, however, it may be possible to improve the stability of the alane complexes by changing the ligands used to stabilize the complex. If successful, the payoff would be the development of a reasonably stable (and safe to handle and transport) liquid with high hydrogen and aluminum content. As an example, N-methylpyrrolidine (NMP) has been used as a Lewis base to synthesize moderately stable alane complexes. The alane-NMP complexes, $AlH_3 \cdot NMP$, $AlH_3 \cdot (NMP)_2$ and $AlH_2Cl \cdot (NMP)_2$, can be prepared by varying the $LiAlH_4/AlCl_3$ ratios in the presence of NMP in an argon filled glove box. In addition, other Lewis bases, such as triazoles and imidazoles can also be used in synthesis of moderately stable alane complexes (Li et al., 2010).
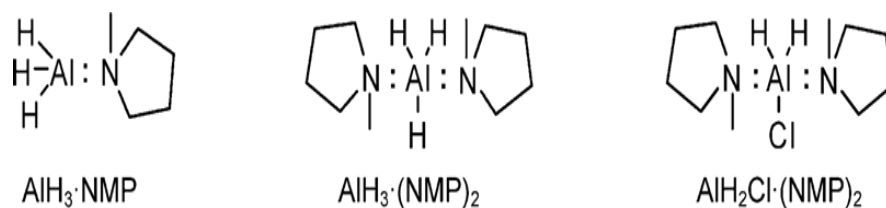
Figure 1. Alane-NMP complexes

3.3.4 On-demand Hydrogen from Al Nanoparticles

The development of technologies that would lead to production of safe and environmentally friendly hydrogen gas is required in order to use it as a future energy source. This can be achieved by an aluminum-water reaction. However, most of the commercially available Al nanoparticles have an aluminum oxide shell around the active Al core and it prevents the reaction between Al and water at ambient conditions. To overcome this problem and facilitate the generation of hydrogen, researchers have applied various reaction-promoting schemes. These have included the use of a strong base, application of high temperature, and activation of aluminum metals. However, our Al core-shell nanoparticles react with water without any promoters to produce hydrogen at room temperature. Therefore, these novel aluminum core-shell nanoparticles might be a potential candidate for providing power based on hydrogen without requiring the direct storage of large quantities of hydrogen; one needs only to add water to produce hydrogen on demand, where and when needed (Bunker et al., 2010).

3.3.5 Synthesis of Metal Decorated Graphene Oxide

Graphene oxide (GO) attracted much recent attention due to its excellent electrical, mechanical, and thermal properties, as well as its wide range of promising applications. For the preparation of GO, graphite powder is oxidized under harsh conditions to yield readily exfoliated GO. In our lab, we used modified Hummer's method to synthesize GO from expanded graphite powder which was obtained from Asbury Carbons Industries. GO, synthesized in our lab, was characterized using transmission electron microscopy (TEM), thermogravimetric analysis (TGA), differential scanning calorimetry (DSC), Raman spectroscopy, and x-ray diffraction (XRD) techniques to evaluate the quality of the sample. Furthermore, the GO synthesized in our lab was decorated with metal nanoparticles such as Ag and Au. In an effort to decorate GO with Ag nanoparticles, we used a sonochemistry method which has a number of advantages, such as simplicity, shorter reaction time, and ease of scale-up compared to existing methods. In a typical procedure of Ag decoration of GO (Ag-GO) using sonochemistry, GO was mixed with Ag acetate in dimethyl formamide and sonicated for 10 minutes active time. After sonication, the sample was allowed to cool for a few minutes and transferred to a round bottom flask. DMF solvent was removed using a rotary evaporator and the Ag-GO sample was washed with water, ethanol, and acetone, respectively to remove unreacted Ag acetate. This Ag-GO sample was also characterized using the aforementioned techniques and results confirmed the GO sheets are well decorated with Ag nanoparticles (Figure 2).
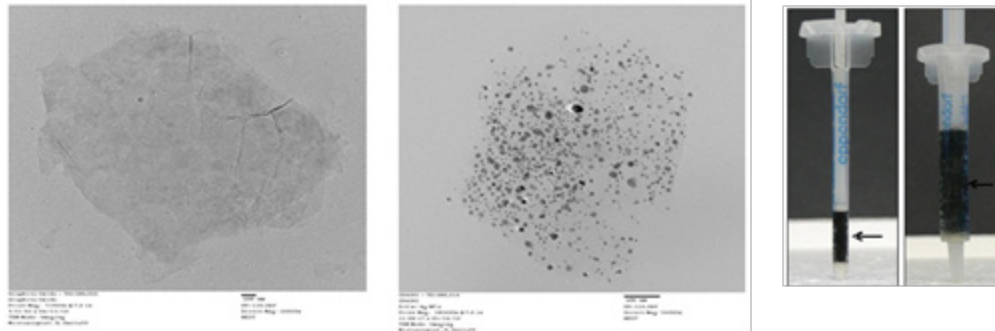
Figure 2. GO sheets synthesized from modified Hummers method (left), Ag decorated GO (middle) and GO columns as fuel filters (right).

3.3.6 Diesel Hybrid-Altitude Testing

ISR aircraft power systems are faced with a difficult mission profile. Aircraft takeoff and climb at very high engine loads, and then are required to throttle down to a relatively small percentage of full load for cruising and loitering. Spark ignited internal combustion engine efficiency suffers at part load operation due to pumping losses of the air throttling mechanism and poor air-fuel mixing. There can also be reliability issues that arise, such as spark plug fouling from low load operation in an SI engine. Spark ignited engines tend to be chosen for their high power density. Diesel engines tend to be more efficient, especially at part load, but suffer from poor power density, as diesel engines are more sturdily built to handle much higher peak pressure in-cylinder.

A power system was investigated to utilize a diesel engine, sized for cruising load, as the primary sustained power source for an aircraft, with an electric motor and battery pack to provide takeoff and climbout power. Both series and parallel hybrid configurations were considered, and a parallel system was chosen for early stage research. Parallel hybrid systems tend to be lighter weight, with just one motor/generator, as the engine and motor/generator are mechanically coupled and the single motor/generator can have a dual function. A theoretical airframe was selected to generate a paper model for cruise power and takeoff/climbout power requirements.

Using an available 70 hp eddy current dynamometer test stand, a mechanically injected, 20 hp diesel engine was selected (from the farm equipment market) and mounted to the test stand. A 34 hp brushless dc motor was coupled, via a synchronous toothed belt, parallel to the engine, and both could feed power to the dyno. Power was successfully generated with the engine and electric motor to simulate takeoff and climb conditions. A load bank was used to absorb electrical power generated from the engine. Current and voltage were measured, and a reduction in dynamometer power was observed as the resistance of the load bank was lowered, generating more electrical power.

Another aspect of this project was to observe the effects of altitude on a small diesel engine. An altitude chamber was designed and built, using a centrifugal supercharger (driven by electric motor) as an air pump to draw a lower pressure, to correspond with given altitudes, in a shared intake and exhaust plenum. Increasing power reductions were observed with increasing altitude with a naturally aspirated engine.

16

Finally an investigation of small turbochargers was conducted to select an appropriately sized turbocharger to turbo-normalize the diesel engine. Turbo-normalization is the use of a turbocharger to return intake pressures to sea level conditions and regain power at altitude. The system was not designed to boost the engine power rating. Turbocharger compressors do generate heat, so an increase in intake air temperature was expected and observed. Testing was conducted at increasing altitudes with three small turbochargers, before one turbocharger was selected for its lower exhaust backpressure characteristics. Specific fuel consumption was measured over a suite of engine speeds, loads, and altitudes, and brake specific fuel consumption (BSFC) maps were generated. General trends showed large increases in BSFC at higher altitudes with a naturally aspirated engine configuration, while the turbo-normalized engine only showed slight increases in BSFC trends with increasing altitude that could be attributed to increased intake air temperatures. It was worth noting that some medium load points showed improved BSFC. This change was attributed to being in a more efficient part of the turbocharger compressor map as turbocharger speeds climbed with increasing pressure differential over the turbine section.

3.3.7 Pulsed Spark Plug

The goal of this work was to verify claims of faster, more complete combustion of fuel in a spark ignition engine using a pulsed power spark plug. The pulsed power spark plug had an integrated capacitor inside the plug which was intended to be used to deliver more spark energy to the combustion chamber to initiate fuel/air combustion. The pulsed plugs did not require any additional electronics to function, and were intended to be used as a drop-in replacement for regular spark plugs.

The stated claims of faster, more complete combustion, and reduced cycle-to-cycle variation in combustion were to be tested on a Rotax 914 four-cylinder, turbo-normalized, port-fuel-injected, spark ignition four-stroke engine using 87 Octane rated gasoline. This engine spends most of its operating life at medium to heavy cruise conditions at medium to high engine speeds.

Combustion analysis used in-cylinder pressure to monitor combustion phasing and heat release, as well as cycle-to-cycle variation to determine if any consistent changes could be seen in combustion properties. Also, specific fuel consumption and engine loading were monitored.

Results showed a small (~1%) fuel consumption decrease at the lower speed set point, while a 1% increase at the higher speed set point. Combustion phasing suffered with the pulsed plugs, compared to regular spark plugs, in that landmark burn durations (0-10%, 10-90% mass fraction burned) and CA50 (50% mass fraction burned) location were extended by up to 2° crank angle and CA50 was pushed further into the expansion stroke by 2°. A re-configuration of engine spark timing maps could reposition the in-cylinder pressures to the most mechanically advantageous crank angle, but that was outside the scope of this testing.

Pulsed spark plug technology is intended to improve combustion efficiency at engine idle and low load cruise conditions. At those conditions, very little in-cylinder gas motion is available to promote thorough mixing, and efficiency can suffer. Additional ignition energy could very well improve flame development and reduce cycle-to-cycle variations at these low load conditions. As engine speeds climb and in-cylinder motion and mixing increases, the benefits of adding ignition energy are less apparent and in the case of this engine testing, without altering ignition

timing maps, combustion durations were unchanged at medium engine load and speed, and impacted negatively at higher engine speeds. An aircraft operates mostly at medium to high engine loads and speeds, so any advantages from pulsed plugs would likely not be seen. Furthermore, with unaltered ignition timing, a small increase in fuel consumption was seen at the higher engine speed. This was likely due to a small lengthening of flame-development angle and rapid-burn angle, which reduced the ability of the engine to convert heat and pressure into mechanical work. At this time continued study of pulsed plugs for use in an aircraft application is not recommended.

3.3.8 Unleaded Avgas

The Air Force utilizes leaded avgas (100LL) to fuel the MQ-1 Predator UAV to help carry out its mission. There are several problems with using 100LL: 1) a future ban on lead in avgas from the EPA, 2) there is only one supplier of the octane-enhancer additive tetraethyl lead (TEL), 3) lead deposits can decrease performance, increase maintenance, and shorten engine lifetime and 4) its costs outside the continental US are quite high. One solution to solving these problems is to find an unleaded high-octane replacement fuel that is lower in cost. This solution would align with USAF's Energy Strategic Plan in multiple ways. First, it could improve resiliency by negating the need for TEL and avoiding a ban on 100LL. Second, it could reduce demand by providing a solution that consumes less fuel. Third, it could ensure supply by utilizing a renewable fuel. The objective of this project was, therefore, to find an available low-cost unleaded fuel that is suitable for operation in the MQ-1 engine.

Two domestic (100-octane: 100SF and G100UL) and two international (91-octane: 91UL and 91/96UL) fuels were identified that could potentially meet this objective. These fuels were tested on a Rotax 914F engine at the Small Engine Research Laboratory. Numerous data were collected to determine and compare the fuels' performance and combustion in the Rotax 914F. Results showed that the lower-octane fuels could not provide the necessary power at high engine speeds (4500 – 5800 rpm), while the 100-octane fuels provided power similar to 100LL. It was also determined through this investigation that one of the fuels (100SF) showed instability during cold-starting; this caused engine hardware damage during testing. Concerning combustion performance, all four fuels were observed to exhibit very similar combustion characteristics. Only the 100SF fuel exhibited combustion instability at 4500 rpm that could limit engine load.

A cost analysis of the data shows that cost savings is linearly dependent with flight hours, increases with engine speed for all fuels, and is higher for the high-octane fuels than the low-octane fuels. Excluding fuel transportation costs, the unleaded 100-octane fuels could provide an estimated $5-10 million in annual savings at operation levels of 100,000 to 150,000 flight hours. A cost analysis of results from a recent investigation into utilizing engine operational changes was also done for comparison purposes. Under a certain combination of adjustments in the equivalence ratio, ignition timing and using dual spark ignition with an 87 AKI mogas, engine power similar to normal operation with 100LL be reached. Although the fuel consumption is up to 30% higher under these conditions, fuel cost savings similar to G100UL could be attained.

The next steps taken to solve the problems associated with 100LL depend upon the route chosen by the USAF. Either G100UL or the combination of engine operation changes at maximum indicated specification fuel consumption (ISFC) may be used to provide similar power out at a reduced operational cost. Both require further steps to implement. Material compatibility and

DISTRIBUTION STATEMENT A: Approved for public release. Distribution is unlimited.

certification testing with G100UL are needed to further ensure its feasibility. Engine operation changes require certification testing, approval, and time to make necessary changes. All of the four options available have the ability to solve the problems associated with 100LL and save the USAF millions of dollars annually.

3.3.9   Diesel/Hydrogen Engine Testing

To increase the fuel efficiency of compression ignition internal combustion engines at low loads and cruise conditions, hydrogen can be used to extend the lean operability limit of combustion.

A test cycle was developed to test a 2.2 liter Ford "Puma" turbodiesel, high pressure common rail engine under a variety of engine speed and load conditions (up to half of the baseline engine load) at Revolve Technologies in England. The test plan included steady-state data points following the test cycle for engine parameters (temperatures, pressures, speeds, torque), in-cylinder pressure data for pressure rise rate, and emissions data (gaseous emissions, smoke opacity, and particulate matter). The test stand engine was set up to use a dual-fuel approach with varying ratios of gaseous hydrogen being injected in the intake manifold to pre-mix with the incoming combustion air and liquid diesel fuel injected via the stock direct injectors. An on-board dry-cell hydrogen generator was used to investigate if significant efficiency gains can be demonstrated to justify the energy investment of the dry-cell hydrogen generator.

Testing was canceled after approximately one year from the start of testing after multiple engine failures and test cell problems were encountered. Revolve Technologies internally decided the project was exceeding the provided funding and decided to no longer support the work with time and resources. It is clear that diesel pilot injection timing, hydrogen port injection timing, and overall equivalence ratio are extremely important and it is likely that one of these characteristics being too far out of range in the Revolve test facility could have contributed to the engine damages sustained. Too high of an equivalence ratio with hydrogen-air can cause uncontrolled combustion in pre-mixed end gas (knocking) that could cause in-cylinder damage that may have been contributing to the smoking engine and rough running. They did mention that intake manifold variations could have contributed to intake flow dynamics that could be creating undesirable combustion characteristics in one or more cylinders.

Few conclusions are able to be drawn for this work due to the incomplete nature of the testing. However, the literature review conducted concurrently with this testing did show that at lower engine loads, and especially from an emissions point of view, the addition of hydrogen can reduce particulate emissions by promoting more complete oxidation of soot, reduce NOx emissions if the air-hydrogen-diesel equivalence ratio is kept low enough to stay away from the NOx formation threshold temperature, and obviously reduce CO_2 and CO production due to the lack of carbon in hydrogen. It is more difficult to make any conclusions about thermal efficiency as some research shows slight decreases in efficiency due to faster heat losses and extension of ignition delay, but that is not to say that an engine couldn't be thoroughly optimized to take advantage of different combustion timing characteristics to regain some of these losses.

3.4 Support of Alternative Fuel Development

3.4.1 'General' Support of Alternative Fuels Efforts

DoD, FAA, and commercial interest in the certification and approval of alternatively (non-petroleum) derived fuel blends for aviation applications has continued since the 2006 certification of the B-52 for use of Fischer-Tropsch derived Synthetic Paraffinic Kerosene (SPK) as a blending feedstock. UDRI has continued to support these efforts by performing basic to applied research which has provided a significant basis for the certification and approval of new alternative fuel chemistries. We have collaborated with AFRL/RQTF to improve the understanding of fuel composition to performance (Corporan et al., 2011a; Corporan et al., 2012; DeWitt, 2014), including the effect of aromatics on thermal-oxidative stability characteristics of SPKs (DeWitt et al., 2014). We have performed extensive combustion and emission evaluations of alternative fuels and blends (Corporan et al., 2013a), including the first on-wing emissions measurements of a C-17 operated with a Hydroprocessed Renewable Jet (HRJ) fuel blend (Corporan et al., 2011b). The UDRI and RQTF team has supported the FAA National Jet Fuel Combustion Program (NJFCP) by performing detailed combustion and emission studies using the new Elevated Pressure Combustor (EPC) facility at AFRL. Overall, these efforts continue to improve the understanding of the complex relationships between fuel composition and performance and assist with identification and certification of future alternative fuel chemistries.

3.4.2 The Performance and Emissions Characteristics of Heavy Fuels in a Small, Spark Ignition Engine

This research was conducted in pursuit of the DoD's plan for the universal use of a heavy, low volatility hydrocarbon fuel, and the increased interest in bio-derived fuels for small Unmanned Aircraft Systems (UAS's). Currently a majority of small UAS's use small spark ignition engines for their high power densities. Typically, these systems use commercial off-the-shelf power plants that are not optimized for fuel efficiency. Increased fuel efficiency is being pursued alongside the ability to utilize military heavy fuels. A test stand using a 33.5 cc four-stroke, spark ignition, air-cooled, single cylinder engine was constructed. Research was conducted to establish the feasibility of converting the existing system to utilize JP-8 with the stock mechanical carburetion. The stock carburetion had difficulty maintaining a consistent air/fuel ratio across the entire engine operating range. To resolve this, an electronic fuel injection system was developed to gain greater control over fuel mixture. An air-assisted electronic fuel injector was sourced from a scooter and adapted to work with the 33.5 cc four-stroke engine. An aluminum injector mount was designed and machined and electronic controls were employed. Sensors on the valve train and crankshaft were developed as control signals for the injection system. The injector was characterized for flow rates and droplet size.

The test stand consisted of a small dynamometer coupled to the engine. Servo throttle actuation was designed and the throttle position was monitored with a throttle position sensor. The air-assisted injector was supplied with regulated shop air, and the fuel pressurized using regulated nitrogen. A fuel flowmeter and mass air flowmeter monitored equivalence ratio. Work was done to facilitate smooth measurement of unsteady air flow intrinsic to single-cylinder engines.

Performance testing showed a decrease in brake specific fuel consumption (BSFC) while utilizing the injection system for the baseline fuel (Avgas 100LL), as greater mixture control

(closer to stoichiometric) was realized. The engine was started using gasoline. Heavy fuel testing showed the ability to achieve required torque values at certain engine speeds. JP-8 was tested on the carbureted engine and fuel injected engine, showing a decrease in BSFC over baseline (carbureted avgas) with the carburetor and a further decrease in BSFC for the injected system.

Biofuels that were tested were plant-based Camelina (carbureted and injected) and a UDRI grown and extracted algae-based fatty acid methyl ester (FAME) biofuel blended with D2 diesel in a 20% algae/80% diesel blend. Performance results for the Camelina showed a decrease in BSFC for the carbureted engine and the largest decrease of all the test fuels for the injected Camelina fuel. The algae blend showed less decrease in BSFC than the 100% diesel fuel.

Emissions data were recorded as well. The injection system demonstrated less CO emissions for the injected fuels over the carbureted fuels due to closer to stoichiometric mixtures. Similarly, unburned hydrocarbon emissions decreased when injection was employed. NOx emissions were higher for the fuel injected engine, as peak NOx emissions will typically occur at slightly lean conditions and the injected fuels were closer to peak NOx emission conditions (Groenewegen et al., 2011; Groenewegen, 2011).

3.5   Materials Compatibility

3.5.1   Tier II & III Material Compatibility Evaluations

UDRI performed Tier II material compatibility testing on 65 candidate alternative fuels and fuel blends with aromatic contents from up to 24.8% using a series of unique small-sample test methods developed with AFRL (Graham and Minus, 2013). Overall, these tests showed that a considerable variety of fuels were likely to be compatible as neat fuels or as fuel blends with materials that have been in service with conventional petroleum-derived jet turbine fuel. These tests also suggested that fuels high in cycloparaffins could exhibit acceptable seal-swell character with little or no aromatics. This observation became a specific topic of investigation through a program supported as part of the Boeing Company's participation in the FAA's CLEEN program (Graham et al., 2013b).

3.5.2   The Effect of Aromatic Type on the Volume Swell of Nitrile Rubber in Selected SPKs

A barrier impeding the full adoption of synthetic paraffinic kerosenes (SPKs) as alternative fuels is their compatibility with fuel system materials, particularly seals and sealants. As-produced SPKs are composed of normal, branched, and cyclic paraffins resulting in fuels that are relatively inert with respect to their interactions with polymers. This contrasts with conventional fuels which can show significant solvent character in the form of swelling and softening polymeric fuel system materials. There is concern that exposing materials that have been in service with conventional fuel to an alternative fuel may cause them to shrink, harden and fail. The most acute concern is for O-rings which rely on their size and resiliency to perform their function. In this study the volume swell of nitrile rubber was measured using six reference JP-8 fuels, four SPKs and 11 aromatic species/mixtures (Graham et al., 2011). The aromatics were selected to examine the influence of molar volume, polarity, and hydrogen bonding on their performance as swelling promoters. It was found that hydrogen bonding had the largest effect followed by polarity and molar volume. Furthermore, it was found that the same rules apply to the SPK itself with lighter fuels providing a higher baseline volume and this characteristic had a significant

effect on the minimum treatment level. Overall, it was found that within the boiling range of jet fuel the individual effects of molar volume and polarity are relatively subtle and the ability to introduce hydrogen bonding is limited. The most effective fuels combine these factors by minimizing molar volume and maximizing polarity and hydrogen bonding.

3.5.3   The Volume Swell of a Self-Sealing Fuel Tank Material

The effect of alternative fuels on the performance of self-sealing fuel tank materials continues to be an active topic of discussion due in part to the uncertainty associated with conventional ballistic testing. In this study an improved method of measuring the volume swell of self-sealing materials using the optical dilatometry was developed and this new technique was used to compare the volume swell as a function of time of a self-sealing material in a JP-4 (10.5% aromatics), two JP-8 fuels (10.9% and 20.3% aromatics), and an FT fuel (0% aromatics). This study is significant as prior research suggested that the primary factor controlling the rate of volume swell of this type of self-sealing material is the molar volume of the fuel components and not necessarily a molecular characteristic specific to aromatics such as polarity or hydrogen bonding, though it should be noted that the aromatics have relatively small molar volume as compared to the alkane fraction of jet fuel. The issue of JP-4 versus JP-8 is significant in that while the aromatic specification of the two fuels is the same, the aromatics found in JP-4 can be smaller and lighter than those found in JP-8 suggesting that the volume swell of self-sealing materials may be higher in JP-4 as compared to JP-8 despite the fact that the two fuels may have the same aromatic content on a volume basis. This is significant in that most of the present experience-base with self-sealing fuel tanks is based on earlier work with JP-4 and the performance of some alternative fuels may appear to be inferior while in fact they may compare well with the current JP-8 fuels. The results of this study showed that the volume swell of the self-sealing material used in this study gradually increased with the aromatic content of the test fuel. Furthermore, the volume swell of this material in the JP-4 used in this study is higher than that observed for the JP-8 with a similar level of aromatics. This suggests that the volume swell of JP-8 in general may be lower than what has been historically observed for JP-4. Furthermore, this study showed a weak dependence on the aromatic content and that this dependence may be linked to the lower molar volume of the aromatic molecules, which in turn allows them to penetrate the self-sealing material faster than the larger alkane molecules found in jet fuel. However, this effect was quite small, indicating that the use of alternative fuels should have a limited impact on the performance of self-sealing materials.

3.5.4   Evaluating the Influence of Alternative Fuels on the Performance of Static O-ring Seals

A significant concern related to the widespread use of alternative jet turbine fuels is that the low aromatic content typical of these fuels could cause O-ring seals to shrink and fail. To moderate this effect, alternative fuels must be blended with conventional fuels at levels of no more than 50% and with a final aromatic content of at least 8%. A growing body of operational experience has demonstrated that this practice is effective and fuel leaks have not been observed. However, there is a lack of engineering data on safety factors associated with the current practice. In this study a large scale test rig was used to evaluate the influence of alternative fuels on the performance of example variable- and fixed-cavity flexible fuel couplings (Graham et al., 2013c). Briefly, the fixed-cavity fuel couplings proved to be very robust with few fuel leaks

being observed despite being subjected to an extreme fuel-switch from a JP-8 with 17.2% to an IPK with 0.5% aromatics. Using witness o-rings as a guide, it was estimated that leaks began to occur in the nitrile rubber o-rings seals as their compression dropped below approximately 6%. This is well beyond the nominal end of service life of static o-ring seals (~12% compression) and near the nominal end of service life of dynamic o-ring seals (~6% compression). This suggests that the presently specified limit of at least 8% aromatics provides sufficient volume swell to ensure the adequate performance of o-ring seals until they approach the end of their normal service life (Graham, 2014).

3.5.5 A Comparison of the Volume Swell of Nitrile Rubber in JP-5, JP-8, and Jet A

JP-8 is often considered to be identical to Jet A, in a materials compatibility sense, with the exception of the JP-8 additives. Jet A has been used as a blending stock for fuels submitted for Tier II material compatibility analysis. Given that it is often assumed that the behavior of JP-8 will be nearly identical to Jet A it was considered valuable to establish the validity of this assumption. In the course of studies for the U.S. Air Force and the Boeing Company there was an opportunity to compare the volume swell of nitrile rubber in JP-8 and Jet A. Furthermore, data was obtained on the volume swell of JP-5 through a separate study for the U.S. Navy. To provide a preliminary comparison of the overall volume swell behavior of these three fuels data was obtained on a single reference population of a nitrile rubber O-ring material whose plasticizer has been extracted. The results of this study showed that the volume swell character of JP-5 is essentially identical to JP-8 over the range of composition used here. This is likely a consequence of the fact that JP-5 is a narrower distillation cut than JP-8 so that the loss of the relatively high swelling lighter fraction is balanced by a reduction in the lower swelling heavy fraction. In contrast, there is a small offset of approximately 1.4% between the JP-8 and Jet A and small difference in slope. This is likely a consequence of the absence of the fuel additive DiEGME in the Jet A. Specifically, it has been previously shown that DiEGME typically contributes approximately 0.5%-1.0% to the volume swell of elastomers in JP-8. Furthermore, the solubility of DiEGME in these elastomers tends to decrease as the aromatic concentration increases. This results from the fuel becoming an increasingly favorable solvent for DiEGME as the aromatic concentration in the fuel increases. Overall, these results show that the volume swell character of JP-5 is essentially identical to JP-8, while the volume swell character of Jet A is slightly lower. The difference between JP-8 and Jet A is unlikely to have serious consequences for the performance of O-ring seals, but it is important to recognize this difference when comparing the volume swell of elastomers aged in Jet A against reference populations aged in JP-8.

3.5.6 The Influence of Fuel Composition on the Physical Properties of Polymeric Materials

In the absence of chemical reactions, the effects of fuel composition on the physical properties of fuel system polymers have a common root in how the absorbed fuel molecules influence the interactions between adjacent polymer chains. Since the changes that occur in the physical properties of fuel system polymers have a common root, they should be related to each other. For example, as a polymer absorbs fuel its volume increases, modulus decreases, glass transition temperature decreases, elongation increases, etc. Since the changes in physical properties are related, they should change proportionally to each other, meaning that if the objective is to show

that the physical properties of fuel system polymers lie within their normal range of behavior when exposed to an alternative fuel, it is not necessary to measure all of the relevant physical properties, but only one representative physical property. Volume swell is a particularly attractive physical property as it is easy to measure and reflects the overall exchange of components between the material and fuel. In this study the volume swell of nitrile rubber was measured in 12 JP-8 fuels with 10.9% to 23.6% aromatics and an SPK with 0% aromatics (Graham and Minus, 2013). It was demonstrated that changes in volume swell correlated with changes in modulus and the glass transition temperature, illustrating that fuels that exhibit volume swell within the normal range would also exhibit modulus and glass transition temperatures that are within the normal range, and that volume swell could be used as a relatively simple screening tool for assessing the material compatibility of alternative fuels.

3.5.7 The Influence of the Molecular Structure of Paraffins on the Volume Swell of Nitrile Rubber

It has been noted that the volume swell of nitrile rubber soaked in aromatic-free fuels such as SPKs tend to be less than the value predicted by extrapolating the volume swell measured in JP-8 to 0% aromatics. This behavior tends to reduce the volume swell character of fuel blends made with these SPKs making it more difficult to prepare fuel blends that exhibit seal swell character that is comparable to a low aromatic JP-8. Consequently, the objective of this study is to investigate the influence of the molecular structure of paraffins on the volume swell of fuel system polymers using nitrile rubber as a model system. Briefly, it was found that the solubility and volume swell of cycloparaffins was higher than that of a comparable linear or branched alkane. It was also found that the solubility and volume swell of cycloparaffins increased as the ring size increased, and decreased as the size of alkyl pendant groups increased. The substitution position of alkyl groups on the ring did not have a significant effect. These results are thought to be a consequence of the limited conformations of cycloparaffins as compared to linear and branched alkanes. This gives the cycloparaffins a slightly more compact structure and a small degree of polarity not found in linear and branched alkanes. This gives cycloparaffins a seal swell character that is intermediate between linear and branched alkanes and aromatics. It is the absence of cycloparaffins from alternative fuels such as SPKs that gives than a volume swell character that is lower than expected based on extrapolating the volume swell of JP-8 to 0% aromatics. The volume swell character of cycloparaffins suggests that it should be possible to formulate a fuel that is low in aromatics and high in cycloparaffins that exhibits acceptable seal swell character (Graham et al., 2013b).

3.5.8 Material Compatibility of Alternative JP-5 and F-76 Fuels

A statistical approach to assessing the basic material compatibility of alternative JP-5 and F-76 fuels was demonstrated by comparing the volume swell of candidate HRJ-5 and HRD-76 fuels with a range of conventional fuels (Graham, 2012). The HRJ-5 fuels exhibits volume swell character towards nitrile rubber O-rings and common sealants were significantly below the normal range for the reference fuels indicating that the neat fuels are likely to be incompatible for use interchangeably with JP-5. However, these fuels may be compatible with fluorosilicone and fluorocarbon O-ring materials. It was also found the 50% blends of these HRJ-5 fuels with JP-5 may be compatible for use interchangeably with JP-5 and the materials used here, though caution is warranted with nitrile rubber and common sealants until operational experience

indicates otherwise as the volume swell of these materials was near the lower limit of the normal range as measured in the reference fuels. Similarly, it was found that the neat HRD-76 fuels are likely to be incompatible for use interchangeably with F-76 and nitrile rubber O-rings and common sealants, though these fuels are likely to be compatible with fluorosilicone and fluorocarbon O-ring materials. It was also found that 50% blends of these HRD-76 fuels with F-76 are likely be compatible for use interchangeably with F-76 and the materials used here. It was also found that JP-5 is likely to be compatible for use interchangeably with F-76 and the materials used here. Analysis of the fuel absorbed by the test materials show that the HRJ-5 fuels were challenged by a lack of any swelling promoters including cycloparaffins. Furthermore, the molecular weight of these fuels is skewed heavy, further reducing their volume swell character. The HRD-76 fuels also lacked any significant swelling promoters. However, the HRD-76 fuels were lighter than the reference F-76s, giving them seal swell character that was higher than the expected value for an F-76 with 0% aromatics. This tended to lift the volume swell character of the F-76 fuel blends resulting in a more favorable overall volume swell character of the 50% HRD-76/F-76 fuel blends.

3.6 Modeling and Simulation

3.6.1 Experimental and Modeling Studies of Heat Transfer, Fluid Dynamics, and Autoxidation Chemistry in the Jet Fuel Thermal Oxidation Tester (JFTOT)

Modern military aircraft use jet fuel as a coolant before it is burned in the combustor. Prior to combustion, dissolved O_2 and trace heteroatomic species react with the heated fuel to form insoluble particles and surface deposits that can impair engine performance. For safe aircraft operation, it is important to minimize jet fuel oxidation and resultant surface deposition in critical fuel system components. ASTM D3241 "Standard Test Method for Thermal Oxidation Stability of Aviation Turbine Fuels," defines the standard test method for evaluation of the thermal oxidation stability of aviation turbine fuels. The JFTOT is a thermal stability test that measures the tendency for fuel to form deposits via heated tube discoloration and/or an increased pressure drop across an outlet filter. It is used to discriminate between fuels of poor and acceptable thermal stability. However, the fluid dynamics, heat transfer characteristics, extent of oxidation and corresponding deposition that occurs in the JFTOT is not fully understood. An improved understanding of these JFTOT characteristics should help in the interpretation of conventional and alternative fuel thermal stability measurements and provide important information for fuel thermal stability specification enhancements and revisions. In this effort, the JFTOT was modified to include a bulk outlet thermocouple measurement and a downstream oxygen sensor to measure bulk oxygen consumption. Tube deposition profiles were measured via ellipsometry. External tube wall temperatures were measured via pyrometry and a computational fluid dynamic (CFD) with chemistry simulation was developed. The experimental temperature measurements show that the cooling of the outlet bus bar creates a wall hot zone near the center of the tube length. A direct relationship was found between the bulk outlet temperature and JFTOT set point temperature with the bulk outlet less than the set point temperature by 60 to 85 °C. Several fuels were tested at varying set point temperatures with complete oxygen consumption observed for all fuels by 320 °C; a wide oxygen consumption range from 10 to 85% was measured at a set point temperature of 260 °C. The CFD simulations demonstrated the importance of complex, three-dimensional fluid flows on the heat transfer, oxygen consumption, and deposition. These three-dimensional simulations showed considerable

flow recirculation due to buoyancy effects which resulted in complex fuel residence time behavior. An optimized chemical kinetic model of autoxidation with a global deposition submechanism was able to reproduce the observed oxidation and deposition characteristics of the JFTOT. Simulations of deposition were of the right order of magnitude and matched the deposit profile of comparable experimental ellipsometric deposition data. This improved CFD with chemistry simulation provides the ability to predict the location and quantity of oxygen consumption and deposition over a wide range of temperatures and conditions relevant to jet fuel system operation (Sander et al., 2015).

3.6.2 Modeling and Simulation Studies Supporting the Air Force Jet A Conversion Program

With recent increases in jet fuel prices, there is potential for significant cost savings for the Air Force if Jet A can be used instead of JP-8 for aircraft operating in and departing from the CONUS. As a consequence, the Air Force Jet A Conversion Program was implemented to convert from JP-8 to Jet A in CONUS. One important issue was the difference in specification freeze point between JP-8 and Jet A. Jet A has a maximum specification freeze point of -40 °C while the maximum specification freeze point of JP-8 is -47 °C. Although an aircraft may not require a fuel with a freeze point of - 47 °C to avoid in-flight fuel freezing, the Air Force had been using JP-8 as the primary fuel for nearly all aircraft and Jet A as an approved alternate fuel for many aircraft. In order to support the Jet A Conversion Program, modeling and simulation studies were performed to determine the operational impact of Jet A specification fuel on B-52, KC-135, B-1, and F-15 aircraft and to determine relevant fuel temperatures for challenging missions. A second goal was to determine the impact of Jet A specification fuel on LC-130, C-5M, and CV-22 operations and to also determine relevant fuel temperatures for challenging missions associated with these aircraft. It was assumed that the aircraft would either be operating in, or departing from, CONUS bases.

Numerical simulations of aircraft fuel temperatures for a given mission used upper atmosphere weather data to include the effects of cooling at altitude. In addition, ground weather temperatures were used to establish the initial fuel temperature in the simulations. Statistical models were used to generate upper atmosphere and ground weather information. The Air Force Fuel Temperature Prediction Program (Boeing, 2005) that was previously developed by Boeing was used to calculate fuel temperatures for an aircraft flying along a specified flight path. Computational fluid dynamics simulations of the flow and temperatures in a B-52 tank together with fuel temperature measurements there provided additional validation of the Air Force Fuel Temperature Prediction Program. With regard to the KC-135, F-15, B-1, LC-130, and CV-22, the use of Jet A was found to not have a significant operational impact. In addition, this study found that the B-52 flight manual cold weather procedure was conservatively adequate for the missions provided in avoiding fuel freezing potential. However, use of the actual, measured Jet A freeze point was recommended for the B-52 in northern regions. The greater speed of the C-5M offered by improved engines did not provide sufficient ram air heating to offset the lower static air temperatures at high altitudes under challenging cold weather conditions (Briones et al., 2014).

3.6.3 Modeling and Simulation Studies Supporting the Navy Jet A Conversion Program

The Navy has been using JP-8 as its primary fuel at a majority of CONUS Naval Air Stations. There is potential for substantial cost savings for the Navy if Jet A can be used instead of JP-8 for aircraft operating in and departing from CONUS. Jet A has a specification freeze point that is 7 $^\circ$C higher than that of JP-8. UDRI performed a modeling and simulation study to determine the potential operational impacts of using Jet A for flights under challenging, cold weather environments for the EA-6B, MV-22, and P-3 flight vehicles. Another goal was to determine relevant fuel temperatures for challenging missions. It was found that the use of Jet A would not have a significant operational impact on the platforms examined. In addition, the missions studied could avert Jet A freeze potential by monitoring the total air temperature (TAT) and avoiding situations where the TAT approaches the specification freeze point of Jet A (Chiasson and Ervin, 2014).

3.6.4 Hypersonic Modeling Summary

The internal component temperatures of a hypersonic vehicle concept were investigated. A notional hypersonic vehicle outer mold line and approximate internal component locations were provided by the customer. Boundary layer recovery temperatures and convection coefficients were also provided. A conduction/convection model was generated in ANSYS FLUENT to study the transient response of internal component temperatures for the duration of the mission profile. Also, 1-D spatial simulations were performed based on transient heat equations with simple one-step time marching. Both modeling techniques were able to provide component lifetime estimates based on historical knowledge of the operating environment.

3.6.5 Bluff-body Stabilized Turbulent Premixed Flames

Afterburners are used to meet requirements for rapid increase in thrust for take-off and climb. This additional thrust producing device provides the demanded extra thrust for these aircraft operations for short durations without significant penalties in weight and engine complexity. However, the specific fuel consumption, noise, and static and dynamic instability during augmentation is substantially higher than that achieved during non-augmented operation. Therefore, it is important to study flame stabilization and lean blowout past flameholders in order to address dynamic and static instability, respectively. We performed a numerical campaign (Briones et al., 2011a) to shed light on the blowout for bluff body stabilized turbulent premixed flames. Our analyses demonstrated that flow past the flameholder leads to a symmetric shear layer containing a turbulent flame (exhibiting a concave shape at the wake). This flame is attached to the trailing edges of the flameholder. This region exhibits the greatest turbulent flame speed, and thermal expansion increases the flow velocity downstream of the concave-like flame region. Baroclinic torque is the largest source of vorticity. Nevertheless, thermal expansion can act either as a source or a sink. A reducing equivalence ratio forces the flame to propagate downstream, where von Kármán vortices extinguish the flame. The baroclinic torque and prevailing Strouhal number are reduced, while drag increases and stretching becomes the major source of vorticity. At sufficiently low equivalence ratio the flame blows out globally and the wake further shrinks. Stretching is the only contributor to vorticity near the wake after blowout (Briones et al., 2011b). Finally, a trade-off between static and dynamic stability is evident during the blowout process (Briones and Sekar, 2012).

3.6.6 Trapped Vortex Cavity (TVC) Ultra Compact Combustor (UCC)

Conflicting challenges of improving gas turbine engine performance, increasing durability, reducing engine weight, and lowering emissions, while maintaining cost, need to be overcome for developing advanced combustor technologies. The ultra-compact combustor (UCC) attains significant length reduction by incorporating high pressure turbine inlet guide vane (IGV) components into the domain of the combustor as well as using a trapped-vortex cavity (TVC) recessed from the core flow to help stabilize the flow. Reducing the combustor length results in engine weight reductions that improve engine thrust-to-weight ratio. Moreover, the systems level approach of a UCC has the potential for significant total pressure loss reduction between the compressor exit and the turbine rotor inlet. Due to the importance of the TVC-UCC, numerical simulations were performed. The results (Briones et al., 2015c) indicated that the effect of combustion on the flow field is to diminish mainstream flow entrainment into the TVC cavity while distorting the single dominating recirculation flow obtained under non-reacting conditions. Flow spillage from the TVC appears to penetrate deeper into the mainstream flow under reacting flow conditions. Thermal gas expansion spreads more flow in the spanwise direction than for the non-reacting flow condition. Multiple partially premixed turbulent flames are present in this combustor within thickened-wrinkled flamelets and thickened flames regimes. The effect of flow injection site on the cavities was also addressed (Briones et al., 2010a). The effect of adding protuberances at the trailing edge of the TVC and IGV designs (Briones et al., 2011c; Briones et al., 2010b) were also explored.

3.6.7 High-g Cavity (HGC) Ultra Compact Combustor (UCC)

The HGC and TVC differ primarily in the manner in which fuel and air are injected in the recessed cavity. In the HGC-UCC, air is injected inwards along the outer wall of the recessed cavity at an angle to the tangent of the cavity outer wall surface, leading to a bulk circumferential flow within the cavity. This bulk swirl in the cavity generates a high centrifugal force that acts as a buoyant-like force on the flame. Therefore, the effect of centrifugal force on flame propagation velocity of turbulent premixed flames was numerically examined in a constant volume setup (Briones et al., 2015a). It was found that the flame propagation velocity increases with centrifugal force. It reaches a maximum, then falls off rapidly with further increases in centrifugal force. However, the centrifugal force does not substantially increase the turbulent flame speed as suggested by previous experimental investigations. Thus, the flame propagates faster due to the action of Rayleigh-Taylor instability and thermal expansion, which increase the pressure inside the test case. The effect of circumferential cavity (CC) air injection angle and CC-to-main stream flow rate were also studied (Briones et al., 2015b). The potential centrifugal force achieved under real combustor operation in an engine would be no more than 2000 g's with the smallest jet angle and largest CC-to mass flow ratio. The numerical results did not suggest that the turbulent flame speed increases with centrifugal force, which is consistent with the former study.

3.6.8 Effusion Cooling Modeling

Modern gas turbine combustors operate at fuel lean conditions in order to reduce environmentally harmful emissions. Consequently, a large amount of air is used for the fuel injection system, reducing the availability of the coolant air for the combustor dome and liner

cooling. This still represents a substantial amount of the combustor total air. Therefore, high-fidelity analyses of combustor performance must consider effusion cooling. Practical effusion cooling models are nearly non-existent in the community. Thus, a novel parallelized, automated, and predictive imprint cooling model (PAPRICO) was developed for modeling of combustor liners using Reynolds-averaged Navier-Stokes (RANS) (Briones et al., 2016). The methodology involves removing the film and effusion cooling jet geometry from the liner while retaining the cooling hole imprints on the liner. The PAPRICO can operate under two modalities, viz., two-sided and one-sided. For the two-sided PAPRICO model, the imprints are kept on the plenum and combustor sides of the liner. For the one-sided PAPRICO model, the imprints are retained only on the combustor side of the liner and there is no need for a plenum. The PAPRICO model neither needs *a priori* knowledge of the cooling flow rates through various combustor liner regions nor specific mesh partitioning. The imprint mass flow rate, momentum, enthalpy, turbulent kinetic energy, and eddy dissipation rate are included in the governing equations as volumetric source terms in cells adjacent to the liner on the combustor side. Additionally, the two-sided PAPRICO model includes corresponding volumetric sinks in cells adjacent to the liner on the plenum side. A referee combustor liner was simulated using PAPRICO under non-reacting flow conditions. The PAPRICO results were compared against predictions of non-reacting flow results of a resolved liner geometry, against a combustor liner with prescribed mass and enthalpy source terms (simplified liner) and against measurements. The investigation concluded that PAPRICO can qualitatively and quantitatively emulate the local turbulent flow field with a reduced mesh size. The simplified liner fails to emulate the local turbulent flow field.

3.6.9   National Jet Fuel Combustion Program (NJFCP) Referee Combustor

The NJFCP is pursuing numerical techniques and high fidelity physical models that can account for blowout sensitivity to fuel properties. Several simulations were performed and the outcomes of these non-reacting flow simulations were in agreement with the measurements in terms of mass flow splits. Several reacting flow simulations using RANS/FGM/PAPRICO models were performed on the referee combustor. The numerical simulations were compared against measurements, which include mass flow rate splits through various combustor regions, tunable diode laser absorption spectroscopy (TDLAS) temperature, and thermocouple temperature on the combustor liner. This comparison in terms of mass flow splits is acceptable for both the mesh resolved regions and the model cooling jet regions (i.e., dome, forward liner, middle liner, downstream liner, aft liner, and side liner cooling flows). Discrepancies are most importantly due to (1) nonlinearity of the flow field solution (total flow rate through combustor is not equal to the sum of individually measured flow rates through combustor regions), and (2) the lack of viscous losses through cooling jets in PAPRICO. Simulations generally overpredicted the pressure drops, which might be due to RANS and its associated (two-dimensional) wall functions ineffectiveness in predicting viscous boundary layer and flow separation. The predicted line-averaged density-averaged temperature marginally underpredicts the time-averaged TDLAS measured temperature. Plausible explanations are the following: (1) Steady RANS lacks fluctuating scalars for converting Favre-average to time-averaged quantities; (2) the TDLAS weighted absorption spectrum is not linear; and (3) the spray model is over-simplified.

3.6.10 Turbulent Flow, Heat Transfer Deterioration, and Thermal Oxidation of Jet Fuel

As part of an active cooling system, heat is rejected to flowing fuel under conditions of high surface temperatures and large heat fluxes relative to those found in conventional gas turbine engines. Computational fluid dynamics simulations can be used to simulate the flow, heat transfer, and fuel chemistry within fuel system cooling passageways. The standard k-ε turbulence model with the standard wall function, renormalization group k-ε model with an enhanced wall function, and the shear stress transport k-ω model were evaluated for their ability to represent turbulent fuel flow and heat transfer under high heat flux and flow rate conditions. The renormalization group k-ε model with an enhanced wall function provided the greatest fidelity in representation of turbulent thermal and flow behavior studied in heated tube experiments conducted at supercritical pressure. Moreover, the renormalization group k-ε model with an enhanced wall function allowed reasonable simulation of heat transfer deterioration, which was more likely for flow conditions involving a large heat flux with low mass flux rate. As the fuel was heated from the liquid to the supercritical phase, the viscosity temperature dependence was the primary transport property leading to heat transfer deterioration. A pseudo detailed chemical kinetic mechanism was used to study the effect of high heat flux and flow rate on dissolved O_2 consumption together with a global submechanism for the simulation of thermal-oxidative surface deposition. The deposition submechanism developed previously for low heat flux conditions provided reasonable agreement between normalized, measured, and simulated deposit profiles (Jiang et al., 2013).

3.6.11 Effects of Flow Passage Expansion or Contraction on Jet Fuel Surface Deposition

The vast majority of previous flow studies of jet fuel autoxidative deposition have been performed using straight cylindrical tubing of a constant diameter despite the fact that real aircraft fuel systems and nozzles contain complex flow passageways. As a result, the role of this complex flow environment and the resulting changes in heat transfer and flow on fuel oxidation/deposition chemistry are poorly understood. In the current work, experiments and computational fluid dynamics (CFD) modeling were performed for jet fuel flowing through heated tubes that have either a sudden expansion or contraction to study the effect of flow path changes on fuel oxidation and deposition. The experiments were conducted under isothermal wall (205 ºC), laminar flow conditions with monitoring of the outlet dissolved O_2 and post-test measurement of the surface carbon profile. The fuel flow rate was varied to study the role of residence time and oxidation extent on deposition near the geometry change. The CFD model includes a chemical kinetic mechanism, which was used to simulate the autoxidative deposition chemistry. With an expansion, the peak deposit occurs in the wide secondary tube. The CFD simulations show increased deposition caused by a recirculation zone after the flow expansion. For the contraction, increased deposition occurs at the beginning of the narrow secondary tube (Jiang et al., 2012).

3.7 Technology Integration and Demonstration for Thermal Management and Fuel System Operability, Supportability, and Maintainability

3.7.1 Thermal Management-Phase Change Heat Transfer Studies

Although complex, phase change heat transfer has many thermal management applications and will likely be important for thermal management systems onboard future advanced aircraft. The goal of our thermal management research was to further the fundamental understanding of heat and mass transfer during liquid/vapor phase change and the key physical mechanisms that limit thermal transport across solid/liquid/vapor interfaces. The research was conducted in two stages. The first stage concerned the study of evaporating microdroplets, and the second focused on evaporating thin liquid films.

In the first stage, evaporating microdroplets on a variety of surfaces were studied. Since the relatively small diameter of a microdroplet (diameter in the range 70-100 microns) captures effects such as curvature but also minimizes the effect of bulk fluid motion, microdroplets were selected for study. In addition, the small size tends to reduce the computational effort required to simulate the fluid mechanics within the drop and surrounding air. Moreover, this size range of droplets had not yet been extensively studied by previous researchers. In this work, it was found that for evaporation (phase change occurring at the liquid/vapor interface) the thermal resistance is dominated by the liquid/vapor interface and solid surface nano-features would not significantly improve the heat transfer rate. Significant progress was made developing reduced order models of the dynamic drop profile during impingement. In addition, it was found that the high resolution numerical models gave better agreement with experiment when droplet depinning was included. The largest drawback was the uncertainty of the independent variables that determine the accommodation coefficient used in the model of evaporation from the free liquid surface (Briones et al., 2010b; Briones et al., 2012; Putnam et al., 2012).

The physical behavior of evaporating thin liquid films of normal alkanes on silicon wafer substrates was studied in the second stage of this research. The laboratory effort involved the creation of a cell in which a reproducible thin film of either n-octane or n-heptane was formed. In this context, the thin films ranged from 10-20 nanometers thick in the non-evaporating adsorbed film region to several hundred micrometers thick in the intrinsic meniscus region. Measurements, both static and transient, were independently performed using both white light reflectometry (Hanchak et al., 2013) and also a Shack-Hartmann wavefront sensor (Hanchak et al., 2016a). The modeling portion of the thin liquid film research concerned the creation of a numerical model to predict the associated heat transfer and evaporation profiles. As the liquid film is very much longer than its height, a CFD analysis would have been difficult. Instead, a 1-D lubrication-type equation set was developed that included liquid transport, heat transfer from the solid substrate, and evaporation physics based on kinetic theory. The simulations, both static (Hanchak et al., 2014) and transient (Hanchak et al., 2016b), were successful in matching the experimental thin film profiles. The simulations were used to gain insight into the characteristics of the thin film that are not so easily measured, such as the evaporation mass flux profile and the particular form of the intermolecular attraction between the liquid and solid.

3.7.2 Emissions Program

An improved understanding of the complex relationships between fuel chemical and physical properties and the corresponding combustion performance is critical to optimizing fuel formulations and identifying acceptable operating regimes. Fuel properties can impact engine design and operation, and affect the corresponding exhaust emissions produced during combustion. Historically, aviation fuel properties have been relatively consistent, with a small variance depending on crude type and refining process used. However, it is expected that the variability of properties for future aviation fuels will increase due to the potential increase in use of non-conventional crude sources (e.g., tar/oil sands, heavy or sour crude) and development of alternative (e.g., bio- or synthetically derived) fuels. Understanding the impact of fuel properties and combustion conditions on the corresponding gaseous and particulate matter (PM) emissions is an important need to ascertain combustion performance and potential environmental impact. The PM emissions of interest include both the total mass and aerosol characteristics (particle number density and distribution). Regulations for aircraft engines currently exist for trace gaseous emissions and total soot emissions (e.g., smoke number); however, the Environmental Protection Agency (EPA) has recently announced an "endangerment finding" that emissions from certain types of plane engines contribute to pollution that results in climate change and creates health risks. This notice may result in future regulatory limits for aircraft emissions. Therefore, an improved understanding of the effect of fuel properties on the resulting emissions characteristics is needed to identify favorable fuel compositional properties.

UDRI continued to collaborate with AFRL Fuels and Energy Branch to perform work related to the sampling, measurement and quantitation of gaseous and PM emissions from research combustors and turbine engines. Characterization of PM emissions is difficult as there is no existing standard methodology for extractive sampling and quantitation. We used and enhanced the capabilities of the Turbine Engine Research Transportable Emissions Laboratory (TERTEL) to study the effects of fuel properties on the corresponding emissions characteristics. The TERTEL was used for many in-house studies performed utilizing the Elevated Pressure Combustor (EPC) Facility and T63 Turboshaft Engine Facility at WPAFB, and several in-field measurement campaigns. One specific in-field campaign was the Alternative Aviation Fuel Experiment (AAFEX)-II study, a NASA-led campaign to characterize the emissions from CFM56 engines of a NASA DC-8 aircraft at Palmdale, CA operated with Hydrotreated Renewable Jet (HRJ) and Fischer-Tropsch derived fuels. The quality of the effort was recognized by receipt of 2012 NASA Group Achievement Award. The fuels used for these various studies ranged from 2-component surrogate mixtures to broad-distilling petroleum- and alternative-derived fuels (Corporan et al., 2011a; Corporan et al., 2011b; Klingshirn et al., 2012; Corporan et al., 2012; Cain et al., 2013; Corporan et al., 2013a; Corporan et al., 2015a; Corporan et al., 2015b). The data obtained in these efforts have been used to improve the understanding of fuel property to performance relationships and to support the development of computational modeling tools. The latter include efforts being performed under SERDP sponsored programs and the FAA sponsored National Jet Fuel Combustion Program (NJFCP).

UDRI investigated various methodologies for sampling and conditioning combustor and turbine engine exhaust for improved quantitation of PM emissions. We performed studies to evaluate various downstream dilution techniques (as opposed to probe-tip dilution) for sampling PM emissions (Corporan et al., 2011b; Corporan et al., 2013b). Under a SERDP funded program, we

DISTRIBUTION STATEMENT A: Approved for public release. Distribution is unlimited.

designed and constructed a Dilution Chamber (DC) to condition engine exhaust to simulate the corresponding mixing and dilution as the exhaust moves downstream of the engine exit plane. A follow-on Environmental Security Technology Certification Program (ESTCP) program was awarded for testing and demonstration of the DC for comparison of emission samples collected 10-30 meters downstream of the exhaust exit plane. We successfully tested the DC using the T63 engine facility at RQTF and on-wing of a C-17 aircraft at WPAFB (Corporan et al., 2016). Further work will be performed with the DC to determine the overall applicability and potential for use in varying applications. We evaluated the impact of sampling conditions on instrument measurement efficiency (DeWitt et al., 2012b) We developed and evaluated various analytical techniques and methodologies for quantifying trace emissions, including Hazardous Air Pollutants and unburned hydrocarbons, and for determining the phase of carbon in soot emissions (Anneken et al., 2015; Klingshirn et al., 2016). Quantitation of these trace constituents assists with developing correlations between fuel properties and performance.

3.7.3 Shock Tube Combustion Emissions Studies

Studies were performed with the UDRI heated shock tube facility to investigate the effect of fuel composition on the corresponding ignition and basic combustion performance over a wide range of reaction conditions. Studies focused on characterizing the impact of fuel properties on the corresponding ignition delay times. A broader goal was to determine if these ignition characteristics can correlate to combustor operational parameters such as lean blow out limits. Studies were conducted with conventional petroleum-derived fuels, alternatively-derived fuels of varying composition, and model compounds. Studies were performed with the fuels fully pre-vaporized to focus on chemical effects on ignition. Ignition delay times for eight formulated fuels including a conventional jet fuel (JP-8), a coal-derived Fisher-Tropsch (FT) from Sasol, a biodiesel-like jet fuel, an alcohol-to-jet fuel (GEVO ATJ) and four bio-jet fuels derived from corn grain, canola, and soy were measured over a temperature range of 1000 to 1600 K, a pressure of 18 atm and equivalence ratio of 0.5. In addition, the following jet fuel surrogate compounds were evaluated: n-heptane, n-dodecane, 2,2,4,6,6-pentamethylheptane, 2,6,10-trimethyl-dodecane, m-xylene and an n-dodecane/m-xylene blend (77%/23% by volume). Experimental results at the high temperatures showed an indiscernible difference between the ignition delay times for JP-8, FT, biodiesel and the four bio-jets, which were also very similar to those of n-heptane, n-dodecane, 2,6,10-trimethyldodecane and the n-dodecane/m-xylene blend under the same conditions. However, GEVO ATJ exhibited longer ignition delay times at higher pre-ignition temperatures. The ignition delay times of m-xylene were significantly longer under identical conditions whereas 2,2,4,6,6-pentamethylheptane exhibited ignition delay times similar to GEVO ATJ (Balagurunathan et al., 2011; Flora et al., 2015a).

Additional hydrocarbon classes were investigated as surrogate components for jet fuels. Methylcyclohexane (MCH), a commonly used surrogate to represent the monocycloparaffin fraction in jet fuels, was tested over pre-ignition temperatures of 975 to 1800 K, pressures of 2 and 20 atm, equivalence ratios of 0.5 and 1, and argon concentrations of 93% and 98%. It was observed that the equivalence ratio significantly affected the ignition delay time. For the lower argon concentration (Ar = 93%) and higher pressure (P = 20 atm), at lower temperatures (T < ~1150 K) ignition delay times were shorter for rich conditions when compared to leaner conditions. An opposite trend was observed at the higher temperatures (T > ~1150 K). In

addition, longer ignition delay times were observed at the lower pressure (P = 2 atm) and higher argon concentration (Ar = 98%) (Nagulapalli et al., 2012).

To understand the effect of chain branching on ignition and increase the ignition database for branched alkanes, the ignition delay behavior of n-pentane, iso-octane, 2-methylheptane and 2,2,4,6,6-pentamethylheptane was investigated. Mixtures of fuel/O_2/Ar were studied at lean (Φ = 0.5) and stoichiometric conditions at pre-ignition pressures of 2 (excluding iso-dodecane) and 16.4 atm over a range of 950 to1580 K for a fixed argon concentration (93%). An impact of equivalence ratio was observed at low pressure (all fuels) and at high pressure (2-methylheptane only) above approximately 1150 to 1250 K: ignition delay time decreased as Φ decreases. Branching effects were clearly seen at low pressure: ignition delay was lengthened by chain branching. However, these effects were attenuated at high pressure; ignition delay was approximately the same for all four fuels tested, and longer delays were only observed above 1350 K for branched heptanes (Flora et al., 2015a; Flora et al., 2011).

Structural upgrades were performed on the shock tube to enhance operating and experimental capability. In particular, a novel shock tube driver configuration was implemented allowing the variation of dwell time while maintaining the same pre-ignition temperature and pressure, as well as achieving longer dwell times for the investigation of low temperature combustion chemistry (Flora et al., 2015b). Using the upgraded system, ignition delay times were measured over the pre-temperature range 650 to 1100K, at a pressure of ~13 atm at stoichiometric equivalence ratio and air-like conditions (Ar = 79%) for five alternative jet fuel surrogates: n-dodecane/n-heptane, n-dodecane/iso-octane, n-dodecane/methylcyclohexane, n-dodecane/m-xylene, and n-dodecane/n-hexadecane. The lower temperature conditions may have more direct applicability to ignition/light-off in larger-scale combustors. Experimental results show a negative temperature correlation behavior of ignition delay time for all the surrogate mixtures in the pre-ignition temperature range of 860 to 740 K. In particular, quantitative differences in ignition delay times were observed in this region. The m-xylene surrogate showed the longest ignition delay times, and a potential correlation of mid-low temperature ignition delay times with single species DCN was also observed. These results are significant in that they demonstrated that chemical composition may have a potential impact on combustor light-off and ignition. Future studies will be performed to determine if correlations exist between the shock tube results and EPC operation.

3.7.4   Best Practices for Fuel System Contamination Detection and Remediation

Fuel contamination is a broad term commonly applied to a material that causes a fuel to fail Quality Assurance (QA) testing when found in sufficient concentration. The Department of Defense, commercial airlines, NATO, ASME and other organizations provide guidance on periodic product sampling and testing to ensure that the quality of fuel is not degraded before aircraft fueling. Guidance for contamination identification, however, is quite limited. The goal of this study was to propose "Best Practice" procedures to perform when fuel contamination is suspected. Current published guidance from DOD, USAF, US Army, and US Navy was examined to catalog procedures for quality assurance testing and testing results that are compatible with fit-for-purpose fuel. The process of identifying a contamination source and the extent of contamination was not spelled out in any detail in any existing government documentation. Electronic records from the AFTAT (AF Test and Analysis Tool) database were

examined for instances of QA test failures. Case studies requested from the Army and Navy fell into the same categories as AF failures with no discernable long term trends. Wright-Patterson AFB, Jacksonville NAS, Fort Rucker AHB, and Barksdale AFB were visited to view normal field sampling operations and document potential areas of emphasis for sampling guidance. Taken together, these installations represented multiple fueling sites, various levels of bulk storage, helicopter operations, pipeline deliveries, tanker deliveries, fleet refueling, F-24 and JP-5 fuels. In order to assist laboratory identification of particulate contaminants, a list of all fuel wetted components in DOD fuel delivery and storage systems was assembled. Polymeric and elemental composition of various fuel handling and pumping hardware was derived from data contained in the Air Force Civil Engineer Support Agency (AFCESA) HRJ Fuel Study. A generic response plan was proposed using basic crisis management principals along with sampling, analysis, and reporting direction to field and laboratory personnel in dealing with unknown contaminants. Partial results of this study were presented at various meetings, (Vangsness, 2014; Vangsness, 2015a; Vangsness, 2015b; Vangsness, 2015c), while the complete report is awaiting public release by DLA Energy (Vangsness, 2015d).

3.7.5 Electrolyzer Development

The purpose of this project was to develop a highly efficient electrolyzer. Initially, we had proposed to use Nickel Iron (NiFe) nano powder coated electrodes. However, as soon as the project was initiated, we found that the material was no longer available. Therefore, we searched for alternative materials, such as NiFe metal alloys and electro-plated electrodes. The project was initiated with a bench scale 1"x1" single cell electrolyzer to evaluate numerous electrode materials described above for their efficiency. The cell design, such as the electrode gap, and gasket design, and the selection of gas separation diaphragm and gasket materials were also evaluated using the bench scale unit cell. It was found that one type of NiFe alloy, Nickel 36 (Inver®) was highly efficient at splitting water and generating hydrogen (H_2). It was also found that a narrow electrode gap design can help to improve the efficiency. After initial evaluation, the system was scaled up gradually by increasing the electrode surface area and the number of unit cells. We eventually developed a commercial size electrolyzer which had a 2.5 kg/day H_2 generation capacity. The system was further examined for its efficiency and durability. Over a 70% thermal efficiency was achieved under practical operation (2.5 kg/day H_2 generation rate) using the high heating value (HHV). Even though the efficiency had been maintained over 70% during the week long operation, some gasket deterioration and electrode surface contamination was observed. Although we successfully achieved the initial goal by developing the commercial scale electrolyzer, further evaluation and improvement are recommended to develop a turnkey system.

3.7.6 Aluminum to Hydrogen

One method of producing on-demand hydrogen for fuel cells is through the use of aluminum which reacts with water under certain conditions to produce hydrogen. This process can be used for applications as small as portable handheld devices, on-board generation for vehicles, or as large as a hydrogen refueling center. However, the utilization of aluminum for generating on-demand hydrogen is critically dependent on the control of the rate of hydrogen generation from the reaction. Therefore, experiments with micron and nano-sized aluminum powder were conducted and the effects of particle size, reagent quantities, temperature and solution

concentration on the hydrogen generation rate and total yield were analyzed and quantified to determine methods to control the reaction rate. Regression models were developed and yield and rate predictions were confirmed. In general, aluminum nanoparticles were found to have poorer hydrogen yields, but marginally faster reaction rates as compared to micron particles (Ahmed, 2010). The efforts were later extended to larger pieces from waste aluminum cans collected from recycle bins and the effect of the paint and liner layers in the cans were evaluated. The work undertaken served as the basis for subsequent efforts to develop and build a full-scale waste aluminum to hydrogen system for demonstration.

3.7.7   SERDP Team Effort

The cooperative agreement FA8650-10-2-2934 covered two Strategic Environmental Research and Development Programs (SERDP): WP-1577 (partially) and WP-2145 (fully).

The primary objective of WP-1577 was to aid the DoD in meeting current and future National Ambient Air Quality Standards (NAAQS) PM2.5 regulations by establishing the fundamental science base needed to develop and validate accurate soot models for realistic fuels. This program focused on understanding the fundamental effects of fuel chemistry and pressure on soot production and burnout, and on evaluating soot models as well as combustion chemistry mechanisms needed for accurate soot predictions.

The approach involved strongly coupled, mutually supportive experimental and simulation efforts conducted in concert with other members of the SERDP Soot Science Team. The approach included a series of well-controlled laboratory experiments that methodically progressed in complexity in a way that supports a systematic analysis and interpretation of results. State-of-the-art soot models and detailed chemical mechanisms for hydrocarbon fuels have been integrated into a unique simulation code called UNICORN. The results and accomplishments include establishing a database for soot emissions in shock tube, co-flow diffusion flames, opposed jet flames, centerbody flames, and swirl stabilized flames. Fuels investigated included: ethylene, m-xylene, dodecane, and a surrogate JP-8, developed in collaboration with the SERDP Soot Science Team. Detailed chemical kinetics models for ethylene and the JP-8 surrogate fuels with PAH chemistry up to pyrene were also developed in conjunction with the SERDP Soot Science Team. UNICORN simulations were used to interpret experimental results and evaluate the detailed soot and combustion chemistry models in the different experiments. A Sooting NETwork of Perfectly Stirred Reactors (SNETPSR) model for estimating the emissions of actual combustors was further developed in this program. The model incorporates the detailed chemical model for the JP-8 surrogate, which can also simulate paraffinic alternative fuels. This model can be used as a design tool for developing low-sooting gas turbine combustors. This program advanced the ability to develop and evaluate models for predicting soot emissions from gas turbine combustors through the creation of a validation database for a surrogate JP-8 and alternative fuels, and through the creation and validation of chemical kinetic models for the surrogate fuels.

The objectives of WP-2145 were to: (1) establish the scientific base needed to develop accurate models for PM, CO, NOx, total UHC and individual HAPs emissions from military gas turbine engines burning alternative fuels and (2) establish a science-based methodology for selecting practical alternative fuels that minimize emissions. Similar to WP-1577, the research approach involved mutually supportive, tightly-coupled experimental and computational efforts. A series

of well-controlled laboratory experiments were designed and conducted that systematically progress in complexity in a way that permits collective analysis of the data to develop a fundamental understanding of the production of emissions from burning alternative fuels under a wide range of conditions. Experimental facilities being used in the program included: a well-stirred reactor in which chemical kinetics are the controlling process; shock tube experiments focusing on kinetics at realistic pressures; premixed and non-premixed co-flow flame experiments with dependence on kinetics and molecular diffusion at variable pressure; and two combustor test rigs - a model combustor at Penn State and the Referee Combustor at WPAFB, which included the composite effects of all the processes occurring in a gas turbine combustor operated at pressure including spray atomization, vaporization, diffusion, turbulent mixing, stretch, kinetics, and turbulent/chemistry interactions. In parallel to the experimental efforts, computations were performed for each of the experiments, except the Referee Combustor and the T-63 engine. The well-stirred reactor and shock-tube are modeled using the commercial CHEMKIN/SHOCKIN software package whereas UNICORN was used to simulate the co-flow flames and the model combustor at Penn State. To achieve the objective of evaluating and developing accurate models for predicting emissions from alternative fuels, a set of alternative fuels with known chemical kinetics is required. A set of test fuels comprised of pure components, for which chemical kinetic mechanisms exist, was used to cover a range of compositions expected in future alternative fuels. The compounds selected to represent each of the major classes of alkanes present in alternative fuels were: n-heptane, iso-octane, and methyl-cyclohexane, and fuel aromatics was represented by m-xylene. A m-xylene/n-dodecane mix served as a simple surrogate for jet fuel and the combustion studies provided direct experimental evidence of the effects of changing jet fuel composition on emissions.

The findings from the experimental and modeling work conducted in this program support the following statements when comparing the binary mixtures of paraffinic compounds representative of alternate fuels to the m-xylene fuel, which is a surrogate for JP-8:

- Effects on NOx, CO and total hydrocarbons were small, generally 10% or less.

- Effect on PM emissions was substantial, with reductions in PM emissions by one order of magnitude.

- Low molecular weight components of UHC emissions were not strongly affected.

- Some high molecular weight UHC species increased in concentration depending on the fuel composition, e.g., benzene emissions were higher for the m-xylene fuel and the methyl-cyclohexane fuel.

- Unique UHC species were present for some of the fuels, e.g., iso-butene for the iso-octane fuel and toluene for the m-xylene fuel.

In addition to these specific findings on alternative fuel effects, the program led to three major insights that advance the state of the art understanding of engine emissions:

- The experimental work in the T-63 engine and the Referee Combustor demonstrated that substantial fractions (30 to 50%) of the UHC emissions can be traced to unreacted fuel.

This finding means that the composition of any fuel directly affects the UHC emissions, including emissions of HAPs that are present in the fuel.

- The experimental and modeling studies conducted to understand the linear behavior in UHC emissions at low power led to the important new insight that UHC emissions form in a gas turbine combustor when reacting premixed fuel-air mixtures are quenched. Thus, the emissions are not determined by reaction kinetics alone, but rather by coupling of chemical kinetics, fluid mechanics, and flame extinction processes. Furthermore, multiple quenching mechanisms can lead to UHC emissions including mixing to very lean fuel-air ratios, quenching due to flame propagation into regions of low fuel-air ratio, and flame stretch. Accurate modeling of the emissions from a gas turbine combustor will require that each of the multiple quenching mechanisms be modelled accurately. The current program included modeling and simulations of quenching via mixing.

- The experimental and modeling work related to chemical effects on PAH and soot formation led to substantial progress toward resolving the longstanding issue within the combustion community related to modeling the effect of aromatic species on soot concentration and the spatial distribution of soot. Enhanced PAH reactions in the chemical kinetic mechanism and improvements in the soot model to track particle size distribution led to substantially improved ability to predict soot concentrations and distributions in all of the co-flow flames.

In addition to these fundamental insights the program also made the following important fundamental contributions:

- The kinetic model with detailed PAH chemistry that was developed in this program is a major contribution from this work because it was a critical element in the advancement of the soot modeling capability. Development of this model was not a part of the original program design, but became necessary when kinetic model development within the combustion community did not evolve as quickly as anticipated. In addition, the modeling studies have demonstrated that this mechanism captures many key trends in gas-phase emissions from gas-turbine engines.

- The data base from the various experiments made using the same set of test fuels is a unique resource for researchers who are simulating gas turbine combustion because of the breadth of chemical and physical processes encompassed across the experimental devices and because of the wide range of experimental conditions used.

The key findings and contributions from this program have substantially extended the fundamental knowledge required to evaluate a science-based methodology for selecting alternative fuels based on their emissions characteristics (Roquemore et al., 2012).

3.8   Subcontracted Programs

UDRI employed substantial subcontracting efforts when a particular expertise was needed to augment research programs. The decision to retain subcontractors was made in consultation with the AFRL project leadership. Below are briefly summarized the primary subcontracting tasks employed during the cooperative agreement period. Additional technical information on these

efforts are included in technical reports and publications listed in the list of publications (Appendix BB).

Aerodyne Research Inc. – A primary goal of this work was to establish a science base that can be used to develop gas turbine combustion models for alternate fuels that can accurately predict emissions. Another goal was to establish a science base methodology for selecting practical alternative fuels that minimize emissions. The subcontractor provided support for the development of a science base for hydrocarbon (HC) emissions from aircraft engines using alternative fuels. This support consisted of consultation and advice for planning alternate fuel experiments, making measurements of HC species in different burners used in the program, interpreting results, and providing ideas for a general methodology for estimating emissions from alternative fuels.

Battelle Memorial Institute – Battelle was tasked with the design and operation of the Aerospace Advanced Fuel Research Facility at AFRL. The upgrading unit was designed to convert feed wax (or other alkane hydrocarbons) to fuel, hydrotreat seed and plant oils as well as hydrogenating oxygenated bio-oils produced by a variety of other processes. The actual jet fuel fraction was separated and collected in a product recovery unit based on naphtha fractionation followed by vacuum distillation of the jet-fuel fraction. Larger molecules were recycled to the front end of the process for further conversion.

Boeing Company – The goal of this program was to provide technical support for modeling of fuel tank temperatures during long-duration flight to support the Jet A CONUS conversion program. Boeing developed a program to assist airlines in conducting route planning on long range polar flights, where fuel temperatures could approach the freeze point of Jet A. This program was modified to accept more general fuel tank and fuel system information. The program was used to evaluate the C-17 fuel system and fuel temperature during simulated aircraft missions. The C-17 was utilized as a validation airframe for this program and based on the successful correlation of the data; other older aircraft in Air Force inventory were modeled and successfully analyzed without costly flight testing. The study developed potential fuel temperature profiles for the F-15, B-52, B-1, and KC-135 when operating out of CONUS airbases utilizing Jet A in support of the aircraft fleet. Boeing Research and Technology conducted the collection of this data and support of this study utilizing the expertise of Boeing Defense, Space & Security.

Clemson University – The goal of this program was to develop methodologies for the synthesis and characterization of reactive nanomaterials, such as nanoscale aluminum particles and related energetic composites. Work was performed in the exploration of new materials and technical approaches toward the development of renewable energy sources, such as hydrogen generation-storage and more effective harvesting of solar energy. This subcontractor was also tasked with improving our understanding of the photoexcited state properties of carbon dots as relevant to their energy conversion and storage functions, thus to guide the further improvements and technological developments.

Creare Inc. – This program was used to develop novel tools for modeling and analyzing ignition in combustion systems. The approach involved breaking up the overall ignition process into three sub-processes: (1) the igniter spark process, (2) local ignition, and (3) propagation. All three sub-

processes are highly complex and deserving of significant investigation. The program focused on developing a sub-model for local ignition.

GE Aviation, Honeywell Aerospace, Rolls-Royce, United Technologies Research Center, and Williams International – The primary gas turbine engine manufacturers were enlisted to provide support to the steering committee of the FAA's National Jet Fuel Combustion Program. The objective of this program is to reduce the cost of ASTM D4054 qualification of alternative fuels for use in gas turbine engines. This objective is to be achieved by developing and demonstrating a new streamlined evaluation methodology to assess combustion risks associated with alternative fuels, eliminating or reducing the need for component/engine tests, and defining a methodology for evaluating fuel effects on combustion. This subcontractors provided the following support to the program:

- Perform program management type tasks including program planning and execution, support of steering committee (and any sub-committee) tasks, travel, internal cost accounting and contracts administration.
- Aid in the selection coordination of test fuels, and identifying fuel properties.
- Establish a streamlined methodology for evaluating test fuels.
- Aid in the kinetics, surrogates, and model development and validation by University team members: including support of planning and execution of basic and advanced combustion tests, definition of the tests to be performed and development of procedures, data reduction.
- Aid in atomization test planning and execution and model development.
- Aid in the development of a vaporization model.
- Aid in the design, fabrication and testing of a referee single-cup combustion rig; define instrumentation and test procedures as necessary to generate combustor operability and emissions data for model validation; testing on-site and provide data reduction.
- Aid in model and tools generation and validation.

Georgia Tech Research Corporation – This program investigated the application of small-scale combustors in the generation of syngas (SG) containing large concentrations of hydrogen and carbon monoxide (without soot) while burning Jet A in fuel-rich mixtures. The dependence of the composition of the generated SG was studied as a function of equivalence ratio, loading and temperature of the combustion process, and the configuration/design of the combustor. The subcontractor investigated the effect of the addition of SG on Jet A ignition in flowing vitiated air-fuel mixtures. The dependence of the ignition process was studied as a function of the composition and temperature of the SG, the composition and temperature of the vitiated air-fuel mixture, and the momentum ratio and relative orientations of the SG and vitiated air-fuel streams.

Lockheed Martin Aeronautics – The goal of this program was to provide technical support for modeling of fuel tank temperatures during long-duration flight to support the Jet A CONUS conversion program. The subcontractor provided aircraft fuel tank geometry, system operating characteristics, and relevant data to evaluate low fuel temperature characteristics of the P-3 aircraft. They supported UDRI modeling of the P-3 based on the Lockheed Martin supplied geometry data and system operation. The input provided was used in a modeling effort

performed by UDRI to help identify fuel freeze point issues that could result from unrestricted operation of the P-3 aircraft from CONUS bases using Jet A fuel.

Northrop Grumman Technical Services – The goal of this program was to provide technical support for modeling of fuel tank temperatures during long-duration flight to support the Jet A CONUS conversion program. The subcontractor helped identify fuel freeze point issues that could result from unrestricted operation of the EA-6 aircraft from CONUS bases using Jet A fuel. They provided aircraft fuel tank geometry, test data, and system operating characteristics to evaluate low fuel temperature characteristics of this aircraft. They supported UDRI modeling of the EA-6 based on supplied geometry data and system operation. This support also included assistance with the Northrop Grumman fuel tank model previously developed for the Air Force. They also provided fuel temperature data cold fuel temperature related information on the EA-6 aircraft.

Pennsylvania State University – A primary goal of this work was to establish a science base that can be used to develop gas turbine combustion models for alternate fuels that can accurately predict emissions. Another goal was to establish a science base methodology for selecting practical alternative fuels that minimize emissions. The subcontractor designed experiments that to provide insight into the formation of unburned hydrocarbons (UHC), hazardous air pollutants (HAPs), non-volatile particulate emissions (PM), carbon monoxide (CO), and oxides of nitrogen (NOx) emissions as a function of alternate fuel properties. They also performed experiments using laboratory flames and model combustors burning selected alternate fuels at pressures up to five atmospheres.

Princeton University – The goal of the effort was to formulate surrogate mixtures to simulate the chemical and prevaporized combustion characteristics of a specific JP-8 fuel. The JP-8 of interest should have properties typical of flight line fuel. Testing of these surrogate mixtures and the specific petroleum-derived JP-8 in the same experimental venue(s) provided evaluation data of a solvent-blending approach to develop cost-effective surrogate fuels. One fuel surrogate blend was to be comprised to meet the target JP-8 prevaporized combustion property targets (H/C ratio, Derived Cetane Number (DCN), Threshold Sooting Index (TSI), Average Molecular Weight (MW ave) while having a distillation range consistent with a typical JP-8 fuel, while the second would be formulated to maintain the same prevaporized combustion prope1iy targets, but with a bi-modal distillation range. Additionally, a four component surrogate mixture composed of n-dodecane, iso-octane, n-propyl benzene, and 1,3,5-trimethyl benzene was be determined to replicate the prevaporized combustion property targets of the specific JP-8 fuel sample.

Saint Louis University – This subcontract was created for the study of new methods for the stabilization of small (< 20 nm) of aluminum nanoparticles (Al NPs). The subcontractor developed a complete thermodynamic model to describe the size-dependence of the reaction enthalpy of pyrophoric nanostructure oxidation. They studied the stabilization of Al NPs to build upon new reaction methodologies of direct epoxide polymerization on the nanoparticle core. They also studied the possibility of direct stabilization of Al NPs with pure hydrocarbons.

United Technologies Research Center – A primary goal of this work was to establish a science base that can be used to develop gas turbine combustion models for alternate fuels that can accurately predict emissions. Another goal was to establish a science base methodology for selecting practical alternative fuels that minimize emissions. The subcontractor identified

alternative fuels to be used in study of emissions. The subcontractor assembled full chemistry models for identified alternative fuels and these emissions models included chemistry for: unburned hydrocarbons (UHC), hazardous air pollutants (HAPs), non-volatile particulate emissions (PM), carbon monoxide (CO), and oxides of nitrogen (NOx) emissions. They used CHEMKIN-based codes and perfectly-stirred reactor codes to evaluate emissions models with data collected by other members of the Air Force Alternate Fuel Emissions Team. They estimated the accuracy of the models and identified chemical reactions that contribute to the errors.

University of Texas at Austin – The goal of this program was the development of parametric models of greenhouse gas emissions of fuel processing based on Fischer Tropsch processing conditions. They performed life cycle analysis of greenhouse gas emissions for the processing of Fischer-Tropsch fuels made from natural gas, coal, and coal - biomass mixtures. The greenhouse gas emission estimates were compared to a petroleum baseline fuel. The estimates indicated that, at least for some FT fuels, the greenhouse gas footprints can be made comparable to, or lower than, the greenhouse gas footprints of petroleum based fuels. However, there were significant uncertainties in the greenhouse gas emission estimates. The two largest uncertainties in the greenhouse gas emission estimates were (1) the method of addressing indirect impacts of biomass production, and (2) the yields of synthetic paraffinic kerosene (SPK) from the coupled Fischer-Tropsch synthesis/upgrading reactions.

4   REFERENCES

1. R. Adams, S. Zabarnick, Z. West, R. Striebich, and D. Johnson, "Chemical Analysis of Jet Fuel Polar Heteroatomic Species via High Performance Liquid Chromatography with Electrospray Ionization-Mass Spectrometric Detection," Energy & Fuels, Vol. 27, pp. 2390-2398, 2013.

2. F. Ahmed, "Experimental Studies in Hydrogen Generation for Fuel Cell Applications Using Aluminum Powder," M.S. Thesis, University of Dayton, Dayton, OH, December 2010.

3. D. Anneken, R.C. Striebich, M.J. DeWitt, C. Klingshirn, and E. Corporan, "Development of methodologies for identification and quantification of hazardous air pollutants from turbine engine emissions," Journal of the Air and Waste Management Association, Vol. 65, pp. 336-346, 2015.

4. J. Balagurunathan, G. Flora, S. Saxena, M.S.P. Kahandawala, M.J. DeWitt, S.S. Sidhu, and E. Corporan, "Ignition Delay Times of a Range of Alternate Jet Fuels and Surrogate Fuel Candidate Hydrocarbons under Fuel-Lean Conditions: a Shock Tube Study," Presented at the 49th American Institute of Aeronautics and Astronautics Aerospace Sciences Meeting including the New Horizons Forum and Aerospace Exposition, American Institute of Aeronautics and Astronautics, Orlando, FL, 2011.

5. D. L. Blunck, J. Cain, R. C. Striebich, S.D. Stouffer, and W.M. Roquemore, "Fuel Rich Combustion Products from a Well-Stirred Reactor Operated using Traditional and Alternative Fuels", 2012 Central States Combustion Meeting, April 22-24, 2012.

6. The Boeing Company, "USAF Fuel Temperature Prediction Program User Guide," August 2005.

7. A. M. Briones and B. Sekar, "Effect of von Kármán Vortex Shedding on Regular and Open-slit V-gutter Stabilized Turbulent Premixed Flames," Spring Technical Meeting of the Central States Section of the Combustion Institute, April 22–24, Dayton, OH, 2012.

8. A.M. Briones, J. Zelina, and V. Katta, "Flame Stabilization in Small Cavities," AIAA Journal, Vol. 48, pp. 224-235, 2010a.

9. A.M. Briones, J.S. Ervin, S. Putnam, L. Byrd, and L. Gschwender, "Micrometer-sized Water Droplet Impingement Dynamics and Evaporation on a Flat Dry Surface," Langmuir, Vol. 26, pp. 13272–13286, 2010b.

10. A.M. Briones, B. Sekar, H. Thornburg, and J. Zelina, "Effect of Vane Notch and Ramp Design on the Performance of a Rectangular Inter-Turbine Burner," 48th AIAA Aerospace Sciences Meeting including the New Horizons and Aerospace Exhibition," Orlando, FL, January, 2010b.

11. A. M. Briones, B. Sekar, and H. Thornburg, "Characteristics of Bluff Body Stabilized Turbulent Premixed Flames," Proceedings of the ASME Turbo Expo 2011: Power for Land, Sea, and Air, Vancouver, British Columbia, Canada, June 6-10, 2011a.

12. A. M. Briones, B. Sekar, H. Thornburg, and K.O. Granlund, "V-gutter Flameholder Lean Premixed Flame Stabilization and Blowout," XX International Symposium on Air Breathing Engines, September 12-16, Goteborg, Sweden, 2011b.

13. A.M. Briones, B. Sekar, and H.J. Thornburg, "Enhanced Mixing in Trapped Vortex Combustor with protuberances Part 2: Two-Phase Reacting Flow," 41st AIAA Fluid Dynamics Conference and Exhibit, Honolulu, HI, June 27-30, 2011c.

14. A.M. Briones, J.S. Ervin, L.W. Byrd, and S.A. Putnam, A. White, J.G. Jones, "Evaporation Characteristics of Pinned Water Microdroplets," J. Thermophys. Heat Transfer, Vol. 26, pp. 480-493, 2012.

15. A. Briones, A. Chiasson, C. Delaney, M. Elsass, J.S. Ervin, and M. Hanchak, "Studies of the Low-Temperature Use of Jet A to Replace JP-8 in Tankers, Fighters, Bombers, and Transport Aircraft," AFRL-RQ-WP-TR-2014-0149, 2014.

16. A.M. Briones, B. Sekar, and T.J. Erdmann, "Effect of Centrifugal Force on Turbulent Premixed Flames," Journal of Engineering for Gas Turbines and Power, Vol. 137, pp. 011501, 2015a.

17. A.M. Briones, D.L. Burrus, T.J. Erdmann, and D.T. Shouse, "Effect of Centrifugal Force on the Performance of High-g Ultra Compact Combustor," Proceedings of ASME Turbo Expo, June 15-19, Montréal, Canada, 2015b.

18. A.M. Briones, B. Sekar, D.T. Shouse, D.L. Blunck, H.J. Thornburg, and T.J. Erdmann, "Reacting Flows in Ultra-Compact Combustors with Combined-diffuser Flameholder," Journal of Propulsion and Power, Vol. 31, pp. 238-252, 2015c.

19. A.M. Briones, B.A. Rankin, S.D. Stouffer, T.J. Erdmann, and D.L. Burrus, "Parallelized, Automated, and Predictive Imprint Cooling Model for Combustion Systems," J. Eng. Gas Turbines & Power, in press, 2016.

20. L.M. Brown, T.S. Gunasekera, and O.N. Ruiz, "Draft genome sequence of *Pseudomonas aeruginosa* ATCC 33988, a bacterium highly adapted to fuel-polluted environments," Genome Announc., Vol. 2, pp. 13-14, 2014.

21. L.M. Brown, T.S. Gunasekera, L.L. Bowen, and O.N. Ruiz, "Draft Genome Sequence of *Rhodovulum* sp. Strain NI22, a Naphthalene-degrading Bacterium", Genome Announc., Vol. 3, pp. 1-2, 2015.

22. L.M. Brown, R.C. Striebich, T.S. Gunasekera, and O.N. Ruiz, "Draft Genome Sequence of *Gordonia sihwensis* S9, a Branched Alkane-Degrading Bacterium," Genome Announc., Vol. 4, pp. 622-616, 2016.

23. C.E. Bunker, M.J. Smith, K.A.S. Fernando, B.A. Harruff, W.K. Lewis, J.R. Gord, E.A. Guliants, and K.D. Phelps, "Spontaneous Hydrogen Generation from Organic-Capped Al Nanoparticles and Water," ACS Appl. Meter. Interf., Vol. 2, pp. 11-14, 2010.

24. J. Cain, D. Blunck, E. Corporan, M.J. DeWitt, R. Striebich, D. Anneken, C. Klingshirn, and W.M. Roquemore, "Characterization of Gaseous and Particulate Emissions from a Turboshaft Engine Burning Conventional, Alternative and Surrogate Fuels" *Prepr.-Am. Chem. Soc., Div Pet. Chem.*, August, 2012.

25. J. Cain, M.J. DeWitt, D. Blunck, E. Corporan, R. Striebich, D. Anneken, C. Klingshirn, W.M. Roquemore, and R. Vaner Wal, "Characterization of Gaseous and Particulate Emissions from a Turboshaft Engine Burning Conventional, Alternative and Surrogate Fuels" Energy & Fuels, Vol. 27, pp. 2290-2302, 2013.

26. A. Chiasson and J.S. Ervin, "Studies of the Use of Jet A to Replace JP-8 in the EA-6B, MV-22, and P-3: Implications of the Difference in Specification Freeze Point," AFRL-RQ-WP-TR-2015-0020, 2014.

27. E. Corporan, M.J. DeWitt, C.D. Klingshirn, R. Striebich, and M.-D. Cheng, "Emissions Characteristics of Military Helicopter Engines with JP-8 and Fischer-Tropsch Fuels," *Journal of Propulsion and Power*, Vol. 26, pp. 317-324, 2010

28. E. Corporan, M.J. DeWitt, C.D. Klingshirn, D. Anneken, and R. Striebich, "Alternative Jet Fuels – Turbine Engine Emissions Characteristics," Presented at the 12th International Conference on Stability, Handling, and Use of Liquid Fuels, Sarasota, FL, 2011a.

29. E. Corporan, T. Edwards, L. Shafer, M.J. DeWitt, C. Klingshirn, S. Zabarnick, Z. West, R. Striebich, J. Graham, and J. Klein, "Chemical, Thermal Stability, Seal Swell, and Emissions Studies of Alternative Jet Fuels," Energy & Fuels, Vol. 25, pp. 955-966, 2011a.

30. E. Corporan, M.J. DeWitt, C.D. Klingshirn, and D. Anneken, "Alternative Fuels Test on a C-17 Aircraft: Emissions Characteristics," AFRL-RZ-WP-TR-2011-2004, 2011b.

31. E. Corporan, M.J. DeWitt, C.D. Klingshirn, D. Anneken, L. Shafer, and R. Striebich, "Comparisons of Emissions Characteristics of Several Turbine Engines Burning Fischer-Tropsch and Hydroprocessed Esters and Fatty Acids Alternative Jet Fuels," *Proceeding of ASME Turbo Expo 2012*, GT2012-68656, Copenhagen, Denmark, June 11-15, 2012.

32. E. Corporan, T. Edwards, M.J. DeWitt, C. Klingshirn, R. Striebich, L. Shafer D. Anneken, and D. Caswell, "Investigation of Combustion and Emissions Performance of Alternative and Conventional Fuels at the Limits of the Jet Fuel Specification," Proceedings of the 13th International Conference on Stability, Handling, and Use of Liquid Fuels, Rhodes, Greece, October, 2013a.

33. E. Corporan, M.J. DeWitt, and C. Klingshirn, "Evaluation of Downstream Dilution Techniques for the Sampling of Turbine Engine Particulate Matter," *SAE 2013 AeroTech Congress & Exhibition, Paper 2013-01-2130,* September, 2013b.

34. E. Corporan, S. Stouffer, M. DeWitt, T. Hendershott, and C. Klingshirn, "Evaluation of Fuel Aromatic Impacts on Combustion Characteristic in a Newly Developed Turbine Engine Combustor Research Facility at AFRL ", IASH 2015, the 14TH International Symposium on Stability Handling and use of Liquid Fuels Charleston, South Carolina USA, 4-8 October 2015a.

35. E. Corporan, T. Edwards, M.J. DeWitt, C. Klingshirn, R. Striebich, L. Shafer, D. E. Corporan, T. Edwards, C. Neuroth, D. Shouse, S. Stouffer, T. Hendershott, C. Klingshirn, M. DeWitt, S. Zabarnick, and J. Diemer, "Initial Studies of Fuel Impacts on Combustor Operability and Emissions at AFRL," Poster presented at IASH 2015, 14TH International Symposium on Stability Handling and use of Liquid Fuels Charleston, South Carolina USA, 4-8 October 2015b.

36. E. Corporan, M. DeWitt, C. Klingshirn, M.-D. Cheng, R. Miake-Lye, J. Peck, Z. Yu, J. Kinsey, and B. Knighton, "Demonstration of Novel Sampling Techniques for Measurement of Turbine Engine Volatile and Non-Volatile Particulate Matter (PM) Emissions", ESTCP Project WP-201317 Final Report, July 2016.

37. M.J. DeWitt, "Development and Evaluation of Alternative Aviation Fuels," Presented at the 5th Annual STARS (Spotlight on Technology, Arts, Research and Scholarship) Symposium, 18 September 2014, University of Dayton, Dayton, OH, 2014.

38. M.J. DeWitt, S. Zabarnick, T. Williams, Z. West, L. Shafer, R. Striebich, S. Breitfield, R. Adams, R. Cook, C.L. Delaney, and D. Phelps, "Overview of Efforts to Determine Minimum Required FSII Use and Procurement Limits for USAF Aircraft," Presented at the 12th International Conference on Stability, Handling, and Use of Liquid Fuels, Sarasota, FL, 2011.

39. M.J. DeWitt, Z. West, A. Mescher, N. Stelzenmuller, S. Zabarnick, and T. Edwards, "Effect of Aromatics Addition on the Thermal-Oxidative Stability of Alternative Jet Fuels," Preprints – American Chemical Society, Division of Energy & Fuels, Vol. 57(2), pp. 826-827, 2012a

40. M.J. DeWitt, E. Corporan, C. Klingshirn, and X. Li-Jones, "Determination of Particle Counting Pressure Correction for Turbine Engine Exhaust Sampling," presented at American Association for Aerosol Research Annual Conference, Minneapolis, MN, October, 2012b.

41. M.J. DeWitt, Z. West, S. Zabarnick, L. Shafer, R. Striebich, and T. Edwards, "Effect of Addition of Aromatics on the Thermal Oxidative Stability of Alternative Aviation Fuels," Proceedings of the 13th International Symposium on Stability, Handling, and Use of Liquid Fuels, October 2013a.

42. M.J. DeWitt, S. Zabarnick, T.F. Williams, Z. West, L. Shafer, R. Striebich, S. Breitfield, R. Adams, R. Cook, D. K. Phelps, and C.L. Delaney, "Determination of the Minimum Use Level of Fuel System Icing Inhibitor (FSII) in JP-8 that Will Provide Adequate Icing Inhibition and Biostatic Protection for Air Force Aircraft (Public Release Version of Technical Report AFRL-RZ-WP-TR-2009-2217)," AFRL-RQ-WP-TR-2013-0271, 2013b.

43. M.J. DeWitt, R. Cook, L. Shafer, S. Zabarnick, and C. McCormick, "Evaluation of ASTM D5006 for Accuracy, Repeatability, and Reproducibility for Fuel System Icing Inhibitor (FSII) Concentrations < 0.10% by Volume and Varying Fuel Composition," AFRL-RQ-WP-TR-2013-0070, 2013c.

44. M.J. DeWitt, Z. West, S. Zabarnick, L. Shafer, R. Striebich, A. Higgins, and T. Edwards, "Effect of Aromatics on the Thermal-Oxidative Stability of Synthetic Paraffinic Kerosene," Energy & Fuels, Vol. 28, pp. 3696-3703, 2014.

45. J. T. Edwards, L. M. Shafer, and J. K. Klein, "U.S. Air Force Synthetic Paraffinic Kerosene (SPK) Fuel Research," AFRL-RQ-WP-TR-2013-0124, 2013.

46. J. T. Edwards, L. M. Shafer, and J. K. Klein, "U.S. Air Force Hydroprocessed Renewable Jet (HRJ) Fuel Research," AFRL-RQ-WP-TR-2013-0108, 2013.

47. J.T. Edwards, S.A. Hutzler, R.E. Morris, and P.A. Muzzell, (Contributions by L. Shafer) "Tri-Service Jet Fuel Characterization for DOD Applications: Compositional Analysis" Task 1, FINAL REPORT, SwRI® Project No. 08.17149.36.100. April 2015.

48. G. Flora, S. Saxena, M.S.P. Kahandawala, M.J. DeWitt, E. Corporan, and S.S. Sidhu, "Ignition Delay Measurements for 2-Methylheptane/O2/Ar Mixtures Behind Reflected Shock Conditions," Presented at the 7th US National Combustion Meeting, Atlanta, GA, 2011.

49. G. Flora, J.P. Cain, M.S.P. Kahandawala, M.J. DeWitt, E. Corporan, and S.S. Sidhu, "The Effect of Chain Branching on Ignition Delay of C5 and C7 Backbone Fuels: n-Pentane, iso-Octane, 2-Methylheptane and iso-Dodecane," Presented at the 9th US National Combustion Meeting, Cincinnati, OH, 2015a.

50. G. Flora, J.P. Cain, M.S.P. Kahandawala, M.J. DeWitt, E. Corporan, and S.S. Sidhu, "Time-dependent Speciation of Ethylene Combustion under Fuel Rich Conditions—a Novel Shock Tube Approach," Presented at the 9th US National Combustion Meeting, Cincinnati, OH, 2015b.

51. J. Graham, "A Statistical Approach to Assessing the Material Compatibility of Alternative JP-5 and F-76 Fuels", Final Report, UDR-TR-2012-153, September, 2012

52. J. Graham, "Assessment of Long Term O-Ring/Fuel Compatibility," Final Report, UDR-TR-2014-129, June, 2014

53. J. Graham, D. Minus, and T. Edwards, "The Effect of Aromatic Type on the Volume Swell of Nitrile Rubber in Selected Synthetic Paraffinic Kerosenes," 12th International Conference on Stability, Handling and Use of Liquid Fuels, Sarasota, Florida, 16-20 October 2011.

54. J. Graham and D. Minus, "Small-Sample Test Methods for Assessing the Compatibility of Alternative Fuels with Polymeric Materials," Proceedings SAMPE 2013 National Meeting, Long Beach, California, May 6-9, 2013.

55. J. Graham, M. Laber, D. Gasper, D. Minus, and T. Edwards, A. Fletcher, "Progress on Evaluating the Influence of Alternative Fuels on the Performance of Static O-ring Seals Using Flexible Fuel Couplings," SAMPE 2013 National Meeting, Long Beach, California, May 6-9, 2013a.

56. J. Graham, T. Rahmes, M. Kay, J. Belières, J. Kinder, S. Millett, J. Ray, W. Vannice, and J. Trela, "Evaluating the Impact of SPK Fuels and Fuel Blends on Non-metallic Materials used in Commercial Aircraft Fuel Systems," DTFA WA-10-C-0030, Final Report, The Boeing Company, Seattle, WA, December, 2013b.

57. J.-R.Groenewegen, S. Sidhu, J. Hoke, C. Wilson, and P. Litke, "The Performance and Emissions Effects of Utilizing Heavy Fuels and Algae Based Biodiesel in a Port-Fuel-Injected Small Spark Ignition Internal Combustion Engine," 47th AIAA/ASME/ SAE/ASEE Joint Propulsion Conference & Exhibit, Joint Propulsion Conferences, (AIAA 2011-5807), 2011.

58. J.-R. Groenewegen, "The Performance and Emissions Characteristics of Heavy Fuels in a Small, Spark Ignition Engine," M.S. Thesis, University of Dayton, Dayton, 2011.

59. T.S. Gunasekera, R.C. Striebich, S.S. Mueller, E.M. Strobel, and O.N. Ruiz, "Transcriptional Profiling Suggests that Multiple Metabolic Adaptations are Required for Effective Proliferation of Pseudomonas aeruginosa in Jet Fuel," Env. Sci Tech., Vol. 47, pp. 13449-13458, 2013.

60. T.S. Gunasekera and O.N. Ruiz, "Transcriptional Response of Pseudomonas aeruginosa to Jet Fuel," Proceedings of the 13th International Conference on Stability, Handling and use of Liquid Fuels, Rhodes, 2014.

61. M.S. Hanchak, M.D. Vangsness, L.W. Byrd, J.S. Ervin, and J.G. Jones, "Profile Measurements of Thin Liquid Films Using Reflectometry," Appl. Phys. Lett., Vol. 103, p. 211607, 2013.

62. M.S. Hanchak, M.D. Vangsness, L.W. Byrd, and J.S. Ervin, "Thin Film Evaporation of n-Octane on Silicon: Experiments and Theory," Int. J. Heat Mass Transfer, Vol. 75, pp. 196–206, 2014.

63. M.S. Hanchak, M.D. Vangsness, J.S. Ervin, and L.W. Byrd, "Transient Measurement of Thin Liquid Films Using a Shack-Hartmann Sensor," International Communications in Heat and Mass Transfer, Vol. 77, pp.100-103, 2016.

64. M.S. Hanchak, M.D. Vangsness, J.S. Ervin, and L.W. Byrd, Model and Experiments of the Transient Evolution of a Thin, Evaporating Liquid Film, Int. J. Heat Mass Transfer, Vol. 92, pp. 757–765, 2016b.

65. H. Jiang, J. Ervin, Z.J. West, and S. Zabarnick, "Effects of Flow Passage Expansion or Contraction on Jet-Fuel Surface Deposition" AIAA Journal of Propulsion and Power, Vol. 28, pp. 694-706, 2012.

66. H. Jiang, J.S. Ervin, Z. West, and S. Zabarnick, "Turbulent Flow, Heat Transfer Deterioration, and Thermal Oxidation of Jet Fuel," Journal of Thermophysics and Heat Transfer, Vol. 27, pp. 668-678, 2013.

67. D.W. Johnson, R.K. Adams, S. Zabarnick, Z.J. West, and R.C. Striebich, "Analysis of Polar Components in Jet Fuel by High Performance Liquid Chromatography/Time of Flight Mass Spectrometry with Electrospray Ionization," Preprints – American Chemical Society, Division of Energy & Fuels, Vol. 57, pp. 798-800, 2012.

68. C. D. Klingshirn, M. DeWitt, R. Striebich, D. Anneken, L. Shafer, E. Corporan, M. Wagner, and D. Brigalli, "Hydroprocessed Renewable Jet Fuel Evaluation, Performance, and Emissions in a T63 Turbine Engine," J. Eng. Gas Turbines Power, Vol. 134, 051506/1-051506/8, 2012.

69. C. D. Klingshirn, Z.J. West, A. Higgins, M. DeWitt, J. Graham, E. Corporan, "Quantitation of Elemental and Organic Carbon in Combustion Soot Using Thermal-Oxidative Carbon Determination," in preparation, 2016.

70. W. K. Lewis, A. T. Rosenberger, J. R. Gord, C. A. Crouse, B. A. Harruff, K. A. S. Fernando, M. J. Smith, D. K. Phelps, J. E. Spowart, E. A. Guliants, and C. E. Bunker, "Multispectroscopic (FTIR, XPS, and TOFMS-TPD) Investigation of the Core-Shell Bonding in Sonochemically Prepared Aluminum Nanoparticles Capped with Oleic Acid" Journal of Physical Chemistry C, Vol. 114, pp. 6377–6380, 2010.

71. W. K. Lewis, B. A. Harruff, J. R. Gord, A. T. Rosenberger, T. M. Sexton, E. A. Guliants, and C. E. Bunker, "Chemical Dynamics of Aluminum Nanoparticles in Ammonium Nitrate and Ammonium Perchlorate Matrices: Enhanced Reactivity of Organically Capped Aluminum," Journal of Physical Chemistry C, Vol. 115, pp. 70-77, 2011.

72. W. K. Lewis, B. A. Harruff-Miller, M. A. Gord, J. R. Gord, E. A. Guliants, and C. E. Bunker, "A Threshold-Based Approach to Calorimetry in Helium Droplets: Measurement of Binding Energies of Water Clusters," Review of Scientific Instruments, Vol. 83, pp. 073109, 2012.

73. W.K. Lewis, C.G. Rumchik, and M.J. Smith, "Emission Spectroscopy of the Interior of Optically Dense Post-Detonation Fireballs," J. Appl. Phys., Vol. 113, pp. 024903/1-024903/4, 2013a.

74. W.K. Lewis, C.G. Rumchik, M.J. Smith, K.A.S. Fernando, C.A. Crouse, J.E. Spowart, E.A. Guliants, and C.E. Bunker, "Comparison of Post-Detonation Combustion in Explosives Incorporating Aluminum Nanoparticles: Influence of the Passivation Layer," J. Appl. Phys., Vol. 113, pp. 044907/1-044907/5, 2013b.

75. W. K. Lewis, B. A. Harruff-Miller, P. Leatherman, M. A. Gord, and C. E. Bunker, "Helium Droplet Calorimetry of Strongly Bound Species: Carbon Clusters from C2 to C12" Review of Scientific Instruments, Vol. 85, pp. 094102, 2014.

76. H. Li, M.J. Meziani, A. Kitaygorodskiy, F. Lu, C.E. Bunker, K.A.S. Fernando, E.A. Guliants, and Y.-P. Sun, "Preparation and Characterization of Alane Complexes for Energy Applications," J. Phys. Chem. C, Vol. 114, pp. 3318-3322, 2010.

77. B. McMasters, M.J. DeWitt, R. Striebich, T. Edwards, and D. Phelps, "Effect of Fuel Chemical Composition on Pyrolytic Reactivity and Deposition Propensity under Supercritical Conditions," Prepr.-Am. Chem. Soc., Div. Pet. Chem., Vol. 57, pp. 819-822, 2012.

78. A. Nagulapalli, G. Flora, S. Saxena, M.S.P. Kahandawala, M.J. DeWitt, E. Corporan, and S.S. Sidhu, "Ignition Delay Measurements of a Methylcyclohexane/O2/Ar Mixture over a Wide Range of Conditions," Presented at the Spring Technical Meeting of the Central States Section of the Combustion Institute, Dayton, OH, 2012.

79. S.A. Putnam, A.M. Briones, L.W. Byrd, J.S. Ervin, M.S. Hanchak, A. White, and J.G. Jones, "Microdroplet Evaporation on Superheated Surfaces," Int. J. Heat Mass Transfer, Vol. 55, pp. 5793-5807, 2012.

80. H.J. Robota and J.C. Alger, "Preparation of a Research Jet Fuel Composition Comprised of Nearly Exclusively Methyl-Branched Tetradecane Isomers Having a Freezing Point below -47 °C," Ind. Eng. Chem. Res., Vol. 51, pp. 10313-10319, 2012.

81. H.J. Robota, J.C. Alger, and L. Shafer, "Converting Algal Triglycerides to Diesel and HEFA Jet Fuel Fractions," Energy & Fuels, Vol., 27, pp. 985-996, 2013.

82. O.N. Ruiz, K.A. Fernando, B. Wang, N.A. Brown, P.G. Luo, N.D. McNamara, M. Vangsness, Y.P. Sun, and C.E. Bunker, "Graphene Oxide: A Nonspecific Enhancer of Cellular Growth," ACS Nano, Vol. 5, pp. 8100–8107, 2011.

83. W. Roquemore, T. Litzinger, M. Colket, V. Katta, K. McNesby, S. Sidhu, and R. Santoro, " Combustion Science to Reduce PM Emissions for Military Platforms," Strategic Environmental Research and Development, Final Report, WP-1577, 2012.

84. O. N. Ruiz, L.M. Brown, R.C. Striebich, S.S. Mueller, and T.S. Gunasekera, "Draft Genome Sequence of *Pseudomonas frederiksbergensis* SI8, a Psychrotrophic Aromatic-Degrading Bacterium," Genome Announc., Vol. 3, pp. 811-815, 2015a.

85. O.N. Ruiz, N.A. Brown, K.A.S. Fernando, B.A. Miller, T.S. Gunasekera, and C.E. Bunker, "Graphene oxide-based nanofilters efficiently remove bacteria from fuel," International Biodegradation and Biodeterioration, Vol. 97, pp. 168-178, 2015b.

86. O.N. Ruiz, L.M. Brown, R.C. Striebich, C.E. Smart, L.L. Bowen, J.S. Lee, B.J. Little, S.S. Mueller, and T.S. Gunasekera, "Effect of Conventional and Alternative Fuels on a Marine Bacterial Community and the Significance to Bioremediation," Energy & Fuels, Vol. 30, pp. 434–444, 2016.

87. Z.H. Sander, Z.J. West, J.S. Ervin, and S. Zabarnick, "Experimental and Modeling Studies of Heat Transfer, Fluid Dynamics, and Autoxidation Chemistry in the Jet Fuel Thermal Oxidation Tester (JFTOT)," Energy & Fuels, Vol. 29, pp. 7036-7047, 2015.

88. L. Shafer, R. Striebich, S. Zabarnick, and Z. West, "Identification and Quantitation of Polar Species in Liquid Transportation Fuels by GCxGC," Proceedings of the 14th International Symposium on Stability, Handling, and Use of Liquid Fuels, October 2015.

89. R.C. Striebich, L.M. Shafer, Z.J. West, R.K. Adams, and S. Zabarnick, "Hydrocarbon Group-Type Analysis of Current and Future Aviation Fuels: Comparing ASTM D2425 to GCxGC," Proceedings of the 12th International Conference on Stability, Handling, and Use of Liquid Fuels, Sarasota, FL, 2011.

90. R.C. Striebich, L.M. Shafer, R.K. Adams, Z.J. West, M.J. DeWitt, and S. Zabarnick, "Hydrocarbon Group-Type Analysis of Petroleum-Derived and Synthetic Fuels Using Two-Dimensional Gas Chromatography," Energy & Fuels, Vol. 28, pp. 5696-5706, 2014a.

91. R.C. Striebich, C.E. Smart, T.S. Gunasekera, S.S. Mueller, E.M. Strobel, B.W. McNichols, and O.N. Ruiz, "Characterization of the F-76 diesel and Jet-A aviation fuel hydrocarbon degradation profiles of *Pseudomonas aeruginosa* and *Marinobacter hydrocarbonoclasticus,*" International Biodeterioration and Biodegradation, Vol. 93, pp. 33-43, 2014b.

92. R.C. Striebich, L.L. Bowen, S.S. Mueller, L.M. Shafer, T.S. Gunasekera, and O.N. Ruiz, "Aviation Fuel Biodegradation using a Stirred-Tank Bioreactor," Proceedings of the 14th International Conference on Stability, Handling, and Use of Liquid Fuels, Charleston, SC, October 2015.

93. B. J. Thomas, B. A. Harruff-Miller, C. E. Bunker, and W. K. Lewis, "Infrared Spectroscopy of Mg-CO2 and Al-CO2 Complexes in Helium Nanodroplets," Journal of Chemical Physics, Vol. 142, pp. 174310, 2015.

94. U.S. Patent (accepted) titled "GRAPHENE OXIDE FILTERS AND METHODS OF USE," Serial No. 20140199777.

95. M.D. Vangsness, "Best Practice for Contamination Testing," CRC Aviation Group Meeting, May 2014.

96. M.D. Vangsness, "Best Practices for Contamination Testing, Some Lessons Learned," CRC Aviation Group Meeting, May, 2015a.

97. M.D. Vangsness, "Best Practices for Contamination Testing," Tri Service Meeting, July 2015b.

98. M.D. Vangsness, "Best Practice for Jet Fuel Contamination Response," Proceedings of the 14th International Conference on Stability, Handling, and Use of Liquid Fuels, Charleston, SC, October 2015c.

99. M.D. Vangsness, "Best Practice for Jet Fuel Contamination Response Final Report", Defense Logistics Agency, November 2015d.

100. Z.J. West, L.M. Shafer, R.C. Striebich, S. Zabarnick, C. Delaney, D.K. Phelps, and M.J. DeWitt, "Equilibrium Partitioning of DiEGME between Fuel and Aqueous Phases at Sub-Ambient Temperatures," Energy & Fuels, Vol 28, pp. 4501-4510, 2014. doi: 10.1021/ef500900p

101. Z. West, M.J. DeWitt, and D. Phelps, "Evaluation of Fuel Tank Topcoat Resistance to Fuel System Icing Inhibitor (FSII)," Presented at the CRC Aviation Meeting, Alexandria, VA, 2–5 May 2016.

102. S. Zabarnick, R. Adams, Z. West, M.J. DeWitt, L. Shafer, R. Striebich, C.L. Delaney, and D.K. Phelps, "Compatibility of DiEGME and TriEGME Fuel System Icing Inhibitor Additives with BMS 10-39 Aircraft Tank Topcoat Material," Energy & Fuels, Vol. 24, pp. 2614-2627, 2010.

103. S. Zabarnick, M.J. DeWitt, R. Adams, Z.J. West, L.M. Shafer, T.F. Williams, R. Cook, R. Striebich, L.M. Balster, D.K. Phelps, and C.L. Delaney, "Evaluation of Triethylene Glycol Monomethyl Ether (TriEGME) as an Alternative Fuel System Icing Inhibitor for JP-8 Fuel, AFRL-RZ-WP-TR-2011-2030, 2011.

LIST OF SYMBOLS, ABBREVIATIONS, AND ACRONYMS

ACRONYM	DESCRIPTION
AAFEX	Alternative Aviation Fuel Experiment
AAFRF	Assured Aerospace Fuels Research Facility
AFB	Air Force Base
AFCESA	Air Force Civil Engineer Support Agency
AFPA	Air Force Petroleum Agency
AFRL	Air Force Research Laboratory
AFRL/RQ	Air Force Research Laboratory Aerospace Systems Directorate
AFRL/RQTF	Air Force Research Laboratory Fuels & Energy Branch
AFTAT	Air Force Test and Analysis Tool
AHB	Assault Helicopter Battalion
AKI	Antiknock index
Al NP	Aluminum nanoparticle
ASIC	Air and Space Interoperability Council
ASME	American Society of Mechanical Engineers
ATJ	Alcohol to Jet
BSFC	Brake specific fuel consumption
CFD	Computational fluid dynamics
CFM	Cubic feet per minute
CLEEN	Continuous Lower Energy, Emissions, and Noise
CONUS	Continental United States
CTIO	Coatings Technology Integration Office
CW	Continuous wave
DCN	Derived Cetane Number
EEE	Energy & Environmental Engineering
EPC	Elevated pressure combustor
EPA	Environmental Protection Agency
ESI	Electrospray Ionization
ESTCP	Environmental Security Technology Certification Program
FAA	Federal Aviation Administration
FAME	Fatty acid methyl ester
FGM	Flamelet generated manifold
FID	Flame ionization detector
FSII	Fuel system icing inhibitor
FT	Fischer-Tropsch
FTTP	Fuel tank topcoat peeling
FPD	Flame photometric detector
GC	Gas chromatography
GC-MS	Gas chromatograph-mass spectrometer
GCxGC	Two dimensional gas chromatography
GFCI	Ground fault circuit interrupt
GHG	Greenhouse gas
GO	Graphene oxide
HAP	Hazardous air pollutant
HC	Hydrocarbon
HEFA	Hydroprocessed esters and fatty acids
HGC	High-g cavity
HHV	High heating value

HPLC	High performance liquid chromatography
HPLC-TOFMS	High performance liquid chromatography-time of flight mass spectrometry
HRD	Hydroprocessed renewable diesel
HRJ	Hydroprocessed renewable jet fuel
ICP	Inductively-coupled plasma
ICP-MS	Inductively-Coupled Plasma Mass Spectrometry
IGV	Inlet guide vane
IPK	Isoparaffinic kerosene
IR	Infrared
ISFC	Indicated specific fuel consumption
LLNL	Lawrence Livermore National Laboratories
MCH	Methylcyclohexane
MS	Mass spectrometer
MW	Molecular weight
NAAQS	National Ambient Air Quality Standards
NAS	Naval Air Station
NASA	National Aeronautical and Space Agency
NATO	North Atlantic Treaty Organization
NJFCP	National Jet Fuel Combustion Program
PAH	Polyaromatic hydrocarbons
PAPRICO	Parallelized, automated, and predictive imprint cooling model
PM	Particulate matter
QCM	Quartz crystal microbalance
RANS	Reynolds-averaged Navier-Stokes
RQTF	AFRL Fuels and Energy Branch
SERDP	Strategic Environmental Research and Development Program
SG	Syngas
SNETPSR	Sooting Network of Perfectly Stirred Reactors
SPE	Solid-phase extraction
SPO	Systems Program Office
SPK	Synthetic paraffinic kerosene
SPU	Sample preparation unit
SRB	Sulfate-reducing bacteria
TCD	Thermal conductivity detector
TDLAS	Tuneable diode laser absorption
TEL	Tetraethyl Lead
TERTEL	Turbine Engine Research Transportable Emissions Laboratory
TOFMS	Time of flight mass spectrometry
TSI	Threshold Sooting Index
TVC	Trapped vortex combustor
UAV	Unmanned aerial vehicle
UCC	Ultra-compact combustor
UD	University of Dayton
UDRI	University of Dayton Research Institute
UHC	Unburned hydrocarbons
USAF	United States Air Force
WPAFB	Wright-Patterson Air Force Base
WSR	Well-stirred reactor

Appendix A. Compatibility of DiEGME and TriEGME Fuel System Icing Inhibitor Additives with BMS 10-39 Aircraft Tank Topcoat Material

energy&fuels
article

Compatibility of DiEGME and TriEGME Fuel System Icing Inhibitor Additives with BMS 10-39 Aircraft Tank Topcoat Material

Steven Zabarnick,*,[†] Ryan Adams,[†] Zachary West,[†] Matthew J. DeWitt,[†] Linda Shafer,[†] Richard Striebich,[†] Charles L. Delaney,[‡] and Donald K. Phelps[§]

[†]*University of Dayton Research Institute, Dayton, Ohio 45469,* [‡]*Consultant, 10011 Bennington Drive, Cincinnati, Ohio 45241, and* [§]*Air Force Research Laboratory, Fuels and Energy Branch AFRL/RZPF, Wright-Patterson AFB, Ohio 45433*

In recent years, the fuel system icing inhibitor (FSII) diethylene glycol monomethyl ether (DiEGME) has been implicated in an increasing incidence of peeling of topcoat material in the ullage space of integral wing tanks in the B-52 and other military aircraft. Work has indicated that, for the combination of DiEGME in JP-8 fuel, the icing inhibitor additive can concentrate in the tank ullage and condense at elevated concentrations on cooled tank walls. These high concentrations of DiEGME cause swelling and subsequent peeling of the epoxy-based topcoat. Here, we report on detailed studies of the compatibility of DiEGME and FSII replacement candidate triethylene glycol monomethyl ether (TriEGME) with BMS 10-39 fuel tank topcoat material. Tests were designed to simulate fuel tank wall exposures with subsequent topcoat degradation measured by icing inhibitor uptake analyses and pencil hardness evaluations. The lower volatility of TriEGME relative to the JP-8 fuel components results in it being less able to concentrate in the tank ullage and promote topcoat failure, as compared to DiEGME. This was confirmed with lower additive levels measured in the ullage, condensed vapors, and the exposed topcoat material. The pencil hardness of topcoat material exposed to fuel vapors was significantly improved upon changing from DiEGME to TriEGME exposure. Simulation experiments were able to reproduce the fuel tank topcoat peeling observed in the field as well as determine the conditions (concentration and temperature) required for topcoat degradation.

Introduction

At high altitudes, the exteriors of aircraft are subjected to cold temperatures ($\leq 60\ ^\circ$C) from the surrounding environment. While the current USAF fuel, JP-8, has a low freezing point ($-47\ ^\circ$C maximum), any free water within the fuel will readily freeze at altitude. To remedy this situation, a fuel system icing inhibitor (FSII) was developed and introduced as a fuel additive to selectively partition into any free water present and suppress the freezing point of the aqueous mixture. This additive became required by the U.S. military in 1961 after a B-52 Stratofortress crash, which was attributed to ice formation that caused fuel line blockages. Initially, ethylene glycol monomethyl ether (EGME)/glycerol mixtures were employed as the FSII additive during the period that JP-4 was used by the United States Air Force (USAF). However, EGME was subsequently shown to have a relatively high toxicity, and problems arose with the volatility of JP-5, the fuel used by the Navy, as it became difficult for EGME-containing fuels to meet the flashpoint specification ($\geq 60\ ^\circ$C).[1] Diethylene glycol monomethyl ether (DiEGME) was found to be an acceptable alternative FSII additive, and transition to this species began in 1987 for JP-5 and was authorized for use in JP-8 in 1992. DiEGME is currently required in both JP-5 and JP-8 fuels, with a specification procurement level of 0.10−0.15 vol % for both fuels.

The current aircraft use limits for DiEGME are currently 0.03 vol% for the U.S. Navy and 0.07 vol % for the U.S. Air Force.

Recently, DiEGME has been implicated in causing degradation and peeling of the protective fuel tank topcoat layer in B-52 aircraft, a process referred to as fuel tank topcoat peeling (FTTP).[2,3] This epoxy topcoat layer is Boeing Material Specification (BMS) 10-39 and serves as a physical barrier between the fuel/air environment and the aluminum tank wall. Peeled surfaces are more likely to support corrosion and pitting of the aluminum substrate. Also, the topcoat flakes that have lost adhesion can cause blockages in fuel filters and valves, resulting in catastrophic failure of the aircraft. Figure 1 shows examples of fuel tank topcoat peeling and the problems it causes.

The BMS 10-39 epoxy topcoat was originally formulated to resist degradation from prolonged exposure to JP-4 fuel. Despite this formulation, FTTP has occurred in fuel containing DiEGME, and high concentrations of DiEGME in fuel and water have been shown to promote swelling and peeling of the topcoat layer.[2,3] FTTP has primarily been observed above the fuel level on the tank walls in the headspace (ullage) of the tank and at the bottom of the tank where water accumulates (Figure 1). Mechanisms of deterioration have been proposed for both of these peeling areas. For the ullage space above the

*To whom correspondence should be addressed. E-mail: zabarnick@udayton.edu.
(1) Martel, C. R. Air Force Wright Aeronautical Laboratories Technical Report AFWAL-TR-2062, Wright-Patterson AFB, OH, 1987.

(2) Aliband, A.; Lenz, D.; Dupois, J.; Alliston, K.; Sorhaug, V.; Stevenson, L.; Whitmer, T.; Burns, D.; Stevenson, W. *Prog. Org. Coat.* **2006**, *56*, 285–296.
(3) Aliband, A.; Lenz, D.; Stevenson, L.; Whitmer, T.; Cash, R.; Burns, D.; Stevenson, W. *Prog. Org. Coat.* **2008**, *63*, 139–147.
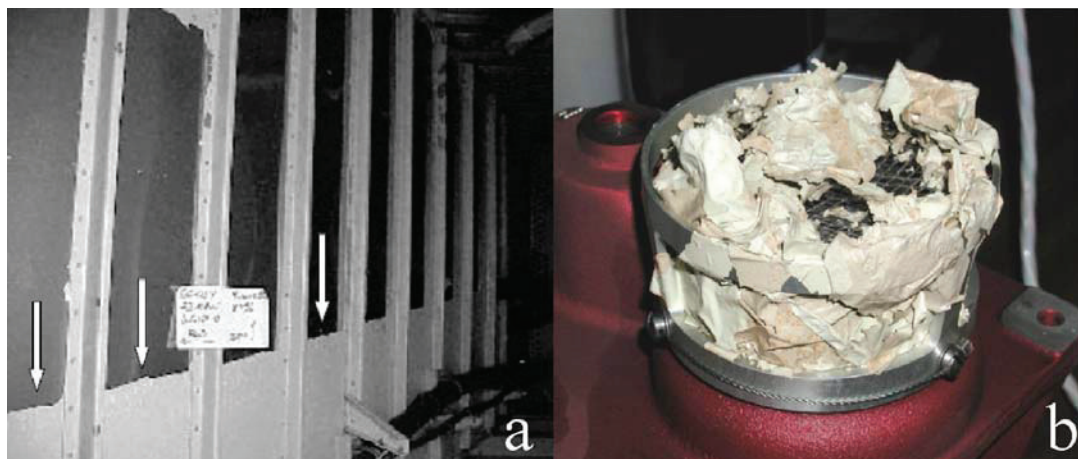
Figure 1. (a) Fuel tank topcoat peeling in a B-52 wing fuel tank[2] and (b) a B-52 boost pump intake screen (4-mesh) clogged with BMS 10-39 flakes.
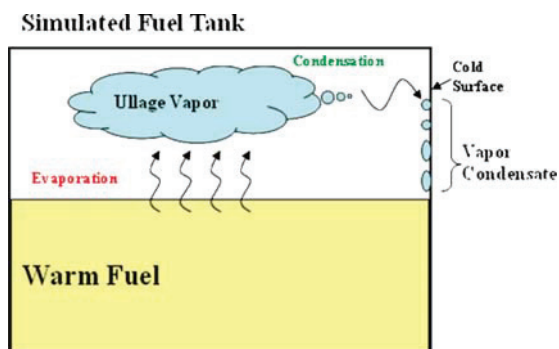
Figure 2. FTTP phenomenon initiated by a DiEGME-rich ullage vapor and condensation on a cold topcoat surface.

fuel level, DiEGME concentrates in the vapor phase due to its high vapor pressure relative to the JP-8 fuel.[2] This DiEGME-rich vapor phase can then condense on cold topcoat surfaces, resulting in a wall wetted with condensate that has a DiEGME concentration which is significantly higher than that of the base fuel. The presence of relatively warm bulk fuel and vapor along with a cold fuel tank wall encourages this process, as demonstrated graphically in Figure 2.

The conditions of relatively warm bulk fuel and a cold wall to promote selective condensation are possible under several scenarios during aircraft operation. For example, after take-off, the fuel tank walls will cool down quickly due to the low outside air temperature at altitude, while the large thermal mass of bulk fuel will result in the fuel cooling down significantly more slowly. These conditions will be repeated for each flight, resulting in continued exposure of DiEGME-rich condensate in contact with the topcoat. Another scenario involves aircraft on the ground in warm climates. If the aircraft is left exposed to the sun throughout a hot day, the bulk fuel temperature in the aircraft fuel tanks can rise substantially. In studies of the temperature of refueling tankers, it was found that the tanker trucks showed fuel temperatures above 55 °C during the middle of the day in a desert location.[4] As the

sun sets, the outside air temperature will decrease quickly, especially in arid climates, while the wall will cool more quickly due to the differences in thermal mass and promote surface condensation. These conditions can be repeated daily if the ambient temperature is sufficiently warm to vaporize the lighter fuel components, such as DiEGME.

Topcoat degradation at lower fuel tank surfaces is likely initiated by high concentrations of DiEGME in water bottoms. The specific gravities of water and DiEGME (1.00 and 1.023, respectively) are higher than that of JP-8 (~0.8), and thus free water that phase-separates will collect at the bottom of the tank. DiEGME and water are completely miscible, and DiEGME typically concentrates in water in the range of 30 to 50 vol % within the fuel tank. Higher concentrations of DiEGME in aqueous solutions have been shown to cause FTTP with seven day liquid exposures.[5] Severe swelling of topcoat flakes has also been shown to occur at similar exposure concentrations.[2]

The chemical and physical mechanisms which result in FTTP are still not fully understood, and thus it is difficult to eliminate or minimize future occurrences. More information needs to be obtained on the required concentrations, temperatures, and time of exposure to induce FTTP. Along with attempting to confirm the mechanisms which cause FTTP, a number of solutions have been proposed to prevent future problems. To reduce the occurrence of peeling in water bottom areas, regular sumping of aircraft tanks ensures that water/FSII mixtures do not accumulate in the fuel tanks and high concentrations of FSII are not in contact with the top-coat for extended periods of time. For the issue of FTTP on the tank ullage surfaces, one solution is to reduce the concentration of DiEGME in JP-8. Decreasing the concentration of DiEGME in the fuel would reduce the concentration in the vapor phase and lower the concentration in the condensate which collects on the ullage topcoat. This approach would also lower the DiEGME levels in tank water bottoms. However, the DiEGME concentration still needs to be high enough to provide the required anti-icing performance. Ideally, a proper balance between reducing the occurrence of FTTP and retaining the inhibiting icing performance of the additive would be found.

(4) Williams, T. F.; Vangsness, M.; Shardo, J.; Ervin, J. Air Force Research Laboratory Report, AFRL-PR-WP-TR-2005-2103, Wright-Patterson AFB, OH, February 2005.

(5) Hufnagle, D. University of Dayton Research Institute Report UDR-TR-2008-00032, Dayton, OH, 2008.

57

Table 1. Selected Properties of DiEGME and TriEGME

FSII additive	vapor pressure (mmHg) @ 20 °C	density (g/mL) @ 20 °C	molecular weight (g/mol)	freezing point (°C)
DiEGME	0.19	1.023	120	−85
TriEGME	<0.01	1.026	164	−47

Another approach is to replace DiEGME with an alternative FSII additive which does not promote FTTP. With the current hypothesized mechanisms for FTTP on the tank ullage walls, a suitable replacement would provide equivalent anti-icing efficacy but exhibit a lower vapor pressure. One such species that may fit these requirements is triethylene glycol monomethyl ether (TriEGME), which has a vapor pressure that is more than an order of magnitude lower than DiEGME, as shown in Table 1.[6] TriEGME should not volatilize as readily from the bulk fuel, resulting in a lower effective concentration in any condensate in contact with the topcoat surfaces. Table 1 also shows other selected property differences between DiEGME and TriEGME.

It is apparent that further investigation of the requisite conditions for the occurrence of FTTP in aircraft is required. A comparison of the topcoat compatibility between DiEGME and TriEGME is also essential to assess TriEGME as an alternative icing inhibitor additive. Determination of the anti-icing efficacy of DiEGME and TriEGME at lower concentrations is being evaluated separately.[6,7] The experiments in this study were designed to assess the effects of DiEGME and TriEGME on BMS 10-39 topcoat degradation using the most probable scenarios relating to FTTP. The absorption of FSII into BMS 10-39 was quantified to analyze the effects of concentration in aqueous or fuel solutions under various exposure conditions. This work also studied differences between DiEGME and TriEGME using topcoat panels that were recently fabricated and those that were exposed to fuel for many years, as well as the conditions which will reduce the topcoat integrity below the minimum specification requirement. After being softened due to DiEGME exposure, BMS 10-39 topcoat has been observed to "reharden",[2] which is most likely due to FSII molecules desorbing from the coating. Thus, preliminary studies were also performed to investigate the desorption rates of FSII from the topcoat. An ultimate goal of this work was to reproduce FTTP in a controlled laboratory setting to assess the differences between DiEGME and TriEGME, as well as to investigate the degradation process and to provide a knowledgebase of the conditions necessary for FTTP.

Experimental Section

BMS 10-39 Panels. Experimental studies were performed to investigate the compatibility of FSII additives with both aged and new BMS 10-39 topcoat panels. The AFRL Coatings Technology Integration Office fabricated one-sided topcoat panels on 1/32 in. aluminum (2024-T3) to meet the 1-mm-thickness specification of BMS 10-39. Prior to coating, the

(6) Zabarnick S.; West Z.; DeWitt M.; Shafer L.; Striebich R.; Adams R.; Delaney C.; Phelps D. IASH 2007, the 10th International Conference on Stability, Handling and Use of Liquid Fuel, Tucson, AZ, October 2007.
(7) DeWitt, M. J.; Zabarnick, S.; Shaeffer, S.; Williams, T.; West, Z.; Shafer, L.; Striebich, R.; Breitfield, S.; Adams, R.; Cook, R.; Delaney, C. L.; Phelps, D. IASH 2009, the 11th International Conference on Stability, Handling and Use of Liquid Fuel, Prague, Czech Republic, October 2009.

aluminum panels were cleaned, acid etched with an alcoholic phosphoric acid solution, and chemically treated with Alodine 1200S, which is a chromium chemical conversion coating surface treatment. These manufactured panels are referred to as "new" panels, as they have not been exposed to fuel or FSII before these studies. The "old" BMS 10-39 panels were obtained from a scrapped B-52G aircraft from Boeing Wichita which had been operated for many years with JP-4 and JP-5/EGME and/or JP-5/DiEGME fuels.

FSII Exposure Solutions. Interactions with the BMS 10-39 topcoat can occur with FSII in solution with various liquids. Three different bulk solutions were used in the experimental studies while varying the FSII concentrations: water, fuel, and a surrogate fuel condensate. Aqueous solutions were used for many of the studies to evaluate the required concentrations for FTTP to occur in water bottoms. The water used to create the solutions was purified via reverse osmosis. A clay treated Jet A-1 (POSF-4877) was used as the base fuel in the experimental studies. The clay treatment was necessary to remove any FSII contamination in the fuel that may have occurred during transportation and storage. Finally, a surrogate fuel was developed to simulate the fuel condensate which would be in contact with the BMS 10-39 coating in the ullage of aircraft tanks. This surrogate was comprised of Exxsol D40 (85% by volume), Aromatic 100 (9%), and Aromatic 150 (6%). The mixture closely simulates the lighter components that are initially vaporized from the bulk fuel and subsequently condense on cold surfaces.[6]

FSII Absorption Study. The uptake study investigated the liquid−solid interactions between FSII and the BMS 10-39 layer by quantifying the FSII absorbed into the topcoat. Aluminum topcoat panel squares (0.25 in.[2]) are submerged in 20 mL of fuel or water with specific concentrations of DiEGME or TriEGME in 30 mL capped vials. This volume of liquid was used to ensure there would not be a significant change in the FSII concentration of the liquid phase due to partitioning into the topcoat. This was verified by analyzing the concentration of the solution before and after exposure to a BMS 10-39 panel.
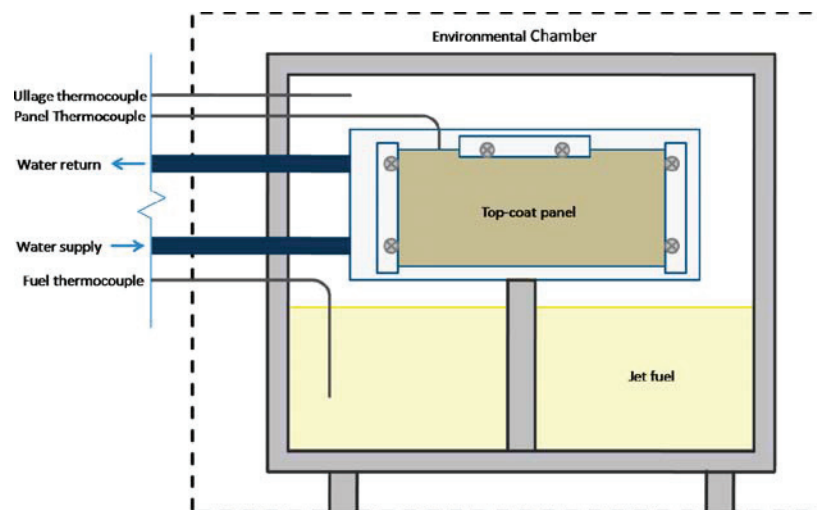
The aqueous solutions ranged from 0 to 100% DiEGME or TriEGME, while the fuel or surrogate solutions ranged from 0 to 2%. This difference in concentration ranges resulted from the typical concentrations expected in these phases. Initially, the solutions were placed into a shaker to be agitated throughout the exposure period; however, further studies revealed that agitation was unnecessary due to the short time required for the FSII in the liquid and topcoat layer to equilibrate. The initial exposure time used was five days, as further time did not increase the absorption of FSII in the topcoat. Later, this was shortened on the basis of the absorption study discussed below. After the exposure period, the panels were removed from the vials and cleaned to remove any liquid droplets by rinsing with a small volume of hexane (1−2 mL) and then blotted dry with Kimwipes. The panel was then submerged in 2 mL of acetone for 1 h to extract the absorbed FSII component from the topcoat. Consecutive acetone extractions on the same panel failed to yield detectable levels of FSII, showing that all of the extractable FSII was removed. The acetone extract was collected and analyzed by GC-MS to obtain the total mass of absorbed FSII. The FSII absorption quantity was normalized by the topcoat volume, measured via thickness measurements, and reported as moles of FSII absorbed per liter of topcoat. Each experimental condition was performed in triplicate to obtain a measure of reproducibility.

This basic approach was modified to investigate the rate of FSII absorption and desorption. To evaluate the absorption rate, the exposure time of the topcoat in contact with a FSII solution was varied to determine when the uptake concentrations reached a plateau. A plateau in the uptake absorption vs time suggests that the topcoat no longer absorbs FSII and equilibrium is reached with the FSII in solution. The panels

Figure 3. FSII simulation box apparatus.

were removed from the solutions at varying times between 10 s and 144 h. This was performed with new panels and 50% aqueous solutions of DiEGME and TriEGME. The results indicated that equilibrium was reached in less than 24 h. These data were used to validate reducing the exposure time for the absorption study to one day for later experiments from the initial five days. Alternatively, the desorption rate was qualitatively analyzed by varying the time between the cleaning of the panel (after removal from the solution) and the acetone extraction.

Pencil Hardness Study. To correlate the quantity of FSII absorbed with the integrity of the coating after exposure, pencil hardness tests were performed. These were performed according to ASTM D3363 procedures. The pencil leads used for this analysis along with the range of acceptable hardness for BMS 10-39 are shown below:

Acceptable Range for BMS 10-39

6B − 5B − 4B − 3B − 2B − B − HB − F − H − 2H − 3H − 4H − 5H − 6H
Softest → → → **Hardest**

The pencil hardness study was performed on 1" × 2" panels of new and old BMS 10-39 on aluminum. The panel size was chosen to allow the use of all leads required to determine the hardness. Two such panels were submerged in 100 mL beakers with 80 mL of a FSII solution for two days. This exposure time permitted two data sets to be collected per week while maintaining equilibrium between the solution and the topcoat. As in the uptake study, this volume of liquid was used to ensure that the concentration of FSII in the solution did not decrease during the duration of exposure. This was verified by analyzing the concentration of DiEGME in a solution before and after exposure, which did not change signficantly over the two days.

When the panels were removed, they were washed with a small amount of hexane to remove the remaining solution from the BMS 10-39 panel. One of the panels was immediately tested for its pencil hardness, while the other was allowed to dry in a fume hood for 2 h prior to evaluation. The latter approach was performed to determine the ability of the topcoat to reharden over time as the FSII evaporates from the topcoat material.

Fuel Tank Topcoat Peeling (FTTP) Simulation Study. This study was designed to simulate the conditions in aircraft fuel tanks which promote topcoat degradation, as well as to quantify the effects of FSII concentration and temperature on the resulting pencil hardness of exposed BMS 10-39 panels.

The experiment was used to test the hypothesis that DiEGME concentrates in the ullage and condenses at high concentrations on the topcoat surface, which results in degradation. This simulation was also used to determine if the lower vapor pressure of TriEGME results in a decreased potential for creating a FSII-rich ullage. The system (Figure 3) consisted of a 28.3 L (1 ft^3) aluminum box which contained the fuel along with a plate heat exchanger with an attached BMS 10-39 panel. The box containing the fuel was placed inside an environmental chamber, allowing control of the fuel and box surface temperatures. The heat exchanger/panel placed above the fuel level allowed independent temperature control of the topcoat panel, which was secured by clamps on the edges and top of the panel. A recirculating cooling water bath was used to control the heat exchanger temperature and the surface temperature of the topcoat panel. This heat exchanger was maintained at a lower temperature than the fuel to promote selective condensation onto the topcoat specimen.

The BMS 10-39 panels used for the simulation were 3" × 6" in size to provide a large surface area for contact with the condensate, and for visible confirmation of topcoat peeling. The box was typically filled with 9 L (approximately 1/3 of the total volume) of jet fuel and agitated throughout the duration of the experiment with a magnetic stir bar. This volume was used to create a similar ratio of total mass of FSII to area of topcoat as shown in the Uptake and Pencil Hardness Study, such that any absorption of FSII in the topcoat panel would not reduce the FSII concentration in the bulk fuel. Thermocouples were placed in the vapor headspace of the box, submerged into the fuel, and placed between the topcoat panel and heat exchanger surface. During the experiment, the box was closed after the fuel was added, and then the environmental chamber was heated to a specified temperature. After the desired test duration (2 to 5 days) and cooling to near ambient temperatures, samples of the bulk fuel and condensate were collected. Condensate samples were obtained using a chromatographic syringe to collect droplets on the panel or the heat exchanger. The initial fuel samples, final fuel samples, and condensate samples were analyzed by GC-MS to obtain FSII concentrations. Data were collected at varying initial FSII concentrations in the bulk fuel, temperatures of the box and/or heat exchanger, and exposure durations of FSII in contact with the topcoat panel. The topcoat panel was removed from the apparatus and immediately evaluated for its hardness at five locations: the center of the panel and each of the four corners.

2617
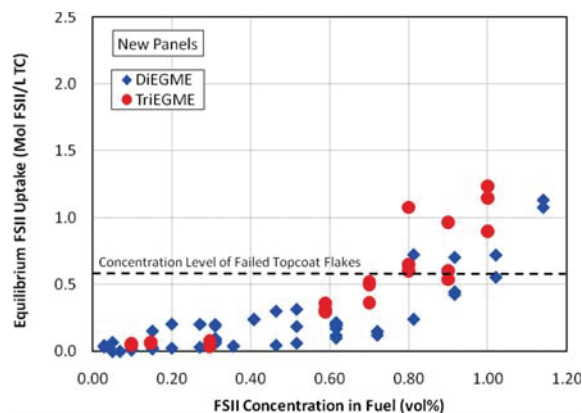
Figure 4. Equilibrium uptake of new panels exposed to DiEGME and TriEGME in Jet A-1.

Figure 5. Uptake of DiEGME and TriEGME in Jet A-1 obtained for old panels that were in service for over 40 years.

Analytical Techniques Used for Quantification of FSII. Analytical techniques were developed for quantification of levels of FSII in water, acetone, and fuel. While there is an ASTM standard for determination of DiEGME in fuel (ASTM D5006), the technique requires a large volume of fuel (80 to 160 mL), which was not available for the current studies. In addition, the variability of this method is greater than required for these studies.

Verification of the FSII concentration in water before exposure to the topcoat material was performed by refractive index using a Reichert AR200 Digital Refractometer over a concentration range of 0 to 100% FSII. Individual calibration curves were determined for DiEGME and TriEGME at approximately 10 vol % increments. The reproducibility is approximately ±10% of the FSII concentration.

Quantifying the concentration of FSII in acetone solutions was required for the topcoat absorption study and was performed by gas chromatography with flame ionization detection (GC-FID). An HP 5890 Series II GC-FID was used to quantify the dilute FSII component in acetone in ranges from 0 to 0.20 vol % to a reproducibility of ±10% of the FSII concentration.

For analysis of FSII in the fuel, fuel surrogate, and fuel condensate, a method was developed which employed gas chromatography with a mass spectrometer (GC-MS) detector. The FSII component in fuel could not be separated chromatographically due to coelution with the other fuel components. Thus, the selective ion mode of the detector was used to monitor the 45, 59, and 89 ions. These ion peaks are selective for both DiEGME and TriEGME, which allows the FSII peak to be resolved from the other fuel components. The reproducibility is approximately ±10% of the FSII concentration.

Results and Discussion

FSII Fuel Absorption Results. Studies were performed to investigate the absorption of DiEGME and TriEGME into BMS 10-39 topcoat panels as a function of concentration and time. The exposure studies were performed at ambient temperature and pressure as these were representative of ground conditions for aircraft fuel tanks. Unless specified, the panels were submerged in 20 mL FSII solutions for five days. The uptake data obtained using new panels in Jet A-1 are shown in Figure 4, with each data point representing the average of two or three panel measurements. The line labeled "concentration level of failed topcoat flakes" at 0.66 mol of FSII/L topcoat is from an uptake measurement obtained from failed topcoat flakes from the field. These failed topcoat flakes, which were obtained from B-52 aircraft, were analyzed by the same acetone extraction methodology as used to analyze the test panels
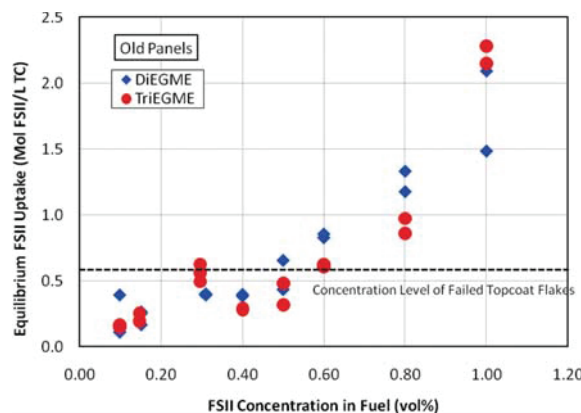
during the absorption studies. Three separate flakes were analyzed in this fashion, and the level of DiEGME was averaged with a reproducibility of ±20% of this concentration.

The figure shows that increasing the initial concentration of FSII in the fuel increases the quantity of FSII absorbed into the topcoat layer. The uptake increases significantly at concentrations greater than 0.50 to 0.80 vol % FSII. The figure shows that DiEGME and TriEGME performed similarly and follow the same trend. The FSII uptake increases above the level of failed topcoat flakes at approximately 0.80 vol % FSII in the fuel. This suggests that the concentration in the fuel required for failure to occur is at least 0.80% FSII in cases of direct contact, although additional analysis and correlation with topcoat integrity (e.g., pencil hardness measurements) is needed for verification. It is likely that the concentration of FSII in these flakes has decreased over time due to evaporation from the coating. The reproducibility of the absorption data can be fairly poor at some concentrations, with the data varying up to ±100% of an average concentration. There are a number of factors that may contribute to this, including variations in the GC analysis, a slightly unequal topcoat thickness, and possible degradation of the topcoat after repeated use of some panels.

To provide an understanding of changes that can occur in the topcoat after 40 years of aging and contact with fuel, the absorption of FSII into BMS 10-39 was also determined using old panels. The absorption data for old panels in Jet A-1 fuel are shown in Figure 5 under ambient temperatures and an exposure time of five days.

The old panels show a significant increase in the topcoat uptake relative to the newer panels at equivalent FSII concentrations. This may be due to the old topcoat having a reduced resistance to absorption due to weakening of the polymer matrix which allows more molecules to absorb into the coating. The old panels reach an uptake value higher than the failed topcoat flakes at 0.50 vol % FSII, which is significantly lower than the 0.80 vol % level found for the new panels. If the ability of the topcoat to absorb FSII correlates with the tendency to exhibit degradation, these data imply that old panels would be expected to exhibit much higher levels of degradation. This correlation is addressed in the Pencil Hardness Study Report below.

When comparing DiEGME and TriEGME on a molar basis, the additives show similar extents of absorption in both the old and new topcoat panels, but on a mass basis,
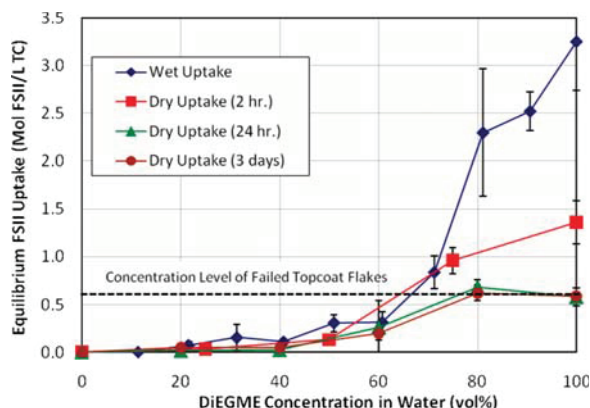
2618

60
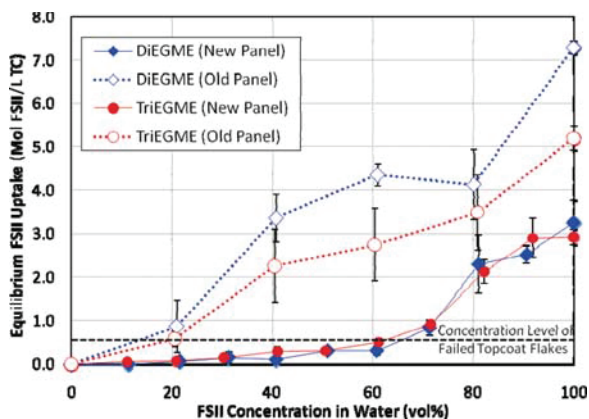
Figure 6. Uptake of DiEGME and TriEGME with new and old panels in aqueous solutions.

Figure 7. Uptake of DiEGME in aqueous solutions as a function of drying time with new panels.

TriEGME has a higher equilibrium uptake than DiEGME. This can be explained by the molecular weight of TriEGME (164 g/mol) being one-third higher than DiEGME (120 g/mol), while the absorption of FSII is likely a function of the number of molecules a given volume of topcoat can absorb, rather than the mass. This FSII absorption data agree qualitatively with the equilibrium solvent uptake (ESU) measurements of topcoat flakes performed by Aliband et al.[2] which were performed via gravimetric differences following exposure. Their data show a relatively level 6% ESU uptake from 0 to 0.75 vol % DiEGME in the fuel, which then increases rapidly at higher DiEGME levels. The higher uptake observed by Aliband et al.[2] is likely caused by absorption of other fuel components into the topcoat, as their technique measures total uptake of all species into the topcoat flakes.

FSII Aqueous Absorption Results. To better understand the occurrence of FTTP from exposure to water bottoms of fuel tanks, measurements were performed to determine the absorption of FSII into the topcoat from FSII/water solutions. These measurements were performed at ambient temperature with the panels exposed to aqueous solutions for five days. Figure 6 shows the results for new and old panels with each data point representing the average of two or three uptake measurements.

The new panels show little uptake until a concentration of approximately 70 vol % FSII is achieved, while the uptake for older panels increases relatively smoothly with increasing FSII concentration. At concentrations greater than approximately 80 vol % FSII, the new panel uptake appears to plateau, or at least not increase as rapidly. These trends are similar to the aqueous ESU data obtained by Aliband et al.[2] Their data show a distinct "S" shaped curve with the ESU measurements reaching a plateau at levels above 75 vol % DiEGME.

The new panel uptakes shown in Figure 6 are above the failed topcoat flakes concentration at 70 vol % FSII and greater, while the old panels achieve this level at a significantly lower concentration of approximately 20 vol % FSII. The older panels absorb more FSII from aqueous mixtures than the newer panels, as also observed in the fuel absorption studies. Overall, the aqueous solutions show a much higher maximum uptake than the FSII in fuel solutions. The maximum uptake for aqueous solutions is ~7.2 mol FSII/L TC at 100 vol % FSII, while the maximum uptake for fuel

exposures was ~2.3 mol FSII/L TC at 1.0 vol % FSII. This may be due to the significantly higher concentration of FSII in the aqueous solutions. While the topcoat was still physically intact after exposure to 100% solutions of DiEGME and TriEGME, it was easily damaged upon contact.

FSII Desorption Results. While the results show that DiEGME and TriEGME have similar absorption rates, it is important to assess relative desorption rates, as a slower desorption can contribute to increased topcoat degradation over time. To evaluate the relative desorption rate of FSII from the topcoat polymer matrix, the exposed panels were allowed to dry in a fume hood at ambient temperatures for various periods of time, rather than being immediately analyzed after exposure. The uptake for aqueous solutions of DiEGME was measured as a function of time and is shown in Figure 7.

The figure shows evidence for DiEGME desorption from the topcoat at the higher concentrations studied. At DiEGME concentrations less than 70 vol %, the equilibrium uptake is very similar for the four tested time periods. At concentrations greater than 70 vol %, there is a very large decrease in the DiEGME absorbed in the topcoat after only 2 h, and at longer times the desorption rate slows down significantly. The DiEGME concentration in the coating reaches its final equilibrium level in less than 24 h. It is interesting to note that DiEGME does not completely desorb from the topcoat, and the resulting final concentration of DiEGME in the topcoat is the same as the uptake level from the failed topcoat flakes at ~0.7 mol FSII/L topcoat for concentrations greater than 80 vol % in the water. In order for the dried flakes to have such a high concentration of FSII, they must have been exposed to an even greater concentration of DiEGME. Once the topcoat is exposed to a sufficient concentration of FSII to cause a failure, it is possible that the FSII in the coating will tend to desorb to this level.

As shown in Figure 8, the equilibrium uptake of TriEGME as a function of time is low up to a concentration of 50 vol % TriEGME. At higher concentrations, the data show evidence of desorption, but the TriEGME desorption is significantly slower at the 2 h mark. At the 100% FSII level, TriEGME is only reduced to 78% of the original concentration after 2 h, while the DiEGME concentration is reduced to 42%. This difference is likely due to the lower vapor pressure of TriEGME, which will cause it to evaporate
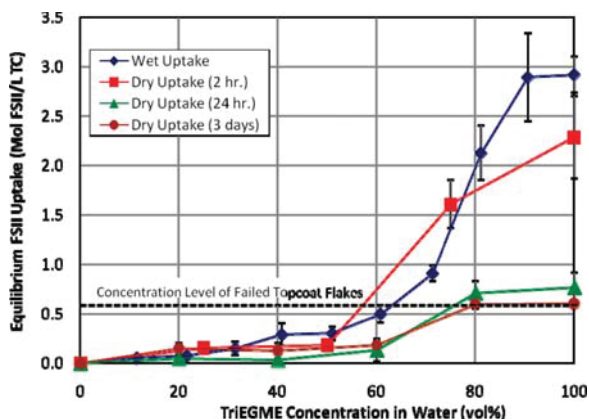
Figure 8. Uptake of TriEGME in aqueous solutions as a function of drying time with new panels.

more slowly from the topcoat. The slower rate of TriEGME desorption may also result from its larger molecular size, causing slower diffusion of the molecules through the polymer matrix. DiEGME and TriEGME desorb to a similar final concentration when given enough time to reach equilibrium.

The results show that TriEGME and DiEGME desorb to similar final equilibrium values, although their initial desorption rates vary. This difference in desorption rates at high concentrations of FSII indicates that it might be possible for high concentrations of TriEGME in the topcoat to be maintained for longer periods of time, with a resulting higher occurrence of topcoat degradation. However, it is expected that these high concentrations of TriEGME will not be achieved due to the lower vapor pressure of the additive, resulting in a reduced concentration in the condensate. This absorption/desorption study does not fully evaluate the entire FTTP process; however, it provides insight into the required concentration of FSII in jet fuel or water that will promote high absorption levels and subsequent topcoat degradation.

Pencil Hardness Study Results. Further studies were performed to evaluate topcoat integrity after the absorption of FSII has occurred. These studies provide insight into what concentration ranges of FSII in fuel or water provide sufficient absorption to cause topcoat degradation and promote FTTP. Pencil hardness measurement after absorption was selected as a simple technique to indicate topcoat degradation. A two day exposure time was selected to complete measurements in a reasonable time, while still maintaining the minimum exposure duration for equilibrium to be reached between the solution and topcoat. Each pencil hardness data point represents a single panel that was tested at the given FSII concentration. The first study used the surrogate condensate, discussed in the Experimental Section, which simulates the condensable fuel components from the fuel ullage. As it is hypothesized that the condensed vapors are the fuel components in contact with the fuel ullage tank walls where FTTP occurs, it is reasonable to study this using the fuel condensate surrogate mixture. Figure 9 shows a plot of the equilibrium uptake and pencil hardness of new panels in the surrogate as a function of the FSII concentration.

The figure shows a strong correlation between the pencil hardness of BMS 10-39 and the equilibrium uptake. The pencil hardness of the panel is unaffected at low FSII concentrations, but as the uptake begins to increase (> 0.80 vol %), a very sharp
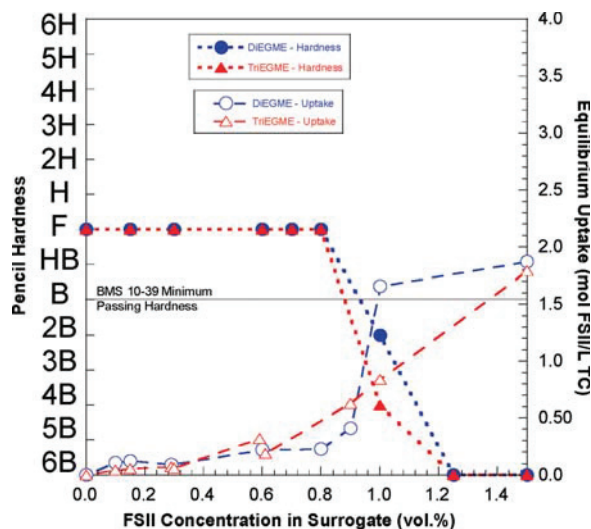
Figure 9. New panel uptake and wet pencil hardness in a fuel condensate surrogate.

decrease is observed. DiEGME and TriEGME behave very similarly in this pencil hardness evaluation. The equilibrium uptake level corresponding to the degradation of BMS 10-39 occurs at uptake levels greater than approximately 1.0 mol FSII/L topcoat. The topcoat integrity continues to decrease, and adhesion is lost as the concentration in the topcoat increases further. Exposure of BMS 10-39 topcoat panels to jet fuel (Jet A-1) containing FSII was compared to the surrogate mixture exposures, and in all cases it was found that the surrogate and jet fuel uptake and pencil hardness measurements were identical within experimental uncertainty. As both fuel and surrogate produce similar results, the surrogate was used for further pencil hardness studies to more closely simulate the conditions for FTTP.

Pencil hardness measurements were also performed with old panels to determine the effect of increased uptake on the hardness of the topcoat. If the older panels represent a worst-case scenario for the current BMS 10-39 coating in B-52 aircraft, then studying the pencil hardness of these panels after exposure to FSII is critical for investigating the requisite conditions for FTTP. The results are shown in Figure 10, along with FSII uptake measurements for old panels in the condensate surrogate.

The pencil hardness begins to decline rapidly at approximately 0.30 vol % FSII, which corresponds to an increase in the uptake. This FSII concentration is only twice the maximum procurement concentration for JP-8. The pencil hardness falls below the minimum passing rating of "B" at a FSII concentration of approximately 0.40 vol % FSII in the surrogate. This is a significant decrease from the concentration necessary to fail newer panels (approximately 1.0 vol % FSII). Overall, the older panels show a highly decreased ability to maintain coating hardness, as is evident by the increased absorption of FSII. These data imply that older panels have increased void spaces and weakened polymer bonds, resulting in a degradation of the topcoat matrix. These results indicate that older panels should be used for conservative analysis of aircraft fuel tank scenarios, due to the degraded properties of the topcoat after exposure to fuel and environmental conditions over many years.
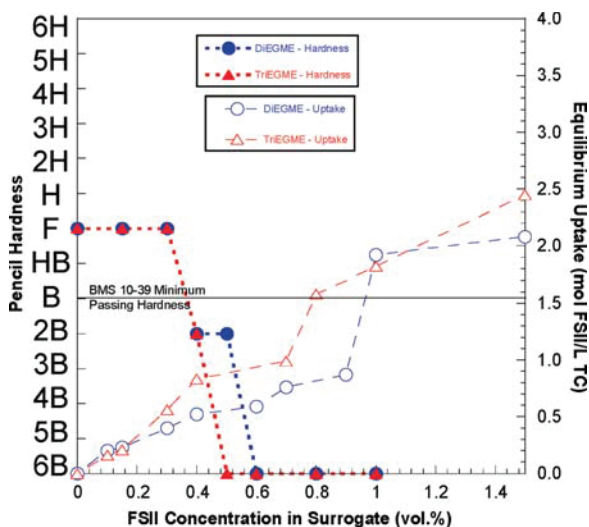
Figure 10. Uptake and pencil hardness of DiEGME and TriEGME in the condensate surrogate for old panels.
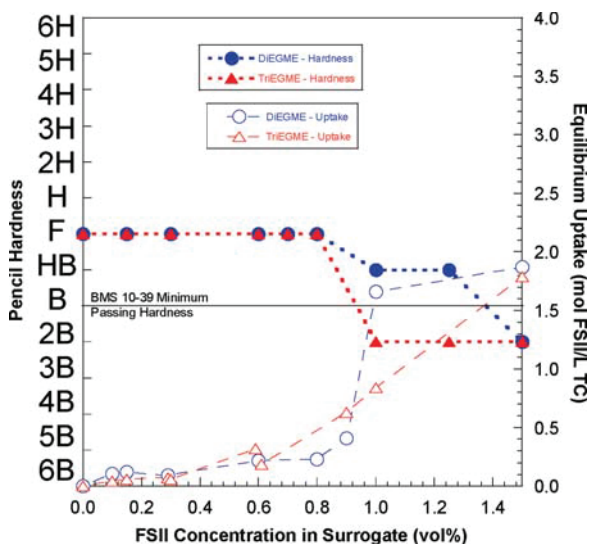

Figure 11. Pencil hardness for new panels in surrogate after 2 h of drying.

Pencil hardness testing was adapted to investigate the effect of FSII desorption from the topcoat. Instead of evaluating the hardness immediately after removal from the solution, testing was performed after drying for 2 h in a fume hood. This study was performed using the condensate surrogate and new panels under ambient conditions. The data are shown in Figure 11. It should be noted that the uptake data included in Figure 11 were obtained from extractions performed without adding a drying time before analysis.

The pencil hardness of BMS 10-39 topcoat decreases as the concentration of FSII in the surrogate increases; however, the hardness does not decrease to nearly the same extent as the panels evaluated immediately after contact with FSII. Panels exposed to DiEGME remain above the minimum passing hardness for BMS 10-39, except for 1.5 vol %
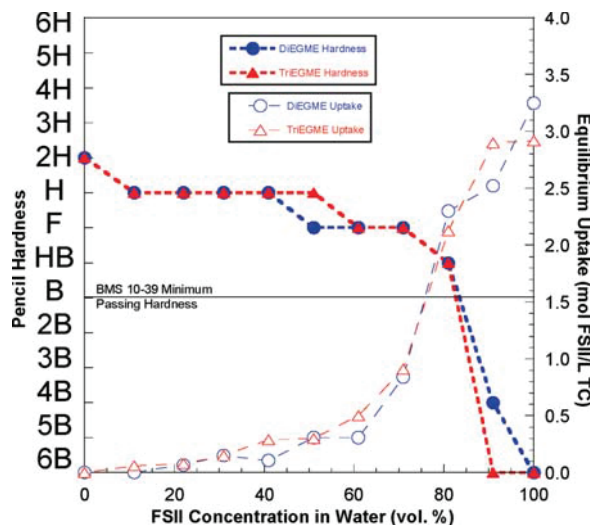
Figure 12. Pencil hardness and equilibrium FSII uptake of new panels in aqueous solutions with varying concentrations of FSII.

DiEGME in the surrogate. Panels exposed to TriEGME fall below the passing level at a concentration of 1.0 vol %. When the panels were evaluated "wet" (Figure 9), both DiEGME and TriEGME decreased the hardness at the same concentration of 1.0 vol % FSII. As discussed above, this difference could be due to the lower vapor pressure of TriEGME, which causes it to desorb and evaporate more slowly from the coating. It would be expected for the pencil hardness to reach the same level in both DiEGME and TriEGME if more time is given for desorption to occur, as the desorption data show that these additives reach the same final level in the topcoat. These data show that BMS 10-39 exposed to high concentrations of TriEGME will have a reduced hardness for a longer period of time compared to DiEGME. This could potentially increase the time frame for FTTP to occur, although these high concentrations of TriEGME in the topcoat are not expected to occur on tank ullage walls, as discussed below.

To study FTTP occurring in fuel tank water bottom areas, the pencil hardness was evaluated for new BMS 10-39 panels after exposure to aqueous solutions. Similar to the fuel and surrogate pencil hardness testing, this provides insight into the requisite concentrations in water bottoms for degradation. Figure 12 shows the "wet" pencil hardness testing and uptake as a function of aqueous FSII concentration for new panels.

The uptake dramatically increases at approximately 70 vol % FSII, while the pencil hardness also begins to decrease rapidly. New topcoat exposed to surrogate or fuel has been shown to degrade at approximately 2.0 mol FSII/L topcoat, and the aqueous solutions also show a very similar uptake concentration for failure. This degradation requires concentrations greater than 70 vol % DiEGME or TriEGME in water in contact with the topcoat. This is much higher than expected concentrations (30 to 50 vol %) in tank bottoms at ambient conditions with specification FSII levels in fuel.[8] The initial hardness of these panels exposed to aqueous solutions was slightly higher than those exposed to fuel surrogate solutions. While there was some variation with the initial hardness from both the new and old

(8) West, Z.; Shafer, L.; Striebich, R.; Zabarnick, S.; Delaney, C.; Phelps, D.; DeWitt, M. J. Manuscript in preparation, 2009.

2621

63

panels used, the surrogate alone seemed to have a very slight softening effect of one pencil lead on the topcoat. This could potentially be due to some slight swelling due to absorption of unknown fuel species into the BMS 10-39 coating.

The pencil hardness testing has been able to provide a comparison between DiEGME and TriEGME, which has shown statistically identical behavior for nearly all absorption measurements. It has also provided a greater understanding into what concentrations are necessary to initiate FTTP. Concentrations of FSII greater than 1.0 vol % are required to severely weaken the topcoat of new panels in a fuel or surrogate. Older panels only require concentrations of FSII greater than approximately 0.40 vol % FSII in the fuel or surrogate to degrade the topcoat below the minimum hardness. As discussed above, this difference in concentration is a result of the reduced capability of the older panels to resist FSII absorption. Aqueous solutions require concentrations greater than 80 vol % for new panels to fail.

The only differences between DiEGME and TriEGME were observed in the desorption studies. The more rapid recovery in the hardness of DiEGME-exposed panels is most likely due to its higher vapor pressure. Because there is less FSII remaining in the topcoat, there is less swelling and the coating retains a higher hardness. While DiEGME and TriEGME performed similarly in the absorption study, different pencil hardness results are expected when the vaporization process of FSII in the bulk fuel is combined with the condensation process of the fuel/FSII vapor onto the topcoat. It is expected for TriEGME to have a much lower concentration in the vapor, and thus a much lower concentration in contact with the topcoat, because of its reduced vapor pressure. The next section demonstrates a simulation system which attempts to reproduce the overall behavior of the fuel/FSII/topcoat system.

Fuel Tank Topcoat Peeling (FTTP) Simulation Results. A fuel tank simulation system was developed to attempt to recreate the required conditions for FTTP, as well as to evaluate the ability of TriEGME to reduce FTTP. In previous work,[6] the concentrations of DiEGME and TriEGME in the fuel condensate were compared. The results show that the concentration of DiEGME in the condensate increased with each distillate fraction and further vaporization, while the concentration of TriEGME in the condensate maintained a level below the initial concentration in the bulk fuel. While this previous work focused only on collecting and analyzing the fuel condensate, the FTTP simulation described here will promote fuel/FSII vaporization with subsequent selective condensation of the fuel vapor on an old topcoat panel. This simulation was designed to recreate all necessary steps for FTTP in a controlled setting. It also serves to investigate the effects of specific conditions on FTTP, such as the initial concentration of FSII in the bulk fuel, the temperature of the fuel, and the temperature of the condensing topcoat surface. Selective condensation on the topcoat panel was achieved by attaching a heat exchanger with a recycling cooled water bath to the back of the panel. Old panels were employed to provide a conservative measure of the effect of the FSII additives. The concentration range of FSII in the fuel was from 0 to 0.15 vol %, while the temperatures investigated were 50 or 60 °C in the environmental chamber, and a cooled panel surface of 10 to 30 °C. These ranges of concentrations and temperatures were selected, as they are believed to closely represent the worst-case ground conditions for FTTP in aircraft fuel tanks.

Table 2. DiEGME and TriEGME Experiments with the Environmental Chamber at 60 °C and the Condensation Surface at 20°C

	Initial FSII Conc. (vol%)	Final FSII Conc. (vol%)	Condensate FSII Conc. (vol%)	Exposure Time (Days)	Pencil Hardness
DiEGME	0	0.006	0.033	3	2H
	0.030	0.026	0.031	3	2H
	0.047	0.049	0.062	3	H-2H
	0.055	0.047	0.077	3	H-2H
	0.067	0.067	0.12	3	F-H
	0.067	0.069	0.076	5	F-H
	0.078	0.076	0.14	3	4B-H
	0.100	0.094	0.67	3	<6B-4B
	0.101	0.100	0.25	4	<6B-4B
	0.140	0.135	0.72	2	<6B
	0.156	0.138	1.09	5	<6B
TriEGME	0.051	0.052	0.065	3	2H
	0.080	0.101	0.12	4	2H
	0.135	0.135	0.15	3	H-2H
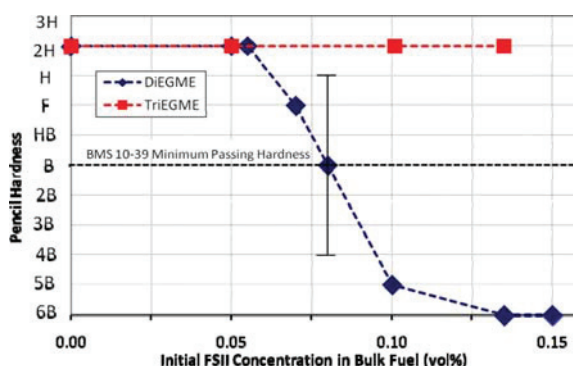
Figure 13. Pencil hardness of older panels after exposure to varying initial FSII concentrations in the bulk fuel.

Fuel and condensate samples were collected, their DiEGME and TriEGME concentrations were quantified after three to five days. This was shown to be sufficient for equilibrium to be reached, as discussed below. The data obtained from this set of experiments, at a fuel temperature of 60 °C and a cooling surface temperature of 20 °C, along with the quantified FSII concentrations are summarized in Table 2. Figure 13 presents the pencil hardness data as a function of the initial concentration for the experimental conditions in Table 2.

At concentrations equal to or below approximately 0.05 vol % DiEGME in the fuel, there were no visible changes in the panel after exposure, and the hardness of the topcoat was unaffected. This is evident by Figure 14, which shows the BMS 10-39 panel exposed to condensate from 0.05 vol % DiEGME in the fuel for three days. At concentrations of 0.06 to 0.10 vol % DiEGME in the fuel, there were initial signs of swelling in the panels. The hardness began to degrade quickly with any further increase in the DiEGME concentration in the fuel, although the panels were still relatively intact and did not show any severe signs of swelling and blistering. Figure 15 shows BMS 10-39 panels after

2622

Figure 14. Old panel exposed to condensed vapors from 0.05 vol % DiEGME in the bulk fuel.
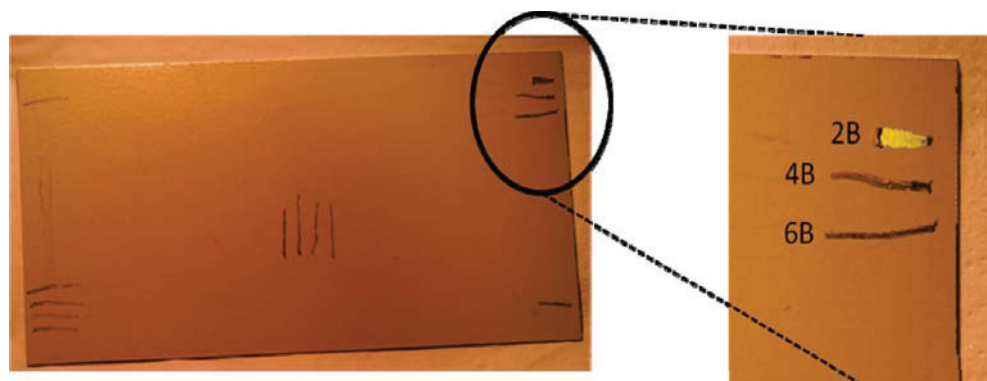
Figure 15. Old panel exposed to condensed vapors from 0.08 vol % DiEGME in the fuel with the pencil hardness measurements shown.

Figure 16. Old panel exposed to condensed vapors from 0.10 vol % DiEGME in the bulk fuel.

a three day exposure to condensate from ~0.08 vol % DiEGME in the bulk fuel. There were no visible changes in the topcoat panel after exposure to the DiEGME-rich condensate in this range; however, the hardness of the panel did decrease significantly on some portions of the coating. The center of the panel did pass a hardness of "H," which is above the minimum passing hardness for BMS 10-39; however, the edges only yielded a hardness of "4B."

A complete failure of the topcoat panels was evident for initial concentrations of approximately 0.10 vol % DiEGME in the fuel or greater. Along with the hardness decreasing below the minimum specification, the coating itself exhibited signs of severe swelling and blistering as well as a loss of adhesion from the aluminum substrate. Figure 16 shows a topcoat panel after three days' exposure to condensate from ~0.10 vol % DiEGME in the fuel. The center of the panel

Figure 17. Old panel exposed to condensed vapors from 0.10 vol % TriEGME in the bulk fuel.

yielded a hardness of 4B, while the edges of the panel were not tested, as they were severely swollen and delaminated from the aluminum substrate. The largest failure regions on the panel typically occurred on the sides and edges of the panel, while the center showed slightly less degradation. This could be explained by a nonuniform condensation on the surface of the panel due to nonuniform surface temperatures created by inadequate contact with the heat exchanger. The panel was attached to the cooled steel heat exchanger plate by clamps on the edges and along the top of the panel. This may have provided better contact to the heat exchanger and a colder surface that selectively condensed the FSII-rich vapor in these regions.

The use of TriEGME in this FTTP simulation study in place of DiEGME provided completely different results for all aspects of this experiment. BMS 10-39 panels showed no degradation after exposure to condensed vapors from TriEGME-containing fuels at all of the concentrations tested. Figure 17 shows a topcoat panel after exposure to condensate from ~0.10 vol % TriEGME in the bulk fuel. The figure shows a topcoat panel that was completely unaffected by contact with concentrations of approximately 0.12 vol % TriEGME in the condensate. There is no visible discoloration or swelling after exposure, and the pencil hardness of the coating did not decrease. At these concentration levels, TriEGME exhibits excellent anti-icing performance.[6]

As DiEGME and TriEGME performed almost identically in the uptake and pencil hardness testing shown above, the reason for the decreased degradation caused by TriEGME is due to the lower concentration in contact with the topcoat, which results from the lower vapor pressure of TriEGME. Gas chromatograms of fuels, DiEGME, and TriEGME (not shown) suggest that DiEGME is more volatile than most jet fuel components, while TriEGME is slightly less volatile than the average fuel components. Thus, at temperatures below the initial fuel boiling point (< 200 °C), DiEGME will preferentially concentrate in the vapor relative to most fuel components, while TriEGME will vaporize along with the fuel components and not increase in concentration in the vapor. Thus, the topcoat will be exposed to concentrations of TriEGME which are far below that shown to cause degradation in the absorption studies reported above.

Table 2 shows a significant difference between the DiEGME and TriEGME concentrations in the sampled condensate. It should be noted that these FSII concentration determina-

tions were difficult to perform, as only microliter volumes could be collected from the panel surface using a GC syringe. The concentrations of DiEGME in the condensate increased by a factor of up to seven compared to the initial bulk fuel concentration. Typically, higher concentrations of DiEGME in the fuel yielded much higher concentrations in the condensate. For example, a concentration of approximately 0.15 vol % DiEGME in the fuel resulted in a condensate of 1.09 vol % DiEGME. TriEGME does not show this large increase in the condensate concentration and only increases by a factor of 1.2 on average for the runs. A maximum value of 0.15 vol % TriEGME in contact with the topcoat is not sufficient to cause degradation, as was also confirmed by the previous pencil hardness study experiments (Figure 10). In the pencil hardness study, the pencil hardness of old panels after exposure to concentrations of 1.0 vol % DiEGME in the surrogate resulted in a hardness of <6B, which is seen under these simulation conditions. The increase in DiEGME concentrations in the condensate is also supported by the ullage box data obtained from previous work.[6] Table 2 shows that the concentration of DiEGME in the condensate clearly increased from the initial concentration in the fuel for each experimental condition. However, the TriEGME result differs from the previous work. The data from Table 2 show an increase of TriEGME in the condensate, while the previous study showed a significant decrease in the TriEGME condensate. This difference could be explained by the relatively low distillation percentage collected in the previous work. Also, the glass collector used previously condensed the fuel condensate at a much lower temperature of −10 °C. This lower temperature may not selectively condense TriEGME from the vapor, but rather, lighter fuel components may be more likely to condense, lowering the concentration of TriEGME.

The time needed to reach equilibrium between the vapor, the condensate, and the topcoat was also studied as shown in Table 2. Degradation could be seen as early as one day for concentrations of 0.07 vol % DiEGME or greater in the bulk fuel; however, more time was given to ensure the entire panel reached equilibrium. Figure 18 shows a BMS 10-39 panel clamped to the heat exchanger while exposed to approximately 0.10 vol % DiEGME after one day. It is evident that there are droplets of the FSII-rich condensate in contact with the topcoat surface, which has begun to swell and blister. Figure 18 also serves to show the increased condensation on

2624

66

Figure 18. Old BMS 10-39 panel in the FTTP simulation box showing severe swelling after one day of exposure to vapors from 0.10 vol% DiEGME in the fuel.

the edges of the panel, where greater amounts of fluid are present. Three days of exposure was found to be sufficient in reaching an equilibrium state between the fuel and the top-coat, as well as to obtain a visual confirmation of the integrity of the topcoat. This was confirmed by running two experiments at 0.067 vol % DiEGME in the fuel, with one panel being exposed for three days and the other for five days. While there was a small difference in the DiEGME concentration in the condensate, the pencil hardness and visual appearance of the panels were identical.

The effects of temperature on the degradation process were also studied to determine the conditions necessary for FTTP to occur. The temperature of the environmental chamber and the cooling surface were varied to determine how they affected the vaporization and condensation processes and topcoat degradation. These additional DiEGME experiments also served to evaluate the minimum concentration of DiEGME in the bulk fuel which would no longer produce FTTP. BMS 10-39 panels were evaluated on the basis of their pencil hardness as a function DiEGME concentration and temperature, as shown in Table 3. The bulk fuel and condensate DiEGME concentrations were also measured.

The environmental chamber was heated to 50 or 60 °C, while the cooling surface temperature was varied between 10 and 30 °C for this study. These temperatures were used to simulate the expected ground conditions in a fuel tank, as well as determine what temperatures will cause the most severe degradation. The initial runs at 60 °C fuel, 20 °C cooling (60/20 °C) showed a significant amount of degrada-tion, especially at concentrations greater than 0.10 vol % DiEGME in the fuel. To further investigate the other temperatures, an initial fuel concentration of approximately 0.07 vol % DiEGME was used, as this was within the transition range for topcoat failure at the 60/20 °C condi-tions. This concentration could then be altered on the basis of the topcoat behavior to further evaluate the effect of temperature.

Table 3. Experimental Simulations with DiEGME Performed at Various Temperatures and Concentrations

Fuel Temperature (°C)	Cooling Surface Temperature (°C)	Initial Conc. (vol%)	Final Conc. (vol%)	Condensate Conc. (vol%)	Test Period (days)	Pencil Hardness
60	20	0	0	0	3	H-2H
		0.047	0.049	0.062	3	H-2H
		0.055	0.047	0.077	3	H-2H
		0.067	0.067	0.12	3	F-H
		0.078	0.076	0.14	3	4B-H
		0.100	0.094	0.67	4	<4B
		0.101	0.100	0.25	4	<4B
		0.140	0.135	0.72	2	<6B
		0.156	0.138	1.09	5	<6B
	30	0.070	0.069	0.046	3	H-2H
		0.088	0.087	0.087	3	H-2H
	10	0.070	0.060	0.19(56.4%)*	3	HB-H
		0.109	0.086	0.28(62.5%)*	3	2B-F
50	20	0.072	0.070	0.10	3	H-2H
		0.093	0.091	0.20	14	F-H
	10	0.079	0.072	0.25(57.1%)*	3	H-2H

(* denotes 2nd aqueous phase concentration)

Increasing the cooling surface to 30 °C increased the hardness of the panel compared to a cooling surface of 20 °C, for the two tested concentrations of approximately 0.07 and 0.09 vol % DiEGME in the bulk fuel. This is most likely due to the surface temperature being high enough such that DiEGME no longer selectively condensed relative to fuel vapors on the panel. The condensate samples did contain lower concentrations of DiEGME than was measured in the 20 °C cooling surface experiments. Lowering the cooling surface temperature to 10 °C also did not promote FTTP as readily. While increasing the initial DiEGME concentration in the fuel to approximately 0.11 vol % did reduce the pencil hardness below the minimum passing hardness at this con-dition, it was still not as severe of a failure as the 60/20 °C condition at a similar initial concentration. Lowering the cooling surface to 10 °C appeared to promote condensation of two phases on the topcoat panel, an aqueous and a hydrocarbon phase. Two condensed liquid phases were observed visually on the topcoat surface. The identity of

2625

67

the phases was confirmed by refractive index as well as GC-MS analysis of the composition and DiEGME concentration. The addition of an aqueous phase on the topcoat surface may provide a benefit to the topcoat integrity, as DiEGME will partition readily into the aqueous phase, reducing the concentration in the hydrocarbon phase. This benefit will only be realized as long as high concentrations (> 70%) are not reached in the aqueous phase.

The other runs involved reducing the fuel temperature to 50 °C to determine if lowering the temperature would significantly reduce the vaporization of DiEGME. The 50/20 °C experiment at approximately 0.07 vol % DiEGME did not produce any detectable change in the pencil hardness, or any visual evidence of failure. It was unclear if sufficient exposure time was given to reach equilibrium at this lower temperature, as it would require more time to vaporize DiEGME and accumulate sufficient amounts in the topcoat to cause degradation. The second run at a higher concentration of approximately 0.09 vol % DiEGME was exposed for 14 days. The BMS 10-39 panel did decrease in pencil hardness slightly, although the coating was still two pencil leads above the minimum passing hardness. This decrease in hardness was most likely a function of the increased concentration of DiEGME in the fuel and subsequent condensate, and not the increased exposure time. An environmental chamber temperature of 50 °C reduced the vaporization of DiEGME in the system such that the condensate concentration did not cause a significant decrease in the topcoat hardness or initiate severe swelling. The final run of 50/10 °C also did not degrade the topcoat panel. This condition created two phases on the panel surface, which seemed to indicate that a cooling surface of 10 °C was sufficient to condense any water within the system.

Overall, experimental simulation of FTTP in this system provided data for the determination of the concentrations and temperatures necessary to promote this phenomenon. The initial conditions of 60/20 °C were ideal for creating an FTTP scenario. While other temperatures did produce some deterioration of the BMS 10-39 coating, the hardness of the panel was still above the minimum specification. The fuel temperature needs to be sufficiently warm such that high concentrations of DiEGME are vaporized, and the condensing surface temperature needs to be low enough to selectively condense DiEGME, but not so low as to condense water. On the basis of this study, continued use of DiEGME as the FSII additive will require a significant decrease in concentration, as FTTP will occur at current procurement concentrations if the correct temperature conditions are reached. The highest concentration that did not cause the hardness of the topcoat to fall below the minimum specification was approximately 0.07 vol % DiEGME. TriEGME did not cause topcoat degradation at any of the concentrations tested in this simulation (up to 0.135 vol %).

Conclusions

The compatibility of DiEGME and TriEGME with BMS 10-39 topcoat material was studied to provide a better understanding of the fuel tank topcoat peeling mechanisms, to determine the requisite conditions for degradation to occur, and to determine the conditions under which degradation can be prevented. Under liquid exposure conditions, both fuel system icing inhibitor additives were found to partition equally, on a molar basis, into the topcoat over a wide range of concentrations. This was demonstrated for aqueous, fuel, and fuel surrogate solution exposures for both old and new topcoat panels. The absorption of FSII was found to increase dramatically for old panels relative to new panels. The old panels are considered to be representative of topcoat surfaces of real fuel tank walls in the current USAF fleet. The new panels studied are likely more resistant to FSII absorption than what is currently present in B-52 aircraft.

The desorption rate of FSII out of the topcoat differed between DiEGME and TriEGME. Initially, TriEGME showed a slower desorption rate than DiEGME, which can be explained by its lower vapor pressure and greater molecular size. After 2 h, the DiEGME and TriEGME concentrations in the panel began to reach similar levels, and eventually reached a final concentration of approximately 0.7 mol FSII/L topcoat after aqueous exposures of 80 vol % FSII or greater. This concentration was similar to that from failed topcoat flakes, which suggests that the FSII component in the topcoat will not completely desorb or evaporate after exposure to high concentrations. In the pencil hardness study, both DiEGME and TriEGME performed identically within experimental error. There was a large difference between the new and old panels, with the old panels falling below the passing hardness lead of "B" when exposed to FSII concentrations as low as 0.40 vol % in the fuel surrogate, while the new panels required concentrations of 1.0 vol % for failure. In pencil hardness measurements of FSII desorption, the hardness of the topcoat was found to increase as desorption occurs. This hardening effect is indicative of relamination of the topcoat after FSII exposure and topcoat softening.

The experimental simulation that was developed to recreate FTTP in a controlled setting was the first laboratory system able to reproduce the entire FTTP process and to determine the requisite conditions for topcoat failure. DiEGME was found to concentrate in the ullage vapor by a factor of 2 to 7 times the initial concentration in the fuel. These high condensate concentrations resulted in severe degradation of the topcoat. The highest concentration in the bulk fuel that did not cause a failure, as rated by the pencil hardness of the coating, was at ~0.07 vol % DiEGME. However, TriEGME proved very effective as it did not lower the pencil hardness of the topcoat panel up to approximately 0.14 vol % TriEGME. The resulting TriEGME condensate concentration did increase on average by a factor of 1.2, although this small increase did not prove detrimental to the BMS 10-39 panel. The lower vapor pressure of TriEGME was determined to be the major reason for its improved topcoat compatibility for fuel tank ullage surfaces. On the basis of these results, TriEGME has been shown to be an excellent FSII replacement in terms of BMS 10-39 topcoat material compatibility. During the scenarios analyzed in these studies, TriEGME would not cause degradation to the topcoat at the current concentrations employed for DiEGME in JP-8. If DiEGME continues to be used as the specification FSII additive, it is recommended that the maximum concentration in aircraft tanks be no more than 0.07 vol % to prevent topcoat degradation. This should prevent high concentrations of DiEGME vaporizing and condensing on topcoat surfaces. Adherence to required maintenance practices, such as sumping of fuel tanks, is essential to the prevention of FTTP in water bottoms when either FSII additive is used.

The occurrence of FTTP in the simulated fuel tank box was dependent on the temperatures of the fuel and condensing

surfaces. Fuel temperatures of 60 °C were able to selectively vaporize levels of DiEGME sufficient to cause swelling and blistering. Lower temperatures were unable to provide condensate concentrations that were sufficient to cause degradation of the coating during the test period. The optimum cooled surface temperature for selective condensation of DiEGME and topcoat degradation is near 20 °C. At higher temperatures, the surface condensate had reduced DiEGME concentrations, and below 20 °C, an aqueous phase condensed on the topcoat surface, which decreased the concentration of DiEGME in contact with the polymer.

Appendix B. Flame Stabilization in Small Cavities

Flame Stabilization in Small Cavities

Alejandro M. Briones[*]
University of Dayton Research Institute, Dayton, Ohio 45469

Joseph Zelina[†]
U.S. Air Force Research Laboratory, Wright-Patterson Air Force Base, Ohio 45433

and

Viswanath R. Katta[‡]
Innovative Scientific Solutions, Inc., Dayton, Ohio 45440

This research is motivated by the necessity to improve the performance of ultracompact combustors, which requires flame stabilization in small cavities. An extensive computational investigation on the characteristics of cavity-stabilized flames is presented. A high-fidelity, time-accurate, implicit algorithm that uses a global chemical mechanism for JP8-air combustion and includes detailed thermodynamic and transport properties as well as radiation effects is used for simulation. Calculations are performed using both direct numerical simulation and standard k-ε Reynolds-averaged Navier–Stokes model. The flow unsteadiness is first examined in large axisymmetric and small planar cavities with nonreactive flows. As with previous investigations on axisymmetric cavities, multiple flow regimes were obtained by varying cavity length (x/D_o): wake backflow regime, unsteady cavity vortex regime, steady cavity vortex regime, and compressed cavity vortex regime. However, planar cavities only exhibit steady cavity vortex and compressed cavity vortex regimes. Two opposed nonaligned air jets were positioned in this planar cavity: the outermost air jet in coflow with the mainstream flow (i.e., normal injection). The fuel jet was injected either in coflow, crossflow, or counterflow with respect to the mainstream flow. Flow unsteadiness was observed to be relatively small for coflow- and crossflow-fuel-jet injection. By reversing the air jet positions (i.e., reverse injection), the flow unsteadiness is promoted regardless of fuel jet positioning. Finally, the effect of combustion and cavity equivalence ratio (ϕ_{CAV}) on flame unsteadiness is addressed. With normal injection (reverse injection), low and high ϕ_{CAV} leads to low (high) and high (low) flame unsteadiness, respectively. Based on these results recommendations are provided to designers/engineers to reduce flame unsteadiness in these cavities.

Nomenclature

C_P = pressure coefficient
D = planar cavity depth
D_o = forebody diameter
D_S = spindle diameter
L = planar cavity length
Re_D = global Reynolds number based on cavity depth, D
Re_x = cavity Reynolds number based on axisymmetric cavity length, x
R_o = forebody radius
x = axisymmetric cavity length
ΔC_D = change in drag
$\Delta C_{D,P}$ = change in pressure drag
$\Delta C_{D,S}$ = change in shear drag
λ_{CAV} = cavity air to fuel jet momentum ratio
ϕ_{CAV} = cavity equivalence ratio

I. Introduction

MAJOR advances in combustor technology are required to meet the conflicting challenges of improving performance, increasing durability, reducing weight, lowering emissions, and

  *Research Engineer, Energy and Environmental Engineering Division, 300 College Park/0043. Member AIAA.
  †Senior Research Engineer, 1950 Fifth Street. Associate Fellow AIAA.
  ‡Senior Research Engineer, 2766 Indian Ripple Road. Senior Member AIAA.

maintaining cost. A novel approach proposed by the U.S. Air Force Research Laboratory/RZTC [1,2] is the development of the ultracompact combustor (UCC). The UCC design uses high swirl in a circumferential cavity (cavity refers to a space lacking of solid and filled with gas) to enhance mixing rates via high cavity gravity loading on the order of $3000g$. The UCC shows how the primary, intermediate, and dilution zones of a conventional combustor can be incorporated into a much smaller footprint using compressor and turbine features that enable a shorter and potentially less complex gas turbine. It combines the high-gravity combustor circumferential cavity and strut with the compressor exit vanes and the high-pressure turbine inlet guide vanes (IGV). Because recent investigations [3] on the UCC have shown promising improvements on performance for future engine implementation, it is envisioned that the UCC could be either used as the main combustor or as an interturbine burner between the high- and low-pressure turbines to operate in a reheat cycle engine.

A schematic of the current UCC is shown in Fig. 1. The main air (or vitiated) flow enters the combustor and flows around the bullet nose of the center body. The turning vanes (indicated as "guide vane") simulate the swirl that would be coming from the compressor rotor in a real gas turbine engine. The flow from the trailing edge of these turning vanes impinges on the IGV (indicated as "blade"). The function of the IGV is the same as that of a conventional gas turbine engine. A radial cavity located in the IGV, aligned with the circumferential cavity, facilitates transport of gases from the circumferential cavity to the main stream. Additional air is admitted through 24 holes equally spaced around the circumferential cavity and angled at 45 deg to the radial direction to promote high swirl in the cavity. At the cavity-in-cavity (CIC), a small amount of air is injected and fuel is sprayed into the circumferential cavity. This allows fuel-rich combustion to occur in the circumferential cavity. Consequently, combustion primarily takes place in the engine circumferential direction rather than in the axial direction as is conventionally done. The circumferential cavity is analogous to a centrifuge; hence, cold nonreactive fuel–air mixture migrates radially outward, whereas hot
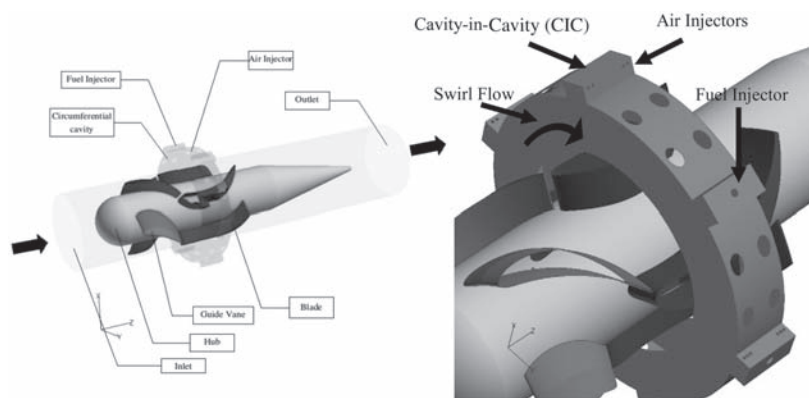
224

Fig. 1 Ultracompact combustor; inlet, hub, guide vane, blade, circumferential cavity, outlet, cavity-in-cavity, air injectors, and fuel injectors are indicated. The swirl flow is also indicated by the bent arrow on the circumferential cavity.

reacted mixture migrates radially inward. The cold mixture remains in the circumferential cavity for a longer period of time to evaporate, mix, and burn. The large density gradient in the cavity along with the high-gravity flow enhances mixing of cold and hot mixtures creating a very well-mixed combustion zone. The intermediate products of combustion are transported by lower wake pressures into the radial cavities where fuel-lean combustion occurs.

Numerous design variations of the selected configurations have been evaluated, leading to improved configurations with optimized performance and higher efficiency [3–7]. Although the UCC exhibits many advantageous features over conventional burners, it poses a particular difficulty regarding lean blowout and flame stability. The CIC shown in Fig. 1 was one of the latest additions to the UCC. Without the CIC, the gaseous flow high speed and acceleration in the circumferential cavity demands fuel injection with low residence times. In addition, the high-gravity loading enhances strain rates and, consequently, promotes extinction. The CIC is a workaround to these problems by channeling a second cavity inside the primary one. The fuel injected with additional air jets through the CIC is to increase fuel-injection residence times and to reduce local strain rates, while enhancing the fuel-air mixing. Hence, the small CIC with dimensions of a few millimeters and inherent global Reynolds number $Re_D \approx 10,000$ acts as a flame holder. [We refer to small cavities as those whose dimensions are very small in comparison with the characteristic length of the combustor. For instance, our planar cavity exhibits cavity length to combustor length of ∼10% (cf. Fig. 1). It turns out that these cavities generally exhibit global Reynolds number $(Re_D) \approx 10,000$. On the other hand, we refer to large cavities as those with cavity length to combustor length greater than ∼50% with usual Re_D greater than 10,000 (e.g., $(Re_D) \approx 70,000$). Large cavities reported in the literature usually exhibit one order of magnitude larger residence time than small cavities.] Even though the CIC concept has proven to enhance the performance of the UCC, there is still further need for improvement [3]. The fuel and air jets in the CIC create vortices, which, depending on the cavity dimensions, equivalence ratio, and injector positions, could lead to highly unstable flow. This in turn leads to flame instability, which induces higher residence times and promotes fuel-rich environments that increase pollution and soot formation. Therefore, current efforts are oriented toward determining design criteria for reducing flame fluctuations in the CIC.

Most previous investigations have dealt with nonreactive and reactive flow stability criteria in large axisymmetric [8–11] and planar [12–15] cavities with dimensions on the order of a few centimeters, $Re_D > 10,000$, and an order of magnitude larger residence time than those expected in the CIC.§ Consequently, the flow/flame stabilization in the CIC is more complicated than in previous studies [8–15]. For instance, for large cavities, the fuel is nearly fully consumed inside the cavity and the flame is contained in

the cavity [10,11,15]. On the contrary, in CIC-like cavities, very little amount of the fuel is burned in the cavity, extending the flame outside it [16]. Despite these facts, it is worth discussing the flow/flame stabilization criteria in large cavities because it provides insights into flame stabilization in CIC-like cavities. Mair [8] experimentally examined the effect of an afterbody disk on the drag of a blunt-based forebody-spindle object. His experiments showed that the drag of the forebody-spindle object is significantly reduced by mounting an afterbody disk. Further reduction in drag was observed by mounting a secondary afterbody disk. Little and Whipkey [9] performed similar experiments. They identified three regimes associated with drag. These are the wake backflow (WBF), unsteady cavity vortex (UCV), and the steady cavity vortex (SCV) regime. In the WBF, flow downstream the afterbody spills upstream into the cavity and the cavity exhibits a counter-rotating vortex¶ with high-drag coefficient. By moving the afterbody disk downstream from where WBF regime exists, the flow in the cavity transitions to the UCV regime. The cavity exhibits a corotating vortex** and the wake backflow does not move upstream past the afterbody disk. The drag coefficient C_D fluctuates from low- to high-drag condition. When the disk is positioned at its optimum from the forebody, the flow in the cavity is said to be in the SCV regime. Here, the vortex rotates (with edge velocity) in the same direction as the mainstream velocity, fits the cavity nearly perfectly, mass transfer into or out of the cavity is minimum, there is no backflow, and is characterized by low drag. Their cavity optimization criterion was based so that, to reduce C_D, the afterbody disk needs to be large enough to separate the wake backflow from the cavity flow so that a locked vortex can exist in the cavity. Therefore, with the proper choice of cavity dimensions, vortices in the cavity can be made stationary. However, a steady vortex yields minimum mass exchange between the vortex and the main flow, which in the CIC means that additional air must be supplied within the cavity for combustion to be sustainable. Consequently, Katta and Roquemore [10,11] conducted an extensive numerical investigation to determine the effect of combustion on cavity-stabilized flames. They showed that, for nonreactive flow, both standard k-ε Reynolds-averaged Navier–Stokes (RANS) model and direct numerical simulation (DNS) can be used to predict ΔC_D with cavity size. They also showed that the optimum cavity length determined from nonreactive flows yields to nonshedding cavity flows, even with combustion and primary injection into the cavities.

Planar cavities better emulate the shape of the CIC (cf. Figure 1). Zdanski et al. [12,13] numerically studied the nonreactive flow past two-dimensional trenchlike cavities and showed that, with increasing

---

§The residence time scales with length for turbulent flows.

¶Throughout the text, counter-rotating vortex means that the vortex edge velocity is in the opposed direction to the mainstream velocity. The mainstream flow is not rotating.

**Throughout the text, corotating vortex means that the vortex edge velocity is in the same direction as the mainstream velocity. The mainstream flow is not rotating.

Table 1   Transport coefficients and source terms appearing in governing equations

Equations	Φ	Γ^Φ	S^Φ
Continuity	1	0	0
Axial momentum	u	μ	$-\frac{\partial P}{\partial z} + (\rho_0 - \rho)g + \frac{\partial}{\partial z}\left(\mu\frac{\partial u}{\partial z}\right) + \frac{\partial}{\partial r}\left(\mu\frac{\partial v}{\partial z}\right) + \frac{\mu}{r}\frac{\partial v}{\partial z} - \frac{2}{3}\left\{\frac{\partial}{\partial z}\left(\mu\frac{\partial u}{\partial z}\right) + \frac{\partial}{\partial z}\left(\mu\frac{\partial v}{\partial r}\right)\right\} + \frac{\partial}{\partial z}\left(\mu\frac{v}{r}\right)$
Radial (transverse) momentum	v	μ	$-\frac{\partial P}{\partial r} + \frac{\partial}{\partial r}\left(\mu\frac{\partial u}{\partial r}\right) + \frac{\partial}{\partial r}\left(\mu\frac{\partial v}{\partial r}\right) + \frac{\mu}{r}\frac{\partial v}{\partial r} - 2\mu\frac{v}{r^2} - \frac{2}{3}\left\{\frac{\partial}{\partial r}\left(\mu\frac{\partial u}{\partial z}\right) + \frac{\partial}{\partial r}\left(\mu\frac{\partial v}{\partial r}\right)\right\} + \frac{\partial}{\partial r}\left(\mu\frac{v}{r}\right)$
Species mass fraction	Y_i	$\rho D_{i-\mathrm{mix}}$	$\dot{\omega}_i$
Energy	H	$\frac{\lambda}{c_p}$	$\nabla\left[\frac{\lambda}{c_p}\sum_1^{N_S}\left\{\left(Le_i^{-1}-1\right)H_i\nabla Y_i\right\}\right] - \sum_1^{N_S}\left\{h_{f,i}^0\dot{\omega}_i\right\} + q_{\mathrm{rad}}$

the cavity aspect ratio, two vortices in the cavity appear. At a critical aspect ratio, the external flow reattaches to the surface that is parallel to the mainstream flow. Similarly, D'yanchenko et al. [14] experimentally studied the nonreactive flow past heated two-dimensional trenchlike cavities with inclined frontal and rear walls. They showed that, for an interval of wall inclination angles, the flow in the cavity becomes unstable with the primary vortex changing its structure from single cellular to double cellular. Recently, Puranam et al. [15] investigated experimentally the flame stabilization in a curving, contracting channel with an inner large cavity. They showed that, at low Reynolds number (1000–10,000), the flame extends outside the cavity, whereas at high Reynolds number ($\geq 40,000$), combustion occurs inside the cavity. In between these regimes, the flame was unstable.

Because flow/flame stabilization in small cavities is so specialized, there are (to the best of our knowledge) only two investigations reported in the literature. Zelina et al. [3] experimentally studied multiple air injection strategies on the performance of the CIC, while the fuel was injected radially as in Fig. 1. The configurations included the following: (config. 1) two-nonaligned opposed air jets with the outermost jet in coflow with the mainstream flow, (config. 2) one single innermost air jet in counterflow with the mainstream flow, and (config. 3) no air jets. Cavity equivalence ratio ϕ_{CAV} at lean blowout was found to be as low as 0.08 for config. 3 and as high as 1.5 for config. 1. Decreasing the cavity air to fuel momentum ratio λ_{CAV} led to higher ϕ_{CAV} at lean blowout for all configurations. Moreover, Katta et al. [16] performed two-dimensional, unsteady, reacting flow numerical simulations on a trenchlike cavity with fuel and air injections. The parametric investigation indicated that there is a cavity optimum size that minimizes flow unsteadiness. Therefore, the purpose of this investigation is to enhance our understanding regarding cavity-stabilized flames that might lead to the development of concepts for the design of higher performance CIC. First, we will start by reviewing and expanding the discussion on the criteria of flow unsteadiness in large axisymmetric cavities. Second, we will apply the concepts related to large axisymmetric cavities to small planar cavities. Third, the effect of fuel and air injections on flow unsteadiness will be addressed for small planar cavities. Fourth, the effect of fuel-injection positioning to flow unsteadiness will be examined in small planar cavities. Then, the effect of air injection positioning on flow unsteadiness will also be investigated in these

cavities. Finally, we will discuss the effect of combustion and cavity equivalence ratio on flow/flame unsteadiness.

II. Physical-Numerical Procedure

A. Gas-Phase Numerical Model

The numerical model is based on the solution of the time-dependent governing equations for a two-dimensional unsteady reacting flow [17,18]. Using cylindrical coordinates (r, z) these equations can be written as

$$\frac{\partial(\rho\Phi)}{\partial t} + \frac{\partial(\rho v\Phi)}{\partial r} + \frac{\partial(\rho u\Phi)}{\partial z} = \frac{\partial}{\partial r}\left(\Gamma^\Phi\frac{\partial\Phi}{\partial r}\right) + \frac{\partial}{\partial z}\left(\Gamma^\Phi\frac{\partial\Phi}{\partial z}\right)$$
$$- \frac{\rho v\Phi}{r} + \frac{\Gamma^\Phi}{r}\frac{\partial\Phi}{\partial r} + S^\Phi \tag{1}$$

Here, t denotes the time, ρ the density, and u and v the axial z and radial r velocity components, respectively. The general form of the equation represents conservation of mass, momentum, species, or energy conservation, depending on the variable used for Φ. The diffusive transport coefficient Γ^Φ and source terms S^Φ are described in Table 1. Introducing the overall species conservation equation and the state equation completes the equation set. In addition, a sink term based on an optically thin gas assumption is included in the energy equation to account for thermal radiation from the flame [19]. The sink term due to the radiation heat loss is expressed as $q_{\mathrm{rad}} = -4\sigma K_p(T^4 - T_o^4)$ [20] where T denotes the local flame temperature. The term K_p accounts for the absorption and emission from the participating gaseous species (CO_2, H_2O, CO, and CH_4) and is expressed as

$$K_p = P\sum_k X_i K_{p,i}$$

where $K_{p,i}$ denotes the mean absorption coefficient of the kth species. Its value is obtained by using a polynomial approximation to the experimental data provided in [21].

The finite difference forms of the momentum equations are obtained using QUICKEST scheme [22], whereas those of the species and energy are obtained using a hybrid scheme of upwind and central differencing. The pressure field is calculated at every time
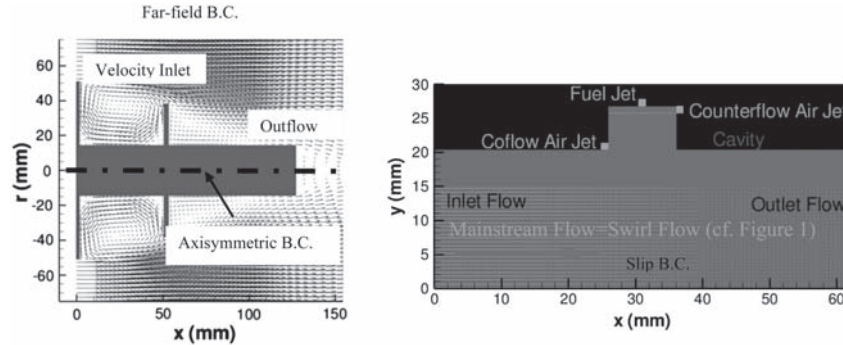
Fig. 2   Computational domains for the axisymmetric cavity (left) and the planar cavity (right). The axisymmetric cavity has been mirrored. The sample axisymmetric cavity corresponds to the case in which the afterbody disk is placed at $x/D_o = 0.5$. The whole computational domain is not shown here. The planar cavity indicates the location of the injections in its normal configuration. The boundary conditions are also indicated. The air mainstream flow direction is also indicated for the small planar cavity case. Note that the air mainstream flow corresponds to the swirl flow in Fig. 1.

step by solving all of the pressure Poisson equations simultaneously and using the lower and upper diagonal matrix-decomposition technique.

Figure 2 illustrates the computational domains for the large axisymmetric and small planar cavities. They consist of 229×229 mm and 62×30 mm in the axial x and radial r (vertical y) directions, respectively, and are represented by a staggered, non-uniform grid system (300×300 and 401×421, respectively). The axisymmetric cavity contains a forebody with diameter D_o of 101.6 mm, spindle diameter D_S of 28.6 mm, afterbody disk diameter D_1 of 38.1 mm, afterbody disk thickness of 1.5 mm, and spindle length of 127 mm. The upstream flow approaches the forebody-spindle-afterbody geometry at uniform and constant velocity and temperature of 30.5 m/s and 300 K, respectively. Throughout this investigation, only the distance of the afterbody disk to the forebody is varied. Only nonreactive flow conditions and standard k-ε RANS simulations are performed on the axisymmetric cavities. The planar cavity consists of a forebody and an afterbody of equal depth D. Although the separation distance of the forebody and afterbody is varied in this study, the depth D is maintained constant at 6.4 mm. For nonreactive flow conditions, the air mainstream approaches the cavity at uniform and constant velocity and temperature of 40 m/s and 300 K. Both DNS and RANS simulations and both nonreactive and reactive flow conditions are performed on the planar cavities. Fuel and air injections are also used in planar cavities. The cavity equivalence ratio ϕ_{CAV} is also varied. Additional details are provided in subsequent sections.

B. Thermodynamic and Transport Properties

The thermodynamic and transport properties appearing in the governing equations are temperature and species dependent. The mixture density is computed using the ideal gas law assuming that the pressure remains constant in the flowfield at 101,325 Pa. The specific heat capacity of individual species is computed with piecewise polynomials [10]. The viscosity, thermal conductivity, and binary diffusivity of the individual species were based on kinetic theory [23]. Whereas the mixture viscosity and thermal conductivity are computed using the Wilke semi-empirical formulas [24], mixture-averaged formulation is used to compute species diffusivities that are used in the governing equations. The Wilke semi-empirical correlations are used because they apply to nonpolar low-density gases; hence, these correlations are useful in our investigation. The mixture-averaged diffusivity is a particularly useful simplification when all species, but one, are not abundant. For instance, the mass fraction of N_2 is ~0.72. The formulation used for the calculation of individual and mixture properties is a common practice used in many in-house source codes [25] and commercial codes [26,27].

C. Combustion Model

The JP8-air chemistry is modeled using a global reaction mechanism involving five species, namely JP8, O_2, CO_2, H_2O, and N_2. JP8 is treated as a surrogate mixture consisting of six parent species: 30% n dodecane, 20% n tetradecane, 10% i octane, 20% methylnaphthalene, 5% tetralin, and 15% m xylene [28]. The global reaction for this surrogate mixture is

$$JP\,8 + 15.425O_2 \rightarrow 10.25H_2O + 10.3CO_2$$
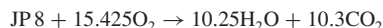
III. Results and Discussion
A. Validation of Numerical Model

The validation of the numerical model has been presented in a previous investigation by Katta and Roquemore [10]. They compared the change in pressure drag $\Delta C_{D,P}$ as a function of afterbody disk distance from the forebody x/D_o for two spindle sizes. Both results of DNS and standard k-ε RANS models were compared with the measurements of Little and Whipkey [9]. Although their RANS simulations did not result in the dynamic flow observed in the experiments, the drag coefficients compared favorably with those

from the experiments. On the contrary, the DNS yielded dynamic flows similar to those observed in the experiments and the drag coefficients were not as favorable with the experiments. For the small and large spindle sizes used in their investigation, the RANS simulations predicted a minimum $\Delta C_{D,P}$ similar to that of the measurements. Moreover, the DNS and RANS algorithms have been extensively validated in many unsteady reacting flow simulations, such as opposed jet flames [29] and buoyant jet diffusion flames [30]. Furthermore, the numerical simulations of the trapped-vortex combustor (TVC) [11], which is similar to our large axisymmetric cavity except that it has fuel and air injections, yielded only qualitative comparison with the experiments in terms of temperature profiles. The DNS results were in closer agreement to the experiments than those obtained with RANS. However, the ability of incorporating standard k-ε RANS model in predicting reacting flows was tested in vertically mounted turbulent jet flames [11]. Good qualitative and quantitative agreements were predicted by both the models. Based on these results and the discrepancies presented in the TVC, it was speculated that the standard k-ε RANS model is only inadequate to predict reacting flows in TVC and in large axisymmetric cavities. Nevertheless, the standard k-ε RANS model can qualitatively obtain general features of large axisymmetric cavities exposed to non-reacting flows as shown in Fig. 2 of [10]. Therefore, in this investigation, the standard k-ε RANS model is used for nonreacting flows, whereas the DNS is used for both nonreacting and reacting flows.

B. Flow Unsteadiness in Large Axisymmetric Cavities

This section is concerned with the drag and flow characteristics of a locked vortex afterbody shapes formed by thin disks spaced along a central spindle. Figure 3 presents the velocity vector flowfields and streamlines for conditions when the afterbody disk is placed at $x/D_o = 0.2, 0.4, 0.5$, and 0.7. Similar simulations were conducted by Katta and Roquemore [10]. In this figure, the upstream flow diverges due to increased cross-sectional area and, consequently, flow separation occurs at the sharp corner of the forebody. The streamwise pressure gradient increases until the flow reattaches to the spindle downstream the afterbody. For $x/D_o = 0.2$, the flow recirculates behind the afterbody disk. This flow spills over the afterbody disk into the cavity and two vortices are formed in the cavity. The innermost vortex is counter-rotating with respect to the direction of the mainstream, whereas the outermost vortex is corotating with the mainstream. There is also a freestanding stagnation point inside the flowfield, indicating the presence of opposed flows. This flow configuration is called the wake backflow regime and the characteristic cavity Reynolds number Re_x is less than 84,000. For $x/D_o = 0.4$, there is still spillover and two vortices within the cavity exist. However, in comparison with the WBF, there are velocity vectors pointing toward the afterbody disk still with the presence of a stagnation point in the flowfield. This contraction around the disk and backflow is responsible for inducing flow oscillations [9] and the flow is said to be in the unsteady cavity vortex regime with Re_x ranging from 84,000 to 105,000. For $x/D_o = 0.5$, there is no longer backflow over the afterbody disk and the stagnation point has moved to the top of the afterbody wall and the vortex fits nearly perfectly in the cavity. The location of the stagnation point is consistent with that reported by Gharib and Roshko [31] for this type of flow. The flow is in the steady cavity vortex regime, exhibiting $Re_x \approx 105,000$. At $x/D_o = 0.7$, the vortex in the cavity becomes elongated, the mainstream impinges on the afterbody disk, and the stagnation point moves to the front of the afterbody wall. This impingement compresses the vortex and the flow becomes unsteady. We named this flow the compressed cavity vortex regime (CCV) and it exhibits $Re_x > 105,000$. Furthermore, the streamlines suggest that the SCV exhibits minimum mass exchange with the mainstream flow, as expected.

Figure 4 presents the change in pressure drag $\Delta C_{D,P}$ coefficient as a function of axial distance x/D_o, resulting from the addition of disk to forebody-spindle geometry, discussed in the context of Fig. 3. Katta and Roquemore [10] presented in their Fig. 2 the total change in drag, whereas we only present the contribution of pressure drag to
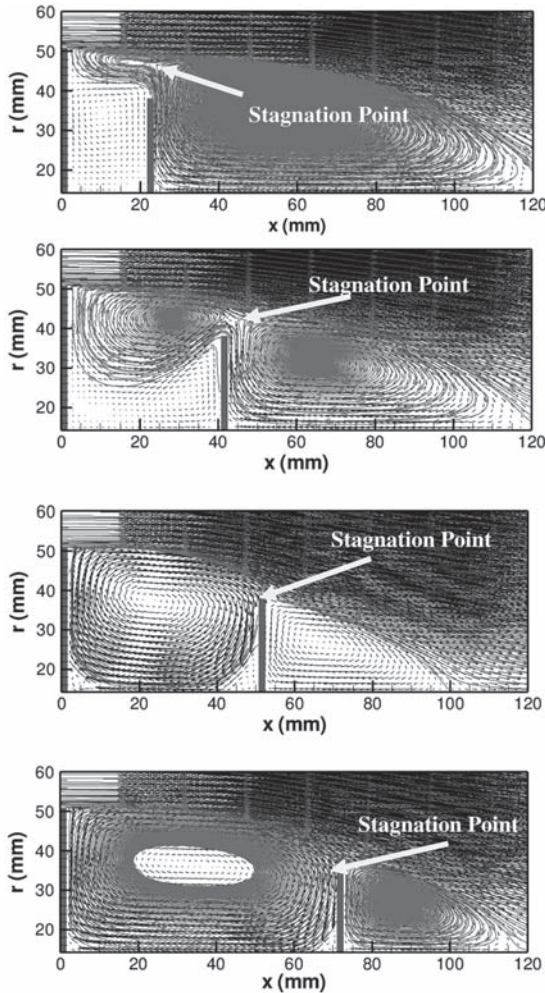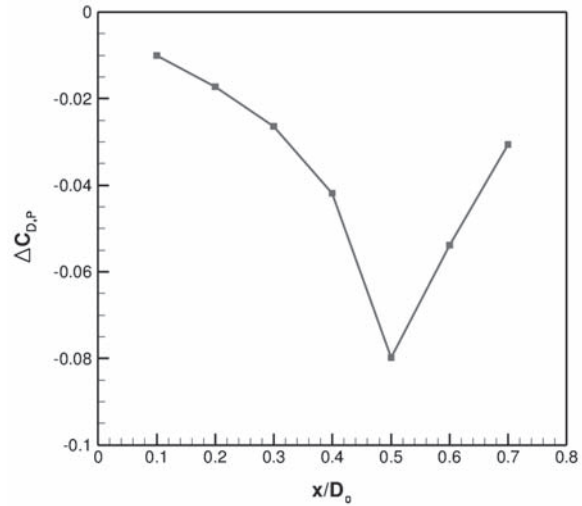
74

Fig. 3 Velocity vectors for the afterbody disk placed at $x/D_o = 0.2$, **0.4, 0.5, and 0.7. The calculations were performed using the standard** $k\text{-}\varepsilon$ **RANS model. The velocity vector lengths are scaled with magnitude. The streamlines are shown. The stagnation points due to reattachment are also indicated.**

Fig. 4 **Change in pressure drag** $\Delta C_{D,P}$ **coefficient as a function of axial distance** x/D_o**, resulting from the addition of disk to forebody-spindle geometry. The calculations were performed using the standard** $k\text{-}\varepsilon$ **RANS model.**

total drag. By comparing our Fig. 4 with Fig. 2 of [10], it is clear that shear drag is nearly negligible. The calculated $\Delta C_{D,P}$ indicates that the drag coefficient decreases monotonically to a minimum value at $x/D_o = 0.5$ and then increases for x/D_o greater than 0.6. Momentum balance on the cavity provides the drag force expressed in terms of the direct forces on the cavity walls or in term of integrated turbulent momentum flux out of the cavity [31]. This momentum flux is inherently unsteady. Increase on the momentum flux indicates increase on flow unsteadiness and thereby increase on drag and drag coefficient (i.e., increase on unbalance forces in the cavity walls). Consequently, the large pressure drag exhibited by the WBF yields oscillations. Similarly, UCV and CCV exhibits larger pressure drags than SCV and these regimes are more unsteady. The flow structure that reduces oscillations is that depicted in Fig. 3 for $x/D_o = 0.5$. Now, in the subsequent paragraph, we relate the minimum $\Delta C_{D,P}$ to the pressure distribution on the forebody face and the upstream face of the afterbody disk.

Figure 5 presents the pressure coefficient C_P as a function of radial coordinate r/R_o at the forebody. The local minima represent the projections of the centers of the vortices on the walls. For the forebody spindle alone without disk, C_P slightly increases from the spindle edge until it reaches an absolute maximum. Further outwardly C_P decreases until it reaches an absolute minimum,

indicating the radial location of the center of the vortex. From the center of this vortex, C_P increases to either side at a rate proportional $\sim(r/R_o)^n$, where n is $-1 \leq n \leq 1$. This indicates that this is a freelike vortex structure. When the disk is added at $x/D_o = 0.2$, C_P decreases drastically, suggesting that velocity magnitude increases. However, the C_p distribution is nearly flat with an increase in the outermost edge and a slight increase near the spindle edge. This indicates that velocity magnitudes and circulations corresponding to the outermost corotating and the innermost counter-rotating vortices are comparable, as shown in Fig. 3. Further increase in x/D_o decreases C_p until it reaches a minimum at $x/D_o = 0.5$. When the disk is at this position, the C_P distribution is no longer flat. First, C_p decreases to a local minimum and then it increases to an absolute maximum. This section of the profile indicates the location of a small vortex near the corner of the cavity, as shown in Fig. 3. Further outwardly C_p decreases to an absolute minimum and then rises. This section indicates the existence of a larger vortex in the cavity. In contrast to $x/D_o < 0.5$, the two vortices indicated by the C_p profile suggest that these vortices are forcedlike vortex. This statement is reached because from the center of the vortices C_P now increases with the square of the radius [i.e., $\sim(r/R_o)^2$], which is characteristic of forced vortices. From Fig. 3, note that the velocity magnitude has increased from $x/D_o = 0.2$ to 0.5 as indicated by the length of the velocity vectors. When the disk is positioned further downstream at $x/D_0 = 0.6$, C_p increases again. By positioning the disk even further downstream, C_p increases monotonically with the same qualitative radial distribution as for when the disk was positioned at $x/D_o = 0.5$ and 0.6 (i.e., $n = 2$). The increase in C_p is associated with decrease in velocity magnitudes in the cavity (as indicated by velocity vector lengths in Fig. 3). It is important to point out that the minimum $\Delta C_{D,P}$, which is associated with steady flow, is also associated with minimum C_P on the forebody face. This is in contradiction with the results of Mair [8] which suggested exactly the opposite (i.e., minimum C_P yields maximum $\Delta C_{D,P}$). We believe that the minimum C_P yields minimum $\Delta C_{D,P}$ since $\Delta C_{D,P} = (1/A) \cdot \int C_P \cdot dA$, where A is the area. In fact, Mair [8] suggested that, in the high-drag regime, the flow was unsteady and the pressures recorded by the manometer may not have been the true mean values. This could have led to data misinterpretation.

Figure 6 presents pressure coefficient C_P as a function of radial coordinate r/R_o at the upstream face of the afterbody disk. At $x/D_o = 0.2$, C_p exhibits a small local minimum near the spindle and then decreases continuously with r/R_o. This indicates that the flow near the disk is moving from the inner regions of the cavity toward
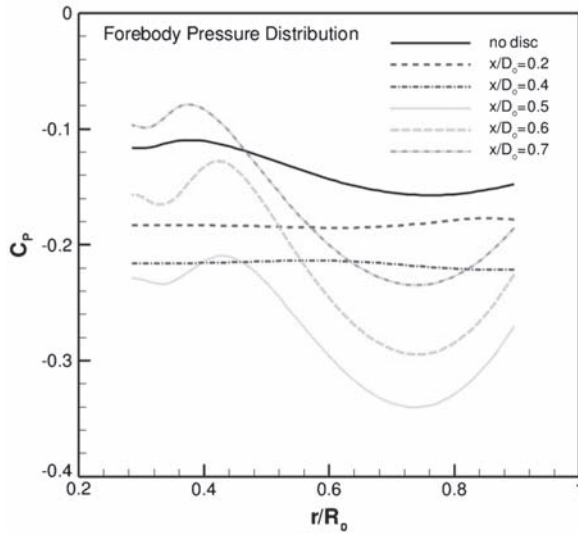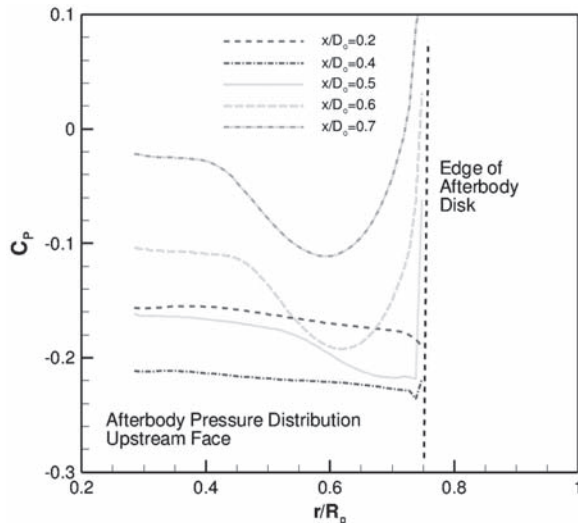
Fig. 5   Pressure coefficient C_P as a function of radial coordinate r/R_o at the forebody. The calculations were performed using the standard k-ε RANS model.

outside (i.e., counter-rotating vortex). With increasing x/D_o to 0.4, the magnitude of C_P decreases and the profile is still nearly similar to that of $x/D_o = 0.2$ because there is still a counter-rotating vortex, as depicted in Fig. 3. Further increase of x/D_o to 0.5 shifts C_P slightly above that of $x/D_o = 0.4$. An absolute minimum C_P is observed to occur. As x/D_o increases to 0.6 and 0.7, the minimum is shifted toward the inside of the cavity. This is due to larger impingement area of the mainstream flow on the afterbody disk, which pushes the vortex toward the spindle. That is why at $x/D_o = 0.6$ and 0.7 the flow is in the CCV regime. According to Zdanski et al. [12,13], if we were to further increase x/D_o, two major vortices would form inside the cavity which depending on x/D_o these vortices could be either encapsulated (i.e., without flow reattachment) or nonencapsulated.

In summary, our results presented from Figs. 3–6 indicate that low flow unsteadiness is achieved when a large corotating vortex with the mainstream, exhibiting forcedlike vortex characteristics, fits the cavity. This leads to low-pressure drag and low-pressure co-efficients in both the forebody face and upstream face of the

afterbody. RANS simulations are sufficient for determining flow configuration exhibiting low flow unsteadiness.

C.   Flow Unsteadiness in Small Planar Cavities

From Fig. 1, it is noticed that the CIC has two major geometrical differences with the large axisymmetric cavities studied in the previous section. In the CIC, the thickness of the afterbody is infinitely long and the heights of the afterbody and forebody walls are equal. Therefore, the CIC is modeled as the small planar cavity shown in Fig. 2. Based on the results from the previous section, we expect the wake spillover to be nonexistent, and, consequently, WBF and UCV regimes will be nonexistent as well.

Figure 7 presents the velocity vectors for the planar cavity with dimensions of $L/D = 1$ and 6. These calculations were performed using the standard k-ε RANS model. As with axisymmetric cavities, flow separation occurs at the sharp corner of the forebody. The streamwise pressure gradient increases until the flow reattaches at the sharp corner of the afterbody for $L/D = 1$ and impinges on the afterbody for $L/D = 6$. For the latter case, the flow momentum is not sufficient, hence flow impingement occurs. For $L/D = 1$, a corotating vortex is seen inside the cavity with its center nearly at the center of the cavity. Thereby, this configuration resembles that of $x/D_o = 0.5$ (shown in Fig. 3). We, consequently, state that the flow is in the SCV regime. Nonetheless, at $L/D = 6$, the vortex is elongated and characterized by flow impingement, exhibiting similarities to that corresponding to $x/D_o = 0.7$ (shown in Fig. 3). Thus, this flow corresponds to the CCV regime. Furthermore, these results plainly suggest that there is a critical cavity length to depth ratio L/D, at which a single vortex does no longer fit in the cavity. For instance, Zdanski et al. [12] showed that, for a trench cavity like this one, vortex encapsulation takes place at $L/D \sim 6.65$. Recall from the previous section that vortex encapsulation refers to two vortices in the cavity without inside-cavity flow reattachment.

Figure 8 presents the change on drag ΔC_D as a function of cavity length to depth ratio L/D. The individual contributions of pressure $\Delta C_{D,P}$ and shear $\Delta C_{D,S}$ drag are also plotted. Both pressure and shear drag increases with increasing L/D. $\Delta C_{D,P}$ increases due to flow impingement on the afterbody wall, as suggested by Fig. 7. It is obvious that shear drag is negligible for both axisymmetric and planar cavities. In comparison with Fig. 4, it is interesting to note that, for our planar cavity, there is no absolute minimum $\Delta C_{D,P}$. This is, however, expected because we modified the cavity to avoid flows in the WBF and UCV regimes. It is evident that, by increasing L/D, the flow transitions from the SCV to the CCV regime. This also suggests that the vortex for the range of L/D studied here exhibits characteristics of forced vortices (i.e., $n = 2$ and the pressure increases almost quadratically with increasing vortex radius). Now it is
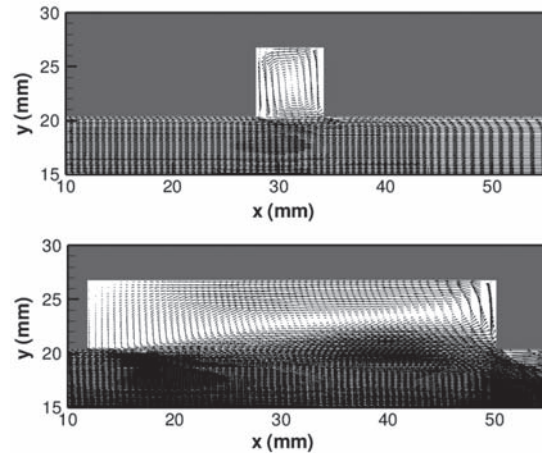

Fig. 6   Pressure coefficient C_P as a function of radial coordinate r/R_o at the upstream face of the afterbody disk. The calculations were performed using the standard k-ε RANS model.

Fig. 7   Velocity vectors for the planar cavity with dimensions of $L/D = 1$ and 6. The calculations were performed using the standard k-ε RANS model.
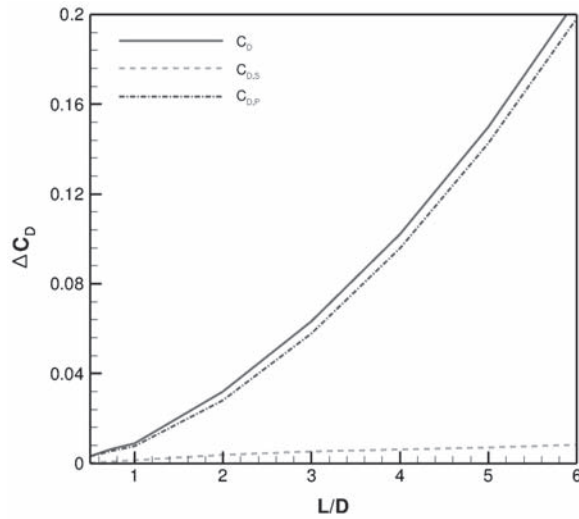
Fig. 8 Change in drag coefficient ΔC_D as function of cavity length to depth ratio L/D. The individual contributions of pressure $\Delta C_{D,P}$ and shear $\Delta C_{D,S}$ drag are also plotted.

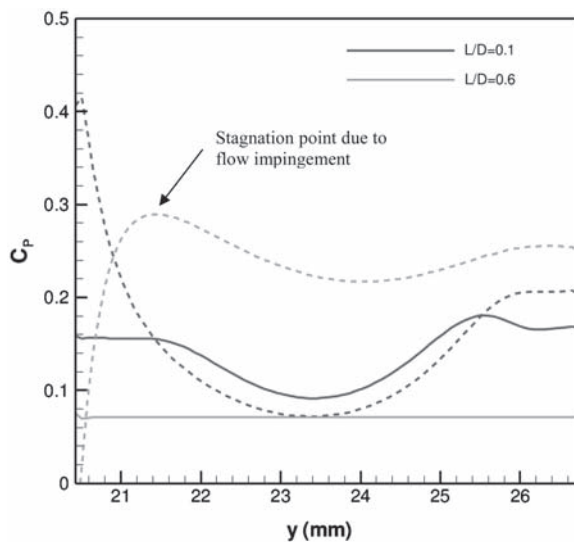important to examine the pressure distribution on the forebody and afterbody walls.

Figure 9 presents the pressure coefficient C_P as function of vertical distance y at the forebody (solid) and afterbody (dashed) walls. For $L/D = 1$, the absolute minimum C_P occurs at the center of the forebody and afterbody walls, indicating that the vortex center is located at the cavity center. Both C_P profiles and magnitudes in the forebody and afterbody walls are very similar, indicating that the horizontal forces are nearly balanced, exhibiting minimum flow oscillations. With increasing length to depth ratio L/D, C_P on the afterbody wall increases, whereas that on the forebody wall decreases. Because both C_p profiles and magnitudes in the forebody and afterbody walls are very different, horizontal forces are not balanced and the flow would exhibit large oscillations. The location of the absolute minimum C_P on the afterbody wall is shifted inward due to flow impingement on the afterbody wall. Note that this shift is consistent with that observed for $x/D_o = 0.6$ and 0.7 in Fig. 5.

Fig. 9 Pressure coefficient C_P as function of vertical distance y at the forebody (solid) and afterbody (dashed) walls. The calculations were performed using the standard k-ε RANS model. The location of the stagnation point due to flow impingement is also indicated.

This again confirms qualitative similarities between that flow configuration in the axisymmetric cavity with afterbody disk at $x/D_o = 0.7$ and the flow in the planar cavity with $L/D = 6$.

DNS calculations were performed for the cavity sizes discussed in the context of Fig. 9 and the change in pressure drag $\Delta C_{D,P}$ as a function of dimensionless time τ^* is presented in Fig. 10. Whereas the RANS simulation provided steady values of $\Delta C_{D,P}$, the DNS provides unsteady values of $\Delta C_{D,P}$. Nevertheless, similar to the results of Fig. 8, the DNS results indicate that with increasing L/D, $\Delta C_{D,P}$ increases. Note that, for $L/D = 1.0$, the average $\Delta C_{D,P}$ is nearly 0.0 consistent with the result in Fig. 8. However, when $L/D = 6.0$, the average $\Delta C_{D,P}$ is ~ 0.7, which is several times larger than that of Fig. 8. DNS and RANS simulations provide qualitative results; however, they might differ on their quantitative results.

D. Effect of Fuel and Air Injections on Flow Unsteadiness in Small Planar Cavities

This section is concerned with the pressure drag and flow characteristics in the small planar cavity due to fuel and air injection configurations. The schematic of normal injection (NI) and reverse injection (RI) configurations for air jets is presented in Fig. 11. In this figure, three possible fuel jet injection configurations are also depicted: coflow, crossflow, and counterflow with respect to the mainstream flow. As discussed in the Introduction, NI with crossflow corresponds to config. 1 examined by Zelina et al. [3]. The temporal pressure drag evolution for the configurations discussed in the context of Fig. 11 is presented in Fig. 12. For the NI of air jets, pressure drag oscillations start to fluctuate after a finite time of ~ 0.4 ms, whereas for RI, pressure drag fluctuations start immediately as the simulation starts. This suggests that flow disturbances propagate faster when RI is used. For NI, the crossflow-fuel-jet position exhibits the lowest pressure drag amplitudes, followed very closely by the coflow fuel jet position. The counterflow fuel jet position, on the other hand, exhibits the highest pressure drag amplitudes. Recall from Secs. III.B and III.C that the optimum flow configuration that leads to lowest flow unsteadiness is that of the SCV regime, which contains a corotating forcedlike vortex with the mainstream with minimum flow impingement on the afterbody wall. Therefore, when the fuel jet is injected in counterflow with respect to the mainstream, the corotating vortex existing in the cavity is distorted. On the contrary, when fuel jet is injected in crossflow or coflow, the corotating vortex is not distorted and possibly enhanced. This explains why the crossflow and coflow fuel-injection positions exhibit superior flow steadiness with respect to the counterflow fuel-injection position. Moreover, RI promotes a counter-rotating cavity
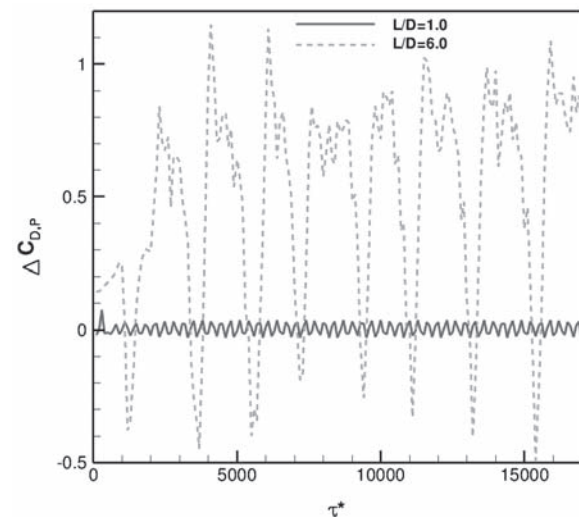

Fig. 10 Change in pressure drag $\Delta C_{D,P}$ as a function of dimensionless time τ^*. The calculations were performed using DNS.
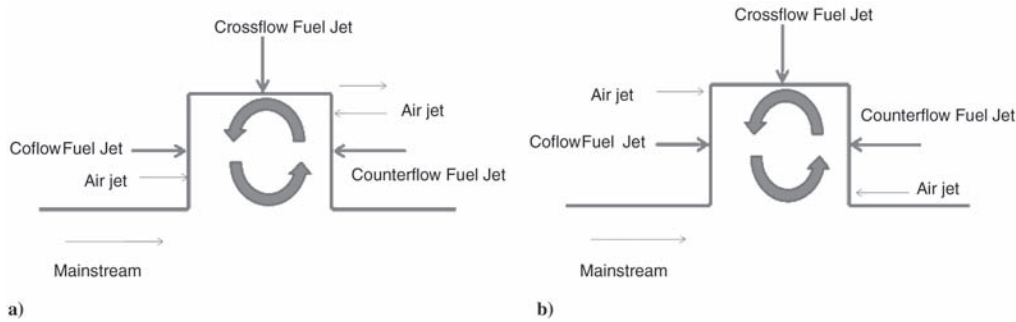
77

Fig. 11   Schematic of the a) normal injection and b) reverse injection configuration of air jets. The multiple positions of fuel jets are also indicated.

vortex (with respect to the mainstream flow). This in turn increases the flow unsteadiness as demonstrated by the larger pressure drag amplitudes. The flow in the RI is nearly insensitive to the fuel-jet injection positions. Counterflow-fuel-jet position and RI provide the worst-case scenario in terms of flow unsteadiness.

E.   Effect of Cavity Equivalence Ratio and Combustion to Flame/Flow Unsteadiness

This section is concerned with the pressure drag and flow/flame characteristics in the small planar cavity due to combustion under various cavity equivalence ratios ϕ_{CAV}. The cavity equivalence ratios ϕ_{CAV} used are 0.85, 1.42, 2.15, 5.67, 8.5, and 11.33. As ϕ_{CAV} is increased, the cavity air to fuel jet momentum ratio λ_{CAV} decreases from 9.9 to 5.85, 3.87, 1.47, 0.97, and 0.74, respectively. The velocity in the main stream is equaled to the velocity of the air jets to reduce the effect of shear between the air mainstream flow and the outermost air jet. The mainstream temperature is constant at 533 K and its profile is uniform. The cavity walls are assumed isothermal at 533 K. A total number of 12 simulations were run corresponding to the six ϕ_{CAV} and two injection configurations for the air jets (cf. Figure 11). The fuel jet is injected in crossflow with the respect to the mainstream air flow. The instantaneous temperature contours, streamlines (lines), and streak lines (dots) for $\phi_{CAV} = 2.15, 5.67, 8.5,$ and 11.33 using NI and RI are presented in Fig. 13. The streamlines are computed from the fuel and air jets, whereas the streak lines are computed from the fuel jet only. These streak lines, in fact, represent massless particles injected through the fuel jet. Temperature contours and streamlines reveal that, when NI is used, two nonpremixed flames attached to the air jet ports are formed. On the other hand, the nonpremixed flames are attached to the fuel jet and the counterflow air jet ports when RI is used. A plausible explanation is that, if the flame were to be attached to the coflow air jet port, the curvature-induced stretch would be high

enough to extinguish the flame. Consequently, the flames established in the NI configuration appeared to be more parallel to the mainstream than the flames in the RI configuration. With NI, the particles are accumulated toward the forebody face of the cavity. On the contrary, particles are clustered toward the afterbody face of the cavity when RI is used. This plainly indicates that fuel is transported toward the forebody face of the cavity and afterbody face of the cavity when NI and RI are used, respectively. Moreover, this fact is consistent with the relatively high temperature encountered in the forward and backward cavity regions for the NI and RI, respectively. Qualitatively, it appears that, regardless of ϕ_{CAV}, it is more difficult for particles to escape the cavity when RI is used. This is because the particles have to go against the flow when they are still in the cavity as illustrated by the streamlines and streak lines.

Figure 14 shows the temporal temperature profiles for the NI (solid) and RI (dashed) for the conditions discussed in the context of Fig. 13. The temperatures are probed at $x = 34$ mm and $y = 22$ mm (cf. Figs. 3 and 13). Note that, at $\phi_{CAV} = 0.85, 1.42, 2.15, 5.67, 8.5,$ and 11.33, the temperature starts increasing and/or oscillating at $\sim$1.5, 0.5, 0.25, 0.11, 0.09, and 0.19 ms, respectively, for the NI case. For ease of discussion, we refer to this time as the ignition time. It is reasonable to qualitatively observe that the mixture ignition time is the slowest at off-stoichiometric conditions (i.e., $\phi_{CAV} = 8.5$ and 11.33). The ignition time is, however, not the lowest at $\phi_{CAV} = 1.42$ because the chemistry model used in this investigation does not account for CO_2 and H_2O dissociation. Therefore, these results can only be interpreted qualitatively. The ignition time for RI is always larger than for their NI counterparts. This is a reasonable result because the large pressure drag fluctuations observed in Fig. 12 for RI would tend to inhibit ignition. For low ϕ_{CAV}, the amplitude of the temperature fluctuations is larger for RI than it is for NI. Nevertheless, as ϕ_{CAV} increases, the amplitude and frequency of temperature oscillations decrease for RI, whereas those for NI
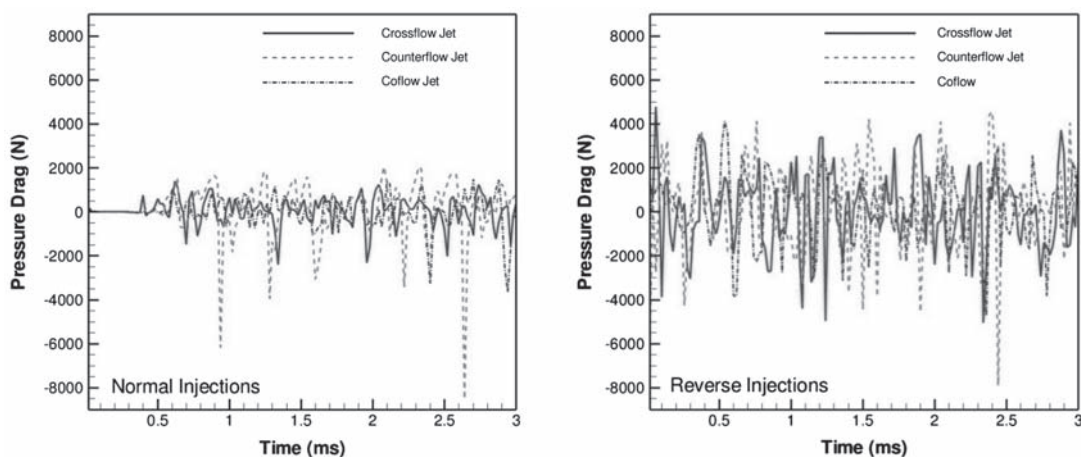

Fig. 12   Pressure drag as a function of time for the normal and reverse injection configurations. DNS were performed for these calculations.
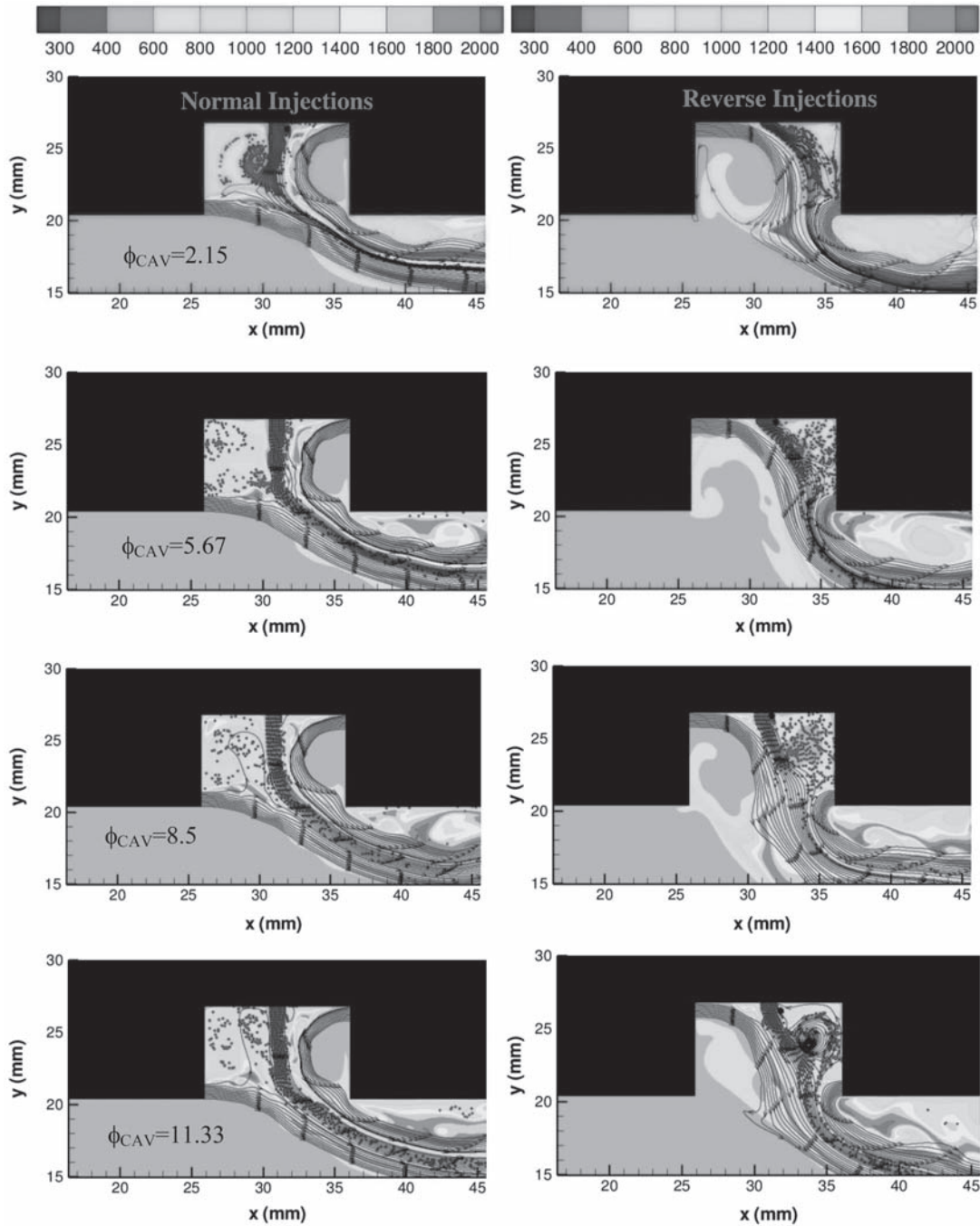
78

Fig. 13 Instantaneous temperature contours, velocity streamlines (lines), and streak lines (dots) after 3 ms for cavity equivalence ratios ϕ_{CAV} of 2.15, 5.67, 8.5, and 11.33 under NI (left) and RI (right) configurations.

generally increase. However, the effect of ϕ_{CAV} appears to be more pronounced for RI. So, at high ϕ_{CAV}, the amplitude and frequency of the temperature fluctuations is larger for NI than it is for RI.

To further examine the effect of ϕ_{CAV} on flow unsteadiness, Fig. 15 presents the pressure drag as a function of time for relatively low and high ϕ_{CAV} (i.e., 2.15 and 8.5). It is evident from Figs. 14 and 15 that, at low ϕ_{CAV}, flow unsteadiness is more pronounced for NI; nonetheless, at high ϕ_{CAV}, the flow unsteadiness for NI and RI become comparable. A possible explanation can be mentally visualized as follows:

1) For NI conditions, as $\phi_{CAV} \to 0$ $\lambda_{CAV} \to \infty$, and the effect of the fuel jet on the air jets becomes negligible. Consequently, we would expect a flow structure resembling that of an axisymmetric cavity with afterbody disk at $x/D_o = 0.5$ (cf. Figure 3) or that of a planar cavity with $L/D = 1.0$ (cf. Figure 7) (i.e., steady cavity vortex). Therefore, low ϕ_{CAV} leads to low flow unsteadiness.

2) For NI, as $\phi_{CAV} \to \infty$ $\lambda_{CAV} \to 0$, and the effect of the fuel jet on the air jets becomes significant. The previously established structure becomes distorted and the flow unsteadiness increases. Therefore, high ϕ_{CAV} leads to high flow unsteadiness. This is consistent
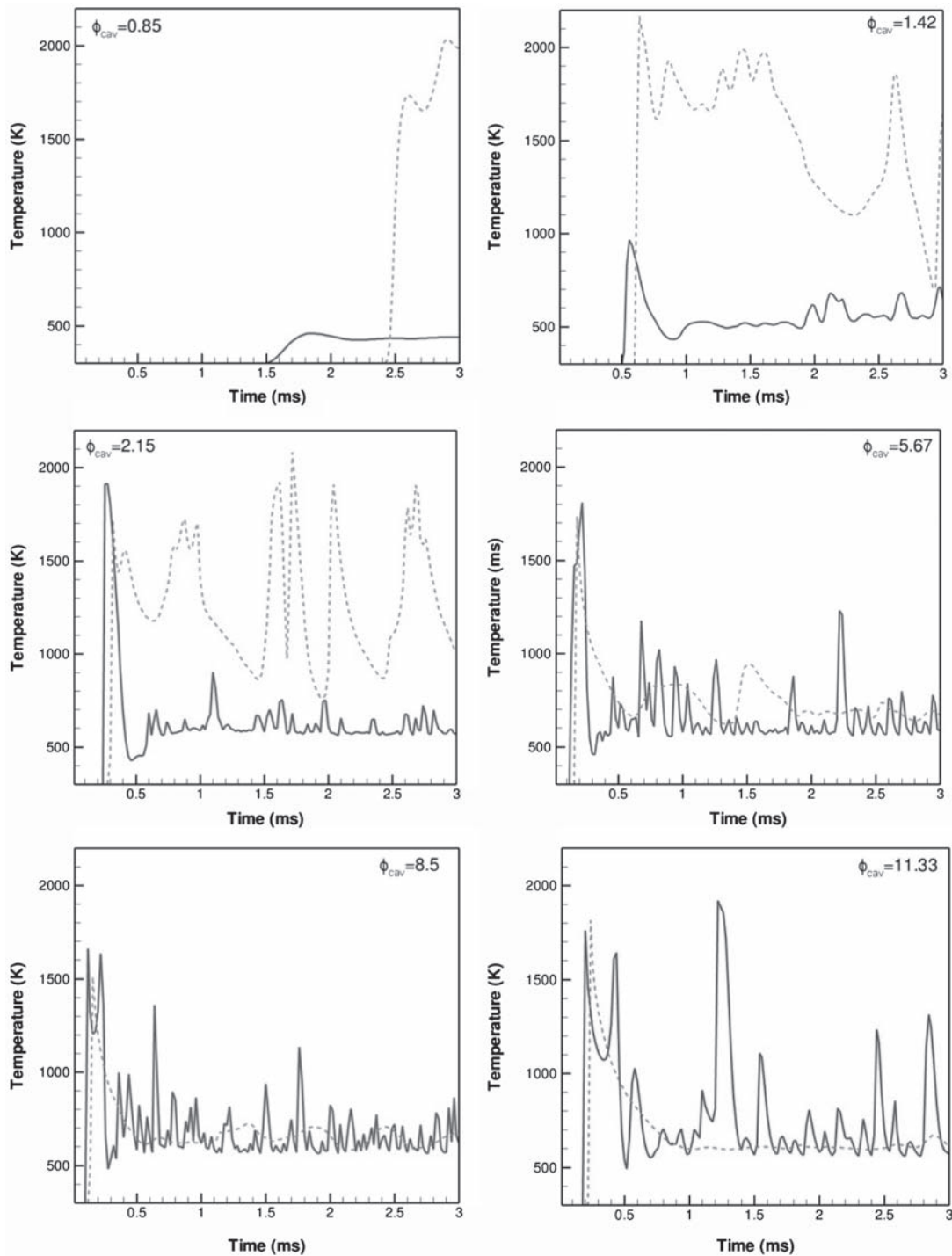
Fig. 14   Temporal temperature profiles for the normal (solid) and reverse (dashed) Injections. The simulations were performed using DNS. The temperatures are probed at $x = 34$ mm and $y = 22$ mm (cf. Figs. 3 and 13).

with Zelina et al. [3] who showed, as discussed in the Introduction, that decreasing λ_{CAV} leads to higher ϕ_{CAV} at lean blowout for NI of air and crossflow fuel injection. Because near-extinction conditions are associated with flow oscillations [32], the higher ϕ_{CAV} at lean blowout is interpreted here as higher flow unsteadiness. Nevertheless, blowout was not observed for any of our simulations because the global chemistry does not include elementary reactions needed for the correct assessment of flame extinction [33].

3) For RI conditions, as $\phi_{CAV} \rightarrow \infty$ $\lambda_{CAV} \rightarrow 0$, and the effect of the fuel jet on the air jets becomes negligible. Consequently, the flow inside the cavity resembles that presented for axisymmetric cavity with afterbody disk at $x/D_o = 0.2$ (cf. Figure 3) (i.e., wake backflow). Therefore, high ϕ_{CAV} leads to high flow unsteadiness.

4) For RI, as $\phi_{CAV} \rightarrow 0$ $\lambda_{CAV} \rightarrow \infty$, and the effect of the fuel jet on the air jets becomes significant. The previously established structure becomes distorted and the flow unsteadiness decreases.
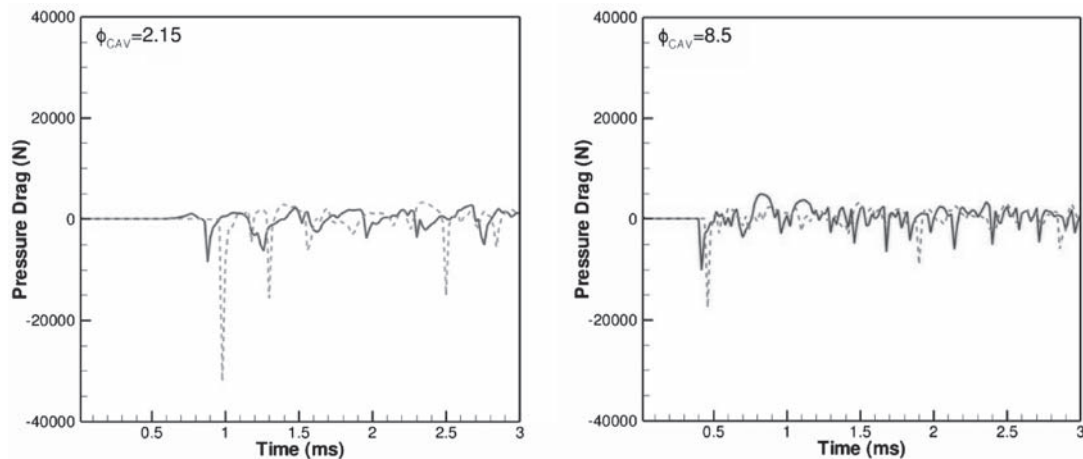
Fig. 15   Pressure drag as a function of time for cavity equivalence ratio ϕ_{CAV} of 2.15 and 8.5. The simulations were performed using DNS. Normal and reverse injections are indicated in solid and dashed lines, respectively.

IV.   Conclusions

An extensive computational investigation on the characteristics of cavity-stabilized flames was presented. We examined the flow unsteadiness in both axisymmetric and (nonreactive and reactive flow past) planar cavities. Important conclusions are as follows:

1) Results indicate that shear drag coefficient $\Delta C_{D,S}$ is negligible in comparison with pressure drag coefficient $\Delta C_{D,P}$, and the former is proportional to flow unsteadiness.

2) The axisymmetric cavity, which consists of a forebody and an afterbody disk, exhibits multiple flow regimes depending on the distance between the forebody and afterbody disk. When the distance between the forebody and afterbody disk x/D_o is small, multiple vortices are formed in the cavity. However, it contains a main counter-rotating freelike vortex with respect to the mainstream flow that is formed due to the backflow (wake backflow regime). As with previous investigations on axisymmetric cavities, results indicate that with increasing cavity length the drag decreases as the flow transitions to the unsteady cavity vortex regime, characterized by backflow and flow contraction around the afterbody disk. Further increase on cavity length reduces the drag to an absolute minimum as the flow transitions to the steady cavity vortex regime. This regime is characterized by a corotating forcedlike vortex with neither backflow nor mainstream flow impingement. With further increase in x/D_o, the drag increases again as the flow transitions to the compressed cavity vortex regime, characterized by an elongated corotating forcedlike vortex with mainstream flow impingement on the afterbody disk.

3) Results indicate that with increasing planar cavity length the pressure drag increases monotonically as the flow in the cavity transitions from SCV to CCV regime. The vortex formed in the cavity exhibits forced-vortex pressure profiles as those present in the axisymmetric cavities. The planar cavity does not exhibit characteristics of the WBF and UCV regimes due to two reasons: 1) the forebody and afterbody depth D are equal, and 2) the afterbody thickness for the planar cavity is infinitely long in comparison with that of the axisymmetric cavity.

4) Normal injections (i.e., the outermost air jet is in coflow with the air mainstream flow, and the innermost air jet is in counterflow) present superior flow steadiness characteristics than their reverse injection counterpart (i.e., the outermost jet is in counterflow with the air mainstream flow and the innermost air jet is in coflow). This is because RI promotes counter-rotating vortex formation, resembling WBF. In the NI, the crossflow fuel jet promotes superior flow steadiness than the counterflow fuel jet. Crossflow-fuel-jet injection is slightly better in terms of flow steadiness than the coflow fuel jet injection. However, with RI, the three fuel jet injection positions (crossflow, coflow, and counterflow) exhibit comparable flow unsteadiness.

5) Cavity-stabilized flames were established at various cavity equivalence ratios ϕ_{CAV} under NI and RI. For NI, low ϕ_{CAV} (with high air to fuel momentum ratio λ_{CAV}) leads to low flow unsteadiness because the air jets promote corotating vortex formation in the cavity. At high ϕ_{CAV} (low λ_{CAV}), on the other hand, the fuel jet distorts the corotating vortex; hence, flow unsteadiness increase. For RI, low ϕ_{CAV} leads to high flow unsteadiness because the air jets promote counter-rotating vortex formation in the cavity. On the contrary, at high ϕ_{CAV}, the fuel jet distorts the formation of corotating vortex(es), increasing flow steadiness.

6) The results presented in this investigation suggest that, for minimizing cavity flow unsteadiness, designers need to focus on geometric dimensions, and fuel/air injection positioning and ϕ_{CAV} that promote corotating forcedlike vortex formation, and reduce both backflow and flow mainstream impingement on the afterbody wall.

References

[1] Zelina, J., Sturgess, G. J., and Shouse, D. T., "The Behavior of an Ultra-Ccompact Combustor (UCC) Based on Centrifugally-Enhanced Turbulent Burning Rates," *40th AIAA/ASME/SAE/ASEE Joint Propulsion Conference and Exhibit*, AIAA Paper 2004-3541, 2004.

[2] Greenwood, R. T., Anthenien, R. A., and Zelina, J., "Computational Analysis of the Ultra Compact Combustor," *43rd AIAA Aerospace Sciences Meeting and Exhibit*, AIAA Paper 2005-220, 2005.

[3] Zelina, J., Anderson, W., Koch, P., and Shouse, D. T., "Compact Combustion Systems Using a Combination of Trapped Vortex and High-g Combustor Technologies," *Proceedings of ASME Turbo Expo 2008: Power for Land, Sea, and Air*, American Society of Mechanical Engineers, GT2008-50090, 2008.

[4] Zelina, J., Ehret, J., Hancock, R. D., Shouse, D. T., and Roquemore, W. M., "Ultra-Compact Combustion Technology Using High Swirl for Enhanced Burning Rate," *38th AIAA/ASME/SAE/ASEE/ Joint Propulsion Conference & Exhibit*, AIAA Paper 2002-3725, 2002.

[5] Zelina, J., Sturgess, G. J., and Shouse, D. T., "The Behavior of an Ultra-Compact Combustor (UCC) Based on Centrifugally-Enhanced Turbulent Burning Rates," *40th AIAA/ASME/SAE/ASEE/ Joint Propulsion Conference & Exhibit*, AIAA Paper 2004-3541, 2004.

[6] Greenwood, R. T., Anthenien, R. A., and Zelina, J., "Computational Analysis of the Ultra Compact Combustor," *43th Aerospace Sciences*

Meeting & Exhibit, AIAA Paper 2005-220, 2005.

[7] Mawid, M. A., Park, T. W., Thornburg, H., Sekar, B., and Zelina, J., "Numerical Analysis of Inter-turbine Burner (ITB) Concepts for Improved Gas Turbine Engine Performance," *43rd Aerospace Sciences Meeting & Exhibit*, AIAA Paper 2005-1162, 2005.

[8] Mair, W. R., The Effect of a Rear-mounted Disc on the Drag of a Blunt-based Body of Revolution, *The Aeronautical Quarterly*, Vol. 16, Pt. 4, Nov. 1965, pp. 350–360.

[9] Little, B. H., Jr., and Whipkey, R. R., "Locked Vortex Afterbodies," *Journal of Aircraft*, Vol. 16, No. 5, 1979, pp. 296–302.
doi:10.2514/3.58522

[10] Katta, V. R., and Roquemore, W. M., "Numerical Studies on Trapped-Vortex Concepts for Stable Combustion," *Transactions of the ASME: Journal of Engineering for Gas Turbines and Power*, Vol. 120, No. 1, 1998, pp. 60–68.
doi:10.1115/1.2818088

[11] Katta, V. R., and Roquemore, W. M., "Numerical Studies of Trapped-vortex Combustor," *32nd AIAA/ASME/SAE/ASEE/Joint Propulsion Conference & Exhibit*, AIAA Paper 1996-2660, 1996.

[12] Zdanski, P. S. B., Ortega, M. A., and Fico, N. G. C. R., Jr., "On the Flow over Cavities of Large Aspect Ratio: A Physical Analysis," *International Communications in Heat and Mass Transfer*, Vol. 33, No. 4, 2006, pp. 458–466.
doi:10.1016/j.icheatmasstransfer.2006.01.007

[13] Zdanski, P. S. B., Ortega, M. A., and Fico, N. G. C. R., Jr., "Numerical Study of the Flow over Shallow Cavities," *Computers and Fluids*, Vol. 32, No. 7, 2003, pp. 953–974.
doi:10.1016/S0045-7930(02)00067-1

[14] D'yanchenko, A. Y., Terekhov, V. I., and Yarygina, N. I., "Vortex Formation and Heat Transfer in Turbulent Flow Past a Transverse Cavity with Inclined Frontal and Rear Walls," *International Journal of Heat and Mass Transfer*, Vol. 51, Nos. 13–14, 2008, pp. 3275–3286.
doi:10.1016/j.ijheatmasstransfer.2007.11.039

[15] Puranam, S., Arici, J., Sarzi-Amade, N., and Dunn-Rankin, D., Sirignano, "Turbulent Combustion in a Curving, Contracting Channel with a Cavity Stablized Flame," *Proceedings of the Combustion Institute*, Vol. 32, No. 2, 2009, pp. 2973–2981.
doi:10.1016/j.proci.2008.06.161

[16] Katta, V. R., Zelina, J., and Roquemore, W. M., "Numerical Studies on Cavity-Inside-Cavity-Supported Flames in Ultra Compact Combustor," *Proceedings of the ASME Turbo Expo 2008: Power for Land, Sea, and Air*, American Society of Mechanical Engineers, GT2008-50853, 2008.

[17] Shu, Z., Aggarwal, S. K., Katta, V. R., and Puri, I. K., "Flame-Vortex Dynamics in an Inverse Partially Premixed Combustor: The Froude Number Effects," *Combustion and Flame*, Vol. 111, No. 4, 1997, pp. 276–286.
doi:10.1016/S0010-2180(97)00018-7

[18] Azzoni, R., Ratti, S., Puri, I. K., and Aggarwal, S. K., "Gravity Effects on Triple Flames: Flame Structure and Flow Instability," *Physics of Fluids*, Vol. 11, No. 11, 1999, pp. 3449–3464.
doi:10.1063/1.870203

[19] Qin, X., Puri, I. K., Aggarwal, S. K., and Katta, V. R., "Gravity, Radiation and Coflow Effects on Partially Premixed Flames," *Physics of Fluids*, Vol. 16, No. 8, 2004, pp. 2963–2974.
doi:10.1063/1.1764835

[20] Siegel, R., and Howell, J. R., *Thermal Radiation Heat Transfer*, Hemisphere, New York, 1981.

[21] Lee, B. J., and Chung, S. H., "Stabilization of Lifted Tribrachial Flames in a Laminar Nonpremixed Flame," *Combustion and Flame*, Vol. 109, Nos. 1–2, 1997, pp. 163–172.
doi:10.1016/S0010-2180(96)00145-9

[22] Katta, V. R., Goss, L. P., and Roquemore, W. M., "Numerical Investigations of Transitional H_2/N_2 Jet Diffusion Flames," *AIAA Journal*, Vol. 32, No. 1, 1994, pp. 84–94.
doi:10.2514/3.11954

[23] Bird, R. B., Stewart, W. E., and Lightfoot, E. N., *Transport Phenomena*, Wiley, New York, 1960.

[24] Reid, R. C., Prausnitz, J. M., and Poling, B. E., *The Properties of Gases and Liquids*, McGraw–Hill, New York, 1987.

[25] Chu, W.-W., Yang, V., and Majdalani, J., "Premixed Flame Response to Acoustic Waves in a Porous-Walled Chamber with Surface Mass Injection," *Combustion and Flame*, Vol. 133, No. 3, 2003, pp. 359–370.
doi:10.1016/S0010-2180(03)00018-X

[26] "Ansys Fluent 12.0 Theory Guide," Ansys, Ann Arbor, MI, www.fluent.com.

[27] Kee, R. J., Rupley, F. M., Miller, J. A., Coltrin, M. E., Grcar, J. F., Meeks, E., Moffat, H. K., Lutz, A. E., Dixon-Lewis, G., Smooke, M. D., et al., "Chemkin Release 4.1.1," Reaction Design, San Diego, CA, 2007.

[28] Katta, V. R., Mawid, M., Sekar, B., Corporan, E., and Montgomery, C. J., "Comparison of Chemical-Kinetics Models for JP-8 Fuels in Predicting Premixed and Nonpremixed Flames," *42nd AIAA/ASME/ASEE Joint Propulsion Conference and Exhibit*, AIAA Paper 2006-4745, 2006.

[29] Katta, V. R., Meyer, T. R., Brown, M. S., Gord, J. R., and Roquemore, W. M., "Extinction Criterion for Unsteady, Opposing-Jet Diffusion Flames," *Combustion and Flame*, Vol. 137, Nos. 1–2, 2004, pp. 198–221.
doi:10.1016/j.combustflame.2004.02.004

[30] Grisch, F., Attal-Tretout, B., Bresson, A., Bouchardy, P., Katta, V. R., and Roquemore, W. M., "Investigation of a Dynamic Diffusion of H_2 in Air with Laser Diagnostics and Numerical Modeling," *Combustion and Flame*, Vol. 139, Nos. 1–2, 2004, pp. 28–38.
doi:10.1016/j.combustflame.2004.08.002

[31] Gharib, M., and Roshko, A., "The Effect of Flow Oscillations on Cavity Drag," *Journal of Fluid Mechanics*, Vol. 177, April 1987, pp. 501–530.
doi:10.1017/S002211208700106X

[32] Füri, M., Papas, M., and Monkewitz, P. A., "Non-Premixed Jet Flame Pulsations Near Extinction," *Proceedings of the Combustion Institute*, Vol. 28, Pt. 1, 2000, pp. 831–838.

[33] Takahashi, F., and Katta, V. R., "A Reaction Kernel Hypothesis for the Stability Limit of Methane Jet Diffusion Flames," *Proceedings of the Combustion Institute*, Vol. 28, Pt. 2, 2000, pp. 2071–2078.

T. Jackson
Associate Editor

Appendix C. Micrometer-Sized Water Droplet Impingement Dynamics and Evaporation on a Flat Dry Surface

Micrometer-Sized Water Droplet Impingement Dynamics and Evaporation on a Flat Dry Surface

Alejandro M. Briones and Jamie S. Ervin

University of Dayton Research Institute

Shawn A. Putnam

Universal Technology Corporation

Larry W. Byrd and Lois Gschwender

Air Force Research Laboratory, Wright-Patterson Air Force Base

A comprehensive numerical and experimental investigation on micrometer-sized water droplet impact dynamics and evaporation on an unheated, flat, dry surface is conducted from the standpoint of spray-cooling technology. The axisymmetric time-dependent governing equations of continuity, momentum, energy, and species are solved. Surface tension, wall adhesion effect, gravitational body force, contact line dynamics, and evaporation are accounted for in the governing equations. The explicit volume of fluid (VOF) model with dynamic meshing and variable-time stepping in serial and parallel processors is used to capture the time-dependent liquid−gas interface motion throughout the computational domain. The numerical model includes temperature- and species-dependent thermodynamic and transport properties. The contact line dynamics and the evaporation rate are predicted using Blake's and Schrage's molecular kinetic models, respectively. An extensive grid independence study was conducted. Droplet impingement and evaporation data are acquired with a standard dispensing/imaging system and high-speed photography. The numerical results are compared with measurements reported in the literature for millimeter-size droplets and with current microdroplet experiments in terms of instantaneous droplet shape and temporal spread (R/D_0 or R/R_E), flatness ratio (H/D_0), and height (H/H_E) profiles, as well as temporal volume ($\forall$) profile. The Weber numbers (We) for impinging droplets vary from 1.4 to 35.2 at nearly constant Ohnesorge number (Oh) of $\sim 0.025-0.029$. Both numerical and experimental results show that there is air bubble entrapment due to impingement. Numerical results indicate that Blake's formulation provides better results than the static (SCA) and dynamic contact angle (DCA) approach in terms of temporal evolution of R/D_0 and H/D_0 (especially at the initial stages of spreading) and equilibrium flatness ratio (H_E/D_0). Blake's contact line dynamics is dependent on the wetting parameter (K_W). Both numerical and experimental results suggest that at $4.5 < We < 11.0$ the short-time dynamics of microdroplet impingement corresponds to a transition regime between two different spreading regimes (i.e., for We ≤ 4.5, impingement is followed by spreading, then contact line pinning and then inertial oscillations, and for We ≥ 11.0, impingement is followed by spreading, then recoiling, then contact line pinning and then inertial oscillations). Droplet evaporation can be satisfactorily modeled using the Schrage model, since it predicts both well-defined transient and quasi-steady evaporation stages. The model compares well with measurements in terms of flatness ratio (H/H_E) before depinning occurs. Toroidal vortices are formed on the droplet surface in the gaseous phase due to buoyancy-induced Rayleigh-Taylor instability that enhances convection.

1. Introduction

Cooling processes are widely found in many industrial applications such as microelectronics,[1−3] transportation,[4,5] metal production and processing,[6−8] and surgical laser equipment.[9] Liquid-based cooling technologies such as spray cooling, heat pipes, thermosyphons, flow boiling, and jet impingement cooling have attracted considerable interest in these industries. Each technology has its own advantages and disadvantages. Water spray cooling, however, is arguably the most attractive due to its ability to (1) uniformly remove large heat fluxes, (2) use small fluid volumes, (3) take advantage of large heat of vaporization, (4) use low droplet impact velocity, and (5) provide optimal control and regulation of system temperatures.[10]

Spray cooling for microelectronic applications generally occurs when liquid flow through small orifices shatters into a dispersion of fine droplets which impact a heated surface. Then, the droplets spread on the surface and evaporate or form a thin liquid film, removing energy at low temperatures. Because of the many interrelated parameters involved in this technology, it has been extensively investigated since the late 1980s. Mudawar and

(1) Cader, T.; Westra, L. J.; Eden, R. C. *IEEE Trans. Device Mater. Reliability* **2005**, *4*, 605–613.

(2) Bash, C. E.; Patel, C. D.; Sharma, R. K. International Electronic Packaging Technical Conference & Exhibition, July 6−11, 2003, Maui, HI; IPACK2003−35058.

(3) Kim, J. H.; You, S. M.; Choi, S. U. S. *Int. J. Heat Mass Transfer* **2004**, *47*, 3307–3315.

(4) Abramzon, B.; Sazhin, A. *Int. J. Heat Mass Transfer* **2005**, *48*, 1868–1873.

(5) Hiroyasu, H.; Kadota, T.; Senda, T. *Bull. JSME* **1974**, 17.

(6) Wendelstorf, J.; Spitzer, K.-H.; Wendelstorf, R. *Int. J. Heat Mass Transfer* **2008**, *51*, 4902–4910.

(7) Hayes, D. J.; Wallace, B. D.; Boldman, M. T. *Proceedings of the 1992 International Symposium on Microelectronics*, October 19−21, 1992, San Francisco, CA; pp 312−321.

(8) Waldvogel, J. M.; Diversiev, G.; Poulikakos, D.; Megaridis, C. M.; Attinger, D.; Xiong, B.; Wallace, D. B. *J. Heat Transfer* **1998**, *120*, 539.

(9) Aguilar, G.; Majaron, B.; Popoe, K.; Svaasand, L. O.; Lavernia, E. J.; Nelson, J. S. *Lasers Surg. Med.* **2001**, *28*, 113–120.

(10) Kim, J. *Int. J. Heat Fluid Flow* **2007**, *28*, 753–767.

Estes[11] studied the effect of nozzle to surface distance and showed that the optimal configuration was when the impact area of the spray is just inscribed within the heated area. Horacek et al.[12] and Sodtke and Stephan[13] experimentally studied FC-72 and water spray cooling, respectively, on a flat surface and showed that the increase in the heat flux is directly related to the increase in the three-phase contact line length. Navedo[14] found that droplet velocity has the greatest impact on the critical heat flux (CHF, the maximum energy transfer rate from the substrate to the liquid at which nucleate boiling ceases to exist) but negligible influence on the heat transfer coefficient (h), whereas increasing the number of droplets increases both CHF and h. An increase in h was associated with a decrease in the Sauter mean diameter (average particle size defined as the diameter of a sphere which has the same volume to surface area ratio as the particles of interest), while the CHF remained unaffected. Moreover, Chen et al.[15] found that CHF varied with droplet velocity and mean droplet flux, and was independent of Sauter mean diameter. More importantly, they found that, in order to increase cooling efficiency with little liquid volume, the droplet diameters need to be small with high impact velocity. Although spray cooling has been extensively investigated, there still remain many questions to be answered: for example, the conditions that lead to maximum droplet spread without rebound, the mechanisms correlating heat transfer with contact line dynamics,[10] the partitioning of energy between single- and two-phase, and the mechanism by which CHF is triggered.

Insight into the fundamental mechanisms responsible for wetting and two-phase mass and heat transfer during spray cooling can be obtained from single droplet studies. There are many studies on droplet impingement and evaporation in the literature. Bhardwaj and Attinger[16] validated a numerical model to study wetting during the impact of millimeter-sized drops on a flat surface. They found that heated drops spread more extensively than cold drops because of a reduction of viscous forces, and not because of an increase in wetting. Lunkad et al.[17] numerically investigated the millimeter-sized drop impact and spreading on horizontal and inclined surfaces using the volume of fluid (VOF) method with both static (SCA) and dynamic contact angles (DCA). Their results were validated against experimental data available in the literature. They found that the SCA can be used to predict the drop impact and spreading behavior in quantitative agreement with measurements for SCA > 90°. For wettable surfaces (SCA < 90°), the DCA observed at initial contact times were ~100° greater than SCA values, and therefore, the DCA is needed for accurate prediction of the spreading behavior. Bernardin et al.[18] experimentally mapped the impact and heat transfer regimes of millimeter-sized water drops impinging on a flat surface. They found that an increasing Weber number (We) decreases the spreading time and increases the instabilities responsible for droplet breakup. Rebound occurred at the film boiling regime at low We. Even though there have been many studies on single droplet impingement and evaporation,

nearly all of these studies focus on millimeter-sized droplets. In fact, we are only aware of three investigations[19−21] that report micrometer-sized droplets impacting on a flat, unheated surface, which are of the same order of magnitude as spray cooling droplets (i.e., 10−80 μm)[22,23]. Moreover, there is no available work in the literature that considers the evaporation of this range of spray-cooling micrometer-sized droplets including both numerical and experimental techniques. However, it is worth mentioning that Bhardwaj et al.[24] conducted both a numerical and experimental investigation of the evaporation of droplets with diameters that were an order of magnitude greater in diameter (i.e., 462−874 μm) than those required in spray cooling applications. Furthermore, Golovko et al.[25] recently reported the evaporation measurements of 10−100 μm water droplets.

Micrometer-sized droplet impingement and evaporation behavior exhibits differences from that of millimeter-sized droplets from both the practical and fundamental point of views. From a practical standpoint, small average droplet diameter increases spray cooling efficiency.[15] For instance, an average droplet diameter of ~60 μm provides a spray cooling efficiency of ~35%, whereas an average droplet diameter of ~200 μm provides a cooling efficiency of ~2%.[15] By increasing We, the spray cooling efficiency decreases.[26] Similarly, spray cooling nozzles that produce small droplets with high impact velocity also increase the cooling efficiency.[15] Therefore, micrometer-sized droplets with high impact velocity would yield low We needed for optimization of spray cooling technology. Now, from a fundamental standpoint, millimeter-sized droplets which are more likely to be characterized by large Bond numbers (Bo) exhibit droplet apex flattening and larger equilibrium spread ratio.[27] In contrast, the final shape of a micrometer-sized droplet on the substrate has to be a truncated sphere because of the strong surface tension force relative to the gravitational force (Bo ≪ 1). Consequently, the deformation history, especially in the final stages, of these droplets impinging on surface is different from that of millimeter-sized droplets. This has implications on spray cooling technology, because the cooling efficiency is affected by both the spreading history and the maximum spread ratio. Moreover, in the few investigations reporting micrometer-sized droplet impingement in the diameter range of interest (~10−80 μm) the maximum We is ~100. Because this range of micrometer-sized droplets inherently exhibits relatively low We, impact phenomena occurring in millimeter-sized droplets such as partial rebound, complete rebound, fingers, prompt splash, corona splash, and crown formation have not been observed. Furthermore, Golovko et al.[25] have shown that hydrophilic pinned microdroplets do not follow the evaporation rate laws established for millimeter-sized droplets at the last stages of evaporation.

Therefore, the purpose of this investigation is to better understand the characteristics of micrometer-sized (refers to droplet diameter of tens of micrometers and not hundreds of micrometers) droplet impingement and evaporation on a flat, dry surface using both numerical and experimental techniques. It is projected that the results of this research will be useful for

(11) Mudawar, I.; Estes, K. A. *J. Heat Transfer* **1996**, *118*, 672–679.
(12) Horacek, B.; Kiger, K. T.; Kim, J. *Int. J. Heat Mass Transfer* **2005**, *48*, 1425–1438.
(13) Sodtke, C.; Stephan, P. *Int. J. Heat Mass Transfer* **2007**, *50*, 4089–4097.
(14) Navedo, J. *Parametric Effects of Spray Characteristics on Spray Cooling Heat Transfer*; Ph.D. Dissertation, University of Central Florida, Florida, 2000.
(15) Chen, R.-H.; Chow, L. C.; Navedo, J. E. *Int. J. Heat Mass Transfer* **2004**, *47*, 5095–5099.
(16) Bhardwaj, R.; Attinger, D. *Int. J. Heat Fluid Flow* **2008**, *29*, 1422–1435.
(17) Lunkad, S. F.; Buwa, V. V.; Nigam, K. D. P. *Chem. Eng. Sci.* **2007**, *62*, 7214–7224.
(18) Bernardin, J. D.; Stebbins, C. J.; Mudawar, I. *Int. J. Heat Mass Transfer* **1997**, *40*, 247–267.

(19) van Dam, D. B.; Le Clerc, C. *Phys. Fluids* **2004**, *16*, 3403–3414.
(20) Zhen-Hai, S.; Rui-Jing, H. *Chin. Phys. B* **2008**, *17*, 1674–1056.
(21) Son, Y.; Kim, C.; Yang, D. H.; Ahn, D. J. *Langmuir* **2008**, *24*, 2900–2907.
(22) Yang, J.; Pais, M. R.; Chow, L. C. *J. Exp. Heat Transfer* **1993**, *6*, 55–67.
(23) Cryer, M. A. *An experimental study of high heat flux removal using micro-droplet spray cooling*, M.S. Thesis, Naval Postgraduate School, Monterey, CA, 2003.
(24) Bhardwaj, R.; Fang, X.; Attinger, D. *New J. Phys.* **2009**, *11*, 075020.
(25) Golovko, D. S.; Butt, H.-J.; Bonaccurso, E. *Langmuir* **2009**, *25*, 75–78.
(26) Estes, K. A.; Mudawar, I. *Int. J. Heat Mass Transfer* **1995**, *38*, 2985–2996.
(27) Bartashevich, M. V.; Kuznetsov, V. V.; Kabov, O. A. *Microgav. Sci. Technol.* **2010**, *22*, 107–114.
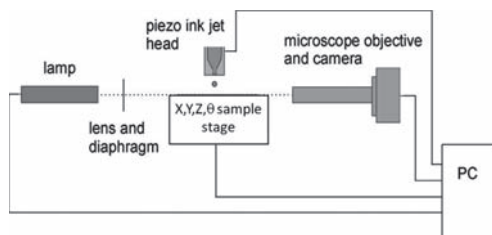
Figure 1. Schematic of experimental setup.

improving single droplet impact dynamics and evaporation models for later enhancement of spray cooling models. Droplet impingement on a heated surface is, however, a very complex phenomenon involving a multitude of physical−chemical events such as deposition, spreading, receding, rebound, jetting, splash, bubble entrapment, pinning, depinning, and evaporation. Therefore, in this study we will only focus on the droplet spreading and receding characteristics upon impingement as well as evaporation from an unheated surface. The explicit VOF model is used for modeling and simulation of the droplet dynamics upon impingement and evaporation. This model is particularly important, because in contrast with other models,[16,28] it allows determination of the gaseous-phase flow field and thermal convection relevant to spray cooling applications. Both the contact line velocity[29] and evaporation[30] models are incorporated in the model. These two models are discussed in detail in subsequent sections. This is the only investigation reporting both molecular-kinetics-based models included within the VOF formulation; therefore, it is a significant contribution to our research.

Although hydrodynamic-theory-based contact line motion[24] and evaporation[31] have been incorporated in interface-tracking numerical formulations,[24] investigations that include the molecular-kinetics-based contact line velocity[29] and evaporation[30] models together in a VOF formulation are unavailable. For instance, Zhen-Hai and Rui-Jing[20] included Blake's contact line velocity[29] in their VOF model (note: the formulation used by Zhen-Hai and Rui-Jing, however, does not include the effect of viscosity on the motion of the contact line), whereas Nikolopoulos et al.[32] incorporated the Schrage evaporation[30] model. Moreover, the VOF model with contact line dynamics and evaporation is superior to interface-tracking methods,[16,28] because the latter neglect the effect of the gas around droplets implicitly assuming that the droplet is traveling in a vacuum. This assumption leaves the interface-tracking methods unable to resolve the complete physics such bubble entrapment and external convection occurring during droplet impingement and during droplet evaporation, respectively. Bubble encapsulation is particularly important for heat removal, because when droplets impinge on a surface, air bubbles act as vapor nuclei and initiate nucleate boiling at much lower superheats than theory predicts.[33] In addition, our numerical results are also compared with measurements reported in the literature and with our experiments as well.

The major objective of this investigation is to develop a numerical model capable of capturing the relevant physics of droplet impact and evaporation under ambient conditions.

Specific objectives are as follows: (1) to validate the numerical model for a single micrometer-sized droplet impinging on an unheated flat surface, (2) to characterize the droplet dynamics in terms of dimensionless groups (We, Oh, and Re), (3) to compare the SCA and DCA modeling approaches with experiments, (4) to determine whether Blake's contact line velocity model[29] can be used to emulate micrometer-sized droplet impingement, and (5) to evaluate the Schrage evaporation[30] model to capture the droplet lifetime as well as the evaporation dynamics.

2. Experimental Setup

Micrometer-sized droplet impingement and evaporation data were acquired with a standard dispensing/imaging system shown in Figure 1. The microdroplets were generated with an inkjet dispensing head from Microdrop Technologies GmbH (Norderstedt, Germany), where the inkjet head consists of a cylindrical piezo element surrounding a glass capillary with a 50 μm inner nozzle diameter. Deionized (DI) water purified and filtered with a Barnstead Nanopure Water Purification System was used. Video recordings were captured with a high-speed camera from Vision Research Inc. (Wayne, New Jersey, USA). The camera is equipped with an internal 8 Gbit buffer, 1280×800 megapixel CMOS sensor, and programmable electronic shutter with a minimum exposure time of 300 ns. The micrometer-sized droplet videos acquired in this study used frame rates up to $\sim$120 000 frames-per-second (fps) using 256×128 pixels of the megapixel sensor. Most short-term microdroplet impingement data were acquired at 66 000 fps (15.14 μs/frame) with 256×256 pixels and $\sim$5 μs exposure intervals. Microdroplet evaporation data were acquired at 58 000 fps (17.24 μs/frame) with $\sim$10 μs exposure intervals, even though a much slower frame rate is adequate. The sample surfaces in all experiments were Al thin films ($\sim$70 nm thick). The Al thin films were deposited by magnetron sputtering on flat ($^1/_{10} \lambda$) fused silica optics windows purchased from Edmund Optics. An external TTL trigger from a computer controlled pulse generator was used to coordinate droplet dispensing and video recordings. We note that, in many cases, footprints of previously evaporated microdroplets were observed on the Al substrate surface, which, in turn, could influence the short-term impingement dynamics of subsequent droplets. To obtain reproducible data, the samples were simply translated and/or rotated after each droplet impingement to ensure that the sample surface was clean prior to each individual impact (as shown in the figures corresponding to section 4.4).

3. Physical−Numerical Procedure

3.1. Liquid−Gas-Phase Numerical Model. The explicit VOF model in FLUENT is used to track the time-dependent volume fractions of liquid (α_l) and gas (α_g) throughout the computational domain.[34] The fields for all variables and properties are shared by the phases and represent volume-averaged values. The liquid phase is composed only of water, whereas the gaseous phase is composed of water vapor (H_2O) and air. The axisymmetric governing equations of continuity, momentum, energy, and species are solved using the segregated pressure-based solver.[35] The governing equations in differential notation are as follows.

VOF Equation.

$$\frac{\partial(\alpha_l \rho)}{\partial t} + \frac{\partial(\alpha_l \rho u)}{\partial r} + \frac{\alpha_l \rho u}{r} + \frac{\partial(\alpha_l \rho v)}{\partial z} = -\dot{m}_{lg} \qquad (1)$$

$$\alpha_g = 1 - \alpha_l$$

(28) Ruiz, O. E.; Black, W. Z. *J. Heat Transfer* **2002**, *124*, 854–863.
(29) Blake, T. D.; De Coninck, J. *Adv. Colloid Interface Sci.* **2002**, *66*, 21.
(30) Schrage, R. W. *A theoretical study of interphase mass transfer*; Columbia University Press: New York, 1953.
(31) Hu, H.; Larson, R. G. *Langmuir* **2005**, *21*, 3972–3980.
(32) Nikolopoulos, N.; Theodorakakos, A.; Bergeles, G. *Int. J. Heat Mass Transfer* **2007**, *50*, 303–319.
(33) Sigler, J.; Mesler, R. *J. Colloid Interface Sci.* **1990**, *134*, 459.

(34) Hirt, C. W.; Nichols, B. D. *J. Comput. Phys.* **1981**, *39*, 201–225.
(35) ANSYS FLUENT 12.0, *Theory Guide*, **2009**.

Momentum Equations.

$$\frac{\partial(\rho u)}{\partial t} + \frac{\partial(\rho uu)}{\partial r} + \frac{\partial(\rho vu)}{\partial z} + \frac{\rho uu}{r} = -\frac{\partial p}{\partial r} + 2\frac{\partial}{\partial r}\left(\mu\frac{\partial u}{\partial r}\right) + \frac{\partial}{\partial z}\left(\mu\frac{\partial u}{\partial z}\right)$$

$$+ \frac{2\mu}{r}\frac{\partial u}{\partial r} + \frac{\partial}{\partial z}\left(\mu\frac{\partial v}{\partial r}\right) - \frac{2\mu u}{r^2} + \frac{2\sigma\rho\kappa_1}{\rho_1 + \rho_g}\frac{\partial\alpha_1}{\partial r}$$

$$\frac{\partial(\rho v)}{\partial t} + \frac{\partial(\rho uv)}{\partial r} + \frac{\partial(\rho vv)}{\partial z} + \frac{\rho uv}{r}$$

$$= -\frac{\partial p}{\partial z} + \frac{\partial}{\partial r}\left(\mu\frac{\partial v}{\partial r}\right) + 2\frac{\partial}{\partial z}\left(\mu\frac{\partial v}{\partial z}\right) + \frac{\mu}{r}\frac{\partial v}{\partial r} + \frac{\partial}{\partial r}\left(\mu\frac{\partial u}{\partial z}\right) + \frac{\mu}{r}\frac{\partial u}{\partial z}$$

$$+ \rho g + \frac{2\sigma\rho\kappa_1}{\rho_1 + \rho_g}\frac{\partial\alpha_l}{\partial z} \tag{2}$$

Energy Equation.

$$\frac{\partial(\rho E)}{\partial t} + \frac{\partial(u(\rho E + p))}{\partial r} + \frac{\partial(v(\rho E + p))}{\partial z} + \frac{u(\rho E + p)}{r}$$

$$= \frac{\partial}{\partial r}\left(k\frac{\partial T}{\partial r}\right) + \frac{\partial}{\partial z}\left(k\frac{\partial T}{\partial z}\right) + \frac{k}{r}\frac{\partial T}{\partial r} \tag{3}$$

$$E = \frac{\alpha_l\rho_l E_l + \alpha_g\rho_g E_g}{\alpha_l\rho_l + \alpha_g\rho_g}$$

Species Equation.

$$\frac{\partial(\rho_g Y_{g,H_2O})}{\partial t} + \frac{\partial(\rho_g u Y_{g,H_2O})}{\partial r} + \frac{\partial(\rho_g v Y_{g,H_2O})}{\partial z} + \frac{\rho_g u Y_{g,H_2O}}{r}$$

$$= \frac{\partial}{\partial r}\left(\rho_g D_{H_2O-air}\frac{\partial Y_{g,H_2O}}{\partial r}\right) + \frac{\partial}{\partial z}\left(\rho_g D_{H_2O-air}\frac{\partial Y_{g,H_2O}}{\partial z}\right)$$

$$+ \frac{\rho_g D_{H_2O-air}}{r}\frac{\partial Y_{g,H_2O}}{\partial r} + \dot{m}_{lg} \tag{4}$$

$$Y_{g,air} = 1 - Y_{g,H_2O}$$

The VOF equation is only solved for the liquid phase and that of the gas phase volume fraction is obtained from the fact that the sum of volume fractions must equal unity. The momentum equation is dependent on the volume fractions (α) by means of the density ($\rho = \alpha_l\rho_l + \alpha_g\rho_g$) and dynamic viscosity ($\mu = \alpha_l\mu_l + \alpha_g\mu_g$). The momentum equation also includes the gravitational body force ($\rho\vec{g}$) as well as the surface tension force ($2\sigma\rho\kappa_1\nabla\alpha_l/(\rho_l + \rho_g)$). The latter is based on the continuum surface force (CSF) model,[36] where $\hat{n} = n/|n|$, $n = \nabla\alpha_l$, and $\kappa_1 = \nabla\cdot\hat{n}$. The surface tension varies linearly with temperature: $\sigma = 116.174 - 0.1477T$. The energy conservation equation treats E as a mass-averaged quantity. The temperature (T) is obtained by knowing c_p and E in each numerical cell. The species continuity equation is only solved for the water vapor (H_2O) in the gaseous phase, since there is only one species component in the liquid phase (i.e., $Y_1 = 1.0$). The diffusion flux is modeled using Fick's law. The mass fraction of air is obtained by knowing that the sum of species in the gaseous phase needs to be equal to unity (see eq 4).

The unsteady terms are first-order accurate in time. The momentum equations are discretized using the QUICK scheme,[37] whereas the species and energy equations are discretized using a second-order upwind scheme.[38] The VOF equation is discretized using the Geo-Reconstruct scheme.[39] The gradients and derivatives of the governing equations are computed using the Green-Gauss Node-Based method[40,41] which is second-order spatially accurate. The pressure values are obtained at the cell faces by using the PRESTO! discretization scheme.[42] The pressure−velocity coupling is achieved by using the PISO algorithm.[43]

3.2. Thermodynamic and Transport Properties. The properties of liquid water are c_p = 4182 J/kg−K, k = 0.6 W/m−K, and μ = 0.001 kg/m−s corresponding to 300 K. The thermodynamic and transport properties appearing in the governing equations for the gaseous phase species (i.e., H_2O and air) are temperature- and species-dependent. The gaseous mixture density is computed using the ideal gas equation. The species individual specific heat capacities are computed using piecewise polynomials.[44] The gaseous mixture specific heat capacity is computed using the species mass-weighted heat capacity (i.e., $\Sigma_{i=1}^{2} Y_i\cdot c_{p,i}$). The thermal conductivity and viscosity of each species are obtained using Chapman-Enskog collision theory, whereas the gaseous mixture thermal conductivity and viscosity are obtained using a mass weighted mixing law (i.e., $\Sigma_{i=1}^{2} Y_i\cdot k_i$ and $\Sigma_{i=1}^{2} Y_i\cdot\mu_i$). The water vapor binary diffusivity coefficient with air is calculated using Chapman−Enskog collision theory and Lennard-Jones potentials.

3.3. Contact Line Dynamics. Three strategies are used to simulate the contact line dynamics. These are the static (SCA) and dynamic contact angle (DCA) approaches and Blake's contact line velocity equation.[29] The SCA and DCA are implemented through the wall adhesion effects using $\hat{n} = \hat{n}_W \cos\theta_W + \hat{t}_W \sin\theta_W$, where θ_W is the wall−liquid contact angle. When the SCA is used, the equilibrium contact angle (θ_E) needs to be obtained from the experiments, so that $\theta_W = \theta_E$ for the entire wall surface at all times. On the other hand, when the DCA is used the dynamic contact angle (θ_D) needs to be obtained from experimental data before the simulation. Thus, $\theta_W = \theta_D$, and consequently, θ_W is time-dependent. DCA is implemented through a C programming language subroutine. Blake's formulation is

$$u_{CL} = \frac{2K_W\lambda}{\mu}\sinh\left[\frac{\sigma}{2nk_BT}(\cos\theta_E - \cos\theta)\right] \tag{5}$$

where the variables n, λ, and K_w represent the number of absorption sites per unit area, displacement length, and wetting parameter, respectively. A typical value of λ is 2×10^{-10} m and $n = \lambda^{-2}$.[16] In eq 5, θ is equal to θ_D, but unlike the DCA, θ is computed from the contact line velocity (u_{CL}). In this regard, $\theta = \theta_D$ is obtained by solving eq 5, where u_{CL} is estimated as the nearest calculated velocity within the interface cell adjacent to the wall. This value of $\theta = \theta_D$ is then used to calculate the surface tension force in eq 2. A similar procedure was implemented in ref 45. In the

(36) Brackbill, J. U.; Kothe, D. B.; Zemach, C. *J. Comput. Physics* **1992**, *100*, 335−354.

(37) Leonard, B. P.; Mokhtari, S. ULTRA-SHARP Nonoscillatory Convection Schemes for High-Speed Steady Multidimensional Flow; NASA TM 1−2568 (ICOMP-90−12); NASA Lewis Research Center, 1990.

(38) Barth, T. J.; Jespersen, D. AIAA 27th Aerospace Sciences Meeting;Reno, NV,1989; AIAA-89−0366.

(39) Youngs, D. L. In *Numerical Methods for Fluid Dynamics*; Morton, K. W., Baines, M. J., Eds.; Academic Press: London, 1982.

(40) Holmes, D. G.; Connell, S. D. AIAA 9th Computational Fluid Dynamics Conference; **1989**, AIAA-1989−1932; pp 25−39.

(41) Rauch, R. D.; Batina, J. T.; Yang, H. T., 32nd AIAA/ASME/ASCE/AHS/ASC Structures, Structural Dynamics, and Materials Conference, Washington D.C., 1991; AIAA-91-1106.

(42) Patankar, S. V. *Numerical Heat Transfer and Fluid Flow*; Hemisphere: Washington, DC, 1980.

(43) Issa, R. I. *J. Comput. Physics* **1985**, *62*, 40−65.

(44) ANSYS FLUENT 12.0, *User's Guide*, **2009**.

(45) Keshavarz-Motamed, Z; Kadem, L; Dolatabadi, A. *Microfluid Nanofluid* **2010**, *8*, 47−56.

current investigation, this methodology is also implemented in FLUENT through a C programming language subroutine.

Blake's contact line velocity model describes wetting as a dynamic absorption/desorption process of liquid molecules to the wall surface. At equilibrium, the contact line would appear to be stationary, but at the molecular level, there is an exchange of molecules from one phase to another at a rate associated with an equilibrium molecular displacement frequency ($f_{W,E}$). Work must be done by the unbalanced Young−Laplace force (i.e., $\sigma(\cos\theta_E - \cos\theta)/n$) at each absorption site to overcome the energy barriers due to molecular displacement (i.e., $\Delta G_W^{\ddagger}/N_A$) in order for the contact line to move. For droplet spreading to occur, the frequency of molecules in the forward direction (f_W^{+}) must exceed those in the backward direction (f_W^{-}). This occurs when the unbalanced Young−Laplace force lowers the energy barriers for displacement in the forward direction and raises them in the backward direction. The converse is true for droplet recoiling. In the context of molecular displacement frequencies, the wetting parameter is equal to $K_W = f_{S,E} \times h_P/v_L$,[29] where $f_{S,E}$ is the equilibrium frequency of molecular displacements associated with droplet surface contributions, h_P is Planck's constant, and v_L is the molecular volume of the liquid phase. Large solid−liquid interactions suggest that the K_W should be small and, consequently, $\theta = \theta_D$ should then be strongly dependent on u_{CL}. In contrast, small solid−liquid interactions suggest the converse.[29] If viscous contributions to molecular displacements are not taken into account (as done by Zhen-Hai and Rui-Jing[20]), then $f_{W,E} = f_{S,E}$ and $K_W = f_{W,E} \times \mu$. We have chosen to use Blake's contact line velocity formulation, such that both the solid−liquid surface interactions and viscous contributions to molecular displacements are taken into account.

3.4. Mass Transfer Rate. The volumetric mass transfer rate that we use to model evaporation is given by

$$\dot{m}_{lg} = |\nabla\alpha_g|\left[\frac{2\varepsilon}{(2-\varepsilon)}\right]\left(\frac{1}{2\pi R \cdot MW_{g,H_2O}}\right)^{1/2}\left(\frac{p_l}{T_l^{1/2}} - \frac{p_g}{T_g^{1/2}}\right)$$

(6)

which is the product of the droplet interfacial surface area density ($|\nabla\alpha_g|$) and Schrage's mass flux.[30] The Schrage equation was derived from kinetic theory for flat surfaces and, consequently, does not include curvature effects.[30] In eq 6, ε is the evaporation efficiency or accommodation coefficient. To date, this quantity is still not well established for a given fluid. For example, Marek and Strub[46] noted the considerable scatter (up to 3 orders of magnitude) in the theoretically and experimentally obtained ε. Equation 6 was adapted to FLUENT through a C programming language subroutine.[47] It is assumed that $T_g = T_l = T$ (i.e., temperature of the cell). P_l is the saturation pressure at T (i.e., $P_{sat}(T)$), whereas P_g is the absolute vapor partial pressure at the cell. If the saturation pressure at T (i.e., $P_{sat}(T)$) is greater than $X_{H_2O} \cdot P_{cell}(T)$, then the liquid evaporates and $\dot{m}_{lg}$ is positive. Condensation occurs when the converse is true; hence, $\dot{m}_{lg}$ is negative.

In the absence of Marangoni flow and in the presence of diffusion-controlled evaporation, the evaporation flux increases
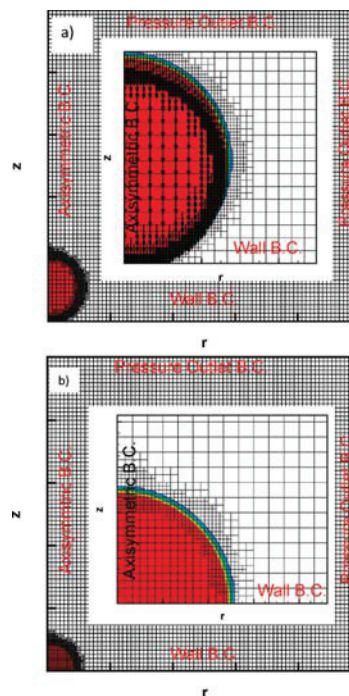
Figure 2. Schematic of computational domain, mesh, boundary conditions, and initial conditions for the (a) impinging and (b) evaporating droplet simulations.

tremendously near the contact line.[48−52] Equation 6 predicts a nearly uniform instantaneous evaporation mass flux along the liquid−gas interface for the evaporating droplets studied here (not shown). This profile is characteristic of kinetically controlled evaporation.[53] Nevertheless, the evaporating droplets studied here exhibit evaporation flux values comparable with the expression given by ref 49 for diffusion-controlled evaporation with suppressed Marangoni flow. Moreover, the analytical solution of Petsi and Burganos[53] also predicts fluid flows from the droplet's apex toward the contact line along the substrate for kinetically controlled evaporation of pinned droplets on hydrophilic substrates, the difference being that diffusion-controlled evaporation exhibits faster flow near the contact line that leads to higher evaporation flux in the vicinity of the contact line[53] and "coffeering" deposition.[48] In the context of droplet lifetime, kinetically controlled evaporation models predict slightly, but non-negligible, longer droplet lifetimes in comparison to the diffusion-controlled evaporation models[54] perhaps due to uniform evaporation flux.

3.5. Geometry and Mesh. A schematic of the computational domain with boundary conditions is presented in Figure 2. The entire geometry is meshed with square elements, where the highest mesh refinement is used at the droplet interface. An extensive grid independence study has been conducted to show that the grid size and meshing scheme shown in Figure 2 resolves the flow field (see section 4.3).

3.6. Dynamic Mesh and Variable Time-Stepping. A dynamic mesh is used for the simulations involving droplet impingement and evaporation. The mesh is refined and coarsened near the

(46) Marek, R.; Straub, J. *Int. J. Heat Mass Transfer* **2001**, *44*, 39–53.
(47) Troshko, A. Report on evaporation model, Internal Report, ANSYS, Inc.
(48) Hu, H.; Larson, R. G. *Langmuir* **2005**, *21*, 3963–3971.
(49) Deegan, R. D.; Bakajin, O.; Dupont, T. F.; Huber, G.; Nagel, S. R.; Witten, T. A. *Nature* **1997**, *389*, 827–829.
(50) Petsi, A. J.; Burganos, V. N. *Phys. Rev. E* **2005**, *72*, 047301.
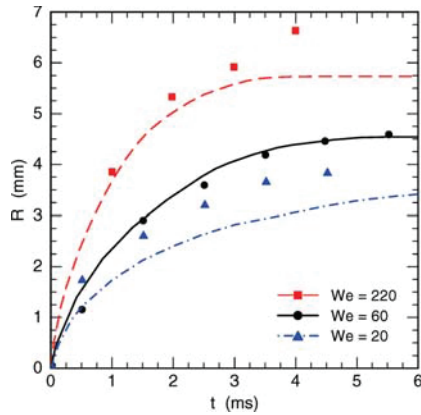(51) Petsi, A. J.; Burganos, V. N. *Phys. Rev. E* **2006**, *73*, 041201.

(52) Hu, H.; Larson, R. G. *J. Phys. Chem. B* **2006**, *110*, 7090–7094.
(53) Petsi, A. J.; Burganos, V. N. *Phys. Rev. E* **2008**, *78*, 036324.
(54) Kryukov, A. P.; Levashov, V. Y.; Sazhin, S. S. *Int. J. Heat Mass Transfer* **2004**, *47*, 2541–2549.

Figure 3. Temporal evolution of the maximum wetting radius (or contact line position) (R) on an isothermal dry surface at $T_s = 180\,°C$ with characteristic Weber numbers of We = 220, 60, and 20. The initial droplet radius is $R_0 = 1.5$ mm, and the Weber numbers correspond to impact velocities of $V_0 = 2.34, 1.21$, and 0.7 m/s, respectively. The experimental results (filled-symbol data) are from Bernardin et al.[18] and the lines are our numerical predictions. The accommodation coefficient used in the Schrage model is $\varepsilon = 0.03$.

liquid−gas interface after each individual time step for impinging droplets, whereas the mesh is dynamically modified once every twenty time steps for evaporating droplets. Dynamic meshing is used in conjunction with noniterative time advancement (NITA)[43] and variable time-stepping. The time step is on the order of $O(10^{-2})$ and $O(10^{-1})\,\mu s$ for the impinging and evaporating microdroplets, respectively.

3.7. Boundary Conditions. Figure 2 also presents the computational domain, which contains the surface, center line, and surroundings. The surface, center line, and surroundings are modeled as wall, axis of symmetry, and pressure-outlet boundary conditions, respectively. For the simulations studied, the initial temperature in the domain is 300 K.

Wall Boundary Condition.

$$\frac{\partial \alpha_l}{\partial z} = 0,\ u = 0,\ v = 0,\ \frac{\partial Y_{H_2O}}{\partial z} = 0,\ \text{and}\ T = 300\ K$$

Axisymmetric Boundary Condition.

$$\frac{\partial \alpha_l}{\partial r} = 0,\ u = 0,\ \frac{\partial v}{\partial r} = 0,\ \frac{\partial Y_{H_2O}}{\partial r} = 0,\ \text{and}\ \frac{\partial T}{\partial r} = 0$$

Pressure-Outlet Boundary Condition.

$$P = 0\ (\text{gauge}); \text{if backflow, then}\ \alpha_l = 0, Y_{H_2O} = 0, \text{and}$$
$$T = 300\ K$$

For positioning the pressure-outlet boundary condition, we conducted an extensive study on the effect of domain size on the numerical simulations by tracking the maximum water vapor as a function of time (not shown). The results showed that when the pressure-outlet boundary conditions are located at a distance corresponding to ten droplet radii away from the wall and axisymmetric boundary conditions, the boundary-induced disturbances are negligible (see Figure 2).

3.8. Parallel Computations. Numerical simulation for the millimeter-sized droplet evaporation required the use of parallel computing. Scalability studies showed that three compute nodes is the optimum number of nodes to achieve high-speed computation.
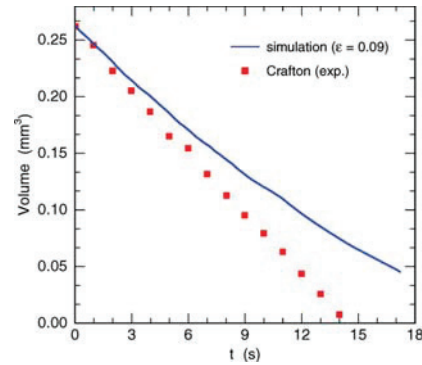
Figure 4. Temporal evolution of droplet volume ($\forall$) for a millimeter-sized water droplet evaporating on an isothermal flat surface at $T_s = 180\,°C$. The initial droplet diameter is $D_0 = 1.0$ mm and the accommodation coefficient is $\varepsilon = 0.09$. The experimental results (filled-square data) are from Crafton.[56]

For these simulations, we used a SGI Altix 4700 parallel computer with 1.6 GHz Itanium 2 processor. The time per iteration was ∼1.5 s leading to a total computational time of ∼24 days.

3.9. Limitations of the Numerical Model. In the context of the axisymmetric configuration, our numerical model is limited to perfect thermal contact between the droplet and the isothermal substrate. In addition, it cannot simulate depinning during evaporation.

4. Results and Discussion

In the remainder of this paper, we present and discuss (1) the validation of our numerical model with millimeter-sized droplets reported in the literature, (2) the operating conditions of cases we investigated for micrometer-sized droplet impingement and evaporation, (3) our grid independence study, and (4) the characteristics of our experimentally and numerically obtained micrometer-sized droplet impact dynamics and evaporation.

4.1. Validation of Numerical Model with Millimeter-Sized Droplets. As mentioned in the introduction, droplet impingement and evaporation are very complex processes since contact line motion and evaporation occur at the molecular level and continuum models are needed for modeling and simulation. Therefore, our numerical model is first compared with widely available measurements on millimeter-sized water droplets regarding impact droplet dynamics and evaporation.

4.1.1. Impact Droplet Dynamics. Figure 3 presents the temporal evolution of the wetted maximum radius (or contact line position) (R) on an isothermal dry surface at $T_s = 180°$ with characteristic We of 220, 60, and 20. The numerical results are compared with the experiments from Bernardin et al.[18] These simulations lasted no more than 24 h. The SCA approach was used to model the contact line dynamics with $\theta_E = 60°$ and $\varepsilon = 0.04$. These values are typical for water droplet impinging and evaporating from an aluminum substrate.[46,55] Experiments and simulations indicate that as We decreases the spreading rate decreases. Therefore, there is good correlation between measured and predicted R on the flat surface as a function of time. This agreement serves to validate the VOF solution technique and evaporative flux expression that is used. Nikolopoulos et al.[32] has also compared the case when We = 220 using the VOF technique with similar conditions as in the present investigation. The main

(55) Bernardin, J. D.; Mudawar, I.; Walsh, C. B.; Franses, E. I. *Int. J. Heat Mass Transfer* **1997**, *40*, 1017–1033.

Table 1. Operating Conditions for Impinging Microdroplets[a]

droplet	$D_0(\mu m)$	V_0 (m/s)	ω_{ana} (kHz)	ω_{exp} (kHz)	We	Ca $\times 10^3$	Re	Oh $\times 10^3$	Bo $\times 10^6$	θ_E (°)
A	40.7	1.56	45.8	70.4	1.4	22	63.4	26	230	87.09
B	35.6	3.02	55.9	59.3	4.5	42	107.3	28	170	79.04
C	55.4	2.45	28.8	29.1	4.6	34	135.5	22	420	50.32
D	36.6	4.02	53.6	61.3	8.2	56	146.8	28	180	65.66
E	32.2	5.14	65.0	69.0	11.8	71	165.2	29	140	64.85
F	33.4	4.97	61.6	62.6	11.4	69	165.7	29	150	66.69
G	43.0	6.41	42.1	44.6	24.5	89	275.1	25	250	60.91
H	43.4	7.30	41.6	42.7	32.1	101	316.2	25	260	54.56
I	44.0	7.61	40.7	42.7	35.3	106	334.2	25	260	54.97

[a] The analytical values of inertial oscillation frequencies were obtained from $\omega_{ana} = \sqrt{(2\sigma/(\rho D_0^3))}$[59].

Table 2. Operating Conditions for Microdroplet Evaporation

	experimental conditions	numerical conditions
RH (%)	17.3	17.3
T (K)	296.35	296.35
D_E (μm)	70.1	70.1
H_E (μm)	35.25	35.25
θ_E (°)	83.5	90.0
τ	1.299 s	---

difference between their simulation and the present is that Nikolopoulos et al.[32] used $\varepsilon = 0.5$. Their result showed good agreement with the measurements as well. Nonetheless, they predicted a larger spreading rate at the end of the spreading process ($t = 5$ ms) when compared to our result (i.e., $R = 6.8$ mm vs 5.8 mm). This suggests that the evaporation mass rate has an effect on droplet spreading on heated surfaces.

4.1.2. Droplet Evaporation. To further validate our numerical results, we compare our simulations with the experiment of Crafton.[56] Figure 4 shows the predicted and measured droplet volume temporal evolution during evaporation. In the experiments, D_0 is in fact 1.05 mm, the temperature of the wall surface is $T_s = 95$ °C, the ambient temperature is $T_\infty = 21$ °C, the relative humidity is RH = 30%, and the SCA is 112°. Crafton[56] gently deposited this water droplet on an aluminum substrate and the results presented here begin with the termination of the spreading process (i.e., once the droplet is pinned and inertial oscillations are damped out). The measurements clearly show that the droplet volume varies linearly with time, and its lifetime is ~14 s. In the numerical simulations, $T_s = 100$ °C, $T_\infty = 25$ °C, RH = 0%, and the droplet is pinned during the simulation. The initial contact angle (θ_0) was set to 90°. These numerical conditions are very close to those of Ruiz and Black[28] who used a front-tracking technique with a hydrodynamic evaporation expression. Their results closely matched the measurements until ~11 s. Their simulation could not be used for later than ~11 s due to convergence deterioration when θ approached the receding angle of 10°. Moreover, Ruiz and Black[28] also suggested that discrepancies between measurements and simulations might be due to three-dimensional effects taking over during the late stages of evaporation (as also observed in the experiments in ref 57).

In our simulations, we attempted to match the measurements with accommodation coefficient of $\varepsilon = 0.09$. The predicted volume at this condition varies nearly linearly until ~10 s. Later on, the droplet starts to evaporate slower and its volume does not decrease as rapidly as before. Our model clearly underpredicts and overpredicts the volumetric evaporation rate and the droplet lifetime, respectively. No further simulations were tried here,

because this simulation is computationally expensive. For instance, the variable time step is in the order of 10^{-5} s leading to ~1.4 million steps with iteration time ~1.5 s that translates to about three weeks of computation. Nevertheless, the present results are satisfactory, because we qualitatively observed the linear volume change during evaporation. To accurately predict the volumetric evaporation rate and droplet lifetime, knowledge of ε is required. Recall, as mentioned in section 3.4, that Marek and Straub[46] noted a significant scatter (up to 3 orders of magnitude) in the theoretically and experimentally obtained ε. As mentioned above, three-dimensional effects might need to be considered as well.

Furthermore, it is worth mentioning that we initially used the CICSAM discretization scheme[58] for the VOF equation instead of Geo-Reconstruct.[39] The droplet lifetime obtained with CICSAM[58] was 2 orders of magnitude smaller. Therefore, Geo-Reconstruct is required for modeling droplet evaporation because CICSAM[58] cannot adequately capture the liquid−gas interface. Resolving the interface is crucial for calculating the interfacial area density needed for computing the mass transfer rate.

**4.2. Operating Conditions for Micrometer-Sized Droplets.** Table 1 presents the conditions for the numerically and experimentally investigated impinging droplets. The impact velocity (V_0), the initial diameter (D_0), the analytically obtained inertial oscillation frequency (ω_{ana}), the measured inertial oscillation frequency (ω_{exp}), the Weber (We), Reynolds (Re), Capillary (Ca), Ohnesorge (Oh), and Bond (Bo) numbers, as well as the equilibrium contact angle (θ_E), are presented. Note that V_0 and D_0 cannot be controlled independently. V_0 and D_0 are used to compute the dimensionless numbers and ω_{ana}. The analytical frequencies are obtained by an order of magnitude analysis between the unsteady inertial term and the surface tension force in the radial momentum equation (see eq 2) and by assuming that $\omega_{ana} \approx V_0/D_0$.[59] The very simple order of magnitude very closely matches the measurements. Both ω_{ana} and ω_{exp} clearly show that the frequency of oscillations of these microdroplets is in the range of tens of kHz, whereas for typical millimeter-sized droplets, it is about 3 orders of magnitude smaller for similar conditions. For instance, for a 3.2 mm water droplet (We = 7.1) impinging under ambient conditions $\omega_{exp} = 50$ Hz,[16] whereas for droplet D (We = 8.2), $\omega_{exp} = 61.3$ kHz. Moreover, for all droplets in Table 1, We is greater than unity and generally increases from droplet A to droplet I. Similarly, Ca and Re increase from droplet A to droplet I. Therefore, based on Ca the parasitic currents (nonphysical currents generated in the fluid adjacent to the liquid−gas interface by local variations in the CSF) inherent to VOF model might become more important in descending order from droplet I to

(56) Crafton, E. F. *Measurements of the evaporation rates of heated liquid droplets*, M.S. Thesis, Georgia Institute of Technology, Atlanta, GA.
(57) Rymkiewicz, J.; Zbigniew, Z. *Int. Comm. Heat Mass Transfer* **1993**, *20*, 687–697.

(58) Ubbink, O. Numerical prediction of two fluid systems with sharp interfaces, PhD Thesis; Imperial College of Science, Technology and Medicine, London, England, 1997.
(59) Schiaffino, S.; Sonin, A. A. *Phys. Fluids* **1997**, *9*, 3172–3187.
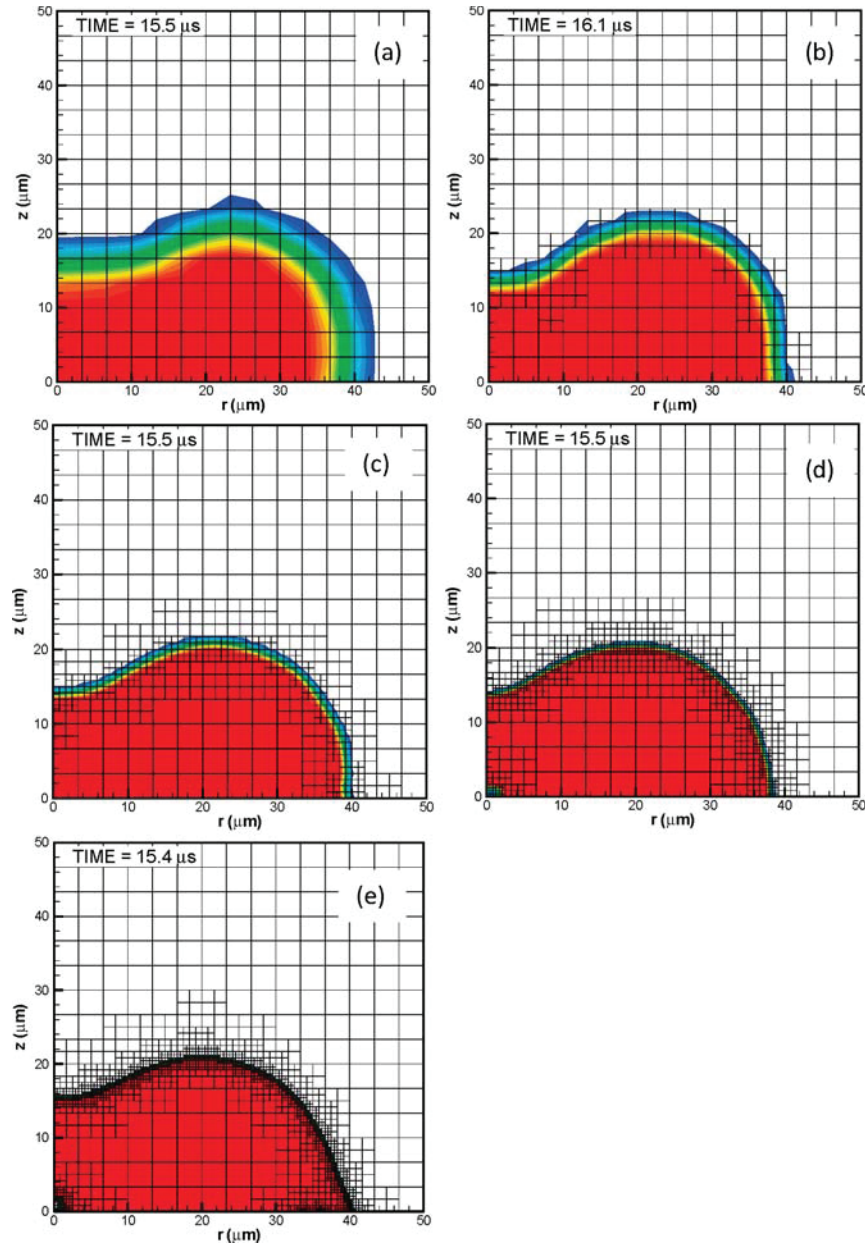
Figure 5. Instantaneous liquid volume fraction (α_l) and mesh ∼16 μs after microdroplet impact for five simulations corresponding to (a) 0, (b) 1, (c) 2, (d) 3, and (e) 4 levels of refinements. Red indicates liquid, blue indicates gas, and colors in between indicate the interface. All five simulations correspond to droplet C (see Table 1).

droplet A. These currents may become so large as to affect the predicted flow field velocity and to even break up the interface in extreme situations.[60] In addition, the very small Bo indicates that the gravitational force is not significant in comparison with surface tension force. Interestingly, droplets A through I exhibit scattered θ_E values varying from nearly 90° to 50°. A plausible explanation is the following: Upon impact, some droplets spread slowly and the instantaneous wetting diameter (D_D) never exceeds the equilibrium wetting diameter (D_E). Therefore, the final

equilibrium contact angle (θ_E) is that of the advancing contact angle (θ_A). Some other droplets spread beyond D_E and then recede to it, and the final θ_E is that of the receding contact angle (θ_R). Consequently, θ_E plainly shows a dependence on the contact line motion (i.e., hysteresis). Furthermore, the measured θ_E at low We and room temperature is $\theta_E \approx 90°$ for both millimeter- and micrometer-sized water droplets on aluminum as reported by Bernardin et al.[55] and by the present investigation (see Table 1), respectively.

The conditions for the numerical and experimental droplet evaporation study are listed in Table 2. It is not expected that the small difference in θ_E between experimental and numerical values

(60) Harvie, D. J. E.; Davidson, M. R.; Rudman, M. *Appl. Math. Model.* **2006**, *30*, 1056–1066.

would have a significant influence on the numerical results. The total evaporation time (τ) is 1.299 s. As will be further discussed in section 4.5, the numerical model can satisfactorily predict the transient and quasi-steady evaporation stages and predict linear temporal evolution of the droplet height (H/H_E) before depinning occurs. However, because our numerical model does not contain a depinning mechanism it does not predict τ accurately.

4.3. Grid Independence. Figure 5 illustrates the instantaneous VOF for droplet C of ~16 μs after impingement for five levels of refinements (0 to 4) of the numerical cells near the liquid−vapor interface. Figure 6 shows their corresponding temporal evolutions of the wetting radius (R) and height (H) for each level of refinement. Refinement level 0 indicates that there is no refinement. Whereas level 1 indicates that an original cell is partitioned into four sections, a refinement level of 2 means that an original cell is partitioned in sixteen, and so on. Therefore, the separation distance between nodes is halved for each level of refinement. As shown in Figure 5a, the original grid spacing of each quadrilateral element is 3.33 μm. After the first refinement, the minimum grid spacing is 1.67 μm, after the second, 0.83 μm, after the third, 0.416 μm, and after the fourth, 0.208 μm. Figure 5 clearly shows that with increasing the level of refinement the thickness of the interface decreases. In addition, not until after a refinement level of 3 do we numerically observe air bubble entrapment near the center line. This indicates that the grid needs to be small enough to capture the air bubble in the droplet. Moreover, all the results show that after impingement the droplet spreads radially very quickly until it reaches a maximum R (R_{max}), which corresponds to a minimum (H_{min}) at $t \approx 20$ μs (see Figure 6). Then, inertial oscillations follow as illustrated by the results obtained with refinement levels from 1 to 4. With no cell refinements (i.e., level of refinement = 0), inertial oscillations are not well captured. Surprisingly, the equilibrium wetting radius (R_E) and the equilibrium height (H_E) are nearly independent of the level of refinement. However, H_{min} and R_{max} at the end of the spreading process decreases and increases, respectively, with level of refinement. The differences in H_{min} and R_{max} between levels of refinement 3 and 4 are negligible. Therefore, level of refinement 3 is used for the numerical simulations.

4.4. Impact Droplet Dynamics. Now, the results on micrometer-sized droplets with Blake's contact line velocity formulation are discussed. The results presented in this section are also useful for validating Blake's contact line velocity model. Figure 7 shows the frame by frame comparison of experimental and numerical images corresponding to droplet C. Whereas the numerical results show the liquid volume fraction (α_l), the experimental results show the high-speed image. Blake's contact line dynamics formulation[29] is used here for the simulations with a wetting parameter, K_w = 2.0 MPa. The experimental results show that, after the droplet has impinged on the substrate, it starts to spread very rapidly. Its contact angle abruptly decreases from 180° at the moment of contact (not shown) to ~80° after ~5.3 μs following impingement. The spreading process ends and the droplet pins on the substrate at ~20.5 μs. Then, inertial oscillations follow and are characterized by motion of the droplet's apex height. The amplitude of these oscillations decreases with time due to viscous dissipation and becomes negligible at ~150 μs after impingement. The numerical result qualitatively matches the experimental result. Interestingly, the numerical model also predicts air bubble entrapment. In the model, the air bubble is attached to the wall (or substrate) at the center line of the droplet. This bubble is observed during the spreading process as indicated in the VOF image at $t \approx 5.4$ μs. The bubble remains inside the droplet throughout the simulation. For our experiments,
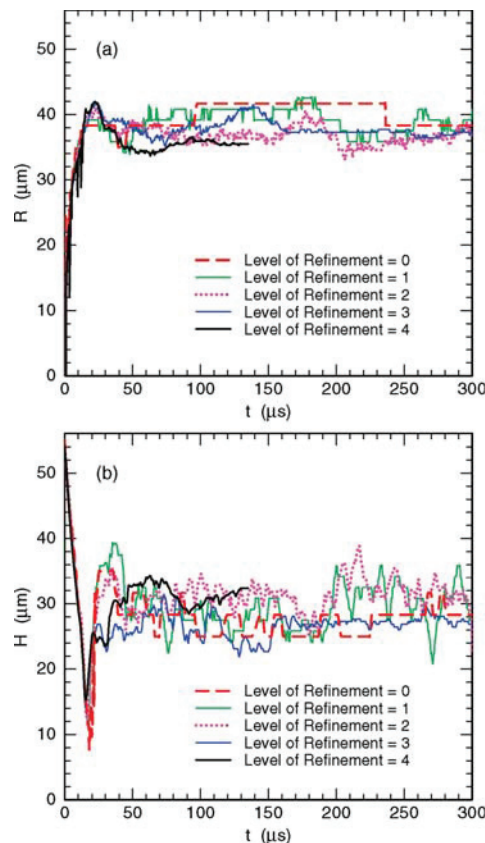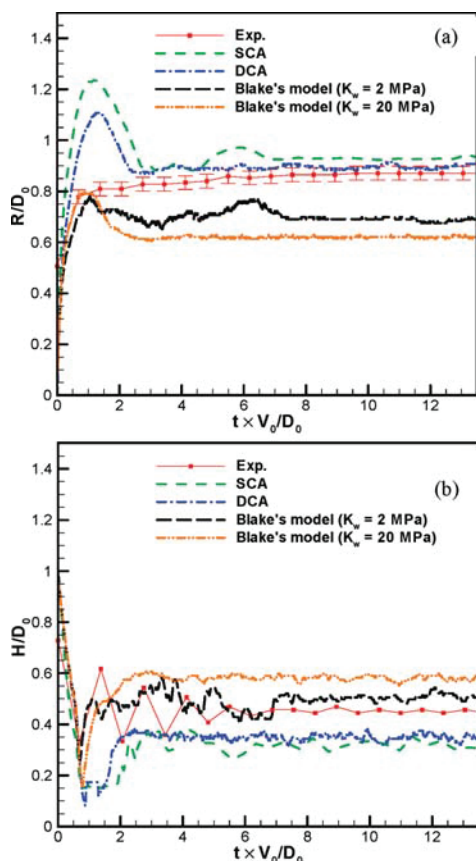

Figure 6. Temporal evolutions of microdroplet (a) wetting radius (R) and (b) apex height (H) for five levels of refinements ranging from 0 to 4 for droplet C (see Table 1).
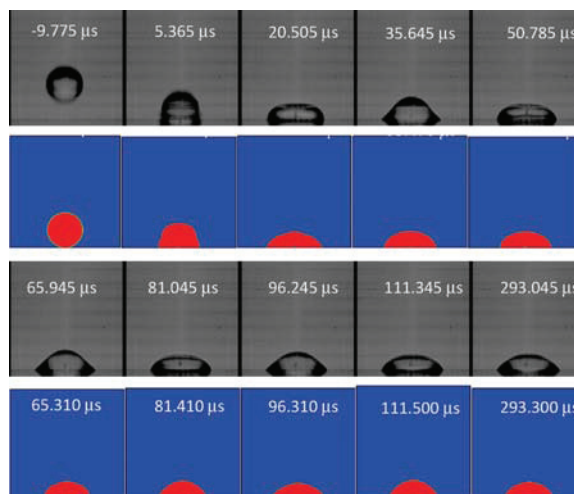
Figure 7. Frame by frame comparison of experimental and numerical images corresponding to droplet C. The experimental results show the high-speed photograph, whereas the numerical results show the liquid volume fraction (α_l). Red indicates liquid, blue indicates gas, and colors in between indicate the interface.

however, the air bubble is not always located at the center line as is shown in a subsequent section. Nevertheless, both our experiments and numerical results are in agreement with previous
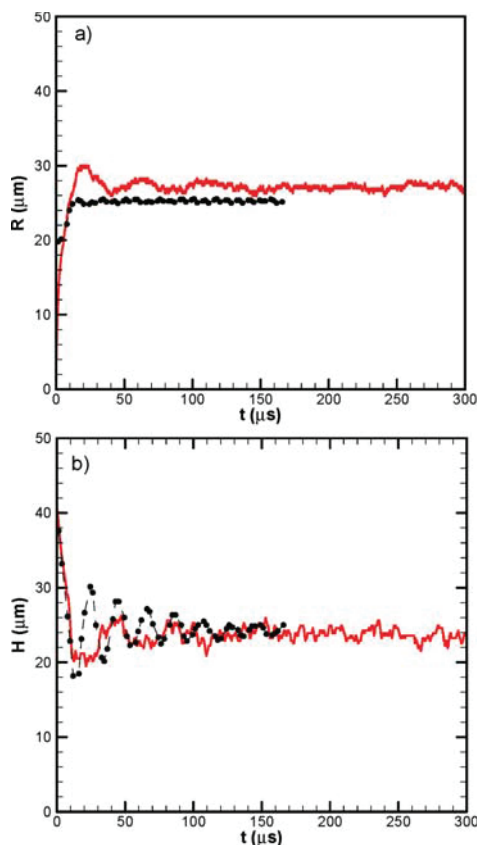
Figure 8. Temporal evolutions of (a) dimensionless microdroplet wetting radius (R/D_0) and (b) dimensionless microdroplet apex height (or flatness ratio) (H/D_0) for droplet C. The experimental results for a single experiment are shown with comparison to our numerical predictions using SCA, DCA, and Blake's molecular kinetic model with K_w = 2.0 MPa and K_w = 20.0 MPa.

Figure 9. Predicted (solid red lines) and measured (dashed lines with filled circle symbols) temporal evolution of the (a) wetting radius (R) and (b) apex height (H) for droplet A (see Table 1). The experimental results correspond to data acquired from four independent experiments/trials. For the simulation, Blake's molecular kinetic model is used with K_w = 2.0 MPa.

investigations.[19,20,61] For instance, Mehdi-Nejad et al.[61] showed that, for millimeter-sized water droplets, the air bubble remains attached to the substrate as observed in our simulations. However, for *n*-heptane droplets, the bubble moved away from the surface, breaking in multiple bubbles and escaping through the interface.[60] van Dam and Le Clerc[19] and Zhen-Hai and Rui-Jing[20] also reported bubble encapsulation in micrometer-sized water droplet impingement with characteristic We varying from 1.1 to 165. This suggests that the bubble entrapment observed in the numerical simulations actually occurs.

To further examine the results presented in Figure 7, Figure 8 presents the predicted and measured temporal evolutions of dimensionless wetting radius (R/D_0) and droplet apex height (or flatness ratio) (H/D_0). The numerical results were obtained using SCA, DCA, and Blake's molecular kinetic model with two test values, viz., K_W = 2.0 and 20.0 MPa, since K_W is not known a priori. These are the same values used by Bhardwaj and Attinger[16] in a similar work. Qualitatively, the results of SCA, DCA, and Blake's molecular kinetic model with K_w = 20.0 MPa provide similar results. These three simulations indicate impact dynamics characterized by spreading followed by a pronounced recoiling and inertial oscillations. The experimental results evidently show
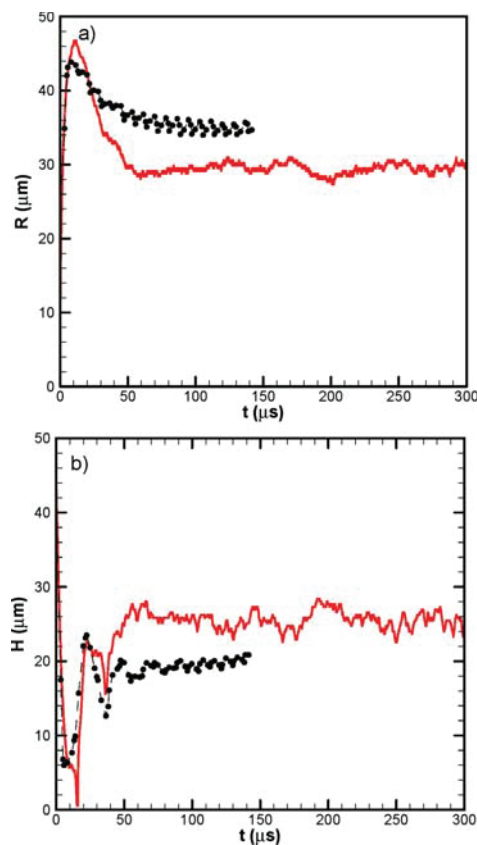
there is no recoiling. Blake's model with K_W = 2.0 MPa provides a better approximation to our measurements. Moreover, SCA overpredicts R_D by more than a factor of 2.4 during the spreading process. Consistent with Lunkad et al.,[17] DCA improves the SCA numerical results by allowing R_D to be overpredicted by no more than a factor of 2.2. Despite these differences between the experimental and numerical results, both SCA and DCA provide accurate results in terms of R_E. With Blake's model, the results are highly dependent on the spreading parameter (K_W). Figure 8 indicates that both values give reasonable results within the spreading process (i.e., $t \times V_0/D_0$ < 0.91 or t < 20.5 μs). During the inertial oscillation process (i.e., $t \times V_0/D_0 \geq$ 0.91), the accuracy of Blake's model decreases in terms of the temporal evolution of R/D_0. Blake's model underpredicts R_E. However, with K_W = 2.0 MPa Blake's model provides more accurate results than with K_W = 20.0 MPa during the inertial oscillation stage. Some of the reasons for these discrepancies are the following: (1) the value of K_W is not known a priori; (2) there are parasitic currents inherent to the VOF model that do not allow full droplet pinning. Moreover, Figure 8 clearly shows that Blake's model with K_W = 2.0 MPa provides the best prediction of H/D_0 as a function of $t \times V_0/D_0$ relative to the other three simulations (i.e., SCA, DCA, and K_w = 20.0 MPa). From the results presented in Figure 7 and Figure 8, K_w was selected to be 2.0 MPa for all droplet impingement simulations.

(61) Mehdi-Nejad, V.; Mostaghimi, J.; Chandra, S. *Phys. Fluids* **2003**, *15*, 173–183.
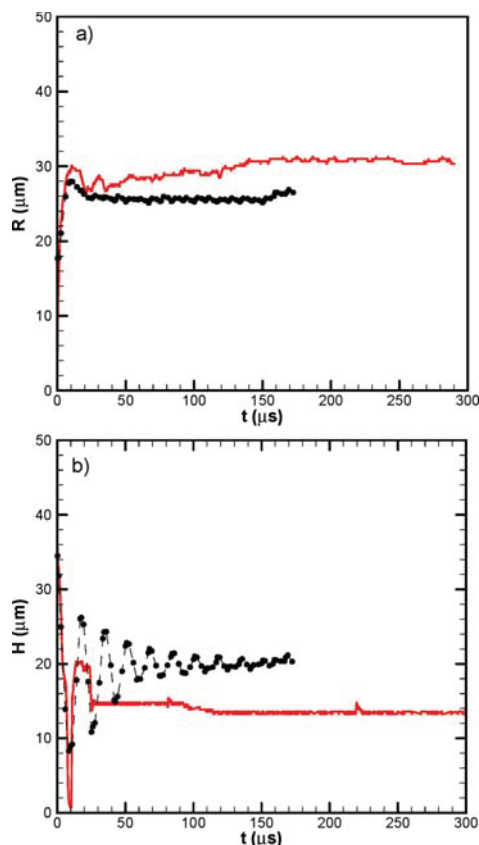
Figure 10. Predicted (solid red lines) and measured (dashed lines with filled circle symbols) temporal evolution of the (a) wetting radius (R) and (b) apex height (H) for droplet D (see Table 1). The experimental results correspond to data acquired from three independent experiments/trials. For the simulation, Blake's molecular kinetics model is used with $K_w = 2.0$ MPa.

Figure 11. Predicted (solid red lines) and measured (dashed lines with filled circle symbols) temporal evolution of the (a) wetting radius (R) and (b) apex height (H) for droplet I (see Table 1). The experimental results correspond to data acquired from four independent experiments/trials. For the simulation, Blake's molecular kinetic model is used with $K_w = 2.0$ MPa.

Now, we analyze the quantitative and qualitative accuracy of our model for other droplets listed in Table 1. So far, we have seen that the spreading process is followed by inertial oscillations (i.e., $R_D \leq R_E$ at all times), but as will be shown, depending on We the spreading process could be followed by recoiling and inertial oscillations (i.e., $R_D > R_E$ at end of spreading and beginning of receding process). For ease of discussion, the former condition is named Regime I and the latter Regime II. Figure 9, Figure 10, and Figure 11 present the temporal evolution of R and H for droplets A, D, and I, respectively. Our numerical simulations present remarkably good quantitative and qualitative results for droplet A. This is because at We = 1.4 and Oh = 0.026 the contact line dynamics play a more critical role in droplet spreading than the dynamic pressure gradient.[59] Hence, the accuracy of Blake's model improves relative to droplet C (see Figure 8). With increasing We while Oh remains nearly constant, the dynamic pressure gradient due to impact becomes more significant for droplet spreading relative to the contact line dynamics.[59] The results of this simulation for droplet D show that there is good qualitative and quantitative comparison between measurements and simulations during the spreading stage. This comparison, however, is no longer so great during the inertial oscillation stage. For instance, Blake's model overpredicts R_D and R_E and underpredicts H_D and H_E. Thus, the numerical model appears to be overdamped as suggested by the lack of temporal changes on

droplet height (H) after the spreading process. With further increase in We, the droplet spread is impact-driven and inertia resisted. The results of droplet I show that both the spreading and the oscillation stage are qualitatively and quantitatively well predicted. Both experiment and simulation indicate that R_D exceeds R_E at ~10 μs, which is then followed by recoiling until it reaches R_E. Numerical simulations overpredict R_E and underpredict R_D. Nevertheless, the numerical model provides satisfactory results at the extreme We studied here (i.e., 1.4 and 35.2), and its accuracy decays with droplets C and D corresponding to 4.5 < We < 11.0. This suggests that these two cases might be in a transitional region between Regime I and Regime II.
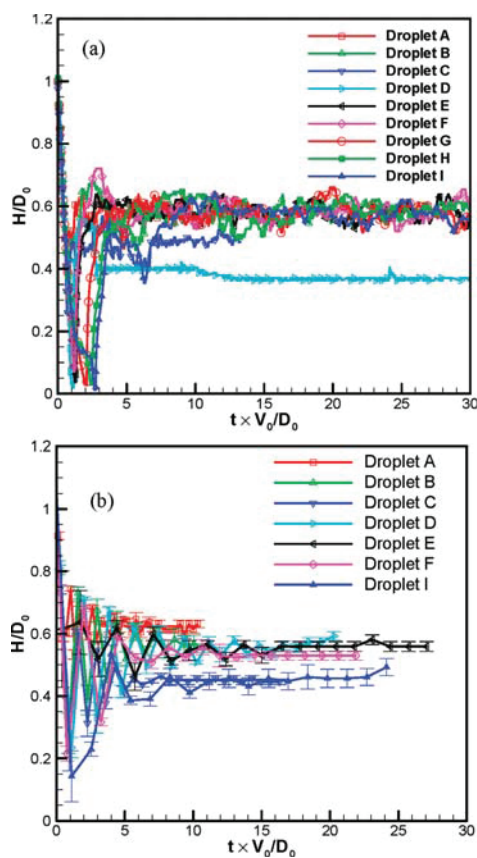
Figure 12 and Figure 13 present the predicted and measured temporal evolutions of wetting radius (R/D_0) and droplet height (H/D_0), respectively. Surprisingly, the numerical results indicate that the equilibrium R_E/D_0 and H_E/D_0 for all droplets except droplet D collapsed at $R_E/D_0 \approx 0.7$ and $H_E/D_0 \approx 0.6$. The experimental results clearly show this trend in Figure 12 except that it is droplet C instead of droplet D which does not collapse. It is evident from both numerical and experimental results that there appears to be a transition regime between Regimes I and II, discussed above. This transition regime occurs at We = 4.5 and We = 11.0 for our experimental and numerical results, respectively. Furthermore, the time for completion of the spreading and the combined spreading and receding process for droplets
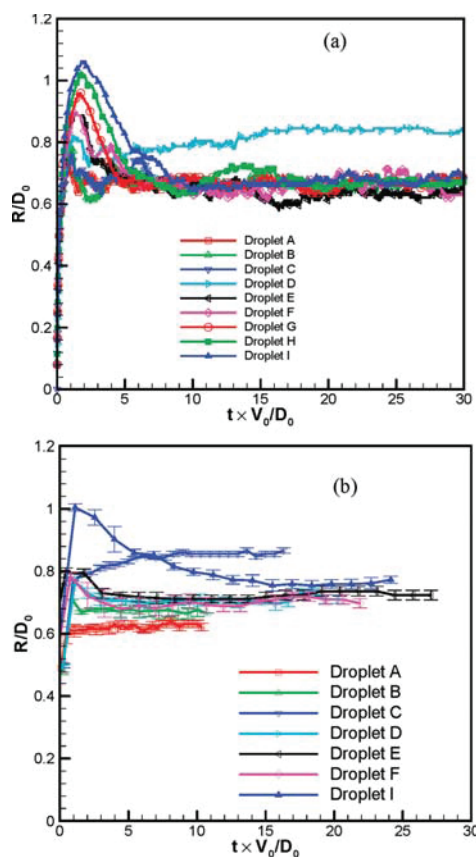
Figure 12. (a) Predicted and (b) measured wetting radius (R/D_0) as a function of dimensionless time ($t \times V_0/D_0$) for all water microdroplets studied in the context of Table 1. The experimental data correspond to a single impingement experiment for each droplet (A−I). Blake's molecular kinetic model is used with $K_w = 2.0$ MPa.

Figure 13. (a) Predicted and (b) measured droplet height (H/D_0) as a function of dimensionless time ($t \times V_0/D_0$) for all water microdroplets studied in the context of Table 1. The experimental data for each droplet (A−I) corresponds to an individual impingement experiments. Blake's molecular kinetic model is used with $K_w = 2.0$ MPa.

in Regimes I and II, respectively, decreases with decreasing We.

4.5. Droplet Evaporation. The results for micrometer-sized droplet evaporation will now be described. In the experiments, the droplet was gently deposited on the surface to avoid the hysteresis discussed in section 4.2. Droplet evaporation is modeled separately from droplet impingement due to 4 orders of magnitude difference in their characteristic time scales. The droplet initial conditions for the simulations were also discussed in section 4.2. Recall that the droplet static pressure is initially at ambient conditions at the beginning of the simulation. This is not realistic, but the static pressure inside the droplet, however, increases due to surface tension forces to a value close to that predicted by the Young−Laplace equation in a few time steps within a few microseconds. This has no implication on the results, since evaporation lifetime is on the order of seconds. Figure 14 illustrates the predicted instantaneous velocity vectors, isobars, and droplet shape in terms of $\alpha_l = 0.5$. In the initial transient stage, the Courant-Friedrichs-Lewy condition $|c\Delta t/\Delta x|$ is set to 0.05 in order to handle the abrupt changes in velocity vector and pressure fields. This transient stage lasted ∼8.5 ms and is depicted by comparing the instantaneous flow field at 3.627 and 8.532 ms in the frames of this figure. The transient stage (i.e., plot at 3.627 ms) is clearly characterized by droplet evaporation at nearly constant apex height with small toroidal vortex formation in both the droplet

and in the gaseous phase adjacent to the liquid−vapor interface. The vortex structures in the gaseous phase are apparently caused by buoyancy-induced Rayleigh-Taylor instability, since the vapor is less dense than air. Therefore, air is drawn from the surroundings creating shear layer roll-ups on the droplet surface. The distorted surface leads to surface tension force gradients that assist in the formation of small toroidal vortices within the droplet during this ephemeral transient stage.

After ∼8.5 ms, a second stage characterized by quasi-steady velocity vector flow field and pressure flow field is observed in plots at 8.532 ms and at 0.7416 s. Now, the droplet's apex height shrinks, whereas the contact line remains pinned. Because the droplet remains pinned, water flows down from the droplet's apex and then turns toward the contact line in order to replenish the volume that evaporates there. This result is consistent with the extensive analytical[51,53,62,63] and numerical[48,64] studies on pinned droplet assuming inviscid flow[51,62] and Stokes flow.[48,53,63,64] Then, the variance in curvature along the liquid−gas interface induces Marangoni flow characterized by fluid flow from the contact line toward the droplet's apex. Similarly, Hu and Larson[31] showed that when the Marangoni number (Ma) is

(62) Tarasevich, Y. Y. *Phys. Rev. E* **2005**, *71*, 027301.
(63) Masoud, H.; Felske, J. D. *Phys. Fluids* **2009**, *21*, 042102.
(64) Petsi, A. J.; Kalarakis, A. N.; Burganos, V. N. *Chem. Eng. Sci.* **2010**, *65*, 2978–2989.
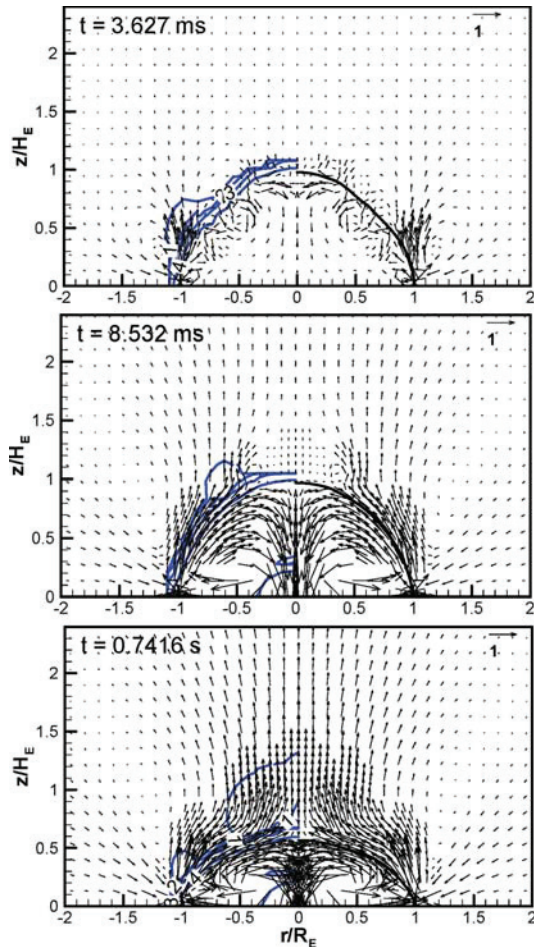
Figure 14. Predicted instantaneous velocity vectors, isobars (blue solid lines), and droplet shape (black solid line) obtained from the liquid volume fraction (α_l) of 0.5. The velocity vector reference is also shown on the upper right corner with units of m/s. The labels for the isobars 1, 2, 3, 4, and 5 correspond to 1, 10, 100, 1000, and 10 000 Pa, respectively.

non-negligible the fluid flows toward the contact line along the substrate and then flows toward the droplet's apex along the liquid−gas interface. Therefore, a toroidal vortex of the size of the droplet is depicted in the snapshots at 8.532 ms and 0.7416 s (cf. Figure 14). Ruiz and Black[28] also reported that droplet evaporation is characterized by a transient and a quasi-steady stage. As mentioned before, the model in ref 28 is interface-tracking and implicitly assumes that the droplet is in a vacuum. Our results show that the velocity flow field in the gaseous phase is time-dependent as illustrated by changes in direction and magnitude of the velocity vector in Figure 14. The gaseous phase exhibits flow oscillations induced by buoyant acceleration. The buoyant acceleration of water vapor causes shear layer rollup, leading to the formation of a toroidal vortex at the droplet's periphery that interacts with the incoming vapor from the droplet surface. The toroidal vortex squeezes the flow toward the center line (e.g., snapshot at 0.7416 s) and also decelerates it (e.g., snapshot at 8.532 ms). The overall effect of this phenomenon might be to enhance external convection for a droplet on a heated surface.

Finally, measured temporal evolution of droplet spread ratio (R/R_E) and height (H/H_E) are presented in Figure 15. Two
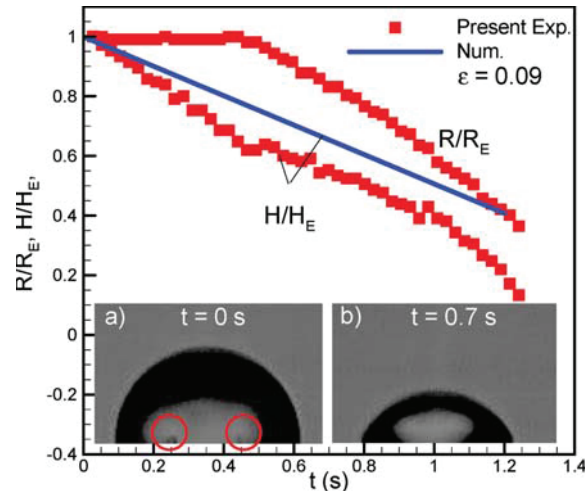
Figure 15. Measured temporal evolution of droplet spread ratio (R/R_E) and flatness ratio (H/H_E) for a water microdroplet evaporating on an Al at room temperature (see Table 2). The red circles circumvent the location of the observable air bubbles within the droplet.

snapshots of droplet evaporation are shown at $t = 0$ and 0.7 s. In addition, the predicted H/H_E is plotted. In the experiments, when this droplet was deposited two small air bubbles were trapped as shown in Figure 15a. In contrast to the numerical simulations shown in Figure 5 and Figure 7, the air bubbles are not at the center of the droplet. This again suggests the need to use VOF model for droplet evaporation since air bubbles can initiate nucleate boiling at much lower superheats than theory predicts.[33] However, we do not expect our numerical simulation to be significantly affected by the air bubbles, since there is negligible heat transfer from the wall to the droplet. The measured R/R_E as a function of time remains nearly constant until ∼0.42 s when depinning occurs. Then, R/R_E varies linearly with time until full evaporation. In contrast, the measured H/H_E varies linearly with time until 1 s. Then, H/H_E varies more rapidly until complete evaporation. Our numerical simulations show that H/H_E varies linearly with time. Therefore, there is good qualitative and quantitative agreement between measurements and predictions. The numerical results beyond 0.42 s do not include depinning, but it is seen that the slope is similar to the experimental data up to ∼1 s. This suggests that depinning may not be as important to H/H_E. As mentioned in section 4.1.2, three-dimensional effects and accurate knowledge of ε are also needed for improved droplet evaporation modeling and simulation.

5. Conclusions

A comprehensive numerical and experimental investigation on micrometer-sized water droplet impact dynamics and evaporation on an unheated flat dry surface was conducted from the standpoint of spray cooling technology. The explicit VOF with axisymmetric time-dependent governing equations of continuity, momentum, energy, and species are solved. Surface tension, wall adhesion effect, gravitational body force, contact line dynamics, and evaporation were also considered. This is the only investigation reporting both Blake's and Schrage's molecular kinetic models for contact line motion and evaporation rate, respectively, within the VOF formulation, and thereby, it is a significant contribution of our research. The numerical model also includes temperature- and species-dependent thermodynamic and transport

properties. An extensive grid independence analysis was conducted. Microdroplet impingement and evaporation data are acquired with a standard dispensing/imaging system with a high-speed camera. Important conclusions are as follows.

The numerical model was validated with millimeter-sized water droplet impingement and evaporation experiments reported in the literature. For the impinging droplet, we found good correlation between measured and predicted maximum wetting radius (or contact line position) (R) as a function of time. Moreover, experiments and simulations indicate that as We decreases the spreading rate decreases. For the evaporating droplet from an isothermal wall, measurements indicate that the droplet's volume varies linearly with time until full evaporation occurs at ~14 s. The predicted volume varies nearly linearly and quantitatively and qualitatively matches the measurement until ~10 s. To accurately predict the volumetric evaporation rate and droplet lifetime, knowledge of the accommodation coefficient (ε) and three-dimensional effect may need to be taken into account.

Both numerical and experimental results indicate that, after the micrometer-sized droplet has impinged on the substrate, it starts to spread very rapidly. Its contact angle abruptly decreases and the spreading rate increases. The spreading process ends and the droplet pins on the substrate. Then, inertial oscillations follow and are characterized by vertical motion of the droplet's apex height. The amplitude of these oscillations decreases with time due to viscous dissipation and becomes negligible.

The VOF model is capable of capturing air bubble entrapment for micrometer-sized droplet impingement. This air bubble is attached to the wall (or substrate) at the center line of the droplet. This bubble is observed during the spreading process. The bubble remains inside the droplet throughout the simulation. For our experiments, however, the location of the air bubble is not always located at the center line.

Numerical results indicate that Blake's formulation provides better results than the static (SCA) and dynamic contact angle (DCA) approach in terms of temporal evolution of R/D_0 and H/D_0, especially at the initial stages of spreading. However, SCA and DCA predict equilibrium wetting radius (R_E/D_0) more accurately than Blake's formulation. The latter provides reasonable results regarding the equilibrium flatness ratio (H_E/D_0). Blake's contact line dynamics is dependent on the wetting parameter (K_W).

The accuracy of our numerical model is good at We away from ~4.5 < We < 11.0, since it appears that at this condition the short-term droplet impingement transitions between two different regimes. For We < 4.5, spreading is followed by pinning and then inertial oscillations, whereas for We > 11.0, spreading is followed by recoiling, pinning, and then inertial oscillations. Moreover, the characteristic dimensionless time ($t \times V_0/D_0$) for completion of the spreading process for We < 4.5 and the combined spreading and receding process for We > 11.0 decreases with decreasing We.

The micrometer-sized droplet evaporation measurements indicate that the droplet remains pinned for about one-third of the droplet's lifetime. Depinning occurs, the contact line recedes, and the droplet radius (R/R_E) varies linearly with time until full evaporation. Most of the evaporation occurs in a depinned mode than in pinned mode. The measurements also show that the droplet's apex height (H/H_E) decreases linearly with time during most of the droplet's lifetime and then it decreases more rapidly near the end of the droplet's lifetime until complete evaporation. Our numerical simulations also show that H/H_E varies linearly with time. Therefore, there is good qualitative and quantitative agreement between measurements and predictions. Since a depinning model has not been used in our simulations, this suggests that depinning may not be as important to H/H_E.

Droplet evaporation was satisfactorily modeled using Schrage's model since the model predicts both well-defined transient and quasi-steady evaporation stages. Vortex layer roll-up and toroidal vortices are formed on the droplet surface in the gaseous phase due to buoyancy-induced Rayleigh-Taylor instability. These vortices interact with the incoming vapor from the droplet's surface, enhancing convection.

Nomenclature

Bo	Bond number = $g(\rho_l)D_0^2/\sigma$
Ca	Capillary number = $\mu V_0/\sigma$
CHF	critical heat flux [W/m^2]
c_p	specific heat capacity at constant pressure [J/kg−K]
D	droplet diameter [μm]
DCA	dynamic contact angle [°]
D_{H_2O-air}	binary diffusivity of water vapor to air [m^2/s]
E	total energy per volume [W/m^3]
H	droplet height at center line [μm]
h	heat transfer coefficient [W/m^2−K]
h_P	Planck's constant [6.626×10^{-34} m^2 kg s^{-1}]
g	gravitational acceleration vector [m/s^2]
K_w	wetting parameter [Pa]
k	thermal conductivity [W/m−K]
k_B	Boltzmann constant [$1.3806503 \times 10^{-23}$ m^2 kg/s^2−K]
N_A	Avogadro's constant [6.0221415×10^{23} mol^{-1}]
MW	molecular weight [kg/kmol]
$\dot{m}$	mass transfer rate per unit volume [kg/m^3−s]
n	surface normal vector or number of absorption sites per unit area [m^{-2}]
$\hat{n}$	unit surface normal vector
Oh	Ohnesorge number = $\sqrt{\text{We}}/\text{Re}$
p	gauge pressure (Pa)
SCA	static contact angle [°]
R	wetting radius [μm] and universal gas constant [8.314 kJ/kmol−K]
Re	Reynolds number = $\rho V_0 D_0/\mu$
T	temperature [K]
t	time [μs, s]
$\hat{t}$	tangential unit vector
u	radial velocity [m/s]
V_0	initial axial velocity [m/s]
v	axial velocity [m/s]
VOF	volume of fluid
v_L	volume of molecule in liquid phase [m^3]
We	Weber number = $\rho V_0^2 D_0/\sigma$
Y	mass fraction
X	mole fraction
$\Delta G_w^{\ddagger}$	activation Gibbs free energy [kJ/kmol]

Greek

$\forall$	droplet volume [mm^3]
α	volume fraction

ε	accommodation coefficient	CL	contact line
κ	curvature [1/m]	D	dynamic or instantaneous
f_W	frequency of molecular displacement [1/s]	E	equilibrium
f_S	frequency of molecular displacement associated with solid−liquid surface interaction [s^{-1}]	exp	experimental
		g	gaseous phase
λ	molecular displacement length [m]	i	species
μ	dynamic viscosity [kg/m−s]	l	liquid phase
θ	contact angle [°]	max	maximum
ρ	density [kg/m^3]	min	minimum
σ	surface tension [mN/m]	R	receding
τ	total evaporation time [s]	S	static
ω	inertial oscillation frequencies [kHz]	W	wall
		w	wetting

Subscripts

0	initial conditions
A	advancing
ana	analytical

Superscripts

+	forward
−	backward

Appendix D. Spontaneous Hydrogen Generation from Organic-Capped Al Nanoparticles and Water

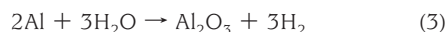# Spontaneous Hydrogen Generation from Organic-Capped Al Nanoparticles and Water

Christopher E. Bunker,*,† Marcus J. Smith,‡ K. A. Shiral Fernando,‡ Barbara A. Harruff,‡
William K. Lewis,‡ Joseph R. Gord,† Elena A. Guliants,‡ and Donald K. Phelps†

Air Force Research Laboratory, Propulsion Directorate, Wright−Patterson Air Force Base, Ohio 45433-7103, and
Metals and Ceramics Division, University of Dayton Research Institute, Dayton, Ohio 45469

ABSTRACT The development of technologies that would lead toward the adoption of a hydrogen economy requires readily available, safe, and environmentally friendly access to hydrogen. This can be achieved using the aluminum−water reaction; however, the protective nature and stability of aluminum oxide is a clear detriment to its application. Here, we demonstrate the spontaneous generation of hydrogen gas from ordinary room-temperature tap water when combined with aluminum−oleic acid core−shell nanoparticles obtained via sonochemistry. The reaction is found to be near-complete (>95% yield hydrogen) with a tunable rate from 6.4×10^{-4} to 0.01 g of H_2/s/g of Al and to yield an environmentally benign byproduct. The potential of these nanoparticles as a source of hydrogen gas for power generation is demonstrated using a simple fuel cell with an applied load.

KEYWORDS: energy • hydrogen • nanoparticles • aluminum

In obtaining hydrogen from water, it is well-known that aluminum metal will react with water to yield hydrogen gas (1, 2):

$$2Al + 6H_2O \rightarrow 2Al(OH)_3 + 3H_2 \qquad (1)$$

$$2Al + 4H_2O \rightarrow 2AlO(OH) + 3H_2 \qquad (2)$$

$$2Al + 3H_2O \rightarrow Al_2O_3 + 3H_2 \qquad (3)$$

The three reactions represent the products that result from varying water conversion efficiencies (bayerite, boehmite, and aluminum oxide, respectively, with hydrogen). These reactions are limited in their utility because of the natural occurrence of a protective aluminum oxide shell on the surface of the aluminum metal. The stability of the aluminum oxide prevents air and moisture from accessing the underlying metal (3, 4). To circumvent this problem and facilitate the generation of hydrogen, researchers have applied various reaction-promoting schemes. These have included the use of strong bases (5, 6), application of high temperature (7), or activation of the aluminum metal (8−11). Recently, Woodall demonstrated the activation concept and produced large quantities of hydrogen from a gallium−aluminum mixture (8, 9). By dissolving the aluminum in liquid gallium, the researchers prevented the formation of the aluminum oxide shell, thus allowing the aluminum−water reaction to proceed.

While able to provide hydrogen from the aluminum−water reaction, the above-mentioned approaches are more complex than what eqs 1−3 imply. A simpler solution might be achieved if the nature of the protective aluminum oxide shell could be altered. Recent research on the combustion of aluminum nanoparticles protected by aluminum oxide shells suggests that this may be possible with data demonstrating enhanced reactivity over micrometer- or bulk-scale aluminum (12, 13). These results can be attributed to the role surfaces and interfaces play in nanoparticle chemistry, noting that, as the particle size decreases, the surface and interfacial areas increase and become dominant in determining the physical and chemical properties. Methods for producing aluminum nanoparticles are well-documented (14−24). However, having particles on the nanoscale alone is not sufficient; commercial aluminum nanoparticles possessing an aluminum oxide shell will not readily react in water under ambient conditions. In fact, the mixing of aluminum oxide protected aluminum nanoparticles with water ice has been demonstrated as a stable and viable propellant formulation (25, 26).

To achieve our desired goal, chemical modification of the aluminum oxide shell is also required. Previously, we reported the synthesis of air-stable AlOA core−shell nanoparticles via the sonochemically assisted thermal decomposition of alane in the presence of the catalyst titanium(IV) isopropoxide (18). The physical and thermal analysis of these particles suggested a structure consisting of an inner aluminum core surrounded by an oxide shell, followed by an outer organic shell, each accounting for ~40, 25, and 35% of the total particle mass, respectively. Because the reaction solutions were vigorously deoxygenated prior to the reaction, the oxide shell is believed to have formed from the oxygen atoms brought to the aluminum surface by the capping agent oleic acid. Thermal analysis of the AlOA particles demon-
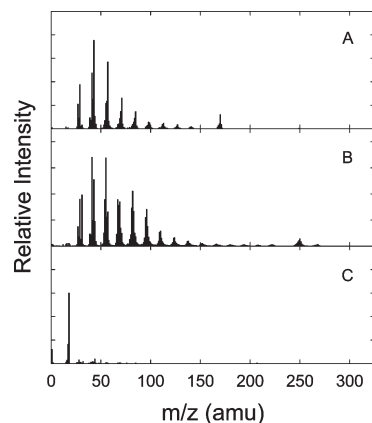
FIGURE 1. TOF mass spectra for the AlOA nanoparticles at (A) 150 °C and (B) 500 °C and for the commercial aluminum nanoparticles with an aluminum oxide coating at (C) 500 °C. The spectra are identified as (A) dodecane, (B) 9-octadecen-1-ol, and (C) water by comparison with the NIST database.
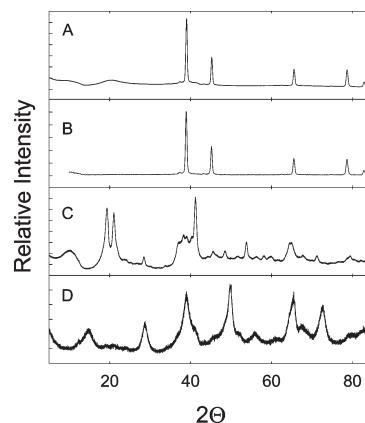

FIGURE 2. Powder X-ray diffraction spectra for (A) the as-synthesized AlOA nanoparticles, (B) the AlOA nanoparticles after exposure to methanol and representative of exposure to hexane, toluene, THF, chloroform, and ethanol, (C) the product of their reaction with water at an AlOA:H_2O ratio of 10^{-3}, and (D) the product of their reaction with water at an AlOA:H_2O ratio of 0.5. The spectra were identified by comparison with the ICPDS database; (A and B) fcc aluminum, (C) a mixture with the main peaks indicating bayerite and boehmite, and (D) boehmite.
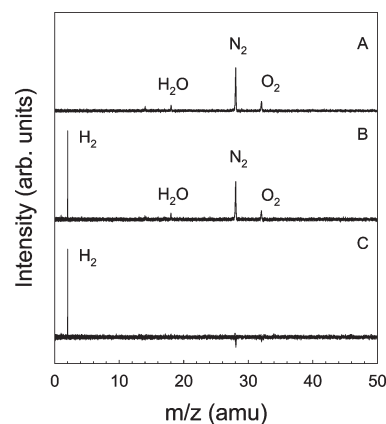

FIGURE 3. Mass spectra demonstrating hydrogen production from reaction of the AlOA nanoparticles and water: (A) background spectrum; (B) reaction spectrum; (C) background-subtracted spectrum.

strated that this oxide shell does not behave as natural aluminum oxide, instead allowing reaction of the nanoparticles at a much lower temperature (~420 vs 600 °C for commercial aluminum nanoparticles) (18). Using a home-built time-of-flight (TOF) mass spectrometer equipped with a thermal desorption stage, we find that the AlOA nanoparticles release dodecane at temperatures between 100 and 150 °C (Figure 1A) and 9-octadecen-1-ol from ~200 to 500 °C (Figure 1B). The dodecane is a residual solvent entrained in the sample. 9-Octadecen-1-ol is consistent with an oleic acid molecule bound to the aluminum particle through the carbonyl oxygen [RC(OH)OAl] and cleaved between carbon and oxygen. The data correlate well with the observed Fourier transform infrared spectrum, showing a strong O−H stretch and no carbonyl band (18). Commercial aluminum nanoparticles (Alpha Asar) analyzed under the same conditions yield only water vapor (Figure 1C).

The AlOA samples were found to be air-stable; however, to provide a more quantitative measure of the stability, an experimental procedure involving exposure of these samples to air-saturated solvents while agitated in a sonic bath was devised. Specifically, samples (~20 mg) were suspended in a series of solvents (5 mL) and agitated in a sonic bath for 90 min. The solvents included nonpolar hydrocarbons (hexane and toluene), heteroatom and halogenated hydrocarbons [tetrahydrofuran (THF) and chloroform], and polar solvents (ethanol, methanol, and water). In each solvent except one, the particles remained unchanged as measured by powder X-ray diffraction (Figure 2A and 2B). Only water showed a change in the particles with a significantly altered X-ray spectrum (Figure 2C). The spectrum is not identifiable as a single aluminum oxide material, but the main peaks suggest the formation of bayerite and boehmite. To test this reaction, a small quantity of sample was mixed with water and the headspace sampled using the mass spectrometer. After subtraction of a background spectrum, the data showed a strong signal for hydrogen gas (Figure 3). It should be noted that, in the above experiments, the AlOA:H_2O mass ratio is

fairly small (AlOA:$H_2O = 10^{-3}$). When performed at a much larger value (e.g., 0.5), the reaction appeared far more vigorous and generated considerable heat. The X-ray spectrum of the oxide product formed under those conditions is quite different (Figure 2D), demonstrating a clear pattern for boehmite (eq 2).

A second experiment was performed to directly measure hydrogen generation (pressure) versus time. To a 25 mL stainless steel pressure vessel was added 1 g of a AlOA sample and 2 mL of water (AlOA:$H_2O = 0.5$). The pressure is plotted versus time in Figure 4 and shows a rapid rise, which then slows to reach a plateau. The pressure at the plateau is 309 psi, or 21 atm. From the knowledge that our samples are ~40% aluminum metal, using the stochiometery of eq 2 and applying the ideal gas law, we calculate a >95% yield for the formation of hydrogen gas. More importantly, if we examine the rate at which hydrogen gas is generated under continuously reacting conditions (i.e., the
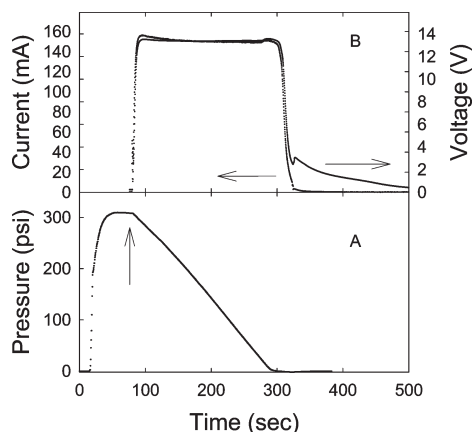
LETTER

FIGURE 4. Plots of pressure versus time (A) and voltage and current versus time (B) for the reaction of 1.0 g of the AlOA nanoparticles with 2.0 mL of water in a 25 mL stainless steel pressure vessel. The pressure was allowed to stabilize before the fuel cell was brought in line. The operating power was approximately 2 W. In plot A, the arrow indicates the point at which the fuel cell was brought in line. In plot B, arrows indicate the applicable axes.

rapid-rise region), we obtain a rate of $\sim$0.01 g of H_2/s/g of Al. The utility of this hydrogen was also demonstrated in Figure 4, where just after the plateau was reached the pressure vessel was placed in line with a fuel cell (TDM Fuel Cell Technology, 20-stack polymer electrolyte membrane cell) using a pressure regulator set to deliver under 5 psi of hydrogen. Attached to the fuel cell was a simple computer fan to serve as the electrical load, and the voltage and current were recorded as the hydrogen was consumed. As can be seen from the plot, once the hydrogen was delivered to the cell, the voltage and current quickly reached stable working values ($\sim$13 V and 0.15 A). The power consumed by this system is $\sim$2 W for a continuous 2.3 min.

Because the reaction appeared to demonstrate a strong dependence on the AlOA:H_2O ratio, a small-scale temperature measurement system was assembled using a thermocouple affixed to an alumina cup to probe this dependence. Water (a constant 60 μL) was added to AlOA samples varying in mass from $\sim$2 to 15 mg (AlOA:H_2O = 0.03−0.25). The temperature was then recorded as a function of time, and the data are plotted in Figure 5. The traces of temperature versus time are all similar in that they exhibit an induction phase, a rapid rise, a maximum, and then a steady decrease, eventually returning to room temperature. The data can be fit using a model that accounts for the heat generated by the reaction q_{rxn}, the heat lost from the system q_{loss}, and the total heat capacity of the system Cp$_{total}$ (a detailed description of the model with definitions for all terms is given in the Supporting Information):

$$T(T) = T(0) + \frac{\int_0^t [q_{rxn}(t) - q_{loss}(t)]\, dt}{Cp_{total}(t)} \quad (4)$$

The q_{rxn} term is obtained assuming a pseudo-first-order kinetic equation modified to account for the time-dependent surface area (SA) of the reacting nanoparticles:

$$q_{rxn} = \Delta H_{rxn} \int_0^t (1 - e^{-k(t)\,t})m_{nanoAl}\, dt \quad (5)$$

where $k(t)$ is

$$k(t) = A\mathrm{SA}(m_{nanoAl})e^{-E_a/RT(t)} \quad (6)$$

The fits to the data are shown in Figure 5 (fit parameters are also provided in the Supporting Information). From the model, we obtain an average activation barrier of 15 kJ/mol. With this information, we can convert the temperature data in Figure 5 to hydrogen volume versus time and obtain the rate of hydrogen production versus the AlOA:H_2O ratio. The modeled data demonstrate a mass-normalized tunable rate between 6.4×10^{-4} and 5.6×10^{-3} g of H_2/s/g of Al (Figure 5), where the aluminum mass was taken as 40 % of the total sample weight. Extending the model to a AlOA:H_2O value of 0.5, we obtain a predicted rate of 0.017 g of H_2/s/g of Al, in very good agreement with the experimentally measured value of $\sim$0.01 g of H_2/s/g of Al (Figure 5).

We have demonstrated that the reaction of aluminum with water to yield hydrogen gas can be performed in a simple fashion, requiring no promoters or initial energy to initiate the reaction. This capability is achieved through the combined effect of using nanoscale aluminum particles coupled with an organic-provided oxide shell, which demonstrates remarkable air and organic solvent stability but allows easy reaction of the aluminum in water. We have shown that the reaction is near-complete, that the rate of hydrogen production can be tuned by controlling the nanoparticle-to-water mass ratio, and that the hydrogen generated by this reaction is sufficient to perform useful work. The simplicity of the reaction, the high energy density of the aluminum−water reaction, and the tremendous stability of these novel aluminum nanoparticles make this system a
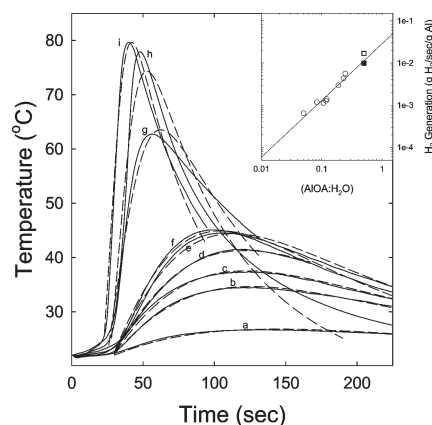
FIGURE 5. Plot of temperature versus time for reaction of the AlOA nanoparticles with water; experimental (—) and calculated (- - -) data for AlOA masses of 3.0, 4.9, 5.0, 6.4, 7.1, 7.3, 11.3, 13.7, and 14.7 mg (curves a−i, respectively). Inset: plot of the hydrogen production rate versus the AlOA:H_2O ratio as calculated from the kinetic model for the data in the main figure (○), calculated for an AlOA:H_2O ratio of 0.5 (□), and measured at a AlOA:H_2O ratio of 0.5 (■).

viable approach for providing power based on hydrogen without requiring the direct storage of large quantities of hydrogen; one need only to add water to produce hydrogen on demand, where and when needed. Future efforts will focus on a better understanding of the nature of the protective shell, the particular role the synthetic method plays in developing these properties, and the effect of the organic capping agent on the reaction parameters.

Supporting Information Available: Additional experimental details for the work presented herein, a full description of the kinetic model and definition of all terms, and a table of fit parameters for the data presented in Figure 5. This material is available free of charge via the Internet at http://pubs.acs.org.

REFERENCES AND NOTES

(1) Wang, H. Z.; Leung, D. Y. C.; Leung, M. K. H.; Ni, M. *Renewable Sustainable Energy Rev.* **2009**, *13*, 845–853.

(2) Roach, P. J.; Woodward, W. H.; Castleman, A. W., Jr.; Reber, A. C.; Khanna, S. N. *Science* **2009**, *323*, 492–495.

(3) Vedder, W.; Vermilyea, D. A. *Trans. Faraday Soc.* **1969**, *65*, 561–584.

(4) Digne, M.; Sautet, P.; Raybaud, P.; Toulhoat, H.; Artacho, E. *J. Phys. Chem. B* **2002**, *106*, 5155.

(5) Belitskus, D. *J. Electrochem. Soc.* **1970**, *117*, 1097.

(6) Soler, L.; Candela, A. M.; Macanás, J.; Muñoz, M.; Casado, J. *J. Power Sources* **2009**, *192*, 21–26.

(7) Astankova, A. P.; Godymchuk, A. Y.; Gromov, A. A.; Il'in, A. P. *Russ. J. Phys. Chem. A* **2008**, *82*, 1913–1920.

(8) Cuomo, J. J.; Woodall, J. M. U.S. Patent 4,358,291, Nov 9, 1982.

(9) Cuomo, J. J.; Leary, P. A.; Woodall, J. M. U.S. Patent 4,745,204, May 17, 1988.

(10) Parmuzina, A. V.; Kravchenko, O. V. *Int. J. Hydrogen Energy* **2008**, *33*, 3073–3076.

(11) Deng, Z.-Y.; Liu, Y.-F.; Tanaka, Y.; Ye, J.; Sakka, Y. *J. Am. Ceram. Soc.* **2005**, *88*, 977–979.

(12) Shafirovich, E.; Diakov, V.; Varma, A. *Combust. Flame* **2006**, *144*, 415.

(13) Sun, J.; Pantoya, M. L.; Simon, S. L. *Thermochim. Acta* **2006**, *144*, 117.

(14) Haber, J. A.; Buhro, W. E. *J. Am. Chem. Soc.* **1998**, *120*, 10847–10855.

(15) Jouet, R. J.; Warren, A. D.; Rosenberg, D. M.; Bellitto, V. J.; Park, K.; Zachariah, M. R. *Chem. Mater.* **2005**, *17*, 2987–2996.

(16) Jouet, R. J.; Carney, J. R.; Granholm, R. H.; Sandusky, H. W.; Warren, A. D. *Mater. Sci. Technol.* **2006**, *22*, 422–429.

(17) Foley, T. J.; Johnson, C. E.; Higa, K. T. *Chem. Mater.* **2005**, *17*, 4086–4091.

(18) Fernando, K. A. S.; Smith, M. J.; Harruf, B. A.; Lewis, W. K.; Guliants, E. A.; Bunker, C. E. *J. Phys. Chem. C* **2009**, *113*, 500–503.

(19) Meziani, M. J.; Bunker, C. E.; Lu, F.; Li, H.; Wang, W.; Guliants, E. A.; Quinn, R. A.; Sun, Y.-P. *ACS Appl. Mater. Interfaces* **2009**, *1*, 703–709.

(20) Chung, S. W.; Guliants, E. A.; Bunker, C. E.; Hammerstroem, D. W.; Deng, Y.; Burgers, M. A.; Jelliss, P. A.; Buckner, S. W. *Langmuir* **2009**, *25*, 8883–8887.

(21) Li, H.; Meziani, M. J.; Lu, F.; Bunker, C. E.; Guliants, E. A.; Sun, Y.-P. *J. Phys. Chem. C* **2009**, *113*, 20539–20542.

(22) Weigle, J. C.; Luhrs, C. C.; Chen, C. K.; Perry, W. L.; Mang, J. T.; Nemer, M. B.; Lopez, G. P.; Phillips, J. *J. Phys. Chem. B* **2004**, *108*, 18601–18607.

(23) Kwon, Y.-S.; Gromov, A. A.; Strokova, J. I. *Appl. Surf. Sci.* **2007**, *253*, 5558–5564.

(24) Mahendiran, C.; Ganesan, R.; Gedanken, A. *Eur. J. Inorg. Chem* **2009**, *14*, 2050–2053.

(25) Ingenito, A.; Bruno, C. *J. Propul. Power* **2004**, *20*, 1056.

(26) Risha, G. A.; Son, S. F.; Yetter, R. A.; Yang, V.; Tappan, B. C. *Proc. Combust. Inst.* **2029**, *31*, 2007.

AM900757R

103

DISTRIBUTION STATEMENT A: Approved for public release. Distribution is unlimited.

Appendix E. Chemical, Thermal Stability, Seal Swell, and Emissions Studies of Alternative Jet Fuels

Chemical, Thermal Stability, Seal Swell, and Emissions Studies of Alternative Jet Fuels

Edwin Corporan,*,[†] Tim Edwards,[†] Linda Shafer,[‡] Matthew J. DeWitt,[‡] Christopher Klingshirn,[‡] Steven Zabarnick,[‡] Zachary West,[‡] Richard Striebich,[‡] John Graham,[‡] and Jim Klein[§]

[†]Air Force Research Laboratory, Fuels and Energy Branch, Wright-Patterson AFB, Ohio 45433, United States

[‡]University of Dayton Research Institute, 300 College Park, Dayton, Ohio 45469, United States

[§]Jim Klein LLC, Wright-Patterson AFB, Ohio 45433, United States

ABSTRACT: This effort describes laboratory evaluations of six alternative (nonpetroleum) jet fuel candidates derived from coal, natural gas, camelina, and animal fat. Three of the fuels were produced via Fischer–Tropsch (FT) synthesis, while the other three were produced via extensive hydroprocessing. The thermal stability, elastomer swell capability, and combustion emissions of the alternative jet fuels were assessed. In addition, detailed chemical analysis was performed to provide insight into their performance and to infer potential behavior of these fuels if implemented. The fuels were supplied by Sasol, Shell, Rentech, UOP, and Syntroleum Corporation. Chemical analyses show that the alternative fuels were comprised of mostly paraffinic compounds at varying relative concentrations, contained negligible heteroatom species, and were mostly aromatic-free. The six paraffinic fuels demonstrated superior thermal oxidative stability compared to JP-8, and therefore, have increased resistance to carbon formation when heated and can be exposed to higher temperatures when used to cool aircraft systems. Material compatibility tests show that the alternative fuels possess significant seal swelling capability in conditioned nitrile O-rings; however, elastomer swelling was significantly lower than for JP-8, which may likely result in fuel leaks in aircraft systems. Engine tests with the alternative fuels demonstrated no anomalies in engine operation, production of significantly lower nonvolatile particulate matter (soot), and moderately lower unburned hydrocarbons and carbon monoxide emissions compared to baseline JP-8 fuel. Also, no penalty (i.e., increase) in fuel flow requirement for equal engine power output was observed. In general, this study demonstrates that paraffinic fuels derived from different feedstocks and produced via FT synthesis or hydroprocessing can provide fuels with very similar properties to conventional fuels consisting of excellent physical, chemical, and combustion characteristics for use in turbine engines. These types of fuels may be considered as viable drop-in replacement jet fuels if deficiencies such as seal swell, lubricity, and low density can be properly addressed.

■ INTRODUCTION

The growing demand and reduced supply of petroleum products, and instability in petroleum-rich countries, results in high uncertainties and volatility in the cost of energy, particularly transportation fuels. As a result, efficient energy technologies and the development of alternative energy options, such as fuels from domestic alternative sources, have become a national priority. Alternative transportation fuels are desirable both from an energy security and environmental perspective as the preponderance of imported oil is converted to liquid transportation fuels. In the United States, liquid fuel production is roughly 200 billion gal/y, with gasoline, diesel, and jet fuel being produced in approximately a 70/20/10 ratio. Thus, domestically produced alternative fuels could increase energy security. Domestic alternatives for gasoline (ethanol) and diesel (biodiesel) exist, but no operational alternative jet fuels are currently being produced in the United States. Alternative aviation fuels are also of interest for mitigating environmental impacts of fuel use, both on the global (climate change) and local (airport) air quality level. Although aviation contributes only 2% to global CO_2 emissions, the U.S. Air Force (USAF) and the aviation industry are committed to contributing to potential solutions.[1] Alternative aviation fuels are being sought as "drop-in" replacements for current aircraft, requiring no modification to equipment, aircraft operations,

handling, and transportation. This rules out ethanol (due to safety, performance, handling, and material compatibility issues) and biodiesel (due to low temperature and combustion performance, and storage stability issues).

Initial U.S. efforts in developing alternative aviation fuels focused on Fischer–Tropsch (FT) fuels produced from coal, biomass, and/or natural gas. Coal-derived "*iso*-paraffinic kerosene" (IPK) produced by Sasol in South Africa was approved for aviation use in blends up to 50% by volume in Jet A-1 (on a producer-specific basis) in 1999.[2] Generic FT "synthetic paraffinic kerosene" (SPK) was approved for use in blends with JP-8 in MIL-DTL-83133G in 2008 and in blends with commercial Jet A in ASTM D7566 in August 2009 (supported by a Research Report outlining the properties of SPK).[3−5] The USAF has been very active in the evaluation, demonstration, and certification of FT fuel blends from natural gas and coal. To date, U.S. military aircraft such as the B-52, C-17, and B-1B have been certified for use of a 50/50 (by volume) JP-8/FT blend. Other aircraft (i.e., F-22, KC-135, F-15, C-5, T-38) have already undergone flight tests and are scheduled to be certified on the FT blend in the near

future. The next class of alternative fuel being studied for military/commercial aviation certification is "hydroprocessed renewable jet" (HRJ), which is a hydrocarbon aviation fuel produced from animal fat/vegetable oils (triglycerides) by hydroprocessing. This fuel has also been called bio-SPK and "green jet". Ground and flight tests were recently (August 2010) completed on the C-17 Globemaster III cargo aircraft operating on blends of a tallow-derived HRJ and JP-8 (50/50) and the tallow-derived HRJ, coal FT and JP-8 (25/25/50). In addition, flight tests on 50/50 HRJ/JP-8 blends have been scheduled for FY11 on F-15 and F-22 aircraft. The ASTM D7566 specification is structured to support various classes of alternative fuels in its Appendices, with HRJ anticipated to be added in the near future as more data become available. It is anticipated that fuel produced from ligno-cellulosic feedstocks will also be added at a future date. In this effort, six alternative jet fuel candidates derived from several feedstocks and processes were evaluated to determine their suitability for use in aircraft. Specifically, the chemical and physical properties, oxidative thermal stability characteristics, elastomer swell compatibility, and combustion emissions were evaluated and compared to specification JP-8 fuels.

■ EXPERIMENTAL SECTION

Techniques for Chemical and Physical Analysis. The chemical composition and physical properties of the alternative fuels were evaluated to provide increased insight into their performance and to infer potential behavior during implementation. The analyses included evaluation of JP-8 specification properties, hydrocarbon type, and nonstandard analysis such as gas chromatography/mass spectrometry (GC/MS), gas chromatography with a flame ionization detector (GC/FID), and high performance liquid chromatography (HPLC). The fuels considered comprise a combination of both commercially available and research fuels.

Thermal Oxidative Stability Evaluation Systems. *Quartz Crystal Microbalance (QCM).* The quartz-crystal microbalance (QCM) has been used extensively to study jet fuel thermal stability and qualify the effects of various jet fuel additives on fuel thermal stability.[6-8] The QCM has the capabilities to monitor both headspace oxygen and carbon deposition in situ during fuel thermal stressing. The in situ mass accumulation is determined based on the well-known relationship between the change in surface mass and resonant frequency of the quartz crystal.[6] The combined oxygen and mass deposition measurements allow for a greater understanding of the autoxidation process for each fuel. The QCM is a batch experiment that is typically operated by thermally stressing 60 mL of fuel at 140 °C for 15 h. Fuel samples are air saturated prior to heating and the system is closed during operation.

Single Tube Flow Reactor System. A single-tube flow reactor system was used to evaluate the relative oxidative stability characteristics of the alternative fuels in a flowing environment. The system has previously been used to evaluate thermal stability characteristics of fuels under both oxidative and pyrolytic conditions.[9-12] The reaction zone is comprised of a 91.4 cm actively heated section where the fuel is exposed to sufficient temperature to promote the desired reaction chemistry. The outer wall temperature profile of the reaction tube is monitored using thermocouples (TC) strap-welded at various locations. The bulk fuel outlet temperature is monitored using a TC that is inserted into the outlet fuel flow approximately 17.8 cm downstream of the actively heated zone. After exiting the reaction zone, the fuel is cooled and passed through a 7-μm sintered filter element to remove any solids that are entrained in the fluid. The stability characteristics are determined by quantifying the total carbon deposition on the internal surface of the reaction tube and on the downstream filter.

Emissions Evaluations. *Turbine Engine.* A T63-A-700 turboshaft engine was used to study the particulate matter (PM) and gaseous emissions characteristics of the alternative jet fuels. The engine is located in the Engine Environment Research Facility (EERF) in the Propulsion Directorate at Wright-Patterson Air Force Base and is used to evaluate turbine engine lubricants, fuels, and sensors in an actual engine environment. Detailed descriptions of the engine and operating methodology have been provided in previous publications.[13,14] Although this engine has a single fuel injector, operates at relatively low pressures (~250–550 kPa), and represents an older technology, the observed emissions trends of more modern technology engines operated with alternative fuels have been consistent with those observed on this platform.[15,16] For this effort, the engine was operated at ground idle (low power) and cruise (high power) conditions. Baseline JP-8 was delivered to the engine fuel pump from a facility underground tank while the neat and blended alternative fuels were supplied from a nitrogen-pressurized (138 kPa) external tank. For all tests, the fuel flow rate was computer controlled to maintain a constant turbine outlet temperature (T_5). This was considered the most appropriate approach for emissions comparison between fuels and for best run-to-run engine condition repeatability. For each evaluation, the engine was initially operated on JP-8 at the two power settings, then with the alternative fuel, and finally returned to JP-8 to verify the baseline emissions.

Emissions Instrumentation. PM and gaseous emissions were sampled from the engine exit plane using oil-cooled probes maintained at 150 °C and transported to the analytical instruments via heated lines (65 °C). The PM sample stream (mostly nonvolatile) was diluted with nitrogen near the probe tip to prevent water condensation, minimize particle losses in the sample lines, and prevent saturation of the particle counting instruments. The PM emissions were characterized using conventional aerosol instruments and corrected for dilution based on the raw and diluted CO_2 measurements. A TSI Model 3022A condensation particle counter (CPC) was used to provide a count of particles per unit volume (particle number (PN)), a TSI Model 3936 scanning mobility particle sizer (SMPS) with a nanodifferential mobility analyzer (nDMA) was used to obtain the particle size distribution from 5 to 150 nm, and a Rupprecht & Patashnick Series 1105 tapered element oscillating microbalance (TEOM) was used to obtain real-time particle mass emissions. For the particle mass emissions, only results for the cruise condition are discussed due to the low particle mass at idle for the SPK fuels. In addition, an in-house designed and built smoke machine was used to collect soot samples for determination of the engine smoke number per SAE ARP 1179.[17] Gaseous emissions were sampled with undiluted probes and transported through heated lines kept at 150 °C per the SAE ARP 1256.[18] Major and minor gaseous species were quantified using an MKS multi gas 2030 Fourier transform infrared (FTIR) based analyzer and total unburned hydrocarbons were quantified using a CAI 600 heated flame ionization detector. A nondisperse infrared analyzer (NDIR) measured the CO_2 for the diluted samples from the particle instruments.

Fuel Elastomer Swell Evaluation System. To measure the overall volume swell character of the paraffinic fuels studied here, the volume swell of a nitrile rubber (Parker N0602) was measured in each fuel. Nitrile rubber was selected as the test material as it is a commonly used elastomer in aircraft systems. The plasticizer was extracted from the nitrile rubber before testing to remove the confounding factor of O-ring shrinkage due to the extraction of plasticizer by the fuel (approximately 10% reduction in original O-ring volume). Generally, the volume swell of elastomers by a fuel is dependent on the fuel's molar volume/geometry, polarity, and ability of the fuel to serve as the hydrogen donor in a hydrogen bond. Nitrile rubber responds to the three factors identified above as influencing the volume swell of O-ring materials. The volume swell of this material was measured using optical dilatometry.[19] Briefly, two O-ring samples were placed in a reservoir with 10 mL of the

test fuel. After 2 min of immersion in the fuel, the samples were digitally photographed every 20 s for the next 3 min. At 6 min total elapsed time, the samples were photographed every 60 min for the next 40 h. After the aging period was completed, the cross-sectional area was determined from the digital images and used as a characteristic dimension proportional to the volume. The final volume swell was calculated as the average value obtained from the two samples.

■ TEST DATA AND DISCUSSION

Chemical and Physical Analysis of Fuels. *Fischer−Tropsch Fuels Produced by Sasol, Shell, and Rentech.* The Sasol, Shell, and Rentech fuels were produced via indirect liquefaction using FT synthesis. The Sasol and Shell fuels are commercially available. During indirect liquefaction, the feedstock (natural gas for Shell and Rentech; coal for Sasol) is partially oxidized either via gasification or steam reforming to produce synthesis gas (carbon monoxide and hydrogen). The synthesis gas (syngas) is fed to an FT reactor where it is converted into higher molecular weight hydrocarbons. The Sasol SPK (also referred to as iso-paraffinic kerosene (IPK)) is produced via oligimerization of C_3 and C_4 olefins followed by hydrotreating and fractionation to produce a fuel with the desired boiling range.[20] This process results in an SPK with a very high degree of branching. The Sasol fuel was the first synthetic fuel to be approved as a blend feedstock with Jet A-1 fuel.[2] The Shell SPK was produced via the Shell middle distillate synthesis (SMDS) process.[21] The SMDS process produces long-chain paraffins from syngas in multitubular fixed bed reactors, followed by hydrocracking, isomerization and fractionation. The submitted Shell SPK fuel is a very narrow-cut kerosene compared to a typical JP-8. The Rentech fuel hydroprocessing process includes hydrotreating to remove oxygenates, followed by hydrocracking/isomerization, hydrotreating, and fractionation to produce a fuel with a volatility range similar to JP-8.

Hydroprocessed Renewable Jet Fuels (HRJ) produced by Syntroleum and UOP. Currently, hydroprocessed renewable jet (HRJ) fuels, also known as Bio-SPKs, are being considered for inclusion as approved blending components for both military and commercial jet fuels.[22] As part of the USAF alternate fuels research program, HRJ fuels have been synthesized and evaluated for their potential application in military systems. Syntroleum Corporation produced a research aviation fuel using the Syntroleum Bio-Synfining process. The research fuel is a renewable SPK termed R-8 (i.e., renewable feedstock and JP-8 like). The Bio-Synfining process can produce SPK from waste fats and greases, which do not compete with food crops. The feedstocks used for the research fuel evaluated in this study are shown in Table 1.

The Syntroleum process includes a feed pretreatment to reduce the contaminants in the solids. Contaminants include animal solids, rust particles, catalyst components, water, and

Table 1. Feedstocks Used to Produce R-8 Fuel

component	mass %
poultry fat	46%
yellow grease	18%
brown grease	18%
floatation grease	9%
prepared foods	9%

solubilized metals. If not removed, these will deposit in the fixed bed reactors causing excessive pressure drop across the catalyst bed and decrease of catalyst activity. The next step in the process is hydrodeoxygenation (HDO). The HDO product effluent, which contains primarily $C_{15}-C_{18}$ n-paraffins, is hydrocracked/isomerized to produce a fuel with a boiling point distribution and freeze point similar to a conventional JP-8. The tested R-8 fuel is very similar to the Fischer−Tropsch (FT) derived fuel produced by Syntroleum, S-8, which was used in the certification of alternative FT fuel blends.[23]

UOP produced two research aviation HRJ fuels using camelina and beef tallow as feedstocks. In the process, pressurized feedstock is mixed with hydrogen and undergoes catalytic deoxygenation to primarily produce n-paraffins. This product is then hydorcracked/isomerized to satisfy required freeze point characteristics and separated to the desired volatility. The beef tallow HRJ fuel evaluated in this effort is very similar to the HRJ used in the recent C-17 tests. Various physical and chemical properties of the alternative fuels were evaluated and compared to a typical specification JP-8. Selected fuel specification properties are shown in Table 2.

In general, all synthetic fuels evaluated had zero to very low aromatic content, negligible sulfur, lower density, and higher hydrogen content compared to conventional JP-8. If used neat, the relative low density of paraffinic fuels is likely to impact aircraft range; however, the impact is highly dependent on whether the aircraft is weight or volume limited.[24] Gas chromatograms of the various fuels (with the n-paraffin peaks identified) are shown in Figure 1.

As shown in Figure 1 and Table 2, the Rentech FT and all HRJ fuels have a boiling point range similar to a typical JP-8, while the Shell and Sasol FT fuels are much narrower. Results of the hydrocarbon type analyses, performed using ASTM D6379 and D2425, are shown in Tables 3 and 4, and a comparison of the n-paraffin content of the fuels is shown in Table 5. As noted previously, the alternative fuels are primarily comprised of normal and branched paraffins with low or negligible aromatic content. On the basis of knowledge of the processing techniques employed for the FT fuels, it was expected that these fuels would be solely comprised of paraffinic compounds and free of aromatics. It appears that aromatic compounds found in the Rentech, Sasol, and R-8 fuels were produced during the upgrading steps of the initial products following FT-synthesis (Rentech and Sasol) or hydrodeoxygenation (R-8). Improved control of the fuel upgrading process parameters will likely eliminate the production of aromatic compounds in these fuels if required. The Shell FT fuel showed a mild degree of branching and was comprised of a much higher n-paraffin concentration than found in typical petroleum-derived jet fuels or the other alternative fuels evaluated.

High concentrations of long n-paraffins can result in poor low temperature properties; however, the narrow distillation range produces a fuel with a sufficient freeze point.[21] On the contrary, the Sasol fuel had no detectable n-paraffins and a very high degree of branching (e.g., tri- and tetra-methylparaffins). The absence of n-paraffins results in an extremely low freeze point for the Sasol SPK.

The Rentech FT and the HRJ fuels have similar n-paraffin distributions, but slightly lower in magnitude than a typical JP-8. These fuels exhibited a mild degree of branching and are very similar in composition to the Syntroleum S-8 fuel used in the FT fuel certification of the B-52.[23] As shown in Table 4, significant

Table 2. ASTM Specification Tests of Fuels Evaluated

| ASTM tests	standard	JP-8	Shell FT	Sasol FT	Rentech FT	R-8 HRJ	tallow HRJ	camelina HRJ
total acid number, mg KOH/g (D3242)	max 0.015	0.005	0.002	0.002	0.004	0.002	0.002	0.002
aromatics, % vol (D1319)	max 25.0	17.2	0.0	0.4	1.7	0.0	0.4	0.0
total sulfur, % wt (D4294 or D2622)	max 0.30	0.064	<0.001	<0.001	<0.001	<0.001	<0.0003	0.0018
distillation, initial boiling point (IBP), °C (D86)	report	152	146	149	152	158	165	151
10% recovered, °C (D86)	max 205	173	162	166	168	175	179	161
20% recovered, °C (D86)	report	179	162	170	179	185	185	166
50% recovered, °C (D86)	report	198	169	180	216	215	210	182
90% recovered, °C (D86)	report	239	184	208	263	260	243	237
final boiling point, °C (D86)	max 300	260	198	228	275	274	255	259
distillation residue, % vol (D86)	max 1.5	1.1	1.0	1.4	1.0	0.8	1.2	1.1
loss, % vol (D86)	max 1.5	0.2	0.4	0.5	0.8	0.2	0.8	0.9
freeze point, °C (D5972)	max −47	−49	−55	<−77	−50	−49	−62	<−77
existent gum, mg/100 mL (D381)	max 7.0	0.4	1.6	1.4	<1	<1	<1	<1
viscosity @ −20 °C, cSt (D445)	max 8.0	4.1	2.6	3.8	5.1	5.5	5.3	3.3
lubricity test (BOCLE) (D5001) wear scar mm	report	0.54	0.75	0.87	0.82	0.92	0.76	0.76
specific gravity (D4052)	0.775−0.840	0.799	0.737	0.762	0.763	0.762	0.758	0.751
smoke point, mm (D1322)	min 19.0	25	40.0	>40	>40	>40	>40	50
flash point °C (D93)	min 38	48	44	44	44	48	55	43
heat of combustion, MJ/kg (D3338)	min 42.8	43	44.1	44.2	44.2	44.1	44.1	44.1
hydrogen content, % mass (D3343)	13.4	13.9	15.6	15.1	15.2	15.3	15.3	15.4
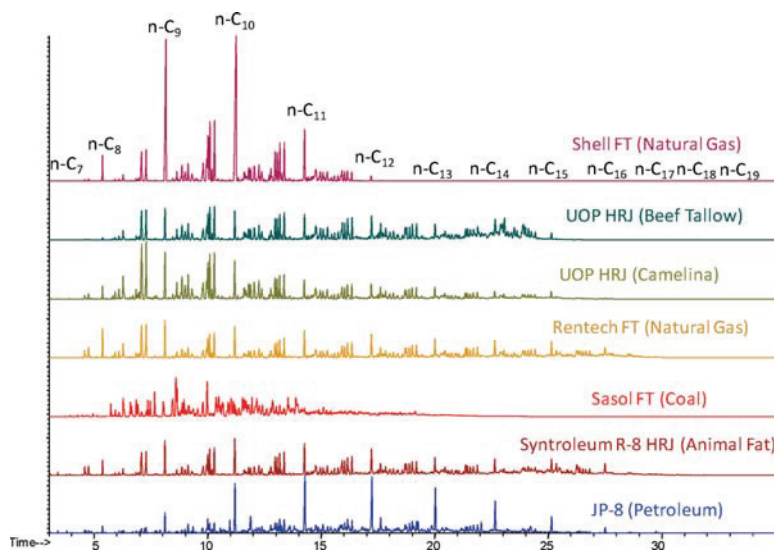
Figure 1. Gas chromatograms of alternative fuels.

Table 3. Aromatic Species Analysis by ASTM D6379 for Alternative Fuels

aromatics (vol %)	JP-8	Shell FT	Sasol FT	Rentech FT	R-8 HRJ	tallow HRJ	camelina HRJ
monoaromatics	15.1	<0.2	0.4	1.5	0.3	<0.2	<0.2
diaromatics	1.6	<0.1	<0.1	<0.1	<0.1	<0.1	<0.1
total aromatics	16.7	<0.2	0.4	1.5	0.3	<0.2	<0.2
total saturates	83.3	>99.8	99.6	98.5	99.7	>99.8	>99.8

concentrations of *cyclo*-paraffins were detected in five of the alternative fuels. It is noteworthy, however, that the technique used for analysis of highly branched SPKs (ASTM 2425) may

result in overestimation of the *cyclo*-paraffin content due to differences in the relative ratio of the *iso*- and *cyclo*-paraffinic characteristic ions found in the alternative fuel compared to those

108

Table 4. Hydrocarbon Type Analysis by ASTM D2425 for Alternative Fuels

hydrocarbon type (vol %)	JP-8	Shell FT	Sasol FT	Rentech FT	R-8 HRJ	tallow HRJ	camelina HRJ
paraffins (normal + iso)	50	>99	88	92	92	98	90
cyclo-paraffins	34	<1	12[a]	7[a]	8[a]	2	10
alkylbenzenes	12	<0.3	0.4	1.3	<0.3	<0.3	<0.3
indans and Tetralins	3	<0.3	<0.3	<0.3	<0.3	<0.3	<0.3
indenes and C_nH_{2n-10}	0.4	<0.3	<0.3	<0.3	<0.3	<0.3	<0.3
naphthalene	<0.3	<0.3	<0.3	<0.3	<0.3	<0.3	<0.3
naphthalenes	1.4	<0.3	<0.3	<0.3	<0.3	<0.3	<0.3
acenaphthenes	<0.3	<0.3	<0.3	<0.3	<0.3	<0.3	<0.3
acenaphthylenes	<0.3	<0.3	<0.3	<0.3	<0.3	<0.3	<0.3
tricyclic aromatics	<0.3	<0.3	<0.3	<0.3	<0.3	<0.3	<0.3
total	100	100	100	100	100	100	100

[a] D2425 may overpredict *cyclo*-paraffins for highly branched SPKs.

Table 5. Weight Percent of *n*-Paraffins for Alternative Fuels

n-paraffins (wt %)	carbon no	JP-8	Shell FT	Sasol FT	Rentech FT	R-8 HRJ	tallow HRJ	camelina HRJ
n-heptane	C_7	0.10	0.012	<0.001	0.007	0.13	<0.001	0.017
n-octane	C_8	0.34	1.63	<0.01	1.88	0.80	0.12	0.71
n-nonane	C_9	1.21	22.4	<0.05	2.75	2.28	2.01	3.20
n-decane	C_{10}	3.48	25.1	<0.03	2.22	2.47	1.88	2.80
n-undecane	C_{11}	4.24	3.78	<0.02	1.81	2.10	1.52	1.20
n-dodecane	C_{12}	3.71	0.29	<0.01	1.52	1.64	1.25	0.87
n-tridecane	C_{13}	2.84	0.003	<0.01	1.40	1.23	0.82	0.60
n-tetradecane	C_{14}	1.79	0.001	<0.01	1.05	0.92	0.86	0.41
n-pentadecane	C_{15}	0.87	<0.001	<0.005	0.90	0.80	0.35	0.37
n-hexadecane	C_{16}	0.27	<0.001	<0.003	0.64	0.60	0.004	0.061
n-heptadecane	C_{17}	0.089	<0.001	<0.001	0.071	0.052	<0.001	0.015
n-octadecane	C_{18}	0.024	<0.001	<0.001	0.002	0.026	<0.001	0.006
n-nonadecane	C_{19}	0.008	<0.001	<0.001	<0.001	<0.001	<0.001	0.001
total *n*-paraffins		19.0	53.3	<0.2	14.3	13.1	8.8	10.2
C_7-C_9		1.7	24.1	<0.06	4.6	3.2	4.0	6.7
$C_{10}-C_{13}$		14.3	29.2	<0.1	7.0	7.4	2.9	4.9
$C_{14}-C_{16}$		2.9	<0.003	<0.02	2.6	2.3	0.35	0.45
$C_{17}-C_{19}$		0.12	<0.003	<0.003	0.07	0.079	<0.001	0.022

for which the correlations were developed. Therefore, the reported *cyclo*-paraffinic values should be regarded as a maximum possible content. It should be noted that *cyclo*-paraffins have recently been reported to be present in the Sasol SPK fuel.[5] Currently, analytical characterization of alternative fuels using two-dimensional gas chromatography (GC × GC) is being pursued as it may be possible to obtain substantially improved resolution for quantitation of paraffinic classes.[25]

The USAF approved the use of blends of SPK produced via FT-synthesis with conventional JP-8 provided that the required SPK and final blend properties are satisfied as detailed in MIL-DTL-83133G. In addition, ASTM also recently approved the use of FT-derived SPK in commercial Jet A and Jet A-1 as detailed in ASTM D7566-09. Both specifications allow a maximum of 50% by volume of SPK to be blended with conventional jet fuel. Selected properties for both the neat SPKs and the resulting fuel blend for each specification are shown in Table 6. The general properties for the neat SPKs are similar for both specifications as each limit the maximum aromatic content while ensuring a minimum volatility range. The major difference between the SPK specifications is the allowable fuel density range, where the

military minimum limit is 0.751 kg/L while the commercial limit is 0.730 kg/L. It should be noted that the Shell FT fuel did not satisfy the minimum military SPK density limit and barely satisfied the minimum volatility distribution. Also, the UOP camelina HRJ was at the lower density limit for the military fuel specification. These properties will need to be addressed in subsequent formulations in order to reliably meet the required fuel specifications. Both blend specifications require a minimum aromatic content of 8.0% by volume. This limit is based highly on operational experience to ensure that required "fit-for-purpose" (FFP) properties (e.g., material compatibility, seal swell, and lubricity) are maintained for the blends. Research is ongoing to better define this lower limit. The Rentech FT fuel did not satisfy the maximum allowable aromatic content, but it is believed that the total aromatic content could be reduced via better control of the processing variables. During blending with petroleum-derived fuels, the addition of the R-8 or Rentech FT fuel is expected to exhibit a linear dependence for all fuel properties proportional to the blend ratio due to the similar volatility range and long chain *n*-paraffin content. The expected behavior is based on similarity to previous studies using S-8.[23,26] The property dependence upon

Table 6. Comparison of Selected Neat SPK and Blend Properties in US Military and Commercial Fuel Specifications

	MIL-DTL-83133G		ASTM D7566-09	
	min	max	min	max
requirements for neat SPK				
aromatic (mass%)		0.5		0.5
density @ 15 °C (kg/L)	0.751	0.770	0.730	0.770
flash point (°C)	38		38	
freezing point (°C)		−47		−40
cyclo-paraffin (mass %)		15		15
sulfur (mass %)		0.0015		0.0015
nitrogen (mg/kg)		2		2
halogens (mg/kg)		1		1
metals (mg per metal/kg)		0.1		0.1
distillation temp (°C)				
10% recovered		205		205
final		300		300
T90−T10 (°C)	22		22	
requirements for petroleum/SPK blend				
aromatic (vol%)	8.0		8.0	
T50−T10 (°C)	15		15	
T90−T10 (°C)	40		40	

blending with the Sasol FT and HRJ fuels is expected to be similar, except for the freeze point of the blend. Blends of either of these with petroleum-derived fuels will result in fuels with reduced freeze points due to dilution of the long-chain *n*-paraffins in the petroleum fuel. In general, the extent of freeze point suppression for the blend will increase as the neat SPK *n*-paraffin concentration and relative molecular weight decrease. Similar formulations of the Shell FT fuel exhibit a linear dependence of fuel properties with blending, with only the freeze point exhibiting nonideal behavior. For these blends, the freeze point is lower than expected based on the JP-8/SPK blend ratio.[21] This is believed to be due to the narrow range and relatively low volatility of the Shell SPK, which reduce the neat JP-8 long chain *n*-paraffins in the blend. However, the blend freeze point will reach a minimum and increase to approach the neat SPK value at relatively high SPK concentrations due to the very high C_9-C_{11} *n*-paraffin content (see Table 5), as these begin to dominate the solidification process.

■ THERMAL OXIDATIVE STABILITY

QCM. The thermal stability characteristics of the six alternative fuels and a typical petroleum derived JP-8 were examined using the QCM under typical operating conditions (i.e., thermal stressing of air saturated fuel samples at 140 °C for 15 h). The resulting mass accumulation and headspace oxygen profiles are shown in Figure 2a and b. These data show that each fuel sample exhibits a unique oxidation/deposition characteristic, with the oxidation profiles providing the highest level of variance. All six alternative fuel samples display typical oxidation profiles for fuels with varying amounts of added synthetic antioxidant (AO) (i.e., minimum oxidation with subsequent rapid and complete oxygen consumption upon depletion of the AO).[8] The Shell FT fuel had sufficient AO to prevent complete oxygen consumption for the
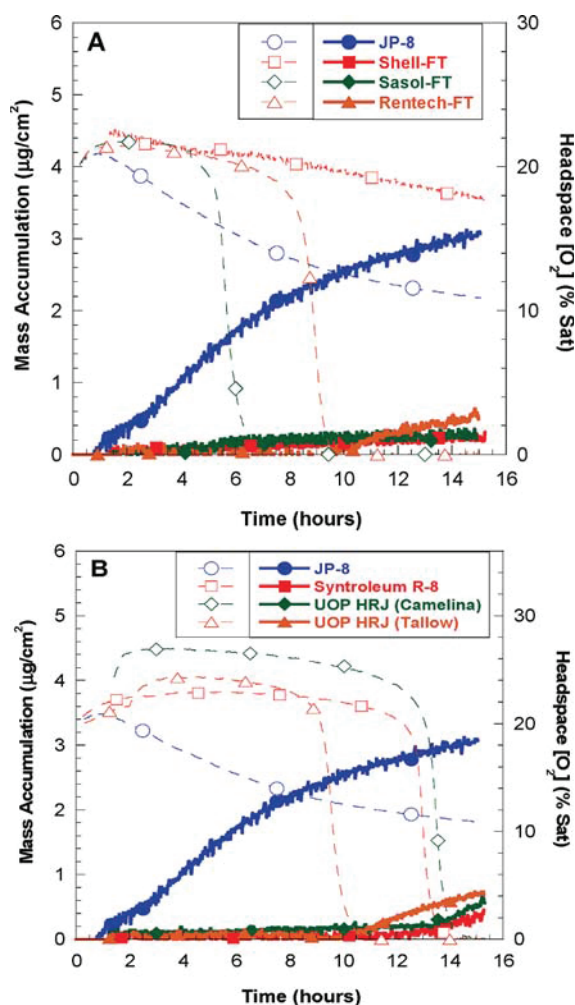
Figure 2. Mass accumulation (solid lines, closed markers) and headspace oxygen (dashed lines, open markers) profiles of alternative fuels in the QCM at 140 °C.

test duration, whereas the added AO in the remaining five alternate fuel samples was consumed within the 15 h stress duration. The JP-8 fuel displayed a slow oxidation rate that typically indicates the presence of natural AO species (e.g., alkyl-substituted phenols). The addition of synthetic AO to heavily hydrotreated fuels is especially important to prevent the buildup of oxidation products during storage. These oxidation products, such as hydroperoxides, alcohols, and acids, may affect the material compatibility and thermal and storage stability of the fuel. The mass accumulation profiles after 15 h of stress duration show that all six alternative fuels exhibit a low deposit tendency (0.2−0.7 μg/cm^2) compared to a typical JP-8 fuel (3.0 μg/cm^2). Therefore, all synthetic fuels exhibit excellent thermal stability characteristics compared to a typical JP-8 under the given experimental conditions.
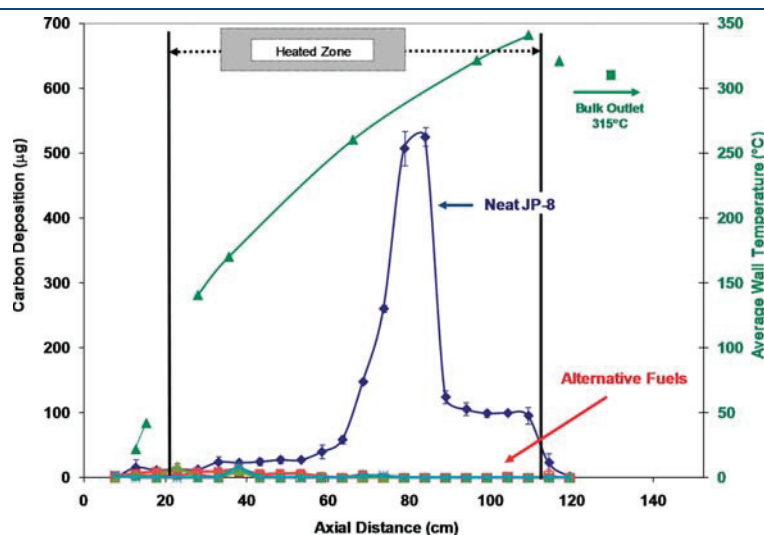
Single-Tube Flow Reactor System. In addition to the QCM tests, oxidation stability experiments were conducted using a 127-cm long, 0.318-cm o.d., 0.216-cm i.d. tube constructed of 316 stainless steel, a reaction pressure of 3.8 MPa and a

volumetric flow rate of 10 mL/min. The furnace temperature was set to obtain a target maximum wall temperature of approximately 340 °C (bulk ∼ 315 °C). These reaction conditions have previously been shown to be adequate for complete consumption of the dissolved oxygen in the fuel within the reaction zone. Studies were conducted to compare the oxidative stability characteristics of the alternative fuels with that of a typical JP-8 fuel. A total reaction time of six hours was used, which has previously been shown to be adequate to discern differences in deposition between various neat and additized fuels. Each test was conducted twice to provide a measure of the reproducibility. Comparisons of the surface deposition profiles and typical average wall temperature measurements for testing with the various fuels are shown in Figure 3. All alternative fuels demonstrated excellent oxidative stability characteristics during the tests resulting in minimal surface deposition on the reaction tube. In addition, the bulk deposits collected on the downstream filter were reduced by at least a factor of 2 compared to testing with the baseline JP-8. The camelina HRJ had a slightly higher level of surface deposition than the other alternative fuels evaluated, most likely due to the slightly higher sulfur content (18 ppm) in this fuel compared to the negligible levels in the other SPK and HRJ fuels. However, this deposition was negligible compared to that of JP-8. The stability characteristics exhibited by these fuels are similar to those observed for a JP-7 fuel,[11] a specialty fuel designed for high-temperature applications. The negligible deposition for these fuels is very similar to that of the S-8 fuel produced by Syntroleum.[11] The single-tube flow reactor results are consistent with the thermal stability evaluation using the QCM.

The improved stability characteristics of the alternative fuels relative to the specification JP-8 are most likely due to the absence of heteroatomic-containing species in these fuels, which have previously been implicated as promoters of undesirable deposit formation in the oxidative regime. The stability of these fuels is significantly better than that observed for a JP-8 fuel with the currently qualified JP-8 + 100 thermal stability additive package.[27] Pyrolytic (>∼480 °C) testing was not conducted in

the current study; however, based on the chemical composition of the fuel and similarities to SPKs previously tested, it is expected that these fuels will exhibit higher reactivity and deposition propensity than a typical JP-8 fuel.[12]

Engine Emissions. *Particulate Matter.* The relative particle number emission index (EI_n) (number of particles per kilogram fuel) for each alternative fuel and the two FT/JP-8 blends (50% by volume) are shown in Figure 4. The JP-8 measurements were the average taken before and after testing of each alternative fuel. As expected, lower EI_n were generated with the paraffinic fuels compared to JP-8. These results agree with previous assessments of SPK fuels on a research combustor and in several engines.[15,16,28,29] Consistent with the previous studies, the largest impacts are produced at low engine power. Between 90 and 98% (idle) and 60−80% (cruise) lower EI_n compared to JP-8 were observed with the SPK fuels. It is believed that at lower combustion temperatures, the rate of molecular soot growth and subsequent particle nucleation with the aromatic-free fuels is relatively low compared to the baseline fuel, thus significantly lower soot is produced. As combustion temperatures increase, the relative role of aromatics on fuel soot formation is reduced as the chemical rates of soot production from the paraffinic compounds (via fragmentation−polymerization reactions) increase. Reductions in unburned hydrocarbons (UHC) aerosols are also believed to impact the resultant particle concentrations, as hydrocarbons may condense on soot nuclei or form nuclei size particles in sample lines. As shown, there were significant differences in particulate emissions between the alternative fuels. The EI_n magnitude varied as follows: Sasol FT > Rentech FT ≥ R-8 > Tallow HRJ = Camelina HRJ > Shell FT. It can be noted that the EI_n trends inversely follow the fuel hydrogen content (i.e., lower hydrogen content SPK fuel produced higher particulate emissions). Another chemical characteristic that affects the particulate production is the iso-to-normal paraffin ratio. Previous research has shown the normal paraffins produce lower particle concentration emissions than *iso*-paraffins, despite having the same H/C ratio.[14] This was attributed to the increased production of specific soot precursors (e.g., propargyl radicals)

Figure 3. Comparison of carbon deposition and wall temperature profiles for oxidative stability testing on single tube flow reactor system with the alternative fuels and a specification JP-8 fuel for 6 h of reaction time.
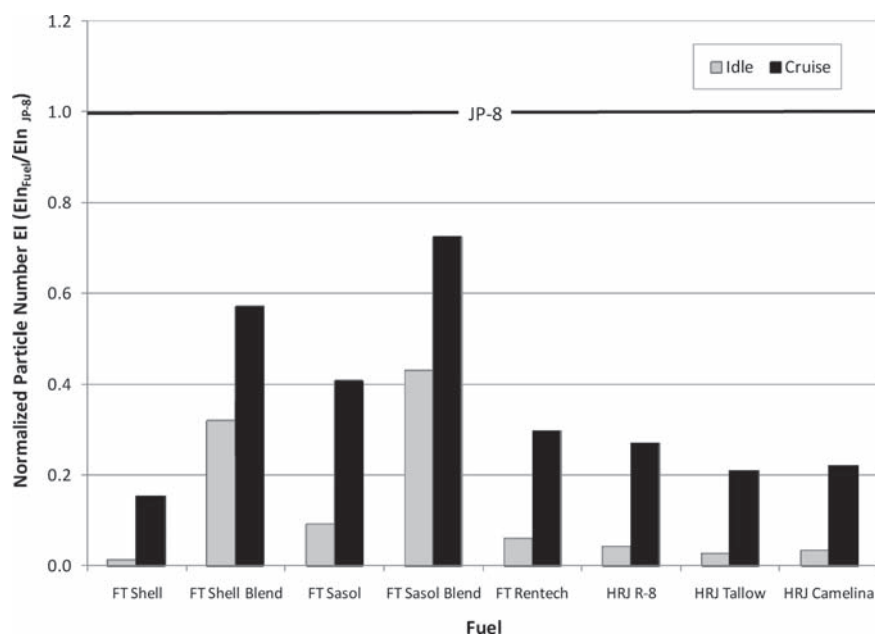
111

Figure 4. Relative particle number emission for T63 engine fueled with alternative fuels.
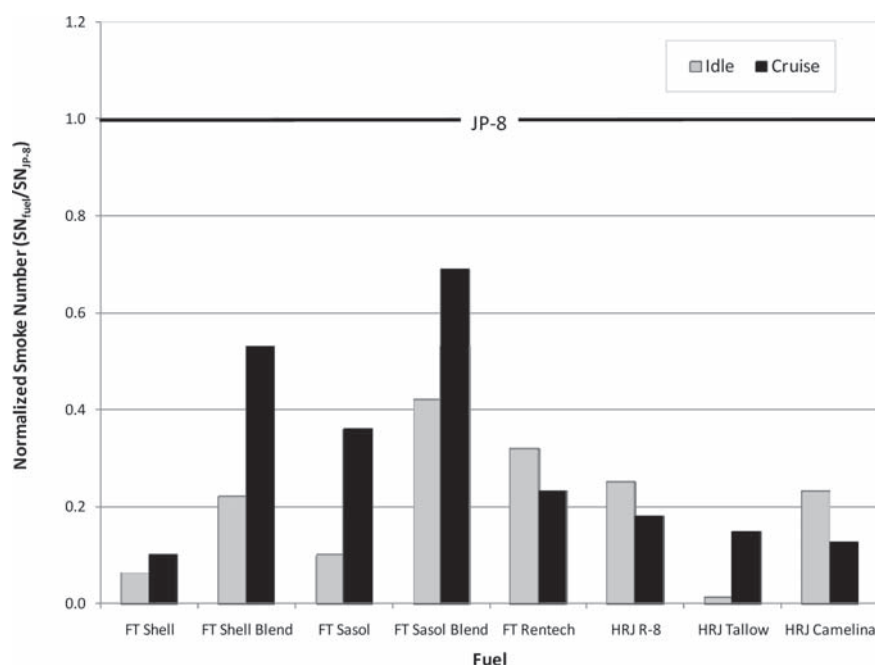

Figure 5. Relative smoke number emission for T63 engine fueled with alternative fuels.

with increased degree of paraffinic branching. Consistent with previous research, the Sasol FT fuel, which has a high degree of branching, produced higher EI_n compared to the other SPKs. Significant reductions in EI_n are also realized for the 50% by volume blends, although as observed, these are not always directly proportional to the exact concentration of FT fuel in the blend (e.g., 50% reduction for 50% FT concentration). The

lower soot production with these SPK fuels is also reflected in the engine smoke number (SN) as displayed in Figure 5. The SN is mostly impacted by the larger particles in the exhaust and, thus, may not correlate directly with the measured particle number; however, the overall trends are similar. Similar to the SN, particulate mass emission index (EI_m) (g/kg fuel) (not shown) also follow the EI_n trends with respect to reductions as a function

of engine power; however, the magnitudes are slightly different as these are a strong function of the particle diameter. Particle size distribution data (acquired with the SMPS system) show single mode log-normal distribution trends for all conditions considered, with no evidence of a particle nucleation mode. The relative mean particle diameter data for each fuel compared to operation with JP-8 evaluated for both engine conditions are displayed in Figure 6. Significantly smaller particles (up to 35%) were observed for the alternative fuels and blends relative to JP-8. This is attributed to the lower concentration of soot nuclei available for surface growth and agglomeration reactions due to the lack or lower concentration of aromatics in the fuel.

Although the smaller particles have higher surface area-to-volume ratios, which may result in increased concentration of harmful compounds on each particle, previous research has demonstrated significantly lower concentration of PAHs in soot particles from FT fuel combustion.[29] Also, even though a particle nucleation mode was not observed, a reduction in volatile PM is also expected for the alternative fuels due to the negligible heteroatomic content and lower unburned hydrocarbon emissions (discussed in the next section).

Gaseous Emissions. Gaseous emissions, quantified with an FTIR-based analyzer, show that the alternative fuels had negligible impact on CO_2, NO_x, and formaldehyde; however, statistically significant reductions in carbon monoxide (CO) and UHC were observed. The normalized CO and UHC emissions for the neat alternative fuels relative to JP-8 for engine idle are shown in Figure 7. Reductions of 10−25% ($\pm5\%$ 1σ) in CO were observed with the various alternative fuels relative to JP-8. The lowest CO emissions were produced with the FT Shell fuel, which also had the highest H/C ratio of all fuels tested. The R-8, Sasol, and Rentech fuels produced similar CO emissions, approximately 10−12% lower than JP-8. Similar reductions in CO have been observed with neat FT fuel on a T701C engine.[15]

Measurement of engine UHC with an FID analyzer show negligible concentrations at cruise, and concentrations of 580−720 ppm UHC for JP-8 at idle during the study. As shown, moderately lower (∼20−30%) UHC were produced with the SPK fuels compared to JP-8. It is well-recognized that the factors that control CO emissions also influence UHC emissions. It is plausible that the lack of relatively stable ring species (i.e., aromatics) in the SPK fuels may facilitate fuel combustion at the relatively low temperatures at idle, thus reducing UHC and CO emissions.

Elastomer Material Volume Swell Characteristics. Although FT and HRJ fuels have shown excellent combustion and thermal stability characteristics, the compatibility of these fuels with aircraft seal materials are a concern and has been receiving considerable attention. Of particular interest is the propensity of conventional fuels to soften and swell O-ring seals to some extent; there is concern that without aromatics and heteroatom exposure, neat paraffinic-type fuels will cause O-ring seals to shrink, harden and fail. However, it has been shown that all of the fuel components can participate in the swelling process and the extent to which they contribute depend primarily on the strength of interaction between the specific fuel component and the O-ring material and the concentration of those components in the overlying fuel.[30−32] Generally, the strength of interaction depends on the molar volume and geometry of the fuel component, the polarity, and the ability to serve as the hydrogen donor in a hydrogen bond. Specifically, volume swell tends to increase as the molar volume of the fuel component decreases and as the polarity and hydrogen bonding increases. In the case of these alternative fuels, the components of the bulk fuel have very little polarity and little if any ability to form even weak hydrogen bonds, leaving only molar volume and geometry as the primary mechanism to induce volume swell in common O-ring materials.

The origin of the functionality of molar volume and geometry in volume swell is the energy required to insert a molecule into a polymer matrix from the bulk fuel.[33,34] Briefly, in order for a fuel
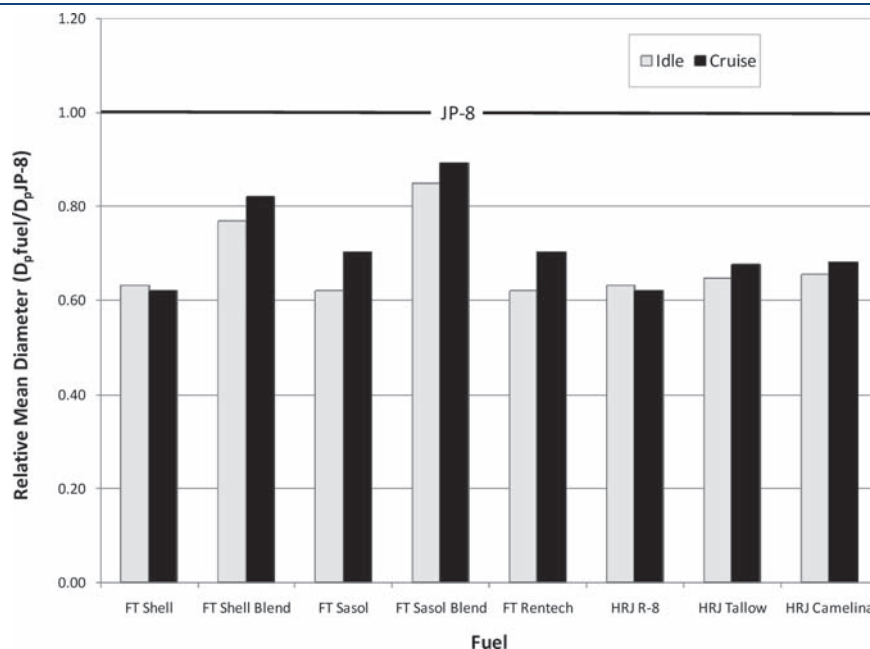

Figure 6. Relative mean particle diameter for T63 engine fueled with alternative fuels.
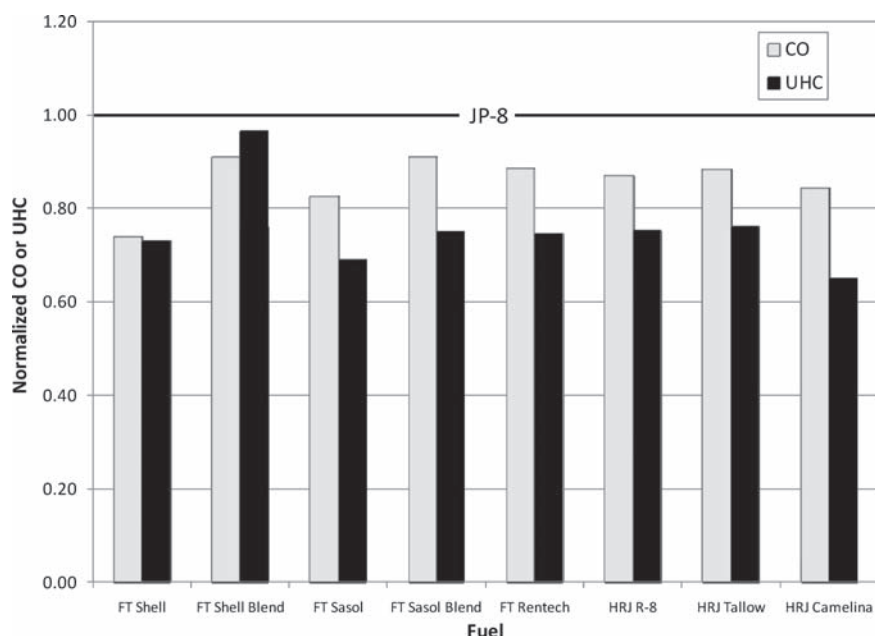
Figure 7. Normalized CO and UHC emissions for T63 engine at idle with alternative fuels.

molecule to penetrate a polymer matrix, adjacent polymer chains must be separated sufficiently to admit the penetrant molecule; the smaller the molecule the less amount of energy it takes to accommodate it in the polymer structure. With respect to the volume swell character of SPKs, this suggests that their ability to impart volume swell in a given O-ring material will depend on their molecular weight distribution (lighter fuels swelling more than heavier fuels) and composition (linear molecules being more mobile than branched). However, it is important to consider that the intermolecular forces involved are primarily very weak (van der Waals) and the extent of these influences can be very material dependent.

The results of the volume swell measurements are summarized in Table 7. Also shown is the volume swell of the Syntroleum S-8 fuel. These results show that nitrile rubber absorbs a significant amount of each fuel even with the absence of aromatics. Furthermore, even though the volume swell varies over a relatively narrow range, the trend is in good agreement with the results expected based on the composition of these fuels. Specifically, comparing these results with the chromatograms shown in Figure 1 illustrates that the volume swell character of these fuels increases as the molecular weight distribution shifts to smaller molecules. For example, the greatest volume swell for the neat fuels (without additives) was observed for the Shell FT, which is a relatively narrow cut dominated by C_9 and C_{10} linear paraffins. The next highest is the Sasol FT which is a similar narrow cut, but with only branched paraffins. The lowest volume swell was observed for Rentech FT and R-8, both of which exhibit very broad molecular weight distributions that more closely match that found in JP-8.

Comparing the volume swell of the neat SPKs with the JP-8 used in this study (which was considered a typical midrange JP-8), if nitrile rubber O-rings were in service with JP-8 and then exposed to the neat SPKs, they will shrink by approximately 7−9% by volume. However, the volume swell of these fuels are

Table 7. Volume Swell of Extracted Nitrile Rubber

fuel	volume swell
Shell FT	9.6%
Sasol FT	9.5%
Rentech FT	7.8%
R-8	7.0%
camelina HRJ	9.1%
tallow HRJ	8.6%
JP-8	16.6%
[a] Syntroleum S-8	8.1%

[a] Previously tested SPK.[19]

comparable to that for the previously flight-tested S-8 fuel,[19] indicating that the alternative fuels used in this study should also serve well as blending stocks for JP-8. It should be noted that the use of these blends will result in some shrinkage relative to operation with neat JP-8. Note that among the O-ring materials commonly used in aircraft fuel systems, nitrile rubber shows the greatest response to the aromatic content and therefore represents a limiting case. The response of other materials such as fluorosilicone and fluorocarbon would be much less.

■ SUMMARY

The chemical and physical characteristics, thermal stability, emissions propensity, and seal swell of six alternative jet fuel candidates from five different feedstocks were evaluated. Detailed chemical analysis of the alternative fuels show that these are primarily composed of paraffins, with negligible or no aromatic and heteroatomic species. Evaluations on two thermal stability systems demonstrated that the alternative fuels possess superior thermal oxidative stability compared to JP-8 and, therefore, have lower tendency to carbon formation when heated to moderate temperatures. Emissions data demonstrate that the neat

paraffinic fuels produced significantly lower soot and moderately lower unburned hydrocarbons and carbon monoxide than baseline JP-8 fuel. Significant swelling capability was observed in nitrile O-rings with the alternative fuels; however, it was substantially less than the aromatic containing JP-8 fuel, which may lead to fuel leaks in aircraft systems.

In general, this effort demonstrates that paraffinic-type fuels, produced via FT synthesis (SPK) or extensive hydroprocessing (HRJ), can provide attractive chemical and physical properties independent of feedstock. Eventual use of these paraffinic fuels as drop-in fuels will require compliance with ASTM 7566-09 and/ or MIL-DTL-83133G and fulfilling lubricity requirements and FFP properties (e.g., seal swell [which may require changing aromatic limits]). The potential penalty on aircraft range with the reduced density of these alternative fuels should also be addressed before implementation.

■ AUTHOR INFORMATION

Corresponding Author
*E-mail: edwin.corporan@wpafb.af.mil.

■ REFERENCES

(1) Intergovernmental Panel on Climate Change. *Summary for Policymakers − Aviation and the Global Atmosphere*; Special Report, 1999.

(2) *Turbine Fuel, Aviation Kerosene Type, Jet A-1 NATO Code: F-35 Joint Service Designation: AVTUR*; Defense Standard 91-91, April, 8 2008.

(3) *Detailed Specification, Turbine Fuel, Aviation, Kerosene Type, JP-8 (NATO F-34), NATO F-35, and JP-8 + 100 (NATO F-37)*, MIL-DTL-83133G, April 30, 2010.

(4) *Standard Specification for Aviation Turbine Fuel Containing Synthesized Hydrocarbons*; ASTM D7566-09, Sept, 1 2009.

(5) Moses, C. *Comparative Evaluation of Semi-Synthetic Jet Fuels*; report on CRC Project AV-2-04a, Coordinating Research Council, September 2008.

(6) Zabarnick, S. Studies of Jet Fuel Thermal Stability and Oxidation Using a Quartz Crystal Microbalance and Pressure Measurements. *Ind. Eng. Chem. Res.* **1994**, *33*, 1348–1354.

(7) Zabarnick, S.; Mick, M. S. Inhibition of Jet Fuel Oxidation by Addition of Hydroperoxide-Decomposing Species. *Ind. Eng. Chem. Res.* **1999**, *38*, 3557–3563.

(8) Grinstead, B.; Zabarnick, S. Studies of Jet Fuel Thermal Stability, Oxidation, and Additives Using an Isothermal Oxidation Apparatus Equipped with an Oxygen Sensor. *Energy Fuels* **1999**, *13*, 756–760.

(9) Edwards, T.; Krieger, J. The Thermal Stability of Fuels at 480C (900F). Effect of Test Time, Flow Rate, and Additives *ASME J. 95-GT-68*; ASME: Houston, TX, **1995**

(10) Corporan, E.; Minus, D. K. Investigation of the Pyrolytic Deposition Characteristics of JP-7 and JP-8 Fuels. *Prepr.—Am. Chem. Soc., Div. Pet. Chem.* **2000**, *45* (3), 474–477.

(11) Edwards, T.; Minus, D.; Harrison, W.; Corporan, E.; DeWitt, M.; Zabarnick, S.; Balster, L. *Fischer-Tropsch Jet Fuels − Characterization for Advanced Aerospace Applications*; AIAA-2004-3885, Fort Lauderdale, FL, July 2004.

(12) Edwards, T.; DeWitt, M. J.; Shafer, L.; Brooks, D.; Huang, H.; Bagley, S. P.; Ona, J. O.; Wornat, M. J. Fuel Composition Influence on Deposition in Endothermic Fuels. *14th AIAA/AHI Space Planes and Hypersonic Systems and Technologies Conference*, Canberra, Australia, Nov 2006; paper AIAA 2006-7973.

(13) Corporan, E.; DeWitt, M. J.; Wagner, M Evaluation of Soot Particulate Mitigation Additives in a T63 Engine. *Fuel Process. Technol.* **2004**, *85*, 727–742.

(14) Corporan, E.; Monroig, O.; Wagner, M.; DeWitt, M. J. Influence of Fuel Chemical Composition on Particulate Matter Emissions of A Turbine Engine. *ASME Turbo Expo*, Vienna, Austria, June 2004; paper GT2004-54335.

(15) Corporan, E.; DeWitt, M.; Klingshirn, C.; Cheng, M. D. Emissions Characteristics of Military Helicopter Engines Fueled with JP-8 and a Fischer−Tropsch Fuel. *J. Propul. Power* **2010**, *26* (2), 317–324.

(16) Bulzan, D., et al. Gaseous and Particulate Emissions Results of the NASA Alternative Aviation Fuel Experiment (AAFEX). *Proceedings of ASME Turbo Expo*, Glasgow, Scotland, June 14−18, 2010; GT 2010-23524.

(17) *Aircraft Gas Turbine Exhaust Smoke Measurement*; SAE: Warrendale, PA, 1970; SAE 1970, SAE Aerospace Recommended Practice ARP 1179.

(18) *Procedure for the Continuous Sampling and Measurement of Gaseous Emissions from Aircraft Turbine Engines*; SAE: Warrendale, PA, 1971; SAE 1971, SAE Aerospace Recommended Practice ARP 1256.

(19) DeWitt, M. J.; Corporan, E.; Graham, J.; Minus, D. Effects of Aromatic Type and Concentration in Fischer−Tropsch Fuel on Emissions Production and Material Compatibility. *Energy Fuels* **2008**, *22* 2411–2418.

(20) Moses, C. A.; Stavinoha, L. L.; Roets, P. *Qualification of SASOL Semi-Synthetic Jet A-1 as Commercial Jet Fuel,* Southwest Research Institute, San Antonio, TX, 1997; Report No. SwRI 8531.

(21) Bauldreay, J. M.; Heins, R. J.; Smith, J. Synthetic Jet Fuels and Their Role in the Future. *Proceedings of the 8th International Conference on Stability and Handling of Liquid Fuels*, Steamboat Springs, CO, Sept 2003.

(22) Kinder, J. D. *Evaluation of Bio-Derived Synthetic Paraffinic Kerosene (Bio-SPKs)*; Draft ASTM Research Report to Subcommittee J on Aviation Fuels, Item Number 05, 2010.

(23) DeWitt, M. J.; Striebich, R.; Shafer, L.; Zabarnick, S.; Harrison, W. E., III; Minus, D. E.; Edwards, T. Evaluation of Fuel Produced via the Fischer-Tropsch Process for Use in Aviation Applications. *Proceedings of the AIChE Spring National Meeting*, 2007; paper 58b.

(24) Young, T. M. Simplified Methods For Assessing The Impact Of Fuel Energy Content On Payload-Range. *26th Congress of International Council of the Aeronautical Sciences*, Anchorage, Alaska, Sept 2008; AIAA paper 8857.

(25) McMall, M. The Status of an Interlaboratory Study to Verify the Ability of D2425 to Determine the Hydrocarbon Composition of Synthetic Paraffinic Kerosene Fuel. Presented at *Coordinating Research Council Aviation Fuels Meeting*, Alexandria, VA, May 3−6, 2010.

(26) Striebich, R.; Shafer, L.; DeWitt, M. J.; West, Z.; Edwards, T.; Harrison, W. E., III *Dependence of Fuel Properties During Blending of Iso-Paraffinic Kerosene and Petroleum-Derived Jet Fuel*; USAF AFRL technical report, AFRL-RZ-WP-TR-2009-2034, 2009.

(27) Heneghan, S. P.; Zabarnick, S.; Ballal, D. R.; Harrison, W. E. JP-8 + 100: Development of a Thermally Stable Jet Fuel. *J. Energy Resource Technol.* **1996**, *118*, 170–179.

(28) Corporan, E.; DeWitt, M. J.; Klingshirn, C.; Striebich, R. DoD Assured Fuels Initiative: B-52 Aircraft Emissions Burning a Fischer-Tropsch/JP-8 Fuel Blend. *10th International Conference on Stability and Handling of Liquid Fuels*, Tucson, Arizona, Oct 2007.

(29) Corporan, E.; DeWitt, M. J.; Belovich, V.; Pawlik, R.; Lynch, A. C.; Gord, J. R.; Meyer, T. R. Emissions Characteristics of a Turbine Engine and Research Combustor Burning a Fischer−Tropsch Jet Fuel. *Energy Fuels* **2007**, *21* (5), 2615–2626.

115

(30) Saleem, M.; Asfour, A. F. A.; De Kee, D.; Harrison, B. Diffusion of Organic Penetrants through Low Density Polyethylene (LDPE) Films: Effect of Size and Shape of Penetrant Molecules. *J. Appl. Polym. Sci.* **1989**, *37* (3), 617–625.

(31) Mathai, A. E.; Thomas, S. Transport of Aromatic Hydrocarbons through Crosslinked Nitrile Rubber Membranes. *J. Macromolec. Sci., Phys.* **1996**, *B35* (2), 229–253.

(32) Graham, J. L.; Striebich, R. C.; Myers, K. J.; Minus, D. K.; Harrison, W. E. Swelling of Nitrile Rubber by Selected Aromatics Blended in a Synthetic Jet Fuel. *Energy Fuels* **2006**, *20*, 759–765.

(33) Flory, P. J. *Principals of Polymer Chemistry*; Cornell University Press: Ithaca, NY, 1953.

(34) Schwarzenbach, R. P.; Gschwend, P. M.; Imboden, D. M. *Environmental Organic Chemistry*, John Wiley and Sons, Inc.: New York, NY, 1993.

116

Appendix F. Effect of Aviation Fuel Type on Pyrolytic Reactivity and Deposition Propensity under Supercritical Conditions

Effect of Aviation Fuel Type on Pyrolytic Reactivity and Deposition Propensity under Supercritical Conditions

Matthew J. DeWitt,*,[†] Tim Edwards,[‡] Linda Shafer,[†] David Brooks,[†] Richard Striebich,[†] Sean P. Bagley,[§] and Mary J. Wornat[§]

[†]University of Dayton Research Institute, 300 College Park, Dayton, Ohio 45469, United States

[‡]Air Force Research Laboratory, Fuels Branch AFRL/RZPF, Wright-Patterson AFB, Ohio 45433, United States

[§]Department of Chemical Engineering, Louisiana State University, Baton Rouge, Louisiana 70803, United States

ABSTRACT: Development of reusable liquid-hydrocarbon-fueled hypersonic vehicles requires improved understanding of the effect of chemical composition on the controlling reaction chemistry and deposition propensity as the fuel is used to cool the system. In this effort, supercritical pyrolytic stressing studies were performed using two petroleum-derived fuels and a Synthetic Paraffinic Kerosene (SPK) comprised predominantly of normal and branched paraffins. All fuels decomposed via free radical pathways with high yields of unsaturates and lower molecular weight products consistent with pyrolysis at high pressures and moderate temperatures. However, the SPK was significantly more reactive than the petroleum-derived fuels due to a lack of efficient hydrogen donors that act to terminate chain reactions (higher net propagation rate). High-pressure liquid chromatography was used to identify and quantify polycyclic aromatic hydrocarbons (PAH) in the stressed fuels, conclusively determining that these are produced during thermal stressing. A notable observation was the presence of PAH during SPK stressing, as the neat fuel did not contain cyclic precursors for growth to PAH. During stressing with stainless-steel tubing, the formation of filamentous deposits via metal-catalyzed reactions of stressed fuel components with reactor surfaces was observed for all fuels studied. However, the SPK fuel exhibited a much higher pyrolytic deposition rate, which was attributed to higher lateral growth rates of surface filaments via noncatalytic free radical addition pathways. The PAH formed during SPK stressing are indicators of the highly reactive intermediates prone to participating in the surface coke addition pathways. Studies blending benzene with the SPK indicated that low PAH solubility in the paraffinic fuel is not the dominant cause for the high deposition propensity. Testing with the petroleum-derived fuels showed that metal sulfide filament formation can occur under endothermic conditions, and higher fuel sulfur content can increase carbon deposition propensity. Studies with surface passivated tubing (Silcosteel) suppressed filamentous carbon formation and rendered a substantial reduction in SPK deposition to levels similar to the petroleum-derived fuels. Overall, these studies provided guidance regarding the controlling chemistry during supercritical pyrolysis of current and potential synthetic hydrocarbon fuels and insight into prevalent deposition pathways.

■ INTRODUCTION

A major complication to the development and implementation of liquid-hydrocarbon-fueled hypersonic vehicles is achieving sufficient heat sink capability in the fuel, which is used to regeneratively cool the vehicle and engine structure and subsystems. One approach, termed an "Endothermic Fuel," achieves high levels of heat sink by supplementing the "sensible heating $(C_p \Delta T)$" via deliberate bulk endothermic (e.g., heat-absorbing) reactions of the fuel, such as thermal (e.g, dehydrogenation) and/or catalytic cracking.[1−3] Current demonstrated endothermic capability is approximately 1500 BTU/lb at fuel temperatures of approximately 700 °C for a 15-min duration.[2,3] A major limitation to viable implementation of endothermic fuels is the undesirable formation of carbonaceous deposits (also known as "coking"). The deposition can reduce fuel flow, increase resistance to heat transfer, and foul injector nozzles. Ideally, the fuel would be selectively converted to low molecular weight products, such as ethylene and propylene, which are favorable for both overall heat sink and combustion efficiency, without forming high molecular weight deposits.[3] However, condensed and supercritical phase pyrolytic reaction pathways produce a wide range of products, with smaller paraffins/olefins and aromatics being predominant products, all of which can form carbonaceous deposits.[2,4−10]

There are varying types of complex deposit mechanisms which have been observed during gas, condensed, and supercritical pyrolysis of hydrocarbons. It is generally accepted that there are three basic mechanisms relevant to deposit formation under these reaction regimes.[3,10−23] These include the formation of filamentous coke via catalytic reactions with surface metals, free radical growth reactions between bulk phase components and surface coke (noncatalytic mechanism), and the production of condensation (amorphous) coke via formation of polycyclic aromatic hydrocarbons (PAH) in the bulk phase which subsequently condense on tubing surfaces. The initial filament formation has been shown to involve metal-catalyzed reactions of fuel components with the reactor surfaces, primarily by nickel and iron, resulting in the formation of metal carbides as intermediates.[12] The metal atoms are extracted from the surfaces

118

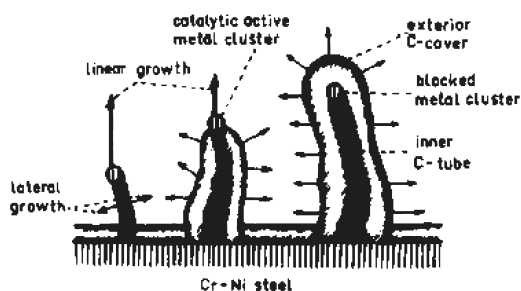DISTRIBUTION STATEMENT A: Approved for public release. Distribution is unlimited.

Figure 1. Comparison of linear and lateral growth mechanisms of carbon filaments.[13]

and catalyze linear filament growth while remaining at the tips of filaments. Sulfur-containing compounds can also promote production of metal sulfide filaments and can potentially have a significant effect on coke formation rates.[18,21−24] Once formed, the filaments can undergo lateral growth (thickening) via free radical reactions between bulk phase components and surface coke; this mechanism has been likened to chemical vapor deposition (CVD) processes.[22] This noncatalytic mechanism can result in significant growth of the filamentous deposits and blockage of the extracted metal atoms. A schematic of the formation of filamentous coke formation via catalytically assisted decomposition (linear growth) and free radical growth reactions (lateral growth) proposed by Kopinke and colleagues,[13] which is consistent with the mechanism discussed by Albright and Marek,[12] is shown in Figure 1.

In general, it is believed that formation of PAH is a key precursor to amorphous coke formation, with PAH concentrations increasing rapidly with pressure and extent of fuel conversion.[25,26] The impact of this mechanism on overall deposition levels becomes more prevalent at higher reaction temperatures and extents of reaction.[3] The formation of aromatics and PAH have been hypothesized to potentially have a dual role, as actual amorphous coke precursors and as an indicator for short living, highly reactive intermediates which participate in coke formation (via free radical growth).[15] Detailed product analyses have confirmed extensive PAH formation during supercritical fuel pyrolysis,[25,27−33] but the PAH distribution is substantially different from that observed at the higher temperatures and lower pressures associated with combustion.[34−38] Thus, deposit formation in supercritical fuel pyrolysis superficially resembles soot formation during combustion in that PAH are believed to be primary intermediates or indicators in the formation of high molecular weight carbonaceous products, but the controlling reactions and growth mechanisms appear to be different in the two reaction environments.

The use of alternative (nonpetroleum derived) aviation fuels derived from coal, natural gas, and biological feedstocks has received significant attention recently.[39] Alternative fuels provide a potential domestic fuel source which can increase energy and economic security. The majority of the initial efforts have focused on Synthetic Paraffinic Kerosene (SPK) derived from the Fischer−Tropsch (FT) process.[40,41] These have resulted in the approval of SPK as a blend feedstock of up to 50% by volume with both commercial Jet A/Jet A-1 (per ASTM D7566[42]) and military JP-8 (MIL-DTL-83133G[43]) fuels, provided the final fuel specification properties are satisfied. Although the potential

feedstock sources (including biological) for the production of alternative fuels are rapidly increasing, near-term drop-in blend candidates will have chemical compositions very similar to currently approved SPKs. As synthesized, neat SPK exhibits excellent thermal-oxidative stability with minimal oxidative deposition propensity,[39,40] however, the behavior under pyrolytic conditions is unknown. Previous studies performed with single-component model compounds and blends have shown differences in relative reactivity and deposition propensity depending on fuel structure. For conditions representative of steam cracking coils (>800 °C, gas phase), studies were performed to investigate the effect of fuel structure on coke formation rates.[3,13,15−17] These were performed by adding small (<0.1 wt %) amounts of a specific ^{14}C-labeled component to a naphtha stream and demonstrated that coking propensity as a function of fuel structure is *n*-paraffins < *iso*-paraffins < olefins ≈ cycloparaffins < aromatics < PAH. However, it is difficult to extrapolate this behavior to expected performance of multicomponent mixtures under aircraft fuel system conditions. One key difference is the high pressure of aircraft fuel systems, which (in combination with the lack of steam dilution) leads to dramatically higher hydrocarbon concentrations in aircraft endothermic fuel systems relative to steam cracking furnaces. It is generally recognized that coking rates are proportional to the hydrocarbon concentration, indicating the key challenge coking presents in endothermic fuel systems.

Due to the need for improved understanding of the effect of fuel type on the relative endothermic reactivity and deposition propensity and the interest in alternative fuels, experimental studies and analyses were performed with the goal to identify major differences in the controlling reaction and deposition mechanisms. The studies herein were performed using two specification petroleum-derived jet fuels (a Jet A-1 and JP-8) and an SPK which conforms to both commercial and military neat specification requirements. Studies with the neat SPK were of particular interest as this fuel is solely comprised of normal, *iso*-, and cycloparaffins and does not contain aromatic compounds or heteroatoms. The following sections will discuss the experimental studies and analyses performed, primary results, and conclusions.

■ EXPERIMENTAL SECTION

Fuels. Conventional jet fuels fall into a broad class of distillate hydrocarbon fuels termed kerosenes, which have a carbon distribution from approximately C_7 to C_{18} and an average molecular weight of approximately 150.[44,45] Petroleum-derived fuels consist of a variable mixture of many hundreds of hydrocarbons, which can be broadly separated into chemical classes such as paraffins, cycloparaffins, and aromatics. Varying the specific constituents and total concentrations in the compound classes, and the presence of trace compounds (e.g., heteroatoms), will strongly affect the physical properties of the formulated fuels and their reactivities during implementation. Currently approved SPK fuels produced via FT synthesis are required to be comprised solely of paraffinic compounds with physical properties which conform to fuel specification requirements, including a volatility range similar to a typical jet fuel.[42,43] However, the specific SPK chemical composition can vary substantially and still satisfy the specification requirements. Differences in composition may result in significant differences in the pyrolytic reactivity and deposition propensity.

The fuels used in this study were selected to provide a comparison between typical specification jet fuels and an FT-derived SPK. The specification fuels used were a Jet A-1 and JP-8. The major difference in these was that the Jet A-1 had very low total sulfur content (<90 ppmV) while that in the JP-8 (1400 ppmV) was more consistent with typical levels.[46] In addition, analysis via high-pressure liquid chromatography[47] showed the phenolic polars content of the JP-8 was ~400 mg/L as compared to only ~30 mg/L for the Jet A-1. It has previously been shown that fuels which have a low heteroatom and phenolic polar content typically exhibit excellent thermal-oxidative stability.[47,48] The JP-8 fuel was treated with the required military specification fuel additives; namely, Fuel System Icing Inhibitor (di-ethylene glycol monomethyl ether), Static Dissipater Additive, and the Corrosion Inhibitor/Lubricity Improver (CI/LI). The Jet A-1 was also treated with CI/LI (~9 ppmV) and artificial antioxidant (~18 ppmV) for storage stability; the extremely low concentrations of these additives in the Jet A-1 are not expected to
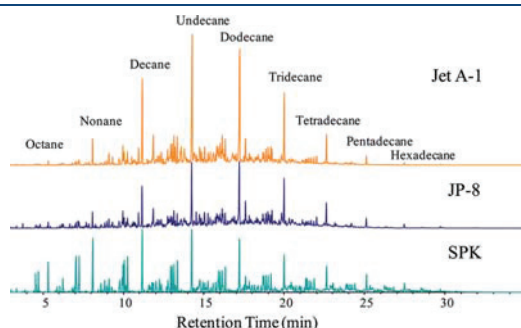

Figure 2. Gas chromatograms of fuels.

significantly affect the pyrolytic reaction chemistry of the bulk fuel. The SPK fuel was derived from natural gas by Syntroleum Corporation, and was used in the first certification of alternative fuel blends with JP-8.[40,41] The SPK is comprised predominantly of normal and branched paraffins, with the possible inclusion of a low quantity of cycloparaffins.[49,50] The latter is uncertain due to difficulty in quantifying this chemical class in highly branched paraffinic mixtures. The SPK has a higher hydrogen content than a typical petroleum-derived fuel (15.4% by mass vs ~13.8%),[51] with negligible sulfur and phenolic polar content. The fuels were extensively characterized for chemical class and primary species composition to assist with interpretation of the experimental results and to deconvolute the controlling reaction mechanism. Gas chromatograms of the various fuels, with the n-paraffins labeled, are shown in Figure 2. As shown, the fuels had similar boiling point distributions with individual n-paraffins comprising a significant portion of the composition. The total n-paraffin contents for the fuels were 24.5% for Jet A-1, 12% for JP-8, and 18% for SPK. Hydrocarbon type analyses of the fuels performed using ASTM D6379 and ASTM D2425 are shown in Table 1; the average Jet A-1 and JP-8 class compositions for a world fuel survey performed in 2006[46] are also shown for comparison. Although the JP-8 and Jet A-1 fuels used in this study vary slightly from the average fuel properties, they were within typical property ranges for specification fuels. The degree of branching in SPKs can vary significantly depending on the feedstock, intermediate product, and upgrading operations employed.[39] Gas chromatography/mass spectrometry analysis indicated that the SPK used in the present study had a mild degree of branching, with the majority comprised of monomethyl substituted n-paraffins.

Supercritical Pyrolysis Studies. Supercritical pyrolytic reactivity and decomposition characteristics of the test fuels were

Table 1. Hydrocarbon Type Analysis (ASTM D2425) and Aromatic Species Analysis (ASTM D6379) for Fuels Evaluated[46]

	present study			world fuel survey	
	Jet A-1 (POSF 4877)[a]	JP-8 (POSF 4177)[a]	SPK (POSF 4820)[a]	Jet A-1 ($n = 33$)[b]	JP-8 ($n = 10$)[b]
	D2425 (vol %)				
paraffins	57	44	97	54	54
cycloparaffins (noncondensed)	20	27	3	19	18
dicycloparaffins (condensed)	4	10	<1	7	7
tricycloparaffins (condensed)	<1	1	<1	1	2
alkylbenzenes	15	9	<0.5	14	14
indans and tetralins	4.2	6.5	<0.5	4.2	4.8
indenes and C_nH_{2n-10}	<0.5	<0.5	<0.5	<0.5	<0.5
naphthalene	<0.5	<0.5	<0.5	<0.5	<0.5
naphthalenes	<0.5	1.1	<0.5	1.3	1.6
acenaphthenes	<0.5	<0.5	<0.5	<0.5	<0.5
acenaphthylenes	<0.5	<0.5	<0.5	<0.5	<0.5
tricyclic aromatics	<0.5	<0.5	<0.5	<0.5	<0.5
total	100	100	100	100	100
	D6379-HPLC (vol %)				
monocyclic aromatics	18.1	15.4	<0.2	18.0	19.1
dicyclic aromatics	0.3	1.1	<0.2	1.6	1.9
total aromatics	18.4	16.5	<0.2	19.4	21.0
total saturates	81.6	83.5	>99.8	80.6	79.0

[a] Internal Fuel identification number. [b] Number of discrete fuels in analysis.

evaluated using a single-tube flow reactor system located at Wright-Patterson Air Force Base (WPAFB). This system has previously been used to evaluate thermal stability characteristics of fuels under both oxidative and pyrolytic conditions.[9,52,53] Fuel is placed into a test reservoir which can be sparged with nitrogen prior to thermal stressing. A single-zone Lindberg furnace is used to provide the required heat input to promote the desired reaction chemistry during testing. The furnace has a 91.4-cm actively heated zone with 13.4-cm insulating adapters at each end. The outer wall temperature profile of the reaction tube is measured using thermocouples (TC) strap-welded at various locations. The bulk fuel temperature is measured using a TC inserted into the outlet flow approximately 17.8 cm downstream of the actively heated zone. Following thermal stressing, the fuel is cooled with a counter-current heat exchanger and passed through a 7-μm sintered filter element to remove any entrained solids. The system pressure ($\pm$3% of set point), which is maintained by a back-pressure valve, is reduced and stressed liquid fuel and gaseous products are collected for off-line analysis.

Pyrolytic stability studies were conducted using a 127cm long, 0.318 cm o.d., 0.216 cm i.d. reaction tube, a reaction pressure of 4.9 MPa, and a standard volumetric inlet flow rate of 10 mL/min. Studies were performed using either 316 stainless steel (316ss) or Silcosteel reaction tubes. The Silcosteel tube is a stainless-steel tube whose inner surface has a commercial vapor-deposited silica coating which has been shown to substantially reduce filamentous carbon deposition.[3] Prior to installation, the reaction tubes were washed with methanol and acetone in sequence to remove any residual contaminants. The test fuel was saturated with air (dissolved oxygen present at ~50−70 ppmV) allowing for investigation of both the relative oxidative and pyrolytic stability during testing. The surface temperature profile was sufficient to prevent merging of the oxidative (<300 °C) and pyrolytic (>450 °C) deposition regimes. Fuel flow was initiated to the reactor under ambient temperature to achieve the target reaction pressure followed by a ramped temperature increase of the furnace. Stressing was conducted for a total test time of either 5 or 6 h; reaction time was initiated when the fuel temperature reached 90% of the pyrolytic reactivity onset temperature. Liquid and gaseous products were collected for off-line analysis; the gaseous products were collected using Tedlar sampling bags. Upon completion of the test duration, the furnace was opened to rapidly quench the reaction chemistry. During this study, the furnace temperature was varied to evaluate from the regime where pyrolytic reactivity is initiated to approximately 30% gaseous product formation by volume. Using computational fluid dynamics (CFD) with temperature dependent fuel properties and the reactor temperature profile, the fluid residence time and flow nature were characterized. The total residence time in the reactive zone was on the order of 8 s of which approximately 2−3 s was in the pyrolytic regime (>450 °C). Fluid flow was laminar at the inlet and transitioning to the turbulent regime (Re 3000−5000) in the pyrolytic zone. Following testing, the reaction tube was removed and sectioned into 5.1-cm segments which were washed in *n*-hexane to remove residual fuel and dried in a vacuum oven at 100 °C for a minimum of 12 h. The total carbon deposition on the internal surface of each segment was determined using a LECO RC-412 multiphase carbon determinator ($\pm$3% accuracy). Selected tube segments were cross-sectioned to allow for deposit morphology analysis using a JEOL JSM-6460LV scanning electron microscopy (SEM) which was also equipped with an energy dispersive spectrometer (EDS).

Gaseous and Liquid Product Quantitation. Analysis of the neat and stressed liquid fuel and gaseous products was performed to provide insight of the controlling reaction chemistry, including the conversion of parent fuel components and relative product yields. Analysis for mono- and dicyclic aromatic hydrocarbon content in the unstressed and stressed fuels was performed using ASTM method D6379. In this method, standards containing mono- and dicyclic aromatics were used to calibrate the HPLC (Agilent model 1100). Both standards and samples were diluted to the same level (1:50) in hexane and the refractive index peak areas were used to quantify the aromatic concentrations in volume percent ($\pm$10% relative accuracy). Quantitative analyses of primary fuel constituents and major products were performed using a gas chromatograph (Agilent model 6890) combined with a mass spectrometer (GC/MS) and a flame ionization detector (GC/FID). Calibration was performed with multicomponent standards to encompass the range and types of products formed ($\pm$15% relative accuracy). For gaseous products, hydrogen concentration was quantified directly with a gas chromatograph/thermal conductivity detector (GC/TCD) (100-μL injection volume) using a multipoint calibration curve. Gaseous hydrocarbon products were quantified using GC/FID (10-μL injection volume). Standards of C_1−C_6 paraffins and α-olefins were used to determine respective retention times. Quantitation was performed assuming FID response is proportional to the total carbon number while correcting for total hydrogen content.[54] The validity of this approach was verified using selected gaseous calibration standards. Quantitation accuracy was estimated at $\pm$5% for each component. Greater than 90% of the total area response was attributable to identified compounds.

High-pressure liquid chromatography (HPLC) with diode-array ultraviolet−visible (UV) absorption detection was used to identify and quantify PAH products in the stressed fuels. As detailed elsewhere in the analyses of other fuel product mixtures,[27,55] products were separated on a reversed-phase HPLC C_{18} column with a time-programmed sequence of the mobile-phase solvents water, acetonitrile, and dichloromethane. UV spectroscopy was employed to determine the isomer-specific identities of each of the separated product components.

Normal-phase HPLC with diode-array UV detection was used to quantify total concentrations of two-, three-, and four-ring PAH products in the stressed liquid fuel product mixtures by integrating the average-UV-absorbance chromatographic peak area corresponding to each PAH ring-number group. Fraction-delineating retention times and ring-number-specific response factors were determined by calibration with appropriate PAH reference standards. PAH quantities, initially measured in terms of mass per volume of total liquid product, were adjusted for liquid to gas conversion and reported in terms of mass per volume of initial fuel.

RESULTS AND DISCUSSION

Chemical Reactivity of Fuels. The pyrolytic reactivities of the SPK, Jet A-1, and JP-8 fuels were evaluated by the extent of low-molecular weight species production, parent fuel component conversion, and relative product yields and selectivities. Comparison of the chemical reactivity for a complex, multicomponent reactant is difficult due to the numerous reaction pathways and products formed. For thermal decomposition chemistry, metrics such as conversion to low molecular weight products (not present in the parent fuel) are typically used for reactivity comparison and

Table 2. Conversion and Deposition Results for Single-Pass Thermal Decomposition Studies of Varying Fuel Composition at 700 psig for 6 h Test Duration

fuel	furnace temperature (°C)	outlet temperature (°C)	liquid to gas conversion (vol %)	heated zone deposition (μg)		deposition rate (μg-deposit/g-fuel)		notes
				oxidative	pyrolytic	oxidative	pyrolyic	
Jet A-1	770	566	6.3	5.8×10^1	3.06×10^2	0.02	0.11	
	785	577	10.0	1.1×10^1	7.11×10^2	0.00	0.25	
	785	577	11.3	1.4×10^1	7.45×10^2	0.00	0.26	
	785	572	11.3	1.3×10^1	6.53×10^2	0.00	0.23	
	800	588	17.5	1.7×10^1	1.38×10^3	0.01	0.48	
	815	603	27.5	5.3	2.24×10^3	0.00	0.94	5 h test
Silcosteel	785	581	13.1	3.1×10^2	1.91×10^3	0.11	0.67	
Silcosteel	800	589	20.6	2.6×10^2	2.62×10^3	0.09	0.91	
Silcosteel	800	604	31.9	3.6×10^2	6.28×10^3	0.13	2.2	
SPK	740	533	1.3	n.d.	n.d.	n.d.	n.d.	
	755	545	6.3	n.d.	1.84×10^4	n.d.	6.76	
	770	556	12.6	n.d.	7.48×10^4	n.d.	27.5	
	770	559	11.9	n.d.	9.00×10^4	n.d.	33.1	
	770	557	12.5	5.5×10^1	5.81×10^4	0.02	21.4	
	785	568	17.5	1.6	9.68×10^4	0.00	35.5	
	800	579	24.4	4.2×10^1	1.22×10^5	0.02	44.9	
	810	588	30.0	1.2	1.19×10^5	0.00	52.7	5 h test
Silcosteel	770	563	16.3	7.7×10^1	1.41×10^3	0.03	0.52	
Silcosteel	785	570	21.3	5.1×10^1	2.13×10^3	0.02	0.78	
Silcosteel	800	582	25.0	9.4×10^1	2.78×10^3	0.03	1.02	
Silcosteel	800	583	31.3	5.3×10^1	3.27×10^3	0.02	1.20	
	770	556	12.5	5.6×10^1	5.79×10^4	0.02	21.3	10% benzene
	785	572	21.3	4.1×10^1	8.66×10^4	0.02	31.8	10% benzene
JP-8	770	558	4.1	2.15×10^3	1.67×10^3	0.73	0.57	
	770	564	6.3	1.78×10^3	2.28×10^3	0.61	0.78	
	770	556	7.3	2.10×10^3	2.76×10^3	0.72	0.94	
	785	567	11.3	1.69×10^3	4.21×10^3	0.58	1.4	
	800	581	18.8	2.15×10^3	8.42×10^3	0.73	2.9	
	810	594	23.1	2.24×10^3	1.07×10^4	0.76	3.6	
Silcosteel	770	567	8.1	1.30×10^2	1.55×10^3	0.04	0.53	
Silcosteel	785	571	10.6	1.22×10^2	4.34×10^3	0.04	1.5	
Silcosteel	800	586	21.9	1.38×10^2	1.30×10^4	0.05	4.4	

[a] Tests performed with 316 ss unless noted for Silcosteel. [b] n.d. denotes not detected/below detection limit.

determination of pseudokinetic measurements.[56,57] Accordingly, the volumetric liquid to gas conversion at standard conditions, defined as the ratio of the difference in the standard volumetric inlet and outlet liquid flow rates to the inlet flow rate, can provide substantial guidance regarding the relative reactivity of the respective fuels and is readily measured during testing (accuracy of $< \pm 1\%$). The gaseous product formation can be also determined on a mass basis, which requires the density for both neat and stressed fuel samples. Regardless of the approach, it should be noted that it can require multiple reaction steps for a high molecular weight component (e.g., n-hexadecane) to form gaseous products, resulting in a slight underestimation of the true extent of reaction at lower conversions. Therefore, detailed analysis of the stressed fuel components further assists to elucidate the overall pyrolytic reactivity and chemistry.

For the testing performed in this study, a compilation of the test conditions, measured volumetric liquid to gas conversion, oxidative and pyrolytic deposition quantities, and calculated deposition rates for the three fuels evaluated are shown in Table 2. A comparison of the volumetric liquid to gas conversion as a function of the bulk fuel outlet temperature for testing with air-saturated fuel and 316ss tubing is shown in Figure 3. The measured outlet temperature is used since the axial fuel temperature is varying throughout the reaction tube. The outlet temperature is slightly lower than the maximum fuel temperature achieved since it is measured downstream of the reactor outlet insulation. The conversion values based on liquid mass recovery were also calculated, but were only slightly higher (between 0 and 2%) and exhibited the same relative trends. It can be clearly observed in Figure 3 that the SPK was more prone to thermal
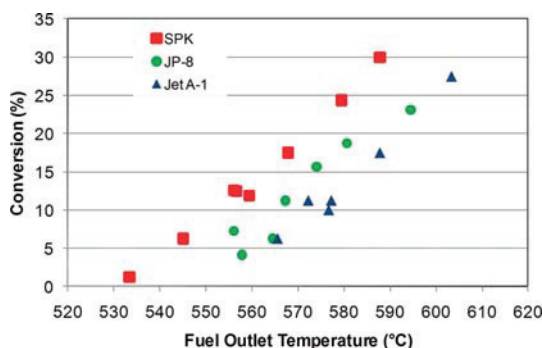
Figure 3. Comparison of volumetric liquid to gas conversion as a function of bulk outlet fuel temperature for varying fuel composition.
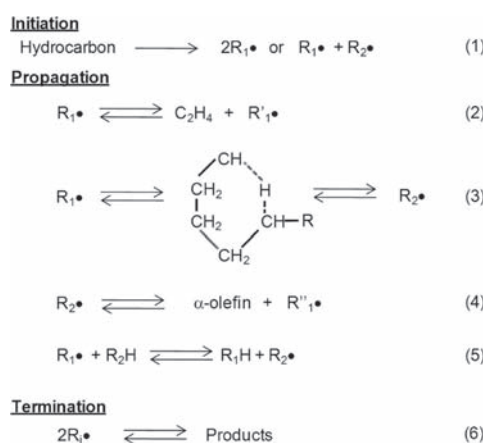

Figure 4. Simplified free radical mechanism for supercritical pyrolysis.

Figure 5. Comparison of JP-8 liquid compositional changes for varying extents of thermal stressing. Temperature is the measured fuel outlet, liquid to gas conversion in parentheses.

cracking than either the Jet A-1 or JP-8, with approximately a $10-20$ °C reduction in outlet temperature to achieve a similar extent of conversion. The Jet A-1 and JP-8 showed comparable pyrolytic reactivity during testing. The increase in reactivity for the SPK will result in an earlier endotherm onset as compared to the petroleum-derived fuels, but the overall endotherm (not directly measured) will be dependent on the specific products formed during stressing.

The pyrolytic decomposition of the fuels proceeds via free radical chemistry, which has been extensively described in the literature.[4−8,58−60] A simplified reaction mechanism is shown in Figure 4. Radicals are initially produced via fission of C−C bonds; these can be either primary ($R_1\bullet$), secondary ($R_2\bullet$), or other (e.g., tertiary, benzylic, etc.) depending upon the composition of the fuel. The radicals propagate via unimolecular or bimolecular reactions; the rates and selectivities of these are dependent on both the reaction conditions and fuel chemistry. Unimolecular reactions include β-scission of primary radicals to form ethylene and a smaller primary radical (eq 2), intramolecular hydrogen abstraction which favors formation of a secondary radical from a primary (eq 3), and β-scission of a secondary radical to produce an α-olefin and smaller primary radical (eq 4). Radical addition to olefins can also occur (reverse of eq 2 or 4) resulting in the formation of a larger product. Bimolecular reactions proceed primarily via intermolecular hydrogen
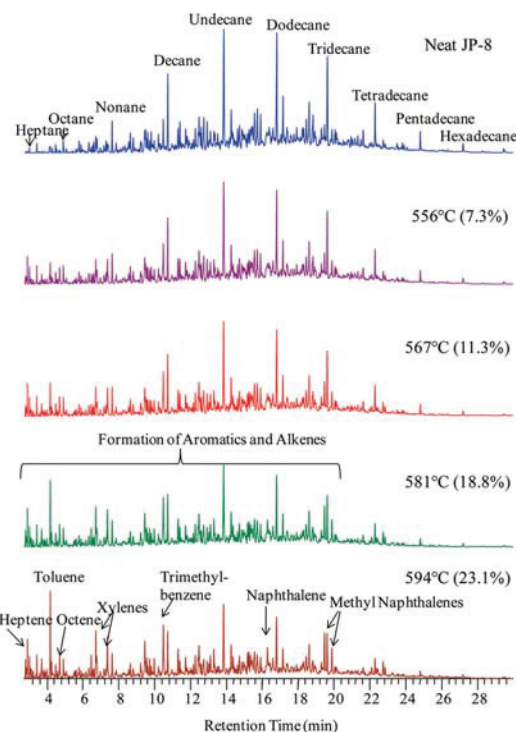
abstraction (eq 5) resulting in the formation of a paraffin (or saturate) and secondary radical. Termination occurs via radical recombination or disproportionation. The overall reactivity of the parent fuel is influenced by the rate of radical initiation and strongly affected by the net propagation rate. Compounds which can act as hydrogen donors and form stable radicals (e.g., benzylic) or can readily produce an unsaturate (e.g., cycloparaffins) can substantially reduce the overall reaction rate.[57,60−63] As discussed earlier, the SPK is comprised predominantly of normal and branched paraffins while the petroleum fuels contain functionalities which act as effective hydrogen donors and suppress the reactivity of the paraffinic compounds.[60] As a result, the SPK will have a higher kinetic chain length (ratio of propagation to initiation) during stressing. Although there were differences between the absolute concentrations of the respective chemical classes in the Jet A-1 and JP-8 (see Table 1), these were not sufficient to result in a considerable difference in overall pyrolytic reactivity of the fuels. This is most likely due to the similarities in the specific types of compounds in each chemical class and the relative overall concentrations (as compared to the SPK). It should be noted that the rate of initiation in the petroleum-derived fuels is most likely higher than the SPK due to the presence of weaker C−C and heteroatomic bonds, but it is the increased propagation rate in the SPK fuel which results in higher overall reactivity.

Gaseous and Liquid Product Analyses. Detailed product analyses were performed on both the gaseous and liquid products of the stressed fuels to assist with understanding the reaction

123

Table 3. Comparison of Molar Concentrations of Primary Gaseous Products as a Function of Conversion and Fuel Type

	Jet A-1				SPK				JP-8		
outlet temperature (°C)	566	577	588	603	559	568	579	588	567	581	594
volumetric conversion (%)	6.3	11.3	17.5	27.5	11.9	17.5	24.4	30.0	11.3	18.8	23.1
hydrogen	0.032	0.036	0.029	0.039	0.009	0.013	0.011	0.019	0.046	0.031	0.043
methane	0.209	0.207	0.205	0.226	0.156	0.160	0.170	0.188	0.226	0.229	0.265
ethane	0.187	0.170	0.171	0.167	0.169	0.162	0.153	0.159	0.161	0.158	0.165
ethylene	0.144	0.128	0.128	0.122	0.129	0.130	0.127	0.134	0.105	0.121	0.112
propane	0.125	0.115	0.114	0.102	0.128	0.119	0.103	0.098	0.115	0.100	0.099
propylene	0.160	0.159	0.165	0.154	0.183	0.181	0.169	0.168	0.145	0.152	0.140
n-butane	0.030	0.032	0.031	0.027	0.038	0.036	0.032	0.028	0.032	0.024	0.023
2-butene	0.006	0.010	0.012	0.013	0.010	0.012	0.013	0.013	0.011	0.013	0.012
1-butene	0.037	0.035	0.043	0.038	0.053	0.054	0.051	0.046	0.037	0.037	0.031
iso-Butylene	0.019	0.022	0.025	0.023	0.035	0.036	0.036	0.032	0.029	0.030	0.026
n-pentane	0.006	0.008	0.008	0.007	0.009	0.009	0.010	0.008	0.008	0.006	0.006
1-pentene	0.011	0.015	0.015	0.014	0.017	0.019	0.021	0.018	0.012	0.013	0.010
butadiene	0.002	0.003	0.003	0.003	0.003	0.003	0.003	0.003	0.002	0.004	0.002

chemistry. As expected during pyrolytic decomposition of hydrocarbons at elevated pressures and moderate temperatures, significant conversion of the parent fuel to lower molecular weight and unsaturated products was observed.[4,5] As an example, Figure 5 shows GC/MS chromatograms comparing JP-8 liquid compositional changes for varying extents of reaction. The analyses clearly show that the higher molecular weight species are thermally decomposed to lighter products, with selective conversion of saturated compounds, such as *n*-paraffins, to olefinic and aromatic compounds (discussed below).

The gaseous products were primarily comprised of C_1-C_4 paraffins and olefins, with moderate yields of H_2. The molar concentrations of the primary products in the gas phase for pyrolytic stressing using the 316ss tubing are shown in Table 3. In addition, a comparison of the C_1-C_3 and H_2 molar concentrations for the varying fuel types at a volumetric conversion of ~11% is shown in Figure 6. The gaseous species concentrations and trends for each fuel were identical for comparable testing with Silcosteel tubing. As shown in Table 3 and Figure 6, the petroleum-derived fuels most selectively produced methane, followed by ethane and propylene. These trends are consistent with similar thermal decomposition testing of kerosene fuels in flow reactor systems at elevated pressure and moderate temperatures.[63,64] Although the petroleum-derived fuels did have varying concentrations of the primary chemical classes shown in Table 1, the selectivities of the gaseous products were very similar. This observation indicates that the primary decomposition pathways for these fuels to form low molecular weight products are similar and that the chemical class effect is minimal provided the fuels have comparable levels.

A notable observation during SPK testing was that the selectivity to propylene and 1-butene was increased with lower methane and minimal H_2. The selectivity to methane did increase for all three fuels with higher overall extent of reaction, possibly due to an increased relative production rate via consumption of primary products. The gaseous product trends for the SPK are consistent with those for similar testing with normal paraffinic mixtures[65−67] and long chain paraffin pyrolysis.[4,5,7] The reduction in H_2 yields for the SPK is most likely related to the inherent types of carbon−hydrogen (C−H) bonding as
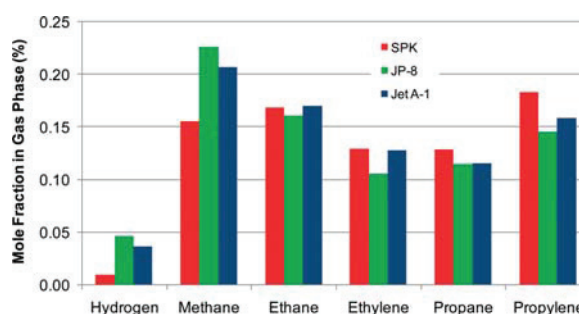
Figure 6. Comparison of primary gaseous products for a volumetric liquid to gas conversion of ~11% as a function of fuel type.

compared to the petroleum-derived fuels. Molecular hydrogen is produced primarily via an intermolecular hydrogen abstraction by a hydrogen radical, which is produced via fission of C−H bonds. Since the SPK is comprised of normal and branched paraffins, all C−H bonds are 1° (101 kcal/mol), 2° (98.5 kcal/mol), or 3° (96.5 kcal/mol). These bonds are substantially stronger than 2° (82 kcal/mol) and 3 °C−C (80 kcal/mol) bonds. Therefore, unimolecular fission of C−C bonds will dominate for the SPK fuel with minimal production of hydrogen radicals. However, the petroleum fuels have compositional functionalities with significantly weaker C−H bonds, such as benzylic hydrogens (82 kcal/mol) in alkylated aromatics (e.g., toluene, xylenes, ethyl-methyl-benzene). Not only will these benzylic hydrogens act as effective hydrogen donors for bimolecular H-abstraction reactions (eq 5), they can directly produce hydrogen radicals. The resulting benzylic radical will also have increased stability relative to 2° and 3° alkyl radicals, which will reduce the overall propagation rate. The lack of these functionalities within the SPK fuel results in a substantial reduction in H•, and hence H_2 formation.

The cause for the lower selectivity to methane for SPK is similar, since CH_4 is produced via intermolecular H-abstraction by methyl radicals. The 2° and 3 °C−C bonds in the SPK will selectively undergo unimolecular fission resulting in longer alkyl radicals rather than formation of methyl radicals.[59]
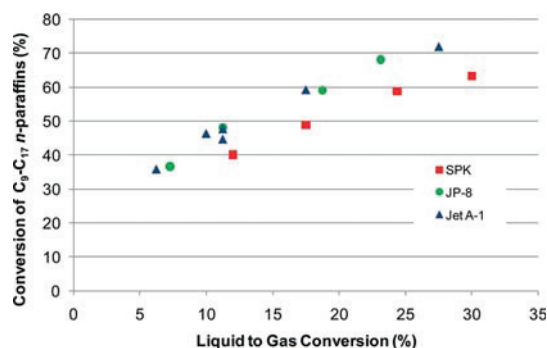
Figure 7. Comparison of cumulative conversion of C_9-C_{17} n-paraffins as a function of conversion and fuel type.

Figure 8. Ratio of 1-heptene to n-heptane as a function of conversion and fuel type.

Methyl radicals must be formed via subsequent decomposition reactions, such as β-scission of a 3-alkyl radical to form a methyl radical and α-olefin. The Jet A-1 and JP-8 fuels have compounds with weaker bonds which can directly form methyl radicals, such as the benzylic C—C bond (72 kcal/mol) in ethylbenzene. The moderate selectivity to ethylene and high yields of n-paraffins during thermal stressing of the fuels tested is consistent with the increase in bimolecular reactions and intramolecular hydrogen transfer as compared to unimolecular decomposition of primary radicals via β-scission, which occurs readily during high-temperature, low-pressure, gas-phase pyrolysis.[58,59] The increase in propylene selectivity for SPK may be due to the relatively high concentration of 2-methyl paraffins in the fuel. Fission of the beta C—C bond in the main chain will produce a 2-propyl and a 1-alkyl radical. The 2-propyl radical can directly form propylene via loss of a hydrogen atom by β-scission or via bimolecular hydrogen-abstraction or disproportionation with another radical.

The neat fuels were also converted into intermediate molecular weight liquid products, as shown in Figure 5. The product trends observed during testing with surface passivated tubing were similar to those with 316ss, indicating that bulk-phase free radical reactions control the decomposition chemistry under the reaction conditions employed with minimal effect of surface catalysis. Reactivity of the higher molecular weight paraffins was predominant with the selective formation of olefinic and cyclic compounds. The cumulative conversions of n-paraffins from C_9 to C_{17} for the three fuels as a function of the measured liquid to gas conversion are shown in Figure 7. The relative conversion of the n-paraffins increased with molecular weight, primarily due to reaction path degeneracy with higher number of equivalent reactive sites and since lower molecular weight paraffins can be produced from larger ones. As shown in Figure 7, the net conversion of the n-paraffins was substantially higher than the corresponding gaseous production rate (Figure 3), supporting the assertion that multiple reaction steps are required to form high yields of C_1-C_5 products. The Jet A-1 and JP-8 n-paraffin conversions were equivalent while that of the SPK was slightly lower. The reduced conversions for the SPK n-paraffins are due to competition with branched paraffins and not to a lower overall extent of reactivity. The branched paraffins are more reactive than the normal paraffins due to the presence of tertiary carbon atoms, which have weaker C—H and C—C bonding.[5] The similar overall reactivity of n-paraffins in the petroleum-derived fuels, despite the Jet A-1 having twice the absolute concentration, is
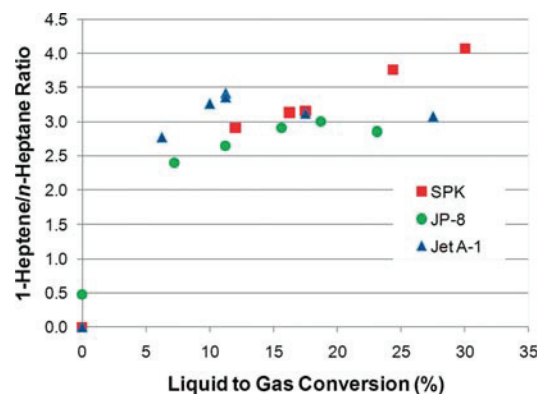
further evidence that these fuels decompose via comparable reaction pathways.

The relative propensity for unimolecular as opposed to bimolecular decomposition was inferred via comparison of 1-heptene and n-heptane yields since these components were either not detectable or in very low concentration in the neat fuels. A comparison of the ratio of 1-heptene to n-heptane for stressing of each fuel as a function of conversion is shown in Figure 8. The ratio was greater than approximately 2.5 for all conditions, indicating that a radical is undergoing several unimolecular decomposition steps prior to bimolecular hydrogen abstraction and stabilization.[4,5,7,60] Specifically, primary alkyl radicals are undergoing several (1—2) intramolecular H-abstraction and β-scission steps prior to bimolecular hydrogen abstraction. A single-step decomposition would result in equivalent yields of olefins and paraffins while multiple isomerization steps of a primary radical would result in negligible n-paraffin yields. The 1-heptene/n-heptane ratio for the SPK increases further at higher extents of reaction, which is likely due to the reduction in abstractable hydrogen at higher conversions. The olefin to paraffin ratio is reported herein to convey that isomerization reactions are prevalent, even under the high pressure reaction conditions employed.

The formation of cyclic and unsaturated products was predominant during the pyrolytic stressing. All fuels showed the production of cycloparaffins, such as cyclohexane, dehydrogenated cycloparaffins (e.g., cyclohexene), and aromatics during stressing. The formation of these types of products is indicative of the pyrolytic reaction pathways and potentially the subsequent deposition propensity (discussed below). Increases in the mono- and dicyclic aromatic concentrations (corrected for gaseous product conversion) for testing with Jet A-1 and JP-8 are shown in Table 4. As shown, both fuels showed a substantial increase in the concentrations of mono- and dicyclic aromatics with increasing degree of stressing. As previously discussed, monocyclic aromatics are formed via dehydrogenation of cycloparaffins (either initially present or formed via ring-closure reactions), which is a prevalent reaction pathway. Increasing concentration of these compounds is further evidence that free radical chemistry is the dominant mechanism for fuel reactivity. As Table 4 shows, a significant increase in dicyclic aromatics was also observed with increased stressing. The large percent increases in dicyclic aromatics with extent of reaction indicates that rates of

Table 4. Concentration Changes of Mono- and Dicyclic Aromatics During Pyrolytic Stressing of Jet A-1 and JP-8[a]

fuel	furnace temperature (°C)	outlet temperature (°C)	liquid to gas conversion (vol %)	monocyclic aromatics		dicyclic aromatics	
				concentration (vol %)	percent increase	concentration (vol %)	percent increase
Jet A-1				18.1		0.3	
	770	566	6.3	19.1	6	0.5	56
	785	577	10.0	20.3	12	0.7	140
	785	577	11.3	20.3	12	0.7	137
	785	572	11.3	20.7	14	0.7	137
	800	588	17.5	21.5	19	1.1	258
	815	603	27.5	22.5	25	1.7	456
JP-8				15.4		1.1	
	770	556	7.3	16.0	4	1.5	35
	785	567	11.3	16.7	8	1.7	53
	800	574	15.7	18.7	22	2.4	115
	800	581	18.8	19.4	26	2.0	85
	810	594	23.1	19.2	25	2.7	145

[a] Aromatic concentrations corrected for volume loss to gaseous products.
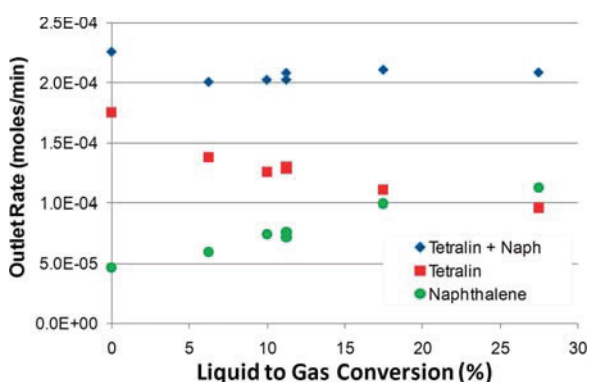
Figure 9. Comparison of the individual and sum of molar outlet rates for tetralin and naphthalene for testing with Jet A-1.

molecular growth pathways increase as direct precursors (e.g., cycloparaffins and monoaromatics) and species prone to molecular addition (e.g., radicals and α-olefins) or hydrogen abstraction increase. An example of a potential dicyclic aromatic production pathway is the conversion of tetralin to naphthalene; tetralin is commonly used as a hydrogen donor additive and solvent.[62,68] A comparison of the molar outlet rates for the individual and sum of tetralin and naphthalene for testing with Jet A-1 is shown in Figure 9. There is a concurrent and near equivalent increase in the naphthalene concentration with tetralin consumption, even though tetralin can also decompose via ring-opening reactions. Trends and pathways such as these further indicate the role of hydrogen donation via bimolecular reactions and support the observation of reduced overall reactivity for the petroleum-derived fuels. Aromatics were observed to be formed during SPK stressing, but the absolute concentrations were low. For example, the monocyclic aromatic content by ASTM 6379 in the most highly stressed SPK sample was 0.8%, while the dicyclic aromatics were below the detection limit. However, the GC/MS analysis did identify the presence of products such as toluene, xylenes, and multialkylated benzenes and naphthalenes. This fuel also produced larger condensed aromatics during stressing, which will be discussed in the following section.

Overall, the detailed liquid and gaseous product analyses provided insight into the prevalent chemical reaction pathways applicable to endothermic reactivity of aviation fuels. The overall reaction mechanism proceeds via free radical reaction pathways in the bulk phase, with the component classes affecting both the relative reactivity (endotherm onset and magnitude) and product selectivities. The latter is especially important when attempting to elucidate and understand the effect of chemical composition on the subsequent deposition propensity and chemistry.

Identification and Quantitation of PAH. The formation of high molecular weight PAH has been linked to the production of carbonaceous deposits, especially condensation coke, under supercritical fuel pyrolysis conditions. Several studies using both single component and fully formulated fuels have conclusively detected large PAH products in stressed product samples.[3,25,27−33,68] Accordingly, HPLC/UV analyses were performed on the stressed fuel samples of this study for the identification and quantification of PAH, with specific focus on the formation of PAH not present in the parent fuels. Because the parent fuels contain large amounts of alkanes, stressing of the fuels produces large numbers of alkylated PAH, not all of which can be resolved by reversed-phase HPLC alone. In cases where the identification and quantification of all of the individual PAH components are needed, normal-phase HPLC fractionation, followed by reversed-phase HPLC analysis can be used, as recently demonstrated in the analysis of supercritical *n*-decane pyrolysis products.[69] In the present study, however, HPLC analyses were performed to provide guidance regarding relative reactivity and molecular growth pathways in the fuels rather than to attempt to identify/quantify all individual PAH formed. Therefore, only reversed-phase HPLC was employed, recognizing that not all PAH components would be sufficiently resolved for identification.
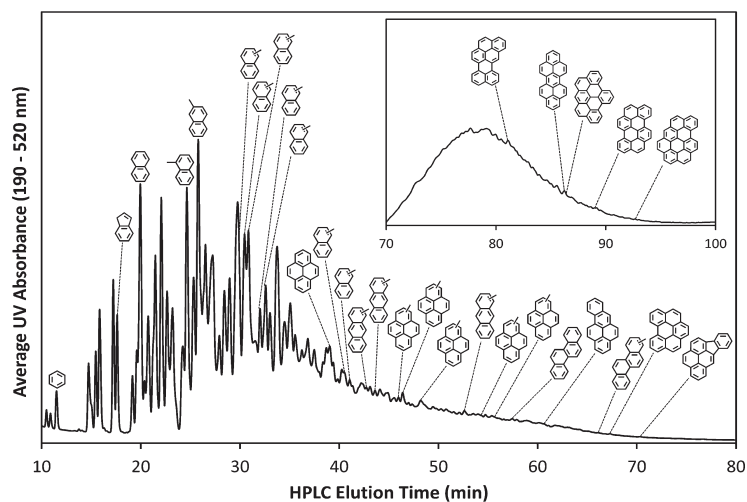
Figure 10. Reversed-phase HPLC chromatogram of the PAH products from supercritical pyrolysis of Jet A-1 (603 °C outlet temperature, 700 psig). Unsubstituted PAH products and singly methylated PAH products in which the positions of the methyl groups are known are labeled with corresponding exact structures. Structures with undesignated alkyl groups correspond to alkylated PAH products in which the aromatic structure is known with certainty but there is uncertainty about the number, position(s), and/or chain length(s) of the alkyl substituent(s). In the inset are the later-eluting products after concentration and separation with a method optimized for the analysis of large-ring-number PAH.

Both the Jet A-1 and JP-8 fuels showed significant formation of large PAH, which was consistent with the increases in mono- and dicyclic aromatic production during stressing, as shown in Table 4. Figure 10 presents the reversed-phase HPLC chromatogram for a typical stressed Jet A-1 fuel sample, along with the structures of the thirty aromatic products sufficiently resolved to be identified by their UV spectra. As Figure 10 reveals, PAH of up to nine fused aromatic rings are produced during the supercritical stressing of the Jet A-1 fuel.

The formation of PAH during supercritical pyrolytic stressing is somewhat similar to that observed during combustion, as PAH are believed to be intermediates in both the production of coke during supercritical pyrolysis and the production of soot during combustion. However, it is generally accepted that during the high temperatures associated with combustion, the hydrogen abstraction/C_2H_2 addition (HACA) reaction sequence is a major pathway to PAH.[70] In the HACA reaction mechanism, repeated addition of acetylene (C_2H_2) to smaller aromatics, followed by ring-closure, produces PAH. Under the high-pressure/intermediate-temperature conditions relevant to supercritical pyrolysis, however, acetylene is not detectable in the gaseous product analysis—either in the present study or in parallel studies;[25,28,31] neither are ethynyl-substituted aromatics, which are frequently found in combustion or high-temperature/low-pressure pyrolysis systems and signify the participation of acetylene in PAH formation reactions.[34,36] Therefore the HACA mechanism is definitely not responsible for the formation of the PAH in the experiments performed in the present study.

The most likely pathways for the formation of the PAH during the stressing of the petroleum-derived fuels are via ring-closure, dehydrogenation, molecular addition, and condensation reactions. Ring-closure and dehydrogenation reactions were evident by observation of increased yields of cyclohexane and dehydrogenated derivatives during stressing. Molecular addition pathways most likely include radical addition to α-olefins, resulting in the formation of larger molecular weight species which can

undergo ring closure. The rates of these types of reactions will be enhanced in petroleum-derived fuels due to the presence of appreciable concentrations of mono- and dicyclic aromatics in the neat fuels, whose concentrations further increase with extent of reaction (see Table 4).

The stressed SPK fuel samples were also analyzed for the presence of PAH. As previously discussed, cycloparaffins and unsaturates were observed during GC/MS analysis, but PAH were below the detectable limit. The higher sensitivity of the HPLC analysis, however, permitted the detection of PAH in the stressed SPK fuel. A reversed-phase HPLC chromatogram of an SPK sample corresponding to a liquid to gas conversion of 30% is shown in Figure 11. Because this sample consists primarily of high concentrations of highly alkylated aromatics, component resolution in Figure 11 is poor, permitting the identification of only four PAH of greater than three rings. Parallel studies show, however, that at higher stressing conditions, this SPK fuel produces significant numbers of large PAH (i.e., up to ten fused aromatic rings).[30,32]

Normal-phase HPLC analysis was used to quantify the 2-, 3-, and 4-ring PAH produced during the stressing of SPK at various temperatures, and the results are shown in Figure 12. Although the absolute concentrations of these compounds are low (relative to those during Jet A-1 and JP-8 testing), the observation that PAH are being formed during stressing is noteworthy as the neat SPK is void of cyclic precursors (cycloparaffins and aromatics). It is believed that pathways for PAH formation in the SPK are similar to those for the petroleum-derived fuels, but the absence of cyclic precursors reduces the overall rate of PAH formation. However, once initial aromatic compounds are formed, continued molecular growth to high molecular weight PAH may proceed readily due to the high concentration of reactive intermediates and net propagation rates. The increased reaction rates may also affect the subsequent deposition rates (discussed below), either directly via PAH formation (to amorphous coke) or via noncatalytic addition pathways of reactive intermediates to
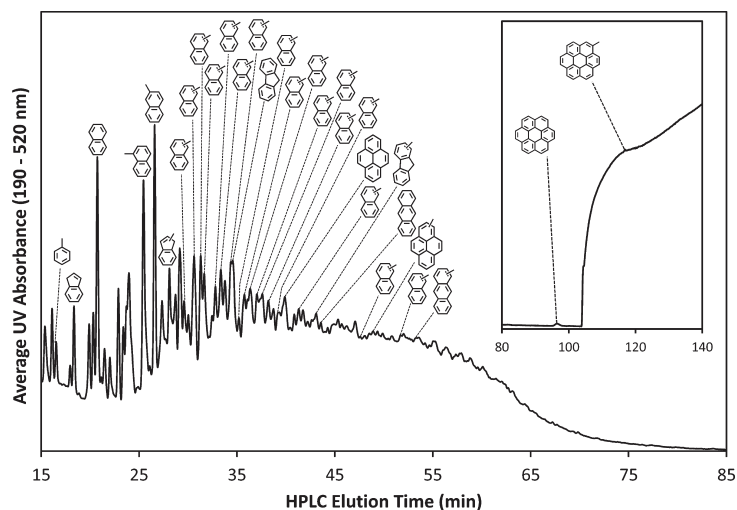
Figure 11. Reversed-phase HPLC chromatogram of the PAH products from supercritical pyrolysis of SPK (588 °C outlet temperature, 700 psig). Unsubstituted PAH products and singly methylated PAH products in which the positions of the methyl groups are known are labeled with corresponding exact structures. Structures with undesignated alkyl groups correspond to alkylated PAH products in which the aromatic structure is known with certainty but there is uncertainty about the number, position(s), and/or chain length(s) of the alkyl substituent(s). In the inset are the later-eluting products after concentration and separation with a method optimized for the analysis of large-ring-number PAH. The rise in baseline at 103 min is due to the UV-absorbing solvent dichloromethane, which is introduced in the HPLC separation method at that time.
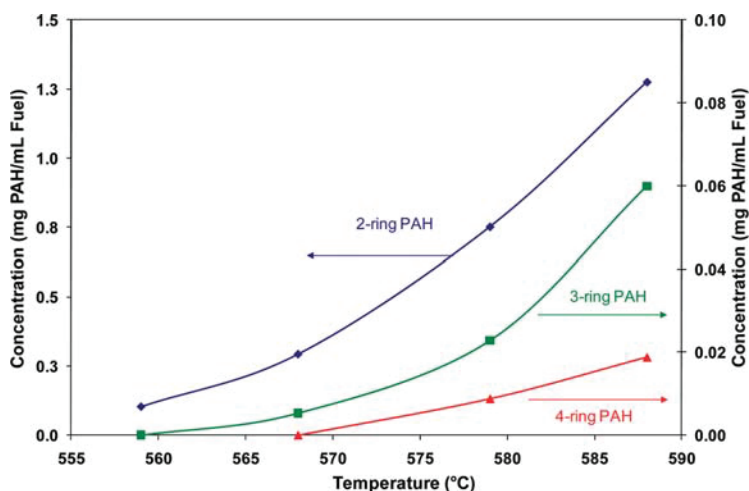
Figure 12. Concentrations of 2, 3, and 4-ring PAH in stressed SPK liquid product as a function of fuel outlet temperature.

surface carbon (e.g., lateral growth of filaments/CVD). During testing with Silcosteel, an increase in PAH concentration in stressed SPK samples relative to 316ss testing was observed during pyrolytic testing. This observation is consistent with the assertion that reactive intermediates which can form PAH participate in surface growth reactions; competition is reduced on the passivated tubing due to the suppression of catalytic filament formation.

Deposition Propensity of Fuels. *Deposition on 316ss Tubing.* The oxidative and pyrolytic deposition propensities of the various fuels were evaluated as a function of the overall extent of reaction and tubing surface material. The compilation of the test conditions, measured volumetric liquid to gas conversion,

oxidative and pyrolytic deposition quantities, and calculated deposition rates for the three fuels evaluated is shown in Table 2. The deposition rates were calculated using the ratio of the total carbon deposit mass (μg) within each region to the total mass of fuel (g) used during the reaction period. For testing with 316ss tubing and air-saturated fuel, a comparison of the surface deposition and wall temperature profiles for each fuel at a liquid to gas conversion of approximately 18% is shown in Figure 13. The deposition profiles are plotted using a logarithmic scale due to the very high pyrolytic deposition quantity for the SPK. The wall temperature was estimated using CFD to be approximately 75−100 °C higher than the bulk fuel temperature. Oxidative deposition occurs within the inlet section
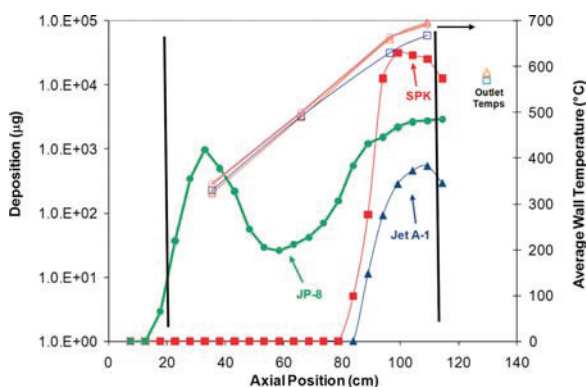
Figure 13. Comparison of surface deposition profile as a function of fuel type with ~18% gaseous product formation. Open symbols correspond to wall temperature profile; symbol type corresponds to fuel; vertical lines correspond to actively heated zone.
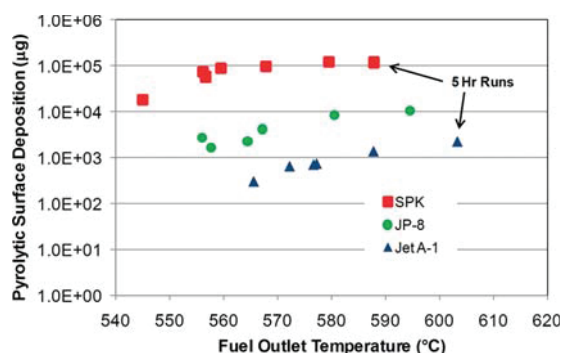

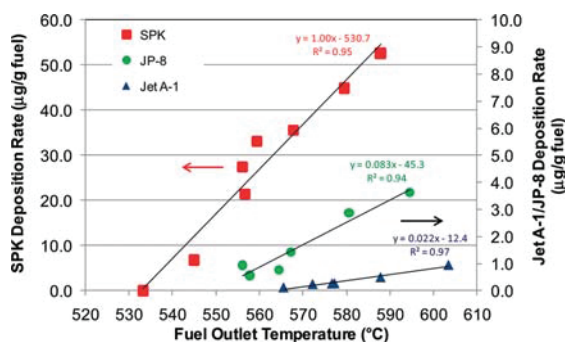**Figure 14.** Comparison of total pyrolytic deposition as a function of fuel type and bulk outlet temperature.

Figure 15. Comparison of pyrolytic deposition rates (μg deposit/g fuel) for SPK (left axis) and petroleum-derived fuels (right axis) as a function of bulk outlet temperature.

(<60 cm) of the reaction zone followed by thermal cracking at fuel temperatures greater than ~450 °C. The JP-8 fuel exhibited a typical oxidative deposition profile and rate. The maximum and subsequent decrease in this region is indicative of complete consumption of the dissolved oxygen within the fuel. The low JP-8 deposition quantities between the oxidative and

pyrolytic regimes (~60−80 cm) are most likely due to oxidative products which subsequently condense on the tubing surface. Both the Jet A-1 and SPK showed negligible oxidative deposition during testing due to the low concentrations of heteroatomic and phenolic polar containing species, which are necessary for deposition within this regime.[39,47,48] It should be reiterated that the Jet A-1 used in this study has very high oxidative stability compared to typical petroleum-derived fuels.

The pyrolytic deposition quantities and rates for the three fuels showed a substantially higher degree of variance with stainless steel tubing; the pyrolytic deposition profiles are also evident at axial positions >80 cm in Figure 13. A comparison of the total pyrolytic deposition quantity as a function of the fuel outlet temperature for testing with 316ss tubing is shown in Figure 14. Although the pyrolytic deposition quantities (especially the SPK) appear to flatten at higher bulk outlet temperatures, comparison of the deposition rates as a function of temperature (see Figure 15) shows a continuing linear increase in deposit formation for all fuels, indicating that the deposit formation is not rate limited at these extents of reaction. The JP-8 and Jet A-1 did show differences in deposition propensity, but are generally consistent with previously reported studies using fully formulated petroleum-derived fuels.[71,72] The potential cause for the lower pyrolytic deposition propensity of Jet A-1 compared to JP-8 will be discussed below. The SPK had over an order of magnitude higher pyrolytic deposition quantity and rate than either of the petroleum-derived fuels. Based on the hypothesis that aromatics and PAH are either precursors to or indicators of deposit formation, it could have been anticipated that highly iso- and normal paraffinic fuels would not be particularly prone to deposit formation due to the low absolute yields of PAH. For testing with Jet A-1 and JP-8, both the total aromatic content in the stressed samples and the deposition rate linearly correlate with the liquid to gas conversion. This result implies that aromatics, and thus, PAH, are intermediates in the deposit formation process. However, it has previously been proposed that these compounds may also be produced by the highly reactive intermediates which form filamentous deposits via metal catalysis and free radical addition pathways.[16] As previously stated, the SPK did form aromatics and PAH, but the absolute concentrations were substantially lower than for the petroleum fuels. If the aromatics were directly involved in the deposit mechanism, the SPK deposition rate would be expected to be lower unless either the increased net propagation rate results in rapid polymerization of the initial aromatics or there is a solubility effect in the base fuel. Limited studies with both normal paraffinic mixtures and paraffinic solvents have also shown increases in the pyrolytic deposition rate relative to the petroleum-derived fuels during testing,[65,71,72] supporting the observations in this study. However, the previously reported deposition increases may have also been related to the paraffinic fuels having a higher relative extent of reaction at a specific test temperature rather than solely due to an inherent increase in the deposition rate. The reactivity comparisons as a function of the bulk outlet fuel temperature in this study clearly show the increased reactivity and deposition propensity of the SPK fuel.

The morphology of the deposits formed during testing was investigated using SEM to obtain insight about the deposit growth mechanisms and formation rate differences. The oxidative deposit morphology for studies with JP-8 with bulk outlet
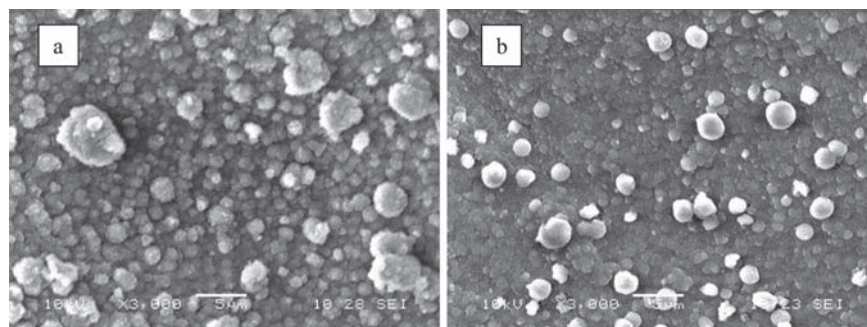
Figure 16. SEM micrographs of oxidative deposit formed during thermal stressing of JP-8: (a) T_{out} = 566 °C, X_{L-G} = 11.3%; (b) T_{out} = 574 °C, X_{L-G} = 15.7%.
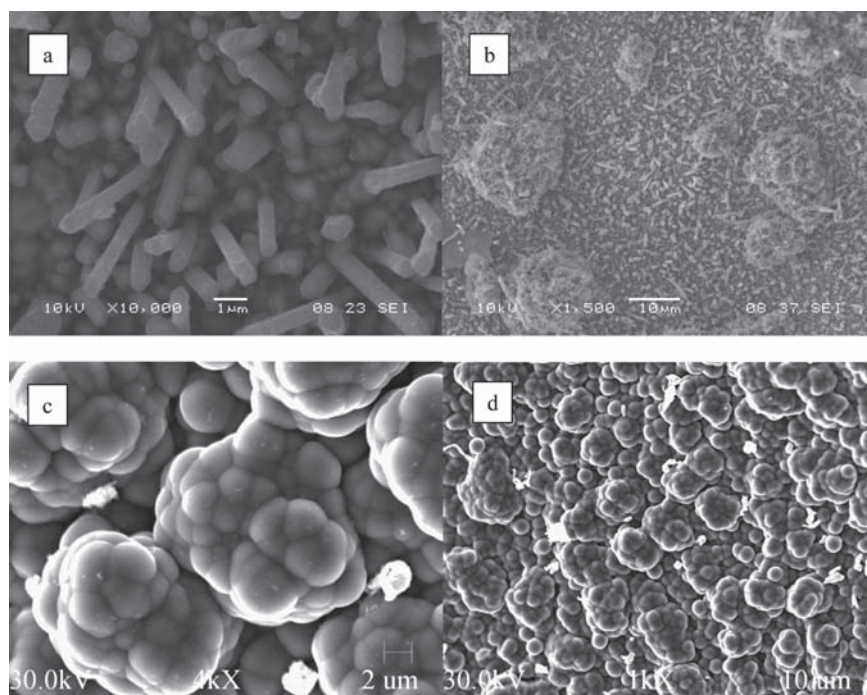
Figure 17. SEM micrographs of pyrolytic deposit formed during thermal stressing of JP-8: (a) and (b) T_{out} = 566 °C, X_{L-G} = 11.3%; (c) and (d) T_{out} = 574 °C, X_{L-G} = 15.7%.

temperatures of 566 °C (Figure 16a) and 574 °C (Figure 16b) showed spherical particles from 1 to 5μm in diameter, which is consistent with the morphology previously reported for this regime.[3] SEM micrographs of the deposit in the pyrolytic regime for various stressing levels of JP-8 are shown in Figure 17. The pyrolytic deposit morphology (Figure 17a and b) for stressing with a bulk fuel outlet of 566 °C (liquid to gas conversion of 11.3%) showed the presence of microscale filamentous carbon with the formation of larger (5−10 μm) agglomerates of filaments. The deposit morphologies observed at the lower extent of stressing in this study are similar to that observed for recent testing of a Chinese commercial jet fuel, RP-3, stressed to a target temperature of approximately 550 °C.[57] For nonpassivated tubing surfaces, filamentous carbon

is formed via catalysis of fuel components with metal atoms extracted from the tubing surface and has been shown to be a prevalent type of carbon deposit morphology under endothermic reaction conditions.[3,10,12,18−24,73−76] The initial formation of the filaments can be promoted via metal carbide and metal sulfide formation on the extracted metal atoms. The role and effect of sulfur components on filamentous deposit formation has been extensively studied by Eser and co-workers, and it has been found that sulfur can be readily incorporated into the catalytically produced filaments.[21−24] The metal sulfides may be more stable than carbides, resulting in a higher incorporation rate of heteroatoms into the filaments. It has also been proposed that sulfur compounds can readily form reactive radicals which can increase the noncatalytic (lateral) growth rate of filaments.[18] The larger
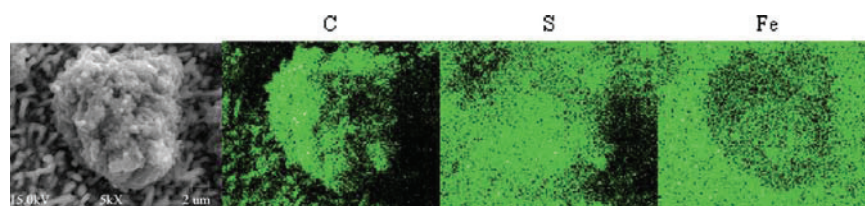
Figure 18. Elemental mapping of pyrolytic deposit formed during thermal stressing of JP-8: T_{out} = 566 °C, X_{L-G} = 11.3%.
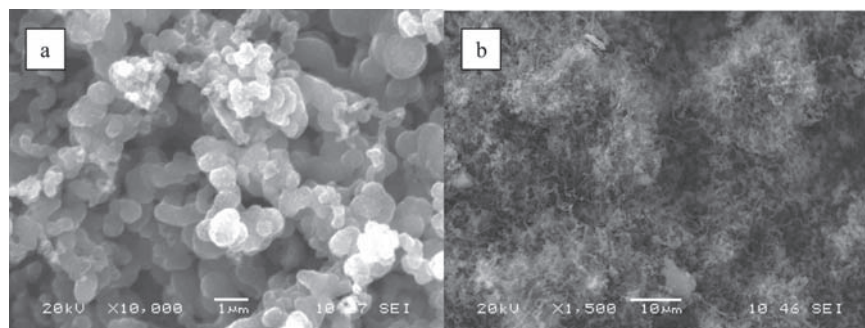
Figure 19. SEM micrographs of pyrolytic deposit formed during thermal stressing of SPK: T_{out} = 558 °C, X_{L-G} = 16.9%.

agglomerates in Figure 17b are most likely formed via similar noncatalytic reaction pathways of fuel decomposition products following initial filament formation, which ultimately cover the extracted metal atoms.

Elemental mapping of the filamentous deposit from JP-8 testing (566 °C bulk outlet temperature) was performed using EDS to provide insight into the composition of the deposit, and is shown in Figure 18. The reduced quality of the micrograph is due to optimizing the elemental mapping. As shown, sulfur is ubiquitous in the surface filaments, while carbon and reduced metal content is most readily evident in the agglomerate structure. Similar behavior has previously been observed during pyrolytic testing with various surface substrates and fuel types.[21,23] The increased deposition propensity of JP-8 compared to the Jet A-1 observed in this study (see Figures 14 and 15) is most likely due to the increased sulfur content of the JP-8 promoting higher rates of catalytic filament formation, and also possibly increasing noncatalytic growth rates.

During stressing of the JP-8 at a slightly higher temperature with a bulk fuel outlet of 574 °C (see Figure 17c and d), the deposits appeared to become agglomerates of spherical particles, and filamentous carbon was not observed on the deposit surface (the bright particles on the micrographs are due to contamination of tubing material during cross-sectioning of the tubes). This change also coincided with a substantial increase in the total aromatic content in the stressed fuel (see Table 4). This morphology is typically referred to as amorphous (or condensation) coke and has been observed during high-temperature stressing using surface-passivated reaction tubing.[3,74] As previously discussed, amorphous coke is formed via bulk-phase free radical reactions and precipitates out of the fluid phase onto reactor surfaces. It has previously been observed that a transitional regime exists where the production of amorphous coke proceeds very rapidly.[74] Elemental mapping (not shown) of these spherical agglomerates in Figures 17c and

d confirmed they were comprised predominantly of carbon with minimal observation of metal atoms. It is believed that filamentous carbon is still formed via catalytic surface growth pathways, but the increased rate of amorphous coke production in the bulk fluid results in higher deposition levels which cover the filamentous carbon. SEM and elemental analysis of a tubing-side flake of deposit (not shown) confirmed filamentous morphology with high sulfur and metal content. Overall, during endothermic stressing of the petroleum-derived fuel using 316ss tubing, filamentous coke is formed, but amorphous deposits are readily produced at higher temperatures and adhere to surfaces during stressing.

The SPK deposit morphology in the pyrolytic regime with a bulk fuel outlet of 558 °C (liquid to gas conversion of 16.9%) is shown in Figure 19. Similar to the petroleum-derived fuels, the SPK showed the presence of filamentous carbon; however, the SPK filaments were more irregular in structure with larger diameters (Figure 19a) and formed much larger agglomerates (Figure 19b). It is believed that the filamentous growth mechanism via catalysis with surface metals is initially occurring (via metal carbide formation due to the absence of fuel sulfur), resulting in the linear growth of carbonaceous deposits. However, the substantial increase in the overall deposition quantity and rate for the SPK is believed to be due to a substantially higher free radical (noncatalytic) growth rate, resulting in lateral (free radical) growth of the carbonaceous filaments (see Figure 1).[12,13,17] The rate of growth via free radical addition (CVD-like process) is strongly affected by the types and concentrations of intermediate fuel products and radicals produced. In particular, olefins and primary alkyl radicals can readily undergo molecular addition to the deposit surface. The aliphatic chain can subsequently undergo decomposition and ring-closure reactions resulting in formation of a compact deposit structure and growth. Other compounds, including alkyl-aromatics, can undergo addition reactions to surface coke,
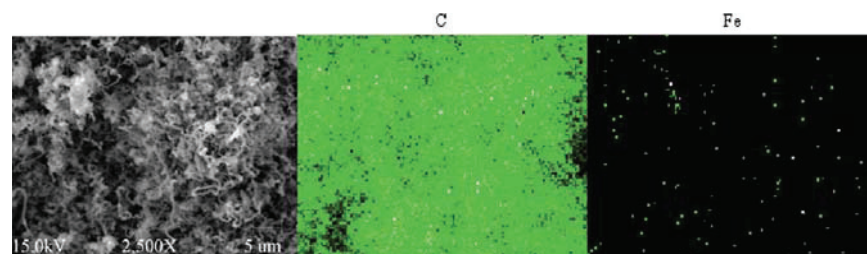
Figure 20. Elemental mapping of pyrolytic deposit formed during thermal stressing of SPK: T_{out} = 558 °C, $X_{L\text{-}G}$ = 16.9%.

but this will most likely proceed at a slower overall rate and result in an initial deposit structure which is less compact and will require multiple reaction steps to form a compact structure. As previously discussed, the SPK fuel has a high selectivity (and yield) to olefinic compounds, high relative extent of reaction, and low concentrations of effective hydrogen donors and cyclic compounds. All of these factors increase the probability and rate of deposit growth via molecular addition and can significantly increase the deposition rate for paraffinic type fuels under supercritical conditions. This result implies that the rate of pyrolytic deposition via filamentous carbon deposition will be higher for chemical classes which have high selectivity to linear and branched olefins, higher net propagation rates and can form condensed and compact structures. Elemental mapping of the SPK deposit, presented in Figure 20, showed the filaments were carbonaceous with minimal metal atoms on the surface. This supports the assertions that the noncatalytic growth mechanism with stressed fuel products is the dominant cause for increased deposition rates, which ultimately cover the metal atoms. The high pyrolytic deposition propensity of the SPK demonstrates that sulfur compounds are not necessary for high filamentous deposit formation rates under these reaction regimes.

The observed deposition propensity in this study is different from the aforementioned effect of chemical class during deposition in stream cracking coils, where larger cyclic and aromatic compounds show higher propensity to deposition. However, it should be noted that the latter operating regime is much lower in pressure and homogeneous free radical reactions in the gas phase significantly affect the overall extent of deposition (similar to condensation coke under endothermic fuel conditions). The cyclic and aromatic compounds in the parent fuel act as seed compounds and increase the production rate of higher molecular weight compounds, similar to particulate matter formation during combustion. In addition, the presence of steam (water vapor) can promote subsequent radical formation on coke surfaces, which results in a further enhancement in the deposition rate.

Therefore, for pyrolytic deposition via pathways related to filamentous carbon production via surface metal catalysis, the quantity of deposition will be related to the overall extent of reaction and propensity of the parent fuel to selectively produce high concentrations of olefinic and linear compounds. Linear and branched paraffinic fuels will be more prone to deposition compared to typical multiclass petroleum-derived fuels as they will have both a higher net reactivity and selectively produce these types of compounds. Sulfur compounds can affect the relative filamentous deposition rate, but are not required for deposit formation. The formation of deposit precursors in the bulk phase (e.g., aromatics) will still occur via parallel reaction pathways, but these compounds will more likely have a secondary role in deposit formation (especially for filamentous carbon on nonpassivated surfaces) than directly participate in deposition pathways.

Deposition on Silcosteel Tubing. Pyrolytic testing was performed with Silcosteel tubing to investigate if the relative deposition rates would be affected by bulk fuel composition. Inerting the tubing surface has previously been shown to substantially reduce oxidative deposition propensity and prevent the formation of filamentous carbon via catalytic growth pathways.[3] Selected experiments were performed using identical reaction conditions for the 316ss testing; results are shown in Table 2. During testing, the passivated tubing did not substantially affect the relative reactivity or primary reaction pathways, as the extents of reaction and product selectivities were very similar to the preceding tests. There was minimal oxidative deposition during testing, which is consistent with previous studies. The pyrolytic deposition for the petroleum fuels was similar to the testing with 316ss, indicating that bulk phase homogeneous reactions to form deposits at higher extents of reaction are prevalent and comparable, in terms of deposition rates, to filamentous carbon formation. On the contrary, the deposition levels for the SPK fuel were reduced by over an order of magnitude compared to testing with 316ss, with levels comparable or below the corresponding petroleum-derived fuels. This result supports the previous assertion that the higher SPK deposition levels with 316ss tubing were due to increased free radical growth on the filamentous deposits that were produced via metal catalysis. Without the catalytic pathway for initial filament production, the primary route for deposit formation transitions to ring formation via condensation pathways with subsequent molecular growth and dehydrogenation. These pathways are prevalent, as supported by the identification and quantitation of multiring PAH in the stressed SPK fuel. The total PAH levels during the SPK studies quantified with normal-phase HPLC were higher during testing with Silcosteel tubing than with 316ss, which potentially indicates the deposition rate of these compounds is further reduced with the suppression of filamentous carbon growth. Overall, it appears that the deleterious propensity of the SPK fuels to form pyrolytic surface deposits may be mitigated via passivation of the tubing surface without affecting the net reactivity of the fuel. This effect could be beneficial as it may be possible to realize a higher net endotherm for a specific reaction temperature compared to typical petroleum-derived fuels. However, as surface coke is produced on reactor surfaces, free radical growth rates may subsequently increase due to the high concentrations of reactive fuel products. Further SPK studies at higher overall extents of reaction could provide insight into this potential effect.

Effect of Benzene on SPK Deposition Propensity. During SPK testing with 316ss tubing, it was proposed that the primary cause for high deposit formation was increased rates of growth via free radical addition reactions on filaments initially produced via metal catalysis. This hypothesis is consistent with the observation of significantly reduced deposition propensity with surface-passivated tubing since metal catalysis is suppressed. It could also be conceivable, however, that the low relative solubility of bulk phase deposit precursors (aromatics and PAH) in the paraffinic fuel could partly impact the deposition rate. It is known that the solubility of PAH is lower in aliphatic solvents as compared to those which contain aromatic constituents,[77] which could contribute to deposition upon formation of PAH in the bulk phase. Solubility effects could be very important if the primary deposition pathway is via a homogeneous noncatalytic mechanism (especially important in heavy feedstock pyrolysis). Therefore, deposition studies were performed with 316ss tubing with addition of benzene (10% by volume) to the SPK to determine if the aromatic would affect the relative deposition rates by increasing the solubility of PAH or other deposit precursors produced during stressing. Benzene was used as it should provide for enhanced solubility of PAH in the SPK, but act as an inert in the reaction process. Previous supercritical pyrolysis studies have shown that benzene should be inert or only minimally reactive for the reaction conditions used in this study.[60,78]

It was found that the deposition rates (see Table 2), deposition profile, and relative product selectivities during testing with benzene/SPK blends with 316ss tubing were identical to those during neat SPK stressing. Because the addition of benzene did not alter the primary reaction pathways or rates, it can be concluded that the benzene had minimal reactivity for the reaction conditions and that low PAH solubility is not the dominant cause for high deposition levels for the neat SPK. These results also indicate that for nonpassivated surfaces, the PAH formed during stressing are most likely produced via reactions that are parallel to molecular addition reactions to the filamentous carbon. It is possible that other types of aromatics or hydrogen donors could be added to selectively interact with these species and stabilize them rather than allow further reaction with the surface filaments. A supplemental study could be performed with Silcosteel tubing to further investigate the potential solubility effect.

■ SUMMARY

Endothermic hydrocarbon fuels are needed to enable high-speed, fuel-cooled aircraft engines. However, major limitations to near-term implementation of these include maximizing the available endotherm for cooling and minimizing undesirable formation of carbonaceous deposits in the fuel systems. The former will allow more available heat sink while the latter will increase the lifetime of the aircraft platform. Improved understanding of the effect of the bulk fuel composition on the overall reactivity, product selectivity, and deposition propensity will substantially assist in the development of viable endothermic fuel candidates. In this effort, supercritical pyrolytic stressing studies were performed using two petroleum-derived fuels and a synthetic paraffinic kerosene (SPK) produced via Fischer—Tropsch (FT) synthesis. The SPK was comprised primarily of normal and branched paraffins with a distillation range similar to a typical aviation fuel. All fuels produced high yields of unsaturates and lower molecular weight products, which is consistent

with hydrocarbon pyrolysis via free radical pathways at high pressures and moderate temperatures. The SPK was significantly more reactive than the petroleum-derived fuels due to a lack of efficient hydrogen donors that act to terminate chain reactions (higher net propagation rate). High-pressure liquid chromatography was used to identify and quantify polycyclic aromatic hydrocarbons (PAH) in the stressed fuels, conclusively determining that these are produced during thermal stressing of the hydrocarbon fuels. A notable observation was the presence of PAH during stressing of the SPK, as the neat fuel did not contain cyclic precursors for molecular growth pathways. PAH can have dual roles as both direct participants in deposition pathways (amorphous coke) and as products of short-lived reactive intermediates which also participate in deposition (free radical addition) reaction pathways.

The SPK had over an order of magnitude higher pyrolytic deposition rate compared to the petroleum-derived fuels during testing with 316ss tubing. Analysis of the deposit morphology for SPK testing indicated the presence of filamentous carbon, which is believed to be initially produced via catalytic reactions with surface metals (linear growth), followed by increased growth via free radical addition pathways (lateral growth). The substantial increase in SPK deposition was attributed to higher rates of free radical addition to surface filaments due to increased propagation rates and selectivity to olefinic products. The formation of PAH during SPK stressing is primarily due to parallel reaction pathways for the highly reactive intermediates prone to participating in lateral growth pathways. Studies blending benzene with the SPK further ruled out the deposition increase being solely due to low PAH solubility in the paraffinic fuel. Pyrolytic stressing of the petroleum-derived fuels with 316ss tubing showed the presence of both filamentous and amorphous coke, with the latter prevalent at higher reaction temperatures and extents of reaction. Filamentous deposit formation during JP-8 studies showed the presence of metal sulfides, which were formed via the catalytic growth mechanism of sulfur compounds in the fuel with surface metals. The higher deposition rate for JP-8 compared to the Jet A-1 used in this study is believed to be due to the significantly higher sulfur content in the former. However, the significantly higher deposition levels for the SPK demonstrate that the rates of noncatalytic surface growth can be dominant under operating conditions relevant to endothermic fuel applications. Testing with surface passivated (Silcosteel) tubing rendered a substantial reduction in the SPK deposition propensity to levels similar to or lower than the petroleum-derived fuels, due to suppression of filamentous carbon formation. Overall, these studies provided guidance regarding the controlling chemistry during supercritical pyrolysis of current and potential synthetic hydrocarbon fuels and insight into prevalent deposition pathways. Future studies at higher extents of conversion, to further identify effects of chemical class composition on deposition propensity, and direct measurement of the overall endotherm are merited.

■ AUTHOR INFORMATION

Corresponding Author
*E-mail: matthew.dewitt@wpafb.af.mil.

■ ACKNOWLEDGMENT

the results of this study. Zachary West, Steven Zabarnick, and Theodore Williams of UDRI are acknowledged for assistance with CFD calculations and useful discussions. The reviewers are thanked for their insightful comments and input which resulted in a manuscript of improved overall quality. This material is based on research sponsored by Air Force Research Laboratory under agreement F33615-03-2-2347. The U.S. Government is authorized to reproduce and distribute reprints for Governmental purposes notwithstanding any copyright notation thereon. The views and conclusions contained herein are those of the authors and should not be interpreted as necessarily representing the official policies or endorsements, either expressed or implied, of the Air Force Research Laboratory or the U.S. Government.

■ **REFERENCES**

(1) Lander, H.; Nixon, A. C. Endothermic fuels for hypersonic vehicles. *J. Aircraft* **1971**, *8* (4), 200.

(2) Huang, H.; Sobel, D. R.; Spadaccini, L. J. Endothermic heat-sink of hydrocarbon fuels for scramjet cooling. *AIAA 2002-3871*, 2002.

(3) Edwards, T. Cracking and deposition behavior of supercritical hydrocarbon aviation fuels. *Combust. Sci. Technol.* **2006**, *178*, 307.

(4) Fabuss, B. M.; Smith, J. O.; Lait, R. I.; Borsanyi, A. S.; Satterfield, C. N. Rapid thermal cracking of *n*-hexadecane at elevated pressures. *Ind. Eng. Chem. Proc. Des. Dev.* **1962**, *1*, 293.

(5) Fabuss, B. M.; Smith, J. O.; Satterfield, C. N. Thermal cracking of pure saturated hydrocarbons. In *Advances in Petroleum Chemistry Refining -Vol. IX*; Interscience: New York, 1964; Ch. 4.

(6) Ford, T. J. Liquid-phase thermal decomposition of hexadecane: Reaction mechanisms. *Ind. Eng. Chem. Fund.* **1986**, *25*, 240.

(7) Khorasheh, F.; Gray, M. R. High-pressure thermal cracking of n-hexadecane. *Ind. Eng. Chem. Res.* **1993**, *32*, 1853.

(8) Song, C.; Lai, W. C.; Schobert, H. H. Condensed-phase pyrolysis of *n*-tetradecane at elevated pressures for long duration. Product distribution and reaction mechanisms. *Ind. Eng. Chem. Res.* **1994**, *33*, 534.

(9) Minus, D.; Corporan, E. Aromatic species formation in thermally stressed jet fuel. *Prepr. - Am. Chem. Soc., Div. Pet. Chem.* **2000**, *45* (3), 484.

(10) Dente, M.; Bozzano, G.; Faravelli, T.; Marongiu, A.; Pierucci, S.; Ranzi, E. Kinetic modeling of pyrolysis processing in gas and condensed phase. *Adv. Chem. Eng.* **2007**, *32*, 51.

(11) Baker, R. T. K.; Yates, D. J. C.; Dumesic, J. A. Filamentous carbon formation over Iron Surfaces. In *Coke Formation on Metal Surfaces*; Albright, L.F., Baker, R.T.K., Eds.; American Chemical Society: Washington, DC, 1982.

(12) Albright, L. F.; Marek, J. C. Mechanistic model for formation of coke in pyrolysis units producing ethylene. *Ind. Eng. Chem. Res.* **1988**, *27*, 755–759.

(13) Kopinke, A.; Zimmermann, G.; Nowak, S. On the mechanism of coke formation in steam cracking—Conclusions from results obtained by tracer experiments. *Carbon* **1988**, *26* (2), 117.

(14) Baker, R. T. K. Catalytic growth of carbon filaments. *Carbon* **1989**, *27* (3), 315.

(15) Kopinke, F.-D.; Zimmermann, G.; Reyniers, G. C.; Froment, G. F. Relative rates of coke formation from hydrocarbons in steam cracking of naphtha. 2. Paraffins, naphthenes, mono-, di-, and cycloolefins, and acetylenes. *Ind. Eng. Chem. Res.* **1993**, *32*, 56.

(16) Kopinke, F.-D.; Zimmermann, G.; Reyniers, G. C.; Froment, G. F. Relative rates of coke formation from hydrocarbons in steam cracking of naphtha. 3. Aromatic hydrocarbons. *Ind. Eng. Chem. Res.* **1993**, *32*, 2620.

(17) Reyniers, G. C.; Froment, G. F.; Kopinke, F.-D.; Zimmermann, G. Coke formation in the thermal cracking of hydrocarbons. 4. Modeling of coke formation in naphtha cracking. *Ind. Eng. Chem. Res.* **1994**, *33*, 2584.

(18) Reyniers, M.-F. S. G.; Froment, G. F. Influence of metal surface and sulfur addition on coke deposition in the thermal cracking of hydrocarbons. *Ind. Eng. Chem. Res.* **1995**, *34*, 773–785.

(19) Orhan, A.; Eser, S. Analysis of solid deposits from thermal stressing of a JP-8 fuel on different tube surfaces in a flow reactor. *Ind. Eng. Chem. Res.* **2001**, *40*, 596–603.

(20) Towfighi, J.; Sadrameli, M.; Niaei, A. Coke formation mechanisms and coke inhibiting methods in pyrolysis furnaces. *J. Chem. Eng. Jpn.* **2002**, *35* (10), 923.

(21) Eser, S.; Venkataraman, R.; Altin, O. Deposition of carbonaceous solids on different substrates from thermal stressing of JP-8 and Jet A Fuels. *Ind. Eng. Chem. Res.* **2006**, *45*, 8946–8955.

(22) Venkataraman, R.; Eser, S. Characterization of solid deposits formed from short durations of jet fuel degradation: Carbonaceous solids. *Ind. Eng. Chem. Res.* **2008**, *47*, 9337–9350.

(23) Mohan, A. R.; Eser, S. Analysis of carbonaceous solid deposits from thermal oxidative stressing of Jet-A fuel on iron- and nickel-based alloy surfaces. *Ind. Eng. Chem. Res.* **2010**, *49*, 2722–2730.

(24) Venkataraman, R.; Eser, S. Characterization of solid deposits formed from jet fuel degradation under pyrolytic conditions: Metal sulfides. *Ind. Eng. Chem. Res.* **2008**, *47*, 9351–9360.

(25) Ledesma, E. B.; Wornat, M. J.; Felton, P. G.; Sivo, J. A. The effects of pressure on the yields of polycyclic aromatic hydrocarbons produced during the supercritical pyrolysis of toluene. *Proc. Combust. Inst.* **2005**, *30*, 1371–1379.

(26) Kalpathy, S. V.; Bagley, S. P.; Nguyen, K.; Wornat, M. J. Pressure-dependent global kinetic rate parameters for the production of polycyclic aromatic hydrocarbons from the supercritical pyrolysis of *n*-decane. Poster presentation at the Thirty-Third International Symposium on Combustion, Beijing, China, August, 2010.

(27) Somers, M. L.; Wornat, M. J. UV spectral identification of polycyclic aromatic hydrocarbon products of supercritical 1-methylnaphthalene pyrolysis. *Polycyclic Aromat. Compd.* **2007**, *27*, 261–280.

(28) McClaine, J. W.; Wornat, M. J. Reaction mechanisms governing the formation of polycyclic aromatic hydrocarbons in the supercritical pyrolysis of toluene: $C_{28}H_{14}$ isomers. *J. Phys. Chem. C* **2007**, *111*, 86–95.

(29) McClaine, J. W.; Oña, J. O.; Wornat, M. J. Identification of a new $C_{28}H_{14}$ polycyclic aromatic hydrocarbon as a product of supercritical fuel pyrolysis: tribenzo[*cd,ghi,lm*]perylene. *J. Chromatogr. A* **2007**, *1138*, 175–183.

(30) Oña, J. O.; Wornat, M. J. Identification of the $C_{30}H_{16}$ polycyclic aromatic hydrocarbon benzo[*cd*]naphtho[1,2,3-*lm*]perylene as a product of supercritical pyrolysis of a synthetic jet fuel. *Polycyclic Aromat. Compd.* **2007**, *27*, 165–183.

(31) Somers, M. L.; McClaine, J. W.; Wornat, M. J. The formation of polycyclic aromatic hydrocarbons from the supercritical pyrolysis of 1-methylnaphthalene. *Proc. Combust. Inst.* **2007**, *31*, 501–509.

(32) Oña, J. O.; Wornat, M. J. The influence of solvents on the ultraviolet-visible absorption spectra of polycyclic hydrocarbons: Applications in the identification of fuel products by HPLC/UV/MS. *Polycyclic Aromat. Compd.* **2008**, *28*, 15–38.

(33) Walker, M. S.; Wornat, M. J. First identification of benzo[*cd*]phenanthro[1,2,3-*lm*]pery-lene by high-pressure liquid chromatography with ultraviolet-visible spectroscopy and mass spectrometry. *J. Chromatogr. A* **2010**, *1217*, 4568–4574.

(34) Wornat, M. J.; Vernaglia, B. A.; Lafleur, A. L.; Plummer, E. F.; Taghizadeh, K.; Nelson, P. F.; Li, C.-Z.; Necula, A.; Scott, L. T. Cyclopenta-fused polycyclic aromatic hydrocarbons from brown coal pyrolysis. *Proc. Combust. Inst.* **1998**, *27*, 1677–1686.

(35) Marsh, N. D.; Zhu, D.; Wornat, M. J. Pyrolysis product absorption by burning benzene droplets. *Proc. Combust. Inst.* **1998**, *27*, 1897–1905.

(36) Marsh, N. D.; Wornat, M. J.; Scott, L. T.; Necula, A.; Lafleur, A. L.; Plummer, E. F. The identification of cyclopenta-fused and ethynyl-substituted polycyclic aromatic hydrocarbons in benzene droplet combustion products. *Polycyclic Aromat. Compd.* **2000**, *13*, 379–402.

(37) Wornat, M. J.; Ledesma, E. B.; Marsh, N. D. Polycyclic aromatic hydrocarbons from the pyrolysis of catechol (*ortho*-dihydroxybenzene), a model fuel representative of entities in tobacco, coal, and lignin. *Fuel* **2001**, *80*, 1711–1726.

10450

dx.doi.org/10.1021/ie200257b |*Ind. Eng. Chem. Res.* 2011, 50, 10434–10451

(38) Thomas, S.; Wornat, M. J. Polycyclic aromatic hydrocarbons from the co-pyrolysis of catechol and 1,3-butadiene. *Proc. Combust. Inst.* **2009**, *32*, 615–622.

(39) Corporan, E.; Edwards, J. T.; Shafer, L.; DeWitt, M. J.; Klingshirn, C.; Zabarnick, S.; West, Z.; Striebich, R.; Graham, J.; Klein, J. Chemical, thermal stability, seal swell and emissions studies of alternative jet fuels. *Energy Fuels* **2011**, *25* (3), 955–966.

(40) Edwards, T.; Minus, D.; Harrison, W.; Corporan, E.; DeWitt, M.; Zabarnick, S.; Balster, L. Fischer—Tropsch jet fuels — Characterization for advanced aerospace applications. *AIAA-2004-3885*, **2004**.

(41) DeWitt, M. J.; Striebich, R.; Shafer, L.; Zabarnick, S.; Harrison, W. E., III; Minus, D. E.; Edwards, J. T. Evaluation of fuel produced via the Fischer-Tropsch process for use in aviation applications. *Proceed. AIChE Spring Natl. Mtng.* **2007**, Paper 58b.

(42) ASTM. *Standard specification for aviation turbine fuel containing synthesized hydrocarbons*; D7566-09; approved 1 Sept 2009.

(43) MIL-DTL-83133G. *Detailed specification, turbine fuel, aviation, kerosene type, JP-8 (NATO F-34), NATO F-35, and JP-8 + 100 (NATO F-37)*; released 30 April 2010.

(44) Edwards, T. "Kerosene" fuels for aerospace propulsion — Composition and properties. *AIAA Paper 2002-3874*, 2002.

(45) Shafer, L., Striebich, R., Gomach, R., Edwards, T. Chemical class composition of commercial jet fuels and other specialty kerosene fuels. *AIAA Paper 2006-7973*, 2006.

(46) Hadaller, O. J.; Johnson, J. M. *World fuel sampling program*; CRC Report 647; June 2006.

(47) Balster, L. M.; Zabarnick, S.; Striebich, R. C.; Shafer, L. M.; West, Z. J. Analysis of polar species in jet fuel and determination of their role in autoxidative deposit formation. *Energy Fuels* **2006**, *20*, 2564–2571.

(48) Zabarnick, S. Studies of jet fuel thermal stability and oxidation using a quartz crystal microbalance and pressure measurements. *Ind. Eng. Chem. Res.* **1994**, *33*, 1348.

(49) Moses, C. *Comparative evaluation of semi-synthetic jet fuels*; Report on CRC Project AV-2-04a; Coordinating Research Council, September 2008.

(50) Moses, C. Comparative evaluation of semi-synthetic jet fuels — Addendum: further analysis of hydrocarbons and trace materials to support D7566; Final Reports for CRC Project AV-2-04a; April 2009.

(51) Defense Energy Support Center. Petroleum quality information system (PQIS) 2009 annual report; http://www.desc.dla.mil/DCM/Files/2009PQISreport.pdf.

(52) Edwards, T.; Krieger J. The thermal stability of fuels at 480 °C (900 °F). Effect of test time, flow rate, and additives. *Proceed. ASME TurboExpo*, **1995**, 95-GT-68.

(53) DeWitt, M. J.; Zabarnick, S. Development and evaluation of additives to inhibit oxidative deposition of jet fuels. *Prepr. Am. Chem. Soc., Div. Pet. Chem.* **2002**, *47*, 183.

(54) Schofield, K. The enigmatic mechanism of the flame ionization detector: Its overlooked implications for fossil fuel combustion modeling. *Progr. Eng. Comb. Sci.* **2008**, *34*, 330–350.

(55) Thomas, S.; Wornat, M. J. $C_{24}H_{14}$ polycyclic aromatic hydrocarbons from the pyrolysis of catechol. *Int. J. Environ. Anal. Chem.* **2008**, *88*, 825–840.

(56) Widegren, J. A.; Bruno, T. J. Thermal decomposition kinetics of the aviation turbine fuel Jet A. *Ind. Eng. Chem. Res.* **2008**, *47*, 4342.

(57) Guo, W.; Zhang, X.; Liu, G.; Wang, J.; Zhao., J.; Mi, Z. Roles of Hydrogen Donors and Organic Selenides in Inhibiting Solid Deposits from Thermal Stressing of *n*-Dodecane and Chinese RP-3 Jet Fuel. *Ind. Eng. Chem. Res.* **2009**, *48*, 8320.

(58) Rice, F. O.; Herzfeld, K. F. Thermal decomposition of organic compounds from the standpoint of free radicals. VI. The mechanism of some chain reactions. *J. Am. Chem. Soc.* **1934**, *56*, 284.

(59) Kossiakoff, A.; Rice, F. O. Thermal decomposition of hydrocarbons, resonance stabilization and isomerization of free radicals. *J. Am. Chem. Soc.* **1943**, *65*, 590.

(60) Khorasheh, F.; Gray, M. R. High-pressure thermal cracking of n-hexadecane in aromatic solvents. *Ind. Eng. Chem. Res.* **1993**, *32*, 1864.

(61) Song, C.; Lai, W. C.; Schobert, H. H. Hydrogen-transferring pyrolysis of long-chain alkanes and thermal stability improvement of jet fuels by hydrogen donors. *Ind. Eng. Chem. Res.* **1994**, *33*, 548.

(62) Probstein, R. F.; Hicks, R. E. *Synthetic Fuels*; pH Press: Cambridge, MA, 1982.

(63) Fan, X.; Yu, G.; Lu, X.; Zhang, X.; Sung, C.-J. Combustion and ignition of thermally cracked kerosene in supersonic model combustors. *J. Prop. Power* **2007**, *23* (2), 317.

(64) Wang, Z.; Guo, Y.; Lin, R. Pyrolysis of hydrocarbon fuel ZH-100 under different pressures. *J. Anal. Appl. Pyrolysis* **2009**, *85*, 534.

(65) Atria, J. V.; Edwards, T. High temperature cracking and deposition behavior of an n-alkane mixture. *Prepr. Am. Chem. Soc., Div. Pet. Chem.* **1996**, *41* (2), 498.

(66) Sheu, J.-C.; Zhou, N.; Krishnan, A.; Jones, E. G.; Katta, V. R. *Thermal cracking of Norpar-13 fuel under near-critical and supercritical conditions.* AIAA 98-3785, 1998.

(67) Sicard, M.; Raepsaet, B.; Ser, F.; Masson, C. Thermal decomposition of a model endothermic fuel. Preliminary study before testing in the MPP-LAERTE supersonic combustion test bench. AIAA 2006-7974, 2006.

(68) Stewart, J.; Glassman, I; Brezinsky, K. Supercritical methylcyclohexane pyrolysis: A flow reactor study. *Prepr. Am. Chem., Div. Pet. Chem.* **1998**, *43* (3), 433.

(69) Bagley, S. P.; Wornat, M. J. Identification of five- to seven-ring polycyclic aromatic hydrocarbons from the supercritical pyrolysis of *n*-decane. *Energy Fuels* **2011**, accepted for publication.

(70) Frenklach, M.; Warnatz, J. Detailed modeling of PAH profiles in a sooting low-pressure acetylene flame. *Combust. Sci. Technol.* **1987**, *51*, 265.

(71) Edwards, T.; Liberio, P. D. The relationship between oxidation and pyrolysis in fuels heated to ~590 °C (1100 °F). *Prepr. Am. Chem. Soc., Div. Per. Chem.* **1994**, *39* (1), 92.

(72) Edwards, T.; Atria, J. V. Thermal stability of high temperature fuels. *Proceed. ASME Int. Gas Turbine Aeroengine Congr. Exhib.* **1997**, 97-GT-143.

(73) Alright, L. F.; Marek, J. C. Mechanistic model for formation of coke in pyrolysis units producing ethylene. *Ind. Eng. Chem. Res.* **1988**, *27*, 755.

(74) Wickham, D. T.; Atria, J. V.; Engel, J. R.; Hitch, B. D.; Karpuk, M. E.; Striebich, R. C. Formation of carbonaceous deposits in a model jet fuel under pyrolysis conditions. *Prepr. Am. Chem. Soc., Div. Pet. Chem.* **1998**, *43*, 428.

(75) Wickham, D. T.; Engel, J. R.; Karpuk, M. E. Additives to prevent filamentous coke formation in endothermic heat exchangers. *Prepr. Am. Chem. Soc., Div. Pet. Chem.* **2000**, *45*, 459.

(76) Woerde, H. M.; Barendregt, S.; Humblot, F.; Brun, C. Mitigate coke formation. *Hydrocarbon Proc.* **2002**, *81* (3), 45–50.

(77) Ruelle, P.; Buchmann, M.; Nam-Tran, H.; Kesselring, U. W. Comparison of the solubility of polycyclic aromatic hydrocarbons in non-associated and associates solvents: The hydrophobic effect. *Int. J. Pharm.* **1992**, *87*, 47.

(78) Savage, P. E. Are aromatic diluents used in pyrolysis experiments inert? *Ind. Eng. Chem. Res.* **1994**, *33*, 1086.

135

Appendix G. Graphene Oxide, A Nonspecific Enhancer of Cellular Growth

Graphene Oxide: A Nonspecific Enhancer of Cellular Growth

Oscar N. Ruiz,[†,*] K. A. Shiral Fernando,[‡] Baojiang Wang,[§] Nicholas A. Brown,[‡] Pengju George Luo,[§] Nicholas D. McNamara,[‡] Marlin Vangsness,[‡] Ya-Ping Sun,[§] and Christopher E. Bunker[†]

[†]Air Force Research Laboratory, Propulsion Directorate, Fuels and Energy Branch, Wright-Patterson AFB, Ohio 45433, United States, [‡]University of Dayton Research Institute, Dayton, Ohio 45469, United States, and [§]Department of Chemistry and Laboratory for Emerging Materials and Technology, Clemson University, Clemson, South Carolina 29634-0973, United States

Graphene oxide sheets are monolayers of carbon atoms that form dense honeycomb structures with unique characteristics.[1,2] They contain a range of reactive oxygen functional groups that facilitate their application in bioengineering.[3] Among the most important properties of GO are low production costs, large surface area, good colloidal behavior, and low cytotoxicity. The solubility of GO in solvents, especially water, is important for applications in bioengineering. The maximum solubility of graphene oxide in a solvent depends both on the solvent polarity and the extent of surface functionalization imparted during oxidation. A few methods are currently available to synthesize GO, and among them, a modified Hummers method is the most popular chemical approach.[4] The surface of GO, made from the aforementioned Hummer's method, has oxygen functional groups, such as hydroxyl, epoxyl, and carboxyl, which enable GO to be readily dispersed in water.[5]

Most reports show that GO materials, including GO films (paper), are superior biocompatible materials that allow the effective proliferation of human and mammalian cells with limited or no cytotoxicity. Such characteristics seem to indicate that GO materials may be used in tissue engineering, tissue implants, wound therapy, and drug delivery applications. These particular characteristics have motivated multiple research groups to further characterize the cytotoxic and antiseptic properties of graphene oxide. Recently, several reports have shown that GO paper promotes the adhesion and proliferation of L-929 cells,[6] osteoblasts,[7] kidney cells,[8] and embryonic cells.[8] However, additional studies have shown that cellular internalization of GO nanosheets applied to the culture media at a concentration of 20 μg/mL can cause

ABSTRACT There have been multiple conflicting reports about the biocompatibility and antimicrobial activity of graphene oxide. To address this, we conducted a study to characterize the antimicrobial properties of graphene oxide (GO) and its biocompatibility with mammalian cells. When GO was added to a bacterial culture at 25 μg/mL, the results showed that bacteria grew faster and to a higher optical density than cultures without GO. Scanning electron microscopy indicated that bacteria formed dense biofilms in the presence of GO. This was shown by a large mass of aggregated cells and extracellular polymeric material. Bacterial growth on filters coated with 25 and 75 μg of GO grew 2 and 3 times better than on filters without GO. Closer analysis showed that bacteria were able to attach and proliferate preferentially in areas containing the highest GO levels. Graphene oxide films failed to produce growth inhibition zones around them, indicating a lack of antibacterial properties. Also, bacteria were able to grow on GO films to 9.5×10^9 cells from an initial inoculation of 1.0×10^6, indicating that it also lacks bacteriostatic activity. Thus, silver-coated GO films were able to produce clearing zones and cell death. Also, graphene oxide was shown to greatly enhance the attachment and proliferation of mammalian cells. This study conclusively demonstrates that graphene oxide does not have intrinsic antibacterial, bacteriostatic, and cytotoxic properties in both bacteria and mammalian cells. Furthermore, graphene oxide acts as a general enhancer of cellular growth by increasing cell attachment and proliferation.

KEYWORDS: nanomaterials · graphene oxide · silver-coated graphene oxide · biomaterials · biocompatible · quantitative real-time PCR · growth enhancer

a 20% decrease in mammalian cell viability, while a concentration of 50 μg/mL can lead to a 50% loss in cell viability, indicating that some inhibitory effect can be observed if a GO suspension is applied to the growth media.[9] The same conditions caused 90% viability loss in *Escherichia coli*.[9] Even after these observations, the authors concluded that GO nanosheets were biocompatible.[9] A recent study showed that graphene and graphene oxide materials are cytotoxic to human erythrocytes and skin fibroblasts.[10] Another study showed that films developed from a suspension of reduced graphene oxide and polyoxyethylene sorbitan laurate (TWEEN) were noncytotoxic to three different types of mammalian cells.[7] These combined results appear to support that GO materials are biocompatible with

137

mammalian cells by promoting cell adhesion and proliferation as effectively as commercial polystyrene tissue culture materials.[6] On the other hand, colloidal GO solutions appeared to be mildly cytotoxic at high concentrations.

The apparent low cytotoxicity of GO materials has led research groups to characterize these materials for antimicrobial effects. A material with low mammalian cell cytotoxicity and increased antimicrobial characteristics may become an ideal material in biomedical applications. A recent report has shown that contact of *E. coli* and *Staphylococcus aureus* bacterial cells with GO can cause growth reductions of about 51 and 61%, respectively.[11] Similar results have been obtained for these two microorganisms when exposed to GO nanowalls.[12] It has been reported that graphene oxide film (paper) can cause growth inhibition zones in *E. coli* and *S. aureus*.[11] On the other hand, recent studies have also indicated that GO is not cytotoxic and also lacks any antibacterial effect. Das *et al.*[13] showed that, when GO was placed in the center of a nutrient media plate previously inoculated with bacteria, a growth inhibition zone was not formed. Alternatively, when silver-decorated GO was used, a clear inhibition zone was formed.[13] In another study, Park *et al.*[8] reported nonspecific binding of Gram-positive and Gram-negative bacteria to GO paper, but functionalization of GO with polyoxyethylene sorbitan laurate reduced bacteria nonspecific binding to GO surfaces. In summary, the numerous conflicting reports about the antimicrobial properties of GO have led us to perform an in-depth characterization of the antimicrobial characteristics of graphene oxide with the goal of addressing the discrepancies in relation to the antimicrobial properties of GO.

The main objective of this investigation is to determine if graphene oxide presents any real antibacterial or bacteriostatic activity. In this study, bacterial and mammalian cellular growth in the presence and absence of graphene oxide materials was determined by the development of carefully designed cell growth bioassays along with the use of quantitative real-time PCR analysis to accurately determine the cells number and the effect of graphene oxide on microbial proliferation. Here, we show that graphene oxide materials do not adversely impact microbial and mammalian cell growth. Furthermore, graphene oxide materials tend to produce a dramatic increase in microbial and mammalian cell proliferation, indicating that graphene oxide is not a bactericidal or bacteriostatic material, but instead a general growth enhancer that acts as a scaffold for cell surface attachment and proliferation. This is the first report that conclusively demonstrates that graphene oxide does not have intrinsic antibacterial properties and cytotoxic properties.

RESULTS AND DISCUSSION

Bacterial Proliferation in the Presence of Colloidal Graphene Oxide (GO). To determine the effect of graphene oxide on bacterial growth, samples containing 5 mL of Luria−Bertani (LB) nutrient broth in 15 mL conical tubes were amended with GO to a final concentration of 25 μg/mL and then inoculated with *E. coli* bacterial cells to a concentration of 0.03 OD. The experimental control was produced by inoculating *E. coli* to 0.03 OD in 5 mL of LB broth without GO. At least, triplicate reactions of each condition were incubated for 16 h at 37 °C and then examined for bacteria growth. Surprisingly, the culture tubes containing graphene oxide did not visually show any apparent reduction in bacterial growth (Figure 1b). Furthermore, they appeared more turbid than the control culture (Figure 1c), and a dense dark precipitate was observed at the bottom of the tube (Figure 1b). The dark precipitate was not produced in the control cultures without GO (Figure 1c). We proceeded to determine growth level in the bacteria cultures by measuring the absorbance at 600 nm. Samples were taken from the supernatant without disturbing the dark precipitates at the bottom of the samples containing GO. The results showed that the GO-containing samples achieved an average absorbance of 1.7 in 16 h of incubation while the bacteria growing in LB broth only achieved an absorbance of 1.3 (Figure 1a). These results indicated that bacteria in the presence of GO grew faster than bacteria in LB media and were able to achieve cell saturation sooner. It was possible that the dark precipitate observed in samples containing GO was responsible for enhancing bacterial growth in the media or harboring bacterial growth itself. To address this, we analyzed samples of the dark precipitate through scanning electron microscopy.

Scanning electron microscopy (SEM) analysis showed that the dark precipitate was formed by a thick bacterial biofilm (Figure 1f,g) containing a large mass of aggregated cells (Figure 1g) and extracellular polymeric material (Figure 1f). A negative control reaction containing just LB broth and GO but not bacteria showed the formation of lower density dark aggregates that did not precipitate to the bottom of the culture tube (Figure 1d). It has been shown that, when a colloidal suspension of GO in water is added to a solution media containing salts, it aggregates and could falloff suspension producing low density aggregates.[14] It is possible that precipitation required bacterial growth. The massive amount of cells observed in the biofilm indicates that there is a direct effect of GO in bacteria proliferation when colloidal GO is added to liquid media. Our results showed that the precipitation of GO in the culture media may be acting as a scaffold for bacterial attachment, proliferation, and biofilm formation. Studies have shown that carbon nanomaterials could act as attachment surfaces where
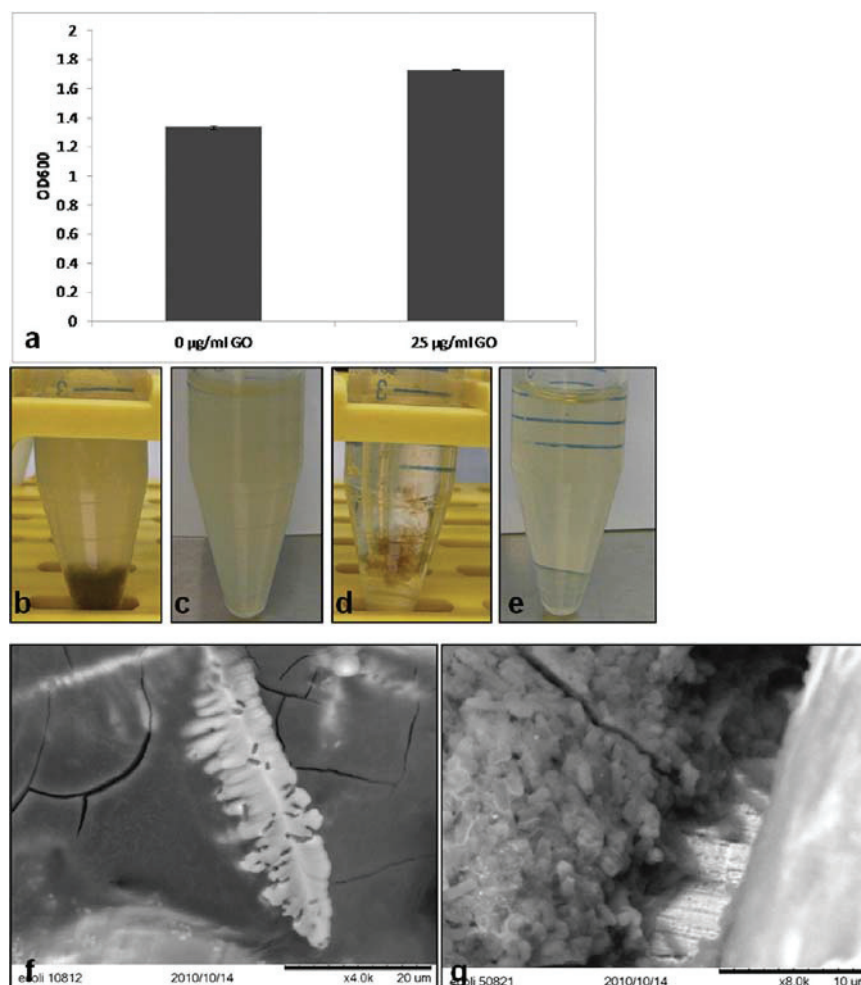
Figure 1. Bacterial proliferation in the presence of colloidal graphene oxide. Pictures showing bacterial growth in test tubes containing 5 mL of Luria—Bertani broth with 0 (c,e) and 25 μg/mL graphene oxide (b,d). *E. coli* was inoculated at a concentration of 0.03 OD_{600} (b,c) and allowed to grow for 16 h at 37 °C. Sterility controls without *E. coli* but with and without GO can be observed (d,e). Note the formation of a dark dense precipitate in the GO sample containing bacteria (b) but not in the sample without GO (c). Graph showing bacterial growth levels in the supernatant of samples containing and lacking GO (a). Scanning electron micrographs showing formation of biofilms in the presence of graphene oxide (f,g). Two characteristic regions were observed within the biofilm, one composed of mostly extracellular polymeric substance (f) and another with a very high bacteria cell density (g).

small colonies grow around tubular carbon nanostructures.[15] Further, it seems that precipitated GO induced massive cell growth, aggregation, and secretion of extracellular polymeric substance (EPS) (Figure 1f,g). In the SEM pictures, it was possible to observe void areas in the EPS with the shape of rod bacteria (Figure 1f). This indicates that bacteria were directly responsible for secreting the EPS. The rod-shape voids observed may be due to the process of bacteria dispersal, a process in which bacteria evacuate the interior of biofilms due to competition or lack of nutrients, leaving behind hollow, shell-like structures.[16]

Characterization of Bacterial Growth on Graphene Oxide Surfaces. To determine the effect of graphene oxide (GO) when coated onto a surface, we coated sterile

PVDF filters with 0 (neat), 100, and 300 μL of a 250 μg/mL colloidal suspension of GO, which equaled 0, 25, and 75 μg of GO per filter. Filters were allowed to dry and were then inoculated with bacteria by submerging them into a solution containing *E. coli* at a concentration of 1×10^6 cells/mL for 1 min. The filters were recovered, allowed to dry, placed onto a sterile LB culture plate, and then incubated for 18 h at 37 °C. After the incubation period, pictures were taken and genomic DNA was extracted from each of the filters for further analysis (Figure 2c—e).

Bacteria growth on filters with or without GO was determined by quantitative real-time PCR (qPCR) analysis of the bacteria genomic DNA. Bacteria growth was observed with the naked eye in all samples, but the

139
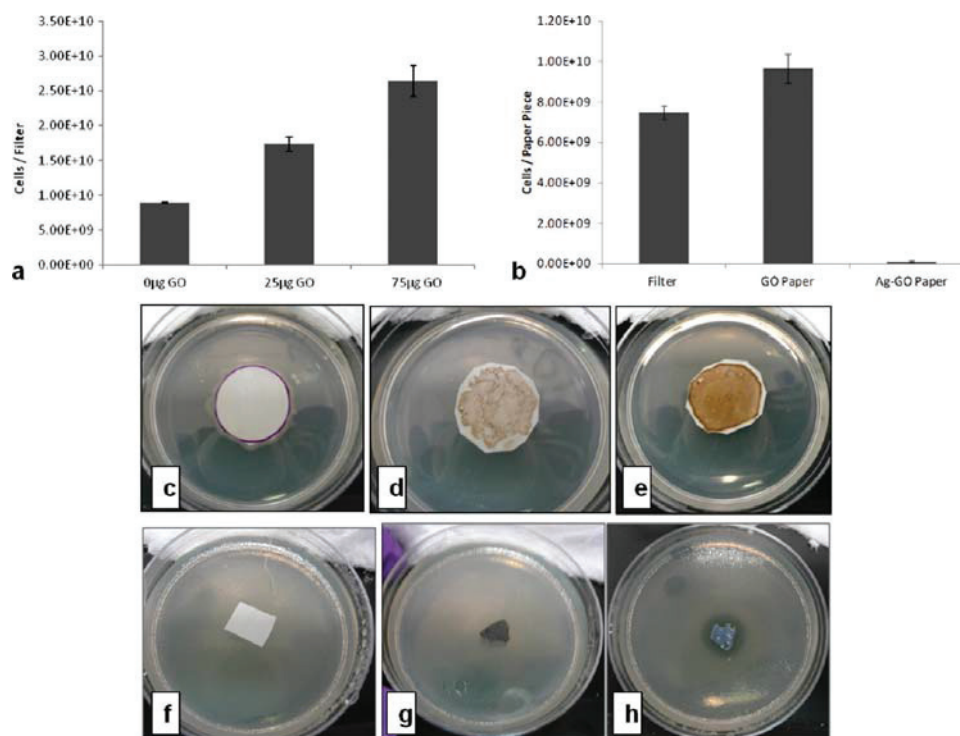
Figure 2. Bacterial growth on graphene oxide surfaces. PVDF filters coated with 0 (c), 25 (d), and 75 μg (e) of GO were inoculated with *E. coli* and incubated at 37 °C for 18 h. Quantitative real-time PCR was used to assess bacterial growth in filters with and without GO (a). Small $\sim$1 cm^2 pieces of PVDF filter (f), GO film (g), and Ag-GO film were inoculated with *E. coli* and culture for 18 h at 37 °C. Bacterial growth was quantified by real-time PCR (b).

filters containing GO presented large bacteria colonies around specific areas that seem to contain more GO (Figure 3a—d). QPCR was chosen over other methods of analysis because it allows precise determination of the level of cellular growth. To achieve cellular quantification, a qPCR assay that targeted the 16S rRNA (*rrn*) gene, a ubiquitous gene in all bacteria, and a synthetic oligonucleotide standard for quantification that spanned the amplicon region were used. This type of analysis provided the number of copies of the 16S *rrn* gene in the sample, which was then used to determine the exact number of cells by dividing the obtained sample gene copy number by the number of 16S *rrn* genes found in the *E. coli* cell; seven copies of the 16S *rrn* gene are found per *E. coli* cell. The qPCR results showed that the bacteria levels in filters containing GO were higher than that in the filters without GO (Figure 2a). The filters containing 25 μg of GO had double the amount of bacteria than the neat filter, while the filter covered with 75 μg of GO had 3 times more cells than the neat filter. These results indicate that GO not only lacks antimicrobial properties, but that it actually enhances microbial growth when coated onto another surface (Figure 2a).

Upon close inspection of the GO-coated and neat filters, we observed some interesting growth patterns
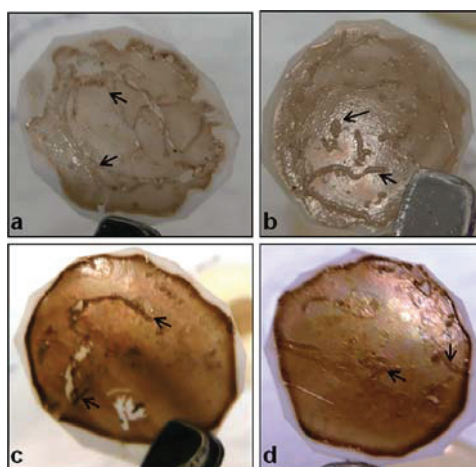
Figure 3. Bacteria interaction with graphene oxide. Black arrows indicate some of the areas with increased bacterial growth observed on filters coated with 25 (a,b) and 75 μg (c,d) of GO. Bacterial colonies can be easily observed as elongated features in GO-coated filters but not in a neat PVDF filter.

that differentiate the GO-coated filters. The GO-coated filters had easy to observe large cell colonies that follow a lined pattern around areas of higher GO content (Figure 3a—d). These areas were observed in

140

ARTICLE
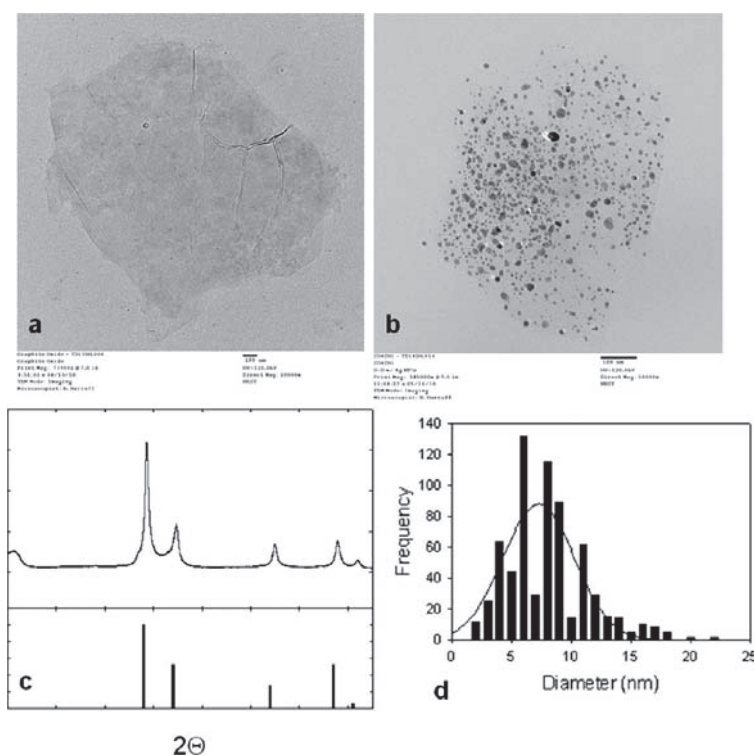
Figure 4. Graphene oxide and silver-coated graphene oxide characterization. (a) TEM image of neat GO, (b) TEM image of Ag-decorated GO, (c) XRD spectrum of Ag-decorated GO and ICDD 00-004-0783 card data for face-centered cubic Ag, and (d) size distribution studies performed using TEM for Ag-decorated GO.
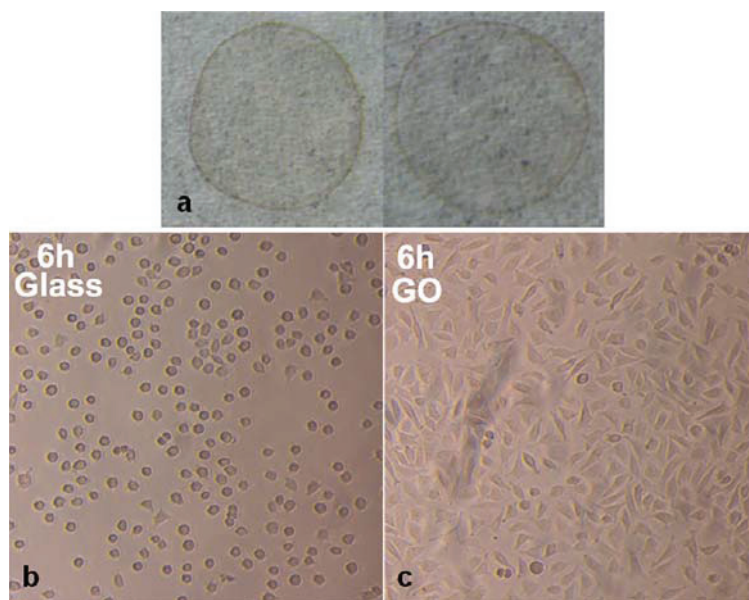
filters with 25 and 75 μg of GO but not in neat filters. Also, we observed that an area of dense bacterial growth in the LB media was produced around all neat filter replicates (Figure 2c). This halo of cells was not observed in any of the GO-coated filters (Figure 2d,e). This was an interesting observation that implied that there is an inherent preference by bacteria to attach and grow in areas containing GO, especially those areas containing the highest GO levels (Figure 3).

Bacteria Interaction with GO and Ag-GO Films (Papers). GO and Ag-GO films were analyzed using TEM and XRD analysis to determine the morphology, size distribution, and the crystal structure of Ag nanoparticles, as shown in Figure 4. TEM analysis clearly showed that the GO sheets were well-decorated with Ag nanoparticles (Figure 4b), and size distribution analysis performed using TEM showed that the average size of Ag nanoparticles on the surface of GO was 8 nm (Figure 4c,d). In addition, XRD analysis revealed that the silver-decorated graphene oxide (Ag-GO) spectrum closely matched the peaks seen in the face-centered cubic silver (ICDD 00-004-0783). The effect of solid GO films on bacteria growth was studied by inoculating GO films, Ag-GO films, and filter pieces with *E. coli* bacteria. Graphene oxide films were placed onto LB culture plates that were previously inoculated with 1 × 10⁶

E. coli cells per plate. Then, 1 × 10⁶ *E. coli* cells were directly inoculated on top of the film pieces and allowed to dry. The plates were incubated for 18 h at 37 °C. After the incubation period, pictures were taken and genomic DNA was extracted from each of the filters for further analysis (Figure 2f–h). The purpose of this type of inoculation was to observe growth over the GO film and also to determine if any growth inhibition zone was formed around the GO film. Growth inhibition zones around GO film have been reported in the past.[11] Inhibition areas would indicate that the material has some toxic effect on the bacteria.

Results showed that growth inhibition zones were not detected in the plate containing either GO film or filter paper (Figure 2f,g). However, Ag-decorated GO showed large growth inhibition zones characterized by a clear area with no cell growth (Figure 2h). These results clearly demonstrate that GO does not have any antimicrobial effects capable of producing a toxic effect in the area surrounding the GO film. By decorating our GO material with silver, we further demonstrate that we can replicate published results for Ag-GO material.[11,13,17] This showed that our GO material was functional and capable of supporting common antimicrobial materials including silver.

Quantitative real-time PCR (qPCR) performed to determine the growth level over the different films

RUIZ *ET AL.* VOL. 5 ■ NO. 10 ■ 8100–8107 ■ 2011 ACSNANO **8104** www.acsnano.org

DISTRIBUTION STATEMENT A: Approved for public release. Distribution is unlimited.

Figure 5. Mammalian cell growth on graphene oxide film. Glass slides coated with graphene oxide (a). Micrographs showing human adenocarcinoma HT-29 cell attachment and growth on glass slides (c) with or (b) without GO film. A GO-coated glass slide and a control uncoated glass slide were placed into the same culture dish, inoculated with HT-29, and allowed to incubate for 6 h at 37 °C.

revealed that GO paper supported bacteria growth more efficiently than a PVDF filter (Figure 2b). The results showed that the surface of the GO film contained 9.5×10^9 cells while the filter paper had 7.5×10^9 cells. The cell level over the Ag-GO paper was determined to be 3.5×10^4 cells, which was lower than the initial inoculation level of 1×10^6 cells, indicating that bacteria cell death was achieved. These results do not indicate any adverse or toxic effect of GO toward bacteria. Furthermore, GO seems to promote bacterial growth by enhancing attachment, proliferation, and biofilm formation.

Mammalian Cell Attachment and Proliferation onto GO Film. A study was performed to test the role of GO film on mammalian cell attachment and proliferation. Control glass slides and glass slides coated with 10 μg of GO (Figure 5a) were placed onto a culture dish to which culture media and 6×10^5 mammalian colorectal adenocarcinoma HT-29 cells were added. The cells were allowed to attach and develop on the slides. At various time intervals, cell attachment was assessed by light microscopy. Shown in Figure 5b,c are representative images of cell morphology after incubation for 6 h. The results indicated that the mammalian cells attached more efficiently to the GO-coated glass slides and grew (Figure 5c). The micrographs showed marked morphological changes and cell enlargement and spreading on the GO-coated slides, which are characteristic of effective cell attachment and cell growth (Figure 5c). However, very few cells became attached to and developed on the plain glass slides (the control)

as observed by the round shape of cells, which indicated lack of cellular enlargement and growth (Figure 5b). These results clearly showed that the GO film, beyond not exerting any cytotoxic effects on the cells, actually promotes mammalian cell attachment and proliferation. During the course of this investigation, several literature reports focusing primarily on biocompatibility of GO films were published,[6−8,18,19] from which the results are generally consistent with what is shown here on the GO film enhancing mammalian cell attachment and proliferation. Taken together these results indicate that GO is a great support for mammalian cell attachment, growth, and proliferation. As shown, GO film coated on glass slides enhances cell attachment, growth, and proliferation. These results compare positively against carbon nanotube materials which have been shown to be cytotoxic at various concentrations.[20−28]

CONCLUSION

The results of this study clearly demonstrate that graphene oxide does not have antibacterial properties. Furthermore, graphene oxide lacks any bacteriostatic property as shown by the prolific growth observed on all forms of GO tested. It seems that GO acts as an enhancer of life, increasing not only mammalian cell growth but also bacterial growth. In the past, several studies have shown that GO is noncytotoxic to mammalian cells, but that it somehow acts as an antibacterial material. In reality, there is no clear reason for which an inert carbon material such as GO could be beneficial

142

to mammalian cell growth and detrimental to bacteria, which are usually less susceptible to biotic and abiotic factors than mammalian cells. It is possible that contaminants retained from the GO preparation or underestimations of GO concentrations might be responsible for some of the detrimental effects on bacteria growth observed in previous reports. Our graphene oxide production process, which includes long-term dialysis, dilution, and sonication, is one that takes great care on removing carryon impurities that could affect the properties of the material. More studies are required to determine which GO synthesis processes are producing the best quality GO material. This study significantly advances our knowledge on the biological properties of graphene oxide and its uses in biomedical and biotechnological application.

MATERIALS AND METHODS

Preparation of Graphene Oxides (GOs). The Hummers method with minor modification was used for the preparation of GO (Figure 4a) from the same graphite sample.[4] Briefly, concentrated H_2SO_4 (10 mL) in a 500 mL flask was heated to 80 °C, to which $(NH_4)_2S_2O_8$ (0.9 g) and P_2O_5 (0.9 g) were added. The mixture was stirred until the reagents were completely dissolved. The graphite sample (1 g) was added, and the resulting mixture was heated at 80 °C for 4.5 h. Upon being cooled to room temperature, the reaction mixture was diluted with water (250 mL) and kept for ~12 h. It was then filtrated and washed repeatedly with water, followed by drying in a vacuum oven. The solid sample was added to concentrated H_2SO_4 (40 mL) in a 500 mL flask cooled in an ice bath. The mixture was added slowly to $KMnO_4$ (5 g over 40 min), during which the temperature was kept at <10 °C. The reaction mixture, with a change in color from black to greenish brown, was heated at 35 °C for 2 h, followed by dilution with water (85 mL; *Caution:* the temperature must be kept at <35 °C throughout) and further stirring for 2 h. The reaction mixture was poured into a large beaker, to which water (250 mL) and then aqueous H_2O_2 (30%, 10 mL) were added. Bubbles from the aqueous mixture along with a color change to brilliant yellow were observed. After the mixture was allowed to settle for ~12 h, the clear supernatant was decanted, and the sediment was washed repeatedly with aqueous H_2SO_4 (5 wt %)-H_2O_2 (0.5 wt %) and HCl solution (10 wt %), followed by washing repeatedly with water until no layer separation was observed after centrifuging. The sample was then dialyzed (MWCO ~ 3500) against water for 7 days to yield a clean aqueous dispersion of GOs. The aqueous GOs thus obtained (acid form) were titrated by aqueous NaOH (0.1 M) until pH reaches 9. The resulting GOs (sodium form) were again dialyzed (MWCO ~ 3500) for 7 days to reach neutral pH. Finally, the aqueous suspension of GOs was diluted (~0.2 wt %) and sonicated for 30 min to achieve complete exfoliation.

Synthesis of Ag-GO. GO was synthesized using the Hummers method as explained previously. Ag-GO (Figure 4b) was prepared using a sonochemical method as follows. First, 50 mg of GO, 25 mg of silver acetate, and 15 mL of DMF were mixed in a three-arm sonochemical flask (Sonics Inc., Suslick flask). The mixture was sonicated at 37% amplitude and 20 kHz for 20 min using a pulsed (1 s on, 1 s off) procedure. After the sonication, the solution turned black and was stable for a few hours without any noticeable precipitation. In the process of recovering Ag-GO, the mixture was transferred to a round-bottom flask and DMF was removed using a rotary evaporator. The remaining solid material was transferred to a centrifuge tube where it was washed with DI water and ethanol five times. The ethanol was dried by blowing nitrogen across the surface of solution, and the final Ag-GO product was recovered as a black powder.

GO and Ag-GO Film (Paper) Preparation. In the film (paper) fabrication of GO and Ag-GO, a suspension of GO or Ag-GO in DMF (0.7 mg/mL, 19 mL) was filtered through a PVDF membrane (Whatman, 0.45 μm, 47 nm diameter). The thin layer of the film formed on the membrane was then subsequently peeled away.

Preparation of GO Film onto a Glass Slide. Graphene oxide (GO) suspension was obtained by sonication of the obtained GO powder in water (~250 μg/mL). Then 40 μL of GO suspension or about 10 μg of GO per slide was spotted using a micropipet onto a glass slide, and the slide was allowed to evaporate in a fume hood to result in a thin GO film on the slide. For the blank control slide, ultrapure sterile water was spotted and allowed to dry. Glass slides with or without GO film were placed into a culture dish (10 cm in diameter) and treated with UV irradiation for 1 h.

Coating of PVDF Filters with GO. PVDF filters (0.22 μm) were coated with a 100 and 300 μL GO suspension containing 25 and 75 μg of GO, respectively. Filter coating took place by releasing the GO solution evenly using a circular motion from a micropipet. The GO-coated filters were allowed to dry in the laminar flow hood under sterile conditions. Once dried, the GO-coated filters were used in the growth bioassay experiments.

Bacterial Cell Culture. *Escherichia coli* strain JM109 was routinely grown in Luria–Bertani (LB) broth or solid media at 37 °C for 16–20 h with or without agitation depending if the study used broth or solid media. The bacteria stocks used to inoculate the different assays were produced as described and the cell level quantified by quantitative real-time PCR. Once the bacterial stocks were quantified, assays were inoculated at a specific starting cell concentration. Bacterial assays were allowed to incubate at 37 °C for 16–18 h before measurements were taken.

Mammalian Cell Culture. Colorectal adenocarcinoma (HT-29) cells were routinely cultured in Eagle's minimum essential medium (EMEM) (ATCC Manassas, VA) supplemented with 10% fetal bovine serum (FBS) and 1% antibiotics (penicillin and streptomycin). The cells were cultured at 37 °C in a humidified atmosphere with 95% air and 5% CO_2 for 48 h (reach 85% of confluency) before subculture.

In experiment, 6×10^5 cells were seeded into the culture dish which contained the glass slides (with or without GO film) and incubated to allow the cells for attachment and development on the glass slides. At various time intervals, the morphology of cell growth was taken under a microscope (Motic) supplied with a camera.

Quantitative Real-Time PCR Analysis of Genomic DNA. Real-time PCR analysis was performed on bacterial genomic DNA samples using the CFX real-time PCR system (BioRad, Hercules, CA) with a two-step amplification program with post-amplification melt curve analysis as described by Ruiz *et al.*[29] The 16S gene-specific real-time PCR primers and synthetic oligonucleotide standard were developed. The synthetic oligonucleotide was serial-diluted from 1×10^8 to 1×10^4 copies/μL and used as standards for absolute quantification purposes. Real-time PCR sample reactions were produced by preparing a master mix containing the 16S gene-specific primers, BioRad SYBR Green SuperMix, water, and the appropriate sample DNA.

REFERENCES AND NOTES

1. Novoselov, K. S.; Geim, A. K.; Morozov, S. V.; Jiang, D.; Zhang, Y.; Dubonos, S. V.; Grigorieva, I. V.; Firsov, A. A. Electric Field Effect in Atomically Thin Carbon Films. *Science* **2004**, *306*, 666–669.
2. Geim, A. K.; Novoselov, K. S. The Rise of Graphene. *Nat. Mater.* **2007**, *6*, 183–191.

143

3. Sabourin, J. L.; Dabbs, D. M.; Yetter, R. A.; Dryer, F. L.; Aksay, l. A. Functionalized Graphene Sheet Colloids for Enhanced Fuel/Propellant Combustion. *ACS Nano* **2009**, *3*, 3945–3954.

4. Hummers, W. S.; Offeman, R. E. Preparation of Graphitics Oxide. *J. Am. Chem. Soc.* **1958**, *80*, 1339.

5. Szabo, T.; Berkesi, O.; Forgo, P.; Josepovits, K.; Sanakis, Y.; Petridis, D.; Dekany, I. Evolution of Surface Functional Groups in a Series of Progressively Oxidized Graphite Oxides. *Chem. Mater.* **2006**, *18*, 2740–2749.

6. Chen, H.; Muller, M. B.; Gilmore, K. J.; Wallace, G. G.; Li, Dan. Mechanically Strong, Electrically Conductive, and Biocompatible Graphene Paper. *Adv. Mater.* **2008**, *20*, 3557–3561.

7. Agarwal, S.; Zhou, X.; Ye, F.; He, Q.; Chen, G. C.; Soo, J.; Boey, F.; Zhang, H.; Chen, P. Interfacing Live Cells with Nanocarbon Substrates. *Langmuir* **2010**, *26*, 2244–2247.

8. Park, S.; Mohanty, N.; Suk, J. W.; Nagaraja, A.; An, J.; Piner, R. D.; Cai, W.; Dreyer, D. R.; Berry, V.; Ruoff, R. S. Biocompatible, Robust Free-Standing Paper Composed of a TWEEN/Graphene Composite. *Adv. Mater.* **2010**, *22*, 1736–1740.

9. Hu, W.; Peng, C.; Luo, W.; Lv, M.; Li, X.; Li, D.; Huang, Q.; Fan, C. Graphene-Based Antibacterial Paper. *ACS Nano* **2010**, *4*, 4317–23.

10. Liao, K. H.; Lin, Y. S.; Macosko, C. W.; Haynes, C. L. Cytotoxicity of Graphene Oxide and Graphene in Human Erythrocytes and Skin Fibroblasts. *ACS Appl. Mater. Interfaces* **2011**, *3*, 2607–2615.

11. Bao, Q.; Zhang, D.; Qi, P. Synthesis and Characterization of Silver Nanoparticle and Graphene Oxide Nanosheet Composites as a Bactericidal Agent for Water Disinfection. *J. Colloid Interface Sci.* **2011**, *360*, 463–470.

12. Akhavan, O.; Ghaderi, E. Toxicity of Graphene and Graphene Oxide Nanowalls Against Bacteria. *ACS Nano* **2010**, *4*, 5731–5736.

13. Das, M. R.; Sarma, R. K.; Saikia, R.; Kale, V. S.; Shelke, M. V.; Sengupta, P. Synthesis of Silver Nanoparticles in an Aqueous Suspension of Graphene Oxide Sheets and Its Antimicrobial Activity. *Colloids Surf., B* **2011**, *83*, 16–22.

14. Li, D.; Muller, M. B.; Gilge, S.; Kaner, R. B.; Wallace, G. G. Processable Aqueous Dispersion of Graphene Nanosheets. *Nat. Nanotechnol.* **2008**, *80*, 101–105.

15. Morozan, A.; Stamatin, L.; Nastase, F.; Dumitru, A.; Vulpe, S.; Nastase, C.; Stamatin, I.; Scott, K. The Biocompatibility Microorganisms−Carbon Nanostructures for Applications in Microbial Fuel Cells. *Phys. Status. Solidi A* **2007**, *204*, 1797–1803.

16. Barraud, N.; Hassett, D. J.; Hwang, S. H.; Rice, S. A.; Kjelleberg, S.; Webb, J. S. Involvement of Nitric Oxide in Biofilm Dispersal of *Pseudomonas aeruginosa*. *J. Bacteriol.* **2006**, *188*, 7344–7353.

17. Zhang, D.; Liu, X.; Wang, X. Green Synthesis of Graphene Oxide Sheets Decorated by Silver Nanoprisms and Their Anti-bacterial Properties. *J. Inorg. Biochem.* **2011**, *105*, 1181–1186.

18. Wang, K.; Ruan, J.; Song, H.; Zhang, J.; Wo, Y.; Guo, S.; Cui, D. Biocompatibility of Graphene Oxide. *Nanoscale Res. Lett.* **2011**, *6*, 1–8.

19. Chang, Y.; Yang, S. T.; Liu, J. H.; Dong, E.; Wang, Y.; Cao, A.; Liu, Y.; Wang, H. *In Vitro* Toxicity Evaluation of Graphene Oxide on A549 Cells. *Toxicol. Lett.* **2011**, *200*, 201–210.

20. Deng, X.; Jia, G.; Wang, H.; Sun, H.; Wang, X.; Yang, S.; Wang, T.; Liu, Y. Translocation and Fate of Multi-walled Carbon Nanotubes *in Vivo*. *Carbon* **2007**, *45*, 1419–1424.

21. Jia, G.; Wang, H.; Yan, L.; Wang, X.; Pei, R.; Yan, T.; Zhao, Y.; Guo, X. Cytotoxicity of Carbon Nanomaterials: Single-Wall Nanotube, Multi-wall Nanotube and Fullerene. *Environ. Sci. Technol.* **2005**, *39*, 1378–1383.

22. Wang, H.; Wang, J.; Deng, X.; Sun, H.; Shi, Z.; Gu, Z.; Liu, Y.; Zhao, Y. Biodistribution of Carbon Single-Wall Nanotubes in Mice. *J. Nanosci. Nanotechnol.* **2004**, *4*, 1019–1024.

23. Wang, J; Deng, X.; Yang, S. T.; Wang, H.; Zhao, Y.; Liu, Y. Rapid Translocation and Pharmacokinetics of Hydroxylated Single-Walled Carbon Nanotubes in Mice. *Nanotoxicology* **2008**, *2*, 28–32.

24. Wang, J.; Sun, R. H.; Zhang, N.; Nie, H.; Liu, J. H.; Wang, J. N.; Wang, H.; Liu, Y. Multi-walled Carbon Nanotubes Do Not Impair Immune Functions of Dendritic Cells. *Carbon* **2009**, *47*, 1752–1760.

25. Wang, X.; Jia, G.; Wang, H.; Nie, H.; Yan, L.; Deng, X.; Wang, S. Diameter Effects on Cytotoxicity of Multi-walled Carbon Nanotubes. *J. Nanosci. Nanotechnol.* **2009**, *9*, 3025–3033.

26. Yang, S. T.; Fernand, K. A. S.; Liu, J. H.; Wang, J.; Sun, H. F.; Liu, Y.; Chen, M.; Huang, Y.; Wang, X.; Wang, H.; *et al.* Covalently PEGylated Carbon Nanotubes with Stealth Character *in Vivo*. *Small* **2008**, *4*, 940–944.

27. Yang, S. T.; Wang, H.; Meziani, M. J.; Liu, Y; Wang, X.; Sun, Y. P. Biodefunctionalization of Functionalized Single-Walled Carbon Nanotubes in Mice. *Biomacromolecules* **2009**, *10*, 2009–2012.

28. Yang, S. T.; Wang, X.; Jia, G.; Gu, Y.; Wang, T.; Nie, H.; Ge, C.; Wang, H.; Liu, Y. Long-Term Accumulation and Low Toxicity of Single-Walled Carbon Nanotubes in Intravenously Exposed Mice. *Toxicol. Lett.* **2008**, *181*, 182–189.

29. Ruiz, O. N.; Alvarez, D.; Torres, C.; Roman, L.; Daniell, H. Metallothionein Expression in Chloroplasts Enhances Mercury Accumulation and Phytoremediation Capability. *Plant Biotechnol. J.* **2011**, *9*, 609–617.

144

Appendix H. Homogeneous Catalysis of Liquid-Phase Hydroperoxide Decomposition in Hydrocarbons

Homogeneous Catalysis of Liquid-Phase Hydroperoxide Decomposition in Hydrocarbons

Zachary J. West,* Ryan K. Adams, and Steven Zabarnick

University of Dayton Research Institute, 300 College Park, Dayton, Ohio 45469-0043, United States

ABSTRACT: The autoxidation of jet fuel takes place via a complex free radical reaction mechanism that involves the decomposition of hydroperoxides. The liquid-phase, unimolecular decomposition of hydroperoxide has been isolated for experimental study. Three hydroperoxides relevant to jet fuel autoxidation, including cumene hydroperoxide (CHP), dodecane hydroperoxide (DHP), and ethylbenzene hydroperoxide (EBHP), were thermally decomposed separately and found to closely fit first-order behavior with respect to hydroperoxide concentration. The activation energy for liquid-phase thermolysis of these hydroperoxides was found to be significantly less than typical gas-phase values. Parameters affecting the rate of hydroperoxide decomposition, such as dissolved metal content, organic acids, and metal deactivator additive (MDA) were explored. Metal type was shown to be a significant factor affecting hydroperoxide decomposition rate, while naphthenic acids (NA) were shown to have little effect on the rate. However, when dissolved metal and NA were added together a strong synergistic effect on hydroperoxide decomposition rate was noted. The increases in decomposition rate due to dissolved metal and/or acid were effectively inhibited by treatment with MDA.

■ INTRODUCTION

Thermal oxidation of liquid hydrocarbons has been a point of study for many decades due to the practical implications of these reactions. A specific area of concern is that of jet fuel thermal stability. Jet fuel is used as a coolant, or heat sink, for critical aircraft and engine components. However, as the fuel is exposed to increasing temperatures and heat loads the rate of thermal oxidative reactions increase. These reactions are due to the presence of ca. 1.8 mM dissolved oxygen. The subsequent autoxidation of fuel hydrocarbons occurs in aircraft fuel lines, often producing undesirable products such as gums, varnishes, and deposits. These bulk and surface deposits foul critical fuel system components, e.g., valves, filters, and nozzles, and if the fouling is left unchecked can ultimately lead to catastrophic system failure. Therefore, a more complete understanding of jet fuel autoxidation and deposition chemistry is desired to both predict deposition *a priori* and present opportunities for deposit mitigation strategies.

Many schemes have been used to model the complex chemical kinetics involved with hydrocarbon autoxidation, pyrolysis, and/or combustion such as global, detailed, and pseudo-detailed mechanisms.[1−3] The global modeling approach obscures the actual chemical mechanisms in order to simplify the problem; however, these models tend to simply fit experimental data and are difficult to extrapolate to other conditions and systems due to the inherent lack of chemically meaningful reactions and rate parameters. The development of detailed chemical kinetic mechanisms provides the greatest chemical realism and allows extrapolation to a range of conditions, but is intractable for complex real fuel mixtures, especially when combined with computational fluid dynamic (CFD) simulations. The pyrolysis community has often used the knowledge of fundamental reaction pathways and applied this knowledge to a more comprehensive "lumped" model using species class reactions rather than individual ones.[2,4] In a similar way, the problem of liquid-phase jet fuel autoxidation has recently been studied using pseudo-detailed oxidation mechanisms.[5] The pseudo-detailed oxidation mechanism groups the bulk hydrocarbon and trace heteroatomic species into classes and is believed to strike a useful balance between the global modeling approach and the use of detailed chemical kinetic mechanisms. These pseudo-detailed mechanisms retain the chemical realism of the detailed mechanisms, yet are small enough to be readily employed into CFD simulations. Pseudo-detailed mechanisms have been used successfully to predict jet fuel oxidation and deposition over a range of fuel samples, temperatures, and flow regimes.[5] Yet more refinement to these pseudo-detailed mechanisms, by both experimental validation and expanded chemical knowledge, is desired especially regarding the catalytic effects of metals and the decomposition pathways of hydroperoxide intermediates. To achieve this refinement, pseudo-detailed models rely upon focused studies of specific reaction pathways that involve classes of chemical species.

It is generally accepted that jet fuel autoxidation proceeds via a free radical chain mechanism, like that reported recently by Kuprowicz, et al.[5] and shown schematically in Figure 1. Where the RH in the figure represents a jet fuel hydrocarbon species, R· and RO$_2$· are the subsequent hydrocarbon radical and peroxy radical, respectively, RO$_2$H is a hydroperoxide, AH is a phenolic species, and SH is a reactive sulfur species. Hydroperoxides are the primary product of autoxidation at lower temperatures, ≤120 °C; however, they decompose at higher temperatures to form radicals which autoaccelerate the oxidation process. Hydroperoxides may also react with other heteroatomic species in fuels, e.g., sulfides and disulfides, to form nonradical products that have been implicated as deposit precursors.[6,7] Dissolved metals and
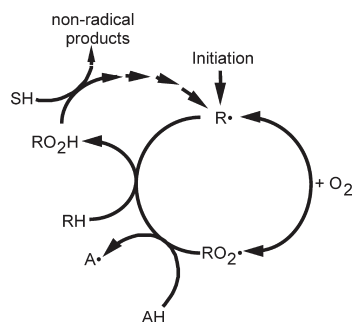
146

Figure 1. Diagram of the autoxidation chain mechanism for jet fuel.[5]

organic acids present in jet fuel are thought to catalyze these hydroperoxide decomposition pathways.

Although hydrocarbons are not conducive to solubilizing metal ions directly, trace amounts of dissolved metals are present in jet fuel with the aid of naturally occurring organic ligands. The exact forms of these organic ligand species are not well-known; however, the most likely is a mixture of carboxylic acids, e.g., naphthenic acids. Fuel contacts various metal components in the production and supply chains, which can bind with the naphthenic acids in the fuel to form fuel soluble metal naphthenates. Even with limited solubility, ppb to low ppm levels of metals have been shown to impact the thermal oxidative stability of jet fuels by increasing the overall oxidation rate and/or increasing the deposition tendency of a given fuel.[8] Experiments investigating the impact of metals on the thermal stability of fuel have generally concentrated on the net effects of oxidation and/or deposition, i.e., a global viewpoint, with few studies focusing on the direct impact of these metals on any one mechanistic step.

Carboxylic acids that act as metal ligands are produced during oxidation of fuel hydrocarbons when excess oxygen is present. Accumulation of organic acids therefore occurs during fuel storage, where oxygen is in abundance, as opposed to aircraft use conditions, where the oxygen in the fuel system tubing is limited and can be consumed. Aside from being able to chelate and solubilize metals in fuel, organic acids have been shown to increase fuel deposition and are typically considered to have a negative impact on fuel thermal stability and material compatibility.[8]

Although many studies of acid catalyzed hydroperoxide decomposition can be found in the literature, the experimental conditions typically involve high reactant concentrations, strong acids, and nonhydrocarbon solvents.[9,10] These conditions are completely unlike the conditions experienced in a typical jet fuel environment where low reactant concentrations are expected due to the low dissolved oxygen content. Moreover, specification tests such as total acid number (TAN), ASTM D3242, and existent gums, ASTM D381, are designed to alert the jet fuel user of excessive oxidation during storage; therefore, accumulation of oxygenated products during storage should be minimized when specification fuels are used. For example the TAN is limited to a maximum concentration of only 0.015 mg KOH/g, or ca. 0.2 mM, for specification JP-8 jet fuels.[11] Also, the acids generated during fuel oxidation are weak organic acids, not the strong mineral acids often studied as catalyzing reagents. Additionally, it has been shown that nonpolar hydrocarbon solvents tend to encourage homolytic reaction pathways and suppress heterolytic ones, whereas polar solvents encourage heterolytic reactions.[12]

Thus, previous studies investigating catalysis of hydroperoxides conducted in polar solvents hold only limited relevance to the chemical pathways in jet fuel.

There is mounting evidence that questions the role of dissolved metals as true catalysts in jet fuel. Zabarnick and Phelps reported[13] the homolytic decomposition of hydroperoxide is believed to have no activation energy barrier, E_a, and thus cannot be truly catalyzed by the lowering of the energy barrier. The reduced E_a of metal "catalyzed" hydroperoxide decomposition could be due to a lower energy pathway forming different radical products, such as the formation of a new metal complex. Additionally, Morris et al.[14] have reported that dissolved copper tends to be removed from the fuel during autoxidation and concentrates in carbonaceous deposits. Thus the copper is actually being consumed during thermal oxidation rather than being regenerated like a true catalyst. It might be more accurate to say hydroperoxide decomposition can be metal assisted, rather than catalyzed.

The aim of this work is to explore the fundamental hydroperoxide decomposition pathways pertinent to jet fuel thermal stability including: simple thermal homolysis, dissolved metal assisted, weak-acid assisted, and a combination of dissolved metal and weak-acid assisted hydroperoxide decomposition. Conditions have been chosen to relate closely to that of real jet fuel thermal stress conditions, i.e., hydrocarbon solvent, 105−205 °C, hydroperoxide concentration of ≤1.8 mM, TAN ≤0.015 mg KOH/g, and dissolved metal levels in the ppb to low ppm range.

■ EXPERIMENTAL SECTION

Hydroperoxide Decomposition Procedure. A 316 stainless steel Parr reaction vessel, ca. 100 mL total volume, equipped with a thermocouple, pressure transducer, headspace dissolved oxygen sensor, and syringe sampling port was used to conduct all of the kinetic experiments. The reaction liquid was well stirred using a magnetic stir bar. The experiments were conducted by first loading the reaction vessel with 60 mL of surrogate fuel, i.e., Exxsol D-80. Exxsol D-80 is an aliphatic hydrocarbon distillate within the jet fuel range which contains very low heteroatom levels. A low flow (≤20 mL/min) of dry nitrogen gas was bubbled through the surrogate fuel for at least 1 h to remove oxygen from the system, which was verified by oxygen sensor readings. Once purged of oxygen, the reactor was then closed and heated to the desired reaction temperature in the range of 105 to 205 °C. After reaching the proper temperature, hydroperoxide reagent was injected via the syringe port and allowed to mix for 1 min. Sample aliquots of ca. 1−2 mL were then pulled via the syringe port at regular intervals for subsequent hydroperoxide analysis. The hydroperoxide quantitative analysis was conducted via a previously reported triphenylphosphine (TPP) method, where the TPP reacts quantitatively with the hydroperoxides in a sample to produce triphenylphosphine oxide (TPPO) with subsequent GC-FID detection of the TPPO.[15] Organometallics, naphthenic acids, and metal deactivator additive were added to the surrogate fuel prior to oxygen removal and heating. Replicate runs were conducted for some rate experiments and the relative standard deviation (RSD) was computed for these rate constants, k. Also, the 95% confidence interval was computed for Arrhenius parameters, E_a and A, when rate data were collected at more than three temperatures.

Hydroperoxide Production Procedure. Dodecane hydroperoxide (DHP) and ethylbenzene hydroperoxide (EBHP) solutions, which were not available commercially, were generated by low temperature oxidations of n-dodecane and ethylbenzene, respectively, with an overpressure of air. The n-dodecane low temperature oxidation was carried out by charging the Parr reactor with 60 mL of solvent and
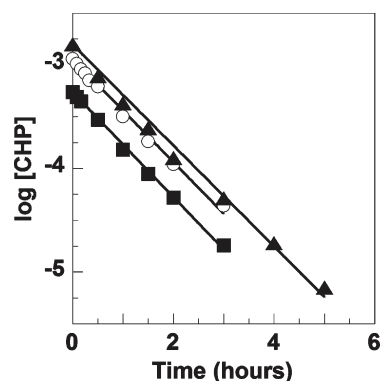
147

Figure 2. Decomposition of CHP in Exxsol D-80 at 165 °C with initial CHP concentrations of (■) 0.55 mM, (○) 1.1 mM, and (▲) 1.6 mM.

Figure 3. First-order decomposition of (■) CHP, (○) DHP, and (▲) EBHP at 145 °C.

Figure 4. Arrhenius plot of the first-order, liquid-phase decomposition of (■) CHP, (○) DHP, and (▲) EBHP.

95 psia of air, and then heating the reactor to 100 °C for 97 h. The ethylbenzene low temperature oxidation was carried out by charging the reactor with 60 mL of solvent and 73 psia of air, and then heating the reactor to 80 °C for 96 h. After the reaction period, both the DHP and EBHP reagent mixtures were allowed to cool to room temperature and then analyzed for hydroperoxide content. The DHP and EBHP reagent concentrations were verified to be 19.5 and 81.8 mM, respectively. The hydroperoxide reagents were kept in refrigerated storage until use.

Reagents. Exxsol D-80 was obtained from ExxonMobil Corp. and used without further purification. The following chemicals were used as received: cumene hydroperoxide (CHP), 88%, Sigma-Aldrich; n-dodecane, anhydrous, 99+%, Sigma-Aldrich; ethylbenzene, anhydrous, 99.8+%, Sigma-Aldrich; copper naphthenates (Cu-na), tech grade, Sigma-Aldrich; iron naphthenates (Fe-na), 12% wt Fe, manganese naphthenates (Mn-na), 6% wt Mn, zinc naphthenates (Zn-na), 10% wt Zn, Strem Chemicals, Inc.; copper bis(2,2,6,6-tetramethyl-3,5-heptanedioate) (Cu-tmhd), 99%, Acros Organics; naphthenic acids (NA), pract., 230−260 mg KOH/g, Acros Organics; N,N'-bis(salicylidene)-1,2-propanediamine (metal deactivator additive [MDA]), CAS 94-91-7, 98%, TCI America.

■ RESULTS

Before measurement of the Arrhenius parameters of hydroperoxide decomposition, experiments were performed to verify the conditions required for first-order, unimolecular hydroperoxide decomposition with minimal secondary reactions. Cumene hydroperoxide (CHP) was thermally decomposed at 165 °C with three initial CHP concentrations of ca. 1.6, 1.1, and 0.55 mM in Exxsol D-80. Exxsol D-80 was selected as a suitable jet fuel surrogate as it is a commercially available, aliphatic solvent that has a very low heteroatomic level and is within the jet fuel distillate range. To completely isolate the hydroperoxide decomposition reaction from interfering autoxidation reactions, the reaction vessel and liquid sample were first sparged with nitrogen to completely remove all oxygen from the system. Figure 2 shows the results of the CHP decomposition experiment, plotting the logarithm of the CHP concentration versus time. As the figure shows, the three sets of data can be fit with similar slopes, i.e., all three fits have a slope within 4% relative to one another and R^2 values of ≥0.991. These linear fits, over a range of initial ROOH concentrations, show that the decomposition of CHP is in accord with a unimolecular first-order process over the concentration range of interest, with no evidence of interference from secondary reactions.
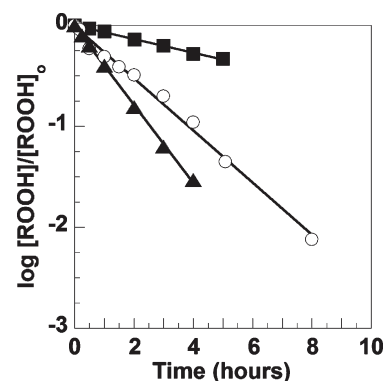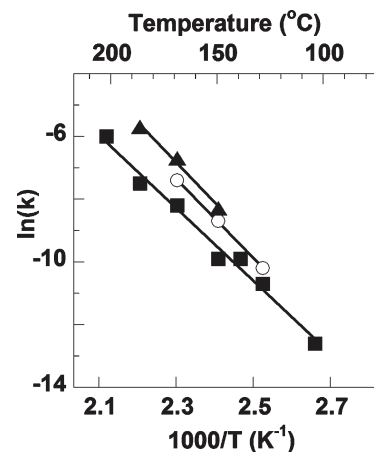
As we have shown that the unimolecular first-order decomposition rate of hydroperoxides can be measured in the liquid phase, we now add other potential fuel hydroperoxides, dodecane hydroperoxide (DHP) and ethylbenzene hydroperoxide (EBHP) to determine their relative reactivity. CHP, DHP, and EBHP were thermally decomposed, separately, in Exxsol D-80 at 145 °C with an initial hydroperoxide level of ca. 0.5 mM. Again oxygen was removed from the system to prevent interfering autoxidation reactions and the hydroperoxide concentrations were monitored over time. Figure 3 shows the resulting logarithm of the normalized hydroperoxide concentrations, i.e., hydroperoxide concentration divided by the initial hydroperoxide concentration, versus time. As the figure shows, the three sets of hydroperoxide data are linear, thus all three hydroperoxide decompositions fit first-order behavior at this temperature. There is also a significant difference in the decomposition rates of the three hydroperoxides where the decomposition rates follow the order EBHP > DHP > CHP. Researchers have often assumed that unimolecular hydroperoxide decomposition rates are independent of the hydroperoxide R group.[16] Although, recent calculations show the O−O bond strength can vary with the R group, especially for vinyl hydroperoxides which exhibit very weak O−O bond strengths.[17]

Table 1. Arrhenius Parameters for First-Order, Liquid-Phase Hydroperoxide Decompositions

hydroperoxide	E_a (kcal/mol)	Log(A) (s^{-1})	no. of exp. temps.
CHP	23 ± 3	7.6 ± 1.5	7
DHP	24	9.0	3
EBHP	25	9.4	3

Table 2. Rate Constants for Liquid-Phase CHP Decomposition

T (°C)	metal species	k (10^{-6}/s)	% RSD^a	k/k_o
105	-	3.5		-
	Cu-na	110		31
	Cu-tmhd	29		8
	Mn-na	1,500		429
125	-	22		-
	Cu-na	200		9
	Cu-tmhd	50		2
	Fe-na	69		3
	Mn-na	1,900		86
	Zn-na	18		0.8
135	-	51	23 (2)	-
	Cu-na	380		7
145	-	48	15 (2)	-
	Cu-na	490		10
	Cu-tmhd	160		3
	Fe-na	310		6
	Mn-na	6,200		129
165	-	280	27 (4)	-
	Cu-na	750	9 (3)	3
	Cu-tmhd	950		3
	Fe-na	1,000		4
	Zn-na	353		1.3
185	-	540		-
	Cu-na	1,900		4
	Cu-tmhd	2,800		5
205	-	2,600		-
	Cu-na	5,800		2

^{a} Values in parentheses are the number of replicate runs used to compute the % RSD.

For development of improved chemical kinetic mechanisms, it is desirable to obtain Arrhenius parameters for the unimolecular, thermal decomposition of hydroperoxides in the liquid phase under representative jet fuel conditions. Thus CHP decomposition rate experiments were conducted at seven temperatures from 105 to 205 °C, with the results shown in Figure 4 and the calculated Arrhenius parameters listed in Table 1. The CHP thermal decomposition data in Table 1 are in good agreement with literature values, as discussed later, which gives confidence in the current experimental procedure. Arrhenius parameters were also determined for DHP and EBHP over a limited temperature range using only three temperatures, with the experimental results shown in Figure 4 and listed in Table 1. The Arrhenius parameters for DHP and EBHP are not significantly different from those of CHP even though the individual rate constant data are significantly different (see, e.g., Figure 3) for the three hydroperoxides, this discrepancy is probably due to the

Table 3. Arrhenius Parameters for Pseudo-First-Order, Liquid-Phase Decomposition of CHP with 1 ppm Dissolved Metal Naphthenates

metal naphthenate	E_a (kcal/mol)	Log(A) (s^{-1})	no. of exp. temps.
Fe	23	8.6	3
Zn	26	9.4	2
Cu	14 ± 3	3.8 ± 1.5	8
Mn	11	3.4	3

Table 4. Rate Constants of Liquid-Phase CHP Decomposition with 0.128 mM Naphthenic Acids

T (°C)	k (10^{-6}/s)	k/k_o
105	9.2	2.6
125	16	0.7
145	90	1.9
165	430	1.5

limited number of temperatures for which data was collected for DHP and EBHP.

With the unimolecular decomposition order and Arrhenius parameters obtained for CHP thermal decomposition, experiments were conducted to determine the effect of dissolved metals on these measured rates. Metals were dissolved in Exxsol D-80 using various metal naphthenates at 0.012–0.015 mM of metal (ca. 1 ppm by weight of metal) prior to oxygen removal, heating, and CHP introduction. The experiments were carried out at a range of temperatures from 105 to 205 °C with an initial CHP concentration of ca. 0.5 mM. The measured pseudo-first-order rate constants, k, of CHP decomposition are listed in Table 2. Also listed in the table for the metal containing experiments is the relative rate constant, k/k_o, that is the pseudo-first-order rate constant of CHP decomposition with metal divided by the rate constant without metal, k_o. The data show that the addition of metal naphthenate increases the relative decomposition rate of CHP, i.e., $k/k_o \geq 1$, in all experimental cases except one: the addition of zinc naphthenate (Zn-na) at 125 °C. Very large increases in k/k_o were noticed for experiments involving copper naphthenate (Cu-na) and manganese naphthenate (Mn-na) at temperatures of 145 °C and lower. The decomposition of CHP proceeded so rapidly with the addition of Mn-na that it became impractical to measure rate data at temperatures of 165 °C and greater. Although the addition of copper increased k/k_o under all experimental circumstances, there was a marked difference in activity between the two copper species examined. The addition of Cu-na increased k/k_o much more than Cu-tmhd, even though the two species were added with equal levels of copper.

The rate data from Table 2 was used to generate Arrhenius parameters, listed in Table 3, for the pseudo-first-order decomposition of CHP with dissolved metal naphthenates. As the data show, iron and zinc do not cause a significant change in the activation energy of CHP decomposition under these experimental conditions. Conversely, copper and manganese both significantly decrease the pseudo-first-order activation energy and A-factor for unimolecular hydroperoxide decomposition. These results indicate that the decomposition of CHP proceeds via lower energy reaction pathways when Cu-na or Mn-na is present.

With the effect of various dissolved metals on the decomposition of CHP determined, we now wish to examine the consequence of dissolved acids on the CHP decomposition rate.

Table 5. Rate Constants for Liquid-Phase Hydroperoxide Decomposition with Metal Naphthenates and Naphthenic Acids

ROOH	T (°C)	metal species	[metal] (mM)	[NA] (mM)	k (10^{-6}/s)	k/k_o
CHP	105	-	-	-	3.5	-
		-	-	0.128	9.2	3
		Cu-na	0.013	-	110	30
		Cu-na	0.013	0.128	2,700	768
	125	-	-	-	22	-
		-	-	0.128	16	0.7
		Cu-na	0.013	-	200	9
		Cu-na	0.013	0.128	9,200	418
		Zn-na	0.012	-	18	0.8
		Zn-na	0.012	0.128	74	3
EBHP	125	-	-	-	85	-
		-	-	0.128	61	0.7
		Cu-na	0.013	-	830	10
		Cu-na	0.013	0.128	12,100	143

Table 6. Rate Constants of Liquid-Phase CHP Decomposition at 125 °C

[Cu-na] (mM)	[NA] (mM)	[MDA] (mM)	k (10^{-6}/s)	k/k_o
-	-	-	22	-
-	-	0.018	35	1.6
0.013	-	-	200	9
0.013	-	0.018	24	1.1
0.013	0.128	-	9,200	418
0.013	0.128	0.018	28	1.3

Experiments were conducted by dissolving naphthenic acids (NA) in Exxsol D-80 to a level of 0.128 mM KOH (0.009 mg KOH/g) prior to oxygen removal, heating, and CHP introduction. Commercially available NA, which is a petroleum-derived mixture of cycloparaffinic carboxylic acids, was selected because NA are believed to be relevant jet fuel acids.[18] As was done previously, the CHP concentration was monitored over time and the resulting pseudo-first-order rate constants are listed in Table 4 for four different temperatures. As the data show, the addition of NA increases the decomposition rate of CHP for three out of the four temperatures examined. However, the maximum observed increase in k/k_o for NA was much less than that observed for the metal naphthenates even though the NA was present at ca. 10 times the concentration of the metal; therefore, the metal naphthenates had a much greater effect on hydroperoxide decomposition than NA.

As we have already shown, reactive metal species such as Cu-na can dramatically increase the rate of hydroperoxide decomposition at low temperatures, ≤145 °C. Conversely, less reactive metal species such as Zn-na and moderately reactive naphthenic acids have shown, at most, a modest increase in the hydroperoxide decomposition rate. However, acids are known to catalyze metal reaction,[19] so experiments were conducted to examine the effect of naphthenic acids on the decomposition rates of hydroperoxides in the presence of a reactive and a less reactive metal species. The experimental procedure was consistent with the previous studies, in that the metal naphthenate and NA were dissolved in Exxsol D-80 prior to deoxygenation, heating, and hydroperoxide addition. Hydroperoxide concentrations were monitored over time and the resulting pseudo-first-order rate constants are listed in Table 5. The unassisted, metal-only assisted, and acid-only assisted data for CHP decomposition shown in Table 5 have been reproduced from previous tables to aid data interpretation. The data in the table clearly show that the combination of metal and acid produce a synergistic increase in the decomposition rate of hydroperoxide for all of the temperatures, metal species, or hydroperoxide species examined. This synergistic effect can be illustrated by examination of the CHP decomposition data at 125 °C, whereby addition of either NA or Zn-na alone has little effect on the relative rate constant of CHP

decomposition, whereas the addition of both NA and Zn-na increases the relative rate constant by a factor of 3.

Having shown the synergistic effects on ROOH decomposition, in the presence of dissolved metals, we now turn to the study of one possible mitigation strategy. The jet fuel community has long used metal deactivator additive (MDA) as a means to reduce the reactivity of dissolved metals, mainly copper, in an effort to improve fuel thermal stability. While it is known that MDA chelates dissolved metals, typically resulting in a net decrease in fuel deposition and oxidation rates, specific examples of the affected chemical pathways are not well documented. To this end, experiments were conducted with combinations of Cu-na, NA, and MDA, under conditions identical to those previously reported herein, to test if MDA has an effect on the metal assisted, weak-acid assisted, and acid–metal assisted hydroperoxide decompositions. The MDA was added at a concentration of 5.0 mg/L (0.018 mM) and the resulting pseudo-first-order rate constants are shown in Table 6. The experimental data generated without MDA have been reproduced from previous tables for ease of interpretation. The data show that the presence of MDA almost eliminates any increase in the relative rate constant for CHP decomposition due to the addition of Cu-na, or both NA and Cu-na. This demonstrates that MDA does effectively reduce the ability of dissolved metal species to assist in hydroperoxide decomposition, even in the presence of organic acids.

■ DISCUSSION

Hydroperoxides, which are formed during jet fuel autoxidation from the bulk fuel components, can be relatively stable at lower temperatures but at higher temperatures become a significant source of radical production. As jet fuel is a complex mixture of normal-, iso-, and cyclo-paraffins, as well as alkyl aromatics, hydroperoxides of various types can be formed in real jet fuel oxidation. The propensity for hydrogen abstraction, and thus subsequent hydroperoxide formation, of a given fuel hydrocarbon depends on both the bond strength and steric factors of the C—H bond. Zabarnick and Phelps calculated that abstraction of benzylic hydrogen from alkyl aromatic species has an E_a of at least 4–5 kcal/mol lower than abstraction of paraffinic hydrogens, making alkyl aromatic species, e.g., ethylbenzene and cumene, likely species that readily produce fuel hydroperoxides.[13] In this study, n-dodecane and ethylbenzene were oxidized separately, under mild conditions, to produce the subsequent hydroperoxides (see Experimental Section). It was found that the ethylbenzene readily produced hydroperoxides at 80 °C, whereas the n-dodecane required a higher temperature, 100 °C, to produce any significant quantity of hydroperoxide over a similar reaction time period. The higher yield of EBHP compared to DHP is experimental evidence supporting the assertion that species with weaker benzylic hydrogen bonds, e.g., ethylbenzene, are more

likely to form hydroperoxides under typical jet fuel thermal oxidation conditions. Therefore, CHP represents a relevant model fuel hydroperoxide since it is a jet fuel distillation range alkyl aromatic hydroperoxide.

The study of CHP decomposition under conditions representative of jet fuel thermal stability has some precedent. Mushrush et al.[20] observed the thermal decomposition products of CHP from 130 to 170 °C in benzene, and from this chemical analysis determined that the predominant reaction pathway must be homolysis of the O—O bond in the hydroperoxide. A wide variety of decomposition products were noted in the study including trace carboxylic acids. Unfortunately, the activation energy was not determined for the CHP decomposition reaction. The activation energy measured in this work for the decomposition of CHP in Exxsol D-80 was 23 ± 3 kcal/mol (see Table 1) and is in good agreement with a previous study which determined a value of 25.4 kcal/mol.[21] The CHP thermal decomposition studies of Mushrush et al., Nurullina et al.,[21] and this work were conducted in the liquid phase, which is relevant to the autoxidation of jet fuel in real fuel systems. However, the observed liquid-phase E_a of ca. 23—25 kcal/mol for CHP thermal decomposition is much less than the average gas-phase E_a value of ca. 43—45 kcal/mol for most hydroperoxides.[16,22] One possible argument to account for the large differences noted in the gas- and liquid-phase activation energies is not the reaction phase, but rather that the R group has an impact on the O—O bond strength. The gas-phase E_a, typically used for combustion modeling, is for an alkyl hydroperoxide, not an alkyl aromatic (or benzylic) hydroperoxide. Indeed it has been shown that the R group can alter the O—O bond strength significantly, whereby the bond energy is reduced by as much as ca. 20 kcal/mol when R is a vinyl or phenyl group compared to an alkyl group.[17] However, DHP also gives a liquid-phase E_a for thermolysis of 24 kcal/mol, which refutes the previous argument. One possible explanation for the disparity between the liquid- and gas-phase activation energies is that cage effects are present in the liquid-phase thermolysis of hydroperoxides. Cage effects are well-known in liquid-phase decompositions and have been demonstrated to affect the reaction rate constants of similar liquid-phase reactions.[19,23] The presence of cage effects may lower the apparent unimolecular liquid-phase E_a of hydroperoxide thermolysis and also decrease the frequency factor. Gas-phase unimolecular thermolysis has a frequency factor of ca. 10^{13} to 10^{16} s^{-1};[24] whereas the measured liquid-phase frequency factor was shown to be ca. 10^7 to 10^{10} s^{-1} for this work (see Table 1) and ca. 10^9 s^{-1} for Nurullina, et al. The large difference in both the E_a and the frequency factor is a significant issue when selecting values to be used for modeling purposes, as the more common gas-phase values have typically been used in pseudo-detailed computations, whereas the liquid-phase values may be more appropriate in light of the current findings.

An effect that has been recently incorporated into pseudo-detailed chemical mechanisms is the catalytic decomposition of hydroperoxides via a single bimolecular reaction involving a catalytic dissolved metal species and a hydroperoxide to produce two radicals.[5] Interestingly, the dissolved metals selected to incorporate into the model were Cu and Mn, while Fe, Mg, and Zn were excluded from the model. The authors' decision to include just these two dissolved metals, of the five that were quantified, was based upon the relatively large sensitivity of the model to the measured Cu and Mn concentrations of the fuel samples. As we have shown above experimentally (see Tables 2

and 3), both Cu and Mn naphthenates have a strong effect on the E_a of hydroperoxide decomposition. Additionally, we have shown that Fe and Zn appear to have little effect on the E_a for hydroperoxide decomposition. Both iron and zinc have been reported to increase the overall oxidation rate of jet fuels, however, only at much higher concentrations.[8] Thus the mode of action of iron and zinc may influence some other portion of the autoxidation chain, or the metals may simply require higher concentrations to affect the hydroperoxide decomposition step.

It was previously mentioned that transition metals are currently believed to take the form of organometallic salts, such as metal naphthenates, when dissolved in jet fuel; however, there is little understanding of the role of the ligand in metal catalysis of hydroperoxide decomposition. Therefore, copper bis(2,2,6,6-tetramethyl-3,5-heptanedioate) (Cu-tmhd) was chosen as a comparison species to Cu-na. The results in Table 2 clearly show that the organic ligand has an effect on the relative reaction rates of the two copper species, i.e., the hindered dioate complex (Cu-tmhd) tends to reduce the severity of catalytic hydroperoxide decomposition compared to the naphthenate complex (Cu-na). These results lead to the conclusion that organometallic speciation, rather than metal atom analysis, is important in determining the potential extent of catalysis of hydroperoxide decomposition. In contrast, the recently adopted approval process for alternative jet fuels (ASTM D4054) employs quantitative analysis of individual metal atoms rather than metal speciation.

Quantification of dissolved metals in petroleum-derived jet fuel is not currently required by specification, let alone the speciation of organometallic compounds; however, the total acid number (TAN) is a required specification property for jet fuel. Even though the TAN specification limit for JP-8 fuel is relatively low (0.015 mg KOH/g), as we have shown above the effects of a small (within specification) amount of acid, in the presence of dissolved metal, can have a synergistic effect on the decomposition rate of hydroperoxides (see Table 5). The synergistic increase in decomposition rate is significant when either a reactive metal, such as Cu, or a less reactive metal, such as Zn, are present with naphthenic acids. The mechanistic details of synergism are poorly understood, but the acid may affect the oxidation state of the metal during hydroperoxide decomposition, making the metal more reactive in encouraging hydroperoxide decomposition. Another possible explanation relates to the earlier mentioned concept that dissolved metal species may not be true catalysts during jet fuel autoxidation. Rather, instead of the metal ion being regenerated after hydroperoxide decomposition, Zabarnick and Phelps[13] proposed the formation of a metal complex, which for the case of divalent copper is CuOH^{+2}. The acid may act to help regenerate a more reactive form of the metal, thus increasing the hydroperoxide decomposition rate. Regardless of the mechanism, the concept of acid/metal catalysis has far reaching implications with regard to jet fuel handling and thermal stability. One unfortunate scenario would involve a high metal containing fuel that accumulates organic acids during storage. It is feasible that this hypothetical jet fuel initially has good thermal stability; however, upon storage, and subsequent acid accumulation, becomes a fuel with poor thermal stability. Therefore, it is useful to consider mitigating strategies to prevent this synergistic increase in hydroperoxide decomposition.

It has been known for some time that MDA has the ability to improve the overall thermal stability of jet fuels containing reactive dissolved metals.[25] Unfortunately, like many jet fuel studies, the global impact of MDA on thermal stability is often

the only cited result. This methodology prevents a fundamental understanding of the chemistry, and therefore, prevents the ability to predict this important fuel chemistry. The results shown in Table 6 provide insight into one chemical pathway that is strongly affected by the presence of MDA, i.e., metal assisted hydroperoxide decomposition. The ability of MDA to strongly complex with Cu effectively renders the dissolved metal unreactive with respect to catalyzing hydroperoxide decomposition. Since MDA is able to "turn off" this lower activation energy pathway to hydroperoxide thermolysis, and MDA has been shown to improve jet fuel thermal stability, the evidence shows the importance of hydroperoxide decomposition to the overall fuel thermal stability.

The goal of this work was to explore the kinetics of the fundamental hydroperoxide decomposition pathways that are relevant to jet fuel thermal stability. While rate parameters and important pathways for hydroperoxide decomposition were identified in the current work, inclusion of these results into improved pseudo-detailed mechanisms for fuel autoxidation will require further experimental and modeling efforts. Proposed mechanism changes that directly follow from this work include the modification of the activation energies for the hydroperoxide decomposition reactions from the previously used higher gas-phase values[5] to the measured lower liquid-phase values, as well as inclusion of the measured metal catalyzed values. Also, a reaction involving the catalyzed decomposition of hydroperoxide by both metals and acids should be considered for inclusion in the mechanism. These changes in the mechanism will require a modeling effort to ensure that the modifications do not negatively impact the previous agreement observed with experimental measurements.[5] Additional experimental measurements may also be required to validate the mechanism changes. Also, the observation that metal speciation effects the catalytic hydroperoxide decomposition rate shows the need for improved methods for metal speciation in hydrocarbons such as the use of liquid chromatography combined with atomic absorption[26] or mass spectrometric detection.[27,28] The recent interest in alternative synthetic jet fuels, e.g., synthetic paraffinic kerosene (SPK) and hydrotreated renewable jet fuel (HRJ), opens the question of the relevance of the current measurements to these new fuels. These alternative fuels are currently being proposed to be used in 50/50 blends with petroleum fuels. The resulting mixtures will have hydroperoxide species that are very much the same as 100% petroleum-derived fuels, and thus the current results are still relevant to the blends. However, the use of 100% SPK or HRJ fuels, which are entirely aliphatic, will produce only aliphatic hydroperoxides during autoxidation. It is suggested that alternative fuel thermal stability experiments and modeling should be performed to validate the usefulness of these mechanisms developed for conventional fuels.

CONCLUSIONS

We have reported on experimental measurements of hydroperoxide decomposition under conditions relevant to liquid-phase jet fuel autoxidation. The unimolecular decomposition of hydroperoxide was shown to closely fit first-order behavior with respect to the hydroperoxide concentration. The first-order behavior occurred for a range of three different hydroperoxides: CHP, DHP, and EBHP. The activation energy for liquid-phase hydroperoxide decomposition was shown to be ca. 20 kcal/mol lower than the gas-phase activation energy, which is primarily attributed to cage effects in the liquid phase. Addition of

dissolved metals increases the decomposition rate of hydroperoxide; however, this effect is dependent upon the metal type and ligand type, where Cu and Mn were shown to be very reactive and Fe and Zn were shown to be less reactive elements. The addition of NA alone was shown to have little effect on the hydroperoxide decomposition rate; however, the combination of NA and dissolved metal proved to synergistically increase the rate of hydroperoxide decomposition. Finally, it was shown that MDA can effectively inhibit the increased hydroperoxide decomposition rate due to dissolved Cu, even in the presence of NA.

AUTHOR INFORMATION

Corresponding Author
*E-mail: Zachary.West@wpafb.af.mil.

DISCLOSURE

ACKNOWLEDGMENT

REFERENCES

(1) Katta, V. R.; Jones, E. G.; Roquemore, W. M. *Combust. Sci. Technol.* **1998**, *139*, 75–111.

(2) Ranzi, E.; Dente, M.; Goldaniga, A.; Bozzano, G.; Faravelli, T. *Prog. Energy Combust. Sci.* **2001**, *27*, 99–139.

(3) Zabarnick, S. *Energy Fuels* **1998**, *12*, 547–553.

(4) Curran, H. J.; Gaffuri, P.; Pitz, W. J.; Westbrook, C. K. *Combust. Flame* **1998**, *114*, 149–177.

(5) Kuprowicz, N. J.; Zabarnick, S.; West, Z. J.; Ervin, J. S. *Energy Fuels* **2007**, *21*, 530–544.

(6) Jones, E. G.; Balster, W. J.; Balster, L. M. *Energy Fuels* **1996**, *10*, 509–515.

(7) Mushrush, G. W.; Beal, E. J.; Slone, E.; Hardy, D. R. *Energy Fuels* **1996**, *10*, 504–508.

(8) Hazlett, R. N. *Thermal Oxidation Stability of Aviation Turbine Fuels*; ASTM: Philadelphia PA, 1991.

(9) (a) Kharasch, M. S.; Fono, A.; Nudenberg, W. *J. Org. Chem.* **1950**, *15*, 748–752. (b) Kharasch, M. S.; Fono, A.; Nudenberg, W. *J. Org. Chem.* **1951**, *16*, 113–127. (c) Kharasch, M. S.; Burt, J. G. *J. Org. Chem.* **1951**, *16*, 150–160.

(10) Petrov, L. V.; Solyanikov, V. M.; Denisov, E. T. *Russ. Chem. Bull.* **1977**, *26*, 670–677.

(11) *Detail Specification: Turbine Fuel, Aviation, Kerosene Type, JP-8 (NATO F-34), NATO F-35, and JP-8 + 100 (NATO F-37)*; MIL-DTL-83133G; 2010.

(12) Gao, F.; Boyles, D.; Sullivan, R.; Compton, R. N.; Pagni, R. M. *J. Org. Chem.* **2002**, *67*, 9361–9367.

(13) Zabarnick, S.; Phelps, D. K. *Energy Fuels* **2006**, *20*, 488–497.

(14) Morris, R. E.; Evans, T.; Hughes, J. M.; Colbert, J. E.; Kamin, R. A.; Nowack, C. J. Oxidation of JP-5 in Single and Multi-Pass Flow Testing. In *Proceedings of the 9th International Conference on Stability and Handling of Liquid Fuels, Sitges, Spain, Sept 18−22*, 2005; pp 244−259.

(15) West, Z. J.; Zabarnick, S.; Striebich, R. C. *Ind. Eng. Chem. Res.* **2005**, *44*, 3377–3383.

(16) Benson, S. W. *Prog. Energy Combust. Sci.* **1981**, *7*, 125–134.

(17) Sebbar, N.; Bockhorn, H.; Bozzelli, J. W. *Phys. Chem. Chem. Phys.* **2002**, *4*, 3691–3703.

(18) Coordinating Research Council. *Handbook of Aviation Fuel Properties*, 3rd ed.; CRC Report No. 635; Alpharetta, GA, 2004.

(19) Denisov, E. T. *Liquid-Phase Reaction Rate Constants*; IFI/Plenum: New York, 1974.

(20) Mushrush, G. W.; Beal, E. J.; Pellenbarg, R. E.; Hazlett, R. N.; Eaton, H. R.; Hardy, D. R. *Energy Fuels* **1994**, *8*, 851–855.

(21) Nurullina, N. M.; Batyrshin, N. N.; Kharlampidi, Kh. E. *Pet. Chem.* **2006**, *46*, 349–352.

(22) Denisov, E. T.; Denisova, T. G. *Handbook of Antioxidants*, 2nd ed.; CRC Press: New York, 2000.

(23) Pryor, W. A.; Smith, K. *J. Am. Chem. Soc.* **1970**, *92*, 5403–5412.

(24) Gardiner, W. C. *Rates and Mechanisms of Chemical Reactions*; W. A. Benjamin: London, 1972.

(25) Waynick, J. A. *Energy Fuels* **2001**, *15*, 1325–1340.

(26) Taylor, D. B.; Synovec, R. E. *J. Chromatogr., A* **1994**, *659*, 133–141.

(27) Gatlin, C. L.; Turecek, F.; Vaisar, T. *Anal. Chem.* **1994**, *66*, 3950–3958.

(28) Taylor, K. B. M.S. Thesis, University of Dayton, Dayton, OH, 2010.

153

Appendix I. Effects of Flow Passage Expansion or Contraction on Jet-Fuel Surface Deposition

Effects of Flow Passage Expansion or Contraction on Jet-Fuel Surface Deposition

Hua Jiang,* Jamie S. Ervin,† Steven Zabarnick,‡ and Zachary West§
University of Dayton Research Institute, Dayton, Ohio, 45469

The vast majority of previous flow studies of jet-fuel autoxidative deposition have been performed using straight cylindrical tubing of a constant diameter despite the fact that real aircraft fuel systems and nozzles contain complex flow passageways. As a result, the role of this complex flow environment and the resulting changes in heat transfer and flow on fuel oxidation/deposition chemistry are poorly understood. In the current work, experiments and computational fluid dynamics (CFD) modeling were performed for jet fuel flowing through heated tubes that have either a sudden expansion or contraction to study the effect of flow path changes on fuel oxidation and deposition. The experiments were conducted under isothermal wall (205°C), laminar flow conditions with monitoring of the outlet dissolved O_2 and post-test measurement of the surface carbon profile. The fuel flow rate was varied to study the role of residence time and oxidation extent on deposition near the geometry change. The CFD model includes a chemical kinetic mechanism, which was used to simulate the autoxidative deposition chemistry. With an expansion, the peak deposit occurs in the wide secondary tube. The CFD simulations show increased deposition caused by a recirculation zone after the flow expansion. For the contraction, increased deposition occurs at the beginning of the narrow secondary tube.

Nomenclature

A	=	pre-exponential factor in Arrhenius rate expression, mol, l, s
D	=	mass diffusivity, $m^2 \cdot s$
R_0	=	radius corresponding to tube centerline, mm
R_e	=	radius corresponding to primary tube wall, mm
R_w	=	radius corresponding to secondary tube wall, mm
r	=	radial location, mm
r_a	=	radius of inner corner, mm
r_b	=	radius of outer corner, mm
V	=	velocity, mm/s

I. Introduction

IN ADDITION to serving as the combustion propellant, jet fuel often serves as a convenient, zero weight penalty cooling media for the lubrication system, environmental control system, and other engine components of military aircraft [1]. Unfortunately, exposing hydrocarbon fuels to high temperatures can promote autoxidative reactions with the production of insoluble products and surface deposition. The insoluble products and surface deposits have the potential to block close tolerance passageways, such as in valves and nozzles, which degrades system performance and may ultimately result in engine failure.

Designers of engines and fuel systems rely heavily on empirically determined rules and limits, such as nozzle fuel and surface temperature limits, to allow the fuel to be used as a coolant while limiting fuel degradation. Because these empirical rules need to be conservative, they can greatly limit the efficiency of using fuel as a coolant. In turn, this limits engine and aircraft capabilities. In recent

*Research Engineer, 300 College Park.
†Senior Research Engineer, 300 College Park. Associate Fellow AIAA.
‡Distinguished Research Chemist, 300 College Park.
§Research Engineer, 300 College Park.

years, work in our laboratory has been directed toward the development of pseudodetailed chemical kinetic mechanisms for fuel autoxidation combined with a global deposition submechanism [2–5]. These chemical kinetic mechanisms have been combined with a computational fluid dynamics (CFD) model to simulate fuel oxidation and deposition in flow-through cylindrical tubes [4,5]. The work has shown that fuel sample variability in oxidation and deposition rates can be understood and predicted based upon quantitative chemical analysis measurements of key species classes (e.g., phenols, reactive sulfur, and metals) in combination with the CFD/chemical kinetic mechanism [5]. In addition, our current model performs reasonably well over a range of temperatures and flow regimes (i.e., both laminar and turbulent flow) relevant for aircraft.

Previous model development efforts concentrated on fuel degradation and flow within straight cylindrical tubes [4,5]. In aircraft fuel systems, the fuel flows through an extremely complex series of flow passages from the fuel tank to the combustor. As an example of this complexity, Fig. 1 shows an image of a sectioned fuel nozzle that has primary and secondary flow passages. The primary circuit is used during combustor ignition and engine idle operation, whereas the secondary passages are actuated during cruise and high power operation [6]. Partial or complete blockage of either circuit would negatively impact engine operation, inhibiting proper combustion with the potential for combustor hot streaks. It is important to better understand the role of complex flow passageways on the resulting fluid dynamics, heat transfer, and thermal-oxidative chemistry that occurs in aircraft fuel systems to prevent catastrophic failure, minimize maintenance, and more efficiently use the fuel heat sink.

Widely used empirical design methods assume that surface deposition is primarily a function of the wetted-wall temperature [6]. However, such design methods cannot account for prior thermal degradation of the fuel that may occur upstream of the component of interest. In addition, these empirical methods do not include the interaction between the fluid dynamics and chemistry. The flow regime (e.g., laminar or turbulent) has an obvious effect on heat transfer, but the coupling of flow geometry changes with temperature, residence time, and autoxidative chemistry has received little attention. The authors have found one previous study of fuel thermal-oxidative degradation within a fuel nozzle involving CFD calculations for a simplified geometry [7]. However, this work used an entirely global kinetic mechanism and did not detail the fluid flow and chemistry interactions. Thus, there is a need to study the

Fig. 1 Image of sectioned fuel nozzle.

Table 1 Experimental parameters

Experiment		Expansion	Contraction
Tube inner diameter, mm	Primary tube	0.69	2.16
	Secondary tube	2.16	0.69
Flow rate, ml/ min		0.1–1.0	0.2–0.8
Residence time, s		138–1384	73–233
Test duration, h		17–165	21–66
Length of primary, mm		203.2	
Length of secondary, mm		609.6	
Tube outer diameter, mm		3.18	
Fuel sample		F4177 and F3084	
Inlet temperature, °C		27	
Wall temperature, °C		205	

effects of flow path geometry on fuel heat transfer, fluid dynamics, autoxidation, and surface deposition.

The simplest flow geometry change occurs when the fuel encounters a sudden expansion or contraction in cylindrical tube flow. Such sudden geometry changes, especially contractions, are encountered in numerous locations in the fuel feed line between the fuel tank and the engine. As fuel flows through a sudden expansion in flow path, a recirculation flow is created that should increase the local fuel residence time. We can hypothesize that this will result in greater dissolved O_2 consumption with a resulting increase in deposition near the expansion. For the contraction case, the fuel will encounter a stagnation zone at the contraction, which will also increase the local fuel residence time. Thus, we can also hypothesize a possible increase in surface deposition near the contraction. Increased local deposition rates can have important implications for the design of fuel systems and nozzles. For example, a fuel system designer would want to avoid close tolerance passageways and high surface temperatures in locations with increased local fuel residence times. No studies have been performed previously to quantify the effect of these flow changes (i.e., determination of the amount of deposition increase and its location) on fuel deposition for aircraft fuel system conditions.

In the present study, we investigate the effects of a sudden change in the inner diameter (ID) of a cylindrical tube on the oxidation and surface deposition rates for jet fuel flowing under isothermal wall and laminar flow conditions using both experimental measurements and CFD simulations. The isothermal surface conditions are employed to focus on the effect of the flow geometry on the fluid dynamics and chemistry without the complication of varying wall temperatures. Both contraction and expansion tube geometries were employed under conditions of complete dissolved O_2 consumption with the goal of having the maximum deposit rate occur near the tube geometry change. The use of the near-isothermal flowing test rig (NIFTR) and isothermal surfaces limits the experiments to laminar flow conditions. The measurements are used to determine the deposition rate along the tube length and the outlet dissolved O_2 level, whereas the calculations are used to increase the understanding of the coupled fluid dynamics and chemistry and to allow extrapolation to other conditions that are not amenable to experiments. Computational fluid dynamics combined with a pseudodetailed chemical kinetic mechanism and global deposition

submechanism are used to simulate the dissolved O_2 consumption and the deposit formation as a function of flow rate. The primary goals of this work are to increase the understanding of the role of flow geometry changes on fuel deposition and to improve the ability of fuel system and nozzle designers to efficiently use the fuel heat sink while preventing the negative impact of fuel degradation associated with high-temperature fuel autoxidation.

II. Experimental

The experiments were performed in the NIFTR (Fig. 2) [8]. A syringe pump was used to pump the fuel through 1.02 m (40 in.) of stainless-steel (316) tubing. A portion of this tubing (0.81 m) was clamped within a heated copper block for heating purposes. A back pressure regulator maintained the system pressure (2.3 MPa) to ensure a single liquid phase during the test duration. In addition, temperature controllers were used to maintain the constant wall temperature of the heated section. The fuel temperature at the outlet of the heated section was monitored to ensure steady-state thermal conditions. Measurements of the dissolved O_2 are obtained by in-line sampling of the fuel and injection into a gas chromatograph and are reproducible to within $\pm 5\%$ [9].

Two geometries (expansion and contraction) and two fuel samples (F4177 and F3084) were used in the experiments. The experimental conditions (Table 1) were chosen to obtain complete dissolved O_2 consumption within the heated section and to have the dissolved O_2 consumption rate and deposit location be a maximum near the tube geometry change. Requiring the O_2 to be fully consumed allows comparison of the total deposit mass for different flow conditions. The fuel reaction time in each experiment was controlled by varying the fuel flow rate. Preliminary experimental measurements and CFD calculations confirmed that the volume (990 ml) of fuel when heated to 478 K was sufficient to produce a measurable level of deposits. In Table 1, primary tube refers to the inlet tube, and secondary tube refers to the downstream passage after the change in ID. Details of the two fuel samples are given elsewhere [5].

At the completion of a run, the heated tube was cut into 17 segments for deposit quantification. Because the area near the geometry change was of primary interest, the tube segment encompassing the weld seam (Fig. 3b) was cut to the smallest length (1.27 cm). The largest segments (5.1 cm in length) were furthest from the weld seam. (Figure 4 gives an indication of the segment length variation.) Bulk insolubles were collected at the tube exit by 0.2 and 0.45 μm filters. The tube segments and filters were rinsed with
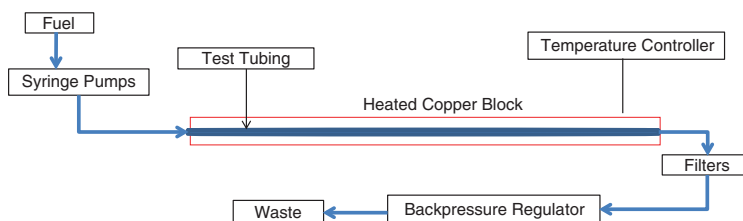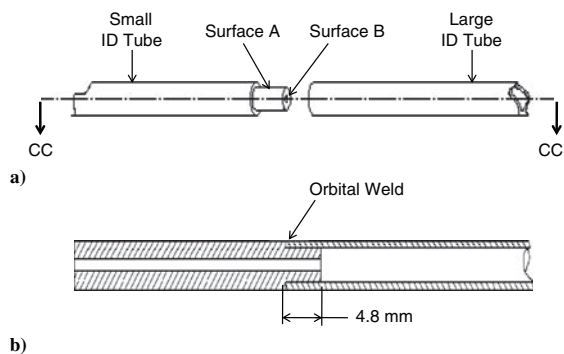

Fig. 2 Schematic diagram of the NIFTR.

Fig. 3 Drawings of the tubes: a) overlapping weld components and b) section view CC–CC.

heptane and dried in a vacuum oven at 100°C. The carbon mass within the tube segments (effectively, the accumulated surface deposit mass) and filters was determined using carbon burn-off measurements (LECO RC-412 surface-carbon analyzer). The carbon burn-off measurements were corrected by subtracting the background carbon present on a clean, untested tube segment of the same dimensions. The measured carbon mass represents an average value over a tube segment for the entire test period.

The heated tubing had either a sudden expansion or contraction in the flow path, depending on the flow direction. Figure 3a depicts how two tubes with the same outer diameter but different IDs were machined and joined to form an abrupt change in the flow passage geometry. At the junction of the two tubes, surface A of the small tube was machined to match the large tube ID, allowing a press fit of the two sections. Surface B was machined flat such that it was perpendicular to the tube axis. Figure 3b shows the cross section of the tubes after they were fit together for welding. The 4.8 mm length of engagement insured that both tubes remained concentric. A welder (Swagelok, SWS-M100-MS-13-202) was used to weld the tubes along the joining seam.

III. Numerical

A. Computational Fluid Dynamics

Numerical simulations were performed to explore the effects of a sudden expansion or contraction in the flow path on the fuel velocity,

autoxidative chemistry, and surface deposition. A commercially available computational fluid dynamics code (Fluent) was used to solve the Navier–Stokes, energy, and species equations for the velocity, pressure, temperature, and species mass fractions [10]. The flow was assumed to be steady, two-dimensional, and axisymmetric. Because the Reynolds number was always below 200 in the simulations, the flow was assumed to be laminar. The enthalpy of reaction was not included in the energy equation because the thermal-oxidative reactions involve trace species, and heating by viscous dissipation was neglected. The transport and thermodynamic properties were assumed to be temperature-dependent.

The governing equations in finite volume form were solved iteratively using a second-order accurate upwind scheme. In addition, the SIMPLEC pressure-velocity coupling scheme was used in the solution of the momentum equations [11]. When the normalized error residuals for all of the calculated variables were reduced by 6 orders of magnitude below their maxima, the solution was considered to be converged. With regard to the boundary conditions, the wall boundary was held at a constant temperature of 205°C. For simplicity, uniform velocity and temperature profiles (25°C) were assumed at the inlet, and the exit plane velocity and temperature profiles were calculated by extrapolation from interior cell values. The length of the thermal entrance region is relatively short, and the fuel becomes isothermal after ∼1 cm (roughly 1% of the heated tube length) at all flow rates. Because the flow is essentially isothermal, the gravitational body force in the momentum equation was neglected. Because the tube wall was thin (<1.5 mm), the radial temperature variation within the tube wall was also neglected. Thus, the wall temperature was assumed to be the same as that of the copper block. The effects of the deposits on the heat transfer and flow were also neglected because the deposits were assumed to be thin.

The computational grids are shown in Fig. 4 and represent the two flow geometries in the experiments. Because the tube length (0.81 m) is significantly greater than the ID (2.16 mm), the grid in the axial direction was spaced nonuniformly to reduce the computational time. The computational cells were clustered near the step region to better capture the larger flow, temperature, and species gradients there. A grid density study was performed to ensure the grid independence of the solutions. The dissolved O_2 concentration is important in the autoxidative mechanism, and large gradients were expected with this species. While monitoring the dissolved O_2 mass fraction, the baseline mesh (14,040 cells) in Fig. 4a was refined by three adaptations (gradient adaption approach [10] for a maximum
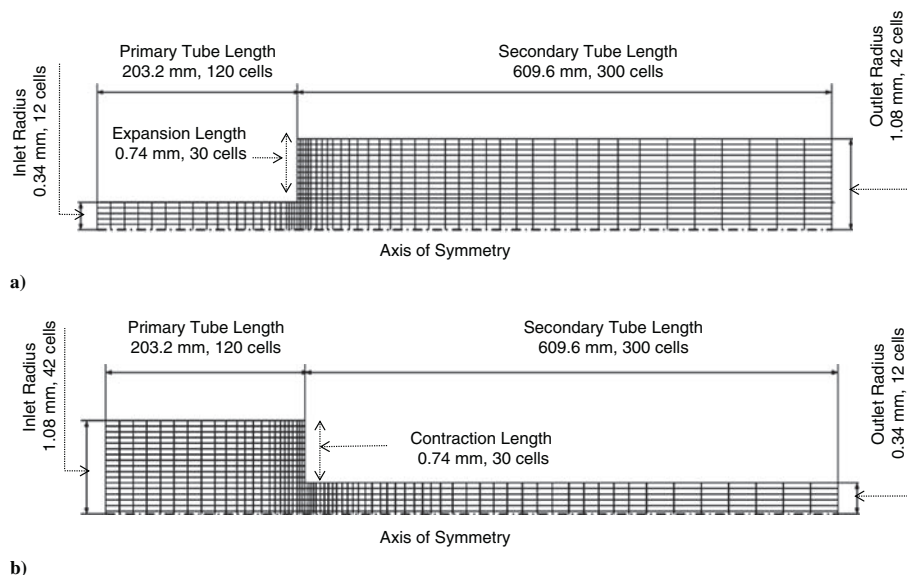
Fig. 4 Axisymmetric computational grids (not to scale): a) expansion (14,040 cells) and b) contraction (8640 cells).

Table 2 Pseudodetailed chemical kinetic mechanism for thermal-oxidative fuel degradation and global submechanism for surface deposition [5]

Reaction	Reactants			Products		Arrhenius "A" factor, mol, l, s	Activation energy, kcal/mol
1	I	—	→	R·	—	$1.00E-03$	0
2	R·	O_2	→	RO_2·	—	$3.00E+09$	0
3	RO_2·	RH	→	ROOH	R·	$3.00E+09$	12
4	RO_2·	RO_2·	→	$TERMRO_2RO_2$	—	$3.00E+09$	0
5	R·	R·	→	R_2	—	$3.00E+09$	0
6	RO_2·	AH	→	ROOH	A·	$3.00E+09$	5
7	A·	RH	→	AH	R·	$1.00E+05$	12
8	A·	RO_2·	→	PRODAH	—	$3.00E+09$	0
9	ROOH	SH	→	PRODSH	—	$3.00E+09$	18
10	ROOH	—	→	RO·	·OH	$1.00E+15$	39
11	RO·	RH	→	ROH	R·	$3.00E+09$	10
12	RO·	—	→	RPRIME	CARBONYL	$1.00E+16$	15
13	·OH	RH	→	H_2O	R·	$3.00E+09$	10
14	RO·	RO·	→	TERMRORO	-	$3.00E+09$	0
15	RPRIME	RH	→	ALKANE	R·	$3.00E+09$	10
16	RO_2·		→	R·	O_2	$1.00E+16$	19
17	RO_2·	R·	→	$TERMRO_2R$	—	$3.00E+09$	0
18	ROOH	M	→	RO·	·OH M	$3.00E+10$	15
19	PRODAH	—	→	SOLUBLES	—	$1.00E+09$	0
20	PRODAH	—	→	INSOLUBLES	—	$3.80E+10$	6.5
21	INSOLUBLES	—	→	DEPOSITS	—	$3.00E+03$	16.3

[a]I, initiator species; R· and RPRIME, hydrocarbon radicals; RO_2·, fuel peroxy radical; RH, hydrocarbon fuel; ROOH, fuel hydroperoxide; AH, peroxy radical inhibitors or antioxidants; SH, hydroperoxide decomposing species; M, dissolved metal species; A·, phenolic radical; RO·, alkoxy radical; PRODAH, product of peroxy radical and phenolic radical; TERMRORO, termination product of RO· pathway; $TERMRO_2R$, termination product of RO_2· and R·; $TERMRO_2O_2$, termination product of RO_2· and R·.

grid density of 37,900 cells). After each adaption, differences in the values of the dissolved O_2 mass fraction and deposition rate between the grids of 14,040 cells and 37,900 cells were negligibly small. Thus, the baseline grid with 14,040 cells was used in the simulations involving the expansion. A similar analysis was performed for the contraction, and the grid density (8,640 cells) of Fig. 4b was found to be sufficient.

B. Chemical Reaction Mechanism

Jet fuel is a complex mixture of hydrocarbons comprised of hundreds of chemical species that vary with the petroleum source and processing conditions. The large number of species prohibits the detailed kinetic modeling of jet-fuel thermal oxidation. Treatment of fuel components as classes of species in a kinetic mechanism has been used successfully in simulating the thermal oxidation of jet fuel [5]. This approach has been referred to as pseudodetailed chemical kinetic modeling. Pseudodetailed kinetic mechanisms are comprised of chemical reactions with rate parameters that are based on literature and theoretical values. Trace heteroatomic species are responsible for differences in the oxidation and deposition behavior among fuel samples. However, knowledge of the detailed behavior of trace heteroatomic species remains incomplete because of the challenges of their concentration measurement and variation among fuel samples. Table 2 lists the reactions used to simulate thermal oxidation and deposit formation [5]. Reactions 1–5 represent the main autoxidation chain. Reactions 6–9 represent antioxidant reactions that interfere with the chain and create surface deposition precursors. Reactions 10–18 represent the chemistry that occurs when hydroperoxides decompose at higher temperatures. Lastly, reactions 19–21 comprise a global submechanism that represents the production of soluble and insoluble products, as well as surface deposits. This mechanism also includes the effect of dissolved metals on hydroperoxide decomposition via reaction 18. Several important species are defined here, and other details of the mechanism are described in Kuprowicz et al. [5].

In the experimental work, JP-8 (F4177) and Jet A (F3084) samples were used to study thermal-oxidative deposition. This particular JP-8 sample produced relatively low levels of deposition upon heating, whereas the Jet A sample tended to produce greater masses of surface deposits. Previous work has shown that the oxidation and deposition behavior of fuel samples can be differentiated by experimental measurements of a few important species classes in the autoxidation

chemical kinetic mechanism [3]. Table 3 lists the mass fractions of the initial trace species for the fuel samples that were obtained from previous work [5]. The initial mass fractions of the listed trace species together with the mass fraction of RH sum to unity. The initial inlet mass fractions of the other 19 species were assumed to be zero.

n-Dodecane has a critical temperature and pressure similar to the pseudocritical temperature and pressure of the jet-fuel samples. Thus for simplicity, the temperature-dependent properties (density, thermal conductivity, dynamic viscosity, and specific heat) of the liquid phase fuel were assumed to be the same as that of n-dodecane and were obtained from SUPERTRAPP software [12]. The system pressure (2.3 MPa) available in the experiments was used for property determination. Because the mass diffusivities of the individual species in jet fuel are unknown, a constant mass diffusivity ($D = 8 \times 10^{-8}$ (m² · s)) was assumed for all species. Mass transfer diffusivities of this order have been shown to sufficiently represent the mass transfer in similar flows [4,5].

IV. Results

It was initially hypothesized that flow recirculation zones and/or areas of low velocity created by an abrupt expansion or contraction would increase dissolved O_2 consumption and surface deposition near the geometry change. Thus, experiments and numerical

Table 3 Initial mass fractions of species used in the chemical kinetic mechanism

Species	Initial mass fraction, kg/kg	
	F4177	F3084
I	2.08×10^{-9}	2.08×10^{-9}
O_2	7.08×10^{-5}	7.12×10^{-5}
ROOH	3.24×10^{-6}	3.29×10^{-6}
AH	5.91×10^{-5}	5.67×10^{-5}
SH	2.35×10^{-3}	9.40×10^{-4}
M	1.41×10^{-6}	3.17×10^{-8}

[a]The assumed molecular weights (atomic mass units) for the pseudospecies classes are: AH = 220, M = 64, ROOH = 202, SH = 202, and RH = 170. These values are based on representative molecules: AH = $C_{15}H_{24}O$ (BHT), M = Cu, ROOH = $C_{12}H_{26}O_2$ (dodecane hydroperoxide), SH = $C_{12}H_{26}S$ (dodecane thiol), and RH = $C_{12}H_{26}$ (n-dodecane).
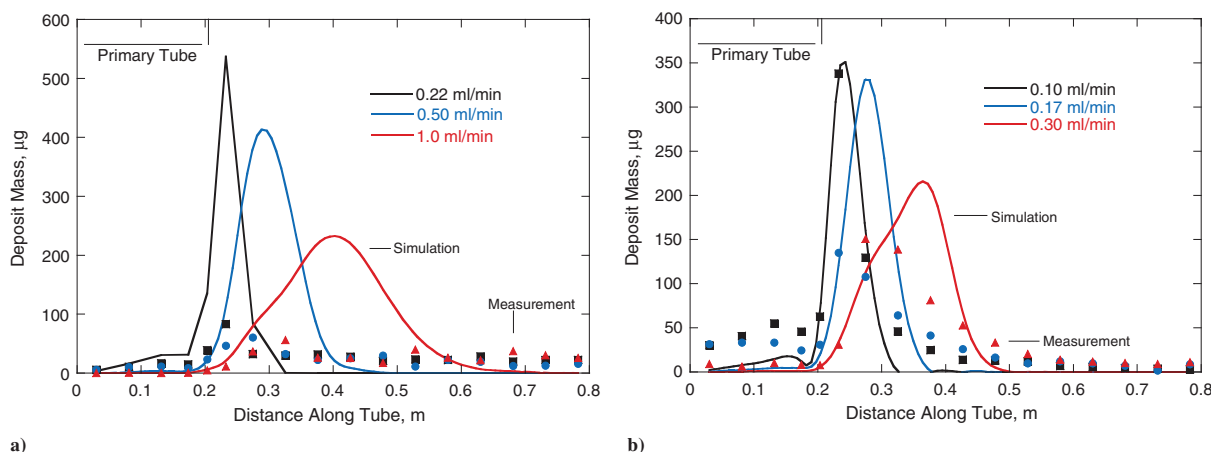
Fig. 5 Deposit masses for flow path expansion with different flow rates: a) JP-8 (F4177) fuel sample and b) Jet-A (F3084) fuel sample.

simulations were performed for fuel flowing in a heated tube for two arrangements, either an expansion or a contraction. The measured and calculated dissolved O_2 consumption, deposition rates, deposit peak locations, and deposit spatial profiles are used to study the effects of the flow changes caused by the step change in geometry on the reaction chemistry. The experimental conditions (wall temperature, flow rate, and test period) were chosen so that the deposition peak and maximum oxidation rates occur at or near the change in flow passage diameter to maximize its effect on the resulting fuel chemistry.

A.   Studies of Flow into an Abrupt Expansion
1.   Validation of Simulations with Surface Deposition Measurements

To use simulations to explore the influence of the fluid dynamics on fuel thermal degradation, it is important to first validate the simulated surface deposition with the measured deposit mass. For the case of the tube expansion, Figs. 5a and 5b show measured and simulated deposit masses from the two fuel samples (F4177 and F3084) along the heated primary and secondary tubes (Figs. 3a and 3b). (In this paper, all plotted solid curves represent simulations.) Three different flow rates were used to study the effect of reaction time and oxidation extent on the surface deposit distribution near the expansion. Previous NIFTR experiments that were performed at 185°C showed that F4177 oxidizes more rapidly than F3084 [5]. As a result of the differences in oxidation characteristics between the fuels, two different flow rate ranges (0.10–0.30 ml/min and 0.22–1.00 ml/min) were used to promote deposition near the step while completely consuming the dissolved O_2 for each fuel.

In previous studies, comparisons were usually made between measured and calculated deposition rates that were normalized by a constant surface area [5]. However in the present study, the flow passage surface area is not constant. Thus, Fig. 5 compares the calculated and measured deposition masses that are not normalized by surface area. In Fig. 5, a measured mass value represents the deposit mass along the entire length of a tube segment and is plotted at the midpoint location of each segment. The CFD simulations provide deposition rates along the interior surface of the flow passages. For purposes of direct comparison with the mass measurements, a deposition rate [kg/(m$^2 \cdot$ s)] was converted to an equivalent mass (μg) by multiplying by the internal tube surface area and the test period for each flow condition. The deposit masses within the computation grid cells adjacent to the solid wall were summed along each tube segment length. The mass sum was located at the midpoint of a segment as in the case of the actual carbon burn off measurements. The simulation curves of Fig. 5 are fits of the calculated tube segment deposit mass with the corresponding midpoint location.

To compare the mass of accumulated deposits for different experiments, the dissolved O_2 was completely consumed at the

heated tube exit for the same initial fuel volume (990 ml). However, to completely consume the dissolved O_2, the total test time was varied for different flow rates. In Fig. 5 at the lowest flow rate, the deposit peak occurs just downstream of the flow path expansion for both fuels. Increasing the flow rate results in the broadening of the deposit profile, and the deposit peak occurs further downstream. Significantly lower flow rates would be required to shift the deposit peak upstream from the tube expansion, which would result in impractically long test durations (many days or weeks) under the present conditions. Similarly, for fuels that oxidize slowly at a given flow rate (i.e., fuel F3084 relative to fuel F4177), the deposit peak shifts downstream, and the deposit distribution along the flow path becomes broader because of the coupling of the deposition rate with the fuel oxidation rate.

The predicted locations of the deposit peaks for both fuels agree well with the experimentally determined peak locations for the lower flow range and are slightly offset from the measured peaks at higher flow rates. This agreement occurs without any modification of the chemical kinetic mechanism developed previously [5]. Figure 5 shows that the simulated deposit masses are higher than the measured values for the F4177 fuel sample but better follow the measured deposit masses of the F3084 sample. In addition, this trend for these fuel samples and the kinetic mechanism was also observed in the past for tubes of constant diameter [5]. The kinetic mechanism was developed to represent deposition behavior for a broad range of jet-fuel samples primarily distinguished by AH, SH, ROOH, and M species and cannot as yet represent all differences caused by trace heteroatoms. Moreover, a goal of our long-term research program has been to obtain measured and simulated surface deposition values that are within 1 order of magnitude of each other. In the current study, we have now applied the previously validated model to the prediction of tubes with flow expansions and contractions. The previous work showed excellent agreement in predicting oxygen consumption and good agreement for predicting deposition mass. The main thrust of the current work is in studying the effect of these flow changes on oxidation and deposition rather than the magnitudes of the absolute deposition quantity. Thus, the differences in deposit magnitudes observed between calculation and experiment (up to a factor of ∼5–10) do not detract from the goals of the study.

2.   Simulations of Dissolved O_2 Consumption and Surface Deposition

The reasonably good agreement between the simulated and measured deposition provides confidence in our ability to perform numerical simulations of other conditions that are beyond the present experimental capability. Ideally, the experimental studies would be performed under conditions where the deposit peak spans the geometry change to emphasize the flow and chemistry effects caused by geometry variation. However, because of the practical limitations of the present experiments, there were relatively low levels of surface
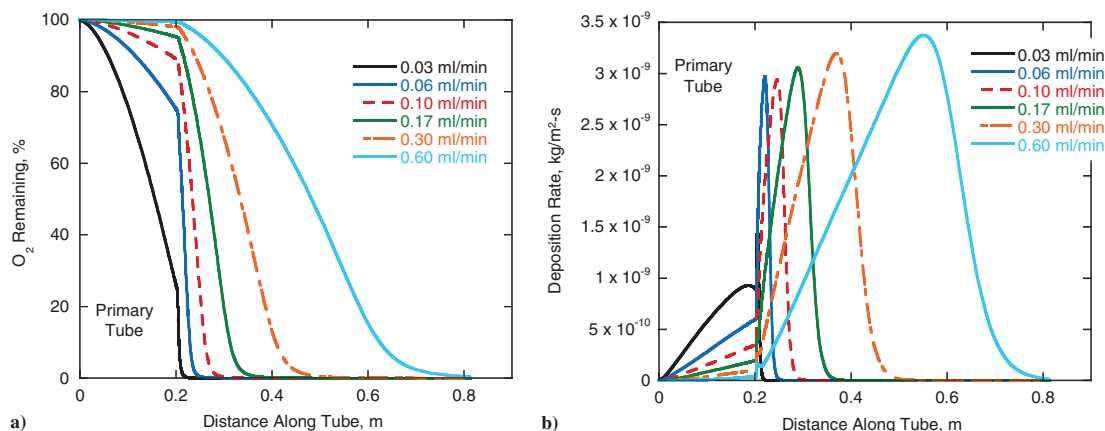
Fig. 6   Simulated profiles along the flow direction for the case of an abrupt expansion with F3084 fuel flowing at different flow rates: a) dissolved O_2 profile and b) deposition profile.

deposition at the flow passage expansion. Thus, two additional slower flow rates (0.03 and 0.06 ml/min) that were expected to produce more surface deposition were simulated in an effort to explore the deposition behavior very near the expansion using fuel F3084. In addition, a faster flow rate of 0.60 ml/min was simulated to study how the deposition rate behaves near the diameter change under conditions of very low dissolved O_2 consumption within the primary tube.

Figure 6 shows the simulated dissolved O_2 remaining and deposition rates along the flow direction for the three flow rates used in the experiments and the additional flow rates. For the lowest flow rate (0.03 ml/min), the peak deposition occurs very near the step with ~75% of the dissolved O_2 consumed in the primary tube. In contrast, less than 1% of the dissolved O_2 is consumed in the primary tube for the highest flow rate (0.60 ml/min), and nearly all of the deposition occurs downstream from the expansion. The figure shows that the dissolved O_2 consumption rates depend on the fuel flow rate and tube radius under isothermal flow conditions. The oxidation rate increases as the fuel flows from the primary to secondary tube because of the factor of 10 increase in cross-sectional area between the tube segments. The increase in cross-sectional area is accompanied by an increase in residence time for oxidation to proceed. In addition, Fig. 6 shows that the deposition rates increase gradually along the primary inner wall but more rapidly in the secondary tube where the maximum deposition occurs. The location of maximum deposition shifts downstream along the flow direction as the flow rate increases because of the close coupling between dissolved O_2 consumption and surface deposition rate [4,5].

Figure 6 shows the effect of flow rate on O_2 consumption and deposition rate along the flow path. Because the fuel encounters the expansion at different residence times for each flow rate, it would seem useful to plot deposition rate with residence time. Figure 7 shows the deposition rates of Fig. 6 as a function of the average residence time rather than as distance along the tubes. Because the experiments were essentially isothermal with known mass flow rates and cross-sectional areas, the residence times within the primary and secondary tubes were calculated from the mean velocity and tube length. For a tube of constant diameter, the deposition profiles at various residence times would collapse to form a single curve, because the oxidation and deposition rates are primarily a function of the chemical reaction time. Thus, any effect of the expansion should be more easily observed with the data plotted versus residence time. Figure 7 shows that for five of the six flow rates, the deposition profiles are very similar except for the residence times, which correspond to the area near the step for each flow rate. In fact, for each flow rate, the deposition rates increase nearly identically in the primary tube until the fuel reaches the expansion plane, which occurs at various residence times based on the flow rate. For example, it takes only 6.2 s for the fuel to reach the expansion for a flow rate of

0.60 ml/min, whereas 62 s is required for a flow rate of 0.06 ml/min.

Figure 7 shows that for all flow rates there is a sudden increase in the deposition rate at the expansion. The deposition rate increases until the peak location is reached at a residence time of 110 s for five of the six flow rates. The deposition rate declines beyond the peak as the dissolved O_2 becomes depleted. The deposition peak normally occurs near the residence time associated with the maximum oxidation rate [5].

Figure 7 shows that the deposition rate behavior for the lowest flow rate (0.03 ml/min) is different from those of the other flow rates. The maximum deposition rate occurs at a residence time (134 s) that is longer than those of the other flow rates. However, Fig. 7 shows that if there was not an expansion along the flow path, the peak deposition rate would occur at the same residence time as the other flow rates (110 s). In fact, there is a peak in the deposition rate at this residence time prior to the expansion for this flow rate. It is important to note that this peak at 110 s occurs in the primary tube, whereas the deposit peak occurs in the secondary tube for the higher flow rates. Thus, the peak in deposition rate at 110 s for the 0.03 ml/min flow rate is lower than those of the other flow rates because of the lower deposition rates in the primary tube. The maximum deposition rate observed near 134 s is due to the increase in deposition rate upon transition of the flow from the primary to the secondary tube. The transition greatly increases the deposition rate because of the increased residence time in the larger tube combined with nearing the complete consumption of dissolved O_2, which reduces the deposition rate after the peak at 134 s. In the next section, the influence of the abrupt geometry change on the fluid dynamics and deposition is more closely examined.
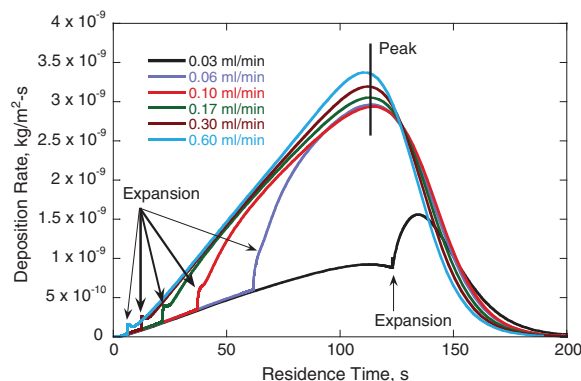

Fig. 7   Simulated deposition rate variation with residence time for F3084 fuel flowing into an abrupt expansion.

3. Influence of the Flow Path Expansion on Fluid Dynamics and Chemistry

Figure 6b for fuel F3084 shows that a flow rate of 0.03 ml/min results in a deposit peak that is nearest the expansion. Thus, this flow rate is selected for further study of how fluid dynamics and chemistry interact to influence the surface deposition near the expansion. Figure 8 shows velocity vectors, remaining dissolved O_2, and deposition rates for (F3084) fuel flowing at 0.03 ml/min. Rather than showing the entire tube length in Fig. 8a, the region near the expansion is enlarged for clarity. The velocity vectors of Fig. 8a show that a recirculation zone occurs after the expansion plane. In Fig. 8a, P represents the axial location of the recirculation zone center, Q is the axial location at the secondary tube inner wall where the recirculation flow ends, and F is the location where the flow becomes fully developed.

Figure 8b shows the simulated dissolved O_2 at three radial locations: the tube center (R_0), the primary inner wall (R_e), and the secondary inner wall (R_w). Upstream of the expansion (before 203 mm in Figs. 8a and 8b), the dissolved O_2 profile in the radial direction is essentially uniform. Thus, the dissolved O_2 concentration along the primary tube inner wall (R_e) has the same concentration as that at the tube center (R_0). Figure 8b shows a small, sudden drop in dissolved O_2 near the inner expansion corner (r_a in Fig. 8a) resulting from the sudden decrease in velocity as the fuel enters the secondary tube. The lowest dissolved O_2 concentration is observed along the secondary inner wall (R_w) within the geometry transition region. This is due to an increase in the local residence time resulting from flow recirculation. The largest dissolved O_2 radial concentration gradient occurs after the expansion, which promotes the advection of dissolved O_2 from the tube center to the secondary inner wall until the fuel flow becomes fully developed (F in Fig. 8a), where the radial gradient of the dissolved O_2 concentration approaches zero.

Figure 8c shows the simulated deposition rate along the primary tube inner wall (R_e) and secondary tube inner wall (R_w). The simulation predicts that the deposition rate increases gradually after the expansion up to the 205 mm axial location, at which point the deposition peaks and decreases thereafter. In the absence of a

recirculation zone, one would expect the deposition to continue decreasing because the dissolved O_2 consumption is ~87% complete in this section of the tube. This is illustrated in Fig. 8c by the dashed line, which is a qualitative estimation of the expected reduction in deposition in the absence of fuel recirculation. The figure also shows the excess deposition caused by the presence of the recirculation zone (indicated by the striped region). As described already, this excess deposition is likely due to the increased dissolved O_2 consumption caused by the longer residence time in the larger tube and an increase in the residence time caused by recirculation (Fig. 8a) near the corner (r_b) created by the transition to the large tube.

Because of the relatively small dimensions of the expansion region, the excess deposition is difficult to observe experimentally and becomes more difficult to observe with increasing flow rate. The simulations of Fig. 7 have a narrow spur-like deposition increase near the expansion plane for the higher flow rates (greater than 0.03 ml/min), and the fluid dynamics and chemistry at a flow rate of 0.30 ml/min are now considered. Figure 9 shows the simulated flow and chemistry profiles near the expansion for fuel F3084 at 0.30 ml/min.

Comparing Figs. 8a and 8b, it is observed that the recirculation zone length increases from 0.55 to 3.8 mm for flow rates of 0.03 and 0.30 ml/min, respectively. In addition, the center of the recirculation zone moves downstream as the flow rate increases with distances from the expansion plane to the recirculation center (P) of 0.2 mm for 0.03 ml/min and 1.1 mm for 0.30 ml/min. The figures show that the velocity magnitude in the recirculation zone is higher for the flow rate of 0.30 ml/min than that for the 0.03 ml/min flow rate. The larger recirculation zone and greater velocities at a higher flow rate result in different characteristics for the dissolved O_2 and deposition profiles.

Figure 9b shows the simulated dissolved O_2 remaining at three radial locations (R_0, R_e, and R_w). Along the tube center (R_0), the dissolved O_2 is gradually consumed, as is the case for the 0.03 ml/min flow rate. Along the primary tube radius (R_e), Fig. 9b shows that the dissolved O_2 concentration is the same as that at the primary tube centerline (R_0). However, there is a sharp drop in the
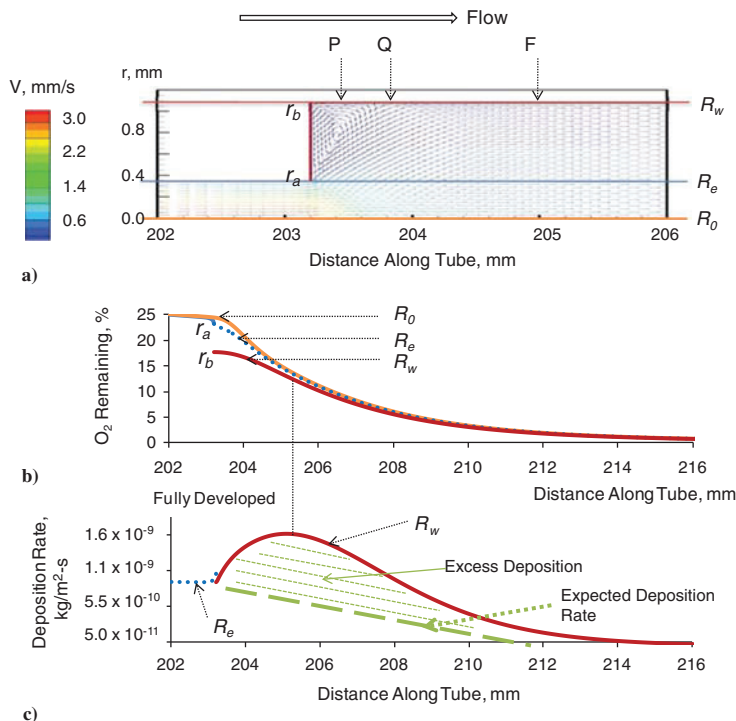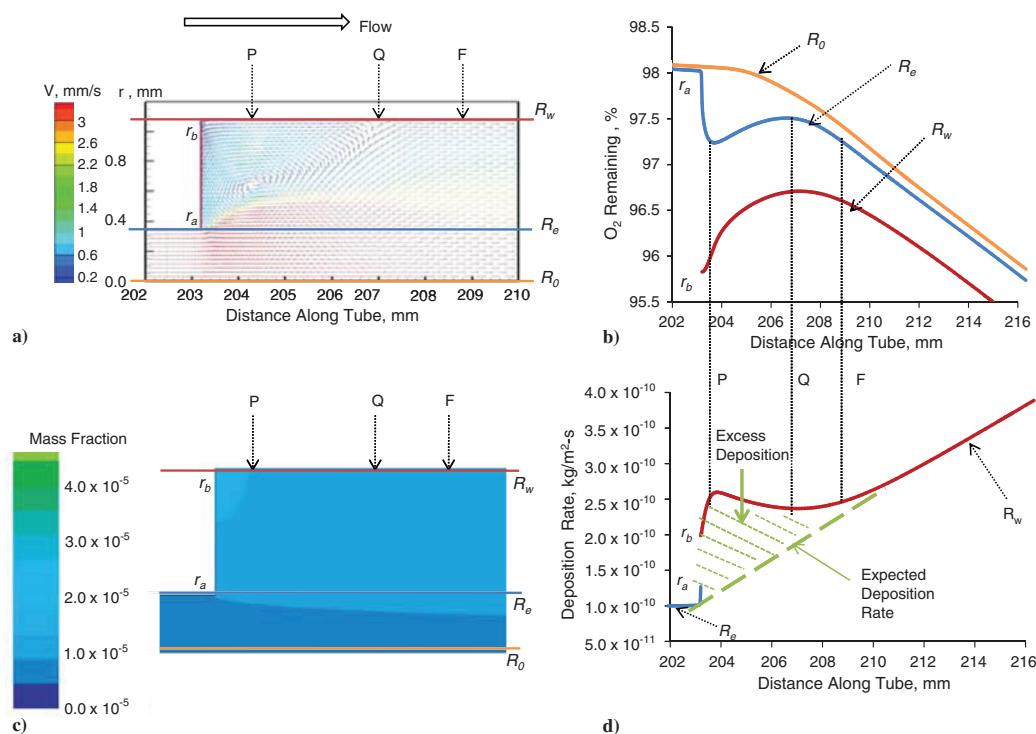

Fig. 8 Simulations of behavior near the expansion plane for a flow rate of 0.03 ml/min: a) velocity vectors, b) dissolved O_2 percentage remaining, and c) deposition rate. The expansion plane is located at 203.2 mm.

Fig. 9 Simulations of fuel behavior near the expansion for flow rate of 0.3 ml/ min: a) two-dimensional velocity vector, b) dissolved O$_2$ remaining, c) ROOH mass fraction, and d) deposition rate.

dissolved O$_2$ concentration after the expansion, followed by an increase in the dissolved O$_2$ as the flow approaches the end of the recirculation zone at axial location Q. There are two possible causes for the dissolved O$_2$ decrease along the primary radius R_e. The first is that the velocity decreases after the expansion, which increases the residence time and dissolved O$_2$ consumption within the fuel. However, this dissolved O$_2$ concentration decrease is much faster than that observed further downstream, after the flow becomes fully developed (point F). More likely, the dissolved O$_2$ decrease is due to the flow of fuel with a low dissolved O$_2$ concentration from near the secondary tube wall towards the tube center. Downstream from the recirculation center, P, the dissolved O$_2$ concentration begins to increase along R_e from the upward flow of O$_2$-rich fuel from near the center region of the tube. Diffusion is not likely to play a significant role in this region because the dissolved O$_2$ concentration gradient is minimal. The velocity vector legend of Fig. 9a indicates that the lowest velocity is near the outer expansion corner (r_b), which corresponds to a long fuel residence time. Thus, the lowest dissolved O$_2$ concentration is at this location and explains the low dissolved O$_2$ concentration near the secondary tube wall (R_w). Along the secondary tube wall (R_w), Fig. 9b shows that the dissolved O$_2$ is initially low, gradually rises until the end of the recirculation zone (as in the case of R_e), and then begins to decrease.

Figure 9c shows color contour plots of the hydroperoxide species (ROOH) mass fraction. The highest mass fraction of ROOH is near the outer expansion corner (r_b) and results from increased dissolved O$_2$ consumption caused by the long residence time there. Figure 9d shows that the deposition rate peaks near this corner. An increased ROOH mass fraction and increased dissolved O$_2$ consumption indicate enhanced autoxidative reactivity, and as a result, the deposition rate is greatest in this location. The deposition rate along the secondary wall (R_w) decreases beyond the center of the recirculation zone (P) because of increased fuel velocities (lower fuel residence times). When the flow becomes fully developed near location F, the deposition rate once again begins to increase as the dissolved O$_2$ consumption rates become similar across the tube.

The phenomenon of a minimum in the dissolved O$_2$ concentration and a peak in the deposition rate near the recirculation zone near the expansion (Fig. 8) is also observed at other flow rates. In Fig. 9d for a flow rate of 0.3 ml/ min, a dashed line qualitatively indicates the expected deposition rate that would occur in the absence of an increased residence time because of recirculation near the expansion. The deposition rate would be expected to increase because of the increased residence time in the wider secondary tube, approaching the simulated deposition rate after the fully developed flow location (F). Figure 9d also shows the excess deposition caused by recirculation near the expansion as a striped region. Although the magnitude of the deposition rate in this region is not large relative to the deposition rate downstream in the secondary tube (Fig. 6), the deposition rate does increase by a factor of 2.5 above that expected without recirculation. Fuel system designers would be concerned with this excess deposition occurring in a narrow region of the tube that could potentially cause flow blockage.

The surface deposition studied thus far in this paper has been limited to horizontal surfaces. We now briefly consider the vertical plane surface at an expansion. This is the surface from point r_a to r_b in Fig. 9a, which is shown in the three-dimensional sketch of Fig. 10a. Figure 10b also shows a two-dimensional view of the vertical plane from the tube exit. Figure 10c shows the simulated deposition rates on the vertical expansion plane at six flow rates. The figure shows that the deposition rates on the vertical wall are larger at the lower flow rates in agreement with the deposition rates on the adjoining horizontal walls, as shown in Fig. 6b. The y axis in Fig. 10c represents the distance from the tube center to the secondary inner wall along the expansion plane, and the x axis represents the deposition rate. The parabolic-like shapes of the deposition rate profiles in Fig. 10c result from the recirculation flow pattern. The simulations indicate that the recirculation center moves towards the tube center in the radial direction as the flow rate increases, resulting in a deposition peak that is skewed toward the tube center.
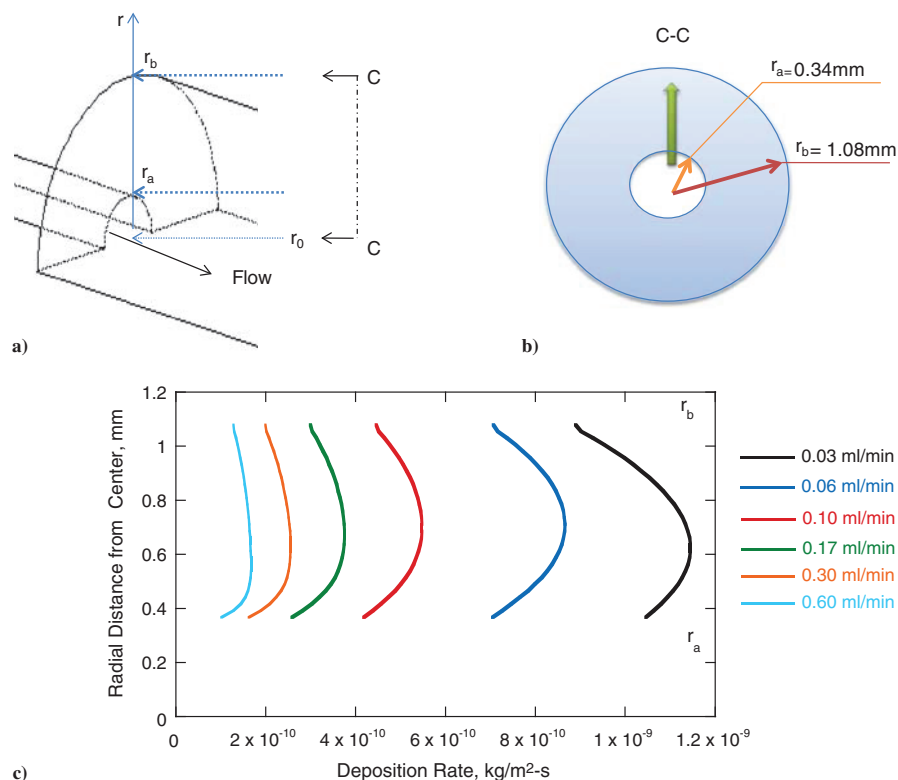
Fig. 10   Expansion region: a) three-dimensional drawing, b) drawing of the expansion plane, and c) deposition rates along the expansion plane at different flow rates.

B. Tube Contraction

1.   Measurement and Simulation of Surface Deposition for a Flow Path Contraction

Now we consider the contraction case, where the primary tube ID is relatively wide, and the secondary tube has a narrow bore. Figure 11 compares measured and simulated deposit masses for the two fuel samples and shows that the calculated peak deposit axial locations agree reasonably well with those of the measurements. As with the expansion case, the agreement in deposit magnitude is better for the Jet A sample (F3084) than for the JP-8 sample (F4177). Figure 11 shows that for both fuels most of the deposition occurs on the primary inner wall at all flow rates. As in the case of the expansion, it is difficult to detect excess deposition near the contraction using experimental measurements.

It is important to examine the dissolved O_2 consumption to better understand deposit formation under different flow conditions. Figure 12 shows the simulated remaining dissolved O_2 and deposition rates along the heated tube with a contraction for the Jet A fuel at four different flow rates. In Fig. 12a, most of the O_2 is consumed before the contraction because of the large ID and relatively long residence time in the primary tube. When the flow enters the secondary tube, the oxidation rates decrease because of higher velocities and shorter residence times. Figure 12b shows the distribution of the simulated deposition rate as a function of tube length that can be compared with the dissolved O_2 profiles of Fig. 12a. The deposition rates quickly grow from the inlet until the maximum oxidation rate is reached and then rapidly decrease until
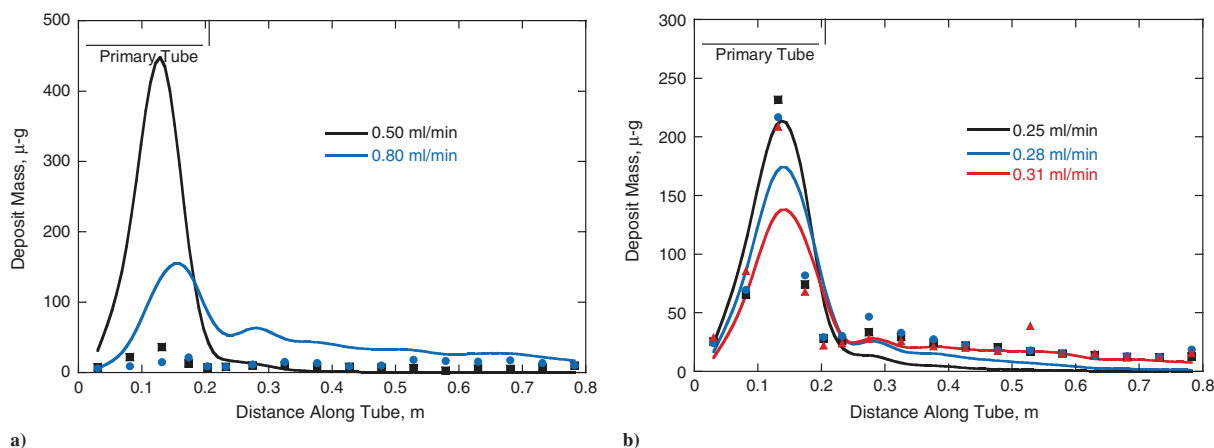
Fig. 11   Deposit mass along the contraction tube at different flow rates: a) F4177 (JP-8) fuel sample and b) F3084 (Jet A) fuel sample.

163
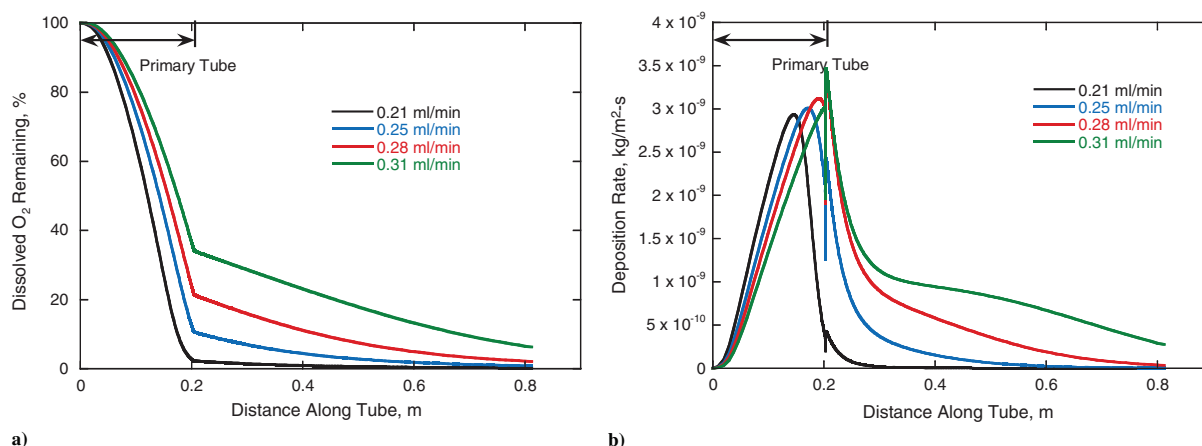
Fig. 12   Simulated profiles: a) dissolved O_2 remaining and b) deposition rates along the flow direction for F3084 fuel flowing in the contraction tube at different flow rates.

the contraction plane is approached. The peak deposition rates for all the flow rates are located on the primary inner wall.

A goal of this study was to perform the experiments at conditions where the deposit peak occurs near the contraction. Unfortunately, it was not possible to increase the flow rate to move the deposit peak further downstream because of the self-imposed requirement of having complete dissolved O_2 consumption within the entire tube. Figure 12 shows that even at a flow rate of 0.31 ml/min, dissolved O_2 consumption is not complete within the tube. As in the expansion case, the figure demonstrates a close coupling between flow rate and dissolved O_2 consumption, as well as a strong correlation between the dissolved O_2 consumption rate and the location of the deposit maximum. As a result, the dissolved O_2 profiles vary only slightly for the different flow rates, and the deposition rate maxima are all in the primary tube. Figure 12b shows interesting behavior in the deposition rate near the contraction, which is most notable for the highest flow rate (0.31 ml/min). At this flow rate, the deposition peak is closest to the contraction and is accompanied by a sharp increase in deposition.

2.   Flow and Chemistry Behavior Near the Contraction

To better understand the flow and chemistry behavior near the contraction, Fig. 13 shows velocity profiles, species concentration contours, and deposition rates for a flow rate of 0.28 ml/min. Figure 13a shows the simulated velocity vectors near the contraction. The fully developed flow in the primary tube becomes disrupted ∼1 mm before the contraction, and the velocity vectors become parallel again ∼2 mm downstream from the contraction plane. In contrast to the expansion case, there is no recirculation flow near the contraction corner (r_b), but instead the fuel flows downward toward the tube center. Also, the velocity rapidly increases as the fuel enters the narrow secondary tube and increases until becoming fully developed. The flow velocity decreases as the r_a-r_b plane is approached, and the velocity tends to zero near the r_b corner. Because the corner is a stagnant flow area, fuel resides at this location for a relatively long period, which results in increased dissolved O_2 consumption, with relatively little (∼1.4%) of the dissolved O_2 remaining there as shown in Fig. 13b. Fuel with a lower dissolved O_2 mass fraction flows away from the r_b corner and around the inner contraction corner (r_a), mixing with the main flow. As a result, the dissolved O_2 mass fraction near the wall at the entrance of the secondary tube is relatively low.

Figure 13c shows a color contour plot of the simulated mass fraction of insoluble species, which are the products of autoxidative reactions and are direct precursors of surface deposition (Reaction 21 of Table 3). Figure 13c shows that a significant insoluble mass fraction is produced within the primary tube because of the long residence time. There are lower mass fractions of insolubles near the

wall because of surface reactions that produce deposits. In the fully developed flow region of the secondary tube, the relatively fast flow rate and low oxidation rate result in fewer insolubles being produced there.

Figure 13d shows the simulated deposition rate along the inner walls of the primary and secondary tubes. The deposition rate on the primary tube wall slowly increases because of O_2 consumption but suddenly drops at the outer contraction corner (r_b) as a result of the low dissolved O_2 mass fraction there. The highest deposition rate occurs in the secondary tube near the inner contraction corner (r_a). This high deposition rate occurs despite the fast flow rate and low oxidation rate there. The deposition rate decreases rapidly over a distance of ∼0.1 m after the contraction plane and then decreases more slowly until the end of the heated tube as shown in Fig. 13d. The higher deposition rate early in the secondary tube is caused by insolubles, produced in the primary tube, being forced into the secondary tube by the high flow rate at the contraction plane. These high levels of insolubles react at the secondary inner wall to form surface deposits. If there were no additional insolubles flowing from the primary tube, the deposition rate in the secondary tube would be significantly lower at the tube entrance. This excess deposition is shown in Fig. 13d as a region above a qualitatively drawn line that estimates the deposition rate expected without insolubles from the primary tube. The narrow tube ID, high velocity, and resulting short fuel residence time result in a low deposition rate expected there in the absence of the insolubles emanating from the primary tube. This excess deposition occurs in a narrow flow passageway, greatly increasing the opportunity for fuel flow blockage. Fortunately here it occurs over the relatively long 10 cm axial distance.

The phenomenon of excess deposition at the secondary tube wall near the contraction is also observed for the other flow rates as shown in Fig. 12b. The deposition rate in the secondary tube rapidly decreases near the contraction but decreases gradually downstream from the contraction for each flow condition. In Fig. 14, the simulated deposition rate is plotted versus residence time with the axial distance converted to residence time at each flow rate. Figure 14a shows that the deposition rate profiles in the primary tube when plotted versus residence time are identical until the contraction is reached. At the contraction, the deposition rate changes rapidly for each flow rate, but the deposition rates again converge at long residence times after the flows become fully developed. Near the contraction plane (enlarged view of contraction plane behavior shown in Fig. 14b), the magnitudes of the deposition rate decrease near r_b and increase near r_a, and both appear to be related to how close the contraction plane is to the maximum in the deposition rate. For example, a large decrease in deposition rate near r_b and large increase near r_a are noted for the 0.31 ml/min flow rate, which occurs closest to the maximum deposition rate. In contrast, at 0.21 ml/min, the changes in
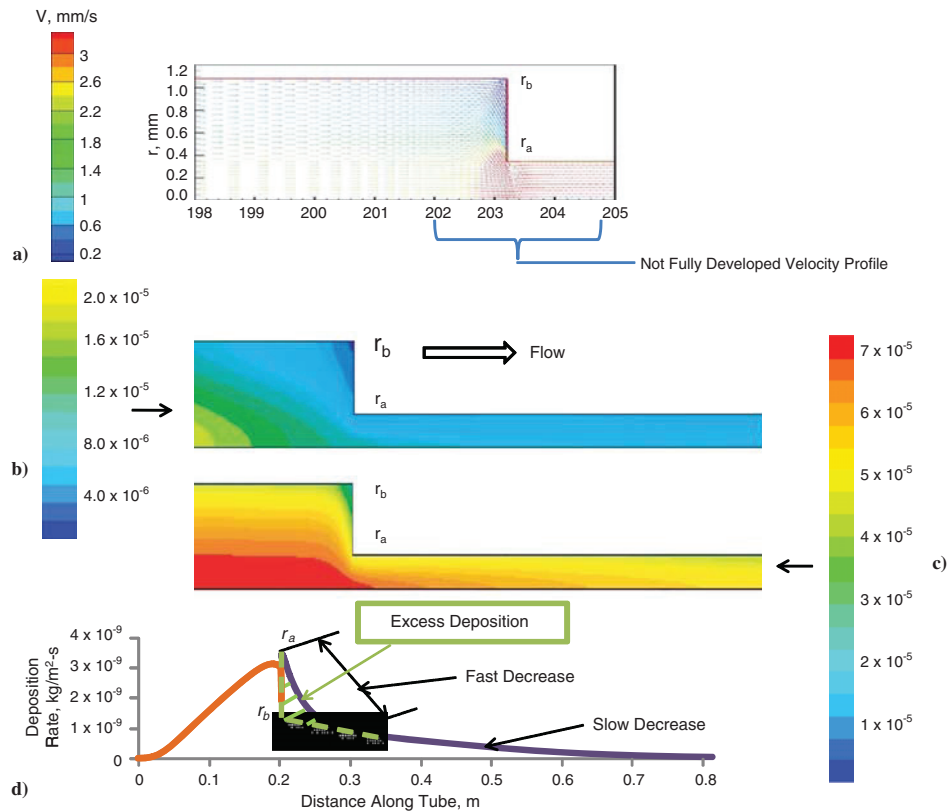
Fig. 13 Simulated behavior: a) velocity vectors, b) dissolved O_2 mass fraction, c) insoluble species mass fraction, and d) deposition rate near the contraction for the F3084 fuel at a flow rate of 0.28 ml/ min.
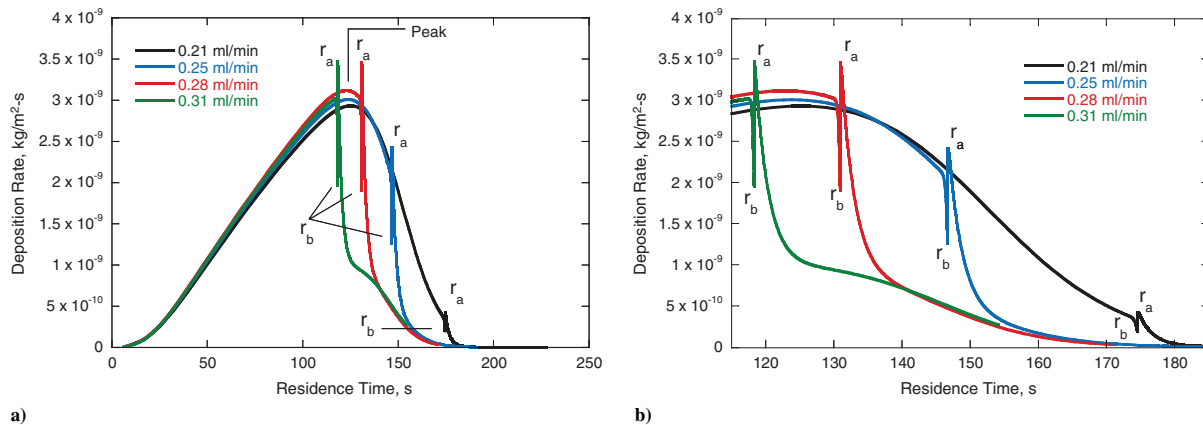

Fig. 14 Simulated deposition rate variation for F3084 fuel flowing in the tube with a contraction at different flow rates: a) 0–250 s residence time and b) 115–185 s residence time.

deposition rate at these locations are significantly smaller. Thus to minimize the excess deposition in a narrow tube, it is important to avoid having the maximum deposition rate (and maximum oxidation rate) occur near sudden flow contractions.

Figure 15 shows the simulated deposition rates for the vertical surface at the contraction for four different flow rates. In contrast to the deposition behavior for the vertical surface of the expansion, the deposition profile is nearly linear from the outer (r_b) to inner (r_a) corners with the deposition increasing towards the tube axis. The lower deposition rate in the outer corner (r_b) is likely due to the lower dissolved O_2 concentration there. In addition, the figure shows that

the deposition rate increases with increasing flow rate, which agrees with the adjoining deposition on the primary and secondary tube horizontal surfaces (Fig. 12b). The deposition rate for the 0.21 ml/ min flow rate is low because of the very low dissolved O_2 level ($\sim$1.5%) adjacent to the wall. For the tube expansion, higher flow rates cause decreased deposition on this vertical surface, whereas the reverse is true for a contraction.

C. Implications for Fuel System Design and Operation

One goal of this work is to improve the ability of fuel system and nozzle designers to efficiently use the fuel heat sink while preventing
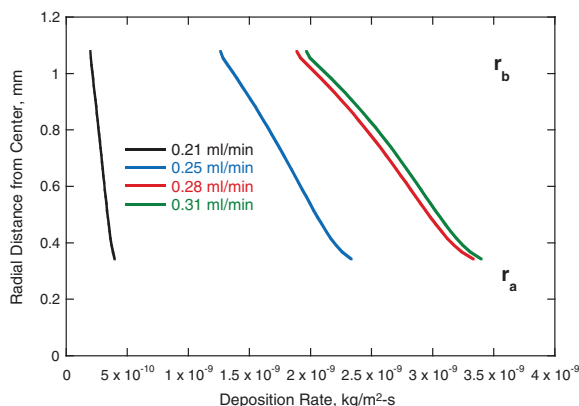
Fig. 15 Simulated deposition rates along the contraction plane at different flow rates.

the negative impact of fuel degradation associated with high-temperature fuel autoxidation. Although aircraft fuel systems and nozzles contain extremely complex flow pathways, the simple cylindrical expansion and contraction systems studied here provide interesting information that can be used to help design fuel system components that minimize excessive surface deposition from fuel autoxidative degradation.

For the expansion case, recirculation flow causes excess deposition at the beginning of the wider secondary tube. Because this deposition occurs in the wider tube it is not as likely to cause problems as if it occurred in the narrower bore tubing. However, the designer needs to consider both the flow rate and the wall and fuel temperatures for this situation. Lower flow rates, such as will occur for fuel flowing through a leaky valve, along with high fuel and wall temperatures will decrease the length of the recirculation zone and shorten the axial length of the tube in which the deposits occur. This will greatly increase the deposit mass per unit area and may cause narrowing of the passageway even for relatively wide flow passages.

The contraction case is more likely to be found in aircraft systems, as fuel is transported through wide tubing in the fuel tank to narrow passageways in the nozzle. For the contraction geometry, the excess deposition occurs at the beginning of the narrow secondary tube, which is the type of tight clearance location in which deposition needs to be avoided. Therefore, the designer should avoid sudden contractions in passageway diameter in locations where the fuel and wall temperatures are high. Fortunately, the acceleration of flow in the narrow tube causes the surface deposition to be spread over a greater axial region than in the expansion case. The fuel flow rate will play a role in the how the deposition is distributed over the length of the tube, with higher flow rates being desirable to minimize deposit quantity per unit surface area in the narrow tubing after a contraction.

In both expansion and contraction situations, the designer should avoid having the peak of oxidation and deposition rates occur near these flow geometry changes. Ideally, performing the CFD with chemistry calculations shown here for the entire heated section of the fuel system would allow prediction of the location of maximum deposition as a function of the engine throttle setting and indicate engine settings and fuel system locations where deposition can be of concern. Although it may not be currently practical to simulate such a large and complex region, it may be possible to perform these calculations on the highest temperature regions of the fuel system.

Future work needs to study other geometry changes that may be of interest for fuel systems, such as a sudden "elbow" change in flow geometry. It would also be interesting to determine whether gradual changes in geometry and/or rounded corners can minimize the increased deposition that occurs at sudden passageway size changes. In addition, deposition experiments need to be performed under nonisothermal and turbulent flow conditions to confirm the general applicability of the model employed here. The study of turbulent conditions is especially desirable because aircraft fuel system flow is

often in this regime, although higher flow rates usually imply lower fuel and wall temperatures and, thus, decreased deposition issues. Also, the current study does not determine the extent to which a passageway is blocked. This requires knowledge of the density of the deposit, whose value may change with the temperature at which it is produced and with the identity of the fuel.

V. Conclusions

This study explores via experiment and computational fluid dynamics with chemistry the effect of a sudden expansion or contraction in the flow path on jet-fuel surface deposition formed in heated cylindrical tubes. Both experiments and simulations show that, under isothermal laminar flow conditions, the peak deposit axial location in the tube is a strong function of the fuel oxidation rate in the flow direction. Although the limited axial resolution of the experimental deposition measurements prevented observation of the effects of the step change on oxidation and deposition, the computational model was successfully used to detect excess deposition caused by the step changes in flow geometry. The model was also used to extrapolate to flow conditions that are experimentally inaccessible. The measurements and calculations were performed for conditions where the deposition peak occurs near the step change location to maximize the effect of the change in geometry on fuel flow.

For the expansion, the simulation predicts that an increase in deposition occurs in the wide secondary tube downstream of the expansion because of a recirculation zone that increases fuel residence and oxidation reaction times. For the contraction, simulations of insoluble species produced during the relatively long residence time in the wide primary tube flow into the secondary tube via acceleration through the contraction. The high level of insolubles in the narrow secondary tube causes excess deposition even though oxidation reactions do not occur readily because of the short residence time in this narrow tube. In the expansion case, the excess deposition is less likely to create conditions where the deposit blocks the flow passage because of its occurrence in the wider secondary tube. For the contraction, the excess deposition is a greater concern because it occurs in the narrow secondary tube and is more likely to result in flow restriction issues.

Fuel system component designers need to consider the fuel and wall temperatures, flow rates, throttle changes, and the locations of changes in flow geometry to maximize fuel heat sink and minimize fuel surface deposition problems caused by fuel oxidative degradation. Future studies need to consider other geometry changes, nonisothermal temperature regimes, turbulent flow, changes in flow geometry caused by deposit accumulation, and the prediction of deposit volume and passageway restriction.

Acknowledgments

References

[1] Hazltett, R. N., *Thermal Oxidation Stability of Aviation Turbine Fuels*, ASTM, Philadelphia, PA, 1991.
[2] Zabarnick, S., "Chemical Kinetic Modeling of Jet Fuel Autoxidation and Antioxidant Chemistry," *Industrial and Engineering Chemistry Research*, Vol. 32, No. 6, 1993, pp. 1012–1017.
doi:10.1021/ie00018a003
[3] Zabarnick, S., "Pseudo-Detailed Chemical Kinetic Modeling of Antioxidant Chemistry for Jet Fuel Applications," *Energy and Fuels*, Vol. 12, No. 3, 1998, pp. 547–553.
doi:10.1021/ef970157l
[4] Ervin, J. S., and Zabarnick, S., "Computational Fluid Dynamics

Simulations of Jet Fuel Oxidation Incorporating Pseudo-Detailed Chemical Kinetics," *Energy and Fuels*, Vol. 12, No. 2, 1998, pp. 344–352.
doi:10.1021/ef970132m

[5] Kuprowicz, N. J., Zabarnick, S., West, Z. J., and Ervin, J. S., "Use of Measured Species Class Concentrations with Chemical Kinetic Modeling for the Prediction of Autoxidation and Deposition of Jet Fuels," *Energy and Fuels*, Vol. 21, No. 2, 2007, pp. 530–544.
doi:10.1021/ef060391o

[6] Graves, C., and Biddle, T., *Verification of JP − 8 + 100 in Full-Scale Fuel Nozzle Testing*, Pratt & Whitney, West Palm Beach, FL, Jan. 1995.

[7] Chin, L. P., and Katta, V. R., "Numerical Modeling of Deposition in Fuel-Injection Nozzles," *33rd Aerospace Sciences Meeting and Exhibit*, AIAA Paper 1995-0497, Reno, NV, 1995.

[8] Jones, G. E., and Balster, W. J., "Phenomenological Study of the Formation of Insolubles in Jet-A Fuel," *Energy and Fuels*, Vol. 7, No. 6, 1993, pp. 968–977.
doi:10.1021/ef00042a038

[9] Rubey, W. A., Striebich, R. C., Tissandier, M. D., Tirey, D. A., and Anderson, S. D., "Gas Chromatographic Measurement of Trace Oxygen and Other Dissolved Gases in Thermally Stressed Jet Fuel," *Journal of Chromatographic Science*, Vol. 33, No. 8, 1995, pp. 433–437.

[10] ANSYS FLUENT, Ver. 12.0, ANSYS, Inc., Canonsburg, PA, 2009.

[11] Vandoormaal, J. P., and Raithby, G. D., "Enhancements of the Simple Method for Predicting Incompressible Fluid Flows," *Numerical Heat Transfer*, Vol. 7, No. 2, 1984, pp. 147–163.
doi:10.1080/01495728408961817

[12] SUPERTRAPP, Thermophysical Properties of Hydrocarbon Mixtures Database, Ver. 3.0, NIST, Gaithersburg, MD, 1999.

L. Maurice
Associate Editor

167

Appendix J. Preparation of a Research Jet Fuel Composition Comprised of Nearly Exclusively Methyl-Branched Tetradecane Isomers Having a Freezing Point below −47 C

Preparation of a Research Jet Fuel Composition Comprised of Nearly Exclusively Methyl-Branched Tetradecane Isomers Having a Freezing Point below −47 °C

Heinz J. Robota* and Jhoanna C. Alger

University of Dayton Research Institute, 300 College Park, Dayton, Ohio 45469, United States

ABSTRACT: The potential for a variety of biologically derived alternative aviation fuels continues to be investigated. The composition of some of these potential fuels contains only a limited number of isomers of only one carbon number. These types of alternative fuels fail the distillation distribution specification in current use. However, it is unclear whether this has actual impact on in-use performance if such an alternative blendstock were used to make a 50/50 alternative/petroleum blend. In order to investigate this question further, the U.S. Air Force seeks a generic surrogate research fuel comprised of isomers of tetradecane that meet the −47 °C freezing point specification of JP-8. We describe our laboratory investigation of a strategy for preparing such an isomer mixture while remaining mindful of the desire to scale the procedures for making hundreds of gallons of such a fuel. We start with a commercially available 1-tetradecene, hydrogenate the olefin to *n*-tetradecane, which is then hydroisomerized using a Pt/US-Y zeolite catalyst, and the raw tetradecane mixture is separated from cracked products by distillation. In order for the isomeric mixture to meet the freezing point specification, the remaining *n*-tetradecane content must be reduced to <1.5%. We describe a solvent dewaxing approach that achieves this goal.

INTRODUCTION

As the military and commercial aviation community certify the 50/50 blends of petroleum-derived and synthetic jet fuels for everyday use, decades of experience with the petroleum-derived specifications provide a foundation upon which to base performance expectations.[1] However, for blends with higher synthetic content, potentially approaching 100%, the empirical foundation of current specifications no longer applies. Consequently, identifying the relationships between composition and specific properties relating to the full spectrum of fit for purpose specifications grows in importance. For example, the role played by alkyl aromatic compounds in ensuring seal swell is well-documented.[1] Conventional petroleum-derived fuel is composed of thousands of individual components that vary considerably in proportion from one lot of fuel to another.[2] Therefore, separating such a mixture into its constituent parts is simply not a viable approach to developing a new specification. Furthermore, petroleum-derived fuels may contain constituent classes, such as aromatics and molecules containing saturated rings, not contained by every synthetic fuel composition.[1,3] As a path forward, an approach where specific classes of constituents can be prepared and the functional performance of these individual classes better understood appears to be preferable.

We report here a preparative approach for making such a reasonably well-defined composition constituting one subset of a constituent class. Broadly speaking, the constituent class can be described as the methyl-branched alkane isomers, which comprise a large proportion of current synthetic fuel blending components.[4] Currently, certified synthetic blending compositions are derived from either a Fischer−Tropsch (FT) process or a natural triglyceride. When compositions of FT origin are used, they are referred to as FT Synthetic Paraffinic Kerosene (FT-SPK). Blendstocks derived from natural triglycerides are

frequently referred to as hydrotreated renewable jet (HRJ) or hydrotreated esters and fatty acids (HEFA).[1,5] Both of these classes of synthetic fuel blendstock are composed of nearly 90% methyl-branched alkane isomers spanning the carbon number range from about C_8 to C_{15}. The remainder of the mixture is the corresponding normal alkanes. Currently, technology developers are investigating several approaches which would produce a synthetic composition composed of very high percentages of a single carbon number rather than the range of carbon number found in FT-SPK or HEFA. An extreme example would be the 15-carbon farnesene, which has the structure shown in Figure 1. For aviation fuel use,[6] it would
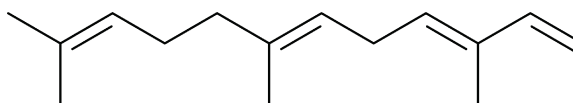
Figure 1. The structure of farnesene.

need to be hydrogenated first in order to improve thermal stability, but this is one of the easiest catalytic transformations. Being a single component, it exhibits a well-defined boiling point rather than a boiling range found in current aviation fuel specifications.[7] Another example would be the narrow distribution of products produced when either 1-butene or iso-butene is oligomerized.[8,9] The distribution of products clusters around C_8, C_{12}, C_{16}, etc. The boiling point would exhibit a range, but would not follow the distribution of boiling points found in current specifications. With these examples in

consideration, the particular methyl-branched alkane isomers that we have selected to produce are those of tetradecane.

Our objective was to produce a distribution of C_{14} alkane isomers that also meet the −47 °C freezing point specification of JP-8.[7] In practice, we found this to mean a residual n-C_{14} content of less than ~1.5%. The eventual goal of this work is to produce a practically useful quantity of this composition, meaning between 500 and 1000 gallons. Therefore, each laboratory step was executed using reagents or methods compatible with larger-scale operations. Rather than use a reagent grade of n-tetradecane as starting material, we started with a 1-tetradecene economically available in bulk and converted it to the corresponding n-tetradecane. Isomerization of the normal alkane was accomplished with a 0.5% Pt/US-Y zeolite catalyst under nearly ideal bifunctional hydrocracking conditions. Operating conditions were selected to achieve an isomeric composition comprising some triply branched isomers as well as high concentrations of the doubly branched isomers, in addition to the singly branched and normal isomers. This resulted in a modest amount of hydrocracking. Since the objective was a single carbon number isomeric composition, the cracked products were removed by distillation. The freezing point achieved with such a product distribution never fell below −25 °C. Since the freezing point of n-tetradecane is 6 °C, the normal alkane needed to be reduced further. This was accomplished with a solvent dewaxing method, yielding a mixture of predominantly methyl branched tetradecane isomers with a freezing point no higher than −65 °C.

■ EXPERIMENTAL SECTION

Fixed-Bed Catalytic Reactor System. The reactor system used in this investigation is based on a $1/2$ in. OD stainless steel tube 24 in. in length, mounted vertically in a three-zone electric furnace. Heater control thermocouples are spot-welded to the exterior of the reactor tube at the center of each 6 in. heated zone and the length of the tube within the heater is covered with a split cylindrical brass tube $1/8$ in. thick for more even heating. The reactor is fitted with a thermowell made from $1/8$ in. stainless steel tubing entering the system at the exit end and extending about halfway into the upper heated zone. Bed temperatures could be measured using a traveling thermocouple within the thermowell. A 20-μm sintered stainless steel filter was located in the exit fitting of the reactor tube upon which a wad of quartz wool was placed. 1.0 g of catalyst was used in these measurements. The Pt/US-Y grains were gently mixed with a 4-fold volumetric excess of SiC of a similar size range. The catalyst charge was located near the center of the middle heated zone by first loading an appropriate volume of the SiC into the reactor bottom. The space above the catalyst was similarly filled with SiC.

Liquid and gaseous feeds enter the reactor immediately above the heated zone. Gas flow is controlled using Brooks mass flow controllers. The liquid feed is delivered by an ISCO high-pressure syringe pump charged from an external reservoir. Reactor effluent enters a cylindrical pressure vessel where liquids condense and gases pass on to the manual back-pressure regulator. Upon exiting the system through the back-pressure regulator, the gas stream is directed to a multiport valve located a short distance from the inlet of an Agilent refinery gas analyzer that could be used to quantify gaseous species. The analyzer was calibrated with certified gas blends. Liquid products were drained from the bottom of the high-pressure receiver cylinder through a valve for external analysis.

0.5% Pt/US-Y Zeolite Hydroprocessing Catalyst. Pt was deposited on a Zeolyst CBV-720 US-Y zeolite via ion exchange to a loading of 0.5 wt %. The required mass of 6.9 wt % tetraammine platinum(II) chloride solution was diluted with distilled water to yield 90 g of solution that was used to slurry 10 g of the zeolite powder. The slurry was stirred with a magnetic stir bar. The pH was frequently checked and adjusted to 9.5 using concentrated aqueous ammonia. After a final pH adjustment at the end of the day, the slurry was allowed to stir overnight resulting in a final pH of 9.4 the following morning. The solid was recovered by vacuum filtration, the cake dried in static air at 120 °C for 4 h, and then calcined at 400 °C for 4 h. After calcination, a 40−60 mesh fraction was recovered by gently breaking and agitating aggregates on a 40 mesh sieve. A Pt dispersion of 0.16 was determined using a dual-isotherm, H_2 volumetric adsorption method at 30 °C.

Producing n-Tetradecane. The starting 1-tetradecene was purchased from Chevron Phillips Chemical Company LP. Hydrogenating an olefin to completion is not a demanding catalytic transformation. A 1 gram reactor charge (~3 mL) of the Pt/US-Y catalyst was used for this purpose. The catalyst was activated in H_2 flow at a system pressure of 110 psig, a flow rate of 100 mL/min, and a temperature of 450 °C. Once activated, the initial reactor temperature was set. We began with a liquid hourly space velocity of LHSV = 3/h and monitored the effluent for residual olefin content via gas chromatography (GC) analysis. Since the reduction consumes H_2, we wanted a sufficiently high excess of H_2 to remain at the catalyst bed exit, to facilitate complete reduction even as the olefinic remnant became vanishingly small. Therefore, we maintained an H_2/1-tetradecene molar feed ratio of 10 at all hydrocarbon feed rates. Eventually, we operated at 140 °C and LHSV = 8/h without detectable residual olefin.

n-Tetradecane Isomerization. The isomerization reactor was loaded as described for hydrogenation and the catalyst activated in the same manner. The initial task was to construct the selectivity/conversion map from which a suitable operating point could be identified. An initial operating temperature of 250 °C was selected with LHSV = 1/h, a pressure of $P = 400$ psig, and an H_2 flow of 8 mol (mol n-C_{14})$^{-1}$. Additional data points were collected at operating temperatures between 240 °C and 280 °C, while holding the remaining conditions fixed, as well as points at 280 °C and LHSV = 10/h and 20/h while maintaining the H_2:n-C_{14} molar ratio of 8 and a total pressure of 400 psig. We selected an operating point of 0.88 fractional conversion, which was achieved at 260 °C, $P = 400$ psig, LHSV = 1/h and H_2:n-C_{14} molar ratio of 8. Conditions were held until ~1 L of liquid products was collected.

Separating C_{14} Isomers from Cracked Products. A spinning band fractionating distillation unit (B/R Instrument Corporation, Model M690) was used to separate the C_{14} isomer mixture from the associated cracked products. Conditions were determined that resulted in a final C_{14} isomer mixture left in the distillation pot which was ~98 wt % C_{14} and roughly equal masses of minor contributions with both larger and smaller carbon numbers. (The initial 1-tetradecene contains slightly over 1% C_{16}.)

Freezing-Point Determinations. Freezing points were measured by the U.S. Air Force Petroleum Agency Specification Laboratory in a manner compliant with ASTM D-5972.

Solvent Dewaxing. Solvent dewaxing is a refining method well-known in the processing of petroleum to a variety of products.[10] Prior to the development of catalytic dewaxing, it

was widely applied to improve the low-temperature properties of lube feedstocks by selectively removing the normal alkanes. Based on several examples from the petrochemical industry, we selected a 50/50 mix of toluene and methyl ethyl ketone (MEK) as the solvent. We examined mixtures of tetradecane isomers with solvent in relative ratios of 1:2, 1:3, and 1:5. In a typical trial, 60 mL of the tetradecane mixture were mixed with the appropriate amount of solvent. The composite mixture was then divided equally among three test tubes 25 mm in diameter and 200 mm in length. These tubes were submerged in a programmable refrigerated methanol bath (normally used for low-temperature viscosity measurements) at a starting temperature of −20 °C. The bath was ramped down in temperature over a 2-h period to −40 °C. After at least 60 min at −40 °C, the solids that had formed were compressed to the bottom of one tube using a wad of filter paper. Once the solids were compressed, the tube was withdrawn from the bath and the remaining liquid recovered. During the compression, it was possible for some solids to slip by the filter paper and end up in the top portion of the tube, which could influence the detected composition. The solids were also thawed and collected. The bath was then cooled to −50 °C and the solids separation and recovery repeated in a second tube before finally lowering the bath temperature to −65 °C and the process was repeated a final time. Samples of both the clear liquid and the thawed solid were analyzed by GC to determine the composition of the tetradecane fraction. Once GC analysis confirmed that the n-C_{14} content of the recovered liquid fraction could be reduced by separation of the solidified portion, an improved compression filter was devised. A perforated washer, near in diameter to the test tube inner diameter, was welded to a $^1/_2$ in. stainless steel tube and used as a plunger. A plug of cotton was secured to the washer with a covering of permeable paper. This resulted in a much-better confinement of solids. With this improvement, recovered liquids as well as remelted solids were separated from the solvent using a rotary evaporator with a water bath held at 80 °C. The recovered C_{14} liquid was analyzed by GC and the freezing point of the solvent-stripped soluble fraction determined.

RESULTS AND DISCUSSION

Hydrogenating the 1-Tetradecene. Hydrogenation of an olefin over a precious metal catalyst proceeds rapidly at modest temperature. An initial 1-tetradecene feed rate equivalent to LHSV = 3/h at a target bed temperature of 150 °C yielded undetectable levels of residual 1-tetradecene. An exotherm at the top of the catalyst bed of ∼20 °C was also detected with the traveling internal thermocouple. Subsequently, the target bed temperature was lowered to 140 °C and the hydrocarbon feed rate increased first to LHSV = 5/h, then to LHSV = 8/h. Under the final conditions, the exotherm diminished to ∼10 °C and was spread slightly deeper into the bed, presumably as a consequence of the increasing flow rate of H_2 with increased hydrocarbon feed rate. In each case, residual 1-tetradecene was undetectable. The system was run continuously during the week and on some weekends. When it was necessary to stop the liquid feed, the H_2 flow rate was lowered to a stand-by flow of ∼20 mL/min while maintaining the bed at 140 °C. Upon restarting conversion, H_2 flow was returned to process conditions, followed by resumption of hydrocarbon feed. Overall, ∼3 L of 1-tetradecene was converted to n-tetradecane.

**Isomerization of n-Tetradecane.** The isomerization reaction sequence is initiated through the establishment of an olefin population in near equilibrium with its alkane counterpart formed on the metal function of the catalyst.[11] The olefins migrate to an acid site where they are protonated as the enabling step to a variety of subsequent possible reactions. When operating under ideal hydroisomerization conditions, a given molecule undergoes only a single isomerization of the alkane backbone before being rehydrogenated to an unreactive alkane. Since the rate at which methyl groups can migrate along the linear carbon chain is typically much faster than the rate at which further isomerization rearrangements occur, the distribution of isomers within a fraction of a given branching degree (monobranched, dibranched, tribranched, etc.) are detected near their equilibrium relative abundances.[11] Thus, as conversion is initiated, monomethyl branching is observed exclusively. As the concentration of the monobranched isomers increases, the rate at which this population undergoes a subsequent isomerization increases, resulting in the appearance and increasing abundance of dibranched isomers.[12] Similarly, as the dibranched population increases, tribranched isomers can begin to form. While cracking through a β-scission can occur in the protonated olefin at any degree of branching, the activation barrier to such a scission is sufficiently higher than the activation barrier to a branching rearrangement that only low levels of cracking are observed. Once tribranched isomers form the protonated olefin, cracking proceeds at a rate higher than further methyl branching.[13] Therefore, when seeking to produce a highly isomerized composition of a given carbon number, there is an operating point where the total fraction of methyl branched isomers is at its highest relative abundance. Further conversion results in rapidly increasing cracking at the expense of the most highly isomerized fraction. Thus, prior to selecting an operating condition, we mapped the net selectivity to monobranched and multibranched feed isomers as well as the loss to cracking as a function of n-tetradecane conversion.

Table 1 compiles the sequentially applied operating conditions used to generate the span of conversions while

Table 1. Sequence of Operating Conditions Used To Span a Range of Conversions for Producing the Selectivity Versus Conversion Data

liquid hourly space velocity, LHSV (1/h)	liquid feed rate (mL/min)	temp (°C)	fractional conversion
1	0.057	250	0.81
1	0.057	240	0.55
1	0.057	280	0.99
10	0.567	280	0.70
20	1.134	280	0.47
1	0.057	250	0.79
1	0.057	255	0.75
1	0.057	260	0.87
1	0.057	265	0.98

maintaining a system pressure of 400 psig and a H_2:n-C_{14} molar feed ratio of 8. Conformity with ideal hydrocracking behavior is confirmed by how well the data points at 280 °C and high LHSV fit with the selectivity data obtained at LHSV = 1/h, while changing only the reactor temperature. Figure 2 shows the selectivity to monobranched and multibranched C_{14} products, along with the fraction lost to cracking as a function of n-C_{14} conversion. Distinguishing the monobranched products from products with higher branching in the chromatogram is simplified by the small number of individual
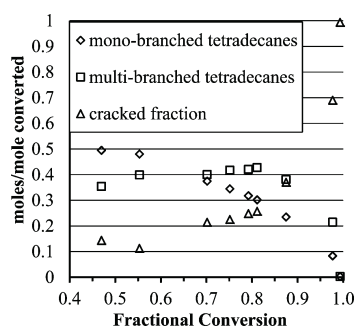
Figure 2. Product selectivity to monobranched feed isomers, multibranched feed isomers, and cracked products as a function of conversion.

products and their clear separation from other constituents in the recovered liquid. Resolution of the multibranched products into individual classes, such as dibranched, tribranched, etc., is not possible, because of the complexity of the chromatogram.[14] The evolution of the product composition with increasing conversion is consistent with the qualitative description of ideal bifunctional hydrocracking presented.[13] Since we seek to produce a C_{14} liquid with the highest degree of isomerization, as well as a residual normal component sufficiently low to suppress the freezing point to less than −47 °C, we have plotted these results to explicitly express the remaining fraction of n-C_{14} in Figure 3. While it is possible to reduce the residual
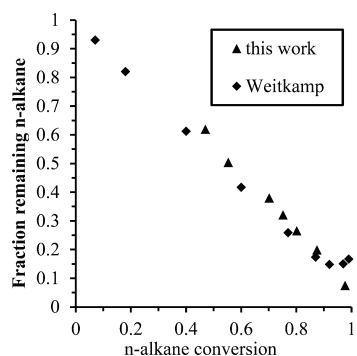
Figure 3. Residual normal alkane fraction in the fed C_n effluent mixture as a function of conversion for n-C_{14} (this work, −0.5% Pt/US-Y zeolite) and n-C_{15} (Weitkamp, −0.5% Pt/CaY zeolite) as a function of conversion.

normal component with increasing conversion, a residual normal fraction of <0.2 requires an overall conversion of >0.85. Unfortunately, at such high conversions, an examination of Figure 2 shows that the cracked fraction increases rapidly above 0.4. We were unable to find previous results for the conversion of n-C_{14} under similar conditions with a similar catalyst. Thus, for comparison, we have recalculated the results of Weitkamp for the conversion of n-C_{15} over a Pt/Ca−Y zeolite catalyst, in terms of the remaining normal alkane fraction, as a function of conversion.[15] The trend is consistent with our observations. Of particular interest is that at the highest conversions, where over 90% of the conversion can be attributed to cracking, the residual normal feed alkane remains a substantial fraction of the C_{15} liquid recovered. This indicates that a strategy for the preparation of hundreds of gallons of highly isomerized C_{14}

based exclusively on a hydroisomerization step, followed by distillation, depends critically on the tolerable remaining normal alkane fraction, which allows compliance with the aviation fuel freezing point specification.

In order to gauge what level of remaining normal alkane might be tolerable, we operated at a conversion of 0.81 sufficiently long to collect enough product liquid for distillation. The light components were distilled over and the liquid remaining in the pot analyzed. C_{14} made up just over 95 wt % of the recovered liquid. This composition, with 23 wt % n-C_{14}, had a freezing point of −13 °C, much closer to the 6 °C freezing point of neat n-C_{14} than the targeted −47 °C JP-8 specification. A second attempt was made by operating for an extended time at a conversion of 0.88. Also, rather than simply distilling off the light cracking components from the mixture and retrieving the entire C_{14} fraction, distillation was continued and small incremental fractions were taken in the hopes of changing the relative concentration of n-C_{14} in each successive cut. This allowed us to collect a small volume of C_{14} with a residual n-C_{14} concentration of 7 wt %, which had a freezing point of −27 °C. While this was an improvement over the previous value, it was still quite distant from our target. As Figure 2 shows, it is doubtful that forcing even higher conversion will reduce the residual normal content much below 10%. Furthermore, at the extremely high conversions that would be required, Figure 2 shows that the amount of C_{14} that could be recovered becomes impractically small. Consequently, a different strategy for achieving the JP-8 freezing point specification, which would be compatible with producing practical quantities of the isomerized C_{14}, is required.

Hydroisomerization and Solvent Dewaxing. Solvent dewaxing is a separation method employed in refining petroleum products for the production of lubricating fluids.[16] Highly paraffinic fractions with carbon numbers in excess of 24 are useful for making these fluids. Unfortunately, even modest percentages of normal alkanes cause these materials to gel or solidify at impractically high temperatures. Solvent dewaxing was developed to remove the normal paraffins with reasonably high selectivity. Similarly, application of solvent dewaxing to middle distillate fractions allows the preparation of diesel fuels compatible with arctic conditions. We were unable to find any previous reports where this method had been applied to removing the normal alkane component from a mixture of alkane isomers comprised of a single carbon number. After reviewing a variety of reports and patent examples, we elected to use a 50/50 mix of toluene and methyl ethyl ketone (MEK). Two further parameters needed to be defined: (1) the ratio of solvent to solute and (2) the temperature required to achieve the required extent of n-C_{14} reduction.

Examination of Figure 2 reveals that at a conversion near 0.8, total isomerization selectivity achieves its highest value while the cracking losses are limited to <25%. This is a reasonable tradeoff, with respect to efficiency when considering larger-scale preparation. In the solvent dewaxing step, we would need to reduce the residual 20% n-C_{14} sufficiently to achieve the freezing point specification. In order to address these questions, several hundred milliliters of isomerized C_{14} were produced and separated by distillation from their associated cracking products. As noted above, initial experiments focused only on determining how effectively the n-C_{14} could be selectively removed from the mixture. This was done exclusively by GC determination of the C_{14} composition using the entire C_{14}:solvent mixture. Only the results for the 1:5 ratio are

172

shown in Table 2, because each ratio yielded the same residual n-C_{14} proportion, indicating that, in this simple system,

Table 2. Residual n-C_{14} Content and Freezing Points for Representative C_{14}:Solvent Ratios and Bath Temperatures[a]

C_{14}:solvent ratio	bath temperature (°C)	residual n-C_{14} mass percent (%)	freezing point (°C)
1:5	−40	9.4	
1:5	−50	8.1	
1:5	−60	4.3	
1:5	−65	1.3	−71
1:3	−65	2.2	−41
1:2	−65	1.3	−71
1:2	−65	0.5	−71

[a]As noted in the text, freezing points were only measured at a bath temperature of −65° C after improving the filtration plunger.

temperature is the most critical factor. This is particularly apparent in going from −60 °C to −65 °C, where the residual n-C_{14} drops from 4.3% to 1.3%.

With the preliminary indication that the n-C_{14} could be nearly eliminated, the improved filtration plunger was used to better segregate the fractions, allowing for freezing-point determination of the solvent-stripped, recovered C_{14} liquid. Clearly, a temperature no higher than −65 °C is required to reliably suppress n-C_{14} to the extent required to meet the −47 °C JP-8 freezing point specification. The results with the 1:3 ratio are presented to underscore this point. In the process of removing the test tube from the bath and separating the liquid from the compressed solid, a delay was encountered which allowed the tube to warm slightly. During the actual execution of the operation, it was unclear how important such a brief delay might be. Clearly, the resulting n-C_{14} content of 2.2% was more than enough to elevate the freezing point of the mixture to above the −47 °C specification. For this reason, we established an operating maximum tolerable residual n-C_{14} content of 1.5%. The last two entries, with a ratio of 1:2 show the same apparent freezing point even though the residual n-C_{14} content differs by more than a factor of 2. This is an artifact of the freezing point measurement. Although several values are reported as −71 °C, this value is the lowest reliable freezing point measurable with the automated unit used for this determination. Thus, once this value is reached, no further information about the true freezing point is available.

When assessing these findings with regard to preparing practical quantities of this C_{14} isomer mixture, three additional factors must be considered. The first is shown in Table 2. Since every gallon of recovered C_{14} isomer mix requires the stripping of a larger volume of solvent, the efficacy of the 1:2 C_{14}:solvent ratio is satisfying. In these measurements, we made no attempts to test the efficacy of even lower ratios, as a scaled-up solid−liquid separation scheme must first be defined before meaningful trials can be undertaken. Second, the partitioning of the C_{14} isomers between the liquid and solid fractions is of interest. These data make clear that the methyl-isomer component of the isomer mixture does not solidify under these conditions, even without the solvent present. Any loss of branched isomers to the solid must therefore be via encapsulation in the freezing n-C_{14} matrix. This can be evaluated simply by looking at the C_{14} GC analysis of the

solids fraction. In these small-scale measurements, the occluded branched C_{14} fraction is quite variable, ranging from as little as 28% to as high as 45% of the solidified mass. These observations would indicate that a reasonable yield of the branched C_{14} would be ∼40% of the starting alkane in the absence of a second round of processing and recovery. This is based on a recovery of 75% C_{14} from the isomerization conversion followed by a 55% recovery of branched isomers from the aggregate. Finally, an indication as to whether the loss of branched C_{14} is due to occlusion or to the onset of further differential solidification would be of interest. This can be done in several ways. We have chosen to compare the signal intensity distribution of the branched fraction in the GC analysis of the liquid recovered containing 0.5% residual n-C_{14} with that observed in the mixture prior to solvent dewaxing, as shown in Figure 4. Both chromatograms have been normalized to peak
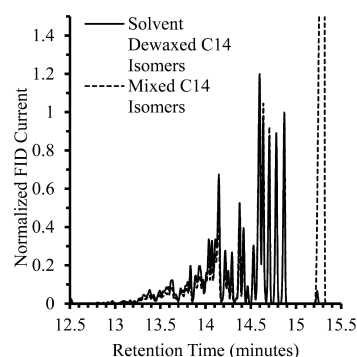
Figure 4. Comparison of the relative populations of single and multiply branched isomers before and after solvent dewaxing. Both distributions are normalized to the peak FID current of the 3-methyltridecane isomer at a retention time of ∼14.87 min. The relative FID current of the multibranched isomers appears larger in the dewaxed mixture than in the initially prepared mixture. This suggests the selective solidification of some proportion of the monomethyl isomers, such that when these are used as the normalization basis, the apparent abundance of the multibranched isomers appears elevated.

FID current of the 3-methyltridecane isomer observed at a retention time near 14.87 min. If there were no differential crystallization, the intensity distribution of the branched C_{14} contribution in both samples would be perfectly superimposed. However, note that the apparent intensity of the multibranched isomer fraction shows a systematic relative attenuation in the full complement of isomers relative to that observed in the solvent-dewaxed isomer distribution. If monomethyltridecanes are preferentially lost to the solid, normalizing on the diminished fraction will artificially elevate the apparent intensity of the higher branched isomers. While this results in a slight yield loss, it actually increases the relative contribution of multibranched isomers to the final isomer composition. Ideally, a distribution of isomers, in which multibranched isomers are in much greater abundance than monobranched isomers, similar to that observed by Claude et al. in their Figure A5,[14] would be desirable, with respect to producing a low-freezing, highly isomerized surrogate fuel in reasonable yield. However, since our work is a precursor to the production of practical quantities of such an isomeric mixture, the use of zeolites like ZSM-22, which are not readily available commercially, precludes their use by us. It is possible to produce an isomer distribution in which the multibranched fraction accounts for over 60% of the

total distribution using our Pt/US-Y zeolite catalyst, as shown in Figure 5. The residual normal fraction accounts for ∼7% of
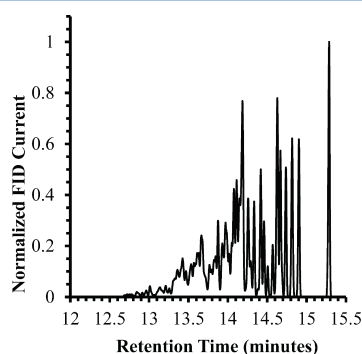
Figure 5. An isomer distribution in which the relative abundance of multibranched isomers is elevated relative to the singly branched isomers. The conditions required to produce such a distribution result in overall conversion of 98% and a corresponding cracking selectivity of 68%, thereby suppressing the overall potential yield of the highly branched isomer distribution following n-C_{14} removal.

the total. However, producing such a distribution comes at the expense of yield. A total conversion of 98% is required with ∼68% cracking. When losses from solvent dewaxing are factored in, a likely net yield of only 10%−15% remains. When making practical quantities, a yield loss of this magnitude is unappealing. However, if a distribution rich in multibranched components is really required, the methods applied in this work provide a pathway for such a composition.

Freezing Point Dependence on n-C_{14} Content. With the availability of a nearly normal alkane-free mixture of C_{14} alkane isomers, we can better quantify the effect of the residual normal fraction on the measured freezing point. Beginning with the dewaxed isomer mixture, containing a normal remnant of 0.44%, we have prepared a series of compositions with increasing normal C_{14} weight percent and had the freezing point determined as prescribed by ASTM D-5972. The result is shown in Figure 6. As the n-C_{14} content decreases, the impact on freezing point becomes incrementally greater. This is most pronounced at the lowest n-C_{14} content, where a 25 °C drop in freezing point occurs with only a 1% absolute change in n-C_{14} content. While refining our solvent dewaxing procedures, we estimated that a residual normal below 1.5% would be required
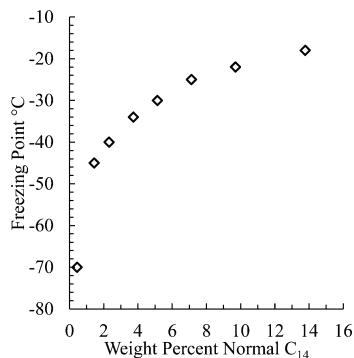
Figure 6. Dependence of the tetradecane mixture freezing point on n-C_{14} content.

to meet the targeted freezing point of −47 °C. That boundary value is reaffirmed through this measurement. What else becomes apparent is just how sensitive the freezing point is to the slightest changes in n-C_{14} content as it becomes vanishingly small. At our lowest n-C_{14} content, the freezing point lies far below the JP-8 specification of −47 °C. At such low true freezing points, the instrumentation used to measure the freezing point according to the applicable ASTM method reaches a minimum meaningful value near −70 °C. If the true freezing point falls below this value, a true freezing point is not returned by the method. A remaining question is how strongly the details of the isomeric composition influence the effect of residual n-C_{14} on freezing point of the mixture. Unfortunately, we have yet to identify a manageable approach for increasing the relative content of multibranched isomers relative to the monobranched fraction.

■ CONCLUSIONS

We have prepared a mixture of predominantly methyl-branched C_{14} alkane isomers with a freezing point below −47 °C, which is the specification value for JP-8 fuel, using an approach that is amenable to scaling for preparing practical quantities of such a mixture. The isomeric composition is achieved by subjecting n-C_{14} to hydroisomerization using a 0.5% Pt/US-Y zeolite catalyst at a fractional conversion just under 0.9. The cracked products formed at this conversion can be efficiently separated from the C_{14} fraction via fractional vacuum distillation. In order to achieve the targeted freezing point, the residual n-C_{14} content must be reduced to <1.5 wt %. n-C_{14} can be reduced to below this amount using a solvent dewaxing method with a solvent composed of a 50/50 mixture of methyl ethyl ketone and toluene at a solvent:C_{14} ratio between 1:2 and 1:5. Direct production of the isomer mixture based only on sequential hydroisomerization and hydrocracking fails, because of an unacceptably high residual n-C_{14} proportion, as well as unacceptably high losses due to cracking at the conversion required to minimize the normal residual. Using the nearly n-C_{14}-free isomer mixture as a starting point, the dependence of the measured freezing point on the n-C_{14} content was determined. This measurement affirms that the permissible residual n-C_{14} must be limited to <1.5 wt % and reveals an extreme sensitivity of the freezing point to quite small changes in n-C_{14} content as it falls below 1 wt %.

■ AUTHOR INFORMATION

Corresponding Author
*Tel.: +1 (937) 229-2349. E-mail: heinz.robota@udri.udayton.edu.
Notes
The authors declare no competing financial interest.

■ ACKNOWLEDGMENTS

174

■ REFERENCES

(1) Corporan, E.; Edwards, T.; Shafer, L.; DeWitt, M. J.; Klingshorn, C.; Zabarnick, S.; West, Z.; Striebich, R.; Graham, J.; Klein, J. Chemical, Thermal Stability, Seal Swell, and Emissions Studies of Alternative Jet Fuels. *Energy Fuels* **2011**, *25*, 955.

(2) McDougal, J. N.; Rogers, J. V. Local and systemic toxicity of JP-8 from cutaneous exposures. *Toxicol. Lett.* **2004**, *149*, 301.

(3) Kahandawala, M. S. P.; DeWitt, M. J.; Corporan, E.; Sidhu, S. S. Ignition and emission characteristics of Surrogate and practical jet fuels. *Energy Fuels* **2008**, *22*, 3673.

(4) Bruno, T. S.; Smith, B. L. Improvements in the Measurement of Distillation Curves. 2. Application to Aerospace/Aviation Fuels RP-1 and S-8. *Ind. Eng. Chem. Res.* **2006**, *45*, 4381.

(5) Hendricks, R. C.; Bushnell, D. M. Shouse, D. T. Aviation Fueling: A Cleaner, Greener Approach. *Int. J. Rotating Machinery* **2011**, 782969.

(6) Ryder, J. A. Jet Fuel Compositions. U.S. Patent 7,589,243 B1, Sept. 15, 2009.

(7) *Detail Specification Turbine Fuel, Aviation Kerosene Type, JP-8 (NATO-F34), NATO F-35, and JP-8 + 100 (NATO F-37)*; MIL-DTL-83133G, U.S. Department of Defense, Washington, DC, April 30, 2010.

(8) Wright, M. E.; Harvey, B. G.; Quintana, R. L. Highly Efficient Zirconium-Catalyzed Batch Conversion of 1-Butene: A New Route to Jet Fuels. *Energy Fuels* **2008**, *22*, 3299.

(9) Harvey, B. G.; Meylemans, H. A. The role of butanol in the development of sustainable fuel technologies. *J. Chem. Technol. Biotechnol.* **2011**, *86*, 2.

(10) Taylor, R. J.; McCormack, A. J. Study of Solvent and Catalytic Lube Oil Dewaxing by Analysis of Feedstocks and Products. *Ind. Eng. Chem. Res.* **1992**, *31*, 1731.

(11) Bouchy, C.; Hastoy, G.; Builoon, E.; Martens, J. A. Fischer–Tropsch Waxes Upgrading via Hydrocracking and Selective Hydro-isomerization. *Oil Gas Sci. Technol.* **2009**, *64*, 91.

(12) Martens, J. A.; Jacobs, P. A.; Weitkamp, J. Attempts to rationalize the distribution of hydrocracked products. I. Qualitative Description of the primary hydrocracking modes of long chain paraffins in open zeolites. *Appl. Catal.* **1986**, *20*, 239.

(13) Martens, J. A.; Tielen, M.; Jacobs, P. A. Attempts to rationalize the distribution of hydrocracked products. III. Mechanistic aspects of the isomerization and hydrocracking of branched alkanes on ideal bifunctional large-pore zeolite catalysts. *Catal. Today* **1987**, *1*, 435.

(14) Claude, M. C.; Vanbutsele, G.; Martens, J. A. Dimethyl Branching of Long *n*-Alkanes in the Range from Decane to Tetracosane on Pt/H-ZSM-22 Bifunctional Catalyst. *J. Catal.* **2001**, *203*, 213.

(15) Weitkamp, J. Isomerization of Long-Chain *n*-Alkanes on a Pt/CaY Zeolite Catalyst. *Ind. Eng. Chem. Prod. Res. Dev.* **1982**, *21*, 550.

10319

dx.doi.org/10.1021/ie301041c | *Ind. Eng. Chem. Res.* 2012, 51, 10313−10319

175

Appendix K. Characterization of Gaseous and Particulate Emissions From a Turboshaft Engine Burning Conventional, Alternative, and Surrogate Fuels

Characterization of Gaseous and Particulate Emissions From a Turboshaft Engine Burning Conventional, Alternative, and Surrogate Fuels

Jeremy Cain,[†] Matthew J. DeWitt,*[‡] David Blunck,[§] Edwin Corporan,[§] Richard Striebich,[‡] David Anneken,[‡] Christopher Klingshirn,[‡] W. M. Roquemore,[§] and Randy Vander Wal[∥]

[†]National Research Council; Wright-Patterson Air Force Base, 1790 Loop Rd. N. Bldg. 490, WPAFB, Ohio 45433-7103, United States

[‡]University of Dayton Research Institute, 300 College Park, Dayton, Ohio 45469-0043, United States

[§]Air Force Research Laboratory/Propulsion Directorate, 1790 Loop Rd. N. Bldg. 490, WPAFB, Ohio 45433-7103, United States

[∥]Pennsylvania State University, 203 Hosler Bldg., University Park, Pennsylvania 16802, United States

ABSTRACT: The effect of fuel composition on the operability and gaseous and particulate matter (PM) emissions of an Allison T63-A-700 turboshaft engine operated at four power settings was investigated in this effort. Testing was performed with a specification JP-8, a synthetic paraffinic kerosene, and four two-component surrogate mixtures that comprise compound classes within current and future alternative fuels. Comparable engine operability was observed for all fuels during this study. Major gaseous emissions were only slightly effected, with trends consistent with those expected based on the overall hydrogen content of the fuels. However, minor hydrocarbon and aldehyde emissions were significantly more sensitive to the fuel chemical composition. Linear correlations between speciated hydrocarbon and aldehyde emissions were observed over the full engine operating range for the fuels tested. The corresponding slopes were dependent on the fuel composition, indicating that fuel chemistry affects the selectivity to specific decomposition pathways. Unburned fuel components were observed in the engine exhaust during operation with all fuels, demonstrating that completely unreacted fuel compounds can pass through the high temperature/pressure combustion zone. Nonvolatile PM emissions (soot) were strongly affected by the fuel chemical composition. Paraffinic fuels produced significantly lower PM number and mass emissions relative to aromatic-containing fuels, with the paraffin structure affecting sooting propensity. The observations are consistent with those expected based on simplified soot formation mechanisms, where fuels with direct precursors for polycyclic aromatic hydrocarbon formation have higher PM formation rates. The effect of a specific chemical structure on the relative PM production is important as this would not be evident when comparing sooting tendencies of fuels based on bulk fuel properties. All fuels produced similar single log-normal size distributions of soot, with higher sooting fuels producing larger mean diameter particles. It is hypothesized that the controlling growth and formation mechanisms for PM production are similar for different fuel chemistries in this regime, with composition primarily affecting soot formation rate. This hypothesis was supported by preliminary TEM analyses that showed similar soot microstructures during operation with either conventional JP-8 or alternative fuels. Overall, this study provides additional and improved insight into the effect of fuel chemical composition on complex combustion chemistry and emissions propensity in a gas turbine engine, and can assist with the successful development of predictive modeling tools.

■ INTRODUCTION

Worldwide aviation growth, rising fuel costs, and limited petroleum resources have resulted in a need to supplement conventional jet fuel production with alternative (nonpetroleum derived) aviation fuels. The U.S. Air Force (USAF) and the Commercial Alternative Aviation Fuel Initiative (CAAFI) have taken lead roles in evaluating and certifying alternatively derived fuels for operation in military and commercial aircraft, respectively.[1] The military aviation fuel specification for JP-8 (MIL-DTL-83133F)[2] was modified in 2008, and a commercial aviation fuel specification (ASTM D7566)[3] was created in 2009 to allow for use of alternatively derived paraffinic kerosene fuels as blending feedstocks up to 50% by volume with petroleum-derived fuels. Specifically, fuels produced via Fischer–Tropsch (F-T) synthesis [termed synthetic paraffinic kerosenes (SPKs)] or hydrodeoxygenation and hydroisomerization of triglyceride-type compounds [termed hydroprocessed esters and fatty acids

(HEFAs)] were certified for use as blending feedstocks in 2009 and 2011, respectively. SPKs and HEFAs are predominantly composed of linear and branched (iso-) paraffins, with minimal concentrations of aromatics (<0.5% by volume) and heteroatomic compounds (<15 ppmv sulfur and <2 ppmv nitrogen), due to the synthesis techniques and current physical and chemical specifications. However, as the diversity of potential feedstocks and processing methods increases, in addition to the desire to produce fully synthetic fuels that do not require blending for use, it is expected that the range and types of chemical functionalities in alternative fuels will significantly increase.

Table 1. Selected Properties of Fuels Evaluated

name	component	volume[a] (%)	mass fraction[b] (%)	hydrogen content[c] (%)	H/C ratio	density[d] (g/mL)	heat of combustion[e] (MJ/kg)	flash point[f] (°C)	surface tension (dyn/cm)[g] @ 22 °C	viscosity (cSt)[h] +40 °C	+90 °C
m-X	m-xylene	25.0	27.7	13.8	1.90	0.778	43.0	44	21.0	1.1	0.7
	n-dodecane	75.0	72.3								
MCH	methylcyclohexane	28.4	28.9	15.1	2.12	0.758	42.9	<5	24.0	1.3	0.7
	n-dodecane	71.6	71.1								
i-C$_8$	iso-octane	30.6	28.9	15.5	2.19	0.737	43.3	<5	20.9	1.1	0.7
	n-dodecane	69.4	71.1								
C$_7$	n-heptane	31.3	29.2	15.6	2.20	0.734	43.4	<5	21.4	1.0	0.6
	n-dodecane	68.7	70.8								
JP-8	aromatics	16.7	19.8	14.0	1.94	0.799	43.1	48	26.6	1.3	0.7
	n-paraffins	19	20.1								
	iso-paraffins	31	32.8								
	cycloparaffins	34	27.4								
	naphthalenes	1.4	2.2								
SPK	aromatics	0.2	0.4	15.4	2.17	0.756	43.9	42	23.6	1.2	0.7
	iso-paraffins	>99	96.8								
	cycloparaffins	<1	2.8								

[a]Two-component blends based on preparation; JP-8 and SPK quantified via ASTM D2425 and D6379. [b]Two-component blends calculated based on volume % and density; JP-8 and SPK quantified via GC×GC analysis. [c]Two-component blends calculated based on volume %, JP-8 via ASTM D7171, and SPK via GC×GC analysis. [d]ASTM D4052. [e]ASTM D4809. [f]ASTM D93. [g]Fisher Surface Tensiomat, model 21. [h]ASTM D445.

178

Understanding the effects of varying fuel composition on engine performance and emissions propensity provides guidance regarding the suitability of potential alternative fuels for use in legacy and future aircraft and the impact on aviation emissions. The latter is important since aircraft emissions, like other sources, can have adverse human health effects[4,5] and may impact the atmospheric environment through direct and indirect processes.[6] There have been a number of experimental investigations into the operational performance and emissions propensity of combustors and turbine engines operated with synthetic paraffinic-like alternative fuels (e.g., SPK and HEFA), both neat and in blends with petroleum-derived fuels.[7−22] These evaluations have shown that similar engine performance and major gaseous emissions (e.g., CO_2 and NO_x) can be obtained with a significant reduction in particulate matter (PM) emissions (mass and particle number), as compared to petroleum-derived fuels. Additionally, the selectivity of certain minor speciated hydrocarbons and oxygenated species has been found to be sensitive to fuel composition.[7,23] This indicates that the fuel structure has an impact on the complex physical and chemical processes occurring within a gas turbine combustor. An improved understanding of the effect of chemical compound class on combustion emissions and performance can help identify optimal compositional properties of alternative fuels and assist in the development of experimental and predictive modeling tools (e.g., "Rules and Tools" program).[1] This understanding is also practical, as supplemental fossil feedstocks (e.g., oil shale, tar sands) are beginning to be used to augment traditional crude-oil resources.

A detailed study was performed with fuels of varying chemical compositions to characterize the operation and emissions of a turboshaft engine over a range of power settings. Testing was performed with a specification jet fuel (JP-8), an SPK that conforms to the specification requirements for an alternative fuel blend feedstock, and four two-component surrogate blends that are composed of compound classes typically found in aviation fuels and are representative of potential classes in future alternative fuels. This effort also supports a current Strategic Environmental Research and Development Program (SERDP) project (WP2145) designed to establish a scientific basis for developing accurate kinetic models for gaseous [e.g., CO, NO_x, total unburned hydrocarbons (UHC), and hazardous air pollutants (HAPs)] and particulate matter (soot) emissions from engines operating with alternative and conventional fuels.

■ EXPERIMENTAL APPROACH

Fuels and Engine Operating Conditions. Two fully formulated fuels and four two-component surrogate mixtures were evaluated to investigate the effect of fuel composition on engine operation and emissions propensity. The fully formulated fuels included a petroleum-derived specification JP-8 and an *iso*-paraffinic kerosene derived from coal via Fischer−Tropsch synthesis produced by Sasol (termed SPK in this paper).[15] The JP-8 conformed to standard fuel specification requirements, with a total sulfur content of ∼700 ppmw and an aromatic content near the average for a typical jet fuel (∼18.0%). The SPK was produced via oligomerization of C_3 and C_4 olefins, followed by hydrotreating and fractionation to produce a fuel with the desired boiling range.[24] This SPK is a highly branched *iso*-paraffinic fuel with low cycloparaffin content and negligible normal paraffin and sulfur content. The surrogates were composed of binary fuel blends that were selected to independently assess the effect of various hydrocarbon classes on emission propensity. All surrogates used *n*-dodecane (C_{12}) as the primary component, while the second component was

interchanged between *m*-xylene (*m*-X), methylcyclohexane (MCH), 2,2,4-trimethylpentane (*iso*-octane: *i*-C_8), and *n*-heptane (C_7). These latter compounds represent aromatic, cycloparaffin, *iso*-paraffin, and *n*-paraffin hydrocarbon classes, respectively. The percentage of the total molar carbon from *n*-C_{12} for each mixture was kept constant (∼70.8%) to provide a basis for comparison of the various fuels. In addition to chemical structure, these mixtures allowed for investigation of the effect of certain physical and chemical properties, such as the overall hydrogen content (or hydrogen-to-carbon (H/C) ratio), which have previously been used when comparing the emissions propensity of petroleum-derived fuels. Selected properties of these fuels are shown in Table 1. The properties shown were either determined using standard ASTM test methods, calculated based on volume blend percentages, or quantified via two-dimensional gas chromatography (GC×GC) analysis. Testing with multicomponent solvents of specific hydrocarbon classes may be more applicable to ultimate implementation in existing engines; however, the current approach allows for direct investigation of the respective individual compounds and assists with ongoing development of predictive engine modeling tools.

Testing was performed using an Allison T63-A-700 turboshaft engine located in the Engine Environment Research Facility of the Aerospace Systems Directorate at Wright-Patterson Air Force Base. This engine model and combustor type have been used extensively in prior studies that investigated the effect of fuel composition on emissions propensity and engine operation.[10−13,15,16,22,25,26] Engine emissions and operability measurements were obtained at four engine power conditions: nominally 3% (low-speed idle), 7% (high-speed idle), 15% (intermediate), and 85% (cruise) of the maximum rated power (nominally 282 HP). The low-speed idle condition was set by controlling the throttle position, while the turbine outlet temperature (T_5) was maintained constant for all other power settings/fuels to provide an equivalent basis for comparison (overall power output). The engine was started with JP-8 for each test to provide baseline operation and emissions data, transitioned to the specific test fuel supplied from an external tank, and subsequently returned to JP-8 to verify consistent operation. This approach minimized the amount of each test fuel required to perform the desired measurements. It should be noted that, although the T63 is an older technology engine, the emissions trends and operational performance with varying fuel compositions from this platform have been consistent with those observed for more modern technology engines.[27]

Gaseous and Particulate Emissions Measurements. Major and minor gaseous and PM emissions were quantified during the engine testing. Samples were extracted from the engine exit plane via temperature-controlled probes (150 °C with recirculating oil) and transported 25 m through heated 0.775 cm i.d. stainless steel tubing to analytical instrumentation located in the Air Force Research Laboratory (AFRL) Turbine Engine Research Transportable Emissions Laboratory (TERTEL). The transfer lines were heated to avoid condensation of volatile organic compounds and water vapor and reduce the loss of soot onto the tube walls. Gaseous (undiluted) and PM (N_2 dilution at the probe tip) emissions were measured using separate probes, with the respective transfer lines maintained at 150 and 75 °C. Sample dilution is used for aerosol measurements to inhibit particle interactions during transport and to prevent saturation of measurement instrumentation. A nondispersive infrared (NDIR) analyzer (California Analytical, model 602P; ± 2% accuracy) was used to determine the dilution ratio for correction based on the diluted and raw CO_2 concentrations.

The total particle number (PN) (number of particles per volume of sample gas) and particle size distributions (PSD; 5−230 nm) were measured in the diluted sample stream using a condensation particle counter (CPC; TSI, model 3022A) and scanning mobility particle sizer (SMPS; TSI, model 3936), respectively. The SMPS consisted of an electrostatic classifier (TSI, model 3080), long differential mobility analyzer (DMA; TSI model 3081), and a CPC (TSI, model 3025A). The reported CPC instrument measurement accuracies are ±10% for the model 3025A, and ±10% for measured concentrations of <5.0 × 10^5 particles/cm^3 and ±20% for higher concentrations for the model 3022A. Measurement repeatability is typically less than ±5% during

179

testing. Black carbon total mass emissions were quantified using a multi-angle absorption photometer (MAAP) (±5% of measured concentration). The MAAP measurements were corrected for the nitrogen dilution used to prevent condensation of moisture and volatile species.

Major and minor gaseous emissions were quantified in the raw gas sample. A Fourier-transform infrared gas analyzer (MKS, MultiGas 2030) measured the concentration of several major and minor gaseous species, including CO_2, CO, NO_x, CH_4, and C_2H_4 (±2% of measured concentration). A flame ionization detector (California Analytical, model 600) measured the total unburned hydrocarbons (UHC) (±3% accuracy). Trace and specific hydrocarbon species were sampled and quantified via two separate methodologies. Charcoal tubes (Supelco, Orbo−32 small) were used to sample unburned hydrocarbons, including low molecular weight aromatics (e.g., mono- and diaromatics). Dinitrophenylhydrazine tubes (DNPH; Supelco, LpDNPH H30) were used to sample aldehydes. Compounds were extracted from the respective tubes using carbon disulfide (charcoal) or acetonitrile (DNPH), and quantification was performed via gas chromatography with flame ionization detection/mass spectrometry (hydrocarbons) and high pressure liquid chromatography with ultraviolet detection (aldehydes). Correction for the respective sampling, extraction, and quantitation efficiencies for each technique was made to determine the actual mass for each species of interest in the exhaust. The relative uncertainties for these methods based on propagation of error analysis are estimated to be ±3% of the reported concentrations. Further details on these specific techniques are provided elsewhere.[28]

Emission Index Calculations. Emission index (EI) values, defined as the amount of the combustion product normalized to the mass of fuel burned, were used for data comparison. This approach provides normalization when comparing engine operation with different fuels and at varying power settings. Emission index values for gas-phase compounds (mass emitted/kg fuel consumed) were calculated with a method similar to that used by Spicer et al.,[29] which determines the mass of fuel burned by assuming all fuel carbon is emitted as CO_2, CO, and UHC

$$EI_x\left(\frac{mass_i}{kg_{fuel}}\right) = \frac{m_i(MW_i \times 10^3)}{(MW_C + \alpha MW_H) \cdot ([CO_2] + [CO] + [UCH])}$$

(1)

where m_i and MW_i are the emitted mass and molecular weight of species i, MW_C and MW_H are the molecular weights of carbon and hydrogen, α is the hydrogen-to-carbon (H/C) ratio of the fuel, and $[CO_2]$, $[CO]$, and $[UHC]$ are the concentrations of CO_2 (background-corrected for atmospheric concentration), CO, and UHC in the exhaust, respectively.

Particle number emission indices were calculated using the methodology included in the current draft of the SAE Aerospace Information Report (AIR) 6037[30]

$$EI_{PN}\left(\frac{\#}{kg_{fuel}}\right)$$
$$= \frac{PN \times 10^6(0.082 \times T_{sample})}{(MW_C + \alpha MW_H) \cdot ([CO_2] + [CO] + [UHC])(P_{sample})}$$

(2)

where PN is the dilution-corrected particle number (i.e., number of particles per mL of sample gas) at the CPC inlet, and T_{sample} and P_{sample} are the sample temperature and pressure, respectively, at the inlet of the CPC.[30]

■ RESULTS AND DISCUSSION

Engine Operability. The basic engine operability, as inferred from the required fuel mass flow rate to achieve the target power setting and short duration operating stability, was similar over the full power range for all fuels evaluated in this

study. A slight reduction (∼1−4%) in the required mass flow rate at the highest power setting relative to operation with JP-8 was observed for the paraffinic fuels with higher overall hydrogen content. This is most likely due to the higher heat of combustion by mass (e.g., see Table 1).

Gaseous Emissions. *Major Emissions.* The major gaseous emissions were similar with different fuels, following trends consistent with those expected primarily based on the overall hydrogen content of the fuels. Emissions indices of CO_2 and CO over the range of power conditions studied are shown in Figures 1 and 2, respectively. Gaseous emissions data were not
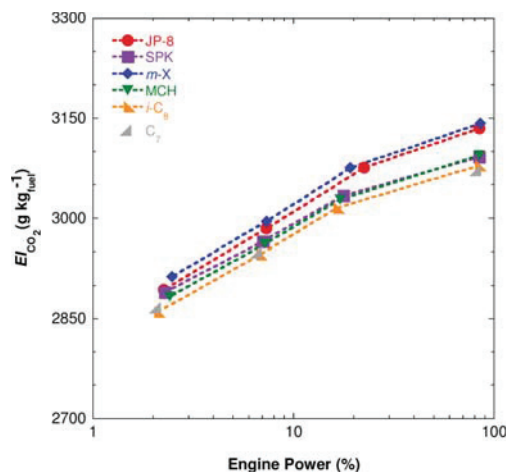
Figure 1. Emission indices for CO_2 as a function of engine power and fuel.
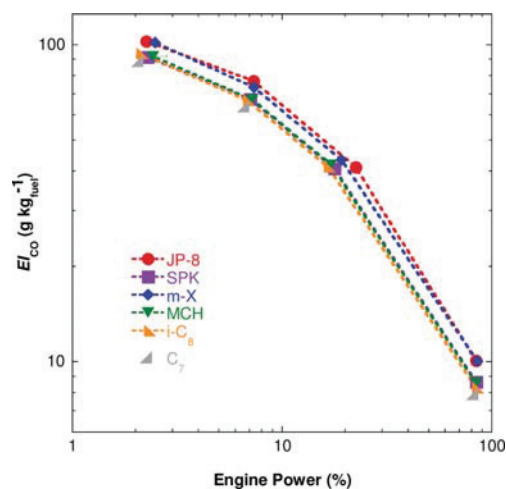
Figure 2. Emission indices for CO as a function of engine power and fuel.

obtained during operation with the C_7/C_{12} blend at the 15% power condition due to a malfunction in the heated transfer line. As shown, the CO_2 emissions increased with increasing engine power with a concurrent decrease in CO emissions; these trends are due to improved combustion efficiency at higher power settings. The measurement uncertainties for these species were 1−2%. The trends observed for CO_2 with fuel type are within the measurement uncertainty, but the trends for

CO are statistically significant (error bars within plot symbols). Both CO and CO_2 emissions were reduced as the fuel H/C ratio increased (e.g., paraffinic mixtures), as expected based on comparable required mass flow rates. The CO emissions for the paraffinic fuels were reduced by approximately 10−20% (compared to JP-8) over the full range of power conditions evaluated. Notably, the CO and CO_2 emissions for the *m*-xylene/C_{12} blend were equivalent to those for JP-8, which could be expected since the hydrogen content of these fuels was almost identical. The trends for the total unburned hydrocarbon emissions (not shown) were consistent with those for CO, with a 10−20% reduction (compared with JP-8) at the lowest power setting. The total NO_x ($NO + NO_2$) emissions were minimally affected during operation with the various fuels, which is reasonable since the formation of these species is primarily thermally driven and the turbine exit temperature was maintained constant. The effect of the specific chemical structure for the paraffinic fuels on the major emissions was not readily evident. In general, the effect of bulk fuel properties (e.g., hydrogen content) on CO, CO_2, and total UHC emissions is consistent with those previously observed during testing with neat synthetic and blends of SPK-type fuels on this and other turboshaft engines.[12,13,15]

Minor Speciated Emissions. The effect of fuel composition and structure was significantly more evident during quantification of the minor speciated gaseous emissions. In particular, the speciated aromatic emissions were very sensitive to the fuel composition, which is important since these classes of compounds are known precursors to polycyclic aromatic hydrocarbons (PAHs), and subsequent soot.[31] Comparisons of the emission indices (EI) of benzene and toluene as a function of engine power and fuel type are shown in Figures 3
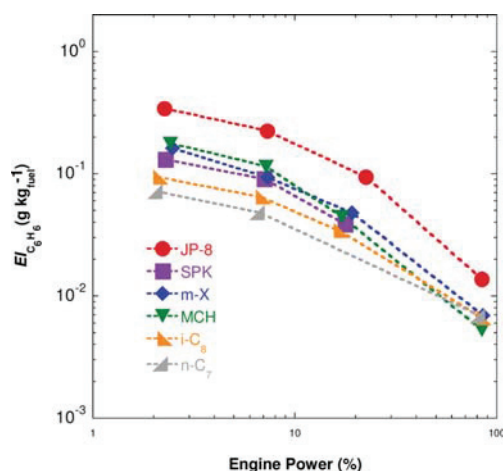

Figure 3. Emission indices for benzene as a function of engine power and fuel.

and 4; these correlations illustrate the dependence of aromatic formation on fuel composition. The measurement uncertainties based on propagation of errors analysis were approximately 4−7% of the measured concentrations; error bars are within plot symbols. For all fuels tested, the emission indices of these species decrease with increasing engine power, which is due to increased combustion efficiency at elevated combustor temperatures and pressures. With respect to the effect of fuel composition on formation of a specific species, a significant
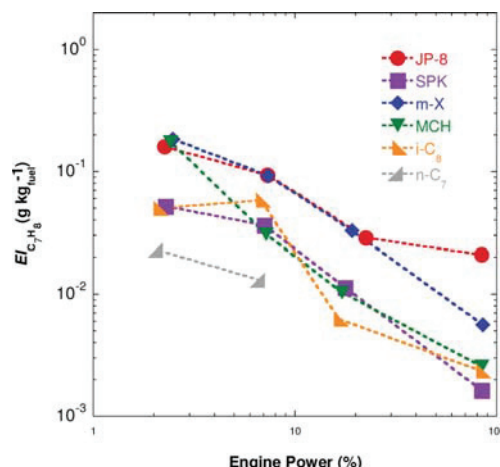

Figure 4. Emission indices for toluene as a function of engine power and fuel.

reduction in both benzene and toluene yields (relative to operation with JP-8) was observed for the paraffinic fuels. In terms of the chemical structure, species that are either direct precursors (e.g., cycloparaffins) to these specific aromatic compounds or selectively form reaction intermediates prone to ring formation have higher aromatic yields. The propensity of the molecular structure of paraffins to produce benzene or toluene was observed to follow cycloparaffin > *iso*-paraffin > *n*-paraffin. For example, the C_7/C_{12} blend produced the lowest benzene yields, followed by the *iso*-paraffinic fuels (*i*-C_8/C_{12} and SPK), and then MCH/C_{12}. Cycloparaffins can form aromatics directly through dehydrogenation of the ring structure via intermolecular hydrogen abstraction reactions (e.g., high yield of toluene for MCH/C_{12} at low power). However, *iso*- and *n*-paraffins must first undergo either ring closure or decomposition to combustion/pyrolytic intermediates prone to ring formation (e.g., propargyl radicals and propylene) to ultimately form cyclic and aromatic compounds. Additionally, an increased branching ratio of *iso*-paraffins results in higher production rates of the C_3-intermediates prone to ring/aromatic formation and growth. These effects were evident in the benzene selectivities, as shown in Figure 3. The SPK most likely had a higher benzene formation than the *i*-C_8/C_{12} blend due to the larger number of potential intermediates and products that could selectively form a six-member ring. It should be reiterated that the SPK in this study was highly branched with no linear paraffins, whereas the *i*-C_8 blend had a high *n*-paraffin percentage (>70% C_{12}). The selective decomposition of the SPK to C_3-intermediates is further illustrated by comparison of ethylene emission indices as a function of engine power and fuel, as shown in Figure 5. The SPK had lower ethylene yields compared to all other fuels, which were similar at all but the highest power condition. Ethylene is produced via β-scission decomposition of primary carbon radicals; the lack of linear character in the SPK inhibits the ethylene formation during pyrolytic decomposition of the fuel. JP-8 had the highest quantified yields of benzene and toluene, which occurs since the base fuel contains these compounds that can be emitted as uncombusted fuel (discussed in next section) and also formed from precursors (e.g., cycloparaffins). The moderate yields of these two specific aromatic compounds for the *m*-X/C_{12} blend occurs since the
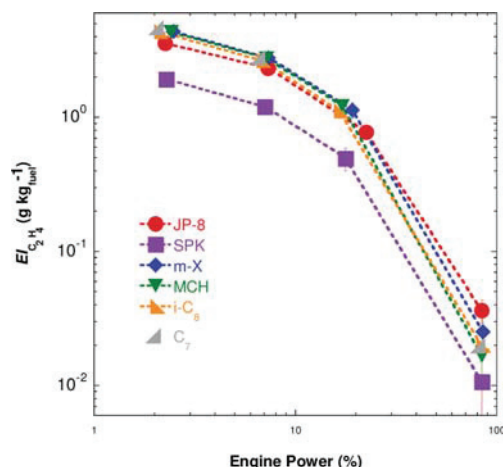
Figure 5. Emission indices for ethylene as a function of engine power and fuel.

direct formation of benzene/toluene from m-X is not inherently favored. However, the measured m-xylene emission index for this blend (~3.2 g/kg_{fuel} at low-speed idle) was 20 times higher than that for JP-8 due to direct emission of unburned fuel (discussed later).

Larger molecular weight aromatics were quantified in the engine exhaust during testing. Mass emissions of naphthalene and pyrene were highest for JP-8, followed by m-X/C_{12} and the SPK (factor of 5−10 lower than JP-8). These trends are consistent with the previous discussion regarding the presence of these compounds in the base JP-8 fuel and production pathways for ring closure and molecular growth. Moreover, JP-8 contains direct precursors for production of naphthalene, such as decalin and tetralin, which will increase the rate of this specific formation pathway. This further illustrates the effect of chemical class and molecular structure on speciated compound formation. The naphthalene and pyrene emissions for the paraffinic surrogates were below the quantitative detection limit of the analytical technique employed. However, these and larger PAHs are present since they are produced via the controlling free-radical pyrolytic pathways in the combustion regime.

Speciated aldehydes were sampled and quantified for the fuels tested. Similar to the results for unburned and speciated hydrocarbons, the emission indices for the aldehydes decreased with increasing engine power. The most prevalent aldehydes emitted for all fuel and engine power combinations were formaldehyde, acetaldehyde, and propionaldehyde. The only exception observed was that the m-tolualdehyde emission was higher than propionaldehyde for the m-X blend testing, which is attributed to the direct formation of this specific aldehyde from m-X in the fuel. Unfortunately, comparison of formaldehyde emissions was not possible for some test conditions due to intermittent moisture condensation at a heated transfer line connection. The high absorption efficiency of formaldehyde in water precluded comparison of the formaldehyde emission trends. All other gaseous species were unaffected by the occurrence of moisture condensation. Similar studies on this T63 engine with the same JP-8 and comparable SPKs have shown that formaldehyde is the aldehyde produced in the highest yield.[28]

Linear Correlations between Speciated Emissions. Recent studies characterizing the emissions from a gas turbine engine operated with petroleum-derived fuels have shown that linear correlations exist between various species in the exhaust stream.[32,33] For example, Yelvington et al.[33] observed linear correlations between various hydrocarbons and formaldehyde with a slope independent of power setting and petroleum fuel composition. These correlations are beneficial because they provide a convenient basis for removing the effect of ambient inlet temperature from the data and allow for comparison with other studies that are performed under significantly different environmental conditions. They can also assist with the development of improved emissions models for gas turbine engines. Such correlations are useful since they could assist with prediction of various speciated emissions by quantifying a few select compounds. For petroleum-derived fuels, linear correlations that are independent of composition indicate that the relative formation rates of the various species are proportional during oxidation/pyrolysis, and slight changes in the base composition do not significantly alter relative production rates.

Recent studies with SPK-type fuels have shown that the relationship (i.e., slope) between speciated products is sensitive to significant changes in the fuel chemistry.[7,23] This implies that the decomposition pathways and rates can be affected by the fuel chemistry in the high pressure/temperature combustion environment. A similar dependency for the emitted ratio of combustion products was observed in the current study. Comparison of the emission indices for benzene and acetaldehyde to that of ethylene as a function of engine power and fuel composition is shown in Figures 6 and 7,
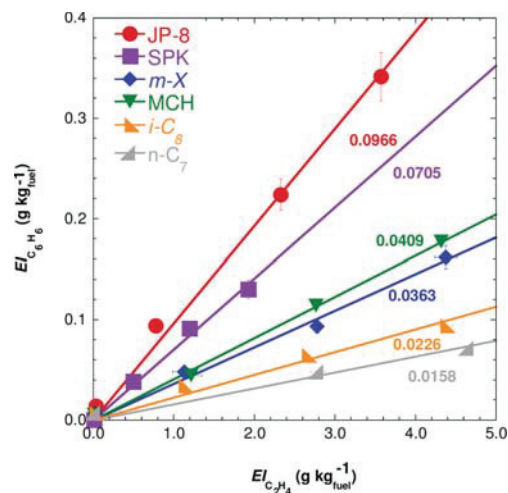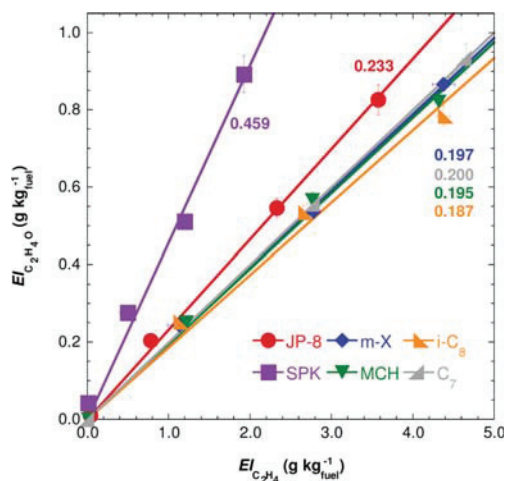

Figure 6. Correlation between the emission indices for benzene and ethylene as a function of fuel composition and engine power settings.

respectively. Ethylene was used for normalization since it was produced in significant yield, while accurate quantification of formaldehyde (used in previous studies) was not obtained in this study. Linear correlations between combustion products as a function of power settings were observed for all fuels used in this study. Similar linear relationships were observed for other primary reaction products measured. Figure 6 shows that the production of benzene relative to ethylene was highly sensitive to fuel composition, with over a factor of 6 difference between

Figure 7. Correlation between the emission indices for acetaldehyde and ethylene as a function of fuel composition and engine power setting.

the highest (JP-8) and lowest (C_7/C_{12}) ratios. These results indicate that decomposition products are formed proportionally, but the relative rates (i.e., slopes) vary with significant changes to the fuel composition, which is consistent with previous studies.[7,23] This occurs since specific reaction pathways will be favored depending on the fuel chemistry. It is noteworthy that the slopes and trends observed for the JP-8 and SPK fuels in this study were very consistent with those from a recent study using the same SPK, but different JP-8, on a CFM-56 engine.[23] This demonstrates that the basic combustion chemistry in these gas turbine engines is similar despite the significant difference in the operating pressures and temperatures. It should also be noted that the slopes can vary with either an increase or decrease in the formation rate of a given species. For example, although the absolute yields of acetaldehyde were similar for the different fuels over the engine power range, a decrease in ethylene selectivity for the SPK fuel resulted in doubling the slope of the correlation for these species (see Figure 7). Hence, the SPK is not more prone to formation of acetaldehyde, but rather this species is formed at a higher rate relative to ethylene. Overall, these linear relationships, which are a function of fuel chemistry, are useful since they can assist with the understanding of the complex combustion process, and can aid the development of predictive computational models.

Unburned Fuel Emissions. During testing with the various fuels, unburned/unreacted fuel compounds were emitted in the engine exhaust at low power settings. The unburned fuel compounds collected on the charcoal tubes were extracted using carbon disulfide and identified and quantified using gas chromatography/flame ionization detection. Chromatograms of samples collected during testing with each of the two-component blends and JP-8 at the lowest power setting are shown in Figure 8 to illustrate the presence of unburned fuel components in the exhaust. For all of the surrogate fuel blends, *n*-dodecane is a primary emission product, along with the second fuel component. Decomposition products (primarily intermediate *n*-alkanes and 1-alkenes) are evident in the chromatograms. For testing with JP-8, it is clear that unburned fuel is being emitted from the engine, as the chromatogram of
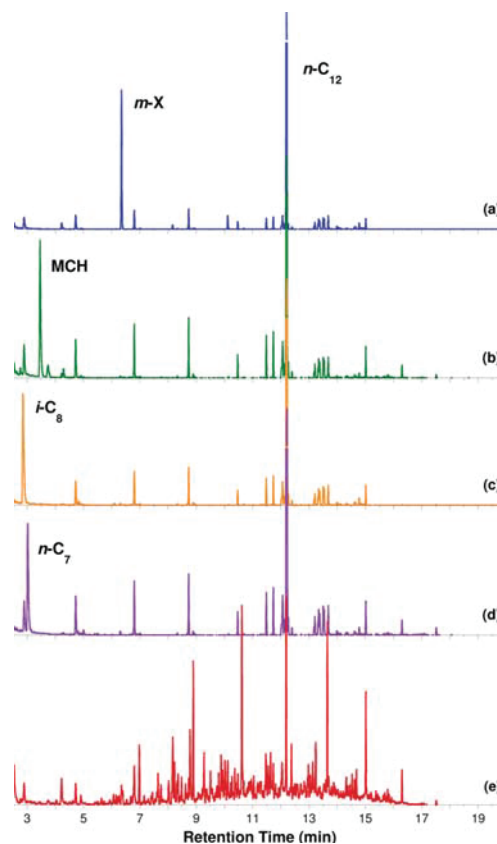

Figure 8. Gas chromatograph analysis of charcoal tube samples collected during testing at the lowest engine power setting: (a) *m*-X/C_{12}, (b) MCH/C_{12}, (c) *i*-C_8/C_{12}, (d) C_7/C_{12}, and (e) JP-8.

the extracted hydrocarbons is identical to that for the fuel. It was estimated from a detailed analysis based on the volume of exhaust gas sampled and mass of total fuel collected that the unburned fuel components comprised a significant percentage (40−70%) of the total unburned hydrocarbon emissions measured online for all fuels evaluated. This phenomenon has also been observed for measurements recently obtained from higher-efficiency turbine engines (e.g., CFM-56 and F117) using the same methodology; these results will be reported elsewhere. These results provide quantitative evidence that uncombusted fuel components are emitted from gas turbine engines during low power operation. In future studies, the use of advanced analytical methods, such as two-dimensional gas chromatography, will provide for improved identification and quantitation of individual species and chemical classes. The presence of specific unburned fuel constituents (e.g., *n*- and *iso*-alkanes) in engine exhaust has previously been reported for measurements from military[34] and commercial[35,36] turbine engines using different sampling and analysis techniques. The identification and quantification of unburned fuel components in engine exhaust is important because the UHCs are typically assumed to be partially oxidized or pyrolyzed fuel products. Furthermore, computational models used to accurately predict combustion efficiency and emissions will need to account for physical effects, such as fuel droplet atomization and vaporization, in addition to reaction kinetics, to accurately predict unburned hydrocarbon emissions.

Particulate Matter Emissions. Particulate matter (PM) emissions were characterized during operation of the T63 engine with the varying fuel compositions over the operating power range. The PM emissions reported herein are primarily nonvolatile, since the exhaust is either highly diluted (aerosol samples) or maintained at a temperature sufficient to prevent condensation of volatile organic compounds (VOCs) or particle nucleation.

PM Aerosol Emissions. The total particle number and size distribution emissions were quantified for the various fuels over the operating range of the T63 engine. It should be noted that these data were not corrected for particle loss during transport from the extraction probe to the instrumentation. There is currently not an accepted standard methodology for determination of the transport efficiency of turbine engine PM through sampling lines. However, estimation of the particle loss percentage as a function of particle diameter was made based on the primary loss modes, which include thermophoresis, diffusion, and impaction, using the particle transport tool developed by Liscinsky and Hollick.[37] For the sampling methodology used in this study, the estimated losses changed the relative particle numbers (PNs) (reported below) by less than 4% for tests at the 3, 7, and 15% power settings, and by approximately 4−7% at the 85% power setting for all fuels except the m-X/C_{12} testing (which was minimally affected by the loss correction). Since these differences have a minimal effect on the trends observed, all aerosol data presented herein were not corrected for particle loss.

A comparison of the particle number (number of particles emitted per kg of fuel burned) (PN-EI) as a function of power setting and fuel type is shown in Figure 9. The total PN
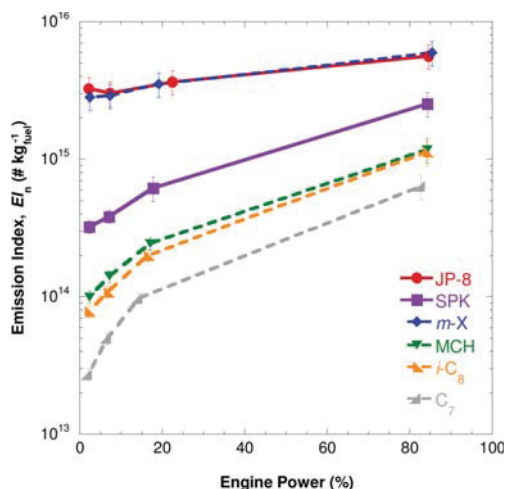
Figure 9. Comparison of particle number emission index as a function of fuel composition and engine power setting.

emissions increased with increasing engine power for all fuels tested, which is due to increased soot formation rates at higher combustion temperatures and pressures. However, there is a very strong dependence of the PN-EI on the fuel chemical composition. The fuels that contain aromatics (JP-8 and m-X/C_{12}) had the highest propensity to form PM since PAHs are precursors to soot.[38] For the paraffinic compounds (inferred from the two-component blends), sooting propensity was lowest for the linear paraffins, with intermediate behavior for

the cyclo- and branched paraffins. The reductions in PN emissions (relative to aromatic-containing fuels) were significantly higher at the lower power settings, with the relative reduction decreasing with increasing engine power.

The relative sooting propensity with respect to fuel chemistry can be explained based on simplified formation mechanisms for PAH, and subsequently soot, formation.[31] Aromatic components present in the parent fuel can act as direct precursors for PAH formation via condensation and addition reactions with products of incomplete combustion and pyrolysis. This can lead to rapid molecular growth of the aromatics to higher molecular weight PAHs. Paraffinic compounds, however, must first undergo decomposition to lower molecular weight (C_2−C_5) intermediates, which subsequently undergo addition and ring closure reactions to form aromatic rings that continue to grow.[31,39−41] These additional reaction steps decrease the overall PM formation rate produced from paraffinic fuels relative to those with aromatics. With respect to molecular structure, an increased branching ratio has been shown to increase sooting propensity in both model and fully formulated fuels, primarily due to the increased selectivity to species (e.g., propene and propargyl radical) that increase ring formation and PAH growth rates.[10,15,41] Cycloparaffins can undergo bond fission, resulting in ring-opening reactions that provide reactivity similar to that with normal paraffins. However, they can also undergo direct dehydrogenation reactions to form aromatics. These competitive pathways result in sooting propensity that is comparable or greater than that in the *iso*-paraffins,[10] depending on the fuel formulation and combustion conditions. As the combustion temperature increases, decomposition and molecular growth reaction rates increase and, thus, reduce the difference in sooting propensities between aromatic and paraffinic fuels.

The fully formulated SPK had a sooting propensity between the aromatic-containing fuels and the paraffinic surrogate blends. It could have been expected that the SPK would exhibit similar sooting propensity to the i-C_8/C_{12} blend. However, this specific SPK has a very high degree of branching with no linear paraffinic content, while the surrogate blend has a significant amount (>70% by mass). This high percentage of n-paraffins substantially reduces the sooting propensity of the i-C_8/C_{12} blend. This behavior was also observed during a recent study performed on the T63 platform using fully formulated SPK fuels with varying branching ratios. It was observed that the SPK fuels with higher *iso*-paraffin contents and degree of branching produced higher soot.[15]

The sooting tendencies of hydrocarbon fuels have previously been compared with respect to their hydrogen content (or H/C ratio) since this has been shown to be a relevant parameter for predicting sooting behavior.[26,31,42] Other parameters, such as the threshold sooting index (TSI), have also been shown to correlate fuel properties (e.g., smoke point and fuel molecular weight) to their sooting tendency. The aromatic content of the fuel is also a primary factor in sooting tendency, as previously discussed; however, this parameter is partially accounted for by hydrogen content. A comparison of the ratio of the PN emission index to that for JP-8 for the six fuels tested at cruise power as a function of the overall hydrogen content is shown in Figure 10 (uncertainty of ±28% of the calculated ratio). These results are consistent with those expected as there is a general correlation of decreasing soot formation with increasing hydrogen content.[26,31,42] However, there is a considerable degree of variability in the relative PN emissions for the
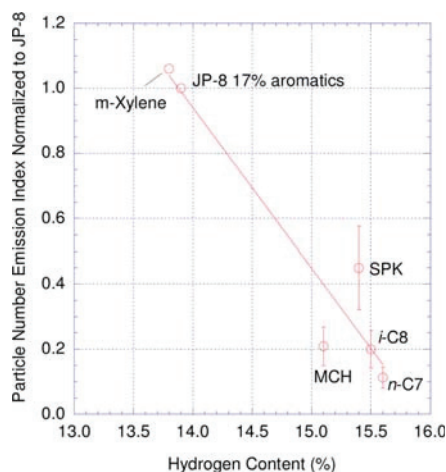
Figure 10. Comparison of particle number emission index at the 85% power condition with respect to the fuel hydrogen content.

Figure 11. Comparison of particle size distributions for the various fuels at the 7% engine power condition.

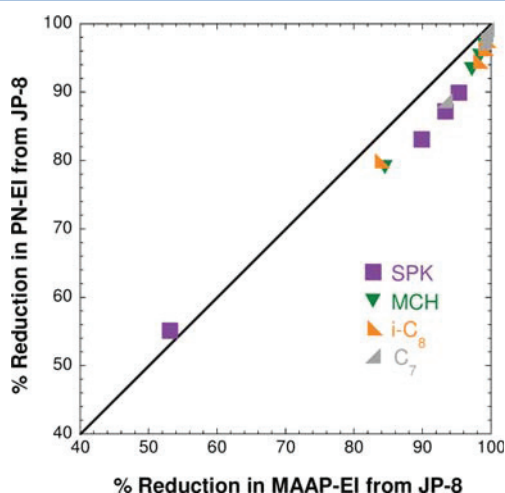**Figure 12.** Comparison of particle size distributions for the various fuels at the 85% engine power condition.

paraffinic surrogate blends, even though the overall hydrogen contents are very similar (e.g., SPK and i-C$_8$/C$_{12}$ blend). This further illustrates that chemical composition can have a significant impact on the overall sooting behavior of the fuel, which is consistent with trends observed during comparable studies.[10,15] The differences in the sooting tendency of fuels shown in Figure 10 are intensified relative to those for petroleum-derived fuels since the chemical character (e.g., branching ratio) was substantially changed while maintaining a constant hydrogen content. For petroleum-derived fuels, the concentrations of multiple chemical classes are typically changed in concert with hydrogen content, which will reduce the overall variability in the corresponding sooting metric. Overall, the observations for sooting propensity as a function of fuel composition are consistent with previous chemical class/alternative fuel studies and with simplified soot formation mechanisms, where the formation rate of reactive intermediates prone to molecular growth reactions affects the overall PM emissions.

Soot particle size distributions (PSDs) were measured over a mobility diameter range of 5−230 nm. As with the total PN-EI, the size distributions are primarily for nonvolatile particles. The PSD for each fuel, shown in PN-EI units for each dynamic mobility diameter, at the high-speed idle (7%) and cruise (85%) power conditions is shown in Figures 11 and 12, respectively. The distributions are an average of multiple (2−5) scans at each fuel and power combination. The PSD for each fuel tested was observed to be unimodal and shifted to larger particle sizes with increasing engine power. This is consistent with characterization of nonvolatile PM emissions (e.g., no nucleation mode < 10 nm observed) and has been reported for previous studies.[9,13,14,43−46] The general trend in the size distributions as a function of fuel composition is consistent with those observed for the total PN emissions. It is also observed that the higher-sooting aromatic fuels have larger mean particle diameters, with decreasing mean particle size for the paraffinic fuels. The larger particles are selectively formed due to higher soot formation and molecular growth rates, which increase the particle size following inception; the decreased formation and molecular growth rates for paraffin compounds renders smaller particle sizes. On the basis of the similarities in the size distributions throughout the engine power range, it is
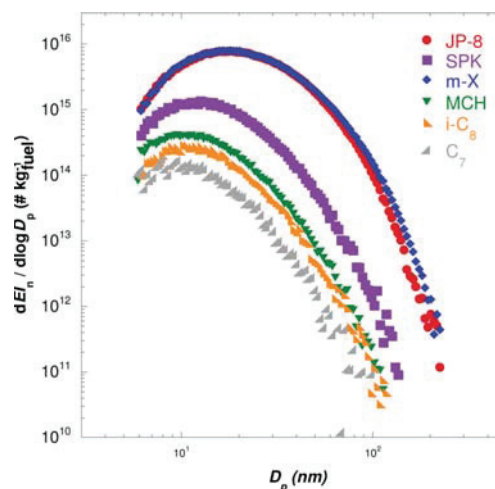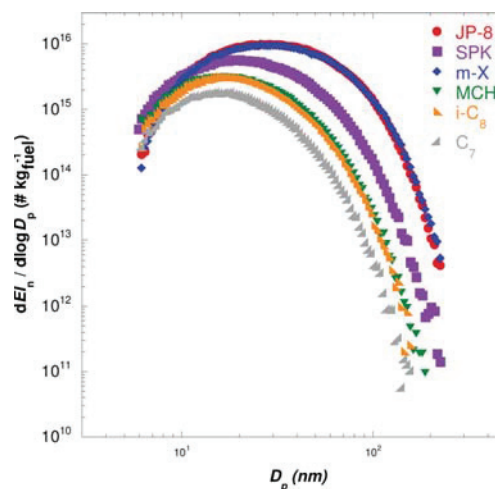
hypothesized that the fuel composition primarily affects the PM formation rate, but the formation and growth mechanism of nonvolatile soot particles is similar. Further discussion is provided during discussion of the nonvolatile soot morphology determined via transmission emission microscopy (TEM). It is acknowledged that subsequent volatile transformations of the PM emissions during cooling and condensation may be dependent on the fuel composition. However, the incipient particles are minimally affected by this volatile fraction.

PM Mass Emissions. The total black carbon mass emissions were measured using a multi-angle absorption photometer (MAAP). Total PM mass emissions showed a strong dependence on the fuel chemical composition, with trends consistent with those for the total PN emissions. The reductions in the mass emissions relative to JP-8 for a specific fuel and engine power setting were proportional to, but slightly greater than, the PN-EI emissions. A parity plot comparing the percent reduction (from JP-8 emission levels) in mass emission index (MAAP-EI; ± 6% relative uncertainty) and PN-EI

($\pm$20% relative uncertainty) is shown in Figure 13. Specific focus is given to the testing with the paraffinic fuels, which


Figure 13. Comparison of percent reduction in PN-EI to percent reduction in MAAP-EI from JP-8 emissions.

showed the greatest relative reduction in both the total PN and mass emissions, and also had the largest reductions in the particle size distribution and corresponding mean particle diameter characteristics relative to operation with JP-8. As shown, the percent reductions in the mass emissions relative to neat JP-8 were greater than the corresponding PN emissions. This is due to the reduction in mean particle diameter on the corresponding mass (i.e., particles are still formed, but impart a smaller impact on the total mass emissions). These results show that characterization of both mass and number emissions is useful to provide improved insight into the effect of fuel chemistry on emissions propensity and soot production pathways.

Effect of Fuel Physical Properties on PM Emissions. The effects of various liquid fuel properties that may potentially impact combustion performance and emissions propensity were examined. Fuel properties that affect fuel droplet spray and atomization characteristics (e.g., viscosity and surface tension) and vaporization rate (e.g., flash point) were measured and are reported in Table 1. Fuel viscosity was measured at 40 and 90 °C (rather than at the specification test temperature of −20 °C) to be more representative of fuel nozzle temperatures. At these elevated temperatures, there is minimal difference between the bulk viscosities for all fuels evaluated. Similarly, the measured surface tensions (between liquid and air) for these fuels did not show a trend consistent with the observed PM emissions. The paraffinic mixtures all had very low flash points (below the +5 °C minimum instrument limit) due to the high concentrations of the blend components with very low flash points (<0 °C) despite that for n-C_{12} (74 °C). The flash point of neat m-xylene (25 °C) is substantially higher, resulting in a moderate flash point for the blend (44 °C), while the wide-distillation ranging SPK and JP-8 have flash points consistent with the production targets. The potential impact of fuel flash point is believed to be minimal compared to the chemical compositional effects. A previous study on the same engine platform with various fuels and solvents showed minimal correlation between fuel physical properties and PM

emissions.[10] It should be noted that the aforementioned properties may affect fuel spray characteristics under combustion conditions (e.g., elevated temperature and pressure) more strongly than indicated by the near-ambient fuel property measurements. Fuel spray visualization studies could be of merit in future investigations.

Transmission Electron Microscopy of Soot Particles. Morphological analysis of the nascent soot structures produced during operation with the JP-8 and SPK fuels was performed by transmission electron microscopy (TEM) to provide insights into the effect of fuel chemical composition on the soot nanostructure. Soot particles were collected on 300 mesh copper TEM grids (Ted Pella, Lacey Formvar/Carbon #01883-F) loaded onto stages of a cascade impactor (MSP, nano-MOUDI II, 125B). Samples were collected from a raw sample line at low-speed idle, intermediate, and cruise conditions. Off-line analysis of the soot particles was performed by a 200 kV field emission TEM (JEOL, EM2010F). Micrographs for samples collected on stage 11 ($D_{p,50\%}$ = 32 nm) of the cascade impactor at the three power conditions for both JP-8 and SPK are shown in Figure 14. These images are representative of soot particles collected on different stages (particle sizes) and for the various two-component fuel blends tested. Overall, the nanostructure is similar for soot particles produced from all fuels evaluated in this study. Particle lamellae are short and
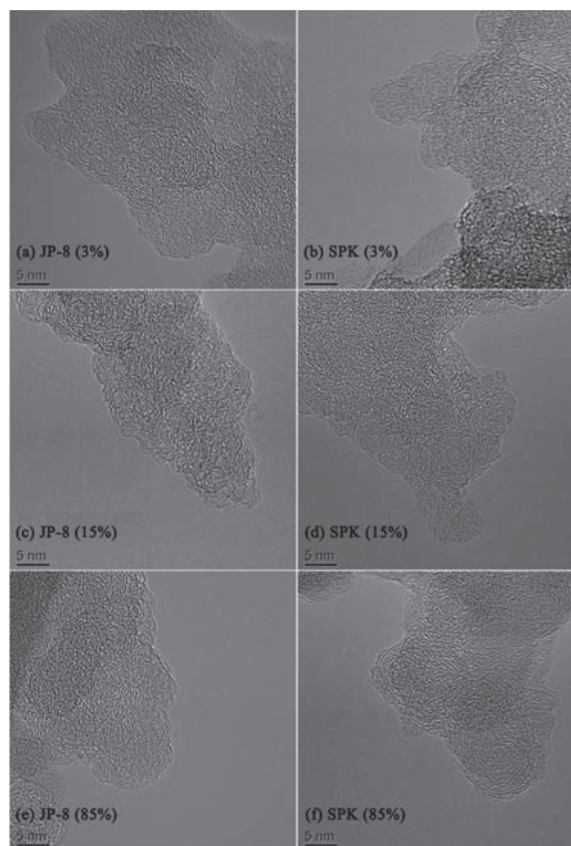
Figure 14. TEM micrographs for particles collected on stage 11 ($D_{p,50\%}$ = 32 nm) of cascade impactor. Production conditions are given in the panels: JP-8 (left), SPK (right), low-speed idle (top), intermediate (middle), and cruise (bottom).

poorly organized overall, and most are randomly oriented with respect to one another rather than exhibiting a stacking order (e.g., graphite). This type of disorder is indicative of chaotic growth conditions wherein diversity of species, coupled with high concentrations, disallows ordered growth.

With respect to engine power, the nanostructures appear more defined at cruise than at the lower power conditions, yet are still highly similar. Despite differences in turbulence and mixing between low and high power levels, the similarity in soot nanostructure is consistent with comparable soot forming environments across engine conditions. Moreover, similarity between both the nonvolatile soot nanostructure and the particle size distributions (as previously discussed) indicates that the mechanisms for (nonvolatile) soot particle formation are similar; changes in gas-phase species concentrations (as affected by fuel composition) or temperature would primarily alter the PM growth rate. The soot nanostructure produced in the turbine engine combustor shown in Figure 14 does not resemble that typically produced in ordinary laboratory flames with simple fuels;[47] such differences are indicative of different environments of formation and growth. Further study and analyses are necessary to provide expanded insight into these observations.

SUMMARY AND CONCLUSIONS

An investigation was conducted to study the effect of fuel composition on the operability and gaseous and particulate matter emissions for an Allison T63-A-700 turboshaft engine. The testing was performed with a specification JP-8, an SPK, and four surrogate mixtures that comprise compound classes representative of current and future alternative fuels. All fuels provided comparable engine operation during testing. Major gaseous emissions were only slightly affected, with trends consistent with that expected based on the overall hydrogen content of the fuels. However, minor hydrocarbon and aldehyde emissions were significantly more sensitive to the fuel composition. The speciated aromatic emissions were highly sensitive to chemical composition, as evidenced by their high formation rates from fuels that contained aromatics or had high selectivity to produce reactive intermediates prone to ring closure and addition. The fuel composition was found to have a significant effect on the specific decomposition and oxidation pathways based on the impact to proportional formation rates between individual species (i.e., slope). These data can assist with understanding the complex combustion and pyrolysis chemistry in addition to the successful development of predictive modeling tools. Evidence of unburned fuel components in the exhaust stream was observed for all fuels evaluated in this study. This demonstrates that completely unreacted fuel compounds can pass through the high temperature and pressure combustion zone.

The nonvolatile PM emissions were strongly affected by the fuel chemistry. Paraffinic fuels were found to produce significantly lower PM emissions than fuels containing aromatic compounds. Additionally, an increased branching ratio of paraffins was observed to increase soot production. These results are consistent with those expected from simplified soot formation mechanisms, where compounds (e.g., aromatics) that can act as direct precursors for PAH formation via condensation and addition reactions with other combustion/pyrolysis products will have higher relative PM formation rates. However, paraffinic compounds must first undergo decomposition to lower molecular weight intermediates prior to molecular growth and soot formation. Paraffinic compounds that have higher selectivity to form reactive intermediates prone to ring growth (e.g., iso-paraffins) had higher soot formation rates. Understanding the effect of chemical structure on emissions propensity is important since the cause for observed differences would not be evident when comparing sooting tendencies of fuels based on bulk fuel properties. All fuels produced similar unimodal particle size distributions, with higher sooting fuels producing larger mean diameter particles. On the basis of similarities in the nonvolatile particle size distributions, it is hypothesized that the fuel composition primarily affects the overall PM formation rate, but the controlling growth and formation mechanisms are similar. This hypothesis was supported by TEM analysis that showed that the soot microstructure was similar during operation with the different fuels. The effect of fuel composition on the total PM mass emissions was consistent with that for the overall particle number emissions, but mass reductions were slightly higher due to shifts in the size distributions to smaller particle size. This study provides additional and improved insight into the effect of fuel chemical composition on gaseous and nonvolatile particulate emissions.

AUTHOR INFORMATION

Corresponding Author
*E-mail: matthew.dewitt@wpafb.af.mil.

Notes
The authors declare no competing financial interest.

REFERENCES

(1) Edwards, T.; Moses, C.; Dryer, F. Evaluation of Combustion Performance of Alternative Aviation Fuels. In *46th AIAA/ASME/SAE/ASEE Joint Propulsion Conference & Exhibit Proceedings*, Nashville, TN, July 25−28, 2010; AIAA: Reston, VA, 2010; Paper No. AIAA 2010-7155.

(2) *Detailed Specification: Turbine Fuel, Aviation, Kerosene Type, JP-8 (NATO F-34), NATO F-35, and JP-8 + 100 (NATO F-37)*; MIL-DTL-83133H w/ AMENDMENT 1; U.S. Department of Defense: Washington, DC, September 14, 2012.

187

(3) *Standard Specification for Aviation Turbine Fuel Containing Synthesized Hydrocarbons*; ASTM D7566-12a; ASTM International: West Conshohocken, PA, September 1, 2012.

(4) Kennedy, I. M. The health effects of combustion-generated aerosols. *Proc. Combust. Inst.* **2007**, *31* (2), 2757−2770.

(5) Pope, C. A., III; Dockery, D. W.; Schwartz, J. Review of epidemiological evidence of health effects of particulate air pollution. *Inhalation Toxicol.* **1995**, *7* (1), 1−18.

(6) Cain, J. P. Development of a novel heterogeneous kinetics reactor and chemical characterization of soot particles. Ph.D. Dissertation, University of Southern California, Los Angeles, 2011.

(7) Anderson, B. E.; Beyersdorf, A. J.; Hudgins, C. H.; Plant, J. V.; Thornhill, K. L.; Winstead, E. L.; Ziemba, L. D.; Howard, R.; Corporan, E.; Miake-Lye, R. C.; Herndon, S. C.; Timko, M.; Woods, E.; Dodds, W.; Lee, B.; Santoni, G.; Whitefield, P.; Hagen, D.; Lobo, P.; Knighton, W. B.; Bulzan, D.; Tacina, K.; Wey, C.; VanderWal, R.; Bhargava, A. *Alternative Aviation Fuel Experiment (AAFEX)*; NASA/TM-2011-217059; National Aeronautics and Space Administration: Hampton, VA, February, 2011.

(8) Bulzan, D.; Anderson, B.; Wey, C.; Howard, R.; Winstead, E.; Beyersdorf, A.; Corporan, E.; DeWitt, M. J.; Klingshirn, C.; Herndon, S.; Miake-Lye, R.; Timko, M.; Wood, E.; Tacina, K. M.; Liscinsky, D.; Hagen, D.; Lobo, P.; Whitefield, P. Gaseous and particulate emissions results of the NASA Alternative Aviation Fuel Experiment (AAFEX). In *Proceedings of ASME Turbo Expo: Power for Land, Sea and Air*, June 14−18, Glasgow, U.K., 2010; ASME: New York, 2010; GT2010-23524.

(9) Cheng, M.-D.; Corporan, E.; DeWitt, M. J.; Landgraf, B. Emissions of volatile particulate components from turboshaft engines operated with JP-8 and Fischer−Tropsch fuels. *Aerosol Air Qual. Res.* **2009**, *9* (2), 237−256.

(10) Corporan, E.; Monroig, O.; Wagner, M. Influence of fuel chemical composition on particulate matter emissions of a turbine engine. In *Proceedings of the ASME Turbo Expo: Power for Land, Sea and Air*, June 14−17, Vienna, Austria, 2004; ASME: New York, 2004; GT2004-54335.

(11) Corporan, E.; Reich, R.; Monroig, O.; DeWitt, M. J.; Larson, V.; Aulich, T.; Mann, M.; Seames, W. Impacts of biodiesel on pollutant emissions of a JP-8-fueled turbine engine. *J. Air Waste Manage. Assoc.* **2005**, *55* (7), 940−949.

(12) Corporan, E.; DeWitt, M. J.; Belovich, V.; Pawlik, R.; Lynch, A. C.; Gord, J. R.; Meyer, T. R. Emissions characteristics of a turbine engine and research combustor burning a Fischer−Tropsch jet fuel. *Energy Fuels* **2007**, *21* (5), 2615−2626.

(13) Corporan, E.; DeWitt, M. J.; Klingshirn, C. D.; Striebich, R.; Cheng, M.-D. Emissions characteristics of military helicopter engines with JP-8 and Fischer−Tropsch Fuels. *J. Propul. Power* **2010**, *26* (2), 317−324.

(14) Corporan, E.; DeWitt, M. J.; Klingshirn, C. D.; Anneken, D. *Alternative Fuels Tests on a C-17 Aircraft: Emissions Characteristics*; AFRL-RZ-WP-TR-2011−2004; Air Force Research Laboratory: Wright-Patterson Air Force Base, December, 2010.

(15) Corporan, E.; Edwards, T.; Shafer, L.; DeWitt, M. J.; Klingshirn, C.; Zabarnick, S.; West, Z.; Striebich, R.; Graham, J.; Klein, J. Chemical, thermal stability, seal swell, and emissions studies of alternative jet fuels. *Energy Fuels* **2011**, *25* (3), 955−966.

(16) DeWitt, M. J.; Corporan, E.; Graham, J.; Minus, D. Effects of aromatic type and concentration in Fischer−Tropsch fuel on emissions production and material compatibility. *Energy Fuels* **2008**, *22* (4), 2411−2418.

(17) Lee, B. H.; Santoni, G. W.; Wood, E. C.; Herndon, S. C.; Miake-Lye, R. C.; Zahniser, M. S.; Wofsy, S. C.; Munger, J. W. Measurements of nitrous acid in commercial aircraft exhaust at the Alternative Aviation Fuel Experiment. *Environ. Sci. Technol.* **2011**, *45* (18), 7648−7654.

(18) Lobo, P.; Whitefield, P. D.; Hagen, D. E.; Rye, L. J.; Blakey, S.; Wilson, C. W.; Williams, P. I.; Christie, S.; Raper, D.; Uryga-Bugajska, I.; Pourkashanian, M. *SAE E31 Methodology Development and Associated PM Emissions Characteristics of Aircraft APUs Burning Conventional and Alternative Aviation Fuels*; PARTNER-COE-2011-005; The Partnership for Air Transportation Noise and Emissions Reduction: Cambridge, MA, July, 2011.

(19) Timko, M. T.; Yu, Z.; Onasch, T. B.; Wong, H. W.; Miake-Lye, R. C.; Beyersdorf, A. J.; Anderson, B. E.; Thornhill, K. L.; Winstead, E. L.; Corporan, E.; DeWitt, M. J.; Klingshirn, C. D.; Wey, C.; Tacina, K.; Liscinsky, D. S.; Howard, R.; Bhargava, A. Particulate emissions of gas turbine engine combustion of a Fischer—Tropsch synthetic fuel. *Energy Fuels* **2010**, *24* (11), 5883−5896.

(20) Snijders, T. A.; Melkert, J. A.; Bauldreay, J. M.; Bogers, P. F.; Wahl, C. R. M.; Kapernaum, M. G. Impact of Fuel Composition on Emissions and Performance of GTL Kerosine Blends in a Cessna Citation II. In *Proceedings of the 12th International Conference on Stability Handling and Use of Liquid Fuels*, October 16−20, Sarasota, FL, 2011; IASH: Atlanta, GA, 2011.

(21) Pucher, G.; Allan, W.; LaViolette, M.; Poitras, P. Emissions from a gas turbine sector rig operated with synthetic aviation and biodiesel fuel. *J. Eng. Gas Turbines Power* **2011**, *133* (11), 111502.

(22) Bester, N.; Yates, A., Assessment of the Operational Performance of Fischer−Tropsch Synthetic-Paraffinic Kerosene in a T63 Gas Turbine Compared to Conventional Jet A-1 fuel. In *Proceedings of the ASME Turbo Expo: Power for Land, Sea and Air*, June 14−18, Orlando, FL, 2009; ASME: New York, 2009; GT2009-60333.

(23) Knighton, W. B.; Herndon, S. C.; Woods, E.; Miake-Lye, R. C.; Timko, M.; Yu, Z.; Beyersdorf, A. J.; Winstead, E. L.; Anderson, B. E.; Wey, C.; Bulzan, D., A method of characterizing aircraft engine exhaust emissions. In *50th AIAA Aerospace Sciences Meeting Proceedings*, Jan 6−9, Nashville, TN, 2012; AIAA:Reston, VA, 2012.

(24) Moses, C. A.; Stavinoha, L. L.; Roets, P. *Qualification of SASOL Semi-Synthetic Jet A-1 as Commercial Jet Fuel*; Report No. 8531; Southwest Research Institute: San Antonio, TX, 1997.

(25) Corporan, E.; DeWitt, M.; Wagner, M. Evaluation of soot particulate mitigation additives in a T63 engine. *Fuel Process. Technol.* **2004**, *85* (6−7), 727−742.

(26) Naegeli, D. W.; Dodge, L. G.; Moses, C. A. Sooting tendency of fuels containing polycyclic aromatics in a research combustor. *J. Energy* **1983**, *7* (2), 168−175.

(27) Corporan, E.; DeWitt, M.; Klingshirn, C.; Anneken, D.; Streibich, R.; Shafer, L. Comparisons of emissions characteristics of several turbine engines burning Fischer−Tropsch and hydroprocessed esters and fatty acids alternative jet fuels. In *Proceedings of the ASME Turbo Expo 2012*, June 11−15, Copenhagen, Denmark, 2012; ASME International: New York, 2012; Paper No. GT2012-68656.

(28) Anneken, D.; Striebich, R.; DeWitt, M. J.; Klingshirn, C.; Corporan, E. Development of a method to identify and quantify hazardous air pollutants from turbine engine emissions. *Prepr. Symp.-Am. Chem. Soc., Div. Fuel Chem.* **2012**, *57* (2), ENFL-188.

(29) Spicer, C. W.; Holdren, M. W.; Cowen, K. A.; Joseph, D. W.; Satola, J.; Goodwin, B.; Mayfield, H.; Laskin, A.; Alexander, M. L.; Ortega, J. V.; Newburn, M.; Kagann, R.; Hashmonay, R. Rapid measurement of emissions from military aircraft turbine engines by downstream extractive sampling of aircraft on the ground: Results for C-130 and F-15 aircraft. *Atmos. Environ.* **2009**, *43* (16), 2612−2622.

(30) *E-31 Aircraft Exhaust Emissions Measurements Committee Aircraft Exhaust Nonvolatile Particle Matter Measurement Method Development*; SAE AIR6037; SAE Aerospace: Warrandale, PA, March 2, 2010.

(31) Lefebvre, A. H.; Ballal, D. R. *Gas Turbine Combustion: Alternative Fuels and Emissions*, 3rd ed.; CRC Press: Boca Raton, FL, 2010.

(32) Knighton, W. B.; Rogers, T. M.; Anderson, B. E.; Herndon, S. C.; Yelvington, P. E.; C., M.-L. R. Quantification of aircraft engine hydrocarbon emissions using proton transfer reaction mass spectrometry. *J. Propul. Power* **2007**, *23* (5), 949−958.

(33) Yelvington, P. E.; Herndon, S. C.; Wormhoudt, J. C.; Jayne, J. T.; Miake-Lye, R. C.; Knighton, W. B.; Wey, C. Chemical speciation of hydrocarbon emissions from a commercial aircraft engine. *J. Propul. Power* **2007**, *23* (5), 912−918.

(34) Spicer, C. W.; Holdren, M. W.; Smith, D. L.; Hughes, D. P.; Smith, M. D. Chemical composition of exhaust from aircraft turbine engines. *J. Eng. Gas Turbines Power* **1992**, *114* (1), 111−117.

(35) Slemr, F.; Giehl, H.; Habram, M.; Slemr, J.; Schlager, H.; Schulte, P.; Haschberger, P.; Lindermeir, E.; Döpelheuer, A.; Plohr, M. In-flight measurement of aircraft CO and nonmethane hydrocarbon emission indices. *J. Geophys. Res.: Atmos.* **2001**, *106* (D7), 7485−7494.

(36) Spicer, C. W.; Holdren, M. W.; Riggin, R. M.; Lyon, T. F. Chemical composition and photochemical reactivity of exhaust from aircraft turbine engines. *Ann. Geophys.* **1994**, *12* (10/11), 944−955.

(37) Liscinsky, D. S.; Hollick, H. H. *Effect of Particle Sampling Technique and Transport on Particle Penetration at the High Temperature and Pressure Conditions Found in Gas Turbine Combustors and Engines*; NASA Report: NASA/CR-2010-NNC07CB03C; NASA: Washington, DC, March, 2010.

(38) Frenklach, M. Reaction mechanism of soot formation in flames. *Phys. Chem. Chem. Phys.* **2002**, *4* (11), 2028−2037.

(39) Bockhorn, H.; Fetting, F.; Wenz, H. W. Investigation of the formation of high molecular hydrocarbons and soot in premixed hydrocarbon-oxygen flames. *Ber. Bunsen-Ges. Phys. Chem.* **1983**, *87* (11), 1067−1073.

(40) Richter, H.; Howard, J. B. Formation of polycyclic aromatic hydrocarbons and their growth to soot—A review of chemical reaction pathways. *Prog. Energy Combust. Sci.* **2000**, *26* (4−6), 565−608.

(41) McEnally, C. S.; Ciuparu, D. M.; Pfefferle, L. D. Experimental study of fuel decomposition and hydrocarbon growth processes for practical fuel components: heptanes. *Combust. Flame* **2003**, *134* (4), 339−353.

(42) Naegeli, D. W.; Moses, C. A. Effects of fuel molecular structure on soot formation in gas turbine engines. In *Proceedings of the ASME Gas Turbine Conference*, March 10-13, New Orleans, LA, 1980; ASME: New York, 1980; Paper 80-GT-62.

(43) Cheng, M.-D.; Corporan, E.; DeWitt, M. J.; Spicer, C. W.; Holdren, M. W.; Cowen, K. A.; Laskin, A.; Harris, D. B.; Shores, R. C.; Kagann, R.; Hashmonay, R. Probing emissions of military cargo aircraft: Description of a joint field measurement strategic environmental research and development program. *J. Air Waste Manage. Assoc.* **2008**, *58* (6), 787−796.

(44) Corporan, E.; DeWitt, M. J.; Klingshirn, C. D.; Mahurin, S. M.; Cheng, M.-D. Emissions Characteristics of a Legacy Military Aircraft. In *Proceedings of the ASME Turbo Expo 2009: Power for Land, Sea and Air*, Orlando, FL, 2009; ASME: New York, 2009; GT2009-59255.

(45) Lobo, P.; Hagen, D. E.; Whitefield, P. D.; Alofs, D. J. Physical characterization of aerosol emissions from a commercial gas turbine engine. *J. Propul. Power* **2007**, *23* (5), 919−929.

(46) Onasch, T. B.; Jayne, J. T.; Herndon, S.; Worsnop, D. R.; Miake-Lye, R. C.; Mortimer, I. P.; Anderson, B. E. Chemical properties of aircraft engine particulate exhaust emissions. *J. Propul. Power* **2009**, *25* (5), 1121−1137.

(47) Vander Wal, R. L.; Tomasek, A. J. Soot oxidation: dependence upon initial nanostructure. *Combust. Flame* **2003**, *134* (1−2), 1−9.

189

Appendix L. Chemical Analysis of Jet Fuel Polar, Heteroatomic Species via High-Performance Liquid Chromatography with Electrospray Ionization Mass Spectrometric Detection

Chemical Analysis of Jet Fuel Polar, Heteroatomic Species via High-Performance Liquid Chromatography with Electrospray Ionization–Mass Spectrometric Detection

Ryan K. Adams,*,[†] Steven Zabarnick,[†,‡] Zachary J. West,[†] Richard C. Striebich,[†] and David W. Johnson[§]

[†]University of Dayton Research Institute, [‡]Department of Mechanical and Aerospace Engineering, and [§]Department of Chemistry, University of Dayton, 300 College Park, Dayton, Ohio 45469-0043, United States

ABSTRACT: High-performance liquid chromatography (HPLC) with electrospray ionization–mass spectrometry (ESI–MS) was used to identify several classes of heteroatomic, polar compounds containing oxygen, nitrogen, and sulfur in a variety of jet fuel samples. While nitrogen, oxygen, and sulfur compounds are present only at low concentrations in jet fuel, they contribute significantly to some important fuel properties. These trace, heteroatomic species can provide positive (e.g., improved lubricity) or negative (e.g., reduced thermal stability) impacts. Reversed-phase liquid chromatography with ESI–MS detection allows for the polar components to be selectively ionized and subsequently identified, despite the complex hydrocarbon fuel matrix. Phenols and carbazoles are detected in negative-ion $[M − H]^-$ mode, while anilines, pyridines, indoles, and quinolines are observed in positive-ion $[M + H]^+$ mode. Accurate mass measurements allow for the molecular formula of the polar components to be determined, while different structural classes of isomeric compounds could be determined via HPLC separation and the formation of derivatives. Derivatization shifts the retention time, species masses, and potentially, the ion charge formed of specific compound classes, allowing them to be positively identified. The usefulness and limits of HPLC with ESI–MS for quantitation of these fuel polar, heteroatomic species are also explored.

■ INTRODUCTION

Aviation jet fuel is a produced via petroleum distillation to yield a kerosene cut primarily consisting of aliphatic and aromatic hydrocarbon species. While these bulk species give fuel many desired combustion properties, such as a high heat of combustion, other trace, heteroatomic species are also present, which can provide positive (e.g., improved lubricity) or negative (e.g., reduced thermal stability) impacts. A number of chemical analysis techniques have been applied to the bulk and trace analyses of jet fuels with separation techniques, such as gas chromatography (GC) with various detection methods[1] and, most recently, two-dimensional GC × GC.[2,3] Pre-separation techniques (e.g., solid-phase extraction) have proven very useful in simplifying the complex fuel matrix for analysis of trace species.[4] Because GC is limited to compounds with relatively high volatility, liquid chromatographic methods have also been employed for analysis of lower volatility fuel species, such as additives and metal species.[5,6] However, many detection methods used in liquid chromatography [e.g., ultraviolet–visible (UV–vis) absorption, refractive index, and electro-chemical] do not readily provide positive identification of unknown compounds and are limited to species that have unique properties particular to that detector. Mass spectro-metric (MS) detection of liquid chromatographic separations provides the promise of a more universal detection method, which can also provide identification of species via exact mass information. The ionization methods currently available for liquid chromatographic detection [e.g., electrospray ionization (ESI) and atmospheric pressure chemical ionization (APCI)] are limited to species that are readily ionizable, and the ionization efficiencies are very sensitive to the conditions employed (e.g., ionization technique and mobile phase). High-performance liquid chromatography (HPLC) with ESI–MS detection appears to hold particular promise for the detection of trace, heteroatomic species in complex hydrocarbon fuel mixtures because these species are more readily ionizable than the bulk hydrocarbon compounds.

In recent years, ESI–MS has been employed for the analysis of many complex hydrocarbon mixtures, including petroleum, diesel fuel, vegetable oil, and jet fuel.[7−12] In limited studies of jet fuel analysis, ESI–MS has been used to identify homologous series of various trace species, including phenols, pyridines, anilines, quinolines, carbazoles, and polar oxidation prod-ucts.[13,14] In this paper, we employ HPLC with ESI–MS detection to explore the qualitative chemical analysis of trace, heteroatomic species in a series of jet fuels. Both positive- and negative-ionization modes are used for the identification of naturally occurring polar, heteroatomic species, fuel additives, and fuel oxidation products. The usefulness and limits of HPLC with ESI–MS for quantitation of these species are also briefly explored.

■ EXPERIMENTAL SECTION

Analyses were conducted using an Agilent 1200 series HPLC equipped with a diode array detector in series with an Agilent 6210 Time-of-flight mass spectrometer (TOF-MS). A reverse-phase column (Agilent C8, 2.1 mm inner diameter, 5 μm particle size, and 100 Å pore size) was used for both negative- and positive-ion modes. The column was temperature-controlled to 30 °C to create a consistent slightly above ambient temperature condition. Electrospray source conditions included a nitrogen drying gas flow rate of 11 L/min at 350 °C, a

nebulizing pressure of 50 psi, a capillary voltage of 3500 V, a fragmentor voltage at 220 V, and an octupole radio frequency (RF) voltage at 60 V. These conditions were used for both negative- and positive-ion mode analyses. The diode array detector extracted a UV absorption response at 254 nm, which was used to verify the repeatability of samples through the column as well as confirm retention times of standards.

Methanol and water were used as mobile-phase solvents, obtained from Fisher Scientific, and of Optima liquid chromatography−mass spectrometry (LC−MS) grade. An acetic acid modifier (Sigma-Aldrich, eluent additive for LC−MS) was added to both mobile phases at 0.1 vol % during the corrosion inhibitor/lubricity improver (CI/LI) additive analysis. Samples analyzed via positive-ion mode were eluted by a gradient of methanol and water, while negative-ion mode analyses were carried out isocractically. All isocratic elutions were performed with 100 vol % methanol for 10 min at 0.3 mL/min. The gradient conditions for positive-ion mode were an isocratic hold at 60:40 (vol %) methanol/water for 4 min and then a ramp to 100 vol % methanol over 5 min, with a final isocractic hold of 11 min. The total analysis time was 20 min at a total flow rate of 0.3 mL/min.

A total of 16 samples of petroleum jet fuels, including Jet A, JP-5, and JP-8 fuels, were obtained from the Air Force Research Laboratory (AFRL) Fuels Branch. Fuel samples were diluted by a factor of 20 in methanol prior to injection. Pure compounds used as standards were typically diluted to approximately 1 parts per million (ppm). These dilutions were necessary because concentrated samples resulted in severe peak tailing, as a result of overloading of the electrospray source and/or MS detector, and decreased mass accuracy for empirical formula generation. The sample volume injected was typically 5 μL, although this was varied if the response was determined to be too high or low. The accuracy of the exact mass measurements of the TOF−MS system was found to be within ±15 ppm by comparison to known standards obtained from Sigma-Aldrich.

For some analyses, liquid−liquid extractions were also performed on the fuels prior to chromatographic injection. This extraction was performed to concentrate the fuel polar species and remove any bulk matrix effects that the fuel may have on the ionization of the desired species. A 10 mL vial was used for the extractions, with 5 mL of fuel being added along with 1 mL of methanol, at which point the two phases were well-mixed. It was assumed that the polar fuel compounds were efficiently extracted by the methanol, although this was not verified. After the methanol was extracted, the mixture was further diluted by a factor of 100 before injection.

Some fuel samples were treated with a derivatization agent to selectively react with a target functional group. The objective of this preparation is to assist with the identification of ionizable compounds, which share similar retention times and molecular formulas. For initial experiments with derivatization, primary amines (in jet fuel, these are predominantly anilines) were targeted by reaction with 2-pyridine carboxaldehyde, as shown in the reaction below.
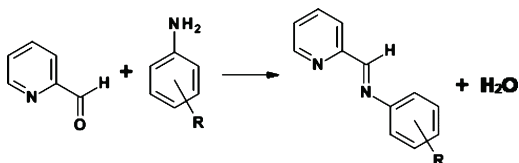
The reaction was carried out by taking 100 μL of jet fuel and adding 10 μL of 2-pyridine carboxaldehyde and 100 μL of toluene to a 2 mL vial. The vial was heated to 75 °C for 1 h. After cooling, 800 μL of methanol was added to further dilute the sample. A series of standards were prepared by treating 1% solutions of standard amines by similar means and then analyzing the solutions by GC−MS. The GC−MS analysis indicated that only the derivatization product and excess pyridine-2-carboxaldehyde were present after the reaction.

RESULTS AND DISCUSSION

HPLC with ESI−MS detection was employed for analysis of polar, heteroatomic species in a variety of jet fuel samples. The goals of this effort were to (a) determine the usefulness of the technique for analysis of these species in jet fuel, (b) determine optimum analysis parameters for detection of these species, and (c) determine the types of heteroatomic, polar species that are commonly found in jet fuel. Initial chromatographic studies were conducted on a JP-8 fuel sample (AFRL accession number F-4177), which has been employed in other published studies.[15]

Negative-Ion Mode Studies. Negative-ion mode with a relatively short 50 mm C8 column was used, and the resulting chromatogram for this fuel is shown in Figure 1. The figure
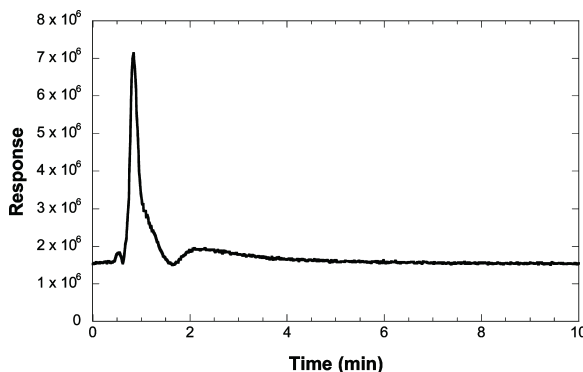

Figure 1. TIC for JP-8 fuel F-4177 in negative-ion mode.

shows a large peak near 1 min retention time with a smaller peak near 2 min retention time. Using an estimated void fraction of 0.66 for the column yields a non-retained time of 0.49 min for this column, demonstrating partial retention of ionizable species with only limited chromatographic separation. While only fuel F-4177 is shown in Figure 1, it was found that all 16 jet fuel samples evaluated here exhibited similar negative-ion chromatograms on this column. The discussion here will center on the 1 min retention time peak, because the second smaller peak at 2 min is the result of increased background response that occurs upon injection of fuel samples.

The presence of a single peak attributed to fuel components indicates that very little chromatographic separation is occurring here, but detailed analysis of the mass spectral information shows evidence of separation. Figure 2 shows extracted mass spectra at retention times of 0.71 and 0.82 min within the single peak of Figure 1. The differences in the mass spectra show that chromatographic separation is occurring within this single peak. It is important to note that ESI is a soft ionization technique that results in no observable ion fragmentation. Also, because fuels are petroleum distillate fractions, homologous series of compounds are expected and their presence is readily observed by a mass series that differs by mass-to-charge ratio (m/z) of 14 (CH_2 mass). The top mass spectrum in Figure 2 shows a m/z series (135, 149, 163, 177, 191, and 205), which are identified as being due to deprotonation of a homologous series of alkyl-substituted phenols. The identification of this series was determined by a comparison of the measured exact m/z to calculated m/z (these agree to ±4 ppm) and mass spectra and retention time agreement with injected phenol standards. The identification of
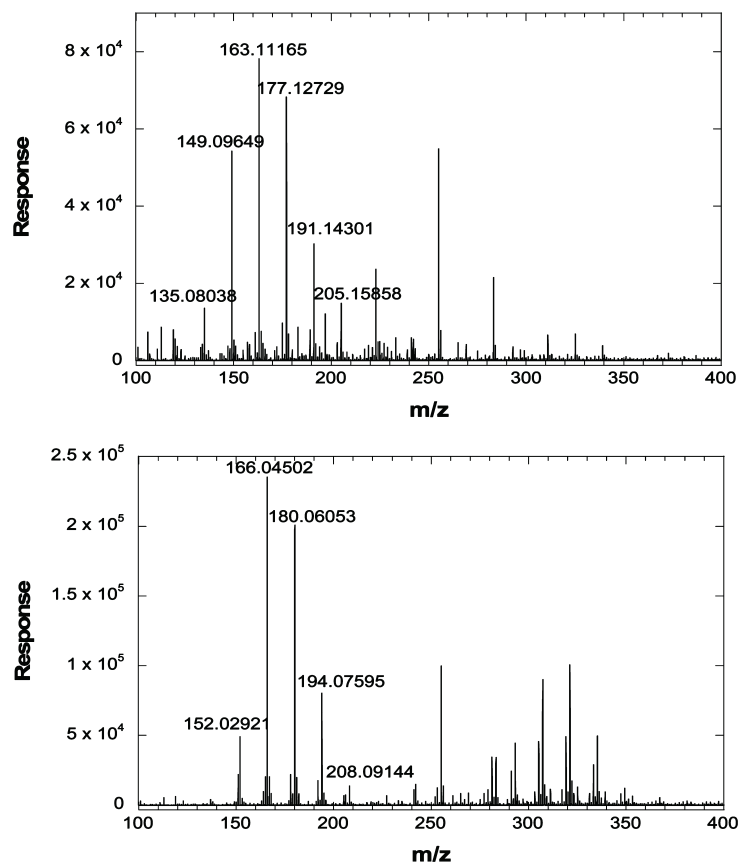
Figure 2. Extracted mass spectra (negative-ion mode) for the chromatogram shown in Figure 1. The top spectrum is at a retention time of 0.71 min, and the bottom spectrum is at a retention time of 0.82 min.

phenols in negative-ion mode ESI−MS in methanol solvent is also supported by the previous work by Rostad.[13] In addition, previous work via other methods has shown that phenols are commonly found in jet fuel at concentrations up to ~1000 ppm.[16]

The phenols observed in these fuels by ESI−MS correspond to substitution on the aromatic ring with 2−10 carbons (CH_3 and CH_2 groups), but the mass spectral data do not reveal the structural identity of the isomers present. GC has previously been used for jet fuels to identify substituted phenols with up to 6 carbons,[4] but detection of larger phenols is likely limited by volatility and concentration. Thus, the current LC method shows an improved ability to detect larger phenols in jet fuel. Of the 16 jet fuel samples evaluated, only 1 showed no evidence of the presence of phenols. This fuel contained high concentrations of jet fuel additives (JP-8 + 100), which may interfere with efficient ion formation in the ESI source. In addition to the phenols, a few unmarked ions are present at 0.71 min (m/z 223, 255, and 283) but should be ignored because they are present in the solvent. The exact masses of these most likely indicate acid functionality.

The bottom of Figure 2 shows the extracted mass spectrum for the 0.82 min retention time of Figure 1. The figure shows a homologous series (m/z 152, 166, 180, 194, and 208), which exhibit greater response than the phenols (note the change in the y axis scale). This relative response cannot be readily related to a corresponding concentration difference because the ESI−

MS response can vary greatly over species classes. This homologous series remains unidentified after significant effort. Exact m/z searches of the observed m/z ratios correspond to unlikely molecular formulas for fuel components, e.g., $C_6H_7N_3S$ for m/z 152. Samples of species classes, such as carbazoles and nitrophenols, which may occur in fuels and have the correct unit masses, were obtained and injected into the system but did not exhibit the correct exact m/z ratios or retention times. It is not clear at what mass this homologous series begins, but for many of the fuels examined, a peak is also obtained at m/z 138, potentially indicating a molecular mass of 139 atomic mass units (amu). This homologous series was observed in 13 of the 16 fuel samples studied, and thus, this unknown homologous series is commonly but not universally found in petroleum-derived fuels. A number of fuel samples also exhibited homologous series of larger molecular weight compounds between m/z 250 and 400, shown in Figure 2 at 0.82 min. These series are outside the typical boiling range of jet fuel, potentially indicating that they may have formed as the fuel aged and are oxygenated compounds. Identification of these series has proven difficult, because the empirical formulas generated by the software yield numerous complex molecules that would not have survived the refining process. Future work with standards and other fuels is warranted to better determine what types of fuels contain these compounds as well as their identity. Table 1 shows a summary of the 16 fuels and the homologous series observed in negative-ion mode.

Table 1. Summary of Homologous Species Classes in Jet Fuel via Negative-Ion Mode

functional group(s) matching exact masses	phenols	unknown	unknown (heavier series)
primary ions present	149, 163, 177, and 191	152, 166, 180, and 194	290−350
potential empricial formula	$C_nH_{(2n-6)}O$	$C_nH_{(2n-5)}N_3S$	

| fuel	type			
2747	Jet A	×	×	×
2959	Jet A	×	×	×
2985	JP-5	×		×
3656	Jet A	×	×	×
3658	Jet A	×		×
3684	JP-8	×	×	×
3773	JP-8	×	×	
3804	JP-8	×	×	
4177	JP-8	×	×	×
4336	JP-8	×	×	×
4339	JP-8	×	×	
4351	JP-8	×	×	×
4718	JP-8	×	×	×
4751	JP-8	×	×	
5098	JP-8			
5699	JP-8	×	×	

Positive-Ion Mode Studies. In negative-ion mode, the phenol series and the unidentified series are the major species observed. An example total ion chromatogram (TIC) for the injection of JP-8 fuel F-4177 in positive-ion mode overlaid with a methanol blank is shown in Figure 3. Unlike in negative-ion
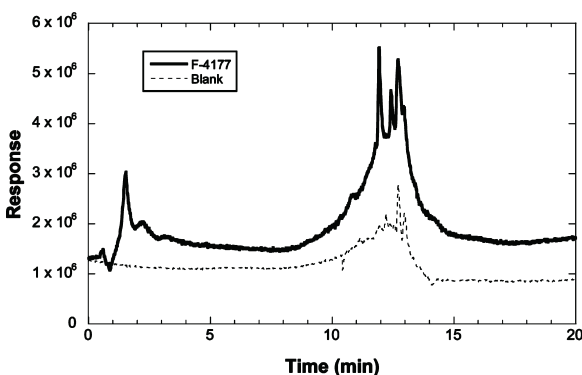
Figure 3. TIC for JP-8 fuel F-4177 in positive-ion mode overlaid with a blank methanol injection as a dotted line.

mode, there is more than a single chromatographic peak present. While there is a relatively small non-retained peak present when the mobile phase is initially at 60:40 (vol %) methanol/water, a larger group of peaks forms from 9 to 15 min as the gradient shifts to 100 vol % methanol. Comparing F-4177 to a blank methanol injection shows that this group of peaks is partially due to the gradient and various contaminants in the mobile phase, while the initial peak at ~2 min is unique to the fuel. Employing a gradient has allowed for some chromatographic separation to occur, although this separation

is still limited because of the similar polarities of the ionizable compounds present in the fuel.

As with the negative-ion case, extracted mass spectra taken at various retention times through the total ion response of the positive-ion mode chromatograms show a number of species classes that are partially separated. Because the ionizable compounds elute over longer periods of time, an average mass spectrum was taken from 5 to 11 min, to better illustrate the multiple series present, as shown in Figure 4. The figure shows
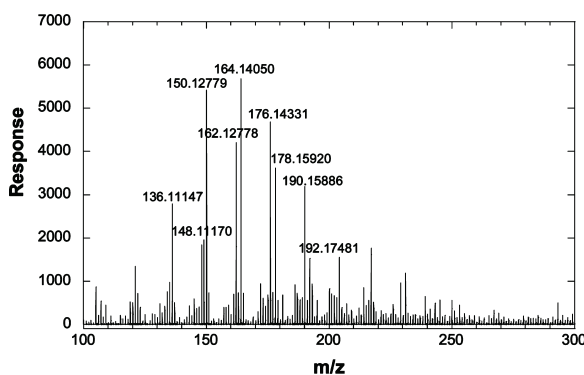
Figure 4. Extracted mass spectra for the chromatogram shown in Figure 3 averaged over 5−11 min.

a number of homologous series, which are tentatively identified as protonated species containing single nitrogen atoms, because the highest abundance homologous series have even m/z ratios. The homologous series consisting of m/z ratios of 136, 150, 164, 178, and 192 are likely anilines and/or pyridines. Although aniline compounds are more commonly found in jet fuels than pyridines,[3] injection of both species classes showed that pyridine compounds exhibit greater response in the ESI−MS detector. This agrees with the higher gas-phase proton affinity of pyridines,[17] which has been shown to correlate with increased response in positive-ion mode ionization.[10] Both anilines and pyridines have the same molecular formulas, and thus, the exact mass measurement cannot be used to differentiate the structural isomers.

The homologous series with m/z 120, 134, 148, 162, 176, 190, and 204 match the exact masses of both indoline and tetrahydroquinoline species classes. These homologous series exhibit similar response to the aniline/pyridine series. Injection of an example of indoline and tetrahydroquinoline compounds indicated that both of these compound classes readily ionize in the ESI source and produce the measured exact m/z ratios.

It is also apparent from Figure 4 that a low but measurable response is obtained in positive-ion mode for a number of odd m/z ratio compounds. At this time, the identity of these species is unclear. The exact m/z ratios yield empirical formulas for protonated single oxygen compounds and/or compounds with both a single oxygen and sulfur atom, although no known fuel species were identified. The odd m/z compounds appear to elute somewhat earlier (1−5 min) than the even m/z compounds, indicating that these unknown compounds are more polar than the nitrogen species. Preliminary work with the analysis of fuel samples after thermal oxidative exposure shows that the even m/z nitrogen compounds decrease in concentration, while the odd m/z compounds increase in concentration. This observation supports the conclusion that

Table 2. Summary of Homologous Species Classes in Jet Fuel via Positive-Ion Mode[a]

|	even molecular ion compounds					odd molecular ion compounds		
functional group(s) matching exact masses	quinolines/ amino-naphthalenes	indolines/ THQ	anilines/ pyridines	pyrroles/ saturated indoles	DHQ	unknown	benzofurans/ benzopyrans	unknown
primary ions present	144, 158, 172, and 186	148, 162, 176, and 190	150, 164, 178, and 192	166, 180, 194, and 208	152, 168, 182, and 196	173, 187, 201, and 215	175, 189, 203, and 217	169, 183, 197, and 211
potential molecular formula	$C_nH_{(2n-11)}N$	$C_nH_{(2n-7)}N$	$C_nH_{(2n-5)}N$	$C_nH_{(2n-3)}N$	$C_nH_{(2n-1)}N$	$C_nH_{(2n-12)}O$/ $C_nH_{(2n-2)}OS$	$C_nH_{(2n-10)}O$/ $C_nH_{(2n)}OS$	$C_nH_{(2n-16)}O$/ $C_nH_{(2n-6)}OS$
fuel — type								
2747 — Jet A	×	×	×			×	×	×
2959 — Jet A						×	×	×
2985 — JP-5	×	×	×	×	×	×	×	×
3656 — Jet A	×	×	×	×		×	×	×
3658 — Jet A	×	×	×	×	×			
3684 — JP-8	×	×	×	×	×	×	×	×
3773 — JP-8	×	×	×			×	×	×
3804 — JP-8	×	×	×	×		×	×	×
4177 — JP-8	×	×	×			×		
4336 — JP-8	×	×	×	×	×	×		×
4339 — JP-8	×	×	×	×		×	×	
4351 — JP-8	×	×	×	×	×	×	×	
4718 — JP-8	×	×	×			×	×	×
4751 — JP-8	×	×	×	×		×	×	
5098 — JP-8	×	×	×	×		×	×	
5699 — JP-8	×	×	×	×				

[a]THQ, tetrahydroquinolines; DHQ, decahydroquinolines.
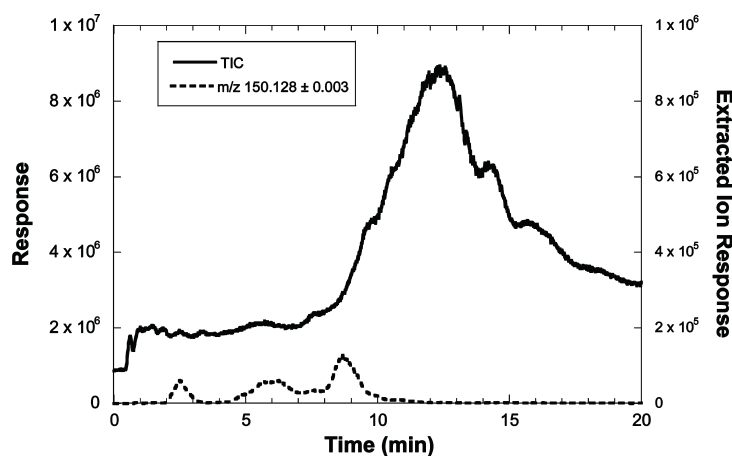
Figure 5. TIC and EIC of underivatized Jet A fuel F-3658 in positive-ionization mode.

these odd m/z peaks are due to oxygen-containing compounds. Previous work in the identification of odd masses from positive-ion ESI of heavy crude oil indicated that most of the odd mass ions were due to ^{13}C isotopic species of the even mass ions rather than from zero or even number of nitrogen species or oxygen species.[11] The large response observed here for the odd masses relative to the even masses (up to 30%) shows that contribution of the ^{13}C isotopes is negligible. Further work in the identification of these odd m/z responses is warranted.

Table 2 lists the homologous series observed in positive-ion mode for the 16 jet fuels studied in this work. Three even m/z series were observed in addition to the two series reported above. These include a m/z 144, 158, 172, and 186 series, which correspond to quinolines and/or amino-naphthalenes; a m/z 166, 180, 194, and 208 series, which correspond to pyrroles and/or indoles; and a m/z 154, 168, 182, and 196 series, which correspond to a homologous series of decahydroquinolines. The peak shape of the decahydroquinoline series is too broad to be observed with a gradient but was identified using an isocratic mobile phase of 100% methanol, because the narrower chromatographic peak gives improved signal response. Also listed in the table are three homologous series of odd m/z ions observed in positive-ion mode. As mentioned previously, these appear to be oxygen-containing species that have not been identified, although a number of
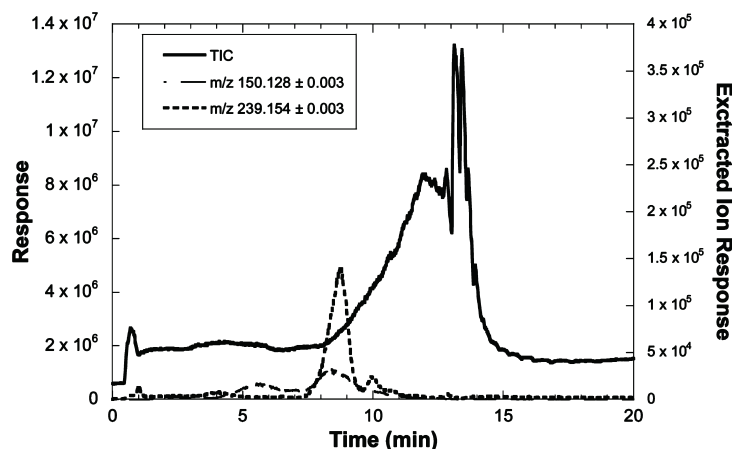
Figure 6. TIC and EIC of Jet-A F-3658 after the reaction with 2-pyridine carboxaldehyde. The extracted ion chromatograms show the exact mass of a C_4-substituted aniline before (- - -) and after (· · ·) derivatization.

heterocyclic oxygen species are potential candidates, e.g., furanones and benzopyrans.

Analysis of Derivatized Fuel Samples by 2-Pyridine Carboxaldehyde. With the larger number of ionizable compounds detected in positive-ionization mode and many that share retention times and molecular formulas, derivatization methods were employed to better identify heteroatom species. Various fuels were analyzed after derivatization to compare the extent of reaction, shift in retention times, and exact masses of the reactants and products. While previous work has been focused on F-4177, which is representative of many JP-8 fuels, it is easier to carry out the discussion with fuel known to contain a high heteroatomic concentration. Jet A fuel F-3658 has been studied previously[16] and contains a high concentration of nitrogen-containing compounds, which will better enable determination of the extent of derivatization and show the ability of derivatization to allow for peak deconvolution. Figure 5 shows the TIC of the underivatized fuel F-3658 with the extracted ion chromatogram (EIC) of [M + H]+: $C_{10}H_{16}N$ at m/z 150. This is the exact mass of a protonated C_5-substituted pyridine or C_4-substituted aniline.

The TIC is similar to F-4177 because it has a large peak with the apex between 10 and 15 min; however, a smaller initial peak is not present. This could be due to the lack of odd m/z compounds (from Table 2), which tend to be more polar and elute earlier. F-3658 also exhibits a higher total response relative to F-4177, most likely indicating a higher concentration of ionizable heteroatoms. The extracted ion chromatogram of m/z 150 shows three peaks between 0 and 10 min. Each peak could represent various isomers of C_5-substituted pyridines, C_4-substituted anilines, or another class of compounds that have a very similar exact mass. Standards that we have analyzed show that anilines typically elute earlier than pyridines, but it is still unclear which peak is representative of each functional group. The derivatization method described previously was employed to verify the identity of the peak representing an aniline. Figure 6 overlays the TIC and EIC of m/z 150.128 and 239.154. The latter is the exact mass of a C_4-substituted aniline derivatized with 2-pyridine carboxaldehyde. The EIC of m/z 239.154 in the neat fuel did not produce any significant peaks of note (not shown).

The TIC has not significantly changed after the reaction, with only two additional narrow peaks eluting slightly after the apex of the large broad peaks. Currently, it has not been determined what these larger peaks represent or what leads to their formation. Overall, the minimal change to the TIC indicates that the bulk of the heteroatomic species has been unaffected by the derivatization, which is the desired result. The EIC of m/z 150 exhibits two broad peaks between 5 and 10 min, while the EIC of m/z 239 shows a larger peak at approximately 9 min and a smaller peak at 10 min. The most significant difference between the neat fuel and the derivatized fuel, with regards to EIC of m/z 150, is the removal of the first peak at approximately 2.5 min. Because the derivatizing agent can only react with primary amines or, in this case, anilines, it is reasonable to assume that the first peak is due to the elution of C_4-substituted anilines. The large peak of m/z 239 is therefore due to the formation of the derivatized product. For this derivatized compound, the retention time is increased from 2.5 to 9 min. This is to be expected from the formation of a larger and less polar hydrocarbon. The analysis has shown similar results to other masses in the aniline/pyridine series of m/z 136, 150, 164, 178, etc. with regards to removal of the first peak in the EIC and producing an additional peak matching the exact mass of the derivatized compound. Additional derivatization schemes will be explored in the future as a means to identify unknown heteroatomic species in fuel.

Analysis and Quantification of Known Standards. Additional HPLC−MS studies were performed for various nitrogen and oxygen species that are relevant to jet fuel analysis. The goal of these studies is to show the response of these species in positive-/negative-ion mode electrospray, to compare the response of the species, and to determine the ability of ESI−MS to quantify these species in fuel. Initially, a range of heteroatomic species were dissolved in methanol at 1−10 ppm and injected into the system while monitoring the response in both negative- and positive-ion mode. The results are summarized in Table 3. The table shows that phenols, carbazoles, and nitrophenols are the only species classes studied, which showed response in negative-ion mode. The phenol observation agrees with our jet fuel results shown above and with the previous work by Rostad.[13] Interestingly, Qian et al.[11] reported a low response for carbazoles in positive-ion

Table 3. Ionization of Polar, Heteroatomic Species via ESI–MS

		ionization mode	
species class	species evaluated	postive (+)	negative (−)
phenols	ethyl, dimethyl, trimethyl, and di-*t*-butyl phenols		×
carbazoles	carbazole		×
nitrophenols	*m*-nitrophenol		×
anilines	methyl and ethyl anilines	×	
indoles	2-methyl and 6-methyl indole	×	
indolines	indoline and 3-methyl indoline	×	
pyridines	2,4,6-trimethyl and 4-ethyl pyridine	×	
quinolines	quinoline, 3-methyl and iso	×	
THQ	tetrahydroquinoline	×	
DHQ	decahydroquinoline	×	
naphthylamines	1-naphthylamine	×	

mode electrospray, while we do not observe a carbazole response in positive-ion mode but do see a response for these species in negative-ion mode. The bulk of the nitrogen species are successfully ionized in positive-ion mode, including both "basic nitrogen species", such as pyridines and quinolines, and "neutral nitrogen species", such as anilines, indoles, indolines, tetrahydroquinolines, decahydroquinolines, and naphthylamines. Other studies indicate that positive-ion mode electrospray response of petroleum is dominated by basic nitrogen species.[12] These differences may be due to the effect of various experimental parameters, such as the mobile phase, presence of modifiers, concentration, presence of other analytes in the spray, spray parameters, etc., on ionization efficiency. Because jet fuel may contain both neutral and basic nitrogen species, the response reported here is desirable but creates challenges in identifying the species classes that exhibit identical exact m/z ratios.

Figure 7 demonstrates the ESI–MS response versus concentration for a series of four alkylphenols. The plot
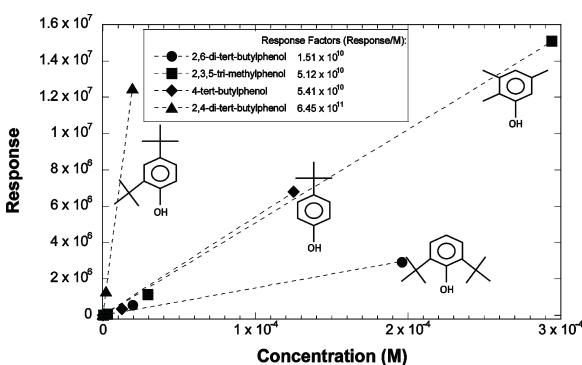
Figure 7. Plots of negative-ion ESI–MS response versus concentration for a series of alkylphenols.

shows that 2,4-di-*t*-butylphenol has the greatest response, with a factor of ~40 greater response than 2,6-di-*t*-butylphenol. The other two phenols (2,3,5-trimethylphenol and 4-*t*-butylphenol) have responses between those two. The data demonstrate that small changes in alkyl substitution have a large effect on the ESI response. Each of the four phenols displayed linear responses over 3–4 orders of magnitude in concentration. The high

responding species 2,4-di-*t*-butylphenol exhibited nonlinearity (not shown) at concentrations above 2×10^{-5} M, possibly indicating that nonlinearity is more a function of signal response than concentration. The varying response may be due to a number of factors, including chemical effects of the structure on ionizability in the liquid and gas phases and the effect of the phenol structure on physical properties, which influence the ability of species to form bare ions from the spray droplets. The data of Figure 7 show the challenge in using ESI–MS for quantification, especially for jet fuels, which contain hundreds or thousands of different species, often including dozens of differently alkyl-substituted species of a given class, e.g., alkyl-substituted phenols.

Analysis of Corrosion Inhibitor/Lubricity Improver Additive Dilinoleic Acid. A corrosion inhibitor additive, which also gives fuel improved lubricity, is added to JP-5 and JP-8 fuels at concentrations of 9–22.5 mg/L. The most common formulation of this additive includes an active ingredient, which is a dimer of linoleic acid, with a molecular weight of ~562 amu. This additive is not amenable to analysis via GC because of its low volatility. Here, we explore the use of HPLC–MS for qualitative and quantitative analyses of the additive. Figure 8 shows the TIC obtained for JP-8 fuel after a liquid–liquid extraction with an additive concentration of 10.2 mg/L. A concentration of 0.1 vol % acetic acid is added to the methanol mobile phase, which results in an improved response for the additive. The initial peak near 0.7 min is due to fuel heteroatomic species, such as phenols and the unidentified homologous series starting at m/z 138, and the peak and shoulder at 0.8 and 1.2 min, respectively, are primarily due to the CI/LI additive. A mass spectrum at a retention time of 1.2 min is also shown in Figure 8, demonstrating a grouping of masses near m/z 561, which we attribute to linoleic acid dimers with various levels of saturation. The signals at m/z 255 and 283 occur as background ions that typically show a slightly increased response when fuel is injected.

Also shown in the figure is an EIC of the m/z 561 ion, showing a peak at 1.2 min. This extracted ion signal at m/z 561 was used for quantitation of the CI/LI additive in jet fuel. An example of using the standard addition method for quantitation is shown in Figure 9. Aliquots (3, 5, and 10 μL) of a 930 mg/L CI/LI standard mixture were added to 1 mL of methanol extracted from a jet fuel using the LLE method. The plot demonstrates quantitation of 0.85 mg/L of additive after accounting for dilution factors via successive addition of additive with excellent response linearity. Standard addition is a good choice for quantitation in jet fuels because of the strong effect of the solution matrix on ionizability using ESI–MS. We estimate a detection limit for the CI/LI additive of ~0.1 mg/L using this method.

■ CONCLUSION

These initial studies have shown a number of potential as well as limited applications for using LC–MS in jet fuel analyses. The functionality of the ESI source in eliminating response of the bulk hydrocarbon matrix is a great asset for targeting trace, heteroatomic species. We have identified many common species present in fuel samples to sub-ppm levels, which is below the typical detection limit of GC–MS analyses. Currently, this analysis is limited to a qualitative analysis. Quantitation in a fuel matrix has proven to be difficult beyond single standards because the ESI response can vary by orders of magnitude for compounds from the same functional group.
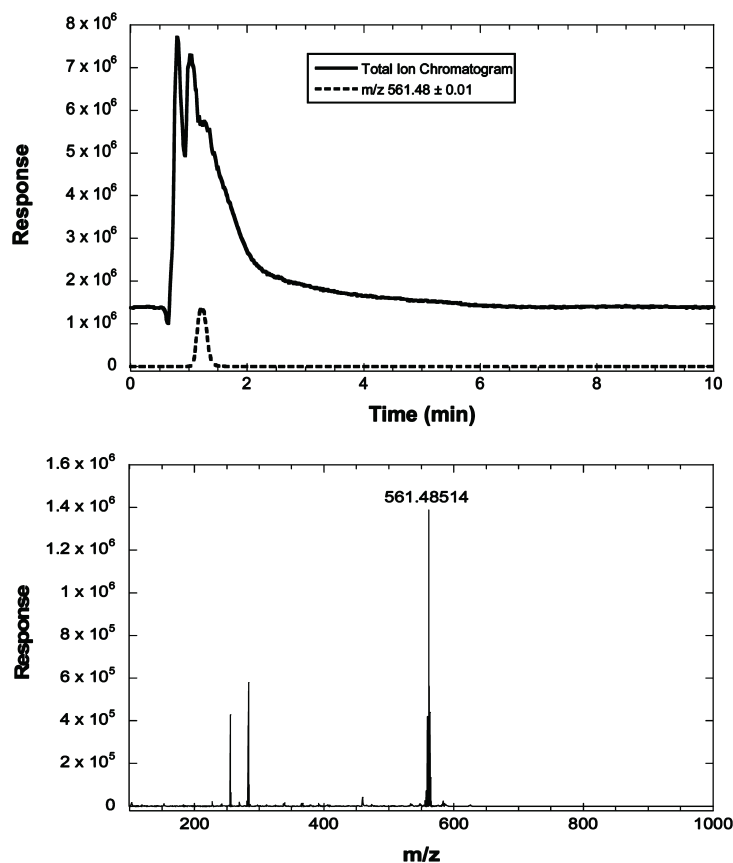
Figure 8. Analysis of dilinoleic acid corrosion inhibitor at 10.2 mg/L in JP-8 fuel after liquid−liquid extraction. The top plot is the TIC (the EIC of 561 amu is shown as the dashed line), and the bottom plot is the mass spectrum at a retention time of 1.2 min.
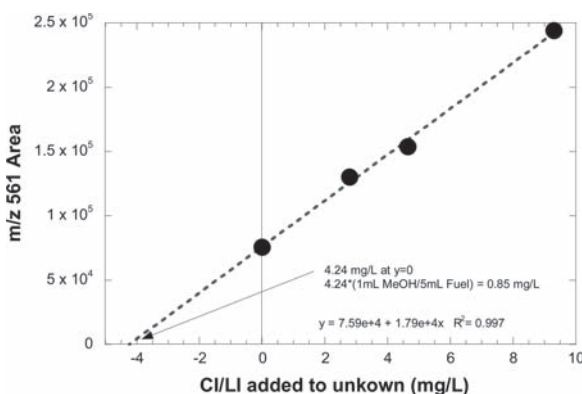
Figure 9. Standard addition method plot for quantitation of the CI/LI additive in jet fuel.

This instrument does show potential for quantitation of the CI/LI additive in JP-8 by means of a standard addition method.

Additional work is being performed to improve the HPLC separation of fuel samples. Separation by species classes would greatly assist with identification and quantification of these heteroatomic species. Derivatization will also be further assessed, because we have shown it to be effective at targeting and altering specific functional groups. Improved species identification could be obtained by coupling a tandem MS to produce ion fragmentation information. HPLC with ESI−MS detection has shown promise for identification of trace, polar species common to jet fuel, which is crucial for studies of fuel thermal oxidation. While limited HPLC−MS work has been performed here and elsewhere, further effort is warranted to improve identification of various ions and to evaluate a larger variety of fuel samples.

■ AUTHOR INFORMATION

Corresponding Author

*E-mail: Ryan.Adams@udri.udayton.edu.

Notes

The authors declare no competing financial interest.

■ REFERENCES

(1) Striebich, R. C.; Motsinger, M. A.; Rauch, M. E.; Zabarnick, S.; Dewitt, M. *Energy Fuels* **2005**, *19*, 2445−2454.

(2) van der Westhuizen, R.; Ajam, M.; De Coning, P.; Beens, J.; de Villiers, A.; Sandra, P. *J. Chromatogr., A* **2011**, *1218*, 4478−4486.

(3) Striebich, R. C.; Contreras, J.; Balster, L. M.; West, Z.; Shafer, L. M.; Zabarnick, S. *Energy Fuels* **2009**, *23*, 5474−5482.

(4) Zabarnick, S.; Striebich, R.; Straley, K.; Balster, L. *Prepr.—Am. Chem. Soc., Div. Pet. Chem.* **2002**, *47*, 223−225.

(5) Hughey, C. A.; Rodgers, R. P.; Marshall, A. G.; Qian, K.; Robbins, W. K. *Org. Geochem.* **2002**, *33*, 743−759.

(6) Taylor, D.; Synovec, R. *J. Chromatogr.* **1994**, *659*, 133−141.

(7) Nakanishi, A.; Ishii, D.; Takeuchi, T. *J. Chromatogr.* **1984**, *291*, 398−403.

(8) Wu, Z.; Rodgers, R. P.; Marshall, A. G. *J. Agric. Food Chem.* **2004**, *52*, 5322−5328.

(9) Gatlin, C.; Turecek, F.; Valsar, T. *Anal. Chem.* **1994**, *66*, 3950−3958.

(10) Cech, N. B.; Enke, C. G. *Mass Spectrom. Rev.* **2001**, *20*, 362−387.

(11) Qian, K.; Rodgers, R. P.; Hendrickson, C. L.; Emmett, M. R.; Marshall, A. G. *Energy Fuels* **2001**, *15*, 492−498.

(12) Qian, K.; Edwards, K. E.; Diehl, J. H.; Green, L. A. *Energy Fuels* **2004**, *18*, 1784−1791.

(13) Rostad, C. E. *Energy Fuels* **2005**, *19*, 992−997.

(14) Commodo, M.; Fabris, I.; Groth, C. P. T.; Gulder, O. M. *Energy Fuels* **2011**, *25*, 2142−2150.

(15) Kuprowicz, N.; Zabarnick, S.; West, Z. J.; Ervin, J. S. *Energy Fuels* **2007**, *21*, 530−544.

(16) Balster, L. M.; Zabarnick, S.; Striebich, R. C.; Shafer, L. M.; West, Z. J. *Energy Fuels* **2006**, *20*, 2564−2571.

(17) Taft, R. W. In *Proton-Transfer Reactions*; Caldin, E., Gold, V., Ed.; Chapman and Hall: London, U.K., 1975; pp 39−44.

199

Appendix M. Comparison of Post-Detonation Combustion in Explosives Incorporating Aluminum Nanoparticles, Influence of the Passivation Layer

Comparison of post-detonation combustion in explosives incorporating aluminum nanoparticles: Influence of the passivation layer

W. K. Lewis,[1,a] C. G. Rumchik,[2] M. J. Smith,[3] K. A. S. Fernando,[1] C. A. Crouse,[4,5] J. E. Spowart,[4] E. A. Guliants,[1] and C. E. Bunker[3]

[1]*University of Dayton Research Institute, Dayton, Ohio 45469, USA*
[2]*U.S. Air Force Research Laboratory, Munitions Directorate, Eglin AFB, Florida 32542, USA*
[3]*U.S. Air Force Research Laboratory, Propulsion Directorate, Wright-Patterson AFB, Ohio 45433, USA*
[4]*U.S. Air Force Research Laboratory, Materials & Manufacturing Directorate, Wright-Patterson AFB, Ohio 45433, USA*
[5]*UES, Inc., Dayton, Ohio 45432, USA*

Aluminum nanoparticles and explosive formulations that incorporate them have been a subject of ongoing interest due to the potential of aluminum particles to dramatically increase energy content relative to conventional organic explosives. We have used time-resolved atomic and molecular emission spectroscopy to monitor the combustion of aluminum nanoparticles within the overall chemical dynamics of post-detonation fireballs. We have studied the energy release dynamics of hexahydro-1,3,5-trinitro-1,3,5-triazine (RDX) charges incorporating three types of aluminum nanoparticles: commercial oxide-passivated nanoparticles, oleic acid-capped aluminum nanoparticles (AlOA), and nanoparticles in which the oxide shell of the particle has been functionalized with an acrylic monomer and copolymerized into a fluorinated acrylic matrix (AlFA). The results indicate that the commercial nanoparticles and the AlFA nanoparticles are oxidized at a similar rate, while the AlOA nanoparticles combust more quickly. This is most likely due to the fact that the commercial nano-Al and the AlFA particles are both oxide-passivated, while the AlOA particles are protected by an organic shell that is more easily compromised than an oxide layer. The peak fireball temperatures for RDX charges containing 20 wt. % of commercial nano-Al, AlFA, or AlOA were $\sim$3900 K, $\sim$3400 K, and $\sim$4500 K, respectively. © *2013 American Institute of Physics*. [http://dx.doi.org/10.1063/1.4790159]

I. INTRODUCTION

Aluminum nanoparticles and explosive formulations that incorporate them have been a subject of significant interest in recent years due to the potential of aluminum particles to dramatically increase energy content relative to conventional organic explosives. To date, a large number of aluminized explosive formulations have been studied, as summarized in several reviews.[1,2] In general, it has been found that oxide-passivated aluminum nanoparticles particles react slowly relative to detonation processes and contribute primarily to "late-time effects" such as post-detonation fireball combustion and air blast[1] due to the high melting point[3] (2054 °C) and mechanical strength of the oxide shell that protects the aluminum metal core from oxidation. Since the properties of the passivation layer are thought to exert an important influence on the post-detonation chemistry, it seems reasonable to suspect that changing the nature of this layer might significantly influence the chemical dynamics.

In recent years, synthesis methods have been developed to produce aluminum nanoparticles which are passivated by an organic layer[4,5] rather the traditional oxide shell. Alternatively, synthesis routes to particles in which a pre-existing oxide layer is functionalized with various organic species have also been discovered.[6,7] We have previously synthesized[5] aluminum nanoparticles capped with oleic acid and characterized their reactivity.[8,9] In these particles, the organic shell is lost at temperatures of 200–300 °C, exposing the reactive core. These particles have also exhibited significantly enhanced reactivity with room temperature water,[8] as well as with ammonium nitrate and ammonium perchlorate matrices and their decomposition products after heating.[9]

The purpose of the current investigation is to study the post-detonation combustion dynamics of hexahydro-1,3,5-trinitro-1,3,5-triazine (RDX) charges incorporating three types of aluminum nanoparticles: commercial oxide-passivated nanoparticles, the oleic acid-capped aluminum nanoparticles (AlOA), and nanoparticles in which the pre-existing oxide shell of the aluminum particle has been functionalized[7] with an acrylic monomer and copolymerized in the presence of a fluorinated acrylate to yield an aluminum-fluorinated acrylic composite material (AlFA). The fluorocarbons in this material have been shown to vigorously react with the Al metal to produce AlF_3 and Al_4C_3 once ignited.[7] Reaction with O_2 in the surrounding air to produce Al_2O_3 also occurs (the material is fuel-rich), but the fluorination reaction is kinetically dominant, making this an intriguing candidate to also study in explosive formulations.

The progress of the post-detonation chemistry is tracked using atomic and molecular emission spectroscopy methods.

[a]Author to whom correspondence should be addressed. Electronic mail: wlewis2@udayton.edu.

Temperatures are obtained using a previously developed atomic emission spectroscopy-based technique[10,11] which involves doping the explosive charge with an inorganic impurity. The temperature is then determined by monitoring the relative intensities of atomic emission lines corresponding to emission from different energy levels of a selected atom. Chemical dynamics are tracked via the time-dependent intensities of electronic emissions from species of interest, such as Al atomic lines and AlO vibronic bands. By combining temperature measurements with the time-resolved emission spectroscopy methods used by earlier groundbreaking investigations[12–18] to characterize the complex chemical dynamics occurring after the detonation of an explosive charge, we are able to monitor the combustion of aluminum particles within the overall chemical dynamics of the explosion and correlate this with the energy release process. We have successfully used this approach to study RDX charges incorporating nano- and micron-sized aluminum particles previously.[11]

II. EXPERIMENT

Pressed right-cylindrical charges (25 mm height $\times$ 25 mm diameter) of 20 g total mass were prepared from a mixture of RDX (73 wt. %), a hydroxyl-terminated polybutadiene (HTPB) binder (6 wt. %), and an aluminum powder (20 wt. %) chosen from commercial nano-Al, AlOA, or AlFA. In order to obtain temperature measurements during the post-detonation combustion via atomic emission spectroscopy, 1 wt. % ball-milled barium nitrate was added to the mixture and mixed thoroughly before pressing. Oxide-passivated nanoparticles (30–70 nm particle size) were obtained from Nano Technologies; the AlOA (20–70 nm particle sizes) and AlFA samples were synthesized as reported previously.[5,7] The AlFA material consisted of micron–sized particles containing oxide-passivated aluminum nanoparticles (30–130 nm size) polymerized into a fluorinated acrylic matrix. We note that the commercial nano-Al is $\sim$80 wt. % active Al metal content. The AlOA particles are $\sim$40 wt. % active Al; the AlFA particles are $\sim$50 wt. % active Al. All charges were initiated using Reynolds RP-80 detonators placed on the end of each cylindrical charge.

Light from the explosions was collected from the end of the charge opposite the detonator using a 5 mm diameter collection lens mounted to the end of a 1000 μm core-diameter fiber optic (Ocean Optics). The collection optics were in a shielded observation room located several meters away from the explosive charge. The collection optic were aligned to view the center of each charge through a BK7 glass viewport. The collected light was sent to a time-resolved emission spectrograph constructed from a 1/8 m spectrometer (Oriel) interfaced to a 4096 pixel line-scan camera (Basler Sprint) with a data collection rate of 1–70 kHz. The resolution and usable spectral range of the spectrograph were 1.2 nm and 380–720 nm, respectively. The wavelength and intensity axes of the spectrograph were calibrated with a mercury-argon lamp (Ocean Optics) and a halogen lamp with a known color-temperature (Thorlabs), respectively. We note that due to the low light output of the color-temperature lamp in the

blue region of the spectrum and the short maximum integration time of the detector (1 ms), the spectrum intensity could not be corrected for instrument response at wavelengths below $\sim$460 nm. The spectrograph was triggered by the fire control circuits used to detonate the explosive charges. Spectra were recorded at an integration period of 15 μs per scan and each shot was repeated several times in order to confirm reproducibility.

We note that in the current investigation, detonation should be complete within $\sim$5 μs of detonator initiation given the length of the charge and the detonation velocity of the formulation, with subsequent emission assigned to the post-detonation fireball resulting from afterburning of under-oxidized detonation products. Interestingly, spectroscopy methods similar to those used in the current study have observed very high temperatures (9700 K) associated with early (t $\leq$ 21 μs) shock breakout into the surrounding air by monitoring atomic emission signals from N and O atoms.[16] We do not expect breakout effects to contribute significantly to the results of the current study on account of the longer delay times and the fact that our temperature measurements are obtained from an atom found in the explosive formulation but not in the surrounding air.

III. RESULTS AND DISCUSSION

In Figure 1, we show typical emission spectra collected from RDX charges incorporating the commercial nano-Al, AlOA, and AlFA. Each spectrum shown was collected at t = 30 μs, where t = 0 corresponds to explosion of the detonator. The spectra are remarkably similar; in each we find a broadband emission covering the entire visible spectrum, Al $^2P_{1/2}$ $^2S_{1/2}$ and $^2P_{3/2}$ $^2S_{1/2}$ atomic emissions at 394 and 396 nm, respectively,[19,20] and the AlO X B vibronic band.[21] We also see a strong Na emission at 589 nm resulting from Na impurities[3] in the sample, as well as peaks at 554 nm and 706 nm due to the $^1S_0$ $^1P_1$ and $^3D_3$ $^3F_4$ transitions in Ba atoms, and peaks at 455, 493, and 614 nm from the $^2S_{1/2}$ $\leftarrow$ $^2P_{3/2}$, the $^2S_{1/2}$ $\leftarrow$ $^2P_{1/2}$, and the $^2D_{5/2}$ $\leftarrow$ $^2P_{3/2}$ transitions in Ba$^+$ ions, respectively.[22] The peak at 650 nm may have contributions[22] from both Ba ($^3D_3$ $^3D_3$) and Ba$^+$ ($^2D_{3/2}$ $^2P_{1/2}$) at the resolution of the spectrograph. In the case of the charges incorporating AlOA, we also see intense Li lines at 610 nm and 671 nm, due to a Li impurity. A number of smaller unassigned peaks and bands are also found throughout the spectra. Unfortunately, no AlF vibronic bands were observed for the RDX-AlFA charges, possibly due to the weak emission character of the AlF bands found in this region of the spectrum.[21] We note that additional AlF bands have been reported[21] at wavelengths outside the spectral range of our spectrometer, and future experiments are planned to focus on any UV emissions.

Although the spectra share the same basic features, the time-dependence of the Al, AlO, and broadband emissions differs between the charges containing the various types of aluminum particles. In Figure 2, we show the intensity of the Al atomic emission and the broadband emission as measured at 600 nm as a function of time. Unfortunately, the AlO band intensities could not be readily extracted and plotted due to
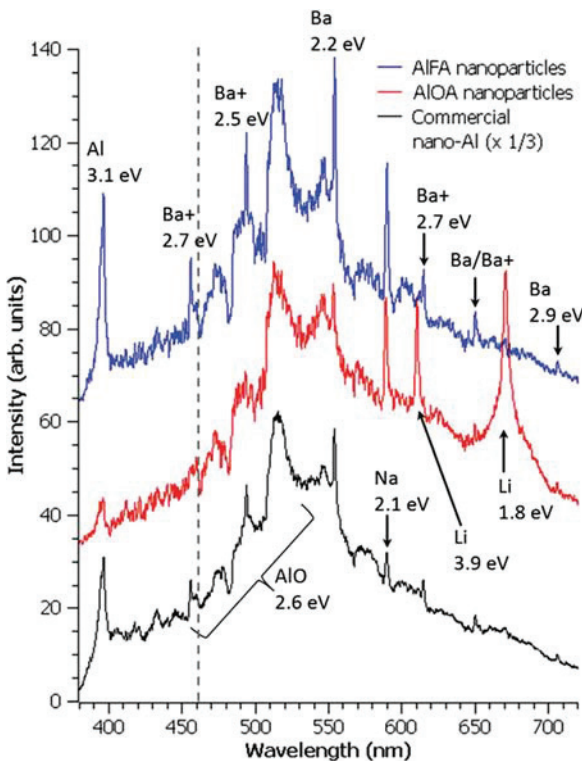
FIG. 1. Emission spectra obtained from detonation of barium-doped 20 g RDX charges containing 20 wt. % aluminum nanoparticles chosen from commercial nano-Al (bottom spectrum), AlOA (middle spectrum), or AlFA (top spectrum). All spectra were captured at t = 30 μs relative to the start of detonation. Prominent peaks and bands are labeled with the identity of the emitting species and the energy of the upper electronic state involved in the transition. The spectra are corrected for instrument response at wavelengths to the right of the vertical dashed line ($\lambda \geq 460$ nm).

the overlapping broadband emission in this region of the spectrum. Nevertheless, visual inspection of the spectra for the various charges as a function of time confirmed that the Al and AlO signals occurred in coincidence, as is typical during Al combustion.[23–27] In Figure 2(a), we see that for the RDX-AlOA charges, the Al atomic emission lines are
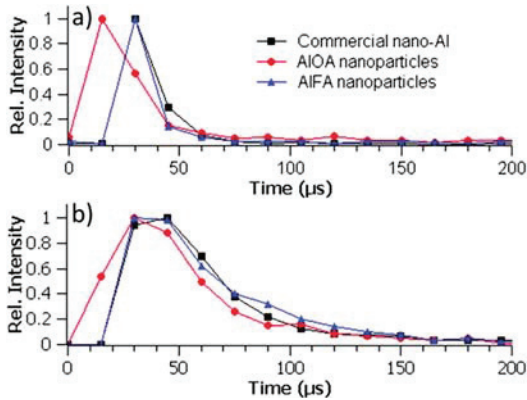

FIG. 2. Time dependence of (a) the Al atomic emission peak at 396 nm and (b) the broadband emission at 600 nm for each of the types of explosives charges studied following detonation.

strongest in the scan obtained at t = 15 μs and then decrease in each subsequent scan. In contrast, the RDX charges containing commercial nano-Al or AlFA exhibit little Al or AlO emission until t = 30 μs. The time-dependence of the Al lines in these two types of charges is virtually identical. The intensity of the broadband emissions shows a similar trend. Strong broadband emissions are typically observed during Al combustion,[23–27] but we must be cautious in the interpretation of this signal since it can also be produced by particulates such as soot. In Figure 2(b), we see that the charges incorporating commercial nano-Al or AlFA again behave similarly to one another, while the evolution of the signals from the RDX-AlOA charges is shifted to somewhat earlier times. Taken at face value, the data in Figure 2 seem to indicate that combustion of the AlOA particles within the post-detonation fireball occurs on a faster timescale than either the commercial nano-Al or AlFA, and that the timescale for oxidation of the latter two particles is quite similar. If indeed this is the case, we might expect to see some evidence of this in the fireball temperatures. Temperature measurements are particularly relevant for the AlFA material, since it may be possible for the aluminum nanoparticles to react exothermically with the fluorinated acrylic matrix before competing oxidation processes can occur,[7] increasing the temperature, but producing only weak AlF vibronic signals, for example.

In Table I, we list the apparent temperatures of the fireballs obtained from the Ba atomic emissions. The temperatures were obtained by the two-line method, utilizing the 554 and 706 nm Ba emission lines since they persisted longest following the detonations. Unfortunately, Ba emission lines were not reliably prominent in the first 1–2 scans (0, 15 μs). The error in the temperatures obtained in subsequent scans was determined by the available signal-to-noise ratio of the Ba peaks in the spectra, with higher Ba signals corresponding to lower error bars. The error bars listed in Table I correspond to either the 95% confidence level calculated from the signal-to-noise ratio of the scan or the inherent accuracy limit of the method,[28] whichever is larger. As mentioned above, each shot was repeated several times to confirm reproducibility. The temperature of the fireball resulting from the RDX charges containing the commercial nano-Al are in the range of 3600–3900 K, in good agreement with earlier measurements.[11] The temperature obtained for the RDX-AlOA charges is initially in the 4000–4500 K range, but then quickly drops to less than 2600 K for t ≥ 45 μs. We

TABLE I. Apparent fireball temperatures for the various types of explosives charges used in the current study, obtained from Ba atomic emission lines evident in the time-resolved spectra. The temperature was calculated by the two-line method using the Ba emission peaks at 554 and 706 nm. The 95% confidence levels are given in parentheses.

Time (μs)	20 wt. % commercial Al in RDX	20 wt. % AlOA in RDX	20 wt. % AlFA in RDX
0	…	…	…
15	…	4000 (400)	…
30	3900 (200)	4500 (500)	3200 (300)
45	3600 (300)	<2600	3400 (500)

can estimate only an upper bound for this temperature based upon the presence of the Ba line at 554 nm and the absence of any other Ba or Ba$^+$ lines in the corresponding spectrum. The temperatures obtained for the RDX-AlFA charges are in the range of 3200–3400 K. It is interesting to note that this is near the expected temperature for aluminum fluorination reactions,[29] although this may be coincidental since these particles are fuel-rich and we know from the emission spectra that oxidation is also occurring. For reference, the apparent temperatures of RDX charges that contain no Al content (obtained previously[10,11] using the same methodology) are in the range of 2600–2900 K.

We note that two Li lines from different energy levels are observed in the RDX-AlOA spectra, resulting from a Li impurity in AlOA. Unfortunately, we cannot use these to obtain an additional temperature measurement since the peak at 671 nm oversaturated the detector in the as-collected spectra (before correction for detector response was applied). The prominent pedestal at the base of this peak is most likely due to charge "bleeding" from the oversaturated pixels into neighboring ones. Additionally, the Li concentration in the sample is currently unknown, thus, we cannot be certain that the Li emissions are not subject to self-absorption effects.

The fact that the temperatures obtained for the RDX-AlOA charges is similar to (or perhaps even a bit higher than) those of the charges with commercial nano-Al, while the RDX-AlFA charges yielded lower temperatures, is consistent with the observed oxidation kinetics discussed above, i.e., that the oxidation timescales are similar for the commercial nano-Al and AlFA but that the AlOA particles burn more quickly. The AlOA and AlFA particles contain ∼40 wt. % and ∼50 wt. % Al metal, respectively,[5,7] only about half of the Al metal content of the commercial particles. The lower percentage of Al metal content correspondingly lowers the energy content of the explosive charge. Consequently, if the AlFA particles burn at a similar rate to the commercial nano-Al, then we would expect the temperature to be intermediate between that of RDX alone and RDX with the commercial nanoparticles. This is precisely what we observe. On the other hand, the observation that the RDX-AlOA charges are able to achieve a peak temperature at least equal to that of RDX with the commercial nanoparticles, despite the substantially lower Al content, lends additional support to the idea that the combustion kinetics for the AlOA particles are faster than those for the other particles studied. Of course, the fact that the temperature drops so quickly for the charges incorporating the AlOA particles also supports this idea.

IV. CONCLUSIONS

The results of the current investigation seem to indicate that the AlOA nanoparticles react more quickly in the fireball than either the commercial nano-Al or the AlFA nanoparticles even though the nanoparticle sizes in the samples are comparable. It also indicates that the oxidation rates of the commercial nano-Al and the AlFA particles (or at least the Al content in the AlFA material) are similar. Clearly, additional experimental investigations and possibly also input

from theory will be required to establish a detailed mechanistic understanding. Nevertheless, the most straightforward interpretation of these results would seem to be that changing the passivation layer of aluminum nanoparticles from an oxide shell to organic passivation can significantly enhance the post-detonation combustion kinetics.

[1]P. P. Vadhe, R. B. Pawar, R. K. Sinha, S. N. Asthana, and A. S. Rao, Combust., Explos. Shock Waves **44**, 461 (2008).
[2]E. Anderson, *Tactical Missile Warheads*, Progress in Astronautics and Aeronautics Vol. 155, edited by J. Carleone (American Institute of Aeronautics and Astronautics, Washington, 1993), Chap. 2.
[3]*CRC Handbook of Chemistry and Physics*, 80th ed., edited by D. R. Lide (CRC, 2000).
[4]R. J. Jouet, A. D. Warren, D. M. Rosenberg, V. J. Bellitto, K. Park, and M. R. Zachariah, Chem. Mater. **17**, 2987 (2005).
[5]K. A. S. Fernando, M. J. Smith, B. A. Harruff, W. K. Lewis, E. A. Guliants, and C. E. Bunker, J. Phys. Chem. C **113**, 500 (2009).
[6]C. A. Crouse, C. J. Pierce, and J. E. Spowart, ACS Appl. Mater. Interfaces **2**, 2560 (2010).
[7]C. A. Crouse, C. J. Pierce, and J. E. Spowart, Combust. Flame **159**, 3199 (2012).
[8]C. E. Bunker, M. J. Smith, K. A. S. Fernando, B. A. Harruff, W. K. Lewis, J. R. Gord, E. A. Guliants, and D. K. Phelps, ACS Appl. Mater. Interfaces **2**, 11 (2010).
[9]W. K. Lewis, B. A. Harruff, J. R. Gord, A. T. Rosenberger, T. M. Sexton, E. A. Guliants, and C. E. Bunker, J. Phys. Chem. C **115**, 70 (2011).
[10]W. K. Lewis and C. G. Rumchik, J. Appl. Phys. **105**, 056104 (2009).
[11]W. K. Lewis, C. G. Rumchik, P. B. Broughton, and C. M. Lindsay, J. Appl. Phys. **111**, 014903 (2012).
[12]J. A. Orson, W. F. Bagby, and G. P. Perram, Infrared Phys. Technol. **44**, 101 (2003).
[13]J. R. Carney, J. S. Miller, J. C. Gump, and G. I. Pangilinan, Rev. Sci. Instrum. **77**, 063103 (2006).
[14]J. Wilkinson, J. M. Lightstone, C. J. Boswell, and J. R. Carney, in *Shock Compression of Condensed Matter*, edited by M. Elert, M. D. Furnish, R. Chau, N. Homes, and J. Nguyen (American Institute of Physics, 2007), p. 1271.
[15]K. C. Gross, J. Wayman, and G. P. Perram, Proc. SPIE **6566**, 656613 (2007).
[16]J. D. Koch, S. Piecuch, J. M. Lightstone, J. R. Carney, and J. Hooper, J. Appl. Phys. **108**, 036101 (2010).
[17]V. Bouyer, G. Baudin, C. Le Gallic, and P. Hervé, in *Shock Compression of Condensed Matter*, edited by M. D. Furnish, N. N. Thadhani, and Y. Horie (American Institute of Physics, 2001), p. 1223.
[18]V. Bouyer, I. Darbord, P. Hervé, G. Baudin, C. Le Gallic, F. Clément, and G. Chavent, Combust. Flame **144**, 139 (2006).
[19]K. B. S. Eriksson and H. B. S. Isberg, Ark. Fys. **23**, 527 (1963).
[20]C. Mendoza, W. Eissner, M. Le Dourneuf, and C. J. Zeippen, J. Phys. B **28**, 3485 (1995).
[21]R. W. B. Pearse and A. G. Gaydon, *The Identification of Molecular Spectra* (Chapman & Hall, 1963).
[22]J. J. Curry, J. Phys. Chem. Ref. Data **33**, 725 (2004).
[23]J. L. Gole and R. N. Zare, J. Chem. Phys. **57**, 5331–5335 (1972).

[24]S. Rosenwaks, R. E. Steele, and H. P. Broida, J. Chem. Phys. **63**, 1963–1965 (1975).

[25]S. Goroshin, J. Mamen, A. Higgins, T. Bazyn, N. Glumac, and H. Krier, Proc. Combust. Inst. **31**, 2011–2019 (2007).

[26]M. Jackson, M. Pantoya, and W. Gill, Combust. Flame **153**, 58–70 (2008).

[27]P. E. Bocanegra, D. Davidenko, V. Sarou-Kanian, C. Chauveau, and I. Gökalp, Exp. Therm. Fluid Sci. **34**, 299–307 (2010).

[28]I. Reif, V. A. Fassel, and R. N. Kniseley, Spectrochim. Acta, Part B **29**, 79 (1974).

[29]C. D. Yarrington, S. F. Son, and T. J. Foley, J. Propul. Power **26**, 734 (2010).

Appendix N. Converting Algal Triglycerides to Diesel and HEFA Jet Fuel Fractions

Converting Algal Triglycerides to Diesel and HEFA Jet Fuel Fractions

Heinz J. Robota,* Jhoanna C. Alger, and Linda Shafer

University of Dayton Research Institute, 300 College Park, Dayton, Ohio 45469, United States

ABSTRACT: Over 2 L of algal triglycerides were first converted to *n*-alkanes using a 3% Pd/carbon catalyst in a fixed bed reactor at 350 °C under 800 psig of H_2. The starting triglyceride was composed of 10.5% C_{16} and 85.2% C_{18} fatty acids. The Pd/C catalyst exhibited primarily decarbonylation and total reduction deoxygenation pathways, which changed in relative contribution over the nearly 200 h of continuous operation. Both the $C_{18}/(C_{18}+C_{17})$ and $C_{16}/(C_{16}+C_{15})$ product ratios changed from 0.3 at the start of the deoxygenation run to 0.6 at its conclusion. Overall, the catalyst became more active during the run. After a first pass deoxygenation, over 85% of the product was composed of *n*-alkanes divided nearly equally between the C_n and C_{n-1} chain lengths corresponding to the starting fatty acid chain lengths. The alkanes along with a few percent 1-alcohols were separated from the remaining incompletely converted components by distillation and subjected to a polishing hydrogenation using a 0.5% Pt/alumina catalyst. A portion of this first pass *n*-alkane composite was hydroisomerized to improve its cold flow properties using a 0.5% Pt/US-Y zeolite catalyst. Even with an iso/normal ratio of just over 1 in the product stream, the mixture solidified near ambient temperature. To further improve the cold flow properties of this diesel composition, it was subjected to a solvent dewaxing procedure, which yielded a product that remained liquid at −20 °C. The incompletely converted components remaining after the first pass deoxygenation were subjected to a second deoxygenation pass under the same conditions used for the fresh triglycerides. The product alkanes were again separated by distillation, alcohols were reduced to alkanes, and a single composite alkane mixture was prepared by combining the first and second pass alkanes. Overall, more than 95% of the product stream produced by the two deoxygenation passes was composed of *n*-alkanes. This final composite mixture was processed further to a HEFA (hydrotreated esters and fatty acids) jet composition using the same 0.5% Pt/US-Y zeolite catalyst at three different conversion severities. With single pass cracking conversions of 43%, 59%, and 93%, yield losses of 41%, 44%, and 75% to a C_{8-} naphtha fraction were observed. Such high yield losses argue against a strategy where HEFA jet is the primarily targeted product. We suggest a strategy in which the yield loss to naphtha can be limited to less than 10% based on making principally a renewable diesel fuel from which a HEFA jet can be extracted as a minority product.

1. INTRODUCTION

To convert renewable triglycerides to liquid transportation fuels, either diesel or HEFA (hydrotreated esters and fatty acids) jet, a number of chemical transformations must be undertaken.[1] First, the triglycerides must be converted to normal alkanes. This can be accomplished by catalytic deoxygenation of (1) triglycerides; (2) free fatty acids derived from triglycerides; or (3) secondary esters produced by the transesterification of triglycerides with an inexpensive alcohol. Next, the normal alkanes must be catalytically isomerized and hydrocracked to a distribution of alkane isomers and the fractions appropriate for diesel and HEFA jet recovered.[2,3] Hydrocracking is required for producing HEFA jet because the naturally occurring distribution of fatty acid chain lengths found in the triglycerides yields alkanes with boiling points near or above the high temperature limit of the boiling point distribution in both commercial and military aviation fuels.[4,5] Similarly, when considering the low temperature requirements for these fuels, any remaining normal alkanes in a very highly isomerized mixture of the initial alkane distribution will have a freezing point considerably higher than the −40 °C required by the Jet-A commercial[4] specification and further still from the −47 °C required for military JP-8.[5] On the other hand, the native distribution of fatty acid chain lengths yields alkanes that are quite suitable for use as a diesel fuel.[5] To improve cold flow properties, the normal paraffins would require only a relatively mild hydroisomerization treatment. Consequently, production

of diesel fuel would result in a much higher yield to a commercial product. However, the European renewable fuels initiative has set targets for renewable fuel use by energy consuming sector.[6] Consequently, it will be necessary to produce aviation fuel from renewable sources. In its roadmap document, the World Energy Council has stated: "...algae biodiesel jet fuel represents the best potential answer for the sustainability of the aviation industry."[7]

The recent review by Kubičková and Kubička on the use of triglycerides as a source of fuel demonstrates a considerable variety of catalysts and feedstocks used to produce normal alkanes.[1] However, not a single example of an algae-derived triglyceride is cited. While algal triglycerides should be chemically similar to many of the seed-oil triglycerides, potential complications from minor constituents entering the triglyceride stream during extraction cannot be appreciated until a variety of oils is evaluated. Also, accumulation of potential contaminants within the deoxygenation catalyst bed requires extended exposures under steady operating conditions. Rapid changes in catalyst activity were most typically observed when deoxygenation was carried out in H_2-free or low H_2 content gas streams.[1] Under conditions with inherently short catalyst lifetimes, it would not be possible to identify more

985

specific feed-related changes in catalyst function. A second type of deactivation was observed with sulfided catalysts operating without further sulfide supplementation.[8] This resulted in slow loss of sulfur from the active sulfides and changed the character of the catalysts over time. With a co-fed source of sulfur, high conversion to alkanes was observed for up to 250 h. To assess the potential effect of minor feed constituents, runs of over many hundreds of hours are required.

While much effort has been focused on the production of alkanes from the triglycerides, much less has been published with regard to the further conversion of these alkanes to actual fuel compositions. Even in instances where selectivity to a single alkane is high, such as with an alumina-supported molybdenum sulfide, detectable amounts of incompletely converted oxygenates remain.[9] When further hydroprocessing these oxygenate contaminated alkanes, water is produced, which can interfere with the acid functionality of the bifunctional hydroisomerization or catalytic hydrocracking catalysts employed.[10] How this affects overall activity, selectivity, and stability remains to be elucidated. Also, it is conceivable that some of the oxygenates will not be completely converted to alkanes over the bifunctional upgrading catalyst. How this might affect fuel fit-for-purpose properties is unknown, but by knowing which compounds are likely to survive the upgrading process and at what concentrations, synthetic test blends could be formulated in order to investigate these issues further.

We report here our investigation of the conversion of algae-derived triglycerides into both a diesel fuel fraction and an aviation fuel fraction (HEFA jet). The triglycerides are converted to a mixture of normal alkanes using a 3% Pd/carbon catalyst in a hydrogen stream with an approximate H_2/triglyceride molar feed ratio of 30. Rather than targeting complete conversion to alkanes in a single reactor pass, we selected operating conditions which gave a product alkane content between 70 and 85 mass percent. Although feed conditions remained unchanged over the course of the initial alkane producing phase, the alkane yield increased as the run progressed with an increasing fraction of the even numbered alkanes. Gas phase compositions were also monitored in order to relate changes in liquid composition to changes in gas phase products. These first pass alkanes were concentrated by distillation into a composite in which the alkane concentration was nearly 95%. The remaining high boiling liquids were then converted in a second catalytic pass to produce additional alkanes, which were again concentrated by distillation and aggregated with the first pass alkanes for further conversion into fuel compositions.

The first pass normal alkane aggregate was subjected to hydroisomerization using a 0.5% Pt/US-Y zeolite catalyst to produce a composition suitable for use as a diesel fuel. The initial conditions resulted in conversion around 60% with the proportion isomerized or cracked dependent on feed alkane carbon number. An initial diesel composition was then recovered by separating the lightest components by distillation. By reducing the remaining normal alkane content using a solvent dewaxing method, a branched isomer enriched diesel composition suitable for low temperature conditions was demonstrated.

Three different bifunctional catalytic cracking strategies for producing HEFA jet were investigated using a composite of first and second pass normal alkanes. Prior to hydrocracking, the entire alkane mixture was first subjected to a polishing

deoxygenation treatment in which predominantly alcohols were reduced to alkanes over a 0.5% Pt/alumina catalyst. In the first hydrocracking approach, conditions were selected which resulted in 50% cracking of the heavier feed alkanes. A second condition was chosen such that secondary cracking of products could just be clearly detected. In the final approach, conditions were selected that resulted in near 100% cracking of the feed alkanes in a single reactor pass. Effluent streams are categorized into the fraction too light for HEFA jet (naphtha), the nominal HEFA jet fraction, and the remaining incompletely converted feed isomers. The relative amounts are considered with respect to lost fuel value for each of the potential single pass conversion conditions. Finally, considering both diesel and HEFA jet fractions, a conversion strategy is suggested which would preserve the greatest fuel value of the original algal alkanes.

2. EXPERIMENTAL SECTION

2.1. Algal Triglycerides. Algal triglycerides, produced by Phycal, were provided by the Air Force Research Laboratory. The roughly 2.5 L of bright orange liquid were derived from a single source. The liquids were clear, but a thin cloudy layer could be seen at the bottom of each sample bottle. We elected to use the triglycerides as delivered without further filtration. The composition of the triglycerides was analyzed by Phycal and is provided in Table 1. At least 95% of the total

Table 1. Fatty Acid Composition of the Algal Triglycerides

fatty acid	carbon no./double bonds	wt %
myristic	14:0	0.79
pentadecanoic	15:0	0.09
palmitic	16:0	10.11
palmitoleic	16:1	0.41
heptadecanoic	17:0	0.23
stearic	18:0	2.66
oleic	18:1	66.92
linoleic	18:2	14.56
linolinic	18:3	1.09
arachidic	20:0	0.28
eicosanoic	20:1	0.16
other		0.23
sum		97.53
wt % C_{16}		10.52
wt % C_{18}		85.23

fatty acid mass is composed of C_{16} and C_{18} fatty acids. The measured density is 0.917 g/mL. On average, there will be one double bond per triglyceride. Based on the analyzed composition, an average formula weight of 850 g/mol is used in relevant calculations.

2.2. 3% Pd/Carbon Deoxygenation Catalyst. The 3% palladium on carbon catalyst was prepared using a $PdCl_4^{-2}$ solution prepared from $PdCl_2$ crystals by dissolving them in a 2 M HCl solution with mild heating. Norit RX 3 Extra was used as the carbon support. The delivered extrudates were crushed and the 40−60 mesh fraction used for this catalyst. A water pore volume of 1.3 g-H_2O/g-carbon was determined and the $PdCl_4^{-2}$ solution was diluted with 2 M HCl to deliver the required amount of Pd in a pore volume impregnation. The granules were dried in static air overnight at 150 °C. Pd dispersion was measured using CO as the adsorbing gas in a Micromeritics volumetric adsorption instrument following reduction in hydrogen at 350 °C. Assuming a CO/Pd adsorption stoichiometry of 1, we determine the proportion of surface accessible Pd to be 20%.

2.3. 0.5% Pt/US-Y Zeolite Hydroprocessing Catalyst. Pt was deposited on a Zeolyst CBV-720 US-Y zeolite by ion exchange. The required mass of a 6.9% tetraammine platinum(II) chloride stock solution was diluted with distilled water to yield 9 kg of solution to which 1.0 kg of the zeolite was added. The slurry was vigorously stirred

208

with an overhead mixer. The pH was frequently checked and adjusted to 9.5 using concentrated aqueous ammonia. After a final pH adjustment at the end of the day, the slurry was allowed to stir overnight resulting in a final pH of 9.4 the following morning. The solid was recovered by vacuum filtration, and the cake was dried in a convection oven at 110 °C for 4 h. The dried cake was then calcined at 400 °C for 4 h in static air. After calcination, a 40−60 mesh fraction was recovered by gently breaking and agitating aggregates on a 40 mesh sieve. The Pt dispersion was determined using volumetric H_2 chemisorption at 30 °C using a Micromeritics adsorption instrument following reduction in hydrogen at 450 °C. Using the dual isotherm method, the proportion of surface accessible Pt was determined to be 17%, using only the irreversibly adsorbed volume.

2.4. Fixed Bed Catalytic Reactor System. Two equivalent reactor systems were used in this investigation, one for converting the algal triglycerides to alkanes and the other for hydroprocessing the aggregate alkanes. The reactors are based on $^1/_2$ in. outer diameter (OD) stainless steel tubes of 24 in. length mounted vertically in a three zone electric furnace. Heater control thermocouples are spot-welded to the exterior of the reactor tube at the center of each heated zone, and the length of the tube within the heater is covered with a split cylindrical brass tube of $^1/_8$ in. thickness to promote uniform temperature. The reactors are fitted with a thermowell made from $^1/_8$ in. stainless steel tubing entering the system at the exit end and extending to about half way into the upper heated zone. Bed temperatures could be measured using a traveling thermocouple within the thermowell. A 20 μm sintered stainless steel filter was located in the exit fitting of the reactor tube.

Liquid and gaseous feeds enter the reactor immediately above the heated zone. Gas flow is controlled using Brooks mass flow controllers. The liquid feed is delivered by a heated ISCO high pressure syringe pump charged from a heated external reservoir. While heating is not required for the original triglycerides, the incompletely converted materials solidified at room temperature. In order to keep this mixture melted and of low viscosity, feed reservoir, pump syringe, and related tubing were heated to 65 °C. Reactor effluent enters a cylindrical pressure vessel where liquids condense and gases pass on to the manual back-pressure regulator. Reactor exit lines and liquid receivers were warmed with heat tape to 65 °C in the case of triglyceride processing and 30 °C for the hydroprocessed algal alkanes. Upon exiting the system through the back-pressure regulator, the gas stream is directed to a multiport valve located a short distance from the inlet of a refinery gas analyzer, which could be used to quantify permanent gases. The analyzer was calibrated with certified gas blends. Liquid products were drained from the bottom of the high pressure receiver cylinder through a valve for external analysis. In cases where separable water was present, the liquids were heated in an oven to 60 °C in their sealed sample bottles in order to promote better phase separation. The water was then extracted using a Pasteur pipet.

2.4.1. Catalyst Charging and Operating Conditions for Triglyceride and Related Feed Conversion. 7.0 g of 40−60 mesh sized 3% Pd/C catalyst were charged without diluent to a reactor tube. This volume of catalyst fills 11 in. of the reactor tube and was placed such that 2.5 in. extended into both the upper and lower heated zones. The volume above and below the catalyst bed was filled with SiC of similar granule size. The triglyceride was charged at the rate of 0.177 mL/min, (WHSV = 1.5/h) roughly 1.91×10^{-4} mol/min. H_2 was fed at 154 mL/min, providing for a molar ratio of H_2/triglycerides slightly in excess of 30. Each zone of the furnace was set to 350 °C. When measuring the temperature profile within the bed at steady state, a nearly constant temperature of 352° ± 2 °C is registered. An exception is the first inch of the bed, where an exotherm of less than 8 °C was observed. This temperature excursion is attributed to the rapid, exothermic hydrogenation of the olefinic fatty acids.

As detailed in the results, the first pass conversion of the triglycerides did not completely convert the triglycerides to alkanes. Also, a plug formed in the reactor at the end of the first pass conversion. The reactor was recharged with catalyst as noted above. After separating the alkanes by distillation, the bottoms were reprocessed using the same hydrocarbon and H_2 feed rates as used

for the fresh triglycerides. In this instance, no exotherm was observed and a constant bed temperature of 352 ± 2 °C was measured throughout this phase of the conversion.

2.4.2. Catalyst Charging and Operating Conditions for Alkane Hydroprocessing to Diesel and HEFA Jet Compositions. The alkanes recovered by distillation from the deoxygenation step contained incompletely reduced alcohols. These alcohols were fully reduced to alkanes in a polishing step using a 0.5% Pt/alumina catalyst at 300 °C, 900 psig H_2 flowing at 150 mL/min and a liquid feed corresponding to LHSV = 6/h. The water produced in the reduction was separated from the organic phase prior to further conversion. For converting the alkanes to fuel compositions, 1.0 g of the 40−60 mesh sized 0.5% Pt/US-Y catalyst was mixed with a 4-fold volumetric excess of similarly sized SiC. The bottom of the reactor tube was filled with sufficient SiC of similar size so as to locate the catalyst charge in the center of the middle heated zone. The volume above the catalyst was then filled with additional SiC. The mixed alkanes were charged at 0.165 mL/min (LHSV = 3/h), H_2 was fed at 140 mL/min, and the system operated at 800 psig. Each zone of the furnace was set to 258 °C for isomerization to diesel. For HEFA jet production, temperatures used are noted in the following.

2.5. Analysis of Product Liquids. Liquid samples were analyzed by gas chromatography-flame ionization detection (GC-FID) using an Agilent model 7890 gas chromatograph fitted with a 30 m DB-5MS column having 0.25 mm inner diameter (ID) and a 0.25-μm film. The GC temperature program began with an initial temperature of 40 °C (3-min hold) followed by ramping (10 °C/min) to 325 °C (20-min hold). The samples were diluted 1 to 10 in carbon disulfide. Samples (1 μL) were injected onto the column using a 100:1 split with a constant column H_2 carrier gas flow rate of 1 mL/min. The GC injector temperature was 300 °C, and the detector was held at 350 °C.

The data analysis method used to quantify the GC-FID results into the abundances of normal and isomerized paraffins was based on ASTM D-5442,[11] which is predicated on the fact that for flame ionization detection of hydrocarbons, area percents of the hydrocarbon peaks translate directly to weight percents. The carbon distribution method used was a modification of D-5442, based on results published by Claude et al., which illustrated where the various branched paraffins chromatographically elute in relation to the normal paraffin of the same carbon number.[12] In mixtures of paraffins, the most highly branched isomers of C_n elute before the n-C_{n-1} peak. Therefore, the total signal assigned to a given carbon number C_n (starting with n = 7) requires summing the area between the monobranched isomers of the C_{n-1} paraffin and the monobranched isomers of the C_n paraffin followed by subtracting the area of the n-C_{n-1} peak. This isomerized C_n signal is then added to the signal of n-C_n paraffin. Because the n-C_{n-1} peak is superimposed on the signal from the more highly branched C_n isomers, the baseline for integrating the n-C_{n-1} peak is drawn from the valley before to the valley following the peak. In addition to the paraffins in the reaction products, small quantities of 1-alcohols also eluted over the same retention time range as the paraffins. Correction factors were determined and used for quantitation of the 1-alcohols, since they have lower responses in FID than the alkanes of the same concentration.

To determine what products other than paraffins were produced from the triglycerides, a gas chromatography mass spectrometry (GC-MS) method was used. Samples were diluted in carbon disulfide as described. The column used in the Agilent Model 6890 gas chromatograph was a 30 m DB-5MS with a 0.25 mm ID and a 0.25 μm film. The GC temperature program employed an initial temperature of 35 °C (5-min hold) followed by first ramping (5 °C/min) to 170 °C and then ramping (10 °C/min) to 310 °C followed by a 20-min hold. 1-μL injections were injected with a 40:1 split and a constant column He carrier gas flow rate of 1 mL/min. The GC injector temperature was 280 °C, and the Agilent Model 5973 mass spectrometer transfer line was held at a temperature of 280 °C. The mass spectrometer was operated in scanning mode to acquire mass spectral data in the range from 33 to 600 Da. The NIST 98 library search software was used to identify the major components in

Table 2. Normal Alkane Composition and Fraction of Total Liquids as a Function of Time on Stream[a]

hours on stream	24	33	52	59.5	76.5	84	100.5	123	146.5	170.5	193.5
normal alkane carbon no.						wt %					
13	0.44	0.38	0.34	0.31	0.32	0.33	0.33	0.34	0.31	0.29	0.30
14	0.56	0.53	0.57	0.53	0.47	0.45	0.43	0.45	0.49	0.53	0.50
15	6.00	5.10	4.61	4.04	4.08	4.32	4.31	4.33	3.94	3.60	3.66
16	2.46	3.51	4.35	5.58	5.62	5.33	5.25	5.39	5.93	6.41	5.91
17	48.19	40.99	36.89	31.98	32.83	34.55	34.73	34.67	31.37	28.57	28.88
18	18.01	26.64	32.68	41.78	43.05	40.58	40.21	40.96	45.03	48.51	44.63
19	0.35	0.32	0.30	0.29	0.29	0.30	0.30	0.30	0.29	0.28	0.28
20	0.13	0.19	0.22	0.28	0.28	0.26	0.27	0.27	0.29	0.32	0.30
21	0.07	0.07	0.06	0.06	0.06	0.06	0.06	0.06	0.06	0.06	0.06
22	0.04	0.05	0.06	0.07	0.07	0.06	0.06	0.06	0.07	0.07	0.07
23	0.06	0.06	0.06	0.06	0.05	0.05	0.05	0.05	0.05	0.06	0.06
24	0.03	0.04	0.04	0.05	0.05	0.04	0.04	0.04	0.05	0.05	0.06
25	0.07	0.06	0.06	0.05	0.04	0.04	0.05	0.05	0.04	0.05	0.05
26	0.12	0.14	0.15	0.15	0.14	0.13	0.14	0.13	0.14	0.17	0.19
total	76.54	78.06	80.38	85.22	87.35	86.51	86.23	87.11	88.07	88.97	84.94
effluent gas constituents						vol %					
CO	4.79	4.11	3.90	3.27	3.81	3.67	3.95	3.83	3.50	3.24	4.37
CO_2	0.36	0.34	0.38	0.42	0.36	0.35	0.35	0.35	0.40	0.46	0.61
methane	0.07	0.05	0.06	0.08	0.07	0.05	0.05	0.05	0.08	0.09	0.16
ethane	0.30	0.24	0.19	0.14	0.30	0.16	0.17	0.16	0.13	0.11	0.18
propane	1.35	1.24	1.57	1.60	1.35	1.77	1.89	1.97	2.13	2.25	1.35
propene	0.01	0.00	0.00	0.00	0.01	0.00	0.00	0.00	0.01	0.00	0.01
exit flow (mL/min)	165	163	158	154	155	158	159	153	154	152	53
recovered H_2O (g)									18.2	19.9	21

[a]The associated exit gas flow rate and composition with mass of water where collected.

the samples. Total ion current area responses were used to assign semiquantitative concentrations to the identified compounds.

2.6. Spinning Band Fractionating Distillation Unit. A spinning band fractionating distillation unit (B/R Instrument Corporation model M690) was used to separate the algal alkanes from the inadequately deoxygenated molecules as well as for separating light cracked products from the diesel. A 1 L round-bottom flask, with a thermowell for measuring the pot liquid temperature, was charged with the mixture to be distilled. A chiller, set to 4 °C, circulates fluid to cool the condenser portion of the spinning band column. Distillations at 50 Torr absolute pressure were executed using the vacuum pump and pressure controller attached to the unit. Multiple aliquots recovered from the fixed-bed reactor system used to convert the algal triglycerides to alkanes were combined into a single mixture. Charges of roughly 800 mL were put into the distillation pot. Distillations of the deoxygenated triglycerides were executed so as to first remove the light ends ($\leq C_{12}$) and water and then to recover the desired alkane fraction ($C_{12}-C_{22}$). The water and light ends fraction was terminated when the reflux atmospheric equivalent vapor temperature reached 155 °C and the targeted mixed alkane fraction collected until the atmospheric equivalent vapor temperature reached 345 °C or all receivers were filled. All liquids remaining in the pot when the final receiver filled were recombined with the remaining undistilled aggregate for further recovery in a subsequent distillation. Product liquids collected from each separate distillation were then combined to make up the algal alkanes used to feed the hydroprocessing conversion reactor.

The same unit operating at atmospheric pressure was used for separating a diesel boiling-range product following catalytic hydro-isomerization and hydrocracking of the initially produced *n*-alkanes. Light components were taken overhead and distillation terminated when the reflux vapor temperature exceeded 135 °C. The entire distribution of products remaining in the distillation flask was recovered as the diesel composition.

2.6. Solvent Dewaxing of the Hydroisomerized Diesel Composition. Solvent dewaxing was achieved by using a 1:1

volumetric mixture of toluene and methyl ethyl ketone. The solvent was mixed with the diesel fraction in a 5:1 volumetric ratio and chilled in a thermostatted, refrigerated methanol bath to −40 °C. The precipitated waxy solids were separated from the remaining liquid by compression filtration, and the liquid was recovered. The solvent was then removed in a rotary evaporator leaving the dewaxed diesel liquid.

3. RESULTS AND DISCUSSION

3.1. First Pass Conversion of Triglycerides to Alkanes. The catalytic conversion of triglycerides to alkanes proceeds by multiple reaction routes.[1] Decarbonylation, in which CO is lost, or decarboxylation, in which CO_2 is lost, can both proceed in either the absence or presence of hydrogen. The resulting alkanes (and alkenes when H_2 is absent) contain one less carbon atom than present in the original fatty acid. Hydro-deoxygenation, the complete reduction of the oxygenated species, produces an alkane with the same number of carbon atoms as the original fatty acid. Much of the previous work has been focused on elucidating reaction pathways and has employed model compounds rather than the more complex compositions found in actual vegetable oils. Also, the aim was not to recover processable quantities of alkanes, so dilute reagents in batch reactors are commonly used. When converting either free fatty acids or fatty acid esters over Pd/C in gas streams at low H_2 partial pressures, deoxygenated products were formed primarily through either decarboxylation or decarbonylation.[13−17] Immer and Lamb found that the preferential pathway switched from decarboxylation to decarbonylation when the H_2 partial pressure exceeded a threshold.[16] Rozmyszłowicz et al. made a similar observation.[17] Under low H_2 partial pressures, even numbered alkanes typically appear as only minor deoxygenation products. Similar results are found with supported Pt catalysts.[18] In contrast,

conversion of rapeseed oil in fixed-bed reactors over sulfided Ni, Mo, or NiMo catalysts in H_2 at 500 psig produced both C_{n-1} and C_n alkanes, depending on catalyst composition.[19] In particular, in the absence of Ni, the sulfided Mo-based catalyst converted rapeseed oil nearly exclusively via hydrodeoxygenation, yielding primarily *n*-octadecane as product. A similar observation was made in the case of supported Mo_2C in the conversion of methylpalmitate, where C_{16} alkanes and alkenes were the predominant products. However, in the same study, Pd/C and Pt/C catalysts produced primarily C_{15} products.[20] Thus, based on these previous observations, we anticipated that we should observe primarily C_{15} and C_{17} alkanes in the conversion of the algal triglycerides over our 3% Pd/C catalyst.

Table 2 shows the alkane analysis observed over the course of processing just over 2 L of the algal triglcyerides. The weight percent of each of the normal alkanes is based upon the FID signal area for that peak relative to the sum of all peaks in the chromatogram of that sample. In every case, the alkanes account for less than 100% of the liquid composition but are always a very high percentage of the total. In the conventional sense, the triglyceride conversion is 100% throughout the run, in that propyl esters of either stearic or palmitic acids represent the only remnants of the original triglycerides. GC-MS analysis of the liquids was used to identify and quantity the major nonalkane contributors to the recovered composition. The remainder of the recovered liquid was composed primarily of a variety of oxygenated species: (1) partially converted esters, such as propyl stearate, acetyl stearate, and propyl palmitate; (2) alcohols, such as octadecanol and hexadecanol; (3) the condensation products of free fatty acids and alcohols, such as stearyl stearate and palmityl stearate; and (4) free fatty acids, primarily stearic acid. The only clearly identified olefin was octadecene, which never exceeded 1% of the total.

At the beginning of the run, the odd numbered alkanes formed from stearic and palmitic acids are, indeed, the most abundant products. Even so, the octadecane and hexadecane still represent roughly a quarter of the yield from conversion of stearic acid and palmitic acid side chains of the original triglycerides. This indicates that the alkane products arise from multiple reaction paths. As the run proceeded, with the external conditions of liquid feed rate, H_2 flow rate, and reactor set point temperature unaltered, the catalyst became more active and exhibited a change in primary reaction pathway. The increased activity is reflected in progressively larger normal alkane content in the recovered liquids, starting at 76% and peaking at 89%. The changing primary reaction pathway results in the octadecane/(octadecane + heptadecane) and hexadecane/(hexadecane + pentadecane) ratios each growing from under 0.3 to over 0.6 as the run proceeded. This shows a shift toward greater hydrodeoxygenation, where the oxidized terminal carbon of the fatty acid becomes fully reduced, and away from pathways that cleave the oxidized carbon from the chain as either CO or CO_2. A similar trend is observed for the other, minor fatty acid side chains with 14 and 20 carbon atoms. Although not noted in the original analysis, fatty acid side chains with 26 carbons appear to be present in meaningful abundance, based upon the yield of normal alkanes with 25 and 26 carbon atoms. The observed activity increase with time on stream has not been previously reported.

A comparison of the relative decarbonylation and decarboxylation rates can be made by comparing the relative amounts of CO and CO_2 detected in the exit gas stream. Generally, the CO_2 content in the gas remains nearly constant over the course

of the run. CO is at its highest at the start, but it declines after the first two days to a somewhat variable but near constant level. Thus, it appears that the relative selectivity between decarbonylation and decarboxylation always favors decarbonylation to about the same extent, even as the overall selectivity between these carbonyl cleavage pathways and complete reduction pathways changes by a factor of 2. Early in the run, a distinct water phase could not be easily separated from the remainder of the liquid products, although droplets of water were observed. As the run progressed, a separate water phase grew in relative abundance. In the three operating periods where water could be readily recovered, an oxygen balance could be estimated. When the oxygen present in effluent CO and CO_2 is integrated over the liquid product collection period and added to the mass of recovered water, it accounts for roughly 90% of the oxygen fed to the reactor in the form of triglycerides. An analysis of the aqueous phase using gas chromatography revealed 1-propanol, 1,2-propanediol, ethanol, and acetic acid. Combined, these minor constituents accounted for only about 5 mass % of the aqueous phase. Since conversion to alkanes is not complete, leaving some oxygenated products in the organic liquid product, accounting for 90% of the fed oxygen in the form of H_2O, CO, and CO_2 is quite satisfactory. Another potential factor that could affect the CO/CO_2 ratio is the water−gas shift (WGS) reaction. If WGS achieved equilibrium at the reactor exit in the three periods where water could be quantified, the expected CO/CO_2 ratio would be roughly 0.4.[21] Since the observed ratio is between 7 and 11, it appears safe to conclude that, under our operating conditions, the Pd/C catalyst is ineffective for equilibrating the WGS reaction and that the observed CO/CO_2 ratios faithfully represent the relative rates of decarbonylation and decarboxylation.

The conversion of stearic acid should be a good indicator of what one might expect when converting a triglyceride. With the triglyceride, following hydrogenation of any double bonds, the first reaction would presumably cleave the fatty acid chain from the glyceryl backbone to yield the free fatty acid. Our observed CO/CO_2 ratio differs decisively from the ratio observed by Immer and Lamb during the first 10 h of stearic acid conversion over a 5% Pd/C catalyst under 0.75 atm H_2 in a semibatch stirred tank reactor. However, they observe a rapid shift from predominantly decarboxylation to decarbonylation at about 10 h without a change in external operating parameters. Further, when operating with only 0.38 atm H_2, decarboxylation predominates exclusively. Since our conversion was operated with 55 atm H_2, it is quite possible that decarbonylation was predominant from the outset. The internal volume of our reactor and product recovery system is such that the effluent gas composition does not reach a representative steady state for many hours. Consequently, we sampled the effluent only immediately prior to draining the liquid product from the receiver at the end of a collection period. If our catalyst also exhibited a transient period in which decarboxylation was dominant over decarbonylation, it would have gone undetected. Immer and Lamb also observed heptadecane exclusively as the alkane product whereas we observe both heptadecane and octadecane at all operating times, but with a growing selectivity toward octadecane. This may be related to the higher H_2 pressure in our measurements. A question that these measurements is unable to resolve is whether the octadecane arises exclusively from total reduction of the free stearic acid, or if under these higher H_2 pressures, cleavage can occur between

Table 3. Normal Alkane Content of Progressive Distillation Fractions between a Minimum and Maximum Atmospheric Equivalent Vapor Temperature of 145 and 345 °C for One of Three Distillations and the Composition of the Major Constituents in the Aggregate of the Distilled Fractions[a]

receiver start/end temp. (°C)	155/298	298/302	302/304	304/307	307/307	307/309	309/311		
normal alkane carbon no.				wt %				aggregate wt %	1-alcohol aggregate wt %
8	0.03	0.00	0.00	0.00	0.00	0.00	0.00	0.00	0.00
9	0.10	0.01	0.00	0.00	0.00	0.00	0.00	0.02	0.00
10	0.19	0.05	0.01	0.00	0.00	0.00	0.00	0.03	0.00
11	0.16	0.08	0.02	0.00	0.00	0.00	0.00	0.03	0.00
12	0.12	0.09	0.03	0.00	0.00	0.00	0.00	0.03	0.00
13	0.91	0.93	0.51	0.13	0.02	0.00	0.00	0.32	0.00
14	1.28	1.54	1.15	0.50	0.18	0.06	0.01	0.69	0.04
15	6.89	8.75	8.02	5.33	3.06	1.65	0.67	4.57	0.00
16	6.97	8.53	8.73	7.60	6.06	4.61	3.06	5.54	0.12
17	35.15	38.56	40.81	41.87	40.89	38.70	35.56	38.54	0.00
18	36.79	34.58	35.61	40.10	44.29	47.84	53.68	43.54	0.55
19	0.24	0.19	0.18	0.21	0.25	0.29	0.37	0.33	0.00
20	0.20	0.13	0.11	0.13	0.17	0.21	0.28	0.25	0.59
21	0.04	0.02	0.02	0.02	0.03	0.03	0.05	0.05	0.00
22	0.04	0.02	0.01	0.01	0.02	0.02	0.03	0.03	0.00
23	0.04	0.02	0.00	0.01	0.01	0.01	0.02	0.02	0.00
24	0.03	0.01	0.00	0.00	0.00	0.01	0.01	0.01	0.00
25	0.03	0.01	0.00	0.00	0.00	0.01	0.01	0.01	0.00
26	0.10	0.04	0.00	0.01	0.01	0.01	0.02	0.02	0.00
total	89.36	93.55	95.21	95.93	94.98	93.45	93.79	94.02	1.31

[a]The start and end temperature for filling each receiver is indicated. In this example, all receivers filled before reaching 345 °C. Only n-alkane carbon numbers contributing at least 0.01 wt % in some fraction are shown. Iso-alkanes, alcohols, and other oxygenates which contribute to the total FID signal are not included. As a result, the given total does not sum to 100%.

the carbonyl carbon and the acid oxygen to produce a free fatty aldehyde and an alcohol? We do observe small quantities of both 1-propanol and 1,2-propanediol in the segregated aqueous phase, which supports a reaction pathway producing a cleaved aldehyde. Krár et al. report high yields of octadecane when hydrotreating sunflower oil using a sulfided $CoMo/Al_2O_3$ catalyst but report only the detection of propane.[22] They make no mention of any product alcohols. Similarly, Kubička and Kaluža report high octadecane yields in vegetable oil deoxygenation over sulfided Ni, NiMo, and Mo catalysts without mention of product propanol.[19] These differing observations suggest a multitude of reaction pathways for converting the fatty acid side chains in biological triglycerides to alkanes depending on catalyst and reaction conditions.

During the final operating period noted in Table 2, a plug began to develop within the reactor, resulting in diminished gas flow. Consequently, the gas composition measured in that final period is likely not truly representative of the operating behavior of the system during that entire period. Following liquid collection in the last noted period, exit gas flow ceased entirely and the liquids collected had developed a yellow color. Such yellow discoloration is common when alkanes are in contact with precious metal catalysts at elevated temperatures and when the local H_2 partial pressure falls due to consumption and stagnation of fresh flow. This development terminated the first pass deoxygenation conversion run.

The relative propane amount follows the shift from carbonyl cleavage reaction pathways to complete reduction pathways. Early in the run, the detected moles of propane account for just under half the moles of triglyceride fed. At the point of highest alkane yield, the detected moles of propane account for just over 70% of the moles of triglyceride fed. The unaccounted-for three carbon glyceryl backbone is distributed over numerous

unquantified species. As noted above, propanol species are found in the aqueous fraction and a remnant of propyl stearate can also be detected. Where ethane, ethanol, and acetic acid arise is unclear but might also have a connection with the glyceryl species. Propene, while detected, never accounts for even 1% of the C_3 molecules detected. Similarly, methane is present in detectable, but not meaningful, quantities.

3.2. Separation of Alkane Products Following First Pass Triglyceride Conversion. Upon completion of the first pass conversion of the algal triglycerides, all of the individually collected fractions were combined for recovery of the targeted alkanes by distillation. The aggregate was large enough that three separate distillations were required. Each distillation was executed with the cut point temperatures noted above. Distillate collected between the lower and upper vapor temperature bounds of 145 and 345 °C was manually switched between receivers as each approached its 100 mL capacity. An example of how the composition evolved from the first to last receiver collected within the target fraction during one particular distillation is given in Table 3. The normal alkanes attributable to the C_{16} and C_{18} fatty acids, n-C_{15}, n-C_{16}, n-C_{17}, and n-C_{18}, account for between 96% and >99% of the recovered normal alkanes in each receiver. All of the aliquots from the first triglyceride conversion pass within the targeted vapor temperature bounds from each of the three distillations were combined into a single algal alkane aggregate with the composition also shown in Table 3. Note that the sum of the C_{14}, C_{16}, C_{18}, and C_{20} normal alcohols account for just over 1% of the total sample weight.

This range of alkanes is well suited for use as a synthetic diesel fuel with a typical composition spanning C_{10} to C_{22}. As normal alkanes, the low temperature properties of this composition are not acceptable, as considerable crystallization

of the n-C_{17} and larger constituents takes place at room temperature. To suppress crystallization to much lower temperature, isomerization of these alkanes using a hydro-isomerization catalyst is required. 700 mL of this aggregate were withdrawn for further processing. For conversion to a jet fuel composition, all of the principal constituents will need to be catalytically hydrocracked into a C_8 to C_{15} fraction. Experience with the hydrocracking of a Fischer–Tropsch wax to a synthetic paraffinic kerosene compliant with MIL-DTL-83133G[5] has taught us that the residual n-C_{15} fraction has a critical influence on the ability of the composition to meet the −47 °C maximum freezing point. In ideal bifunctional hydrocracking, the largest cracked constituent is three carbon atoms shorter than the cracked molecule.[23] If the objective were to convert all of the algal alkanes to a fully compliant HEFA jet, complete cracking of the C_{18} fraction alone will be inadequate, as this will result in a residual n-C_{15} fraction on the order of several percent. To reduce this residual to an acceptable level, estimated at less than 1 wt % of the total HEFA jet composition, some secondary cracking will be necessary. However, secondary cracking is unavoidable, as it will also be necessary to completely crack the C_{17} and C_{16} fractions from the starting composition. Unfortunately, this will result in considerable waste of the algal alkanes, since the likelihood of cracking is nearly equal for each of the n-4 to $n/2$ internal bonds of the original normal alkane.[23] Only a limited amount of a C_8 fraction can be tolerated, and nearly none of the C_7 and smaller fraction can remain in the HEFA jet in order to meet the flash point requirements. We explore this issue of maximizing useful output by exploring three approaches to producing a HEFA composition detailed below. To adjust the catalytic hydrocracking operating parameters to achieve the targeted conversions, multiple adjustments in response to product composition will be required. This will consume considerable feed before an acceptable product composition is achieved. Therefore, a larger fraction of the algal alkane mixture has been reserved for exploring conversion to a HEFA jet composition.

3.3. Second Pass Conversion of Partially Converted Triglycerides to Alkanes. The second pass conversion of the distillation bottoms recovered from separating the first pass alkanes was also done at 350 °C and with the liquid volumetric and H_2 feed rate the same as that employed in the first pass conversion of the triglycerides. The complex nature of the incompletely converted mixture precludes determining a measure of conversion. About 20% of the mixture is made up of n-C_{17} and n-C_{18}, and the remainder is a multitude of partial conversion products such as 1-octadecanol, stearic acid, and propyl stearate and secondary reaction products such as the esters formed by condensation of 1-hexadecanol or 1-octadecanol with stearic acid to form heavy esters. These latter components make up about 60% of the mixture. The effluent gas composition, shown in Table 4, has a higher relative contribution of CO_2 than observed during the first pass conversion, but CO still dominates the reaction products resulting from carbonyl cleavage from the rest of the fatty acid chain. GC-MS was used to identify the principal constituents in the liquid product stream. Table 5 shows the relative normalized peak areas corresponding to all constituents registering greater than 0.1% of the total area. Normal alkanes made up 55% of the liquid product, which is a much smaller relative amount than observed when the neat triglycerides were fed in the first deoxygenation pass, especially when accounting

Table 4. Major Effluent Gas Constituents Other than Feed H_2 during the Second Pass Deoxygenation

effluent gas constituents	vol %
CO	0.89
CO_2	0.13
ethane	0.01
propane	0.16
exit flow (mL/min)	130

**Table 5. GCMS Analysis of the Product Composition during the Second Catalytic Deoxygenation Pass**

mass spectrometer analysis of principal GC peaks	
area %	compound
0.31	n-tridecane
1.26	n-tetradecane
3.63	n-pentadecane
2.81	n-hexadecane
25.73	n-heptadecane
19.32	n-octadecane
0.24	heptadecenal
0.33	n-nonadecane
0.15	n-hexadecanoic acid
0.29	n-eicosane
0.14	1-octadecanol
0.67	propyl palmitate
0.2	heneicosane (n-C_{21})
5.26	stearic acid
0.81	acetyl stearate
0.21	n-C_{22}
3.85	propyl stearate
0.25	n-C_{23}
0.19	n-C_{24}
0.29	n-C_{25}
0.78	n-C_{26}
0.59	nonacosanol
5.64	palmityl stearate
22.75	stearyl stearate

for their presence in the feed. Also, in contrast to the even/odd ratios found during the first deoxygenation pass, the odd numbered n-1 alkanes are now in higher abundance than their even numbered companion. Nevertheless, this second pass conversion brings to nearly 95% the total mass of alkane recovered from the conversion of the initial triglyceride. As with the first pass alkane product, the desired fraction in this second pass product was recovered by distillation and combined with the remaining first pass alkanes to yield the final alkane composition used in further conversions to HEFA jet compositions.

3.4. Conversion of the First Pass Alkane Aggregate to a Diesel Fuel Composition. The aggregate product described in Table 3 was used as a starting material for preparing a diesel fuel composition. As prepared, the range of carbon numbers falls within the usual C_{10}–C_{22} range considered as diesel fuel. However, being nearly exclusively normal alkanes, this composition would be unsuitable by itself as a fuel due to the crystallization of the heavier components in the mixture at temperatures near 25 °C. While it might be possible to blend this renewable composition into a petroleum-derived fuel at a proportion that would allow the composite to meet relevant pour point specifications, a desire for a purely renewable fuel

Table 6. Detailed Composition of the Raw and Distilled Product Obtained by Hydroprocessing the Aggregate Product Described in Table 3 over a 0.5% Pt/US-Y Zeolite Catalyst

hydroprocessed product composition				distilled product composition				dewaxed product composition			
carbon no.	total wt %	normal wt %	isomer wt %	carbon no.	total wt %	normal wt %	isomer wt %	carbon no.	total wt %	normal wt %	isomer wt %
5	0.88	0.20	0.68	5	0.02	0.00	0.01	5	0.01	0.00	0.01
6	1.40	0.28	1.11	6	0.04	0.01	0.03	6	0.00	0.00	0.00
7	1.90	0.33	1.57	7	0.17	0.04	0.13	7	0.21	0.02	0.19
8	2.30	0.33	1.96	8	0.71	0.13	0.57	8	0.22	0.10	0.12
9	2.47	0.33	2.14	9	1.73	0.28	1.45	9	1.60	0.25	1.35
10	2.48	0.32	2.16	10	2.61	0.35	2.25	10	2.89	0.35	2.54
11	2.28	0.25	2.02	11	2.59	0.29	2.30	11	3.00	0.32	2.68
12	1.94	0.19	1.75	12	2.19	0.21	1.98	12	2.73	0.27	2.46
13	1.87	0.32	1.55	13	2.11	0.35	1.76	13	2.63	0.44	2.19
14	2.11	0.68	1.44	14	2.30	0.73	1.57	14	6.92	3.44	3.48
15	4.56	2.10	2.46	15	4.94	2.29	2.64	15	6.29	2.33	3.97
16	9.25	3.43	5.81	16	9.74	3.60	6.15	16	8.47	1.73	6.74
17	33.34	14.59	18.75	17	35.79	15.94	19.85	17	31.88	4.07	27.81
18	32.25	15.28	16.97	18	34.36	16.61	17.75	18	30.46	1.75	28.71
19	0.26	0.10	0.16	19	0.26	0.11	0.16	19	0.50	0.00	0.50
20	0.19	0.07	0.12	20	0.20	0.08	0.12	20	0.27	0.00	0.27
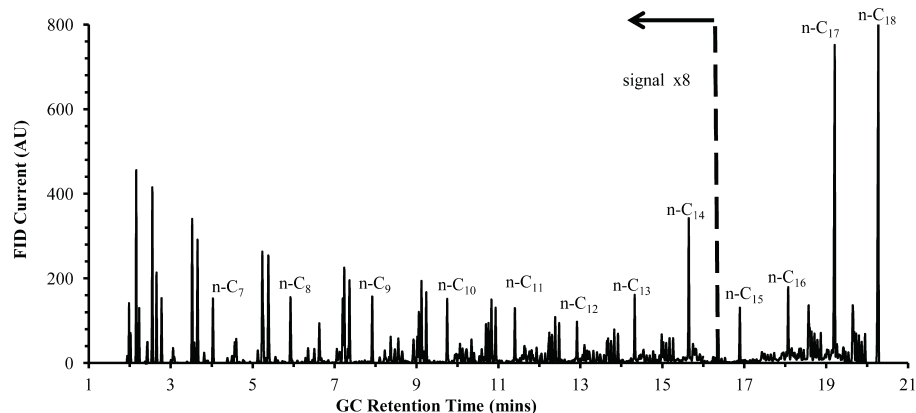
Figure 1. Chromatogram of the composite product obtained by hydroprocessing the normal alkane aggregate described in Table 3. Conditions were selected that produced a feed isomer/normal ratio a bit larger than 1. At that condition, hydrocracking does occur and gives rise to the distribution of cracked products shown.

would require isomerization of these normal alkanes into a suitably isomer-rich mixture. We have undertaken further processing of these normal alkanes to produce a diesel fuel composition that would have a pour point suitable for use in extreme low temperature applications.

The selected catalyst operating conditions of 258 °C, LHSV = 3/h, 140 mL/min H_2 at 800 psig result in conversions ranging from about 65% for the n-C_{18} to about 50% for the n-C_{15}. Under these conditions, about 25% of the C_{18} undergoes hydrocracking while less than 5% of the C_{15} cracks. For the diesel composition, we would like to preserve as high a proportion of the alkanes in an uncracked state as possible while achieving as high a state of isomerization as possible. Since we have a limited amount of the algal alkanes with which to work, we elected conditions that produced a feed isomer/ normal ratio a bit larger than 1. The feed isomer composition is a mixture of primarily mono- and dimethyl branched alkanes also in roughly equal relative abundance. The detailed alkane product composition is shown in Table 6 along with the corresponding chromatogram in Figure 1. Since cracking yields

molecules too light for typical diesel use, it again became necessary to separate the light fraction from the heavier fraction to be further processed into a cold-weather suitable fuel. The distilled product composition is also given in Table 6.

With over 30% of the distilled diesel fraction coming from n-C_{17} and n-C_{18}, this potential fuel begins shedding crystals just below room temperature, making it unsuitable for practical use as a neat fuel. A higher degree of feed isomerization would produce a composition that would remain solids-free down to temperatures near 0 °C but at the expense of additional cracking. At even lower temperatures, such as those encountered in high latitude climates during winter, where temperatures of −20 °C are frequently encountered, this entire composition solidifies. Therefore, we have undertaken a solvent dewaxing procedure, to reduce the residual normal alkanes to the point where the overall composition remains a liquid at −20 °C. The chromatogram for this dewaxed composition is shown in Figure 2, and the detailed composition also shown in Table 6. With dewaxing, the n-C_{17} and n-C_{18} contribution is now just under 11% while the distribution of isomers has
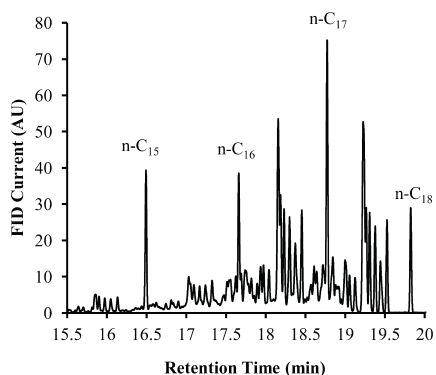
Figure 2. Chromatogram of the $C_{15}-C_{18}$ range in the dewaxed diesel fraction.

remained virtually unchanged. We have employed a solvent dewaxing method to accomplish this improvement in low temperature properties. For practical applications, a more desirable approach would be selective catalytic dewaxing in which the normal alkanes are preferentially isomerized rather than cracked.[24]

As can be seen in Table 6, the C_{8-} fraction is just under 7% of the total mass. With higher isomerization of the feed, additional cracking will also occur. An optimum conversion would be greater than observed here at 258 °C but not as high as observed when focusing on an aviation fuel at 268 °C, as described more fully below. At the 268 °C operating point, the C_{8-} fraction is about 15%. Thus, we believe that a strategy for preserving the overall fuel value of the algal alkanes while also producing practically useable fractions will focus on feed isomerization to a diesel composition with acceptable low temperature properties while recovering the cracked fraction in

the jet fuel range for use as a HEFA jet. Such an approach should limit losses to the C_{8-} fraction to less than 10%.

3.5. Conversion of the Composite Alkane Aggregate to a HEFA Jet Composition. Synthetic paraffinic kerosene (SPK) has been approved for both U.S. military and commercial aviation use as a 50/50 blend with petroleum derived Jet-A or Jet-A1 fuel.[25] The appropriate specification for this SPK can be found in MIL-DTL-83133G.[5] When derived from renewable triglycerides, these SPKs are typically referred to as HEFA jet, hydroprocessed esters and fatty acids. The algal compositions of this work fall into this designation. Typically, C_9-C_{15} alkane isomers make up the bulk of these SPK compositions with minor contributions from C_{8-} and C_{16+} isomers.[25] Since C_{17} and C_{18} will contribute the majority of the deoxygenated mass from natural triglycerides, hydrocracking is required to shift the composition into the SPK range. This results in an unavoidable yield loss, since only minor shifts in cracking selectivity can be effected through a combination of catalyst and operating conditions.[23] When catalytically hydrocracking a C_n alkane, the range of cracked products will be predominantly found in the C_3 to C_{n-3} range.[23] Consequently, the portion in the C_3-C_8 range (naphtha) will be unsuitable for use in SPK. These losses become relatively greater as the starting molecule becomes progressively smaller. Under practical conditions, as much as 40−50 wt % of the cracked distribution from a triglyceride-derived n-alkane mixture can be shifted out of the useful range.

In this work, we have examined three approaches to converting the algal n-alkane starting mixture to a HEFA jet. In the first approach, the single pass conversion is higher than that used for mildly isomerizing the feed alkanes to a diesel type of composition, with net cracking targeted near 50%. In so doing, the feed n-alkanes become substantially isomerized and can be separated from the jet fraction and used directly as a diesel fuel composition. Alternatively, this heavier fraction could be recombined with fresh feed in a recycle to extinction

Table 7. Feed and Product Compositions at the Three Levels of Conversion Severity when Targeting HEFA Jet

alkane composition	feed n-alkanes			modest feed cracking T = 268 °C			higher feed cracking T = 272 °C			feed alkanes cracked to extinction T = 278 °C		
carbon no.	total mass %	n-alkane mass%	iso-alkane mass %	total mass %	n-alkane mass%	iso-alkane mass %	total mass %	n-alkane mass%	iso-alkane mass %	total mass %	n-alkane mass%	iso-alkane mass %
4	0.00	0.00	0.00	0.63	0.21	0.42	0.82	0.27	0.54	2.37	0.74	1.63
5	0.00	0.00	0.00	1.88	0.44	1.43	2.45	0.58	1.87	6.06	1.38	4.68
6	0.01	0.00	0.00	3.02	0.66	2.36	3.98	0.88	3.09	8.85	1.90	6.95
7	0.04	0.01	0.03	4.22	0.80	3.41	5.76	1.11	4.65	11.72	2.20	9.52
8	0.12	0.03	0.10	5.36	0.85	4.51	7.50	1.20	6.30	14.07	2.17	11.90
9	0.23	0.06	0.17	5.98	0.85	5.13	8.37	1.19	7.18	14.36	1.92	12.44
10	1.03	0.79	0.24	7.14	1.37	5.77	9.72	1.65	8.06	14.75	2.02	12.73
11	0.18	0.07	0.12	5.77	0.60	5.17	8.08	0.81	7.27	11.14	0.99	10.15
12	0.17	0.08	0.09	5.09	0.51	4.58	7.03	0.67	6.36	7.97	0.63	7.34
13	0.62	0.45	0.17	4.46	0.59	3.87	5.75	0.67	5.09	4.64	0.33	4.31
14	2.93	2.03	0.90	4.48	0.81	3.68	4.78	0.63	4.14	2.14	0.12	2.01
15	5.17	5.07	0.10	3.94	1.11	2.82	3.37	0.69	2.68	0.59	0.04	0.56
16	6.08	5.94	0.14	5.38	0.88	4.50	4.30	0.46	3.84	0.30	0.01	0.29
17	38.03	37.43	0.60	21.02	4.37	16.65	14.81	1.97	12.83	0.43	0.02	0.41
18	43.38	42.21	1.16	21.08	3.87	17.21	12.89	1.49	11.40	0.19	0.01	0.18
19	0.82	0.34	0.48	0.20	0.02	0.18	0.10	0.01	0.09	0.02	0.00	0.02
20	0.51	0.30	0.21	0.11	0.02	0.10	0.05	0.01	0.05	0.02	0.00	0.02
21	0.17	0.07	0.10	0.03	0.00	0.03	0.02	0.00	0.02	0.02	0.00	0.02
22	0.10	0.05	0.04	0.02	0.00	0.02	0.02	0.00	0.02	0.02	0.00	0.02
23	0.09	0.03	0.06	0.02	0.00	0.02	0.01	0.00	0.01	0.01	0.00	0.01

strategy and eventually wholly converted to jet and naphtha fractions. Under these mildest of cracking conditions, the cracked product distribution would remain unchanged by further, secondary cracking of the initial product distribution. In a second approach, a more aggressive operating point is selected such that the onset of secondary product cracking is just detected. Again, the heavier-than-jet fraction can be separated and either used directly as diesel or recycled to extinction. In the most aggressive approach, the feed is converted so fully in a single pass that only a negligible portion of the composition heavier than jet remains. This would result in no diesel and require only the separation of the naphtha fraction from the jet fraction. Since water can affect the performance of the acid function in the bifunctional Pt/US-Y zeolite catalyst used in these transformations,[10] we elected to reduce any remaining oxygenates to a minimum prior to further fuel-making processing, as noted in the experimental description. Table 7 presents the feed and effluent compositions as well as the reactor temperature required to achieve them while holding pressure at 800 psig and LHSV at 1/h.

As an estimate of cracking conversion, we have taken the difference between the sum of the $C_{15}-C_{23}$ amounts in the feed and effluent compositions. While the feed components larger than C_{18} can contribute cracked products into this range, their total amount is sufficiently small that the fraction of cracked products overlapping with the feed composition presents a negligible error. A slightly larger error arises from counting C_{15} exclusively as feed, since the first major cracking product from C_{18} will be C_{15}. However, in the two intermediate cracking cases, this results in a modest error. In the extinction case, the error is reduced by the high extent of both primary and secondary cracking. Using these criteria, the three conditions result in about 43%, 59%, and 93% cracking at temperatures of 268 °C, 272 °C, and 278 °C, respectively. A second figure of merit is the fraction of the effluent that falls in the C_{8-} naphtha fraction. This fraction is lost from the useable HEFA jet fuel range. In the three examples of Table 7, the C_{8-} fractions comprise 15%, 21%, and 43% of the recovered reactor effluent. By comparing liquid mass fed with liquid mass recovered, potential additional losses to vapor products are found to be inconsequential. Clearly, conversion of these algal alkanes to a HEFA jet fuel with the selected catalyst is not a high yield undertaking. If we normalize the naphtha loss to the mass found in the C_9-C_{15} fraction, the relative losses become 41%, 44%, and 75%, respectively. The increase from 41% to 44% reflects the added loss resulting from the onset of secondary cracking. In principle, the normalized cracked fraction molar distribution should be similar at all conversions until secondary cracking sets in. This is supported by the 40% obtained when comparing the relative amounts of C_4-C_8 with C_9-C_{15} observed under diesel isomerization conditions noted in Table 6. From the standpoint of fuel-making efficiency, a strategy in which only the jet fraction is targeted clearly results in much lower yields of high value fuel. The observed 40% loss to naphtha agrees well with the estimates made based on bifunctional hydrocracking chemistry.

The fuel freezing point is an important characteristic of HEFA jet and is limited to −47 °C in JP-8.[5] In other work, we have found that the normal alkane content of the higher carbon numbers has the most direct influence on this property. When converting these algal alkanes, the feed contains normal $C_{14}-C_{16}$. However, the C_{16} content is sharply reduced through

distillation, as the SPK is primarily constituted of the C_9-C_{15} alkanes. Thus, under partial cracking conditions, the relative contribution of normal alkanes in this range is a combination of residual feed normal as well as the normal alkanes formed from the cracking reaction. As can be seen in Table 7, the (n-C_{14} + n-C_{15})/SPK mass ratio is 0.052, 0.028, and 0.003 for conversion at 268 °C, 272 °C, and 278 °C, respectively. In the separation of SPK from the remainder of the stream, the C_{15} content will be reduced further, with the normal alkane reduced relatively more than the isomerized portion of that carbon number. With that in mind, we have examined the (n-C_{14} + n-C_{15})/SPK mass ratio found in a variety of SPKs held by the Air Force Research Laboratory. They range from a high of 0.034 to a low of 0.004. Therefore, we believe SPK recovered from a stream with a composition like that obtained at 268 °C would not meet the freezing point specification unless half of the C_{15} fraction were excluded from the product. The ratio at 272 °C is sufficiently low that the small further diminution in this part of the distribution by separation from the heavier remnants will likely allow it to achieve the required freezing point. We have no doubt that the highly cracked and isomerized product obtained at 278 °C will meet the freezing point requirement.

3.6. Maximizing the Fuel Value of the Algal Alkanes. To be used as a fuel, the alkanes obtained from deoxygenation of triglycerides must undergo some isomerization if they are to constitute a significant fraction of a final fuel. As shown, accompanying that isomerization will necessarily be some cracking as well. Once cracking occurs, loss of fuel value to the C_{8-} naphtha fraction is unavoidable. However, an overly high normal alkane content will produce a diesel fraction with unacceptable cold flow properties. Therefore, the deciding factor in maximizing the fuel yield from any natural triglyceride is the required low temperature properties of the produced diesel fuel. Although the typical ASTM specification for diesel fuel, D-975, provides methods for determining low temperature properties such as cloud or pour point, no firm value is specified.[26] Another factor influencing the required extent of isomerization is whether a SPK product is also required. Since the diesel fuel fraction could accommodate the cracked product down to C_{10}, these highly isomerized, lower molecular weight constituents could help improve the lower temperature properties of the composite diesel fuel by helping to solvate the higher weight normal alkanes, thereby reducing the need for further cracking. However, if SPK is required as a separate product, then the boiling point range specification in MIL-DTL-83133G[5] forces the inclusion of some heavier components. However, as evidenced by the Shell FT fuel described by Corporan et al., the distribution need not extend fully to C_{15}.[25]

From a process economic perspective, minimizing the number of operations required to produce the product slate is desirable. We employed a solvent dewaxing operation to improve the low temperature properties of a mildly isomerized algal alkane aggregate. The fraction removed by freezing can then also be separated from the solvent and returned to the hydroisomerization feed stream for further processing. A more efficient approach employs catalytic, rather than solvent, dewaxing.[24] In catalytic dewaxing, the normal fraction of the mixture is selectively isomerized while minimizing the further reaction of the already isomerized constituents. We have been unable to ascertain how much such an approach would reduce parasitic cracking losses from either open or patent literature. Such an approach has the benefit of being continuous but is best suited to producing diesel, rather than aviation, fuel. A

216

general conclusion is that the value of alkanes derived from natural triglycerides is maximized when they are used primarily as a diesel fuel. However, in light of renewable aviation fuel requirements, the most economically appealing product distribution will depend critically on the exact triglyceride composition, or potential range of compositions, to be converted to aviation fuel.

4. CONCLUSIONS

We have demonstrated the conversion of algal triglycerides to both diesel and HEFA jet fuel compositions. Using a 3% Pd/C catalyst at the fixed conditions of WHSV = 1.5/h, T = 350 °C, P = 800 psig and an H_2/triglyceride molar ratio of 30, normal alkanes comprise over 85% of the aggregate recovered effluent. Both the C_{n-1} and C_n alkanes stemming from an initial $C_{n-1}COOH$ fatty acid side chain are recovered, with the C_n alkanes being 15–20% more abundant in the combined aggregate of all the produced alkanes. We observe decarbonylation to be the predominant pathway to the C_{n-1} alkane, with the CO/CO_2 typically in excess of 9. The catalyst maintained high activity for over 190 continuous hours and exhibited considerable performance evolution over that time. Most notably, decarbonylation accounted for the majority of the alkanes formed at the beginning of the run, but complete reduction produced the majority of alkanes at the end of the run. Further, the catalyst became more active for the reduction pathway with time on stream. Decarboxylation appeared to operate at a near constant and much lower rate than the other two main pathways. Rather than catalyst deactivation forcing run termination, a physical obstruction of uncertain origin resulted in a plugged reactor. The desired n-alkanes were separated from the remaining free acids and heavy esters by distillation, although a small but significant amount of 1-alcohol was also recovered with the alkanes.

The incompletely converted material recovered from the distillation pot was processed a second time over a fresh charge of the same catalyst at the same temperature, pressure, and flow rates used for the fresh triglyceride feed. In contrast to first pass conversion of the triglycerides, the heavy esters formed in the first pass from condensation of partially reduced alcohols and free fatty acids undergo only modest conversion to alkanes in the second pass. Also, the combined decarbonylation plus decarboxylation pathways predominate, as indicated by the much higher proportion of recovered odd numbered n-alkanes. The relative contribution of decarbonylation and decarboxylation still strongly favors decarbonylation but to a slightly smaller degree than observed during first pass conversion.

Before converting the n-alkane mixture over the Pt/US-Y zeolite bifunctional hydrocracking catalyst, residual oxygenates were converted to water over a Pt/alumina catalyst. The water was separated from the remaining hydrocarbon mixture. The first pass alkanes, comprised principally of 4.6% n-C_{15}, 5.5% n-C_{16}, 38.5%, and 43.5% n-C_{18} were mildly hydroisomerized using a Pt/US-Y zeolite catalyst in order to improve cold flow properties. Isomerization was held to just over 50% so as to limit undesired cracking to even lighter products. The combined isomerized and cracked composition was distilled so as to remove the fraction too light for a diesel fuel. With the high concentration of remaining n-C_{17} and n-C_{18}, cold flow properties were still unacceptable for low temperature use. Further reduction in n-alkane content relative to the isomerized fraction was achieved using solvent dewaxing to produce a fuel composition which remained fluid at −20 °C.

Three approaches for converting the algal alkanes to a HEFA jet only composition were investigated. The three approaches differ in the extent of single pass cracking conversion targeted. The three conditions result in about 43%, 59%, and 93% net cracking at temperatures of 268 °C, 272 °C, and 278 °C, respectively. Only under the most aggressive single pass conditions are the heaviest molecules sufficiently reduced in abundance that no recycle of the insufficiently converted fraction would be needed in a continuous conversion process. Under the least aggressive conditions, it is doubtful that the amount of remaining n-C_{14} and n-C_{15} is low enough that the HEFA jet fraction would meet the −47 °C freezing point requirement under MIL-DTL-83133G for JP-8. Under these three conditions, losses to the C_{8-} naphtha fraction when normalized to the C_9–C_{15} fraction comprise 41%, 44%, and 75%, respectively. Because of these high losses, a renewable aviation turbine fuel strategy that preserves the overall highest liquid fuel yield would target the production of primarily diesel fuel. The aviation fuel would then be recovered from the cracked fraction that naturally accompanies the hydroisomerization of the original n-alkanes to the extent required for meeting an appropriate diesel fuel pour point specification. Such an approach would limit the loss of algal alkane fuel value to less than 10%.

■ AUTHOR INFORMATION

Corresponding Author
*Phone: +1 (937) 229-2349. E-mail: heinz.robota@udri.udayton.edu.
Notes
The authors declare no competing financial interest.

■ REFERENCES

(1) Kubičková, I.; Kubička, D. *Waste Biomass Valorization* **2010**, *1*, 293−308.
(2) Bezergianni, S.; Voutetakis, S.; Kalogianni, A. *Ind. Eng. Chem. Res.* **2009**, *48*, 8402−8406.
(3) Šimáček, P.; Kubička, D.; Kubičková, I.; Homola, F.; Pospíšil, M.; Chudoba, J. *Fuel* **2011**, *90*, 2473−2479.
(4) ASTM D-1655 *Standard Specification for Aviation Turbine Fuels*; ASTM: West Conshohocken, PA, 1994.
(5) MIL-DTL-83133G *Detail Specification, Turbine Fuel, Aviation, Kerosene type, JP-8 (NATO F-34), NATO F-35, and JP-8 + 100 (F-37)*; Department of Defense: Washington DC, 2010.
(6) Directive 2009/28/EC of the European Parliament and of the Council of 23 April 2009 on the Promotion of the Use of Energy from Renewable Sources and Amending an Subsequently Repealing

Directives 2001/77/EC and 2003/30/EC. *Official Journal of the European Union* **2009**, L 140/15.

(7) *Biofuels: Policies, Standards, and Technologies*; World Energy Council: London, 2010.

(8) Kubička, D.; Horáček, J. *Appl. Catal. A* **2011**, *394*, 9−17.

(9) Kubička, D.; Kaluža, L. *Appl. Catal. A* **2010**, *372*, 199−208.

(10) Lekel, D. *Energy Fuels* **2007**, *21*, 662−667.

(11) ASTM D-5442-93 *Standard Test Method for Analysis of Petroleum Waxes by Gas Chromatography*; ASTM: West Conshohocken, PA, 2008.

(12) Claude, M. C.; Vanbutsele, G.; Martens, J. A. J. *Catalysis* **2001**, *203*, 213−231.

(13) Kubičková, I.; Snåre, M.; Eränen, K.; Mäki-Arvela, P.; Murzin, D. Y. *Catal. Today* **2005**, *106*, 197−200.

(14) Snåre, M.; Kubičková, I.; Mäki-Arvela, P.; Chicova, D.; Eränen, K.; Murzin, D. Y. *Fuel* **2008**, *87*, 933−945.

(15) Mäki-Arvela, P.; Kubičková, I.; Snåre, M.; Eränen, K.; Murzin, D. Y. *Energy Fuels* **2007**, *21*, 30−41.

(16) Immer, J. G.; Lamb, H. *Energy Fuels* **2010**, *24*, 5291−5299.

(17) Rozmysłowicz, B.; Mäki-Arvela, P.; Tokarev, A.; Leino, A. R.; Eränen, K.; Murzin, D. Y. *Ind. Eng. Chem. Res.* **2012**, *51* (26), 8922−8927.

(18) Do, P. T.; Chiappero, M.; Lobban, L. L.; Resasco, D. E. *Catal. Lett.* **2009**, *130*, 9−18.

(19) Kubička, D.; Kaluža, L. *Appl. Catal. A* **2010**, *372*, 199−208.

(20) Han, J.; Duan, J.; Chen, P.; Lou, H.; Zheng, X.; Hong, H. *Green Chem.* **2011**, *13*, 2561−2568.

(21) Moe, J. M. *Chem. Eng. Progress* **1962**, *58* (3), 33−36.

(22) Krár, M.; Kovács, S.; Kalló, D.; Hancsók, J. *Bioresour. Technol.* **2010**, *101*, 9287−9293.

(23) Bouchy, C.; Hastoy, G.; Guillon, E.; Martens, J. A. *Oil Gas Sci. Technol.—Rev. IFP* **2009**, *64*, 91−112.

(24) Degnan, T. F., Jr. *Stud. Surf. Sci. Catal.* **2007**, *170*, 54−65.

(25) Corporan, E.; Edwards, T.; Shafer, L.; DeWitt, M. J.; Klingshirn, C.; Zabarnick, S.; West, Z.; Striebich, R.; Graham, J.; Klein, J. *Energy Fuels* **2011**, *25*, 955−966.

(26) ASTM D-975 *Standard Specification for Diesel Fuel Oils*; ASTM: West Conshohocken, PA, 1999.

218

Appendix O. Transcriptional Profiling Suggests that Multiple Metabolic Adaptations are Required for Effective Proliferation of Pseudomonas aeruginosa in Jet Fuel

Transcriptional Profiling Suggests that Multiple Metabolic Adaptations are Required for Effective Proliferation of *Pseudomonas aeruginosa* in Jet Fuel

Thusitha S. Gunasekera,[†] Richard C. Striebich,[†] Susan S. Mueller,[†] Ellen M. Strobel,[‡] and Oscar N. Ruiz*[,‡]

[†]University of Dayton Research Institute, University of Dayton, Dayton Ohio 45469, United States

[‡]Aerospace Systems Directorate, Fuels and Energy Branch, Air Force Research Laboratory, 1790 Loop Road, Bldg. 490, Wright-Patterson AFB, Ohio 45433, United States

Ⓢ *Supporting Information*

ABSTRACT: Fuel is a harsh environment for microbial growth. However, some bacteria can grow well due to their adaptive mechanisms. Our goal was to characterize the adaptations required for *Pseudomonas aeruginosa* proliferation in fuel. We have used DNA-microarrays and RT-PCR to characterize the transcriptional response of *P. aeruginosa* to fuel. Transcriptomics revealed that genes essential for medium- and long-chain *n*-alkane degradation including *alkB1* and *alkB2* were transcriptionally induced. Gas chromatography confirmed that *P. aeruginosa* possesses pathways to degrade different length *n*-alkanes, favoring the use of *n*-C_{11-18}. Furthermore, a gamut of synergistic metabolic pathways, including porins, efflux pumps, biofilm formation, and iron transport, were transcriptionally regulated. Bioassays confirmed that efflux pumps and biofilm formation were required for growth in jet fuel. Furthermore, cell homeostasis appeared to be carefully maintained by the regulation of porins and efflux pumps. The Mex RND efflux pumps were required for fuel tolerance; blockage of these pumps precluded growth in fuel. This study provides a global understanding of the multiple metabolic adaptations required by bacteria for survival and proliferation in fuel-containing environments. This information can be applied to improve the fuel bioremediation properties of bacteria.
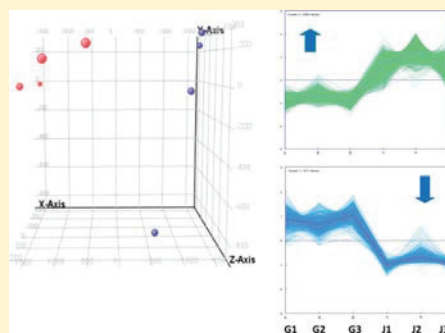
■ INTRODUCTION

Pseudomonas aeruginosa can adapt to diverse ecological niches due to its metabolic versatility.[1] *P. aeruginosa* has been shown to grow in jet fuel storage systems and petroleum oil fields and is able to degrade a wide range of hydrocarbons.[2,3] Thus, *P. aeruginosa* has been proposed as an important microorganism for bioremediation of light non-aqueous phase liquids (LNAPLs).[4,5] Normal alkanes in fuels are metabolized via oxidation and are used as a sole carbon source for energy and growth. The *P. aeruginosa* genome encodes two membrane-bound alkane hydroxylases (AlkB1 and AlkB2) and essential electron transfer proteins, rubredoxins (RubA1, RubA2), and FAD-dependent NAD(P)H2 rubredoxin reductases required for alkane degradation.[6,7] In addition to AlkB1 and AlkB2 monooxygenases, bacteria also utilize soluble heme-thiolate prokaryotic-P450 monooxygenases to oxidize *n*-alkanes. Both membrane-bound AlkB and cytochrome P450 act efficiently on medium chain alkanes ranging from C_5-C_{16}.[8] However, the physiological signal that regulates the alkane degradation pathway of *P. aeruginosa* is not well known. On the other hand, it is known that in *Pseudomonas putida* GpO1 the *alk* genes are regulated by AlkS, which activates the expression of the alkane degradation pathway in presence of alkanes. The expression of the alkane degradation pathway is also regulated by a catabolic repression control (CRC) system that represses the *alk* genes depending on the availability of simple carbon sources in the growth environment.[9,10] Another difference between *P. aeruginosa* PAO1 and *P. putida* GpO1 is that the alkane degradation genes in GpO1 are grouped in two clusters located on the OCT plasmid,[11] whereas in *P. aeruginosa* PAO1 the *alk* genes are located in the chromosome.

Although *P. aeruginosa* is equipped with the basic machinery to consume fuel as a carbon source, fuel is considered a harsh environment for bacteria to survive. Therefore, bacteria prefer to proliferate in the water phase or fuel−water interface. To encounter these adverse conditions, bacterial cells have developed multiple adaptations, including the ability to change the cell surface hydrophobicity and form biofilms,[12] regulate outer membrane porins and membrane permeability, and extrude toxic compounds. Biofilms are the aggregation of cells enclosed in a matrix of polymeric compounds, primarily

220

exopolysaccharides (EPS).[13,14] Biofilms are important for bacteria to survive when environmental conditions deteriorate. Bacteria are capable of producing biofilms on a number of different surfaces including fuel tank walls, fuel lines, and the fuel−water interfaces.[15,16] *P. aeruginosa* secretes alginate that produces the specific characteristic observed in the biofilms formed in the lungs of cystic fibrosis patients.[14] EPS helps to avoid direct contact of cells with fuel. In this study, we show that genes responsible for alginate biosynthesis and alginate transport across the cell inner membrane have been transcriptionally induced, indicating that the fuel environment can promote biofilm formation.

Jet fuel contains aromatic and cyclic hydrocarbons which are toxic to the cell.[17−19] Also, fuel can capture heavy metals during transport and storage, which may also affect bacteria. It has been proposed that membrane proton antiporter-pumps of the resistance-nodulation-division (RND) family can function in the extrusion of toxic compounds including antimicrobials, organic solvents, and heavy metals.[20] The tripartite efflux pumps MexAB-OprM, MexCD-OprJ, and MexEF-OprN have been shown to provide broad resistance to antibiotics and different aromatic compounds in *P. aeruginosa*.[20,21] Homologous proteins in *E. coli* encoded by the *acrAB/EF*-Tol genes have shown similar activity.[19,22] Deletion of these efflux pump systems rendered the cell susceptible to toxic molecules.[20] Outer membrane porins have been shown to have an essential role in the adaptation of bacteria to different environments. Porins can transport everything from glucose and carbohydrates to phosphate, polyphosphate, and even organic solvents, such as toluene and naphthalene.[23−25] Previous studies showed that *P. aeruginosa* cells lacking the outer membrane proteins OprF were highly resistant to the toxic effects of toluene.[23] The protein OprG has also been linked to the transport of solvents, such as naphthalene into the cell.[24,25]

Although the fundamental aspects of the metabolic machinery and pathways involved in the utilization of hydrocarbons may be known, the transcriptional expression profiles of genes involved in survival, adaptation, and proliferation of bacterial cells in fuel have not been well characterized. Therefore, we initiated a whole genome expression analysis using Affymetrix microarray chips against *P. aeruginosa* PAO1 in order to study the transcriptional profile of the fuel degrading strain *P. aeruginosa* ATCC 33988, which was originally isolated from a fuel tank. We utilized the available microarray chip for the PAO1 strain, which also encodes functional genes responsible for fuel degradation.[2,26,27] In addition, we have used quantitative reverse transcription polymerase chain reaction (qRT-PCR) to confirm the results obtained through microarray analyses. Chemical analyses using gas chromatography−mass spectrometry (GC-MS) allowed us to describe the degradation profile of jet fuel and the progression and consumption rate of fuel hydrocarbons, including *n*-alkanes, and cyclic and aromatic hydrocarbons. Finally, we performed functional assays in the presence of fuel to determine the formation of biofilms and the role of efflux pumps in the resistance of toxic compounds and proliferation of bacteria in fuel. Here, we provide a comprehensive description of the transcription profile of *P. aeruginosa* when exposed to jet fuel. The results demonstrate how multiple metabolic pathways and adaptations take place for effective proliferation of bacteria in fuel. This study provides a new global understanding of the genetic and metabolic plasticity of bacterial cells. This knowledge can be used in combination with genetic engineering, biotechnological, and environmental engineering approaches to enhance characteristics such as nutrient uptake, biofilm formation, surfactant production, and tolerance to toxic compounds in order to improve the potential of bacteria for detoxification and bioremediation of hydrocarbons and LNAPLs.

■ MATERIALS AND METHODS

Bacteria Strains and Growth Condition. The *P. aeruginosa* strain ATCC 33988 originally isolated from a fuel storage tank was used in this study. *P. aeruginosa* ATCC 33988 was initially grown in LB (Lysogeny broth) medium overnight at 28 °C. Cells were harvested by centrifugation at 10,000 rpm for 5 min. Cells were then washed twice with M9 minimal medium to remove trace amounts of LB before inoculation to M9 minimal medium. Four independent cultures of *P. aeruginosa* were grown in M9 minimal media with filter sterilized Jet A fuel at 28 °C with aeration. The chemical composition of Jet A was confirmed by GCxGC (Table S6, Supporting Information). As a control, bacteria were grown in M9 minimal media with glycerol as the sole carbon source. Bacteria were grown to mid log phase (0.5−0.6 OD_{600}), and cells were cooled rapidly on ice. Cells were harvested by centrifugation (4 °C) with 10% ethanol/phenol (19:1) solution, and the pellet was frozen immediately on dry ice.

RNA Isolation, cDNA Synthesis, and Affymetrix GeneChip Analysis. Total RNA was extracted from cells using the Qiagen Total RNA kit as described by the manufacturer. Any DNA contamination was removed by DNAase treatment. The quality of RNA was initially assessed by electrophoresis through a 1% agarose gel and by the Agilent Bioanalyzer System (Agilent Technologies, Palo Alto, CA). Total RNA, free of genomic DNA, was used to synthesize cDNA. First strand cDNA was synthesized with random primers using SuperScript II Reverse transcriptase. The cDNA was fragmented and labeled with biotin. Subsequently, the labeled-cDNA was hybridized to the Affymterix microarray chips. Arrays were then washed and stained as described in the Affymetrix GeneChip Expression Analysis Technical Manual, using the instructions specifically for *P. aeruginosa* PAO1. After washing and staining, Microarray chips were scanned using the Affymetrix GeneChip Scanner 3000. The initial data analyses were performed using Affymetrix Microarray Analysis Suite (MAS), version 5.1. Signal values, detection calls (present, absent, marginal), and *P* values for each detection call were generated using Affymetrix gene chip operating software (GCOS). PCA analyses of microarray chips distinguished four replicates of glycerol chips different to four replicates of jet fuel chips based on their expression profiles. However, to reduce dimensionality, we removed the outlier chip from each condition; three chips from each condition were considered for further analyses. All nine possible comparison analyses were performed using Glycerol CHP files as baseline values to obtain signal log ratio (SLR), change call, and *P* values associated with the change call. Nonspecific hybridization probes were eliminated by removing signals from a defined cutoff. Data were normalized across the two different conditions. Data were filtered based on the presence call, consensus changed call (CCC), and SLR to obtain significantly up-regulated and down-regulated genes as described previously.[28]

Quantitative Reverse Transcription PCR (qRT-PCR). Quantitative RT-PCR was used to validate the microarray data. Gene-specific qRT-PCR primers (Table S1, Supporting
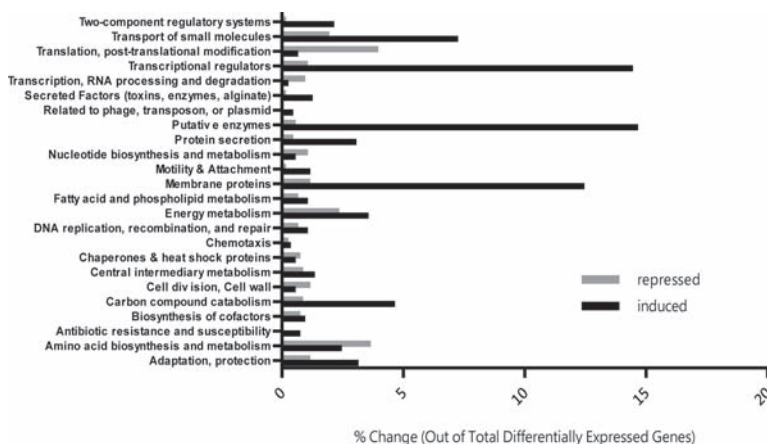
Figure 1. Regulation of *P. aeruginosa* functional genetic classes when grown in fuel. Functional classifications are according to *P. aeruginosa* genome project (www.pseudomonas.com). Black and gray bars represent % induced and % repressed genes of total differentially expressed genes, respectively.

Information) were designed for several genes representing some of the important biological processes identified by microarray. A SYBR-Green mediated two-step RT-PCR method was used to measure gene expression using the CFX quantitative real-time PCR instrument (BioRAD). PCR-amplified target sequences for each gene were amplified from *Pseudomonas aeruginosa* ATCC 33988 genomic DNA, quantified, and used as external standards for quantification during qPCR. Reverse transcription was carried using 100 ng of total RNA, random primers, and 75 U of iScript MMLV-RT (RNaseH+). The threshold cycle values (Ct) were obtained from amplification curves and the gene expression fold changes was calculated using $2^{-\Delta\Delta CT}$ method.

Fuel Degradation Profiles by GC X GC. Studies were conducted to investigate which specific compounds or compound types in Jet A fuel were preferentially degraded by *P. aeruginosa*. The bioassays were performed by using 10 μL of Jet A aviation fuel in 1 mL of M9 minimal media containing *P. aeruginosa* at 0.03 OD in a 10 mL glass vial sealed with a Teflon-lined lid. The samples were maintained in a 28 °C incubator for a period of 13 days, without opening the vial. Multiple sample replicates were incubated at the same time, and then sample vials were removed from the incubator at the time of testing, and finally extracted and analyzed by GC X GC as explain in Table S7 of the Supporting Information.

Fluorescent Staining of Cell Aggregates and Biofilm Assay. An Olympus BX50 F4 fluorescence microscope was used to visualize cell aggregations and biofilms. Cells were carefully collected from the fuel−M9 interface and live/dead staining was performed using the BacLight LIVE/DEAD kit (Life Technologies, U.S.A.) to visualize viable cells. A biofilm assay to quantify the formation of bacterial biofilms was conducted as described by Gunasekera et al.[29]

Efflux Pump Blockage Assay. To demonstrate that the Mex efflux pumps were important in the adaptation and resistance of *P. aeruginosa* to fuel, we used the known Mex-efflux pump inhibitor, c-capped dipeptide Phe-Arg β-naphthylamide dihydrochloride (Sigma-Aldrich P4157−250MG), to block the efflux pumps and determine the impact on cell growth in the presence of fuel. *P. aeruginosa* ATCC 33988 was inoculated at 0.03 OD_{600} into 5 mL M9 medium, and the c-capped dipeptide added at 0, 20, 40, 60, 80, and 100

μg/mL. Cultures were overlaid with 2 mL of Jet A fuel. Control samples were produced by adding 0.2% glycerol as the carbon source to samples containing efflux pump inhibitor but not fuel. The experiments were performed in triplicate and repeated twice each. Cultures were grown at 28 °C aerobically in a shaking (200 rpm) incubator, and the growth was monitored by measuring OD_{600}.

■ RESULTS AND DISCUSSION

To date, there has been no comprehensive study describing the diverse synergistic cellular adaptations that have to be triggered in *P. aeruginosa* to survive and thrive in toxic fuel-containing environments. Using DNA microarrays, we surveyed the global expression profile of *P. aeruginosa* genes to gain a deeper understanding into the complex machinery required for fuel degradation and adaptation.

The *P. aeruginosa* core genome has been shown to be highly conserved across different strains, irrespective of their origins, regardless of whether a strain is an environmental or clinical strain.[1] It has also been shown that environmental strain isolates have physiological properties similar to the clinical strain PAO1.[2] Moreover, alkane hydroxylase genes are present in both clinical and environmental isolates.[30] The PAO1 strain can utilize Jet A fuel (data not shown), dodecane,[24] and hexadecane[26] as carbon sources. Whole genome sequencing of *Pseudomonas aeruginosa* ATCC 33988 revealed that this genome is at least 99% similar to the PAO1 strain for the known genes contained in PAO1 chips. DNA sequence analyses of the genes selected for the qPCR study showed 100% sequence homology to the PAO1 strain. However, *P. aeruginosa* ATCC 33988 grows faster in jet fuel than the clinical strain PAO1 and appears to be better adapted to the fuel environment. Therefore, we used the *P. aeruginosa* ATCC 33988 strain for this study.

The Affymetrix gene-chip of *P. aeruginosa* PAO1 (Pae_G1a) genome consists of 5900 probe-sets representing 5549 protein-coding sequences, 18 tRNA genes, a representative of the rRNA cluster, 117 genes from different strains other than PA01, and 199 probe sets of intergenic regions. We used clustering algorithms to analyze expression data. Of 5549 genes, 3778 genes were called present in all 6 conditions and 5461 genes were called present or marginally present in at least 2 chips with

an alpha-1 value of 0.05. Of 5570 annotated Open Reading Frames (ORFs) in the *P. aeruginosa* PAO1 genome (www.pseudomonas.com[31]), here we found that under fuel growth, 2963 genes were induced and 617 genes were repressed over 2-fold. Additionally, differentially expressed genes were assigned to different functional classes (Figure 1). Analyses showed that 47% of the induced and 22.5% of the repressed genes were hypothetical with unknown functions in *P. aeruginosa*. Of the induced known genes, 12.4% were membrane proteins, 14.6% were putative enzymes, and 14.4% were transcriptional regulators (Figure 1). Up-regulation of large number transcriptional regulators during fuel growth allowed cells to adapt to the fuel environment rapidly. Among the down-regulated genes, the functional class of translation and post-translational modification were most notable (Figure 1). Almost every gene involved in the formation of ribosomal small (S) and ribosomal Large (L) proteins were significantly down-regulated probably due to slower growth rates in fuel compared to glycerol. In addition, a large number of genes related to translational and post-translational modification, amino acid biosynthesis and metabolism, energy metabolism, cell division, and cell wall were down-regulated.

The microarray results were further validated using quantitative reverse transcription−PCR (qRT-PCR) for several candidate genes that represented the different pathways studied through microarray (Figure 2). The results showed that the mRNA expression levels detected by qRT-PCR were consistent with the expression levels obtained by microarray.
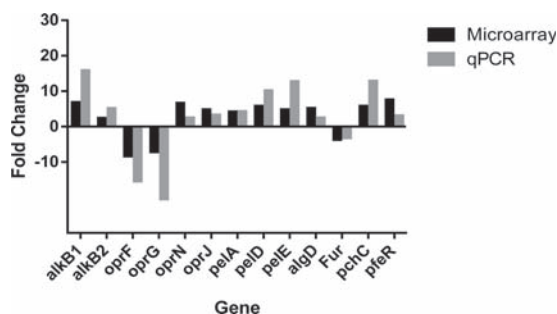
Figure 2. Validation of microarray gene expression data using qRT-PCR. A few candidate genes that represented some of the important biological processes identified by microarray including alkane degradation (*alkB1*, *alkB2*), EPS biosynthesis mechanism (*pelA*, *pelD*, *pelE*, *algD*), efflux pumps, and porin regulation (*oprF*, *oprG*, *oprN*, *oprJ*), iron transport, and metabolism (*Fur*, *pchF*, *pfeR*) were selected to be tested by qRT PCR. Microarray fold-change data were compared against the qRT-PCR data.

Alkane Degradation Pathways. Alkanes are highly reduced saturated hydrocarbons with high energy content. Therefore, alkanes can serve as a rich carbon and energy source for bacteria to grow. Alkane degradation is a complex process that involves the uptake of alkanes from a hydrophobic environment to the inside of the cell, followed by oxidation using substrate specific enzymes. *P. aeruginosa* is known to secrete surfactant rhamnolipids that emulsify hydrocarbons, thereby improving the uptake process.[32−34] In addition, rhamnolipids increase the hydrophobicity of the cell surface improving adaptability of *P. aeruginosa* to fuel-containing environment. A complex gene regulatory network is involved in rhamonlipid production. The *rhlAB* gene operon encoding

the rhamnosyltransferase involved in rhamnolipid biosurfactant production was up-regulated in our experiment over 5-fold, suggesting that rhamnolipid plays a role in fuel uptake.

Degradation of alkanes involves hydroxylation of the terminal methyl group to render a primary alcohol, followed by further oxidation to an aldehyde, and then conversion to fatty acids. Fatty acids are conjugated to co-enzyme A (CoA) and further processed by β-oxidation to generate acetyl CoA. Activation of medium chain ($C_5−C_{11}$) or long chain alkane molecules (C_{12} and greater) require the expression of the alkane hydroxylase genes, which encode membrane bound monooxygenases. The *alkB1* and *alkB2* genes are known to be present in *P. aeruginosa*, and our results showed that both genes were up-regulated by 6.75- and 2.33-fold (Table S2, Supporting Information), respectively, when grown in jet fuel. In agreement with a previous study,[35] the *alkB1* and *alkB2* genes were differentially expressed during the exponential phase of growth. However, the genes encoding two soluble electron transfer proteins rubredoxins (PA5350, PA5351) and rubredoxin reductase (PA5349) were not transcriptionally induced by fuel. These results are in agreement with Marin et al.,[35] in which they showed that rubredoxins and rubredoxin reductase encoding genes are constitutively expressed even in the presence of alkanes. Rubredoxin transfers electrons from NADH-dependent flavoprotein to rubredoxin reductase and to AlkB and the cytochromes. AlkB1 and AlkB2 have overlapping substrates ranging from medium chain length alkanes to long chain alkanes. The AlkB1 and AlkB2 were shown to be particularly active on $C_{10}−C_{22}/C_{24}$ alkanes but were differentially express at different stages of the growth phase.[32] In addition to AlkB1 and AlkB2, cytochrome P450 alkane hydroxylases (PA2475, PA 3331), which are ubiquitous among all kingdoms of life,[7] were also induced in *P. aeruginosa* when grown in fuel.

Several ferrodoxins and ferrodoxin reductase (PA4331) were up-regulated when *Pseudomonas* was grown in fuel, indicating the possible involvement of these enzymes in jet fuel degradation (Table S2, Supporting Information). Both AlkB and Cytochrome P450 monooxygenase oxidize medium-chain ($C_5−C_{11}$) and long-chain alkanes ($>C_{11}$). The up-regulation of *alkB1* (6.75-fold), *alkB2* (2.33-fold), and P450 (4.89- and 3.85-fold) indicates that these enzymes were activated by the presence of fuel and likely involved alkane degradation. In addition to *alkB* and P450 genes, a number of enzymes involved in terminal oxidation pathways were induced including, alcohol dehydrogenase, aldehyde dehydrogenase, and acyl-CoA-synthetase (Table S2, Supporting Information). The fatty acid degradation pathway plays a critical role in consumption of jet fuel by *P. aeruginosa*. The initial oxidation step of beta-oxidation is catalyzed by acyl-CoA dehydrogenase. We observed that multiple acyl-CoA dehydrogenases were induced in the presence of fuel. A number of enzymes in the enoyl-CoA hydratase family that catalyze the second step of β-oxidation pathway were also induced (Table S2, Supporting Information).

Selective Consumption of *n*-Alkanes in Jet-A Fuel by *P. aeruginosa*. Jet fuel composition analyses performed by two-dimensional gas chromatography (GC × GC) provided new insights into the type of hydrocarbons degraded by *P. aeruginosa* ATCC 33988. These results further confirmed activity of *n*-alkane degradation pathways detected by microarray. The results showed that n-C_9, C_{10}, and C_{11} presented a slower rate of decomposition over the 13 days, while a much greater decline in concentrations occurred for n-C_{12} through n-

C_{18} alkanes (Figure 3a). These results agreed with the degradability profiles shown for the PAO1 strain by Smits et
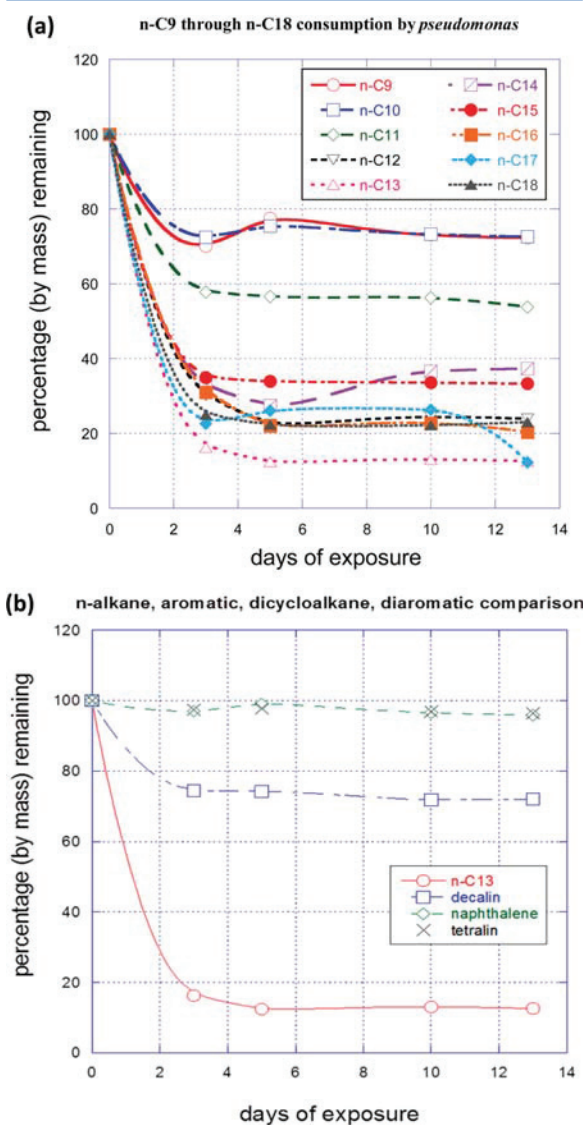

Figure 3. Selective consumption of Jet A fuel hydrocarbons by *P. aeruginosa*. (a) Degradation rate of normal alkanes based on molecular weight. (b) Comparison of the consumption of four different jet fuel hydrocarbons representing four important compound classes in fuel: n-C13 ($C_{13}H_{28}$), indicative of paraffins and isoparaffins; decalin ($C_{10}H_{20}$), indicative of cycloparaffins; naphthalene ($C_{10}H_8$), indicative of diaromatics; and tetralin ($C_{10}H_{14}$), indicative of monoaromatics. The samples were analyzed by GC × GC with dual flame ionization detection (FID) and mass spectrometry detection.

al.,[30] which indicated higher degradability of n-C_{12} to n-C_{16} compared to shorter chain alkanes <n-C_{10}. We also observed that the *P. aeruginosa* ATCC 33988 strain degraded n-alkanes longer than C_{20} (data not shown), suggesting that additional alkane degradation pathways may exist in this organism. The consumption rate of 10-carbons aromatic napthalene, tetralin, and the dicyclicloparaffin decalin was compared to the consumption rate of n-C_{13}, the most degraded normal alkane

(Figure 3b). Naphthalene and tetralin were entirely undegraded. However, the concentration of decalin was reduced from its original concentration by 25% as compared to an approximate 85% loss of the n-alkane C_{13}. Clearly, cells preferentially consumed the n-alkane in favor of the aromatics (Figure 3b). The results demonstrated that saturated cyclic compounds that have no aromaticity such as decalin are also degraded but to a lesser degree than the n-alkanes. These observations are in general agreement with the studies conducted on oil spills where bacteria consume hydrocarbons in the order of n-alkanes > branched alkanes > low molecular weight aromatics > cyclic alkanes > higher molecular weight aromatics.[3]

Biosynthesis of Extracellular Polysaccharides and Biofilm Formation. The formation of biofilms in the fuel environment has been indicated previously.[15,16] *P. aeruginosa* successfully colonizes fuel tanks by secreting extracellular polysaccharides and forming biofilms. We observed that *P. aeruginosa* produced a significant amount of biofilm at the fuel and M9 media interface (Figure 4a). Microscopic analyses showed that most of the cell aggregations were alive (Figure 4b). Under static condition, *P. aeruginosa* formed a significant ($P < 0.01$) amount of biofilm when compared to *P. aeruginosa* grown in glycerol in as short as 3 days (Figure 4c). Using expression microarray, we identified genes likely responsible for extracellular polysaccharide (EPS) and biofilm formation. We noticed that in the presence of fuel, alginate, and Pel protein biosynthesis and export mechanisms were induced (Table S3, Supporting Information). Alginate, a linear polymer of β-1,4-linked D-mannuronic acid, is known to play a role in the development of biofilms of *P. aeruginosa* in the upper and lower airways of cystic fibrosis patients.[9,32] With the exception of *algC*, which does not reside in the *algD* operon, all the other genes involved in biosynthesis and secretion of alginate were induced in the presence of fuel. The *algC* gene, which has additional functions in lipopolysaccharide (LPS) biosynthesis,[36] was down-regulated in presence of fuel (Table S3, Supporting Information). The *algA* and *algD* genes which encode the enzymes required for synthesis of the alginate precursor guanosine diphosphate (GDP) mannuronic acid were up-regulated over 4-fold in fuel (Table S3, Supporting Information). Once the alginate precursor is synthesized in the cytoplasm, it is polymerized and exported across the outer membrane. The genes that encode the alginate precursor transport proteins, *alg8* and *alg44*, were induced over 7-fold. The genes encoding three periplasmic proteins (AlgG, AlgK, AlgX) involved in forming a scaffold to protect alginate degradation from alginate lyase were also induced. The gene products of *algI*, *algJ*, *algF*, which serve as the reaction center for O-acetylation in the membrane were also induced in fuel. Additionally, the *algE* gene that encodes the outer membrane protein that exports alginate from periplasm to the environment was up-regulated. Overall, our study provides novel insight into the production of alginate by *P. aeruginosa* during fuel growth. Exopolysaccharides make cells more mucoid, enabling cells to attach to fuel tank surfaces and produce biofilms, which prevent direct contact of cells with fuel. The regulation of alginate biosynthesis is a complex process controlled at the transcriptional level, which involves a number of proteins including AlgT, AlgR, MucA, and MucB.[9] However, the expression of these transcriptional regulator genes was not changed under fuel condition suggesting that transcription of the alginate biosynthetic genes might be activated by an
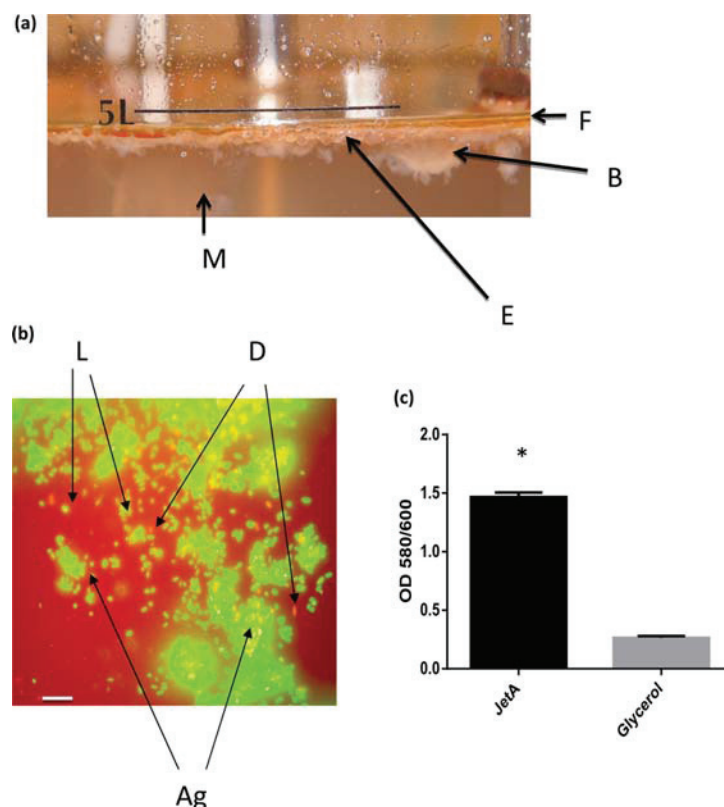
Figure 4. (a) Biofilm formations by *Pseudomonas aeruginosa* ATCC 33988 when grown in Jet A fuel aerobically in a bioreactor. Note that cell aggregates and biofilms are mainly formed at the fuel water interface. F, fuel layer; B, biofilm; E, emulsified fuel; and M, M9 buffer. (b) Epifluorescent microscope image of biofilm/cell aggregates induced by fuel. Cells were stained with Syto9/propidium iodide. Live cells are green, and dead cells are red. L, live cells; D, dead cells; and Ag, cell aggregation. Bar indicates 5 μm. (c) Quantification of Jet A-induced biofilm formation after 3 days incubation at 28 °C. Biofilms were quantified by crystal violet staining. A significant difference is indicated by $*$ for $p < 0.01$.

unknown mechanism in the presence of fuel. However, it is likely that slight fluctuations of these regulatory proteins can produce a strong change in the expression of their target genes. Alternatively, mutation of the coding region of these transcriptional regulators could affect the way they interact with the operator region of the alginate genes, leading to increased expression. Increased production of alginate due to mutation of the inner-membrane antisigma factor *mucA* gene has been reported.[12]

In addition to alginate, pal and psl exopolysaccharides are also implicated in playing a role in biofilm formation in *P. aeruginosa*. Our study showed that the entire pel operon (*pelA-G*) was induced in the presence of fuel. This suggests that extracellular pel may be playing a role in cell aggregation and biofilm formation. PEL-polysaccharide production is regulated by PelD,[37] a degenerate diguanylate cyclase receptor; this gene was induced 5.4-fold during fuel growth. It has been shown that *P. aeruginosa* PA14 strain produced Pel protein in air–water interface biofilms.[36] In our study, we consistently observed the formation of this biofilms at the fuel–water interface (Figure 4a); it is possible that increased Pel production may be playing a role in cell aggregation. The formation of biofilms, particularly at the fuel–water interface was clearly demonstrated in our growth characterization experiments (Figure 4b,c).

Efflux Pumps and Porin Regulation. The role of membrane proteins is crucial in regulating cell homeostasis.

The two major general porins, OprF and OprG, were down-regulated 8.25- and 7.02-fold, respectively, when *P. aeruginosa* was grown in jet fuel. The down-regulation of these porins was also confirmed by qRT-PCR (Figure 2). Aromatic compounds present at about 20% (v/v) in fuel are highly toxic to cells. It has been shown that aromatics such as toluene and naphthalene can be transported into the cell through the porins OprF and OprG, respectively.[23,25] Li et al.,[23] showed that mutant cells defective in OprF were highly tolerant to toluene. Volker et al.,[38] showed that when the solvent-tolerant *Pseudomonas putida* S12 was exposed to toluene *oprF* was repressed. Previous studies indicated that OprG is required by *P. fluorescens* to grow in pure naphthalene,[25] and that it works in *P. putida* and *P. aeruginosa* by forming a diffusion channel with emulsifying activity.[25] However, our GC × GC analysis revealed that when grown in jet fuel, *P. aeruginosa* ATCC 33988 does not degrade aromatic hydrocarbons (Figure 3b).

Besides prevention of the internalization of toxic hydrocarbons, bacterial cells may activate multiple efflux pump mechanisms to extrude toxic hydrocarbons and ions from the cells in order to maintain a low intracellular level that can be managed by biodegradative pathways. It has been shown that multidrug efflux pumps of the RND family, which are highly conserved among bacteria, are involved in the resistance of bacteria to toxic compounds and small molecules. Furthermore, efflux pumps MexAB-OprM, MexCD-OprJ, and MexEF-OprN
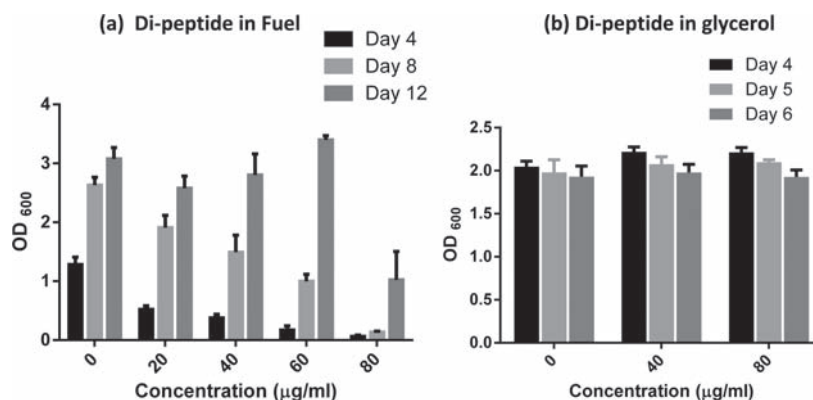
Figure 5. (a,b) Effect of efflux pump inhibitor (c-capped dipeptide) on *Pseudomonas* growth in the presence and absence of fuel. Bacteria were grown in M9 minimal media containing Jet A fuel (a) and glycerol (b) as sole carbon sources for growth in the presence of 0, 20, 40, 60, and 80 μg/mL Phe-Arg-β-naphthylamide efflux pump inhibitor.

have been proposed as possible mechanisms of aromatic solvent extrusion.[20,23,39] These tripartite pumps can move solutes from the cytoplasm and from the periplasm to the cell exterior.[40] Our results showed the MexCD-OprJ and MexEF-OprN efflux pumps were up-regulated in fuel about 4-to 6-fold and 5-to 8-fold, respectively (Table S4 and Figure S1, Supporting Information). However, the MexAB-OprM efflux pump was repressed by about 2-fold. This result indicated that in *Pseudomonas aeruginosa* ATCC 33988, the MexAB-OprM efflux may not be a major contributor to the solvent extrusion system. In *P. aeruginosa*, the mexAB-oprM operon has been shown to be expressed at a basal level as a primary system for intrinsic multidrug resistance.[41] However, it has also been observed that the *mexCD-oprJ* and *mexEF-oprN* can be activated in cases where the mexAB-oprM is not expressed or when exposure to a specific compound makes the activation of these efflux pumps advantageous over the expression of the mexAB-oprM pump.[42]

We also observed that a great number of other efflux transporters were up-regulated in the presence of fuel. For example, 21 probable RND efflux pumps and probable drug efflux pumps were up-regulated (Table S4, Supporting Information). Out of these genes, PA1238, PA1541, PA3523, and PA4990 were highly up-regulated, 16.50-, 33.00-, 15.40-, and 10.93-fold, respectively (Table S4, Supporting Information). Furthermore, we have observed that the RND-divalent metal cation efflux transporters *czcA, czcB, czcC, czcD* were up-regulated 6.75-, 7.13-, 16.63-, and 2.85-fold, respectively (Table S4, Supporting Information). The Czc proteins have been involved in the extrusion of toxic metal ions such as cadmium, zinc, cobalt, magnesium, and copper.[43] The manner in which jet fuel is transported and stored provides a great chance that metal ions, including heavy metals, might get dissolved in the fuel. While the level of these toxic metals in most instances can be very low, they tend to partition and concentrate into the aqueous phase where microorganisms prefer to grow. Also, many heavy metal ions, such as Pb, Hg, and Cd, are highly toxic even at very low concentrations. Because of the susceptibility of organisms to metal toxicity, bacteria have evolved mechanisms, such as active efflux pumps, that can reduce the intracellular levels of metal and its toxicity. The metal efflux pumps appeared to be required for effective growth in fuel. It is also likely that some of these efflux pumps could be activated by the same trigger signals that activate the Mex efflux pumps. Our

results revealed a great complexity of efflux systems that may likely be activated to reduce the intracellular concentration of toxic molecules. As shown here, these efflux pumps provide protection to the cell and are important systems for homeostasis regulation and resistance to toxic compounds (Figure S1, Supporting Information).

Role of Efflux Pumps in Cell Resistance to Fuel. To demonstrate that Mex efflux pumps were truly important in the adaptation and resistance of *P. aeruginosa* to fuel, we decided to use a known efflux pump inhibitor to block the efflux pumps and observe any effects of this blockage. The efflux pump inhibitor Phe-Arg-β-napthylamide (PAβN), a c-capped dipeptide, was applied at different concentrations to M9 minimal media containing fuel or glycerol as the sole carbon source. PAβN has been shown to bind and inhibit the function of MexAB-OprM, MexCD-OprJ, and MexEF-OprN efflux pumps,[44−49] reducing the resistance of bacteria to antibiotics. It was expected, as in the case of antibiotics resistance, that if efflux pumps were involved in protecting the cell by reducing the intracellular levels of organics and other toxic compounds from fuel that their blockage would lead to an observable growth reduction.

The results showed that addition of PAβN efflux pump inhibitor to fuel-containing minimal media samples effectively inhibited *P. aeruginosa* growth for several days (Figure 5a). For the first 4 days, growth inhibition was observed at every concentration tested from 20 to 80 μg/mL. However, only the highest concentration, 80 μg/mL, was able to permanently inhibit the growth of *P. aeruginosa* (Figure 5a). However, when 40 and 80 μg/mL PAβN were added to glycerol-containing minimal media samples, no growth reduction was observed (Figure 5b). This result demonstrated that the inhibitory effect was not due to direct antimicrobial activity of the efflux pump inhibitor on the bacteria. Furthermore, the results clearly support that blockage of the efflux pumps by PAβN led to the toxic accumulation of fuel compounds in the cell cytoplasm that prevented the bacteria from growing. Additional experiments performed with the Gram-negative fuel-degrading bacteria *Acinetobacter venetianus* showed a similar result, indicating that PAβN mediated efflux pump blockage can lead to fuel toxicity and growth inhibition in other bacteria (data not shown). Efflux pump blockers may be applied to prevent biodeterioration of fuel.

Iron Acquisition. Iron is an essential element for living cells, but it is strictly regulated because iron is toxic to the cell in excess.[50] In fuel-degrading bacteria, there are a number of iron enzymes including integral membrane di-iron alkane hydroxylases (e.g., AlkB), cytochrome P450 enzymes, ferredoxin reductase, and ferredoxin that utilize iron to transfer electrons to P450. Also, several iron-containing alcohol dehydrogenases require iron as a cofactor. Significant up-regulation of these genes during fuel growth indicated a greater demand for iron during alkane degradation. *P. aeruginosa* employs multiple acquisition pathways to transport iron inside the cell. It has also been observed that critical iron concentration serves as a signal for *P. aeruginosa* to produce biofilms.[51] Our study revealed that both high affinity pyoverdine and the lower affinity pyochelin systems[51,52] were induced in *P. aeruginosa* while growing in fuel (Table S5, Supporting Information). Both pyoverdin and pyocheline act as siderophores, binding to extracellular iron (Fe+3), which is then transported across the outer and inner membranes. All the genes encoding the pyoverdine biosynthesis pathway (*pvcA-F*) and genes encoding the pyochelin biosynthesis pathway (*pchC*, *pchD*, *pchF*), along with its outer membrane receptor FptA, were highly induced (Table S5, Supporting Information). The genes encoding the proteins PvdS[53] and PchR,[54] which positively regulate the biosynthesis of pyroverdine and pyocheline, respectively, were induced about 7-fold during fuel growth. In the iron-depleted condition, Fe2+ prevents FUR repression, and as a result the iron regulatory protein PvDS is activated. In our study, during fuel growth, genes encoding the FUR and PvdS proteins were down-regulated and up-regulated, respectively. Fur down-regulation was also confirmed by qRT-PCR (Figure 2). In *P. aeruginosa*, Fur is an essential protein that negatively regulates the expression of number of genes involved in iron uptake.[52] Fur down-regulation activates a cascade of regulatory and iron uptake mechanisms including several extra-cytoplasmic sigma factors (Table S5, Supporting Information) known to be iron-regulated.[55] Fur regulates the *fepBDGC* operon, which encodes an ABC transporter involved in the transport of ferric enterobactin; this operon was also up-regulated during fuel growth. Fur also regulates the expression of the two component systems for the uptake of ferric enterobactin; we noticed that the genes *pfeS* and *pfeR*, which encode the ferric enterobactin sensor and response regulator, respectively, were up-regulated. Additionally, the genes encoding a second low affinity ferri-enterbactin receptor, PirA, and the PirR-PirS regulatory system, were induced. Overall, a significant number of genes related to iron transport and metabolism were up-regulated in our study, indicating a greater demand for iron during fuel growth. Therefore, depleting iron in the fuel tank environment could potentially inhibit or compromise *P. aeruginosa* growth in jet fuel. It is clear that survival and proliferation in fuel requires multiple synergistic cellular responses.

ASSOCIATED CONTENT

⑤ Supporting Information

Table S1 presents the RT-qPCR primers. Table S2−S5, describe the transcript fold change for genes detected by microarray. Tables S6−S7 present the Jet A composition and the GC × GC analysis method, respectively. Figure S1 is the schematic representation of regulated efflux pumps and porins. This material is available free of charge via the Internet at http://pubs.acs.org.

■ AUTHOR INFORMATION

Corresponding Author
*Tel.: +1-937-255-6237. Fax 1-937-255-3893. E-mail: oscar.ruiz@us.af.mil.

Notes
The authors declare no competing financial interest.

■ ACKNOWLEDGMENTS

■ REFERENCES

(1) Kung, V. L.; Ozer, E. A.; Hauser, A. R. The accessory genome of *Pseudomonas aeruginosa*. *Microbiol. Mol. Biol Rev.* **2010**, *74* (4), 621−641.

(2) Belhaj, A.; Desnoues, N.; Elmerich, C. Alkane biodegradation in *Pseudomonas aeruginosa* strains isolated from a polluted zone: Identification of alkB and alkB-related genes. *Res. Microbiol.* **2002**, *153* (6), 339−344.

(3) Das, N.; Chandran, P. Microbial degradation of petroleum hydrocarbon contaminants: an overview. *Biotechnol Res Int.* **2011**, DOI: 10.4061/2011/941810.

(4) Szoboszlay, S.; Atzél, B.; Kriszt, B. Comparative biodegradation examination of *Pseudomonas aeruginosa* (ATCC 27853) and other oil degraders on hydrocarbon contaminated soil. *Commun. Agric. Appl. Biol. Sci.* **2003**, *68* (2), 207−10.

(5) Wongsa, P.; Tanaka, M.; Ueno, A.; Hasanuzzaman, M.; Yumoto, I.; Okuyama, H. Isolation and characterization of novel strains of *Pseudomonas aeruginosa* and *Serratia marcescens* possessing high efficiency to degrade gasoline, kerosene, diesel oil, and lubricating oil. *Curr. Microbiol.* **2004**, *49* (6), 415−22.

(6) Rojo, F. Degradation of alkanes by bacteria. *Environ Microbiol.* **2009**, *11* (10), 2477−2490.

(7) Rojo, F. Enzymes for aerobic degradation of alkanes. In *Handbook of Hydrocarbon and Lipid Microbiology*; Timmis, K. N., Ed.; Springer-Verlag: Berlin, Heidelberg, 2010; pp 781−797.

(8) Liu, C.; Wang, W.; Wu, Y.; Zhou, Z.; Lai, Q.; Shao, Z. Multiple alkane hydroxylase systems in a marine alkane degrader, *Alcanivorax dieselolei* B-5. *Environ. Microbiol.* **2011**, *13* (5), 1168−1178.

(9) Yuste, L.; Rojo, F. Role of the crc gene in catabolic repression of the *Pseudomonas putida* GPo1 alkane degradation pathway. *J. Bacteriol.* **2001**, *183* (21), 6197−6206.

(10) Dinamarca, M. A.; Aranda-Olmedo, I.; Puyet, A.; Rojo, F. Expression of the *Pseudomonas putida* OCT plasmid alkane degradation pathway is modulated by two different global control signals: evidence from continuous cultures. *J. Bacteriol.* **2003**, *185* (16), 4772−4778.

(11) Chakrabarty, A. M.; Chou, G.; Gunsalus, I. C. Genetic regulation of octane dissimilation plasmid in *Pseudomonas*. *Proc. Natl. Acad. Sci. U.S.A.* **1973**, *70* (4), 1137−1140.

(12) Baumgarten, T.; Sperling, S.; Seifert, J.; von Bergen, M.; Steiniger, F.; Wick, L. Y.; Heipieper, H. J. Membrane vesicle formation as a multiple-stress response mechanism enhances *Pseudomonas putida* DOT-T1E cell surface hydrophobicity and biofilm formation. *Appl. Environ. Microbiol.* **2012**, *78* (17), 6217−6224.

(13) Vu, B.; Chen, M.; Crawford, R. J.; Ivanova, E. P. Bacterial extracellular polysaccharides involved in biofilm formation. *Molecules* **2009**, *14* (7), 2535−2554.

(14) Ramsey, D. M.; Wozniak, D. J. Understanding the control of *Pseudomonas aeruginosa* alginate synthesis and the prospects for management of chronic infections in cystic fibrosis. *Mol. Microbiol.* **2005**, *56* (2), 309−322.

(15) Passman, F. J. Standard Guide for Microbial Contamination in Fuels and Fuel Systems. In *Fuel and Fuel System Microbiology:*

Fundamentals, Diagnosis, and Contamination Control; Passman, F. J., Ed.; ASTM International: West Conshohocken, PA; 2003; pp 81−91.

(16) Sabirova, J. S.; Becker, A.; Lünsdorf, H.; Nicaud, J. M.; Timmis, K. N.; Golyshin, P. N. Transcriptional profiling of the marine oil-degrading bacterium *Alcanivorax borkumensis* during growth on n-alkanes. *FEMS Microbiol. Lett.* **2011**, *319* (2), 160−168.

(17) Hansch, C.; Anderson, S. M. The effect of intramolecular hydrophobic bonding on partition coefficients. *J. Org. Chem.* **1967**, *32*, 2583−2586.

(18) Inoue, A.; Horikoshi, K. A. A *Pseudomonas* thrives in high concentrations of toluene. *Nature* **1989**, *338*, 264−266.

(19) Li, X. Z.; Zhang, L.; Poole, K. Role of the multidrug efflux systems of *Pseudomonas aeruginosa* in organic solvent tolerance. *J. Bacteriol.* **1998**, *180* (11), 2987−2991.

(20) Fraud, S.; Campigotto, A. J.; Chen, Z.; Poole, K. MexCD-OprJ multidrug efflux system of *Pseudomonas aeruginosa*: Involvement in chlorhexidine resistance and induction by membrane-damaging agents dependent upon the AlgU stress response sigma factor. *Antimicrob. Agents Chemother.* **2008**, *52* (12), 4478−4482.

(21) Baum, E. Z.; Crespo-Carbone, S. M.; Morrow, B. J.; Davies, T. A.; Foleno, B. D.; He, W.; Queenan, A. M.; Bush, K. Effect of MexXY overexpression on ceftobiprole susceptibility in *Pseudomonas aeruginosa*. *Antimicrob. Agents Chemother.* **2009**, *53* (7), 2785−2790.

(22) Aono, R.; Aibe, K.; Inoue, A.; Horikoshi, K. Preparation of organic solvent-tolerant mutants of *Escherichia coli* K-12. *Agric. Biol. Chem.* **1991**, *55*, 1935−1938.

(23) Li, L.; Komatsu, T.; Inoue, A.; Horikoshi, K. A toluene-tolerant mutant of *Pseudomonas aeruginosa* lacking the outer membrane protein F. *Biosci. Biotechnol. Biochem.* **1995**, *59* (12), 2358−2359.

(24) Neher, T. M.; Lueking, D. R. *Pseudomonas fluorescens* ompW: Plasmid localization and requirement for naphthalene uptake. *Can. J. Microbiol.* **2009**, *55* (5), 553−563.

(25) Touw, D. S.; Patel, D. R.; van den Berg, B. The crystal structure of OprG from *Pseudomonas aeruginosa*, a potential channel for transport of hydrophobic molecules across the outer membrane. *PLoS One* **2010**, *5* (11), e15016.

(26) Alonso, A.; Rojo, F.; Martínez, J. L. Environmental and clinical isolates of *Pseudomonas aeruginosa* show pathogenic and biodegradative properties irrespective of their origin. *Environ. Microbiol.* **1999**, *1* (5), 421−430.

(27) Smits, T. H.; Balada, S. B.; Witholt, B.; van Beilen, J. B. Functional analysis of alkane hydroxylases from gram-negative and gram-positive bacteria. *J. Bacteriol.* **2002**, *184* (6), 1733−1742.

(28) Gunasekera, T. S.; Csonka, L. N.; Paliy, O. Genome-wide transcriptional responses of *Escherichia coli* K-12 to continuous osmotic and heat stresses. *J. Bacteriol.* **2008**, *190* (10), 3712−3720.

(29) Gunasekera, T. S.; Herre, A. H.; Crowder, M. W. Absence of ZnuABC-mediated zinc uptake affects virulence-associated phenotypes of uropathogenic *Escherichia coli* CFT073 under Zn(II)-depleted conditions. *FEMS Microbiol. Lett.* **2009**, *300* (1), 36−41.

(30) Smits, T. H.; Witholt, B.; van Beilen, J. B. Functional characterization of genes involved in alkane oxidation by *Pseudomonas aeruginosa*. *Antonie Van Leeuwenhoek* **2003**, *84* (3), 193−200.

(31) Winsor, G. L.; Lam, D. K.; Fleming, L.; Lo, R.; Whiteside, M. D.; Yu, N. Y.; Hancock, R. E.; Brinkman, F. S. *Pseudomonas* Genome Database: Improved comparative analysis and population genomics capability for *Pseudomonas* genomes. *Nucleic Acids Res.* **2001**, *39* (Database issue), D596−600.

(32) Smits, T. H.; Röthlisberger, M.; Witholt, B.; van Beilen, J. B. Molecular screening for alkane hydroxylase genes in Gram-negative and Gram-positive strains. *Environ. Microbiol.* **1999**, *1* (4), 307−317.

(33) Nie, M.; Yin, X.; Ren, C.; Wang, Y.; Xu, F.; Shen, Q. Novel rhamnolipid biosurfactants produced by a polycyclic aromatic hydrocarbon-degrading bacterium *Pseudomonas aeruginosa* strain NY3. *Biotechnol. Adv.* **2010**, *28* (5), 635−643.

(34) Rocha, C. A.; Pedregosa, A. M.; Laborda, F. Biosurfactant-mediated biodegradation of straight and methyl-branched alkanes by *Pseudomonas aeruginosa* ATCC 55925. *AMB Express* **2011**, *1* (1), 9.

(35) Marín, M. M.; Yuste, L.; Rojo, F. Differential expression of the components of the two alkane hydroxylases from *Pseudomonas aeruginosa*. *J. Bacteriol.* **2003**, *185* (10), 3232−3237.

(36) Franklin, M. J.; Nivens, D. E.; Weadge, J. T.; Howell, P. L. Biosynthesis of the *Pseudomonas aeruginosa* extracellular polysaccharides, alginate, Pel, and Psl. *Front. Microbiol.* **2001**, *2*, 167.

(37) Whitney, J. C.; Colvin, K. M.; Marmont, L. S.; Robinson, H.; Parsek, M. R.; Howell, P. L. Structure of the cytoplasmic region of PelD, a degenerate diguanylate cyclase receptor that regulates exopolysaccharide production in *Pseudomonas aeruginosa*. *J. Biol. Chem.* **2012**, *287* (28), 23582−23593.

(38) Volkers, R. J.; de Jong, A. L.; Hulst, A. G.; van Baar, B. L.; de Bont, J. A.; Wery, J. Chemostat-based proteomic analysis of toluene-affected *Pseudomonas putida* S12. *Environ. Microbiol.* **2006**, *8* (9), 1674−1679.

(39) Meguro, N.; Kodama, Y.; Gallegos, M. T.; Watanabe, K. Molecular characterization of resistance-nodulation-division transporters from solvent- and drug-resistant bacteria in petroleum-contaminated soil. *Appl. Environ. Microbiol.* **2005**, *71* (1), 580−586.

(40) Piddock, L. J. Clinically relevant chromosomally encoded multidrug resistance efflux pumps in bacteria. *Clin. Microbiol. Rev.* **2006**, *19* (2), 382−402.

(41) Poole, K.; Krebes, K.; McNally, C.; Neshat, S. Multiple antibiotic resistance in *Pseudomonas aeruginosa*: evidence for involvement of an efflux operon. *J. Bacteriol.* **1993**, *175* (22), 7363−7372.

(42) Poole, K.; Srikumar, R. Multidrug efflux in *Pseudomonas aeruginosa*: Components, mechanisms and clinical significance. *Curr. Top Med. Chem.* **2001**, *1* (1), 59−71.

(43) Silver, S.; Ji, G. Newer systems for bacterial resistances to toxic heavy metals. *Environ. Health Perspect.* **1994**, *102* (Suppl. 3), 107−113.

(44) Zechini, B.; Versace, I. Inhibitors of multidrug resistant efflux systems in bacteria. *Recent Pat. Antiinfect Drug Discovery* **2009**, *4* (1), 37−50.

(45) Hasdemir, U. O.; Chevalier, J.; Nordmann, P.; Pagès, J. M. Detection and prevalence of active drug efflux mechanism in various multidrug-resistant *Klebsiella pneumoniae* strains from Turkey. *J. Clin. Microbiol.* **2004**, *42* (6), 2701−2706.

(46) Renau, T. E.; Léger, R.; Flamme, E. M.; Sangalang, J.; She, M. W.; Yen, R.; Gannon, C. L.; Griffith, D.; Chamberland, S.; Lomovskaya, O.; Hecker, S. J.; Lee, V. J.; Ohta, T.; Nakayama, K. Inhibitors of efflux pumps in *Pseudomonas aeruginosa* potentiate the activity of the fluoroquinolone antibacterial levofloxacin. *J. Med. Chem.* **1999**, *42* (24), 4928−4931.

(47) Mazzariol, A.; Tokue, Y.; Kanegawa, T. M.; Cornaglia, G.; Nikaido, H. High-level fluoroquinolone-resistant clinical isolates of *Escherichia coli* overproduce multidrug efflux protein AcrA. *Antimicrob. Agents Chemother.* **2000**, *44* (12), 3441−3443.

(48) Baucheron, S.; Imberechts, H.; Chaslus-Dancla, E.; Cloeckaert, A. The AcrB multidrug transporter plays a major role in high-level fluoroquinolone resistance in *Salmonella enterica* serovar typhimurium phage type DT204. *Microb. Drug Resist.* **2002**, *8* (4), 281−289.

(49) Malléa, M.; Chevalier, J.; Eyraud, A.; Pagés, J. M. Inhibitors of antibiotic efflux pump in resistant *Enterobacter aerogenes* strains. *Biochem. Biophys. Res. Commun.* **2002**, *293* (5), 1370−1373.

(50) Wandersman, C.; Delepelaire, P. Bacterial iron sources: From siderophores to hemophores. *Annu. Rev. Microbiol.* **2004**, *58*, 611−647.

(51) Banin, E.; Vasil, M. L.; Greenberg, E. P. Iron and *Pseudomonas aeruginosa* biofilm formation. *Proc. Natl. Acad. Sci. U.S.A.* **2005**, *102* (31), 11076−11081.

(52) Vasil, M. L.; Ochsner, U. A. The response of *Pseudomonas aeruginosa* to iron: genetics, biochemistry and virulence. *Mol. Microbiol.* **1999**, *34* (3), 399−413.

(53) Leoni, L.; Orsi, N.; de Lorenzo, V.; Visca, P. Functional analysis of PvdS, an iron starvation sigma factor of *Pseudomonas aeruginosa*. *J. Bacteriol.* **2000**, *182* (6), 1481−1491.

(54) Heinrichs, D. E.; Poole, K. PchR, a regulator of ferripyochelin receptor gene (fptA) expression in *Pseudomonas aeruginosa*, functions

both as an activator and as a repressor. *J. Bacteriol.* **1999**, *178* (9), 2586−2592.

(55) Cornelis, P.; Matthijs, S.; Van Oeffelen, L. Iron uptake regulation in *Pseudomonas aeruginosa. Biometals* **2009**, *22* (1), 15−22.

229

Appendix P. Turbulent Flow, Heat Transfer Deterioration, and Thermal Oxidation of Jet Fuel

Turbulent Flow, Heat Transfer Deterioration, and Thermal Oxidation of Jet Fuel

Hua Jiang,* Jamie Ervin,† Zachary West,* and Steven Zabarnick‡
University of Dayton Research Institute, Dayton, Ohio 45469

Computational fluid dynamics simulations can be used to simulate the flow, heat transfer, and fuel chemistry within fuel system cooling passageways. The standard k-ε turbulence model with the standard wall function, renormalization group k-ε model with an enhanced wall function, and the shear stress transport k-ω model were evaluated for their ability to represent turbulent fuel flow and heat transfer under high heat flux and flow rate conditions. The renormalization group k-ε model with an enhanced wall function provided the greatest fidelity in representation of turbulent thermal and flow behavior studied in heated tube experiments conducted at supercritical pressure. Moreover, the renormalization group k-ε model with an enhanced wall function allowed reasonable simulation of heat transfer deterioration, which was more likely for flow conditions involving a large heat flux with low mass flux rate. As the fuel was heated from the liquid to the supercritical phase, the viscosity temperature dependence was the primary transport property leading to heat transfer deterioration. A pseudodetailed chemical kinetic mechanism was used to study the effect of high heat flux and flow rate on dissolved O_2 consumption together with a global submechanism for the simulation of thermal-oxidative surface deposition. The deposition submechanism developed previously for low heat flux conditions provided reasonable agreement between normalized, measured, and simulated deposit profiles.

Nomenclature

A	=	preexponential factor in Arrhenius rate expression, mole, L, s
A_c	=	interior cross-sectional area of tube, m
C_p	=	specific heat, J/kg-K
D_i	=	inner diameter of tube, m
G	=	mass flux, $\dot{m}/A_c$, kg/m²-s
K	=	thermal conductivity, W/m-K
k	=	turbulent kinetic energy, kJ/kg
$\dot{m}$	=	mass flow rate, kg/s
P	=	pressure, MPa
$\dot{q}$	=	volumetric heat generation, kW/m³
q''	=	heat flux, kW/m²
R	=	internal radius of tube, m
r	=	radial distance from tube centerline, m
Re	=	Reynolds number, $\rho V D_i/\mu$
T	=	temperature, K
u_τ	=	friction velocity, $(\tau_\omega/\rho)^{1/2}$, m/s
y	=	distance of wall-adjacent cell centroid from wall, m
y^+	=	dimensionless distance of wall-adjacent cell centroid from wall, $u_\tau y/\nu$

Greek

ε	=	turbulence dissipation rate, kJ/kg-s
μ	=	dynamic viscosity, kg/m-s
μ_t	=	turbulent viscosity, kg/m-s
ρ	=	density, kg/m³
τ_w	=	wall shear stress, N/m²
ν	=	kinematic viscosity, m²/s

*Research Engineer, 300 College Park.
†Group Leader, 300 College Park, Associate Fellow AIAA.
‡Distinguished Research Chemist, 300 College Park.

I. Introduction

IN ADDITION to providing propulsive energy for hypersonic vehicles, hydrocarbon fuels are used for the regenerative cooling of the combustion chamber and nozzles. As part of an active cooling system, heat is rejected to flowing fuel under conditions of high surface temperatures and large heat fluxes relative to those found in conventional gas turbine engines [1,2]. These high temperatures promote fuel degradation and the formation of deposits on heat transfer surfaces. Surface deposits inhibit cooling by increasing the thermal resistance for conduction heat transfer from flow passage walls. If there is sufficient deposit accumulation in the presence of large heat fluxes, wall-material temperature limits can be reached with the potential for catastrophic vehicle failure. In addition, surface deposits can create an increased pressure drop in regenerative cooling channels and cause nozzle injection problems. Thus, surface deposition is the limiting issue for the use of hydrocarbon fuels in regenerative cooling [2]. In order for vehicle designers to minimize the potential for deposit formation from the use of hydrocarbon fuels, it is important to understand how surface deposition is influenced by flow turbulence, convective heat transfer deterioration, and fuel degradation chemistry.

Computational fluid dynamics (CFD) simulations can be used to help understand how the turbulent flow in regenerative cooling passageways influences the heat transfer and fuel chemistry within the fuel system of a hypersonic vehicle. Thus, selection of a turbulence model that adequately represents the turbulent behavior under these conditions is vital. In the past, the standard k-ε (SKE) turbulence model with the standard wall function (here, referred to together as the SKE-st turbulence model) was used to successfully simulate the fuel flow and thermal conditions relevant for military jet aircraft [3–5]. The SKE-st turbulence model has been employed in nearly all previous simulations of fuel thermal degradation due to its simplicity and fidelity with experimental measurements [5,6]. However, the SKE-st model may be inaccurate under conditions of large temperature gradients. Thus, it is necessary to investigate the performance of the SKE-st turbulence model relative to other turbulence models for heat fluxes and Reynolds numbers that are greater than those of past fuel thermal degradation studies. In this paper, simulations of turbulent fuel flow under high heat flux conditions that used the SKE-st baseline model are compared with those that used the SKE turbulence model with an enhanced wall function (SKE-en turbulence model), the renormalization group k-ε turbulence model with an enhanced wall function (RNG-en

turbulence model), and the shear stress transport k-ω (SST) turbulence model [7–10].

Previous studies of high heat flux cooling have noted a sudden, local rise in the wall temperature that occurs as the fluid reaches the supercritical phase near the heat transfer surface [11–13]. In this past research, the rise in wall temperature was attributed to heat transfer deterioration (HTD), which was defined as a reduction in the heat transfer rate below the normal heat transfer rate [14]. Although high temperatures can significantly reduce the wall-material strength and result in increased surface deposition rates, avoidance of HTD is particularly important for the regenerative cooling designs of hypersonic vehicles. The majority of HTD studies have employed water as the heat transfer fluid and were relevant for the nuclear power industry. In addition, CO_2 was used in a number of studies [14,15]. Relatively few HTD studies have employed hydrocarbons fluids [16,17]. CFD simulations and experiments are used in this paper to explore the flow and thermal conditions, which lead to HTD involving a hydrocarbon fuel.

The high fuel velocity within regenerative cooling passages implies short bulk fuel residence times. Short residence times are desirable for limiting thermal-oxidative deposit reactions. On the other hand, the temperature of the surface contacting the fuel is relatively high under these conditions. High surface temperatures may result in the fuel being in the supercritical phase near the wall, while remaining in the liquid phase in the bulk fuel flow. This results in varied reaction chemistry and flow physics across the tube radius. At wall temperatures that are higher than in the current study, it may be possible for both thermal oxidation and pyrolysis reactions to occur at the same axial tube location, such that pyrolysis occurs very near, or at, the wall, while thermal oxidation occurs away from the wall in the bulk fuel. Calculations and experiments are performed here to study thermal oxidation and deposition under conditions of high temperatures and flow rates representative of those found in hypersonic vehicles. A recently developed thermal-oxidative chemical kinetic mechanism is used to represent oxidation chemistry and surface deposition reactions under these conditions.

II. Experimental

Experiments were performed in which JP-8 fuel flowed vertically upward at 300 ml/min through a 0.0032-m-o.d. (1/8 in.) resistively heated stainless steel (316) tube. The surface roughness (arithmetic average) of the tube samples was 0.2 to 0.4 μm. Figure 1 shows the tube held between two electrical clamps. The tube downstream from the upper clamp, as well as the tube upstream from the lower clamp, is unheated. The electrical power from a 50 kVA dc power supply was adjusted to obtain the desired fuel outlet bulk temperature that was limited by the maximum temperature (746°C) allowed for the safe use of the stainless-steel tubing. The exterior temperature profiles along the tube were measured by fourteen K-type thermocouples welded to the outer tube surface. In later sections of this paper, the heated length (Fig. 1) refers to the tubing between the electrical clamps, and the unheated length is downstream from the downstream clamp but prior to the thermocouple Tee where the outlet bulk temperature was measured.

Two different groups of experiments were performed using the resistively heated tube. The first group was used in the study of turbulence models and jet fuel thermal-oxidative behavior. The second series were used to study heat transfer behavior. All experiments were carried out at a pressure of 5.5 ± 1.0 MPa, which is above the fuel critical pressure of roughly 1.8 MPa. At this pressure, liquid fuel transitions to the supercritical phase without boiling. The duration of each experiment was limited to 25 min to avoid flow disruptions from blockage by fuel deposits.

A. Turbulence Model and Thermal-Oxidative Chemistry Studies

Table 1 summarizes the flow and heating conditions in the experiments used to study turbulence models and thermal-oxidative behavior. The use of a constant inlet flow rate, 300 ± 10 mL/min, and two heated tube lengths provided different fuel residence times and outlet Reynolds numbers. The heating power supplied to the tube
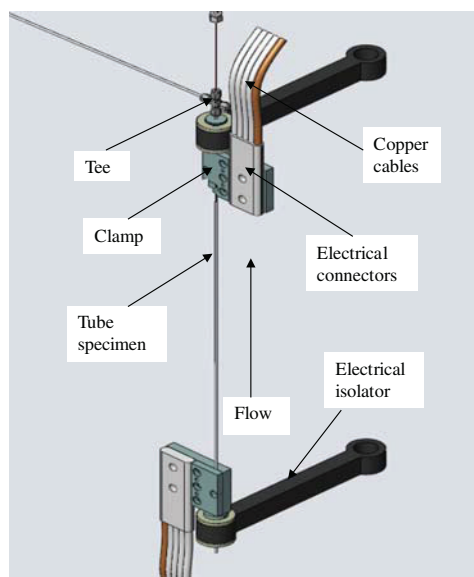

Fig. 1 Resistively heated stainless-steel tube that heated vertically upward flowing jet fuel.

was estimated from the difference between the inlet and outlet fuel enthalpies multiplied by the mass flow rate. The enthalpies were determined from the bulk inlet and outlet temperatures at 5.5 MPa using SUPERTRAPP (Version 3.0) with the assumption that the fuel was n-dodecane [18]. Since jet fuel is a complex mixture of hydrocarbons, the enthalpy for n-dodecane was used for simplicity [19]. The mass flow rate was measured using a turbine flow meter (Max Machinery, Model 284-542). This energy balance neglects ambient heat losses. Using a natural convection correlation [20] for a vertical cylinder in air, and assuming an emissivity of 0.8 for the stainless-steel tube, the sum of the convective and radiative losses from the tube exterior was estimated to be less than ~3% of the input power. Thus, it was reasonable to neglect heat losses from the tube. Lastly, the volumetric heating rate $\dot{q}$ was estimated by dividing the heating power by the metal tube volume in the heated region. The experimental parameters for the two tube lengths are summarized in Table 1.

For the thermal-oxidative chemistry studies, measurements of the dissolved O_2 are obtained by in-line sampling of the fuel and injection into a gas chromatograph and are reproducible to within 5% [21]. The dissolved O_2 was measured before the inlet (from a Tee not shown) and near the outlet (from the Tee in Fig. 1) of the heated tube. The mass of the surface carbon deposits was measured by sectioning the tube and performing carbon burn-off measurements on the sections using a LECO RC-412 multiphase carbon determinator (each section length is ~0.025 m).

Table 1 Experimental parameters for turbulence model and deposition studies

Parameter	Long tube	Short tube
Inner diameter, m	0.00069	
Outer diameter, m	0.0032	
Heated (unheated) length, m	0.254 (0.15)	0.127 (0.15)
Inlet flow rate, mL/min	300	
Inlet Reynolds number	5,000	
Inlet fuel temperature, K	300	
Outlet fuel temperature, K	677	570
Outlet Reynolds number	67,000	43,000
Heating power, W	4,500	3,100
Heat flux, q'', kW/m^2	8,200	11,000
Volumetric heating, $\dot{q}$, MW/m^3	2,300	3,200
Average residence time, ms	15	8

Table 2   Thermal and flow conditions for HTD studies (tube length 25.4 cm, inner diameter 0.069 cm, outer diameter 0.32 cm)

Parameters	Experiment 1	Experiment 2	Experiment 3	Experiment 4	Experiment 5
Flow rate, mL/min	373	452	457	300	109
Inlet Re	5,800	7,050	7,130	4,680	1,700
Heated zone exit Re	19,900	52,000	97,000	111,000	43,000
Measured outlet temperature, K	402	502	598	677	683
$\dot{q}$, MW/m^3	616	1,590	2,420	2,110	790
q'', kW/m^2	2,150	5,550	8,400	7,370	2,750
q''/G, kJ/kg	0.17	0.37	0.55	0.74	0.76

Note: $q'' =$ heat flux (kW/m^2), $G =$ mass flux (kg/m^2-s)

B. Studies of Heat Transfer Behavior

In the second group of experiments, the inlet flow rates and heat fluxes were varied within a long tube (0.254 m) with constant inner and outer diameters (0.00069 m and 0.0032 m, respectively) to study the effect of the flow rate on the heat transfer behavior. For these experiments, Table 2 lists the involved parameters, including inlet and exit Re and $\dot{q}$.

III. Numerical

A commercially available CFD code (Fluent 12.0) was used to simulate the fuel behavior within the heated tube [22]. The simulations involved the finite volume solution of the Navier–Stokes, turbulent energy, thermal energy, and species equations. Convective terms were represented by a second-order accurate upwind scheme, and a version of the SIMPLEC algorithm was used in the solution procedure. The upward flow inside the vertical tubes was assumed to be axisymmetric and steady. For the relatively large velocities involved in this study, buoyancy forces within the fuel were assumed to be negligible and, thus, the gravity term was not included in the momentum equations. The effect of surface deposition on the flow itself (i.e., flow blockage and heat transfer resistance) was not modeled, as the deposits measured in the present experiments were very thin. Similar to the calculations involving the fuel enthalpy as described in the experimental section, n-dodecane was used in the CFD simulations as a surrogate fuel for simplicity [19]. The temperature-dependent thermal and transport properties (density, viscosity, thermal conductivity, and specific heat) for n-dodecane were obtained from the SUPERTRAPP property program and used for all numerical computations [18]. The tube inlet velocity and temperature (300 K) profiles were assumed to be uniform for simplicity, and the inlet velocity was estimated from the cross-sectional flow area together with the inlet volumetric flow rate. When the normalized residuals for all calculated variables were reduced below four orders of magnitude from their maximum values, the solution was considered to be converged.

Axisymmetric computational grids were used to simulate the flow within the heated tubes. Figure 2 shows a representative grid with the number of cells used in the simulations. Cells comprising the relatively thick tube walls were included in the computational

domain. The unheated section was also included in the computations such that the measured bulk temperature at the outlet could be used as one form of validation of the simulations.

Uniform cell spacing was used in the axial (flow) direction (Fig. 2) of the fuel and metal tubing zones. In addition, the cells within the tube wall were spaced uniformly in the radial direction. Because of the high heat flux, relatively large radial temperature gradients were expected in the fuel near the solid–liquid interface and, thus, the structured grids were clustered more densely in this region. A description of the grid independence of the solutions is given in Sec. IV.

A. Turbulence Models

Unlike the SST turbulence model, the SKE and RNG turbulence models do not provide values of the flow variables near the wall and wall functions are used for this purpose. In this paper, the SKE and RNG models were used with the enhanced wall function and are referred to as the SKE-en and RNG-en models, respectively. The enhanced wall function combines a blended law-of-the-wall and a two-layer zonal model to describe the flow within the inner layer of the wall [22,23]. For the enhanced wall function, the first grid point is located within the viscous sublayer, so that $y^+ < 1$. The SKE-st turbulence model was used as a baseline comparison with the other turbulence models.

The numerical study and evaluation of the turbulence models was conducted by two methods. In the first, the simulations were performed by imposing the measured exterior wall temperature profile as a boundary condition. The bulk temperature at the unheated outlet was calculated using the four turbulence models, and these values were compared with the measured temperature there. In the second method, simulations were performed using volumetric heat generation in the tube wall together with an adiabatic boundary condition for the exterior tube wall. For this second stage of simulations, the measured and simulated exterior wall temperature profiles were compared.

B. Thermal-Oxidative Chemistry

In this work, the dissolved O_2 consumption and surface deposition resulting from liquid phase thermal-oxidative reactions are
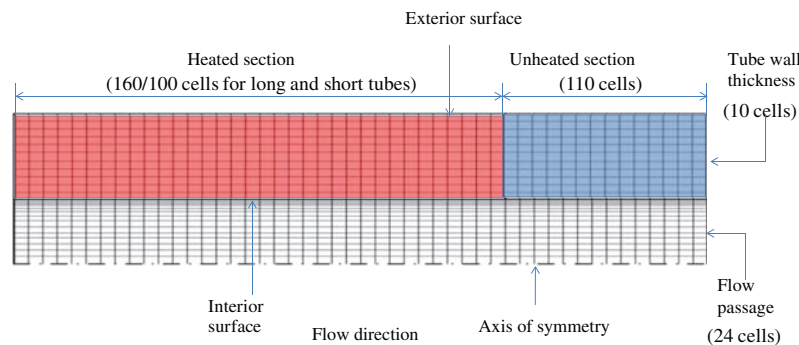
Fig. 2   Representative axisymmetric computational grid (not to scale). Red is associated with the heated wall, and blue represents the unheated wall. The uncolored grid corresponds to the fuel.

Table 3   Pseudodetailed chemical kinetic and global deposition mechanism [5]

Rxn	Reactants			Products		A factor (mol, L, s)	Activation energy (kcal/mol)
1	I	-	→	R·	-	1.00E − 03	0
2	R·	O_2	→	RO_2·	-	3.00E + 09	0
3	RO_2·	RH	→	ROOH	R·	3.00E + 09	12
4	RO_2·	RO_2·	→	$TERMRO_2RO_2$	-	3.00E + 09	0
5	R·	R·	→	R_2	-	3.00E + 09	0
6	RO_2·	AH	→	ROOH	A·	3.00E + 09	5
7	A·	RH	→	AH	R·	1.00E + 05	12
8	A·	RO_2·	→	PRODAH	-	3.00E + 09	0
9	ROOH	SH	→	PRODSH	-	3.00E + 09	18
10	ROOH	-	→	RO·	·OH	1.00E + 15	39
11	RO·	RH	→	ROH	R·	3.00E + 09	10
12	RO·	-	→	RPRIME	CARBONYL	1.00E + 16	15
13	·OH	RH	→	H_2O	R·	3.00E + 09	10
14	RO·	RO·	→	TERMRORO	-	3.00E + 09	0
15	RPRIME	RH	→	ALKANE	R·	3.00E + 09	10
16	RO_2·	-	→	R·	O_2	1.00E + 16	19
17	RO_2·	R·	→	$TERMRO_2R$	-	3.00E + 09	0
18	ROOH	M	→	RO·	·OH M	3.00E + 10	15
19	PRODAH	-	→	SOLUBLES	-	1.00E + 09	0
20	PRODAH	-	→	INSOLUBLES	-	3.80E + 10	6.5
21	INSOLUBLES	-	→	DEPOSITS	-	3.00E + 03	16.3

Note: Symbol Expression: *I*, initiator species; *R*·, hydrocarbon radical; RO₂·, peroxy radical; RH, hydrocarbon; ROOH, hydroperoxide; AH, phenol; SH, reactive sulfur species (e.g., sulfide); M, dissolved metal species.

simulated. A pseudodetailed chemical kinetic mechanism has been developed to represent jet fuel autoxidation reactions [5]. This kinetic mechanism treats the fuel as a mixture of compound classes and is comprised of reactions with rate parameters that are estimates from literature values. A global deposition submechanism was used to simulate the deposition rate [5]. The chemical reactions, activation energies, and *A* factors are listed in Table 3. Table 4 lists the initial species mass fractions for a JP-8 fuel sample, designated as F4177, with the remaining mass fraction assigned to the bulk hydrocarbon species, RH. These values were obtained from the correlation of measurements performed previously. In Tables 3 and 4, *I* is an initiator species. Determining the exact identity of this species remains an active area of research. This trace species only has the role of starting the chain mechanism. The initial inlet concentrations of the other nineteen species (Table 3) were set to zero.

As described later in this paper, the fuel is heated to the supercritical regime only in thin regions adjacent to the wall. Since the pyrolytic temperature regime is confined to thin regions and the residence times are short, cracking and the effects of pyrolysis on bulk fuel properties were ignored in the simulations. Thus, the present work does not numerically simulate the pyrolytic chemistry of jet fuel.

IV.   Results and Discussion

It is important to assess the grid independence of a numerical simulation. Thus, the results of the grid refinement study are described next. The selection of a turbulence model is crucial in the correct modeling of the fluid dynamics, heat transfer, and fuel chemistry. In the following paragraphs, we describe the selection of a turbulence model based on its ability to simulate the measured bulk outlet fuel temperature and external wall temperature profile. An accurate simulation of these temperatures, in turn, is an indirect

confirmation of a reasonable representation of the fluid dynamics and heat transfer. This is followed by a discussion of an unexpected heat transfer deterioration observed in the experiments, which is also simulated here. Lastly, the results from simulations of thermal-oxidative deposition in long and short tubes are described.

A.   Grid Study

The grids were refined via grid adaption in Fluent using values of the outlet fuel temperature to establish grid independence of the solution. Table 5 shows the grid refinement study involving the RNG-en model for both long and short tubes. For both tubes, the difference between the first and third refinements in the calculated outlet fuel bulk temperatures is less than 1.5 K. The chemical kinetic mechanism used to represent the fuel thermal-oxidative chemistry is employed by equations that are numerically stiff. As a result, prohibitively long run times are required for very fine grids. Thus, to save computational time, the grid with the first level of refinement was used in all simulations. In addition, grid refinement studies were conducted for all the turbulence models, but only the results for the RNG-en model are shown here for brevity.

B.   Turbulence Model Studies

The SKE-st, SKE-en, RNG-en, and SST turbulence models were evaluated in two stages. In the first stage, the measured exterior wall temperature profile was used as a boundary condition for the energy equation, and the outlet bulk temperature was compared to measurements. Table 6 shows the calculated bulk temperatures at the end of the unheated section (for the long tube) resulting from the use of the measured exterior wall temperatures. A thermocouple also measured the outlet fuel temperature, and ΔT_{outlet} in Table 6 represents the difference between the simulated and measured outlet

Table 4   Initial concentrations of species used in the chemical mechanism

Species	Initial mass fraction fuel F4177
I	2.08×10^{-9}
O_2	7.08×10^{-5}
ROOH	3.24×10^{-6}
AH	5.91×10^{-5}
SH	2.35×10^{-3}
M	1.41×10^{-6}

Table 5   Calculated outlet bulk temperature and cell numbers simulated by RNG-en model

Tube type	Grid	Total cells	Outlet fuel $T(K)$
Long tube	1st refinement	9,180	667.1
	2nd refinement	18,944	667.7
	3rd refinement	39,429	668.1
Short tube	1st refinement	7,140	566.4
	2nd refinement	18,300	567.3
	3rd refinement	37,584	567.6

Table 6   Outlet bulk temperatures calculated by different turbulence models for the long tube of Table 1

Turbulence model	Wall treatment	y^+	Simulated outlet temperature (K)	$\Delta T_{\text{outlet}}(K)$ $(T_{\text{simulated}} - T_{\text{measured}})$
SKE-st	standard wall function	20–120	712	35
SKE-en	enhanced wall function	0.3–0.6	650	−27
RNG-en	enhanced wall function	0.2–0.8	667	−10
SST	standard k-ω model	0.3–0.6	662	−15

Note: SKE = standard k-ε, RNG = renormalization group, SST = shear stress transport, st = standard wall function, en = enhanced wall function.

fuel temperatures. The listed y^+ values for the location of the first cell adjacent to the wall (and along the entire flow path) are an indication of the grid density near the wall and satisfy the requirements for the different wall models. The largest $|\Delta T_{\text{outlet}}|$ is associated with the SKE-st model. Although a coarse grid near the wall is required by the standard wall function, it results in inaccurate temperatures for this high heat flux condition. In contrast, fine grid spacing is used near the wall for the SKE-en, RNG-en, and SST turbulence models such that the first grid point lies within the viscous sublayer ($y^+ < 1$). The smallest value of $|\Delta T_{\text{outlet}}|$ occurs with the use of the RNG-en model.

Figure 3 shows simulated bulk fuel temperatures along the flow path in the long tube calculated using the four turbulence models. The fuel temperature determined with the SKE-st model rises more rapidly than those calculated by the other models. Thus, the use of the SKE-st model predicts a relatively high convective heat transfer to the fuel. In contrast, SKE-en allows a finer grid spacing near the wall than the SKE-st model, and the bulk temperature profile is closer in agreement with the other models. Figure 3 shows that the use of fine grid spacing in the vicinity of the wall yields bulk temperatures that agree with the measured outlet fuel temperature. In particular, the bulk temperatures calculated using the RNG-en and SST models agree well with each other along the entire flow path. For conditions of a relatively high flow rate and heat flux, the thermal boundary layer will be thin. For this situation, a turbulence model must have the ability to resolve the thin boundary layer behavior, and a fine grid spacing near the wall is necessary. This is an important observation because nearly all previous thermal stability simulations used the SKE-st turbulence model, which requires a relatively coarse grid near the wall. Recent work has also demonstrated that the enhanced wall function can provide accurate simulations of the velocity profile in turbulent channel flow [24]. Lastly in Fig. 3, the calculated bulk temperatures (SKE-en, RNG-en, and SST) continue to rise somewhat after the heated section. This is due to the rise in the fit of the external wall temperatures that was used as a temperature boundary condition in the calculations. For example, Fig. 4 shows that the measured exterior wall temperatures have a relatively small rise, which is due to the uncertainty in the measurements, as indicated by the error bars.

In the majority of past fuel degradation simulations [3–5], the measured wall temperature profile was used as a thermal boundary condition, and the relative agreement between the measured and

calculated exit bulk temperatures was used as a metric of success for adequate simulation of the heat transfer behavior. The focus of these previous studies was primarily on the fuel chemistry rather than on the heat transfer itself. However, the unique high heat flux and high temperature conditions of this paper require additional consideration. In the second stage of turbulence model evaluations, the exterior tube surface was considered to be adiabatic, due to the small heat losses to the ambient, and $\dot{q}$, the volumetric heating within the tube wall, was imposed. The exterior wall temperature of the tube was then calculated for comparison with measured profiles. As will be shown later, this boundary treatment proved to be a more stringent measure of the performance of the turbulence models rather than imposing the measured temperature profile.

In this work, $\dot{q}$ was not directly measured. Instead, the enthalpy difference for the surrogate fuel (n-dodecane) between the exit and entrance of the heated section was obtained from SUPERTRAPP and used to estimate $\dot{q}$, assuming no heat losses. The enthalpy at the heated region exit is based on the bulk temperature there. Since the heated region exit temperature could not be directly measured, it was obtained from the first stage of turbulence model evaluations that used the measured wall temperature profile as a boundary condition and the RNG-en turbulence model. With $\dot{q}$ known, it was used in the energy for a given turbulence model for comparison of the measured and simulated exterior surface temperature profiles.

Figure 4 shows measured and simulated exterior wall temperatures for both the heated and unheated tube segments of the long tube. The measured exterior wall temperature profile has a peak near the inlet. In contrast, the exterior wall temperature profiles simulated using the SKE-st and SST models do not have a well-defined initial peak and have a wall temperature that roughly varies linearly with distance along the heated tube. The SKE-en model captures the initial peak in the exterior wall temperature, but the simulated temperatures in the heated segment are high relative to the measured values. A requirement for use of the standard wall function is that the first cell is located between a y^+ of 30 and 300. In contrast, for the enhanced wall function, the first grid point is located within the viscous sublayer so that $y^+ \leq 1$. Figure 4 shows that the fine grid spacing near the wall
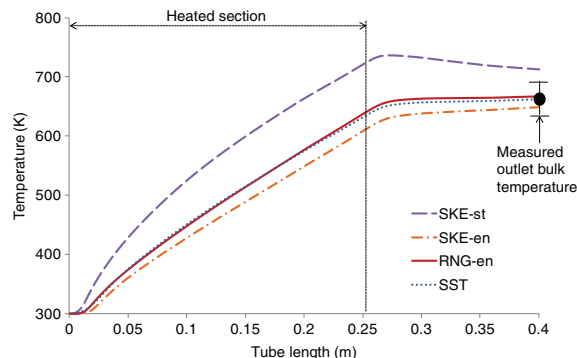
Fig. 3   Calculated bulk fuel temperatures along the length of the long tube using different turbulence models.
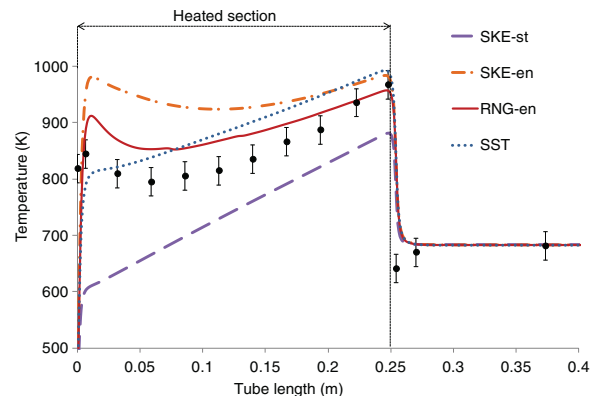
Fig. 4   Exterior surface temperatures calculated using volumetric heat generation with an adiabatic exterior surface for the long tube and different turbulence models.

provides significant improvement over the SKE-st model, in that the temperature profile shape obtained from the SKE-en model is more correct. However, the SKE-en model underpredicts the convective heat transfer in the fuel, which is reflected by the highest exterior wall temperature. Thus, the SKE-en model is inadequate for representation of the turbulent behavior under the present thermal and flow conditions. Figure 4 shows that the RNG-en model produces the initial peak in the exterior wall temperature with a temperature profile that has the best agreement with the measurements. The wall temperatures predicted by the RNG-en model are somewhat higher than the measurements. This may be due in part to the assumption of an adiabatic exterior surface. As described in the experimental section, this assumption is not strictly true, as there are small losses. In addition, there are differences between the actual and surrogate fuel properties. However, the influence of these differences on the resulting temperature simulations is expected to be small [19]. The difference between the measured exterior surface temperature and that simulated using the RNG-en model shows that there are limits in the ability of the RNG-en model to fully capture the physics of HTD.

In addition, the SKE-st, SKE-en, RNG-en, and SST turbulence models were used to simulate the flow and heat transfer within the short tube (not shown). The trends in heat transfer characteristics that were observed in the long tube were also found with the short tube and the use of these turbulence models. The RNG-en model provided the greatest fidelity with measurements for both the short and long tubes. Thus, it was used in all remaining simulations described in this paper.

C. Studies of Heat Transfer Behavior

Figure 4 shows a peak in the measured exterior surface temperature near the inlet of the heated tube. This peak has a corresponding local maximum interior surface temperature due to heat conduction through the tube wall. A peak in the interior surface temperature is a concern because there is potential for increased surface deposition and eventual flow blockage at this location. In addition, any unexpected peak in the wall temperature in a fuel system can result in exceeding material temperature limits. To explore the conditions that result in this surface temperature peak, experiments were performed in which the fuel flow rate and heat flux were varied. In parallel, simulations of the experiments were performed using $\dot{q}$ within the tube wall together with an adiabatic exterior surface boundary. Table 2 lists inlet and exit Re, $\dot{q}$, and the q''/G (kJ/kg) used in the experiments. The mass flux G is the mass flow rate divided by the cross-sectional flow area of the tube. Here, q'' was estimated by dividing the heating power by the interior surface area of the tube in the heated region. The ratio q''/G (kJ/kg) has been used in past studies to characterize the rate of applied heating relative to its convective removal rate [15].

Figure 5a shows the calculated temperatures of the interior tube surface in contact with the fuel. These temperatures correspond to the exterior surface temperatures in Fig. 5b for five different experiments that were performed. To include a range of flow conditions, the experiments involved either laminar or turbulent flow at the entrance of the heated portion of the tube. For example, the inlet Re for experiment 5 was laminar (Re of 1700), while those of the other experiments were turbulent (Re of 4680 to 7130). In all experiments, the outlet Re were highly turbulent (19,900 to 111,000). Experiment 3 had the greatest heating rate (2420 kW/m³) while experiment 1 used roughly one-fourth of that value. The peaks in the inner wall temperature profiles of experiments 4 and 5 are above the critical temperature of the fuel (shown for reference). Since the pressure is above the critical pressure, the fuel adjacent to the wall has transitioned to the supercritical phase. In addition, for experiment 3, there is a relatively small peak in the interior surface temperature, which approaches the critical temperature. In previous studies using other fluids, HTD has been associated with transition from the liquid to supercritical phase [11–15]. As indicated in Fig. 5a, it is believed that the temperature peaks near the inlet for experiments 3 through 5 are evidence of HTD. Past studies involving the heating of water by a large heat flux have found similar behavior in that the interior wall
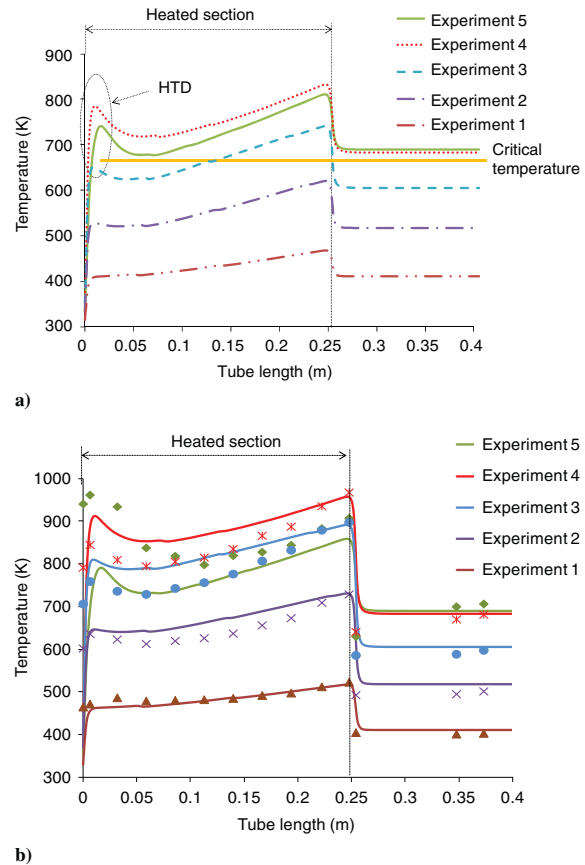

Fig. 5 Plots of a) simulated interior wall temperatures and b) measured (dashed curves) and simulated (solid curves) exterior surface temperatures for the conditions of Table 2.

temperature sharply increases and then rapidly decreases as water is heated from the liquid to the supercritical phase [11–13]. Although somewhat less obvious, an emerging peak for experiment 2 that has interior wall temperatures below the critical temperature seems to also suggest the presence of HTD.

A plot of the heat transfer coefficient along the interior wall provides an explicit means of demonstrating HTD. As an example, Fig. 6a shows the simulated inner wall temperature and heat transfer coefficient along the heated section for experiment 4 of Fig. 5a. Figure 6a shows that the heat transfer coefficient drops sharply near the location where the fuel contacting the wall transitions to the supercritical phase. Rather than monotonically decreasing or leveling, the heat transfer coefficient rises again after the heat transfer coefficient minimum near the inlet. Similar reduction in the heat transfer coefficient (i.e., HTD) for CO_2 systems has been observed previously [14]. Figure 6b shows an image of the heated tube containing flowing fuel during experiment 4. The red, glowing section in the image occurs in the region of HTD and the accompanying temperature rise shown in Fig. 6a. Figure 6b provides a visual demonstration of the occurrence of HTD and suggests the importance of understanding HTD, particularly for the design of advanced fuel systems.

Previous research involving supercritical water found that HTD occurs for a critical q''/G value that, in turn, depends on the pressure and flow path geometry [25]. Referring to the q''/G values in Table 2, Fig. 5a shows that the wall temperature peaks associated with HTD is most obvious for q''/G above 0.5, that is for experiments 3 through 5. For those thermal and flow conditions, the wall heating rate becomes sufficiently high such that the convective flow cannot adequately transport the thermal energy from the interior tube
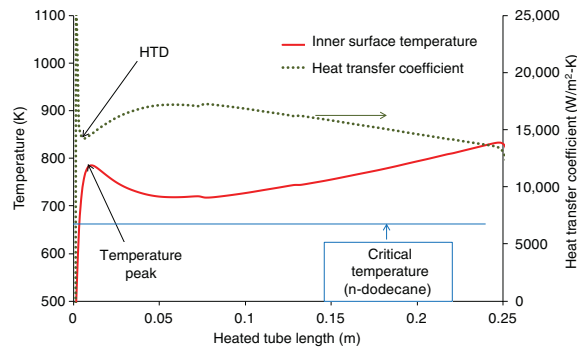
a)
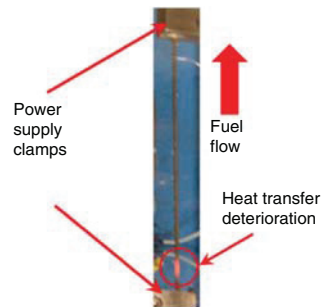
b)

Fig. 6 Experiment 4 data a) simulated and b) photo image of heated tube.

surface, and this is demonstrated by the presence of large temperature gradients near the tube interior surface. As an example, Fig. 7a shows simulations of the fuel temperature in the form of color contours along the heated (short) tube for dimensionless radial locations and the conditions listed in Table 1. Figure 7a shows that the temperature variation in the radial direction is relatively small over most of the tube radius, except very near the tube interior surface. Near the axial location where HTD occurs (~0.4 cm), there is a subcritical bulk flow and a thin layer of fuel in the supercritical phase adjacent to the wall. The enlarged view of Fig. 7b further emphasizes the presence of large temperature gradients near the heated surface. For example, at a distance of roughly 0.4 cm along the tube length, there is a temperature difference of roughly 400 K between $r/R = 0.88$ and $r/R = 1$.

a)
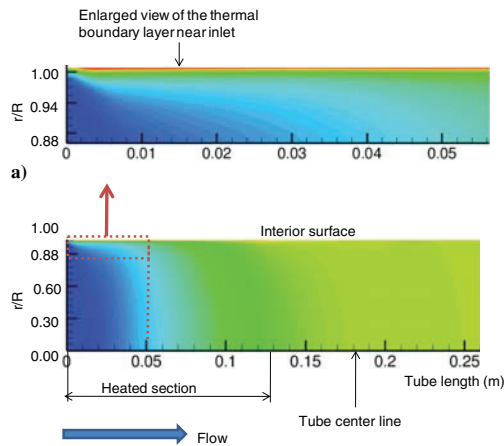
b)

Fig. 7 Simulated temperature contours for short tube a) near-wall and b) axisymmetric views.

The ratio q''/G gives an indication of the potential for HTD but does not offer insight into the HTD mechanism itself. In attempts to explain HTD, several mechanisms have been proposed. Some researchers purport that a buoyancy dominated (upward) flow is necessary for the occurrence of HTD [26]. The present simulations were performed with (upward flow) and without gravitational acceleration in the momentum equations and essentially the same fuel temperature profiles were obtained. Thus, buoyancy was not required here for the occurrence of HTD. This agrees with the work of Palko and Anglart [27] who studied the influence of buoyancy on HTD in flowing water. Some researchers have attributed HTD to the changes in transport properties as a fluid transition from a compressed liquid to a supercritical fluid, but explanations of this mechanism do not agree [11,12,15,25,27]. We now explore the effect of properties on HTD in following paragraphs.

D. Effect of Properties on HTD

To understand the effect of temperature-dependent transport properties on HTD, simulations were performed in which the fuel temperature at the entrance of a tube (0.069-cm-i.d. × 0.32-cm-o.d.× 12.7-cm-long) was varied over the range 300 to 600 K. The temperature of the exterior tube surface was held at 1000 K for simplicity, and the short tube was simulated since the inlet section is the region of concern. In addition, a high inlet flow rate of 300 mL/min, along with the RNG-en turbulence model, was used in the simulations. Because of the large Re along the tube ($Re \sim 100,000$ at the tube outlet), buoyancy forces were neglected.

Figure 8 shows simulated interior surface temperatures associated with different tube-inlet temperatures. Although the calculated interior surface temperatures are above the critical temperature, a temperature peak indicating the occurrence of HTD is most evident for a subcritical inlet temperature of 300 K. With increasing inlet temperature, the peak in the interior surface temperature diminishes. This behavior shows that HTD is maximized when there is a large ΔT between the inlet bulk fuel temperature and the hot wall. This observation is also supported by the simulations shown in Fig. 5a, which also showed that the phase change from liquid to supercritical phase also encourages HTD. Similarly, it was observed in past experiments with CO_2 that the greatest deterioration in heat transfer occurred with the lowest inlet temperatures for a given pressure [11]. It appears likely that the observation that a large ΔT and a liquid supercritical fluid phase change promote HTD is due to the sudden change in the temperature-dependent transport properties near the wall.

It is desirable to understand how properties (e.g., density ρ, dynamic viscosity μ, specific heat C_p, thermal conductivity K, or a combination of these) play a role in the occurrence of HTD in the present hydrocarbon studies. Thus, a series of simulations were performed by holding one property constant while allowing the others to vary with the temperature. Again, the inlet fuel temperature was 300 K for a flow rate of 300 mL/min with an exterior surface
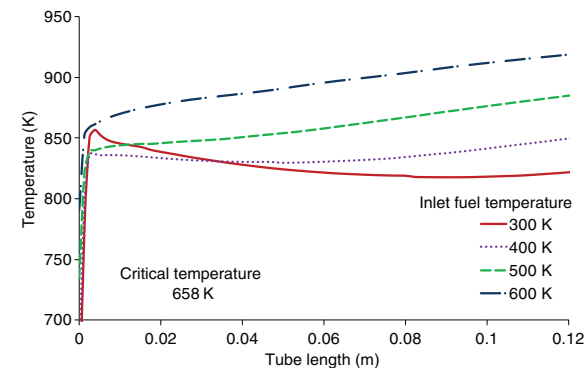
Fig. 8 Simulated interior surface temperatures using different inlet fuel temperatures and a constant exterior wall temperature (1000 K) and inlet flow rate (300 mL/min).

temperature of 1000 K. Figures 9 and 10 show simulated interior surface temperatures for each property that is sequentially held constant. In the legend of Fig. 9 for example, ρ-Constant means that the density was held constant and μ, C_p, and K varied with the temperature. The legend none held constant means that all transport properties were simultaneously varied with fuel temperature. Each property value was held constant at a single temperature in the liquid phase (390 K) and also in the supercritical phase (780 K). Figures 9 and 10 show the interior wall temperatures for constant properties evaluated in the liquid phase and supercritical phase, respectively.

Figures 9 and 10 show that the fuel viscosity has the largest effect on the occurrence of HTD under these conditions. When the dynamic viscosity is held constant at either the liquid (390 K) or supercritical phase (780 K) values, the inlet peak temperature profile is eliminated, showing that HTD is inhibited. These results indicate that viscosity is the dominate transport property leading to HTD under these conditions. Figure 11 shows a plot of the dynamic viscosity in the (compressed) liquid and supercritical phases for a constant pressure of 5.52 MPa between 300 and 950 K for n-dodecane and generated using SUPERTRAPP [18]. In addition, dynamic viscosity values along the saturated liquid and vapor curves are shown for reference. Figure 11 shows that the viscosity decreases by roughly two orders of magnitude in the temperature range 300 to 900 K. This is a large change with temperature relative to ρ, C_p, and K, which all vary by less than a factor of five in this same temperature range. It is apparent from the figures that other transport properties can also play a role in HTD (e.g., density). While the fuel viscosity decreases by roughly two orders of magnitude (in the temperature range 300 to 900 K), the resulting heat transfer is ultimately a complex function of

Fig. 11 Dynamic viscosity of n-dodecane along a constant pressure curve (5.52 MPa) and along the saturated liquid and vapor curves.
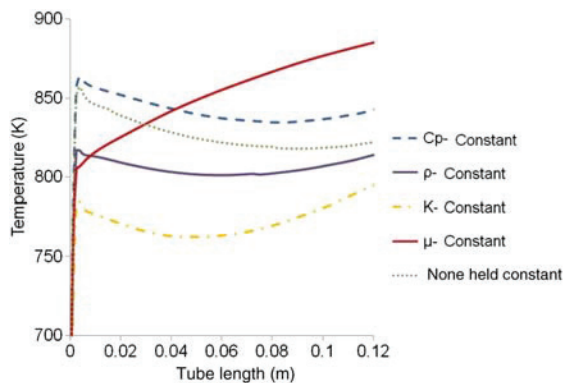
Fig. 9 Simulated interior wall temperatures with one property held constant (liquid phase value determined at 390 K) while the other properties vary with temperature.
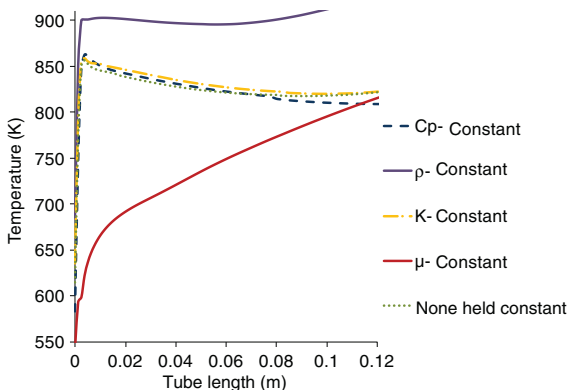
Fig. 10 Simulated interior surface temperatures with one supercritical phase property held constant (value determined at 780 K) while the other properties vary with temperature.
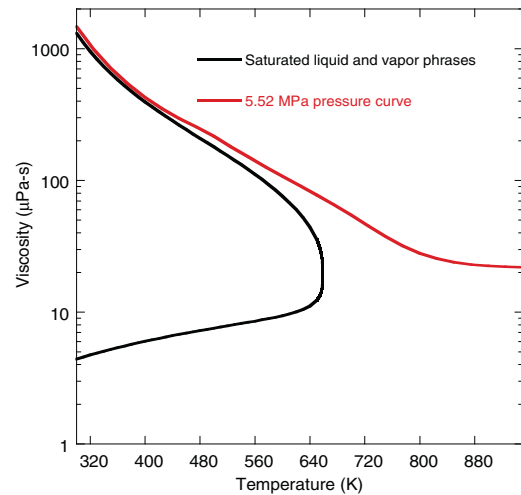
the coupled temperature-dependent behavior of all of the transport properties and their effect on the velocity and thermal boundary layers.

A decrease in the wall shear stress near the location of HTD was observed in the present CFD simulations. In light of the similarity between heat and momentum transport in the turbulent boundary layer, the heat transfer coefficient would then be expected to decrease there as well. In addition, our CFD simulations showed a reduction in the turbulence intensity near the wall in regions of HTD. A reduction in turbulence intensity translated to a decreased turbulent mixing and heat transport from the wall. The current results are supported by an early study of HTD by Shiralkar and Griffith [11] who heated CO_2 from the subcooled liquid phase to the supercritical phase under supercritical pressures. They believed that decreases in viscosity and density within the supercritical phase adjacent to the heated surface reduced the local wall shear stress. As a consequence, this resulted in HTD because the effects of low viscosity and density near the heated surface were not yet offset by increased velocities in the core of the flow [11]. In our study (Fig. 8) as well as that of [11], it was necessary for the inlet temperature to be below some value (with the fluid still in the liquid phase) and for the wall temperature to be above the critical temperature for a given supercritical pressure in order for HTD to be observed. This condition ensured a thin layer in the supercritical phase adjacent to the heated wall with a bulk temperature below the critical temperature and, consequently, a reduction in the wall shear stress. Figure 8 emphasizes the importance of the effects of the inlet fuel conditions for a heated section within an advanced fuel system and would be of concern for designers.

To summarize, a series of experiments and simulations were conducted to investigate HTD involving jet fuel, and the following were observed:

1) The RNG-en turbulence model allowed reasonable simulation of HTD within a supercritical layer near the wall.

2) HTD occurred for flow conditions of a large heat flux q'' with low mass flux rate G.

3) Buoyancy dominated flow was not required for the occurrence of HTD in the present study.

4) HTD was reflected by a rapid decrease in the heat transfer coefficient and a rapid increase in the wall temperature above the fuel critical temperature. A peak in the wall temperature was related to the large temperature difference between the interior wall and bulk fuel, which was associated with transition from the subcritical to supercritical phase in the fluid near the interior surface.

5) As fuel was heated from the liquid to the supercritical phase, the viscosity temperature dependence was the primary transport property leading to HTD.

E. Thermal-Oxidative Chemistry Studies

It is important to study the effect of high heat flux on surface deposit formation to enable the development of software tools that allow fuel system designers to use the cooling capacity of the fuel most efficiently while avoiding excessive deposit production. Previously, a pseudodetailed chemical kinetic mechanism was developed to numerically simulate dissolved O_2 consumption and surface deposition over the temperature range 458 to 673 K [5]. This mechanism demonstrated good agreement between simulations and experiments for deposits produced over a range of fuel samples at relatively low heat flux conditions. Here, the use of this chemical kinetic mechanism to simulate dissolved O_2 consumption under the present high heat flux and high wall temperature conditions is explored.

Figure 12a shows a plot of the simulated dissolved O_2 along the interior surface and centerline for the long tube. In the heated section, little dissolved O_2 (less than 0.8%) is consumed in agreement with the experimental measurements (<2% O_2 consumed) due to the short residence time (~12 ms) there. Figure 12a shows that the O_2 profiles along the interior surface and tube centerline are nearly identical, despite the higher temperature at the interior surface of the heated tube. Dissolved O_2 consumption depends on both the residence time and fuel temperature, and this result emphasizes the importance of residence time in fuel oxidation. A nearly uniform fuel temperature of 667 K is maintained within most of the downstream unheated section. Because of the longer times (that is up to a residence time of ~8 ms in the unheated section and ~12 ms in the heated section) at higher temperatures, the resulting O_2 consumption is greater in the unheated section than in the heated section. Figure 12b shows similar dissolved O_2 consumption behavior in the short tube.

The pseudodetailed kinetic mechanism used to simulate dissolved O_2 consumption also included a global deposit submechanism for the simulation of thermal oxidative deposition [5]. This deposition submechanism demonstrated good agreement between calculations and experiments for deposits produced for a range of different fuel samples under relatively low heat flux conditions. Here, this global deposit submechanism developed previously is employed without modification to simulate deposition under our high heat flux and high wall temperature conditions. The purpose of this work is to better understand the deposition process at these conditions, and to examine the usefulness of the deposition submechanism at these extrapolated conditions.

The simulated and measured deposit profiles are compared on a normalized basis, where the simulated and measured deposits are normalized to their respective peak values. This normalization is performed to assess the ability of the simulation to correctly predict the deposition profiles, while initially not being concerned with absolute deposit quantities. The normalized deposit profiles (simulated and measured) are plotted in Figs. 13a and 13b for the long and short tubes, respectively. The figures show reasonable agreement in the measured and simulated deposit profiles for both tubes. For both the long and short tubes, the simulations and measurements show a peak near the end of the heated section, with a drop in deposition upon entering the unheated tube, followed by an increase in deposits near the end of the unheated section. The good agreement in deposit profiles between the simulation and measurement gives confidence in the ability of employing the deposit submechanism for the current conditions, which are beyond the conditions for which it was developed.

It is important to note that the absolute magnitude of the simulated deposit prediction using this deposition submechanism is not in good agreement between simulation and experiment, with the simulation being lower than the experiment by up to a factor of 6×10^3 (for the peak deposition in the long tube). This lack of agreement is not unexpected as the deposition submechanism is a global mechanism that was developed for a particular set of fuels under lower heat flux and temperature conditions. One goal of this work is to obtain these comparisons between the simulation and experiments to allow
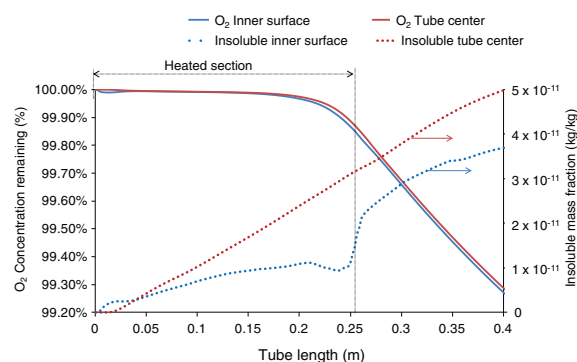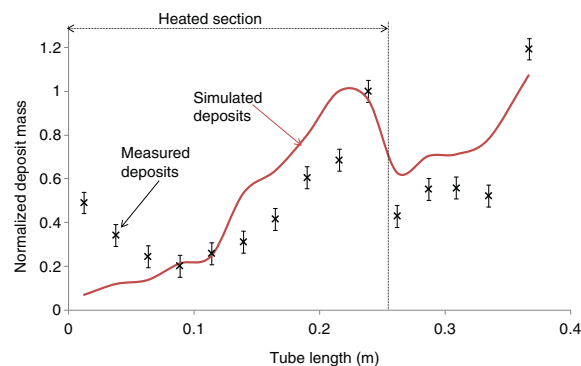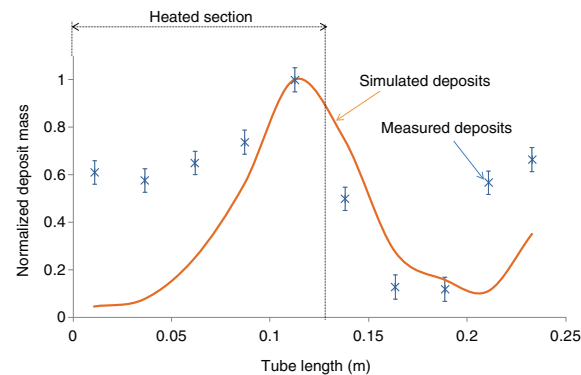

a)
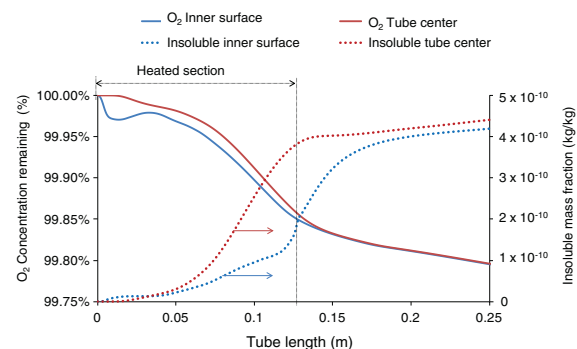
b)

Fig. 12 Simulated dissolved O_2 (solid lines) and insoluble species (dashed lines) along the interior surface and centerline of the a) long tube and b) short tube.

a)

b)

Fig. 13 Comparison of the measured and simulated deposit mass along the a) long tube and b) short tube.

development of improved deposition submechanisms that can be used to predict deposition over a wide range of flow and temperature conditions. We have chosen not to modify the Arrhenius parameters in the deposition submechanism to match the deposition of the current study, but rather use the differences between simulation and experiment to help determine future modifications required for a deposit submechanism that is more globally applicable.

One important difference between the simulated and measured deposit profiles occurs near the tube entrance region for both the long and short tubes. The measured deposit profiles both show significantly higher normalized deposition than the simulations. We have previously shown that the wall temperatures in these regions are above the fuel supercritical temperature and, thus, fuel pyrolysis may occur in the near-wall region. Simple kinetic calculations (assuming a global fuel pyrolysis activation energy of ∼60 kcal/mol) show that the extremely short residence times (<1 ms) for which the fuel is exposed to these supercritical temperatures results in only minor extents of fuel pyrolysis. At this time, it is unclear whether fuel pyrolysis at the near-wall region of the tube entrance can be the cause of the increased deposition observed experimentally for both tubes. Future chemical kinetic mechanisms can combine pyrolytic reactions along with the current oxidative reaction scheme to further elucidate the chemistry occurring in the near-wall regime.

Another interesting observation in the deposition profiles of both long and short tubes is the increase in deposition near the end of the unheated section. This increase in deposition occurs despite the relatively low temperatures in this region, especially for the short tube (Fig. 13b). An examination of the profiles of the global insolubles species is instructive in determining the cause of this increased deposition. The insolubles species concentrations are plotted in Figs. 12a and 12b for the long tube and short tubes. The plots show that for the long tube, the insolubles continue to be produced in the unheated section due to increased O_2 consumption. This is less apparent in the short tube, but this tube exhibits a higher level of insoluble production in the heated section due to the higher temperatures. The increase in deposition in the unheated section of the long tube can be explained by the continued increase in the insolubles deposit precursor species in this section, which is caused by increased O_2 consumption at relatively high temperatures. The short tube simulation only shows a minor increase in deposition at the end of the unheated section despite a larger increase demonstrated in the measured profile. The short tube exhibits a significant cooling of the fuel when entering the unheated section. Cooling can result in the increased formation of insolubles due to decreased solubility at lower temperatures. The current deposit submechanism does not consider this process of insoluble formation and thus, may underpredict deposition in cooled regimes. Future deposit submechanisms may need to consider the effect of fuel cooling on insoluble formation. The extent of fuel cooling after heating depends on fuel system design, with some fuel systems having insignificant cooling due to fuel combustion soon after fuel heat exposure.

V. Conclusions

The first challenge of this work was to select an appropriate turbulence model so that simulation results would correctly represent the fuel behavior under high heat flux conditions. In the past, the standard k-ε turbulence model (SKE) was used successfully to simulate high Reynolds number flow. For the current flow and heating conditions, poor agreement was found for the SKE model incorporating a standard wall function (SKE-st), which used coarse grid spacing near the wall. The fine grid spacing of the SKE turbulence model with an enhanced wall function (SKE-en model) provided a significant improvement over the SKE-st model. Thus, the grid density in the vicinity of the wall is important and fine grid spacing may likely be required when large heat fluxes are imposed on the interior wall surface. However, simulations using the SKE-en model also showed an underprediction of the fuel heat transfer compared with the shear stress transport k-ω (SST) turbulence model and the renormalization group k-ε turbulence model with an enhanced wall function (RNG-en) and measured temperatures. The

SST model failed to predict the physical phenomena of the initial peak in the wall temperature that was observed in the experiments. The RNG-en turbulence model provided an accurate solution for representation of the turbulent behavior under the present high heat flux conditions. The simulated temperatures obtained using the RNG-en model yielded reasonable heat transfer rates, which were reflected by the agreement between measured and simulated outlet fuel bulk temperatures and by the ability to reproduce the measured exterior wall temperature.

The understanding and simulation of heat transfer deterioration (HTD) and, ultimately, how it may be avoided is important for the design of high speed aircraft. HTD was manifested by a rapid decrease in the heat transfer coefficient and a rapid increase in the wall temperature above the fuel critical temperature. An unexpected local maximum in the wall temperature may create a local maximum deposition rate on the interior tube surface that could lead to increased heat transfer resistance and tube material failure or flow path blockage. Experiments and simulations involving jet fuel flowing under conditions of high heat flux and supercritical pressure were performed to investigate HTD. It was found that an initial peak in the wall temperature was caused by HTD within the supercritical layer adjacent to the interior tube surface and that the RNG-en turbulence model allowed reasonable simulation of HTD there. In addition, it was found that HTD occurs for flow conditions involving a large q'' with a low G. The observed wall temperature peaks were related to the large temperature difference between the interior surface and bulk fuel, which was associated with transition from the subcritical to supercritical phase in the fluid layer adjacent to the interior tube surface. As the fuel was heated from the liquid to the supercritical phase, the viscosity temperature dependence was the primary transport property leading to HTD. Lastly, buoyancy dominated flow was not required for the occurrence of HTD in the present study.

A pseudodetailed chemical kinetic mechanism was incorporated in the present simulations to study the effect of high heat flux and flow rate on dissolved O_2 consumption together with a global submechanism for the simulation of thermal-oxidative surface deposition. Dissolved O_2 consumption depends on both the residence time and the temperature. Because of the longer residence times at higher temperatures in the long tube, it was found that the resulting O_2 consumption was greater in the unheated section than in the heated section. Most thermal-oxidative stability studies of jet fuel report results involving only heated flow paths while ignoring the behavior in unheated passages. However, the current research showed that there was greater O_2 consumption in the unheated section and demonstrates that O_2 consumption in unheated passages should not necessarily be ignored. Increased consumption of O_2 is a concern as it may lead to increased surface deposition there. The deposition submechanism was developed previously for use under low heat flux conditions and was considered here to assess the usefulness of the deposition submechanism at the present extrapolated conditions. Reasonable agreement was found between the measured and simulated deposit profiles that were normalized by the peak deposit values for both tubes. This agreement provided a degree of confidence in the use of the deposit submechanism for the current conditions. Because of differences between the measured and simulated absolute deposition magnitudes, the global deposition submechanism needs to be further investigated for use over a wide temperature range. In addition, the role of fuel pyrolysis near the heated interior surface at the tube entrance should be studied in future work. A long-range goal of this work is to develop improved deposition submechanisms that can be used to predict deposition over a wide range of flow and temperature conditions.

representing the official policies or endorsements, either expressed or implied, of Air Force Research Laboratory or the U.S. Government.

References

[1] Heiser, W. H., and Pratt, D. T., *Hypersonic Airbreathing Propulsion*, AIAA, Washington, 1994, pp. 479–496.

[2] Bates, R., Edwards, T., and Meyer, M. L., "Heat Transfer and Deposition Behavior of Hydrocarbon Rocket Fuels," *41st Aerospace Sciences Meeting and Exhibit*, AIAA Paper 2003-0123, 2003.

[3] Katta, V. R., and Roquemore, W. M., "Numerical Method for Simulating Fluid-Dynamic and Heat-Transfer Changes in Jet-Engine Injector Feed-Arm Due to Fouling," *Journal of Thermophysics and Heat Transfer*, Vol. 7, No. 4, 1993, pp. 651–660.
doi:10.2514/3.474

[4] Ervin, J. S., and Zabarnick, S., "Computational Fluid Dynamics Simulations of Jet Fuel Oxidation Incorporating Pseudo-Detailed Chemical Kinetics," *Energy Fuels*, Vol. 12, No. 2, 1998, pp. 344–352.
doi:10.1021/ef970132m

[5] Kuprowicz, N. J., Zabarnick, S., West, Z. J., and Ervin, J. S., "Use of Measured Species Class Concentrations with Chemical Kinetic Modeling for the Prediction of Autoxidation and Deposition of Jet Fuels," *Energy Fuels*, Vol. 21, No. 2, 2007, pp. 530–544.
doi:10.1021/ef060391o

[6] Launder, B. E., and Spalding, D. B., "The Numerical Computation of Turbulent Flows," *Computer Methods in Applied Mechanics and Engineering*, Vol. 3, No. 2, 1974, pp. 269–289.
doi:10.1016/0045-7825(74)90029-2

[7] Yakhot, V., Orszag, S. A., Thangam, S., Gatski, T. B., and Speziale, C. G., "Development of Turbulence Models for Shear Flows by a Double Expansion Technique," *Physics Fluids A*, Vol. 4, No. 7, 1992, pp. 1510–1520.
doi:10.1063/1.858424

[8] Menter, F. R., "Two-Equation Eddy-Viscosity Turbulence Models for Engineering Applications," *AIAA Journal*, Vol. 32, No. 8, 1994, pp. 1589–1605.
doi:10.2514/3.12149

[9] Menter, F. R., Kuntz, M., and Langtry, R., "Ten Years of Industrial Experience with the SST Turbulence Model," *Turbulence, Heat and Mass Transfer 4: Proceedings of the Fourth International Symposium on Turbulence, Heat and Mass Transfer, Antalya, Turkey, Oct. 12–17, 2003*, edited by Hanjalic, K., Nagano, Y., and Tummers, M. J., Begell House, Redding, CT, 2003.

[10] Wilcox, D. C., *Turbulence Modeling for CFD*, DCW Industries, La Canada, CA, 1993, pp. 73–128.

[11] Shiralkar, B. S., and Griffith, P., "The Deterioration in Heat Transfer to Fluids at Super-critical Pressure and High Heat Fluxes," Massachusetts Institute of Technology Report No. 70332-5, Engineering Projects Laboratory, Department of Mechanical Engineering, 1968.

[12] Koshizuka, S., Takano, N., and Oka, Y., "Numerical Analysis of Deterioration Phenomena in Heat Transfer to Supercritical Water," *International Journal of Heat and Mass Transfer*, Vol. 38, No. 16, 1995, pp. 3077–3084.
doi:10.1016/0017-9310(95)00008-W

[13] Mokry, S., Pioro, I., Kirillov, P., and Gospodinov, Y., "Supercritical-Water Heat Transfer in a Vertical Bare Tube," *Nuclear Engineering and Design*, Vol. 240, No. 1, 2010, pp. 568–576.
doi:10.1016/j.nucengdes.2009.09.003

[14] Duffey, R. B., and Pioro, I. L., "Experimental Heat Transfer of Supercritical Carbon Dioxide Flowing Inside Channels (Survey)," *Nuclear Engineering and Design*, Vol. 235, 2005, pp. 913–924.
doi:10.1016/j.nucengdes.2004.11.011

[15] Pioro, I. L., Khartabil, H. F., and Duffey, R. B., "Heat Transfer to Supercritical Fluids Flowing in Channels-Empirical Correlations (Survey)," *Nuclear Engineering and Design* Vol. 230, Nos. 1–3, 2004, pp. 69–91.
doi:10.1016/j.nucengdes.2003.10.010

[16] Zhong, F., Fan, X., Yu, G., and Li, J., "Heat Transfer of Aviation Kerosene at Supercritical Conditions," *Journal of Thermophysics and Heat Transfer*, Vol. 23, No. 3, 2009, pp. 543–550.
doi:10.2514/1.41619

[17] Hua, Y. X., Wang, Y. Z., and Meng, H., "A Numerical Study of Supercritical Forced Convective Heat Transfer of *n*-Heptane inside a Horizontal Miniature Tube," *Journal of Supercritical Fluids*, Vol. 52, No. 1, 2010, pp. 36–46.
doi:10.1016/j.supflu.2009.12.003

[18] SUPERTRAPP, Thermophysical Properties of Hydrocarbon Mixtures Database, Ver. 3.0, NIST, Gaithersburg, MD, 1999.

[19] Ervin, J. S., Ward, T. A., Williams, T. F., and Bento, J., "Surface Deposition Within Treated and Untreated Stainless Steel Tubes Resulting from Thermal-Oxidative Degradation of Jet Fuel," *Energy Fuels*, Vol. 17, No. 3, 2003, pp. 577–586.
doi:10.1021/ef020180t

[20] Arpaci, V. S., Kao, S., and Selamet, A., *Introduction to Heat Transfer*, Prentice–Hall, Upper Saddle River, NJ, 1999, Chap. 6.

[21] Rubey, W. A., Striebich, R. C., Tissandier, M. D., and Tirey, D. A, "In Line Gas Chromatographic Measurement of Trace Oxygen and Other Dissolved Gases in Flowing High-Pressure Thermally Stressed Jet Fuel," *Journal of Chromatographic Science*, Vol. 33, No. 8, 1995, pp. 433–437.
doi:10.1093/chromsci/33.8.433

[22] ANSYS FLUENT, Ver. 12.0, ANSYS, Inc. Canonsburg, PA, 2009.

[23] Ciofalo, M., and Collins, M. W., "*k-ε* Predictions of Heat Transfer in Turbulent Recirculating Flows Using an Improved Wall Treatment," *Numerical Heat Transfer*, Part B, Vol. 15, No. 1, 1989, pp. 21–47.

[24] El Gharbi, N., Absi, R., Benzaoui, A., and Amara, E. H., "Effect of Near-Wall Treatments on Airflow Simulations," *Proceedings of 2009 International Conference Computational Methods for Engineering and Environment*, 2009, pp. 185–189.

[25] Wang, J., Li, H., Guo, B., Yu, S., Zhang, Y., and Chen, T., "Investigation of Forced Convection Heat Transfer of Supercritical Pressure Water in a Vertically Upward Internally Ribbed Tube," *Nuclear Engineering and Design*, Vol. 239, No. 10, 2009, pp. 1956–1964.
doi:10.1016/j.nucengdes.2009.04.012

[26] Sharabi, M., and Ambrosini, W., "Discussion of Heat Transfer Phenomena in Fluids at Supercritical Pressure with the Aid of CFD Models," *Annals of Nuclear Energy*, Vol. 36, No. 1, 2009, pp. 60–71.
doi:10.1016/j.anucene.2008.10.006

[27] Palko, D., and Anglart, H., "Theoretical and Numerical Study of Heat Transfer Deterioration in High Performance Light Water Reactor," *Science and Technology of Nuclear Installations*, Vol. 2008, 2008, pp. 1–5.
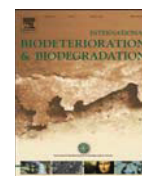doi:10.1155/2008/405072

Appendix Q. Characterization of the F-76 Diesel and Jet A-1 Aviation Fuel Hydrocarbon Degradation Profiles of Pseudomonas aeruginosa and Marinobacter hydrocarbonoclasticus

CrossMark

Characterization of the F-76 diesel and Jet-A aviation fuel hydrocarbon degradation profiles of *Pseudomonas aeruginosa* and *Marinobacter hydrocarbonoclasticus*

Richard C. Striebich [a], Caitlin E. Smart [b], Thusitha S. Gunasekera [a], Susan S. Mueller [a], Ellen M. Strobel [b], Brett W. McNichols [b], Oscar N. Ruiz [b],*

[a] University of Dayton Research Institute (UDRI), 300 College Park, Dayton, OH 45469-0043, USA
[b] Air Force Research Laboratory, Aerospace Systems Directorate, Fuels and Energy Branch, Wright-Patterson AFB, OH 45433, USA

ABSTRACT

To better understand the process of fuel biodeterioration, Jet-A and F-76 diesel fuel were exposed to *Pseudomonas aeruginosa*, a common fuel contaminant, and *Marinobacter hydrocarbonoclasticus*, a marine hydrocarbon degrader, and the extent of hydrocarbon decomposition produced by these bacteria determined. Degradation assays containing fuel-minimal media mixtures and bacteria were analyzed by gas chromatography (GC) to discern the consumption of fuel hydrocarbons. Experiments were conducted in closed systems to prevent evaporation of hydrocarbons and allow accurate quantitation. Results indicated that *P. aeruginosa* preferred to consume mid-range normal alkanes (C_{12}–C_{18}) followed by higher chain n-alkanes (C_{19}–C_{23}). Cycloparaffins were consumed at much lower rates, while aromatic and isoparaffins were not consumed. However, *M. hydrocarbonoclasticus* showed a different profile with preferential degradation of shorter n-alkanes (C_8–C_{11}) and specific aromatic compounds. Both types of bacteria were incapable of degrading branched alkanes. During larger scale bioreactor tests, bacteria were able to degrade similar hydrocarbons. This study clearly demonstrated that the effects of fuel biodeterioration can go well beyond corrosion and filter fouling, with different bacteria metabolizing different fuel hydrocarbons and presenting the possibility for microbes to directly change fuel composition and properties. Results are discussed in light of the use of newer alternative fuels which can have dramatically different hydrocarbon profiles compared to conventional petroleum fuels.

Published by Elsevier Ltd.

1. Introduction

Biological growth and its effect on the cleanliness of aviation, marine and ground fuels is a significant concern to fuel users. Water introduced into fuel by condensation or through leaky infrastructure can often collect at the bottom of tanks exacerbating microbial growth and biodegradation. Bacteria are ubiquitous in the environment but once in fuel, extensive growth and biofilm formation can lead to costly and disruptive problems in fuel systems including tank corrosion, fuel pump failures, filter plugging, injector fouling, topcoat peeling, and engine damage (Edmonds and Cooney, 1967;

Passman et al., 2001, 2012; Jung et al., 2002; Rauch et al., 2006; Brown et al., 2010; Korenblum et al., 2010; White et al., 2011). Besides these effects, there has been speculation about the effects of microbes on the actual fuel composition and quality. Microbes can severely reduce the concentration of lubricity improvers present in diesel fuels, increasing wear in pumps and at other high friction surfaces (Stamper et al., 2012). Because kerosene and diesel distillate products may serve as food and energy source to microorganisms, it is possible that rampant growth could lead to measureable changes in fuel composition.

Multiple bacterial species have been isolated from environments exposed to fuel (Edmonds and Cooney, 1967; White et al., 2011) with *Pseudomonas aeruginosa* and *Marinobacter hydrocarbonoclasticus* being ubiquitous hydrocarbon degraders of terrestrial and marine environments, respectively (Belhaj et al., 2002). Bacteria and other microorganisms in fuel tanks prefer to

* Corresponding author. Air Force Research Laboratory, Aerospace Systems Directorate, Fuels and Energy Branch, 1790 Loop Road, Bldg. 490, Wright-Patterson AFB, OH 45433, USA. Tel.: +1 937 255 6237.
  E-mail address: oscar.ruiz@us.af.mil (O.N. Ruiz).

live in the water/fuel interface, feeding on the hydrocarbons, thereby having a limitless supply of fuel available to grow. While the fuel is a source of energy for the bacteria, components of it may be toxic to the organism; many bacteria have evolved protection mechanisms such as the formation of biofilms and the activation of efflux pumps for protection (Gunasekera et al., 2013). Biofilms are collections of cells enclosed in a matrix of polymeric compounds, primarily exopolysaccharides (EPS) (Vu et al., 2009). Biofilm formation in fuel tanks and its importance have been described (Passman, 2003). The combination of biofilms and the cellular material from organisms can create significant masses that can disable filters, plug flow paths and generally upset the intricate nature of the fuel delivery system for aircraft and ground engines.

P. aeruginosa, a rod-shaped, gram-negative bacteria, is known to metabolize normal alkanes in fuels *via* oxidation and use them as the sole carbon source for growth. *P. aeruginosa* has two alkane hydroxylases (alkB1 and alkB2), cytochrome P450 and other essential electron transfer proteins that allow it to metabolize medium and long normal alkanes (Gunasekera et al., 2013). The *P. aeruginosa* strain ATCC 33988, originally isolated from a fuel storage tank, was used in this study. Some *Pseudomonas* species have also been known to consume other hydrocarbons including aromatics and cyclic hydrocarbons but generally these hydrocarbons appear to be more toxic to microorganisms (Corwin and Anderson, 1967; Inoue and Horikoshi, 1989; Li et al., 1998). *Marinobacter hydrocarbonoclasticus* is also a rod-shaped, gram-negative aerobic halophilic heterotrophic bacteria recently isolated from marine environments polluted with hydrocarbons. While the exact pathways by which *Marinobacter* can metabolize multiple hydrocarbons are not well understood, this bacteria is known to degrade normal alkanes by the action of the alkane monooxygenases encoded by the *alk*B genes (Smith et al., 2013). Also this bacteria is well-known for its ability to use hydrocarbon as the sole source of carbon and energy and for being an important player in the biodegradation of polycyclic aromatic hydrocarbons (PAH) in seawater (Vila et al., 2010). However, the degradation of Jet-A and diesel fuels by *Marinobacter* has not been studied.

The objective of this investigation was to characterize the hydrocarbon degradation profile of *P. aeruginosa* and *M. hydrocarbonoclasticus* when grown on Jet-A and F-76 marine diesel fuels as the sole carbon source. Further, the biodegradation rate of major hydrocarbon components in these fuels by each bacteria was investigated to ascertain which compounds could be consumed most readily to determine the possible impact of fuel biodegradation. The effect of bacteria on fuel was studied by performing fuel bioassays in which fuel and minimal media mixtures exposed to bacteria were carefully analyzed by two-dimensional gas chromatography (GCxGC) in order to characterize fuel hydrocarbon degradation rate and profile. Experiments using alternative fuels and larger scale bioreactors were also conducted to confirm the results observed in small vial experiments, extending the applicability of this study to the effect of biodegradation on larger volumes of conventional fuel and new alternative fuels.

2. Materials and methods

2.1. Fuel bioassay

Studies were conducted to investigate which specific compounds or compound types in Jet-A and F-76 fuel were preferentially degraded by *P. aeruginosa*. The fuel-degrading bacteria *P. aeruginosa* strain ATCC 33988, originally isolated from a fuel storage tank, was grown in Luria–Bertani (LB) broth overnight in a shaker incubator at 28 °C. The cells were then pelleted and washed three times with M-9 minimal media to remove any residues of LB

broth before being added to the bioassay mixture. The bioassays were performed by using 10 µL of Jet-A or F-76 fuel in 990 µL of M-9 minimal media (90 mM $Na_2HPO_4 \cdot 7H_2O$, 22 mM KH_2PO_4, 8.5 mM NaCl, 18.6 mM NH_4Cl, 2 mM $MgSO_4$, 0.1 mM $CaCl_2$ and 0.02 mM $FeSO_4$) containing *P. aeruginosa* at 0.03 OD (optical density measured at 600 nm) in a 8 mL glass vial sealed with a PTFE-lined lid. The lids were tightened and sealed with parafilm. The samples were maintained in a 28 °C incubator for a period of between 10 and 13 days, without opening the vial. Multiple samples (triplicate for each time point) were incubated at the same time, and then sample vials were removed from the incubator at the time of testing. Control samples were also prepared in separate vials containing the same proportions of fuel and minimal media but without bacteria. Each vial was used for a single test, including optical density measurement or measurement of the fuel components remaining in the sample by GC. The OD of the inoculated medium was measured using a SmartSpec Plus Spectrophotometer (Bio RAD).

M. hydrocarbonoclasticus cells were grown in marine broth overnight in a shaker incubator at 28 °C. The cells were then pelleted and washed three times with M-9 minimal media to remove any residual marine broth before being added to the bioassay mixture at a final concentration of 0.040 OD. The slightly higher OD was used because of the slower growth rate of *Marinobacter* in comparison to *Pseudomonas*. Because *M. hydrocarbonoclasticus* was a marine bacteria requiring seawater for growth and did not grow well in pure M-9, we tested different minimal media and found that an aqueous media mixture comprised of 50% (v/v) seawater (Nutri-SeaWater Natural Live Ocean Saltwater by Nature's Ocean), 40% (v/v) deionized sterile water and 10% (v/v) M-9 media was optimal for growing *Marinobacter*. Samples containing fuel were incubated for up to 21 days at 28 °C.

Jet-A and F-76 fuels were examined. Jet-A, commercial aviation fuel closely resembling Air Force aviation fuel JP-8, contained no fuel system icing inhibitor which is known to act as a biocide. F-76 is the marine diesel fuel used by the US Navy for non-nuclear ship propulsion and other non-aviation functions. Both the Jet-A and F-76 were filter-sterilized through a 0.22 µm filter to remove any microbes from extraneous sources.

2.2. Sample preparation and GC analysis

The fuel/M-9 samples were analyzed using a liquid–liquid extraction with methylene chloride (Fisher Optima, purity, >99.9%), followed by GCxGC analysis on an Agilent 7890/5975 GCxGC with flow modulation. Methylene chloride extraction of water, soils and other solids is a routine technique for isolating organics from aqueous or solid matrices (Burford et al., 1993). For each sample, an internal standard (Base/Neutrals Surrogate Standard, Ultra Scientific) and 2.0 mL of methylene chloride were added to the M-9/fuel mixture and shaken by hand for one minute. The vials were then placed in an ultrasonic bath for 10 min to assist the methylene chloride extraction process and break emulsions within the sample. The samples were centrifuged; the methylene chloride, containing any organic components from the original 10 µL of fuel, or decomposition products from the bacteria, was removed to a GC vial for analysis. Because different jet fuel components have different solubility in aqueous systems, this liquid–liquid extraction technique removed all the organics from the sample to be collected, whether in the organic phase or aqueous phase.

GCxGC was conducted using a non-polar 30 m primary column (DB5-MS, Agilent Technologies) and a shorter, 5 m secondary column (DB-17, Agilent Technologies), using hydrogen carrier gas; other analytical conditions are previously described (Johnson and Synovec, 2002; Striebich et al., 2011; Van der Westhuizen et al.,

2011). An example of a 2-dimensional separation is given in Figure S1 (Supporting Information). Because GCxGC provides two distinct separations, better resolving power between the components is possible. Another significant advantage of this system was that a flame ionization detector (FID) and a mass spectrometer (MS) measured chromatographic response simultaneously, providing the ability to perform qualitative and quantitative analysis of the samples.

Gas chromatography with thermal conductivity detection (GC-TCD) was used to examine the organism's use of oxygen within the vial system. Caps with septa replaced the typical hard caps used in the majority of experiments, so that the headspace could be sampled. A gastight syringe was used to extract a 0.5 mL gas phase sample at regular intervals during the 10 and 21 day experiments, to characterize the oxygen usage. A 30 m HP-Molesieve (Agilent) column was used to separate the components of the headspace.

2.3. Bioreactor hydrocarbon degradation experiment

A bioreactor (BIOFLO 110 Fermentor, New Brunswick Scientific) was used to provide a more realistic experiment to simulate biological growth in fuel tanks than the small vials could provide. This reactor was filled with 5 L of M-9 inoculated with the *P. aeruginosa* at 0.03 OD. In order to keep the same ratio of nutrient to organism as in the vials, a total of 50 mL of Jet-A was added to the reactor. The bioreactor system containing fuel and bacteria was incubated for a period of 3 months at 28 °C with agitation. The system was vented and agitated using an automatic impeller at 125 rpm in order to maintain optimal air diffusion and to prevent the formation of anaerobic conditions. The bioreactor oxygen probe was used to track the oxygen levels over the duration of the experiment; normal oxygen levels similar to those observed at the beginning of the experiment were maintained during the three month test.

2.4. Alternative fuel bioassay

Vial experiments such as those described in Section 2.1 were conducted using the alternative fuel Synthetic Paraffinic Kerosene (SPK) and the isoparaffinic hydrocarbon mixture Isopar-M; both of these fuels contained only branched alkanes. To determine whether fuels comprised of isoparaffins were less susceptible to biodegradation, *P. aeruginosa* was grown in SPK and in Isopar-M. Briefly, *P. aeruginosa* cells were cultured overnight in LB at 28 °C in a shaker incubator. Next day, the cells were pelleted, washed three times with M-9 minimal media to remove any traces of the LB media, and the cell culture diluted to 0.03 OD in M-9 minimal media. Cells were then added to 8 mL glass vials already containing either 10 μL of pure isoparaffinic fuels or 10 μL of isoparaffinic fuel with 5% (v/v) of n-hexadecane. A total of 15 sample vials containing *Pseudomonas* and 8 negative control vials without *Pseudomonas* were used for GCxGC analysis. An additional 8 sample vials were used to track growth by measuring OD.

3. Results and discussion

Analyses of Jet-A and F-76 marine diesel fuel composition before and after exposure to *P. aeruginosa* and *M. hydrocarbonoclasticus* was investigated using GCxGC. This technique was used because it separates complex mixtures better than traditional GC−MS and is especially suited to study Jet-A and diesel fuel range hydrocarbon mixtures (Striebich et al., 2001, 2011; Johnson and Synovec, 2002; Van der Westhuizen et al., 2011). The original Jet-A fuel investigated contained almost 22% aromatics and nearly 24% normal alkanes, with the balance containing isoparaffins and cycloparaffins, while F-76 diesel contained more aromatics (27.9%) and less than

half the normal alkanes (11.8%) as shown in Table 1. It was important to accurately know the hydrocarbon composition of the fuels before exposure so that changes in composition could be attributed to degradation by the bacteria following exposure.

3.1. Optimization of fuel bioassays

In order to demonstrate how fuels were consumed by *P. aeruginosa* and *M. hydrocarbonoclasticus*, a number of fuel bioassays were attempted with different volumes of fuel and combinations of water and minimal media. The M-9 minimal media was found to be the best supporter of *Pseudomonas aerugionosa* growth when fuel was used as the sole carbon source. For the marine bacteria, *M. hydrocarbonoclasticus*, a combination of 10% (v/v) M-9 media, 50% (v/v) seawater and 40% (v/v) ultrapure water provided the best aqueous phase for growth in the presence of fuel. Growing bacteria in 1:1 and 1:5 fuel to aqueous media ratios did not produce measurable changes in fuel hydrocarbon concentration in incubation of up to 14 days. However, by reducing the fuel to media ratio to 1:100, the degradation of fuel hydrocarbon components was clearly detected and measured.

The accurate quantitation of hydrocarbons consumed could not be easily measured in early experiments due to the evaporation of volatile compounds. Although open vials prevent the depletion of oxygen and provide faster biodegradation, trial experiments using loose caps showed a large reduction of volatiles (less than C_{11}), such that it was difficult to clearly determine how much of each component was either degraded or lost to evaporation. Therefore, airtight vials were used in subsequent experiments. Because the vial headspace was the only source of oxygen for the bacteria, a headspace volume 8-times larger than the media/fuel matrix was maintained.

Investigations were conducted to demonstrate that the system was not deprived of oxygen during the experiment. Fig. 1 shows the oxygen concentration and *Pseudomonas* growth for samples in

Table 1
Fuel hydrocarbon composition using GCxGC analysis.

	Jet-A	F-76
	Weight %	Weight %
Alkylbenzenes	**16.76**	**11.35**
Alkylnaphthalenes	**0.54**	**4.54**
Indan/tetralins	**4.54**	**12.03**
Isoparaffins	**32.82**	**19.87**
n-paraffins		
n-C$_{07}$	0.02	0.01
n-C$_{08}$	0.17	0.05
n-C$_{09}$	1.05	0.15
n-C$_{10}$	4.18	0.48
n-C$_{11}$	7.52	0.73
n-C$_{12}$	5.91	0.81
n-C$_{13}$	3.28	0.77
n-C$_{14}$	1.27	1.05
n-C$_{15}$	0.35	1.15
n-C$_{16}$	0.09	1.29
n-C$_{17}$	0.03	1.58
n-C$_{18}$	<0.01	1.14
n-C$_{19}$	<0.01	0.81
n-C$_{20}$	<0.01	0.73
n-C$_{21}$	<0.01	0.52
n-C$_{22}$	<0.01	0.34
n-C$_{23}$	<0.01	0.23
Total n-paraffins	**23.89**	**11.84**
Cycloparaffins		
Monocycloparaffins	18.15	27.40
Dicycloparaffins	3.21	12.93
Tricycloparaffins	0.10	0.05
Total cycloparaffins	**21.45**	**40.39**
Total	100.0	100.0

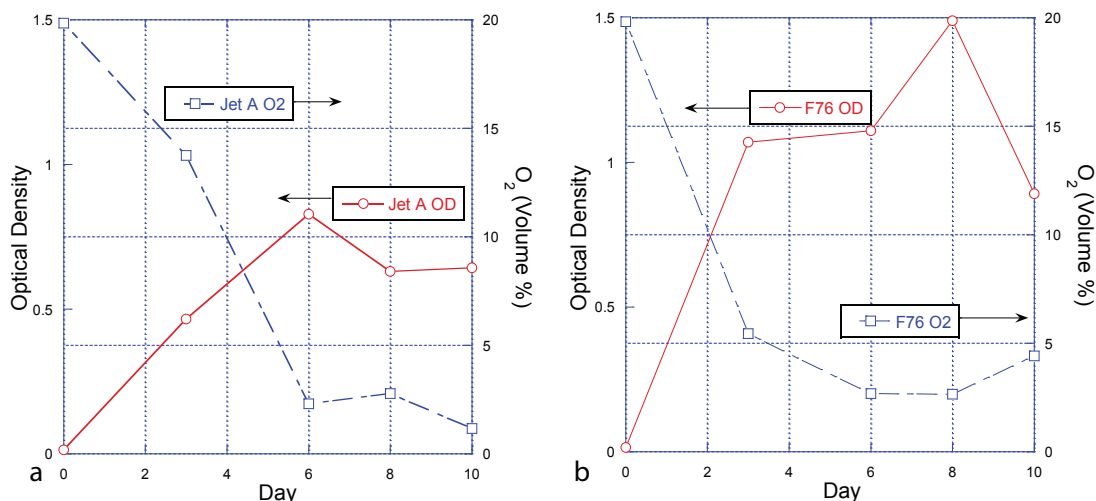Bold indicates the subtotals from the groups.

Fig. 1. Growth curve and headspace oxygen usage for 10 days with *Pseudomonas* in sealed vials with Jet-A (a) and F-76 (b).

sealed vials (with septa) taken over a 10 day experiment. A similar experiment was performed with *Marinobacter* over a period of 21 days (Fig. 2). As expected, after a few days, the cell count increased dramatically as measured by optical density, and headspace measurements of the sealed vials indicated declining oxygen concentrations inversely proportional to cell growth through day 6 for *Pseudomonas*; by day 6, oxygen concentration fell below 5% (v/v), which is not conducive to aerobic fuel degradation and growth. As observed, by day 6 *Pseudomonas* had reached its maximum growth in Jet-A, and after that, the culture optical density was reduced (Fig. 1a). Interestingly, *Pseudomonas* was able to achieve higher cell density in F-76 than in Jet-A and that growth continued through day 8 in F-76 even though a greater reduction in oxygen levels was observed by day 3 (Fig. 1b). In the case of *Marinobacter*, oxygen concentration stayed above 15% at all times. The higher oxygen levels in the headspace of the *Marinobacter* samples in comparison with the *Pseudomonas* samples may be due to the fact that *Marinobacter* grew at a lower rate and to a lower cell density than *Pseudomonas* (Fig. 2).

The observation that *Pseudomonas* was able to grow to a higher cell density in F-76 than in Jet-A may be due to this organism's preference for the heavier n-alkanes in fuel. Although the total n-alkane content in Jet-A is 23.9% while in F-76 is only 11.8%, the F-76 fuel contains a concentration of heavier n-alkanes ($\geq$n-C_{15}) that is 16-times higher than that found in Jet-A (7.8% in F-76 versus 0.47% in Jet-A) (Table 1). *Pseudomonas* appeared to be very selective to the higher molecular weight alkanes and found more of them in F-76 than Jet-A.

The development of a small scale vial test using a 1:100 ratio of fuel to media proved to be an optimal system for rapid and accurate characterization of the hydrocarbon degradation profile of bacteria. The small vial system prevented multiple issues that have often affected the study of hydrocarbon biodegradation, including preventing the evaporation of volatile hydrocarbon compound, achieving abundant cell growth while using a small amount of fuel that can be readily degraded in a short amount of time before the cells reach the stationary phase, and preservation of oxygen long enough to maintain rapid oxygenic biodegradation of
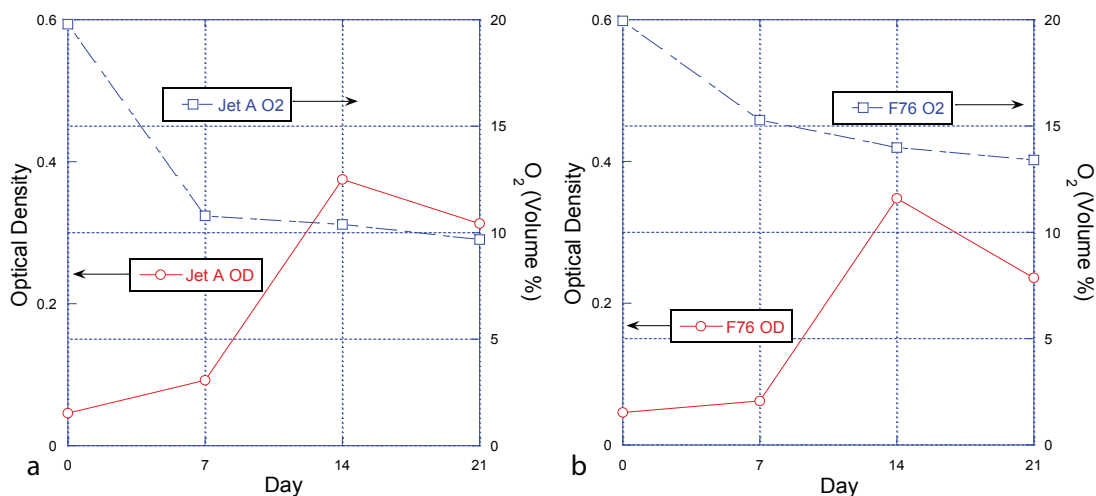

Fig. 2. Growth curve and headspace oxygen usage for 21 day with *Marinobacter* in sealed vials with Jet-A (a) and F-76 (b).
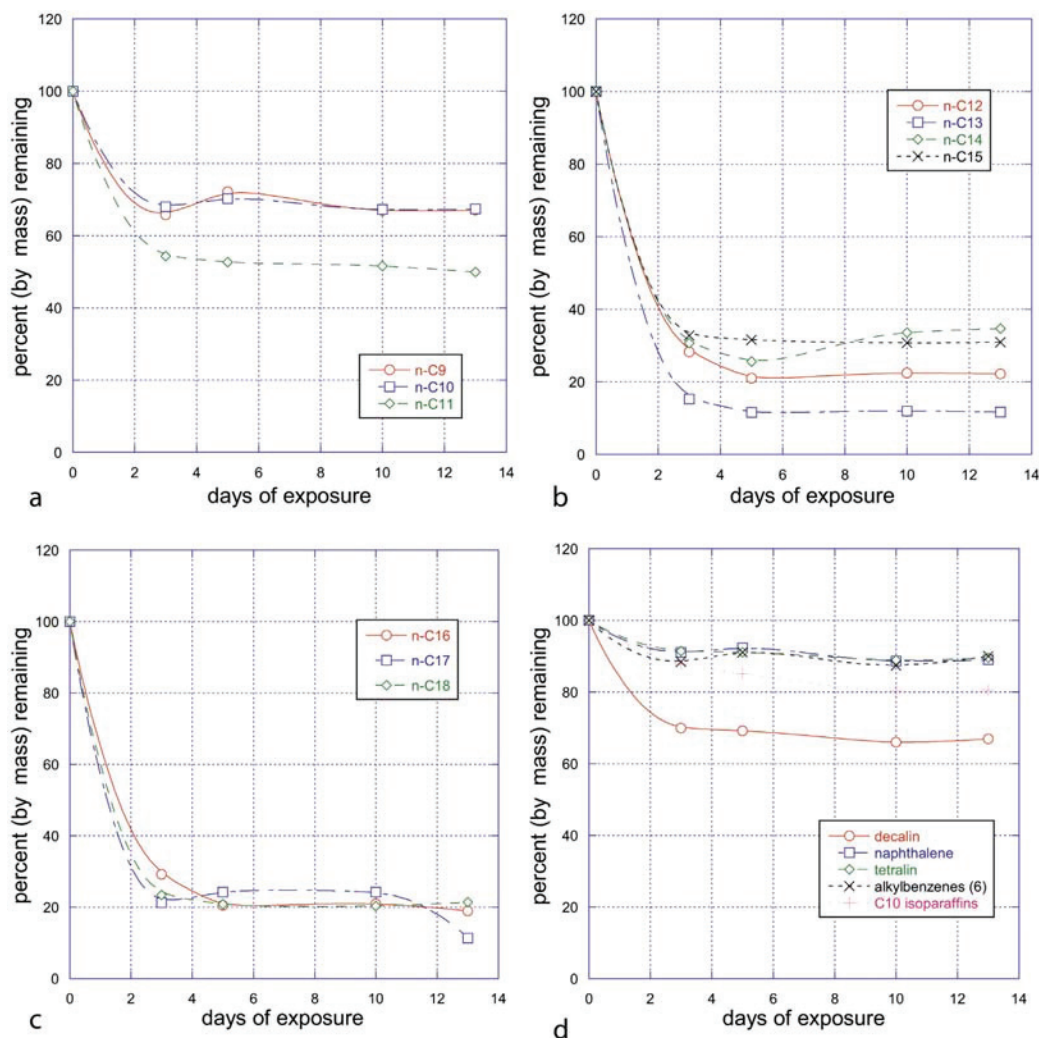
Fig. 3. Degradation of hydrocarbon components of Jet-A by *Pseudomonas aeruginosa* over a 13 day period in sealed vials. (a) C_9 through C_{11} n-alkanes; (b) C_{12}–C_{15} n-alkanes; (c) C_{16}–C_{18} n-alkanes; (d) 5 types of C_{10} compounds.

hydrocarbons. This method allowed us to accurately characterize the hydrocarbon degradation profile of *P. aeruginosa* ATCC 33988 and *M. hydrocarbonoclasticus* when exposed to Jet-A and F-76 fuel.
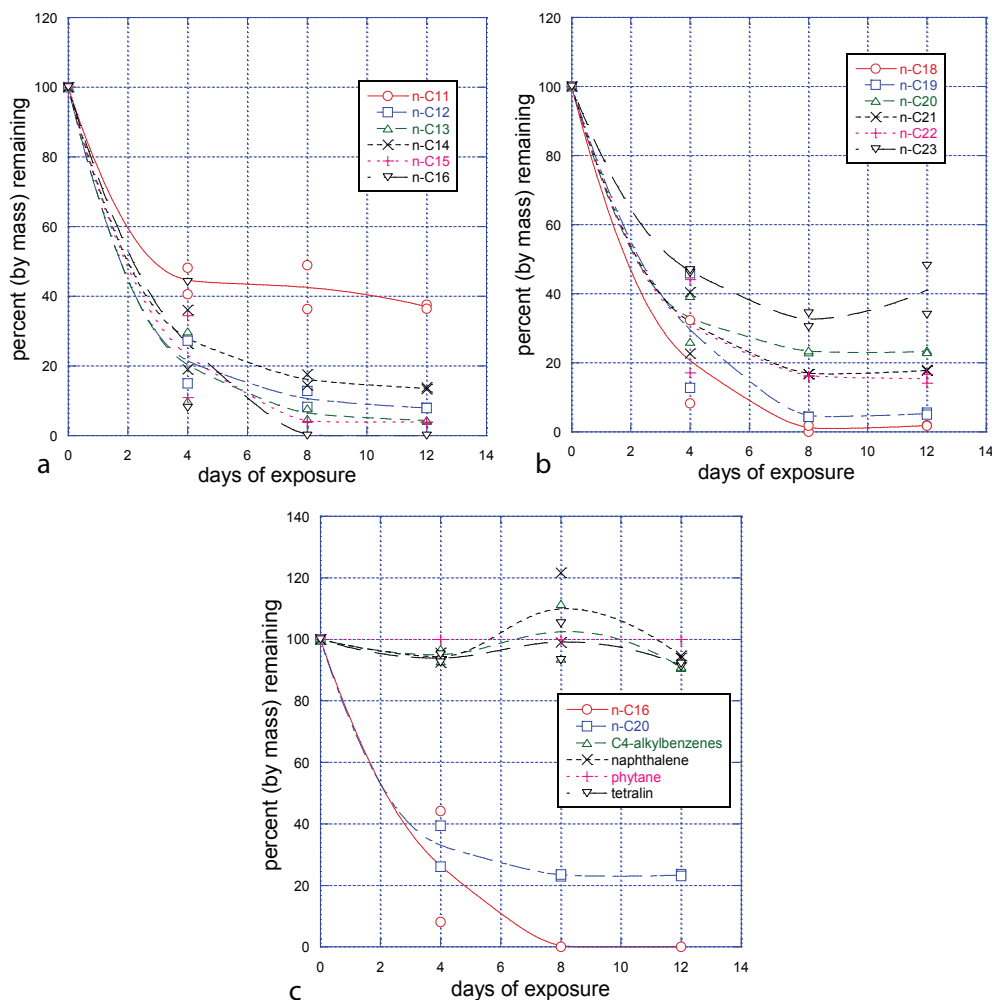
3.2. Hydrocarbon consumption by Pseudomonas

Degraded samples were compared to control fuel samples without bacteria, and the percentage degradation for *Pseudomonas* with Jet-A and F-76 was determined (Figs. 3 and 4). Results showed that the terrestrial and fresh water bacteria *P. aeruginosa* ATCC 33988 degrades normal alkanes from C_9 to C_{23} preferentially, independently of the fuel used. Most of these compounds showed concentration reductions of more than 60% in less than 4 days (Fig. 3b,c and 4a,b). Similarly, F-76 showed that mid-chain n-alkane (C_{13}, C_{15}, C_{16}, C_{18} and C_{19}) degradation was favored over the other n-alkanes with degradation levels over 90% by day 8 (Fig. 4a, b). C_{17} was not well quantified due to the coeluting interferent, pristane. The lighter n-alkanes degraded less than the heavier alkanes, with

n-C_9 and n-C_{10} degraded by 30% and n-C_{11} degraded more than 40% (Figs. 3a and 4a).

In terms of the degradation of aromatics, for the conditions tested, this *P. aeruginosa* strain lacked the ability to degrade aromatics such as naphthalene, tetralin and alkylbenzenes, under the experimental conditions tested. Interestingly, the C_{10} dicycloparaffin, decalin, was degraded to about the same extent as n-C_{10} (Fig. 3d). However, naphthalene ($C_{10}H_8$) and tetralin ($C_{10}H_{12}$), also C_{10} compounds, did not degrade significantly, most likely due to their aromatic nature (Figs. 3d and 4c). Other C_{10} alkylbenzenes (6 isomers) were examined and summed using GCxGC and were found to be wholly unaffected by *Pseudomonas* under these conditions (Fig. 3d). In spite of the fact that the normal alkanes were degraded so readily, the branched alkanes including the C_{10} isoparaffins and the phytane did not significantly degrade. The observation that mid-range n-alkanes degrade more than other components in the fuel has been previously reported (Sanger and Finnarty, 1984; Saadoun, 2002). Alkanes are relatively easy for bacteria to degrade because of the number of oxygenase,

247

Fig. 4. Degradation of hydrocarbon components of F-76 by *Pseudomonas* over a 12 day period in sealed vials. (a) C_{11} through C_{16} n-alkanes; (b) C_{18}–C_{23} n-alkanes; (c) comparison of various compounds of different hydrocarbon classes.

dioxygenase, P450 and hydroxylase enzymes available to oxidize the alkanes readily to alcohols (Gunasekera et al., 2013).

Phytane is a compound which is often used as a biomarker to date oil spills in marine and terrestrial ecosystems because is very resistant to biodegradation (Senn and Johnson, 1987). This isomer of C_{20} (2,6,10,14-tetramethylhexadecane) is chromatographically adjacent to n-C_{18} on most non-polar columns, such as those used in these analyses. In this study, phytane was entirely unaffected by the *Pseudomonas* while the n-C_{18} alkane was readily degraded (Fig. 5). The organism under these conditions clearly prefers to consume specific isomers of compounds with the same molecular formula as observed by the great difference in degradation between phytane and its isomer, n-C_{20} (Fig. 4c). How the organism could be so selective is not well understood.

3.3. Hydrocarbon consumption by Marinobacter

To characterize the role of other bacteria in the degradation of fuels, the fuel hydrocarbon degradation pattern produced by the marine fuel-degrading bacteria *Marinobacter hydrocarbonoclasticus*

was also investigated. This specie was isolated from a fuel-seawater sample and is known to grow well in fuel-aqueous systems. F-76, a naval propulsion fuel, is commonly stored in the ballast tanks of vessels with seawater; consequently, a study of the behavior of oceanic hydrocarbonoclastic bacteria with F-76 is pertinent.

Even though *Marinobacter* presented lower growth rate and lower total growth than *Pseudomonas*, the clear difference in the hydrocarbon degradation profile of each of these bacteria allowed us to draw some general conclusions. Like *Pseudomonas*, *Marinobacter* appeared to prefer n-alkanes over other types of hydrocarbons. In contrast to *Pseudomonas*, *Marinobacter* highly favored the degradation of shorter chain normal alkanes from C_8–C_{10} with no degradation of longer n-alkanes from C_{15} through C_{23} (Figs. 6 and 7). The degradation of the shorter n-C_9 and n-C_{10} by *Marinobacter* was so efficient that they were completely consumed in F-76. However, the degradation of n-alkanes between C_{11} and C_{14} appeared to be more variable, with higher degradation of n-C_{11} and C_{12} in F-76 diesel than in Jet-A fuel (Fig. 6a,b and 7a). In F-76, degradation decreased with increasing carbon number for normal alkanes greater than n-C_{11}. Even after some of the shorter alkanes
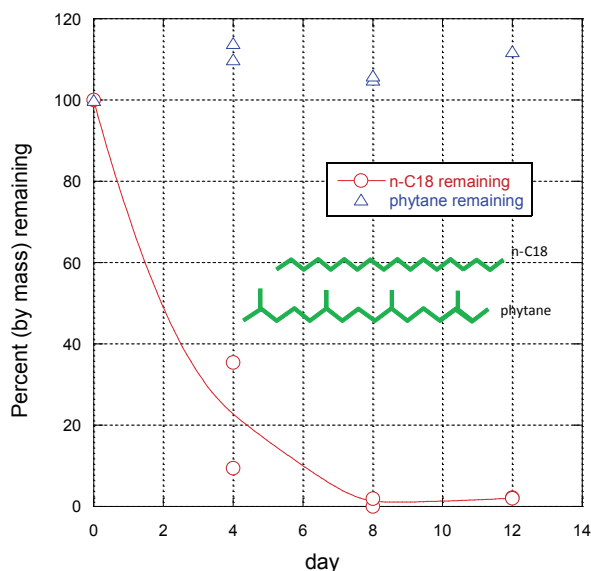
Fig. 5. Biodegradation rate of the C_{20} branched alkane phytane versus the C_{18} normal alkane octadecane by *Pseudomonas* in F-76.

were completely consumed, *Marinobacter* did not appear to significantly degrade the longer n-alkanes.

Another difference between the two organisms was that *Marinobacter*, unlike *Pseudomonas*, was able to degrade certain aromatic compounds under the conditions tested (Figs. 6d and 7c). *Marinobacter* degraded ethylbenzene very efficiently to concentrations of less than 5% remaining in both Jet-A and F-76. Jet-A has a higher concentration of ethylbenzene and other low molecular weight aromatics than does F-76 (due to its distillation range), which may explain why the *Marinobacter* grew slightly better in Jet-A. Aromatics consumption was highly selective since the bacteria showed a preference for ethylbenzene (C_8H_{10}), but no preference for any of the three other isomers of xylene (C_8H_{10}). In addition, while most C_3-alkylbenzenes were completely undegraded, the two isomers of ethyl-methylbenzene were significantly degraded with less than 60% remaining (Fig. 6d). Normal-propylbenzene was only degraded by about 20% (Fig. 6d) in Jet-A. Only one isomer of the C_4-alkylbenzenes (n-butylbenzene) was degraded while other isomers were completely undegraded. Overall, *Marinobacter* showed an unusual and distinct preference for specific isomers of alkyl-aromatics. But in all cases, the diaromatic compound naphthalene, like the other diaromatic compounds in both fuels, was completely resistant to degradation by *Marinobacter* and *Pseudomonas*.

Clearly, *Marinobacter* has a metabolism that differs from *Pseudomonas* because *Marinobacter* degrades some alkyl substituted benzenes. An increase in lower carbon number aromatic compounds was not evident; there were no indications of the organisms degrading alkylbenzenes to benzene or toluene products. In fact, toluene itself was degraded by about 40% (Fig. 6d). It is not clear why *Marinobacter* targets alkylbenzenes with specific alkyl groups. It is possible that metabolizing compounds with less steric hindrance such as n-paraffins (versus isoparaffins) or n-alkyl substituted benzene isomers may be thermodynamically favored by the organism. A good example of this preference is the consumption of ethylbenzene with no consumption of xylene (dimethylbenzene).

3.4. Bioreactor degradation study

Previous studies concerning the degradation of petroleum products in the environment have indicated that microbes first degrade n-alkanes, followed by cyclic alkanes, then isoparaffins and finally the aromatic components (Vila et al., 2010). Although our vial tests with the bacteria *Pseudomonas* showed a similar pattern of hydrocarbon degradation with preferential consumption of n-alkanes followed by cyclic alkanes, we did not observe the degradation of branched and aromatic hydrocarbons. It may be possible that the short timeframe, small volumes and limited oxygen availability in the vial experiments may have prevented further degradation of other hydrocarbon classes. To test this hypothesis, a larger scale Jet-A fuel degradation study was performed using a bioreactor with constant aeration to maintain optimal oxygen levels and an incubation period of three months. It was apparent that the bioreactor showed the same behavior as the smaller scale experiments conducted in individual vials, in that the normal alkanes were significantly consumed by the *Pseudomonas* (Fig. 8). After 3 months, some evaporation was evident in the bioreactor as all of the early eluting volatile compounds between 5 and 15 min on the GC tracing were removed. However, the later eluting n-alkanes (n-C_{12-17}) were not being removed by evaporation as shown by the consistent amount of chromatographically adjacent branched alkane compounds of similar molecular weight and volatility at time zero and after 3 months. The dotted lines in the figure indicate the location of the missing normal alkanes consumed by the bacteria, while the branched alkanes around the n-alkanes remain relatively unaffected (Fig. 8). The levels of the heavier normal alkanes C_{12} through C_{16} that remained after 3 months were quantified using GC–MS by extracted ion analysis (Table 2). Generally, the heavier alkanes were highly degraded with a loss of more than 90% from their original concentration. However, degradation of branched alkanes and aromatic compounds was not observed by using the bioreactor, indicating that the degradation profile of a microorganism is highly determined by its intrinsic genetic and metabolic function and not as much by the growth conditions. Having said that, optimal growth conditions did increase the degradation of those compounds for which the cell is equipped to degrade.

3.5. Implication of alternative fuels hydrocarbon composition in biodegradation

In the complex relationship between fuel composition, bacterial growth and biodegradation it would appear from this study that conventional fuels with high normal alkane content are a suitable environment for microbial growth and biodegradation. On the other hand, *Pseudomonas* and *Marinobacter* appeared incapable of degrading the branched alkane components in the conventional fuels. Currently, a wide variety of alternate fuels are being produced from many feedstocks, processes and conditions. In many cases, these new alternative fuels may contain minimal amounts of n-alkanes and high levels of branched alkanes, products of the specific processing conditions used to generate these fuels. One may expect this type of fuel to be less susceptible to biological growth in tanks, hoses and carts. While *Pseudomonas* and *Marinobacter* are just two species from the vast richness of microbes in nature, they are important and common representatives of those bacteria capable of degrading fuel, and they may be used as examples to describe the general characteristics of fuel-degrading bacteria.

To determine whether fuels comprised of isoparaffins were less susceptible to bacterial degradation, the alternative fuel SPK and the surrogate fuel Isopar-M were exposed to the bacteria *P. aeruginosa*. The results showed that neither SPK nor Isopar-M

could support the growth of *Pseudomonas*, indicating that this organism cannot use branched alkanes (isoparaffins) as the sole carbon source for growth (Fig. 9). However, addition of the n-alkane hexadecane at 5% (v/v) to SPK and Isopar-M allowed *Pseudomonas* to thrive initially until the n-C_{16} was completely consumed at which time the growth of the bacteria slowed and then stopped. The addition of n-C_{16} to the isoparaffinic fuels also revealed that the lack of growth in SPK or Isopar-M was not caused by toxicity of components in the two fuels but by the lack of a readily metabolizable carbon source. Bacteria exposed to both fuels showed a complete lack of growth (as measured by OD) when n-C_{16} was not added to the isoparaffin mixture.

These results indicate that it may be possible to design a fuel which is more resistant to microbial growth and degradation by reducing the compounds that bacteria prefer to consume. Such a fuel could potentially save money in purchasing additives and reducing expensive fuel system maintenance. Isoparaffinic fuels are not the only alternative fuels being considered for aircraft use, but are a major class within a gamut of potential alternative fuels.

Other studies in marine settings with environmental organisms have shown that linear and branched alkanes are biodegradable, as are aromatic compounds (Hua, 2006). Our study clearly showed that n-alkanes are preferentially degraded by *Pseudomonas* and *Marinobacter* and these results correlate with multiple reports that indicate that mid-range n-alkanes degrade more than other components in the fuel (Sanger and Finnarty, 1984; Saadoun, 2002). Alkanes are relatively easy for bacteria to degrade because of the number of oxygenase, dioxygenase, P450 and hydroxylase enzymes available to oxidize the alkanes readily to alcohols. Under the conditions of this study, only *Marinobacter* degraded aromatics, and then only specific isomers.
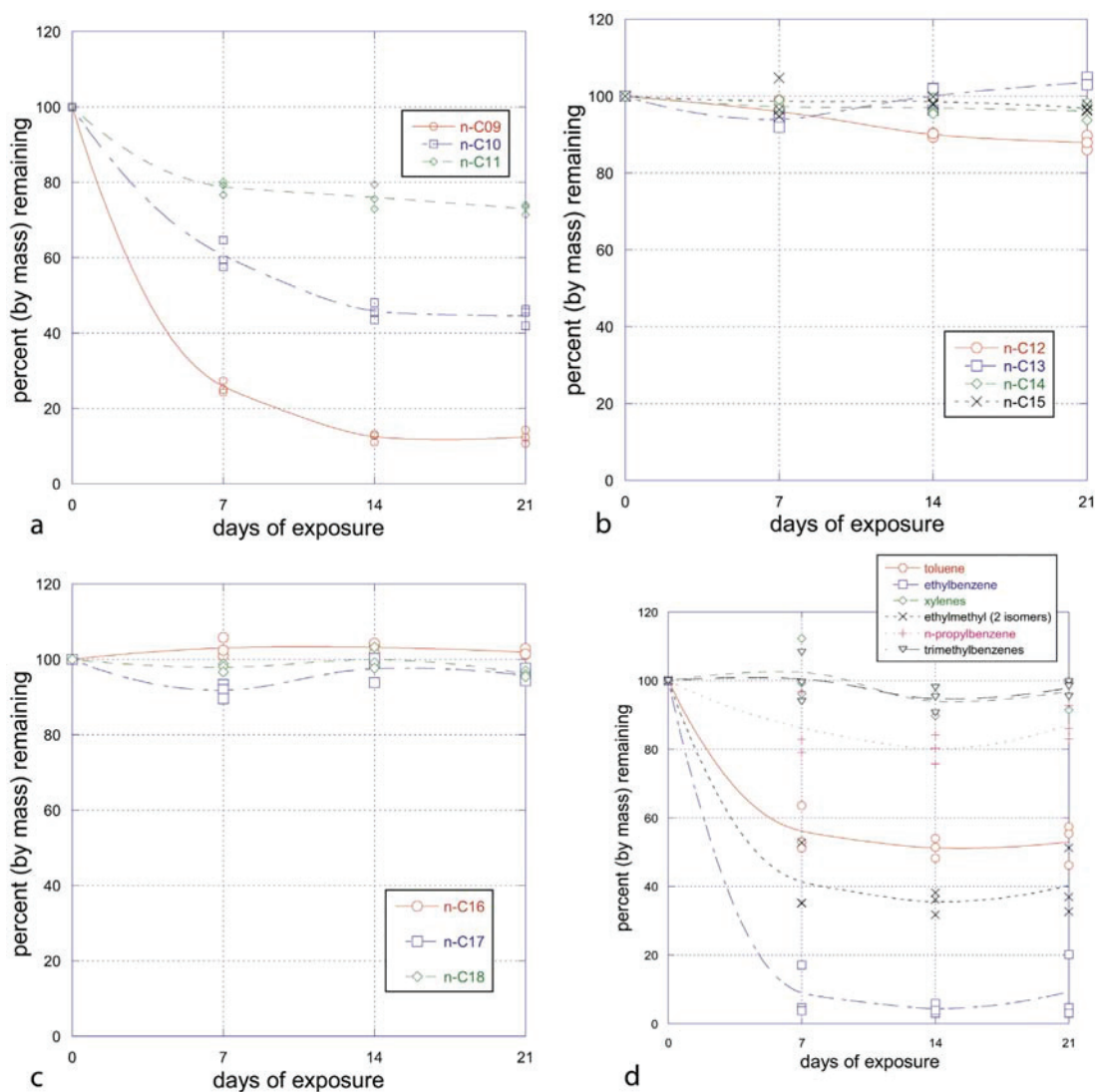

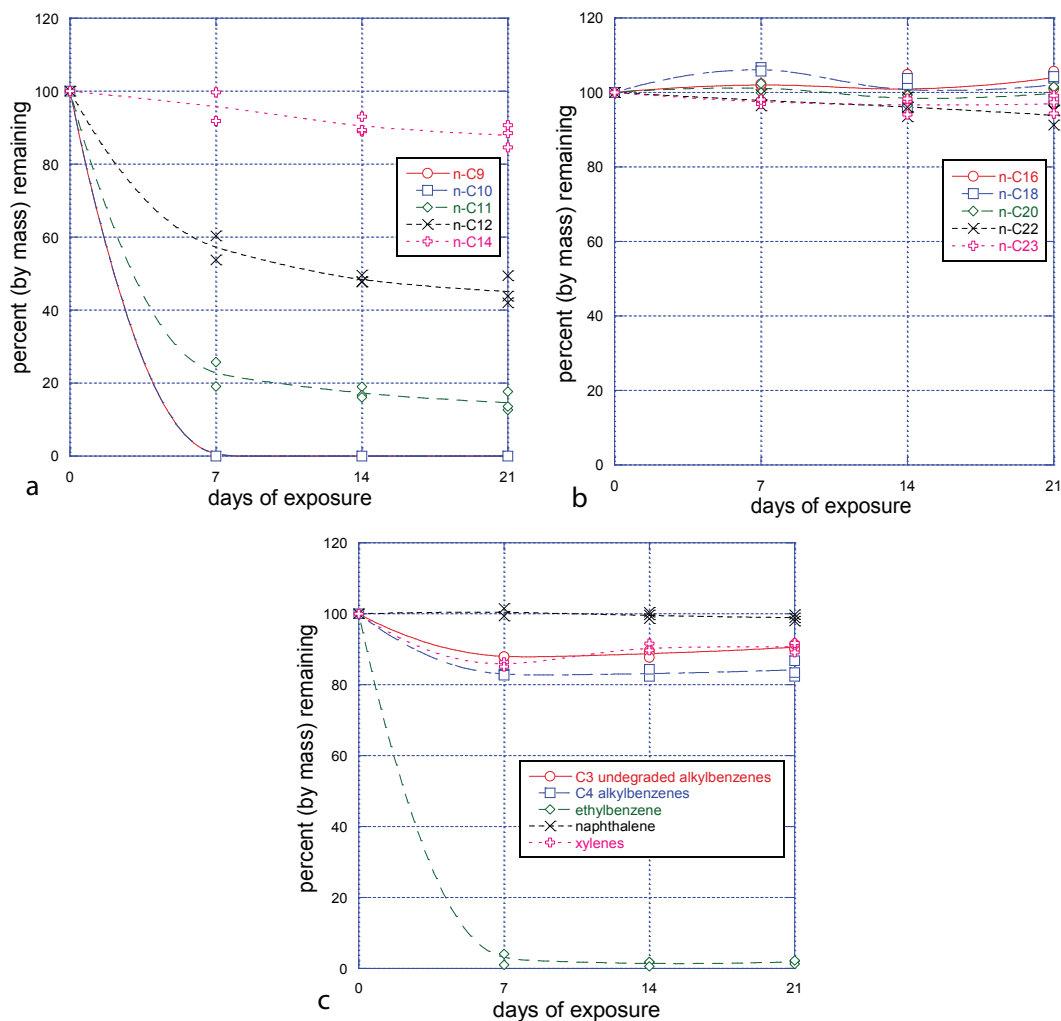**Fig. 6.** Degradation of hydrocarbon components of Jet-A by *Marinobacter* over a 21 day period in sealed vials. (a) C_9 through C_{11} n-alkanes; (b) C_{12} through C_{15} n-alkanes; (c) C_{16} through C_{22} n-alkanes; (d) comparison of various aromatic hydrocarbons.

Fig. 7. Degradation of hydrocarbon components of F-76 by *Marinobacter* over a 21 day period in sealed vials. (a) C_9 through C_{14} n-alkanes; (b) C_{16}–C_{23} n-alkanes; (c) comparison of various aromatic hydrocarbons.
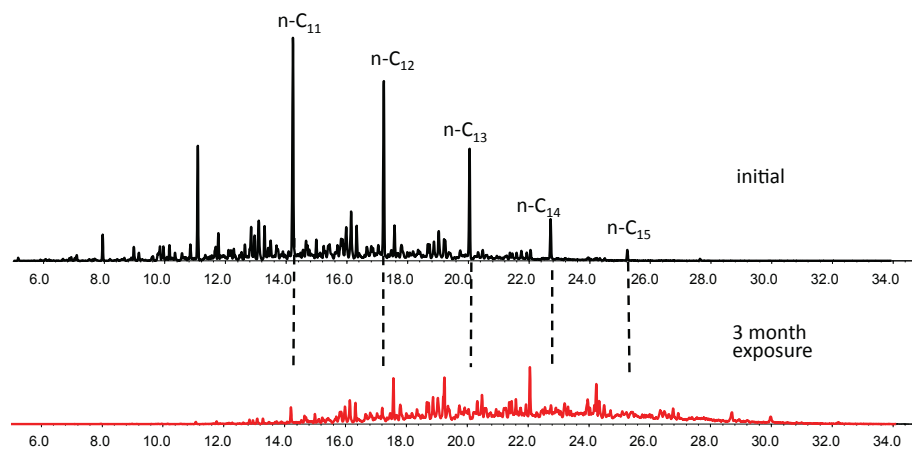

Fig. 8. Jet-A degradation profile after 3 month exposure to *Pseudomonas* in a bioreactor. Biodegraded fuel was compared to untreated (time = 0) fuel by GC−MS. The dotted lines indicate the location of the degraded n-alkanes.

251

Table 2
Loss of normal alkanes in the 3 month bioreactor experiment.

Compound	Ion	Time, min	Response, $t = 0$ months	Response, $t = 3$ months	% Remaining
n-C_{12}	170	17.22	318,000	17,100	5.4
n-C_{13}	184	20.049	145,000	3200	2.2
n-C_{14}	198	22.72	41,000	3980	9.7
n-C_{15}	212	25.24	8190	740	9.0
n-C_{16}	226	27.641	585	ND	NA

ND indicates not detected.

Biodegradation may be limited by many factors, including lack of catabolic pathways in the microorganism and slow rates of dissolution, desorption or transport. The tendency not to consume aromatics structures or even branched paraffins of similar carbon number to the degraded alkanes must indicate that the degradation of these hydrocarbons is not thermodynamically favorable, or that the compounds may be toxic to the organism. Previously we have shown that in order for bacteria to proliferate in fuel, multiple adaptations that go well beyond hydrocarbon consumption have to be activated to maintain cell homeostasis in the adverse fuel environment (Gunasekera et al., 2013).

The degradation of the fuel, due to significant disappearance of the normal alkanes, may cause a change in fuel properties. In fuels, n-alkane concentrations are often related to the fuel's freeze point, pour point, and other low temperature properties such as viscosity. Interestingly, the heavy normal alkanes are generally believed to be detrimental to fuel freeze point (higher concentrations create higher freeze point). For example, higher concentrations of normal C_{16}–C_{20} for jet fuels have been shown to correlate with higher freeze points (Striebich et al., 2005). Normal alkanes are sometimes removed from process streams by isomerization in order to improve freeze point. Other techniques involve reactions with specific compounds to remove n-alkanes and improve freeze point (Zabarnick et al., 2002). While the amount of fuel examined here is too small to be able to accurately measure freeze point, a scaled-up exposure of fuel to *Pseudomonas* is possible. Additional studies conducted with more fuel are being considered to investigate the possibility of organisms changing both trace and bulk fuel properties.

4. Conclusion

Marinobacter and *Pseudomonas* consistently showed very different metabolism of fuel. *Marinobacter* consumes low carbon number n-alkanes and some aromatics, while *Pseudomonas* only consumes mid-range and long range n-alkanes. It appeared that both microorganisms almost exclusively prefer n-alkanes over their isoparaffinic counterparts. Undoubtedly, studying the differences in these two microbes' metabolic pathways will afford greater understanding of their hydrocarbon degradation potential. It was clear that the components of isoparaffinic fuels were not toxic to the bacteria because the organisms grew well in isoparaffinic mixtures spiked with n-hexadecane. Isoparaffins were not consumed, but neither did they create significant toxicological response. However, isoparaffinic fuels without added n-alkanes will not sustain these microorganisms. The future implications of this study include the possibility of predicting the rate of fuel biodeterioration based on the hydrocarbon profile of a particular fuel and the development of fuels impervious to biodeterioration with improved storage properties. The results presented here also extend to the field of environmental bioremediation by proving a detailed description of the hydrocarbon degradation rate of different fuels and how different environmental bacteria react to those fuels.

Fig. 9. Growth of *Pseudomonas* in the isoparaffinic alternative fuel SPK (a), and isoparaffin fuel surrogate Isopar-M (b) before and after addition of 5% (v/v) n-C_{16}. The green curves represent the degradation of n-C_{16}.(For interpretation of the references to colour in this figure legend, the reader is referred to the web version of this article).

Appendix A. Supplementary data

Supplementary data related to this article can be found at http://dx.doi.org/10.1016/j.ibiod.2014.04.024.

References

Belhaj, A., Desnoues, N., Elmerich, C., 2002. Alkane biodegradation in *Pseudomonas aeruginosa* strains isolated from a polluted zone: identification of alkB and alkB-related genes. Res. Microbiol. 153, 339–344.

Brown, L.M., McComb, J., Vangsness, M., Bowen, L., Mueller, S., Balster, L., Bleckmann, C., 2010. Community dynamics and phylogenetics of bacteria fouling Jet-A and JP-8 aviation fuel. Int. Biodeterior. Biodegrad. 64, 253–261.

Burford, M.D., Hawthorne, S.B., Miller, D.J., 1993. Extraction rates of spiked versus native PAHs from heterogeneous environmental samples using supercritical fluid extraction and sonication in methylene chloride. Anal. Chem. 65, 1497–1505.

Corwin, H., Anderson, S.M., 1967. The effect of intramolecular hydrophobic bonding on partition coefficients. J. Org. Chem. 32, 2583–2586.

Edmonds, P., Cooney, J., 1967. Identification of microorganisms isolated from jet fuel systems. J. Appl. Microbiol. 15, 411–416.

Gunasekera, T.S., Striebich, R.C., Mueller, S.S., Strobel, E.M., Ruiz, O.N., 2013. Transcriptional profiling suggests that multiple metabolic adaptations are required for effective proliferation of *Pseudomonas aeruginosa* in jet fuel. Environ. Sci. Technol. 47, 13449–13458.

Hua, J., 2006. Biodegradation of dispersed marine fuel oil in sediment under engineered pre-spill application strategy. Ocean Eng. 33, 152–167.

Inoue, A., Horikoshi, K.A., 1989. *Pseudomonas* thrives in high concentration of toluene. Nature 338, 264–265.

Johnson, K.J., Synovec, R.E., 2002. Chemom. Intelligent Lab. Syst. 60, 225–237.

Jung, C.M., Broberg, C., Giuliani, J., Kirk, L.L., Hanne, L.F., 2002. Characterization of JP-7 jet fuel degradation by the bacterium Nocardioides luteus strain BAFB. J. Basic Microbiol. 42, 127–131.

Korenblum, E., Valoni, E., Penna, M., Seldin, L., 2010. Bacterial diversity in water injection systems of Brazilian offshore oil platforms. Appl. Microbiol. Biotechnol. 85, 791–800.

Li, X.Z., Zhang, L., Poole, K., 1998. Role of the multidrug efflux systems of *Pseudomonas aeruginosa* in organic solvent tolerance. J. Bacteriol. 180, 2987–2991.

Passman, F.J., 2003. Standard guide for microbial contamination in fuels and fuel systems. In: Fuel and Fuel System Microbiology: Fundamentals, Diagnosis, and Contamination Control. ASTM International, PA, USA, pp. 81–91.

Passman, F.J., 2012. Microbial contamination control in fuels and fuel systems since 1980 — a review. Int. Biodeterior. Biodegrad. 81, 88–104.

Passman, F.J., McFarland, B.L., Hillyer, M.J., 2001. Oxygenated gasoline biodeterioration and its control in laboratory microcosm. Int. Biodeterior. Biodegrad. 47, 95–106.

Rauch, M.E., Graft, H., Rozenzhak, S., Jones, S., Bleckmann, C., Kruger, R., Naik, R., Stone, M., 2006. Characterization of microbial contamination in United States Air Force aviation fuel tanks. J. Industrial Microbiol. Biotechnol. 33, 29–36.

Saadoun, I., 2002. Isolation and characterization of bacteria from crude petroleum oil contaminated soil and their potential to degrade diesel fuel. J. Basic Microbiol. 42, 420–428.

Sanger, M., Finnarty, W., 1984. Microbial metabolism of straight chain and branched alkanes. In: Atlas, R.M. (Ed.), Petroleum Microbiology. Macmillan, New York, pp. 1–61.

Senn, R.B., Johnson, M.S., 1987. Interpretation of gas chromatographic data in subsurface hydrocarbon investigations. Ground Water Monit. Rev., 58–63. Winter Ed.

Smith, C.B., Tolar, B.B., Hollibaugh, J.T., King, G.M., 2013. Alkane hydroxylase gene (alkB) phylotype composition and diversity in northern Gulf of Mexico bacterioplankton. Front. Microbiol. 4, 370–378.

Stamper, D.M., Morris, R.E., Montgomery, M.T., 2012. Depletion of lubricity improvers from hydrotreated renewable and ultralow-sulfur petroleum diesels by marine microbiota. Energ. Fuels 26, 6854–6862.

Striebich, R.C., Rubey, W.A., Klosterman, J.R., Balster, L.M., 2001. HPLC Pre-separation with High Resolution gas Chromatography (HRGC): a Comparison to Multidimensional GC (MDGC). Proceedings of the 24th International Symposium on Capillary Chromatography and Electrophoresis, Las Vegas, NV.

Striebich, R.C., Motsinger, M.A., Rauch, M.E., Zabarnick, S., DeWitt, M., 2005. Estimation of select specification tests for aviation turbine fuels using fast gas chromatography. Energ. Fuels 19, 2445–2454.

Striebich, R.C., Shafer, L.M., West, Z.J., Adams, R.K., Zabarnick, S., 2011. Hydrocarbon group-type analysis of current and future aviation fuels: comparing ASTM D2425 to GCxGC. Proceedings of the 12th International Conference on Stability, Handling, and Use of Liquid Fuels, Sarasota, FL.

Van der Westhuizen, R., Ajam, M., De Coning, P., Beens, J., de Villiers, A., Sandra, P., 2011. J. Chromatogr. A vol. 2018, 4478–4486.

Vila, J., Nieto, J.M., Mertens, J., Springael, D., Grifoll, M., 2010. Microbial community structure of a heavy fuel oil-degrading marine consortium: linking microbial dynamics with polycyclic aromatic hydrocarbon utilization. FEMS Microbiol. Ecol. 73, 349–362.

Vu, B., Chen, M., Crawford, R.J., Ivanova, E.P., 2009. Bacterial extracellular polysaccharides involved in biofilm formation. Molecules 14, 2535–2554.

White, J., Gilbert, J., Hill, G., Hill, E., Huse, S.M., Weightman, A.J., Mahenthiralingam, E., 2011. Culture-independent analysis of bacterial fuel contamination provides insight into the level of concordance with the standard industry practice of aerobic cultivation. Appl. Environ. Microbiol. 77, 4527–4538.

Zabarnick, S., Widmore, N., Vangsness, M., 2002. Studies of urea treatment on the low-temperature properties of jet. Energy Fuels 16, 1565–1570.

Appendix R. Effect of Aromatics on the Thermal-Oxidative Stability of Synthetic Paraffinic Kerosene

Effect of Aromatics on the Thermal-Oxidative Stability of Synthetic Paraffinic Kerosene

Matthew J. DeWitt,*,[†] Zachary West,[†] Steven Zabarnick,[†] Linda Shafer,[†] Richard Striebich,[†] Ashil Higgins,[†] and Tim Edwards[‡]

[†]University of Dayton Research Institute, 300 College Park, Dayton, Ohio 45469-0043, United States

[‡]Air Force Research Laboratory/Propulsion Directorate, 1790 Loop Road North, Building 490, Wright-Patterson Air Force Base (WPAFB), Ohio 45433-7103, United States

ABSTRACT: The effect of aromatic type and concentration on the thermal-oxidative stability characteristics of a synthetic paraffinic kerosene (SPK) aviation fuel was performed using batch and flow reactor systems, in combination with detailed chemical fuel analyses. An improved understanding of the impact of aromatic addition will assist in optimizing beneficial operational characteristics of the SPK feedstocks and the development of fully synthetic jet fuels. A primary goal of this study was to elucidate the controlling reaction chemistry and identify the cause for differing stability characteristics for varying types of aromatics. Studies were performed using a SPK comprised primarily of mildly branched iso- and *n*-paraffins as the base feedstock; limited studies were performed using a highly branched SPK. Commercially available aromatic solvents were used to represent petroleum-derived jet fuel and potential synthetic aromatic blending streams. These solvents were composed of mono- and diaromatic compounds of varying average molecular weight and size. The resulting thermal-oxidative stability characteristics were highly sensitive to the blend composition, with both increasing aromatic size and concentration, resulting in a higher deposition propensity upon stressing. It was determined that oxidation and molecular growth of the aromatic compounds are the probable primary pathways of surface deposit formation for these blends. Larger aromatic compounds (e.g., diaromatic) require fewer successive growth steps to produce insoluble deposit precursors, resulting in significantly higher deposition propensity than lower molecular weight (e.g., monoaromatic) species. Limited testing showed that the impact of aromatic type on deposition is consistent for different SPK compositions, but the deposit magnitude may be affected.

■ INTRODUCTION

There has been significant interest during recent years in the development and approval of alternative (non-petroleum) aviation fuels. Alternative fuels have the potential to increase the supply and availability of reliable domestic sources while reducing associated cost volatility. Extensive laboratory and full-scale testing have resulted in the approval of synthetic paraffinic-type fuels for use as a blending feedstock (up to 50% by volume) in both commercial and military aviation fuels (per ASTM D1655-11 and MIL-DTL-83133H). This includes synthetic paraffinic kerosene (SPK) produced via Fischer–Tropsch synthesis and hydroprocessed esters and fatty acids (HEFA) derived from plant oils and animal fats. These SPK and HEFA blend stocks are predominantly paraffinic (normal and iso-) in composition and contain minimal aromatic and heteroatomic compounds. The neat paraffinic blend stocks exhibit favorable characteristics, such as excellent thermal-oxidative stability and significantly reduced particulate matter (PM) propensity during combustion, which is attributable to the lack of the aromatics and heteroatomic compounds.[1] However, the lack of these compound classes results in fuels with insufficient material compatibility/seal swell and lubricity characteristics. Therefore, the current fuel specifications have taken a conservative approach, requiring a minimum total aromatic concentration of 8% by volume (%v) for synthetic blends to ensure that fit-for-purpose (FFP) requirements are satisfied. This constraint reduces the beneficial aspects of the neat paraffinic fuels, resulting in behavior that is generally consistent with petroleum-derived fuels. Studies have been performed that demonstrate that specific types of aromatics can be added to SPK-type fuels, which provide acceptable seal swell characteristics while maintaining reduced PM emission production relative to petroleum-derived fuels.[2] Determination of favorable characteristics and required concentrations of desired aromatics would also allow for the formulation of fully synthetic jet fuels (FSJF), which would not require blending with petroleum-derived fuels and could maximize favorable operational characteristics of the fuel. However, an improved understanding of the effect of the aromatic type and concentration on other FFP characteristics is needed.

Thermal-oxidative stability, which is the propensity of a fuel to produce undesirable deposits in fuel system passages, controls, and nozzles as it absorbs waste heat from aircraft components and other fluids because of reaction with dissolved oxygen, is an important operational characteristic of a fuel. Fuel specifications evaluate the relative thermal stability using ASTM D3241 with a jet fuel thermal oxidation tester (JFTOT). The thermal stability of the fuel is evaluated via the amount of deposit on the aluminum heater tube using visual tube rating (VTR) methods and the rate of plugging [e.g., pressure drop (ΔP)] on a filter downstream of the heater tube. A VTR ≥ 3, a $\Delta P > 25$ mmHg, a "peacock" rating, or an "abnormal" tube

color (defined in ASTM D3241 as "a tube deposit color that is neither peacock nor like those of the Color Standard") result in a failure. Recent studies have investigated the effect of aromatic addition (e.g., aromatic solvents and synthetic fuel streams) on the thermal-oxidative stability of synthetic paraffinic fuels.[3−7] These have included the use of both petroleum-derived and synthetically produced aromatic compounds and evaluated thermal stability by measuring the JFTOT breakpoint temperature (highest temperature at which fuel passes the rating criteria). Studies performed by Sasol using synthetically derived aromatics, primarily composed of alkylbenzenes, have shown that the base SPK thermal stability is not affected.[4,5] However, studies using petroleum-derived aromatics (mono- and diaromatics) have shown that the addition at concentrations ≥10%v can decrease the fuel thermal stability.[3,6] The failures reported were attributed to the corresponding VTR rating of the JFTOT tube, because there was a minimal increase in ΔP during the testing.

A separate study performed to investigate the effect of blending similar petroleum-derived aromatics at varying concentrations into several SPK and HEFA fuels also showed a corresponding decrease in thermal stability with an increasing aromatic concentration.[7] However, there was not a distinct trend in the specific breakpoint temperature with respect to base fuel composition, aromatic type, or total concentration. In addition, many of the failures were due to "abnormal" deposit color. For example, photographs of JFTOT tubes with the corresponding VTR from this testing are shown in Figure 1.
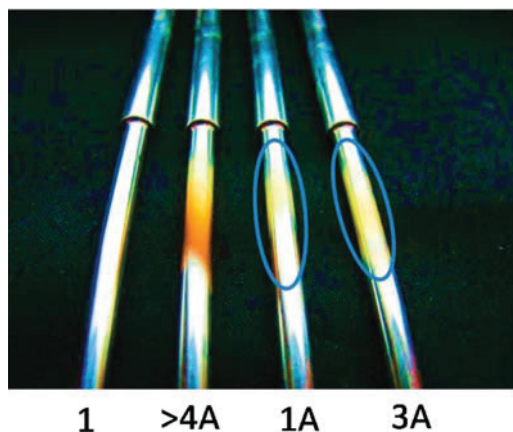
Figure 1. Photographs of JFTOT tubes and reported VTR following JFTOT testing with blends of an aromatic solvent blend in various SPK and HEFA feedstocks.

The 1A and 3A failures were reported because of the deposit having a "whitish/tannish" color, which is not typically observed for petroleum-derived fuels. The deposits were analyzed using infrared spectroscopy and elemental analysis (not previously reported); it was determined that the deposits were predominantly composed of carbon and oxygen and the color was hypothesized to be related to the deposit thickness. To provide improved insight into the experimental results, the JFTOT tubes from this study were analyzed using ellipsometry (Falex model 430) to quantify the deposit profile and thickness. A comparison of the maximum average deposit thickness (nm) over a 2.5 mm^2 area to the corresponding VTR is shown in Figure 2. Results are shown as either normal or abnormal for
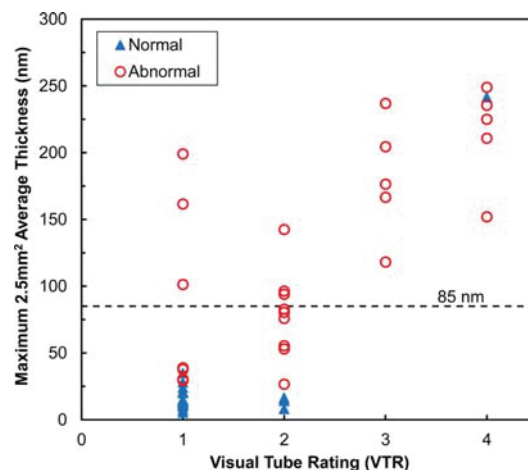
Figure 2. Comparison of JFTOT tube maximum average deposit thickness determined using ellipsometry to VTR from testing with varying concentrations and types of aromatics in several SPK and HEFA feedstocks.

each VTR; a thickness level of 85 nm is highlighted because this is the proposed value that ASTM is considering as a pass/fail criteria for use of an interferometer in the D3241 test method. As shown, a VTR of 3 or greater correlates well with a high maximum deposit level and may be able to discern unacceptable thermal stability characteristics. However, there is a wide range of deposit thickness levels for tubes with abnormal VTRs of 1 and 2, with many "failures" having low deposition levels. It may be necessary to determine appropriate test conditions and rating criteria for using the JFTOT to evaluate the effect of aromatics on synthetic fuel thermal stability characteristics.

Because of the varying observations reported in previous studies, a detailed study was performed herein to provide an improved understanding of the effect of the aromatic type and concentration on the thermal stability of SPK-type fuels. Primary objectives were to supplement the previous JFTOT studies with a more quantitative basis for evaluation and improve the understanding between chemical composition and properties on resulting performance. This approach will provide improved ability to identify optimal aromatic compounds and concentrations, which can be added to paraffinic fuels to maximize desired operational characteristics and allow use without blending with petroleum-derived fuel.

■ EXPERIMENTAL SECTION

Two reactor systems were used to evaluate the thermal stability of a SPK blended with varying concentrations of different aromatic solvents. This included a batch [quartz crystal microbalance (QCM)] and a flowing (single-tube reactor) system. These systems have been previously used to successfully evaluate the thermal-oxidative stability characteristics of aviation-type fuels. The design and operation of these have previously been described in detail;[1,8,9] a brief description of each is provided below.

QCM. The QCM is a batch reactor system that provides isothermal stressing of a test fuel for an extended duration with an oxygen headspace. Headspace oxygen and mass deposition are monitored *in situ* to provide time-dependent information regarding the thermal-oxidative stability characteristics of the sample. For this testing, 60 mL of the test fuel was air-saturated under ambient conditions. The reactor was closed, heated to 140 °C, and stressed isothermally for 15 h. The

time-dependent deposition and oxygen consumption characteristics were used to evaluate relative thermal stability characteristics.

Single-Tube Flow Reactor System. Thermal stability was evaluated using a single-tube, single-pass flow reactor.[1,9] The reaction system has a 91.4 cm (36 in.) long actively heated section, where the temperature is sufficient to promote the desired reaction chemistry. Studies were performed using 0.216 cm (0.085 in.) inner diameter and 0.318 cm (0.125 in.) outer diameter reaction tubes constructed of 316 stainless steel. The fuel was air-saturated, and thermal stressing was performed with an inlet volumetric flow rate of 10 mL/min, reaction pressure of 38.9 bar (550 psig), and test duration of 6 h. The external wall temperature was measured at various axial locations using strap-welded K-type thermocouples. The temperature profile $[T_{wall,max} \approx 357\ °C\ (675\ °F)$, and $T_{bulk,out} \approx 316\ °C\ (600\ °F)]$ was sufficient to consume all dissolved oxygen in the heated reaction zone. For the reaction condition studies, the bulk fuel temperature is estimated to be approximately 75−100 °C higher than the measured wall temperature.[9] Following testing, the reaction tube was removed and cut into 5.1 cm (2 in.) long sections. The total carbon deposit on each tube segment was determined via temperature-programmed oxidation using a LECO RC612 multiphase carbon analyzer. The stability characteristics were determined by comparing the total mass quantity and axial deposition profile.

Fuels and Aromatic Solvents. Experimental testing and analysis was performed to investigate the effect of the aromatic type and concentration on the thermal-oxidative stability characteristics of a SPK. The primary SPK used in this study was produced from natural gas via indirect liquefaction by Syntroleum Corporation (also termed S-8). This fuel is composed of mildly branched (e.g., monomethyl-substituted) isoparaffins with ~20%v n-paraffins and a distillation range similar to a typical JP-8 specification fuel. This SPK was used during the certification of alternative blends for the B-52 platform. Limited testing was performed using a SPK [also referred to as isoparaffinic kerosene (IPK)] produced by Sasol. This fuel is produced via oligimerization of C_3 and C_4 olefins, followed by hydrotreating and fractionation, to produce a fuel with the desired boiling range.[4,5,10] This process results in a SPK with a very high degree of branching and low concentration (~10%v) of cycloparaffins. The Sasol fuel was the first synthetic fuel to be approved as a blend feedstock with Jet A-1 fuel. Both neat SPKs exhibit excellent thermal-oxidative stability, with negligible deposition during stressing.[1,11] Additional details on the chemical and physical properties of these SPKs are provided elsewhere.[1,4,5,10−13] The thermal stability of the neat SPK and aromatic blends was compared to a specification JP-8 (designated POSF 6169). This JP-8 had a total aromatic concentration of ~15.7% v, total naphthalenes of ~1.1%v, and a total sulfur content of ~540 ppm by mass.

Commercially available aromatic solvents were used to represent petroleum-derived jet fuel and potential synthetic aromatic blending streams. Aromatic 100, 150, and 200 (designated A100, A150, and A200) solvents were obtained from ExxonMobil and used in this study. The solvents were analyzed for chemical composition via gas chromatography/mass spectrometry (GC/MS) and two-dimensional gas chromatography (GC × GC). These solvents are composed of a range of mono- and diaromatic compounds with varying average molecular weight ranges,[2,6] which are listed in Table 1. A100 is comprised primarily of C_3 (83.6%v) and C_4 (12.8%) alkylated benzenes, with a low concentration of indane (1.1%). A150 is comprised primarily of C_3 (2.6%v), C_4 (62.2%), C_5 (18.3%), and C_6

(1.3%) alkylated benzenes, C_{10^-} and C_{11}-alkylated indans and tetralins (7.3%), and naphthalene (6.7%). A200 is primarily composed of $C_5−C_8$-alkylated benzenes (5.3%), $C_{11}−C_{13}$-alkylated indans and tetralins (10.1%), naphthalene (6.7%), and $C_1−C_{4+}$-alkylated naphthalenes (76.3%). The chemical compositions of these solvents are slightly different but generally consistent with those previously reported when used during previous research efforts.[6] Analysis of these solvents showed negligible heteroatomic or polar compounds present. Testing with multi-component solvents allows for the evaluation of the effect of the chemical class and structure on reactivity, without favoring a specific reaction path, which could occur with single-component testing. Studies were performed with each of these solvents at varying overall concentration in the SPK fuel. In addition to the individual solvents, a composite blend (referred to as "A-Blend") was formulated (30%v A100/60%v A150/10% A200), which simulates the range of aromatic compounds in a "typical" aviation fuel. In comparison of the gas chromatography/flame ionization detection (GC/FID) chromatograms of the individual and composite aromatic solvents, S-8, neat JP-8, and the aromatic fraction of the JP-8 extracted using high-pressure liquid chromatography[14] are shown in Figure 3.
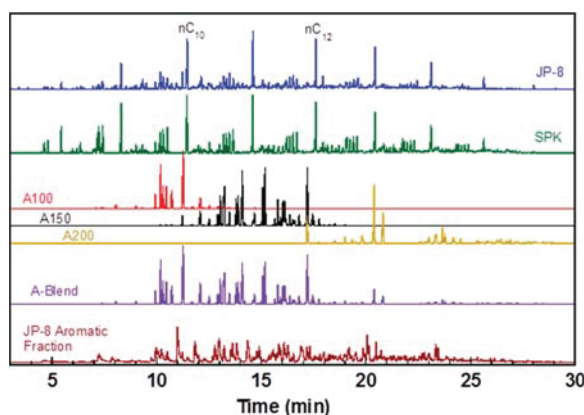
Figure 3. Comparison of chromatograms of aromatic solvents, aromatic solvent blend (30:60:10), S-8, JP-8, and aromatic fraction of JP-8.

RESULTS AND DISCUSSION

Effect of the Aromatic Concentration. The effect of the overall concentration of aromatics on the resulting thermal stability characteristics was investigated using the composite aromatic blend. Studies were performed varying the concentration of the blend at 5%v increments in the SPK (S-8 unless otherwise specified). Results from QCM testing are shown in Figure 4; mass accumulation (solid lines) and headspace oxygen (dashed lines) profiles are shown as a function of the test duration and aromatic concentration. The corresponding profiles are also shown for the neat SPK and JP-8. The neat SPK exhibited excellent thermal stability characteristics, with minimal deposition during stressing. This behavior is consistent with that observed for other neat SPK and HEFA fuels.[1]

The specification JP-8 had a deposition level and profile consistent with that typically observed for a petroleum-derived fuel with good thermal stability evaluated using the QCM. A higher total aromatic content in the SPK blends increased the total mass deposition while decreasing the onset time for oxidation. Testing with 5−15%v total aromatic content resulted in comparable deposition to that for the JP-8. It should be noted that the deposition for the petroleum-derived fuel is also affected by heteroatomic compounds within the fuel, which are

Table 1. Aromatic Solvent Composition

|	concentration (%v)		MW range (g/mol)	MW$_{ave}$ (g/mol)
solvent	monoaromatic	diaromatic		
aromatic 100	100		106−148	122
aromatic 150	94	6	120−162	136
aromatic 200	18	82	128−196	152
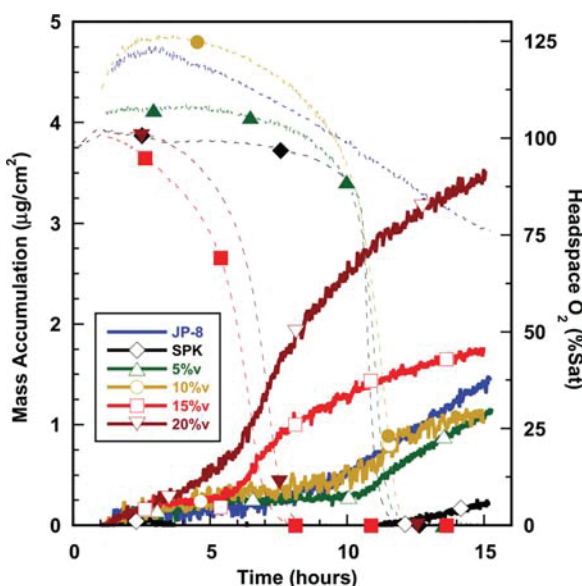
Figure 4. QCM mass accumulation (solid lines and open markers) and headspace oxygen profiles (dashed lines and closed markers) at 140 °C with a varying total concentration of the aromatic solvent blend (30:60:10) in SPK.

negligible in both the aromatic solvents and the neat SPK. The 20%v blend had a substantially higher quantity of deposition relative to the other concentrations and JP-8 fuel. However, the total magnitude is within the typical range observed for evaluation of petroleum-derived fuels on the QCM (≤ 8 $\mu g/cm^2$).

The flow reactor system was used to evaluate the thermal stability of the solvent blends for concentrations of 5−15%v in a flowing environment with a total dissolved oxygen concentration representative of actual systems (e.g., ~70 ppm by weight). The carbon deposition and measured wall temperature profiles as a function of the axial position and aromatic concentration from this testing are shown in Figure 5. The neat SPK results are not shown because negligible deposition was observed during stressing. Consistent with the QCM results, an increase in the total deposition quantity was observed with an increasing total aromatic content. The onset of the deposition was similar for each of the aromatic/SPK blends, indicating that the aromatics do not significantly affect the initial rate of fuel oxidation for the reaction conditions studied. The observation of a maximum in the deposition profile with a subsequent decrease is indicative of complete consumption of the dissolved oxygen within the heated zone. The significantly higher deposition characteristics for the JP-8 fuel are most likely due to heteroatomic (e.g., oxygen, sulfur, and nitrogen) components within the fuel, which are known to promote undesirable deposit formation under oxygen-limited conditions.[14−16] It is possible that slight differences in the specific aromatic compounds in the petroleum-derived fuel and aromatic solvents also impact the deposition propensity, but this is believed to be minor compared to the role of heteroatoms in the deposition process. Overall, the observation that the magnitude of deposit formation correlates with the total aromatic content indicates that this compound class participates in and promotes deposit formation pathways.
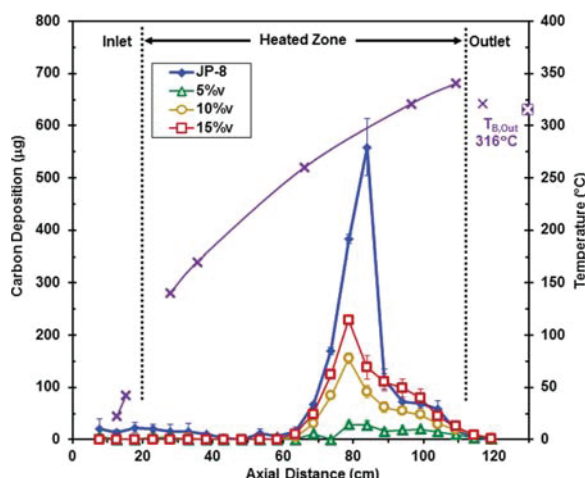
Figure 5. Carbon deposition and measured wall temperature profiles from flow reactor testing with a varying total concentration of the aromatic solvent blend (30:60:10) in SPK.

Effect of the Aromatic Type. The effect of the type of aromatic on the deposition propensity of the SPK was evaluated by performing studies with the individual aromatic solvents blended at a varying concentration in the SPK. These were performed to determine if the aromatic structure and molecular size (e.g., mono- versus diaromatic) have a significant impact on thermal stability characteristics. QCM experiments were performed by blending each of the individual solvents or composite blend at 20%v with SPK and using the same reaction conditions as previously reported. This relatively high concentration was used to intensify the effect of the molecular type on deposition. The results from this testing are shown in Figure 6. The type of aromatic solvent had a major impact on both the total mass accumulation and the corresponding rate of oxygen consumption during thermal stressing. The total mass deposition with A100, comprised solely of alkylated mono-aromatics, was similar to that for the neat SPK, even though the
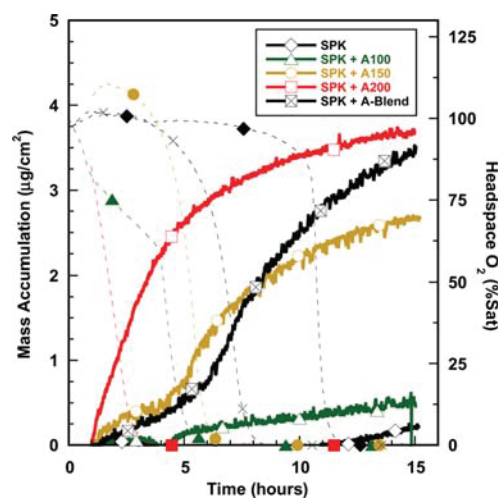
Figure 6. QCM mass accumulation (solid lines and open markers) and headspace oxygen profiles (dashed lines and closed markers) at 140 °C with a varying aromatic solvent type in SPK at 20%v.

aromatic solvent was present at 20%v. A100 did increase the rate of fuel oxidation; however, this is believed to be primarily due to dilution of the synthetic antioxidant in the neat SPK. The addition of both A150 and A200 significantly increased deposition levels, while testing with the 30:60:10 composite blend resulted in deposition levels between the individual solvent results. This observation is reasonable because of the inclusion of both solvents within the blend. These results imply that the molecular type of aromatics can affect the thermal stability characteristics of synthetic fuels, with diaromatics having a higher impact on the resulting deposition propensity.

The impact of the aromatic type on the SPK thermal stability was also evaluated using the flow reactor system. Testing was performed by blending each of the individual and composite solvents at 10%v in the SPK using reaction conditions consistent with the aforementioned studies. The carbon deposition and measured wall temperature profiles as a function of the axial position and aromatic type are shown in Figure 7.
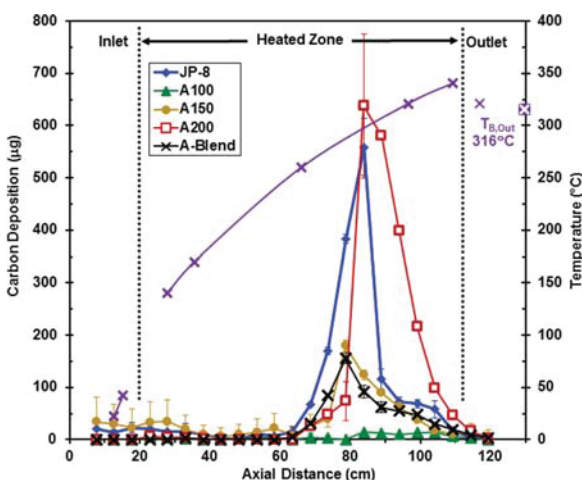

Figure 7. Carbon deposition and measured wall temperature profiles from flow reactor testing with a varying aromatic solvent type in SPK at 10%v.

Similar to the QCM testing, the addition of A100 showed minimal effect on surface deposition levels, which were similar to that for the neat SPK. The A100 is comprised solely of alkylated monoaromatics, which are similar in composition to the synthetic aromatic streams produced by Sasol. As previously mentioned, JFTOT breakpoint studies showed that the thermal stability of the Sasol SPK was not significantly impacted by this type of aromatic stream.[4,5] The A150 blend showed very similar deposition characteristics to the 30:60:10 composite blend, while the A200 promoted a significant increase in deposition, which was substantially higher than that for the JP-8 fuel. These results further indicate that aromatic compounds participate in deposit formation pathways, with diaromatics having an increased propensity to produce high-molecular-weight compounds.

Pathways for Deposit Formation from Oxidation of Aromatics. The thermal-oxidative stability characteristics of petroleum-derived fuels have been related to the presence of trace heteroatomic compounds within the fuels. These deleterious compounds include oxygenates (e.g., phenols) and reactive sulfur/nitrogen species.[8,14−16] These species can

increase deposit formation via pathways that promote oxidation and molecular growth at elevated reaction temperatures. The presence of heteroatomic compounds in the neat fuels prior to stressing intensifies deposition propensity, with increased concentrations typically promoting higher deposition levels. The SPK and aromatic solvents used in this study contained negligible concentrations of these heteroatomic compounds. However, the observation of significant carbon deposition during oxidation, with sensitivity to the aromatic type and concentration, indicates that molecular growth pathways do occur within the synthetic fuel blends. The neat SPK readily undergoes oxidation during thermal stressing but primarily produces stable oxygenated compounds, which are not prone to significant molecular growth. This is most likely due to the paraffinic nature (mild branching and primarily linear structure) of the SPK. Aromatic compounds undergo oxidation under these reaction conditions, with rates competitive with those for the neat SPK. This is due to the presence of weak bonds within alkylated aromatics (e.g., benzylic hydrogens), which provide energetically favorable sites for hydrogen donation and subsequent oxidation. Alkylated aromatics can undergo oxidation, producing compounds, such as phenols, aldehydes, ketones, and carboxylic acids. Once formed, these species can subsequently undergo ring-closure reactions, producing species, such as benzofuranones.[17] These products have the potential to undergo molecular growth via further oxidation or reaction with other aromatic compounds. It is likely that larger aromatic compounds, such as diaromatics, require fewer consecutive reaction steps to produce high-molecular-weight, low-solubility species, which are prone to surface deposition. This would increase the deposition propensity for blends, which contain high concentrations of diaromatics, especially under oxygen-limited conditions.

Analysis was performed on neat and thermally stressed samples to determine if there was quantitative evidence of molecular growth products following oxidative stressing. Polar species/products were separated and concentrated using a solid-phase extraction (SPE) pre-separation technique with subsequent gas chromatographic (GC) analysis. A total volume of 5−20 mL of sample was passed through 1 g of silica gel, followed by a wash of three aliquots of hexanes and extraction with 1 mL of methanol. Each extract was analyzed using GC × GC, GC/MS, and/or high-temperature GC/FID. GC/FID chromatographs from the analysis of polars for a mixture of the SPK with 10%v of the A-Blend (both neat and following stressing in the flow reactor system) and the A-Blend following stressing on the QCM are shown in Figure 8. Similarly, GC × GC chromatograms (color intensity correlates with the mass concentration) from the analysis of polar products following QCM stressing of the individual aromatic solvents (non-blended with SPK to intensify product formation) are shown in Figure 9. The unstressed SPK/aromatic blend had very low concentrations of polar compounds (representative of all aromatic solvents/blends used in this study). The oxidation products from both the aromatic solvents and aromatic/SPK blends exhibited a distribution consistent with sequential molecular growth steps. The primary product region (1°) is attributed to initial oxidation of the parent aromatic or SPK compounds to produce oxygenated species. The secondary (2°), tertiary (3°), and subsequent product distributions (evident from high-temperature GC/FID analysis; not shown) had molecular weight ranges (elution times) and mass spectra ion fragmentation patterns [from mass spectro-
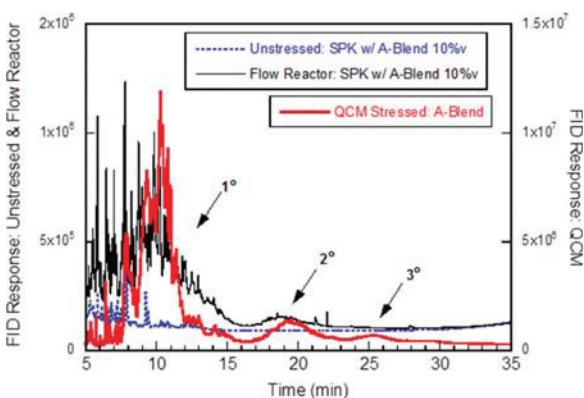
Figure 8. Chromatographic analysis of polar compounds in neat and stressed samples.
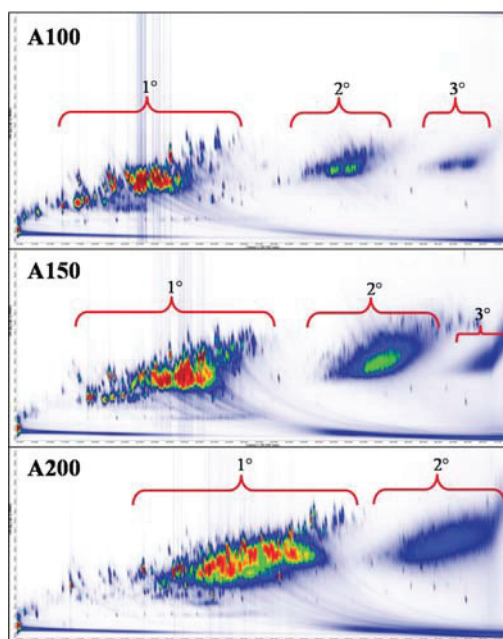

Figure 9. GC × GC analysis of polar compounds following stressing of varying aromatic solvents in QCM.

metric (MS) analysis] consistent with species formed via molecular growth and oligomerization of the oxidation products and/or parent fuel molecules (e.g., $1° + 1°$ or fuel $\rightarrow 2°$, and $1° + 2° \rightarrow 3°$). For example, approximate carbon number ranges for the A100 product regions shown in Figure 9 were $1°$, C_9-C_{13}; $2°$, $C_{16}-C_{22}$; and $3°$, $C_{24}-C_{30}$. It was not feasible to identify specific structures because of the various isomers and types of alkylated aromatics in the solvent and co-elution during analysis. Similar to the aromatic solvent testing, the stressed flow reactor sample had products consistent with molecular growth, as shown in Figure 8. There is a more diverse range of the initial oxidation products for this sample, most likely because of products formed directly from the SPK. However, there is clear evidence of molecular growth products consistent with those observed during the QCM stressing. GC/MS analysis also confirmed these species as having an aromatic base structure. This is an important observation because it

provides further evidence of molecular growth under conditions more representative of actual fuel systems (e.g., oxygen-limited, flowing reaction environment). The lower absolute concentration of higher molecular weight products for the flow reactor sample is most likely due to the loss of these species to surface deposit formation within the heated or post-reactor zones and the reduced oxygen availability (i.e., lower concentration of the limiting reagent).

The significantly higher propensity of diaromatics to promote surface deposition during flow reactor stressing occurs because these larger precursors require fewer oxidation and oligomerization steps to produce higher molecular weight products, which are more prone to producing surface deposits.[15] For example, the A100 and A150 appear to require 2−3 molecular growth steps to form products with molecular weight ranges observed following a single growth step for the A200 solvent (see Figure 9). This result supports the assertion that molecular growth and oligimerization are the primary steps required for oxidative deposition, especially for fuels with a low heteroatomic content. In addition, molecular type/size can have a significant effect on the resulting thermal stability behavior, especially under oxygen-limited conditions, where rapid growth to deposit precursors is necessary for high deposition levels.

Effect of the SPK Composition on Deposition Propensity. There is evidence that oxidation products of aromatics can produce surface deposits, with increasing propensity for higher concentration and larger molecular size. It is possible that the type and composition of the SPK can also affect the deposition propensity of the aromatic compounds. A limited flow reactor testing was performed with a highly branched SPK produced by Sasol. This type of SPK contains monocycloparaffinic compounds (~10−12%v) with negligible normal paraffins and was used during previous aromatic blending JFTOT studies.[4,5] Testing was performed blending the individual solvents and A-Blend at 10%v in this SPK; results are shown in Figure 10. Consistent deposition trends with those for S-8 testing were observed with respect to the effect of the aromatic type. However, the absolute magnitude and initial onset of the deposit were affected by the base SPK, with the Sasol blends having a higher deposition quantity. For example,
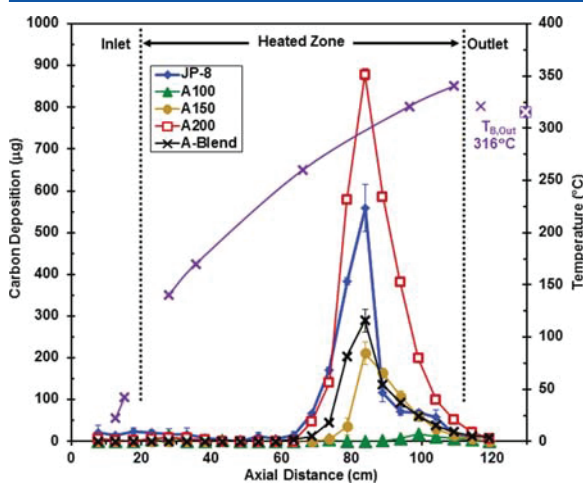
Figure 10. Carbon deposition and measured wall temperature profiles from flow reactor testing with a varying aromatic solvent type in Sasol SPK at 10%v.

the total heated zone deposit quantity for testing with the A-Blend in S-8 and Sasol was approximately 580 and 910 μg, respectively. This is most likely due to competition for oxidation of the parent SPK species and the subsequent propensity of these to undergo further molecular growth steps. Therefore, it is most likely feasible to assume that the impact of aromatic addition will be consistent for different SPKs, but the magnitude of the deposit quantity may be affected. The impact of the base SPK composition and properties on the resulting deposition characteristics with the addition of aromatics merits further study.

SUMMARY

Improved insight into the effect of aromatic addition on the thermal-oxidative stability characteristics of synthetic paraffinic feedstocks can assist in maximizing desirable operational characteristics of paraffinic fuels (e.g., reduced emission propensity and improved thermal stability). This can also provide a basis for producing FSJF compatible with legacy and future aircraft. SPKs exhibit excellent oxidative thermal stability, which has been attributed to the lack of heteroatomic and aromatic compounds within these fuels. Previous studies have shown differing impacts of adding petroleum-derived or synthetically produced aromatics on the resulting thermal stability characteristics. An improved understanding of the effect of aromatic type and concentration will assist in identifying optimal aromatic types that will satisfy FFP requirements while maximizing beneficial aspects of the paraffinic base feedstocks. Batch and flowing thermal stability tests were performed to examine the effect of the aromatic type and concentration on oxidative deposition characteristics. It was found that, for a specific aromatic type, the deposition propensity is higher with an increasing concentration. This result indicates that oxidation and growth products of aromatic compounds can promote undesirable surface deposits. The molecular size of the aromatic compounds also affected deposition propensity, with larger species (e.g., diaromatics) producing significantly higher quantities of insoluble deposits because fewer successive molecular growth reaction steps are required for deposition. Analysis of the oxidative products following fuel stressing provided further evidence of molecular growth of aromatic oxidation products. Additional studies can provide improved insight and understanding into the effect of the aromatic type on thermal stability, guidance for selection of optimal aromatic compounds to satisfy FFP requirements, and assistance in the development of viable test methodologies for fuel implementation.

AUTHOR INFORMATION

Corresponding Author
*E-mail: matthew.dewitt@wpafb.af.mil.

Notes
The authors declare no competing financial interest.

ACKNOWLEDGMENTS

REFERENCES

(1) Corporan, E.; Edwards, T.; Shafer, L.; DeWitt, M. J.; Klingshirn, C.; Zabarnick, S.; West, Z.; Striebich, R.; Graham, J.; Klein, J. Chemical, thermal stability, seal swell, and emissions studies of alternative jet fuels. *Energy Fuels* **2011**, *25* (3), 955−966.

(2) DeWitt, M. J.; Corporan, E.; Graham, J.; Minus, D. Effects of aromatic type and concentration in Fischer−Tropsch fuel on emission production and material compatibility. *Energy Fuels* **2007**, *22* (4), 2411−2418.

(3) Klettlinger, J.; Rich, R.; Yen, C.; Surgenor, A. Thermal stability testing of Fischer−Tropsch fuel and various blends with Jet A, as well as aromatic blend additives. *Proceedings of the IEEE EnergyTech*; Cleveland, OH, May 25−26, 2011.

(4) Ajam, M.; Viljoen, C. L. Synergies between renewable kerosene and Fischer−Tropsch Synthetic Paraffinic Kerosene (FT-SPK). *Proceedings of the 12th International Conference on Stability, Handling and Use of Liquid Fuels*; Sarasota, FL, Oct 16−20, 2011.

(5) Moses, C. A.; Roets, P. N. J.; Ajam, M.; Viljoen, C. L.; van der Westhuizen, R.; Wilson, G. R. An evaluation of synthetic jet fuel containing aromatics. *Proceedings of the 12th International Conference on Stability, Handling and Use of Liquid Fuels*; Sarasota, FL, Oct 16−20, 2011.

(6) Klettlinger, J. L. S.; Edwards, T.; Rich, R. Effect of aromatic concentration of a Fischer−Tropsch fuel on thermal stability. *Proceedings of the ASME Turbo Expo 2012*; Copenhagen, Denmark, June 11−15, 2012; GT2012-68626.

(7) DeWitt, M. J.; West, Z.; Mescher, A.; Stelzenmuller, N.; Zabarnick, S.; Edwards, T. Effect of aromatics addition on the thermal-oxidative stability of alternative jet fuels. *Prepr.—Am. Chem. Soc., Div. Energy Fuels* **2012**, *57* (2), 826−827.

(8) Zabarnick, S. Studies of jet fuel thermal stability and oxidation using a quartz crystal microbalance and pressure measurements. *Ind. Eng. Chem. Res.* **1994**, *33*, 1348−1354.

(9) DeWitt, M. J.; Edwards, T.; Shafer, L.; Brooks, D.; Striebich, R.; Bagley, S. P.; Wornat, M. J. Effect of aviation fuel type on pyrolytic reactivity and deposition propensity under supercritical conditions. *Ind. Eng. Chem. Res.* **2011**, *50* (18), 10434−10451.

(10) Moses, C. A. *Qualification of SASOL Semi-synthetic Jet A-1 as Commercial Jet Fuel*; Southwest Research Institute: San Antonio, TX, 1997; Report SwRI 8531.

(11) Edwards, T.; Minus, D.; Harrison, W.; Corporan, E.; DeWitt, M.; Zabarnick, S.; Balster, L. Fischer−Tropsch jet fuels—Characterization for advanced aerospace applications. *Proceedings of 40th AIAA/ASME/SAE/ASEE Joint Propulsion Conference and Exhibit*; Ft. Lauderdale, FL, July 11−14, 2004; Paper AIAA-2004-3885.

(12) Corporan, E.; DeWitt, M. J.; Belovich, V.; Pawlik, R.; Lynch, A. C.; Gord, J. R.; Meyer, T. R. Emissions characteristics of a turbine engine and research combustor burning a Fischer—Tropsch jet fuel. *Energy Fuels* **2007**, *21* (5), 2615−2626.

(13) DeWitt, M. J.; Striebich, R.; Shafer, L.; Zabarnick, S.; Harrison, W. E., III; Minus, D. E.; Edwards, T. Evaluation of fuel produced via the Fischer−Tropsch process for use in aviation applications. *Proceedings of AIChE Spring National Meeting*; Houston, TX, April 22−27, 2007; Paper 58b.

(14) Balster, L. M.; Zabarnick, S.; Striebich, R. C.; Shafer, L. M.; West, Z. J. Analysis of polar species in jet fuel and determination of their role in autoxidative deposit formation. *Energy Fuels* **2006**, *20*, 2564−2571.

(15) Hazlett, R. N. *Thermal Oxidation Stability of Aviation Turbine Fuels*; American Society for Testing and Materials (ASTM): West Conshohocken, PA, 1991; pp 68−69 and 111152.

(16) Kuprowicz, N. J.; Zabarnick, S.; West, Z. J.; Ervin, J. S. Use of measured species class concentrations with chemical kinetic modeling

261

for the prediction of autoxidation and deposition of jet fuels. *Energy Fuels* **2007**, *21*, 530−544.

(17) Webster, R. L.; Evans, D. J.; Rawson, P. M.; Mitrevski, B. S.; Marriott, P. J. Oxidation of neat synthetic paraffinic kerosene fuel and fuel surrogates: Quantitation of dihydrofuranones. *Energy Fuels* **2013**, *27*, 889−897.

262

Appendix S. Equilibrium Partitioning of Di-ethylene Glycol Monomethyl Ether (DiEGME) between Fuel and Aqueous Phases at Sub-Ambient Temperatures

Equilibrium Partitioning of Di-ethylene Glycol Monomethyl Ether (DiEGME) between Fuel and Aqueous Phases at Sub-Ambient Temperatures

Zachary J. West,[†] Linda M. Shafer,[†] Richard C. Striebich,[†] Steven Zabarnick,[†] Charles Delaney,[‡] Donald Phelps,[§] and Matthew J. DeWitt*,[†]

[†]University of Dayton Research Institute, 300 College Park, Dayton, Ohio 45469, United States

[‡]Encore Support Systems, 303 Clarence Tinker Drive, San Antonio, Texas 78226, United States

[§]Air Force Research Laboratory, Fuels and Energy Branch, Wright-Patterson Air Force Base (WFAFB), Ohio 45433, United States

ABSTRACT: Improved understanding of the effect of temperature and concentration on the equilibrium partitioning of Fuel System Icing Inhibitor (FSII) additive between fuel and aqueous phases can assist in identifying required dose concentrations for safe aircraft operability. A novel experimental system was designed and used to quantify the equilibrium partitioning of the currently approved FSII, di-ethylene glycol monomethyl ether (DiEGME), under conditions relevant to actual aircraft fuel system operation. This included temperatures from ambient to -47 °C, total water contents from 130 to 560 ppmV, and initial FSII concentrations from 100 to 1500 ppmV. The partitioning of DiEGME was a strong function of temperature, exhibiting nonideal solution behavior. For a constant temperature, the resulting phase partitioning was independent of initial FSII and total water concentrations, with a single equilibrium correlation established. FSII partitioning into the aqueous phase increased with both decreasing temperature and initial FSII dose concentration in the fuel. The overall behavior was attributed to hydrophilic interactions between the glycol ether and water, which become more favored at lower temperatures and concentrations. The behavior is consistent with that expected based on the effect of temperature and concentration on the corresponding FSII activity coefficients in each phase, and has previously been observed for analogous glycol ethers. Based on the partitioning behavior, very low concentrations of FSII are expected to be sufficient to prevent water solidification to temperatures below the specification freeze point of the fuel.

■ INTRODUCTION

Fuel system icing inhibitor (FSII) is one of three additives currently required in U.S. military aviation fuels JP-5 and JP-8, per specifications MIL-DTL-5624V[1] and MIL-DTL-83133H,[2] respectively. The primary function of FSII is to prevent water, present in fuel systems at parts per million levels, from solidifying and inhibiting aircraft operation. The requirement for FSII was added in 1961 following several reported incidents that attributed fuel system malfunctions and aircraft losses to ice formation in the fuel system; an extensive research and development program was performed to evaluate and approve a FSII additive.[3−5] The FSII additive currently approved for use is di-ethylene glycol monomethyl ether (DiEGME) (CAS No. 111-77-3); the structure is shown in Figure 1. DiEGME has
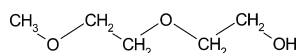

Figure 1. Structure of DiEGME.

both hydrophilic and hydrophobic functionalities and is soluble, to varying degrees, in both fuel and water. FSII is required at the highest concentration of the military fuel additives with procurement ranges of 0.07−0.10 vol % (JP-8) and 0.10−0.15 vol % (JP-5), and on-aircraft minimum use limits of 0.03 vol % (300 ppm) for JP-5 (per NAVAIR 00-80T-109[6]) and 0.04 vol % for JP-8 (per USAF T.O. 42B-1-1[7]). The higher procurement range allows for possible FSII loss via water extraction during

fuel transport and storage, thus ensuring the minimum requirement for aircraft use. Commercial aviation fuels Jet A and Jet A-1 do not require FSII, but the additive is permitted for use with a fuel procurement range of 0.10−0.15 vol % (per ASTM D1655-13a[8]). ASTM is currently considering reduction of the minimum procurement limit to 0.07 vol %, which will be consistent with the USAF requirement.

There are many motivating factors for determining the lowest FSII dose concentration which can provide the desired anti-icing efficacy during operation. These range from logistical and economic issues to application-based concerns. A lower FSII requirement would significantly reduce the associated logistical footprint and procurement issues of the additive, rendering a considerable cost savings, especially for operation outside of the United States. In addition, water bottoms containing DiEGME are considered hazardous waste and have disposal- and toxicity-related concerns. DiEGME has been implicated in the peeling of fuel tank topcoat material in the ullage space of integral wing fuel tanks in the B-52 and other military aircraft; a lower concentration may reduce the frequency of failure occurrences.[9,10] From an application perspective, the need for FSII may be reduced or eliminated due to more stringent maintenance practices (e.g., improved

sump draining), alternate system designs for newer aircraft, and hardware modifications made to legacy aircraft (e.g., water scavenge rakes). In addition, FSII is not required during commercial aircraft flight, indicating the potential for safe operation without the additive. However, there are significant differences in the operation cycle of commercial and military aircraft.

Extensive studies have been performed to determine the minimum required DiEGME concentration to prevent blockage of close tolerance flow paths due to ice formation. Most notably, the U.S. Navy performed the majority of this testing using the Fuel System Icing Simulator (FSIS), which evaluates the plugging of a fine flow restriction (typically, a 30 μm wire mesh filter) by recirculating fuel with a specified total water and FSII content.[11,12] These studies demonstrated that the DiEGME concentration can be significantly lower than the 0.07 vol % procurement limit and still prevent solidification of water at very low temperatures (<−40 °C). However, the FSII concentration needed to prevent solidification was highly dependent on the total quantity of water and test conditions used. Many factors can affect the formation of ice in fuel systems, including undercooling effects, fluid velocity, boundary conditions, and the freezing transition temperature for FSII/water mixtures.[13] Because of the varying complexity, geometry, and operating conditions experienced by different aircraft platforms, it is difficult to independently evaluate the required DiEGME concentration for all applications.

DiEGME primarily prevents ice formation in jet fuel by selectively partitioning into any free water present and suppressing the solidification temperature of the aqueous phase. Several possible mechanisms for the freeze point suppression by anti-icing inhibitors have been proposed, including the role of hydrogen bonding and the resulting effect on water activity.[14−16] Determination of the extent of DiEGME partitioning from fuel as a function of the total FSII/water concentrations and temperature is useful because it provides insight regarding the minimum freeze point suppression that can be obtained. The measured freeze point of binary DiEGME/water mixtures as a function of DiEGME concentration is shown in Figure 2.[13] The freeze point suppression is minor at low concentrations, but rapidly improves as the DiEGME concentration increases above ∼50 vol % (0.13 mol
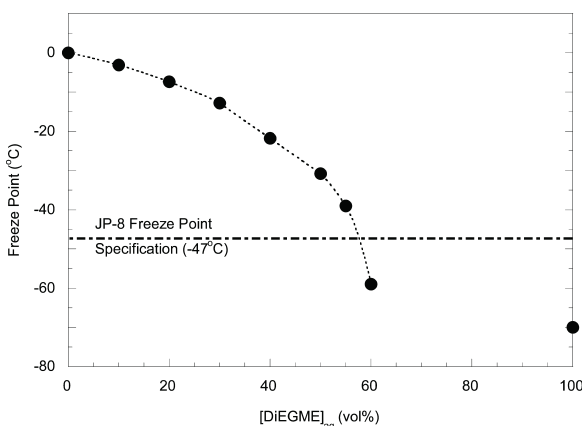

Figure 2. Measured freeze point of DiEGME/water mixtures using differential scanning calorimetry (≤50 vol %) and ASTM D1177 (>50 vol %).

%). The freeze point dependence shown in Figure 2 indicates that a single eutectic point may exist at temperatures below −70 °C; however, it was not possible to obtain quantitative freeze point measurements within this concentration range because of the reduced amount of latent heat released. The inability to obtain quantitative freeze points could also potentially be due to a larger number of molecular conformations formed at higher glycol ether concentrations, which can result in multiple types of solid phases. Similar behavior has previously been reported for the solid−liquid phase transition of ethylene glycol/water mixtures, where different phase formation could be promoted, depending on the cooling methodology used.[17] For the ethylene glycol system, a stable hydrate phase could be produced by seeding crystals for nucleation and growth resulting in a phase diagram with two eutectic points. The DiEGME/water system is more complex because of the varying types of oxygen bonding within the molecule and may allow formation of multiple crystal structures. Regardless of whether the DiEGME/water system has a single or multiple eutectic points, the respective freeze points within the 60−100 vol % range are most likely well below −50 °C. Since the specification fuel freeze points for JP-5 and JP-8 are −46 and −47 °C, respectively, there should be minimal concerns with ice formation once the freeze point of the FSII/water phase is below these values. In fact, this would provide for safe operability, regardless of the aircraft platform or mission profile. Since FSII is added to the fuel, and must subsequently partition into any free water present, determination of the final phase equilibrium as a function of FSII/water concentration and temperature is highly relevant. This would not only provide a measure of the "potential protection" during flight (via freeze point depression) and guidance for a minimum required additive dose concentration, it would also provide guidance of potential losses during fuel procurement and transfer.[18,19]

Partition Coefficients of FSII in Fuel/Water Systems. The equilibrium ratio of FSII between fuel and aqueous phases provides guidance regarding the potential anti-icing efficacy with varying FSII dosage concentrations. For aviation applications, this ratio has previously been estimated using the Partition Coefficient (PC), defined as

$$\text{Partition Coefficient (PC)} = \frac{[\text{DiEGME}]_{\text{aq}}}{[\text{DiEGME}]_{\text{fuel}}} \quad (1)$$

where $[\text{DiEGME}]_{\text{aq}}$ and $[\text{DiEGME}]_{\text{fuel}}$ are the concentrations (in volume percent) of DiEGME in the aqueous and fuel phases at equilibrium, respectively. A desired characteristic of FSII is that it is soluble in the base fuel, but readily partitions into any aqueous liquid present (e.g., has a high PC). The higher the value of the PC, the greater the final $[\text{DiEGME}]_{\text{aq}}$. However, a high PC value may also result in higher loss during fuel transport and storage. Although the equilibrium ratio is most likely a function of temperature and concentration, there is only limited data available pertaining to the functional dependence of the PC. The majority of the studies were performed using the previously approved FSII, ethylene glycol monomethyl ether (EGME) (with and without glycerol) in JP-4 fuels.[20,21] Netzel and Gadberry[20] measured the PC at equilibrium with final concentrations of 0.10 and 0.20 vol % EGME in JP-4 fuel under ambient conditions. A PC value of 163 ± 10 was obtained, which was found to be independent of the FSII/water volume ratio or the total EGME concentration

studied. Orrell and co-workers[21] performed a more-detailed study investigating the PC of EGME as a function of temperature and concentration for varying fuel compositions. These studies were primarily conducted with high water concentrations (2500 ppmV) for temperatures from −50 °C to +24 °C. The $[DiEGME]_{aq}$ was quantified while the fuel phase concentration was calculated by mass balance based on initial concentrations. The PC was found to increase significantly as the temperature was reduced at constant FSII/water concentrations. For example, the PC values for testing with initial concentrations of 0.60% EGME and 0.25% water (FSII/water ratio of 2.4) were 119 (24 °C), 172 (−5 °C), 197 (−30 °C), and 353 (−50 °C). However, the PC value was found to decrease as the EGME/water ratio increased with a constant total water or EGME concentration.

Limited studies have been performed to estimate the PC of DiEGME in aviation fuels, and all have been performed at ambient temperature. PC measurements were conducted for EGME and DiEGME in JP-4 and JP-5 (400 mL fuel), using consecutive extractions of the FSII from the fuel using large quantities of water.[22] The first extract (10 mL water) was analyzed to quantify $[DiEGME]_{aq}$ while the second extract (40 mL water) was used to determine $[DiEGME]_{fuel}$. Reported values from the study are shown in Table 1. DiEGME was

Table 1. Comparison of Partition Coefficients for EGME and DiEGME in JP-4 and JP-5 Jet Fuels[a]

	Partition Coefficient	
initial concentration of FSII (vol %)	JP-4	JP-5
0.15% EGME	280 ± 3	402 ± 136
0.50% EGME	243 ± 27	305 ± 52
0.20% DiEGME	749 ± 32	661 ± 102
0.50% DiEGME	566 ± 57	642 ± 51

[a]Data taken from ref 22.

found to have a higher degree of partitioning than EGME. With respect to the EGME measurements, JP-4 values were higher than previously reported,[20] but it should be noted that the aforementioned study reported the PC achieved at the final FSII concentration while Table 1 values are for the initial EGME concentration (which will decrease during partitioning). Two more recent studies reported PC values of DiEGME in Jet A of 480 (±20%)[23] and 538.[12] The former study employed the use of a DiEGME/water ratio of ~1, while the latter methodology used consecutive FSII extractions with large volumes of water. The primary purpose for quantifying the PC of DiEGME in Jet A for these two studies was for screening of potential alternative FSII additives.

All of the aforementioned PC values were estimated using DiEGME/water ratios of one or less with a total water concentration much higher than expected in the fuel. The ratio of DiEGME/water required to inhibit solidification at reduced temperatures will likely be in excess of one (i.e., ≥ 50% FSII, see Figure 2). Accordingly, significant variance of the PC as a function of the DiEGME/water ratio, total concentrations of FSII and water, or temperature could result in a large overestimation or underestimation of the required FSII concentration. Although these variables would not affect the behavior for an ideal solution at constant temperature, it is reasonable to assume this system will deviate from ideality. These trends were all observed during the temperature-dependent study with EGME,[21] but extension of the data to

current applications is limited due to the high water concentrations used. Therefore, this study was performed to investigate the effect of the pertinent variables on FSII partitioning using concentration and temperature ranges relevant to current aircraft fuel system operation.

■ EXPERIMENTAL SECTION

A novel experimental system and testing methodology were developed to quantify the PC of DiEGME between fuel and water under aircraft relevant conditions. The variables of interest included the temperature and the total concentrations of DiEGME and water. The temperature range of interest is from ambient conditions to the minimum that bulk fuel could experience during flight, −47 °C, per the JP-8 and Jet A-1 fuel freeze point specifications. The DiEGME concentration range is bound by a minimum level of interest, 0.01% by volume, to the current maximum procurement limit (0.15 vol % in JP-5). The expected total water content is difficult to specify directly, but recent estimations and measurements of the total water content expected on aircraft indicate that low quantities of water (<120−130 ppmV) should be encountered during standard operation.[19,24] In addition, the SAE provides recommendations regarding the total water concentration that should be used when performing aircraft fuel system and component icing testing.[25,26] The recommended total water contents range from water saturated fuel at 80 °F (~90 ppmV) for "Continuous System Operation" to ~618 ppmV for "Filter Bypass Function Operation". This range was deemed relevant to aircraft operation and was implemented in the current study. It should be noted that these levels are substantially lower than those employed during previous FSII partitioning studies.

A primary objective of this work was to improve the overall accuracy of the PC quantification. This was accomplished by individually sampling the fuel and aqueous phases at the experimental temperature, with direct quantitation of DiEGME in each phase rather than determination via mass balance or consecutive water extractions of the fuel phase. This approach allows calculation of a FSII mass balance and can provide direct guidance regarding the minimum protection afforded against solidification (i.e., aqueous phase freeze point). It was desirable to use a total fuel volume which could be readily handled and conditioned, yet sufficient to obtain the required data. A total fuel volume of 1500 mL satisfied these requirements using small, but manageable total water volumes (e.g., 195−840 μL to achieve 130−560 ppmV). Sampling an extremely small aqueous volume is very difficult and requires accumulation at a single point. This prompted the use of Teflon wetted surfaces and a system low point to allow proper aqueous phase shedding to an accumulation point. Additional test requirements were sampling of the test fluids at the equilibrium temperature and an acceptable test duration. The former ensures that back-diffusion to the fuel would not occur prior to sampling while the latter allows a wide range of test conditions to be readily explored.

Procedure and Apparatus. Mixtures of Jet A-1 fuel (designated POSF 4877), DiEGME (≥98% purity from Sigma−Aldrich), and water (purified by reverse osmosis) were prepared over the applicable range of interest in 2-L Teflon separatory funnels (Nalgene, Teflon-FEP, P/N 4301-2000). Thw Jet A-1 was a low sulfur fuel (~82 ppm) with a typical total aromatic content (~18.8 vol %). Although it is possible that the absolute PC values may vary slightly with differing chemical class composition,[27] the trends with respect to each test variable should be consistent. The separatory funnels were initially filled with 1500 mL of jet fuel, dosed with the appropriate volume of DiEGME (0.03−0.15 vol %) via syringe, and vigorously shaken. The fuel was then sampled to quantify the initial DiEGME concentration via gas chromatography with mass-selective detection (GC/MS) using extracted-ion area response (m/z = 90), this technique has a relative accuracy of approximately ±10% for concentrations of <500 ppmV (0.05 vol %) and approximately ±5% for higher concentrations. The initial water content of the fuel was determined prior to filling the separatory funnels via Karl Fischer analysis using a Mettler Toledo Model DL39 coulometric Karl Fischer instrument. The initial water content ranged from ~11 to 39 ppmV (~27 ppmV average) for the

266

measurements performed in this study. The required water volume for addition was determined based on the desired total target and initial water content.

The separatory funnel was outfitted with two thermocouples (T-type, $^1/_{32}$-in.-diameter), two capillary sampling lines (PEEK, $^1/_{16}$-in. outer diameter (o.d.), 0.020-in. inner diameter (i.d.)), and a single "fluid ejector" tube. The fluid ejector tube consisted of a $^5/_{16}$-in. i.d. Teflon tube that narrowed at the tip (via successively smaller tube segments) to $^1/_{16}$-in. i.d.. Collectively, the thermocouples, capillary sample lines, and fluid ejector were supported with a rubber stopper, and will be referred to as the "dip-tube-assembly". The thermocouples and capillary sample lines were positioned at the midpoint (fuel phase) and bottom (aqueous phase) of the funnel, while the fluid ejector was located ~1 in. from the bottom of the funnel. A schematic of the assembled apparatus, termed the Sub-Ambient Liquid Equilibrium Measurement System (SALEMS), is shown in Figure 3. Four SALEMS
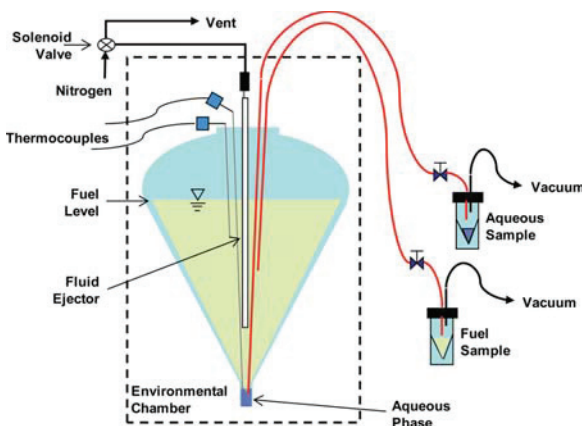
Figure 3. Schematic of SALEMS apparatus; dashed line indicates environmental chamber boundary.

were simultaneously used to increase sample throughput. The separatory funnels were placed into an environmental chamber (Cincinnati Sub-Zero, Model Z8) capable of precise temperature control within the range of −73 to +190 °C (±1 °C) with the capillary sample lines connected to external shutoff valves. During testing, the chamber was cooled at a constant ramp rate of −5 °C/h until the target temperature was achieved. A minimum equilibration time of 3 h was established prior to sample collection from both the fuel and aqueous phases. Nitrogen was slowly sparged (~1 mL/min) through both capillary sample lines to prevent fluid solidification within the transfer lines during cooling. Sample collection was performed by connecting these lines to 3.0 mL cylindroconical glass collection vials and drawing liquid via vacuum. The fuel phase was analyzed using the aforementioned GC/MS technique while the aqueous phase DiEGME concentration was determined using a temperature compensated digital refractometer (Reichert Model AR200) and DiEGME/water calibration curve (accuracy of ±10% of the absolute concentration).

Sufficient contacting of the fluid phases was achieved via fluid displacement from the Teflon ejector nozzle. Nitrogen was pulsed through the fluid ejector with a frequency of 1 pulse (0.5 s duration) per 10 s, with every sixth pulse having a duration of 1.0 s. The fluid ejector was vented to atmosphere between nitrogen pulses to allow fluid refill. The shorter duration pulses (0.5 s) expelled ~75% of the liquid volume in the ejector tube, which was sufficient to agitate the aqueous phase and the lower half of the separatory funnel. The longer duration (1.0 s) pulse was performed to completely expel the ejector liquid contents and thoroughly mix all fluid in the apparatus. This pulsing scheme provided adequate contacting of the fuel and aqueous phases, even at very low temperatures, to prevent solidification of the aqueous phase during cooling due to diffusion limitations of DiEGME. In addition, it minimized undesirable effects of other possible mixing

schemes, such as a complex setup for impeller mixing or loss of water and volatiles because of continuous dry nitrogen sparging.

■ RESULTS AND DISCUSSION

Partitioning studies were conducted over a wide range of initial water and DiEGME concentrations, and equilibrium temperature conditions that encompass conditions pertinent to actual aircraft operation. The ranges used for the three experimental variables are listed in Table 2. The test conditions were

Table 2. List of Experimental Variables Used for Partitioning Studies

experimental parameter	range
total water (ppmV)	130, 220, 300, and 560
initial fuel DiEGME concentration (ppmV)	300, 400, 500, 700, 1000, and 1500
temperature (°C)	20, 0, −10, −30, and −47

specified to provide adequate resolution for each temperature of interest. It was not practical to perform testing with total water concentrations below 130 ppmV and initial DiEGME levels below 300 ppmV since aqueous phase samples could not be reliably obtained for quantitation. The experimental results for the partitioning studies performed at each test temperature are shown in Tables 3−7. The reported data includes the total

Table 3. Equilibrium Data for Jet Fuel/Water/DiEGME Mixtures at 20 °C

[DiEGME]$_0$ (vol %)	[DiEGME]$_{fuel}$ (vol %)	[DiEGME]$_{aq}$ (vol %)	MB	PC
W_{tot} = 560 ppmV
0.149	0.115	43	1.05	370
0.102	0.075	35	1.03	470
0.100	0.070	36	1.01	510
0.070	0.051	30	1.06	580
0.071	0.050	31	1.05	610
0.051	0.032	25	1.00	800
0.042	0.027	22	1.01	840
0.032	0.019	18	0.99	990
0.019	0.013	13	1.10	1100
0.011	0.008	9	1.24	1100
0.011	0.007	9	1.23	1200
W_{tot} = 220 ppmV
0.146	0.125	49	1.00	400
0.099	0.084	40	1.00	480
0.072	0.061	33	1.00	530
0.050	0.047	26	1.09	560
0.041	0.035	19	1.00	560
0.032	0.025	19	0.95	750
0.022	0.018	18	1.03	1000
0.020	0.015	17	1.02	1100
0.010	0.008	11	1.07	1300
W_{tot} = 130 ppmV
0.148	0.139	52	1.03	370
0.099	0.090	43	1.01	480
0.070	0.067	29	1.04	430
0.050	0.048	28	1.07	590
0.041	0.040	24	1.05	600
0.031	0.030	22	1.07	740
0.022	0.020	19	1.05	920
0.010	0.009	11	1.01	1300

Table 4. Equilibrium Data for Jet Fuel/Water/DiEGME Mixtures at 0 °C

[DiEGME]$_0$ (vol %)	[DiEGME]$_{fuel}$ (vol %)	[DiEGME]$_{aq}$ (vol %)	MB	PC
	W_{tot} = 560 ppmV			
0.154	0.094	54	1.04	580
0.155	0.093	55	1.04	590
0.100	0.065	45	1.11	700
0.102	0.065	49	1.17	760
0.100	0.059	46	1.07	780
0.099	0.060	47	1.10	780
0.103	0.063	49	1.14	780
0.101	0.059	47	1.08	800
0.072	0.034	42	1.02	1200
0.051	0.022	36	1.06	1700
0.042	0.017	35	1.14	2100
0.032	0.012	31	1.17	2600
	W_{tot} = 220 ppmV			
0.146	0.120	62	1.07	520
0.149	0.122	59	1.04	490
0.101	0.088	56	1.15	640
0.099	0.082	53	1.08	650
0.101	0.084	54	1.09	650
0.099	0.084	55	1.11	650
0.071	0.058	49	1.10	840
0.052	0.040	43	1.09	1100
0.041	0.031	41	1.13	1300
0.031	0.023	38	1.16	1700
	W_{tot} = 130 ppmV			
0.150	0.108	63	0.87	590
0.097	0.088	53	1.06	600
0.099	0.091	56	1.09	620
0.052	0.062	48	1.41	770
0.070	0.066	52	1.14	790
0.051	0.047	47	1.14	1000
0.042	0.033	40	1.00	1200
0.042	0.037	42	1.11	1100
0.032	0.030	39	1.18	1300

Table 5. Equilibrium Data for Jet Fuel/Water/DiEGME Mixtures at −10 °C

[DiEGME]$_0$ (vol %)	[DiEGME]$_{fuel}$ (vol %)	[DiEGME]$_{aq}$ (vol %)	MB	PC
	W_{tot} = 560 ppmV			
0.156	0.079	59	1.02	750
0.156	0.080	59	1.03	740
0.144	0.077	59	1.10	770
0.145	0.076	60	1.09	780
0.104	0.054	52	1.11	970
0.103	0.052	52	1.08	990
0.094	0.047	51	1.13	1100
0.093	0.047	51	1.14	1100
0.071	0.028	45	1.05	1600
0.051	0.016	40	1.03	2500
0.042	0.013	37	1.10	3000
0.032	0.009	35	1.22	3700
	W_{tot} = 220 ppmV			
0.148	0.125	71	1.19	570
0.098	0.074	60	1.08	810
0.074	0.055	54	1.09	970
0.051	0.036	50	1.14	1400
0.041	0.025	45	1.05	1800
0.032	0.021	43	1.19	2100
	W_{tot} = 130 ppmV			
0.147	0.136	71	1.13	530
0.098	0.087	62	1.09	720
0.073	0.066	57	1.14	870
0.051	0.045	51	1.14	1100
0.043	0.034	47	1.06	1400

water concentration (W_{tot}), initial DiEGME concentration in the fuel ([DiEGME]$_0$), equilibrium DiEGME concentrations in the fuel ([DiEGME]$_{fuel}$) and aqueous ([DiEGME]$_{aq}$) phases, and the calculated mass balance (MB) and partition coefficient (PC). The mass balance (ratio of total DiEGME volume at equilibrium condition to the initial volume dosed) was calculated based on the initial volumes of fuel and total water, the final concentration of DiEGME in each phase, and assuming negligible water remained dissolved. The validity of the last assumption increases at higher total water contents and lower test temperatures. It should be reiterated that this study employed the use of realistic total water and FSII concentrations, which should improve the applicability of the data obtained. The experiments performed herein can be considered "single mixing events", since pure water (DiEGME-free) was added to the DiEGME/fuel mixture only once. In a fuel storage tank or aircraft, a water bottom previously exposed to FSII-treated fuel will already contain DiEGME, resulting in a lower overall quantity of additional DiEGME extracted into the aqueous phase to achieve equilibrium. During this study, there were specific measurements at the lowest test temperatures where the initial ratio of DiEGME/water employed was insufficient (i.e., too low) to prevent solidification of the aqueous phase. Since the primary objective was to characterize the FSII partitioning under equilibrium conditions, these data are not included in the subsequent discussion. However, this further demonstrates the necessity to ensure sufficient FSII is dosed into the fuel if the goal is to prevent solidification of free water throughout the complete operating temperature range.
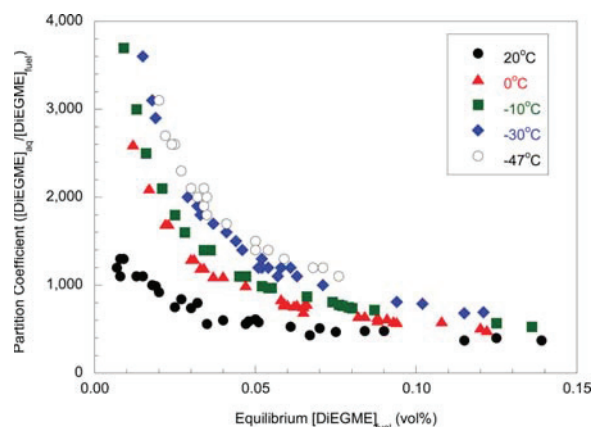
The calculated PC values as a function of temperature and the equilibrium concentration of DiEGME in the fuel phase are plotted in Figure 4. Comparison of the PC with respect to the equilibrium fuel concentration shows that partitioning at a constant temperature is independent of the initial DiEGME and water concentrations in the system, which is an important result with respect to application. It can be clearly observed that the PC is not constant (e.g., propensity of DiEGME to migrate from fuel to aqueous phase) and significantly increases with both decreasing temperature and DiEGME concentration. For example, the PC increases by a factor of ∼3 at the lowest equilibrium concentrations evaluated as the temperature is decreased from ambient to −10 °C, with a further increase at lower temperatures. This behavior is in contrast to the aforementioned partitioning studies, which reported a constant PC value (e.g., ideal behavior).[20] However, there is general agreement on the magnitude of the PC at ambient temperature and concentrations greater than ∼0.04% in the fuel with previous studies (relatively constant value of ∼350−500).[12,23] It should be reiterated that the reported PC values are those achieved at equilibrium with the final fuel concentration; the specific fuel and aqueous concentrations achieved during a single mixing event (and corresponding PC) are dependent on the initial FSII/water contents and temperature (see Tables 3−7).

**Table 6. Equilibrium Data for Jet Fuel/Water/DiEGME Mixtures at −30 °C**

[DiEGME]$_0$ (vol %)	[DiEGME]$_{fuel}$ (vol %)	[DiEGME]$_{aq}$ (vol %)	MB	PC
	W_{tot} = 560 ppmV			
0.152	0.057	65	1.07	1100
0.156	0.054	66	1.03	1200
0.103	0.033	58	1.08	1800
0.103	0.033	60	1.12	1800
0.071	0.019	54	1.21	2900
	W_{tot} = 300 ppmV			
0.101	0.052	65	1.07	1300
0.098	0.054	65	1.13	1200
0.069	0.033	60	1.12	1800
0.068	0.032	59	1.11	1900
	W_{tot} = 220 ppmV			
0.153	0.102	81	1.28	790
0.148	0.094	76	1.12	810
0.102	0.063	71	1.15	1100
0.097	0.061	71	1.18	1200
0.071	0.044	65	1.21	1500
0.070	0.037	61	1.04	1700
0.071	0.041	64	1.14	1600
0.051	0.029	56	1.12	2000
0.041	0.018	55	1.09	3100
0.032	0.015	53	1.24	3600
	W_{tot} = 130 ppmV			
0.150	0.121	84	1.25	690
0.148	0.115	78	1.09	680
0.101	0.071	73	1.05	1000
0.070	0.058	69	1.24	1200
0.071	0.051	62	1.03	1200

Table 7. Equilibrium Data for Jet Fuel/Water/DiEGME Mixtures at −47°C

[DiEGME]$_0$ (vol %)	[DiEGME]$_{fuel}$ (vol %)	[DiEGME]$_{aq}$ (vol %)	MB	PC
	W_{tot} = 300 ppmV			
0.079	0.035	64	1.13	1800
0.079	0.032	64	1.09	2000
0.070	0.025	66	1.19	2600
0.073	0.030	63	1.11	2100
0.060	0.024	63	1.27	2600
0.062	0.024	62	1.17	2600
0.049	0.020	61	1.38	3100
0.045	0.020	63	1.58	3100
	W_{tot} = 220 ppmV			
0.153	0.076	85	1.32	1100
0.102	0.050	75	1.14	1500
0.148	0.068	82	1.11	1200
0.148	0.071	84	1.28	1200
0.069	0.041	68	1.28	1700
0.069	0.034	64	1.06	1900
0.070	0.035	71	1.26	2000
0.068	0.034	71	1.28	2100
	W_{tot} = 130 ppmV			
0.101	0.059	78	1.06	1300
0.069	0.050	70	1.16	1400
0.070	0.054	77	1.39	1400
0.042	0.027	62	1.15	2300
0.032	0.022	59	1.28	2700

Figure 4. Partition coefficient (PC) of DiEGME as a function of temperature and equilibrium concentration of DiEGME in the fuel phase.

Comparison of the equilibrium [DiEGME]$_{aq}$, rather than the PC, as a function of [DiEGME]$_{fuel}$ (shown in Figure 5), is
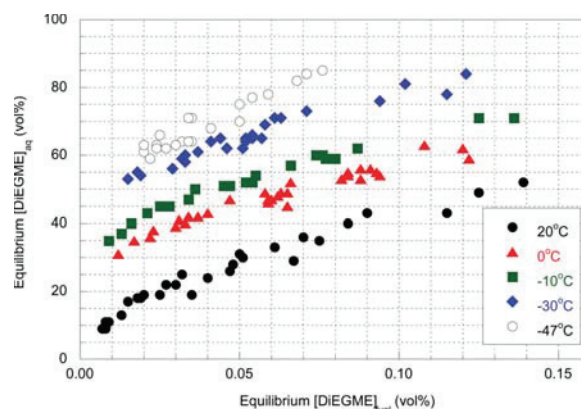
Figure 5. Equilibrium concentration of DiEGME in the aqueous phase as a function of the fuel phase concentration and temperature.

simpler to understand, with respect to ultimate application. For example, the aqueous phase concentrations at ambient temperature for fuel concentrations greater than 0.07% (current USAF minimum procurement limit) are consistent with those typically reported during sumping of aircraft and ground storage fuel tanks (i.e., 30% ≤ [DiEGME]$_{aq}$ ≤ 50%).[19] It can be clearly observed that for a constant [DiEGME]$_{fuel}$, the equilibrium aqueous phase concentration increases significantly as the temperature is reduced. This behavior is extremely favorable for potentially reducing the required FSII use concentration since the aqueous phase freeze point will be suppressed due to increased FSII partitioning. In fact, the aqueous phase equilibrium concentrations shown in Figure 5 have freeze points that are either comparable or below that for the respective temperature (see Figure 2), indicating that blockage of fuel flow by ice formation would not be a concern, regardless of the aircraft platform or mission profile.

The calculated mass balances (MB) for DiEGME shown in Tables 3−7 have an average value of 1.12 ± 0.10 (1σ). Although this indicates a considerable level of confidence in the experimental data, it is greater than desired. The variance of the

MBs can be affected by the accuracy of the analytical techniques employed, but random variance around 1.00 would be expected if the resulting values were not biased in some manner. Potential causes for the slight offset could be due to the methodology used for estimation. As previously discussed, mass balance calculations were performed using the total volumes of fuel (V_{fuel}), water (V_{water}), and DiEGME (V_{DiEGME}), and the measured equilibrium $[DiEGME]_{aq}$ and $[DiEGME]_{fuel}$. The V_{water} value used in the calculations was the total water content (free plus dissolved); this may overestimate the actual DiEGME volume in the aqueous phase, since a percentage of the water may remain dissolved, resulting in a MB value of >1.00. The same net effect would result if low water quantities were lost due to volatilization during mixing/sparging. Regardless of the cause, the partitioning data quantified herein represent the equilibrium achieved within this multicomponent system. Since the resulting equilibrium behavior at a constant temperature is independent of the initial DiEGME and water volumes (see Figures 4 and 5), the slight imbalances do not affect interpretation as would be the case when DiEGME is quantified in one phase and calculated in the other via closure of the mass balance.

Factors Affecting DiEGME Partitioning. Experimental results indicate that the ternary fuel/water/DiEGME system does not exhibit ideal solution behavior. This nonideality is due to the corresponding molecular interactions between DiEGME and water/fuel in each respective phase. Solubility characteristics are a relative means to infer the effect of temperature on the corresponding molecular interactions. Although some glycol ether/water systems exhibit a lower critical solution temperature (LCST) at which two-phase formation occurs, the LCST is typically at elevated temperatures (above ∼50 °C).[28−30] It has been proposed that increased molecular motion at higher temperatures is sufficient to disrupt hydrogen bonding interactions between the glycol ethers and water, resulting in more-prominent hydrophobic interactions.[30] The prevalence of hydrophilic/hydrophobic interactions in these solutions is further supported by measurements that show both the number and structure of the oxyalkylene group can affect the resulting LCST behavior.[29] For temperatures of interest to aircraft operation, water and DiEGME are infinitely miscible,[13,28] indicating hydrophilic interactions are sufficient to provide solution stability. With respect to the organic phase, DiEGME has a limited solubility in aviation fuel, which decreases with temperature. Chang and Krizovensky measured the solubility of DiEGME in JP-5 (chemically very similar to Jet A, Jet A-1, or JP-8) at temperatures of 15, 0, −18, and −51 °C, with volumetric DiEGME solubility limits of ∼2.0%, ∼1.5%, ∼1.0%, and ∼0.4%, respectively.[31] Stirling and Ripley measured the low-temperature solubility of DiEGME in a JP-5 and found a similar dependence.[32] Although this behavior indicates that lower temperature increases hydrophilic self-interactions of DiEGME, relative to DiEGME/fuel interactions, the solubility limits are greater than current procurement limits for aviation fuel.

The concentration of glycol ether can also influence the stability of the FSII/solvent complexes in each phase, and subsequently, the partitioning behavior. It is reasonable to assume that the concentration of DiEGME in the fuel (organic phase) remains sufficiently dilute. However, $[DiEGME]_{aq}$ can achieve high levels, as demonstrated in Tables 3−7 and Figure 5. The corresponding stability of the aqueous mixtures can be inferred by considering concentration-dependent property

behavior. Experimental measurements have been performed for the excess molar volume (V_M^E) and viscosity of DiEGME/water mixtures as a function of DiEGME mole fraction.[33] For measurements at 35 °C, the V_M^E value had a negative parabolic dependence with a minimum established between 0.20 to 0.40 mole fraction of DiEGME (i.e., ∼60−80% by volume). Fluid viscosity showed an opposite trend, increasing with addition of DiEGME to the aqueous phase. Both properties were highly sensitive to incremental changes of DiEGME concentration in the water-rich region (<0.20 mole fraction). The V_M^E behavior implies that each DiEGME molecule effectively interacts with ∼2−4 water molecules and that the hydrogen bonding interactions are maximized near 0.30 mole fraction DiEGME. The property dependences were primarily attributed to favorable association via intermolecular hydrogen bonding between DiEGME and water, with formation of a more compact lattice.[33] Establishment of favorable molecular interactions are also supported by calorimetric studies of the heats of mixing of binary aqueous mixtures of DiEGME or other comparable glycol ethers.[34,35] The heats of mixing were exothermic for all compositions studied, with a decrease in magnitude for increasing test temperature. This latter observation can be attributed to increased molecular motion, promoting more hydrophobic behavior of the solution. Additionally, exothermic behavior was observed for partial molar excess enthalpy calculations of aqueous mixtures with analogous glycol ethers.[30] For the concentration ranges typically pertinent to aircraft operation, it can be expected that the favorable interactions will continue to provide stabilization as DiEGME partitions into the aqueous phase.

The effect of hydrogen bonding on the equilibrium partitioning of DiEGME between the aqueous and fuel (e.g., organic) phases is further supported by experimental measurements made between 40 °C and 90 °C investigating the effect of organic solvent type and temperature on partitioning of an analogous glycol ether, propylene glycol *n*-propyl ether (PnP) ($C_3H_7-O-CH_2-CH(CH_3)-OH$).[30] The PnP studies showed that, at a constant temperature, the partitioning of DiEGME into the aqueous phase increased with decreasing organic solvent polarity. Additionally, the partitioning of PnP into the aqueous phase decreased with increasing temperature, which was attributed to glycol ether/water interactions becoming less attractive, because of the disruption of hydrogen bonding from enhanced molecular motion. Similar behavior with temperature has been observed for the partitioning of the surfactant dodecyl pentaethylene glycol ether between heptane and water.[36]

The partitioning behavior of glycol ether-type compounds between fuel and aqueous phases can also be considered from a thermodynamic perspective, employing the concepts of chemical potential and activity coefficients.[16,30,37,38] Dacre[38] provided a derivation for the dependence of the partitioning ratio (on a mole fraction basis) by initially considering the chemical potential of a FSII in each phase. The chemical potential of a solute in solution (μ_i) can be defined as

$$\mu_i = \mu_i^* + RT \ln(a_i) \qquad (2)$$

where μ_i^* and a_i are the chemical potential at a specified reference state and activity of the solute (i). The activity of component i can be defined as

$$a_i = \gamma_i x_i \qquad (3)$$

where γ_i is the activity coefficient and x_i is the mole fraction in the phase. The chemical potentials of DiEGME in the aqueous and fuel phases, respectively, can be expressed as

$$\mu_{D,\text{fuel}} = \mu_{D,\text{fuel}}^* + RT\ln(a_{D,\text{fuel}}) \tag{4}$$

and

$$\mu_{D,\text{aq}} = \mu_{D,\text{aq}}^* + RT\ln(a_{D,\text{aq}}) \tag{5}$$

For simplicity, the reference state within each phase can be selected to be identical as pure DiEGME. Equilibrium for a FSII will be established when the corresponding chemical potentials in each phase are equal:

$$\mu_{D,\text{fuel}} = \mu_{D,\text{aq}} \tag{6}$$

Since the reference states are selected to be identical, combining and rearranging eqs 4 and 5 results in

$$\frac{a_{D,\text{aq}}}{a_{D,\text{fuel}}} = 1 \tag{7}$$

Substituting eq 3 for the activity of DiEGME in each phase results in

$$\frac{x_{D,\text{aq}}}{x_{D,\text{fuel}}} = \frac{\gamma_{D,\text{fuel}}}{\gamma_{D,\text{aq}}} \tag{8}$$

where the left-side is the partition coefficient expressed in terms of mole fraction rather than volumetric concentration (see eq 1). Accordingly, insight regarding the behavior of DIEGME activity coefficient in the fuel and aqueous phases with varying temperature and concentration can further elucidate the causes for the observed partitioning behavior. The activity coefficients measured for several glycol ethers at infinite dilution in water were observed to increase with temperature, indicating less favorable interactions due to increased molecular motion allowing hydrophobic interactions to become more significant.[30] In contrast, calculated fuel phase activity coefficients were shown to decrease with increasing temperature, indicating more favorable solute/solvent interactions. Consistent behavior of increasing activity coefficient dependence with temperature for various aromatics, alcohols, ketones, and esters at infinite dilution in water were also reported, with exothermic mixing behavior for oxygenated compounds.[37]

Taylor considered the concentration dependence for the activity of DiEGME in aqueous mixtures as a potential method to describe the partitioning, surface tension and freeze point suppression behavior.[16] The role of hydrogen bonding in both the partitioning and the resulting physical properties was proposed and supported by several of the experimental trends. However, Flory–Huggins analysis of experimental water activity measurements resulted in a positive binary interaction parameter, indicating that DiEGME/water mixing is endothermic. This contrasts calculated binary interaction parameters for aqueous mixtures of other oxygenated compounds, such as ethylene glycol,[39] and the aforementioned measured exothermic mixing and negative V_M^E behavior for DiEGME/water mixtures.[33−35] Although the magnitude of the water activities reported by Taylor are believed to be inaccurate, a strong correlation between water activity and fuel properties, including freeze point suppression, most likely exists, which merits future study.

Implications of FSII Partitioning for Aircraft Applications. The propensity of DiEGME to migrate from the fuel to

the aqueous phase, as the temperature and concentration is reduced, is favorable for potential reduction of the required dose concentration while maintaining safe aircraft operability. Although the overall efficacy of the FSII will depend on multiple operational factors, such as fuel system design, hardware, and mission profile, estimation of the aqueous-phase DiEGME concentration can provide guidance regarding the minimum achievable level of protection for a specific initial DiEGME and water content. This can be accomplished via calculation of the overall mass balance of DiEGME within each phase following partitioning. The most conservative scenario is when any water present is initially DiEGME-free (which is inaccurate if the water has previously been contacted with FSII-treated fuel). Mass balance calculations were performed assuming 100 ppm free (in excess of dissolved) water with initial fuel concentrations of DiEGME of 0.04, 0.07, and 0.10 vol %. The highest DiEGME level is representative of the maximum procurement concentration in the JP-8 fuel specification. The mass balance relationships were overlaid with curve fits of the partitioning data from Figure 5; these comparisons are shown in Figure 6. The intersection point of
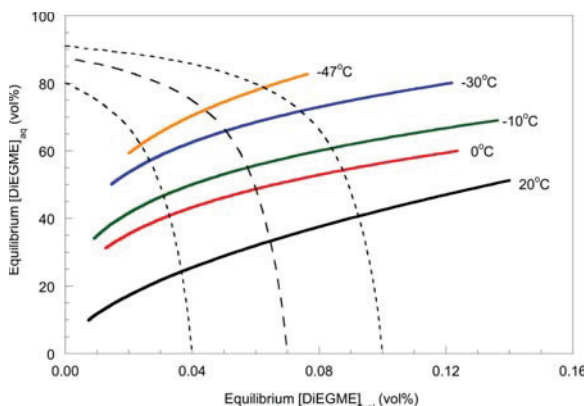
Figure 6. Phase equilibrium of DiEGME in water and fuel; curve fits of equilibrium data from this work (solid curves), and calculated mass balance with 100 ppmV free water as basis (dashed curves).

the mass balance and partitioning curves are the expected aqueous and fuel phase equilibrium concentrations at each temperature (assuming homogeneous mixing). For an initial fuel concentration of 0.10%, the calculated aqueous-phase equilibrium concentration at ambient temperature is consistent with the range typically reported in aircraft and fuel storage tanks (30%−50%). At the lowest test temperature, the aqueous phase equilibrium concentration is sufficient to prevent solidification with a significant residual DiEGME concentration in the fuel phase. This residual fuel phase DiEGME provides no immediate benefits to the system; however, should the fuel be exposed to additional free water, this excess DiEGME will subsequently partition into the aqueous phase and establish a new equilibrium. With initial fuel concentrations of 0.04 and 0.07%, the aqueous phase equilibrium concentrations achieve levels which have very low freeze points with lower residual amounts remaining in the fuel.

Although the partitioning propensity of FSII is favorable for reducing the required initial dose concentration, the potential for a further reduction in FSII concentration is also dependent on dynamic factors. These include time scales for fuel

271

temperature cool-down and contacting of fuel/water in the fuel system. In addition, the ability of FSII to prevent blockage due to ice formation in a flowing environment must be evaluated. A nonspecification, but desired, characteristic of FSII is the role as a biostat/biocide within bulk storage and aircraft fuel systems.[24,40−42] It has been shown that DiEGME can inhibit the growth of bio-organisms and films, which cause detrimental effects to fuel system operation. One potential concern with a reduced dose concentration of FSII is that this functionality would be diminished. Previous studies have demonstrated that, for selected laboratory organisms, aqueous phase concentrations as low as 10−15% will still provide equivalent bioefficacy to current levels.[40,42] As shown in Figure 5, aqueous phase concentrations equivalent or greater than these levels are expected to be achieved, even with fuel concentrations as low as 0.01%−0.02%, reducing the concern regarding a lack of bioefficacy with reduced FSII fuel dose levels.

SUMMARY

Improved understanding of the partitioning behavior of fuel system icing inhibitor (FSII) additive between fuel and aqueous phases, as a function of temperature and concentration, will significantly assist in determining conditions to ensure safe operability of aircraft. A novel experimental system was designed and used to quantify the equilibrium partitioning of the currently approved FSII (di-ethylene glycol monomethyl ether, DiEGME) under conditions relevant to actual aircraft fuel system operation. This included a temperature range from ambient conditions to −47 °C, and total water contents from 130 to 560 ppmV. The partitioning of DiEGME between fuel and aqueous phases exhibited nonideal solution behavior, with the equilibrium dependence being a strong function of temperature. For a constant temperature, the resulting phase equilibrium was independent of the initial FSII and total water concentrations, with a single equilibrium curve established. FSII partitioning increased with both decreasing temperature and decreasing FSII concentration in the fuel. This behavior is attributed to favorable hydrophilic interactions between the glycol ether and water and the effect of temperature and concentration on the chemical activity of FSII in each phase. For conditions expected during typical aircraft operation, fuel phase equilibrium concentrations greater than ∼0.02% are expected to be sufficient to prevent water solidification to temperatures below the specification freeze point of the fuel.

AUTHOR INFORMATION

Corresponding Author
*E-mail: matthew.dewitt@wpafb.af.mil.

Notes
The authors declare no competing financial interest.

ACKNOWLEDGMENTS

REFERENCES

(1) MIL-DTL-5624V. *Detail Specification: Turbine Fuel, Aviation, Grades JP-4 and JP-5.* Released July 11, 2013.

(2) MIL-DTL-83133F with AMENDMENT 1. *Detail Specification: Turbine Fuel, Aviation, Kerosene Type, JP-8 (NATO F-34), NATO F-35, and JP-8 + 100 (NATO F-37).* Released Sept. 14, 2012.

(3) Langer, G. *JP-4 Fuel System Icing*; Armour Research Foundation of Illinois Institute of Technology: Chicago, IL, 1960; Report No. ARF 3165-3/Wright Air Development Division (WADD) Technical Report 60-826.

(4) Martel, C. R. *Military Jet Fuels, 1944−1987*; Air Force Wright Aeronautical Laboratories: Wright-Patterson Air Force Base (WPAFB), OH, 1987; Report AFWAL-TR-2062.

(5) Edwards, T. Liquid Fuels and Propellants for Aerospace Propulsion: 1903−2003. *J. Propulsion Power* **2003**, *19* (6), 1089−1107.

(6) NAVAIR 00-80T-109. *NATOPS Aircraft Refueling Manual.* Released Aug. 1, 2011.

(7) USAF T.O. 42B-1-1. *Technical Manual: Quality Control of Fuels and Lubricants, change 1.* Released Nov. 19, 2012.

(8) Standard D1655-13a. *Standard Specification for Aviation Turbine Fuels.* Released Dec. 1, 2013.

(9) Aliband, A.; Lenz, D. W.; DuPois, J.; Allison, K.; Storhaug, V.; Stevenson, L. E.; Whitmer, T.; Cash, R.; Burns, D. Epoxy paint failure in B-52 fuel tanks Part I—Preliminary development of a model for the process. *Progr. Org. Coat.* **2006**, *56*, 285−296.

(10) Zabarnick, S.; Adams, R.; West, Z.; DeWitt, M. J.; Shafer, L.; Striebich, R.; Delaney, C. L.; Phelps, D. K. Compatibility of DiEGME and TriEGME Fuel System Icing Inhibitor additives with BMS 10-39 aircraft tank topcoat material. *Energy Fuels* **2010**, *24*, 2614−2627.

(11) Cummings, J. R. *Performance Evaluation of Potential Fuel System Icing Inhibitors in Aviation Jet Fuel Using the U.S. Navy Aircraft Fuel System Icing Simulator*; Naval Air Systems Command: Patuxent River, MD, 1997; Report NAVAIRWARCENAC-DIVTRENTON-LR-PPE-97-3.

(12) Krizovensky, J. M. Fuel System Icing Inhibitor: U.S. Navy Experience. Presented at *Fuel System Icing Inhibitor Workshop*; Patuxent River, MD, 2000.

(13) DeWitt, M. J.; Williams, T. F.; Shafer, L.; Striebich, R.; Riehl, L.; Delaney, C. Investigation of the effectiveness of DiEGME to suppress solidification of water in aircraft fuel systems. In *Proceedings of the 9th International Conference on Stability and Handling of Liquid Fuels*; Sitges, Spain, Sept. 18−22, 2005.

(14) Trohalaki, S.; Pachter, R. Modeling of fuel-system icing inhibitors. *Energy Fuels* **1999**, *13*, 992−998.

(15) Koop, T.; Luo, B.; Tsias, A.; Peter, T. Water activity as the determinant for homogeneous ice nucleation in aqueous solutions. *Nature* **2000**, *406*, 611−614.

(16) Taylor, S. E. Component interactions in jet fuels: Fuel system icing inhibitor additive. *Energy Fuels* **2008**, *22* (4), 2396−2404.

(17) Cordray, D. R.; Kaplan, L. R.; Woyciesjes, P. M.; Kozak, T. F. Solid−liquid phase diagram for ethylene glycol + water. *Fluid Phase Equilib.* **1996**, *117*, 146−152.

(18) Shaeffer, S. K. Loss of Fuel System Icing Inhibitor additive during fuel transport and storage. *Proceedings of the 10th International Conference on the Stability and Handling of Liquid Fuels*; Tucson, AZ, Oct. 7−11, 2007.

(19) DeWitt, M. J.; Zabarnick, S.; Shaeffer, S.; Williams, T. F.; West, Z.; Shafer, L.; Striebich, R.; Breitfield, S.; Adams, R.; Cook, R.; Delaney, C.; Phelps, D. K. Determination of minimum required Fuel System Icing Inhibitor (FSII) use and procurement limits for USAF aircraft. *Proceedings of the 11th International Conference on the Stability*

and Handling of Liquid Fuels; Prague, Czech Republic, Oct. 18−22, 2009.

(20) Netzel, D. A.; Gadberry, H. M. *Investigation of Anti-Icing Additives in JP-4 Fuel*; Midwest Research Institute, 1960; WADD Technical Report, pp 60−226.

(21) Orrell, L. *The Performance of Anti-Icing Additive in Aviation Fuel*; Shell Research Limited: Thornton Research Centre, 1966; Report K.166.

(22) Stirling, K. Q.; Ripley, D. L. *Partition Coefficients of Icing Inhibitors in JP-4 and JP-5 Jet Fuels*; ITT Research Institute: Bartlesville, OK, 1990. (Report prepared for U.S. Department of Energy and Naval Air Propulsion Center under Cooperative Agreement DE-FC22−83FE60149.)

(23) Grosjean, D. F. *Efforts to Advance Fuel-System Ice-Inhibitor (FSII) Technology*; Innovative Scientific Solutions, Inc.: Dayton, OH, 1998. (Report prepared for AFRL/PRSF.)

(24) DeWitt, M. J.; Williams, T. F.; Shafer, L.; Striebich, R.; Riehl, L.; Delaney, C. Determination of minimum required FSII dosage for use on USAF aircraft. *Proceedings of the 10th International Conference on the Stability and Handling of Liquid Fuels*; Tucson, AZ, Oct. 7−11, 2007.

(25) SAE. *Aerospace Information Report 790C—Considerations on ice formation in aircraft fuel systems*. Revised Aug. 1, 2006.

(26) SAE. *Aerospace Recommended Practice 1401B—(R) Aircraft fuel system and component icing test*. Revised June 1, 2012.

(27) DeWitt, M. J.; Cook, R., Shafer, L.; Zabarnick, S.; McCormick, C. *Evaluation of ASTM D5006 for Accuracy, Repeatability, and Reproducibility for Fuel System Icing Inhibitor (FSII) Concentrations <0.10% by Vol. and Varying Fuel Composition*; Air Force Research Laboratory: WPAFB, OH, 2012; AFRL Technical Report: AFRL-RQ-WP-TR-2013−0070.

(28) *Dow The Glycol Ethers Handbook*; Dow Chemical Company, 2001.

(29) Christensen, S. P.; Donate, F. A.; Frank, T. C.; LaTulip, R. J.; Wilson, L. C. Mutual solubility and lower critical solution temperature for water + glycol ether systems. *J. Chem. Eng. Data* **2005**, *50*, 869−877.

(30) Frank, T. C.; Donate, F. A.; Merenov, A. S.; Von Wald, G. A.; Alstad, B. J.; Green, C. W.; Thyne, T. C. Separation of glycol ethers and similar LCST-type hydrogen-bonding organics from aqueous solutions using distillation of liquid−liquid extraction. *Ind. Eng. Chem. Res.* **2007**, *46*, 3774−3786.

(31) Chang, P.; Krizovensky, J. M. *Fuel System Icing Inhibitor (FSII) Deterioration Use Limits Study*; Naval Air Systems Command: Patuxent River, MD, 2003; Report NAVAIRSYSCOM Report 445/03-009.

(32) Stirling, K. Q.; Ripley, D. L. *Equilibrium Solubility of Icing Inhibitors in JP-4 and JP-5 Jet Fuel*; ITT Research Institute: Bartlesville, OK, 1990; Report prepared for U.S. Department of Energy and Naval Air Propulsion Center under Cooperative Agreement DE-FC22-83FE60149.

(33) Pal, A.; Singh, Y. P. Excess molar volumes and viscosities for glycol ether-water solutions at the temperature of 308.15K: Ethylene Glycol Monomethyl, Diethylene Glycol Monomethyl, and Triethylene Glycol Monomethyl Ethers. *J. Chem. Eng. Data* **1996**, *41*, 425−427.

(34) Pathak, G.; Katti, S. S.; Kulkarni, S. B. Calorimetric studies of the heats of mixing of cellosolve−water systems. *Indian J. Chem.* **1970**, *8* (5), 357−361.

(35) Pathak, G.; Katti, S. S.; Kulkarni, S. B. Calorimetric studies of the heats of mixing of carbitol−water systems. *Indian J. Chem.* **1970**, *8* (5), 444−447.

(36) Aveyard, R.; Binks, B. P.; Clark, S.; Fletcher, P. D. I. Effects of temperature on the partitioning and adsorption of $C_{12}E_5$ in heptane−water mixtures. *J. Chem. Soc. Faraday Trans.* **1990**, *86* (18), 3111−3115.

(37) Atik, Z.; Gruber, D.; Krummen, M.; Gmehling, J. Measurement of activity coefficients at infinite dilution of benzene, toluene, ethanol, esters, ketones, and ethers at various temperatures in water using dilutor technique. *J. Chem. Eng. Data* **2004**, *49*, 1429−1432.

(38) Dacre, R. Some thoughts on the behaviour of Fuel System Icing Inhibitor. In *Newsletter of the International Association for Stability, Handling and Use of Liquid Fuels*, No. 33; 2005.

(39) Nagarajan, R.; Wang, C.-C. Theory of surfactant aggregation in water/ethylene glycol mixed solvents. *Langmuir* **2000**, *16*, 5242−5251.

(40) Hill, G. C.; Hill, E. C.; Collins, D. J.; Anderson, S. Investigation of the anti-microbial characteristics of Di-Ethylene Glycol Mono Methyl Ether (Di-EGME) in relation to its use ixntermittently and at sub-lethal concentrations. *Proceedings of the 9th International Conference on the Stability and Handling of Liquid Fuels*; Sitges, Spain, Sept. 18−22, 2005.

(41) Balster, L. M.; Vangsness, M. D.; Bowen, L. L.; Mueller, S. S.; Brown, L. M.; Strobel, E. M. *The effect of DiEGME on microbial contamination of jet fuel: A minimum concentration study*; Air Force Research Laboratory: WPAFB, OH, 2010; AFRL Technical Report AFRL-RZ-WP-TR-2010−2002.

(42) Ruiz, O.; Brown, N. Advances in microbial mitigation of aviation fuels: characterization of the antimicrobial activity of DiEGME in fuel by quantitative real-time PCR. In *Proceedings of the 12th International Conference on the Stability and Handling of Liquid Fuels*, Sarasota, FL, Oct. 16−20, 2011.

273

Appendix T. Hydrocarbon Group-Type Analysis of Petroleum-Derived and Synthetic Fuels Using Two-Dimensional Gas Chromatography

Hydrocarbon Group-Type Analysis of Petroleum-Derived and Synthetic Fuels Using Two-Dimensional Gas Chromatography

Richard C. Striebich,* Linda M. Shafer, Ryan K. Adams, Zachary J. West, Matthew J. DeWitt, and Steven Zabarnick

University of Dayton Research Institute (UDRI), 300 College Park, Dayton, Ohio 45469-0043, United States

ABSTRACT: A group-type analysis of hydrocarbons in a complex jet fuel may be more useful than attempting to analyze every component because the latter inevitably leaves a large portion of the fuel unidentified. While it may be difficult to accurately determine the identity of a particular compound, that compound can often be classified as belonging to a group or compound class because of its chromatographic retention and mass spectral properties. Compound class quantitation is often capable of relating compositional information to fuel properties. Two-dimensional gas chromatography (GC × GC) is a technique capable of providing this group-type separation and quantitation in jet fuels. This technique was used to examine a large set of fuels (Jet A, Jet A-1, JP-5, and JP-8, primarily) from petroleum sources and non-petroleum alternative sources, such as synthetic paraffinic kerosene (SPK). By comparing results from GC × GC analysis to established techniques and model compound studies, we have found that the accuracy of GC × GC for group-type analysis is excellent. Quantitation of group types for alternative fuel sources were also investigated and compared to conventional techniques. The possible uses and applications of group-type measurements using GC × GC for fuels and fuel-related materials are discussed.

1. INTRODUCTION

1.1. Petroleum-Derived and Synthetic Jet Fuels. The use of synthetic fuels is becoming more widespread with the desire for energy independence and the threat of unstable costs. The U.S. Air Force has been investigating the use of emerging synthetic fuels since the early 2000s.[1] Fischer–Tropsch (FT) and other hydrocarbon processes can be used to create synthesized paraffinic kerosenes (SPKs) from sources such as coal, biomass, and natural gas, which can be blended to a maximum of 50% with conventional petroleum-derived sources. These mixtures can then be used as replacements for the current military jet fuels, such as JP-8. Other sources of hydrocarbons have also been produced for blending into current fuels to create a semi-synthetic hydrocarbon, which could meet the specification established for SPKs, ASTM D7566.[2] These other sources have recently included animal fats, vegetable oils, and algae, all processed and classified as hydroprocessed esters and fatty acids (HEFAs).[3]

FT-SPK and HEFA-SPK products consist mainly of paraffins (normal and/or iso-) and cycloparaffins and generally lack a significant concentration of aromatics. ASTM D7566 describes the specification of these fluids before being blended into conventional fuels. Currently, the D7566 specification calls for limited aromatic levels (≤0.5% by mass) and low cycloparaffin content (≤15 mass %). To characterize these fuels as well as the mixtures that are produced when the SPKs are blended with petroleum fuels, a dependable group-type analysis technique is needed, which quantifies the major hydrocarbon types. Particularly, it is important to be able to separate the compound classes accurately at low levels of aromatics and cycloparaffins.

1.2. Hydrocarbon Types and Their Properties in Jet Fuel. Jet fuel is mainly composed of normal paraffins, isoparaffins, cycloparaffins (primarily single and double ring), alkylbenzenes, indans and tetralins, naphthalene, and alkylnaph-thalenes. All of these hydrocarbon group types provide particular properties to a fuel. For example, normal paraffins are important because of their energy content and their effect on the fuel freezing point. Isoparaffins have the same chemical formulas as their *n*-paraffin counterparts, but because of shape irregularities of branching, they have much lower freezing points. The branching provided by isoparaffins may be an important factor in cetane number, a measure of combustion stability, similar to knocking tendency in gasoline engines. Cycloparaffins have lower freezing points and higher densities than normal paraffins and isoparaffins of the same carbon number. Substituted, single-ring aromatics (alkylbenzenes) impart energy density per unit volume and affect elastomer (O-ring) swelling, both of which are necessary for fuel system integrity. Naphthalene, alkylnaph-thalenes, and indans and tetralins are multi-ring aromatics, which are generally thought to have an adverse effect on combustion by contributing to soot formation. Each hydrocarbon class, containing potentially tens or hundreds of individual chemical compounds, provides some contribution to the properties of a fuel.

1.3. Hydrocarbon Group-Type Separations. It is tedious to conduct complete analyses of aviation fuel because petroleum-based aviation fuels may contain 1000 or more components (Figure 1a).[4] Identification of each individual component is difficult and often unnecessary, because fuel component classes (not individual compounds) tend to impart chemical or physical properties. The use of "group-type" separations gives a more complete picture of the chemical makeup of the fuel and is often preferred in the sense that it is easier to describe and document from a chemical perspective.
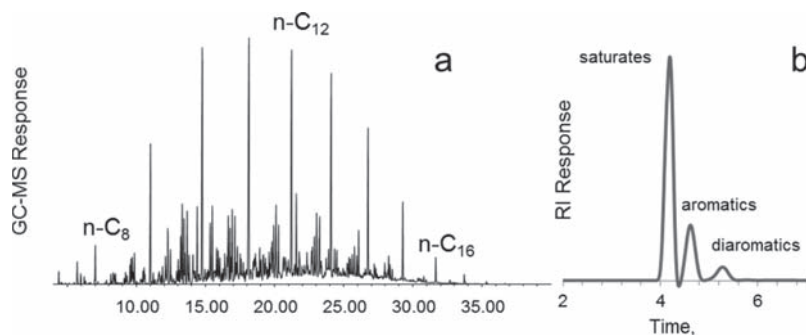
Figure 1. (a) Jet-A sample analyzed by GC−MS. Each peak represents at least one compound. (b) Group-type HPLC separation of saturates, aromatics, and diaromatics for a similar fuel with RI detector.

Figure 1b[4] shows an example chromatogram of a simple group-type separation of fuel components by high-performance liquid chromatography (HPLC), containing three major peaks eluting from a polarity separation of the whole fuel: saturates, single-ring aromatics, and diaromatics. This normal-phase separation is the basis for one of the class separations discussed here: hydrocarbon type by mass spectrometry. Hydrocarbon type by mass spectrometry, as practiced in our laboratory, is a modified version of ASTM D2425.[5] The basis of this technique is to conduct the same separation shown in Figure 1b, physically collect the saturates and total aromatics in separate fractions, and then separate each fraction based on volatility using gas chromatography−mass spectrometry (GC−MS). The second technique is GC × GC, which is a two-dimensional gas chromatographic separation (the first separation based on volatility and the second separation based on polarity).[6−9]

1.3.1. Hydrocarbon Type by Mass Spectrometry (ASTM D2425). ASTM D2425[5] was developed for middle distillates having a boiling range of 204−343 °C (5−95% recovered). In this technique, hydrocarbon samples are pre-separated as saturate and aromatic fractions by ASTM method D2549,[10] which is a glass-column separation that also measures the percentages of saturates and aromatics. In the modified version of the method employed here, ASTM D6379,[11] a HPLC technique was used to quantify the saturate and aromatic fractions. These fractions were also separated by HPLC and collected for mass spectral analysis by GC−MS. While no GC separation is required by the ASTM D2425 method, it was used here for convenience of sample introduction into the mass spectrometer and increased confidence in the accuracy of the HPLC separation. The mass spectral information obtained for each fraction was summed over the length of the chromatographic analysis.

Because compounds in the same class fragment similarly, ion responses tend to be similar in a compound class. These summed ion responses determine the concentration of hydrocarbon types. Interferences exist, however, and empirical relationships provided in method D2425 adjust for many of the major interferences. These calculated adjustments are based on analyses of petroleum-based fuels, which have ion responses based on higher aromatic and (perhaps) higher cycloparaffin levels, and may be less valid for alternative fuels, which may contain highly branched isoparaffins. The classified ions are summed, and their responses are normalized to the aromatic and saturate fraction percentages obtained from the saturate/aromatic group separation (D6379 in our laboratory). Results for ASTM D2425 are reported for the hydrocarbon type categories listed in Table 1. It is unclear whether the empirical

**Table 1. Categories of Hydrocarbon Type Analysis by ASTM D2425**

compound classes	
paraffins	indenes (C_nH_{2n-10})
monocycloparaffins (non-condensed)	naphthalenes
dicycloparaffins (condensed)	acenaphthenes
tricycloparaffins (condensed)	acenaphthylenes
alkylbenzenes	tricyclic aromatics
indans and tetralins	

relationships used in this method are appropriate for new, alternative fuels (non-petroleum), even though they may be of similar boiling range. In addition, this technique can be tedious, labor-intensive, and equipment-prohibitive, using four analytical separations (two HPLC and two GC) with three different detectors (refractive index detector, ultraviolet detector, and mass selective detector) and a fraction collector.

1.3.2. Two-Dimensional Gas Chromatography (GC × GC). GC × GC is well-described previously.[6−9,12] This technique is performed using either (1) thermal modulation (cooling to trap and then heating to release) or (2) flow modulation.[13] In either case, a primary column separation occurs, followed by a repeated modulation of a narrow zone onto a secondary column. The separation from this shorter column occurs fast enough to keep up with the primary column separation. The result is a two-dimensional separation with zones containing a retention time having both primary column and secondary column coordinates and response in the z axis. This response is measured with a traditional chromatographic detector, such as a flame ionization detector (FID), a mass selective detector (MSD), or both.

A popular arrangement of GC × GC is to have the primary column as nonpolar and the secondary column as polar; the resulting separation is mostly a function of volatility on the primary (x) axis and a function of polarity on the secondary (y) axis.[7] Thus, hydrocarbon group types are separated as shown in the example of a GC × GC output (Figure 2). Each of the group types are contained inside the regions shown. By summing the responses in these regions and normalizing based on carbon number to the total response, hydrocarbon type concentrations (weight percent) can be calculated.

The objective of the work described in this contribution is to examine, evaluate, and compare the use of ASTM D2425 and GC × GC for performing accurate analyses of hydrocarbon group-type separations of jet fuels, from both petroleum and synthetic sources.
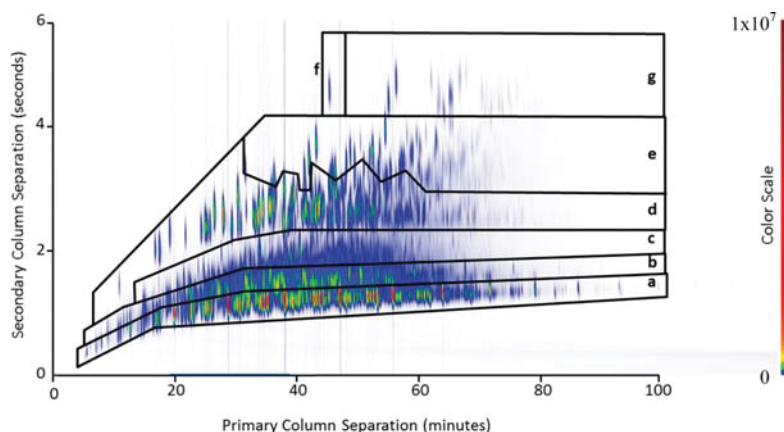
Figure 2. Example GC × GC chromatogram (FID detection) of a jet fuel with the primary axis separation by a nonpolar column and the secondary axis separation by a polar column. Section identifications: (a) *n*- and isoparaffins, (b) monocycloparaffins, (c) dicycloparaffins, (d) alkylbenzenes, (e) indans and tetralins, (f) naphthalene, and (g) alkylnaphthalenes. Response is in arbitrary volume units.

2. EXPERIMENTAL SECTION

2.1. ASTM D2425. As mentioned previously, quantitation of saturate and aromatic fractions was performed using a HPLC technique (ASTM D6379) with conditions described in Table 2. Saturate and

Table 2. Conditions for HPLC and GC−MS Separations in ASTM D2425

HPLC	Agilent 1100
column	cyano column (4.6 × 150 mm)
mobile phase	hexane (normal phase)
injection	1:50 dilution, 20 μL injection (50 μL for fraction collection)
saturate/aromatic quantitation detector	refractive index detection
cut point detector	UV−vis diode array detector
fraction collector	Gilson model FC203B
GC−MS	Agilent 6890-5973, splitless injection, 1 μL
GC column	DB5-MS, 0.25 mm inner diameter, 0.25 μm
program	40 °C (3) to 280 °C (5) at 10 °C/min

aromatic fractions were separated via HPLC with ultraviolet−visible (UV−vis) detection and were collected with a Gilson fraction collector.

These fractions were examined for hydrocarbon type analysis using an Agilent 6890-5973 GC−MS system. Mass spectrometry results were then processed using routines that summed ion responses[14] and reported results according to the D2425 method.

2.2. GC × GC. This technique was conducted using an Agilent 5975 GC−MS system equipped with capillary flow technology (CFT) flow modulation. A 20 m, DB-5MS, 0.18 mm inner diameter primary column and a 5 m, DB-17MS, 0.25 mm inner diameter secondary column were used. A programming rate of 1.5 °C/min was used to obtain the primary separation, and a 6 s modulation time was chosen. Data were evaluated using GC Image software (Zoex, version 2.2b0). Both FID and MS data were taken simultaneously, using post-column splitting and short transfer lines to each detector. The primary column flow rate used was 0.4 mL/min, and the secondary column flow was 36 mL/min. This high flow through the secondary column allowed peaks from the polar column to be relatively narrow compared to other flows examined. A template was developed for sample evaluation by close examination of MS results and subsequent translation to the co-generated FID file. These templates or two-dimensional boundaries (Figure 2) included the following hydrocarbon classes: paraffins (isoparaffins and normal paraffins), monocycloparaffins, dicycloparaffins, alkylbenzenes, indans and tetralins, naphthalene, and alkylnaphthalenes. Quantitation of classes was performed by the total FID response of the compounds in each hydrocarbon class, because FID has been shown to respond

Table 3. Mixtures and Fuel Samples Evaluated by Hydrocarbon Type Analysis

|		Model Mixtures		
mixture class	components	description	range (wt %)	source
paraffins	7	*n*-C_9−*n*-C_{15}	13−32[a]	Restek PN30713
isoparaffins	20	C_8−C_{11} isoparaffins	13−32[a]	Restek PN30715
cycloparaffins	21	C_9−C_{10} cycloparaffins	6−16	Restek PN30719
alkylbenzenes	38	benzene−C_6-alkylbenzene	0−27	Restek PN30717
indans/tetralins	3	tetralin, indan, and indene	0−13	Sigma-Aldrich
naphthalenes	3	naphthalene and C_1- and C_2-alkylnaphthalenes	0−6	Sigma-Aldrich
		Petroleum-Derived Fuel Sets		
name	number of fuels	description		source
world survey	54	JP-8 (10), Jet A (13), Jet A-1 (27), JP-5 (2), synthetic Jet A-1 (1), semi-synthetic Jet A-1 (1)		Air Force, Navy, airports
specialty set	8	JP-8, Jet A, Jet A-1, JP-5, JP-7, F-76 (diesel), RP-1, RP-2		Air Force
		Non-petroleum (Synthetic) Fuel Sets		
name	number of fuels	description		source
USAF samples	8	FT-SPK, HEFA-SPK, others		Air Force, alternate fuel producers

[a]Isoparaffins + *n*-paraffins.

277

consistently by the number of carbons for a wide range of hydrocarbons.[15]

2.3. Mixtures Investigated. Model compound mixtures were purchased for their complexity and documented concentrations (Table 3). Together, they represent a mixture with 118 unique, quantitative components, similar to JP-8 or Jet-A. Military fuels (JP-8, JP-5, etc.), commercial fuels (Jet-A and Jet A-1), and alternative (non-petroleum) jet fuels were also analyzed using both ASTM D2425 and GC × GC. These mixtures are also provided in Table 3.

3. RESULTS AND DISCUSSION

3.1. Model Mixture Studies. The accuracy of both ASTM D2425 and GC × GC is most readily evaluated using model mixtures. ASTM D2425 had been evaluated in previous work using hydrocarbons with 1−5 compounds per group type.[6] This work showed that ASTM D2425 successfully predicted the concentration of hydrocarbon group types in model mixtures.

GC × GC analysis of model mixtures was evaluated in this current work, using complex mixtures available from Restek. Table 3 shows the large number of chemicals in these mixtures from 6 different hydrocarbon groups. The 6 hydrocarbon groups were blended together in 12 different mixtures to provide a wide range of concentrations. These available mixtures simulated gasoline components and contained some components in the C_5-C_7 region that are not typically in middle distillate jet fuels in any significant concentrations. The GC × GC configuration used here (without cryogenic oven temperatures) could not separate paraffins from cycloparaffins in the C_5-C_7 range; therefore, these components were not included in the calculations. Figure 3
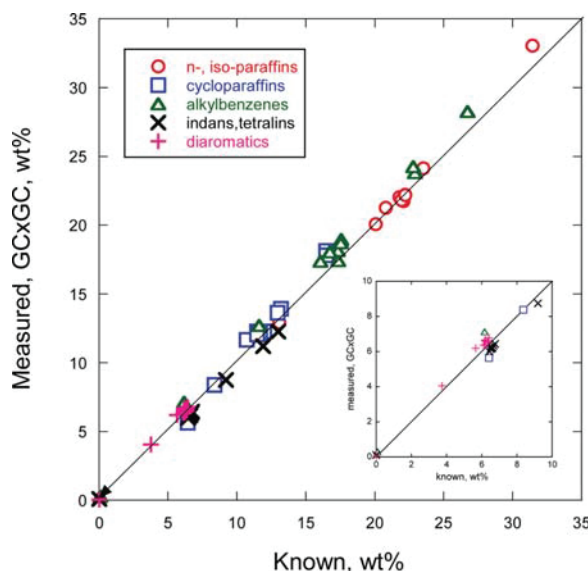
Figure 3. GC × GC results for 92 different chemical components blended into 12 different mixtures reflecting jet fuel ranges of hydrocarbon group types.

shows the comparison of actual versus measured results using GC × GC. There were some slight biases between GC × GC predictions and known levels of some group types. Figure 4 shows the relative errors of the compound classes as a function of the mean. Generally, the deviation from known results was less than 10% relative to the known concentration. Indans and tetralins, as a class, showed a slight negative bias of −5%, while the alkylnaphthalenes showed a corresponding positive bias of
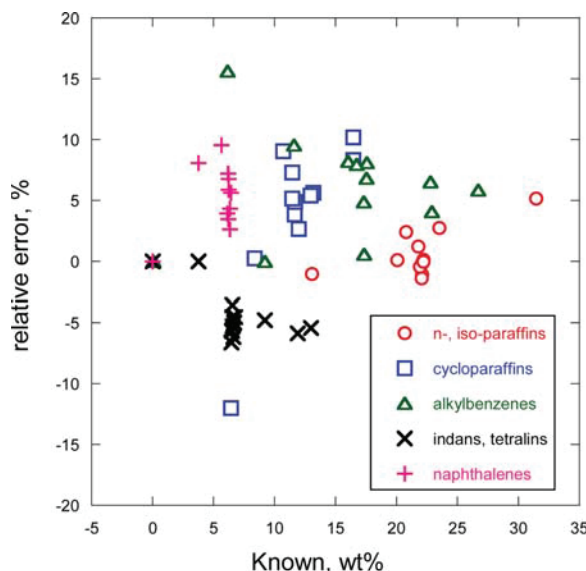
Figure 4. Relative error versus compound class for the 12 model mixtures examined using GC × GC.

about +5%. These two classes are adjacent to each other in the chromatographic separation; therefore, a slight consistent deviation may represent an impurity or a slight misidentification of a particular compound. Cycloparaffins were slightly over-predicted (less than 10% relative to known values), probably because of normal paraffinic and isoparaffinic peaks, which may have been misidentified. Overall, however, the agreement between predicted and actual levels of compound classes is excellent. Both ASTM D2425 and GC × GC successfully predict the concentration of group types from known mixtures.

The linearity of the plot in Figure 3 shows that the FID is responding quantitatively to the mass of the carbon in the compounds being detected without regard to compound class. This observation is consistent with other studies, which have examined the use of FIDs for different compound types.[15] These studies show that FID response factors (in the great majority of hydrocarbon compounds) are directly related to the weight percentage of carbon in each compound in a mixture and not directly related to the weight percentage of each compound in the mixture. Consequently, the concentration of each compound must be calculated from the weight percentage of carbon that is obtained from the FID response.

Precision for the two methods was measured through replicate analyses of jet fuel samples. The measurements indicate that statistical deviation because of the sampling, injection, GC × GC separation, detection, and quantitation is ≤2.1% for the general types of hydrocarbons in jet fuel (Table 4). This table shows the mean and standard deviation values (expressed in volume percentage) for an $n = 4$ sampling of a JP-8 fuel analyzed by both GC × GC and D2425 at four different points in time that were a minimum of 6 months apart. Assuming that real world, complex jet fuels would show higher standard deviations from replicate measurements than standard mixtures, any error bars for the data in Figure 3 would generally be smaller than the symbols used in the figure.

3.2. GC × GC Results for Middle Distillate Jet Fuels. The modified ASTM D2425 method was used as a reference technique for comparison to GC × GC measurements for

Table 4. Replicate Analysis of Fuel for GC × GC and D2425 Hydrocarbon Class Determination

	GC × GC (vol %; n = 4)		
	mean	standard deviation	RSD (%)
alkylbenzenes	12.9	0.20	1.6
naphthalene and alkylnaphthalenes	1.23	0.02	2.0
indans and tetralins	5.37	0.07	1.3
cycloparaffins	25.1	0.67	1.2
paraffins and isoparaffins	55.3	0.53	2.1
	D2425 (vol %; n = 4)[5]		
	mean	standard deviation	RSD (%)
alkylbenzenes	11.9	0.2	1.7
naphthalene and alkylnaphthalenes	1.3	0.1	8.8
indans and tetralins	5.6	0.6	10.1
cycloparaffins	27	1.3	4.7
paraffins and isoparaffins	54	1.3	2.4

hydrocarbon type analysis applied to a variety of jet fuel petroleum samples (along with one synthetic and one semi-synthetic fuel) collected during a worldwide survey.[16] Because the first part of the D2425 analysis employed here was to measure aromatic content using ASTM D6379, results from GC × GC and D6379 are compared in Figure 5 for the 54 fuels available. The methods are in excellent agreement for nearly every fuel tested. Plots for the more specific hydrocarbon classes (paraffins, alkylbenzenes, cycloparaffins, and indans/tetralins) are shown in Figure 6.

The agreement between ASTM D6379 and GC × GC for saturate and aromatic contents is very acceptable. The complete baseline resolution of saturates and aromatics in D6379 using HPLC (see Figure 1b) makes quantitation for this measurement very accurate. The refractive index (RI) detector used for D6379 is very linear for measuring aromatic compounds. GC × GC also shows reasonable chromatographic separation between these two major classes (Figure 2), which is reflected in the ability to accurately quantify the responses for each class. GC × GC is typically quantified in weight percent, which is calculated using FID response for mixtures with low heteroatomic content, whereas ASTM D6379 is often quantified in volume percent to evaluate against fuel specifications. To compare the two techniques, class densities were calculated from individual compound densities to convert GC × GC results from weight

percent to volume percent. These class densities were estimated from the available densities of one or more compounds from the class.

Figure 6 also shows good agreement between the two techniques for the more difficult separations within the saturate or aromatic compound classes. Paraffins and cycloparaffins share similar fragmentation ions by mass spectrometry; therefore, they are more reliant on the empirical corrections in ASTM D2425, which were developed for middle distillate fuels. In the situation where highly branched isoparaffins are present (e.g., the synthetic and semi-synthetic fuels), ion ratios that are used to calculate concentrations by D2425 are very similar to those for higher concentrations of cycloparaffins. Consequently, there may be some misclassification of these two groups, especially if highly branched isoparaffins are present in greater amounts. We have observed some instances where, for fuels containing highly branched isoparaffins, the concentration of cycloparaffins by D2425 may be overestimated in comparison to GC × GC cycloparaffin content. This situation may exist for two of the fuels in Figure 6, marked "A" and "B" on the "paraffins" and "cycloparaffins" plots, where the cycloparaffins are significantly higher by D2425 than those by GC × GC. More work is anticipated to verify these initial observations, and more discussion follows for synthetic fuel measurements. As for the GC × GC separation between the chromatographically adjacent monocycloparaffins and isoparaffins, it is not ideal, because the polarity differences between these two groups are small. Despite these difficulties, both techniques are in good agreement with each other for a wide range of petroleum-derived jet fuel samples.

Results initially reported for indans and tetralins using GC × GC[6] were re-examined for these fuels. New identifications of indans and tetralins were made, which affected the results for both indans/tetralins and alkylbenzenes, improving both. These updated results are shown in Figure 6.

Table 5 summarizes the hydrocarbon type results of the world survey fuels by fuel type for both GC × GC and ASTM D2425. This table is not a direct comparison of GC × GC to ASTM D2425, because it compares averages of different JP-8, Jet-A, Jet A-1, and JP-5 fuels. The data give a snapshot view of the general hydrocarbon composition of an average JP-8 or other petroleum fuel, as measured by both techniques. It is important to note that the GC × GC technique presented here does not adequately measure indenes (C_nH_{2n-10}) or some of the aromatics that are not typically present in jet fuel (acenaphthenes, acenaphthalenes,
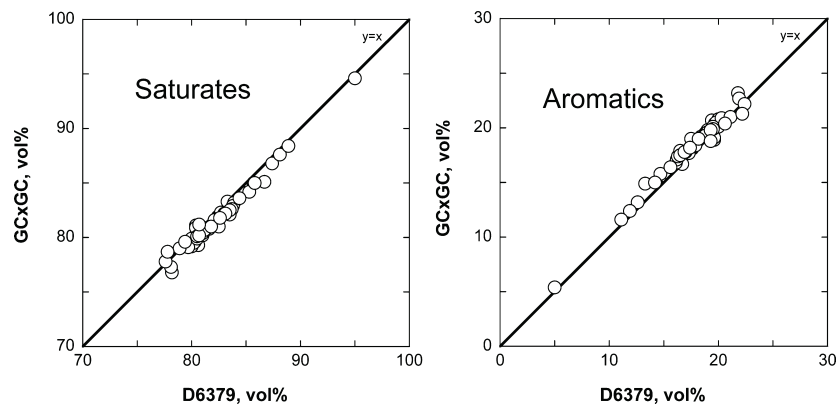
Figure 5. Comparison of saturates and aromatics by GC × GC to measurements made by ASTM D6379, a HPLC-based method.
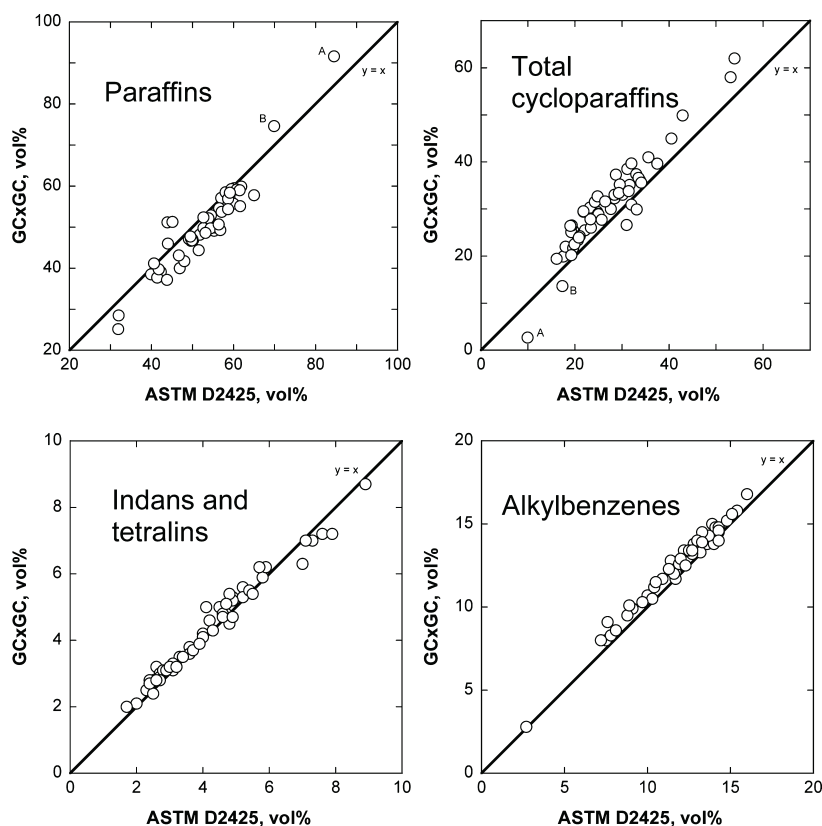
Figure 6. JP-8, Jet A-1, JP-5, and Jet A sample hydrocarbon type analysis conducted by GC × GC and compared to ASTM D2425. Data points labeled "A" and "B" in the paraffins and cycloparaffins plot represent a synthetic fuel (A) and a 50:50 synthetic fuel/petroleum fuel blend (B).

Table 5. Average Measured Hydrocarbon Type Compositions of Samples by Fuel Type[6][a]

	JP-8 ($n = 10$)	Jet A ($n = 13$)	Jet A-1 ($n = 28$)	JP-5 ($n = 2$)	JP-8 ($n = 10$)	Jet A ($n = 13$)	Jet A-1 ($n = 28$)	JP-5 ($n = 2$)
		D2425 (vol %)				GC × GC (vol %)		
paraffins	52	46	48	41	52.2	45.8	50.0	38.8
total cycloparaffins	29	35	34	39	28.7	35.6	31.4	41.4
alkylbenzenes	12.6	10.9	12.6	10.4	13.2	11.6	13.2	11.0
indans and tetralins	4.3	4.6	4.0	6.0	4.3	4.9	4.1	6.2
indenes C_nH_{2n-10}	<0.3	0.4	<0.3	0.6	ND[b]	ND	ND	ND
naphthalene	<0.3	<0.3	<0.3	0.3	c	c	c	c
naphthalenes	1.3	1.8	1.1	2.2	1.6	2.0	1.4	2.6
acenaphthenes	<0.3	<0.3	<0.3	<0.3	ND	ND	ND	ND
acenaphthylenes	<0.3	<0.3	<0.3	<0.3	ND	ND	ND	ND
tricyclic aromatics	<0.3	<0.3	<0.3	<0.3	ND	ND	ND	ND
total	100	100	100	100	100	100	100	100
D6379 HPLC (vol %)						GC × GC (vol %)		
monoaromatics	17.0	15.9	16.8	17.1	17.5	16.5	17.3	17.2
diaromatics	1.5	2.2	1.3	2.7	1.6	2.2	1.4	2.6
total aromatics	18.5	17.9	18.0	19.8	19.1	18.6	18.6	19.9
total saturates	81.5	82.1	82.0	80.2	80.9	81.4	81.4	80.2

[a]n = number of fuels averaged. [b]ND = not determined. [c]Naphthalene is included in naphthalenes for GC × GC.

and tricycloaromatics). The mass spectrometry technique of D2425 is capable of this measurement because of the unique masses of these compounds. GC × GC is capable of separating these compounds; however, because they are almost never significantly present in petroleum or synthetic jet fuels, it is not demonstrated here. These compounds may be added to analysis schemes in GC × GC should they be present in particular

mixtures. The results shown in Table 5 are different from those previously reported[6] as a result of improvements in the GC × GC method because initial results were obtained, particularly with regard to indan and tetralin concentrations.

3.3. Hydrocarbon Type Analysis for Alternative Fuels with Low-Level Cycloparaffins. Even though traditional petroleum jet fuels can contain large amounts of cycloparaffins
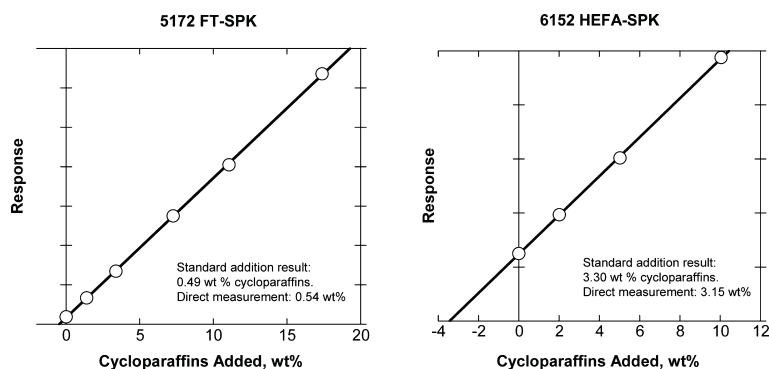
Figure 7. Standard addition experiment for alternative fuels showing low-level cycloparaffin measurement.
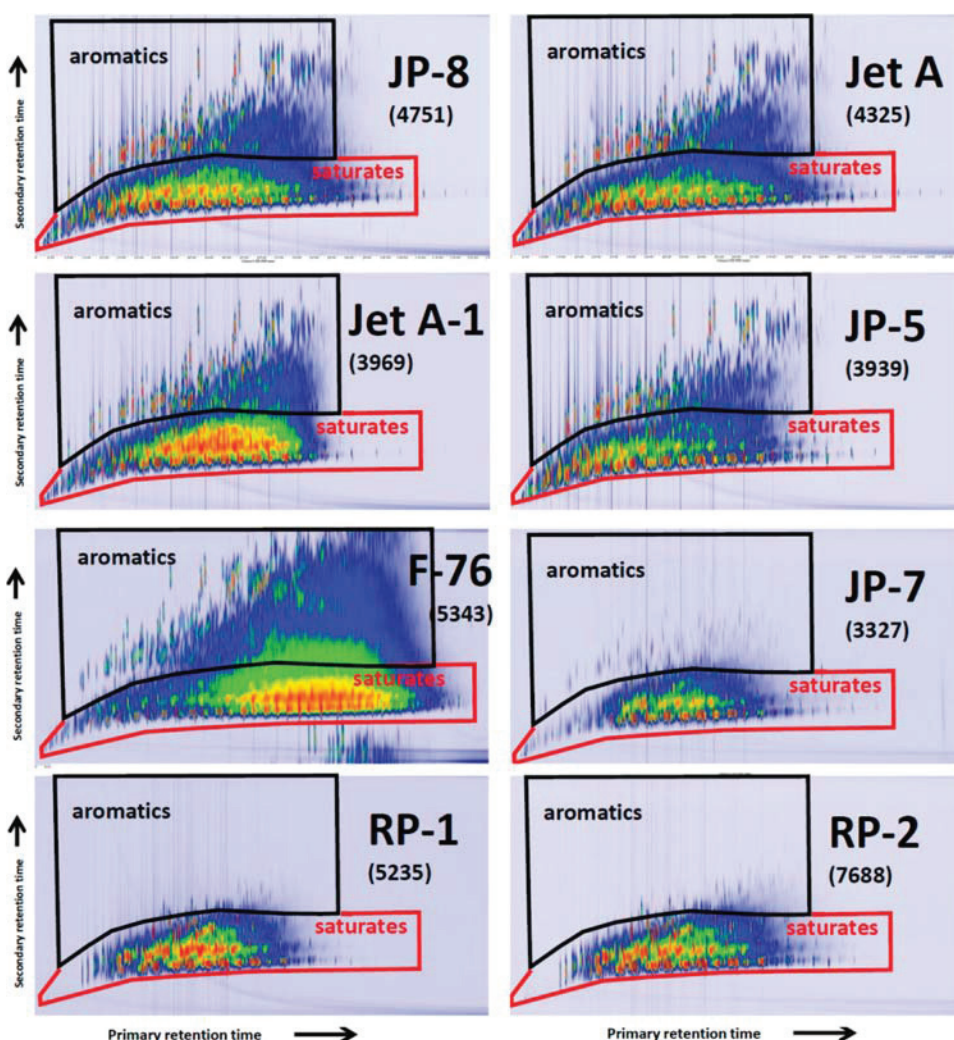

Figure 8. Petroleum-derived military and commercial fuels.

(about 20−50%), SPK blend stocks must contain less than or equal to 15 wt % total cycloparaffins by specification.[2] Figure 6 shows that there are substantial differences in the cycloparaffin concentration from D2425 and GC × GC for highly branched isoparaffinic fuels. In addition, Figure 2 shows that, for GC × GC,

the cycloparaffin region is located very near the isoparaffins, making low-level quantitation of cycloparaffins more difficult. To evaluate GC × GC for these low-level measurements, 0−5% cycloparaffin mixtures were analyzed using GC × GC and the technique of standard addition. The standard additions to two

281

Table 6. Hydrocarbon Type for the Eight Different Petroleum-Derived Fuels Shown in Figure 8

	JP-8 (4751) (wt %)	JP-8 (standard deviation) (n = 4)	Jet A (4325) (wt %)	Jet A-1 (3969) (wt %)	JP-5 (3939) (wt %)	F-76 (5343) (wt %)	JP-7 (3327) (wt %)	RP-1 (5235) (wt %)	RP-2 (7688) (wt %)
alkylbenzenes									
benzene	<0.01	NA	0.01	<0.01	<0.01	<0.01	<0.01	<0.01	<0.01
toluene	0.10	0.01	0.14	0.19	0.05	<0.01	0.03	<0.01	<0.01
C_2-benzene	0.59	0.02	0.90	2.21	0.48	0.05	0.03	<0.01	<0.01
C_3-benzene	2.27	0.04	3.15	4.03	1.39	0.28	0.13	<0.05	<0.01
C_4-benzene	3.47	0.04	3.45	3.41	2.32	0.48	0.37	<0.05	<0.05
C_5-benzene	2.73	0.03	2.48	2.12	2.23	0.51	0.10	<0.05	<0.02
C_{6+}-benzenes	4.95	0.04	4.28	2.13	4.75	6.87	0.44	<0.2	<0.2
total alkylbenzenes	14.12	0.16	14.41	14.10	11.22	8.18	1.10	<0.3	<0.3
alkylnapthalenes									
naphthalene	0.09	0.00	0.24	0.35	0.13	0.04	<0.01	<0.01	<0.01
C_1-naphthalenes	0.34	0.00	0.72	0.92	0.42	0.29	0.02	<0.01	<0.01
C_2-C_4-alkylnaphthalenes	1.13	0.03	1.79	1.59	1.15	7.43	<0.01	<0.01	<0.01
total alkylnaphthalenes	1.55	0.03	2.75	2.85	1.70	7.76	0.03	<0.02	<0.02
indans and tetralins	6.30	0.08	5.63	3.21	8.07	9.96	0.34	<0.2	<0.2
isoparaffins									
C_7- and lower iso	0.21	0.04	0.24	0.23	0.05	0.02	0.02	<0.01	<0.01
C_8-iso	0.51	0.05	0.43	0.79	0.15	0.04	0.02	<0.01	<0.01
C_9-iso	1.28	0.15	1.27	2.70	0.57	0.17	0.08	<0.01	<0.01
C_{10}-iso	4.05	0.21	4.19	5.42	1.70	0.47	0.39	1.38	2.21
C_{11}-iso	6.46	0.38	5.13	5.57	3.07	0.78	6.10	5.42	6.92
C_{12}-iso	5.93	0.46	4.47	3.81	3.67	0.70	6.61	8.30	8.20
C_{13}-iso	5.83	0.15	4.13	3.10	3.62	0.87	8.66	8.66	6.79
C_{14}-iso	4.30	0.33	3.56	2.59	3.65	1.52	5.75	7.05	6.43
C_{15}-iso	3.08	0.02	2.37	1.55	2.98	2.44	2.10	2.47	3.45
C_{16}-iso	1.22	0.01	1.04	0.31	0.82	2.92	0.36	0.31	0.69
C_{17}- and greater iso	0.48	0.01	0.64	0.13	0.07	23.42	0.10	0.05	0.28
total isoparaffins	32.86	0.66	27.46	26.20	20.35	33.34	30.20	33.65	34.99
n-paraffins									
n-C_7	0.11	0.01	0.10	0.16	0.02	0.01	<0.01	<0.01	<0.01
n-C_8	0.43	0.01	0.43	1.39	0.23	<0.01	<0.01	<0.01	<0.01
n-C_9	1.19	0.02	1.45	3.05	0.71	0.12	0.11	0.02	0.03
n-C_{10}	3.38	0.05	3.43	5.18	1.56	0.57	1.16	0.09	0.17
n-C_{11}	4.09	0.09	3.74	5.44	3.31	0.67	6.43	0.33	1.48
n-C_{12}	3.70	0.03	3.50	4.24	3.34	0.68	6.77	0.61	1.33
n-C_{13}	2.87	0.03	2.74	3.10	2.81	0.70	6.09	0.28	0.25
n-C_{14}	2.06	0.02	1.93	2.02	2.32	0.96	2.40	0.22	0.25
n-C_{15}	1.01	0.01	1.16	0.80	1.41	1.43	0.51	0.02	0.03
n-C_{16} and greater	0.51	0.00	0.81	0.31	0.14	9.28	0.13	<0.01	<0.01
total n-paraffins	19.34	0.16	19.27	25.67	15.85	14.43	23.62	1.57	3.55
cycloparaffins									
monocycloparaffins	20.33	0.36	22.95	19.93	28.72	14.38	33.11	42.10	37.03
dicycloparaffins	5.45	0.22	7.36	7.83	13.90	11.93	11.41	21.19	20.65
tricycloparaffins	0.05	0.01	0.16	0.22	0.19	<0.01	0.20	1.02	3.33
total cycloparaffins	25.83	0.53	30.47	27.98	42.80	26.32	44.71	64.31	61.00

fuels (FT-SPK and HEFA-SPK with identification numbers 5172 and 6152, respectively) were made using a mixture of 27 monocycloparaffins, which were previously described in model mixture experiments. The results (Figure 7) show the GC × GC−FID response to be linear with each standard addition. The FT-SPK was measured as 0.54 ± 0.01 wt %, using typical GC × GC quantitation methods, and the standard addition calculation gave a 0.49 ± 0.01 wt % response. The HEFA-SPK was also evaluated with this technique. Direct measurement using GC × GC yielded 3.15 wt % cycloparaffins, whereas the standard addition technique gave a 3.30 wt % result. These results demonstrate the ability of GC × GC to accurately quantify low levels of cycloparaffins, even in highly isoparaffinic SPKs.

3.4. GC × GC Analysis for Petroleum-Derived Fuels. Examples of GC × GC chromatograms for petroleum-derived military and commercial fuels are shown in Figure 8. JP-8, Jet A, and Jet A-1 exhibit very similar patterns and are difficult to distinguish from each other. Similar to GC−MS, even highly detailed GC × GC chromatograms would not reveal many significant differences between these fuel types. JP-5 also looks similar to JP-8/Jet A, because it has the same hydrocarbon range and similar aromatic compounds. JP-7 and the rocket propulsion (RP) fuels have a dramatic reduction of aromatic compounds compared to JP-8 or Jet A fuels, whereas F-76, a military diesel fuel, has higher levels of aromatics as well as a wide boiling range of hydrocarbons. Note that the F-76 sample contains
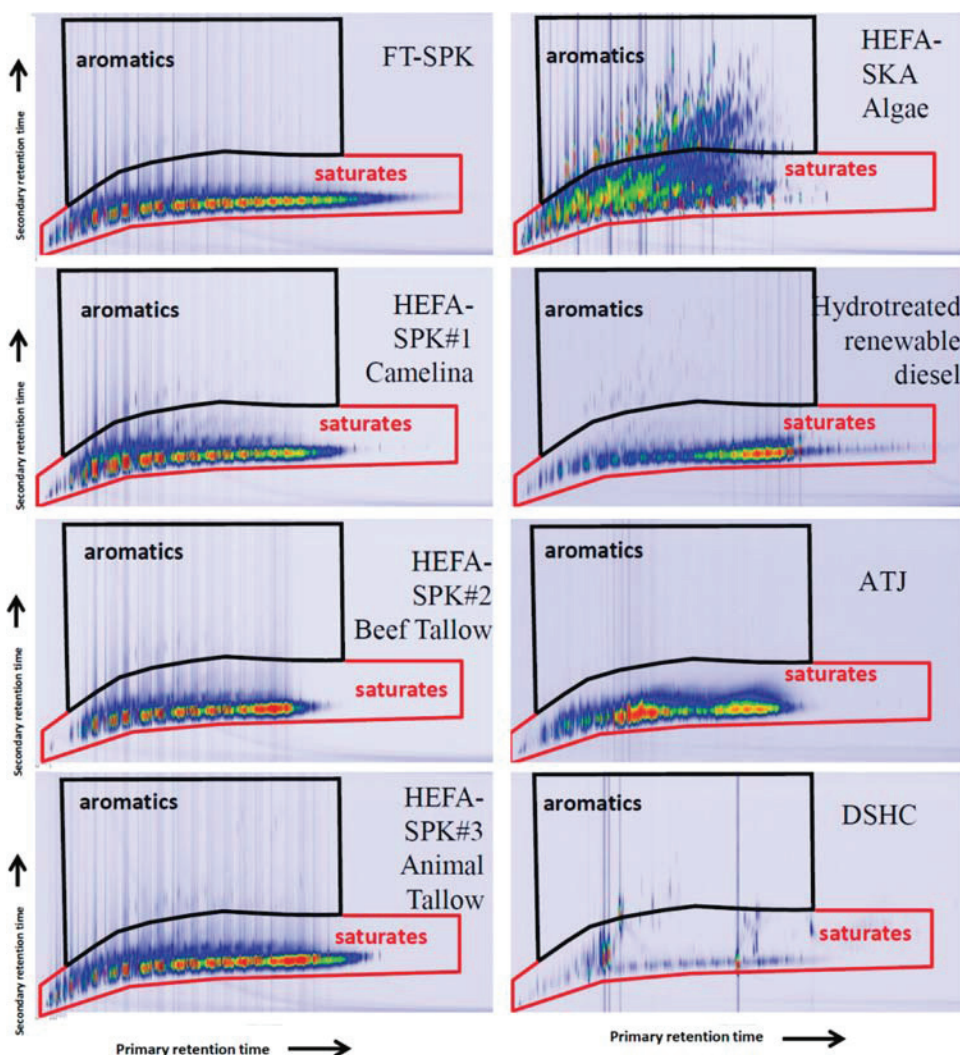
Figure 9. Two-dimensional chromatograms of alternative jet fuel candidates and blendstocks using GC × GC.

components that are more polar than the alkylnaphthalenes [biphenyls and other polycyclic aromatic hydrocarbons (PAHs)], which show up as "wrap-around" peaks at the very bottom of the plot.[17] GC × GC images can be used to distinguish fuel types and visually indicate compositional differences, unlike other chromatographic techniques.

When these chromatograms are evaluated using the templates developed for hydrocarbon type analysis, the data from Table 6 is produced. Fuels with similar chromatograms (JP-8, Jet A, and Jet A-1) do show detectable, quantitative differences for the categories of hydrocarbon types. These particular fuels happen to have very similar alkylbenzene concentrations, which is not the case for all jet fuels (Table 5). They do, however, differ in indan and tetralin levels (ranging from 3.2 to 8.1%) as well as in the levels of alkylbenzenes (1.6−29%). Normal paraffin concentrations differ between the rocket fuels (RP) and conventional fuels, because rocket fuels have been processed to obtain more density without aromatics by emphasizing the cycloparaffins. The mono- and dicycloparaffin concentrations are double those of the aircraft fuels, thereby decreasing the freezing point and

increasing the density without substantially affecting the hydrogen content. The F-76 diesel fuel is visually different in the boiling range (Figure 8) but also shows higher levels of heavier aromatics (C_6 and greater alkylbenzenes and naphthalenes but not indans and tetralins). The most abundant normal paraffins for F-76 are in the C_{17+} range, which is also indicative of its higher boiling nature.

3.5. GC × GC Analysis for Non-petroleum Alternative Fuels. The hydrocarbon type analysis of non-petroleum fuels is a natural and useful extension of this technique. Frequently, the development of alternative fuels involves processing streams that may be entirely aliphatic, as is true with SPK fuels, which, in most cases, contain mainly isoparaffins. In these instances, it may be important to be able to measure trace amounts of other compound classes, such as cycloparaffins or trace aromatics, to satisfy specifications. In addition, different types of compounds created in processing alternative sources of fuel may be unlike those in petroleum mixtures and may not be categorized as consistently as the petroleum fuels. For example, it is difficult to distinguish many alkenes from isoparaffins or cycloparaffins

Table 7. Hydrogen Content and Average Molecular Weight Calculations from GC × GC Data

POSF	average MW (GC × GC)	average MW[19]	hydrogen mass percent (GC × GC) (%)	hydrogen mass percent (D3343) (%)	hydrogen mass percent (D7171 NMR) (%)
JP-8 (6169)	159	158	14.1	14.0	14.1
FT-SPK 1 (5729)	143	152	15.5	15.5	15.5
JP-8/SPK 1 (1:1)	150	152	14.8	14.8	14.6
FT-SPK 2 (7629)	154	152	15.4	15.1	15.3
JP-8/SPK 2 (1:1)	156	152	14.8	14.5	14.4
tallow-SPK 3 (6308)	169	171	15.4	15.3	15.2
JP-8/SPK 3 (1:1)	164	164	14.8	14.6	14.7
Camelina-SPK 4 (7720)	176	176	15.3	15.3	15.1
JP-8/SPK 4 (1:1)	167	167	14.8	14.6	14.7

using the configuration of GC × GC from our laboratory. Oxygenates are not well identified by GC × GC, because the polarity of the compounds produced frequently cause intrusion into other compound classes. Fortunately, in the case of finished fuels (even from non-petroleum sources), the alkene and oxygen concentrations are usually low, allowing GC × GC to be used with confidence for the other compound classes. GC × GC chromatograms for many non-petroleum fuels are provided in Figure 9. The names of the mixtures shown are general in nature to protect the intellectual property of the fuel processors.

The GC × GC chromatograms in Figure 9 show that many of the processes to make alternative fuels result in a very similar product. The SPKs shown, with one exception, have a notable lack of aromatic components. The one exception, HEFA-SKA, is algae-derived feedstock, which was processed with aromatics. The others fuels are various mixtures of mainly isoparaffins and normal paraffins, with different volatilities, depending upon distillation cut points desired. Some, such as the hydrotreated renewable diesel, emphasize the heavier (greater than C$_{15}$) hydrocarbons instead of a more balanced collection of hydrocarbons in most of the other fuels. The alcohol-to-jet (ATJ) sample contains two distinct areas of component concentration (heavy range and mid-range) that are all isoparaffins. The direct sugar to hydrocarbon (DSHC) is a different type of mixture, which consists of three or four major compounds from a renewable feedstock. All of these mixtures have different properties and are being evaluated as aviation fuel candidates, which currently do or may in the future require group-type or class measurements as part of a specification.

3.6. Group-Type Analysis Used To Calculate Properties. One benefit of accumulating detailed information about a fuel, as shown in Table 6, is that the calculation of fuel properties, such as molecular weight and hydrogen content, are relatively straightforward. Once the weight percentages of the individual compound classes are determined from GC × GC, the molecular weight and hydrogen content contributions can be calculated for each class. The sums of these contributions are the average molecular weight and hydrogen content of the fuel, which can be used to calculate the molecular formula. The molecular formula is useful in determining stoichiometric ratios for fuel and air in combustion experiments. The hydrogen content in fuel has been shown to relate to important properties, such as combustor durability, smoke point, and others.[18] Average molecular weights and hydrogen contents measured in this way were compared to those generated from an established molecular weight estimation technique[19] and ASTM methods, and they compared favorably. The established technique was based on distillation ranges and other general fuel information. As shown in Table 7, the average molecular weights of 50:50 blends of fuels calculated from GC ×

GC are consistent with the arithmetic mean of the two blended fuels.

Work is continuing on hydroprocessed alternative fuels, which can be produced from unusual feedstocks. Many of the alternative fuels are more difficult to analyze for group type, because the majority of components are crowded into the isoparaffin region. This can make the accurate determination of cycloparaffins and low-level aromatics more difficult. We have begun this work by comparing the D2425 and GC × GC methods to determine whether GC × GC can be extended to the more unusual alternative fuels. A graphical comparison of the GC × GC output is provided in Figure 10 for eight different types of
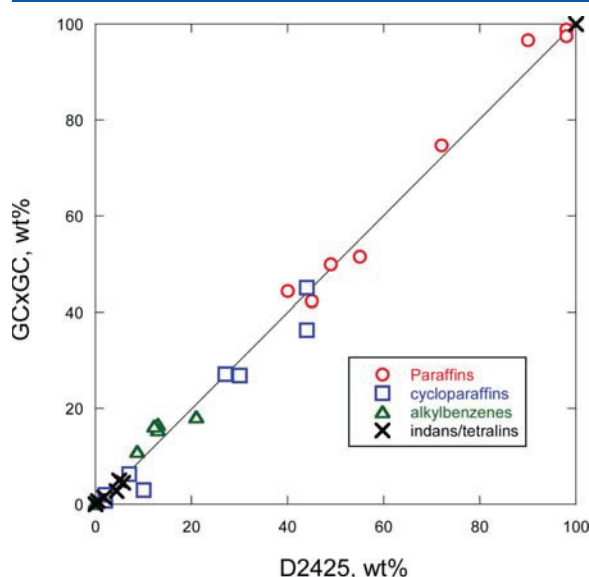

Figure 10. Comparison of alternative fuel hydrocarbon type results by two techniques, D2425 and GC × GC, for these alternative fuel sources: FT SPK, *Camelina* HEFA-SPK, tallow HEFA-SPK, algal oil product, ATJ fuel process, and mixed fat conversion process.

alternate fuels. In most cases, the agreement is good between the methods. The fact that GC × GC provides essentially the same results as D2425 is encouraging for GC × GC as a new technique; however, agreement between the two is also an indication that ASTM D2425 is capable of measuring these important group concentrations. Despite the fact that the method was developed for a certain (relatively small) group of middle distillate fuels, it is able to accurately measure these alternative fuels. While the analysis may take longer and use more

instrumentation, it has greatly aided in the development of GC × GC for this application and will likely continue as a capable technique for this measurement. Investigations continue with regard to the use of these two methods with non-conventional fuels and processing intermediates.

Two of the comparisons of cycloparaffin content by the two methods were of some concern. The GC × GC cycloparaffin predictions for two fuels were much lower than those measured by ASTM D2425. Investigation of this deviation revealed that some alternative streams that are highly hydroprocessed or isomerized have multi-branched isoparaffins (more than 3 side chains). Because the mass spectral patterns for these compounds are different from those of mildly branched (1−3 side chains) isoparaffins and ASTM D2425 ion ratios are based on conventional petroleum fuels, it is possible that these highly branched isoparaffins are misidentified in D2425 as cycloparaffins. For fuels with a small number of components, this misidentification could lead to the type of error that was observed in this instance. Continued used of both techniques to distinguish these types of compounds is warranted for analysis of these unusual fuels.

4. CONCLUSION

ASTM D2425 and GC × GC are in excellent agreement in their abilities to measure hydrocarbon group-type concentrations for aviation fuels. The analysis of a large set of Jet A, JP-8, Jet A-1, and JP-5 fuels was conducted using both techniques with good agreement. Model mixture results for GC × GC indicated that it was very capable of accurate determination of complex mixtures. The GC × GC analyses were expanded to alternative fuels (SPKs) with similar results. The expense of the GC × GC instrumentation while significant may be offset by the time, effort, and equipment necessary for the ASTM D2425 analysis (HPLC with two detectors, followed by fraction collection and two MS determinations). As more laboratories invest in GC × GC instrumentation, the use of this technique should prove to compare favorably to the more established technique of ASTM D2425 for hydrocarbon type analysis for many petroleum and non-petroleum fuels.

■ AUTHOR INFORMATION

Corresponding Author
*E-mail: richard.striebich@wpafb.af.mil.

Notes
Disclaimer: The views and conclusions contained herein are those of the authors and should not be interpreted as necessarily representing the official policies or endorsements, either expressed or implied, of the Air Force Research Laboratory or the U.S. Government.
The authors declare no competing financial interest.

■ REFERENCES

(1) Edwards, T.; Minus, D.; Harrison, W.; Corporan, E.; DeWitt, M. J.; Zabarnick, S.; Balster, L. Fischer−Tropsch jet fuels—Characterization for advanced aerospace applications. *Proceedings of the 40th AIAA/ASME/SAE/ASEE Joint Propulsion Conference and Exhibit*; Fort Lauderdale, FL, July 11−14, 2004; AIAA-2004-3885.

(2) ASTM International. *ASTM D7566-11a. Aviation Turbine Fuel Containing Synthesized Hydrocarbons*; ASTM International: West Conshohocken, PA, 2011.

(3) Pearlson, M.; Wollersheim, C.; Hileman, J. *Biofuels, Bioprod. Biorefin.* **2013**, 7, 89−96.

(4) Striebich, R. C.; Rubey, W. A.; Klosterman, J. R.; Balster, L. M. HPLC pre-separation with high resolution gas chromatography (HRGC): A comparison to multidimensional GC (MDGC). *Proceedings of the 24th International Symposium on Capillary Chromatography and Electrophoresis*; Las Vegas, NV, May 20−24, 2001.

(5) ASTM International. *ASTM D2425-93. Standard Test Method for Hydrocarbon Types in Middle Distillates by Mass Spectrometry*; ASTM International: West Conshohocken, PA, 1997.

(6) Striebich, R. C.; Shafer, L. M.; West, Z. J.; Adams, R. K.; Zabarnick, S. Hydrocarbon group-type analysis of current and future aviation fuels: Comparing ASTM D2425 to GC × GC. *Proceedings of the 12th International Conference on Stability, Handling, and Use of Liquid Fuels*; Sarasota, FL, Oct 16−20, 2011.

(7) van der Westhuizen, R.; Ajam, M.; De Coning, P.; Beens, J.; de Villiers, A.; Sandra, P. *J. Chromatogr. A* **2011**, *2018*, 4478−4486.

(8) Dimandja, J-M. D. *Anal. Chem.* **2004**, 76 (9), 167 A−174 A.

(9) Johnson, K. J.; Synovec, R. E. *Chemom. Intell. Lab. Syst.* **2002**, *60*, 225−237.

(10) ASTM International. *ASTM D2549-02. Standard Test Method for Separation of Representative Aromatics and Nonaromatics Fractions of High-Boiling Oils by Elution Chromatography*; ASTM International: West Conshohocken, PA, 2012.

(11) ASTM International. *ASTM D6379-04. Standard Test Method for Determination of Aromatic Hydrocarbon Types in Aviation Fuels and Petroleum Distillates—High Performance Liquid Chromatography Method with Refractive Index Detection*; ASTM International: West Conshohocken, PA, 2004.

(12) Striebich, R. C.; Rubey, W. A.; Klosterman, J. R. *Waste Manage.* **2002**, 22, 413.

(13) Seeley, J. V.; Kramp, F.; Hicks, C. J. *Anal. Chem.* **2000**, 72, 4346−4352.

(14) Edwards, T.; Shafer, L.; Striebich, R.; Gomach, J. Chemical class composition of commercial jet fuels and other specialty kerosene fuels. *Proceedings of the 14th AIAA/AHI Hypersonics Technology Conference*; Canberra, Australian Capital Territory, Australia, 2006; Paper 2006-7972.

(15) Schofield, K. *Prog. Energy Combust. Sci.* **2008**, 34, 330−350.

(16) Hadaller, O. J.; Johnson, J. M. *World Fuel Sampling Program*; CRC Aviation Fuel, Lubricant & Equipment Research Committee of the Coordinating Research Council, Inc.: Alpharetta, GA, June 2006; CRC Report 647.

(17) Ong, R.; Marriott, P.; Morrison, P.; Haglund, P. *J. Chromatogr. A* **2002**, *962*, 135−152.

(18) Obringer, C. *Fuel Property Effects on Combustion*; Air Force Wright Aeronautical Laboratories: Wright-Patterson Air Force Base, OH, 1985; AFWAL-TR-85-2051.

(19) Nelson, W. L. *Petroleum Refining Engineering*, 4th ed.; McGraw-Hill: New York, 1958.

285

Appendix U. Migration of Silver Nanoparticles from Silver Decorated Graphene Oxide to Other Carbon Nanostructures

# Migration of Silver Nanoparticles from Silver Decorated Graphene Oxide to Other Carbon Nanostructures

K. A. Shiral Fernando,*[†] Venroy G. Watson,[†] Xifan Wang,[†] Nicholas D. McNamara,[†] Mary C. JoChum,[‡] Dylan W. Bair,[‡] Barbara A. Miller,[†] and Christopher E. Bunker[‡]

[†]Energy Technology and Materials Division, University of Dayton Research Institute, Dayton, Ohio 45469, United States
[‡]Propulsion Directorate, Air Force Research Laboratory, Wright-Patterson Air Force Base, Ohio 45433-7103, United States

Ⓢ Supporting Information

ABSTRACT: Decoration of graphene oxide (GO) sheets with Ag nanoparticles has been demonstrated using a simple sonication technique. By changing the ratio between Ag-decorated-GO and GO, a series of Ag-decorated-GO samples with different Ag loadings were synthesized. These Ag-decorated-GO samples were characterized using transmission electron microscopy (TEM), X-ray diffraction (XRD) spectroscopy, thermal gravimetric analysis (TGA), and differential scanning calorimetric (DSC) techniques. TEM analysis showed that Ag nanoparticles were evenly distributed on GO sheets, and the size analysis of the particles using multiple TEM images indicated that Ag nanoparticles have an average size of 6−7 nm. TEM analysis also showed that Ag nanoparticles migrated from Ag-decorated-GO to later-added GO sheets. In XRD, all the Ag-decorated GO samples showed the characteristic peaks related to GO and face-centered-cubic (fcc) Ag. Thermal analysis showed peaks related to the combustion of graphitic carbon shifted to lower temperatures after GO sheets were decorated with Ag nanoparticles. In addition, further experiments performed using Ag-decorated-GO and multiwalled carbon nanotubes (MWNTs) confirmed that Ag nanoparticles migrated from Ag-decorated-GO to later-added carbon nanotubes without a noticeable coalescence of Ag nanoparticles.
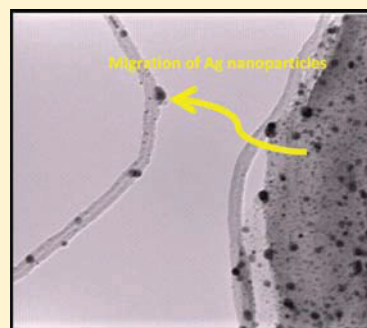
■ INTRODUCTION

Much recent effort has gone into research of metal-decorated carbon nanostructures because these nanostructures possess very attractive featues.[1−6] As a result, a wide range of metal-decorated carbon nanostructures have been prepared that exhibit promising applications in nanotechnology and nano-biotechnology.[2,3,7−11] For example, Sun and co-workers demonstrated that metal-decorated carbon nanoparticles might be used to convert carbon dioxide to fuel and split water in order to produce hydrogen in the presence of light.[2,8] Silver is widely known for its antimicrobial activity, and therefore, Ag-decorated carbon supports are used in biomedical applications, such as in wound dressing and medical catheters.[12,13] Ruiz et al. have reported that GO was highly biocompatible with bacterial and mammalian cells, with no cytotoxicity, and that in fact GO promotes bacterial and mammalian cell growth by enhancing cell attachment and proliferation, while Ag-decorated-GO inhibits the growth of bacterial cells.[7] In this paper, we present the preparation and characterization of Ag-decorated-GO samples with different Ag concentrations/loadings using simple sonochemical methods that mix different ratios of Ag-decorated-GO and GO. GO was prepared using a modified Hummers method.[14−16] This method involves the chemical oxidation of graphite to produce highly exfoliated graphene sheets that contain a large amount of oxygen functional groups (epoxides, alcohols, ketones, carbon-yls, and carboxylic groups).[17−23] The oxygen functional groups

on the GO surface have a major role in the nucleation and growth of Ag nanoparticles.[25−42] For example, Pasricha et al. reported that oxygen functional groups act as nucleation sites for formation and anchoring of metal nanoparticles.[42] In addition, metal (Ag and Au) nanoparticles can interact with GO sheets through physisorption, electrostatic interactions, and charge-transfer interactions.[42] Furthermore, this study shows that Ag nanoparticles migrate from Ag-decorated-GO to later-added GO and produce a new Ag-decorated-GO sample with less Ag content. The microscopy characterization shows that Ag nanoparticles are evenly distributed without any noticeable ripening effect or coalescence. To the best of our knowledge, this is the first report showing migration of metal nanoparticles from one carbon nanostructure to another (inter). However, Lu et al. have reported that, at elevated temperatures (>100 °C), small Ag nanoparticles moved on GO surface to form larger Ag nanoparticles.[51] Lu et al. observed that the coalescence of Ag nanoparticles happened in same GO sheet (intra), and they did not report any Ag nanoparticles migration between GO sheets (inter). They speculated that two possible mechanisms, Oswald ripening and particles coalescence, are likely to have been responsible for the ripening process.[51]
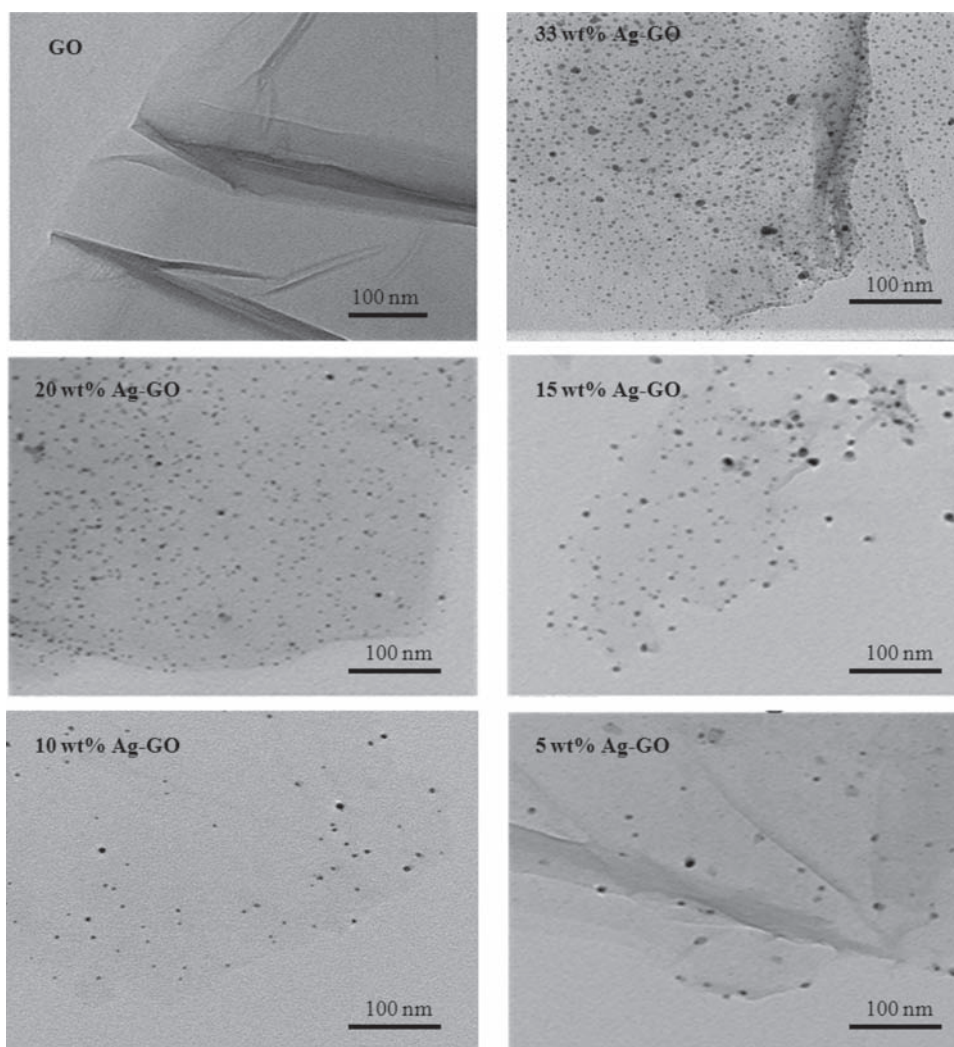
Figure 1. TEM images for Ag-GO samples with different Ag loadings.

RESULTS AND DISCUSSION

GO was prepared by oxidation of natural graphite powder using a modified Hummers method.[14−16] Graphite consists of stacked graphene layers with a plane distance of 0.335 nm.[17,43] The severe oxidation process in a modified Hummers method separates these stacked graphene layers and introduces many oxygen-containing functional groups, as noted before.[17−23] GO powder readily exfoliates into individual or few-layers-thick nanosheets in polar solvents (water, DMF, ethanol, etc.) upon a simple sonication forming a suspension that is stable for a long period of time. In addition, it has been reported that metal ions could be adsorbed on GO nanosheets because these oxygen functional groups provide reactive sites for nucleation and growth of metal nanoparticles.[24−42] Both GO and silver acetate are readily soluble in DMF, and so DMF was used as the solvent in our Ag decoration of GO reactions. In addition, Pastoriza-Santos and co-workers have reported that DMF is a mild reducing agent that reduces silver acetate to silver nanoparticles easily at elevated temperatures.[44] Furthermore, DMF has a desired vapor pressure and viscosity, which are important properties to use in a sonochemical reaction.

Controlling the Ag Content of GO. A 33 wt % Ag loaded sample was prepared by mixing 50 mg of GO with 25 mg of silver acetate in DMF and sonicated for 20 min. The same experiment was repeated five more times to obtain a sufficient amount of 33 wt % Ag-decorated-GO stock sample. The other Ag-decorated-GO samples with different Ag loadings (20, 15, 10, and 5 wt %) were synthesized by changing the ratio between 33 wt % Ag-decorated-GO and GO. In synthesis the precise ratio between 33 wt % Ag-decorated-GO and GO was sonicated in DMF for an hour in a bath sonicater. The reproducibility of this experiment was performed by replicating above experiments multiple times in the same conditions. These Ag-decorated-GO samples (33−5 wt %) were characterized using TEM, XRD, and simultaneous TGA/DSC analysis.

TEM analysis was performed to determine morphology, extent of nanoparticle decoration, and size distribution of Ag nanoparticles. TEM samples were prepared by dropping the dispersions of GO and Ag-decorated-GO samples in

isoproponol onto carbon-coated or plain copper TEM grids and then drying at room temperature. As seen in Figure 1a, GO has a typical flaky structure that is a few layers thick and has a wrinkled surface. Ag-decorated-GO with different Ag loadings (33−5%) are shown in Figure 1b−f. Ag nanoparticles appear as dark dots and are evenly decorated on GO sheets in each sample. The population of Ag nanoparticles on GO surface decreases from 33 wt % sample to 5 wt % sample, as expected. For Ag-decorated-GO samples with different Ag loadings, we did not observe in TEM the areas where Ag nanoparticles are agglomerated or larger undecorated areas of GO. The size analysis of Ag nanoparticles on GO surface was performed using multiple TEM images of each Ag-decorated-GO. The size analysis of Ag nanoparticles using TEM showed an average size of 6−7 nm, with a size distribution of 1−22 nm, as shown in Figure 2a−e.
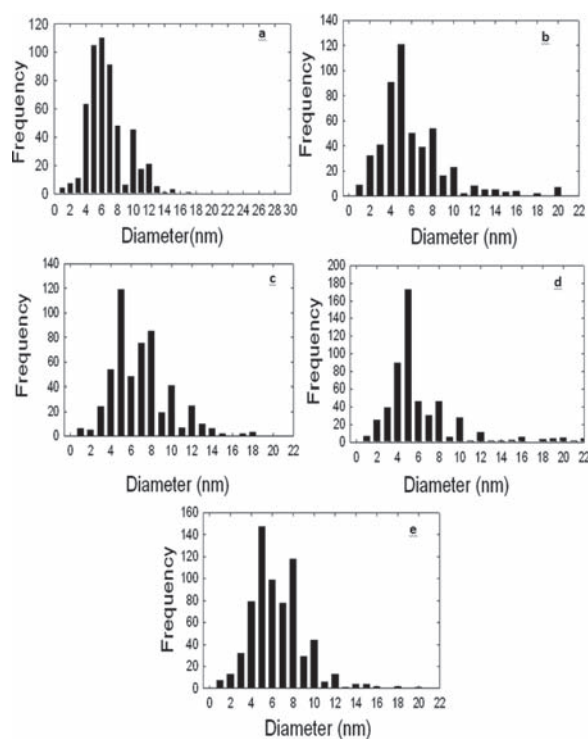
Figure 2. Size distributions of Ag nanoparticles on GO for 33 (a), 20 (b), 15 (c), 10 (d), and 5 wt % (e).

XRD analysis was performed to determine the crystallinity of GO and Ag-decorated-GO samples, as shown in Figure 3. In XRD analysis, GO exhibits a carbon (002) diffraction peak at 2θ value in the range of 10°−12°, which is considerably lower than the diffraction peak of graphite at 2θ value of ∼26°.[45−47] GO shows a lower 2θ value in XRD because the vigorous oxidation process during GO synthesis introduces oxygen functional groups and water molecules between graphene layers; therefore, GO has a higher interlayer distance. The interlayer distance of graphene sheets of GO is ∼0.709−0.804 nm, and the interlayer distance of graphene sheets of graphite is ∼0.335 nm.[17,43,45] In XRD, all the Ag-decorated-GO samples show the characteristic peaks related to GO and face-centered-cubic (fcc) Ag, which are well matched to ICDD card data. In
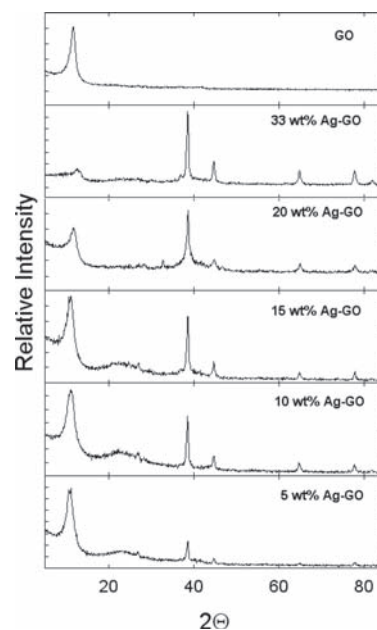
Figure 3. XRD analysis of the GO and Ag-decorated-GO samples.

addition to GO peak and fcc Ag peaks, a broad peak appeared at a 2θ value of 24°, which is related to reduced graphene oxide (r-GO). Qui et al. reported a similar observation of a new broad peak appearing at 2θ value of ∼24° after GO was decorated with Pt nanoparticles, and later they identified it as a r-GO peak.[28] The observation of the peak at 2θ value of ∼24° indicates GO is partially reduced during the sonochemical reaction. The intensity ratio between XRD peak of GO and Ag peaks increases when Ag percentage decreases, as expected. Therefore, 33 wt % Ag-decorated-GO sample has the lowest intensity and 5 wt % Ag-decorated-GO sample has highest intensity of GO peak. Simultaneously, 33 wt % Ag-decorated-GO sample has the highest intensity and 5 wt % Ag-decorated-GO sample has the lowest intensity of fcc Ag peak.

In addition, TGA and DSC analyses were performed using a simultaneous TGA/DSC instrument at a temperature range from 25 to 800 °C to obtain the Ag loading and thermal behavior of Ag-decorated-GO samples, as shown in Figure 4. It has been reported that Ag nanoparticles are stable in air up to ∼1000 °C, and therefore, in thermal analysis, Ag nanoparticles are not oxidized.[48,49] In DSC analysis, GO and Ag-decorated-GO samples showed two exothermic peaks, with the first peak centered at ∼222 °C and the second peak centered at 578 °C. The first peak is related to the removal of oxygen functionality from GO surface, and the second peak is related to the combustion of graphene sheets.[17,50] The intensity of the first peak at ∼222 °C depends on the Ag content of sample. A 33 wt % Ag-decorated-GO sample has the lowest intensity for the first peak because it has the highest percentage of Ag loading, while a 5 wt % sample has the highest intensity for first peak because it has the lowest percentage of Ag loading. As noted before, the oxygen functional groups on the surface of GO act as nucleation sites for formation and anchoring of the metal nanoparticles. Therefore, the highest Ag loaded sample has the lowest amount of free oxygen functional groups and the lowest Ag loaded sample has the highest amount free oxygen functional groups. As a result, the 33 wt % Ag-decorated-GO
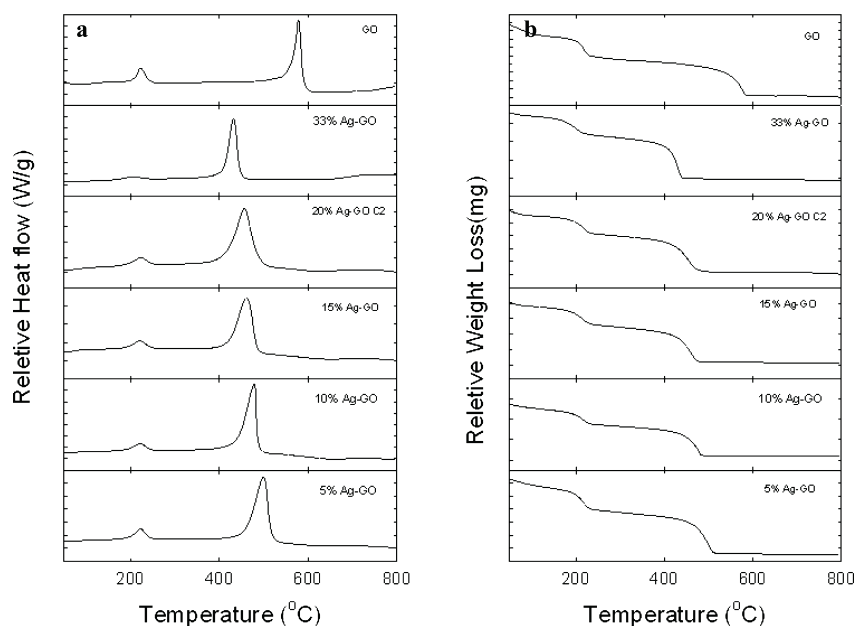
Figure 4. DSC (a) and TGA (b) traces for GO and Ag-decorated-GO samples with different Ag loadings.

sample showed the lowest intensity for the first peak at ~222 °C and the 5 wt % Ag-decorated-GO showed the highest intensity for the same peak. This DSC results provide direct evidence that nucleation and the growth of Ag nanoparticles occurred in oxygen functional groups of GO surface. The second peak at 578 °C of GO, which is related to the combustion of carbon of graphene sheets, is shifted to lower temperature for all the Ag-decorated-GO samples. A 33 wt % Ag-decorated-GO has the highest shift, while 5 wt % Ag-decorated-GO has the lowest shift of the carbon combustion peak, as shown in Table 1. The exact reason behind this carbon

Table 1. Actual Ag Content, Average Nanoparticle Size from TEM and the Position of Carbon Combustion Peak from DSC for Ag-Decorated-GO Samples Synthesized by Changing the Ratio between 33 wt % Ag-Decorated-GO and GO

sample	actual Ag loading from TGA (wt %)	av size from TEM (nm)	position of carbon combustion peak
GO			578
33 wt % Ag-GO	32	6	418
20 wt % Ag-GO	15	7	457
15 wt % Ag-GO	12	7	461
10 wt % Ag-GO	8	6	478
5 wt % Ag-GO	5	7	499

combustion peak shift to a lower temperature is not yet understood. However, we speculate this could likely be due to three effects. First, Ag behaves as a catalyst and catalyzes the combustion of graphitic carbon. Second, silver is an excellent conductor, absorbing heat and passing to graphene sheets efficiently, and thus the combustion of GO occurs at lower temperature in the presence of Ag nanoparticles on GO sheets. Third, it has already been published that metal nanoparticles intercalate between graphene sheets during the metal decoration of GO,[28] so metal nanoparticles behave as spacers

and increase the interlayer distance further. Subsequently, Ag-decorated-GO samples have a larger surface area than regular GO to absorb heat from heating source. Therefore, the combustion of Ag-decorated-GO samples occurs at a lower temperature than regular GO. In TGA, weight loss between 25 and 100 °C is attributed to the removal of water between graphene sheets of GO. Then, there are two regions of noticeable weight loss: from 150 to 250 °C and 550 to 600 °C. The former is attributed to the removal of oxygen functional groups from GO surface while the latter is related to the combustion of graphitic carbon sheets of GO. The two weight loss regions in TGA correlate well with two exothermic peaks observed in DSC. As noted before, Ag nanoparticles are stable in air up to ~1000 °C without making their oxide. As GO is completely burned out before ~600 °C, TGA analysis could be utilized to determine the Ag content of Ag-decorated-GO samples (Table 1). Ag loading of Ag-decorated-GO samples that were obtained from TGA showed a good agreement with calculated values.
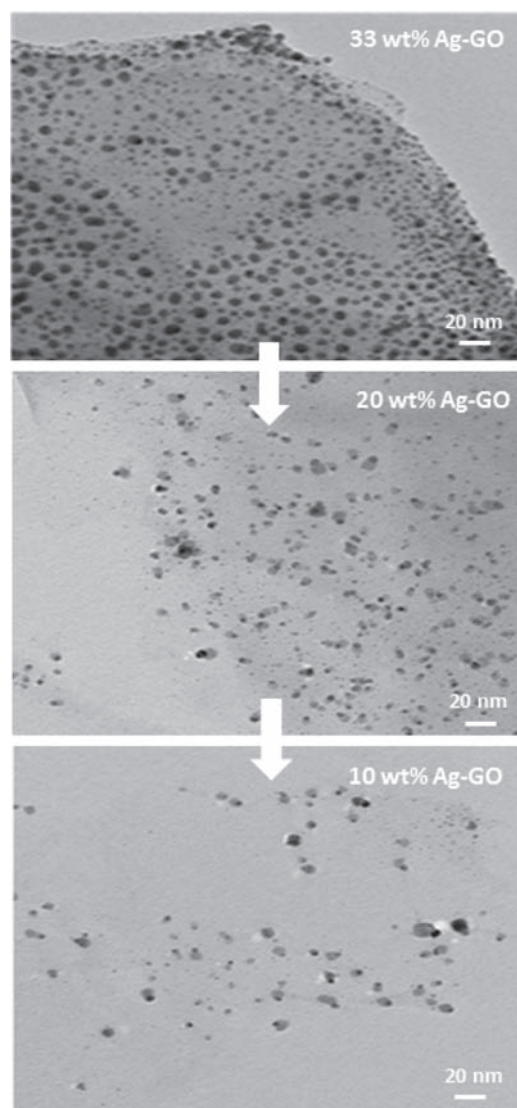
Migration of Ag Nanoparticles. In the synthesis of Ag-decorated-GO samples with different Ag loadings, a 33 wt % Ag-decorated-GO sample was used as a starting material, and it was mixed with GO to obtain desired Ag loading. In order to synthesize new Ag-decorated-GO samples with different Ag loading, Ag nanoparticles should leave the 33 wt % Ag-decorated-GO sample and migrate to later-added GO. TGA, DSC, and XRD analyses show the presence of Ag in newly synthesized Ag-decorated-GO samples. Nevertheless, these characterization techniques do not provide any information about the migration of Ag nanoparticles from 33 wt % Ag-decorated-GO to later-added GO. Therefore, these techniques cannot be utilized to characterize the migration and distribution of Ag nanoparticles. Microscopic techniques, especially TEM, are useful to characterize the distribution of Ag nanoparticles on GO sheets. As shown in Figure 1, all the newly prepared Ag-decorated-GO samples show that Ag nanoparticles are evenly distributed on GO surface. The content of Ag nanoparticles on

GO surface of each sample depends on ratio between 33 wt % Ag-decorated-GO and GO used during synthesis. A 5 wt % Ag-decorated-GO sample has the lowest content of Ag nanoparticles, while 33 wt % Ag-decorated-GO has the highest content of Ag nanoparticles.

Even though TEM analysis confirms that Ag nanoparticles are evenly distributed in newly synthesized Ag-decorated-GO samples with less Ag loading, we need further investigation to confirm the migration of Ag nanoparticles from 33 wt % Ag-decorated-GO to later-added GO because later-added GO has the similar morphology to GO with Ag nanoparticles. Therefore, a couple of new experiments were designed to confirm the migration of Ag nanoparticles from Ag-decorated-GO to later-added GO. The first experiment was designed to determine whether the migration of Ag nanoparticles from Ag-decorated-GO to GO is continuous. In this experiment, 10 wt % Ag-decorated-GO sample was synthesized from 20 wt % Ag-decorated-GO sample instead from 33 wt % Ag-decorated-GO sample, as shown in Figure 5. Analysis of this sample confirmed that successive migration of Ag nanoparticles occurred and that 10 wt % Ag-decorated-GO can be synthesized from 20 wt % Ag-decorated-GO sample. As noted before, size analysis was performed using multiple TEM images of 10 wt % Ag-decorated-GO sample, and it indicated the average size of Ag nanoparticles is ∼10 nm with a size distribution of 1−20 nm. In addition to TEM analysis, this sample was analyzed by XRD and simultaneous TGA/DSC. These characterizations showed that there were no meaningful differences between the 10 wt % Ag-decorated-GO samples synthesized from 20 or 33 wt % Ag-decorated-GO. Therefore, this experiment has proved the successive migration of Ag nanoparticles from Ag-decorated-GO to later-added GO.

The second experiment was designed by adding MWNTs to 33 wt % Ag-decorated-GO sample instead of GO because in TEM the tubular structure of MWNTs can be easily differentiated from GO sheets. A 33 wt % Ag-decorated-GO sample was mixed with MWNTs in DMF and sonicated similar to previous Ag-decorated-GO synthesis experiments. TEM analysis of product (Ag-decorated-GO-MWNTs) indicated both GO and MWNTs are evenly decorated with Ag nanoparticles, as shown in Figure 6. Size distribution analysis was performed to evaluate the size distribution of Ag nanoparticles on MWNTs and GO. Analysis of particles revealed the average size of Ag nanoparticles on both GO and MWNTs surfaces are ∼6−7 nm, with a size distribution of 1−24 nm. These numbers are well matched with an average size and a size distribution of Ag nanoparticles obtained for our previous Ag-decorated-GO samples. Therefore, this experiment confirms that Ag nanoparticles are migrating from Ag-decorated-GO to later-added MWNTs without any noticeable ripening or damage of particles. Similar to this, Ag nanoparticles should migrate from 33 wt % Ag-decorated-GO to later-added GO in the synthesis of 5−20 wt % Ag-decorated-GO samples. To the best of our knowledge, no papers have been published related to the migration of metal nanoparticles from one carbon substrates to another (inter). However, as mentioned before, Lu et al. reported that, in elevated temperatures, Ag nanoparticles, especially smaller ones, moved on same GO sheet (intra) and agglomerated to form larger nanoparticles.[51] In addition, there are other reports of the migration, coalescence, and agglomeration of small metal nanoparticles to form larger metal nanoparticles in a same GO sheet.[51−55] The exact mechanism of the migration of Ag nanoparticles

Figure 5. TEM analysis to prove the migration of Ag nanoparticles from Ag-decorated- GO to GO is not limited to one time. The successive migration of Ag nanoparticles occurs between Ag-decorated-GO to GO.

from Ag-decorated-GO to later-added GO or MWNTs is not clear at this point. We speculate that sonochemistry activates some of the silver nanoparticles that are attached to GO surface, so silver nanoparticles release to DMF solution. Later-added GO and MWNTs also have reactive sites, including defect sites and oxygen functional groups. Therefore, Ag nanoparticles in DMF solution can attach to the surface of later-added GO or MWNTs. We should note here that the simple mixing of 33 wt % Ag-decorated-GO with GO or MWNTs in the absence of aforementioned experimental conditions (in DMF and sonication) did not show any silver presence on later-added GO or MWNTs. Therefore, sonication and a solvent (DMF) are essential for migration of Ag nanoparticles from one carbon substrate to another. In the synthesis of Ag-decorated-GO samples (20−5 wt %), the 33 wt % Ag-decorated-GO sample was mixed with GO and sonicated

291
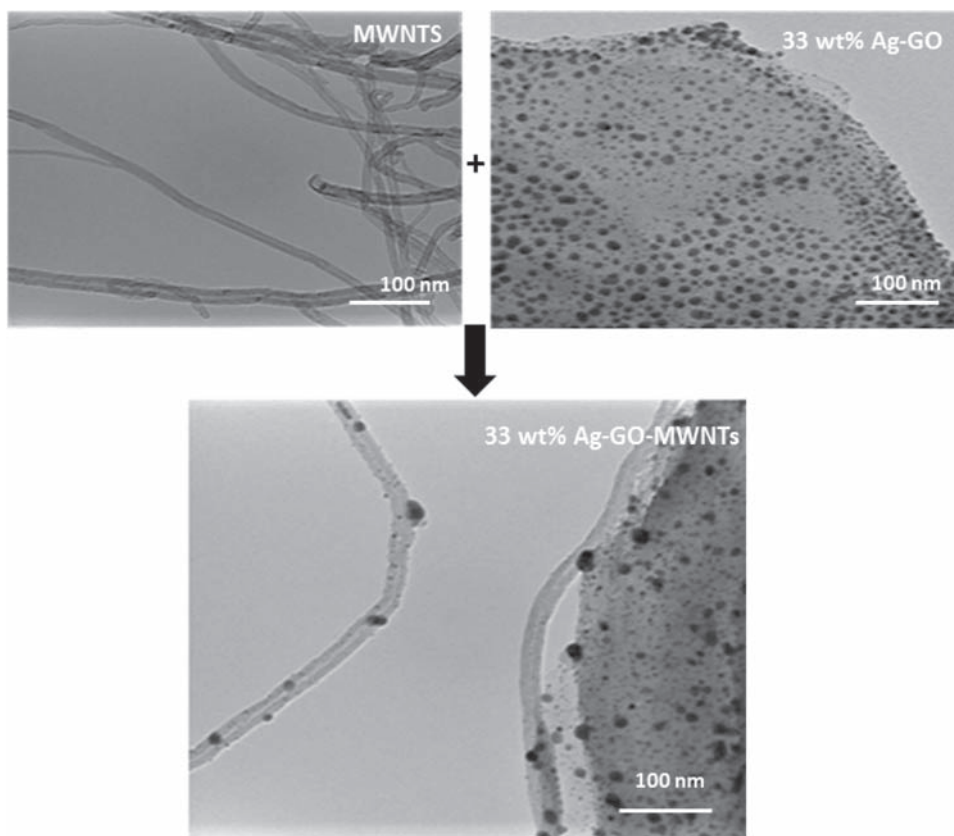
Figure 6. TEM analysis to show the migration of Ag nanoparticles from Ag-decorated-GO to MWNTs: acid-treated MWNTs (a), 33 wt % Ag-decorated-GO (b), and 20 wt % Ag equivalent Ag-decorated-GO-MWNTs (c).

in a round-bottom flask. In this reaction both Ag-decorated-GO and later-added GO are in close proximity in DMF solvent. Sonication provides the required kinetic energy to mix and collide Ag-decorated-GO with later-added GO. Therefore, Ag nanoparticles might also migrate from Ag-decorated-GO to later-added GO because of these rapid collisions.

It has been reported in the literature that synthesis of Ag and other metal nanoparticles using passivation agents to prevent agglomerations and then attaching these passivated-metal nanoparticles to GO and other carbon nanostructures via covalent bonds or weak intermolecular interactions such as $\pi-\pi$ stacking, hydrophobic, and electrostatic interactions.[3,56] The nature of chemical interaction between GO and Ag nanoparticles is completely different in these samples compared to our Ag-decorated-GO. Our Ag nanoparticles do not have a passivation agent, and therefore, Ag nanoparticles are directly attached to the surface of GO or any other carbon nanostructures. This migration of metal nanoparticles between nanostructures is significant because this method might be utilized to introduce metal nanoparticles to the substrates that are inherently difficult to functionalize with metal nanoparticles. GO, carbon nanoparticles, and purified carbon nanotubes are easy to functionalize with metal nanoparticles because they have oxygen functional groups on the surface. As noted before, these oxygen functional groups provide platforms for nucleation and growth of metal nanoparticles. Metal nanoparticles do not agglomerate because the nucleation and growth of metal nanoparticles happens in distinct places on these

nanostructures. However, the materials and substrates that do not have defects and functional groups cannot be decorated with metal nanoparticles easily because of the absence of nucleation centers. Therefore, migration of metal nanoparticles might be useful in decorating the substrates and materials with metal nanoparticles that do not possess nucleation centers.

CONCLUSIONS

GO was successfully decorated with Ag nanoparticles in DMF using sonochemistry. The loading of Ag nanoparticles on GO surface was controlled by mixing 33% Ag-decorated-GO with known amounts of GO. TEM analyses revealed that GO surfaces are evenly decorated with Ag nanoparticles in all the Ag-decorated-GO samples prepared in this study. Size analysis using TEM indicated an average size of 6−7 nm, with a size distribution of 1−22 nm. Simultaneous TGA and DSC analysis of GO and Ag-decorated-GO samples with different Ag loadings indicated that the carbon combustion peak of GO at ~578 °C shifted to lower temperature after Ag nanoparticles were added to GO surfaces. Further experiments performed using MWNTs confirmed that Ag nanoparticles migrated from Ag-decorated-GO to later-added MWNTs.

EXPERIMENTAL SECTION

Materials. Silver acetate (99.99%), ammonium persulfate, phosphorus pentoxide, potassium permanganate, multiwall carbon nanotubes (MWNTs), sulfuric acid, hydrochloric acid, 13.3 M nitric acid (>69%), and N,N-dimethylformamide (DMF) (99.6%) were

purchased from Sigma-Aldrich. Graphite powder was obtained from Asbury Carbon (grade 3805). Dialysis tubes (MWCO ~ 6000−8000) and reagent ethanol (90%) were also purchased from Fisher Scientific. All the solvents were used as received without any further treatment or purification.

Synthesis of Graphene Oxide. Graphene oxide was synthesized by using modified Hummers method. H_2SO_4 (10 mL) was heated at 80 °C in a 500 mL round-bottom flask, and then $(NH_4)_2S_2O_8$ (0.9 g) and P_2O_5 (0.9 g) were added. The mixture was stirred well until all the reagents were dissolved well and make a homogeneous solution. Graphite powder was introduced to the flask, and the mixture was allowed to heat for 4.5 h at 80 °C and then cooled down to room temperature. The reaction mixture was diluted with 250 mL of deionized water and kept for 12 h. The mixture was filtered, and a solid residue in filter paper was washed repeatedly with water and dried in an oven for overnight. The solid residue was added to H_2SO_4 (40 mL) in a 500 mL round-bottom flask and cooled in an ice bath. $KMnO_4$ (5 g over 40 min) was added to the mixture while the temperature was kept <10 °C. Upon achieving a color change from black to greenish brown, the mixture was kept at 35 °C for 2 h. Then the mixture was diluted with 85 mL of water. Ice bath was used to maintain the inside temperature of the mixture below 35 °C during this water addition. After the temperature reached room temperature, the flask was heated at 60 °C overnight. 250 mL of water was added to the mixture and kept another 5 h at ~60 °C. Then the mixture was poured into a beaker, and 10 mL of aqueous H_2O_2 was added after mixture was reached room temperature. Effervescence and a color change to yellow were observed. The reaction mixture was allowed to sit for 12 h, after which the transparent supernatant was removed, and H_2SO_4 (5 wt %)−H_2O_2 (0.5 wt %) and a solution of HCl (10 wt %) were used to repeatedly wash the sediment. The washing with water was performed repeatedly until the sample did not show layers separation. Then, the sample was transferred to dialysis tubes, which were kept in a deionized filled water beaker for 7−10 days, and water was changed once a day. The final product was recovered as a black flaky powder after water was removed by rotary evaporation.

Acid Treatment of MWNTs. 500 mg of MWNTs was added to a 2.6 M solution of 250 mL of nitric acid and refluxed for 24 h. Upon completion of refluxing, the mixture was cooled to room temperature, centrifuged, and washed with deionized water many times until the pH of supernatant was neutral. Then, the recovered sample was washed with acetone several times to remove water. Nitrogen was blown over the sample to remove acetone, and a final product was recovered as a black powder.

Sonochemical Synthesis of Ag-Decorated-GO with 33 wt % Ag Loading. 50 mg of GO, 15 mL of DMF, and 25 mg of silver acetate were mixed in a sonication flask (Sonics Inc., Suslick flask). The mixture was sonicated using a horn sonicator at 1-s-on and 1-s-off at 37% amplitude for 20 min. After sonication, the mixture turned to a black solution, and the final temperature was measured as ~90 °C. After cooling to room temperature, the solution in a sonication flask was transferred to a round-bottom flask. Then, DMF was removed using a rotary evaporator, leaving a black powder in the round-bottom flask. In order to remove any unreacted Ag acetate and loosely bound Ag nanoparticles, the sample needed to be washed with water and ethanol. For this purpose, the sample was transferred to centrifuge tubes and washed with water and ethanol five times. Ethanol was dried by blowing nitrogen across the surface of the solution, and a final product was recovered as a black powder. This synthesis procedure was repeated multiple times to synthesize enough Ag-decorated-GO for experiments that are discussed in this article.

Synthesis of Ag-Decorated-GO Sample with 20 wt % Ag Loading. In a round-bottom flask, 30.77 mg of Ag-decorated-GO (33 wt % Ag loading) and 19.23 mg of GO were mixed with 15 mL of DMF and sonicated for 1 h in a bath sonicator. Upon completion of sonication, DMF was removed from sample using a rotary evaporator. Then, the sample was transferred to centrifuge tubes and washed with ethanol 5 times. The final product was recovered as a black powder with 46 mg yield after blowing nitrogen across the surface of the sample.

Synthesis of Other Ag-Decorated-GO with 15, 10, and 5 wt % Ag Loading. These Ag-decorated-GO samples were synthesized in the same way as described in 20 wt % Ag-decorated-GO synthesis procedure. In these reactions, the weight ratio between GO and Ag-decorated-GO were changed to obtain the new Ag-decorated-GO samples with desired Ag loadings.

Successive Dilution of 33 wt % Ag-Decorated-GO To Obtain 20 and 10 wt % Ag-Decorated-GO. First, the 20 wt % Ag-decorated-GO sample was synthesized in the same way as described earlier. In the preparation of 10 wt % Ag-decorated-GO sample, 20 wt % Ag-decorated-GO (25 mg) was mixed with GO in DMF (15 mL) and sonicated for 1 h. The recovery and cleaning procedures were performed in the same way as stated in previous synthesis procedures.

Synthesis of 20 wt % Ag-GO-MWNTs. In a round-bottom flask, 9.13 mg of MWNT and 15.38 mg of 33 wt % Ag-decorated-GO were mixed with 15 mL of DMF and sonicated in a bath sonicator for 1 h. Cleaning and recovery of the sample were performed in the same way as described in the previous synthesis procedures.

Measurements. Transmission electron microscopy (TEM) images were obtained using a Hitachi H-7600 operated at 100−120 kV. Samples for TEM were prepared in butanol and drip spotted on copper grids coated with carbon. X-ray diffraction (XRD) studies were performed using a Bruker D8-Advance equipped with a Cu Kα source and a Sol-X detector. Observed XRD patterns were identified with the ICDDS crystallographic database. The mass and energetic behavior of the samples as a function of temperature were determined using thermogravimetric analysis (TGA) and differential scanning calorimetry (DSC) on a TA Q600. The solid sample was heated in an opened alumina pan from room temperature to 800 °C at 10 °C/min with air flow rate kept at 100 mL/min. A PerkinElmer 400F equipped with a continuous 785 nm laser was used to record the Raman spectrum over a wavenumber ranging from 100 to 3000 cm^{-1} by placing the solid sample on a glass slide in the sample holder for analysis.

■ ASSOCIATED CONTENT

Ⓢ Supporting Information

Experimental details and Figures S1−S6. This material is available free of charge via the Internet at http://pubs.acs.org.

■ AUTHOR INFORMATION

Corresponding Author

*E-mail Shiral.Fernando@udri.udayton.edu (K.A.S.F.).

Notes

The authors declare no competing financial interest.

■ ACKNOWLEDGMENTS

■ REFERENCES

(1) McNamara, N. D. Sonochemical synthesis and characterization of metal nanoparticle-decorated carbon supports. Master of Science Thesis, University of Dayton, OH, 2011.

(2) Cao, L.; Sahu, S.; Anilkumar, P.; Bunker, C. E.; Xu, J.; Fernando, K. A. S.; Wang, P.; Guliants, E. A.; Tackett, K. N.; Sun, Y. P. Carbon Nanoparticles As Visible-Light Photocatalysts for Efficient CO_2 Conversion and Beyond. *J. Am. Chem. Soc.* **2011**, *133*, 4754−4757.

(3) Georgakilas, V.; Gourinis, D.; Tzitios, V.; Pasquato, L.; Guldi, D. M.; Prato, M. Decorating Carbon Nanotubes with Metal or Semiconductor Nanoparticles. *J. Mater. Chem.* **2007**, *17*, 2679−2694.

(4) Rangari, V. K.; Mohammad, G. M.; Jeelani, S.; Hundley, A.; Vig, K.; Singh, S. R.; Pillai, S. Synthesis of Ag/CNT Hybrid Nanoparticles

and Fabrication of Their Nylon-6 Polymer Nanocomposite Fibers for Antimicrobial Applications. *Nanotechnology* **2010**, *21*, 1−11.

(5) Ma, P. C.; Tang, B. Z.; Kim, J.-K. Effect of CNT Decoration with Silver Nanoparticles on Electrical Conductivity of CNT-Polymer Composites. *Carbon* **2008**, *46*, 1497−1505.

(6) Li, S.; Yu, X.; Zhang, G.; Ma, Y.; Yao, J.; Keita, B.; Louis, N.; Zhao, H. Green Chemical Decoration of Multiwalled Carbon Nanotubes with Polyoxometalate-Encapsulated Gold Nanoparticles: Visible Light Photocatalytic Activities. *J. Mater. Chem.* **2011**, *21*, 2282−2287.

(7) Ruiz, O. N.; Fernando, K. A. S.; Wang, B.; Brown, N. A.; Luo, P. G.; McNamara, N. D.; Vangsness, M.; Sun, Y. P.; Bunker, C. E. Graphene Oxide:A Nonspecific Enhancer of Cellular Growth. *ACS Nano* **2011**, *5*, 8100−8107.

(8) Suhant, S.; Yamin, L.; Ping, W.; Christopher, B.; Fernando, K. A. S.; Lewis, W.; Guliants, E.; Yang, F.; Jinping, W.; Sun, Y.-P. Visible-Light Photoconversion of Carbon Dioxide into Organic Acids in Aqueous Solution of Carbon Dots. *Langmuir* **2014**, *30*, 8631−8636.

(9) Dai, L.; Chang, D. W.; Baek, J.-B.; Lu, W. Carbon Nanomaterials for Advanced Energy Conversion and Storage. *Small* **2012**, *8*, 1130−1166.

(10) Liu, R.; Li, S.; Yu, X.; Zhang, G.; Ma, Y.; Yao, J. Facile Synthesis of a Ag Nanoparticle/Polyoxometalate/Carbon Nanotube Tri-Component and Its Activity in the Electrocatalysis of Oxygen Reduction. *J. Mater. Chem.* **2011**, *21*, 14917−14924.

(11) Liu, R.; Yu, X.; Zhang, G.; Zhang, S.; Cao, H.; Dolbecq, A.; Mialane, P.; Keita, B.; Zhi, L. Polyoxometalate-Mediated Green Synthesis of a 2D Silver Nanonet/Graphene Nanohybrid as a Synergistic Catalyst for the Oxygen Reduction Reaction. *J. Mater. Chem. A* **2013**, *1*, 11961−11969.

(12) Kong, H.; Jang, J. Antibacterial Properties of Novel Poly(methyl methacrylate) Nanofiber Containing Silver Nanoparticles. *Langmuir* **2008**, *24*, 2051−2056.

(13) Yoon, K. Y.; Byeon, J. H.; Park, C. W.; Hwang, J. Antimicrobial Effect of Silver Particles on Bacterial Contamination of Activated Carbon Fibers. *Environ. Sci. Technol.* **2008**, *42*, 1251−1255.

(14) Brodie, B. C. On the Atomic Weight of Graphite. *Philos. Trans. R. Soc. London* **1859**, *14*, 249−259.

(15) Hummers, W. S.; Offeman, R. E. Preparation of Graphitic Oxide. *J. Am. Chem. Soc.* **1958**, *80*, 1339.

(16) Marcano, D. C.; Kosynkin, D. V.; Berlin, J. M.; Sinitskii, A.; Sun, Z.; Slesarev, A.; Alemany, L. B.; Lu, W.; Tour, J. M. Improved Synthesis of Graphene Oxide. *ACS Nano* **2010**, *4*, 4806−4814.

(17) Dryer, D.R; Park, S.; Bielawski, C. W.; Ruoff, R. The Chemistry of Graphene Oxide. *Chem. Soc. Rev.* **2010**, *39*, 228−240.

(18) Navarro, C. G.; Meyer, J. C.; Sudara, R. S.; Chuvilin, A.; Kurasch, S.; Burghard, M.; Kern, K.; Kaiser, U. Atomic Structure of Reduced Graphene Oxide. *Nano Lett.* **2010**, *10*, 1144−1148.

(19) Lerf, A.; He, H.; Forster, M.; Klinowski, J. Structure of Graphite Oxide Revisited. *J. Phys. Chem. B* **1998**, *102*, 4447−4482.

(20) Gao, W.; Alemany, L. B.; Ci, L.; Ajayan, P. New Insights into the Structure and Reduction of Graphite Oxide. *Nat. Chem.* **2009**, *281*, 1−6.

(21) Acik, M.; Lee, G.; Mattevi, C.; Pirkle, A.; Wallace, R. M.; Chhowalla, M.; Cho, K.; Chabal, Y. The Role of Oxygen during Thermal Reduction of Graphene Oxide Studied by Infrared Absorption Spectroscopy. *J. Phys. Chem. C* **2011**, *115*, 19761−19781.

(22) Park, S.; An, J.; Jung, I.; Piner, R. D.; An, S. J.; Li, X.; Velamakanni, A.; Ruoff, R. S. Colloidal Suspensions of Highly Reduced Graphene Oxide in a Wide Variety of Organic Solvents. *Nano Lett.* **2009**, *9*, 1593−1597.

(23) Si, Y.; Samulski, E. T. Synthesis of Water Soluble Graphene. *Nano Lett.* **2008**, *8*, 1679−1682.

(24) Allen, M. J.; Tung, V. C.; Kaner, R. B. Honeycomb Carbon: A Review of Graphene. *Chem. Rev.* **2010**, *110*, 132−145.

(25) Kamat, P. V. Graphene-Based Nanoarchitectures. Anchoring Semiconductor and Metal Nanoparticles on a Two-Dimensional Carbon Support. *J. Phys. Chem. Lett.* **2010**, *1*, 520−527.

(26) Niyogi, S.; Bekyarova, E.; Itikis, M. E.; McWilliams, J. L.; Hammon, M. A.; Haddon, R. C. Solution Properties of Graphite and Graphene. *J. Am. Chem. Soc.* **2006**, *128*, 7720−7721.

(27) Compton, O. C.; Nguyen, S. T. Graphene Oxide, Highly Reduced Graphene Oxide, and Graphene: Versatile Building Blocks for Carbon-Based Materials. *Small* **2010**, *6*, 711−723.

(28) Qiu, J.; Wang, G.; Liang, R.; Xia, X.; Yu, H. Controllable Deposition of Platinum Nanoparticles on Graphene as an Electrocatalyst for Direct Methanol Fuel Cells. *J. Phys. Chem. C* **2011**, *115*, 15639−15645.

(29) Park, S.; Lee, K. S.; Bozoklu, G.; Cai, W.; Nguyen, S. T.; Ruoff, R. S. Graphene Oxide Papers Modified by Divalent Ions—Enhancing Mechanical Properties *via* Chemical Cross- Linking. *ACS Nano* **2008**, *3*, 572−578.

(30) Rao, C. N. R.; Sood, A. K.; Subrahmanyam, K. S.; Govindaraj, A. Graphene: The New Two-Dimensional Nanomaterial. *Angew. Chem., Int. Ed.* **2009**, *48*, 7752−7777.

(31) Raveendran, P.; Fu, J.; Wallen, S. L. Completely "Green" Synthesis and Stabilization of Metal Nanoparticles. *J. Am. Chem. Soc.* **2003**, *125*, 13940−13941.

(32) Xua, C.; Wangb, X. *Colloids Surf., A* **2012**, *404*, 78−82.

(33) Doty, R. S.; Tshikhudo, T. R.; Brust, M.; Fernig, D. G. Extremely Stable Water-Soluble Ag Nanoparticles. *Chem. Mater.* **2005**, *17*, 4630−4635.

(34) Bei, F.; Hou, X.; Chang, S. L. Y.; Simon, G. P.; Li, D. Interfacing Colloidal Graphene Oxide Sheets with Gold Nanoparticles. *Chem.—Eur. J.* **2011**, *17*, 5958−5964.

(35) Gao, L.; Yue, W.; Tao, S.; Fan, L. Antibacterial Properties of Novel Poly(methyl methacrylate) Nanofiber Containing Silver Nanoparticles. *Langmuir* **2013**, *29*, 957−964.

(36) Faria, A. F.; Martinez, D. S. T.; Maraes, A. C.; Costa, M. E. H.; Barros, E. B.; Filho, A. G. S.; Paula, A. J.; Alves, O. L. Unveiling the Role of Oxidation Debris on the Surface Chemistry of Graphene through the Anchoring of Ag Nanoparticles. *Chem. Mater.* **2012**, *24*, 4080−4087.

(37) Goncalves, G.; Marques, P. A. A. P.; Granadeiro, C. M.; Nogueira, H. I. S.; Singh, M. K.; Gracio, J. Surface Modification of Graphene Nanosheets with Gold Nanoparticles:The Role of Oxygen Moieties at Graphene Surface on Gold Nucleation and Growth. *Chem. Mater.* **2009**, *21*, 4796−4802.

(38) Muszynki, R.; Seger, B.; Kamat, P. V. Decorating Graphene Sheets with Gold Nanoparticles. *J. Phys. Chem. C* **2008**, *112*, 5263−5266.

(39) Yang, H.; Zhou, W.; Yu, B.; Wang, Y.; Cong, C.; Yu, T. Uniform Decoration of Reduced Graphene Oxide Sheets with Gold Nanoparticles. *J. Nanotechnol.* **2012**, 1−8.

(40) Ismaili, H.; Geng, D.; Sun, A. X.; Kantzas, T. T.; Workentin, M. S. Light-Activated Covalent Formation of Gold Nanoparticle Graphene and Gold Nanoparticle Glass Composites. *Langmuir* **2011**, *27*, 13261−13268.

(41) Liu, M.; Zhao, H.; Chen, S.; Yu, H.; Quan, X. Interface Engineering Catalytic Graphene for Smart Colorimetric Biosensing. *ACS Nano* **2012**, *6*, 3142−3151.

(42) Pasricha, R.; Gupta, S.; Srivastava, A. K. A Facile and Novel Synthesis of Ag-Hgraphene-Based. *Nanocomposites* **2009**, *5*, 2253−2259.

(43) Schniepp, H. C.; Li, J. L.; McAllister, M. J.; Sai, H.; Alonso, M. H.; Adamson, D. H.; Prud'homme, R. K.; Car, R.; Saville, D. A.; Aksay, I. A. Functionalized Single Graphene Sheets Derived from Splitting Graphite Oxide. *J. Phys. Chem. B* **2006**, *110*, 8535−8539.

(44) Santos, I. P.; Marzen, L. M. L. Reduction of Silver Nanoparticles in DMF. Formation of Monolayers and Stable Colloids. *Pure Appl. Chem.* **2000**, *72*, 83−90.

(45) Jeong, H. K.; Jin, M. H.; An, K. H.; Lee, Y. H. Structural Stability and Variable Dielectric Constant in Poly Sodium 4-Styrensulfonate Intercalated Graphite Oxide. *J. Phys. Chem. C* **2009**, *113*, 13060−13064.

(46) Worsley, M. A.; Olson, T. Y.; Lee, J. R. I.; Willey, T. M.; Nielsen, M. H.; Roberts, S. K.; Pauzauskie, P. J.; Biener, J.; Satcher, J. H.;

294

Baumann, T. F. High Surface Area, sp^2-Cross-Linked Three-Dimensional Graphene Monoliths. *J. Phys. Chem. Lett.* **2011**, *2*, 921−925.

(47) Fan, W.; Lai, Q.; Zhang, Q.; Wang, Y. Nanocomposites of TiO$_2$ and Reduced Graphene Oxide as Efficient Photocatalysts for Hydrogen Evolution. *J. Phys. Chem. C* **2011**, *115*, 10694−10701.

(48) Sun, J.; Ma, D.; Zhang, Z.; Liu, X.; Han, X.; Bao, X.; Weinberg, G.; Pfander, N.; Su, D. Toward Monodispersed Silver Nanoparticles with Unusual Thermal Stability. *J. Am. Chem. Soc.* **2006**, *128*, 15756−15764.

(49) Zheludkevich, M. L.; Gusakov, A. G.; Voropaev, A. G.; Vecher, A. A.; Kozyrski, E. N.; Raspopov, S. A. Oxidation of Silver by Atomic Oxygen. *Oxid. Met.* **2004**, *61*, 39−48.

(50) McAllister, M. J.; Li, J.-L.; Adamson, D. H.; Schniepp, H. C.; Abdala, A. A.; Schniepp, H. C.; Abdala, A. A.; Herrera-Alonso, M.; Liu, J.; Milius, D. L.; Car, R.; Prud'homme, R. K.; Aksay, I. A. Single Sheet Functionalized Graphene by oxidation and Thermal Expansion of Graphite. *Chem. Mater.* **2007**, *19*, 4396−4404.

(51) Lu, G.; Mao, S.; Park, S.; Ruoff, R. S.; Chen, J. Facile, Noncovalent Decoration of Graphene Oxide Sheets with Nanocrystals. *Nano Res.* **2009**, *2*, 192−200.

(52) Kebaili, N.; Benrezzak, S.; Cahuzac, A.; Masson, A.; Schmidt, M.; Brechignac, C. Deposition Migration and Coalescence of Silver Nanoparticles on Carbon Surfaces. Comparison between Bent Graphite and Carbon Nanotubes from Multi Microscopy Investigation. *AMTC Lett.* **2008**, *1*, 216−217.

(53) Zhu, L.; Lu, G.; Mao, S. Chen, Ripening of Silver Nanoparticles on Carbon Nanotubes. *J. Nano: Brief Rep. Rev.* **2007**, *2*, 149−156.

(54) Jin, Z.; Nackashi, D.; Lu, W.; Kittrell, C.; Tour, J. M. Decoration, Migration, and Aggregation of Palladium Nanoparticles on Graphene Sheets. *Chem. Mater.* **2010**, *22*, 5695−5699.

(55) Muhich, C. L.; Westcott, J. Y.; Morris, T. C.; Weimer, A. W.; Musgrave, C. B. The Effect of N and B Doping on Graphene and the Adsorption and Migration Behavior of Pt Atoms. *J. Phys. Chem. C* **2013**, *117*, 10523−10535.

(56) Dutta, S.; Ray, C.; Sarkar, S.; Pradhan, M.; Negishi, Y.; Pal, T. Silver Nanoparticle Decorated Reduced Graphene Oxide (rGO) Nanosheet: A Platform for SERS Based Low-Level Detection of Uranyl Ion. *ACS Appl. Mater. Interfaces* **2013**, *5*, 8724−8732.

295

Appendix V. Development of Methodologies for Identification and Quantification of Hazardous Air Pollutants from Turbine Engine Emissions

TECHNICAL PAPER

Development of methodologies for identification and quantification of hazardous air pollutants from turbine engine emissions

David Anneken,[1] Richard Striebich,[1,*] Matthew J. DeWitt,[1] Christopher Klingshirn,[1] and Edwin Corporan[2]

[1]*University of Dayton Research Institute, Dayton, OH, USA*
[2]*Air Force Research Laboratory, Fuels Branch AFRL/RQTF, WPAFB, Dayton, OH, USA*
Please address correspondence to: Richard Striebich, University of Dayton Research Institute, 300 College Park, Dayton, OH 45469, USA; e-mail: richard.striebich@wpafb.af.mil

Aircraft turbine engines are a significant source of particulate matter (PM) and gaseous emissions in the vicinity of airports and military installations. Hazardous air pollutants (HAPs) (e.g., formaldehyde, benzene, naphthalene and other compounds) associated with aircraft emissions are an environmental concern both in flight and at ground level. Therefore, effective sampling, identification, and accurate measurement of these trace species are important to assess their environmental impact. This effort evaluates two established ambient air sampling and analysis methods, U.S. Environmental Protection Agency (EPA) Method TO-11A and National Institute for Occupational Safety and Health (NIOSH) Method 1501, for potential use to quantify HAPs from aircraft turbine engines. The techniques were used to perform analysis of the exhaust from a T63 turboshaft engine, and were examined using certified gas standards transferred through the heated sampling systems used for engine exhaust gaseous emissions measurements. Test results show that the EPA Method TO-11A (for aldehydes) and NIOSH Method 1501 (for semivolatile hydrocarbons) were effective techniques for the sampling and analysis of most HAPs of interest. Both methods showed reasonable extraction efficiencies of HAP species from the sorbent tubes, with the exception of acrolein, styrene, and phenol, which were not well quantified. Formaldehyde measurements using dinitrophenylhydrazine (DNPH) tubes (EPA method TO-11A) were accurate for gas-phase standards, and compared favorably to measurements using gas-phase Fourier-transform infrared (FTIR) spectroscopy. In general, these two standard methodologies proved to be suitable techniques for field measurement of turbine engine HAPs within a reasonable (5–10 minutes) sampling period. Details of the tests, the analysis methods, calibration procedures, and results from the gas standards and T63 engine tested using a conventional JP-8 jet fuel are provided.

Implications: HAPs from aviation-related sources are important because of their adverse health and environmental impacts in and around airports and flight lines. Simpler, more convenient techniques to measure the important HAPs, especially aldehydes and volatile organic HAPs, are needed to provide information about their occurrence and assist in the development of engines that emit fewer harmful emissions.

Introduction

As worldwide air travel continues to increase, so does the consumption of jet fuel. This increase in overall fuel usage further intensifies the need for reliable and quantitative methods for characterizing gaseous emissions from aviation sources. However, implementation of viable techniques can be difficult due to the complex sampling environment for turbine engine exhaust. Although the overall mass emissions from aircraft may be significantly lower in magnitude than other mobile sources (e.g., gasoline and diesel engine sources), they can be locally concentrated at high altitude, at flight lines, and near airports (Federal Aviation Administration, 2005). These concentrated emissions can have adverse local health and environmental impacts.

Gaseous emissions of general interest from turbine engines include carbon dioxide (CO_2), carbon monoxide (CO), nitrogen oxides (NO and NO_2), sulfur oxides (SO_x), and total unburned hydrocarbon (UHC) emissions. The UHC emissions, which are primarily released at low power conditions, include unburned fuel constituents and oxidized or pyrolyzed combustion products. Some of these compounds may have higher potential environmental and health impacts and are considered hazardous air pollutants (HAPs). HAPs are chemical species which are regulated emissions under the Clean Air Act (CAA) Amendment of 1990 (U.S. Environmental Protection Agency [EPA], 2007); however, they are only regulated for stationary sources and not for aircraft. The International Civil Aviation Organization (ICAO) has established limits for emissions of total NO_x, CO, UHC, and particulates (smoke number) from

336

commercial jet engines, but these guidelines do not include speciated emissions of individual UHCs, but rather, total response for all UHCs (Anderson et al., 2006; Kurniawan and Khardi, 2011). Consequently, there are presently no federal regulatory guidelines that address aircraft engine-related HAP emissions. The CAA Amendment of 1990 defines a major (stationary) emission source as one that emits 10 tons per year of any single HAP or 25 tons per year of any combination of HAPs. While airports are not technically regulated by the CAA, some may have HAPs emissions comparable to stationary sources (Federal Aviation Administration, 2005). Therefore, it is important to identify the levels of HAPs emitted from aircraft since they may represent a significant local emission source that may be regulated in the future.

The original list of HAPs from the CAA of 1990 includes many compounds not typically present in aircraft emissions (EPA, 1990). Spicer and others have examined HAPs from this original list, and produced shorter lists of HAPs from aircraft emissions (see Table 1) (URS Corp., 2003; Federal Aviation Administration, 2009; Spicer et al., 2009; EPA, 1999a; Kinsey, 2009). The aldehydes in this list constitute a significant fraction of the total engine emissions; formaldehyde levels alone have been reported to comprise approximately 12% of the organic emissions from military engines tested (Federal Aviation Administration, 2009). Spicer estimates the average formaldehyde levels to be more than 1,300 mg/kg fuel for specific aircraft (Spicer et al., 2009). Kinsey examined six commercial engines and found formaldehyde levels between 130 and 357 mg/kg fuel using a DNPH sampling technique (Kinsey, 2009). This study also showed the aldehydes to represent more than half of the total organic emissions. Since the Air Force used more than 2

billion gallons of JP-8 jet fuel in 2010 (Defense Logistics Agency, 2010), a significant amount of formaldehyde and other pollutants were likely emitted near airports or bases. Overall, the amount of emitted HAPs by aircraft may be both significant and similar in concentration to many stationary source emissions.

Development and implementation of simple methodologies that can be used to accurately and reliably sample and quantify selected HAPs from aviation sources would be useful to characterize the potential environmental burden of current and future systems. Specific compounds of interest pertinent to turbine engine exhaust include carbonyls (primarily aldehydes), C_1–C_6 hydrocarbons, unburned fuel components, and polycyclic aromatic hydrocarbons (PAHs). In addition to the general need for quantifying HAPs, both the Federal Aviation Administration (FAA) and the Department of Defense (DoD) have been actively pursuing the approval and certification of alternative (non-petroleum-derived) aviation fuels for use as blending feedstocks with petroleum-derived aviation fuel (Corporan et al., 2011). This may lead to substantial changes in the base fuel chemical composition and resulting emissions characteristics. Improved understanding of the impact of fuel formulation on HAPs emissions will assist in assessing the potential environmental impact of these fuels.

Measurement Methodologies for HAPs

Previous efforts have been performed to sample and quantify HAPs emissions from aircraft engines (Spicer et al., 2009; Spicer et al., 1994; Knighton et al., 2009; Corporan et al., 2005; Kinsey, 2009). The most complete of these methods for measuring a wide range of hydrocarbon species, including low-molecular-weight hydrocarbons (C_1–C_5), aromatics, and unburned fuel constituents, was completed by Spicer (Spicer et al., 2009). Exhaust sampling was performed in the field directly into passivated canisters, followed by subsequent laboratory analysis. Spicer also quantified speciated aldehydes by collection on dinitrophenylhydrazine (DNPH)-coated tubes and analysis using proton transfer reaction–mass spectrometry (PTR-MS) analysis. Aldehydes are important species for quantification due to their high relative concentrations in the exhaust and their classification as HAPs. Alternative methodologies for sampling and quantitation of aldehydes have been implemented.

Kinsey (2009) also presented a complete methodology of sampling HAPs including DNPH cartridges and gas sample canister work for nonmethane volatile organic compounds (NMVOCs) in six aircraft turbine engines. This work showed emission indexes for both the aldehydes and NMVOCs in which the aldehydes represented between 31% and 53% of the emissions measured. NMVOCs measured included C_2 through C_4 components, in addition to alkenes and alkanes. While the great majority of these were not HAPs, most of the HAPs were measured and quantified using these methods.

For example, EPA compendium Method TO-11A (EPA, 1999b) measures aldehydes by sampling in DNPH coated silica

Table 1. Table of hazardous air pollutants commonly emitted from jet engines and their chemical properties (EPA, 2009)

HAP		MW (g/mol)	BP (ºC)
Oxygenated compounds			
Formaldehyde	CH_2O	30.0	–21
Acetaldehyde	C_2H_4O	44.0	20
Propanal	C_3H_6O	58.1	48
Acrolein	C_3H_4O	56.1	53
Methanol	CH_4O	32.0	64.7
Phenol	C_6H_6O	94.1	181.7
Hydrocarbons			
1,3-Butadiene	C_4H_6	54.1	–4.4
Benzene	C_6H_6	78.1	80
Toluene	C_7H_8	92.1	111
Ethylbenzene	C_8H_{10}	106.2	136
p-Xylene	C_8H_{10}	106.2	138
m-Xylene	C_8H_{10}	106.2	139
o-Xylene	C_8H_{10}	106.2	144
Styrene	C_8H_8	104.2	145
Isopropylbenzene (cumene)	C_9H_{12}	120.2	152
Naphthalene	$C_{10}H_8$	128.2	218
2-Methylnaphthalene	$C_{11}H_{10}$	142.2	241

tubes followed by off-line solvent extraction and quantification using high-pressure liquid chromatography (HPLC). TO-11A was created to quantify 14 different aldehyde compounds for ambient air monitoring, but could be appropriate for sampling combustion or engine emissions if the required total sample volume remains low (<10 L) and the adsorptive capacity of the sampling tubes is not exceeded. This sampling approach has been used in combination with either HPLC–ultraviolet (UV) or gas chromatography–mass spectrometry (GC-MS) detection for quantitation. Real-time measurement techniques, such as tunable diode laser absorption spectroscopy (TDLAS) and gas-phase Fourier-transform infrared (FTIR) spectroscopy, can be used for characterizing engine emissions, but quantitation can be challenging and must be developed for each individual aldehyde due to measurement interferences.

Several techniques are available for the sampling of speciated (nonaldehyde) hydrocarbons from engine exhaust streams. The aforementioned studies by Spicer and coworkers used passivated sampling containers for collection, followed by detailed GC and GC-MS analysis. Although these containers can be convenient for field work due to their ease of implementation during sampling (e.g., pumps and electricity are not required), storage/transport of the large containers and posttest cleaning present several logistical challenges. An alternate methodology is to use charcoal tubes to sample and extract gas-phase hydrocarbons in exhaust streams. Charcoal tubes have been effectively used for ambient sampling of organic species (C_6–C_{20} and speciated aromatics) and occupational safety applications (National Institute for Occupational Safety and Health [NIOSH] Method 1501) (NIOSH, 2003). The potential exists to incorporate charcoal tubes for adsorbing hydrocarbons in jet engine exhaust due to their simplicity and suitability for the species of interest. Charcoal tubes are relatively inexpensive, can be used for relatively short-term sampling (5–10 minutes), and are readily transportable and stored. Following sampling, the adsorbed hydrocarbons can be extracted using a solvent (e.g., carbon disulfide) and analyzed via gas chromatography–mass spectrometry (GC-MS) or GC–flame ionization detection (GC-FID). The methods for these tubes were developed for occupational safety applications and have reduced application for some compounds and quantitation levels, especially higher polarity compounds. However, they are appropriate for many occupational exposure compounds that are also found in jet engine exhaust.

In this effort, the potential use of DNPH-coated tubes and charcoal tubes for sampling and quantitation of speciated aldehydes and hydrocarbons in jet engine exhaust was investigated. This included development of a viable methodology for sampling a known volume of engine exhaust under relevant conditions, evaluation of the collection and extraction efficiencies of the two types of tubes, identification of appropriate analytical techniques following extraction, and demonstration on a turbine engine platform. While other researchers have conducted successful HAPs analysis using canister sampling and other methods, the simplicity of sorbent tubes such as these is suitable in terms of HAP

characterization. Charcoal tubes are much less expensive and easier to transport in the field than canisters.

Experimental Methods

Exhaust gas sampling

Turbine engine gaseous emissions measurements are typically performed via extractive probe sampling at the engine exit plane. Samples are transported to analytical instrumentation using heated lines to prevent condensation of moisture and condensable hydrocarbons (Corporan, 2010). Major and minor gaseous emissions (e.g., CO_2, CO, NO_x, UHCs) are typically quantified on-line using nondispersive infrared (NDIR), chemiluminescence, FTIR, and FID instrumentation. FTIR can provide real-time on-line simultaneous measurement of several major and minor gaseous emissions, which is also extremely beneficial for determining steady-state engine operation and stabilization following engine transients. It is possible to use FTIR to attempt to monitor and quantify speciated HAPs emissions, but this can be difficult due to spectral interferences during measurement (e.g., multiple species absorbing at the same wavenumber range), making it difficult to fully resolve and quantify individual species.

For practical purposes, it is desirable to implement techniques for HAPs sampling using existing gas analysis systems. A basic flow schematic for implementing charcoal and DNPH tube sampling within a typical sampling system is shown in Figure 1. In this configuration, the heated transport line is split to provide a parallel sampling path for transport of raw sample to the DNPH and charcoal tubes. Total volume of sample gas through each sample tube can be independently controlled and quantified using high-precision mass flow controllers and sampling pumps, while specifying the total sampling duration with constant flow. The total sample duration can be varied to insure quantifiable total mass of the target HAPs are collected without exceeding the total adsorption capacity. While not used in this study, backup DNPH tubes can be used to monitor for
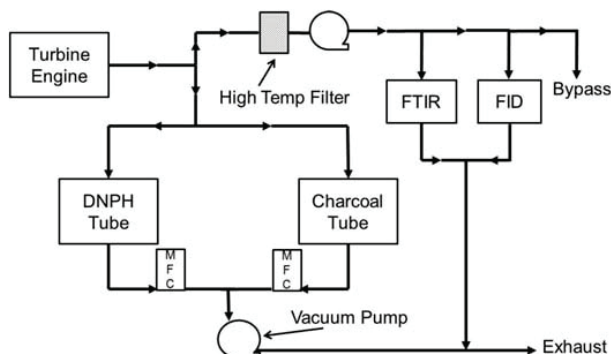
Figure 1. Schematic for implementation of DNPH and charcoal tube sampling in a gaseous emissions sampling system. Mass flow controllers (MFC) are used to control rates through the sampling media.

breakthrough; in this study, short sampling times were used to reduce breakthrough through a single DNPH tube. Charcoal tubes have a separate breakthrough region in each tube. Following sample collection, the tubes can be removed and stored for subsequent laboratory analysis, and new sampling tubes can be inserted into the flow path. A parallel bypass pathway can be implemented to allow for continuous flow of exhaust through the sample pathway during inactive sampling. The following subsections describe how this sampling approach has been used with both DNPH and charcoal tubes.

Aldehyde collection, extraction, and quantitation

Measurement of aldehydes was performed using DNPH tubes (Supelco LpDNPH H30) via a modified EPA Compendium Method TO-11A. The method is based on a specific reaction between the organic carbonyl compounds and DNPH-coated silica gel in the presence of a strong acid to form a stable hydrazone derivative, and provides a time-weighted average (TWA) measurement. DNPH tubes can adsorb a wide range of aldehyde/ketone compounds pertinent to turbine engine exhaust, with representative compounds shown in Table 2. Of the 14 components typically measured using the DNPH-coated tubes, only four are classified as HAPs: formaldehyde, acetaldehyde, acrolein, and propanal (propionaldehyde).

During exhaust sampling through the DNPH tube, a constant flow rate (between 1 and 2 SLPM) was maintained for a predetermined amount of time (typically 5–10 minutes). These parameters were determined to be appropriate for typical aldehyde levels in turbine engine exhaust. While it was difficult to know beforehand how long to collect sample through tubes, short sampling times were used so that breakthrough was avoided. No backup tubes were used due to the shorter sampling times. An ozone scrubber (Supelco, 505285) was placed immediately upstream of the DNPH tube to prevent undesired

reaction of the DNPH and aldehyde derivatives with ozone (Knighton et al., 2009). Following sample collection, the cartridges were removed and capped, placed into aluminum foil lined bags, and stored at 4ºC prior to posttest laboratory analysis. Derivatized aldehydes were extracted from the DNPH tubes using 5 mL acetonitrile (total collected volume). Analysis of the extracted compounds was performed using an HPLC-UV technique using the conditions listed in Supplemental Table 1.

A commercial standard mixture (Supelco 47285) of derivatized aldehydes (0–15 µg/mL) was used to develop a calibration curve for the HPLC-UV analysis and to determine the extraction and recovery efficiency for each compound of interest. In the event that a measured species concentration is greater than 15 µg/mL, the sample is diluted with additional acetonitrile to be within the calibration range. The corresponding gas-phase concentration of each species (C_x in µg/L) is determined as

$$C_x = \frac{m_x}{V_T} \qquad (1)$$

where m_x is the mass of component x quantified from the DNPH tube (µg), and V_T is the total standard volume of exhaust gas sampled (L). The mass of each extracted compound is determined by

$$m_x = C_i \cdot V_{ACN} \cdot \frac{100\%}{EE} \qquad (2)$$

where C_i is the concentration of compound x from the HPLC-UV analysis (µg/mL), V_{ACN} is the total volume of acetonitrile recovered during extraction (mL), and EE is the extraction efficiency (%) for each compound from the DNPH tubes.

Aromatics and C_6–C_{20} hydrocarbons sampling, extraction, and quantitation

Sampling of aromatic compounds and C_6–C_{20} hydrocarbons was performed via adsorption with charcoal tubes (Supelco ORBO 32). The charcoal tubes comply with all NIOSH and OSHA specifications for tube dimensions, adsorbent quality and particles size, divider composition, and pore size. Prior to sampling, the tube ends are removed using a tube cutter and the tube is installed in the sampling system (Figure 1). A constant sample flow rate (typically 1.0 SLPM) was drawn through the tube for a predetermined amount of time (typically 5 minutes). Following sample collection, the tubes are removed and capped, and stored at 4ºC prior to analysis. Each charcoal sample tube is comprised of two adsorbent beds separated by a section of urethane foam: The front bed (100 mg charcoal with glass wool) is used for primary sample collection while the back bed (50 mg charcoal and two foam plugs) is used to identify the occurrence of sample breakthrough. If sample analytes break through the first charcoal bed and get adsorbed on the foam, they will be counted with the smaller 50-mg bed. During laboratory analysis, the charcoal tube is scored and broken, separating each bed, with its glass wool or foam plug, into a separate GC vial. Extraction is performed

Table 2. Extraction efficiencies (EE) of an aldehyde standard solution, evaluated by EPA Method TO-11A

Compound	Extraction efficiency (EE),%	Relative standard deviation, % for EE ($n = 4$)
Acetaldehyde	95	2.6
Acrolein	59	25
Benzaldehyde	93	2.7
Butyraldehyde	85	9.6
Crotonaldehyde	51	39
Formaldehyde	94	2.1
Hexaldehyde	112	13
Isovaleraldehyde	85	7.5
m-Tolualdehyde	93	2.6
o-Tolualdehyde	93	3.0
p-Tolualdehyde	92	3.4
Propanal	93	3.2
Valeraldehyde	94	2.1

directly in the vial via addition of 1.0 mL carbon disulfide (CS_2) and manual agitation. An internal standard (n-C_{20}) is added to each vial prior to GC-MS or GC-FID analysis. Aromatic species are measured via GC-MS using a characteristic ion for each specific compound while GC-FID response and retention time is used to quantify other hydrocarbons. The conditions used during GC analysis are shown in Supplemental Table 2. The corresponding gas phase concentrations of speciated and total hydrocarbon emissions is performed using the same methodology described in eqs 1 and 2.

Results and Discussion

Evaluation of aldehydes in turbine engine exhaust

HPLC-UV analysis. Prior to implementation of DNPH tubes for sampling of turbine engine exhaust, evaluation of the analytical accuracy and adsorption/extraction efficiencies was performed. A standard solution of 14 derivatized carbonyl compounds (15 µg/mL of each), Supelco 47285, was analyzed using the HPLC-UV method and conditions shown in Supplemental Table 1. A representative HPLC chromatogram for analysis under these conditions is shown in Supplemental Figure 1. As shown, there was good separation and resolution for most compounds of interest, with the exception of acrolein and acetone, which coelute. However, the impact of coelution of these two specific compounds during actual implementation is minimized since acrolein is typically emitted in turbine engine exhaust at more than an order of magnitude higher level than acetone (Federal Aviation Administration, 2009) (acetone and acrolein were at the same concentration for this standard sample). Figure 2 displays the linearity of the

calibration curves for the HPLC response versus concentrations for the aldehydes of interest in this study.

Extraction efficiency of derivatized DNPH compounds. The extraction efficiency (EE) of derivatized compounds from the DNPH tubes is required to accurately quantify the mass of each species adsorbed during exhaust sampling. The extraction efficiencies were determined by injecting known volumes of the derivatized standard (15 µg/mL) onto DNPH tubes and performing acetonitrile extraction and quantification. Four measurements were conducted; the results with relative standard deviations (RSD) are shown in Table 2. Three important HAPs (formaldehyde, acetaldehyde, and propionaldehyde) showed extraction efficiencies greater than 93% with low standard deviations. Two specific aldehydes, acrolein and crotonaldehyde, had extraction efficiencies of 59% and 51%, respectively, with relative standard deviation (standard deviation/mean [or RSD]) of 25 and 39%. Attempts to perform additional extraction with acetonitrile showed negligible improved recovery. The poor results for crotonaldehyde and acrolein are most likely due to decomposition of these compounds on the DNPH tubes (Ho et al., 2011; Goelen et al., 1997) and the inability to separate acrolein from acetone. This known decomposition of crotonaldehyde and acrolein on DNPH tubes precludes the use of this method for accurate quantitation of these specific compounds in turbine engine exhaust. Overall, the magnitude and consistency of the EE for the majority of compounds of interest were good, providing confidence in the application of the technique for this purpose.

Recovery efficiency from sampling of gas-phase aldehydes. The potential use of a modified EPA Method TO-11A for turbine engine exhaust applications was assessed by measuring the overall efficiency of transport of HAP species through the sampling system, adsorption on the DNPH tubes under representative conditions, and solvent extraction for off-line quantitation. The combined transport, collection, and recovery efficiencies were evaluated using a standard gas mixture containing formaldehyde, acetaldehyde, and acrolein with concentrations of 6.56, 2.20, and 1.10 ppmv (parts per million volume), respectively, in nitrogen. Tests were performed using a flow system configured as represented in Figure 1, with the standard gas mixture introduced at the inlet of the sampling system. The standard mixture was drawn via a vacuum pump through heated lines maintained at 150ºC. The sample was split to provide separate streams for DNPH tube sampling and on-line measurement using an MKS Multi Gas 2030 FTIR based analyzer. This instrument was operated at a scanning rate of 1 scan/8 seconds at a spectral resolution of 0.5 cm^{-1} and a 5.11-m gas cell. The cell was operated at ambient pressure with a temperature of 150°C. The FTIR measurement provided a concurrent formaldehyde measurement and verified a steady sample flow and exhaust stream concentration. Tube sampling was performed using a constant sample flow rate of 1.0 SLPM with durations of 5, 10, 15, and 20 minutes. The total sampling time was varied to investigate the effect of tube sample loading on the measurement accuracy. Concentrations of each
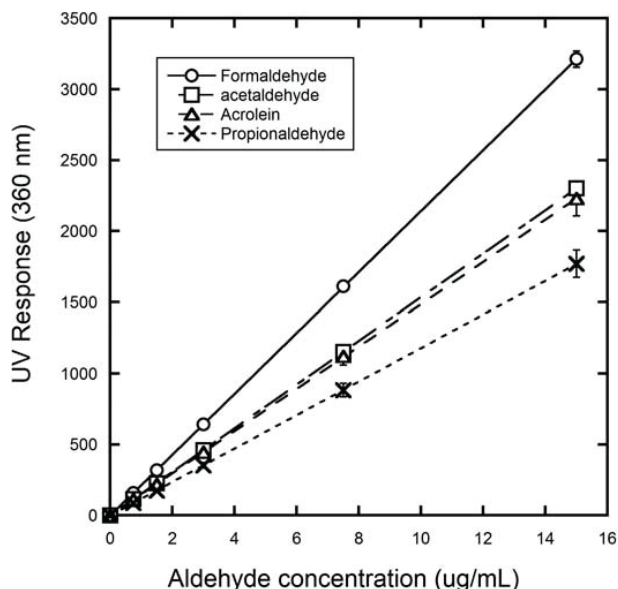

Figure 2. HPLC-UV calibration curves for representative compounds of interest.

component quantified using HPLC-UV were corrected to equivalent gas phase concentrations using eqs 1 and 2 and the corresponding EE shown in Table 2.

Experimental results are shown in Figure 3. The horizontal lines correspond to the concentration of each species in the gas standard. For the sample transport system and conditions employed, the DNPH tube method (EPA Method TO-11A) provided excellent accuracy for recovery and quantitation of both formaldehyde and acetaldehyde, with a larger uncertainty for acrolein. The average corrected gas-phase concentrations for the four different sample durations were 6.36 ± 0.12 ppmv for formaldehyde, 2.22 ± 0.05 ppmv for acetaldehyde, and 1.37 ± 0.46 ppmv for acrolein. Consistent, accurate values were obtained for sampling with higher total gas volumes, indicating sufficient adsorption capacity for the quantity of compounds extracted.

These experiments were conducted to understand the absolute accuracy of the measurement for a known mixture sampled over a wide range of total volume sampled and mass of analyte. Sampling up to 20 L of gas with excellent accuracy and precision for three solutes indicated that breakthrough of components was not readily occurring. If breakthrough were occurring, this experiment would have yielded poor or inconsistent results, especially in the higher gas volumes sampled. The 20 L of sample used in this study was 2–4 times more sample than typically used in this technique, indicating the high capacity of these sampling tubes.
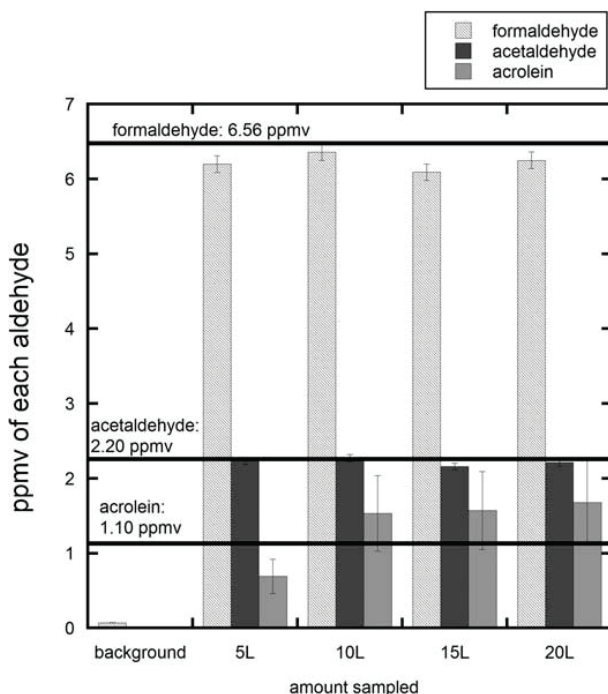
The formaldehyde measurement from the FTIR was also consistent over the test duration, but was approximately 20% higher than the DNPH measurement, with an average concentration of 7.45 ± 0.14 ppmv. The cause of the differences is not readily known, but could be due to the FTIR calibration or more likely, interferences with the other compounds in the gas mixture. On-line FTIR analysis of formaldehyde is an important measurement in the field, as it can indicate when background levels are high or if memory effects are present.

In the case of acrolein, the corrected concentrations were overestimated for the higher sample volumes and significantly underestimated for the lowest sample volume. The inaccuracies are believed to be primarily due to the poor extraction consistency and efficiency for this compound, and also possibly influenced by degradation on the DNPH tube. In general, poor extraction efficiency, poor stability, and (generally) low concentrations of this compound in turbine engine exhaust make acrolein quantitation inappropriate using this method.

Uncertainty analysis for aldehyde quantitation. Propagation of error analysis was performed to estimate the measurement uncertainty for the quantitation of aldehydes using the modified method TO-11A. The relative errors, shown in Table 3, account for the respective uncertainties in the total volume of gas sampled, solvent extraction from the DNPH tube and HPLC quantitation. In general, the RSD associated with aldehyde measurement is less than 10%. Limits of detection (LOD) were estimated using the minimum respective concentration for which there is a quantifiable HPLC response. This HPLC response was used for each component to calculate the amount possible to detect, given a 10 L sample of exhaust emissions.

Overall, the calculated relative errors are consistent with the aforementioned experiment results from testing using the gas

Figure 3. Comparison of measurement accuracy for DNPH tube sampling of selected gas-phase compounds with varying total sample gas volume. The horizontal lines represent the standard gas concentration.

Table 3. Relative errors of aldehyde compounds evaluated by EPA Method TO-11A and their limits of detection

Compound	Relative standard deviation (%)	Estimated limits of detection (LOD), ppmv**
Acetaldehyde	4.6	0.097
Acrolein	NA*	NA*
Benzaldehyde	4.6	0.23
Butyraldehyde	10	0.17
Crotonaldehyde	NA*	NA*
Formaldehyde	4.4	0.071
Hexaldehyde	13	0.11
Isovaleraldehyde	8.5	0.21
m-Tolualdehyde	4.8	0.28
o-Tolualdehyde	5.0	0.30
p-Tolualdehyde	6.1	0.31
Propanal	7.2	0.13
Valeraldehyde	4.2	0.20

Notes: *NA signifies quantitation of analyte not appropriate for this method.
**For LOD, assume a 10-L gas sample.

standard mixture, shown in Figure 3. The low estimated relative errors associated with formaldehyde and acetaldehyde are also consistent with the good experimental agreement between the measured and known concentrations.

Evaluation of modified NIOSH Method 1501 for aromatics and C_6–C_{20} hydrocarbon analysis

An initial motivation for using the NIOSH Method 1501 was to quantify individual aromatic compounds in turbine engine exhaust. In addition to being health hazards and harmful for the environment (designated as HAPs, such as benzene), these compounds are of interest due to the potential role as intermediates in the formation of polycyclic aromatic hydrocarbons (PAHs), and subsequently soot. Charcoal has a high affinity for hydrocarbon adsorption, making it a viable adsorbent for this application. Following sample collection and extraction with carbon disulfide, quantitation of specific aromatics can be performed via GC-MS using extracted ion analysis. Extracted ion response is necessary due to the presence of partially combusted and unburned fuel components, which coelute with the aromatic compounds of interest. For example, Figure 4a shows a gas chromatogram of hydrocarbons extracted from a charcoal tube following sampling from a T63 turboshaft engine operated with JP-8 fuel at idle power. The chromatogram in Figure 4b represents a standard solution of several mono- and diaromatic compounds of interest.

An internal standard (n-C_{20}) was added to both solutions for quantitation. Individual calibration curves are developed for each species of interest. As shown, there are numerous hydrocarbon species that are present in the engine exhaust, with many being residual unburned fuel species. Due to coelution, it is not feasible to fully speciate and quantify individual components using a universal detection method (e.g., FID); however, extracted ion analysis allows for measurement of species with unique ions and is used for

Figure 4. Gas chromatographic analysis of a charcoal tube sampled from a previous test on a T63-A-700 turboshaft engine operating at idle power (a) and a standard solution of several aromatic compounds (b).

quantitation of aromatics, which are the primary hydrocarbon HAPs of interest for this application. No breakthrough of organics into the second charcoal bed occurred during these analyses due to the short sampling duration. The short sampling times may have resulted in less sensitivity for these compounds than longer times would have allowed.

The presence of unburned fuel constituents in turbine engine exhaust is noteworthy. It is typically assumed that UHC emissions are partially oxidized or pyrolyzed products, and not unreacted fuel constituents, especially for high-efficiency turbine engines. Identification and quantification of unreacted fuel in turbine engine exhaust demonstrates that fuel-rich pockets can survive the high pressure and temperature combustion zone without reaction. Unreacted fuel constituents have been observed in the exhaust of the aforementioned T63 engine, and during recent testing from higher-efficiency turbine engines (CFM56 and F117) (Cain et al., 2013). The measurement and quantitation of the unreacted fuel make up a relatively simple analysis that can be performed directly using a flame ionization detector (FID).

Extraction efficiency from sampling of aromatic HAP compounds. Similar to the DNPH tube methodology, estimation of the extraction efficiency of aromatic compounds from the charcoal tubes is required to determine the mass of each species adsorbed during sample collection. Efficiencies were determined by injecting small volumes of a standard solution of aromatic compounds onto the front bed of the charcoal tubes using a microliter syringe. Following injection, the front bed was removed and extracted using the solvent extraction method described previously. The corresponding extraction efficiencies were calculated using the ratio of the extracted concentrations to those obtained for the standard solutions injected directly into 1.0 mL of carbon disulfide.

The extraction efficiencies, shown in Table 4, were evaluated over a wide concentration of aromatic compounds (1–500 μg). Averages of lower concentrations (1–20 μg) and higher concentrations (21–500 μg) show that for most compounds, there is a reasonable agreement in extraction efficiency over this wide concentration range. However, styrene and phenol showed significantly different and inconsistent extraction efficiencies depending on the concentration range. At low concentrations, it is more difficult to recover these two polar compounds. Diaromatics, such as naphthalene and alkylnaphthalenes, also have lower extraction efficiencies than alkylbenzenes, likely due to their increased polarity. In general, compounds present at higher concentrations were extracted with a slightly better efficiency than when present at lower concentrations. Highly polar compounds, such as phenol, have very low extraction efficiencies, indicating that this methodology is not appropriate for accurate quantitation of such compounds, even though it may occasionally be detected.

The RSD for the extraction efficiencies were calculated over 4–6 different concentrations between 1 and 500 μg/mL by
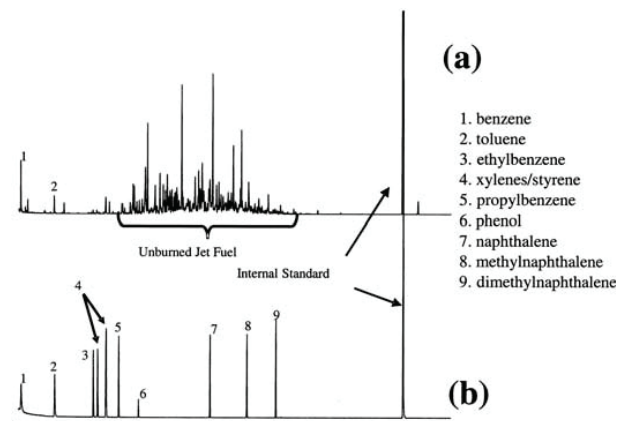
303

Table 4. Extraction efficiencies of select aromatic compounds from charcoal tubes

Compound	Extraction efficiency (EE), 1—20 µg	Relative standard deviation, %, 1–20 µg	Extraction efficiency (EE), 20–500µg	Relative standard deviation, %, 20–500 µg
Benzene	98	4.8	99	0.9
Toluene	96	7.1	100	0.6
Ethylbenzene	97	6.6	100	0.3
m,p-Xylene	96	7.8	99	1.3
Styrene	38	65	74	29
o-Xylene	88	14	**ND	**ND
Isopropylbenzene	94	12	**ND	**ND
Phenol	1	180	8.0	96
Naphthalene	29	33	49	24
Naphthalene, 2-methyl	35	20	51	24
Naphthalene, 1, 3-dimethyl*	48	21	59	13

Notes: *Not a regulated HAP. **ND indicates the extraction efficiency of this compound was not determined.

comparing spiked tube samples to spiked solvent samples; these show excellent consistency for mono-aromatic compounds. Averages for EE are shown in Table 4 for two ranges (1–20 and 20–500 µg). Diaromatics have relatively low extraction efficiencies (29–45% for the 1–20 µg range) with extraction efficiency RSD of 25–34%. These allow reasonable estimation of the emission levels of these types of compounds, but with a high uncertainty interval.

Based on previously reported emission inventories (Spicer et al., 2009), it is expected that exhaust gas concentrations for several engines of interest should be on the order of 0–2 µg/L gas sampled for individual alkyl aromatics and 0–0.5 µg /L gas sampled for naphthalene. For expected sampling durations (5–10 minutes) and flow rates (1 liter per minute) used with this technique, it is anticipated that the mass range of approximately 1–20 µg of each compound will be adsorbed during sampling.

Relative errors for aromatic HAP analysis. Propagation of error analysis was performed for the measurement of aromatic species via the NIOSH 1501 method, assuming a total adsorbed mass of 0–20 µg. Table 5 lists the calculated relative error of each compound under sample conditions of 1 SLPM for 10 minutes. In this propagation of error analysis, the replicate (n = 3) analyses of a 5 µg spike of a standard solution on a charcoal tube were used to estimate the standard deviation of the extraction and analysis.

Limits of detection were calculated using the lowest concentration of the standard solution. A 1-µL spike of this mixture provided some minimally detectable responses, from which were calculated concentrations, adjusted using blank correction and EE for each compound. There were two compounds that were not well quantified using this method, styrene and phenol. Low extraction efficiencies (shown in Table 4) are the primary reason for not including limits of detection.

Table 5. Relative errors of selected HAPs from charcoal tubes and their limits of detection

Compound	Relative error (%)	Limit of detection (µg/L gas)**
Benzene	8.1	0.16
Toluene	11.4	0.14
Ethylbenzene	11.3	0.12
m,p-Xylene	12.1	0.12
Styrene	NA*	NA*
o-Xylene	16.8	0.12
Isopropylbenzene	15.7	0.12
Phenol	NA*	NA*
Naphthalene	10.9	0.15
Naphthalene, 2-methyl	11.0	0.12
Naphthalene, 1,3-dimethyl***	17.5	0.079

Notes: *Not appropriate analytes for this method.
**For LoD, assume a 10-L gas sample.
***Not classified as a HAP.

Demonstration of DNPH and charcoal tube sampling methodologies during sampling from a turboshaft engine

Demonstration of the two modified methods was performed during measurement of turbine engine exhaust from a T63-A-700 turboshaft engine housed in the Engine Environment Research Facility at Wright-Patterson Air Force Base. This engine has been used to investigate the effect of fuel chemical and physical properties, additives, and engine power setting on gaseous and PM emissions; details on the engine are provided elsewhere (Corporan et al., 2005, 2009; Wilson et al., 2013). During this effort, the engine was operated at several power

settings, 3% (idle) and 30% and 85% (cruise) of maximum rated power, with a specification-quality, conventional JP-8 fuel. Results reported here are for the engine operated at idle and 30% power.

Exhaust measurements were performed using a sampling system consistent with the flow schematic shown in Figure 1. Raw engine exhaust was extracted at the engine exit plane using an open bore probe (1.19 mm orifice diameter) installed parallel to the exhaust flow. The sample was transported through 25 m of 7.75-mm internal diameter stainless-steel heated lines maintained at 150ºC to prevent condensation of moisture and hydrocarbons. For HAPs sampling, the gas sample was split and connected to a manifold assembly. In addition to tube sampling, real-time FTIR (formaldehyde response) measurements were performed.

Comparisons of speciated aldehyde and aromatic measurements for several separate test cycles for the idle and 30% power settings are shown in Figures 5 and 6, respectively. As expected, the absolute emissions of these compounds are highest at the lower power setting, and decrease significantly with increasing power setting due to higher combustion efficiencies. The levels of compounds emitted at the two higher power conditions were below the lower detection limit of the respective methods. In Figure 5, the average aldehyde concentrations for the three test cycles, conducted over a 3-day period, are shown for the engine operated at idle and intermediate (30%) power. The relative standard deviation (RSD) based on $n = 6$ samples taken at idle and $n = 4$ samples at 30% power over the 3-day test period are below 18% for formaldehyde and acetaldehyde. The data variation is believed to be mostly due to variation in engine operation over three separate days. All other aldehyde compounds of interest were below the lower
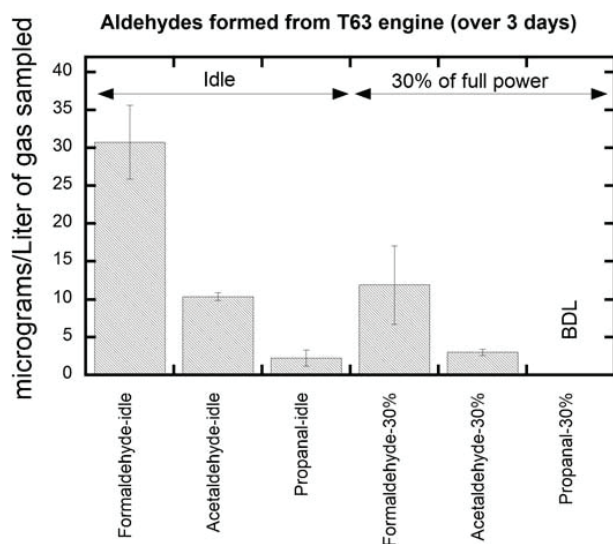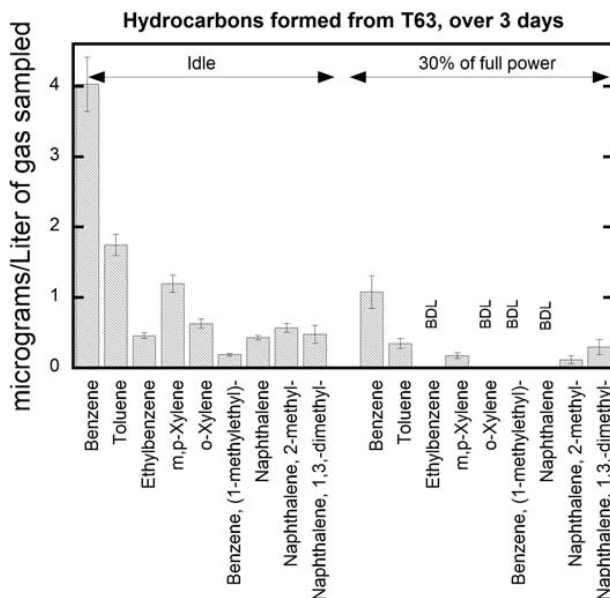
Figure 6. T63 HAP emissions captured by charcoal tubes and measured by GC-MS at idle and 30% conditions. The sampling was conducted over three consecutive days at each condition; error bars represent 2 standard deviations, calculated using mean extraction efficiencies from Table 4.

detection limit of the method. It is possible to quantify these other aldehyde species by increasing the total volume of exhaust sampled.

Because acrolein degrades on the tube and extraction efficiencies are poor, quantitation levels for these engine tests are not reported. However, acrolein was detected at idle power conditions and was below detectable levels at 30% power. Poor extraction efficiencies did not allow acrolein to be accurately and confidently quantified.

The HAPs measured using charcoal tubes are shown in Figure 6. Benzene levels over the three days of test cycles show an RSD of 16% for the idle condition; in contrast, the RSD for the method using standard solutions (Table 5) was less than 10%, indicating that the engine variability contributes to the measurement uncertainty. As observed in Figure 6, aromatic compounds were present in the exhaust in significant concentrations at low engine power. These compounds can be emitted directly as unburned fuel constituents, in addition to being produced during combustion. Monoaromatic compounds were emitted at the highest concentrations, while diaromatics such as naphthalene and alkyl naphthalenes were observed at lower, but measurable, levels. These results agree in general with those of Spicer (Spicer et al., 1994), which are reported in an emission index format (mg/kg fuel). Like acrolein, styrene and phenol are both detected under idle conditions, but because of poor extraction efficiencies, their concentrations could not be reported accurately. Their detection implies that their actual concentration in the engine exhaust is likely higher than the amount detected (about 4 µg/L gas sampled).

Figure 5. Aldehydes from T63 engine at two conditions, idle and 30% power. The sampling was conducted over three consecutive days at each condition; error bars represent 2 standard deviations, calculated using mean extraction efficiencies from Table 2.

The error bars shown in Figure 6 indicate one standard deviation from the mean for the measurements of hydrocarbon at idle ($n = 6$) and 30% ($n = 4$) engine power for the T63 over 3 consecutive days. The major components of those measured using charcoal tubes (benzene and toluene) have approximately half the RSD for idle measurements as for the 30% power setting. Like the aldehyde measurements, it is suspected that much of the deviation present in the measurements was likely due to the operation of the engine over a period of 3 days. Like acrolein, styrene and phenol are not well quantified using this method, as explained earlier. However, styrene was formed at detectable levels during idle combustion.

It was difficult to compare emissions levels with literature data (Spicer, 2009; Kinsey, 2009) because the aircraft engines and operating conditions were different. However, at low power conditions (idle) the benzene concentration determined during this study was lower than that reported by the other two studies: emissions index of 0.4 mg/kg fuel as compared to 9.25 mg/kg fuel (Spicer, 2009) or 32.4 mg/kg fuel (Kinsey, 2009). The T63, a helicopter engine, is very different than the engines from the F-15 or C-130 used in the two studies as it is older, and T63 testing was conducted on the engine in a laboratory, not while the engine was on the wing of an operational aircraft.

This technique could have been improved by sampling a higher volume of gaseous emission, either by increasing the flow rate through each tube, or sampling for longer times. However, the pressures of keeping short sampling times to reduce engine time-at-condition (especially in the field) were significant and larger samples from higher flow rates increased the amount of water coating the sorbents, as well as concerns about breakthrough. The conditions and methods chosen represented a reasonable, simple, and inexpensive way to obtain the aldehyde and hydrocarbon data. While methods of canister sampling have advantages in measuring polar hydrocarbons (which are not well measured in sorbent tubes), the simplicity and economy of sorbent tubes provide a reasonable alternative for many labs.

Conclusion and Recommendations

Two established methods, EPA Method TO-11A and NIOSH Method 1501, typically used for the sampling and analyses of hydrocarbon pollutants in ambient air monitoring, were evaluated for the potential to quantify HAP emissions in turbine engine aircraft exhaust. Results show that the EPA Method TO-11A (DNPH tubes) is suitable for measuring speciated aldehydes for the expected concentration ranges, except for acrolein and crotonaldehyde, which decompose following adsorption. Among the aldehydes, formaldehyde and acetaldehyde are well measured by this technique, as validated using gas-phase standards. This result is promising, as these two species have been reported to be present at high concentrations in turbine engine exhaust. Real-time monitoring of selected aldehydes, which can be performed using FTIR in conjunction with DNPH sampling, can provide an effective approach to verify the stability of engine operation and transfer line background before conducting composite DNPH tube sampling.

NIOSH Method 1501 (charcoal tubes) offers an effective technique for sampling and measuring organic volatiles in engine exhaust. A wide range of unburned hydrocarbons, including unreacted jet fuel and single-ring aromatics, can be characterized with a reasonable degree of accuracy using this methodology. Higher molecular weight hydrocarbon compounds (e.g., naphthalene) have lower extraction efficiencies than monoaromatics; however, the consistent extraction efficiencies provide the potential for accurately quantifying these types of species in engine exhaust. This method has limitations with regard to polar species such as phenol and styrene due to poor extraction from the charcoal matrix. Efforts are underway to characterize the sampling and solvent extraction efficiency of unburned fuel onto charcoal tubes, which will allow correlation to total UHC concentrations using a standard on-line FID.

Supplemental Materials

Supplemental data for this article can be accessed at http://dx.doi.org/10.1080/10962247.2014.991855.

References

Anderson, B.E., G. Chen, and D.R. Blake. 2006. Hydrocarbon emissions from a modern commercial airliner. *Atmos. Environ*. 40:3601–12. doi:10.1016/j.atmosenv.2005.09.072

Cain, J., M.J. DeWitt, D. Blunck, D, Corporan, E., R.C. Striebich, D. Anneken, C. Klingshirn, W.M. Roquemore, and R. Vander Wal. 2013. Characterization of gaseous and particulate emissions from a turboshaft engine burning conventional, alternative, and surrogate fuels. *Energy Fuels* 27: 2290–302. doi:10.1021/ef400009c

Corporan, E., R. Reich, O. Monroig, M. J. DeWitt, V. Larson, T. Aulich, M. Mann, and W. Seames. 2005. Pollutant emissions of a JP-8-fueled turbine engine. *J. Air Waste Manage. Assoc*. 55(7): 940−49. doi:10.1080/10473289.2005.10464680

Corporan, E., M.J. DeWitt, C.D. Klingshirn, R. Striebich, and M.-D. Cheng. 2010. Emissions characteristics of military helicopter engines with JP-8 and Fischer–Tropsch fuels, *J. Propulsion Power* 26:317–24. doi:10.2514/1.43928

Corporan, E., T. Edwards, L. Shafer, M.J. DeWitt, C. Klingshirn, S. Zabarnick, Z. West, R. Striebich, J. Graham, and J. Klein. 2011. Chemical, thermal stability, seal swell, and emissions studies of alternative jet fuels. *Energy Fuels*, 25:955–66. doi:10.1021/ef101520v

Defense Logistics Agency. 2010. Petroleum Quality Information System (PQIS) annual report (2010). Fort Belvoir, VA. http://www.energy.dla.mil

Federal Aviation Administration, 2005. Primer on emissions from aircraft engines. http://www.faa.gov/regulations_policies/policy_guidance/envir_policy/media/aeprimer.pdf

Goelen, E., M. Lambrechts, and F. Geyskens. 1997. Sampling intercomparisons for aldehydes in simulated workplace air. *Analyst* 122:411–19. doi:10.1039/a607047g

Ho, S.S.H., K.F. Ho, W.D Liu, S.C. Lee, W.T. Dai, J.J. Cao, and H.S.S Ip. 2011. Unsuitability of using the DNPH-coated solid sorbent cartridge for determination of airborne unsaturated carbonyls. *Atmos. Environ.* 45: 261–65. doi:10.1016/j.atmosenv.2010.09.042

Kinsey, J.S. 2009. Characterization of emissions from commercial aircraft engines during the Aircraft Particle Emissions eXperiment (APEX) 1 to 3. EPA-600/R-09/130. http://nepis.epa.gov/Adobe/PDF/P1005KRK.pdf

Kline, S.J., and F.A. McClintock. 1953. Describing uncertainties in single-sample experiments. *Mech. Eng.* **75**:3–8.

Knighton, W.B., S.C. Herndon, and R.C Miake-Lye. 2009. Aircraft engine speciated organic gases: speciation of unburned organic gases in aircraft exhaust. EPA-420-R-09-902. http://www.epa.gov/nonroad/aviation/420r09901

Kurniawan, J.S., and S. Khard. 2011. Comparison of methodologies estimating emissions of aircraft pollutants, environmental impact assessment around airports. *Environ. Impact Assess. Rev.* 31:240–52. doi:10.1016/j.eiar.2010.09.001

National Institute for Occupational Safety and Health. 2003. Method 1501. *NIOSH Manual of Analytical Methods*, 4th ed. http://www.cdc.gov/niosh/docs/2003-154/pdfs/1501.pdf

Spicer, C.W., M.W Holdren, R.M. Riggin, and T.F. Lyon. 1994. Chemical composition and photochemical reactivity of exhaust from aircraft turbine engines. *Ann. Geophys*. 12(10/11): 944−55. doi:10.1007/s005850050116

Spicer, C.W., M.W. Holdren, K.A. Cowen, J.D. Joseph, J. Satola, B. Goodwin, H. Mayfield, A. Laskin, L. Alexander, J.V. Ortega, M. Newburn, R. Kagann, and R. Hashmonay. 2009. Rapid measurement of emissions from military aircraft turbine engines by downstream extractive sampling of aircraft on the ground: Results for C-130 and F-15 aircraft. *Atmos. Environ.* 43:2612–22. doi:10.1016/j.atmosenv.2009.09.034

URS Corporation. 2003. Select resources materials and annotated bibliography on the topic of hazardous air pollutants (HAPs) associated with aircraft, airports and aviation. DTFA 01-00-Y-01002. http://www.epa.gov/nscep/index.html.

U.S. Environmental Protection Agency. 1990. Hazardous air pollutants list. http://www.epa.gov/ttnatw01/orig189.html

U.S. Environmental Protection Agency. 1999a. Evaluation of air pollutant emissions from subsonic aircraft. EPA 420-R-99-013. http://www.epa.gov/oms/regs/nonroad/aviation /r99013.pdf

U.S. Environmental Protection Agency. 1999b. Compendium Method TO-11a (1999). EPA/625/R-96/010b. http://www.epa.gov/ttnamti1/files/ambient/airtox/to-11ar.pdf

U.S. Environmental Protection Agency. 2007. Plain English guide to the Clean Air Act. Publication EPA-456/K-07-001, Office of Air Quality. http://www.epa.gov/airquality/peg_caa/pdfs/peg.pdf

U.S. Environmental Protection Agency. 2009. Recommended best practice for quantifying speciated organic gas emissions from aircraft equipped with turbofan, turbojet and turboprop engines. Federal Aviation Administration, U.S. EPA. www.epa.gov/nonroad/aviation/420r09901.pdf

Wilson, G.R., J.T. Edwards, E. Corporan, and R.L. Freerks. 2013. Certification of alternative aviation fuels and blend components *Energy Fuels* 27: 962–66. doi:10.1021/ef301888b

About the Authors

David Anneken and **Christopher Klingshirn** are research engineers, **Richard Striebich** is a senior research engineer, and **Matthew J. DeWitt** is a distinguished senior research engineer at the University of Dayton Research Institute (UDRI), Dayton, OH, USA.

Edwin Corporan is a senior research engineer at the Air Force Research Laboratory at Wright-Patterson Air Force Base, Dayton, OH, USA.

Appendix W. Effect of Centrifugal Force on Turbulent Premixed Flames

Effect of Centrifugal Force on Turbulent Premixed Flames

Alejandro M. Briones[1]
Mem. ASME
University of Dayton Research Institute,
300 College Park,
Dayton, OH 45469
e-mail: alejandro.briones.1.ctr@us.af.mil

Balu Sekar
AFRL/RQTC, Wright-Patterson AFB,
Dayton, OH 45433

Timothy Erdmann
Innovative Scientific Solutions, Inc.,
Dayton, OH 45459
e-mail: timothy.erdmann.3.ctr@us.af.mil

The effect of centrifugal force on flame propagation velocity of stoichiometric propane–, kerosene–, and n-octane–air turbulent premixed flames was numerically examined. The quasi-turbulent numerical model was set in an unsteady two-dimensional (2D) geometry with finite length in the transverse and streamwise directions but with infinite length in the spanwise direction. There was relatively good comparison between literature-reported measurements and predictions of propane–air flame propagation velocity as a function of centrifugal force. It was found that for all mixtures the flame propagation velocity increases with centrifugal force. It reaches a maximum, then falls off rapidly with further increases in centrifugal force. The results of this numerical study suggest that there are no distinct differences among the three mixtures in terms of the trends seen of the effect of centrifugal force on the flame propagation velocity. There are, however, quantitative differences. The numerical model is set in a noninertial, rotating reference frame. This rotation imposes a radially outward (centrifugal) force. The ignited mixture at one end of the tube raises the temperature and its heat release tends to laminarize the flow. The attained density difference combined with the direction of the centrifugal force promotes Rayleigh–Taylor instability. This instability with thermal expansion and turbulent flame speed constitute the flame propagation mechanism towards the other tube end. A wave is also generated from the ignition zone but propagates faster than the flame. During propagation the flame interacts with eddies that wrinkle and/or corrugate the flame. The flame front wrinkles interact with streamtubes that enhance Landau–Darrieus (hydrodynamic) instability, giving rise to a corrugated flame. Under strong stretch conditions the stabilizing equidiffusive-curvature mechanism fails and the flame front breaks up, allowing inflow of unburned mixture into the flame. This phenomenon slows down the flame temporarily and then the flame speeds up faster than before. However, if corrugation is large and the inflow of unburned mixture into the flame is excessive, the latter locally quenches and slows down the flame. This occurs when the centrifugal force is large, tending to blowout the flame. The wave in the tube interacts continuously with the flame through baroclinic torques at the flame front that further enhances the above mentioned flame–eddy interactions. Only at low centrifugal forces, the wave intermingles several times with the flame before the averaged flame propagation velocity is determined. The centrifugal force does not substantially increase the turbulent flame speed as commented by previous experimental investigations. The results also suggest that an ultra-compact combustor (UCC) with high-g cavity (HGC) will be limited to centrifugal force levels in the 2000–3000 g range. [DOI: 10.1115/1.4028057]

Introduction

There is a need to develop advanced combustors for aircraft gas turbine engines with improved thrust-to-weight ratio and gaseous emissions, and lower pressure losses and specific fuel consumption. Such combustors would have to be able to preserve low maintenance cost and high durability. In order to accomplish this goal, it is necessary to reduce the size of the combustors. Every inch of a combustor length reduction translates to about 200 lbs. in weight savings (this is highly dependent on the engine size and type) [1]. Reductions in engine length and weight favorably impact engine thrust to weight ratio and fuel burn performance. A shorter length and smaller volume equates to a shorter residence time compared to conventional combustors. Since gaseous emissions such as NO_x tend to form in long residence time regions at elevated temperature, this is an advantage because these emissions would have less time to form within the combustor. However, a shorter combustor imposes some difficult challenges to overcome. All the fuel would have to mix with the combustor air and completely react in a shorter distance. Therefore, faster mixing of fuel with air and reactants with products as well as increased turbulent flame speeds must occur. This phenomenon could potentially lead to an increase in pressure losses in order to enhance mixing. To mitigate these increased pressure losses and further reduce engine length, the advanced UCC integrates the turbine inlet guide vanes (IGVs) within the combustor.

There are two general concepts of the UCC, viz., HGC and trapped-vortex combustor (TVC). Both concepts incorporate a circumferential cavity that is recessed from the mainstream flow. Liquid fuel spray and hot air are injected in this circumferential cavity where fuel evaporates and burns in a fuel-rich primary zone. Low pressure wakes transport the products, unburned fuel and intermediate species from the cavity to the mainstream flow to complete burning in a secondary zone at fuel-lean equivalence ratios. The reacted mixture then flows through the IGVs, which act as a nozzle to increase the Mach number and swirl angle for entry into the high pressure turbine rotor stage for power extraction. The HGC and TVC differ primarily in the manner in which fuel and air are injected in the recessed cavity, as illustrated in Fig. 1. For the UCC–TVC concept, air is axially injected into the cavity in nonaligned opposite directions, leading to a
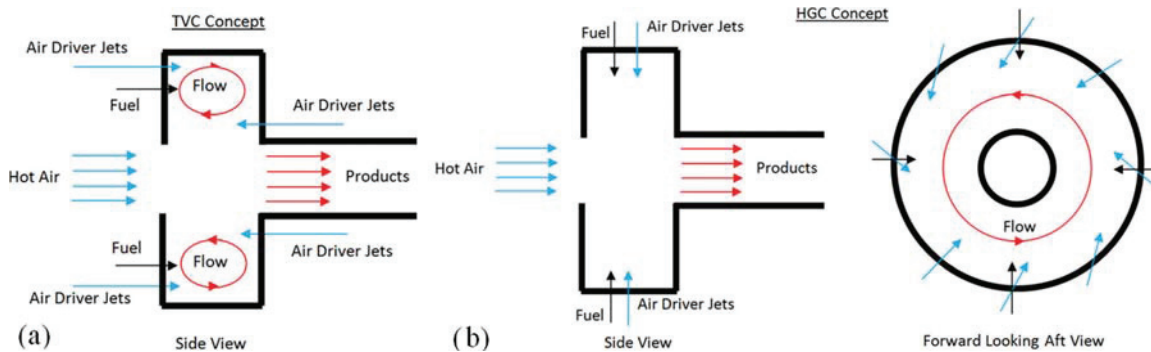

Fig. 1 Schematics of the (*a*) TVC and (*b*) HGC concepts. The IGVs are not shown.

cavity-stabilized flame vortex with its axis tangentially aligned to the circumference of the combustor. Therefore, there is no actively forced bulk swirl flow in this concept. On the other hand, the UCC–HGC cavity air is injected inwards along the outer wall of the recessed cavity at an angle to the tangent of the cavity outer wall surface, leading to a bulk circumferential flow within the cavity around the combustor annulus. This bulk swirl in the cavity generates a high centrifugal force that acts as a buoyant-like force. It impulses the hot, lower-density reacted gases in the recessed cavity radially inwards, while pushing the colder, higher-density nonreacted gases radially outward. This allows for a shorter flame that oxidizes fuel at a "bubble" flame speed [2–4] faster than its corresponding fuel–air turbulent flame speed.

The concept of the HGC was conceived from the experiments of Lewis in the 1970s. Lewis et al. [2–4] used a cylindrical tube that was filled with a premixed mixture of fuel and air. Propane and hydrogen were used in these experiments. Like a propeller, the tube was rotated about its center, and once it had reached its intended rotational speed, an igniter positioned at one end of the tube sparked a flame in the fuel–air mixture. The centrifugal force induced Rayleigh–Taylor instability by negatively stratifying the mixture density in the direction of this force. Therefore, the centrifugal force is measured in factors of the Earth's gravitational acceleration. Depending on the calculated g-load, the flame propagated toward the other end of the tube at a flame propagation velocity[2] equal or greater than the mixture's corresponding turbulent flame speed. They claimed that at low centrifugal forces (less than 500 g) there was no effect on the propane–air flame propagation velocity. However, when the centrifugal force was increased substantially above 500 g, they claimed that the turbulent flame speed increased by up to a factor of four. They reasoned that the flame propagated at a "bubble" velocity that exceeded its corresponding turbulent flame speed. The sensitivity of the flame speed of hydrogen to g-loads was impacted by the equivalence ratio of the mixture. The flame speed of stoichiometric hydrogen–air was independent of g-load whereas that of leaner premixed hydrogen–air showed sensitivity to g-load similar to stoichiometric propane–air premixed flames. It was stated that at very high centrifugal forces of nearly 3500 g the "bubble" velocity peaked and then began to decrease abruptly until the flame extinguished due to very high stretch rates.

For fuel jets such as JP-8 and S-8 that can be used in UCC–HGCs, it is critical to define the stability limits. Besides being expensive and laborious, such experiments are extremely complex because it would require the fuel to be prevaporized. This could auto-ignite the mixture and jeopardize the measurements. Therefore, computational fluid dynamics can be used to

investigate the problem at hand. Katta et al. [5] have previously investigated this problem. They simulated Lewis experiments by imposing a body force in the momentum equation parallel to the flow mainstream motion. However, their simulations also differ from those of Lewis et al. [2–4] because the tube was opened at one end. This did not allow for pressure rise that actually occurred in the experiments. However, the results compared well with Lewis experiments. In addition, Katta et al. [6] conducted a 2D simulation where they imposed high-g forces in a JP-8 fuel-rich recessed cavity for a UCC application. They found that the high-g forces had nearly negligible effect on their 2D numerical results. The unexpected result could have been due to the simplicity of the numerical model, which lacks a mainstream crossflow integral to the UCC–HGC design.

In order to shed light into this controversy, we numerically investigate the effect of centrifugal forces on the turbulent flame speed of propane–air, kerosene–air, and octane–air premixed flames by modeling a rotating cylindrical tube similar to that used in Lewis experiments. The numerical studies were first conducted using stoichiometric propane–air mixture for direct comparisons with the data available from Lewis experiments. In addition, propane is a major byproduct of natural gas, which constitutes a fossil fuel. Kerosene is used because JP-8 is a kerosene-based fuel, which is in turn derived from petroleum. According to Gokulakrishnan et al. [7], the atomic hydrogen mass percentage and the H/C atomic ratio of S-8 [7] is greater than that of JP-8. The latter, however, exhibits greater molecular weight than that of S-8. The alkane compounds concentration of S-8 is almost twice that of JP-8. For these reasons we use *n*-octane as our surrogate for S-8. Octane has lower molecular weight with greater hydrogen concentration and H/C atomic ratio than kerosene. Therefore, propane and kerosene represent the conventional fuels, whereas octane represents the alternative fuel.

The purpose of this investigation is to provide feedback to the UCC–HGC designers on how much centrifugal force will lead to improved turbulent flame speed as well as identifying the maximum centrifugal force level that could lead to blowout due to high stretch rates. Therefore, we use transient 2D scale-adaptive simulations (SAS) with global reaction model for conventional and alternative fuel premixed flame propagation in a rotating tube with a rectangular cross-sectional area. A 2D geometry is used instead of an axisymmetric geometry because the latter would demand two axes (one for the axis of symmetry and one for the axis of rotation), which is not possible in the current FLUENT software [8]. However, the major differences between the 2D planar and axisymmetric geometries are the centrifugal and Coriolis forces with respect to the axis of symmetry that explicitly appear in the latter. However, because there is no swirl with respect to the axis of symmetry in the current model, both forces are zero. Very importantly, there is another nonzero centrifugal force that is caused by rotation. Now, the only other term in an axisymmetric geometry that is not zero is the tangential shear stress on the tangential

---

[2]Flame propagation velocity is the observed flame velocity from a reference frame rotating in the same direction and angular speed as the tube, which is also located at the axis of rotation. In other words, flame propagation velocity is the summation of the local flow velocity and the turbulent flame speed.

plane. In the absence of swirl, its value is proportional to the product of the effective viscosity times the radial velocity divided by the radius. Because most of the flame propagates along the rotating tube, this shear stress would have a minor effect on the results. The reason for using global chemical mechanisms is to capture the laminar flame speed without having to solve for detailed chemistry that would be otherwise computationally expensive. The fuel–air mixture is spark ignited at one end of the rotating tube. The rotation of the tube (i.e., centrifugal force) with the negatively stratified density will induce Rayleigh–Taylor instability. The high-g loads will force unburned mixture radially outward while forcing burned mixture radially inward. This information will be critical for the UCC–HGC designers to determine the size of the circumferential cavity, and the number, the alignment, and the angle of the radial air jets.

Physical–Numerical Procedure

The commercial code FLUENT [8] has been utilized for the simulations presented here. Details of species transport equations with global reaction mechanisms are presented here such as gas-phase formulation, geometries, initial and boundary conditions, reaction mechanism, and computations.

Governing Equations and Discretization. The unsteady 2D governing equations of continuity, momentum, turbulence, and species transport are solved using the PISO segregated pressure-based solver of FLUENT [8]. Turbulence is modeled using the SAS governing equations. Standard-wall functions [9] are used to determine the near wall flow velocity. The numerical model is second-order accurate in space [10], but first-order accurate in time. The gradients and derivatives of the governing equations are computed using the least-square cell-based gradient [11], which is second-order spatially accurate. The governing equations in differential notation with absolute velocity formulation can be represented in general form as follows:

$$\frac{\partial(\bar{\rho}\Phi)}{\partial t} + \frac{\partial(\bar{\rho}(\tilde{u}-\phi y)\Phi)}{\partial x} + \frac{\partial(\bar{\rho}(\tilde{v}+\phi x)\Phi)}{\partial y}$$
$$= \frac{\partial}{\partial x}\left(\Gamma^\Phi \frac{\partial\Phi}{\partial x}\right) + \frac{\partial}{\partial y}\left(\Gamma^\Phi \frac{\partial\Phi}{\partial y}\right) + S^\Phi \qquad (1)$$

Depending on the value of Φ, this equation represents the continuity, momentum, turbulent kinetic energy, specific dissipation rate, species transport equations, and enthalpy, as shown in Table 1. This table also describes the transport coefficient Γ^Φ and the source term S_Φ for each equation. The Reynolds stresses in the momentum equations are related to the mean velocity gradients through the Boussinesq hypothesis [12]. The turbulent kinetic energy and specific dissipation rate Prandtl numbers are $\sigma_k = 1.0$ and $\sigma_\omega = 1.2$ [8], respectively. The turbulent Schmidt numbers (σ_t and Sc_t) are, respectively, 0.85 and 0.7 [8]. The ideal gas equation is dependent on both pressure and temperature. The thermodynamic and transport properties of the mixtures are both temperature- and species-dependent.

Boundary and Initial Conditions. The geometry is represented by adiabatic, impermeable wall boundary conditions, and a symmetric boundary. The axis of rotation is at the center of the tube on the symmetric plane and points out of the page. Figure 2 presents the computational domain and boundary conditions. The operating pressure of the cylindrical tube is 101,325 Pa. The fuel–air mixture is homogeneously distributed inside the tube at 300 K. All mixtures are at stoichiometric conditions because this data is ready available. In addition, this condition is chosen because it reduces thermal-diffusive instabilities that arise due to nonequidiffusive and curvature effects (i.e., there is negligible cellular instability). Moreover, stoichiometric mixtures increase their flame speeds and decrease their flame thicknesses, which, in turn, enhances the equidiffusive (Le = 1) and curvature stabilizing mechanism [13]. In other words, stoichiometric mixtures are easier to examine.

The initial and boundary conditions are as follows:

Initial conditions

$$\tilde{Y}_{C_a H_b} = \frac{1 \cdot MW_{C_a H_b}}{\left(\begin{array}{c} 1 \cdot MW_{C_a H_b} + \left(a + \dfrac{b}{4}\right) \cdot MW_{O_2} \\ + 3.76\left(a + \dfrac{b}{4}\right) \cdot MW_{N_2} \end{array}\right)}$$

Table 1   Variables, transport coefficients, and source terms appearing in the governing equation

Equations	Φ	Γ_Φ	S_Φ
Continuity	1	0	
Favre mean streamwise momentum	$\tilde{u}$	$\mu + \mu_t$	$-\dfrac{\partial\bar{p}}{\partial x} + \bar{\rho}\tilde{v}\phi + \dfrac{\partial}{\partial x}\left((\mu+\mu_t)\dfrac{\partial\tilde{u}}{\partial x}\right) + \dfrac{\partial}{\partial y}\left((\mu+\mu_t)\dfrac{\partial\tilde{v}}{\partial x}\right) + 2\mu_t\dfrac{\partial\tilde{u}}{\partial x} - \dfrac{2}{3}\left(\rho k + \mu_t\left(\dfrac{\partial\tilde{u}}{\partial x}+\dfrac{\partial\tilde{v}}{\partial y}\right)\right) + \mu_t\left(\dfrac{\partial\tilde{u}}{\partial y}+\dfrac{\partial\tilde{v}}{\partial x}\right)$
Favre mean transverse momentum	$\tilde{v}$	$\mu + \mu_t$	$-\dfrac{\partial\bar{p}}{\partial y} + \bar{\rho}\tilde{u}\phi + \dfrac{\partial}{\partial x}\left((\mu+\mu_t)\dfrac{\partial\tilde{u}}{\partial y}\right) + \dfrac{\partial}{\partial y}\left((\mu+\mu_t)\dfrac{\partial\tilde{v}}{\partial y}\right) + 2\mu_t\dfrac{\partial\tilde{v}}{\partial y} - \dfrac{2}{3}\left(\rho k + \mu_t\left(\dfrac{\partial\tilde{u}}{\partial x}+\dfrac{\partial\tilde{v}}{\partial y}\right)\right) + \mu_t\left(\dfrac{\partial\tilde{u}}{\partial y}+\dfrac{\partial\tilde{v}}{\partial x}\right)$
Turbulent kinetic energy	k	$\mu + \dfrac{\mu_t}{\sigma_k}$	$\mu_t\left[\left(\dfrac{\partial\tilde{u}}{\partial x}\right)^2 + \left(\dfrac{\partial\tilde{v}}{\partial y}\right)^2 + \dfrac{1}{2}\left(\dfrac{\partial\tilde{u}}{\partial y}+\dfrac{\partial\tilde{v}}{\partial x}\right)^2\right] - \rho c_\mu k\omega$
Specific dissipation rate	ω	$\mu + \dfrac{\mu_t}{\sigma_\omega}$	$\dfrac{\alpha\omega\mu_t}{k}\left[\left(\dfrac{\partial\tilde{u}}{\partial x}\right)^2 + \left(\dfrac{\partial\tilde{v}}{\partial y}\right)^2 + \dfrac{1}{2}\left(\dfrac{\partial\tilde{u}}{\partial y}+\dfrac{\partial\tilde{v}}{\partial x}\right)^2\right] - \rho\beta\omega^2 + \max\left[3.51\rho\kappa\left[\left(\dfrac{\partial\tilde{u}}{\partial x}\right)^2 + \left(\dfrac{\partial\tilde{v}}{\partial y}\right)^2\right]\right.$ $\left. + \dfrac{1}{2}\left(\dfrac{\partial\tilde{u}}{\partial y}+\dfrac{\partial\tilde{v}}{\partial x}\right)^2\right]\left(\dfrac{L}{L_{vk}}\right)^2 - 6\rho k \cdot \max\left[\dfrac{1}{\omega^2}\left(\left(\dfrac{\partial\omega}{\partial x}\right)^2 + \left(\dfrac{\partial\omega}{\partial y}\right)^2\right), \dfrac{1}{k^2}\left(\left(\dfrac{\partial k}{\partial x}\right)^2 + \left(\dfrac{\partial k}{\partial y}\right)^2\right)\right], 0\right]$
Species transport	$\tilde{Y}_i$	$\rho D_{im} + \dfrac{\mu_t}{Sc_t}$	R_i
Sensible enthalpy	$\tilde{h}$	$\dfrac{\lambda + \dfrac{c_p\mu_t}{Pr_t}}{c_p}$	$\dfrac{\partial}{\partial x}\left(\dfrac{\lambda + \dfrac{c_p\mu_t}{Pr_t}}{c_p}\sum_{i=1}^{N_s}(Le_i^{-1}-1)\tilde{h}_i\dfrac{\partial\tilde{Y}_i}{\partial x}\right) + \dfrac{\partial}{\partial y}\left(\dfrac{\lambda + \dfrac{c_p\mu_t}{Pr_t}}{c_p}\sum_{i=1}^{N_s}(Le_i^{-1}-1)\tilde{h}_i\dfrac{\partial\tilde{Y}_i}{\partial y}\right) - \sum_{i=1}^{N_s}h_{f,i}^\circ R_i + \left[\dfrac{Ig}{\Delta t \cdot V_{cell}}\right]_{t \le t_{ig}}$

$$\tilde{Y}_{O_2} = \frac{\left(a + \dfrac{b}{4}\right) \cdot MW_{O_2}}{\left(\begin{array}{c} 1 \cdot MW_{C_a H_b} + \left(a + \dfrac{b}{4}\right) \cdot MW_{O_2} \\ +3.76 \cdot \left(a + \dfrac{b}{4}\right) \cdot MW_{N_2} \end{array}\right)}$$

$$\tilde{Y}_{N_2} = 0.0$$

$$\tilde{u} = \tilde{v} = \tilde{h} = \tilde{Y}_{CO_2} = \tilde{Y}_{H_2O} = \tilde{Y}_{CO} = 0$$

$$k = 10 \ \mathrm{m^2/s^2} \ \text{(whole domain)}$$

$$\omega = 1/s \ \text{(whole domain)}$$

Ig = 300 J in a 1 cm × 3.35 cm area adjacent to the left end for t_{ig} = 100 μs

Wall boundary condition

$$\tilde{u} = \tilde{v} = k = \omega = \tilde{h} = \tilde{Y}_i = 0$$

Symmetric boundary condition

$$\frac{\partial \tilde{u}}{\partial y} = \tilde{v} = \frac{\partial k}{\partial y} = \frac{\partial \omega}{\partial y} = \frac{\partial \tilde{H}}{\partial y} = \frac{\partial \tilde{Y}_i}{\partial y} = 0$$

Global Reaction Mechanisms. Three global reaction mechanisms are used for propane–air [14], kerosene–air [8,14], and octane–air [14] combustion, respectively. These mechanisms are now discussed.

Propane–air global reaction mechanism

$$C_3H_8 + 3.5(O_2 + 3.76N_2) \rightarrow 3CO + 4H_2O + 18.8N_2$$
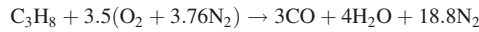
$$k_1 = 5.62 \times 10^9 \exp\left(\frac{1.256 \times 10^8}{8345T}\right)[C_3H_8]^{0.1}[O_2]^{1.65}$$

$$CO + 0.5O_2 \leftrightarrow CO_2$$
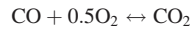
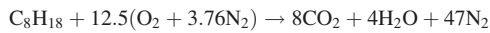$$k_{2f} = 2.239 \times 10^{12} \exp\left(\frac{1.7 \times 10^8}{8345T}\right)[CO][O_2]^{0.25}[H_2O]^{0.5}$$

$$k_{2b} = 5.0 \times 10^8 \exp\left(\frac{1.7 \times 10^8}{8345T}\right)[CO_2]$$

Kerosene–air global reaction mechanism

$$C_{12}H_{23} + 17.75(O_2 + 3.76N_2) \rightarrow 12CO_2 + 11.5H_2O + 66.74N_2$$
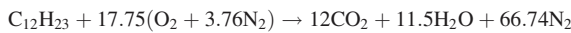
$$k_1 = 2.587 \times 10^9 \exp\left(\frac{1.256 \times 10^8}{8345T}\right)[C_{12}H_{23}]^{0.25}[O_2]^{1.5}$$

Normal octane–air global reaction mechanism

$$C_8H_{18} + 12.5(O_2 + 3.76N_2) \rightarrow 8CO_2 + 4H_2O + 47N_2$$

$$k_1 = 2.587 \times 10^9 \exp\left(\frac{1.256 \times 10^8}{8345T}\right)[C_8H_{18}]^{0.25}[O_2]^{1.5}$$

The units of the above Arrhenius parameters are in Joules, kilomoles, meters, seconds, and Kelvin. For propane–air, we used a two-step chemical reaction mechanism. For kerosene and *n*-octane, we used single-step reaction mechanism. Notice that the reaction rates of both kerosene and *n*-octane are the same. Therefore, differences between these two mechanisms will be attributed to molecular weights and density differences.

Computations. The three mixtures are ignited with a constant energy of 300 J applied to a region on the left end of the tube for
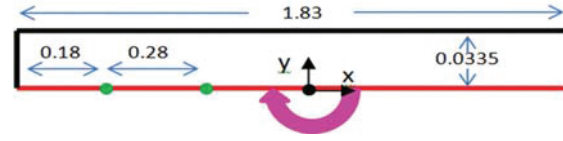
Fig. 2 Schematic of computational domain. The black lines represent impermeable adiabatic walls, whereas the red lines represent the plane of symmetry. The center of the tube and the rotation direction are also indicated. The location of the probes to measure the averaged propagation velocity is indicated by the green solid circles. The units are in meters.

100 μs (cf. Fig. 2). The ignition energy was chosen heuristically, so that all mixtures could be ignited with the same energy. The energy used here is vastly larger than the typical ignition energies used in gas turbine engine combustors because the global reaction mechanism are tuned to predict laminar flame speeds over a range of equivalence ratios and not to model ignition phenomena, which involves chain branching, propagating, and termination reactions. Consequently, the first stages of flame propagation are far from reality. Fortunately, the ignition stage in the order of hundreds of microseconds is a very small fraction of the total propagation time, which is in the order of unity to tens of milliseconds. Furthermore, there are two heat release rate probes placed in the tube symmetry plane, as indicated in Fig. 2. The locations of these probes are consistent with Lewis experiment [2]. One probe is located 18 cm away from the left wall, whereas the other is positioned 28 cm away from the previous probe. The flame propagation velocity is recorded as the time that it takes for the flame to travel between these two probes.

A constant and fixed time step of 1 μs was used for all the simulations. The same grid is used for all simulations. The grid is uniform in both *x* and *y* directions with a mesh size of 0.5 mm. It will be shown that the maximum averaged flame propagation velocity is ca. 120 m/s. Therefore, it would take the flow ca. 4.2 μs to cross a cell or more than four time steps. The simulations were conducted in the DoD Supercomputing Resource Center (DSRC) system of the Air Force Research Laboratory (AFRL). For the simulations, 16-core parallel computations were used in a supercomputer. This 64-bit supercomputer uses two 16-core Intel Xeon E5 2600 series processors at 2.6 GHz.

Results and Discussion

The results and their discussions are now presented. First, the turbulent propane–air premixed flame results are presented in detail and are compared to the results from the Lewis experiments. Then, they are followed by comparing those of the kerosene–air and *n*-octane–air premixed flames.

Propane–Air Premixed Flame. Figures 3 and 4 present, respectively, the instantaneous temperature and static pressure contours for 1 g stoichiometric turbulent propane–air premixed flame at various times. A flame is generated with the ignition source and a flat flame is observed at 2 ms. The heat release from the flame tends to laminarize the flow by decreasing density and increasing viscosity. At the same time, a weak wave departs from the left end of the tube toward the other end. The speed of this wave is ca. Mach 1.2. As time evolves, the flame moves forward due to the imposed Rayleigh–Taylor instability, thermal expansion, and the turbulent flame speed. The flame becomes corrugated, as illustrated at the snapshot at 8 ms. At ca. 9 ms, the weak wave interacts with the flame (not shown). The already wrinkled regions of the flame exhibit a flame front in an angle with the weak wave. This interaction reduces flame thickness and enhances baroclinic torque near the flame front. The latter, in turn, generates eddies with fluctuating intensities that sometimes exceed the local burning rate, corrugating the flame front. This front is exposed to
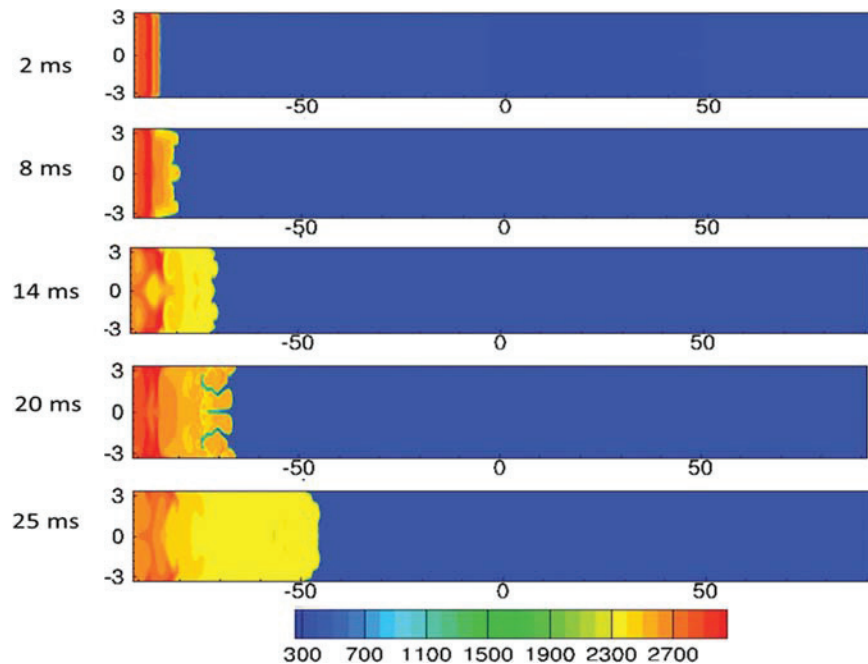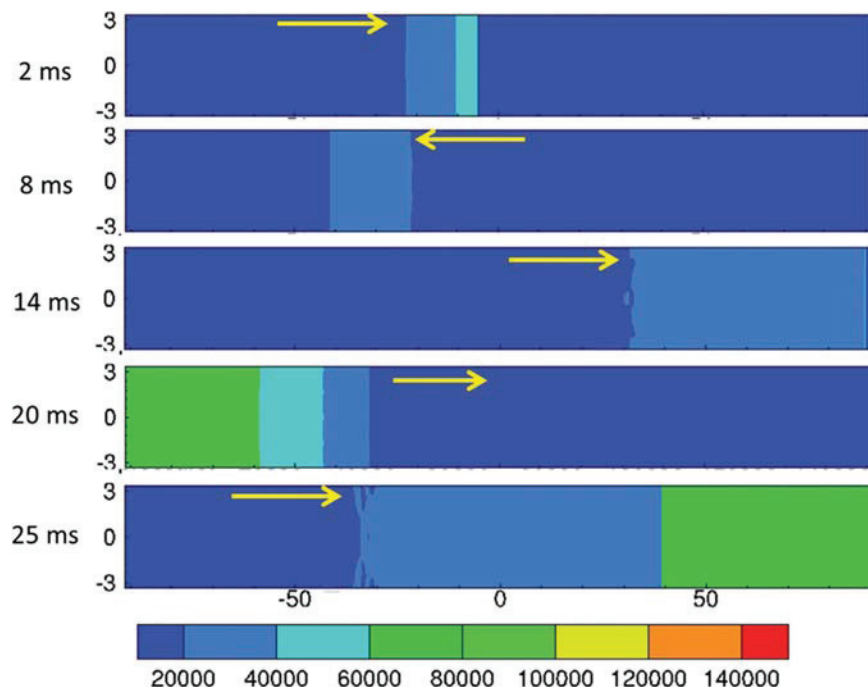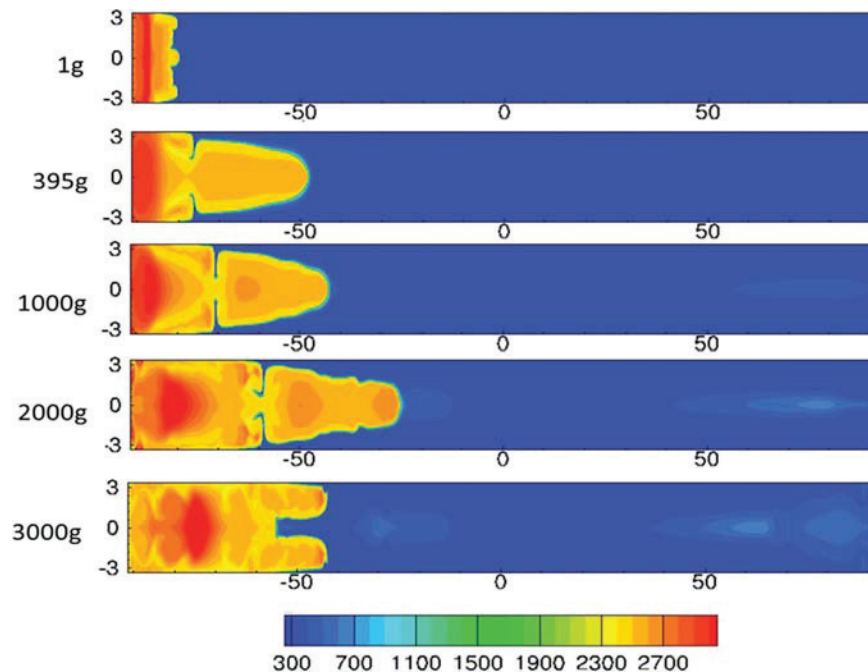
Fig. 3 Instantaneous temperature contours for 1 g stoichiometric propane–air premixed flame at $t = 2, 8, 14, 20,$ and 25 ms. The contour units are in Kelvin. Dimensions are in centimeters.

streamtubes that converge and diverge in concave and convex flame front regions (with respect to the unburned mixture). In the concave regions, the flow velocity exceeds the local burning speed and the flame front moves away from the axis of rotation (i.e., in the negative x direction). In the convex regions, the conversed

occurs. The equidiffusive-curvature stabilizing mechanism [13] cannot oppose these Landau–Darrieus (or hydrodynamic) instability [15] because the imposed stretch ends up breaking the flame front, allowing unburned mixture to penetrate into the hot gases. During this event, the flame is briefly pushed back. However, the

Fig. 4 Instantaneous static gauge pressure contours for 1 g stoichiometric propane–air premixed flame at $t = 2, 8, 14, 20,$ and 25 ms. The contour units are in Pascals. Dimensions are in centimeters.

Fig. 5 Instantaneous temperature contours for 1 g, 395 g, 1000 g, 2000 g, and 3000 g stoichiometric propane–air premixed flame at $t = 8$ ms. The contour units are in Kelvin. Dimensions are in centimeters.

preheating of this unburned mixture accelerates the flame again. At 14 ms, the flame has further propagated and exhibits a wrinkled flame front. In the next 6 ms, the flame is further corrugated and wrinkled with unburned mixture penetrating deeply into the flame. This is because there was a second interaction of the weak wave with the flame front at ca. 19 ms. Then, the flame accelerates and doubles its volume in just an additional 5 ms. After each interaction of the weak wave with the flame, the pressure in the wave increases again. The flame front again appears to be flat. For this mixture at this centrifugal force, the flame has reached the second probe needed to calculate the averaged flame propagation velocity.

Figure 5 shows the instantaneous temperature contours for 1 g, 395 g, 1000 g, 2000 g, and 3000 g stoichiometric turbulent propane–air premixed flame at $t = 8$ ms. At 1 g, the flame propagation velocity is very slow. It is evident that with increasing centrifugal force, the flame propagation velocity increases and reaches a maximum at 2000 g. Then, it decreases at 3000 g. The flame front shapes at 395 g, 1000 g, and 2000 g are very similar. The flame exhibits two parts. These flames have a convex shape toward the unburned mixture. This part of the flame structure does not reach the parallel walls, permitting unburned mixture to flow around this convex shape. A small neck of hot gases allows this part to join the other part of the flames. A faster flame exhibits a more wrinkled and corrugated flame front than the slower flame front (e.g., 2000 g flame versus 395 g flame or 1000 g flame versus 395 g flame). The 3000 g flame, on the other hand, exhibits a concave shape toward the unburned mixture. At this condition, corrugation is excessive, and vast amounts of unburned mixture enter the flame, locally quenching the flame. Moreover, the calculation procedure used to calculate the averaged flame propagation velocity will underestimate the results because these flames propagate faster at the walls than at the center. The flame propagation velocity primarily depends on centrifugal force/Rayleigh–Taylor instability. The fastest flames are more corrugated than wrinkled. Excessive corrugation, however, breaks the flame flowing unburned mixture into the flame. This, in turn, locally quenches the flame that ultimately slows it down.

The predicted flame propagation velocity as a function of centrifugal force is compared with measurements [3] in Fig. 6. The measurements show that there is a large scatter. At 1 g, the measurements vary from 25 to 55 m/s. It was reported that the averaged of these measurements is 40 m/s. The simulation underpredicts this value (40 versus 20 m/s). Even though there are no data below 150 g (besides that of 1 g), it was stated by Lewis [2] that the flame propagation velocity does not increase until it reaches about 500 g. This statement is dubious because the experimental data at 150 g and 300 g suggests that the arithmetic averaged flame propagation velocity increases above 40 m/s. For example, at 300 g, the measured data report a maximum of 60 m/s and minimum of 40 m/s, averaging 50 m/s. The measured flame propagation velocity peaks at nearly 2500 g[3] and then it abruptly decreases. The predictions indicate that the flame propagation velocity first increases gradually until 395 g. Then, the flame propagation velocity increases abruptly until 2000 g. Further, increase in centrifugal force decreases the flame propagation velocity. There is relatively good agreement between measurements and predictions both qualitative and quantitative. Discrepancies may be due to: (1) the 2D numerical model, which in turn suggests that the calculations are quasi-turbulent; and (2) the fact that there is no detailed chemistry to account for the correct ignition event as well as no account for extinction and re-ignition processes during flame propagation.

To determine the cause for the enhanced flame propagation due to centrifugal force, the temporal flame surface area was calculated and plotted in Fig. 7. The flame surface area was calculated by assuming that the flame rests on the isocontour of $T = 2000$ K. Note that the flame surface area is the summation of discretized flame length sectors along the isotherm multiplied by 1 cm. It is a well-known fact that turbulent flames propagate faster than laminar flames because turbulent flames are wrinkled and/or

---

[3]In the Introduction we refer to a maximum of 3500 g because that is what Lewis et al. state in their papers. However, a careful examination of the data suggests that the maximum occurs at 2500 g. Consequently, there is a better agreement of the simulations with experiments (2000 g versus 2500 g).
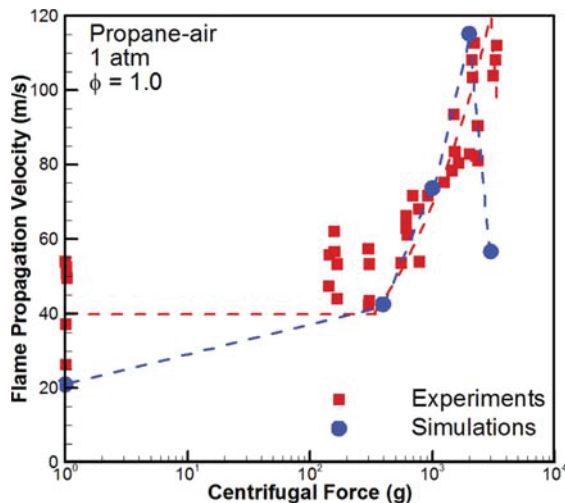
Fig. 6 Measured [3] and predicted flame propagation velocity as a function of centrifugal force for propane–air mixtures at 1 atm and $\phi = 1.0$. The dashed lines represent the trends.

corrugated. The unwrinkled flame area is 6.7 cm^2. For all cases, the temporal flame areas are larger than this value by various factors. The 1 g flame exhibits a flame area of ca. 50 cm^2 and 60 cm^2 at 10 ms and 20 ms, respectively. These peak values correspond to the time at which the flame interacted with the weak wave, as discussed above in the context of Figs. 3 and 4. As the centrifugal force increases the temporal flame surface area increases. However, it appears that at 3000 g, the flame surface area no longer increases. This is observed by comparing the lines corresponding to 2000 g and 3000 g. Even though all flames eventually interact with the weak wave, not all the measurements of averaged flame propagation velocity are affected by these events. Above 395 g, the flame propagation velocity is measured before the wave interacts with the flame. The reason we have discussed flame–wave interactions throughout this section is to provide comprehensive understanding that calculated flame propagation velocities in the rotating tube may be influenced by disturbances. However, in the UCC–HGC waves do not interact with turbulent flames.
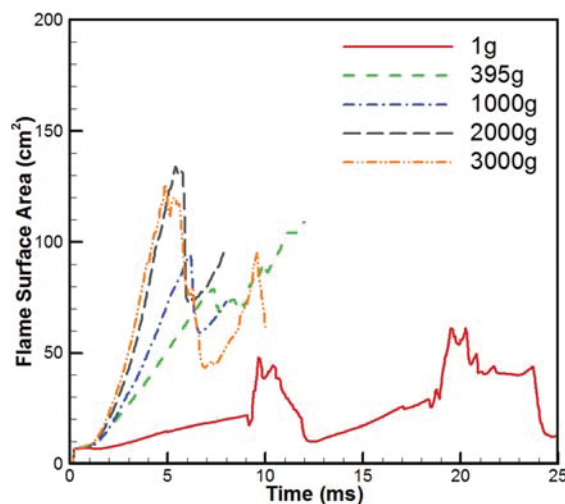

Fig. 7 Temporal flame surface area for the propane–air flames presented in Fig. 6
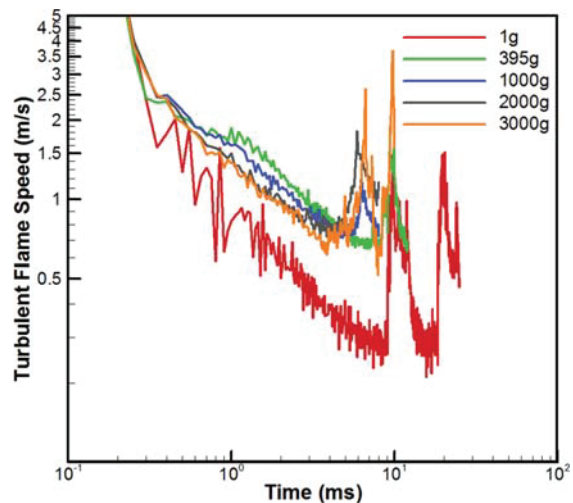

Fig. 8 Turbulent flame speed as a function of time for propane–air premixed flames presented in Fig. 6

The values reported in Fig. 6 do not represent the true turbulent flame speed (U_{T}). This speed is that value measured by an observer traveling at the flame front. The flame propagation velocity (V_{f}) is the absolute velocity measured from an observer at a rotating reference frame located at the axis of rotation. This noninertial reference frame rotates at the same speed as the tube. Therefore, the flame propagation velocity (V_{f}) is the summation of the turbulent flame speed (U_{T}) and the local flow velocity (V_{flow}) (i.e., $V_{\mathrm{f}} = U_{\mathrm{T}} + V_{\mathrm{flow}}$). The latter is due to thermal expansion and Rayleigh–Taylor instability. The turbulent flame speed is $U_{\mathrm{T}} = \dot{m}_b/(\rho_u A_u)$. It is acceptable to assume that the change in flame area from the 300 K to 2000 K isotherms is nearly negligible and, consequently, $A_u = A_b$. This is the value plotted in Fig. 7. The burning rate can be calculated by $\dot{m}_b = \left(m_b^{n+1} - m_b^n\right)/\Delta t$, where $n + 1$ and n represent two consecutive time steps. This expression means that the difference between two instantaneous burned mass regions ($m_b = \sum \bar{\rho} \cdot \Delta V_{\mathrm{cell}}$ only if $T \geq 2000\,\mathrm{K}$) provides the mass flow rate of unburned reactants entering the flame front. The temporal turbulent flame speeds for the flames discussed in the context of Fig. 7 are illustrated in Fig. 8. The figure demonstrates that the turbulent flame speed (U_{T}) varies as a function of time. Each interaction with the weak wave enhances U_{T}; however, the maximum for all centrifugal forces does not exceed 4 m/s. Therefore, at some time during propagation, U_{T} is about 10 times its corresponding laminar flame speed (i.e., ca. 0.4 m/s). Above 1 g, U_{T} is not severely affected. Consequently, it is obvious that flame propagation is due primarily to Rayleigh–Taylor instability and thermal expansion and not to enhance turbulent flame speed.

Kerosene–Air Versus n-Octane–Air Premixed Flames. The UCC–HGC will operate at high g-loads, and therefore, we are not interested in the low centrifugal forces. Propane is not a good fuel candidate for an aircraft gas turbine combustor used in the transportation sector. Kerosene and *n*-octane are better representatives of typical aviation gas turbine engine fuels. Figures 9 and 10 illustrate the results achieved for both of these fuels. Figure 9 shows the instantaneous temperature contours for 2000 g stoichiometric kerosene–air and *n*-octane–air premixed flame. Qualitatively, kerosene–air flames exhibit a more triangular flame structure than that of propane (cf. Fig. 9). The *n*-octane–air flame is clearly more elongated than both kerosene– and propane–air flames. This suggests that there are small variations on the effect of eddies on the local flame speeds. It is clear from these images that this kerosene–air flame is faster than its corresponding *n*-octane–air. For instance, at 7 ms, the kerosene flame is at ca. $x = -35$ cm location,

Journal of Engineering for Gas Turbines and Power
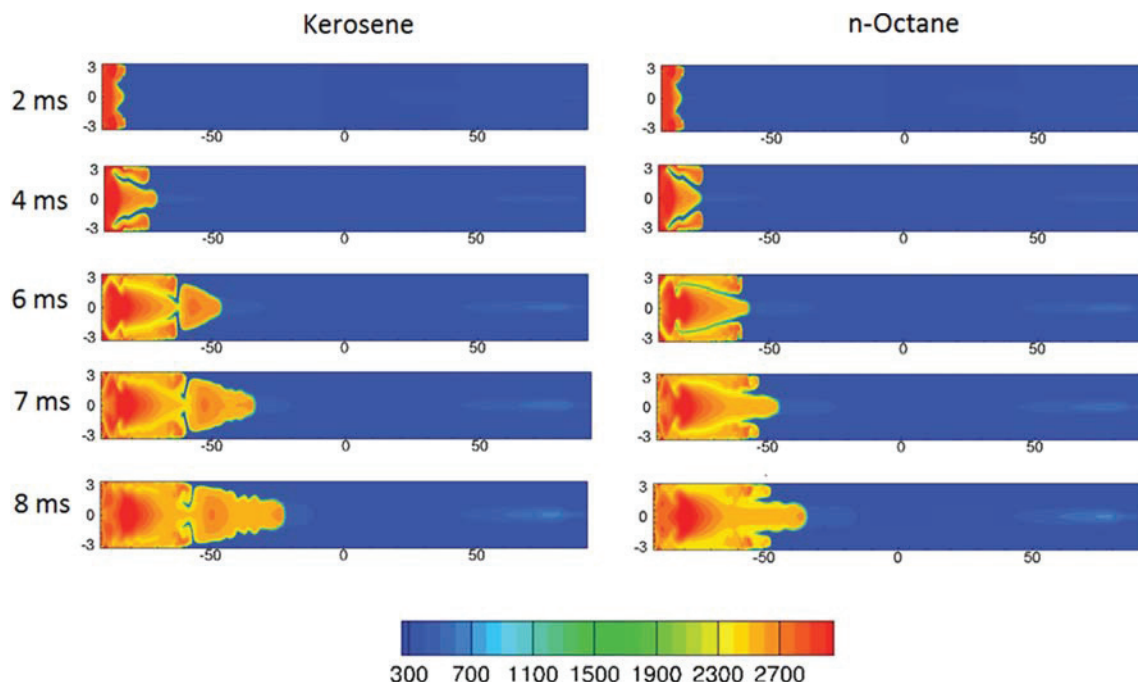
JANUARY 2015, Vol. 137 / **011501-7**

315

Fig. 9 Instantaneous temperature contours for 2000 g stoichiometric kerosene–air and *n*-octane–air premixed flame at *t* = 2, 4, 6, 7, and 8 ms. The contour units are in Kelvin. Dimensions are in centimeters.

whereas the *n*-octane–air flame is at ca. $x = -50$ cm location. As discussed above for propane–air flames, these flames exhibit two parts connected by a high temperature region neck. Unburned mixture enters the flames at 4 ms (cf. Fig. 9). This unburned mixture is preheated by the flame. This portion of the flame starts accelerating for both kerosene–air and *n*-octane–air flames. However, the latter speeds up slower than the former. At 8 ms, the kerosene–air flame is clearly corrugated. This is the maximum time needed to measure both kerosene–air and *n*-octane–air flames.

Figure 10 presents the flame propagation velocity as a function of centrifugal force for the three mixtures under investigation. It is obvious that the qualitative behavior of all flames is the same. The
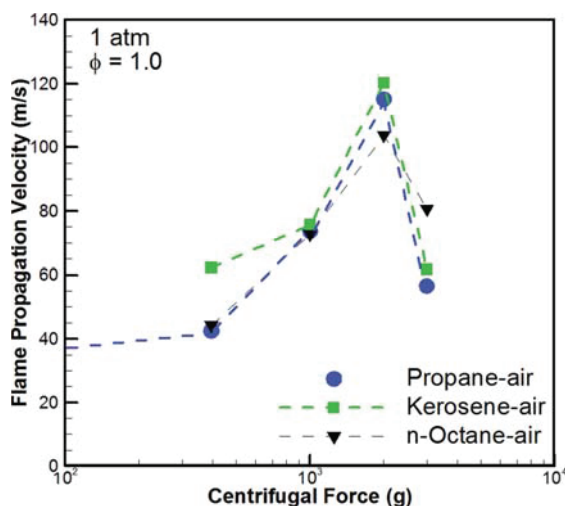

Fig. 10 Flame propagation velocity as a function of centrifugal force for atmospheric, stoichiometric turbulent propane–, kerosene–, and *n*-octane–air premixed flames

flame propagation velocity increases with increasing centrifugal force. Interestingly, all flames peak at 2000 g. This again suggests that physical forces are dominating over chemical kinetics. Even though kerosene–air and *n*-octane–air premixed flames have the same Arrhenius parameters, the flame propagation velocity of kerosene–air is larger. This is because the molecular weight and density of kerosene is larger than that of *n*-octane (1.47 kg/m^3 versus 1.27 kg/m^3). The maximum temperatures for both mixtures are the same, but the density of unburned mixture is larger for that of kerosene–air. This enhances centrifugal force and Rayleigh–Taylor instability. The propane–air mixture is lighter than that of *n*-octane (0.44 kg/m^3 versus 1.27 kg/m^3). However, the flame propagation velocity of the former is larger than that of the latter (at 2000 g). This can be attributed to the fact that the pre-exponential factor of the propane–air mixture is twice that of *n*-octane. Moreover, the propane–air and kerosene–air flames appear to be more sensitive to centrifugal forces than *n*-octane–air flames at 3000 g. Recall that at high centrifugal forces the flame is concave toward the unburned mixture (cf. Fig. 5). When the flame exhibits this shape the calculation method underpredicts the flame propagation velocity. Even though it is not shown the temporal flame surface areas and the temporal turbulent flame speeds at various g-loads are similar for the three mixtures (cf. Figs. 7 and 8). Therefore, there are no outstanding differences among the three mixtures in terms of the effect of centrifugal force on flame propagation velocity, temporal flame area, and temporal turbulent flame speed. There are, however, quantitative differences. In descending order, kerosene–air, propane–air, and lastly *n*-octane–air flames respond with high propagation velocity to centrifugal force.

Furthermore, the results presented for kerosene–air turbulent premixed flames are in contradiction with the findings of Katta et al. [6]. Recall that they showed that high-g forces in a JP-8 fuel-rich recessed cavity have no effect on the combustion field. A plausible explanation is that they used partially premixed flames where only the flame front exhibits premixed-like characteristics while most of the flame is nonpremixed. This suggests that partially premixed flames and premixed flames may respond differently to centrifugal forces. The results of Katta et al. [6] may,

however, more closely describe the effect of centrifugal forces on the current UCC–HGC design and operating conditions. In addition, the results of the current investigation proposes that the UCC–HGC should operate at fuel-rich, but near-stoichiometric cavity equivalence ratio in order to experience enhanced flame propagation velocity through centrifugal force/Rayleigh–Taylor instability and thermal expansion.

Conclusions

A numerical investigation of reacting flows for a rotating tube containing premixed mixtures of propane–, kerosene–, and n-octane–air is conducted. The tube was rotated and ignited at one end, and a flame was allowed to propagate toward the other end. The unsteady (planar) 2D governing equations of continuity, momentum, turbulence, species, and sensible enthalpy are solved using the FLUENT solver. Turbulence is modeled using the SAS. Global chemistry is used to model the chemical kinetics. The corresponding mechanisms for the before mentioned mixtures have been used to compute laminar flame speeds in the past by numerous researchers. Ignition is modeled by temporarily applying a constant energy source at one end of the tube. The numerical simulations with the propane–air mixture are validated against experimental data reported in the literature. Important conclusions are as follows:

(1) There was a relatively good agreement between literature-reported measurements and predictions of propane–air flame propagation velocity as a function centrifugal force.

(2) It was found that for all mixtures studied the flame propagation velocity increases with centrifugal force. It reaches a maximum and further increase on centrifugal force reduces the flame propagation velocity. There are no distinct differences among the three mixtures in terms of the effect of centrifugal force on flame propagation velocity. There are, however, quantitative differences. In descending order, kerosene–air, propane–air, and lastly n-octane–air flames respond with high propagation velocity to centrifugal force.

(3) The ignited mixture at one end of the tube raises the temperature and its heat release tends to laminarize the flow. The attained density difference combined with the direction of the centrifugal force promotes Rayleigh–Taylor instability. This instability with thermal expansion and turbulent flame speed constitute the flame propagation mechanism toward the other tube end.

(4) A wave is also originated but propagates faster than the flame. During propagation the flame interacts with eddies that wrinkle and/or corrugate the flame. The flame front wrinkles interact with streamtubes that enhance Landau–Darrieus (hydrodynamic) instability, giving rise to a corrugated flame.

(5) Under strong stretch conditions, the stabilizing equidiffusive-curvature mechanism fails and the flame front breaks up, allowing inflow of unburned mixture into the flame. This phenomenon slows down the flame temporarily and then the flame speeds up faster than before.

(6) If corrugation is large and the inflow of unburned mixture into the flame is excessive, the latter locally quenches and slows down the flame. This occurs when the centrifugal force is large, tending to blowout the flame.

(7) Only at low centrifugal forces, the wave intermingles several times with the flame before the averaged flame propagation velocity is determined.

(8) The centrifugal force does not substantially increase the turbulent flame speed as commented by previous experimental investigations. The peak values of turbulent flame speed ($U_T \approx 10 \times U_L$) are due to turbulent flame–wave interactions that do not occur in constant pressure configurations. The nonpeak values of U_T correspond to typical turbulent flame speeds.

(9) The results also suggest that the UCC with HGC will be limited to ca. 2000–3000 g because around these centrifugal forces, corrugation stretches the flame so much that starts to locally extinguish the flame.

Nomenclature

a = number of C atoms
A = flame area (m^2)
b = number of H atoms
c_p = specific heat capacity (J/kg K)
D_{im} = mixture-averaged diffusivity of species "i" to the mixture
Da = Damköhler number
$\tilde{h}$ = Favre mean sensible enthalpy (J/kg)
$h_{f,i}^\circ$ = enthalpy of formation at standard temperature of species "i" (J/kg)
Ig = ignition energy (J)
m_b = burned mass (kg)
$\dot{m}_b$ = mass burning rate (kg/s)
k = kinetic turbulent energy (m^2/s^2)
k_j = Arrhenius elementary reaction rate
l_t = integral length scale (m)
Le = Lewis number
$\bar{p}$ = time-averaged pressure (Pa)
Pr$_t$ = turbulent Prandtl number
S^Φ = generic source term (units depend upon variable Φ)
Sc$_t$ = turbulent Schmidt number
t = time (s)
T = temperature (K)
$\tilde{u}$ = Favre mean streamwise velocity (m/s)
U_L = turbulent flame speed (m/s)
U_T = turbulent flame speed (m/s)
$\tilde{v}$ = Favre mean transverse velocity (m/s)
V_{cell} = cell volume (m^3)
V_f = absolute flame propagation velocity (m/s)
V_{flow} = local flow velocity (m/s)
x = streamwise Cartesian coordinate (m)
y = transverse Cartesian coordinate (m)

Greek Symbols

α = specific dissipation rate constant
β = specific dissipation rate constant
Γ^Φ = generic diffusion coefficient (units depend upon variable Φ)
κ = von Kármán constant
λ = thermal conductivity (W/m K)
μ = kinetic viscosity (kg/m s)
ρ = density (kg/m^3)
σ_k = turbulent kinetic energy Prandtl number
σ_ω = specific dissipation rate Prandtl number
τ_{ij} = stress tensor (Pa/m^3)
ϕ = equivalence ratio

Φ = generic transport variable (unit depends open the variable)

ω = specific dissipation rate (1/s)

Subscripts

b = burned

i = species "i"

ig = ignition

j = reaction number "j" (e.g., 1, 2f, 2b)

p = particle

st = stoichiometry

t = turbulent

u = unburned

References

[1] Burrus, D., 2013, internal communication.

[2] Lewis, G. D., Shadowen, J. H., and Thayer, E. B., 1977, "Swirling Flow Combustion," J. Energy, **1**(4), pp. 201–205.

[3] Lewis, G. D., 1973, "Centrifugal-Force Effects on Combustion," Symp. (Int.) Combust., **14**(1), pp. 413–419.

[4] Lewis, G. D., 1971, "Combustion in a Centrifugal-Force Field," Symp. (Int.) Combust., **13**(1), pp. 625–629.

[5] Katta, V. R., Blunck, D., and Roquemore, W. M., 2013, "Effect of Centrifugal Effects on Flame Stability in an Ultra-Compact Combustor," AIAA Paper No. 2013-1046.

[6] Katta, V. R., Zelina, J., and Roquemore, W. M., 2008, "Numerical Studies on Cavity-Inside-Cavity-Supported Flames in Ultra Compact Combustor," ASME Paper No. GT2008-50853.

[7] Gokulakrishnan, P., Fuller, C. C., Klassen, M. S., and Huang, H., 2011, "Kinetic Modeling of Thermal and Catalytic Cracking of Paraffinic Surrogate Fuels Relevant to Supersonic Applications," AIAA Paper No. 2011-6106.

[8] ANSYS, 2013, ANSYS FLUENT 14.5, Theory Guide, ANSYS, Inc., Canonsburg, PA.

[9] Kader, B., 1981, "Temperature and Concentration Profiles in Fully Turbulent Boundary Layers," Int. J. Heat Mass Transfer, **24**(9), pp. 1541–1544.

[10] Barth, T. J., and Jespersen, D., 1989, "The Design and Application of Upwind Schemes on Unstructured Meshes," AIAA Paper No. 89-0366.

[11] Anderson, W., and Bonhus, D. L., 1994, "An Implicit Upwind Algorithm for Computing Turbulent Flows on Unstructured Grids," Comput. Fluids, **23**(1), pp. 1–21.

[12] Hinze, J. O., 1975, Turbulence, McGraw-Hill, New York.

[13] Law, C. K., 2006, Combustion Physics, Cambridge University, Cambridge, UK.

[14] Westbrook, C. K., and Dryer, F. L., 1981, "Simplified Reaction Mechanisms for the Oxidation of Hydrocarbon Fuels in Flames," Combust. Sci. Technol., **27**(1–2), pp. 31–43.

[15] Landau, L. D., and Lifshitz, E. M., 1959, Fluid Mechanics, Addison-Wesley, Reading, MA.

318

Appendix X. Experimental and Modeling Studies of Heat Transfer, Fluid Dynamics, and Autoxidation Chemistry in the Jet Fuel Thermal Oxidation Tester (JFTOT)

Experimental and Modeling Studies of Heat Transfer, Fluid Dynamics, and Autoxidation Chemistry in the Jet Fuel Thermal Oxidation Tester (JFTOT)

Zachary H. Sander, Zachary J. West, Jamie S. Ervin, and Steven Zabarnick*

University of Dayton Research Institute, Dayton, Ohio 45469-0043, United States

ABSTRACT: Modern military aircraft use jet fuel as a coolant before it is burned in the combustor. Prior to combustion, dissolved O_2 and trace heteroatomic species react with the heated fuel to form insoluble particles and surface deposits that can impair engine performance. For safe aircraft operation, it is important to minimize jet fuel oxidation and resultant surface deposition in critical fuel system components. ASTM D3241, "*Standard Test Method for Thermal Oxidation Stability of Aviation Turbine Fuels*" (ASTM International: West Conshohocken, PA, 2014), defines the standard test method for evaluation of the thermal oxidation stability of aviation turbine fuels. The JFTOT is a thermal stability test that measures the tendency for fuel to form deposits via heated tube discoloration and/or an increased pressure drop across an outlet filter. It is used to discriminate between fuels of poor and acceptable thermal stability. However, the fluid dynamics, heat transfer characteristics, extent of oxidation, and corresponding deposition that occurs in the JFTOT are not fully understood. An improved understanding of these JFTOT characteristics should help in the interpretation of conventional and alternative fuel thermal stability measurements and provide important information for fuel thermal stability specification enhancements and revisions. In the current effort, the JFTOT was modified to include a bulk outlet thermocouple measurement and a downstream oxygen sensor to measure bulk oxygen consumption. Tube deposition profiles were measured via ellipsometry. External tube wall temperatures were measured via pyrometry and a computational fluid dynamic (CFD) with chemistry simulation was developed. The experimental temperature measurements show that the cooling of the outlet bus bar creates a wall hot zone near the center of the tube length. A direct relationship is found between the bulk outlet temperature and JFTOT set point temperature with the bulk outlet less than the set point temperature by 60−85 °C. Several fuels were tested at varying set point temperatures with complete oxygen consumption observed for all fuels by 320 °C; a wide oxygen consumption range from 10% to 85% was measured at a set point temperature of 260 °C. The CFD simulations demonstrated the importance of complex, three-dimensional fluid flows on the heat transfer, oxygen consumption and deposition. These three-dimensional simulations showed considerable flow recirculation due to buoyancy effects, which resulted in complex fuel residence time behavior. An optimized chemical kinetic model of autoxidation with a global deposition submechanism is able to reproduce the observed oxidation and depositions characteristics of the JFTOT. Simulations of deposition were of the right order of magnitude and matched the deposit profile of comparable experimental ellipsometric deposition data. This improved CFD with chemistry simulation provides the ability to predict the location and quantity of oxygen consumption and deposition over a wide range of temperatures and conditions relevant to jet fuel system operation.

■ INTRODUCTION

Jet fuel plays a vital role in modern aircraft systems beyond its primary use for propulsion via combustion in the gas turbine engine. With dramatically increasing heat loads in modern aircraft, jet fuel is used as a coolant during its passage through numerous aircraft fuels systems (e.g., avionic, hydraulic, lubrication, and environmental control) prior to combustion. Using jet fuel as a heat sink is an enabling technology for thermal control of such subsystems, but the resultant temperature rise in jet fuel can have detrimental effects. When the fuel bulk temperature approaches ∼140 °C, dissolved oxygen (∼70 ppm) reacts with fuel hydrocarbons via an autoxidation mechanism, resulting in the formation of surface deposits and bulk insolubles.[1] ASTM D3241,[2] "*Standard Test Method for Thermal Oxidation Stability of Aviation Turbine Fuels*", defines the standard test method for thermal oxidation stability of aviation turbine fuels. The apparatus defined in the method is commonly referred to as the JFTOT, for Jet Fuel Thermal Oxidation Test. JFTOT is a trademark of the

Petroleum Analyzer Company, LLP, but specification instruments are also produced by the Falex Corporation. The JFTOT determines the tendency of an aviation turbine fuel to produce surface and bulk insolubles under such thermal-oxidative stresses. It is used to discriminate between fuels of poor and acceptable thermal stability. The test measures the formation of surface deposits on a heated aluminum rod (referred to as the JFTOT heater tube) and formation of insoluble deposits via an increase in pressure across a downstream filter. The ASTM D3241 specification rates thermal stability via a visual or metrological rating of tube surface deposition and the differential pressure increase during a test. ASTM D3241 does not attempt to closely reproduce jet fuel system deposit formation that might cause servo valve sticking, heat exchanger degradation, and/or filter plugging over the typical thousands

of hours of aircraft operation and tens of thousands of gallons of fuel usage. But rather, this relatively rapid test (2.5 h) uses a small volume of fuel (500 mL) for rating the tendency of individual fuel samples to produce deposits within a fuel system. Most current petroleum-based jet fuel specifications require a set point test temperature of 260 °C, which is significantly higher than fuel temperatures in current aircraft which are typically <140 °C. The higher test temperature is used to accelerate the deposition rate when employing these short test times and low fuel volumes. Other test temperatures are used for specialty fuels. For example, synthetic blend stocks use a test temperature of 325 °C (ASTM D7566)[3] and the JPTS specification (MIL-DTL-25524E)[4] uses a test temperature of 335 °C.

Despite the use of ASTM D3241 in nearly all jet fuel specifications, the fluid dynamics, heat transfer characteristics, extent of oxidation, and corresponding deposition that occurs in the JFTOT have not received significant experimental or modeling study. One previous study measured the oxygen consumption in the JFTOT.[5] In this work, fuel from the exit of the heater test section was routed to a gas chromatograph. Oxygen consumption was found to start near a set point temperature of 220 °C, and complete oxygen consumption occurred for all fuels tested at a set point temperature of 310 °C. This study was limited in its relevance to standard JFTOT tests since it used a custom stainless steel heater tube that had a heated length twice that of current heater tubes (127 mm compared to 60 mm).

Two previous studies reported on computational simulations of the flow and temperature distributions in the JFTOT. The first study[6] utilized a computational fluid dynamics (CFD) code to simulate the three-dimensional fluid dynamics using the measured internal temperature profile and a constant external wall temperature as boundary conditions. The second study focused on developing a time-dependent model of flow/heat transfer/chemistry interactions,[7] but only explored a two-dimensional, axisymmetric geometry. Neither modeling study considered the role of gravity in inducing buoyancy in this vertical upward flow. Both studies were limited to a single temperature-dependent, empirical surface deposition rate rather than including a chemical kinetic fuel autoxidation mechanism. The second study also failed to consider the effects of the JFTOT's cooled bus bars, forcing use of a nonuniform heat flux to empirically match the axial temperature profile. Neither of these studies was able to compare their calculations to experimental measurements, as the experiments were used to create boundary conditions for the calculations.

The recent development of chemically realistic chemical kinetic mechanisms for fuel oxidation and deposition,[8] along with improved capabilities in CFD and greater computational power, provides the ability to model the three-dimensional flow, heat transfer, and autoxidative chemistry within the JFTOT fuel flow path. In this paper, we employ a modified JFTOT to include a bulk outlet thermocouple measurement and a downstream oxygen sensor to measure oxygen consumption and outlet fuel temperature as a function of set point temperature. An ellipsometric technique is used for quantitative determination of deposit thickness along the tube.[9−11] With these experimental and computational methodologies, a range of conventional petroleum jet fuels and alternative fuels have been used to study the fluid dynamics, heat transfer, and chemistry that occur at various set point temperatures in the JFTOT.

■ EXPERIMENTAL SECTION

Experiments were conducted using an Alcor JFTOT II Jet Fuel Thermal Oxidation Tester Model 230. The inlet fuel was at ambient temperature (21−23 °C), and the JFTOT system pressure was 3.45 MPa. The JFTOT system was modified to permit measurement of both the fuel outlet temperature and the outlet dissolved oxygen concentration. The outlet temperature of the fuel leaving the JFTOT tube holder was measured by adding a 1/32 in. OD Type K thermocouple between the test tube outlet and the outlet filter in the location shown in Figure 1. Outlet fuel oxygen concentration
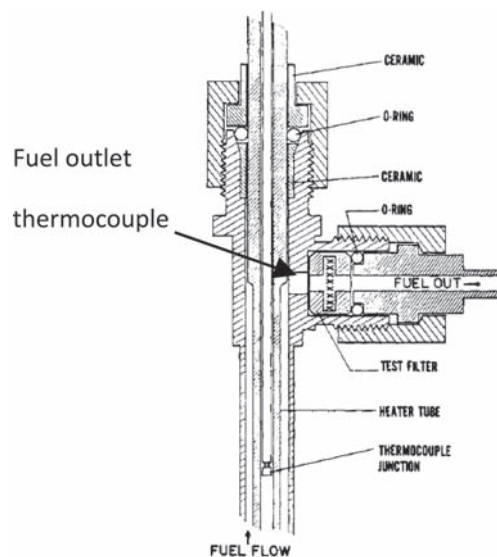
Figure 1. Location of bulk outlet temperature thermocouple near the JFTOT flow exit (modified from Hazlett et al.[12]).

measurements were made using a 12 mm Mettler-Toledo Dissolved Oxygen Sensor (InPro 6800). The oxygen sensor could not be placed immediately downstream of the JFTOT heater test section exit due to poor accessibility and the high fuel exit temperature. Instead, the outlet fuel flow was split through a tee connection and one-third of the flow (about 1 mL/min) was diverted to the oxygen sensor. A double needle metering valve was used to reduce the pressure to atmospheric pressure. With the goal of minimizing additional oxygen consumption in the oxygen sensor sampling line, a four foot length of narrow stainless steel tubing (1/16 in. O.D.) was used to reduce the fuel temperature (slowing fuel oxidation) with a minimum fuel residence time. The residence time in this narrow tubing is very small relative to the JFTOT system, and simple calculations show that additional oxygen consumption is very low due to the combined effect of reduced temperature and low residence time.

CFD modeling required accurate measurements of the internal and external wall temperature profiles to impose the correct boundary conditions. The internal metal wall temperature profile was obtained via the built-in JFTOT set point thermocouple. During specification runs, this thermocouple is placed inside an axial channel in the aluminum heater tube, 39 mm downstream of the inlet. The JFTOT uses this thermocouple to control the heater power output. After establishing and fixing the correct heater setting, this movable thermocouple was translated along the internal tube wall to obtain temperature profiles for a range of set point temperatures at 11 locations along the tube length. Examples of these measurements over the set point range 240−300 °C are shown in Figure 2. These measurements were used to create fitted curves for use as internal temperature boundary conditions for the CFD model. The shape of the temperature profiles, with a temperature peak between 30 and 40 mm and lower temperatures near the entrance and exit, is due to heat

321
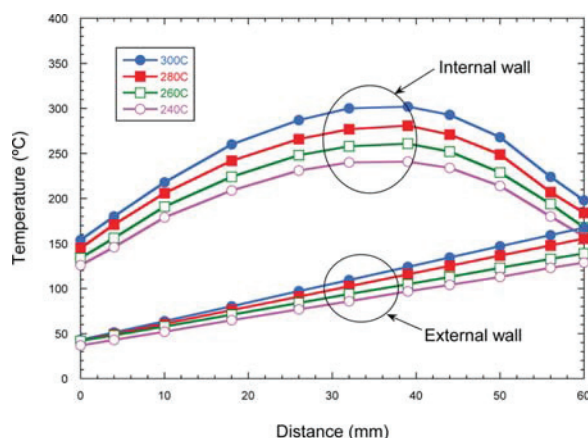
Figure 2. Measured internal and external wall temperatures vs distance from the inlet for various set point temperatures.

transfer to the water-cooled JFTOT bus bars, which are at the entrance and exit ends of the tube.

The external temperature profiles of the JFTOT tube holder were measured using a FLIR ThermoVision SC6000 infrared camera. All images were taken with a Janos Technology Inc. midwave infrared lens with a 50 mm focal length and F-stop of 2.3. Temperature profiles were obtained every 10 °C for set points from 240 to 340 °C. Multiple images were taken at different radial angles around the tube holder. The temperatures were extracted from these images, and the data were averaged to obtain temperature profiles along the external tube length. An example of these external tube holder temperatures over the set point range 240−300 °C is shown in Figure 2. The plots demonstrate that the external tube holder temperature increases linearly from the bottom fuel inlet to the top fuel outlet. These temperature measurements were used as boundary conditions in the CFD modeling.

Tube deposit depth profiles were measured using a Falex Model 430 Ellipsometer. This instrument is designed specifically for measurement of deposit depth of ASTM D3241 JFTOT heater tubes. The ellipsometric method of tube deposit rating has recently been added as an annex to the D3241 specification and to the ASTM D1655[13] Jet Fuel specification with a passing criterion of a maximum deposit depth of 85 nm at 260 °C[1] over a 2.5 mm area (i.e., maximum spot thickness). The ellipsometer deposition depth curves reported here are presented as average depths around the tube circumference at each axial location. Additional details of the experimental measurements have been reported separately.[14]

■ COMPUTATIONAL SIMULATIONS

The JFTOT system consists of a vertically oriented, electrically heated aluminum rod surrounded by an outer stainless steel tube (Figure 3). The fuel flow is upward in the annular region between the rod (heater tube) and outer tube. The annular flow region is ∼0.89 mm in width and ∼60.3 mm long for a volume of ∼0.68 mL. The standard 3 mL/min inlet flow rate yields a nominal unheated flow residence time of 13.6 s in the annular region, but the simulations performed here show that the residence time behavior is complex due to buoyancy-induced recirculation. The fuel inlet and outlet tubes are at right angles, creating a complex three-dimensional flow. Three dimensional computational simulations were performed using a refined mesh consisting of 78 618 nodes. When the temperature and species profiles changed negligibly with mesh refinement, the simulations were considered to be mesh-independent. The structured mesh was based on hexahedrons with mesh inflation
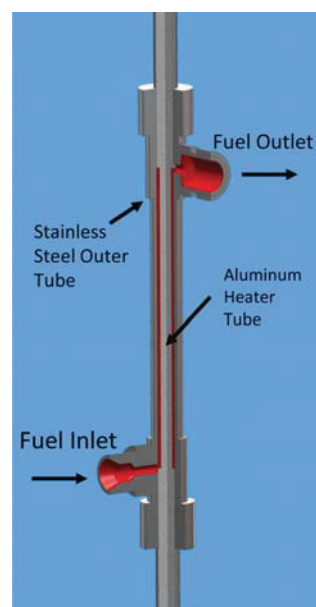
Figure 3. Diagram of the JFTOT flow geometry, three-quarter section shown; red colored surfaces are fuel wetted walls.

near the tube walls to correctly capture the behavior in this laminar flow.

Temperature-dependent fuel properties were obtained via SUPERTRAPP software.[15] SUPERTRAPP is an interactive program for predicting thermodynamic and transport properties of pure hydrocarbon fluids and mixtures. Temperature-dependent thermodynamic and transport properties were generated using the "petroleum fraction" (with an average boiling point of 207 °C and an API gravity of 42.3) capability of SUPERTRAPP at a pressure of 500 psig.

Three dimensional simulations were conducted using Fluent (v15.0) software,[16] which solved the mass, species transport, energy, and momentum equations by the finite volume method. The laminar form of the governing equations was solved for all simulations, as the average Reynolds number was less than 20 for all cases. The SIMPLEC pressure based solver was used with a skewness correction factor of zero. The least-squares cell based discretization scheme was used for gradients, the second-order scheme was used for pressure, and a second-order upwind scheme was used for all other calculations. Gravity was important due the presence of buoyancy effects, so a gravitational force term of 9.81 m/s^2 was used in the direction opposite to the flow in all simulations. All simulations were carried out using double precision computations.

The internal and external measured wall-temperature profiles on either side of the annular fuel flow were used as boundary conditions, and heat conduction in the radial direction through the metal walls was not modeled. This assumption is reasonable for thermally thin metal walls (∼0.85 mm external walls).

The complex interactions of heat transfer, fluid flow, and chemistry which occur in this system result in variation of the observed behavior (e.g., deposition rates) as a function of the azimuthal location around the tube. These variations were found to be relatively minor in the calculation of surface deposition compared to the changes observed along the axial direction (azimuthal deposit variations change <10% compared

322

with the deposit maximum). These differences may help explain previous observations of deposit "streaking" on JFTOT tubes. Future efforts may help elucidate the causes of these streaks, but this study did not further explore these observations.

Diffusion. Initial CFD runs used a temperature-independent diffusion coefficient for all species (8×10^{-8} m/s^2) as in previous CFD studies.[17] Further efforts indicated the importance of using accurate diffusion coefficients for this laminar flow. Modifying the diffusion coefficient in the CFD calculations over a reasonable range showed the strong influence of the magnitude of the diffusion coefficient on the species profiles. As a consequence, a more detailed study of species diffusion coefficients was undertaken. There are very few temperature-dependent measurements of binary diffusion coefficients for the relevant species over the temperature range of interest in this study. Lee and Chang[18] used molecular dynamics (MD) united-atom simulations to calculate self-diffusion constants for a range of n-alkanes (C$_{12}$, C$_{20}$, C$_{32}$, and C$_{44}$) over the temperature range 0−200 °C. As jet fuel carbon numbers usually average near C$_{12}$,[19] we employed an extrapolation of the Lee and Chang's n-dodecane self-diffusion coefficient calculations over the temperature range 0−99 °C. The temperature dependence of diffusion coefficients is often expressed in Arrhenius form over limited temperature ranges.[20] Thus, these data were fit to the Arrhenius form

$$D = D_0 \exp(-E_D/RT)$$

where D_0 is the pre-exponential factor and E_D is the activation energy of the diffusion coefficient. The Arrhenius fit was chosen to allow extrapolation to higher temperatures, as this form has been used previously by other workers.[20] The fitted parameters ($D_0 = 1.38 \times 10^{-7}$ m^2/s and $E_D = 2.82$ kcal/mol) were used to create a third-order polynomial fit for input into Fluent

$$D = -4.82 \times 10^{-9} + 9.61 \times 10^{-12}T + 3.28 \times 10^{-14}T^2$$

where T is in Kelvin. A plot of the resulting diffusion coefficients along with the low temperature MD calculated values are shown in Figure 4 over the relevant temperature range for the JFTOT runs. The calculated diffusion coefficients in the figure are significantly lower than the temperature-independent values used in many previous fuel CFD studies (8
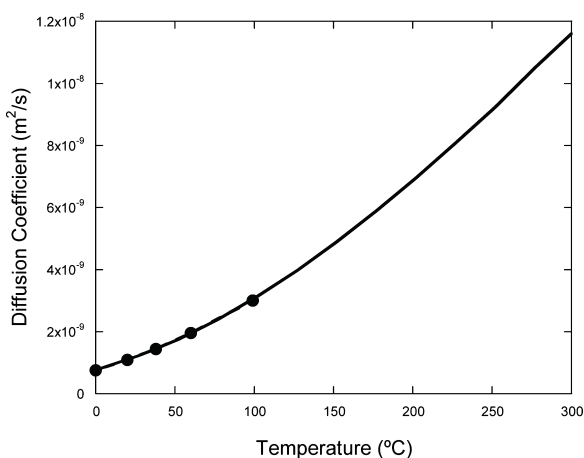
Figure 4. Plot of extrapolated n-dodecane self-diffusion coefficient vs temperature. Markers are the data of Lee and Chang.[18]

$\times 10^{-8}$ m^2/s). Calculations performed with the lower diffusion coefficient values used here result in radial species profiles which are less well mixed due to slower diffusive transport. Future efforts in determining more accurate values for the temperature-dependent diffusion coefficients for fuel species will be an important contribution to improving the ability to predict fuel reactivity and deposition.

Of course, each of the species present in oxidatively reacting fuel exhibits its own temperature-dependent diffusion coefficient with every other species present. Thus, using a single temperature-dependent diffusion coefficient is still an approximation to the real system behavior. However, it is also important to note that some species in the reacting fuel will exhibit diffusion behavior that may be significantly different than the n-dodecane temperature behavior used here. The smallest species present in the chemical kinetic mechanism is the O$_2$ molecule, which is likely to exhibit higher temperature-dependent diffusion rates due to its small size relative to most of the fuel species. We explored the effect of using higher O$_2$ diffusion coefficients on the calculated oxygen radial and axial profiles. A factor of 5 increase in the diffusion coefficient resulted in negligible changes, and as a result, the diffusion coefficient values of Figure 4 were used for all species in the present calculations.

Chemical Kinetic Mechanism. The jet fuel autoxidation chemistry and deposition were modeled in Fluent using a 19-step autoxidation chemical kinetic mechanism (Table 1) that is based on the mechanism developed by Kuprowicz et al.,[8] along with a global submechanism for the deposition reactions. The mechanism employs grouped fuel species and chemically realistic rate parameters for the bulk fuel autoxidation reactions. The deposition submechanism (Table 2) employs global kinetic reactions and parameters to represent the poorly understood deposition chemistry. Species transport was enabled in Fluent as well as volumetric (i.e., bulk/liquid phase) and wall reactions, including a mass deposition source on the inner annulus wall to allow surface deposit formation. Grid convergence studies were performed for 3D CFD calculations. The mesh was refined until no further changes were observed in the calculated temperature and species profiles. Table 3 lists the initial mass fractions of the reactive species for the two fuels for which the chemistry study was performed. An initial oxygen mass fraction of 7.12×10^{-5} (i.e., ~70 ppm) was used for all air-saturated calculations. Deposit depths (nm) were calculated from the rates of the deposition wall reaction (Reaction 19) in units of kg/m^2 s multiplied by the 2.5 h test time with an assumed deposit density of 2.0 g/cm^3 (this deposit density is an average of the densities of graphite and coal).[21]

■ RESULTS AND DISCUSSION

The goal of this study is to gain a better understanding of the heat transfer, fluid dynamics, and oxidation/deposition chemistry processes which occur in the JFTOT system under various set point conditions with a range of fuels. Experimental measurements of wall and outlet temperatures and outlet dissolved oxygen concentrations, along with computational fluid dynamics, were performed. Five different jet fuel samples were used. They are labeled here by their fuel type (e.g., Jet A-1, JP-8, etc.) and their Air Force Research Laboratory (AFRL) sample identification numbers (POSF Number), which are shown in Table 4. The two alternative "fuels" are not fully

Table 1. Chemical Kinetic Mechanism for Autoxidation of Jet Fuel

no.	reaction	Arrhenius factor (mol, L, s)	E_a (kcal/mol)
1	$R\cdot + O_2 \rightarrow RO_2\cdot$	3.0×10^9	0
2	$RO_2\cdot \rightarrow R\cdot + O_2$	1.0×10^{16}	23
3	$RO_2\cdot + RH \rightarrow RO_2H + R\cdot$	3.0×10^9	12
4	$RO_2\cdot + RO_2\cdot \rightarrow ROH + Aldehyde + O_2$	3.0×10^9	0
5	$RO_2\cdot + AH \rightarrow RO_2H + A\cdot$	3.0×10^9	5
6	$A\cdot + RH \rightarrow AH + R\cdot$	1.0×10^5	12
7	$A\cdot + RO_2\cdot \rightarrow Products_{AH}$	3.0×10^9	0
8	$RO_2H \rightarrow RO\cdot + \cdot OH$	1.0×10^{15}	39
9	$RO_2H + M \rightarrow RO\cdot + \cdot OH + M$	3.0×10^{10}	15
10	$RO\cdot + RH \rightarrow ROH + R\cdot$	3.0×10^9	10
11	$RO\cdot \rightarrow R'\cdot + Carbonyl$	1.0×10^{16}	15
12	$\cdot OH + RH \rightarrow H_2O + R\cdot$	3.0×10^9	10
13	$R'\cdot + RH \rightarrow Alkane + R\cdot$	3.0×10^9	10
14	$RO_2H + SH \rightarrow Products_{SH}$	3.0×10^9	18
15	$RO_2\cdot + R\cdot \rightarrow RO_2R$	3.0×10^9	0
16	$R\cdot + R\cdot \rightarrow R_2$	3.0×10^9	0

Table 2. Global Deposition Submechanism

no.	reaction	Arrhenius factor (m, s)	E_a (kcal/mol)
17	$Products_{AH} \rightarrow Solubles_{AH}$	1.5×10^{10}	3
18	$Products_{AH} \rightarrow Insolubles_{AH}$	5×10^7	1.3
19	$Insolubles_{AH} \rightarrow Surface\ Deposits_{AH}$	3.0×10^3	16.3

Table 3. Initial Mass Fractions of Reactive Species for Chemistry Mechanism

fuel	AH	M	ROOH	SH
2747	2.04×10^{-5}	4.00×10^{-8}	5.24×10^{-6}	1.00×10^{-6}
4177	5.93×10^{-5}	1.42×10^{-7}	3.25×10^{-6}	2.36×10^{-3}

formulated and blended specification jet fuels, but rather are isoparaffinic blend stocks.

Measured Bulk Outlet Temperatures. The JFTOT bulk outlet temperature was measured using a 1/32 in. thermocouple (Figure 1) for set point temperatures ranging from 215 to 325 °C. The bulk outlet temperature was recorded for the five different fuels listed in Table 4 and is shown in Figure 5. The figure shows a direct relationship between the JFTOT set point temperature and the bulk outlet temperature for these
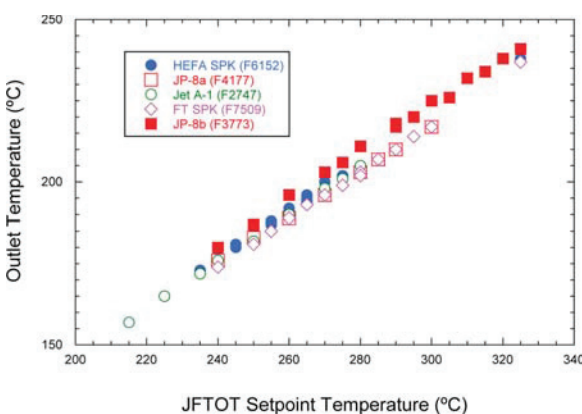

Figure 5. Measurements of the bulk outlet temperature as a function of the JFTOT set point temperature for various fuels.

fuels. There is a variability of less than ±3 °C in the measured outlet temperature of all fuels for a given set point, which may be due to either fuel inlet temperature variations and/or fuel heat capacity variations. The inlet fuel temperature varied with the ambient laboratory temperature. The figure shows that the fuel outlet temperature is lower than the set point temperature by 60−85 °C over the conditions studied. The cooled outlet bus bar is likely the reason that the fuel outlet temperature is significantly lower than the set point temperature, as the outlet temperatures are similar to the internal wall temperatures at the outlet as shown in Figure 2 for a given set point. Averages of these measured bulk fuel outlet temperatures will be used as one validation measure of the CFD simulations.

Table 4. Fuels Employed

POSF number	fuel type	fuel process
2747	Jet A-1	petroleum distillate
3773	JP-8	petroleum distillate
4177	JP-8	petroleum distillate
6152	HRJ (HEFA)	hydroprocessed fats/oils
7509	FT	Fischer−Tropsch isoparaffinic kerosene from coal

Measured Oxygen Profiles. The measured dissolved oxygen profiles are shown in Figure 6 for the five jet fuel samples at varying set point temperatures. The data were recorded after the JFTOT was set to a specific temperature set point with fuel flow and the oxygen sensor reading stabilized. The data show that oxidation starts to occur near a set point temperature of 220 °C for all fuels. The set point of 220 °C corresponds to an average bulk exit temperature of ∼160 °C. For all the fuels tested, the dissolved oxygen is fully consumed by a set point temperature of 325 °C, corresponding to a bulk exit temperature of ∼240 °C. Thus, oxidation occurs over an ∼80 °C fuel temperature range for these fuels in the JFTOT. Within this 80 °C temperature range, the individual fuels oxidize over a wide range of rates. For example, the HRJ fuel reaches complete oxygen consumption by 275 °C, but the JP-8 (POSF-3773) fuel has only reached 19% oxygen consumption at this set point temperature. Our previous studies (e.g., Kuprowicz et al.[8]) have shown that fuel oxidation rates and deposition tendencies are a function of the identities and
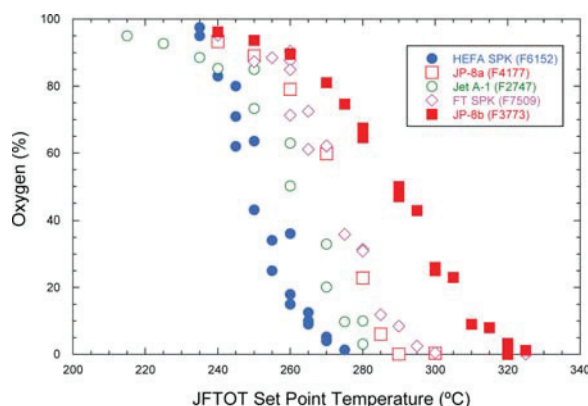
Figure 6. Oxygen consumption profiles for five different fuels at various set point temperatures.

concentrations of various heteroatomic (including hydro-peroxides, phenols, and reactive sulfur species) and dissolved metal species that may be present.

With regard to jet fuel specifications, the 260 °C specification JFTOT test temperature (for Jet A, Jet A-1, JP-8, and JP-5 fuels) shows a wide variation in oxygen consumption, varying from 10% to 85% for these fuels. For the petroleum-based fuels tested, only partial oxygen consumption occurs (10−50%) at the 260 °C set point temperature. For these fuels, raising or lowering the set point temperature by a relatively small amount (e.g., 10−20 °C) has a large effect on the extent of oxygen consumption. Increasing the JFTOT set point temperature normally results in increases in deposition on the heated tube. These observations suggest the following question: Is the increase in deposition rate observed with increasing temper-ature in the JFTOT due to increased oxygen consumption (as observed here), to an increase in the rate of deposit forming reactions, or to both effects? The CFD with chemistry simulations may help answer this question.

Interestingly, the two synthetic fuels (i.e., FT and HRJ) reach 100% oxygen consumption by 300 °C, which is below the synthetic fuel JFTOT specification set point temperature of 325 °C (ASTM D7566).[3] Previous work in other thermal stability experimental systems has shown that deposition rates decrease substantially after complete oxygen consumption.[22] In the case where oxygen has been completely consumed, the effect of raising the set point temperature beyond 325 °C for synthetic fuels might result in little increase in deposition if oxygen consumption is the controlling influence, in contrast to when the temperature dependence of the deposition formation reactions dominates the kinetics. Thus, the effect of the extent of oxygen consumption and temperature on deposition rates needs further study under JFTOT conditions to better guide the development of fuel thermal stability specifications for alternative fuels.

■ COMPUTATIONAL FLUID DYNAMIC MODELING

The measured fuel outlet temperatures are used here for validation of the CFD simulation, with boundary conditions taken from the measured temperature profiles. The calculated mass-weighted average at the outlet was used to represent the bulk outlet temperature. A comparison of measured and calculated fuel outlet temperatures over the set point temperature range 240−320 °C is shown in Figure 7. The
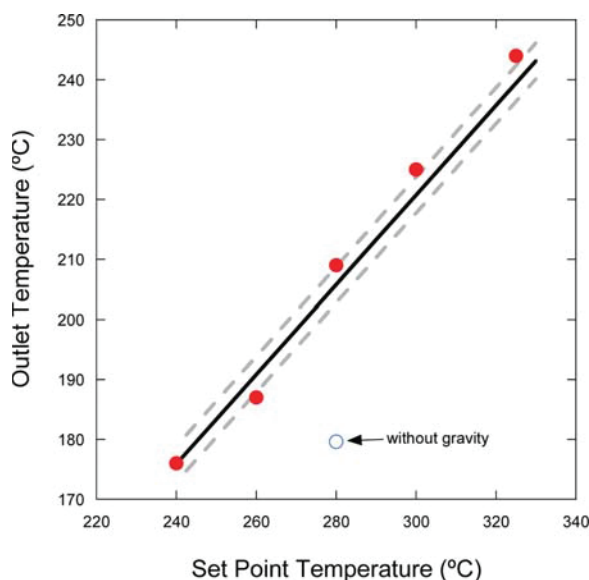

Figure 7. Plots of outlet temperature vs JFTOT set point temperature: averaged measurements (line) and calculated (symbols). The red data points are simulations which include gravity, while the blue data point omits gravity.

solid line is a linear fit to the measured data of Figure 5 for all five fuels. The gray dashed lines represent the ±3 °C uncertainty of these measurements. The red data points are the calculated outlet temperatures for the CFD model when gravity was included. The blue data point at a set point of 280 °C shows that omitting gravity from the simulation results in a substantial under prediction of the outlet temperature. The inclusion of gravity results in excellent agreement between simulation and measurement. Therefore, gravity is very important in correctly modeling the heat transfer which occurs in the JFTOT system. This is confirmed via calculation of a Richardson number of ∼100, indicating buoyancy dominated flow.

Figure 8 shows a contour plot of simulated temperatures for a slice through the JFTOT axial length for a set point temperature of 260 °C. The figure shows that there is a large temperature gradient near the hot (inner) side of the annulus. This temperature gradient results in a thin layer (∼0.05 mm) that approaches the temperature of the heated wall. The presence of the cooled bus bars at the inlet and outlet (in particular at the outlet) of the tube causes a hot region in the axial direction at the inner wall. This hot, thin, near-wall region is the location where the majority of the autoxidation and deposition chemistry occurs during a JFTOT test.

Contours of axial velocity can help one visualize the flow complexities. An example axial velocity contour plot is shown in Figure 9 for a 260 °C set point temperature. The figure shows that there is a region of high upward flow (in orange/red) near the hot inner wall. This high velocity region is due to buoyancy forces on the relatively low density fluid in this region. The figure also shows a reverse, downward flow (dark blue) near the cooler outer wall. This reverse flow is caused by the relatively high density fluid near the outer wall. The buoyancy forces result in a flow with a recirculating cell that occurs along the entire tube length. The forced and natural convection simultaneously contribute to the overall heat transfer. As a
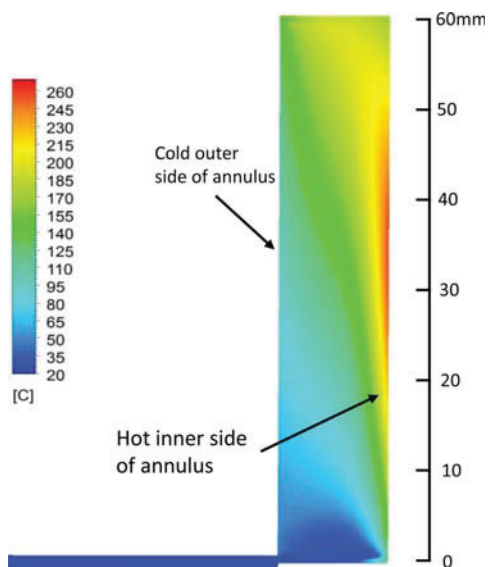
Figure 8. Contour plot of calculated temperature for the JFTOT at a 260 °C set point temperature. This contour plot is on a plane through the central axis of the bottom inlet tube and the heated JFTOT tube. Bulk fuel flow is in the vertical upward direction. The radial dimension (horizontal) is scaled (stretched) by a factor of 12.5. Color legend temperature values are in °C.
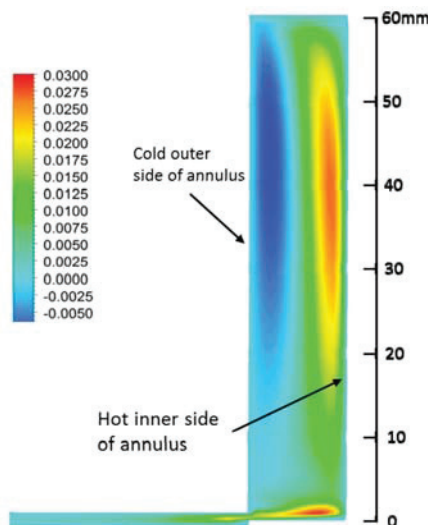
Figure 9. Contour plot of calculated axial velocity (m/s) for the JFTOT at a 260 °C set point temperature. This contour plot is on a plane through the central axis of the bottom inlet tube and the heated JFTOT tube. Bulk fuel flow is the vertical upward direction. The radial dimension (horizontal) is scaled (stretched) by a factor of 12.5. Color legend velocity values are in m/s.

result, the presence of gravity significantly increases the outlet temperature, as observed in the simulations of Figure 7.

Buoyancy Effects on Residence Time. Figure 10 shows a histogram for the distribution of residence times for fuel flowing through the JFTOT at a set point of 260 °C. The residence times were obtained by simulating streamlines of velocity from the inlet to the exit and computing the time of the
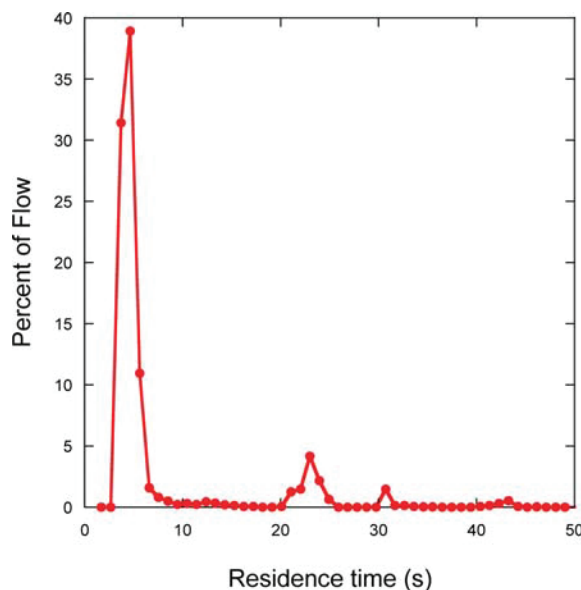
Figure 10. Residence time histogram for the three-dimensional simulation of the JFTOT at 260 °C.

fluid particles on those streamlines. The figure is a histogram that shows these residence times using 1 s discrete intervals (i.e., the histogram shows the percent of the fluid particles that experience specific residence times). A constant inlet flow rate of 3 mL/min results in an average residence time of about 11 s for the computational simulation, but buoyancy forces accelerate the fuel near the hot internal wall, decreasing the residence time for 50% of the total flow to less than 5.5 s. This leaves a distribution of longer residence times for the remainder of the flow. For example, 10% of the flow has a residence time over 30 s and 1.5% of the flow is well over 1 min with a maximum residence time of 2 mins. The longer residence times are the result of a portion of the fuel becoming entrained in flow recirculation cells. Examination of the histogram data shows a repeating pattern with peaks occurring roughly every 5−6 s. This indicates that the recirculation time for a fluid particle within the recirculating cell corresponds to fuel recirculation over the entire length of the tube. Recirculation behavior in the JFTOT adds complexity to the deposition and oxidation processes since the recirculated fuel introduces reaction intermediates (such as hydroperoxides) and products to the unreacted fuel upstream near the inlet.

■ CFD WITH CHEMISTRY MODELING

A previous study employed a simplified chemical kinetic mechanism and global deposition submechanism to simulate the complex chemistry which occurs during jet fuel autoxidation and deposition.[8] This previous work primarily relied on isothermal experimental oxygen consumption and deposition measurements at 185 °C (NIFTR rig), although a limited comparison between experiment and model was performed for nonisothermal flow experiments over a 340−400 °C maximum wall temperature range (ECAT rig). Limited CFD calculations were performed using a standard k-ε turbulence model to simulate this nonisothermal turbulent flow environment. Laminar flow in the JFTOT eliminates the need to select a turbulence model but still includes complex

recirculating flow and interactions among flow, chemistry, and heat transfer. The experimental work performed in the current study provides additional oxygen consumption and deposition data that will be used here to further refine the chemical kinetic mechanism. In addition, the CFD with chemistry model will be "exercised" to help elucidate the chemistry, heat transfer, and fluid dynamics which occur in the JFTOT system over a range of initial oxygen levels and extents of dilution.

Initial CFD with chemistry modeling of the JFTOT using the previous chemical kinetic mechanism[8] showed that the mechanism under-predicted oxygen consumption and deposition. As a result, the chemical kinetic mechanism was reevaluated against the previous and present data to determine chemically realistic kinetic parameters which worked well in simulating oxygen consumption and deposition over the full range of temperatures and flow environments in the JFTOT and the previous NIFTR/ECAT experiments. The goal was to provide equivalent agreement between the experimental measurements and simulations as demonstrated in the previous work while refining the chemical mechanism to enable improved simulations of JFTOT conditions. An improved mechanism which correctly models this wide range of conditions would increase the usefulness of the mechanism for simulating fuel oxidation and deposition over a broad range of temperature and flow environments.

Changes were made to two parts of the chemical kinetic mechanism to provide improved agreement with the wide range of previous oxidation/deposition data and the current JFTOT measurements. The activation energy of the unimolecular decomposition reaction of peroxy radicals, RO_2, via

$$RO_2 \rightarrow R + O_2 \qquad \text{(Reaction 2)}$$
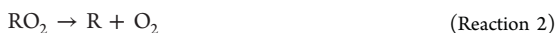
was changed from 19 to 23 kcal/mol. The previous selection of the lower activation energy (19 kcal/mol) was based on the assumption that the peroxy radicals involved in jet fuel autoxidation consist entirely of benzylic peroxy radicals.[23] Significantly higher peroxy radical decomposition activation energies (31.8−39.4 kcal/mol) are found for alkyl hydrocarbon peroxy radicals.[24] The current activation energy (23 kcal/mol) is reasonable for a peroxy radical pool that consists of a mixture of benzylic and nonbenzylic peroxy radicals (i.e., alkyl peroxy radicals), as is to be expected during the oxidation of the complex hydrocarbon mixture that constitutes jet fuel. The lower activation energy (19 kcal/mol) resulted in a significant slowing of oxidation at higher temperatures (approaching 280 °C), which has not been observed in experiments at these temperatures. This slowing of oxidation with increasing temperature (negative temperature coefficient behavior) is well-known in low temperature combustion (e.g., cool flames), but is overexpressed beyond the experimental observations using the lower activation energy value.

Arrhenius parameters were changed in the global deposition submechanism (Table 2) for Reactions 17 and 18 to provide improved agreement between model and experiment over the full range of conditions of the previous[8] and current work. In addition, the "artificial" initiation reaction used in the previous study (I → R) was found to be unnecessary as the decomposition of the initial concentration of hydroperoxides in these fuels (via reactions 8 and 9) is sufficient to initiate oxidation.

Figure 11 shows a comparison between experiments and the CFD with chemistry model for the JFTOT outlet oxygen concentration as a function of JFTOT set point temperature for
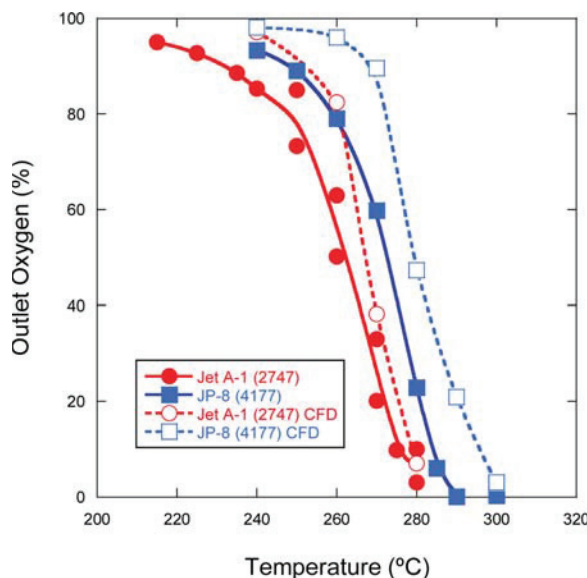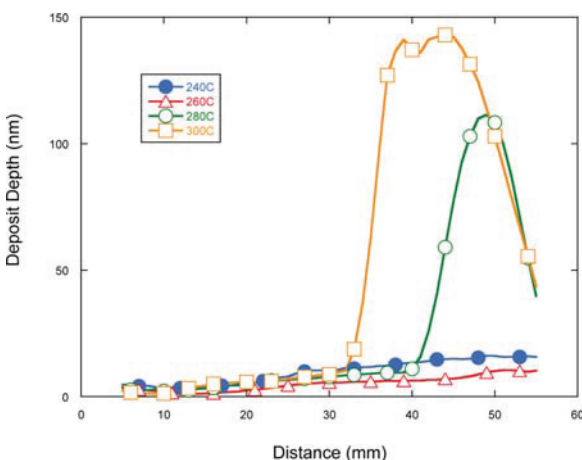

Figure 11. Comparison of measured and simulated oxygen outlet concentrations as a function of set point temperature for two fuels: filled symbols (solid lines) are experiments, and open symbols (dashed lines) are CFD with chemistry model results.

two fuels. The experimental results show that oxygen consumption begins in the temperature range 210−230 °C and is complete at 290−300 °C. The inflection point of the S-shaped oxygen consumption vs temperature curves occurs over the range 255−280 °C. The model results for both fuels show very good agreement in the shapes of the oxygen consumption curves, but they are shifted to slightly higher temperatures (by up to 10 °C), or lower oxygen consumptions at a constant temperature (by ∼20−30% oxygen outlet content), relative to the experimental measurements. Further improvement between these oxygen consumption experiments and simulations could not be realized using chemically realistic autoxidation rate parameters without adversely affecting the agreement shown below for the deposition profiles. Differences between model and experiment could be due to additional oxidation that occurs between the JFTOT tube exit and the oxygen sensor in the experimental measurements, although a narrow tube was used to rapidly cool the fuel and minimize additional oxygen consumption. Estimates of oxygen consumption in this sampling tube indicate that additional oxygen consumption should be negligible. The observed agreement shown in Figure 11 gives confidence in the ability of the chemical kinetic mechanism to provide reasonable predictions of oxygen consumption over a range of temperatures and conditions, particularly considering that the mechanism also provides good agreement in oxidation rates and deposition quantities at the lower temperatures of the previous study.[8]

CFD with chemistry modeling of surface deposit production was also performed for these two fuels and compared with experimental deposition profiles obtained using ellipsometry. As mentioned above, the Arrhenius parameters of the global deposition submechanism were modified to provide adequate agreement for both the current higher temperature JFTOT conditions and the previous NIFTR runs at 185 °C and ECAT runs over the range 340−400 °C (wall temperatures). It was found here that the relative deposit production tendencies of
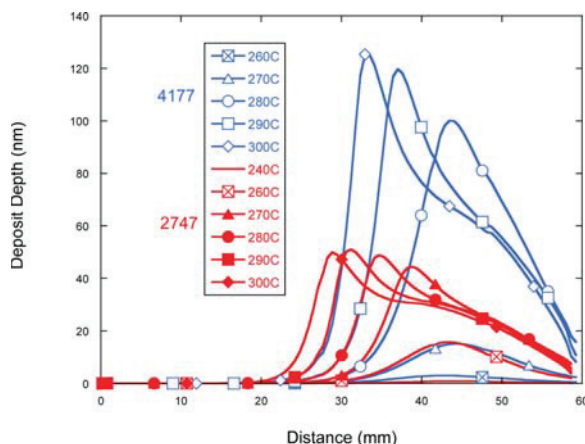
the two fuels (2747 and 4177) in this study have changed greatly since the original low temperature and chemical analysis work was performed.[8] The lower depositing fuel is now higher depositing, which is not reflected in the original composition measurements. Thus, a quantitative comparison of predicted and measured deposition is not feasible as the analytical measurements (AH, SH, metals, and ROOH concentrations) were conducted before the fuel changes, while the deposition measurements were conducted after. We will, therefore, emphasize a qualitative comparison of deposition profiles and levels. The fuel 4177 deposits were quite small and the results noisy; therefore, we concentrate here on the fuel 2747 deposition profiles. A comparison between experimental and modeling results for surface deposition is shown in Figures 12

Figure 13. Plots of CFD with chemistry calculated deposit depths vs distance for two fuels at various JFTOT set point temperatures. The markers are not actual data points; they are used to identify the curves only.

Figure 12. Plots of deposit depth vs distance obtained via ellipsometry for a single fuel (2747) at multiple JFTOT set point temperatures. Each curve is an average of deposition profiles from three separate JFTOT runs.

and 13 for a range of JFTOT set point temperatures. Figure 12 shows measured deposit depth profiles for fuel 2747 at set point temperatures covering the range 240−300 °C. Three separate JFTOT runs were performed at each temperature, and the resulting ellipsometric deposit profiles shown are an average of the three. The figure shows that, at 240 and 260 °C, deposition is very low. Significant deposits are formed at 280 °C with a peak deposition of 110 nm near 49 mm in the tube. At 300 °C, the deposit begins earlier in the tube and is broader with a peak deposition above 140 nm. The deposition onset moves upstream with increasing temperature due to the increase in oxidation rate with temperature, as demonstrated in Figure 11. This type of deposition behavior, with a sudden increase in deposition with increasing set point temperature, is typical of the behavior of most fuels in the JFTOT,[25] although deposition profiles have low reproducibility at lower deposition levels (<50 nm). The fuel 4177 deposit profiles were in this lower range and are not shown as they displayed poor reproducibility.

The deposition profile modeling results are shown in Figure 13 for two fuels at JFTOT set point temperatures over the temperature range 240−300 °C. The simulations show very low deposition, ≤10 nm at 260 °C for fuel 4177 and at 240 °C for fuel 2747, where oxygen consumption is low (<20%; see Figure 11). At higher set point temperatures, both fuels begin

to deposit more significantly, with deposit peak amounts increasing up to the highest temperature simulated, 300 °C. The deposit peak and onset locations move upstream with increasing temperature, in good agreement with the measurements of Figure 12; however, the simulation peaks do occur slightly earlier (i.e., upstream) in the tube. Both the experimental measurements and simulations show a broadening of the deposit peak with increasing temperature.

As mentioned above, the absolute deposition amounts cannot be compared between the model and experiment due to changes in the fuels over time. However, the absolute deposition amounts simulated can be compared with expected deposition levels from the fuel specifications. The ASTM D1655 jet fuel specification currently limits deposition to a maximum of 85 nm (measured via ellipsometry) for a JFTOT set point of 260 °C. Both the experiments (Figure 12) and model (Figure 13) show very low deposition (≤15 nm) at this temperature, which is to be expected for on-specification fuels. The model and experiment show greatly increased deposition once the oxygen consumption increases above 20%. This rather sudden rise in deposition with temperature has been observed previously,[25] but the current study is the first to show the role of oxygen consumption in its temperature dependence. In addition, both the model and experiment show deposition that varies over the range 0−150 nm for the JFTOT set point temperatures employed here. Thus, while a quantitative comparison cannot be made for each fuel, the modeled results show qualitative behavior that closely matches that observed in the experiments.

The modeling and experimental results show good agreement for both oxidation and deposition over a range of temperatures and flow environments. The kinetic mechanism is highly constrained by the range of acceptable kinetic parameters for the class of reactions and by the range of experimental measurements of oxygen consumption, hydroperoxide formation,[8] and deposition. One important constraint in the current data is the oxygen consumption levels at various temperatures and the location of the deposition profiles. Figure 11 shows that the simulated oxygen consumption curves are shifted to slightly higher temperatures than the measurements. In contrast, the deposition curves in Figures 12 and 13 show

that the simulated deposition curves occur slightly earlier in the tube than the experiments. These observations are interesting considering that the oxidation reactions are linked to and initiate the deposition process. These small differences in oxidation and deposition simulations relative to the measurements closely constrain the selection of deposition submechanism kinetic parameters and imply that some part of the simulation may need further refinement. This includes possible modifications to the chemistry and/or flow physics in the simulation. Targets for further study include improved handling of temperature-dependent transport parameters, such as diffusion coefficients which determine the diffusion rate to the surface, and/or modifications of reaction mechanism Arrhenius parameters to speed up oxidation relative to deposition. It is possible that a combination of refinements to both chemistry and physics will be required to improve the agreement between experiment and simulation.

Many previous jet fuel deposition modeling studies employed global oxidation chemistry which could only be applied to the particular experimental system being studied (e.g., Katta et al.[17]). The autoxidation mechanism used in the current study was developed using realistic grouped chemical reactions and Arrhenius parameters. Using real chemistry and chemical kinetic parameters allows the mechanism to be broadly applicable over a range of conditions and flow systems. The refined mechanism used for the current study expands the temperature range and flow conditions to which the mechanism can be applied. In contrast to the autoxidation mechanism, the deposition chemistry of fuels is poorly understood and modeled here using a simplified global submechanism. Thus, the kinetic parameters used in the deposit submechanism are not based on known chemical reactions with readily estimated Arrhenius parameters. Nevertheless, the experimental oxidation and deposition behavior closely restricts the global deposition reactions and rate parameters that are used, and therefore, further analysis of these parameters can be useful. The only wall reaction in the mechanism is Reaction 19, where insoluble species react at the wall to form deposits. The A factor used here (3000 m/s) was estimated based on an extrapolation of the hard sphere encounter frequency of fuel species with the surface.[26] The activation energy selected allows the observed deposition temperature dependence to be closely matched for the current JFTOT results and the previous lower temperature results.[8] Reactions 17 and 18 distribute the deposition precursor "Products AH" species, between soluble and insoluble products. The difference in activation energies for these two reactions (i.e., 3 and 1.3 kcal/mol, respectively) determines the temperature dependence of formation of soluble vs insoluble species. The selected activation energies dictate that, at the temperatures of interest in autoxidation, the formation of solubles increase faster with temperature than insoluble species. This is consistent with the typical increase in solubility with temperature.

Exercising the Model. With the observed agreement for oxygen consumption and deposition over a range of temperatures in the previous[8] and current work, we now employ the model to explore the chemistry which occurs in the JFTOT flow environment to better understand the role of flow, temperature, and chemistry on autoxidation and deposition. Figure 14 is a contour plot of oxygen percent at a set point of 280 °C for a cross section through the center of the JFTOT tube. The plot shows that oxygen consumption begins near the midpoint of the hot inner wall (which correlates to the
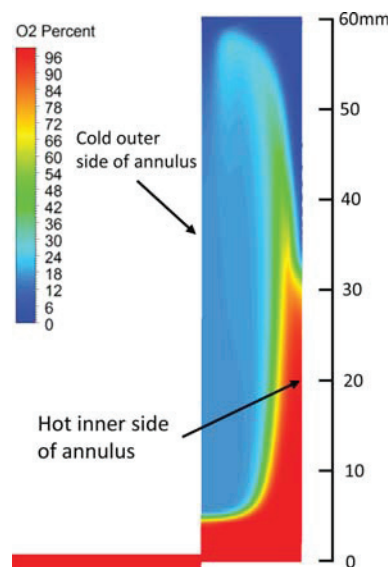

Figure 14. Calculated contour plot of oxygen percent for fuel 2747 at a 280 °C set point temperature.

maximum wall temperature; see Figure 8) and is rapidly consumed in this near wall region. This low oxygen fuel is carried downstream and then recirculates upstream near the colder outer wall, resulting in a lower oxygen level on the cold outer wall compared to the hot inner wall. Normally, one would expect lower oxygen consumption in the colder parts of the system, but here, the radial temperature gradients induce buoyancy effects to create this unusual situation.

One benefit of a having a CFD with chemistry simulation is the ability to readily perform "computational experiments" where system conditions are varied over a range of values more readily than would be feasible via experiment. Here, we show the predictions of such computations on the effect of partial deoxygenation and fuel dilution on deposition profiles. Figure 15 shows the results for a 280 °C set point temperature using fuel 2747 where the initial oxygen level (Figure 15a) and fuel dilution (Figure 15b) is varied. These figures show the value of the simulation in providing simple predictions which would be difficult to generate experimentally. Figure 15a shows that reducing initial oxygen levels from 100% (i.e., air saturated, ∼70 ppm, mass fraction of 7.12×10^{-5} used in the simulation) to 50, 10, and 2% results in a significant reduction of deposition without changes in the deposition profile. The inset shown in Figure 15a is a plot of the integrated deposition over the length of the tube vs the oxygen level. The plot shows a linear relationship between oxygen and total deposition. For complete oxygen consumption conditions, this is in agreement with previous experimental measurements, but the situation for partial oxygen consumption is more complex.[27−29] Partial oxygen consumption can result in a nonlinear relationship between initial oxygen levels and deposition which will require an improved chemical kinetic mechanism to correctly model.

Figure 15b demonstrates simulations of diluting a fuel sample with relatively nonreactive hydrocarbon solvent or low heteroatomic fuel (e.g., a heavily hydrotreated petroleum-based fuel or a HEFA/FT synthetic paraffinic alternative fuel). These dilution simulations were performed by lowering the initial AH, SH, ROOH, and dissolved metals concentrations by

329
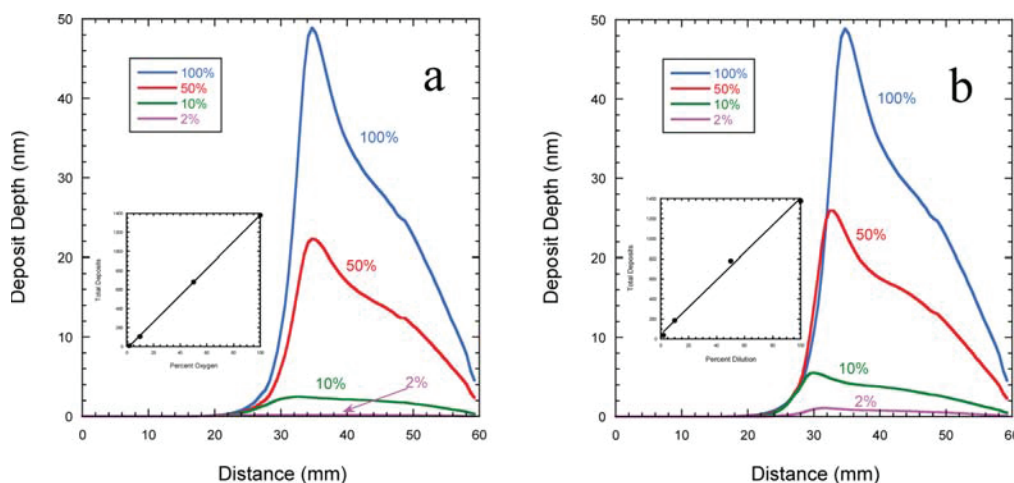
Figure 15. Plots of CFD with chemistry simulated deposition profiles for the effect of initial (a) oxygen level and (b) fuel dilution on deposition in the JFTOT for a set point of 280 °C (fuel 2747). Insets show the effect on total (summed) deposits.

the dilution level (e.g., for a dilution level of 50%, these initial concentrations were reduced in half). The simulation shows that fuel dilution is very similar to oxygen reduction (Figure 15a) in reducing deposition levels, with the inset of Figure 15b showing a linear relationship between integrated deposition and dilution level. Figure 15b also shows subtle effects of dilution on the onset of fuel deposition, with the simulation predicting the deposition onset to occur slightly upstream in the tube. This is likely due to the role of fuel heteroatomics in slowing fuel oxidation by intercepting peroxy radicals.[8] In fuel dilution, this can be offset by the lower initial concentration of hydroperoxides and dissolved metals, which would result in moving oxygen consumption and the deposition onset downstream. The results show that the lowering of fuel heteroatomics dominates this competition.

CONCLUSIONS

Experimental measurements of wall and fuel temperatures, outlet dissolved oxygen, and surface deposit depth in combination with a CFD with chemistry simulation were used to provide improved characterization of the heat transfer, fluid dynamics, autoxidation chemistry, and deposition which occur in the JFTOT system. The study shows that the flow is dominated by buoyancy effects with inner/outer wall temperature gradients inducing fuel recirculation and complex residence time behavior. Oxidation rates vary greatly over a range of fuel types, which results in a wide range of oxygen consumption levels at the standard 260 °C set point temperature. This oxygen consumption extent is shown to be a primary driver of the deposition extent in the JFTOT with oxygen consumption over ∼20% required before significant deposition is observed. An optimized chemical kinetic model of autoxidation with a global deposition submechanism is able to reproduce the observed oxidation and depositions characteristics. This improved CFD with chemistry simulation provides the ability to predict the location and quantity of oxygen consumption and deposition over a wide range of temperatures and conditions relevant to jet fuel system operation. This improved model can be used to predict the effect of fuel system modifications (e.g., fuel system geometry and/or fuel

composition changes) on the location and amount of oxygen consumption and surface deposition.

AUTHOR INFORMATION

Corresponding Author
*Tel: 937-255-3549. E-mail: Steven.Zabarnick@udri.udayton.edu.

Notes
Disclosure: The U.S. Government is authorized to reproduce and distribute reprints for Governmental purposes notwithstanding any copyright notation thereon. The views and conclusions contained herein are those of the authors and should not be interpreted as necessarily representing the official policies or endorsements, either expressed or implied, of Air Force Research Laboratory or the U.S. Government.
The authors declare no competing financial interest.

REFERENCES

(1) Hazlett, R. N. *Thermal Oxidation Stability of Aviation Turbine Fuels*; ASTM: Philadelphia, 1991.
(2) *Standard Test Method for Thermal Oxidation Stability of Aviation Turbine Fuels*; ASTM D3241-14b; ASTM International: West Conshohocken, PA, 2014.
(3) *Standard Specification for Aviation Turbine Fuel Containing Synthesized Hydrocarbons*; ASTM D7566-14c; ASTM International: West Conshohocken, PA, 2015.
(4) *Detail Specification Turbine Fuel, Aviation, Thermally Stable*; MIL-DTL-25524E; U.S. Air Force: Wright-Patterson Air Force Base, OH, 1997.
(5) Morris, R. E.; Hazlett, R. N. *Energy Fuels* 1989, 3, 262−267.
(6) Oh, C. H.; Merrill, B. J.; Wadkins, R. P. *Three-Dimensional Analysis on Flow and Temperature Distributions for Aircraft Fuel Thermal Stability*; WRDC-TR-89-2138; Wright Research and Development Center: Wright-Patterson Air Force Base, OH, 1989.
(7) Menon, S. *Development of a Mathematical Code to Predict Thermal Degradation of Fuel and Deposit Formation in a Fuel System*; WRDC-

330

TR-90-2084; Wright Research and Development Center: Wright-Patterson Air Force Base, OH, 1990.

(8) Kuprowicz, N. J.; Zabarnick, S.; West, Z. J.; Ervin, J. S. *Energy Fuels* **2007**, *21*, 530−544.

(9) Baker, C.; David, P.; Taylor, S. E.; Woodward, A. J. Thickness Measurement of JFTOT Tube Deposits by Ellipsometry. In *Proceedings of the 5th International Conference on Stability and Handling of Liquid Fuels*, Rotterdam, The Netherlands, Oct 3−7, 1994; Department of Energy: Washington, DC, 1994.

(10) Baker, C.; David, P.; Love, I.; Mogford, R.; Taylor, S.; Woodward, A. In *Proceedings of the 6th International Conference on Stability and Handling of Liquid Fuels*, Vancouver, BC, Canada, Oct 13−17, 1997; Department of Energy: Washington, DC, 1997; pp 185−200.

(11) David, P.; Mogford, R.; Paduscheck, P.; Taylor, S.; Woodward, A. *Proceedings of the 6th International Conference on Stability and Handling of Liquid Fuels*, Vancouver, BC, Canada, Oct 13−17, 1997; Department of Energy: Washington, DC, 1997; pp 947−55.

(12) Hazlett, R. N.; Hall, J. M.; Matson, M. *Ind. Eng. Chem. Prod. Res. Dev.* **1977**, *16*, 171−177.

(13) *Standard Specification for Aviation Turbine Fuels*; ASTM D1655-15; ASTM International: West Conshohocken, PA, 2015.

(14) Sander, Z. H. Heat Transfer, Fluid Dynamics, and Autoxidation Studies in the Jet Fuel Thermal Oxidation Tester (JFTOT). M.S. Thesis, Department of Mechanical Engineering, University of Dayton, Dayton, OH, 2012.

(15) Huber, M. L. *NIST Thermophysical Properties of Hydrocarbon Mixtures (SUPERTRAPP)*, Version 3.2; U.S. Department of Commerce: Gaithersburg, MD, 1999.

(16) *ANSYS Fluent*, version 15; ANSYS, Inc.: Canonsburg, PA, 2010.

(17) Katta, V. R.; Jones, E. G.; Roquemore, W. M. *Combust. Sci. Technol.* **1998**, *139*, 75−111.

(18) Lee, S.-H.; Chang, T.-H. *Bull. Korean Chem. Soc.* **2003**, *24*, 1590−1598.

(19) Edwards, T.; Zabarnick, S. *Ind. Eng. Chem. Res.* **1993**, *32*, 3117−3122.

(20) Mondello, M.; Grest, G. S. *J. Chem. Phys.* **1995**, *103*, 7156−7165.

(21) Haynes, W. M., Ed. *CRC Handbook of Chemistry and Physics*, 95th; CRC Press: Boca Raton, FL, 2014.

(22) Zabarnick, S.; Zelesnik, P.; Grinstead, R. *J. Eng. Gas Turbines Power* **1996**, *118*, 271−277.

(23) Kuprowicz, N. J.; Ervin, J. S.; Zabarnick, S. *Fuel* **2004**, *83*, 1795−1801.

(24) Knyazev, V. D.; Slagle, I. R. *J. Phys. Chem. A* **1998**, *102*, 1770−1778.

(25) Abdallah, D. J.; Kreno, L. E.; Thompson, K. E.; Gaughan, R. G.; Hoskin, D. H. In *IASH 2013: The 13th International Symposium on Stability, Handling, and Use of Liquid Fuels*, Rhodes, Greece, Oct, 2013.

(26) Gardiner, W. C., Jr. *Rates and Mechanisms of Chemical Reactions*; W. A. Benjamin: New York, 1969.

(27) Zabarnick, S.; Zelesnik, P.; Grinstead, R. R. *J. Eng. Gas Turbines Power* **1996**, *118*, 271−77.

(28) Ervin, J. S.; Williams, T. F. *Ind. Eng. Chem. Res.* **1996**, *35*, 899−904.

(29) Ervin, J. S.; Williams, T. F.; Heneghan, S. P.; Zabarnick, S. *J. Eng. Gas Turbines Power* **1997**, *119*, 822−829.

Appendix Y. Reacting Flows in Ultra-Compact Combustors with Combined-Diffuser Flameholder

Reacting Flows in Ultra-Compact Combustors with Combined-Diffuser Flameholder

Alejandro M. Briones*
University of Dayton, Dayton, Ohio 45469
Balu Sekar[†] and Dale T. Shouse[‡]
U.S. Air Force Research Laboratory, Wright–Patterson Air Force Base, Ohio 45433
David L. Blunck[§]
Oregon State University, Corvallis, Oregon 97331
Hugh J. Thornburg[¶]
High Performance Technologies, Inc., Reston, Virginia 20190
and
Timothy J. Erdmann[**]
Innovative Scientific Solutions, Inc., Dayton, Ohio 45459

In ultra-compact combustors, the length of the system is reduced by integrating the turbine turning vanes within the combustor and the primary zone is in a cavity recessed from the core flow. To understand the combustion characteristics of an ultra-compact combustor, the turning vanes were removed and a combined-diffuser flameholder was integrated upstream of a trapped-vortex combustor cavity. Two variants of the combined-diffuser flameholder are compared. In configuration **A**, the row of passages nearest the trapped-vortex combustor is opened, whereas for configuration **B**, an additional row of flow passages vertically adjacent is also open. Grid-independent three-dimensional simulations of these geometries are performed following a steady, multiphase, Reynolds-averaged Navier–Stokes, *C*-progress variable/flamelet approach with source terms to model effusion cooling. Nondispersive infrared analyzers were used to measure the concentrations of CO_2, O_2, and CO at the exit of the test section using three sets of emission rakes, with each having five vertically aligned, quick quenching sampling probes. Reasonable comparison was obtained between predictions and measurements of CO_2 and O_2 mass fraction profiles. Besides comparison between the two configurations, the effect of combustion on the flowfield/flamelet/flame structure is provided. Recommendations on further improvement of the design and numerical model are also discussed.

Nomenclature

A	=	area, m^2
C_D	=	drag coefficient
$\tilde{C}$	=	Favre mean *C*-progress variable
c_p	=	specific heat capacity, J/kg · K
Da	=	Damköhler number
d	=	diameter, m
f	=	mixture fraction in the flamelet domain
$\tilde{f}$	=	Favre mean mixture fraction
$\tilde{f}'^2$	=	Favre mean mixture fraction variance
$\tilde{H}$	=	Favre mean total enthalpy, J/kg
Ka	=	Karlovitz number
k	=	kinetic turbulent energy, m^2/s^2
lt	=	integral length scale, m
$\dot{m}$	=	mass flow rate, kg/s
Pr_t	=	turbulent Prandtl number
$\tilde{P}$	=	Favre mean pressure, Pa
Re	=	Reynolds number
SR	=	strain rate, 1/s
Sc_t	=	turbulent Schmidt number
S^{Φ}	=	generic source term (units depend upon variable Φ)
U_t	=	turbulent flame speed, m/s
U_l	=	laminar flame speed, m/s
$\tilde{u}$	=	Favre mean streamwise velocity, m/s
$\tilde{v}$	=	Favre mean transverse velocity, m/s
$\tilde{w}$	=	Favre mean spanwise velocity, m/s
x	=	streamwise Cartesian coordinate, m
y	=	transverse Cartesian coordinate, m
z	=	spanwise Cartesian coordinate, m
α	=	thermal diffusion coefficient, m^2/s
Γ^{Φ}	=	generic diffusion coefficient (units depend upon variable Φ)
ε	=	eddy dissipation rate, m^2/s^2
μ	=	kinetic viscosity, kg/m · s
ξ	=	random number from 0 to 1
ρ	=	density, kg/m^3
σ_k	=	turbulent kinetic energy Prandtl number
σ_t	=	turbulent Schmidt number for mean mixture fraction and mean mixture fraction variance equations
σ_{ε}	=	eddy dissipation rate Prandtl number
τ_{ij}	=	stress tensor, Pa/m^3
Φ	=	generic transport variable (unit depends open the variable)
ϕ	=	equivalence ratio

*Senior Research Engineer, University of Dayton Research Institute, Energy and Environmental Engineering Division, 300 College Park/0043.

†Senior Aerospace Engineer, Combustion Branch, 1950 Fifth Street. Associate Fellow AIAA.

‡In-House Research Manager, 1950 Fifth Street.

§Assistant Professor, School of Mechanical, Industrial and Manufacturing Engineering, 204 Rogers Hall. Member AIAA.

¶Senior Research Engineer, U.S. Department of Defense High-Performance Computing Modernization Program Office for User Productivity Enhancement, Technology Transfer, and Training, 2435 Fifth Street Bldg. 676. Associate Fellow AIAA.

**Research Engineer, 7610 McEwen Road. Member AIAA.

238

χ_{st} = scalar dissipation rate in flamelet domain, 1/s
$\tilde{\chi}_{st}$ = scalar dissipation rate, 1/s

Subscripts

b = wall boundary condition
bface = face of a cell adjacent to a wall boundary condition
ecj = effusion-cooling jets
p = particle
st = stoichiometry
t = turbulent
$\frac{1}{2}$ = half-injection angle

I. Introduction

CONFLICTING challenges of improving gas turbine engine performance, increasing durability, reducing engine weight, and lowering emissions, while maintaining cost, need to be overcome for developing advanced combustor technologies. The ultra-compact combustor (UCC) attains significant length reduction (~30% [1]) by incorporating high-pressure turbine inlet guide vane (IGV) components into the domain of the combustor as well as using a trapped-vortex cavity recessed from the core flow to help stabilize the flow. Reducing the combustor length results in engine weight reductions that improve engine thrust-to-weight ratio. Moreover, the systems-level approach of a UCC has the potential for significant total pressure loss reduction [1] between the compressor exit and the turbine rotor inlet. The UCC/trapped-vortex combustor (TVC)/IGV operates by spraying fuel and injecting air jet streams into the TVC cavity to produce a vortex-like structure within this cavity for stable flameholding. Typically, the cavity operates as a fuel-rich primary combustion zone. Then, the unburned fuel and intermediate products are transported into the main burner channel across a set of struts that bridge the main inlet airstream, seeking lower pressures in between the IGV passages, where quick quench occurs. Complete combustion follows at fuel-lean conditions further downstream. Because of the associated low residence times, and because the UCC/TVC/IGV operates in a rich-burn quick-quench lean-burn cycle, this combustor could drastically reduce NO_x, CO, and unburned hydrocarbon emissions. The body of this combustor is cooled by a combination of film- and effusion-cooling jets to ensure the durability of the liner.

There have been numerous UCC/TVC/IGV variants [1–8], but our current notional design operates as a main combustor situated in between the compressor exit and the high-pressure turbine inlet using a trapped-vortex combustor cavity as a primary zone [9] and a combined-diffuser flameholder (CDF) as a core flow entrainment mechanism. Xing et al. [3,4] have used the UCC as an interturbine burner with a prevaporized premixed fuel/air mixture to experimentally and numerically study the effect of Mach number, inlet air temperature, and TVC air driver jet flow rates on ignition, blowout, efficiency, and temperature exit profiles. Even though they obtained stable combustion at Mach numbers between 0.3 and 0.6, the temperature pattern factor and pressure losses were inferior to that corresponding to conventional combustors. In the past, IGVs have been used [3,6–8] for the dual purpose of turning the flow and enhancing mass transport from the cavity into the core flow to acquire desirable temperature profiles. Previous investigations [3,6–8] using turning vanes with or without enhanced entrainment mechanisms, such as radial vane cavities, did not produce the desired exit temperature profile. The entrainment mechanisms and the low-pressure region developed around the vane were not sufficient to transport the combustion products from the primary zone of the cavity and evenly distribute them across the mainstream reaction zone. Thus, the radial temperature profile was skewed toward the cavity-side wall. This may in part be due to the unbalanced flow splits distribution between the mainstream and the TVC cavity air (90 vs 10% [excluding cooling]). This, in turn, led to flow spillage from the TVC cavity [3]. To generate better entrainment and mixing between these two flows, the mainstream to TVC cavity air flow split must decrease in order to generate a more balanced momentum ratio. In addition, struts or blockages can be used to create low-pressure regions and enhance transport of the combustion products out of the cavity.

In an effort to improve flow distribution and mass transport, and to provide a baseline for future studies with vanes, the IGVs were removed and replaced with the CDF. The latter contain three rows of diffuser flow passages traversing from near the TVC-cavity-side wall to the UCC top wall. This device is useful in order to study how the mainstream to TVC cavity air flow split and how the front-end air jet configurations affect cavity transport and overall combustion performance. Moreover, rows of flow passages within the CDF can be opened or closed, providing some flexibility to vary flow splits and mixing. Because the core flow air enters the combustor through discrete jets through the CDF (in contrast to a single opening), the CDF has two functions: 1) to integrate the TVC with the upstream diffuser and provide a balanced flow distribution between the mainstream and the TVC cavity, which, in turn, creates a shear layer between the TVC cavity and the mainstream, enhancing mixing; and 2) to act as a bluff body, providing low-pressure wakes in between and above the discrete air jets in order to enhance product transport from the TVC cavity to the mainstream, leading to a suitable temperature profile. Two CDF configurations were tested at the High-Pressure Combustor Research Facility at constant operating pressure, pressure drop, and inlet temperature. Configuration A contained a single row of discrete air jets blowing downstream directly across the opening of the TVC cavity (i.e., near-TVC rows of passages opened), and configuration B contained an additional row of air jets near the center of the mainstream (i.e., middle row of passages opened). The IGVs are removed in this study in order to determine if the correct flow distribution and bluff body provide high combustor performance. As will be shown in this paper, this concept provides the desirable exit temperature profile. The IGVs will need to be incorporated into future designs in a manner that does not distort the current flow performance.

Previous UCC investigations have made major strides into understanding the fundamental and practical characteristics of this combustor. Blunck et al. [1] found that higher combustion efficiencies typically correspond to higher vortex strengths within the cavity, and that the configuration with mainstream air jets passing over the cavity produced the highest vortex strength and combustion efficiencies. The combustor tested is the same as configuration A, which is used in the current study, and comparisons between the experiments and computations are presented in a subsequent section. Erdmann et al. [6] demonstrated experimentally that the TVC can experience Rayleigh losses of approximately 1.4% and that a compact, turbulent flame can be obtained using a CDF upstream of the TVC cavity. In addition, they showed that maintaining an overall inlet Mach number less than 0.1 can help keep the Rayleigh losses to less than 3%. Sekar et al. [2], Xing et al. [3], and Briones et al. [7,8] have demonstrated that the exit temperature profile and the pressure losses can be affected by geometric features on the IGV such as ramps, dimples, and cavities. In addition, they have shown that the flow is highly three-dimensional and, consequently, the combustor has to be fully modeled without significant simplification, such as a single vane passage combustor section with translationally periodic boundary conditions. Briones et al. [7] have also shown that reasonable qualitative comparisons between measurements and predictions can be achieved using the *C*-progress variable/flamelet model with the Zimont source-term closure. However, the results are sensitive to the arbitrary Zimont model coefficient.

We do not fully understand how well the CDF with the TVC works in terms of mixing and combustor exit profiles. The problem is extremely challenging and requires analytical, numerical, and experimental efforts. From the numerical standpoint, to solve the aforementioned problem, high-fidelity reacting flow simulations are necessary in order to reduce the research and development cost and time. Consequently, insight into the final UCC design can be obtained with modeling and simulation of reacting flows using the progress variable/flamelet model approach for faster turnaround. For now, we will limit our examination to look at the interaction between the CDF and the TVC cavity in terms of the transport of cavity combustion products and mixing with the mainstream air, since very little

research has been conducted in this regard [6]. This, in turn, will provide insight into the future shape and location of the IGVs. Therefore, the numerical model needs to be compared against experimental measurements in order to assess the numerical model.

The major purposes of this investigation are to provide insight into the development of the UCC based on further understanding of the interaction between the CDF and TVC cavity and to assess the numerical model. The specific objectives of this study are the following: 1) to appraise the numerical models in terms of predicted and measured CO_2, O_2, and CO species mass fraction profiles; 2) to determine the effect of combustion on the flowfield structure; 3) to scrutinize the flow and flame structures for both UCC/TVC/CDF configurations in terms of streamlines, product formation rate, and temperature distribution; 4) to determine the characteristics of local turbulent flame speeds and turbulent flame regimes; and 5) to assess mixing between the TVC cavity flow and the CDF flow.

II. Physical-Numerical Procedure

The commercial code FLUENT [10] has been used for the simulations presented. The fuel is injected as a liquid spray through six fuel injectors, and a discrete phase is used to model the transition of liquid fuel spray into gas phase, employing both Eulerian and Lagrangian frames of reference. Details of the nonadiabatic C-progress variable/flamelet model are presented here, such as gas-phase formulation, in-house effusion-cooling sources, geometries and meshes, and boundary conditions.

A. Gas-Phase Numerical Model

The steady three-dimensional governing equations of continuity, momentum, turbulence, total enthalpy, mixture fraction, mixture fraction variance, and the C-progress variable are solved using the coupled pressure-based solver of FLUENT [10]. Turbulence is modeled using the realizable k-ε Reynolds-averaged Navier–Stokes (RANS) governing equations. Turbulent kinetic energy is only generated due to mean velocity gradients. Standard-wall functions [11] are used to determine the near-wall flow velocity. The governing equations are discretized using a second-order upwind scheme [12]. The gradients and derivatives of the governing equations are computed using the least-square cell-based gradient [13], which is

second-order spatially accurate. The discrete phase was set to interact with the continuous phase every 20 iterations. The continuity, momentum, total enthalpy, and the mixture fraction equations contain source terms that couple the continuum phase with the discrete phase. The governing equations in differential notation can be represented in general form as follows:

$$\frac{\partial(\bar{\rho}\,\tilde{u}\,\Phi)}{\partial x} + \frac{\partial(\bar{\rho}\,\tilde{v}\,\Phi)}{\partial y} + \frac{\partial(\bar{\rho}\,\tilde{w}\,\Phi)}{\partial z} = \frac{\partial}{\partial x}\left(\Gamma^{\Phi}\frac{\partial\Phi}{\partial x}\right) + \frac{\partial}{\partial y}\left(\Gamma^{\Phi}\frac{\partial\Phi}{\partial y}\right)$$
$$+ \frac{\partial}{\partial z}\left(\Gamma^{\Phi}\frac{\partial\Phi}{\partial z}\right) + S^{\Phi} \qquad (1)$$

Depending on the value of Φ, this equation represents the continuity, momentum, turbulent kinetic energy, eddy dissipation rate, total enthalpy, mixture fraction, mixture fraction variance, and C-progress variable equations, as shown in Table 1. This table also describes the transport coefficient Γ^{Φ} and the source term S_{Φ} for each equation. The Reynolds stresses in the momentum equations are related to the mean velocity gradients through the Boussinesq hypothesis [14]. The turbulent kinetic energy and eddy dissipation equation Prandtl numbers are $\sigma_k = 1.0$ and $\sigma_\varepsilon = 1.2$ [10], respectively. The enthalpy-equation turbulent Prandtl number (Pr_t) is 0.85 [10]. The turbulent Schmidt numbers (σ_t and Sc_t) are, respectively, 0.85 and 0.7 [10]. The β-shape probability density function (PDF) equations and discrete phase model are given in [3] and [8], respectively.

B. Effusion-Cooling Source Term Modeling

The mass continuity and momentum equations contain source terms that model the effusion-cooling jets in the combustor. Modeling is required instead of resolving the effusion-cooling injections because there are thousands of tiny injections with geometrical sizes comparable to that of the cells near the boundary conditions. Therefore, meshing these inlet conditions would be prohibitive. Nevertheless, accurate numerical predictions call for modeling these effusion-cooling jets because their total air mass flow rate constitutes a substantial fraction of the total mass flow rate. For instance, for configurations A and B, effusion cooling constitutes 32 and 25% of the total mass flow rate, respectively. In addition, these

Table 1   Variables, transport coefficients, and source terms appearing in the governing equation

Equations	Φ	$\Gamma\Phi$	S_Φ
Continuity	1	0	$\frac{\dot{m}_b}{V_{cell}} + \frac{m_{p_{in}} - m_{p_{out}}}{m_{p,0} V_{cell}}\dot{m}_{p,0}$
Favre mean streamwise momentum	$\tilde{u}$	$\mu + \mu_t$	$-\frac{\partial\bar{p}}{\partial x} + \frac{\partial}{\partial x}\left((\mu+\mu_t)\frac{\partial\tilde{u}}{\partial x}\right) + \frac{\partial}{\partial y}\left((\mu+\mu_t)\frac{\partial\tilde{v}}{\partial x}\right) + \frac{\partial}{\partial z}\left((\mu+\mu_t)\frac{\partial\tilde{w}}{\partial x}\right) - \frac{\partial\tau_{yx}^{turb}}{\partial x} - \frac{\partial\tau_{yy}^{turb}}{\partial y} - \frac{\partial\tau_{zx}^{turb}}{\partial z} + \frac{\dot{m}_b\cdot u_b}{V_{cell}} + \sum\left[\frac{18\mu}{\rho_p d_p^2}\frac{C_D Re_p}{24}\left(u_p - \left(\tilde{u} + \xi\sqrt{\frac{2k}{3}}\right)\right)\right]\frac{\dot{m}_p\Delta t}{V_{cell}}$
Favre mean transverse momentum	$\tilde{v}$	$\mu + \mu_t$	$-\frac{\partial\bar{p}}{\partial y} + \frac{\partial}{\partial x}\left((\mu+\mu_t)\frac{\partial\tilde{u}}{\partial y}\right) + \frac{\partial}{\partial y}\left((\mu+\mu_t)\frac{\partial\tilde{v}}{\partial y}\right) + \frac{\partial}{\partial z}\left((\mu+\mu_t)\frac{\partial\tilde{w}}{\partial y}\right) - \frac{\partial\tau_{yx}^{turb}}{\partial x} - \frac{\partial\tau_{yy}^{turb}}{\partial y} - \frac{\partial\tau_{yz}^{turb}}{\partial z} + \frac{\dot{m}_b\cdot u_b}{V_{cell}} + \sum\left[\frac{18\mu}{\rho_p d_p^2}\frac{C_D Re_p}{24}\left(u_p - \left(v + \xi\sqrt{\frac{2k}{3}}\right)\right)\right]\frac{\dot{m}_p\Delta t}{V_{cell}}$
Favre mean spanwise momentum	$\tilde{w}$	$\mu + \mu_t$	$-\frac{\partial\bar{p}}{\partial z} + \frac{\partial}{\partial x}\left((\mu+\mu_t)\frac{\partial\tilde{u}}{\partial z}\right) + \frac{\partial}{\partial y}\left((\mu+\mu_t)\frac{\partial\tilde{v}}{\partial z}\right) + \frac{\partial}{\partial z}\left((\mu+\mu_t)\frac{\partial\tilde{w}}{\partial z}\right) - \frac{\partial\tau_{zx}^{turb}}{\partial x} - \frac{\partial\tau_{zy}^{turb}}{\partial y} - \frac{\partial\tau_{zz}^{turb}}{\partial z} + \frac{\dot{m}_b\cdot u_b}{V_{cell}} + \sum\left[\frac{18\mu}{\rho_p d_p^2}\frac{C_D Re_p}{24}\left(w_p - \left(\bar{w} + \xi\sqrt{\frac{2k}{3}}\right)\right)\right]\frac{\dot{m}_p\Delta t}{V_{cell}}$
Turbulent kinetic energy	k	$\mu + \frac{\mu_t}{\sigma_k}$	$\mu_t\underbrace{\left[\left(\frac{\partial\tilde{u}}{\partial x}\right)^2 + \left(\frac{\partial\tilde{v}}{\partial y}\right)^2 + \left(\frac{\partial\tilde{w}}{\partial z}\right)^2 + \frac{1}{2}\left(\frac{\partial\tilde{u}}{\partial y} + \frac{\partial\tilde{v}}{\partial x}\right)^2 + \frac{1}{2}\left(\frac{\partial\tilde{w}}{\partial y} + \frac{\partial\tilde{v}}{\partial z}\right)^2 + \frac{1}{2}\left(\frac{\partial\tilde{u}}{\partial z} + \frac{\partial\tilde{w}}{\partial x}\right)^2\right]}_{SR^2} - \rho\varepsilon$
Eddy dissipation rate	ε	$\mu + \frac{\mu_t}{\sigma_\varepsilon}$	$\rho\cdot\max\left(0.43\frac{SR\cdot k/\varepsilon}{5+SR\cdot k/\varepsilon}\right)\cdot\left[\left(\frac{\partial\tilde{u}}{\partial x}\right)^2 + \left(\frac{\partial\tilde{v}}{\partial y}\right)^2 + \left(\frac{\partial\tilde{w}}{\partial z}\right)^2 + \frac{1}{2}\left(\frac{\partial\tilde{u}}{\partial y} + \frac{\partial\tilde{v}}{\partial x}\right)^2 + \frac{1}{2}\left(\frac{\partial\tilde{w}}{\partial y} + \frac{\partial\tilde{v}}{\partial z}\right)^2 + \frac{1}{2}\left(\frac{\partial\tilde{u}}{\partial z} + \frac{\partial\tilde{w}}{\partial x}\right)^2\right]^{1/2}\varepsilon - 1.9\rho\frac{\varepsilon^2}{k+\sqrt{\mu_t\varepsilon/\rho}}$
Favre mean total enthalpy	$\tilde{H}$	$\mu + \frac{\mu_t}{Pr_t}$	$\frac{\dot{m}_{p,0}}{m_{p,0} V_{cell}}\left[(m_{p_{out}} - m_{p_{in}})h_{fg} - m_{p,out}\int_{T_{ref}}^{T_{p,out}}C_{p_p}\,d\tilde{T} + m_{p,in}\int_{T_{ref}}^{T_{p,in}}C_{p_p}\,d\tilde{T}\right]$
Favre mean mixture fraction	$\tilde{f}$	$\frac{\mu_t}{\sigma_t}$	$\frac{m_{p_{out}} - m_{p_{in}}}{m_{p,0} V_{cell}}\dot{m}_{p,0}$
Favre mean mixture fraction variance	$\tilde{f}'^2$	$\frac{\mu_t}{\sigma_t}$	$2.86\cdot\mu_t\left(\frac{\partial\tilde{f}}{\partial x} + \frac{\partial\tilde{f}}{\partial y} + \frac{\partial\tilde{f}}{\partial z}\right)^2 - 2.0\cdot\rho\frac{\varepsilon}{k}\tilde{f}'^2$
Favre C-progress variable	$\tilde{C}$	$\frac{\mu_t}{Sc_t}$	ρS_C

cooling air flow rates could react with the fuel vapor, substantially altering the numerical results. Consequently, the effusion-cooling jets are removed from the geometry for meshing and they are introduced in the model as volumetric mass flow rate and momentum source terms in the cells adjacent to the relevant boundary conditions. These source terms are modeled as follows:

$$\frac{\dot{m}_b}{V_{\text{cell}}} = \frac{(\dot{m}_{\text{ecj}}/A_b)A_{\text{bface}}}{V_{\text{cell}}} \quad (2)$$

$$\frac{\dot{m}_b \cdot u_b}{V_{\text{cell}}} = \frac{(\dot{m}_{\text{ecj}}/A_b)A_{\text{bface}}}{V_{\text{cell}}} \cdot \left(\frac{\dot{m}_{\text{ecj}} \cdot \sin(\theta_{\text{ecj}})}{\rho(T_{\text{inlet}})A_{\text{ecj}}}\right) \quad (3)$$

$$\frac{\dot{m}_b \cdot \mathrm{v}_b}{V_{\text{cell}}} = \frac{(\dot{m}_{\text{ecj}}/A_b)A_{\text{bface}}}{V_{\text{cell}}} \cdot \left(\frac{\dot{m}_{\text{ecj}} \cdot \cos(\theta_{\text{ecj}})}{\rho(T_{\text{inlet}})A_{\text{ecj}}}\right) \quad (4)$$

$$\frac{\dot{m}_b \cdot w_b}{V_{\text{cell}}} = \frac{(\dot{m}_{\text{ecj}}/A_b)A_{\text{bface}}}{V_{\text{cell}}} \cdot \left(\frac{\dot{m}_{\text{ecj}} \cdot \cos(\theta_{\text{ecj}})}{\rho(T_{\text{inlet}})A_{\text{ecj}}}\right) \quad (5)$$

The mass flow rate through a boundary cell face $\dot{m}_b$ is the (measured) total mass flow rate of the effusion-cooling jets through that boundary condition $\dot{m}_{\text{ecj}}$ divided by that boundary condition area A_b times the cell face area adjacent to the boundary A_{bface}. Then, $\dot{m}_b$ is divided by the cell volume V_{cell}. Equation (2) is introduced as a source term in Eq. (1) with $\Phi = 1$ and appropriate Γ^Φ and S_Φ. There is also a corresponding momentum associated with $\dot{m}_b$ for Eq. (1) with $\Phi = u$, v, and w. Since information of our effusion-cooling jet inlet areas A_{ecj} and direction of the jets θ_{ecj} are known, the jet's velocity components (u_b, v_b, and w_b) can be calculated as shown in the term within parentheses in Eqs. (3), (4), and (5). These jet's velocity components are multiplied by $\dot{m}_b$ and divided by V_{cell} in order to obtain the corresponding momentum source terms. We developed, coded, compiled, and linked this procedure to FLUENT using a C programming language subroutine to account for the effusion-cooling jet's mass flow rate and momentum. Further details can be found in [3]. The user provides values of inlet temperature T_{inlet}, $\dot{m}_{\text{ecj}}$, θ_{ecj}, and A_{ecj} for this subroutine for the various wall boundary conditions with effusion-cooling jet modeling. The cooling air density is calculated from T_{inlet}.

C. Flamelets for the Probability Density Function

The flamelets are calculated by solving the laminar $n - C_{12}H_{26}$/air counterflow non-premixed flame equations in a mixture fraction space [15,16] using the JetSurf-1.0 [17] chemical reaction mechanism containing 194 species and 1459 Arrhenius reactions. Only the 20 most abundant species are kept in the β-shaped PDF lookup table. The flamelet calculation computes the mixture density ρ, species Y_i, and temperature T_b as a function of mixture fraction f for a given stoichiometric scalar dissipation rate χ_{st}. The thermodynamic properties appearing in the flamelet equations (not shown) are temperature and species dependent. The specific heat capacity c_p of the individual species is computed from piecewise polynomials [10]. The PDF equation is a function of mixture fraction $\tilde{f}$ and mixture fraction variance $\tilde{f}'^2$ as described in [3]. Then, the computational flowfield scalar variables ($\tilde{\rho}$, $\tilde{T}$, $\tilde{Y}_i$) are obtained by using the probability density function PDF(f), the mean stoichiometric scalar dissipation rate $\tilde{\chi}_{\text{st}}$, the mean enthalpy $\tilde{H}$, and the flamelet variables (ρ, T_b, Y_i) [3]. If the variables ρ, T_b, and Y_i do not exist for a given f, $\tilde{\chi}_{\text{st}}$, and $\tilde{H}$, they are linearly interpolated. The unburned density ρ_u, unburned thermal diffusivity α_u, unburned temperature T_u, and specific heat capacity c_p are fitted to third-order polynomials of the mixture fraction $\tilde{f}$ using linear least squares [10].
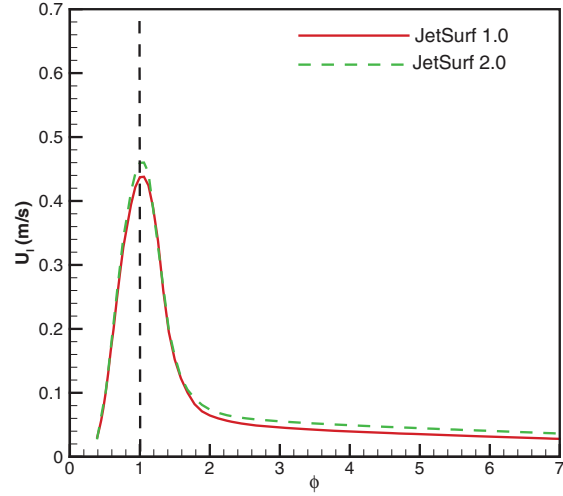
Fig. 1 N-dodecane/air unstretched laminar flame speed U_l as a function of equivalence ratio ϕ. The calculations were performed at a 440 K inlet temperature and 689,475.3 Pa constant pressure using the JetSurf-1.0 chemical kinetics mechanism [17].

D. C-Progress Variable Source Term S_C and Laminar Flame Speed U_l

The laminar flame speed U_l as a function of the equivalence ratio ϕ is needed to calculate the turbulent flame speed U_t. This in turn is used to compute the source term in the C-progress variable equation with the Zimont closure. That is, $\rho S_C = \rho_u U_t |\nabla \tilde{C}|$ and

$$U_t = A\left(\sqrt{\frac{2k}{3}}\right)^{3/4} U_l^{1/2}(\alpha)^{-1/4} l_t^{1/4}$$

Explanation of the Zimont model can be found elsewhere [7,8]. Consequently, the calculation of U_l is critical for the prediction of U_t. Calculations of U_l were conducted in the freely propagating configuration premixed $n - C_{12}H_{26}$/air mixture at 440 K and 689,475.2 Pa. These conditions correspond to the operating conditions of the combustor. CHEMKIN-PRO [18] was used for these calculations. The laminar flame speed predicted with JetSurf-1.0 [17] was compared with that of JetSurf-2.0 in Fig. 1. Because there are no substantial differences between the two mechanisms, the results of JetSurf-1.0 were used. This reduced the computational effort for calculating the various flamelets needed for the PDF table, as described in the previous section. Finally, the laminar flame speed as a function of mixture fraction f was programmed using a C programming subroutine.

E. Boundary Conditions

The geometry is represented by mass flow inlet, pressure inlet, pressure outlet, and wall boundary conditions. Figure 2 presents the computational domain and boundary conditions. The hot air driver jets and film-cooling jets are modeled with the mass flow inlet boundary condition. The mainstream hot air entering the CDF is modeled as a pressure inlet boundary condition. The outflow is modeled with the pressure outlet boundary condition. The reason for using inlet and outlet pressure boundary conditions is because the two UCC/TVC/CDF configurations are compared at constant pressure drop, operating pressure, and inlet temperature. The rest of the walls are modeled as impermeable adiabatic wall boundary conditions. The operating pressure of the combustor is 689 kPa. The fuel is injected as liquid from six injection sites equally distributed at the upstream wall of the TVC. The injections are conical, with a half-angle of injection set to $\theta_{1/2} = 45$ deg and the Rosen–Rammler droplet distribution with a spread factor of 3.5 varying from 0.1 to 100 μm. The average diameter is 20 μm. The fuel droplets can escape the inlet and outlet boundaries; however, they bounce off the walls. The boundary
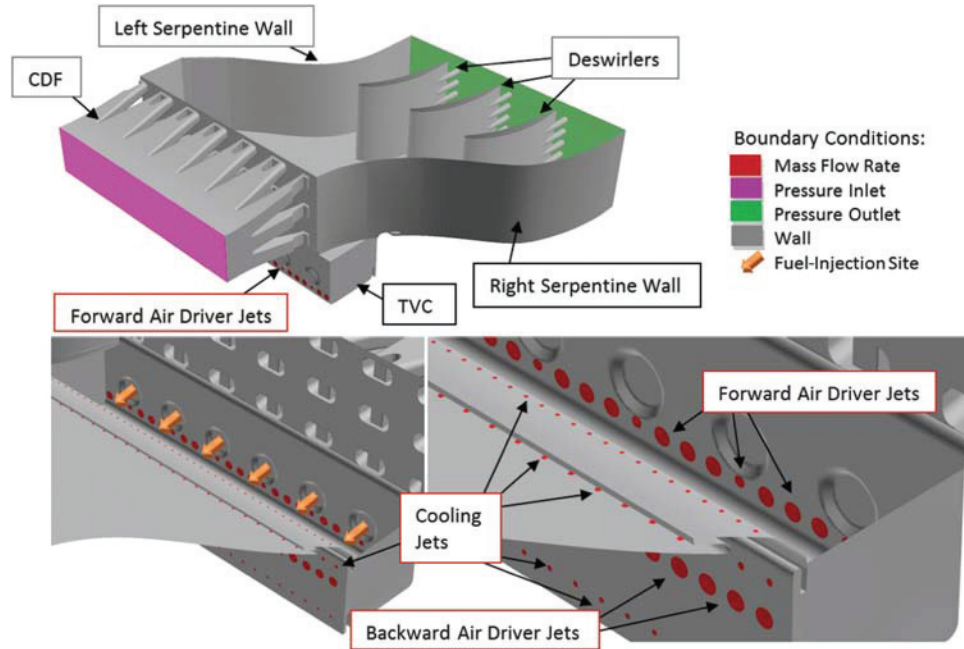
Fig. 2 Computational domain and boundary conditions. The types of boundary conditions are color coded by representing mass flow rate boundary conditions (red), pressure outlet boundary conditions (green), and impermeable adiabatic wall boundary conditions (gray). The orange arrows indicate the locations at which the injectors are mounted onto the trapped-vortex combustor cavity. However, the arrows do not represent the direction of the injections. The injectors are at a 45 deg half-angle $\theta_{1/2}$. The various components of the ultra-compact combustor are labeled. The labels are colored with the applied boundary condition.

conditions for the continuum and discrete phase governing equations presented before are as follows:

Mass flow inlet boundary condition[††]:
$\dot{m} = 15.5\%$ and 10.9% (total forward driver jets), 16.8 and 12.8% (total aft driver jets),
0.8 and 0.6% (total A cooling jets), 1.7 and 1.3% (total B cooling jets), 1.8 and 1.4% (total C cooling jets), or 1.6 and 1.3% (total D cooling jets)

$$\tilde{T} = 540 \text{ K}, \quad \tilde{C} = \tilde{f} = \tilde{f}'^2 = \tilde{H} = 0, \quad u' = 0.1\tilde{u}, \quad l_{\text{turb}} = D_H$$

Pressure inlet boundary condition:

$$\tilde{P} = 35907.9 \text{ Pa}, \quad \tilde{T} = 540 \text{ K}, \quad \tilde{C} = 0,$$
$$\tilde{f} = \tilde{f}'^2 = \tilde{H} = 0, \quad u' = 0.1\tilde{u}, \quad l_{\text{turb}} = D_H$$

Pressure outlet boundary condition:

$$\tilde{P} = 0.0 \text{ (gauge)}$$

Wall boundary condition:

$$\tilde{u} = \tilde{v} = \tilde{w} = 0, \quad \nabla_n\tilde{C} = \nabla_n\tilde{f}'^2 = \nabla_n\tilde{H} = 0, \quad k = \epsilon = 0,$$
$$\boldsymbol{v}_p \cdot \hat{n}_w = -\boldsymbol{v}_p \cdot \hat{n}_w, \quad \text{and} \quad \boldsymbol{v}_p \cdot \hat{t}_w = \boldsymbol{v}_p \cdot \hat{t}_w$$

Discrete phase injections:

[††]Mass flow rates are given in percentage values of the total mass flow rates though configurations A and B, respectively. The percentage values drop from A to B because more mass flows through B at a constant pressure drop.

$$\dot{m}_p = 0.00525 \text{ kg/s (per injector)}, \quad |\boldsymbol{v}_p| = 93 \text{ m/s},$$
$$T_p = 296.8 \text{ K}, \quad \theta_{1/2} = 45 \text{ deg}, \quad d_{p,\min} = 0.1 \text{ } \mu m,$$
$$d_{p,\text{avg}} = 20 \text{ } \mu m, \quad d_{p,\max} = 100 \text{ } \mu m$$

F. Geometry, Mesh and Computation

The geometries were created in Unigraphics. Gambit was used for geometry cleanup, decomposition, and meshing. Two geometries were meshed. The two geometries contain a combined-diffuser flameholder upstream of trapped-vortex combustor cavity, as shown in Fig. 3. They only differed in the row of passages that were opened or closed in the CDF. Out of the three rows of passages in the CDF (i.e., near TVC, intermediate, and away from TVC), configuration A had only the near-TVC row of passages opened, whereas configuration B had the additional intermediate row of passages opened. Therefore, the meshes were similar in all respects, and the boundary conditions were adjusted between the two configurations. The meshes were sized to use standard wall functions. The meshes for configurations A and B contained approximately 53 million mixed cells. It arrived to this mesh size by conducting a grid-independence study, as illustrated in Fig. 4. This figure shows the normalized area-averaged temperatures as a function of dimensionless streamwise coordinate, just downstream of the combined-diffuser flameholder, for three mesh sizes. The temperature was normalized by the ratio of the temperature difference between the local and inlet temperatures to the difference between the maximum and inlet temperature. Three meshes were evaluated, viz., 17, 53, and 63 million cells. From 17 to 53 million cells, the mesh grew 212% and the maximum difference in temperature was 16%. Similarly, from 53 to 63 million cells, the mesh grew 18% and the maximum difference in temperature profile was 6%. However, the differences between the largest meshes were only localized in a small region near the TVC. On the other hand, the quantitative difference between the 17 and 53 million cell meshes was pronounced almost everywhere downstream of the CDF. In fact, the average temperature difference between the two largest meshes
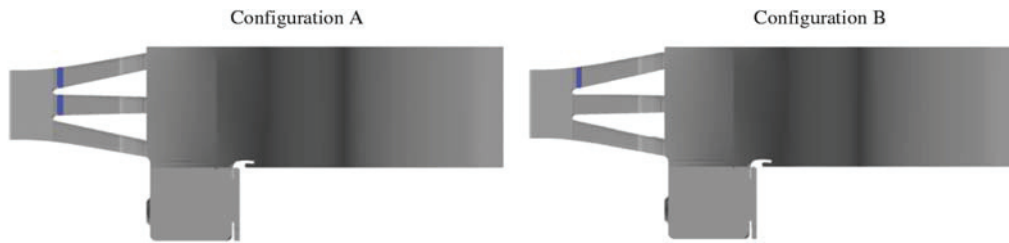
Fig. 3   Side view of the computational domain for configurations A (left) and B (right). The CDF is semitransparent, and the blockages to the CDF passages (colored in blue) are observed.

was negligible downstream of the TVC. Therefore, the 53 million cell mesh suffices for a grid-independent study. Furthermore, the simulations were conducted in the U.S. Department of Defense Supercomputing Resource Center system of the U.S. Air Force Research Laboratory. For the simulations, 160 parallel-core computations were used in a supercomputer. This 64 bit supercomputer uses two 16-core AMD Opteron processors at 2.4 GHz.

III.   Experimental Procedure

Testing of the UCC was performed in the High-Pressure Combustor Research Facility at the U.S. Air Force Research Laboratory. This facility provides high-temperature and high-pressure air to replicate conditions in a gas turbine engine. A side-view cross section of the UCC is shown in Fig. 5. The cavity is the primary combustion zone of the UCC. The fuel-rich combustion products from the cavity are mixed with extra air and further react with the mainstream flow as they migrate from the TVC cavity and into the core flow along the forward face of the CDF. The walls are cooled with a combination of film- and effusion-cooling jets. The deswirling vanes do not represent components in an engine or constitute a key element of the UCC design under development. These are used to turn the flow in the streamwise direction before passing into the facility exhaust section. The exit of the UCC is at the leading edges of the deswirler vanes, which straighten the flow to minimize lateral stresses within the rig. The two UCC/TVC/CDF configurations tested here are illustrated in Fig. 3. The configuration with only the bottom row of air jets open along the CDF (i.e., A) provided the best combustion efficiency and temperature profile [1]. Additional information regarding testing with the CDF is reported by Blunck et al. [1] and Erdmann et al. [6]. Testing on the UCC was performed at nearly 689 kPa and 540 K for

both configurations. JP-8 was used as fuel. The TVC cavity operated at fuel-rich conditions ($\phi_{TVC} = 1.55$–1.68), whereas the overall UCC operated at fuel-lean conditions ($\phi_{UCC} = 0.53$–0.74). Three rakes of emission probes were placed in the same streamwise plane as the trailing edges of the deswirlers, as shown in Fig. 6. Each rake had five quick-quench gas sampling probes distributed across the height of the main combustor channel. Nondispersive infrared analyzers were used to measure the concentrations of CO_2, O_2, and CO at the exit of the rig using a set of three rakes, with each having five vertically aligned quick-quenching sampling probes. The uncertainty
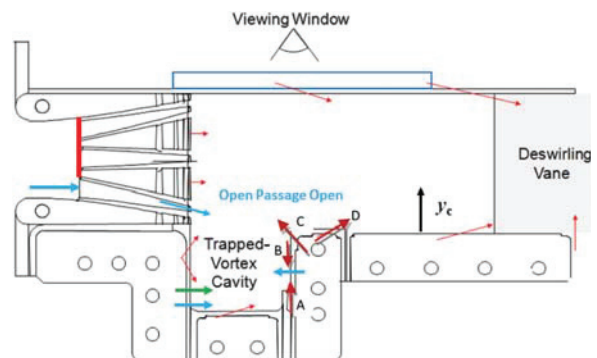

Fig. 5   Schematic of the experimental setup showing the combined-diffuser flameholder, the trapped-vortex combustor cavity, and deswirler vanes. Because the two upper passages of the combined-diffuser flameholder are closed, this setup corresponds to that of configuration A. The viewing window is also indicated. The blue arrows indicate the air jets, the green indicate the fuel injection site, and the red arrows indicate the effusion-cooling jets.
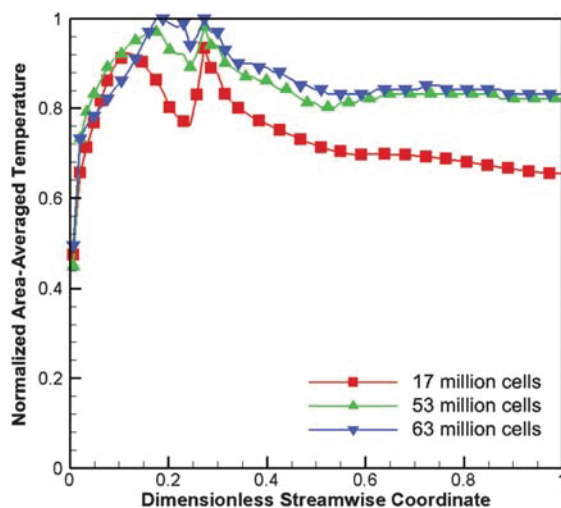

Fig. 4   Normalized area-averaged temperatures as a function of the dimensionless streamwise coordinate. The dimensionless streamwise coordinate of zero represents the location just downstream the combined-diffuser flameholder, whereas the value of unity represents the exit of the combustor, as discussed in the context of Fig. 2.
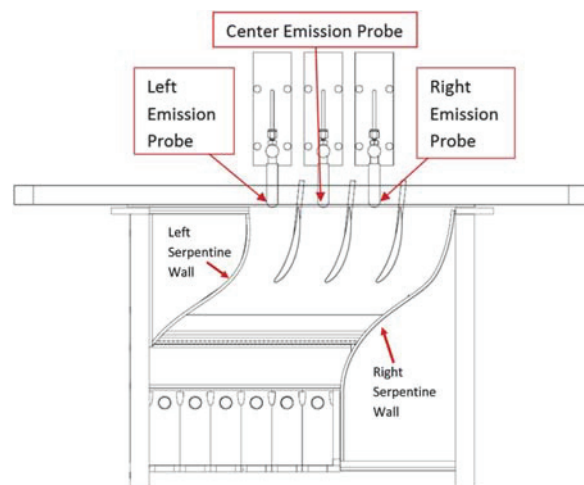

Fig. 6   Top view of the rig showing the location of the multiple emission probe rakes. The locations of the serpentine walls are also indicated.

of the emission rake measurements was ±3%, based on manufacturer specifications. The CO_2, O_2, and CO measurements are compared with predictions in the Results and Discussion section (Sec. IV).

IV. Results and Discussion

In this section, we initially discuss the assessment of the numerical model by comparing measurements with predictions and qualitatively inspecting the Zimont model closure. Subsequently, we examine the effect of combustion on the flowfield in terms of streamlines. Then, we qualitatively compare the reacting flowfield of configurations A and B in terms of streamlines, velocity contours, product formation rate, and temperature distribution. Finally, we examine the turbulent flame regimes within the combustors.

A. Assessment of the Numerical Model

As described in the previous section, the physical-numerical model is complex, since it involves many submodels that are compiled into a more intricate model that captures multiphysics such as liquid fuel evaporation, liquid fuel boiling, molecular mixing, turbulence-induced mixing, turbulence–chemistry interactions, and flame stabilization. These submodels can be individually assessed/validated (e.g., chemical mechanism, evaporation, etc.) or can be assessed altogether. We have evaluated the models in both manners. Although not shown, the unstretched laminar flame speed U_l, calculated using CHEMKIN-PRO's freely propagating application [18], was compared with the data reported by Kumar and Sung [19]. The conditions correspond to atmospheric pressure and inlet temperatures of 400 and 470 K, respectively. The chemical mechanism provided remarkably good results at lean conditions, but it underestimated the data at rich conditions. This suggests that our three-dimensional model will be more accurate at downstream locations where the flow is leaner and less accurate at the TVC cavity where the flow is richer. In an earlier [3] investigation, we compared the heat signature with the predicted IGV temperature distribution, and good qualitative comparison was obtained. Moreover, the good qualitative comparison between measured and predicted exit CO_2 mass fraction profiles was previously obtained [3]. Further comparisons between measured CO_2, O_2, and CO mass fraction profiles and predictions are presented here.

The comparisons between predicted and measured species profiles are presented in Fig. 7 for both configurations: A and B. The locations of these measurements are illustrated in Fig. 6 and were discussed in the previous section. The measured CO_2, O_2, and CO profiles are qualitatively similar between configurations A and B, suggesting similar combustion characteristics. For a given configuration, the CO_2 mass fraction is greatest at the center probe (cf. Fig. 6), especially closer to the UCC bottom wall. This indicates the location for a hot spot. At the left probe, the CO_2 mass fraction is generally lower than at the center probe. However, the CO_2 also peaks near the UCC bottom wall for this probe. The CO_2 mass fraction is pronouncedly lower at the right probe, with a peak closer to the UCC top wall. The calculations follow the probe-rake individual CO_2 profiles as well as the trend among probe rakes. The calculations are best for the left and center probes, whereas discrepancies are more prominent for the right probe.

Moreover, the measurements in Fig. 7 show that the O_2 profiles of individual probes are qualitatively opposite to that of CO_2 profiles. For instance, the location of the CO_2 maximum peak corresponds to the location of the O_2 minimum peak, and when CO_2 increases, O_2 decreases. This figure also indicates that the O_2 mass fraction is greater at the right probe (cf. Fig. 6), suggesting the location for fuel-lean combustion and a cooler spot. At the left probe, the O_2 mass fraction is generally lower than at the right probe. The O_2 mass fraction is markedly lower at the center probe, where we have observed a high-CO_2 mass fraction. The predictions evidently follow the probe-rake individual O_2 profiles as well as the trend among probe rakes. The O_2 predictions are better for the left and center probes, whereas discrepancies are more pronounced for the right probe, as with the CO_2 measurements. In addition, the model generally overpredicts the CO measurements. The discrepancies are

greater between measured and predicted CO mass fractions than for CO_2 and O_2 mass fractions. Lastly, it is interesting to note that, even though the calculated laminar flame speed U_l is more accurate at lean conditions, as previously discussed, the numerical model shows the greater discrepancies at fuel-lean conditions (i.e., right probe). This shows that accurate U_l is necessary but not sufficient to guarantee the predictability of the model.

The discrepancies between predictions and measurements are plausible because 1) in the experiments, JP8 was used, whereas in the model, an n-dodecane surrogate was used; 2) the fact that the physics that was being modeled corresponded to a dynamic system and not a steady-state solution; 3) the numerical progress variable/flamelet model lacks the middle (unsteady) and lower (weak) branches of the s-curve response to strain. Therefore, local extinction and reignition cannot be captured in the simulations [20,21]; and 4) it is expected to have partially premixed flames in the combustor. Consequently, a model is needed to correlate the multiple flames containing rich premixed (RPRZ), lean premixed (LPRZ), and non-premixed (NPRZ) with their corresponding rich premixed, lean premixed, and non-premixed flamelets.

Another manner to evaluate the numerical model is to examine whether or not the results uphold the Zimont theory [22]. This can be done by plotting the turbulent flame speeds U_t as a function of the product of a fluctuating velocity and Damköhler number ($\sqrt{k} \cdot Da^{1/4}$), as illustrated in Fig. 8. Note that $\sqrt{k} \cdot Da^{1/4}$ is essentially the same as the source term in Eq. (1) for $\Phi = \tilde{C}$. This figure shows that, by increasing $\sqrt{k} \cdot Da^{1/4}$, the turbulent flame speed U_t increases nearly linearly, even though there is some scattering, especially at low $\sqrt{k} \cdot Da^{1/4}$. The locations of these scatterings are also revealed in both UCC/TVC/CDF configurations in Fig. 8. These scatterings mostly occur near the CDF front face and the TVC for both configurations, where there are large gradients. A plausible explanation for these scatterings is that, at those locations there are severe stretch rates, which the current Zimont model is not accounting for. However, the Zimont model could address stretch effects [22], but in our current model, stretch effects (or scalar dissipation rates) are only introduced through the flamelet model and not through the C-progress variable model. Anyway, the results are consistent with theory because, by increasing the Damköhler number Da, the chemical equilibrium state is approached and, consequently, the maximum heat release rate is obtained. It is also consistent with the theory that U_t increases with turbulent kinetic energy k because flame wrinkling is increased. This, in turn, leads to a turbulent flame area greater than that of its corresponding laminar flame area. Consequently, U_t increases, by several factors, its corresponding laminar flame speed U_l. Moreover, the results in this plot are similar for configurations A and B. This indicates that the result is independent of the geometry and/or conditions as long as it is a reacting turbulent flow.

B. Effect of Combustion on the Flowfield Structure

To understand the effect of combustion on the flowfield we compare the nonreacting flow to the reacting flow of configuration A. Figure 9 shows isometric, top, and side views of streamlines for configuration A. The results presented in this figure correspond to nonreacting and reacting flow simulations. For the nonreacting condition, the mainstream flow seals the cavity flow, i.e., there is very little penetration of the mainstream flow into the TVC cavity. However, the streamlines emanating from the CDF mix with the TVC driver jet and cooling jet streamlines in the main channel flow above the TVC. Then, the streamlines pass the deswirlers and exit the computational domain. For both conditions, it is evident that the results are not periodic in the spanwise direction, as discussed in the Introduction section (Sec. I). Most of the flow passes in between the left serpentine wall and the center deswirler (i.e., through the two leftmost passages) (cf. Figs. 6 and 9). The flow rate decreases abruptly from the center deswirler toward the right serpentine wall. However, for the reacting flow condition, there is more flow in the passage between the center and right deswirler than for the nonreacting flow condition, which is due to thermal expansion.
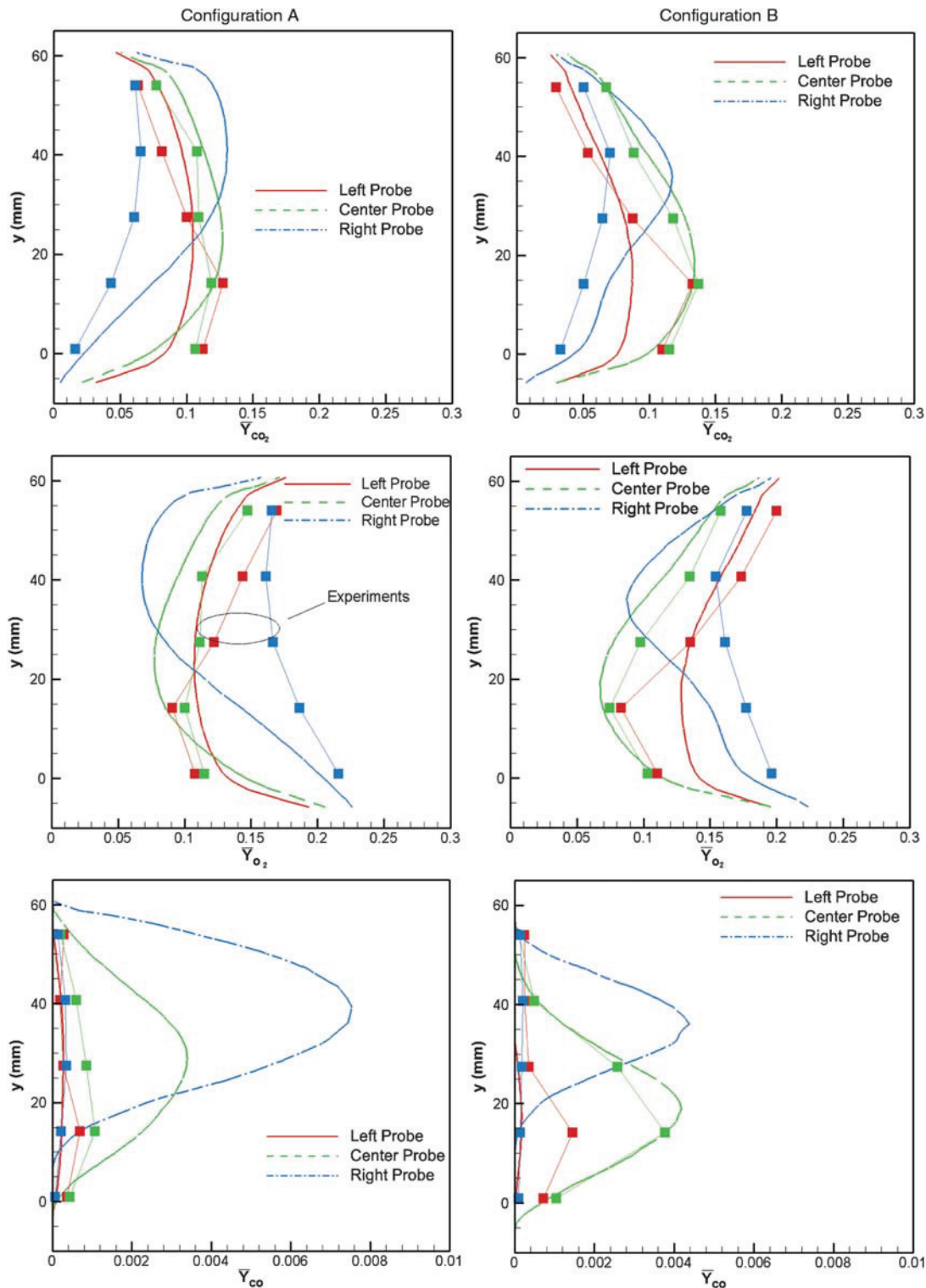
Fig. 7 Predicted and measured CO_2, O_2, and CO mass fraction profiles as a function of dimensionless height (y/H) for both configurations A and B. Measurements are represented by square symbols and lines. The location measurements are discussed in the context of Fig. 6.

Between the right deswirler and the right serpentine wall, there is almost negligible flow for both conditions (cf. Figs. 6 and 9). This indicates that the IGVs on the TVC are needed to make the flow turn. The preference of the flow to move along the left wall is observed experimentally and is attributed to the orientation of the main flow relative to the walls of the combustor.

Furthermore, the very little entrainment of the mainstream flow into the TVC cavity vanishes under reacting conditions. The single
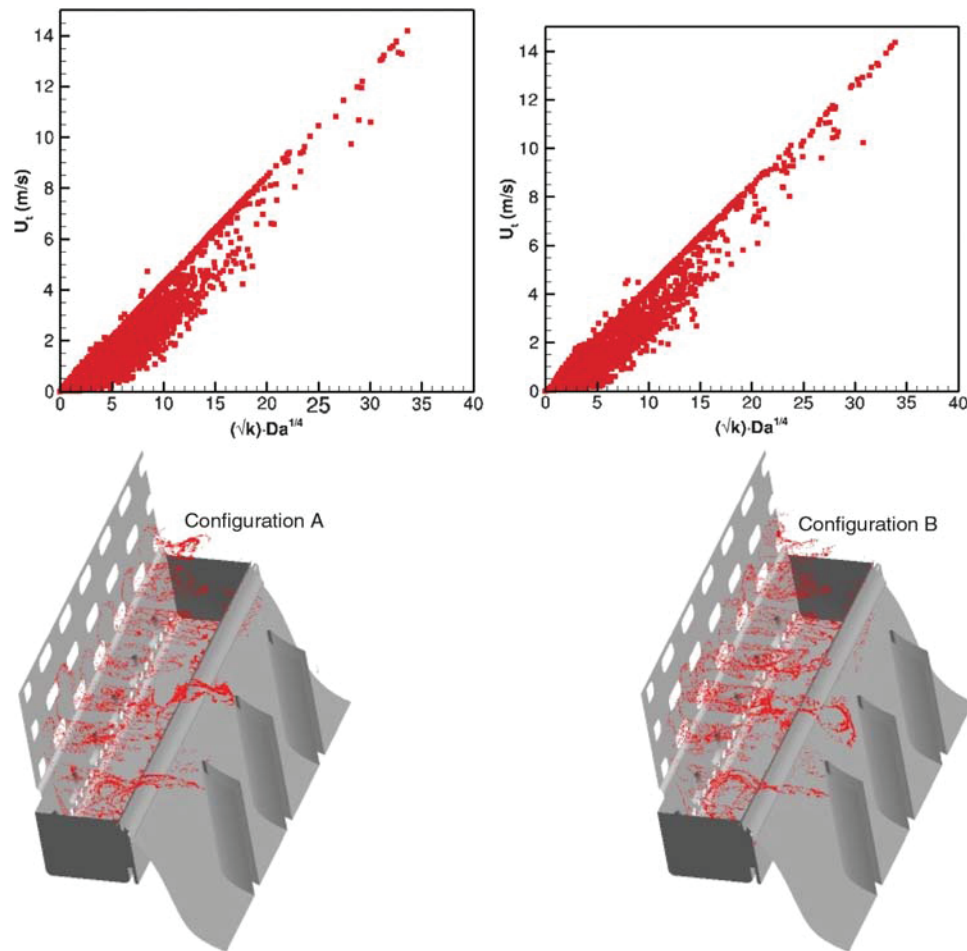
Fig. 8   Zimont model representation of the turbulent flame speed U_t as a function of $\sqrt{k} \cdot Da^{1/4}$ for both configurations A (top-left) and B (top-right). The points that deviate from the linear variation of U_t with $\sqrt{k} \cdot Da^{1/4}$ are shown below for configurations A (bottom-left) and B (bottom-right). The bottom figures only show the region of interest.

dominating recirculation flow in the TVC under nonreacting conditions is distorted due to combustion. That is, the forward driver jets impinge on the TVC aft wall and then spill out into the mainstream. Combustion enhances vorticity sinks such as baroclinic torque [23–25], thermal expansion [26], and vortex diffusion [27]. These phenomena have been considered in previous bluff-body investigations [23–27] to destroy large flow structures, such as the single recirculation region in the TVC. In the current UCC/TVC/ CDF, since the primary fuel-rich combustion occurs in the TVC, density generally decreases towards the mainstream (as reactions are completed), whereas the pressure decreases from the CDF plenum toward the exit of the rig. Consequently, the pressure and density gradient vectors are not in parallel, which would enhance baroclinic torque. Thermal expansion increases under combustion due to an increase in temperature, which, in turn, decreases density and causes velocity vector acceleration in order to maintain mass continuity. Although considered weaker than the other sink terms, vorticity diffusion increases because the rise in temperature enhances molecular viscosity. In addition, the TVC flow spilling pushes the mainstream flow upward. For both conditions, the cooling jets as well as the aft driver jets just spill out the TVC. A major consequence of this result is that there will be, in the TVC, a higher equivalence ratio than expected, and that corner will be overly cooled. In contrast with the nonreacting flow, the reacting flow exhibits a recirculating flow at the corner of the CDF and UCC top wall. The nonreacting and reacting flow results for configuration B are qualitatively similar to the ones presented here for configuration A.

Further understanding of the effect of combustion on the flowfield is obtained by comparing the velocity magnitude contours between nonreacting and reacting flows in Fig. 10. The observed horizontal plane cuts the bottom row of the flow passages of the CDF in half. The flow is accelerated through the CDF passages, reaching a maximum velocity of ∼136 and ∼120 m∕s for nonreacting and reacting flow simulations, respectively. The velocity through the CDF is lower for the reacting simulations due to a lower pressure drop across the CDF caused by an increase in Rayleigh pressure losses due to sensible heat release to the flow. The air jets enter the UCC at different penetration lengths for both conditions. This finding could potentially cause flow instability, because the flames will be stabilized at different locations where the turbulent flame speed U_t matches the incoming flow velocity. For the nonreacting flow condition, the flow is highly stratified. Fluid from the cooling jets is even observed at this height above the cavity (cf. Figs. 2 and 10). On the other hand, for the reacting flow condition, thermal expansion causes the flow to be less stratified. Nevertheless, for both conditions, it is evident that there is little flow on the right side of the combustor. This confirms our observations made in the previous paragraph.

C.   Reacting Flowfield: Further Comparison Between Configurations A and B

Figure 11 shows the side views of the streamlines of configurations A and B under reacting flow conditions. The isometric and top views of the streamlines for the reacting flow condition for configuration B
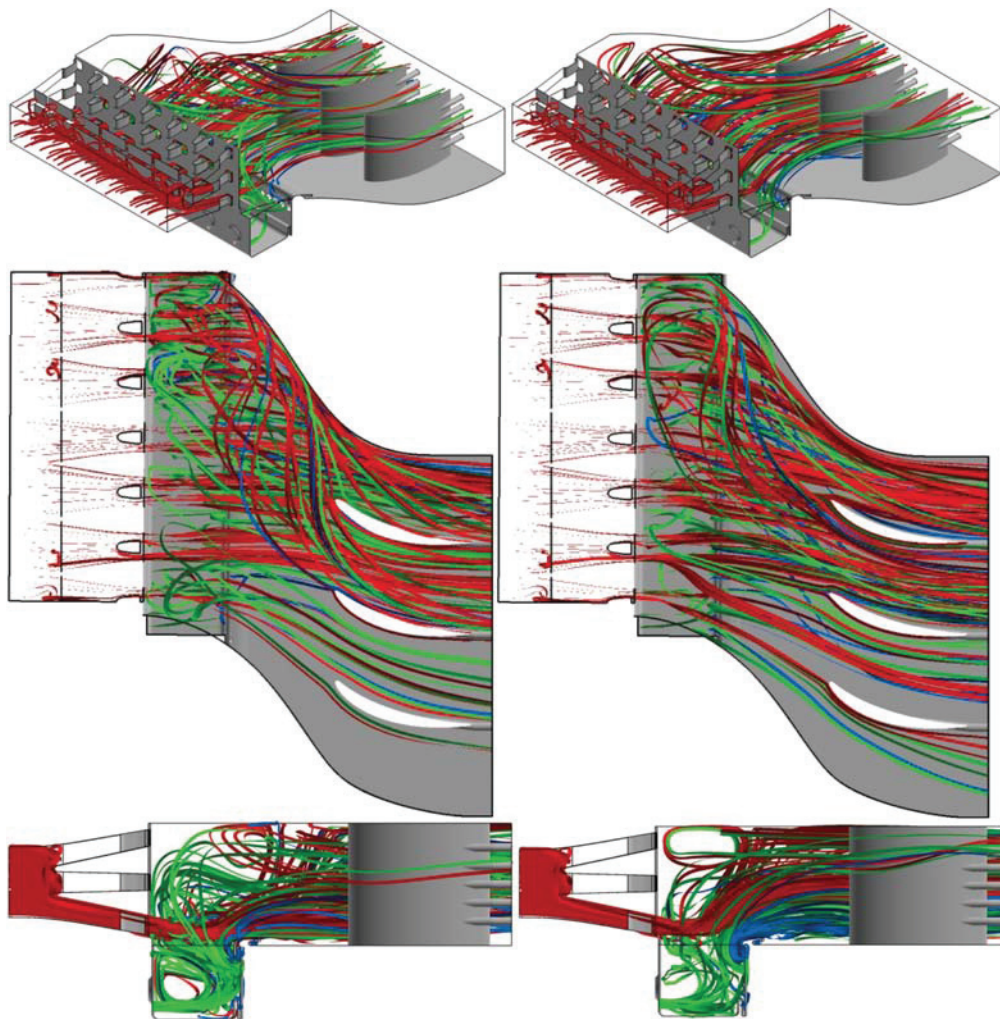
Fig. 9   Isometric, top, and side views of nonreacting (left) and reacting (right) flow streamlines emanating from the inlet boundary condition (red), the forward and aft air driver jets (green), and the cooling jets (blue) for configuration A.

Nonreacting Flow

Reacting Flow

Fig. 10   Comparison between velocity magnitude contours of nonreacting (left) and reacting (right) flow solutions for configuration A. The horizontal plane cuts the bottom row of passages of the CDF in half, as discussed in the context of Figs. 2 and 3. The velocity magnitude is given in meters per second.
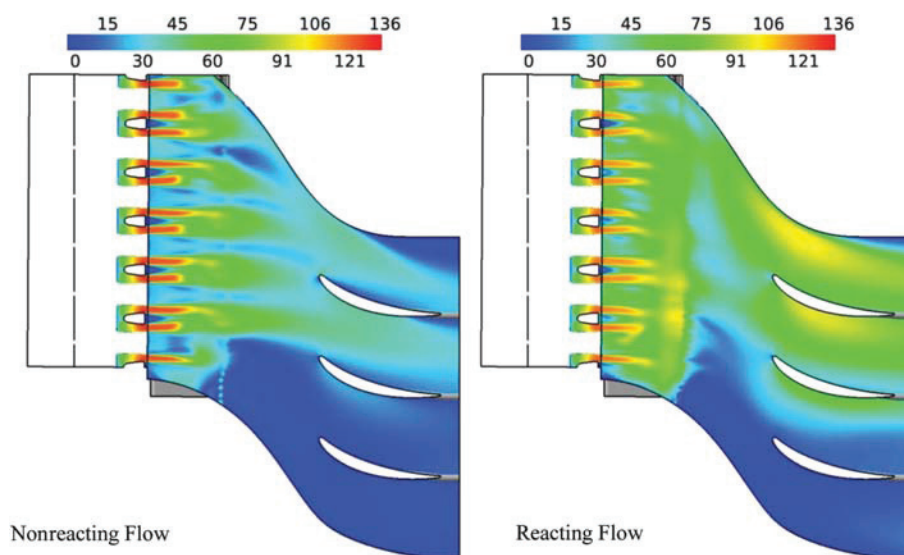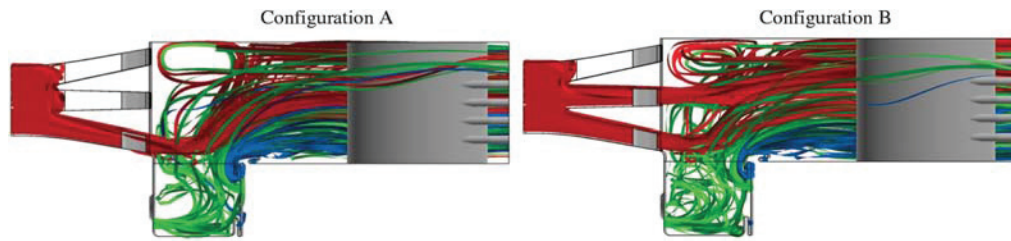
Fig. 11   Side views of configuration A (left) and configuration B (right) flow streamlines emanating from the inlet boundary condition (red), the forward and aft air driver jets (green), and the cooling jets (blue).
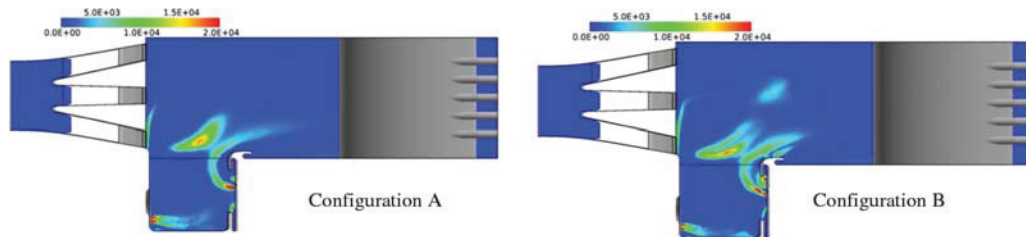

Fig. 12   Product formation rate ρS_C contours at centerplane. The units are in kilograms per cubic meter per second. The product formation rate is the same progress variable source term.

are similar to the ones presented in Fig. 9 for configuration A. However, subtle differences between the two configurations are observed in the TVC. Qualitatively, the flow inside the TVC in configuration A appears to more orderly follow a path, whereas for configuration B, the streamlines are in various directions inside the TVC. In addition, the latter configuration also appears to further enhance the secondary recirculation region in the corner of the CDF face and the UCC top wall.

Figure 12 shows the product formation rate ρS_C contours at the centerplanes for configurations A and B. Both configurations exhibit multiple regions of product formation rate (or progress variable source term). There is one region at the forward driver jets, another at the aft driver jets, another at the exit of the CDF bottom row passages, and another just above the TVC. These reaction zones are discrete and distributed in the spanwise direction, although they are not shown. These regions also indicate the multiple flames contained in
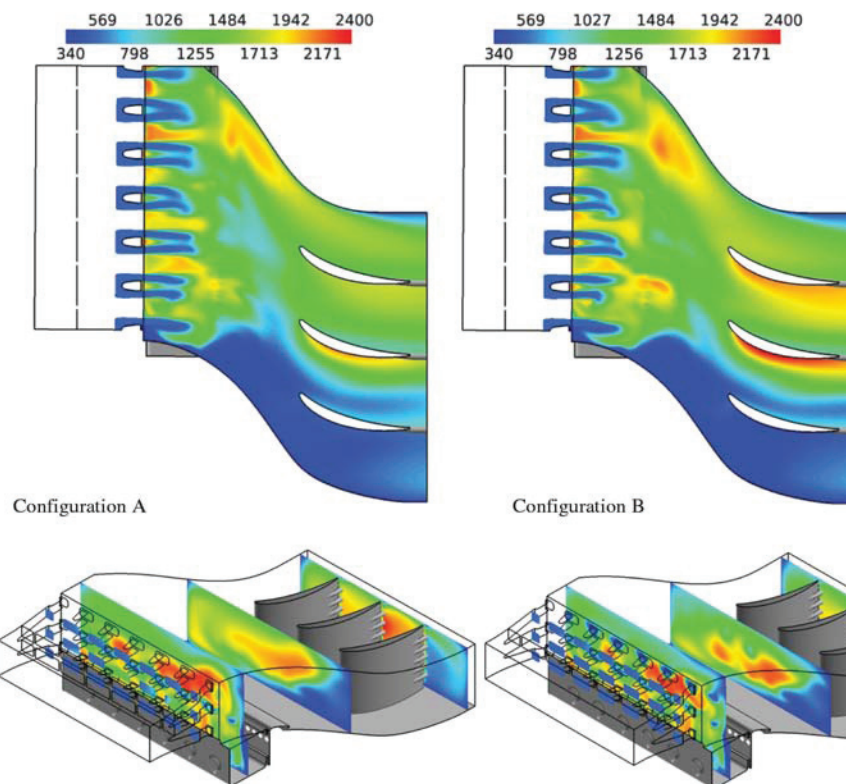

Fig. 13   Temperature contours at various planes for configurations A and B. The plane on the upper images is located at a normal position that cuts the CDF near TVC passages in half. The temperature is in Kelvin.
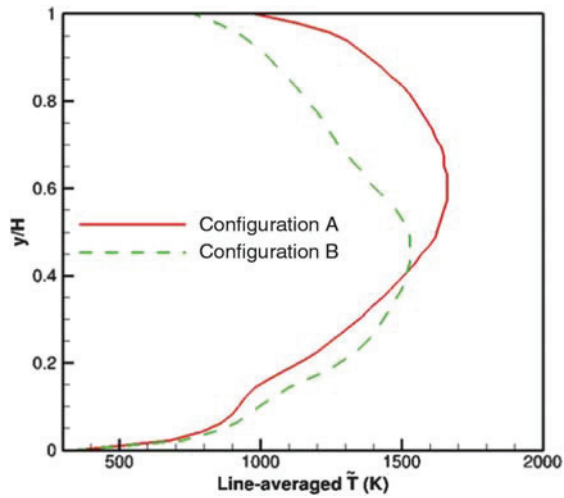
343

Fig. 14   Line-averaged temperature profiles at the plane just upstream of the deswirlers. This plane is shown in Fig. 13.

the flow domain. Therefore, there is not a single turbulent flame, but many. Because the flames are anchored to the discrete jets, increasing the number of driver jets will also increase the number of individual turbulent flames. In addition, each of these individual turbulent flames is formed by multiple reaction zones containing rich premixed, lean premixed, and non-premixed reaction zones [3]. Moreover, there are small ρS_C on the TVC aft wall on either side of the aft driver jets, suggesting that the cooling jets impinging on the metal (cf. Fig. 2) and forming a film are also reacting with the fuel. The ρS_C regions at the forward and aft driver jets follow their corresponding flow direction (cf. Fig. 11). The ρS_C region just above the TVC is actually attached to the exit of the CDF. However, in this figure, it looks as it were lifted. This is because this ρS_C region is bent. For configuration A, there are no individual turbulent flames attached to the CDF's upper row of flow passages because there is no air exiting through this region. In contrast, configuration B contains a few product formation rate regions attached to the CDF's middle row of passages. These flames are also bent; therefore, in this figure, they look like they were lifted. Nonetheless, the reacting flowfields for both configurations are very similar.

Figure 13 illustrates the temperature contours at various planes for configurations A and B. The plane on the upper images is located at a
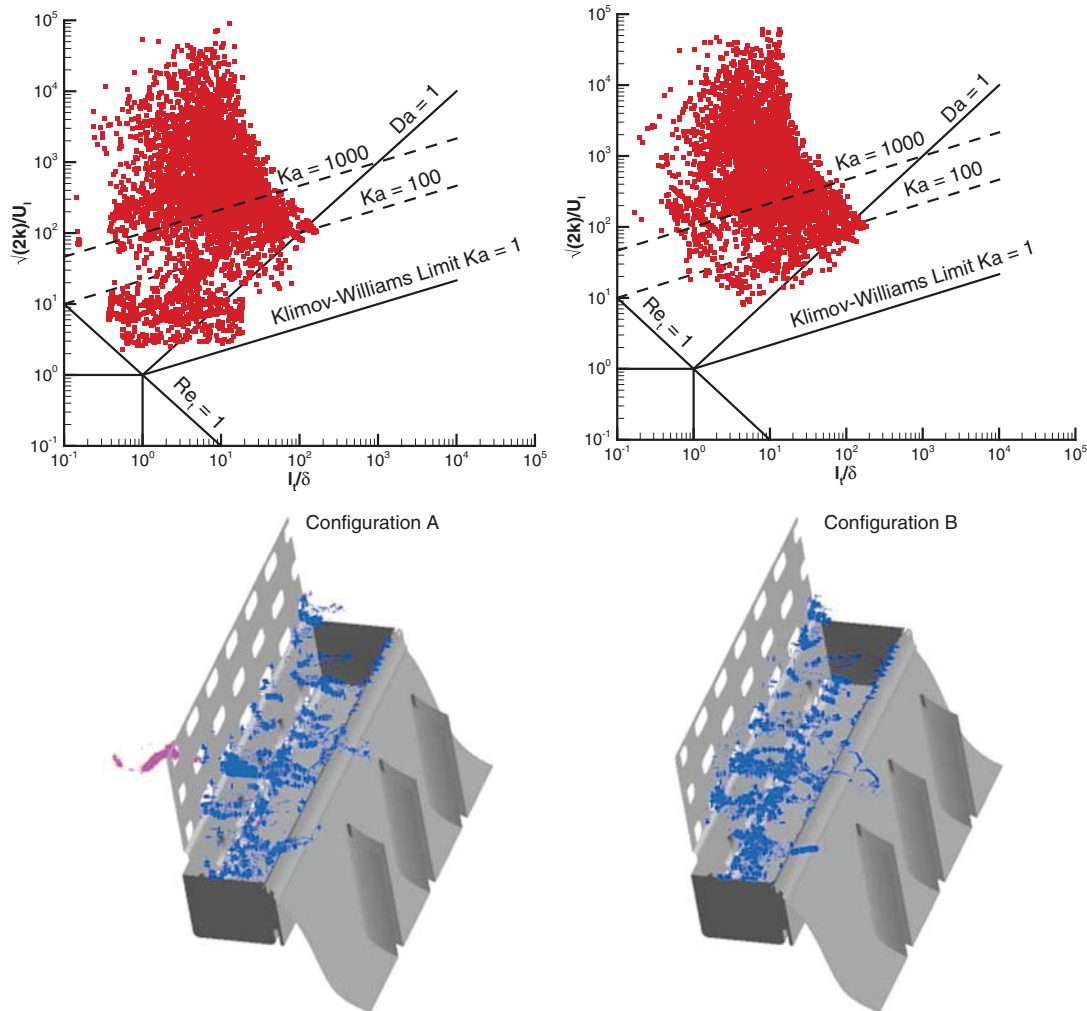

Fig. 15   Borghi diagram for the entire flowfields of configurations A (top-left) and B (top-right). The thickened–wrinkled flamelets ($1 < Ka < 100$) and thickened flamelets ($Ka > 100$) are indicated in magenta and blue, respectively, for both configurations A (bottom-left) and B (bottom-right). The bottom figures only show the region of interest.

normal position that cuts the CDF near-TVC flow passages in half. The results indicate that the fuel, which is injected as a liquid, evaporates and boils within the TVC. The vapor fuel mixes with the air, burning and raising the temperature. Some fuel also seems to mix stoichiometrically above the TVC, as indicated by the high-temperature region at ~2400 K. Then, these hot gases are transported toward the deswirlers. Due to additional mixing, the temperature becomes more uniform and the maximum temperature slightly drops. Recall from the Experimental Procedure section (Sec. III) that the deswirlers are not to be used in the actual UCC. They are used in the experiment only to protect the downstream equipment from lateral forces resulting from the flow. Therefore, the plane just ahead of the deswirlers is the exit temperature profile that the gas turbine will interact with. In this context, the contour of configuration A is more appropriate for gas turbine blades than that of configuration B. No high temperature is observed on the suction side of the right serpentine wall because the flow cannot turn without IGVs, as discussed earlier. At the exit of the rig, both configurations clearly exhibit a hot spot in between the trailing edges of the center and right deswirlers.

Attainment of the desired temperature profile is of paramount importance because an adverse temperature profile can damage the turbine blades and deteriorate turbine performance. Since stresses are highest at the turbine hub and seal materials need to be protected at the turbine blade tip, the temperature profile needs to be center peaked for modern high-performance engines [28]. Therefore, Fig. 14 shows the line-averaged temperature profile just upstream of the deswirler leading edges for both configurations. Both configurations exhibit similar temperature profiles. However, the peak temperature of that of configuration A peaks at $y/H \sim 0.6$, whereas that of configuration B peaks at $y/H \sim 0.5$. Because the temperature of the former configuration is, in addition, about 200 K above that of the latter, we expect that the former will perform better than the latter even, though it is slightly off center. Because the pressure drop is maintained constant for both configurations, configuration B exhibits greater mass flow rate due to more opened passages (i.e., more cross-sectional area). Therefore, configuration B has a leaner overall equivalence ratio ϕ_{UCC} than configuration A. Under equilibrium conditions, the area-averaged exit temperature for configuration A should be higher than that of B. However, combustors are exposed to high stretch effects that could lower the actual temperature from its corresponding equilibrium temperature. To account for these stretch effects, a flamelet model with a PDF-lookup table containing flow-field data (e.g., temperature) as a function of scalar dissipation rates χ_{st} is used. Therefore, the nonequilibrium flow temperature depends not just on equivalence ratio but also on scalar dissipation rate. Because the area-averaged exit temperature of configuration A is greater than that of configuration B, it can be asserted that the characteristic scalar dissipation rate of the former is not sufficient to lower its exit temperature below that of configuration B. In addition, experimental results reported in [1,6] suggested that configuration A provided the best combustion efficiency, temperature profile, and vortex strength within the cavity.

D. Borghi Diagram

To determine the turbulent flame regime, Fig. 15 illustrates the Borghi diagram [29] for the entire flow domain for both configurations under investigation. The ratio of fluctuating velocity to laminar flame speed ($\sqrt{2k}/U_l$) and the ratio of the turbulent integral scale to laminar flame thickness (l_t/δ) were computed all over the computational domain at the flame interfaces (where $\tilde{C} = 0.5$) for both configurations. The integral scale is computed as $l_t = 0.37(\sqrt{2k})^3/\varepsilon$ [10], whereas the laminar flame thickness is estimated as $\delta = \alpha/U_l$. According to Peters [30], the laminar combustion occurs at $Re_t < 1$, turbulent wrinkled flamelets occur at Karlovitz number $Ka < 1$, turbulent thickened–wrinkled flamelets occur in between $Ka < 100$ and $Ka > 1$, and thickened flames occur at $Ka > 100$. Previous experimental [31] and numerical [32] simulations have usually placed the operating conditions of a combustor in a single point in the Borghi diagram. This is because authors have

used inlet conditions to determine the flame regime within the Borghi diagram and/or because the flame corresponds to an individual equivalence ratio ϕ turbulent premixed flame. Results show that both configurations show somewhat similar distributions in the Borghi diagram. However, configuration A spreads from the low turbulent Reynolds number near $Re_t = 1$, whereas configuration B is considerably above $Re_t = 1$. Therefore, the former configuration is exposed to lower turbulence levels. Configuration A contains more fluid particles that are exposed to lower Damköhler numbers than unity. For both configurations, however, the Karlovitz number expands from $Ka = 10$ to 10^6. This latter value exceeds the value reported in the literature. The greater resistance to extinction from stretch may result from two phenomena. Recall that, in these cases, we have turbulent partially premixed flames that have been found to extend the flammability limits and extinction limits due to synergistic interaction between the non-premixed and premixed reactions zones [33–35]. The former improves the stabilization characteristics, whereas the latter enhances emissions. Nevertheless, it is quite possible that the model is overpredicting the flame strength to withstand large stretch rates. This is because the current PDF lookup table does not include the middle (unsteady) and lower (weak) branches of the s-curve response to the stretch rate. Therefore, local extinction and reignition cannot be captured in the simulations [20,21]; hence, the flame survives high Karlovitz numbers. Despite the fact that both configurations do not enclose wrinkled flamelets, they exhibit thickened–wrinkled flamelets and thickened flames. These two regimes are also illustrated in both UCC/TVC/CDF configurations in Fig. 15. The thickened flames are predominantly distributed in the TVC region, whereas the thickened–wrinkled flamelets are concentrated in small regions. For configuration A, the wrinkled–thickened flamelets are found in one of the CDF middle passages that has been closed upstream, whereas for configuration B, the wrinkled–thickened flamelets are found in a small spot in the TVC underneath the thickened flamelets (that it is hard to see in the current image).

V. Conclusions

A numerical and experimental investigation of reacting flows for two ultra-compact combustors configurations was conducted. In this study, a combined-diffuser flameholder was integrated upstream of the trapped-vortex combustor cavity. The CDF, which has three rows of passages at different heights above the cavity, was designed to distribute the inlet air to different regions of the combustor. Two variants of the CDF are compared at constant operating pressure, pressure drop, and inlet temperature. In configuration A, the row of holes nearest the TVC is opened, whereas configuration B has the bottom row of holes opened as well as an adjacent row. Liquid fuel is injected through six fuel injectors in the TVC cavity. The TVC operates at fuel-rich conditions ($\phi_{\text{TVC}} = 1.55$–1.68), whereas the UCC as a whole operates at fuel-lean conditions ($\phi_{\text{UCC}} = 0.53$–0.74). Grid-independent three-dimensional numerical simulations of the UCC are performed following a steady, multiphase, RANS, C-progress variable/flamelet approach using FLUENT. The unstretched laminar flame speeds U_l and flamelets are, respectively, calculated by solving the laminar $n - C_{12}H_{26}/\text{air}$ premixed and non-premixed flame equations using the JetSurf-1.0 detailed chemical reaction mechanism (194 species and 1459 reactions). Jets involved in film cooling are resolved, whereas the effusion-cooling jets are modeled as source terms. Nondispersive infrared analyzers are used to measure the concentrations of CO_2, O_2, and CO at the exit of the rig using a set of three rakes, with each having five vertically aligned quick-quenching sampling probes. Important conclusions are as follows:

1) Reasonable qualitative and quantitative comparisons are obtained between calculations and measurements of CO_2 and O_2 mass fraction profiles. The CO mass fraction profiles are, however, more strongly overpredicted.

2) For nonreacting conditions, there is very little entrainment of the mainstream flow into the TVC cavity for both configurations A and B. The streamlines emanating from driver and cooling jets inside the TVC mix with the mainstream flow in the main channel just

345

above the TVC. Then, the streamlines pass the deswirlers and exit the computational domain. The nonreacting flow results for configurations A and B are qualitatively similar. For both configurations, the results indicate that the flow is not periodic in the spanwise direction because most of the flow passes through the two leftmost passages.

3) The effect of combustion on the flowfield is to diminish mainstream flow entrainment into the TVC cavity while distorting the single dominating recirculation flow obtained under nonreacting conditions. Flow spillage from the TVC appears to penetrate deeper into the mainstream flow under reacting flow conditions. Thermal gas expansion spreads more flow in the spanwise direction, and there is more flow in the passage between the center and right deswirlers (i.e., third passage from left to right) than for the nonreacting flow condition. There is, however, still negligible flow on the fourth rightmost passage, indicating that the IGVs are still needed to turn the flow and must be included in subsequent investigations.

4) For both conditions and configurations, the TVC aft cooling jets as well as the aft driver jets just spill out of this cavity. A major consequence of this result is that there will be richer conditions (in the TVC) than intended and that the corner will be overly cooled. In contrast with the nonreacting flow, the reacting flow exhibits a recirculating flow at the corner of the CDF and UCC top walls that would assist flame stabilization. Future TVC cavity design should consider relocating the aft driver and cooling jets and/or redesigning the TVC corner through which leaking occurs in order to avoid this flow spilling.

5) The reacting flow results for configurations A and B are qualitatively similar. Both configurations exhibit multiple partially premixed turbulent flames attached to the driver jets and the CDF near-TVC flow passages. However, configuration B exhibits subtle differences such as additional turbulent flames attached to some of the CDF middle row of passages. These dissimilarities between the two configurations give rise to qualitative and quantitative differences in the temperature distribution, with both producing near-center peaked exit temperature profiles. Even though the nonequilibrium flow temperature depends not just on equivalence ratio but also on scalar dissipation rate, the area-averaged exit temperature of configuration A (closer to stoichiometric ϕ_{UCC}) is greater than that of configuration B (leaner ϕ_{UCC}). Consequently, the characteristic scalar dissipation rate of the former is not sufficient to lower its exit temperature below that of the latter. Anyway, configuration A performs (overall) better than configuration B when evaluating them in terms of temperature profile, combustion efficiency, and vortex strength.

6) For both configurations, the turbulent flame speed U_t varies linearly with $\sqrt{k} \cdot Da^{1/4}$. This is consistent with theory because, by increasing the Damköhler number Da, the chemical equilibrium state is approached and, consequently, the maximum heat release rate is obtained. In addition, U_t increases with turbulence kinetic energy k because flame wrinkling is increased, which in turn leads to a turbulent flame area greater than that of its corresponding laminar flame area. This indicates that this result is independent of the geometry and/or conditions as long as it is a reacting turbulent flow.

7) For both configurations, their multiple partially premixed turbulent flames contain rich (RPRZs), lean (LPRZs), and non-premixed (NPRZs) reaction zones. According to a Borghi diagram analysis, these reaction zones are within thickened–wrinkled flamelets ($Ka < 100$ and $Ka > 1$) and thickened flames ($Ka > 100$). The reason why these flames can withstand high $Ka > 100$ may be due to the synergistic interaction between the NRPZ, RPRZ, and LPRZ. Nevertheless, it is also possible that the model is overpredicting the flame strength to withstand large stretch rates such as $Ka > 10^6$. This is perhaps because the current PDF lookup table does not include the middle (unsteady) and lower (weak) branches to the s-curve response to the stretch rate. Therefore, local extinction and reignition cannot be captured in the simulations; hence, the flame survives large Karlovitz numbers. The future model should include the capability to account for local extinction and reignition in order to improve the model's robustness. For this, the model will also have to discern among rich premixed, lean premixed, and non-premixed zones, whereas the PDF lookup table will also have premixed flamelets.

Reference

[1] Blunck, D., Shouse, D., Neuroth, C., Battelle, R., Lynch, A., Sekar, B., Zelina, J., Erdmann, T.J., Burrus, D., Howard, R., Briones, A., Richardson, D., and Caswell, A., "Experimental and Computational Studies of an Ultra-Compact Combustor," American Society of Mechanical Engineers Paper GT2013-94372, Fairfield, NJ, June 2013.

[2] Sekar, B., Thornburg, H. J., Briones, A., and Zelina, J., "Effect of Trapped Vortex Combustion with Radial Vane Cavity Arrangements on Predicted Inter-Turbine Burner Performance," AIAA Paper 2009-4603, Aug. 2009.

[3] Xing, F., Zhang, S., Wang, P., and Fan, W., "Experimental Investigation of a Single Trapped-Vortex Combustor, with a Slight Temperature Raise," Aerospace Science and Technology, Vol. 14, No. 7, 2010, pp. 520–525.
doi:10.1016/j.ast.2010.04.007

[4] Xing, F., Wang, P., Zhang, S., Zou, J., Zheng, Y., Zhang, R., and Fan, W., "Experiment and Simulation Study on Lean Blow-Out of Trapped Vortex Combustor," Aerospace Science and Technology, Vol. 18, No. 1, 2012, pp. 48–55.
doi:10.1016/j.ast.2011.03.010

[5] Briones, A. M., Thornburg, H., Sekar, B., Neuroth, C., and Shouse, D., "Numerical-Experimental Research of Ultra Compact Combustors Containing Film and Effusion Cooling," AIAA Paper 2013-1045, Jan. 2013.

[6] Erdmann, T. J., Blunck, D. L., Shouse, D., Neuroth, C., Lynch, A., Caswell, A. W., Richardson, D., and Briones, A. M., "Rayleigh Loss Analysis and Mitigation in Ultra-Compact Combustors," AIAA Paper 2013-0873, Jan. 2013.

[7] Briones, A. M., Sekar, B., and Thornburg, H., "Modeling and Simulation of Enhanced Reactant-Product Mixing in Ultra-Compact Combustors," AIAA Paper 2012-3779, Aug. 2012.

[8] Briones, A. M., Sekar, B., and Thornburg, H. J., "Enhanced Mixing in Trapped Vortex Combustor with Protuberances Part 2: Two-Phase Reacting Flow," AIAA Paper 2011-3422, June 2011.

[9] Katta, V. R., and Roquemore, W. M., "Numerical Studies on Trapped-Vortex Concepts for Stable Combustion," Journal of Engineering for Gas Turbines and Power, Vol. 120, No. 1, 1998, pp. 60–68.
doi:10.1115/1.2818088

[10] ANSYS FLUENT Theory Guide: Release 14, ANSYS, Inc., Canonsburg, PA, 2012.

[11] Kader, B., "Temperature and Concentration Profiles in Fully Turbulent Boundary Layers," International Journal of Heat and Mass Transfer, Vol. 24, No. 9, 1981, pp. 1541–1544.
doi:10.1016/0017-9310(81)90220-9

[12] Barth, T. J., and Jespersen, D., "The Design and Application of Upwind Schemes on Unstructured Meshes," AIAA Paper 1989-0366, Jan. 1989.

[13] Anderson, W., and Bonhus, D. L., "An Implicit Upwind Algorithm for Computing Turbulent Flows on Unstructured Grids," Computers and Fluids, Vol. 23, No. 1, 1994, pp. 1–21.
doi:10.1016/0045-7930(94)90023-X

[14] Hinze, J. O., Turbulence, McGraw–Hill, New York, 1975.

[15] Pitsch, H., Barths, H., and Peters, N., "Three-Dimensional Modeling of NO_x and Soot Formation in DI Diesel Engines Using Detailed Chemistry Based on the Interactive Flamelet Approach," SAE-962057, SAE International, Warrendale, PA, 1996.

[16] Pitsch, H., and Peters, N., "A Consistent Flamelet Formulation for Non-Premixed Combustion Considering Differential Diffusion Effects," Combustion and Flame, Vol. 114, Nos. 1–2, 1998, pp. 26–40.
doi:10.1016/S0010-2180(97)00278-2

[17] Sirjean, B., Dames, E., Sheen, D. A., You, X.-Q., Sung, C., Holley, A. T., Egolfopoulos, F. N., Wang, H., Vasu, S. S., Davidson, D. F., Hanson, R.

K., Bowman, C. T., Kelley, A., Law, C. K., Tsang, W., Cernansky, N. P., Miller, D. L., Violi, A., and Lindstedt, R. P., "A High-Temperature Chemical Kinetic Model of N-Alkane Oxidation," JetSurF Ver. 1.0, Sept. 2009, http://web.stanford.edu/group/haiwanglab/JetSurF/JetSurF1.0/index.html.

[18] CHEMKIN-PRO 15113, Software, Reaction Design, San Diego, CA, 2012.

[19] Kumar, K., and Sung, C.-J., "Laminar Flame Speeds and Extinction Limits of Preheated n-Decane/O_2/N_2 and n-Dodecane/O_2/N_2 Mixtures," *Combustion and Flame*, Vol. 151, Nos. 1–2, 2007, pp. 209–224.
doi:10.1016/j.combustflame.2007.05.002

[20] Ihme, M., Cha, C. M., and Pitsch, H., "Prediction of Local Extinction and Re-Ignition Effects in Non-Premixed Turbulent Combustion using a Flamelet/Progress Variable Approach," *Proceedings of the Combustion Institute*, Vol. 30, No. 1, 2005, pp. 793–800.
doi:10.1016/j.proci.2004.08.260

[21] Dhuchakallaya, I., Rattanadecho, P., and Watkins, P., "Auto-Ignition and Combustion of Diesel Spray using Unsteady Laminar Flamelet Model," *Applied Thermal Engineering*, Vol. 52, No. 2, 2013, pp. 420–427.
doi:10.1016/j.applthermaleng.2012.12.016

[22] Zimont, V., Polifke, W., Bettelini, M., and Weisenstein, W., "An Efficient Computational Model for Premixed Turbulent Combustion at High Reynolds Numbers Based on a Turbulent Flame Speed Closure," *Journal of Engineering for Gas Turbines and Power*, Vol. 120, No. 3, 1998, pp. 526–532.
doi:10.1115/1.2818178

[23] Briones, A. M., Sekar, B., Thornburg, H., and Granlund, K. O., "V-Gutter Flameholder Lean Premixed Flame Stabilization and Blowout," *XX International Symposium on Air Breathing Engines*, ISABE, Cincinnati, OH, Sept. 2011.

[24] Ghoniem, A. F., Chorin, A. J., and Oppenheim, A. K., "Numerical Modeling of Turbulent Flow in a Combustion Channel," *Philosophical Transactions of the Royal Society of London*, Series A: Mathematical and Physical Sciences, Vol. 304, No. 1484, March 1982, pp. 303–325.
doi:10.1098/rsta.1982.0014

[25] Soteriou, M. C., and Ghoniem, A. F., "The Vorticity Dynamics of an Exothermic, Spatially Developing, Forced, Reacting Shear Layer," *Proceedings of the Combustion Institute*, Vol. 25, No. 1, 1994, pp. 1265–1272.
doi:10.1016/S0082-0784(06)80767-8

[26] Mehta, P., and Soteriou, M., "Combustion Heat Release Effects on the Dynamics of Bluff Body Stabilized Premixed Reacting Flows," AIAA Paper 2003-0835, Jan. 2003.

[27] Coats, C. M., "Coherent Structures in Combustion," *Progress in Energy and Combustion Science*, Vol. 22, No. 5, 1996, pp. 427–509.
doi:10.1016/S0360-1285(96)00011-1

[28] Lefebvre, A. H., *Gas Turbine Combustion*, Taylor and Francis, New York, 1983.

[29] Borghi, R, *Recent Advances on Aeronautical Sciences*, edited by Bruno, C., and Casci, C., Plenum, New York, 1984.

[30] Peters, N., "The Turbulent Burning Velocity for Large-Scale and Small-Scale Turbulence," *Journal of Fluid Mechanics*, Vol. 384, April 1999, pp. 107–132.
doi:10.1017/S0022112098004212

[31] Abraham, J., Williams, F. A., and Bracco, F. V., "A Discussion of Turbulent Flame Structure in Premixed Charges," Paper 850345, SAE-P-156, SAE International, Warrendale, PA, 1985.

[32] Veynante, D., and Vervisch, L., "Turbulent Combustion Modeling," *Progress in Energy and Combustion Science*, Vol. 28, No. 3, 2002, pp. 193–266.
doi:10.1016/S0360-1285(01)00017-X

[33] Briones, A. M., Som, S., and Aggarwal, S. K., "Effect of Multistage Combustion on NO_x Emissions in Methane–Air Flames," *Combustion and Flame*, Vol. 149, No. 4, 2007, pp. 448–462.
doi:10.1016/j.combustflame.2007.01.007

[34] Shu, Z., Aggarwal, S. K., Katta, V. R., and Puri, I. K., "Flame-Vortex Dynamics in an Inverse Partially Premixed Combustor: The Froude Number Effects," *Combustion and Flame*, Vol. 111, No. 4, 1997, pp. 276–286.
doi:10.2514/6.1997-259

[35] Amantini, G., Frank, J. H., Smooke, M. D., and Gomez, A., "Computational and Experimental Study of Standing Methane Edge Flames in Two-Dimensional Axisymmetric Counterflow Geometry," *Combustion and Flame*, Vol. 147, Nos. 1–2, 2006, pp. 133–149.
doi:10.1016/j.combustflame.2006.05.006

A. Gupta
Associate Editor

Appendix Z. Effect of Conventional and Alternative Fuels on a Marine Bacterial Community and the Significance to Bioremediation

Effect of Conventional and Alternative Fuels on a Marine Bacterial Community and the Significance to Bioremediation

Oscar N. Ruiz,*,[†] Lisa M. Brown,[‡] Richard C. Striebich,[‡] Caitlin E. Smart,[†] Loryn L. Bowen,[‡] Jason S. Lee,[§] Brenda J. Little,[§] Susan S. Mueller,[‡] and Thusitha S. Gunasekera[‡]

[†]Air Force Research Laboratory, Aerospace Systems Directorate, Fuels and Energy Branch, Wright-Patterson AFB, Ohio 45433, United States
[‡]University of Dayton Research Institute, Dayton, Ohio 45469, United States
[§]Naval Research Laboratory, Stennis Space Center, Mississippi 39559, United States

Ⓢ Supporting Information

ABSTRACT: Understanding the effect of conventional and alternative fuels on the marine bacterial community is crucial, as it pertains to the impact, biodegradation, and final fate of these fuels in the environment. Metagenomics analysis demonstrated that conventional and alternative fuels promoted the growth of *Proteobacteria*. *Marinobacter* and *Desulfovibrio* were predominant in seawater exposed to conventional jet propellant-5 (JP-5), while *Hyphomonas* and *Rhodovulum* were most abundant in seawater with hydroprocessed renewable jet fuel (HRJ) and conventional F-76 diesel, respectively. The phyla *Bacteroidetes, Firmicutes*, and *Lentisphaerae* were underrepresented in samples with fuel, and these phyla were largely comprised of unclassified bacteria. Culture-dependent tests isolated several of the same genera detected in high abundance by metagenomics DNA sequencing, including *Marinobacter, Rhodovulum*, and *Halobacillus*. Growth studies in fuel and gas chromatography analysis demonstrated that isolates grew in fuel and metabolized hydrocarbons efficiently. The hydrocarbon degradation profile of each bacterium was conserved from conventional to alternative fuels. The study indicated that bacteria must out-compete others to get established and proliferate. Competition between hydrocarbon degraders was an important factor affecting the bioremediation process. This study provides insights into the growth characteristics of hydrocarbon-degrading bacteria and the effects of fuel on marine bacterial communities.

INTRODUCTION

A wide range of bacteria have been isolated from marine and terrestrial environments contaminated with hydrocarbons.[1−5] Bacteria of the phyla *Proteobacteria, Bacteroidetes, Actinobacteria,* and *Firmicutes* are often found in hydrocarbon polluted marine and terrestrial environments.[6−11] *Gammaproteobacteria*, including *Marinobacter, Alcanivorax, Pseudomonas*, and *Acinetobacter* were recovered from salt marshes and ocean surface water contaminated with hydrocarbons.[12] Studies have shown that biostimulation of indigenous marine bacteria at spill sites can enhance the biodegradation of crude oil.[11,13−15]

Hydrocarbon fuel can be divided into two classes: conventional and alternative fuels. Conventional fuels are liquid hydrocarbon mixtures such as gasoline, kerosene, jet fuel, and diesel derived from the distillation of nonrenewable crude oil (petroleum). Alternative fuels are liquid hydrocarbon fuels derived from renewable feedstock and, on rare occasions, from unconventional nonrenewable resources (i.e., natural gas and coal) through advanced physicochemical and biological processes.[16,17] Unlike biodiesel (fatty acid methyl esters or FAME) and ethanol biofuels, which are not comprised of hydrocarbons, alternative fuels are considered "drop in" fuels, meaning they resemble the corresponding conventional hydrocarbon fuel in composition and physicochemical properties, and may be used directly in vehicles without having to modify any of their systems. While alternative fuels derived from renewable feedstocks may prove more environmentally

friendly than conventional fuels due to a reduced carbon footprint, their complex hydrocarbon composition presents environmental challenges similar to those of conventional fuels, including biodegradability and environmental impact. Because of these factors, it is important to assess the effect of these new fuels on the environment.

The metabolic flexibility of bacteria was observed in the crude oil plumes of the Deepwater Horizon blowout in the Gulf of Mexico in 2010, where the indigenous marine microbial population remediated the oil plume.[18] While the microbial population in the oil plume was enriched with hydrocarbon-degrading bacteria, the microbial diversity was drastically reduced in comparison to the clean surrounding water column.[18] Similarly, exposure of seawater to biodiesel (fatty acid methyl ester fuel) substantially altered the microbial community.[19] These observations indicate that not every bacterium has the genetic adaptation required to persist and proliferate in environments contaminated with hydrocarbons.

Bacteria grow at the interface between fuel and water, secreting emulsifiers such as rhamnolipids to increase the solubility of hydrocarbons in water and facilitate utilization.[20−22] While fuel can be an excellent source of carbon, some of its components may be toxic to living cells.
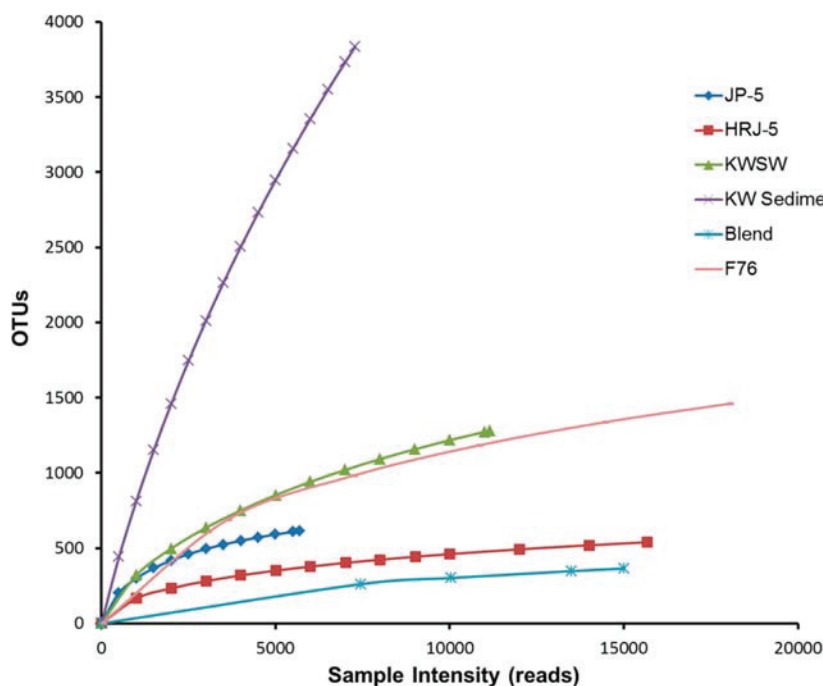
Figure 1. Rarefaction curve showing the effect of different fuels on bacterial diversity. OTUs assigned at 5% distance.

Hydrocarbon fuels may contain aromatics, cyclic hydrocarbons, branched and normal alkanes, and additives which often are toxic to microorganisms.[9,23,24] Hence, bacteria that grow in fuel have evolved mechanisms such as the formation of biofilms, secretion of biosurfactants, regulation of efflux pumps and porins, and hydrocarbon catabolism for protection against toxic compounds.[25,26] Important nutrients such as nitrogen, phosphorus, and iron are often in low availability in oil-contaminated environments. The up-regulation of multiple iron uptake genes including pyoverdin and pyochelin in *P. aeruginosa* during growth in Jet-A fuel was reported.[26] Due to the diversity of hydrocarbon compounds in alternative and conventional fuels, no single bacterium can metabolize every compound. Bacteria selectively consume hydrocarbon components within fuel with many showing specificity for *n*-alkanes and simple aromatics.[10,27−29]

The goal of this study is to understand how fuels with different hydrocarbon composition affect the bacterial community in a sample of coastal seawater from Key West, Florida. Members of the fuel-enriched population were isolated, identified, and characterized for their ability to grow and metabolize fuel. The effect of competition between hydrocarbon degraders was evaluated. Culture-independent metagenomic analysis was used to identify and quantify bacteria before and after exposure to conventional and alternative fuels of different compositions.[4,30,31] Bacteria were isolated from the fuel-seawater enrichments by culturing. Their growth rate in fuel and hydrocarbon degradation profile were determined by gas chromatography−mass spectrometry (GC-MS) to confirm the hydrocarbon bioremediation potential. The fuel-degrading isolates were used in fuel growth assays to test the degradability of several conventional and alternative fuels. Finally, fuels of different hydrocarbon composition were evaluated to see how they affected a consortium of hydrocarbon degraders. This

study expands our understanding on the effects of fuel contamination on marine environments and demonstrates that marine bacterial communities contain active metabolic pathways for the degradation of diverse hydrocarbon classes.

■ EXPERIMENTAL SECTION

Conventional and Alternative Fuels. Conventional fuels U.S. military petroleum marine diesel (F-76), petroleum jet propellant 5 (JP-5), petroleum jet propellant 8 (JP-8), and commercial jet fuel (Jet-A) were used in this study. Jet-A, JP-8, and JP-5 are all kerosene jet fuel of similar composition and characteristics. What makes JP-8 and JP-5 different from Jet-A is the addition of specific additive packages that may serve to improve lubricity, reduce corrosion, prevent the formation of ice and dissipate static charges. Also, JP-5 has a higher flash point than Jet-A and JP-8 so it can be used in shipboard aircrafts. Alternative fuels camelina-derived hydro-processed renewable JP-5 (HRJ-5), algal-derived hydro-processed renewable F76 diesel (HRD), and catalytic hydrothermal conversion diesel (CHCD) were used in this study. In addition, JP-5 and HRJ-5 were blended in a 50/50 volume percent ratio (v/v) to produce 50/50 JP-5/HRJ-5 (Blend) which was also tested. These fuels were selected because they are representative of middle-range distillate fuels commonly used in civilian and military transportation.

Seawater Exposure to Fuel. Oligotrophic coastal seawater containing sediment was collected from Key West, FL, and used as inoculum and growth medium.[32] Throughout this paper, the natural seawater with sediment is abbreviated as NKWSW. During metagenomic analysis (Figures 1−3, and Figure S1, Supporting Information), the coastal seawater inoculum was separated into the liquid fraction (KWSW) and the solid sediment fraction (KW sediment) to facilitate DNA extraction and characterization of bacterial populations.

Seven chambers were constructed to contain seawater and fuel combinations. The chambers (Tank Depot, Pompano Beach, FL) were rectangular and constructed from heavy gauge, chemical and fuel resistant, opaque black cross-linked polyethylene plastic. A schematic representation of the fuel/seawater exposure chamber is provided in Figure S2, Supporting Information. NKWSW (4.5 L) with fuel (3 L),
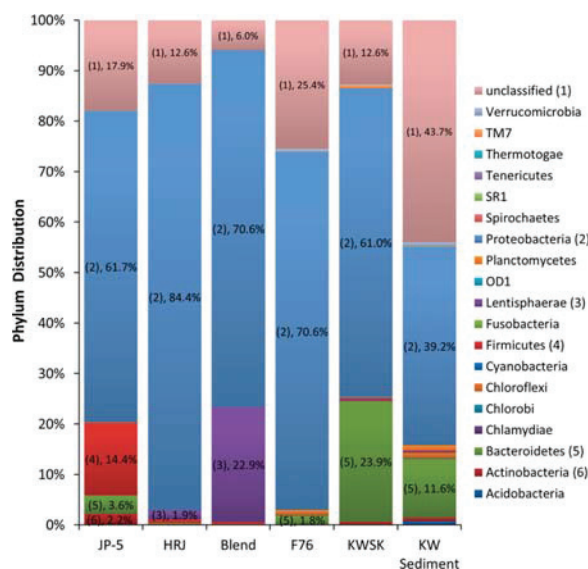
Figure 2. Phylum distribution per sample. Bacteria identity was assigned at 95% similarity. The following phyla have a relative abundance above 1% and have been identified in the graph by a number and their respective relative abundance: *Actinobacteria* (6), *Bacteroidetes* (5), *Firmicutes* (4), *Lentisphaerae* (3), *Proteobacteria* (2), *Unclassified* (1).

and NKWSW (7.5 L) with no fuel were sealed in the chambers with approximately 7 L of air in the headspace as previously described.[32] The fuels examined were F-76, JP-5, HRJ-5, and JP-5/HRJ-5 (Blend). No attempt was made to remove oxygen from the fuel, seawater, or head space prior to sealing the chamber. Chambers were placed in an anaerobic glovebox (0.01% CO_2, 10% H_2, balance N_2). Temperature was maintained at 23 °C. After 90 days, NKWSW was sampled and used in genomics and microbiological studies.

Metagenomic Analysis. Genomic DNA extractions were performed by filtering 50 mL of water from fuel-KWSW samples through a 0.22 μm filter (Durapore, Millipore Billerica, MA, USA). Genomic DNA was extracted from the filter using a Power Water Kit (MoBio Laboratories, Inc. Carlsbad, CA, USA). Genomic DNA was extracted from 4.35 g of wet Key West (KW) sediment using a MoBio Power Max Soil Kit.

An approximate 500bp region of the 16S *rrn* gene was amplified by PCR using 100 ng of DNA from each sample in a reaction consisting of 13 μL sterile water, 2.5 μL 10X PCR buffer, 1.5 μL 25 mM $MgSO_4$, 2.5 μL 2 mM dNTP's, 0.5 μL KOD Polymerase (EMD Millipore, Billerica, MA, USA), 200 nM of FuelbugF (tggagagtttgatcctggctca) and 200 nM of FuelbugR (gctgctggcacgtagttagc) primers.[33] These primers included sequences for the multiplexing barcodes and 454 sequencing primers (454 Sequencing Bulletin No. 005−2009). The PCR amplification was performed by an initial 2 min denaturing step at 94 °C followed by 30 cycles of denaturation (94 °C, 30 s), annealing (51 °C, 20 s), and extension (72 °C, 30 s), and finished with a final 72 °C extension step for 5 min. Small fragment removal was performed with AMPURE XP beads (Beckman Coulter Brea, CA, USA). The cleaned DNA amplicons were quantified prior to sequencing by using the 454 GS Titanium Kit (KAPA Biosystems Wilmington, MA, USA). Finally, 5×10^5 DNA amplicon molecules from each sample were pooled, amplified via emulsion PCR using a 0.4 to 1 DNA molecules to beads ratio and sequenced on a Roche 454 Junior platform (Branford, Connecticut, USA) as described by the Roche emPCR amplification and sequencing manuals.

DNA sequence reads were first parsed using the Roche 454 Junior software (Branford, Connecticut, USA) and each sample library cleaned by the Ribosomal Database Project (RDP) Initial Processor to remove short sequence reads (<200 bp), reads with a Q-score less than 20, reads with any mismatch in the forward primer or any read with a 'N'-called base pair. Chimeric sequences were detected using DECIPHER and removed using RDP.[34,35] Libraries were then aligned and classified in RDP at a 95% confidence cutoff.[34,36]

The 16S *rrn* metagenomics libraries derived from the KWSK, KW sediments and NKWSW exposed to different fuels are available in MGRAST (metagenomics.anl.gov) under the accession number 4544004.3−4544009.3.

Isolation and Identification of Marine Bacteria from Fuel-Exposed Seawater. To obtain individual bacteria isolates, 1 mL of KWSW from samples containing JP-5, HRJ-5, Blend and F-76 and KWSW unexposed to fuel were serially diluted and plated on Marine Agar 2216 and incubated at 28 °C until colonies were visible (approximately 48 h). Individual colonies were subcultured on marine agar and grown in Marine Broth 2216 (Difco) to produce glycerol stocks and for subsequent DNA extraction. DNA was extracted from each pure bacterial isolate using the Mo-Bio UltraClean Microbial DNA Isolation Kit. Identification of bacterial isolates to genus and, in some cases, to species level was determined by BLAST analysis of a 500 bp fragment sequences from the 16S rRNA gene generated by the bacterial universal primers FuelbugF (tggagagtttgatcctggctca) and 200 nM of FuelbugR (gctgctggcacgtagttagc) primers.[33] A species name was only provided for DNA sequences presenting at least 99% homology with known GenBank species. Isolates were preserved for long-term storage, frozen at −80 °C in glycerol stocks.

Fuel Growth Assay. Marine bacterial isolates were grown in marine broth (BD Difco), harvested by centrifugation and washed three times with 0.1 μm filter sterilized seawater. Cells were then inoculated at a final concentration of 0.03 OD_{600} into sterilized KWSW supplemented with an equal volume of Bushnell-Haas (BH) minimal media.[37] Cultures were grown aerobically at 28 °C in a shaking (200 rpm) incubator. Growth was monitored periodically measuring absorbance at 600 nm in a spectrophotometer or by quantitative real-time PCR (qPCR).

Quantitative Real-Time PCR (qPCR). Quantitative real-time PCR analysis was performed on bacterial genomic DNA isolated at different time points during the growth assays as previously described.[38−40] The qPCR reaction was performed in a CFX real-time PCR system (BioRad, Hercules, CA) using a two-step amplification program at 60 °C with a postamplification melt curve for quality control. Total bacteria and specific species were quantified and detected by using a universal 16S *rrn* gene primer set[41] or species-specific 16S *rrn* primer sets as follows: *M. hydrocarbonoclasticus* (FW: CCT ACG GGA GGC AGC AGT/RV: GTA GGT AAC GTC AAG CCT CAT GGG TAT), *Rhodovulum* sp., NI22 (FW: CCT ACG GGA GGC AGC AGT/RV: CGG CTA CCG TCA TTA TCT TCA CCG T), *Halobacillus* sp. (FW: CCT ACG GGA GGC AGC AGT/RV GTA CCG CTC TAT TCG CAC GGT). For absolute quantification, synthetic oligonucleotides spanning the amplicon length were serial-diluted from 1×10^8 copies/μL to 1×10^3 copies/μL, and used as standards. The qPCR sample reaction contained 1 μL primer set (200 nM final concentration), 12.5 μL Biorad SYBR Green SuperMix, 10.5 μL water and 1 μL of the appropriate sample DNA for a total volume of 25 μL.

Fuel Degradation Prolife by GC Analysis. Assays were conducted to identify specific compounds in fuel F76, HRD and CHCD that were degraded by *Marinobacter hydrocarbonoclasticus* strain NI9 and *Rhodovulum* sp., strain NI22.[29,42] The assays were performed using 10 μL of fuel in 1 mL of supplemented KWSW containing *M. hydrocarbonoclasticus* and *Rhodovulum* at 0.01 OD in a 10 mL glass vial sealed with a Teflon-lined lid. The samples were maintained in a 28 °C incubator for a period of up to 21 days, without opening the vials. Multiple sample replicates were incubated simultaneously and sample vials (n = 3 per time point) were removed from the incubator at the time of testing. Sample extractions were prepared as previously explained.[29] The methylene chloride containing the extracted hydrocarbons was recovered and analyzed by GC-MS (Agilent 5890/5973). This GC-MS analysis was conducted in split-injection mode. A HP-5MS (Agilent) column was heated from 40 to
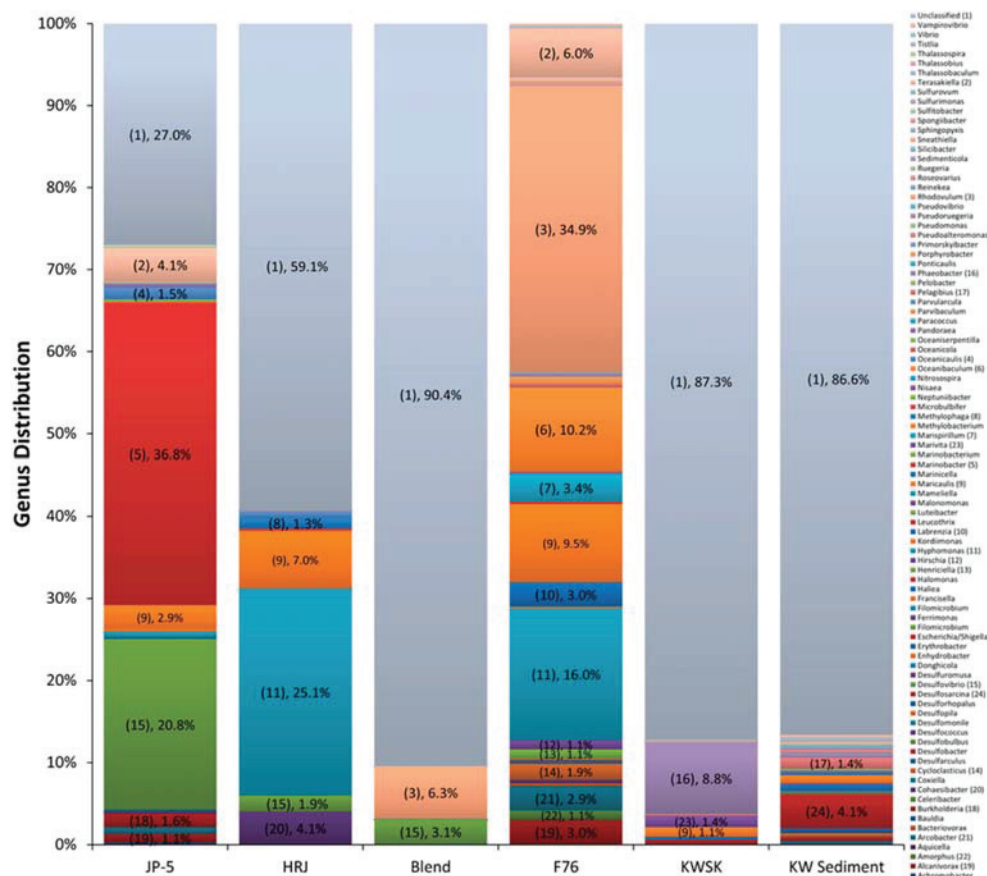
Figure 3. Genera within phylum *Proteobacteria*. Bacteria identity was assigned at 95% similarity. The following genera have a relative abundance above 1% and have been identified in the graph by a number and their respective relative abundance: *Alcanivorax* (19), *Amorphus* (22), *Arcobacter* (21), *Burkholderia* (18), *Cohaesibacter* (20), *Cycloclasticus* (14), *Desulfosarcina* (24), *Desulfovibrio* (15), *Henriciella* (13), *Hirschia* (12), *Hyphomonas* (11), *Labrenzia* (10), *Maricaulis* (9), *Marinobacter* (5), *Marivita* (23), *Marispirillum* (7), *Methylophaga* (8), *Oceanibaculum* (6), *Oceanicaulis* (4), *Pelagibius* (17), *Phaeobacter* (16), *Rhodovulum* (3), *Terasakiella* (2), *Unclassified* (1).

280 °C at 5 °C per minute to elute the 1 μL sample. The MS scanning range was 33−350 Da and extracted ions were used for quantitation of the signal. The analyzed samples were compared to control samples using an extracted ion signal for each compound of interest. Sample responses for each compound were adjusted for the internal standard concentration to measure concentration of compounds of interest as the jet fuel degraded.

■ RESULTS AND DISCUSSION

**Seawater Bacterial Community Characterization.** Rarefaction analysis of KWSW and KW sediment not exposed to fuel showed high bacterial diversity with 1,272 and more than 3,835 operation taxonomic units (OTUs), respectively (Figure 1). The diversity in KW sediment was greater than in KWSW. In fact, the rarefaction analysis indicated the coverage provided by the sequencing reaction was insufficient to discover all the different bacteria present in the KW sediment sample (Figure 1). Ocean sediments and sands may be orders of magnitude more biodiverse than the surrounding water column, serving as reservoirs of biodiversity.[43] Phylum distribution analysis indicated that KWSW and KW sediment samples were highly diverse with 18 different phyla and a large portion of unclassified members. *Proteobacteria* was the predominant phylum in KWSW and KW sediment with

39.2% (2857 reads) and 61% (6813 reads) of the total reads, respectively (Figure 2). *Bacteroidetes* was highly represented with 23.9% (2,667 reads) and 11.6% (844 reads) of the total population in KWSK and KW sediment (Figure 2). The unclassified group represented 12.6% and 43.7% of the population in KWSW and KW sediment, respectively (Figure 2). At least 86% of the bacteria in the phylum *Proteobacteria* were unclassified at the genus level (Figure 3). The *Bacteroidetes* in KWSW and KW sediment were 98.8% and 46.4% unclassified, respectively (Figure S1a, Supporting Information). The phyla *Firmicutes* and *Lentisphaerae* were comprised almost in their entirety of novel unclassified genera (Figure S1b-c, Supporting Information). These results indicated that marine bacterial communities were very complex and largely uncharacterized.

Effect of Hydrocarbon Fuels on Seawater Bacterial Population. Exposure of NKWSW (combined liquid and sediments fractions) to JP-5, HRJ, and Blend jet fuels for 90 days reduced the biodiversity to less than 600 OTUs (Figure 1). Exposure of NKWSW to F-76 diesel fuel produced a less dramatic reduction in OTUs than that observed in the jet fuels (Figure 1). The phylum diversity dropped from 18 in unexposed NKWSW to less than ten after exposure to any of
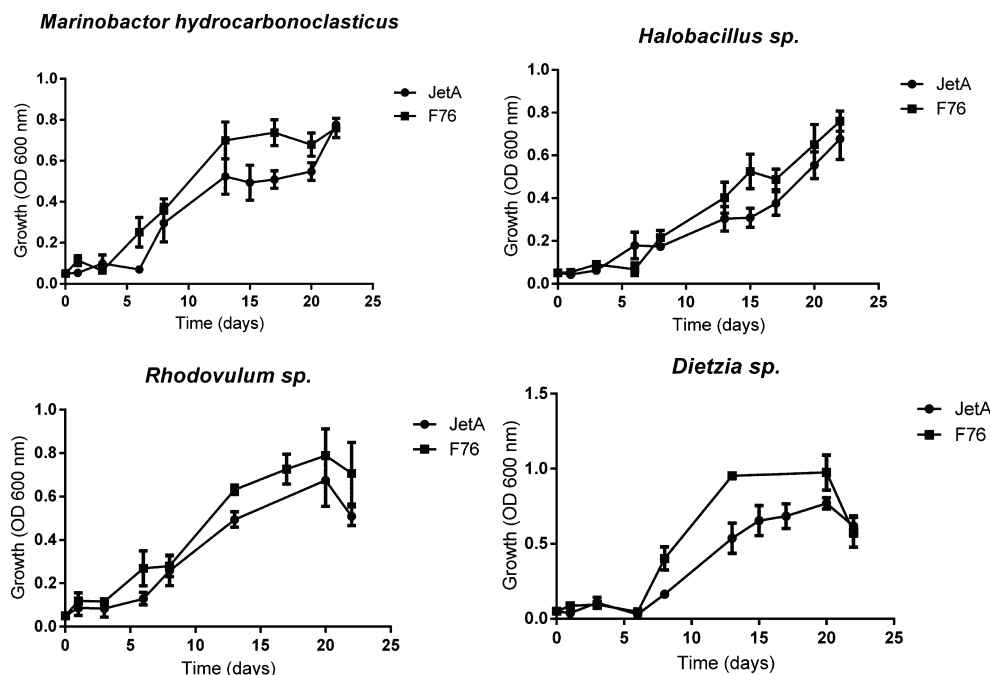
Figure 4. Bacterial fuel growth assay. The bacteria *M. hydrocarbonoclasticus*, *Halobacillus* sp., *Rhodovulum* sp., and *Dietzia* sp. were grown in seawater-BH minimal media in the presence of Jet-A and F-76 marine diesel for 24 days and their growth determined by measuring the OD_{600}.
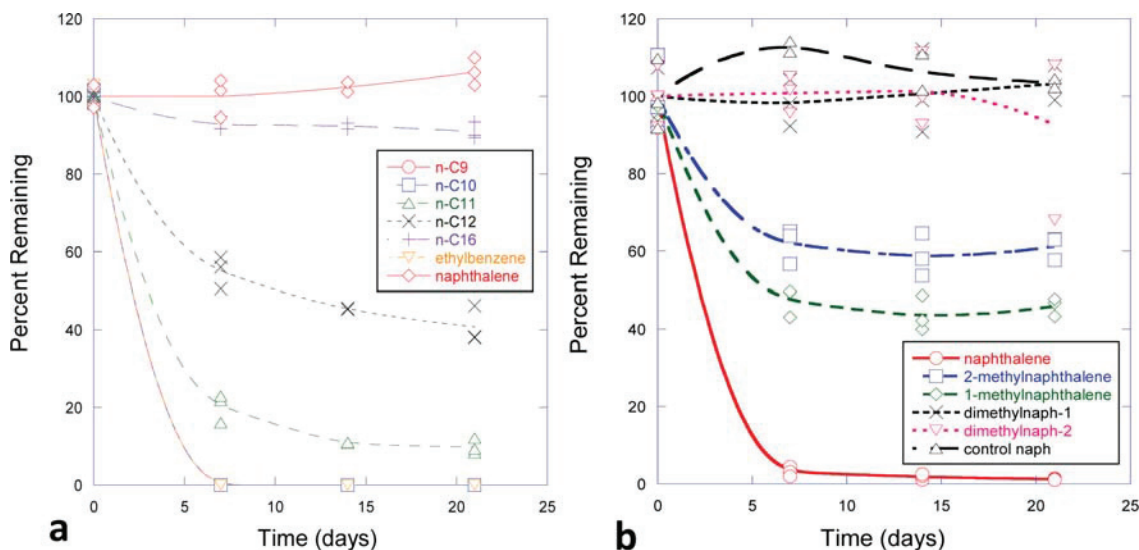
Figure 5. Selective consumption of F-76 diesel hydrocarbons by *Marinobacter hydrocarbonoclasticus* (a) and *Rhodovulum navalis* (b). The samples were analyzed by scanning GC-MS using extracted ion signals and compared to controls. Two isomers of methyl naphthalene and dimethyl naphthalene are shown in panel b.

the four fuels (Figure 2). The phylum *Proteobacteria* was the most abundant with 62% to 84% of the total population (Figure 2). *Firmicutes* and *Lentisphaerae* were abundant in JP-5 and Blend samples, accounting for 14.4% and 22.9% of the total population, respectively (Figure 2). The phylum *Proteobacteria* was generally promoted by all four fuels, while the *Firmicutes* and *Lentisphaerae* were enhanced by JP-5 and Blend, respectively. The abundance of *Bacteroidetes* was substantially reduced by the presence of fuel.

The effect of the fuels on the type of bacteria was more obvious at the genus level (Figure 3). The *Proteobacteria* genera *Marinobacter* and *Desulfovibrio* were most abundant in JP-5 while *Hyphomonas* and *Rhodovulum* were most abundant in HRJ and F-76 respectively. The Blend increased the numbers of unclassified *Proteobacteria* (Figure 3). Interestingly, the opposite effect was observed with F-76 which actually promoted known genera (Figure 3). The phyla *Bacteroidetes*, *Firmicutes* and *Lentisphaerae* were largely comprised of
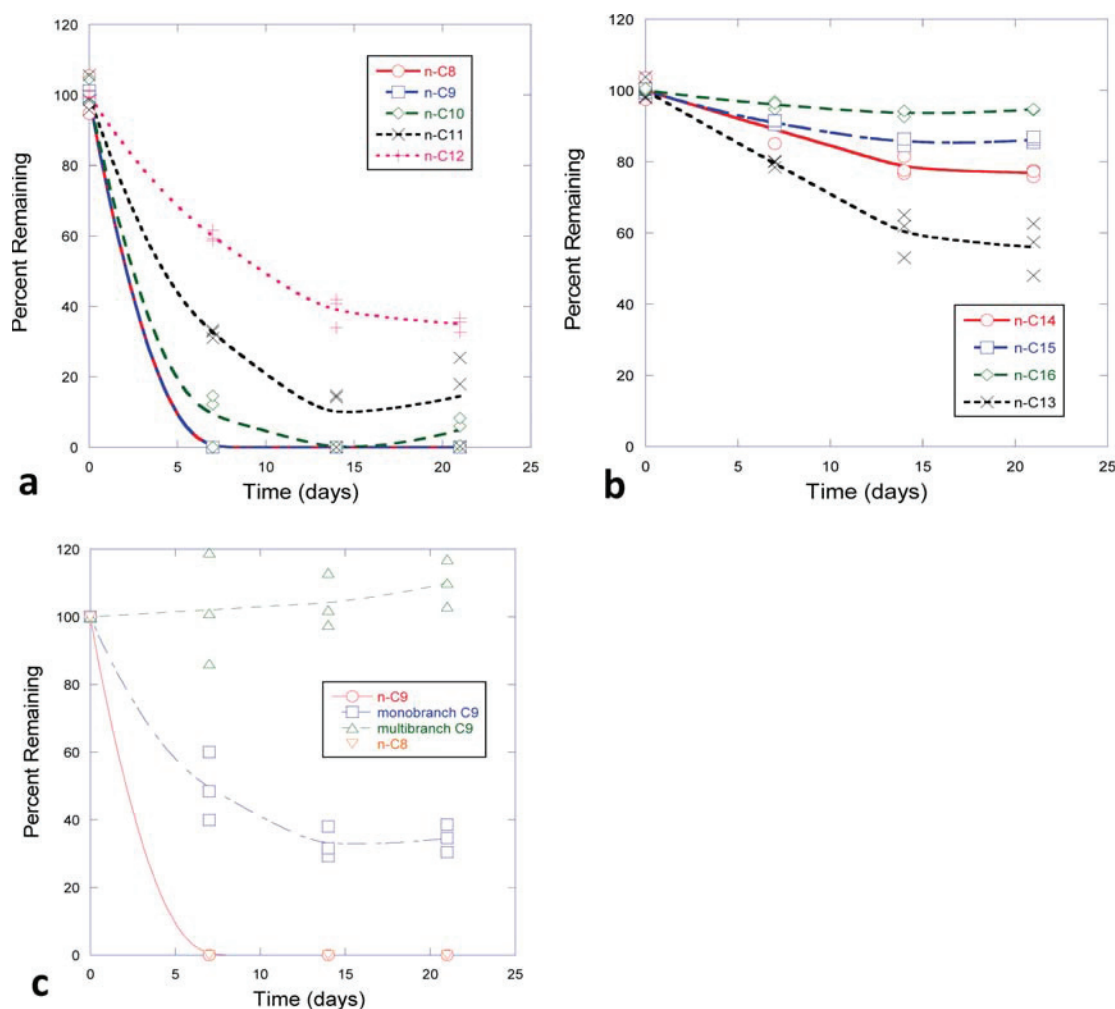
Figure 6. Degradation of HRD normal and branched alkanes by *Marinobacter hydrocarbonoclasticus* over 21 days.

unclassified bacteria with some important exceptions that included the genera *Maricauda*, *Halobacillus*, *Croceitalea*, *Mesoflavibacter*, *Sporobacter* and *Clostridium*. The genus distribution for the phyla *Bacteroidetes*, *Firmicutes* and *Lentisphaerae* in the different samples is provided in Figure S1, Supporting Information.

Sulfate-reducing bacteria (SRB) of the genus *Desulfovibrio* were present in all four fuel samples but predominantly in JP-5 (Figure 3). The JP-5 exposed sample also contained a high level of the fast growing *Marinobacter hydrocarbonoclasticus*. Striebich et al.,[29] showed that *M. hydrocarbonoclasticus* grew fast in the presence of Jet-A and F-76 diesel fuel, depleting oxygen rapidly from the headspace of airtight containers during hydrocarbon consumption. *Marinobacter* sp., in chemostat coculture with *Desulfovibrio oxyclinae*, rapidly depleted oxygen allowing anaerobic growth of *Desulfovibrio*.[44] Syntrophic interaction between cyanobacteria, *Marinobacter* sp., and SRB in marine microbial mats provided a suitable environment for aerobic and anaerobic metabolism.[45] This observation indicates that hydrocarbon fuel could promote syntrophic relationships between aerobic and anaerobic bacteria.

Fuel exerts high selective pressure on bacteria communities promoting those members with the adaptations to withstand and metabolize hydrocarbons. JP-5, HRJ and F-76 have different hydrocarbon composition (Figure S3 and S4, Supporting Information). Petroleum derived jet fuel contains about 23% *n*-paraffins, 33% isoparaffins, 22% aromatics and 21% cycloparaffins, while F-76 diesel contains about 11% *n*-paraffins, 20% isoparaffins, 28% aromatics and 40% cycloparaffins.[29] HRJ lacks aromatics and has a higher proportion of branched alkanes to *n*-alkanes than JP-5. These compositional differences may help explain why different bacteria were promoted by these fuels. For example, the ability to metabolize highly branched alkanes and toxic polycyclic aromatics appears to be a less general trait than the ability to degrade *n*-alkanes.[27−29] Thus, it would be expected that a fuel with a high proportion of these compounds would select for novel microorganisms.

Isolation and Characterization of Fuel-Degrading Bacteria. Bacteria were isolated in nutrient marine agar from unexposed NKWSW and NKWSW exposed to JP-5, HRJ and F-76 to determine if at least some hydrocarbon degraders detected through metagenomics sequencing could be isolated.
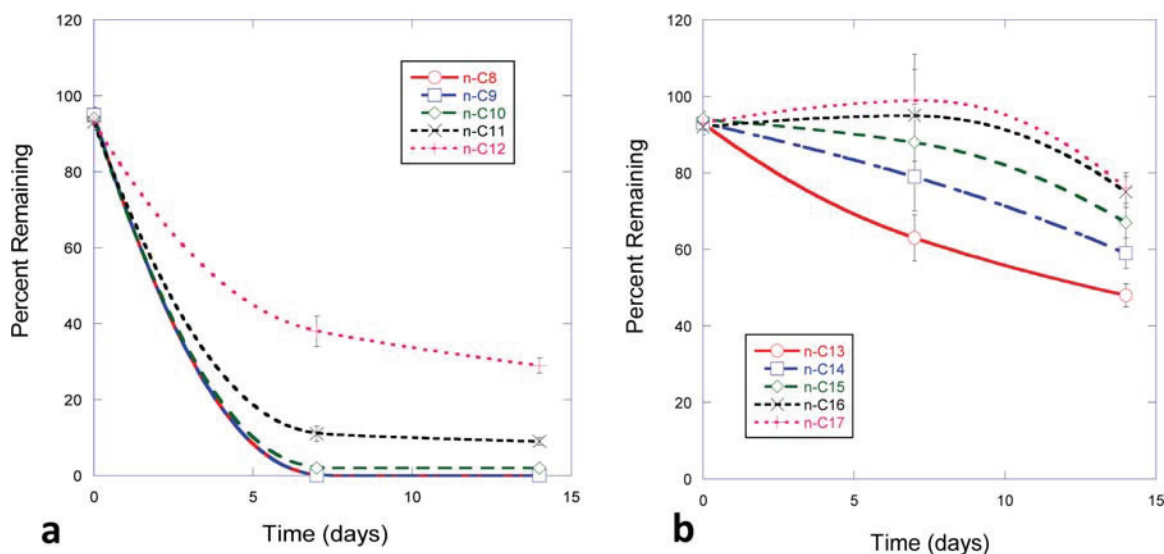
Figure 7. Degradation of hydrocarbon components of CHCD by *Marinobacter hydrocarbonoclasticus* over 14 days.
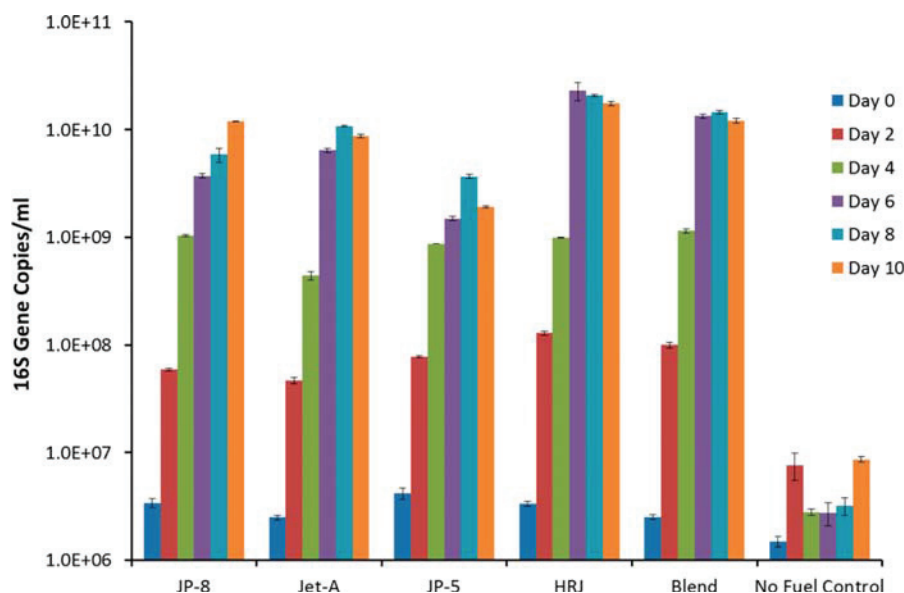
Figure 8. Quantification of total bacterial growth in different alternative and conventional fuels. Quantitative real-time PCR with a universal 16S *rrn* primer set was used for quantification.

Upon inspection of culture plates, it was apparent that plates inoculated with NKWSW presented a more diverse bacterial population than plates inoculated with NKWSW exposed to fuel (Figure S5, Supporting Information). While NKWSW showed colonies of different morphology and color, fuel-exposed samples presented uniform colonies of similar shape and color (Figure S5, Supporting Information). The ability of the bacterial isolates to grow in jet fuel as sole carbon source was examined. Table S1 presents the identity of 25 isolates, sample sources, and indications of fuel metabolism (Table S1, Supporting Information). The identity of each isolate was determined by 16S DNA sequencing. From the six species isolated from NKWSW seawater only *Halobacillus sp.*, and *Marinobacter hydrocarbonoclasticus* degraded fuel. *Photobacte-*

rium sp., *Bacillus* sp., *Phaeobacter* sp., *Loktanella* sp., did not degrade fuel. However, from the seven species isolated from fuel-exposed seawater, five, *M. hydrocarbonoclasticus*, *M. salsuginis*, *M. alkaliphilus*, *Rhodovulum* sp., and *Dietzia* sp., metabolized hydrocarbons (Table S1, Supporting Information). Only *Paracoccus* sp., did not degrade fuel.

Growth curves with fuel as the sole carbon source showed that *M. hydrocarbonoclasticus*, *Rhodovulum sp.*, *Dietzia sp.*, and *Halobacillus sp.*, grew well with Jet-A and F-76 (Figure 4). Members of the genera *Marinobacter, Dietzia, Halobacillus* and *Rhodovulum* are often found in marine environments contaminated with hydrocarbons.[1,11,46−52]

Biodegradation of Hydrocarbons by *M. hydrocarbonoclasticus* NI9 and *Rhodovulum* sp. NI22. To demonstrate
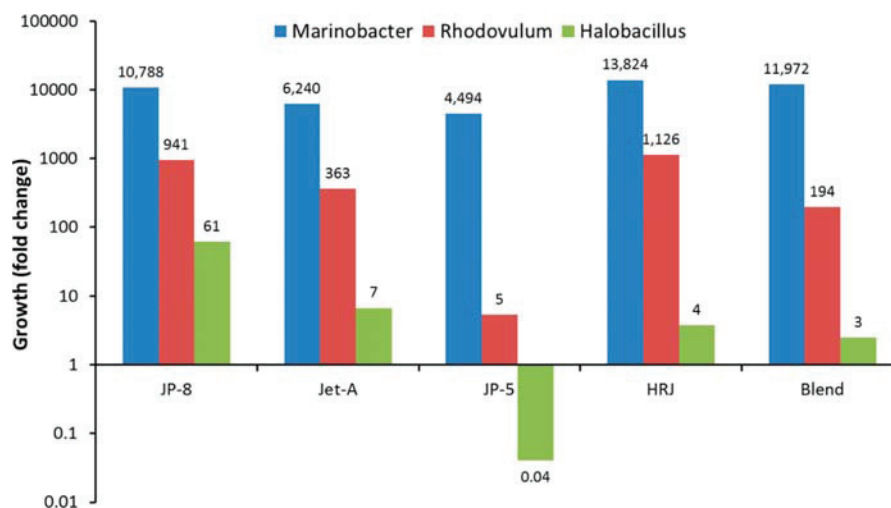
Figure 9. Effect of different alternative and conventional jet fuels on *Marinobacter, Rhodovulum,* and *Halobacillus* growth. Results show the growth fold change after 10 days from the initial cell inoculation level. Values <1 represent a reduction in abundance from the initial inoculation cell levels. Quantitative real-time PCR with species-specific 16S *rrn* primer sets was used for quantification.

that bacterial isolates obtained from the fuel enrichments degraded hydrocarbons, the hydrocarbon degradation profiles of *M. hydrocarbonoclasticus* isolate NI9 and *Rhodovulum* sp., isolate NI22 in F-76 diesel were determined. GC-MS showed that *M. hydrocarbonoclasticus* preferentially degraded short-chained *n*-alkanes from C_9 to C_{11} while *n*-alkanes longer than C_{15} were not consumed (Figure 5a). *M. hydrocarbonoclasticus* also degraded specific aromatics including 70% of the toluene and ethylmethylbenzene (data not shown), and all of the ethylbenzene in F-76 (Figure 5a). However, *M. hydro-carbonoclasticus* was unable to degrade naphthalene. M. *hydrocarbonoclasticus* degrades alkanes by the action of the alkane monooxygenase encoded by the *alk*B.[53] Analysis of *Rhodovulum* sp., strain NI22 indicated that it preferentially degraded naphthalene (Figure 5b) and some light *n*-alkanes, branched alkanes and aromatics but not the longer normal and branched alkanes like *n*-heptadecane and pristane (Figure S6, Supporting Information). *Rhodovulum* sp., strain NI22 harbors aromatic degradation genes including naphthalene 1,2-dioxygenase, benzene 1,2-dioxygenase, catechol 1,2-dioxygenase, and gentisate 1,2-dioxygenase, and the *alk*B gene for alkane degradation.[42]

The previous results indicated that each bacterial strain presented a specific hydrocarbon degradation profile. To determine whether the degradation profile of a specific bacterial strain is constant in different fuels, the hydrocarbon degradation profile of *M. hydrocarbonoclasticus* was evaluated in two alternative diesel fuels. The results showed that *M. hydrocarbonoclasticus* efficiently degraded the shorter normal (C_{8-10}) alkanes in a HRD (Figure 6a). Compounds with more than 13 carbons were not degraded (Figure 6b). Short monobranched alkanes were degraded but not the dibranched (Figure 6c). It was apparent that HRD contained sufficient concentration of short normal and branched alkanes to sustain the growth of *Marinobacter*.

M. hydrocarbonoclasticus degraded the same type of hydrocarbons in CHCD. GC results showed that *Marinobacter* efficiently consumed over 90% of n-C_9, n-C_{10} and n-C_{11}, 65% of n-C_{12} and 50% of n-C_{13} in the CHCD fuel even though *n*-

nonane, *n*-decane and *n*-undecane were 12-, 5.4-, and 3.2-times more abundant in CHCD than in F-76 (Figure 7).

Effect of Fuel Composition on Bacterial Growth. The metagenomics analysis indicated that different hydrocarbon fuels can enhance the growth and abundance of specific bacteria within a community. To test if hydrocarbon-degrading bacteria were differentially affected by fuel hydrocarbon composition, the growth of a bacterial consortia comprised of 0.01 OD of *M. hydrocarbonoclasticus*, 0.01 OD of *Rhodovulum* sp., and 0.01 OD of *Halobacillus* sp., in seawater-BH supplemented with either JP-8, Jet-A, JP-5, HRJ and Blend fuel was monitored. Over a ten-day period the total bacterial growth and the growth of individual bacterial species was determined by quantitative real-time PCR (qPCR) using a 16S universal primer set and species-specific primer sets. *M. hydrocarbonoclasticus*, *Rhodovulum* and *Halobacillus* were selected because they had similar growth rates in seawater-BH with Jet-A fuel when cultured individually (Figure 4). The results showed that the total bacterial abundance was highest in HRJ followed by Blend, JP-8 and Jet-A fuel (Figure 8). JP-5 supported the least growth of all five fuels (Figure 8). A closer look at the growth levels of individual bacteria showed that by day ten, *Marinobacter* was the dominating species in all five fuels (Figure 9). *Marinobacter* and *Rhodovulum* growth appeared to be enhanced by HRJ while *Halobacillus* grew better in JP-8 (Figure 8). JP-5 appeared to be the harshest fuel for the three bacteria but especially for *Halobacillus* which saw its abundance reduced by 40-fold from the original inoculation level (Figure 9).

It is possible that because *M. hydrocarbonoclasticus* and *Rhodovulum* sp., specialize in the degradation of low molecular weight alkanes such as *n*-C8 and *n*-C9, and since more of these compounds are present in HRJ, their growth was promoted (Figure S3, Supporting Information). However, it cannot be assumed that HRJ will biodegrade more than Jet-A or JP-5 in the environment because there are many bacteria capable of degrading different hydrocarbon classes in the environment. For example, *P. aeruginosa* 33988 preferentially degrades longer *n*-alkanes (*n*-C_{12-18}), which are in higher abundance in Jet-A.[29] Striebich et al.[29] showed that *P. aeruginosa* 33988 grew better

than *M. hydrocarbonoclasticus* in minimal media containing Jet-A and that F-76. *P. aeruginosa* 33988 did not grow in minimal media containing highly branched isoparaffinic fuels unless *n*-hexadecane, a metabolizable carbon source, was added.[29]

Bacteria are very specific in the type of hydrocarbon they can consume. The metabolic flexibility of the bacterial community and competitive interactions between biodegraders appear to be two main factors influencing the bioremediation process. The role of competition and how it may limit the biodegradation process should be studied in further detail. From the metagenomics and *in vitro* tests, it is clear that better adapted bacteria presenting more robust growth can out-compete other bacteria. For example, *Marinobacter* and *Rhodovulum* prevented *Halobacillus* from growing *in vitro* even though the bacterium grew well in Jet-A in pure culture. This finding indicates that the bioremediation process could benefit from selective and systematic addition of specific hydrocarbon degraders once specific hydrocarbon components have been depleted from the system. Equally important is the possibility that out-competed members can survive long enough to grow back once the aggressive growers have stopped or died down because they have consumed their preferred hydrocarbon source. Clearly, the alternative fuels present environmental challenges similar to those posed by conventional fuels. However, the biodegradability of a given fuel will largely depend on its hydrocarbon composition, with fuels comprised of *n*-alkanes and specific aromatic compounds degrading faster in the environment than their isoparaffinic counterparts. The information presented here will be valuable in the development of best practices to maximize the potential of bioremediation systems, and could be applied to the development of fuels with specific biodegradation properties.

ASSOCIATED CONTENT

Ⓢ Supporting Information

The Supporting Information is available free of charge on the ACS Publications website at DOI: 10.1021/acs.energy-fuels.5b02439.

Table S1, bacteria isolated from different fuel/seawater samples; Figure S1, genera within the phyla *Bacteroides*, *Firmicutes*, and *Lentisphaerae*; Figure S2, schematic representation of the fuel/seawater exposure chamber; Figure S3, hydrocarbon profile of JP-5 and HRJ fuel; Figure S4, Jet-A, F76, and HRD hydrocarbon profile; Figure S5, morphological characterisitics of bacterial colonies isolated from seawater and HRJ/seawater samples; Figure S6, degradation of aromatics and the stability of longer alkanes while exposed to *Rhodovulum* sp., strain NI22. (PDF)

AUTHOR INFORMATION

Corresponding Author

*Tel.: +1 937 255 6237. E-mail: Oscar.Ruiz@us.af.mil.

Notes

Disclosure: The U.S. Government is authorized to reproduce and distribute reprints for Governmental purposes notwithstanding any copyright notation thereon. The views and conclusions contained herein are those of the authors and should not be interpreted as necessarily representing the official policies or endorsements, either expressed or implied, of Air Force Research Laboratory or the U.S. Government.

The authors declare no competing financial interest.

REFERENCES

(1) Belhaj, A.; Desnoues, N.; Elmerich, C. Alkane biodegradation in Pseudomonas aeruginosa strains isolated from a polluted zone: identification of alkB and alkB-related genes. *Res. Microbiol.* **2002**, *153*, 339−344.

(2) Mnif, S.; Chamkha, M.; Sayadi, S. Isolation and characterization of Halomonas sp. strain C2SS100, a hydrocarbon-degrading bacterium under hypersaline conditions. *J. Appl. Microbiol.* **2009**, *107*, 785−974.

(3) Berlendis, S.; Lascourreges, J. F.; Schraauwers, B.; Sivadon, P.; Magot, M. Anaerobic biodegradation of BTEX by original bacterial communities from an underground gas storage aquifer. *Environ. Sci. Technol.* **2010**, *44*, 3621−3628.

(4) White, J.; Gilbert, J.; Hill, G.; Hill, E.; Huse, S. M.; Weightman, A. J.; Mahenthiralingam, E. Culture-independent analysis of bacterial fuel contamination provides insight into the level of concordance with the standard industry practice of aerobic cultivation. *Appl. Environ. Microbiol.* **2011**, *77*, 4527−4538.

(5) Sharma, N. K.; Philip, L.; Murty Bhallamudi, S. Aerobic degradation of phenolics and aromatic hydrocarbons in presence of cyanide. *Bioresour. Technol.* **2012**, *121*, 263−273.

(6) Brown, L. M.; McComb, J.; Vangsness, M.; Bowen, L.; Mueller, S.; Balster, L.; Bleckmann, C. Community dynamics and phylogenetics of bacteria fouling Jet A and JP-8 aviation fuel. *Int. Biodeterior. Biodegrad.* **2010**, *64*, 253−261.

(7) Korenblum, E.; Valoni, E.; Penna, M.; Seldin, L. Bacterial diversity in water injection systems of Brazilian offshore oil platforms. *Appl. Microbiol. Biotechnol.* **2010**, *85*, 791−800.

(8) Beazley, M. J.; Martinez, R. J.; Rajan, S.; Powell, J.; Piceno, Y. M.; Tom, L. M.; Andersen, G. L.; Hazen, T. C.; Van Nostrand, J. D.; Zhou, J.; Mortazavi, B.; Sobecky, P. A. Microbial community analysis of a coastal salt marsh affected by the Deepwater Horizon oil spill. *PLoS One* **2012**, *7*, e41305.

(9) Suflita, J. M.; Aktas, D. F.; Oldham, A. L.; Perez-Ibarra, B. M.; Duncan, K. Molecular tools to track bacteria responsible for fuel deterioration and microbiologically influenced corrosion. *Biofouling* **2012**, *28*, 1003−1010.

(10) Vila, J.; Nieto, J. M.; Mertens, J.; Springael, D.; Grifoll, M. Microbial community structure of a heavy fuel oil-degrading marine consortium: linking microbial dynamics with polycyclic aromatic hydrocarbon utilization. *FEMS Microbiol. Ecol.* **2010**, *73*, 349−362.

(11) Jiménez, N.; Viñas, M.; Bayona, J. M.; Albaiges, J.; Solanas, A. M. The Prestige oil spill: bacterial community dynamics during a field biostimulation assay. *Appl. Microbiol. Biotechnol.* **2007**, *77*, 935−945.

(12) Kostka, J. E.; Prakash, O.; Overholt, W. A.; Green, S. J.; Freyer, G.; Canion, A.; Delgardio, J.; Norton, N.; Hazen, T. C.; Huettel, M. Hydrocarbon-degrading bacteria and the bacterial community response in gulf of Mexico beach sands impacted by the deepwater horizon oil spill. *Appl. Environ. Microbiol.* **2011**, *77*, 7962−74.

(13) Venosa, A. D.; Zhu, X. Biodegradation of crude oil contaminating marine shorelines and freshwater wetlands. *Spill Sci. Technol. Bull.* **2003**, *8*, 163−178.

(14) Gallego, J. R.; Fernandez, J. R.; Diez-Sanz, F.; Ordonez, S.; Sastre, H.; Gonzalez-Rojas, E.; Peláez, A. I.; Sanchez, J. (2007). Bioremediation for shoreline cleanup: in situ vs. on-site treatments. *Environ. Eng. Sci.* **2007**, *24*, 493−504.

(15) Venosa, A. D.; Campo, P.; Suidan, M. T. Biodegradability of lingering crude oil 19 years after the Exxon Valdez oil spill. *Environ. Sci. Technol.* **2010**, *44*, 7613−7621.

(16) Edwards, T. In Jet Fuel Composition. *Jet Fuel Toxicology*; Witten, M. C., Zeiger, E., Ritchie, G. D., Eds.; CRC Press: 2011; pp 21−26.

(17) Edwards, T.; Moses, C.; Dryer, F. Evaluation of combustion performance of alternative aviation fuels. *46th AIAA/ASME/SAE/ASEE Joint Propulsion Conference & Exhibit*, Nashville, TN, July 25−28, 2010, AIAA Paper 2010−7155. http://arc.aiaa.org/doi/abs/10.2514/6.2010-7155.

(18) Hazen, T. C.; Dubinsky, E. A.; DeSantis, T. Z.; Andersen, G. L.; Piceno, Y. M.; Singh, N.; Jansson, J. K.; Probst, A.; Borglin, S. E.; Fortney, J. L.; Stringfellow, W. T.; Bill, M.; Conrad, M. E.; Tom, L. M.; Chavarria, K. L.; Alusi, T. R.; Lamendella, R.; Joyner, D. C.; Spier, C.; Baelum, J.; Auer, M.; Zemla, M. L.; Chakraborty, R.; Sonnenthal, E. L.; D'haeseleer, P.; Holman, H. Y.; Osman, S.; Lu, Z.; Van Nostrand, J. D.; Deng, Y.; Zhou, J.; Mason, O. U. Deep-sea oil plume enriches indigenous oil-degrading bacteria. *Science* 2010, *330*, 204−208.

(19) Lee, J. S.; Ray, R. I.; Little, B. J.; Duncan, K. E.; Oldham, A. L.; Davidova, I. A.; Suflita, J. M. Sulphide production and corrosion in seawaters during exposure to FAME diesel. *Biofouling* 2012, *28*, 465−478.

(20) Smits, T. H.; Röthlisberger, M.; Witholt, B.; van Beilen, J. B. Molecular screening for alkane hydroxylase genes in Gram-negative and Gram-positive strains. *Environ. Microbiol.* 1999, *1*, 307−317.

(21) Nie, M.; Yin, X.; Ren, C.; Wang, Y.; Xu, F.; Shen, Q. Novel rhamnolipid biosurfactants produced by a polycyclic aromatic hydrocarbon-degrading bacterium Pseudomonas aeruginosa strain NY3. *Biotechnol. Adv.* 2010, *28*, 635−643.

(22) Rocha, C. A.; Pedregosa, A. M.; Laborda, F. Biosurfactant-mediated biodegradation of straight and methyl-branched alkanes by Pseudomonas aeruginosa ATCC 55925. *AMB Express* 2011, *1*, 9.

(23) Rodríguez-Rodríguez, C. E.; Rodríguez-Cavallini, E.; Blanco, R. Bacterial contamination of automotive fuels in a tropical region: the case of Costa Rica. *Rev. Biol. Trop.* 2009, *57*, 489−504.

(24) Stamper, D. M.; Morris, R. E.; Montgomery, M. T. Depletion of lubricity improvers from hydrotreated renewable and ultralow-sulfur petroleum diesels by marine microbiota. *Energy Fuels* 2012, *26*, 6854−6862.

(25) Vu, B.; Chen, M.; Crawford, R. J.; Ivanova, E. P. Bacterial extracellular polysaccharides involved in biofilm formation. *Molecules* 2009, *14*, 2535−2554.

(26) Gunasekera, T. S.; Striebich, R. C.; Mueller, S. S.; Strobel, E. M.; Ruiz, O. N. Transcriptional profiling suggests that multiple metabolic adaptations are required for effective proliferation of Pseudomonas aeruginosa in jet fuel. *Environ. Sci. Technol.* 2013, *47*, 13449−13458.

(27) Sanger, M.; Finnarty, W. In Microbial metabolism of Straight Chain and Branched Alkanes. *Petroleum Microbiology*; Atlas, R. M., Ed.; Macmillan: New York, 1984; pp 1−61.

(28) Saadoun, I. Isolation and characterization of bacteria from crude petroleum oil contaminated soil and their potential to degrade diesel fuel. *J. Basic Microbiol.* 2002, *42*, 420−428.

(29) Striebich, R. C.; Smart, C. E.; Gunasekera, T. S.; Mueller, S. S.; Strobel, E. M.; McNichols, B.; Ruiz, O. N. Characterization of the F-76 Diesel and Jet-A Aviation Fuel Hydrocarbon Degradation Profiles of Pseudomonas aeruginosa and Marinobacter hydrocarbonoclasticus. *Int. Biodeterior. Biodegrad.* 2014, *93*, 33−43.

(30) McHardy, A. C.; Rigoutsos, I. What's in the mix: phylogenetic classification of metagenome sequence samples. *Curr. Opin. Microbiol.* 2007, *10*, 499−503.

(31) Tringe, S. G.; Rubin, E. M. Metagenomics: DNA sequencing of environmental samples. *Nat. Rev. Genet.* 2005, *6*, 805−814.

(32) Lee, J. S.; Ray, R. I.; Little, B. J.; Duncan, K. E.; Aktas, D. F.; Oldham, A. L.; Davidova, I. A.; Suflita, J. M. Issues for storing plant-based alternative fuels in marine environments. *Bioelectrochemistry* 2014, *97*, 145−153.

(33) Rauch, M. E.; Graft, H.; Rozenzhak, S.; Jones, S.; Bleckmann, C.; Kruger, R.; Naik, R.; Stone, M. Characterization of microbial contamination in United States Air Force aviation fuel tanks. *J. Ind. Microbiol. Biotechnol.* 2006, *33*, 29−36.

(34) Cole, J. R.; Wang, Q.; Cardenas, E.; Fish, J.; Chai, B.; Farris, R. J.; Kulam-Syed-Mohideen, A. S.; McGarrell, D. M.; Marsh, T.; Garrity, G. M.; Tiedje, J. M. The Ribosomal Database Project: improved alignments and new tools for rRNA analysis. *Nucleic Acids Res.* 2009, *37* (Database issue), D141−D145.

(35) Wright, E. S.; Yilmaz, L. S.; Noguera, D. R. DECIPHER, a search-based approach to chimera identification for 16S rRNA sequences. *Appl. Environ. Microbiol.* 2012, *78*, 717−725.

(36) Wang, Q.; Garrity, G. M.; Tiedje, J. M.; Cole, J. R. Naïve Bayesian classifier for rapid assignment of rRNA sequences into the new bacterial taxonomy. *Appl. Environ. Microbiol.* 2007, *73*, 5261−5267.

(37) Bushnell, L. D.; Haas, H. F. The Utilization of Certain Hydrocarbons by Microorganisms. *J. Bacteriol.* 1941, *41*, 653.

(38) Ruiz, O. N.; Brown, N. A. Advances in microbial mitigation of aviation fuels: characterization of the antimicrobial activity of DIEGME in fuel by quantitative real-time PCR. *Proceeding of the 12th International Conference on Stability, Handling and Use of Liquid Fuels*, Sarasota, FL, Oct 16−20, 2011. http://iash.omnibooksonline.com/.

(39) Ruiz, O. N.; Brown, N. A.; Fernando, K. A. S.; Miller, B. A.; Gunasekera, T. S.; Bunker, C. E. Graphene oxide-based nanofilters efficiently remove bacteria from fuel. *Int. Biodeterior. Biodegrad.* 2015, *97*, 168−178.

(40) Ruiz, O. N.; Fernando, K. A.; Wang, B.; Brown, N. A.; Luo, P. G.; McNamara, N. D.; Vangsness, M.; Sun, Y. P.; Bunker, C. E. Graphene Oxide: A Nonspecific Enhancer of Cellular Growth. *ACS Nano* 2011, *5*, 8100−8107.

(41) Maeda, H.; Fujimoto, C.; Haruki, Y.; Maeda, T.; Kokeguchi, S.; Petelin, M.; Arai, H.; Tanimoto, I.; Nishimura, F.; Takashiba, S. Quantitative real-time PCR using TaqMan and SYBR Green for Actinobacillus actinomycetemcomitans, Porphyromonas gingivalis, Prevotella intermedia, tetQ gene and total bacteria. *FEMS Immunol. Med. Microbiol.* 2003, *39*, 81−86.

(42) Brown, L. M.; Gunasekera, T. S.; Bowen, L. L.; Ruiz, O. N. Draft genome sequence of *Rhodovulum* sp. strain NI22, a naphthalene-degrading bacterium. *Genome Announcements* 2015, *3*, 1−2.

(43) Gobet, A.; Böer, S. I.; Huse, S. M.; van Beusekom, J. E.; Quince, C.; Sogin, M. L.; Boetius, A.; Ramette, A. Diversity and dynamics of rare and of resident bacterial populations in coastal sands. *ISME J.* 2012, *6*, 542−53.

(44) Sigalevich, P.; Baev, M. V.; Teske, A.; Cohen, Y. Sulfate reduction and possible aerobic metabolism of the sulfate-reducing bacterium Desulfovibrio oxyclinae in a chemostat coculture with Marinobacter sp. Strain MB under exposure to increasing oxygen concentrations. *Appl. Environ. Microbiol.* 2000, *66*, 5013−5018.

(45) Cohen, Y. Bioremediation of oil by marine microbial mats. *Int. Microbiol.* 2002, *5*, 189−193.

(46) Gauthier, M. J.; Lafay, B.; Christen, R.; Fernandez, L.; Acquaviva, M.; Bonin, P.; Bertrand, J. C. Marinobacter hydrocarbonoclasticus gen. nov., sp. nov., a new, extremely halotolerant, hydrocarbon-degrading marine bacterium. *Int. J. Syst. Bacteriol.* 1992, *42*, 568−76.

(47) Iwaki, H.; Nishimura, A.; Hasegawa, Y. Isolation and characterization of marine bacteria capable of utilizing phthalate. *World J. Microbiol. Biotechnol.* 2012, *28*, 1321−1325.

(48) Li, H.; Zhang, Q.; Wang, X. L.; Ma, X. Y.; Lin, K. F.; Liu, Y. D.; Gu, J. D.; Lu, S. G.; Shi, L.; Lu, Q.; Shen, T. T. Biodegradation of benzene homologues in contaminated sediment of the East China Sea. *Bioresour. Technol.* 2012, *124*, 129−36.

(49) Liu, Z.; Liu, J. Evaluating bacterial community structures in oil collected from the sea surface and sediment in the northern Gulf of Mexico after the Deepwater Horizon oil spill. *MicrobiologyOpen* 2013, *2*, 492−504.

(50) Riis, V.; Kleinsteuber, S.; Babel, W. Influence of high salinities on the degradation of diesel fuel by bacterial consortia. *Can. J. Microbiol.* 2003, *49*, 713−21.

(51) Takai, K.; Moyer, C. L.; Miyazaki, M.; Nogi, Y.; Hirayama, H.; Nealson, K. H.; Horikoshi, K. Marinobacter alkaliphilus sp. nov., a

358

novel alkaliphilic bacterium isolated from subseafloor alkaline serpentine mud from Ocean Drilling Program Site 1200 at South Chamorro Seamount, Mariana Forearc. *Extremophiles* **2005**, *9*, 17−27.

(52) Teramoto, M.; Suzuki, M.; Hatmanti, A.; Harayama, S. The potential of Cycloclasticus and Altererythrobacter strains for use in bioremediation of petroleum-aromatic-contaminated tropical marine environments. *J. Biosci. Bioeng.* **2010**, *110*, 48−52.

(53) Smith, C. B.; Tolar, B. B.; Hollibaugh, J. T.; King, G. M. Alkane hydroxylase gene (alkB) phylotype composition and diversity in northern Gulf of Mexico bacterioplankton. *Front. Microbiol.* **2013**, *4*, 370−378.

359

Appendix AA. Transient Measurement of Thin Liquid Films using a Shack–Hartmann Sensor

CrossMark

Transient measurement of thin liquid films using a Shack–Hartmann sensor☆

M.S. Hanchak [a,*], M.D. Vangsness [a], J.S. Ervin [a], L.W. Byrd [b]

[a] University of Dayton Research Institute, Dayton, OH 45469, USA
[b] Air Force Research Laboratory, WPAFB, OH 45433, USA

ARTICLE INFO

ABSTRACT

A Shack–Hartmann (SH) wavefront sensor was used to measure the thickness of thin liquid films of n–octane on silicon substrates. A SH device consists of an array of microlenses spaced from an image sensor by their effective focal length. A planar wavefront imposed on a SH device would produce uniformly spaced foci on the sensor for each lenslet. A distorted wavefront would then shift the foci by a calculable amount. Typically used for optical system alignment and calibration, the SH device was coupled with magnifying optics to determine the distortion of a planar wavefront source upon refraction through a film and reflection by a polished substrate. Geometrical optics, in the form of ray transfer matrices, were used to determine the location and orientation of rays emanating from the film surface given their positions and angles recorded by the SH device. The SH foci movements were translated into sample coordinates and film slopes, which were subsequently integrated to produce the film profile.

© 2016 Elsevier Ltd. All rights reserved.

1. Introduction

Liquid to vapor phase change provides an effective way to absorb a large amount of heat energy. Often, devices are cooled through the evaporation of a liquid in direct contact with a heated solid substrate. Heat flux enhancement can occur when the liquid layer is sufficiently thin such that heat conduction through it allows the liquid–vapor interface to be nearly the same temperature as the substrate, which enhances evaporation. This occurs, for example, when a liquid meniscus decreases in thickness near a substrate. Such situations are found in spray cooling, microchannel devices, and heat pipes [1]. If the liquid layer becomes thin enough (an adsorbed film), intermolecular forces between the liquid and solid molecules can actually suppress evaporation, even at increased temperatures. Between the adsorbed film and the thicker meniscus region, there exists a region of maximal heat flux [2]. For this reason, the characterization of the liquid film in this transition is important.

Previously, we measured the film thickness from the adsorbed film to the meniscus region using a reflectometer [3,4]. The reflectometer measured the reflected spectrum of light from a broad-band source and determined the thickness using its internal model of the complex indices of refraction of the various layers. Spectra were taking at discrete locations along the film using motorized positioning stages. However, this method lacks the acquisition speed required for sub-second transients in the film movement.

The objective of this paper is to present the use of the SH technique and basic optical principles to obtain transient thicknesses of thin liquid films.

2. Methodology

2.1. Measurement technique

This work relies on a commercially available Shack–Hartmann (SH) wavefront sensor to characterize the thin film region. The SH technique has been used previously to determine the topology of thin, transparent solids [5]. It was also coupled with a laser light source to measure the static surface profiles of liquid microlenses, which were then fit to both spherical and conical surface shapes [6]. The sensor consists of three components (Fig. 1). First, there is a microlens array, often called a lenslet array, consisting of 29 × 29 individual but identical lenslets spaced 0.150 mm apart, each with an effective focal length of 5.2 mm. Second, a CCD image sensor is situated a distance from the array equal to the focal length. Finally, software is provided that converts the image data from the sensor into centroid positions of the mean foci locations of each lenslet and ultimately provides a reconstructed wavefront [7]. The advantage of this device over reflectometry is twofold. First, the SH sensor covers a two-dimensional area without needed translation stages to otherwise scan the sample. Second, since it uses conventional imaging sensors, it acquires images much faster than the spectrometer of the reflectometer.

The SH sensor provides the angle of incidence of lights rays that impinge it. To illustrate, we examine a single lenslet (Fig. 2). Given the small aperture of the lenslet, the light rays from a sample in question

Fig. 1. A Shack–Hartmann wavefront sensor (most foci removed for clarity).

Fig. 3. Diagram of the optical path used to collimate and direct light to the SH sensor.

70 mm. This provides a magnification of 1.25. Specifically, the lenslet centers cover an area of 4.2 × 4.2 mm; this is mapped to an area on the sample of 3.4 × 3.4 mm. The region of interest could be varied by changing magnification.

2.2. Liquid sample

The sample is a meniscus of n–octane residing on a polished silicon wafer. It is produced by micropositioning a 0.01 mm thick plastic shim against the wafer at a shallow angle (Fig. 4). N–octane was introduced using a syringe under the shim and was subsequently wicked to the working side of the shim.

In the absence of liquid, the entire optical system was calibrated to provide a baseline of lenslet focal centroids. By adjusting each component in series, the presence of a planar wavefront at the silicon substrate was confirmed. The centroid locations of the planar (or collimated) illumination were then recorded as the baseline. When the liquid was introduced, the centroids formed by the light traveling through the n–octane were displaced relative to the baseline.

2.3. Interface reconstruction

To determine the geometry of the interface, a known ray was traced back to a point on the interface using the inverse ray transfer matrix of the optical path. A ray transfer matrix, when multiplied by a column-vector consisting of ray displacement and ray angle at the input plane, will provide the ray displacement and angle at the output plane of an optical system. However, the SH gives ray information at the output plane, thus the matrix was inverted. The lenslets lie on a square grid spaced by the array pitch. For each lenslet center, the ray angle was known (from Fig. 2), and the inverse matrix gave the ray location and angle at the sample. This was done for each lenslet center. What resulted was a non-uniform grid of ray origin points and angles at the sample plane.

will be nearly parallel and will intersect the lenslet at a given angle. Because the sensor is located at precisely the lenslet focal length, the nearly parallel rays will be focused to a spot at some distance from the calibration spot. The centroid of the focused light is calculated, and the nominal ray angle relative to the SH device is the displacement of the centroid divided by the focal length. This is done in both x and y components to capture the three-dimensional direction of each ray.

When the sample is non-uniform in the manner in which it reflects or refracts light, each lenslet will receive rays at different angles. By tracing each lenslet ray back to the sample, one can infer its geometry. This requires a light source with a planar wavefront (parallel and normally incident rays).

Fig. 3 shows the optical path of the system. An optical fiber originating from a monochromatic LED (385 nm) enters the system from the top and is collimated by an achromatic triplet. The light passes through a beam splitter down to the sample were it is reflected and refracted. Light from the sample is reflected from the beam splitter toward a pair of relay lens which collect and direct the reflected light to the SH sensor. For this specific implementation, the focal lengths of the relay lenses are $f_1 = 40$ mm and $f_2 = 50$ mm, and the distance L is
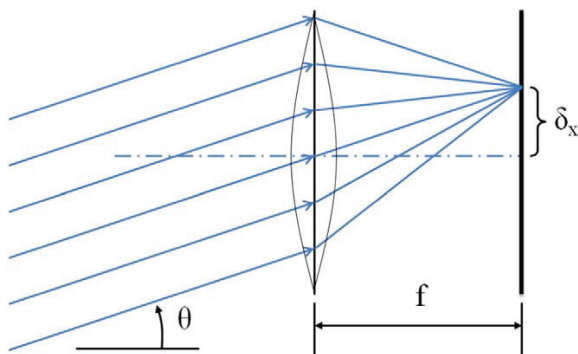

Fig. 2. Geometry of a single lenslet is shown in one dimension, x. A similar displacement also occurs in the y direction.
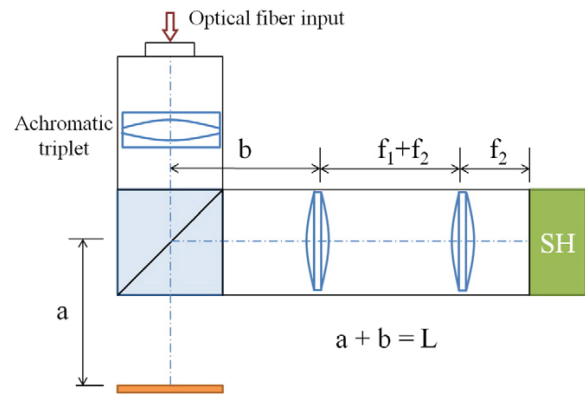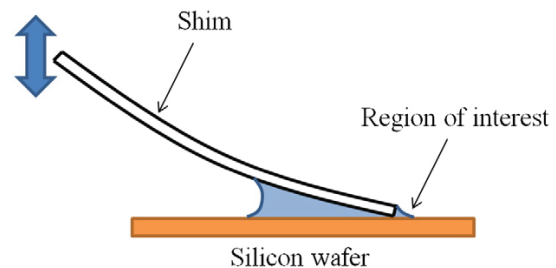

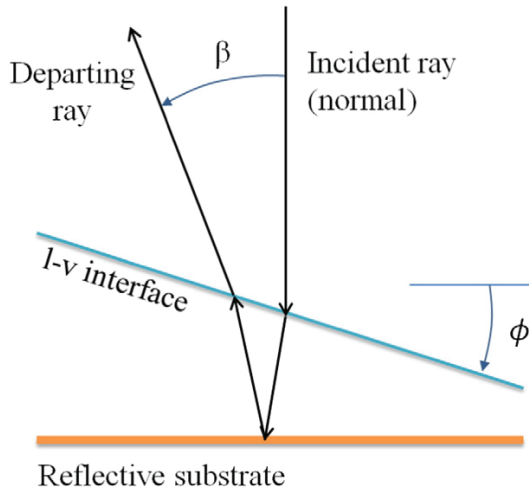Fig. 4. Method of supplying n–octane to the region of interest.

Fig. 5. Relation between film slope and departing ray angle at the sample.

The slope of the liquid–vapor interface is given by $\phi = \frac{\beta}{2(1-n)}$, where β is the departing ray angle, n is the index of refraction of the liquid, and ϕ is the film slope (Fig. 5). Again, there is a slope in both x and y directions. In one dimension, the film profile could be found simply by integrating the slopes across the non-uniform grid. However, in two dimensions, the integration is nontrivial, since a) the ray departure points are non-uniform and b) measurement errors may not guarantee a direction independent result (for example, integrating first in x then in y and vice versa).

To remedy this, let the film profile be an unknown scalar function of x and y, i.e., $z = f(x,y)$. The result of inverse ray tracing has essentially provided us with the gradient of the level surface on a non-uniform grid. So, the gradient is first interpolated onto a square, uniform grid that is entirely encompassed within the experimental data. Therefore, we have $\nabla f = \vec{a}(x,y)$, where $\vec{a}(x,y)$ is the measured vector field of interface slopes under the small angle approximation, with $\tan(\phi) \approx \phi$. Taking the divergence of the previous expression yields $\nabla^2 f = \nabla \cdot \vec{a}(x,y)$. This is Poisson's equation for f and can be solved a number of ways. We chose a finite-difference method with iteration [8]. A central, finite-difference stencil applied to the Poisson equation yields

$$\frac{f_{i+1,j}-2f_{i,j}+f_{i-1,j}}{\Delta x^2} + \frac{f_{i,j+1}-2f_{i,j}+f_{i,j-1}}{\Delta y^2}$$
$$= \frac{a_{x_{i+1,j}}-a_{x_{i-1,j}}}{2\Delta x} + \frac{a_{y_{i,j+1}}-a_{y_{i,j-1}}}{2\Delta y}. \tag{1}$$

On a square grid, the length steps are equal in both directions. Solving Eq. (1) for the (i,j) value produces an average of neighboring grid points and a source term,

$$f_{i,j} = \frac{1}{4}\left(f_{i+1,j} + f_{i-1,j} + f_{i,j+1} + f_{i,j-1}\right) - \frac{\Delta x}{8}\left(a_{x_{i+1,j}} - a_{x_{i-1,j}} + a_{y_{i,j+1}} - a_{y_{i,j-1}}\right). \tag{2}$$

This equation is iterated at every interior point of grid; the first term in parentheses is calculated every iteration, but the second term in parentheses is only calculated once. However, the boundary condition for the finite-difference equations must be prescribed beforehand and consists of the film height at the exterior points of the computational grid. It is determined by contour integration of the tangential component of the gradient (slope) along the four edges of the square grid. Thus, along the boundaries parallel to the x axis, $\frac{\partial z}{\partial x}\big|_{y=y_1,y_N} \approx \phi_x$ is integrated to give $z(x)$, and along the boundaries parallel to the y axis, $\frac{\partial z}{\partial y}\big|_{x=x_1,x_N} \approx \phi_y$ is integrated to give $z(y)$. The four constants of integration are reduced to one by equating common heights at the corners. The last constant cannot be determined unless there is an independent measure of the absolute height somewhere in the field of view. However, the relative height of the boundary is now known. In the case where the end point is not at the same height as the starting point, then either measurement error or lack of data on the boundary has occurred. In the latter case, entire rows or columns of data may be truncated to produce a new, smaller boundary.

3. Results

The integration scheme was numerically coded in MATLAB [9], where Eq. (2) is calculated using matrix indexing, not looping. Approximately 150 iterations are required to achieve convergence of the Poisson equation. The code imports the x and y centroid files provided by the SH software suite, traces the $29^2 = 841$ incident rays backwards to the sample, interpolates the data onto a 50×50 square grid, and then solves the Poisson equation. To process 440 time-steps of data took approximately 40 s. Since the current capture rate of the SH sensor is 7.5 Hz, the data processing could be implemented in real time. The result of these calculations is a series of matrices representing the height function of the liquid–vapor interface in x–y coordinates. There is one matrix for each time-step. To validate the method, a concave mirror of known radius was imaged and processed with the algorithm (Fig. 6). Our system calculated the correct radius of curvature of the mirror within 2%.

We used this measurement technique to reveal the time evolution of the thin film upon introducing n–octane at the shim, which in turn filled the region of interest (Fig. 7). This is a typical thin film profile. The adsorbed film region is fairly constant in thickness, approximately 30–40 nm. The transition region extends up to around 150 nm, where the evaporation mass flux begins to recede as the film thermal
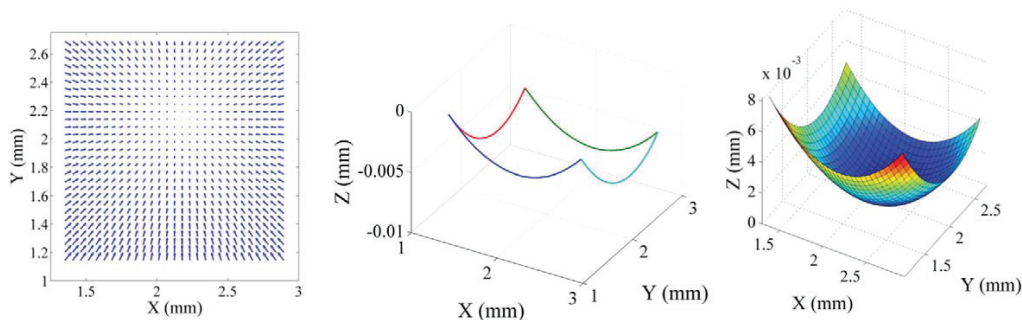

Fig. 6. Algorithm applied to a concave mirror: the gradient field (left), the integrated boundary condition (center), and the reconstructed surface profile (right).
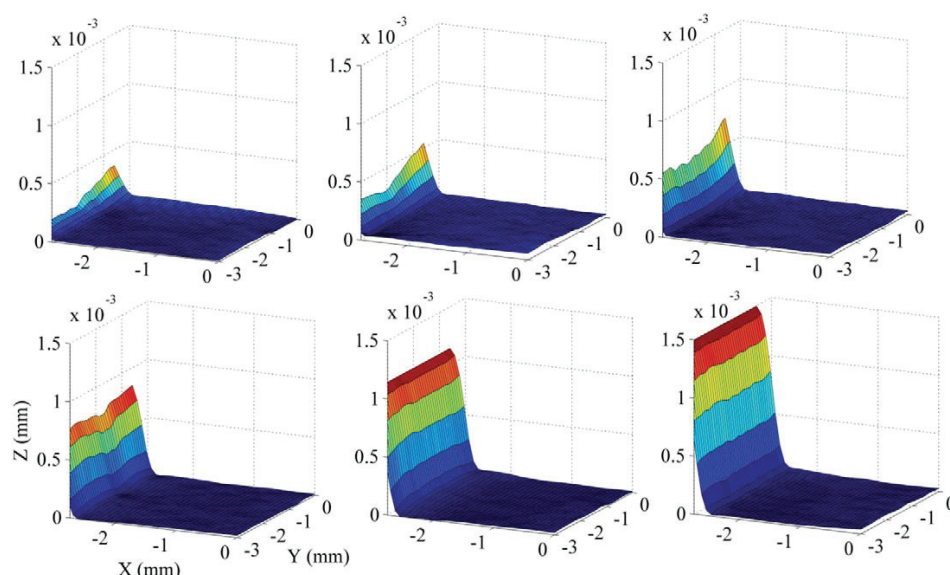
Fig. 7. Selected transient measurements are shown upon filling the capillary region. These images are 0.27 s apart. Time increases from left to right, then top to bottom.

resistance increases. Beyond that, the meniscus region is described by a near-constant film slope. The transition from adsorbed film to meniscus occurs over approximately 300 μm in the X direction.

4. Conclusion

The SH sensor has provided a means to observe a two-dimensional area of interest of a liquid film, measuring the thickness of the liquid using basic optical principles. The system described provides transient measurements at the rate of 7.5 Hz, although this could be increased significantly with a faster image sensor. While the data here was post-processed, the workflow could be altered to provide real-time observation of the film thickness. This technique has distinct advantages to the previous use of reflectometry, including both greater speed and larger observable area.

To our knowledge, this is the first use of the SH technique in measuring transient, thin liquid films. With this information, it may be possible to develop better models of the liquid and evaporative transport during thin film phase change.

Acknowledgment

References

[1] V.P. Carey, Liquid–Vapor Phase-Change Phenomena, Hemisphere Publ Corp., 1992
[2] P.C. Wayner Jr., Y.K. Kao, L.V. LaCroix, The interline heat-transfer coefficient of an evaporating wetting film, Int. J. Heat Mass Transf. 19 (1976) 487–492.
[3] M.S. Hanchak, M.D. Vangsness, L.W. Byrd, J.S. Ervin, J.G. Jones, Profile measurements of thin liquid films using reflectometry, Appl. Phys. Lett. 103 (2013) 211607.
[4] M.S. Hanchak, M.D. Vangsness, L.W. Byrd, J.S. Ervin, Thin film evaporation of n-octane on silicon: experiments and theory, Int. J. Heat Mass Transf. 75 (2014) 196–206.
[5] C.R. Forest, C.R. Canizares, D.R. Neal, M. McGuirk, M.L. Schattenburg, Metrology of thin transparent optics using Shack–Hartmann wavefront sensing, Opt. Eng. 43 (3) (2004) 742–753.
[6] C. Li, G. Hall, D. Zhu, H. Li, K.W. Eliceiri, H. Jiang, Three-dimensional surface profile measurement of microlenses using the Shack–Hartmann wavefront sensor, J. Microelectromech. Syst. 21 (3) (2012) 530–540.
[7] WFS-K2, www.thorlabs.com.
[8] J.C. Tannehill, D.A. Anderson, R.H. Pletcher, Computational Fluid Mechanics and Heat Transfer, Taylor & Francis, Philadelphia, PA, 1997.
[9] MATLAB R2013a, The MathWorks Inc., Natick, MA (1984–2013)

Appendix BB. AWARDS, PUBLICATIONS, AND PRESENTATIONS
Air Force Cooperative Agreement No. FA8650-10-2-2934
(December 2009 to September 2016)

Honors and Awards

1. S. Stouffer, Session Chair, 35th Annual DCASS, March 2010.

2. M.J. DeWitt, Session Chair, 35th Annual DCASS, March 2010.

3. S. Stouffer, Second Place in Art-In Science Competition, 35th Annual AIAA DCASS, March 2010.

4. S. Zabarnick, Selected as At-Large Steering Committee Member of the Coordinating Research Council Aviation Meetings, May 2010.

5. M. Vangsness, Plenary Speaker, International Symposium on Aircraft Materials-ACMA 2010, Marrakech, Morocco, May 12-14, 2010.

6. S. Zabarnick, Organizer and Session Chair of Chemistry and Materials for Alternative Energy, Central Regional Meeting of the American Chemical Society (CeRMACS), Dayton, OH, June 16-19, 2010.

7. M.J. DeWitt, External Advisory Board Member, Mechanical, Industrial and Manufacturing Engineering Department of the University of Toledo, June, 2010.

8. K.E. Binns, Keynote Address, Joint Symposium of SAE-AE-5 and A-6 Committees, September, 2010

9. K.E. Binns, Special performance recognition award, SAE-6 Committee, September 2010.

10. E. Corporan, M.J. DeWitt, C. Klingshirn, J. Mantz, NASA Group Achievement Award to Alternative Aviation Fuel Experiment (AAFEX) Team, May, 2010.

11. L.M. Balster, Invited Speaker, Air Force Institute of Technology (AFIT) Research Seminar, Dayton, OH, Nov. 16, 2010.

12. S. Stouffer, Session Chair, 36th Annual DCASS, March 2011.

13. M.J. DeWitt, liaison to SAE AE-5 Aerospace Fuel, Oil and Oxidizer Systems Committee, March 2011.

14. M.J. DeWitt, Session Chair, 36th Annual DCASS, March 2011.

15. A. Briones, Session Chair, 2011 ASME Turbo Expo, Vancouver, Canada, June 2011.

16. S. Stouffer, Session Chair, 7th Annual ASME- DESS, Oct 2011.

17. W. Roquemore, D. Blunck, J. Cain, M. Colket, V. Katta, T. Litzinger, V. Katta, R.J. Santoro, S. Sidhu, S. Stouffer, and J. Zelina, SERDP Project of the Year—Weapon Systems and Platforms, "Soot Science Program," November 2011

18. S. Zabarnick, Invited Speaker, ExxonMobil, Lubricants Product Division, Paulsboro, NJ, January 2012.

19. Z. West, Invited Speaker, ExxonMobil, Lubricants Product Division, Paulsboro, NJ, January 2012.

20. J.S. Ervin, Organizer and University Host, Central States Combustion Meeting, Dayton, OH, April 2012.

21. M.J. DeWitt, Session Chair, 37th Annual DCASS, March 2012.

22. L. M. Balster, Chair-Elect, American Chemical Society (ACS), Dayton section, January-December 2012.

23. Scott Stouffer, Session Chair, Central States Combustion Meeting, Dayton, OH, April 2012.

24. M.J. DeWitt, External Advisory Board Member, Mechanical, Industrial and Manufacturing Engineering Department of the University of Toledo, June, 2012.

25. M.J. DeWitt, Invited Panel Member, Northwestern University Hulburt-Thodos Department of Chemical and Biological Engineering Professional Development Symposium, July, 2012.

26. E. Corporan, M.J. DeWitt, C. Klingshirn, D. Anneken, J. Mantz, NASA Group Achievement Award to Alternative Aviation Fuel Experiment (AAFEX) Team, August, 2012.

27. S. Stouffer, Session Chair, 8th Annual ASME- DESS, Oct 2012.

28. W. K. Lewis, AFRL Munitions Directorate Publication of the Year, 2012

29. W. K. Lewis, Co-chair of the 2012 Workshop on Time-Dependent Temperature Measurements in Energy Release Processes, 2012.

30. M.J. DeWitt, External Advisory Board Member, Mechanical, Industrial and Manufacturing Engineering Department of the University of Toledo, 2013.

31. L. M. Balster, Chair, American Chemical Society (ACS), Dayton section, January-December 2013.

32. S. Zabarnick, Elected Vice-Chair, Coordinating Research Council Aviation Meetings, May 2013.

33. S. Zabarnick, IASH Lifetime Achievement Award, International Association for Stability, Handling, and Use of Liquid Fuels, October 2013.

34. M.J. DeWitt, Invited Panel Member, Northwestern University Hulburt-Thodos Department of Chemical and Biological Engineering Professional Development Symposium, July, 2013.

35. M.J. DeWitt, Session Chair, 13th International Conference on Stability, Handling, and Use of Liquid Fuels, Rhodes, Greece, October, 2013.

36. M.J. DeWitt, External Advisory Board Member, Mechanical, Industrial and Manufacturing Engineering Department of the University of Toledo, April, 2014.

37. S. Zabarnick Invited Speaker, "Alternative Transportation Fuels- Issues & Technologies," Kettering College, February 2014.

38. S. Stouffer, Session Chair, 39th Annual DCASS, March 5 2014.

39. M.J. DeWitt, Invited Speaker, 5th Annual STARS (Spotlight on Technology, Arts, Research and Scholarship) Symposium, University of Dayton, Dayton, OH, September 18, 2014.

40. M.J. DeWitt, External Advisory Board Member, Mechanical, Industrial and Manufacturing Engineering Department of the University of Toledo, April, 2015.

41. M.J. DeWitt, 2015 Affiliate Council of Dayton Outstanding Engineer and Scientists Award for Excellence in Research, April, 2015.

42. A. Briones, Session Chair, 2015 ASME Turbo Expo, Montreal, Canada, June 2015.

43. M.J. DeWitt, Invited Speaker, 62nd JANNAF Propulsion Meeting, 8th Liquid Propulsion Subcommittee, Nashville, TN, June 2, 2015.

44. S. Zabarnick, Elected Chair, Coordinating Research Council Aviation Meetings, May 2015.

45. M.J. DeWitt, Session Chair, 14th International Conference on Stability, Handling, and Use of Liquid Fuels, Charleston, SC, October, 2015.

46. A. Briones, Session Chair, 2016 ASME Turbo Expo, Seoul, South Korea, June 2016.

47. M.J. DeWitt, External Advisory Board Member, Mechanical, Industrial and Manufacturing Engineering Department of the University of Toledo, April, 2016.

Journal Publications and Pre-Prints Papers

1. S. Zabarnick, R. Adams, Z. West, M.J. DeWitt, L. Shafer, R. Striebich, C.L. Delaney, and D.K. Phelps, "Compatibility of DiEGME and TriEGME Fuel System Icing Inhibitor Additives with BMS 10-39 Aircraft Tank Topcoat Material," Energy & Fuels, Vol. 24, pp. 2614-2627, 2010.

2. E. Corporan, M.J. DeWitt, C.D. Klingshirn, R. Striebich, and M.-D. Cheng, "Emissions Characteristics of Military Helicopter Engines with JP-8 and Fischer-Tropsch Fuels," Journal of Propulsion and Power, Vol. 26, pp. 317-324, 2010

3. L. M. Brown, J. P. McComb, M. D. Vangsness, L. L. Bowen, S. S. Mueller, L. M. Balster, and C. A. Bleckmann, "Community Dynamics and Phylogenetics of Bacteria Fouling in Jet A and JP-8 Aviation Fuel," International Journal of Biodeterioration & Biodegradation, Vol. 64, pp. 253-261, 2010.

4. W.S. Anderson, M.D. Polanka, J. Zelina, D.S. Evans, S.D. Stouffer, and G. Justinger, "Effects of a Reacting Cross-Stream on Turbine Film Cooling," ASME Journal of Engineering for Gas Turbines and Power, Vol. 132, pp. 051501/1-051501/7, 2010.

5. W.K. Lewis, A.T. Rosenberger, J.R. Gord, C.A. Crouse, B.A. Harruff, K.A.S. Fernando, M.J. Smith, D.K. Phelps, J.E. Spowart, E.A. Guliants, and C.E. Bunker "Multispectroscopic (FTIR, XPS, and TOFMS-TPD) Investigation of the Core-Shell Bonding in Sonochemically-Prepared Aluminum Nanoparticles Capped with Oleic Acid," J. Phys. Chem. C, Vol. 114, pp. 6377-6380, 2010.

6. S.W. Chung, E.A. Guliants, C.E. Bunker, P.A. Jelliss, and S.W. Buckner, "Size-Dependent Al Nanoparticle Oxidation Enthalpy," Prepr. Pap.-Am. Chem. Soc., Div. Fuel Chem., 2010.

7. M.A. Burgers, C.D. Oberle, S.W. Chung, E.A. Guliants, V. Kalugotla, C.E. Bunker, D.W. Hammerstroem, P.A. Jelliss, and S.W. Buckner, "Long-Term Air Stability of Organically-Capped Aluminum Nanoparticles," Prepr. Pap.-Am. Chem. Soc., Div. Fuel Chem., 2010.

8. H. Li, M.J. Meziani, A. Kitaygorodskiy, F. Lu, C.E. Bunker, K.A.S. Fernando, E.A. Guliants, and Y.-P. Sun, "Preparation and Characterization of Alane Complexes for Energy Applications," J. Phys. Chem. C, Vol. 114, pp. 3318-3322, 2010.

9. C.E. Bunker, M.J. Smith, K.A.S. Fernando, B.A.Harruff, W.K. Lewis, J.R. Gord, E.A. Guliants, and D.K.Phelps "Spontaneous Hydrogen Generation from Organic-Capped Al Nanoparticles and Water," ACS Appl. Mater. Interfaces, Vol. 2, pp. 11-14, 2010.

10. A.M. Briones, J. Zelina, and V. Katta, "Flame Stabilization in Small Cavities," AIAA Journal, Vol. 48, pp. 224-235, 2010.

11. A.M. Briones, J.S. Ervin, S. Putnam, L. Byrd, and L. Gschwender, "Micrometer-sized Water Droplet Impingement Dynamics and Evaporation on a Flat Dry Surface," Langmuir, Vol. 26, pp. 13272–13286, 2010.

12. M.T. Timko, Z. Yu, T.B. Onasch, H.-W. Wong, R.C. Miake-Lye, A.J. Beyersdorf, B.E. Anderson, K.L. Thornhill, E.L. Winstead E. Corporan, M.J. DeWitt, C.D. Klingshirn, C.

Wey, K. Tacina, D.S. Liscinsky, R. Howard and A. Bhargavi, "Particulate Emissions of Gas Turbine Engine Combustion of a Fischer-Tropsch Synthetic Fuel," Energy & Fuels, Vol. 24, pp. 5883-5896, 2010.

13. M. Billingsley, T. Edwards, L. Shafer, and T. Bruno, "Extent and Impacts of Hydrocarbon Fuel Compositional Variability for Aerospace Propulsion Systems," Presented at the 46th AIAA/ASME/SAE/ASEE Joint Propulsion Conference & Exhibit, AIAA No. 2010-6824, Nashville, TN, July 25-28, 2010.

14. D. Bulzan, B. Anderson, C. Wey, R. Howard, E. Winstead, A. Beyersdorf, E. Corporan, M. DeWitt, C. Klingshirn, S. Herndon, R. Miake-Lye, M. Timko, E. Wood, K. Tacina, D. Liscinsky, D. Hagen, P. Lobo, and P. Whitefield, "Gaseous and Particulate Results of the NASA Alternative Aviation Fuel Experiment (AAFEX)," Proceedings of ASME Turbo Expo, Power for Land, Sea and Air, Paper GT2010-23524, Glasgow, UK, 2010.

15. M.J. DeWitt, T. Edwards, L. Shafer, D. Brooks, R. Striebich, S.P. Bagley, and M.J. Wornat, "Effect of Aviation Fuel Type on Pyrolytic Reactivity and Deposition Propensity under Supercritical Conditions," Ind. Eng. Chem. Res., Vol. 50, pp. 10434-10451, 2011.

16. E. Corporan, T. Edwards, L. Shafer, M.J. DeWitt, C. Klingshirn, S. Zabarnick, Z. West, R. Striebich, J. Graham, and J. Klein, "Chemical, Thermal Stability, Seal Swell, and Emissions Studies of Alternative Jet Fuels," Energy & Fuels, Vol. 25, pp. 955-966, 2011.

17. Z. West, R.K. Adams, and S. Zabarnick, "Homogeneous Catalysis of Liquid-Phase Hydroperoxide Decomposition in Hydrocarbons," Energy & Fuels, Vol. 25, 897-904, 2011.

18. S. Saxena, M.S.P Kahandawala, and S.S. Sidhu, "A Shock Tube Study of Ignition Delay in the Combustion of Ethylene," Combustion and Flame, Vol. 158, pp. 1019–1031, 2011.

19. C.-X. Lin, R.J. Holder, B. Sekar, J. Zelina, M.D. Polanka, H.J. Thornburg, and A.M. Briones, "Heat Release in Turbine cooling II: Numerical Details of Secondary Combustion Surrounding Shaped Holes," Journal of Propulsion and Power, Vol. 27, pp. 269-281, 2011.

20. C.D. Klingshirn, M.J. DeWitt, R. Striebich, D. Anneken, L. Shafer, E. Corporan, M. Wagner and D. Brigalli, "Hydroprocessed Renewable Jet Fuel Evaluation, Performance, and Emissions in a T63 Turbine Engine," Proceeding of ASME Turbo Expo 2011, GT2011-46572, Vancouver, British Columbia, 2011.

21. M.T. Timko, S.C. Herndon, E. de la Rosa Blanco, E.C. Wood, Z. Yu, R.C. Miake-Lye, W.B. Knighton, L. Shafer, M. DeWitt, and E. Corporan, "Combustion Products of Petroleum Jet Fuel, a Fischer Tropsch Synthetic Fuel, and a Biomass Fatty Acid Methyl Ester Fuel for a Gas Turbine Engine," Combustion Science and Technology, Vol. 183, pp. 1039-1068, 2011.

22. A. Parambath, K.A.S. Fernando, C. Li, L. Fushen, Y. Fengchun, S. Weili, S. Sushant, Q. Haijun, T. Tim, A. Ankoma, and Y.-P. Sun, "Noncovalent Interactions of Derivatized Pyrenes with Metallic and Semiconducting Single-Walled Carbon Nanotubes," Journal of Physical Chemistry, Vol. 115, pp. 11010-11015, 2011.

23. L. Cao, S. Sahu, P. Anilkumar, C. E. Bunker, J. Xu, K.A.S. Fernando, P. Wang, E.A. Guliants, K.N. Tackett, and Y.-P. Sun, "Carbon Nanoparticles as Visible-Light

Photocatalysts for Efficient CO_2 conversion and Beyond," Journal of the American Chemical Society, Vol. 133, pp. 4754-4757, 2011.

24. V.R. Katta, R.A. Forlines, W.M. Roquemore, W.S. Anderson, J. Zelina, J.R. Gord,S.D. Stouffer, and S. Roy, "Experimental and Computational study on Partially Premixed flames in a Centerbody Burner," Combustion and Flame, Vol. 158, pp. 511-524, 2011.

25. O.N. Ruiz, K.A.S. Fernando, B. Wang, N.A. Brown, P.G. Luo, N.D. McNamara, M. Vangsness, Y.-P. Sun, and C.E. Bunker, "Graphene Oxide: A Nonspecific Enhancer of Cellular Growth," ACS Nano, Vol 5, pp. 8100-8107, 2011.

26. V.R. Katta, W.M. Roquemore, S. Stouffer, and D. Blunck, "Dynamic Lifted Flame in Centerbody Burner," Proceedings of the Combustion Institute, Vol 33, pp. 1187-1194, 2011.

27. M. D. Polanka, J. Zelina, W. S. Anderson, B. Sekar, D.S. Evans, C.-X. Lin, and S.D. Stouffer, "Heat Release in Turbine Cooling I: Experimental and Computational Comparison of Three Geometries," Journal of Propulsion and Power, Vol. 27, pp. 257-268, 2011.

28. Z. West, H. Jiang, and S. Zabarnick, "Jet Fuel Degradation during Supercritical High Heat Flux Heat Transfer," Proceedings of the 12th International Conference on Stability, Handling, and Use of Liquid Fuels, Sarasota, FL, 2011.

29. R.C. Striebich, L.M. Shafer, Z.J. West, R.K. Adams, and S. Zabarnick, "Hydrocarbon Group-Type Analysis of Current and Future Aviation Fuels: Comparing ASTM D2425 to GCxGC," Proceedings of the 12th International Conference on Stability, Handling, and Use of Liquid Fuels, Sarasota, FL, 2011.

30. L.M. Shafer and T. Edwards, "Speciated Naphthalene Analysis in Liquid Transportation Fuels," Proceedings of the 12th International Conference on Stability, Handling, and Use of Liquid Fuels, Sarasota, FL, 2011.

31. Z.J. West, R.K. Adams, M. Flake, and S. Zabarnick, "Catalytic Decomposition of Hydroperoxides: Implications for Jet Fuel Stability," Proceedings of the 12th International Conference on Stability, Handling, and Use of Liquid Fuels, Sarasota, FL, 2011.

32. S.S. Mueller, L.L. Bowen, L.M. Brown, N.A. Brown, O.N. Ruiz, M. Vangsness, L. Balster, S. Zabarnick, L. Shafer, R. Cook, and E.M. Strobel, "A Comparison Study of the Effects of Bacterial Contamination on Alternative Fuels Versus Petroleum-Derived Fuels," Proceedings of the 12th International Conference on Stability, Handling, and Use of Liquid Fuels, Sarasota, FL, 2011.

33. J. Balagurunathan, G. Flora, S. Saxema, M.S.P. Kahandawala, M.J. DeWitt, S.S. Sidhu, and E. Corporan, "Ignition Delay Times of a Range of Alternative Jet Fuels and Surrogate Fuel Candidate Hydrocarbons under Fuel-Lean Conditions: a Shock Tube Study," Proceedings of the 49th AIAA Aerospace Sciences Meeting, Orlando, FL, 2011

34. O.N. Ruiz and N.A. Brown, "Advances in Microbial Mitigation of Aviation Fuels: Characterization of the Antimicrobial Activity of DiEGME in Fuel by Quantitative Real-Time PCR," Proceedings of the 12th International Conference on Stability, Handling, and Use of Liquid Fuels, Sarasota, FL, 2011.

35. W.K. Lewis, B.A. Harruff, J.R. Gord, A.T. Rosenberger, T.M. Sexton, E.A. Guliants, and C.E. Bunker, "Chemical Dynamics of Aluminum Nanoparticles in Ammonium Nitrate and Ammonium Perchlorate Matrices: Enhanced Reactivity of Organically Capped Aluminum," J. Phys. Chem. C, Vol. 115, pp. 70-77, 2011.

36. J.C. Servaites, J.L. Faeth, and S.S. Sidhu, "A Dye Binding Method for Measurement of Total Protein in Microalgae," Anal. Biochem., Vol. 421, pp. 75-80, 2012.

37. A.R. O'Neil, S.D. Stouffer, S. Kostka, S. Roy, A. Lynch, D.L. Blunck, J.R. Gord and M. Polanka, "Chemiluminescence and High Speed Imaging of Reacting Film Cooling Layers," AIAA Paper 2012-325 presented at the AIAA Aerospace Sciences Conference Nashville, TN, 2012

38. B.A. Rankin, D.L. Blunck, V.R. Katta, S.D. Stouffer, and J.P. Gore, "Experimental and computational infrared imaging of bluff body stabilized laminar diffusion flames," Combustion and Flame, Vol. 159, pp. 2841-2843, 2012.

39. A.M. Briones, J.S Ervin, L. Byrd, S. Putnam, A. Ashley, and J.G. Jones, "Evaporation Characteristics of Pinned Water Microdroplets," Journal of Thermophysics and Heat Transfer, Vol. 26, pp. 480-493, 2012.

40. A.M. Briones, J.S Ervin, S. Putnam, L. Byrd, and J.G. Jones, "A Novel Kinetically-controlled De-pinning Model for Evaporating Water Microdroplets," International Communications in Heat and Mass Transfer, Vol. 39, pp. 1311-1319, 2012.

41. Y. Lin, C.E. Bunker, K.A.S. Fernando, J.W. Connell "Aqueously Dispersed Silver Nanoparticles-Decorated Boron Nitride Nanosheets for Reusable, Thermal Oxidation-Resistant SERS Devices," ACS Applied Materials & Interfaces, Vol. 4, pp. 1110-1117, 2012.

42. J. Xu, S. Sahu, L. Cao, C.E. Bunker, G. Peng, Y. Liu, K.A.S. Fernando, P. Wang, E.A. Guliants, M.J. Meziani, H. Qian, Y. P. Sun, "Efficient Fluorescence Quenching in Carbon Dots by Surface-Doped Metals - Disruption of Excited State Redox Processes and Mechanistic Implications," Langmuir, Vol. 28, pp. 16141-16147, 2012.

43. W.K. Lewis, C.G. Rumchik, P.B. Broughton, and C.M. Lindsay, "Time-Resolved Spectroscopic Studies of Aluminized Explosives: Chemical Dynamics and Apparent Temperatures," J. Appl. Phys., Vol. 111, pp. 014903/1-014903/6, 2012.

44. C. D. Klingshirn, M. DeWitt, R. Striebich, D. Anneken, L. Shafer, E. Corporan, M. Wagner, and D. Brigalli, "Hydroprocessed Renewable Jet Fuel Evaluation, Performance, and Emissions in a T63 Turbine Engine," J. Eng. Gas Turbines Power, Vol. 134, 051506/1-051506/8, 2012.

45. D. L. Blunck, J. Cain, R. C. Striebich, S.D. Stouffer, and W.M. Roquremore, "Fuel Rich Combustion Products from a Well-Stirred Reactor Operated using Traditional and Alternative Fuels," 2012 Central States Combustion Meeting, Dayton, OH, 2012.

46. E. Corporan, M.J. DeWitt, C.D. Klingshirn, D. Anneken, L. Shafer, and R. Striebich, "Comparisons of Emissions Characteristics of Several Turbine Engines Burning Fischer-Tropsch and Hydroprocessed Esters and Fatty Acids Alternative Jest Fuels," Proceeding of ASME Turbo Expo 2012, GT2012-68656, Copenhagen, Denmark, 2012.

47. A. Nagulapalli, G. Flora, S. Saxema, M.S.P. Kahandawala, M.J. DeWitt, E. Corporan, and S.S. Sidhu, "Ignition Delay Measurements of Methylcyclohexane/O2/Ar Mixture Over a Wide Range of Conditions," Proceedings of the Spring Technical Meeting of the Central States Section of the Combustion Institute, Dayton, OH, 2012.

48. M.S. Hanchak, L.W. Byrd, A.M. Briones, J.S. Ervin, and S.A. Putnam, "Model of Droplet Impingement Based on Least-Squares Solution of Proper Orthogonal Decomposition Basis Matrices," Journal of Fluids Engineering, Vol. 134, 041301-041301-8, 2012.

49. S.A. Putnam, A.M. Briones, L.W. Byrd, J.S. Ervin, M.S. Hanchak, A. White, and J.G. Jones, "Microdroplet Evaporation on Superheated Surfaces," International Journal of Heat and Mass Transfer, Vol. 55, pp. 5793-5807, 2012.

50. S.A. Putnam, L.W. Byrd, A.M. Briones, M.S. Hanchak, J.S. Ervin, and J.G. Jones, "Role of Entrapped Vapor Bubbles during Microdroplet Evaporation," Applied Physics Letters, Vol. 101, pp. 071602 - 071602-4, 2012.

51. S.A. Putnam, A.M. Briones, J.S. Ervin, M.S. Hanchak, L.W. Byrd, and J.G. Jones, "Interfacial Heat Transfer during Microdroplet Evaporation on a Laser Heated Surface," International Journal of Heat and Mass Transfer, Vol. 55, pp. 6307-6320, 2012.

52. J. Cain, D. Blunck, E. Corporan, M.J. DeWitt, R. Striebich, D. Anneken, C. Klingshirn, and W.M. Roquemore, "Characterization of Gaseous and Particulate Emissions from a Turboshaft Engine Burning Conventional, Alternative and Surrogate Fuels," Prepr.-Am. Chem. Soc., Div Pet. Chem., August, 2012.

53. D. Anneken, R. Striebich, M.J. DeWitt, C. Klingshirn, and E. Corporan, "Development of a Method to Identify and Quantify Hazardous Air Pollutants from Turbine Engine Emissions," Prepr.-Am. Chem. Soc., Div Pet. Chem., August, 2012.

54. B. McMasters, M.J. DeWitt, R. Striebich, T. Edwards, and D. Phelps, "Effect of Fuel Chemical Composition on Pyrolytic Reactivity and Deposition Propensity under Supercritical Conditions," Prepr.-Am. Chem. Soc., Div. Pet. Chem., Vol. 57, pp. 819-822, 2012.

55. H. Jiang, J. Ervin, Z.J. West, and S. Zabarnick, "Effects of Flow Passage Expansion or Contraction on Jet-Fuel Surface Deposition" AIAA Journal of Propulsion and Power, Vol. 28, pp. 694-706, 2012.

56. D.W. Johnson, R.K. Adams, S. Zabarnick, Z.J. West, and R.C. Striebich, "Analysis of Polar Components in Jet Fuel by High Performance Liquid Chromatography/Time of Flight Mass Spectrometry with Electrospray Ionization," Preprints – American Chemical Society, Division of Energy & Fuels, Vol. 57, pp. 798-800, 2012.

57. M.J. DeWitt, Z. West, A. Mescher, N. Stelzenmuller, S. Zabarnick, and T. Edwards, "Effect of Aromatics Addition on the Thermal-Oxidative Stability of Alternative Jet Fuels," Preprints – American Chemical Society, Division of Energy & Fuels, Vol. 57, pp. 826-827, 2012.

58. W.K. Lewis, B.A. Harruff-Miller, M.A. Gord, J.R. Gord, E.A. Guliants, and C.E. Bunker, "A Threshold-Based Approach to Calorimetry in Helium Droplets: Measurement of Binding Energies of Water Clusters," Rev. Sci. Instrum., Vol. 83, pp. 073109/1-073109/5, 2012.

59. D.K. Minus and L. M. Balster, "Jet Fuel Parameter Prediction and Quality Assessment Analysis Using Nuclear Magnetic Resonance Spectroscopy Coupled with Chemometrics," Prepr.-Am. Chem. Soc., Div Pet. Chem., Vol. 57, 2012.

60. H.J. Robota and J.C. Alger, "Preparation of a Research Jet Fuel Composition Comprised of Nearly Exclusively Methyl-Branched Tetradecane Isomers Having a Freezing Point below -47 °C," Ind. Eng. Chem. Res., Vol. 51, pp. 10313-10319, 2012.

61. R. Adams, S. Zabarnick, Z. West, R. Striebich, and D. Johnson, "Chemical Analysis of Jet Fuel Polar Heteroatomic Species via High Performance Liquid Chromatography with Electrospray Ionization-Mass Spectrometric Detection," Energy & Fuels, Vol. 27, pp. 2390-2398, 2013.

62. H. Jiang, J.S. Ervin, Z. West, and S. Zabarnick, "Turbulent Flow, Heat Transfer Deterioration, and Thermal Oxidation of Jet Fuel," Journal of Thermophysics and Heat Transfer, Vol. 27, pp. 668-678, 2013. doi: 10.2514/1.T4103

63. H.J. Robota, J.C. Alger, and L. Shafer, "Converting Algal Triglycerides to Diesel and HEFA Jet Fuel Fractions," Energy & Fuels, Vol., 27, pp. 985-996, 2013.

64. M.S. Hanchak, A.M. Briones, J.S. Ervin, and L.W. Byrd, "One-dimensional Models of Nanoliter Droplet Evaporation from a Hot Surface in the Transition Regime," International Journal of Heat and Mass Transfer, Vol. 57, pp. 473-483, 2013.

65. W.K. Lewis, C.G. Rumchik, M.J. Smith, K.A.S. Fernando, C.A. Crouse, J.E. Spowart, E.A. Guliants, and C.E. Bunker "Comparison of Post-Detonation Combustion in Explosives Incorporating Aluminum Nanoparticles: Influence of the Passivation Layer," J. Appl. Phys., Vol. 113, pp. 044907/1-044907/5, 2013.

66. W.K. Lewis, C.G. Rumchik, and M.J. Smith "Emission Spectroscopy of the Interior of Optically Dense Post-Detonation Fireballs," J. Appl. Phys., Vol. 113, pp. 024903/1-024903/4, 2013.

67. E. Corporan, M.J. DeWitt, C. Klingshirn, "Evaluation of Downstream Dilution Techniques for the Sampling of Turbine Engine Particulate Matter," SAE 2013 AeroTech Congress & Exhibition, Paper 2013-01-2130, September, 2013.

68. S. Zabarnick, L. Shafer, R. Cook, and Z. West, "Use of Scanning Brookfield Viscometry as a Viscosity Equivalent Method for Jet Fuel Freezing Point," Proceedings of the 13th International Symposium on Stability, Handling, and Use of Liquid Fuels, October 2013.

69. O.N. Ruiz, C. Smart, W. Foley, T. Gunasekera, and R.C. Striebich (presented by S. Zabarnick), "Effects of Bacterial Transcriptional Response and Metabolism on Fuel Composition and Performance," Proceedings of the 13th International Symposium on Stability, Handling, and Use of Liquid Fuels, October 2013.

70. M.J. DeWitt, B. McMasters, T. Williams, T. Hendershott, R. Striebich, S. Zabarnick, T. Edwards, and D.K. Phelps, "Effect of Fuel Chemical Composition on Supercritical Reactivity and Deposition Propensity," Proceedings of the 13th International Symposium on Stability, Handling, and Use of Liquid Fuels, October 2013.

71. M.J. DeWitt, Z. West, S. Zabarnick, L. Shafer, R. Striebich, and T. Edwards, "Effect of Addition of Aromatics on the Thermal Oxidative Stability of Alternative Aviation Fuels,"

Proceedings of the 13ᵗʰ International Symposium on Stability, Handling, and Use of Liquid Fuels, October 2013.

72. E. Corporan, T. Edwards, M.J. DeWitt, C. Klingshirn, R. Striebich, L. Shafer, D. Anneken, and D. Caswell, "Investigation of Combustion and Emissions Performance of Alternative and Conventional Fuels at the Limits of the Jet Fuel Specification," Proceedings of the 13th International Conference on Stability, Handling, and Use of Liquid Fuels, Rhodes, Greece, October, 2013.

73. S. Zabarnick, Z.J. West, L.M. Shafer, and R. Cook, "Studies of Scanning Brookfield Viscometry as a Replacement for Freezing Point in Aviation Fuel Specifications," Coordinating Research Council, CRC Project No. AV-16-11, 2013.

74. M.S. Hanchak, M.D. Vangsness, L.W. Byrd, J.S. Ervin, and J.G. Jones, "Profile Measurements of Thin Liquid Films using Reflectometry," Appl. Phys. Lett., Vol., 103, pp. 211607/1-211607/4, 2013.

75. D. Blunck, D. Shouse, C. Neuroth, R. Battelle, A. Lynch, B. Sekar, J. Zelina, T.J. Erdmann, D. Burrus, R. Howard, A. Briones, D. Richardson, A. Caswell, "Experimental and Computational Studies of an Ultra-compact Combustor," ASME Turbo Expo 2013, San Antonio, TX, 2013.

76. J. Cain, M.J. DeWitt, D. Blunck, E. Corporan, R. Striebich, D. Anneken, C. Klingshirn, W.M. Roquemore, and R. Vaner Wal, "Characterization of Gaseous and Particulate Emissions from a Turboshaft Engine Burning Conventional, Alternative and Surrogate Fuels" Energy & Fuels, Vol. 27, pp. 2290-2302, 2013.

77. T.S. Gunasekera, R.C. Striebich, S.S. Mueller, E.M. Strobel, and O.N. Ruiz, "Transcriptional Profiling Suggests that Multiple Metabolic Adaptations are Required for Effective Proliferation of *Pseudomonas aeruginosa* in Jet Fuel," Env. Sci Tech., Vol. 47, pp. 13449-13458, 2013.

78. B.T. Bohan, D.L. Blunck, M.D. Polanka, S. Kostka, N. Jiang, and S.D. Stouffer, "Impact of an Upstream Film Cooling Row on Mitigation of Secondary Combustion in a Fuel Rich Environment," ASME Journal of Turbomachinery, Vol. 136, pp. 031008-031008-8, 2013.

79. W. K. Lewis, B. A. Harruff-Miller, P. Leatherman, M. A. Gord, and C. E. Bunker "Helium Droplet Calorimetry of Strongly Bound Species: Carbon Clusters from C2 to C12" Review of Scientific Instruments, Vol. 85, pp. 094102-094102-10, 2014.

80. K.A.S. Fernando, V. Watson, X. Wang, C.E. Bunker, "Synthesis and Characterization of Metal Decorated Carbon Substrates for Energy Applications," ACS Conference Proceedings, Division of Energy & Fuels, Dallas, TX, ISBN: 9781632660039, Volume 59, 319, 2014.

81. K.A.S. Fernando, V.G. Watson, X. Wang, N.D. McNamara, M.C. JoChum, D.W. Bair, B. A. Miller, and C.E. Bunker, "Migration of Silver Nanoparticles from Silver Decorated Graphene Oxide to Other Carbon Nanostructures," Langmuir, Vol. 30, pp. 11776-11784, 2014.

82. S. Suhant, L. Yamin, W. Ping, C.E. Bunker, K.A.S. Fernando, W. Lewis, E. Guliants, F. Yang, W. Jinping, Y.-P. Sun "Visible-Light Photoconversion of Carbon Dioxide into

Organic Acids - A Pressure Dependence Study in Aqueous Solution of Carbon Dots," Langmuir, Vol. 30, pp. 8631-8636, 2014.

83. A.M. Briones, B. Sekar, T.J. Erdmann, "Effect of Centrifugal Force on Conventional and Alternative Fuel Surrogate Turbulent Premixed Flames," Proceedings of the ASME Turbo Expo 2014, Düsseldorf, Germany, GT2014-27327.

84. Z.J. West, L.M. Shafer, R.C. Striebich, S. Zabarnick, C. Delaney, D.K. Phelps, and M.J. DeWitt, "Equilibrium Partitioning of DiEGME between Fuel and Aqueous Phases at Sub-Ambient Temperatures," Energy & Fuels, Vol 28, pp. 4501-4510, 2014. doi: 10.1021/ef500900p

85. M.J. DeWitt, Z. West, S. Zabarnick, L. Shafer, R. Striebich, A. Higgins, and T. Edwards, "Effect of Aromatics on the Thermal-Oxidative Stability of Synthetic Paraffinic Kerosene," Energy & Fuels, Vol. 28, pp. 3696-3703, 2014. doi: 10.1021/ef500456e

86. A.K. Janeczko, E.B. Walters, S.J. Schuldt, M.L. Magnuson, S.A. Willison, L.M. Brown, O.N. Ruiz, D.L. Felker, L. Racz, "Fate of Malathion and a Phosphonic Acid in Activated Sludge with Varying Solids Retention Times," Water Research, Vol. 57, pp. 127-139, 2014.

87. R.C. Striebich, C.E. Smart, T.S. Gunasekera, S.S. Mueller, E.M. Strobel, B.W. McNichols, and O.N. Ruiz, "Characterization of the F-76 diesel and Jet-A aviation fuel hydrocarbon degradation profiles of *Pseudomonas aeruginosa* and *Marinobacter hydrocarbonoclasticus,*" International Biodeterioration and Biodegradation, Vol. 93, pp. 33-43, 2014.

88. M.J. DeWitt, B. McMasters, Z. West, A. Higgins, L. Shafer, S. Zabarnick, D.K. Phelps, T. Edwards, R. Wills, and S.T. Bailie, "Evaluation of the Supercritical Decomposition of JP-10, "Proceedings of the 61st JPM/42nd SMBS/38th PEDCS/29th RNTS/27thSEPS JANNAF Meeting," Charleston, SC, 2014.

89. R.C. Striebich, L.M. Shafer, R.K. Adams, Z.J. West, M.J. DeWitt, and S. Zabarnick, "Hydrocarbon Group-Type Analysis of Petroleum-Derived and Synthetic Fuels Using Two-Dimensional Gas Chromatography," Energy & Fuels, Vol. 28, pp. 5696-5706, 2014. doi: 10.1021/ef500813x.

90. M.S. Hanchak, M.D. Vangsness, L.W. Byrd, and J.S. Ervin, "Thin Film Evaporation of n-Octane on Silicon: Experiments and Theory," Int. Journal of Heat and Mass Transfer, Vol. 75, pp. 196–206, 2014.

91. A.M. Briones, B. Sekar, and T.J. Erdmann, "Effect of Centrifugal Force on Turbulent Premixed Flames," ASME Journal of Engineering for Gas Turbines and Power, Vol. 137, pp. 011501-011501-10, 2014.

92. M.J. DeWitt, P. Kennedy, T. Williams, D.K. Phelps, T. Hendershott, A. Higgins, L. Shafer, J. Mantz, and T. Edwards, "Hydrocarbon-Based Fuel Selection and Characterization for Medium Scale Scramjet Engine Tests," Proceedings of the 46th Combustion/34th AP/38th EP and S/28th PSH, JANNAF Meeting, Paper 3624, Albuquerque, NM, 2014.

93. L.M. Brown, T.S. Gunasekera, and O.N. Ruiz, "Draft Genome Sequence of *Pseudomonas aeruginosa* ATCC 33988, a Bacterium Highly Adapted to Fuel-polluted Environments," Genome Announcements, Vol. 2, pp. 13-14, 2014.

94. T.S. Gunasekera and O.N. Ruiz, "Transcriptional Response of *Pseudomonas aeruginosa* to Jet Fuel," Proceedings of the 13th International Conference on Stability, Handling and use of Liquid Fuels, Rhodes, 2014.

95. B.J. Thomas, B.A. Harruff-Miller, C.E. Bunker, and W.K. Lewis "Infrared Spectroscopy of Mg-CO2 and Al-CO2 Complexes in Helium Nanodroplets," Journal of Chemical Physics, Vol. 142, pp. 174310, 2015.

96. R.C. Striebich, L.L. Bowen, S.S. Mueller, L.M. Shafer, T.S. Gunasekera, and O.N. Ruiz, "Aviation Fuel Biodegradation using a Stirred-Tank Bioreactor," Proceedings of the 14th International Conference on Stability, Handling, and Use of Liquid Fuels, Charleston, SC, October 2015.

97. D. Anneken, R.C. Striebich, M.J. DeWitt, C. Klingshirn, and E. Corporan, "Development of Methodologies for Identification and Quantification of Hazardous Air Pollutants from Turbine Engine Emissions," Journal of the Air and Waste Management Association, Vol. 65, pp. 336-346, 2015.

98. A.M. Briones, B. Sekar, D.T. Shouse, D.L. Blunck, H.J. Thornburg, and T.J. Erdmann, "Reacting Flows in Ultra-Compact Combustors with Combined-diffuser Flameholder," Journal of Propulsion and Power, Vol. 31, pp. 238-252, 2015.

99. T. Cleaver, K. Granlund, A. Comer, A.M. Briones, and V. Belovich, "Bluff-body wake stability for unsteady inflow conditions," AIAA 2015-1295, 53rd Aerospace Sciences Meeting, 2015.

100. L.M. Brown, T.S. Gunasekera, and O.N. Ruiz, "Draft Genome Sequence of *Rhodovulum navalis* NI22, a Novel Naphthalene Degrading Marine Bacterium" Genome Announcements, Vol. 3, pp. 1-2, 2015.

101. E.K. Brown, M. Palmquist, D. Lunning Prak, S.S. Mueller, L.M. Bowen, K. Sweely, O.N. Ruiz, and P.C. Trulove, "Interaction of Selected Fuels with Water: Impact on Physical Properties and Microbial Growth," Journal of Petroleum & Environmental Biotechnology, Vol. 6, pp. 204-212, 2015.

102. O.N. Ruiz, N.A. Brown, K.A.S. Fernando, B.A. Miller, T.S. Gunasekera, and C.E. Bunker, "Graphene Oxide-based Nanofilters Efficiently Remove Bacteria from Fuel," International Biodegradation and Biodeterioration, Vol 97, pp. 168-178, 2015.

103. K.A.S. Fernando, S. Sahu, Y. Liu, W.K. Lewis, E.A. Guliants, A. Jafariyan, P. Wang, C.E. Bunker, and Y.-P. Sun, "Carbon Quantum Dots and Applications in Photocatalytic Energy Conversion," ACS Applied Materials & Interfaces, Vol. 7, pp. 8363-8376, 2015.

104. S. Sahu, L. Cao, M.J. Meziani, C.E. Bunker, K.A.S. Fernando, P. Wang, and Y.-P. Sun, "Carbon Dioxide Photoconversion Driven by Visible-Light Excitation of Small carbon Nanoparticles in Various Configurations," Chemical Physics Letters, Vol. 634, pp. 122-128, 2015.

105. G. Flora, J. Cain, M. Kahandawala, M.J. DeWitt, E. Corporan, and S. Sidhu, "The Effect of Chain Branching on Ignition Delay of C_5 and C_7 Backbone Fuels: *n*-Pentane, *iso*-Octane, 2-Methylheptane and *iso*-Dodecane," Proceedings of the 9th U.S. Combustion Meeting, Paper #114RK-0263, 2015.

106. G. Flora, J. Cain, M. Kahandawala, M.J. DeWitt, E. Corporan, S. Sidhu, "Time-dependent Speciation of Ethylene Combustion under Fuel Rich Conditions—a Novel Shock Tube Approach," Proceedings of the 9th U.S. Combustion Meeting, Paper #114RK-0266, 2015.

107. Z.H. Sander, Z.J. West, J.S. Ervin, and S. Zabarnick, "Experimental and Modeling Studies of Heat Transfer, Fluid Dynamics, and Autoxidation Chemistry in the Jet Fuel Thermal Oxidation Tester (JFTOT)," Energy & Fuels, Vol. 29, pp. 7036-7047, 2015.

108. L. Shafer, R. Striebich, S. Zabarnick, and Z. West, "Identification and Quantitation of Polar Species in Liquid Transportation Fuels by GCxGC," Proceedings of the 14th International Symposium on Stability, Handling, and Use of Liquid Fuels, October 2015.

109. M.J. DeWitt, T. Williams, T. Hendershott, R. Striebich, L. Shafer, S. Zabarnick, Z. West, M. Hanchak, T. Edwards, and D.K. Phelps, "Reactivity and Deposition Propensity of Hydrocarbons Under Supercritical Pyrolytic Reaction Conditions," Proceedings of the 14th International Conference on Stability, Handling, and Use of Liquid Fuels, Charleston, SC, October 2015.

110. O.N. Ruiz, L.M. Brown, R.C. Striebich, S.S. Mueller, T.S. Gunasekera, "Draft Genome Sequence of Pseudomonas frederiksbergensis SI8, a Psychrotrophic Aromatic-Degrading Bacterium. Genome Announcements," Vol 3, pp. 811-815, 2015.

111. M.S. Hanchak, M.D. Vangsness, J.S. Ervin, and L.W. Byrd, "Model and Experiments of the Transient Evolution of a Thin, Evaporating Liquid Film," International Journal of Heat and Mass Transfer, Vol. 92, pp. 757-765, 2016.

112. M.S. Hanchak, M.D. Vangsness, J.S. Ervin, and L.W. Byrd, "Transient Measurement of Thin Liquid Films Using a Shack-Hartmann Sensor," International Communications in Heat and Mass Transfer, Vol. 77, pp.100-103, 2016.

113. A.M. Briones, B.A. Rankin, S.D. Stouffer, T.J. Erdmann, and D.L. Burrus, "Parallelized, Automated, Predictive Imprint Cooling Model for Combustor Liners, 2016 ASME Turbo Expo, GT2016-56187, Seoul, South Korea, 2016.

114. L.M. Brown, R.C. Striebich, T.S. Gunasekera, and O.N. Ruiz, "Draft Genome Sequence of Gordonia sihwensis S9, a Branched Alkane-Degrading Bacterium," Genome Announcements, Vol. 4, pp. 622-616, 2016.

115. O.N. Ruiz, L.M. Brown, R.C. Striebich, C.E. Smart, L.L. Bowen, J.S. Lee, B.J. Little, S.S. Mueller, and T.S. Gunasekera, "Effect of Conventional and Alternative Fuels on a Marine Bacterial Community and the Significance to Bioremediation," Energy & Fuels, Vol. 30, pp. 434–444, 2016.

116. T.S. Gunasekera, L.L. Bowen, S.C. Howard-Byerly, W.S. Foley, R.C. Striebich, C.E. Zhou, and O.N. Ruiz, "Transcriptomic Analyses Elucidate Adaptive Differences of Closely-Related Strains of *P. aeruginosa* in Fuel," Applied and Environmental Microbiology, under review, 2016.

117. L.M. Brown, R.C. Striebich, T.S. Gunasekera, and O.N. Ruiz, "Draft Genome Sequence of Nocardioides luteus Strain BAFB, an Alkane-Degrading Bacterium Isolated from JP-7 Polluted Soil," Genome Announcements, under review, 2016.

118. O.M. Pavlyuk and O.N., Ruiz, "Peptide-Biofunctionalized Quantum Dot Chemistry for Rapid Detection of Microbial Contamination in Fuel Systems" ACS Nano, in preparation, 2016.

119. Y. Liu, P. Wang, K.A.S. Fernando, G.E. LeCroy, B.A. Harruff-Miller, K. Lewis, C. E. Bunker, Z.-L. Hou, and Y.-P. Sun "Enhanced Fluoresence Propeties of Carbon Dots in Polymer Films," Journal of Materials Chemistry C., Vol. 4, pp. 6967-6974, 2016.

120. G.E. LeCroy, S.-T. Yang, F. Yang, Y. Liu, K.A.S. Fernando, C.E. Bunker, Y. Hu, P.G. Luo, and Y.-P. Sun, "Functionalized Carbon Nanoparticles Synthesis and applications in Optical Bioimaging and Energy Conversion," Coordination Chemistry Reviews, Vol. 320-321, pp. 66-82, 2016.

Presentations

1. M.J. DeWitt, "Overview of R&D Efforts Related to Aviation Fuel Chemistry and Engineering," presented at University of Dayton Senior Chemical Engineering Seminar, March, 2010.

2. S.S. Mueller, M.D. Vangsness, L.M. Balster, L.L. Bowen, L.M. Brown, E.M. Strobel, "Comparing Microbial Contamination in Different Types of Fuel," 4th Annual Alternative Energy NOW Conference, Orlando, FL, February 9-10, 2010.

3. A.M. Briones, B. Sekar, H. Thornburg, and J. Zelina, "Effect of Vane Notch and Ramp Design on the Performance of a Rectangular Inter-Turbine Burner," 48th AIAA Aerospace Sciences Meeting including the New Horizons and Aerospace Exhibition," Orlando, FL, January, 2010.

4. H. Thornburg, B. Sekar, and A.M. Briones, "Analysis of Wake Characteristics of Several Two-dimensional Flame Holders for Combustion Systems," 34th Dayton-Cincinnati Aerospace Sciences Symposium, Dayton, OH, March, 2010.

5. B. Sekar, A.M. Briones, and H. Thornburg, "Analysis of Wake Characteristics of Several Two-dimensional Flame Holders for Combustion Systems," Augmentor Design Systems Conference, Jacksonville, FL, March, 2010.

6. L.M. Balster, L.L. Bowen, L.M. Brown, S.S. Mueller, L.M. Shafer, E.M. Strobel, M. Tsao, M.D. Vangsness, "Microbial Growth and Biofilm Formation: GC-MS Analysis and Traditional Culture of Jet A-1 and Alternative Fuels," Central Regional Meeting of the American Chemical Society (CeRMACS), Dayton, OH, June 16-19, 2010.

7. M.D. Vangsness and K. Lafdi, "Nano Technology Approach to Prevent Bacterial Contamination in Aircraft Fuel Systems," International Symposium on Aircraft Materials-ACMA 2010, Marrakech, Morocco, May 12-14, 2010.

8. M.D. Vangsness and E.M. Strobel, "Bio-Contamination Suppression by Antimicrobial Cotton Coalescer Element," Coordinating Research Council (CRC) Aviation Meeting, Alexandria, Virginia, May 3-6, 2010.

9. L.M. Balster, L.L. Bowen, L.M. Brown, S.S. Mueller, L.M. Shafer, E.M. Strobel, M. Tsao, M.D. Vangsness, "Microbial Growth and Biofilm Formation: Jet A-1 vs. Six Alternative Fuels," Coordinating Research Council (CRC) Aviation Meeting, Alexandria, Virginia, May 3-6, 2010.

10. H. Jiang, Z. West, S. Zabarnick, and J. Ervin, "Effects of a Step Change in Flow Geometry on the Surface Deposition from Jet Fuel within a Tube," Coordinating Research Council (CRC) Aviation Meeting, Alexandria, Virginia, May 3-6, 2010.

11. E. Corporan, M.J. DeWitt, C. Klingshirn, J. Mantz, and D. Anneken, "AFRL Efforts on Turbine Engine PM Emissions," presented at SAE E31 Committee Meeting, Interlaken, Switzerland June 29, 2010.

12. Z. West, R. Adams, and S. Zabarnick, "Homogeneous Catalysis of Hydroperoxide Decomposition in Liquid Hydrocarbons," Central Regional Meeting of the American Chemical Society (CeRMACS), Dayton, OH, June 16-19, 2010.

13. H.J. Robota, J. Jones, M. Luo, and A. Stewart, "Hexadecane Hydrotreating as a Surrogate for Fischer-Tropsch Upgrading to Aviation Fuel Using a Co/MoO3/Silica-Alumina Catalyst," Central Regional Meeting of the American Chemical Society (CeRMACS), Dayton, OH, June 16-19, 2010.

14. B. Sekar, H. Thornburg, and A.M. Briones, "Design and Analysis of Flame Holders for Instability-Free Operation of Combustion Systems," Proceedings of the HPCMP User's Group Conference, Schaumburg, IL, June 14-17, 2010.

15. A.M. Briones and B. Sekar, "Characteristics of Multi-Cavity Trapped Vortex Combustors," ASME Turbo Expo 2010: Power for Land, Sea, and Air, Glasgow, Scotland, UK, June 14-18, 2010.

16. K.A.S. Fernando, "Sonochemical Assisted Synthesis of Aluminum and Silver Nanoparticles and Decoration of Single-walled Carbon Nanotubes and Graphene Oxide with These Nanoparticles," ACS Regional Conference, Dayton OH, Aug. 2010.

17. K.E. Binns, "Fueldraulic and Hydraulic Technology for Future Military Aircraft," Joint SAE AE-5 and A-6 Committee Meeting, Anchorage, Alaska, September 2010.

18. H. Jiang, Z. West, S. Zabarnick, and J.Ervin, "Effect of a Step Change in Flow Geometry on the Surface Deposition from Jet Fuel within a Tube," 35th Dayton-Cincinnati Aerospace Sciences Symposium, Dayton OH, March 2010.

19. L. Balster, "Microbial Growth and Biofilm Formation in Jet Fuel: Current Projects," AFIT Research Seminar, Dayton, OH, Nov. 16, 2010.

20. D. Anneken, R. Striebich, M.J. DeWitt, C.D. Klingshirn, and E. Corporan, "Identification and Quantitation of Hazardous Air Pollutants (HAPs) from Aircraft Engines," *6th Annual Dayton Engineering Sciences Symposium*, Dayton, OH, October 25, 2010.

21. B. Sekar, A.M. Briones, and H. Thornburg, "Numerical Simulation of Lean Blowout of Flame Attached to a V-gutter," *Augmentor Design Systems Conference*, Jacksonville, FL, March 16-18, 2011.

22. A.M. Briones, B. Sekar, H. Thornburg, "Characteristics of Bluff Body Stabilized Turbulent Premixed Flames," *Proceedings of the ASME Turbo Expo 2011: Power for Land, Sea, and Air*, Vancouver, British Columbia, Canada, June 6-10, 2011.

23. A.M. Briones, B. Sekar, H. Thornburg, K.O. Granlund, "V-gutter Flameholder Lean Premixed Flame Stabilization and Blowout," *XX International Symposium on Air Breathing Engines*, September 12-16, Goteborg, Sweden, 2011.

24. C.D. Klingshirn, M.J. DeWitt, R. Striebich, D. Anneken, L. Shafer, E. Corporan, M. Wagner and D. Brigalli, "Hydroprocessed Renewable Jet Fuel Evaluation, Performance, and Emissions in a T63 Turbine Engine," *ASME Turbo Expo 2011*, Vancouver, British Columbia, June 6-10, 2011.

25. V.R. Katta, A. O'Neil, S. Stouffer, and W.M. Roquemore, "Experimental and Numerical Studies on JP-8 Flames in Centerbody Burner," 7th U. S. National Combustion Meeting, Atlanta, GA, March 20-23, 2011.

26. D. Blunck, S. Kostka, A. Lynch, M. Polanka, S. Stouffer, S. Roy, J. Zelina, J.R. Gord, "Flame Structure of Vitiated Fuel Rich Inverse Diffusion Flames in a Cross-Flow," PaperT05, 7th U. S. National Combustion Meeting, Georgia Institute of Technology, Atlanta, GA, March 20-23, 2011.

27. B.A. Rankin, D.L. Blunck, V.R. Katta, S.D. Stouffer, and J.P. Gore, "Infrared Imaging, Computations, and Tomography of Bluff Body Stabilized Laminar Diffusion Flames," AIAA Paper 2011-690, 2011.

28. M.J. DeWitt, T. Edwards, L. Shafer, D. Brooks, R. Striebich, S.P. Bagley, and M.J. Wornat, "Fuel Composition Effect on Endothermic Reactivity and Deposition Propensity," Coordinating Research Council (CRC) Aviation Fuel Meeting, Seattle, WA, 2011.

29. Z. West, H. Jiang, and S. Zabarnick, "Jet Fuel Degradation During Supercritical High Heat Flux Heat Transfer," Presented at the 12th International Conference on Stability, Handling, and Use of Liquid Fuels, Sarasota, FL, 2011.

30. R.C. Striebich, L.M. Shafer, Z.J. West, R.K. Adams, and S. Zabarnick, "Hydrocarbon Group-Type Analysis of Current and Future Aviation Fuels: Comparing ASTM D2425 to GCxGC," Presented at the 12th International Conference on Stability, Handling, and Use of Liquid Fuels, Sarasota, FL, 2011.

31. L.M. Shafer and T. Edwards, "Speciated Naphthalene Analysis in Liquid Transportation Fuels," Presented at the 12th International Conference on Stability, Handling, and Use of Liquid Fuels, Sarasota, FL, 2011.

32. Z.J. West, R.K. Adams, M. Flake, and S. Zabarnick, "Catalytic Decomposition of Hydroperoxides: Implications for Jet Fuel Stability," Presented at the 12th International Conference on Stability, Handling, and Use of Liquid Fuels, Sarasota, FL, 2011.

33. S.S. Mueller, L.L. Bowen, L.M. Brown, N.A. Brown, O.N. Ruiz, M. Vangsness, L. Balster, S. Zabarnick, L. Shafer, R. Cook, and E.M. Strobel, "A Comparison Study of the Effects of Bacterial Contamination on Alternative Fuels Versus Petroleum-Derived Fuels," Presented at the 12th International Conference on Stability, Handling, and Use of Liquid Fuels, Sarasota, FL, 2011.

34. O.N. Ruiz and N.A. Brown, "Advances in Microbial Mitigation of Aviation Fuels: Characterization of the Antimicrobial Activity of DiEGME in Fuel by Quantitative Real-Time PCR," Presented at the 12th International Conference on Stability, Handling, and Use of Liquid Fuels, Sarasota, FL, 2011.

35. E. Corporan, M.J. DeWitt, C.D. Klingshirn, D. Anneken, and R. Striebich, "Alternative Jet Fuels – Turbine Engine Emissions Characteristics," Presented at the 12th International Conference on Stability, Handling, and Use of Liquid Fuels, Sarasota, FL, 2011.

36. M.J. DeWitt, S. Zabarnick, T. Williams, Z. West, L. Shafer, R. Striebich, S. Breitfield, R. Adams, R. Cook, C.L. Delaney, and D. Phelps, "Overview of Efforts to Determine Minimum Required FSII Use and Procurement Limits for USAF Aircraft," Presented at

the 12th International Conference on Stability, Handling, and Use of Liquid Fuels, Sarasota, FL, 2011.

37. H.J. Robota, R.K. Smith, and R.W. Morris, Jr., "The U.S. Air Force's Assured Aerospace Fuels Research Facility Fischer-Tropsch Liquids Upgrading Reactor," Presented at the 12th International Conference on Stability, Handling, and Use of Liquid Fuels, Sarasota, FL, 2011.

38. J. Graham, D. Minus, and T. Edwards, "The Effect of Aromatic Type on the Volume Swell of Nitrile Rubber in Selected Synthetic Paraffinic Kerosenes," Presented at the 12th International Conference on Stability, Handling, and Use of Liquid Fuels, Sarasota, FL, 2011.

39. G. Flora, S. Saxena, M.S.P. Kahandawala, and S.S. Sidhu, "Investigation of Ignition Delay Time for n-Dodecane and n-Dodecane/m-Xylene Mixture," 7th US National Combustion Meeting, March. 20-23, 2011, Atlanta (GA), Paper 2A19-RK71.

40. G. Flora, S. Saxena, M.S.P. Kahandawala, M.J. DeWitt, E. Corporan, and S.S. Sidhu, "Ignition Delay Measurements for 2-Methylheptane/O2/Ar Mixtures Behind Reflected Shock Conditions," 7th US National Combustion Meeting, March. 20-23, 2011, Atlanta (GA), Paper 2A13-RK73.

41. G. Flora, A. Nagulapalli, S. Saxena, M.S.P. Kahandawala, and S.S. Sidhu, "Simulation of Reflected Shock Combustion Experiments Using Multiple Computational Approaches," 7th US National Combustion Meeting, March. 20-23, 2011, Atlanta (GA), Paper 2A06-RK72.

42. S. Saxena, G. Flora, M.S.P. Kahandawala, and S.S. Sidhu, "A Shock Tube Experimental Study and Kinetic Modeling of M-xylene Ignition Delay," 49th AIAA Aerospace Sciences Meeting including the New Horizons Forum and Aerospace Exposition, January 4-7, 2011, Orlando (FL), AIAA 2011-314.

43. J. Balagurunathan, G. Flora, S. Saxena, M.S.P. Kahandawala, and S.S. Sidhu, "Ignition Delay Times of a Range of Alternate Jet Fuels and Surrogate Fuel Candidate Hydrocarbons under Fuel-Lean Conditions: a Shock Tube Study," 49th AIAA Aerospace Sciences Meeting including the New Horizons Forum and Aerospace Exposition, January 4-7, 2011, Orlando (FL), AIAA 2011-696.

44. F. Ahmad, M. Kahandawala, A. Krishnan and S. Sidhu, "Hydrogen Generation using Aluminum Powder for Fuel Cell Applications", Proceedings of ASME 2011 5th International Conference on Energy Sustainability & 9th Fuel Cell Science, Engineering and Technology Conference ESFuelCell2011 Aug 7-10, 2011 Washington, DC, USA

45. M. Kahandawala, T. Naguy, A. Krishnan and S. Sidhu, "Impact of Particle Size and Aluminum Type on Hydrogen Generation Rates," 4th World Hydrogen Technologies Convention, 2011, Glasgow, U.K. Paper ID: 0139

46. J.S. Ervin, A. Chaisson, M. Elsass, and S. Zabarnick, "Impact of Jet A Freeze Point on B-1, B-52, F-15E, & KC-135 Operations for Flights Departing CONUS," AFPETA, Ft. Belvoir, VA, November 2011.

47. H. Thornburg, B. Sekar, A.M. Briones, "Conceptual Design Analysis for Enhanced Mixing and Combustion in Re-heat Combustion Devices," *Physics Based Modeling and Design & Development for US Defense Conference*, November 14-17, Denver, CO, 2011.

48. S. Zabarnick and Z. West, "Modeling of Fuel Autoxidation," Invited Lecture, ExxonMobil Lubricants Product Division, Paulsboro, NJ, January 2012.

49. L. Balster and D. Minus, "Fuel Property Prediction Using ^{13}C NMR," Coordinating Research Council (CRC) Aviation Meeting, Alexandria, Virginia, April 30 – May 3, 2012.

50. Col. Redford, J.S. Ervin, A. Chiasson, and M. Elsass, "Jet A CONUS Conversion - An AFSO21 Initiative," AFSOC Head Quarters, Hurlburt Fld, FL, February 28, 2012.

51. Col. Redford, J.S. Ervin, A. Chiasson, and M. Elsass, "Jet A CONUS Conversion - An AFSO21 Initiative," AFRC Head Quarters, Robins AFB, GA, February 29, 2012.

52. J.S. Ervin, A. Chiasson, and M. Elsass, "Impact of Jet A Freeze Point on B-52 Operations for Flights Departing CONUS," AFGSC Head Quarters, Barksdale AFB, LA, March 2, 2012.

53. J.S. Ervin, A. Chiasson, and M. Elsass, "Impact of Jet A Freeze Point on KC-135 Operations for Flights Departing CONUS, AMC Head Quarters, Scott AFB, IL, March 6, 2012.

54. J.S. Ervin, A. Chiasson, and M. Elsass, "Impact of Jet A Freeze Point on B-1 and F-15E Operations for Flights Departing CONUS, ACC Head Quarters, Langley AFB, VA, March 14, 2012.

55. E. Corporan, M.J. DeWitt, C.D. Klingshirn, D. Anneken, L. Shafer, and R. Striebich, "Comparisons of Emissions Characteristics of Several Turbine Engines Burning Fischer-Tropsch and Hydroprocessed Esters and Fatty Acids Alternative Jest Fuels," *ASME Turbo Expo 2012*, GT2012-68656, Copenhagen, Denmark, June 11-15, 2012.

56. J. Cain, D. Blunck, E. Corporan, M.J. DeWitt, R. Striebich, D. Anneken, C. Klingshirn, and W.M. Roquemore, "Characterization of Gaseous and Particulate Emissions from a Turboshaft Engine Burning Conventional, Alternative and Surrogate Fuels" presented at American Chemical Society National Meeting, Philadelphia, PA, August, 2012.

57. D. Anneken, R. Striebich, M.J. DeWitt, C. Klingshirn, and E. Corporan, "Development of a Method to Identify and Quantify Hazardous Air Pollutants from Turbine Engine Emissions," presented at American Chemical Society National Meeting, Philadelphia, PA, August, 2012.

58. M.J. DeWitt, Z. West, A. Mescher, N. Stelzenmuller, S. Zabarnick, and T. Edwards, "Effect of Aromatics Addition on the Thermal-Oxidative Stability of Alternative Jet Fuels" presented at American Chemical Society National Meeting, Philadelphia, PA, August, 2012.

59. B. McMasters, M.J. DeWitt, R. Striebich, T. Edwards, and D. Phelps, "Effect of Fuel Chemical Composition on Pyrolytic Reactivity and Deposition Propensity under Supercritical Conditions," presented at American Chemical Society National Meeting, Philadelphia, PA, August, 2012.

60. M.J. DeWitt, E. Corporan, C. Klingshirn, and X. Li-Jones, "Determination of Particle Counting Pressure Correction for Turbine Engine Exhaust Sampling," presented at American Association for Aerosol Research Annual Conference, Minneapolis, MN, October, 2012.

61. A.M. Briones, B. Sekar, H. Thornburg, "Modeling and Simulation of Enhanced Reactant-Product Mixing in Ultra Compact Combustors," *48th AIAA/ASME/SAE/ASEE Joint Propulsion Conference & Exhibit and 10th International Energy Conversion Engineering Conference,* 30 July - 1 August, Atlanta, GA, 2012.

62. Z. Sander, S. Zabarnick, and J. Ervin, "Experimental and Numerical Studies of Autoxidation in the JFTOT," Coordinating Research Council (CRC) Aviation Meeting, Alexandria, Virginia, April 30 – May 3, 2012.

63. D.W. Johnson, R.K. Adams, S. Zabarnick, Z.J. West, and R.C. Striebich, "Analysis of Polar Components in Jet Fuel by High Performance Liquid Chromatography/Time of Flight Mass Spectrometry with Electrospray Ionization," American Chemical Society National Meeting, Philadelphia, PA, 2012.

64. K.A.S. Fernando, "Synthesis and Characterization of Metal Decorated Graphene Oxide" 244th American Chemical Society National Meeting, Philadelphia, PA, Aug. 2012.

65. K.A.S. Fernando, "Synthesis of Silver Decorated Graphene Oxide with Different Concentrations of Ag using Sonochemistry, 244th American Chemical Society National Meeting, Philadelphia, PA, Aug. 2012.

66. J.T. Gross, S.D. Stouffer, J. Hoke, A. Caswell, D.L. Blunck, F.R. Schauer, "Simultaneous Temperature and Species Probe," 8th Annual Dayton Engineering Sciences Symposium 29 October, 2012, Dayton, OH.

67. J.T. Gross, S.D. Stouffer, and D.L. Blunck, "Atmospheric Combustion Experiments with a High Pressure Well Stirred Reactor," 8th Annual Dayton Engineering Sciences Symposium 29 October, 2012, Dayton, OH.

68. D.K. Minus and L. M. Balster, "Jet Fuel Parameter Prediction and Quality Assessment Coupled with Chemometrics," 244th American Chemical Society National Meeting, Philadelphia, August 19-23, 2012.

69. S. Zabarnick, L. Shafer, R. Cook, and Z.J. West, "Development of a Cold Fuel Flowability Test," Coordinating Research Council (CRC) Aviation Meeting, Alexandria, Virginia, 2013.

70. M.J. DeWitt, T. Williams, T. Hendershott, B. McMasters, R. Striebich, and L. Shafer, "Evaluation of Endothermic Reactivity and Deposition Propensity of JP-7 and RP-2 Fuels," presented at JANNAF Spring Meeting, Colorado Springs, CO, May 1, 2013.

71. S.Z. Vijlee, J.C. Kramlich, A.M. Mescher, S.D. Stouffer, and A.R. O'Neil-Abels, "Characterizing Combustion of Synthetic and Conventional Fuels in a Toroidal Well-Stirred Reactor," Proceedings of ASME Turbo Expo 2013: Turbine Technical Conference and Exposition, GT2013, June 3-7, 2013, San Antonio, Texas, USA.

72. S. Zabarnick, L. Shafer, R. Cook, and Z. West, "Use of Scanning Brookfield Viscometry as a Viscosity Equivalent Method for Jet Fuel Freezing Point," IASH 2013, the 13th

International Symposium on Stability, Handling, and Use of Liquid Fuels, Rhodes, Greece, October 2013.

73. T.J. Erdmann, D.L. Blunck, D. Shouse, C. Neuroth, A. Lynch, A.W. Caswell, D. Richardson, A.M. Briones, "Raleigh Loss Analysis and Mitigation in Ultra-Compact Combustors," *51st AIAA Aerospace Science Meeting*, Grapevine, TX, 2013.

74. A.M. Briones, H. Thornburg, B. Sekar, C. Neuroth, D. Shouse, "Numerical-Experimental Research of Ultra Compact Combustors containing Film and Effusion Cooling," *51st AIAA Aerospace Science Meeting*, Grapevine, TX, 2013.

75. O.N. Ruiz, C. Smart, W. Foley, T. Gunasekera, and R.C. Striebich (presented by S. Zabarnick), "Effects of Bacterial Transcriptional Response and Metabolism on Fuel Composition and Performance," IASH 2013, the 13th International Symposium on Stability, Handling, and Use of Liquid Fuels, Rhodes, Greece, October 2013.

76. M.J. DeWitt, B. McMasters, T. Williams, T. Hendershott, R. Striebich, S. Zabarnick, T. Edwards, and D.K. Phelps, "Effect of Fuel Chemical Composition on Supercritical Reactivity and Deposition Propensity," IASH 2013, the 13th International Symposium on Stability, Handling, and Use of Liquid Fuels, Rhodes, Greece, October 2013.

77. M.J. DeWitt, Z. West, S. Zabarnick, L. Shafer, R. Striebich, and T. Edwards, "Effect of Addition of Aromatics on the Thermal Oxidative Stability of Alternative Aviation Fuels," IASH 2013, the 13th International Symposium on Stability, Handling, and Use of Liquid Fuels, Rhodes, Greece, October 2013.

78. S. Stouffer, R. Townsend, M. Laber, J. Grieselhuber, M.J. DeWitt, J. Diemer, H. Day, R. Zierhing, E. Corporan, and D. Shouse, "Development of an Advanced Combustion Research Facility for Fuels, Emissions and Combustor operability Studies," poster presented at the 13th International Conference on Stability, Handling, and Use of Liquid Fuels, Rhodes, Greece, October 7, 2013.

79. E. Corporan, T. Edwards, M.J. DeWitt, C. Klingshirn, R. Striebich, L. Shafer, D. Anneken, and A. Caswell, "Investigation of Combustion and Emissions Performance of Alternative and Conventional Fuels at the Limits of the Jet Fuel Specification," poster presented at the 13th International Conference on Stability, Handling, and Use of Liquid Fuels, Rhodes, Greece, October 7, 2013.

80. M.S. Hanchak, M.D. Vangsness, N. Gheorghiu, J.S. Ervin, L.W. Byrd, and J.G. Jones, "Thin Film Evaporation Model with Retarded Van Der Waals Interaction," ASME 2013 International Mechanical Engineering Congress and Exposition, San Diego, November 2013.

81. D. Blunck, D. Shouse, C. Neuroth, R. Battelle, A. Lynch, B. Sekar, J. Zelina, T.J. Erdmann, D. Burrus, R. Howard, A. Briones, D. Richardson, A. Caswell, "Experimental and Computational Studies of an Ultra-compact Combustor," ASME Turbo Expo 2013, June 3-7, San Antonio, TX, 2013.

82. Z. West, M. DeWitt, S. Zabarnick, L. Shafer, R. Striebich, and T. Edwards, "Impact of Aromatics on Jet Fuel Thermal Stability: Implications for Synthetic Fuel Formulation and Abnormal JFTOT Deposits," Coordinating Research Council (CRC) Aviation Meeting, Alexandria, Virginia, 2014.

83. K.A.S. Fernando, "Synthesis and Characterization of Metal Decorated Carbon Substrates for Energy Applications" 247th ACS National Meeting, Division of Energy and Fuels, Dallas, TX, March 2014.

84. T.S. Gunasekera, L.L. Brown, S.S. Mueller, R.C. Striebich, O.N. Ruiz, "Molecular mechanisms of *Pseudomonas aeruginosa* growth and adaptation in Jet fuel," American Society for Microbiology 114th General Meeting, Boston, USA, May 17-20, 2014.

85. M.J. DeWitt, B. McMasters, Z. West, A. Higgins, L. Shafer, S. Zabarnick, D.K. Phelps, T. Edwards, R. Wills, and S.T. Bailie, "Evaluation of the Supercritical Decomposition of JP-10," presented at the 61st JPM/42nd SMBS/38th PEDCS/29th RNTS/27th SEPS JANNAF Meeting, 22 May 2014, Charleston, SC.

86. T.S. Gunasekera and O.N. Ruiz, "Transcriptional Response of Pseudomonas aeruginosa to Jet Fuel," Proceedings of the 13th International Conference on Stability, Handling and use of Liquid Fuels, Rhodes, 2014.

87. A.M. Briones, B. Sekar, T.J. Erdmann, "Effect of Centrifugal Force on Conventional and Alternative Fuel Surrogate Turbulent Premixed Flames," Proceedings of the ASME Turbo Expo 2014, Düsseldorf, Germany, GT2014-27327.

88. M.J. DeWitt, "Development and Evaluation of Alternative Aviation Fuels," *Presented at the5th Annual STARS (Spotlight on Technology, Arts, Research and Scholarship) Symposium*, 18 September 2014, University of Dayton, Dayton, OH.

89. M.J. DeWitt, P. Kennedy, T. Williams, D.K. Phelps, T. Hendershott, A. Higgins, L. Shafer, J. Mantz, and T. Edwards, "Hydrocarbon-Based Fuel Selection and Characterization for Medium Scale Scramjet Engine Tests," Presented at the 46th Combustion/34th AP/38th EP and S/28th PSH, JANNAF Meeting, Paper 3624, 8 December 2014, Albuquerque, NM.

90. B. C. Huelskamp, P. Gokulakrishnan, C.D. Klingshirn, N. J. Kuprowicz and V. M. Belovich "Addition of Ammonia to a Bluff-Body Stabilized Flame and Its Effect on NOx Emissions and Static Stability," AIAA 2015.

91. D. Blunck, S. Zeppari, J.Gross, S.Stouffer, and M.Colket, "Hydrocarbon Emissions from a Well-Stirred Reactor Near Lean Blow-Off", AIAA 2015-0415.

92. Z. West, S. Zabarnick, D. Fisher, T. Edwards, "Replacement of Obsolete Tube Deposit Rater (TDR) with Ellipsometer for JPTS (MIL–DTL–25524) Conformance," Presented at the CRC Aviation Meeting, Nashville, TN, 4–7 May 2015.

93. Z. West, and T. Yamada, "Impact of Alternative Aviation Fuels on Water Solubility & Demulsibility Characteristics," Presented at the CRC Aviation Meeting, Nashville, TN, 4–7 May 2015.

94. Z. Sander, S. Zabarnick, Z.J. West, and J.S. Ervin, "Experimental and CFD with Chemistry Studies of Autoxidation & Deposition in the JFTOT," Presented at the CRC Aviation Meeting, Nashville, TN, 4–7 May 2015.

95. M.J. DeWitt, T. Williams, T. Hendershott, A. Higgins, L. Shafer, R. Striebich, S. Zabarnick, Z. West, J. Mantz, D.K. Phelps, T. Edwards, and P. Kennedy, "Development and Evaluation of Hydrocarbon-Based Fuels for Hypersonic Platforms," Presented at the

62nd JPM/10th MSS/8th LPS/7th SPS Joint Subcommittee Meeting, JANNAF Meeting, 2 June 2015, Nashville, TN.

96. L. Shafer, R. Striebich, S. Zabarnick, and Z. West, "Identification and Quantitation of Polar Species in Liquid Transportation Fuels by GCxGC," IASH 14, the 14th International Symposium on Stability, Handling, and Use of Liquid Fuels, Charleston, SC, October 2015.

97. Z. West, M. Evanhoe, and M. Griesenbrock, "Aviation Turbine Fuel Properties Based on Hydrocarbon Type and Size Distribution," Presented at IASH 2015, the 14th International Symposium on Stability, Handling and Use of Liquid Fuels, Charleston, SC, USA, 4-8 October 2015.

98. M.J. DeWitt, T. Williams, T. Hendershott, R. Striebich, L. Shafer, S. Zabarnick, Z. West, T. Edwards, and D.K. Phelps, "Reactivity and Deposition Propensity of Hydrocarbons Under Supercritical Pyrolytic Reaction Conditions," Presented at IASH 2015, the 14th International Symposium on Stability, Handling and Use of Liquid Fuels, Charleston, SC, USA, 4-8 October 2015.

99. R.C. Striebich, L.L. Bowen, S.S. Mueller, L.M. Shafer, T.S. Gunasekera, and O.N. Ruiz, "Aviation Fuel Biodegradation Under Static Conditions and in a Stirred-Tank Bioreactor," Presented at IASH 2015, the 14th International Symposium on Stability, Handling and Use of Liquid Fuels, Charleston, SC, USA, 4-8 October 2015.

100. M. Vangsness, "Best Practice for Fuel Contamination Response," Presented at IASH 2015, the 14th International Symposium on Stability, Handling and Use of Liquid Fuels, Charleston, SC, USA, 4-8 October 2015.

101. E. Corporan, S. Stouffer, M. DeWitt, T. Hendershott, C. Klingshirn, "Evaluation of Fuel Aromatic Impacts on Combustion Characteristic in a Newly Developed Turbine Engine Combustor Research Facility at AFRL," IASH 2015, the 14TH International Symposium on Stability Handling and use of Liquid Fuels Charleston, South Carolina USA, 4-8 October 2015.

102. E. Corporan, T. Edwards, C. Neuroth, D. Shouse, S. Stouffer, T. Hendershott, C. Klingshirn, M. DeWitt, S. Zabarnick, and J. Diemer, "Initial Studies of Fuel Impacts on Combustor Operability and Emissions at AFRL," Poster presented at IASH 2015, 14TH International Symposium on Stability Handling and use of Liquid Fuels Charleston, South Carolina USA, 4-8 October 2015.

103. R. Stachler, J. Heyne, J.D. Miller, M.X. Liu, S.D. Stouffer, and W.M. Roquemore, "Well Stirred Reactor Emission Studies of Fuel Surrogates," DESS15-0011, Presented at ASME 11th Annual Dayton Engineering Sciences Symposium, 2 November 2015, Wright State University, Dayton, OH.

104. B. Long, A. Briones, B. Rankin, "Modeling and Simulation of High-Pressure High-G Ultra Compact Combustor," DESS15-0095, Presented at ASME 11th Annual Dayton Engineering Sciences Symposium, 2 November 2015, Wright State University, Dayton, OH.

105. R.D. Stachler, J.S. Heyne, J.D. Miller, S.D. Stouffer, S.P. Zeppieri, M.B. Colket, and . W.M. Roquemore, "Well Stirred Reactor Emission Studies of Fuel Surrogates," Paper for

Central States Section of the Combustion Institute, Knoxville, Tennessee, May 15-17, 2016.

106. S.D. Stouffer, T.H. Hendershott, J.R. Monfort, and E. Corporan, "Combustion Characteristics in a Single Cup Combustor Using Jet A and Research Fuels," Paper for Central States Section of the Combustion Institute, Knoxville, Tennessee, May 15-17, 2016.

107. M.J. DeWitt, T. Williams, T. Hendershott, R. Striebich, L. Shafer, S. Zabarnick, Z. West, M. Hanchak, T. Edwards, and D.K. Phelps, "Development of Hydrocarbon-Based Fuels for High-Speed Applications," Presented at the CRC Aviation Fuels Meeting, Alexandria, VA, 4 May 2016.

108. Z. West, M. DeWitt, and D. Phelps, "Evaluation of Fuel Tank Topcoat Resistance to Fuel System Icing Inhibitor (FSII)," Presented at the CRC Aviation Meeting, Alexandria, VA, 2–5 May 2016.

109. Z. West, T. Yamada, and C. Bruening, "Impact of Alternative Aviation Fuels on Water Solubility & Demulsibility Characteristics – Program Update," Presented at the CRC Aviation Meeting, Alexandria, VA, 2–5 May 2016.

110. S. Zabarnick, Z.J. West, L. Shafer, R.C. Striebich, S.S. Mueller, and M.M. Griesenbrock, "Role of Nitrogen and Sulfur Species in Jet Fuel Thermal Stability," Presented at the CRC Aviation Meeting, Alexandria, VA, 2–5 May 2016.

111. J. Gross, S. Stouffer, D. Shouse, and C. Neuroth, "Lean Blowout with a High Pressure Well Stirred Reactor," AIAA-2016-4899.

Technical Reports

1. D.T. Allen, C. Allport, K. Atkins, J. Cooper, R. Dilmore, L. Draucker, K.E. Eickmann, J.C. Gillen, W. Gillette, M.W. Griffin, W.E. Harrison III, J. Hileman, J.R. Ingham, F.A. Kimler III, A. Levy, C.F. Murphy, M. O'Donnell, D. Pamplin, G. Schivley, T. Skone, S. Strank, R.W. Stratton, P.H. Taylor, V. Thomas, M.l Wang, and T. Zidow, "Framework and Guidance for Estimating Greenhouse Gas Footprints of Aviation Fuels," The Aviation Fuel Life Cycle Assessment Working Group, Interim Report, AFRL-RZ-WP-TR-2009-2206, April, 2009

2. E. Shafer, R. Striebich, M.J. DeWitt, T. Edwards, and W. Harrison, "Variation of JP-8 Properties in CONUS and Potential Implications During Blending with Synthetic Paraffinic Kerosene," AFRL-RZ-WP-TR-2010-2079, 2010.

3. L. M. Balster, M. D. Vangsness, L. L. Bowen, S. S. Mueller, L. M. Brown, E. M. Strobel, D. D. Pike, "Effects of Diethylene Glycol Monomethyl Ether (DiEGME) and Triethylene Glycol Monomethyl Ether (TriEGME) on Microbial Contaminants in Aviation Fuel," AFRL-RZ-WP-TR-2010-2094, 2010.

4. L. M. Balster, M. D. Vangsness, L. L. Bowen, S. S. Mueller, L. M. Brown, E. M. Strobel, "The Effect of DiEGME on Microbial Contamination of Jet Fuel: A Minimum Concentration Study," AFRL-RZ-WP-TR-2010-2002, 2010.

5. M.J. DeWitt, S. Zabarnick, T.F. Williams, Z. West, L. Shafer, R. Striebich, S. Breitfield, R. Adams, R. Cook, D.K. Phelps and C.L. Delaney, "Determination of the Minimum Use Level of Fuel System Icing Inhibitor (FSII) in JP-8 that Will Provide Adequate Icing Inhibition and Biostatic Protection for Air Force Aircraft," AFRL-RZ-WP-TR-2009-2217, 2010.

6. E. Corporan, M.J. DeWitt, C.D. Klingshirn, and D. Anneken, "Alternative Fuels Test on a C-17 Aircraft: Emissions Characteristics," AFRL-RZ-WP-TR-2011-2004, 2010.

7. D.K. Thomas, G. Marcum, E. Griesenbrock, R. Smith, W. Jones and H. Conkle, "Assured Aerospace Fuels Research Facility (AAFRF) Hydrocracking System, System Acceptance Test (SAT)," AFRL-RZ-WP-TR-2011-2068, 2011.

8. D.K. Thomas, G. Marcum, E. Griesenbrock, R. Smith, W. Jones and H. Conkle, "Assured Aerospace Fuels Research Facility (AAFRF) Hydrocracking System, Run 1 Evaluation of the Naphtha Splitter," AFRL-RZ-WP-TR-2011-2069, 2011.

9. D.K. Thomas, H.N. Conkle, R.K. Smith, E.W. Griesenbrock, and W.A. Jones, "Assured Aerospace Fuels Research Facility (AAFRF) Hydrocracking System, Run 2A Evaluation of Vacuum Column Performance Following Reboiler Modification," AFRL-RZ-WP-TR-2011-2029, 2011.

10. H.J. Robota, D.K. Thomas, G. Marcum, E. Griesenbrock, R. Smith, W. Jones and H. Conkle, "Assured Aerospace Fuels Research Facility (AAFRF) Hydrocracking System, Run 4 Evaluation of the Integrated Upgrader," AFRL-RZ-WP-TR-2011-2070, 2011.

11. D.K. Thomas, W.A. Jones, H.N. Conkle, R.K. Smith, and E. Griesenbrock, "Assured Aerospace Fuels Research Facility (AAFRF) Hydrocracking System, Run 2 Evaluation of Fractionator and Vacuum Column Performance," AFRL-RZ-WP-TR-2011-2100, 2011.

12. S. Zabarnick, M.J. DeWitt, R. Adams, Z.J. West, L.M. Shafer, T.F. Williams, R. Cook, R. Striebich, L.M. Balster, D.K. Phelps, and C.L. Delaney, "Evaluation of Triethylene Glycol Monomethyl Ether (TriEGME) as an Alternative Fuel System Icing Inhibitor for JP-8 Fuel, submitted for publication, AFRL-RZ-WP-TR-2011-2030, 2011.

13. S. Zabarnick, D.R. Ballal, J.S. Ervin, A. Briones, J.L. Graham, M.J. DeWitt, R. Adams, Z.J. West, S.D. Stouffer, P.H. Taylor, L.M. Shafer, T.F. Williams, E.A. Guliants, R. Striebich, and L.M. Balster, "Versatile Affordable Advanced Fuels and Combustion Technologies," AFRL-RZ-WP-TR-2011-2028, 2011.

14. W. Roquemore, T. Litzinger, M. Colket, V. Katta, K. McNesby, S. Sidhu, and R. Santoro, " Combustion Science to Reduce PM Emissions for Military Platforms," Strategic Environmental Research and Development, Final Report, WP-1577, 2012.

15. H.J. Robota, D.K. Thomas, H.N. Conkle, G. Marcum, and E.W. Griesenbrock, "Assured Aerospace Fuels Research Facility (AAFRF) Hydrocracking System, Run 6A Report: Production of Isomerized Tetradecane" AFRL-RQ-WP-TR-2013-XXX, submitted to Robert Morris 2013

16. H.J. Robota, D.K. Thomas, H.N. Conkle, G. Marcum, E.W. Griesenbrock, and S. Howe, "Assured Aerospace Fuels Research Facility (AAFRF) Hydrocracking System, Run 6C Report: Purification of Isomerized Tetradecane" AFRL-RQ-WP-TR-2013-XXX, submitted to Robert Morris, 2013

17. H.J. Robota, D.K. Thomas, H.N. Conkle, G. Marcum, and E.W. Griesenbrock, "Assured Aerospace Fuels Research Facility (AAFRF) Hydrocracking System, Run 7 Report: Production of Isomerized Decane" AFRL-RQ-WP-TR-2013-XXX, submitted to Robert Morris, 2013

18. H.J. Robota, D.K. Thomas, H.N. Conkle, E.W. Griesenbrock, S. M. Howe S.K. Nejfelt, and C.P. Kehnell, "Assured Aerospace Fuels Research Facility (AAFRF) Hydrocracking System, Run 8: Renewable Jet Production" AFRL-RQ-WP-TR-2013-XXX, submitted to Robert Morris, 2013

19. H.J. Robota, D.K. Thomas, H.N. Conkle, E.W. Griesenbrock, S. M. Howe S.K. Nejfelt, and C.P. Kehnell, "Assured Aerospace Fuels Research Facility (AAFRF) Hydrocracking System, Post Run 8 Report: Renewable Jet Production" AFRL-RQ-WP-TR-2013-XXX, submitted to Robert Morris, 2013

20. H.J. Robota, D.K. Thomas, H.N. Conkle, E.W. Griesenbrock, S. M. Howe S.K. Nejfelt, and C.P. Kehnell, "Assured Aerospace Fuels Research Facility (AAFRF) Hydrocracking System, Run 9: Renewable Diesel Production" AFRL-RQ-WP-TR-2013-XXX, submitted to Robert Morris, 2013

21. E. Edwards, J. Boyce, and C. Lukuch, "Final Report on the Scale-Up of a Dewaxing Process to Remove n-Tetradecane from a Mixture of Tetradecanes in Solvent" Prepared for H.J. Robota and Submitted to Robert Morris, 2013

22. E. Edwards, J. Boyce, and C. Lukuch, "Phase 1 Final Report on the Scale-Up of a Dewaxing Process to Remove n-Tetradecane from a Mixture of Tetradecanes in Solvent" Prepared for H.J. Robota and Submitted to Robert Morris, 2013

23. M.J. DeWitt, R. Cook, L. Shafer, S. Zabarnick, and C. McCormick, "Evaluation of ASTM D5006 for Accuracy, Repeatability, and Reproducibility for Fuel System Icing Inhibitor (FSII) Concentrations < 0.10% by Volume and Varying Fuel Composition," AFRL-RQ-WP-TR-2013-0070.

24. M.J. DeWitt, C. Klingshirn, E. Corporan, and X. Li-Jones, "Determination of Particle Counting Pressure Correction Factors and Particle Number Emission Indices in Turbine Engine Exhaust Using Concentration Particle Counters," RQ-WP-TR-2013-XXXX. *in preparation*.

25. S. Zabarnick, L. Shafer, Z. West, R. Cook, M. DeWitt, and T. Williams, "Low Temperature Additive Performance in Jet A Fuels," AFRL Technical Report, AFRL-RQ-WP-TR-2013-0093, 2013.

26. S. Zabarnick, Z.J. West, L.M. Shafer, and R. Cook, "Developing a Cold Fuel Flowability Test," UDR-TR-2013-100.

27. J.T.Edwards, L.M. Shafer J.K. Klein, "U.S. Air Force Synthetic Paraffinic Kerosene (SPK) Fuel Research", AFRL-RQ-WP-TR-2013-0124, 2013.

28. J.T.Edwards, L.M. Shafer J.K. Klein, "U.S. Air Force Hydroprocessed Renewable Jet (HRJ) Fuel Research", AFRL-RQ-WP-TR-2013-0108, 2013.

29. M.J. DeWitt, S. Zabarnick, T.F. Williams, Z. West, L. Shafer, R. Striebich, S. Breitfield, R. Adams, R. Cook, D.K. Phelps, C.L. Delaney, "Determination of the Minimum Use Level of Fuel System Icing Inhibitor (FSII) in JP-8 that Will Provide Adequate Icing Inhibition and Biostatic Protection for Air Force Aircraft (Public Release Version of Technical Report AFRL-RZ-WP-TR-2009-2217)," AFRL-RQ-WP-TR-2013-0271, 2013.

30. M.J. DeWitt, B. McMasters, Z. West, A. Higgins, L. Shafer, S. Zabarnick, D.K. Phelps, T. Edwards, R. Wills, and S.T. Bailie, "Evaluation of the Supercritical Thermal Decomposition of JP-10," AFRL-RQ-WP-TR-2013-0258.

31. R.W. Morris, Jr. and D. Davis, "Evaluation of Water Separation and Filter/Coalescer Impact on JP-8 by Next-Generation +100 Thermal Stability Additives," AFRL-WP-TR-2013-0276, 2013.

32. S. Zabarnick, Z.J. West, L.M. Shafer, and R. Cook, "Studies of Scanning Brookfield Viscometry as a Replacement for Freezing Point in Aviation Fuel Specifications, Coordinating Research Council, CRC Project No. AV-16-11, October 2013.

33. R.W. Morris, Jr., J.R. Shardo, A.K. Higgins, Z. West, S. Tanner, R. Cook, and J. Kelley, "Evaluation of FAME-Contamination on the Thermal Stability Characteristics of Military Jet Fuels (JP-8 and JP-5)," AFRL-RQ-WP-TR-2014-0060; Interim Report for the Propulsion Directorate, Air Force Research Laboratory, WPAFB, OH, December 2013.

34. R.W. Morris, Jr., J.R. Shardo, A.K. Higgins, Z. West, S. Tanner, R. Cook, and J. Kelley, "Evaluation of the Impact of KeroJet Aquarius Water Scavenger Additive on the Thermal Stability of Jet A Fuels," AFRL-RQ-WP-TR-2015-0014; Interim Report for the Aerospace Systems Directorate, Air Force Research Laboratory, WPAFB, OH, December 2014.

35. R.W. Morris, Jr., J. Shardo, K. Higgins, R. Cook, S. Tanner, Z. West, and L. Shafer, "Evaluation of the Impact of Fatty Acid Methyl Ester (FAME) Contamination on the Thermal Stability of Jet A," AFRL-WP-TR-2014-0017, 2014.

36. A. Briones, A. Chiasson, C. Delaney, M. Elsass, J.S. Ervin, and M. Hanchak, "Studies of the Low-Temperature Use of Jet A to Replace JP-8 in Tankers, Fighters, Bombers, and Transport Aircraft," AFRL-RQ-WP-TR-2014-0149, 2014.

37. A. Chiasson and J.S. Ervin, "Studies of the Use of Jet A to Replace JP-8 in the EA-6B, MV-22, and P-3: Implications of the Difference in Specification Freeze Point," AFRL-RQ-WP-TR-2015-0020, 2014.

38. J.S. Ervin and A. Chiasson, "Fuel Tank Heat Transfer Simulations of the A-10," Submitted to Lt. J.D. Carpenter, AFLCMC/WWAEB, Hill AFB, September 2015.

Student Theses/Dissertations

1. K.B. Taylor, "Comparative Study of Alternative Fuel Icing Inhibitor Additive Properties & Chemical Analysis of Metal Speciation in Aviation Fuels," M.S. Thesis Mechanical Engineering, University of Dayton, July 2010.

2. H. Jiang, "Effect of Changes in Flow Geometry, Rotation and High Heat Flux on Fluid Dynamics, Heat Transfer and Oxidation/Deposition of Jet Fuels," Ph.D. Dissertation in Mechanical Engineering, University of Dayton, December 2010.

3. F. Ahmed, "Experimental Studies in Hydrogen Generation for Fuel Cell Applications Using Aluminum Powder," M.S. Thesis, University of Dayton, Dayton, December 2010.

4. N.D. McNamara, "Sonochemical Synthesis and Characterization of Metal Nanoparticle-Decorated Carbon Supports," M.S. Thesis, Chemical Engineering, August 2011.

5. Z.J. West, "Studies of Jet Fuel Autoxidation Chemistry: Catalytic Hydroperoxide Decomposition & High Heat Flux Effects," Ph.D. Dissertation in Mechanical Engineering, University of Dayton, December 2011.

6. A.R. O'Neil "Chemilumenscence and High Speed Imaging of Reacting Shear Layers," MS Thesis Mechanical Engineering, M.S. Thesis Mechanical Engineering, University of Dayton, Dec 2011.

7. J.-R. Groenewegen, "The Performance and Emissions Characteristics of Heavy Fuels in a Small, Spark Ignition Engine," M.S. Thesis, University of Dayton, Dayton, 2011.

8. Z.H. Sander, "Heat Transfer, Fluid Dynamics, and Autoxidation Studies in the Jet Fuel Thermal Oxidation Tester (JFTOT)," M.S. Thesis Mechanical Engineering, University of Dayton, December 2012.

9. G. H. Parker, "Pyrolytic Decomposition of Synthetic Paraffinic Kerosene Fuel Compared to JP-7 and JP-8 Aviation Fuels," M.S. Chemical Engineering, University of Dayton, August 2013.

10. K.R. Kerr, "Deposit Formation of Deoxygenated JP-8 Fuel with Added Hydroperoxides," M.S. Thesis Chemical Engineering, University of Dayton, September 2013.

11. B. McMasters, "Effect of Fuel Chemical Composition on Pyrolytic Reactivity and Deposition Propensity under Supercritical Conditions," M.S. Chemical Engineering, University of Dayton, April, 2014.

12. V.G. Watson, "Decoration of Graphite Oxide with Silver Nanoparticles and Controlling the Silver Nanoparticle Loading on Graphene Oxide," M.S. Chemical Engineering, May 2014.

13. J.T. Gross, "Experiments with a High Pressure Well Stirred Reactor," M.S. thesis, Aerospace Engineering, University of Dayton, December 2014.

14. J.R. Monfort, "Experimental Investigation into Thermoacoustic Instability in Pre-mixed, Pre-vaporized Bluff-Body Stabilized Flames," Ph.D. Dissertation, Mechanical Engineering, University of Dayton, August 2015.

15. G. Flora, "Fuel Structure Effects on Surrogate Alternative Jet Fuel Emission," Ph.D. Dissertation, Mechanical Engineering, University of Dayton, August 2015.

LIST OF PUBLIC AFFAIRS CLEARANCE NUMBERS FOR INCLUDED PAPERS

A.   Compatibility of DiEGME and TriEGME Fuel System Icing Inhibitor Additives with BMS 10-39 Aircraft Tank Topcoat Material, ASC Case Number: 88ABW-2009-4315

B.   Flame Stabilization in Small Cavities, ASC Case Number: 88ABW-2009-0797

C.   Micrometer-Sized Water Droplet Impingement Dynamics and Evaporation on a Flat Dry Surface, ASC Case Number: 88ABW-2010-1717

D.   Spontaneous Hydrogen Generation from Organic-Capped Al Nanoparticles and Water, ASC Case Number: 88ABW-2009-3067

E.   Chemical, Thermal Stability, Seal Swell, and Emissions Studies of Alternative Jet Fuels, ASC Case Number: 88ABW-2009-4316

F.   Effect of Aviation Fuel Type on Pyrolytic Reactivity and Deposition Propensity under Supercritical Conditions, ASC Case Number: 88ABW-2012-2383

G.   Graphene Oxide, A Nonspecific Enhancer of Cellular Growth, ASC Case Number: 88ABW-2011-4103

H.   Homogeneous Catalysis of Liquid-Phase Hydroperoxide Decomposition in Hydrocarbons, ASC Case Number: 88ABW-2010-6630

I.   Effects of Flow Passage Expansion or Contraction on Jet-Fuel Surface Deposition, ASC Case Number: 88ABW-2011-2786

J.   Preparation of a Research Jet Fuel Composition Comprised of Nearly Exclusively Methyl-Branched Tetradecane Isomers Having a Freezing Point below -47 C, ASC Case Number: 88ABW-2012-0822

K.   Characterization of Gaseous and Particulate Emissions From a Turboshaft Engine Burning Conventional, Alternative, and Surrogate Fuels, ASC Case Number: 88 ABW-2012-2496

L.   Chemical Analysis of Jet Fuel Polar, Heteroatomic Species via High-Performance Liquid Chromatography with Electrospray Ionization Mass Spectrometric Detection, ASC Case Number: 88ABW-2012-4635

M.   Comparison of Post-Detonation Combustion in Explosives Incorporating Aluminum Nanoparticles, Influence of the Passivation Layer, ASC Case Number: 88ABW-2012-5732

N.   Converting Algal Triglycerides to Diesel and HEFA Jet Fuel Fractions, ASC Case Number: 88ABW-2012-5618

O.   Transcriptional Profiling Suggests that Multiple Metabolic Adaptations are Required for Effective Proliferation of Pseudomonas aeruginosa in Jet Fuel, ASC Case Number: 88ABW-2013-3240

P.   Turbulent Flow, Heat Transfer Deterioration, and Thermal Oxidation of Jet Fuel, ASC Case Number: 88ABW-2012-6137

Q.   Characterization of the F-76 Diesel and Jet A-1 Aviation Fuel Hydrocarbon Degradation Profiles of Pseudomonas aeruginosa and Marinobacter hydrocarbonoclasticus, ASC Case Number: 88ABW-2013-3479

R.   Effect of Aromatics on the Thermal-Oxidative Stability of Synthetic Paraffinic Kerosene, ASC Case Number: 88ABW-2012-2423

S.   Equilibrium Partitioning of Di-ethylene Glycol Monomethyl Ether (DiEGME) between Fuel and Aqueous Phases at Sub-Ambient Temperatures, ASC Case Number: 88ABW-2014-1814

T.   Hydrocarbon Group-Type Analysis of Petroleum-Derived and Synthetic Fuels Using Two-Dimensional Gas Chromatography, ASC Case Number: 88ABW-2014-1213

U.   Migration of Silver Nanoparticles from Silver Decorated Graphene Oxide to Other Carbon Nanostructures, ASC Case Number: 88ABW-2014-2759

V.   Development of Methodologies for Identification and Quantification of Hazardous Air Pollutants from Turbine Engine Emissions, ASC Case Number: 88ABW-2013-5183

W.   Effect of Centrifugal Force on Turbulent Premixed Flames, ASC Case Number: 88ABW-2013-4567

X.   Experimental and Modeling Studies of Heat Transfer, Fluid Dynamics, and Autoxidation, Chemistry in the Jet Fuel Thermal Oxidation Tester (JFTOT), ASC Case Number: 88ABW-2015-3804

Y.   Reacting Flows in Ultra-Compact Combustors with Combined-Diffuser Flameholder, ASC Case Number: 88ABW-2013-3562

Z.   Effect of Conventional and Alternative Fuels on a Marine Bacterial Community and the Significance to Bioremediation, ASC Case Number: 88ABW-2015-4196

AA.   Transient Measurement of Thin Liquid Films using a Shack–Hartmann Sensor, ASC Case Number: 88ABW-2015-4227